2009

Very High Energy Phenomena in the Universe

Sponsored by

. CNRS (Centre National de la Recherche Scientifique)
. CEA (Commissariat à l'Énergie Atomique)
. EU (European Union)
. FNRS (Fond National de la Recherche Scientifique)
. IN2P3 (Institut National de Physique Nucléaire et de Physique des Particules)
. NSF (National Science Foundation)
. BSP (Belgian Science Policy)

XLIVth Rencontres de Moriond
La Thuile, Aosta Valley, Italy – February 1-8, 2009

2009 Very High Energy Phenomena in the Universe

Proceedings of the XLIVth RENCONTRES DE MORIOND

Very High Energy Phenomena in the Universe

La Thuile, Aosta Valley Italy *February 1-8, 2009*

2009

Very High Energy Phenomena in the Universe

edited by

Jacques Dumarchez

and

Jean Trân Thanh Vân

The XLIVth Rencontres de Moriond

2009 Very High Energy Phenomena in the Universe

was organized by :

J. Trân Thanh Vân (Orsay)

with the active collaboration of :

R. Ansari (LAL, Orsay)
J.L. Atteia (Toulouse)
L. Celnikier (Meudon)
A. De Angelis (Udine)
J. Dumarchez (LPNHE, Paris)
Y. Giraud-Héraud (APC, Paris)
C. Magneville (IRFU, Saclay)
E. Parizot (Paris)
G. Sigl (Hamburg)
D. Smith (Bordeaux)
Th. Stolarczyk (Saclay)

2009 RENCONTRES DE MORIOND

The XLIVth Rencontres de Moriond were held in La Thuile, Valle d'Aosta, Italy.

The first meeting took place at Moriond in the French Alps in 1966. There, experimental as well as theoretical physicists not only shared their scientific preoccupations, but also the household chores. The participants in the first meeting were mainly french physicists interested in electromagnetic interactions. In subsequent years, a session on high energy strong interactions was added.

The main purpose of these meetings is to discuss recent developments in contemporary physics and also to promote effective collaboration between experimentalists and theorists in the field of elementary particle physics. By bringing together a relatively small number of participants, the meeting helps develop better human relations as well as more thorough and detailed discussion of the contributions.

Our wish to develop and to experiment with new channels of communication and dialogue, which was the driving force behind the original Moriond meetings, led us to organize a parallel meeting of biologists on Cell Differentiation (1980) and to create the Moriond Astrophysics Meeting (1981). In the same spirit, we started a new series on Condensed Matter physics in January 1994. Meetings between biologists, astrophysicists, condensed matter physicists and high energy physicists are organized to study how the progress in one field can lead to new developments in the others. We trust that these conferences and lively discussions will lead to new analytical methods and new mathematical languages.

The XLIVth Rencontres de Moriond in 2009 comprised three physics sessions:

- February 1 - 8: "Very High Energy Phenomena in the Universe"
- March 07 - 14: "Electroweak Interactions and Unified Theories"
- March 14 - 21: "QCD and High Energy Hadronic Interactions"

We thank the organizers of the XLIVth Rencontres de Moriond:

- R. Ansari, J.L. Atteia, L. Celnikier, A. De Angelis, Y. Giraud-Héraud, C. Magneville, E. Parizot, G. Sigl, D. Smith, Th. Stolarczyk for the "Very High Energy Phenomena in the Universe" session.

- A. Abada, A. Blondel, J. Conrad, S. Davidson, P. Fayet, J.-M. Frère, H. Frisch, L. Iconomidou-Fayard, P. Hernandez, M. Knecht, J. P. Lees, S. Loucatos, F. Montanet, L. Okun, A. Pich, S. Pokorski, G. Unal, D. Wood for the "Electroweak Interactions and Unified Theories" session.

- U. Bassler, E. Berger, S. Bethke, A. Capella, A. Czarnecki, D. Denegri, Y. Dokshitzer, N. Glover, B. Klima, L. Kluberg, M. Krawczyk, L. McLerran, B. Pietrzyk, Chung-I Tan, U. Wiedemann for the "QCD and High Energy Hadronic Interactions" session.

and the conference secretariat and technical staff:

C. Bareille, C. Barthelemy, I. Cossin, V. de Sa-Varanda, G. Dreneau, M. Joguet, N. Ribet, H. Schenten, Pham Duy Tu, V. Zorica.

We are also grateful to Andrea Righetto, Marcello Torre, Gioacchino Romani and the Planibel Hotel staff who contributed through their hospitality and cooperation to the well-being of the participants, enabling them to work in a relaxed atmosphere.

The Rencontres were sponsored by the European Union "Marie Curie Conferences and Training Courses" Activity, the Centre National de la Recherche Scientifique, The Centre National d'Etudes Spatiales, the Institut National de Physique Nucléaire et de Physique des Particules (IN2P3-CNRS), the Commissariat à l'Energie Atomique (DSM and IRFU), the Fonds de la Recherche Scientifique (FRS-FNRS), the Belgium Science Policy and the National Science Foundation. We would like to express our thanks for their encouraging support.

It is our sincere hope that a fruitful exchange and an efficient collaboration between the physicists and the astrophysicists will arise from these Rencontres as from previous ones.

E. Augé, J. Dumarchez and J. Trân Thanh Vân

Contents

2. High Energy Cosmic Rays

3. Gamma Ray Bursts

1.
Gamma Ray Astronomy

Latest results on Galactic sources as seen in VHE gamma-rays

M. Renaud

Laboratoire APC, CNRS-UMR 7164, Université Paris 7,
10, rue Alice Domon et Léonie Duquet, 75025 Paris Cedex 13, France

As of early 2009, latest results on Galactic sources (mainly shell-type and plerionic supernova remnants), as observed in the very-high-energy domain, are reviewed. A particular attention is given to those obtained with the H.E.S.S. experiment during its Galactic Plane Survey which now covers the inner part of the Milky Way. From the well identified VHE γ-ray sources to those without any obvious counterpart and the putative Galactic diffuse emission, this observational window fully deserves to be celebrated during this International Year of Astronomy, as a new mean to image the Galaxy and reveal sites of particle acceleration, potentially at the origin of Galactic cosmic rays.

1 Introduction

Current generation of Imaging Atmospheric Cherenkov Telescopes (hereafter, IACTs) have recently revealed a new population of Galactic sources emitting in the very-high energy (VHE; E $>$ 100 GeV) gamma-ray domain [26]. In particular, the H.E.S.S. experiment, through a Galactic Plane Survey performed over the last five years and covering the inner Galaxy ($\ell \in$ [-90°,60°], $|b| < 3°$, see Figure 1), has accomplished a major breakthrough by revealing most of these new VHE γ-ray sources, as shown in Figure 2. A variety of source classes, identified (*i.e.* coincident) with sources known at traditional wavelengths, was found, among them several shell-type supernova remnants (hereafter, SNRs), isolated or interacting with the surrounding medium, many young and middle-aged offset pulsar wind nebulae (hereafter, PWNe), some young massive star clusters, and a bunch of γ-ray binaries. In regards with SNRs and PWNe, one of the main pending question concerns the nature of the observed VHE γ-ray emission, which relates to the parent population of accelerated particles, or, in other words, the difficulty in disentangling the hadronic and leptonic contributions to the observed emission. This is in turn intimately linked to the more general question of the origin of Galactic cosmic rays (hereafter, CRs). As we shall see in the following, these questions can be efficiently addressed through a detailed investigation of the broadband spectrum of these sources, from radio to VHE γ-ray domains, coupled with the recent theoretical developments of acceleration mechanisms.

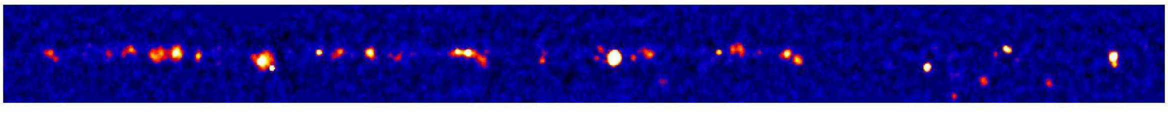

Figure 1: H.E.S.S. significance image of the inner part of the Galaxy ($\ell \in$ [-60°,40°], $|b| < 3°$), as of 2008 (from Chaves et al., H.E.S.S. collaboration, 2008). The color transition from blue to red is set to 5 σ.

Besides these sources whose nature is firmly established thanks to the existing multi-wavelength observations, many others fall into the category of the so-called dark sources (*i.e.* with no clear counterpart at other wavelengths) [44]. This can be first explained by the fact that the majority of the VHE γ-ray sources are extended, on scales of the order of tens of arcminutes, with no clear sub-structure. Although current IACTs have reached unprecedented sensitivities and angular resolutions, the morphology of most of the faint sources can not be characterised precisely. Moreover, instruments in other domains (radio, infrared, X-rays) usually feature angular resolutions at the arcsecond / subarcminute scales, often coupled with relatively small field of views, which (1) does not permit one to perform deep surveys of the whole Galactic Plane, and (2) makes it difficult to reveal large-scale structures coincident with these newly discovered sources.

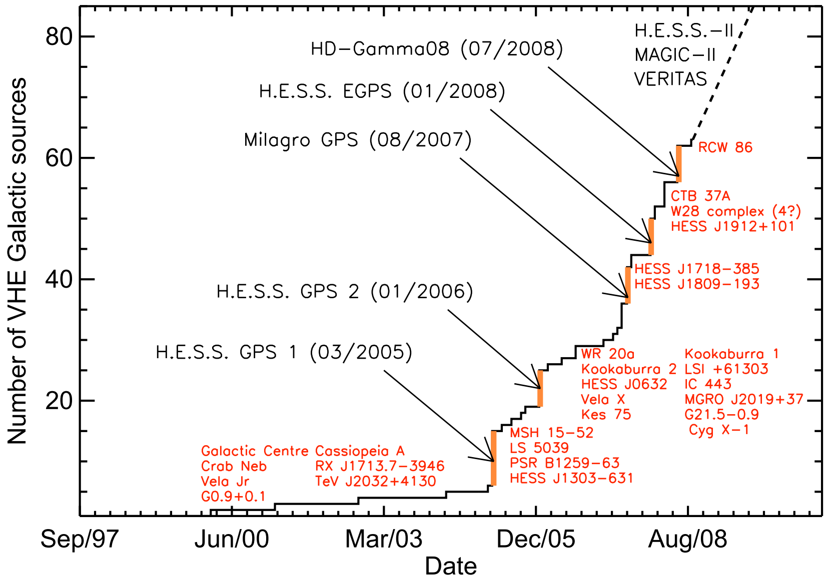

Figure 2: A history of VHE Galactic astronomy. The number of VHE Galactic sources is shown against the date, which corresponds to either the date of the publication or the date of the conference where the discovery has been officially announced. The number of Galactic sources has tremendously increased by steps over the last five years, particularly through the Galactic Plane Surveys (GPS, EGPS standing for the extension of the GPS) conducted with H.E.S.S.. HD-Gamma08 corresponds to the 4^{th} International Meeting on High Energy Gamma-Ray Astronomy which was held in Heidelberg, july 2008. The sources marked in red have been revealed in between these steps, mainly thanks to dedicated observations. The extrapolation in time depicted by the dashed line serves as an estimate of the number of new sources which might be revealed in the incoming era of H.E.S.S. II (Southern Hemisphere), MAGIC II and VERITAS (Northern Hemisphere).

In this contribution, latest results on VHE Galactic sources are reviewed, with a particular attention to those obtained with H.E.S.S.. The well-identified cases, such as shell-type SNRs and PWNe, are discussed in sections 2 and 3 respectively, together with the implications and new questions related to the acceleration mechanisms and the nature of the VHE γ-ray emission. Some interesting cases of dark sources are exposed in section 4, and the origin of the putative VHE Galactic diffuse emission is discussed in section 5. The conclusion focuses on the interest of population studies, through the log N − log S distribution of all the VHE Galactic sources known so far, and the perspectives with the next generation of IACTs (CTA [84], AGIS [83]).

2 Shell-type supernova remnants

Since the first speculation of Baade & Zwicky in 1934, the question of SNRs as the main sources of Galactic CRs up to the knee (~ 3 PeV) and beyond is not yet settled, in spite of several decades of important observational [70] and theoretical investigations [6,9,60]. The broadband spectrum of these sources, from radio to VHE γ-ray domains, is the signature of particles accelerated at the shock fronts and radiating photons through several channels (synchrotron SC, non-thermal bremsstralhung, inverse-Compton IC and π^0-decay). Therefore, it represents by far our best access to the acceleration processes in SNRs [32]. Up to now, five previously known shell-type SNRs, namely Cas A [4,34], RX J1713.7-3946 [10,29,35], RX J0852-4622 [13,19,24,36], RCW 86 [74], and more recently SN 1006 [82], have been discovered in VHE γ-rays, the last four exhibiting a shell-type morphology matching that observed in X-rays. As discussed before, the main question concerns the nature of the VHE γ-ray emission from these shell-type SNRs (leptonic through IC emission or hadronic through π^0-decay decay from p-p interactions) and gives rise to an intense debate [33,54,55,57,56,58]. On one hand, the correlation between X-ray and VHE γ-ray emission would support the leptonic scenario but implies, in a simple one-zone model, a spatially-averaged magnetic field of the order of a few tens of μG (except Cas A). This value seems uncomfortably low in comparison with the theoretical prediction of magnetic field amplication associated with the efficient production of CRs at forward shocks, by the (non-linear) diffusive shock acceleration (DSA) mechanism [6,59]. Magnetic fields of $\gtrsim 100\ \mu$G have been derived from the measured thickness of the X-ray filaments in several young SNRs [11,22], and, more recently, from the fast variability of small-scale X-ray dots and clumps [33], in case these localized structures effectively reflect the SC losses of high-energy electrons in strong (amplified) magnetic fields[a]. On the other hand, for the four resolved shell-type SNRs, the lack of clear correlation between the tracers of the ISM and the VHE γ-ray emission, together with the tight constraints on the local density derived from the absence (or the faint level) of thermal X-ray emission [3,43], does not permit one to draw firm conclusions in favor of an hadronic origin in these shell-type SNRs[b].

Table 1: Observational constraints on VHE shell-type SNRs. Distances d_{SNR} assumed here are 1, 1, 1, 2.2, 3.4, 4.8 and 2.3 kpc, for RX J1713, Vela Jr, RCW 86, SN 1006, Cas A, Kepler and Tycho, respectively. The first column gives the magnetic field values assuming a one-zone leptonic model, with standard seed radiation fields (CMB and Galactic infra-red and star-light emissions). The second column shows the magnetic field values derived from the thickness of the X-ray filaments. Third and fourth colums give the widths of VHE shells and of X-ray filaments, respectively. η_{CR} in the sixth column represents the fraction of the energy of the explosion, E_{51} (in units of 10^{51} erg), injected into CR protons, at the distance d_{SNR} and for a gas density $n_\alpha = n/\alpha$ cm^{-3}. Such density can then be compared to those given in the last column, mainly derived from the level of thermal X-ray emission.

	$B_{X\text{-}VHE}$ (μG)	$B_{filaments}$ [$\times d_{d_{SNR}}^{-2/3}$] ($\mu$G)	$Width_{VHE}$ [$\times d_{d_{SNR}}$] (pc)	$Width_{filaments}$ [$\times d_{d_{SNR}}$] (pc)	η_{CR} [$\times E_{51} d_{d_{SNR}}^2$]	n_{obs} (cm^{-3})
RX J1713	~ 10	58–271	~ 4.5	0.1–0.2	0.8–2.6/$n_{0.1}$	$< 0.02\ d_{d_{SNR}}^{-1/2}$
Vela Jr	~ 6	200–240	2.2–3.9	0.18–0.44	$\sim 2.5/n_{0.1}$	$< 0.03\ d_{d_{SNR}}^{-1/2}$
RCW 86	~ 30	50–115	2.2–4.7	0.29–0.5	0.05–0.3/$n_{0.5}$	$(0.3\text{–}0.7)_N$, $\sim 10_S$
SN 1006	~ 30	57–143	2.4–3.5	0.13–0.2	$\sim 0.2/n_{0.05}$	0.05_{SE}, $\sim 0.2_{NW}$
Cas A	~ 100	485–550	unresolved	0.03–0.05	$\sim 0.01/n_{11}$	$\sim 11_{\text{shocked shell}}$
Kepler	> 70	172–258	–	0.07–0.11	$< 0.05/n_{0.7}$	$< 0.15_{SE}$
Tycho	> 70	240–360	–	0.04–0.05	$< 0.02/n_{0.4}$	$< 0.3_{\text{SC rim}}$

Table 1 summarizes the relevant parameters of the five shell-type SNRs detected in VHE γ-rays and of the two historical SNRs, Kepler and Tycho, for which upper limits have been obtained so far [5,49]. It appears clearly that the magnetic field values estimated from a one-zone

[a]However, it was proposed that the thickness of the X-ray filaments would trace the magnetic field damping downstream of the forward shock and, therefore, would not be a measure of the magnetic field strength [12]. As for dots and clumps, which would reflect the inherent turbulence of the magnetic field, even in the case of a steady particle distribution [61].

[b]Note that, in the framework of the non-linear DSA, the post-shock gas temperature, which is expected to lie in the X-ray domain for young SNRs, and consequently the thermal X-ray emission, can be reduced (shifted towards lower temperatures) due to strong particle acceleration [75]. However, there are still discrepancies on the level at which the thermal X-ray emission could be suppressed [76].

leptonic model ($f_X/f_{VHE} \propto B^2$), are significantly below those derived from the thickness of the X-ray filaments. The situation looks even worse in the case of Kepler and Tycho SNRs, for which only rather strongly amplified magnetic fields seem to be compatible with the non-detection of VHE γ-rays, within these simple assumptions [54]. On the other hand, the typical width of the X-ray filaments, over which amplified magnetic fields of about hundreds of μG may exist, are an order of magnitude below the widths of the resolved VHE γ-ray shells. Hence, in case the magnetic field has been damped quickly behind the forward shock, the observed emission could still be explained by IC emission, with a fairly weak *spatially-averaged* value. Moreover, a detailed modeling of the interstellar radiation field for the calculation of the IC spectrum may help to improve the fit to the VHE γ-ray spectra [23]. In regards with the hadronic scenario, the energy injected into CR protons, required to explain the VHE γ-ray flux, is quite demanding, especially if the constraints on the gas density from the level of thermal X-ray emission are taken at face value. Apart from these energetical considerations, π^0-decay from p-p interactions seems to better explain the highest energy ($>$ 10 TeV) data points measured in RX J1713.7-3946, where the Klein-Nishina limit of IC scattering takes place [77]. Therefore, both scenarios, in their simpliest form, suffer from severe limitations. The question of these shell-type SNRs as efficient Galactic CR accelerators can only be efficiently addressed through spectro-imaging analysis in X-rays and VHE γ-rays, two domains whose current instrumental characteristics are quite different [c], together with theoretical developments of the DSA mechanism.

3 Plerionic supernova remnants

Besides shell-type SNRs, a significant fraction of VHE γ-ray sources is (or at least seems to be) associated with energetic pulsars [71,67]. These sources can generate bubbles of relativistic particles and magnetic field when their ultra-relativistic wind interacts with the surrounding medium (SNR or interstellar medium) [20]. Their confinement leads to the formation of strong shocks, which can accelerate particles up to hundreds of TeV and beyond, thus generating luminous nebulae seen across the entire electromagnetic spectrum in the SC emission from radio to hard X-rays, and through IC process and potentially π^0-decay from p-p interactions [21], in the VHE γ-ray domain. On one hand, recent advances in the study of PWNe have been made from mainly radio and X-ray observations of the complex morphology of the inner PWN structure at the arcsecond scales [20]. On the other hand, in the VHE domain, H.E.S.S. has proven to be capable to measure, in at least one case [31], spatially resolved spectra at the tenths of degree scales. These complementary VHE observations then permit one to probe the electron spectra in these sources and to investigate the associated magnetic field distribution [72].

Two classes of VHE γ-ray PWNe have recently emerged, based on observational grounds: young systems such as the Crab nebula [30], G0.9+0.1 [16], MSH 15-52 [17] and the newly discovered VHE γ-ray sources associated with the Crab-like pulsars of G21.5-0.9 [64] and Kes 75 [69], and evolved (extended and resolved) systems (*i.e.* with characteristic ages $\tau_c \gtrsim 10^4$ yr), as exemplified by Vela X [28], HESS J1825-137 [31], HESS J1718-385 and HESS J1809-193 [38]. In the former case, the VHE γ-ray emission, when resolved, matches quite well the morphology seen in X-rays, while in the latter case, these VHE γ-ray PWNe were found to be significantly offset from the pulsar position, with large size ratios between the X-ray and VHE γ-ray emission regions. The evolution of the SNR blastwave into an inhomogeneous ISM [2] and/or the high velocity of the pulsar [8], together with a low magnetic field value (~ 5 μG [72]), may explain these large offset filled-center VHE γ-ray sources as being the relic nebulae from the past history of the pulsar wind inside its host SNR. Since VHE-emitting electrons are usually less energetic than X-ray-emitting ones, they do not suffer from severe radiative losses and the majority of them may survive from

[c] While soft X-ray ($<$ 10 keV) telescopes feature angular resolutions at the arcsecond scales, both the imaging instruments above 10 keV and current IACTs reach angular resolutions of the order 5-10$'$ at best.

(and hence probe) early epochs of the PWN evolution. This interpretation has been further supported by the discovery of the spectral softening of the VHE nebula HESS J1825-137 as a function of the distance from the pulsar [31]. Given the discovery of this large population of middle-aged PWNe [73], many new sources regularly revealed by the on-going H.E.S.S. Galactic Plane Survey could fall into this category, some of them being classified as PWN *candidates*. For instance, HESS J1356-645 [67] lies close to the young (τ_c = 7.3 kyr) and energetic ($\dot{\rm E} = 3.1 \times 10^{36}$ erg s^{-1}) 166 ms pulsar PSR J1357-6429 [7], for which only a marginal evidence of a 3″ diffuse X-ray emission (*i.e.* of a putative PWN) was found [40,41]. Interestingly, the extended VHE γ-ray source coincides with a diffuse radio emission, originally catalogued as a SNR candidate [1]. The on-going analysis of archival radio and X-ray data should thus help to constraint the nature of HESS J1356-645 (Aharonian et al., in prep.). Therefore, these sources can be confirmed as VHE γ-ray PWNe thanks to a detailed investigation of all the available multi-wavelength data, together with follow-up observations in radio (*e.g.* HESS J1857+026 - PSR J1856+0245) [44,62] and with now *Fermi*/LAT (*e.g.* MGRO J1908+06 - HESS J1908+063 - 0FGL J1907.5+0617) [39,81,80], in order to reveal the associated (presumably energetic) pulsars.

4 VHE γ-ray "nebulae"

From the well-identified cases such as shell-type SNRs and PWNe, to the PWN candidates for which further data are required to firmly establish the putative association, it is presented here some cases of VHE γ-ray nebulae, also called dark sources [44]. HESS J1731-347 represents the best example in this regard. Originally classified as a dark source, a faint and extended (R $\sim 0.25°$) non-thermal radio and X-ray shell-type SNR, named G353.6-0.7, coincident with the extended VHE γ-ray emission, was discovered in the archival data [53]. At a distance of $\sim$ 3.2 kpc, estimated from HI absorption measurements toward an adjacent HII region, this SNR would have a physical diameter of $\sim$ 28 pc, significantly larger than the known VHE shell-type SNRs described in section 2. This would then suggest that G353.6-0.7 is an old ($\sim 2.7 \times 10^4$ yrs) and intrinsically very bright SNR. However, its distance and the nature of the X-ray emission are poorly constrained. Even though some theoretical studies have proposed that old SNRs ($\sim 10^{4-5}$ yrs) could still emit in the VHE γ-ray domain [25], it is commonly thought that multi-TeV particles usually leave the acceleration site on timescales of a few thousands of years [14]. Therefore, follow-up radio and X-ray observations are needed in order to shed further light on the nature of this newly discovered shell-type SNR.

This example serves as a discussion about the VHE γ-ray emission from SNRs. During the Sedov phase of the SNR evolution, accelerated particles are gradually injected in the ISM, the most energetic ones being released first. In case the SNR lies close to a molecular cloud (MC, at $\lesssim$ 100 pc), delayed VHE γ-ray (and neutrino) emission of the latter, through p-p interactions, may arise at detectable levels with the current IACTs [42]. The duration of VHE γ-ray emission from the cloud ($\gtrsim 10^4$ yrs) would then last much longer than that of the SNR itself, since it is determined by the time of propagation of CRs from the accelerator to the target. On a theoretical side, the detection of such emission would then indicate that the nearby SNR was acting *in the past* as an effective Galactic CR accelerator or PeVatron [d]. On an observational side, in this recently revisited scenario [42], (some of) the unidentified VHE γ-ray sources could be *indirectly* associated with old SNRs, the γ-ray emission being produced during the interaction of escaping CRs with nearby MCs. One would then expect a correlation between the VHE γ-ray emission and the tracers of molecular material (^{12}CO, ^{13}CO and masers in case the SNR shock encounters the MC), as it might be the case for the VHE γ-ray emission detected by

[d] Thus, the cutoff measured in RX J1713.7-3946 at $\sim$ 20 TeV [35], which translates into an E_{max} of particles at $\gtrsim$ 100 TeV (well below the knee in the CR spectrum observed at Earth), would imply that RX J1713.7-3946 *was a PeVatron in the past* and that the highest energy CRs have already been released in the surrounding medium

H.E.S.S. toward the old SNRs W41 (HESS J1834-087 [26]) and W28 (HESS J1800-240/J1801-233 [45]), the CTB 37 complex [50,48], and HESS J1745-303 [46]. However, it is worth noting that some of these nebulae could be instead VHE γ-ray PWNe [79], as discussed in section 3: the large lifetime of VHE γ-ray emitting electrons in low magnetic field environments ($\sim$ 20 $B_{5\mu G}^{-2}$ $E_{\gamma,\mathrm{TeV}}^{-1/2}$ kyr) makes the ratio of the VHE γ-ray luminosity to the X-ray luminosity an increasing function of the source age and size [78]. Therefore, one would expect VHE γ-ray PWNe to be hardly detectable with current X-ray instruments, and more generally at any other wavelength (leading to a VHE-*only*, dark, source). Moreover, for most of these nebulae, the morphology is poorly characterized, where only the source barycenter and gaussian extension are usually provided. Many of them may well be multiple sources of different kinds, as for HESS J1800-240 (A, B, & C) [45] and HESS J1745-303 [46]. Observations with the next generation of IACTs such as CTA and AGIS, with better sensitivities and angular resolutions, will undoubtedly help to search for counterparts with small field-of-view instruments and, thus, constrain the nature of the VHE γ-ray emission(s).

5 VHE Galactic diffuse emission... or unresolved sources?

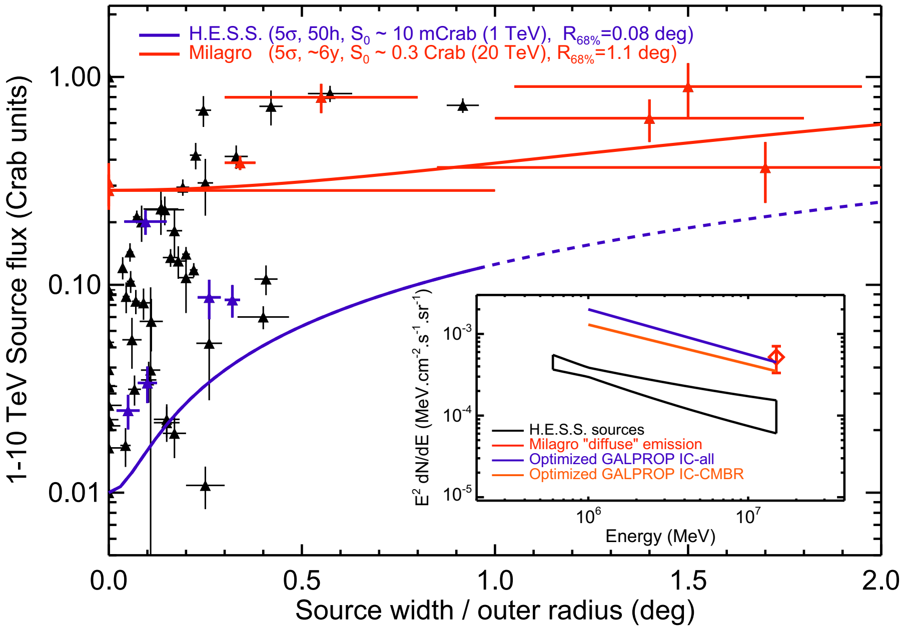

Figure 3: Flux – Size plot of the VHE Galactic sources detected so far. The integrated flux is given between 1 and 10 TeV, in units of the Crab nebula in the same energy band. The size correponds to either the intrinsic mean source width or, in the case of shell-type SNRs, the outer radius, in units of degrees. The red points represent the sources detected by Milagro during its Galactic Plane survey ($\ell \in$ [30,65]°, |b| < 2°), while the blue points correspond to those revealed by H.E.S.S. in the same region of the sky. The solid lines show the sensitivities of the two instruments, according to their respective characteristics given in brackets, which degrades with the source extent as: $S = S_0 \times (R_s^2 + \sigma_{psf}^2)^{1/2}/\sigma_{psf}$, where S_0 is the nominal sensitivity and R_s is the effective source size. Note that this law does not hold anymore when the source size becomes comparable to the instrument field of view, which explains why the H.E.S.S. sensitivity curve is valid only for $R_s \lesssim 1°$. The inset plot shows the Milagro diffuse emission measured at 15 TeV, the expected diffuse flux from the optimized GALPROP model and the summed spectrum of all the H.E.S.S. sources falling into the region probed by Milagro.

This section is devoted to the recent detection by Milagro of a large-scale VHE γ-ray diffuse emission (30° < ℓ < 110° and 136° < ℓ < 216°, |b| < 10°) [51], after removing the contribution of the sources detected by this experiment [39]. In the inner part of the Galaxy (between 30 and

65° in longitude, *i.e.* excluding the peculiar Cygnus region), the traditional GALPROP model fails to fit the measured flux at ~ 15 TeV. An optimized version of GALPROP has been designed to reproduce the *EGRET* data by relaxing the restriction of the local CR measurements. In this model, the electron spectrum is contrained by the *EGRET* data themselves, such that any hard and faint (relatively to the standard π^0-decay spectrum from CR protons) IC spectrum, as proposed by the authors, would not violate the GeV measurements, while explaining the measured flux at 15 TeV. Diffuse emission would thus be almost entirely explained by ~ 100 TeV electrons scattering off the CMB, with a flux, after propagation, of four times the one measured locally. Interestingly, this region has also been surveyed by H.E.S.S., featuring much better sensitivity and angular resolution than Milagro at the expense of a much smaller field of view (see Figure 3), though with a non-uniform coverage [66]. So far, five VHE γ-ray sources have been detected by H.E.S.S. (and unresolved by Milagro) in this region, and the resulting summed spectrum is shown in Figure 3, together with the Milagro measurement. Roughly 20 % of the diffuse emission is already explained by these H.E.S.S. sources, and a larger fraction should be reached in a next future once the existing H.E.S.S. data will be carefully analyzed and the survey will become uniform. First studies of the VHE γ-ray source population, based on the second H.E.S.S. survey catalogue [26], had already suggested that at least 10 % of the VHE Galactic diffuse emission should be attributed to unresolved sources [63].

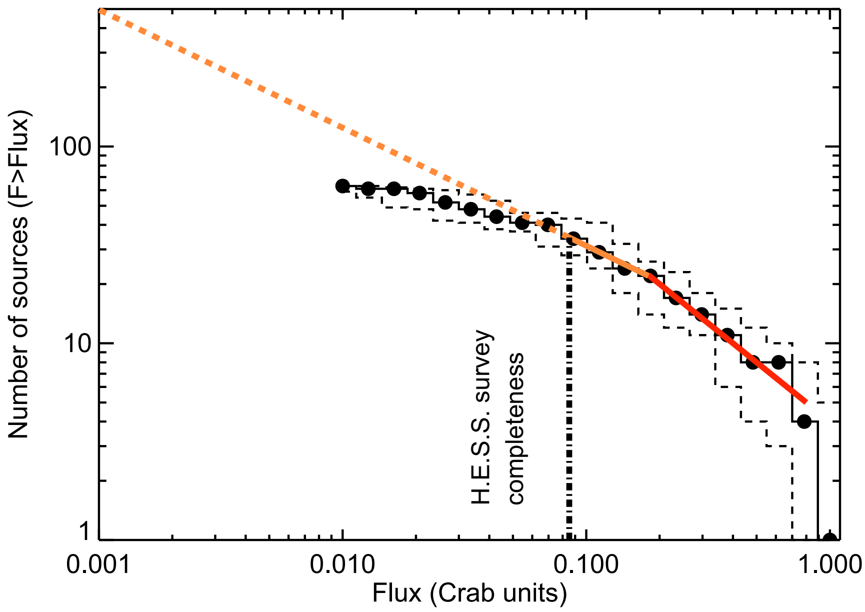

Figure 4: Log N(>S) – log S diagram of the VHE Galactic sources. The dashed lines represent the dispersion of the distribution after taking into account the statistical and systematical errors on the source spectra through a Monte-Carlo simulation. The red and orange solid lines correspond to the expectations from a uniform distribution in a thin disk (slope of -1) and a source population distributed along the spiral arms (slope of -0.6), respectively. The transition between these two regimes was set arbitrarly. The dot-dashed line shows the completeness limit of the H.E.S.S. survey (for a source extent of 0.2° in radius, and five hours of observations everywhere in the inner part of the Galaxy). The extrapolation down to 1 mCrab, a sensitivity that should be reached by the next generation of IACTs like CTA and AGIS, would then lead to the detection of about 500 VHE Galactic sources.

6 Conclusion

To conclude this review, the log N(>S) – log S distribution of all the VHE Galactic sources known so far is shown in Figure 4. A slope of -1 corresponds to a uniform infinite plane distribution while a slope of $\sim$ -0.6 indicates that the population follows the spiral arm distribution on Galactic scales (*i.e.* at distances of $\gtrsim 8\,\mathrm{kpc}$), as expected from young stellar population generating SNRs and PWNe. Even though there are inherent complications in the interpretation of such plot, the transition between the two regimes (at ~ 0.15 Crab) seems to take place above the completeness limit of the H.E.S.S. survey. Extrapolating the curve down to 1 mCrab in sensitivity then implies that the next generation of IACTs like CTA [84] and AGIS [83] should detect at least 500 sources. As discussed in section 4, many faint sources could actually be several sources, not clearly resolved yet, leading the log N(>S) − log S to soften toward low fluxes. The paper focused mainly on the latest results and open questions related to shell-type SNRs and PWNe. Besides them, new classes of VHE γ-ray emitters in the Milky-Way are expected to emerge, either from multi-wavelength follow-up observations of the so-called dark sources, as it might be the case of HESS J1503-582 [68], or through dedicated observations of sky regions of interest, as exemplified by the recent detection of VHE γ-rays towards the young stellar cluster Westerlund 2 [37]. Such detection has triggered many exciting questions on the nature of the VHE γ-ray emission and more generally on the contribution of such wind-blown bubbles to the Galactic CR flux. HESS J1848-018 could be the second case of this kind, where the VHE γ-ray emission is found to be slightly offset from the massive star-forming (Galactic "mini-starburst") region W 43 [65]. Moreover, γ-ray binaries have now joined the club of VHE γ-ray emitters and many pending issues still need to be investigated. Next generation of VHE observatories, in tight link with incoming multi-wavelength instruments, will undoubtedly play a crucial role in the understanding of all these acceleration sites in the Galaxy and, very likely, in the discovery of an even larger diversity of VHE γ-ray sources than expected.

References

1. A.R. Duncan et al. , MNRAS **287**, 722 (1997)
2. J.M. Blondin, R.A. Chevalier & D.M. Frierson, ApJ **563**, 806 (2001)
3. P. Slane et al. , ApJ **548**, 814 (2001)
4. F.A. Aharonian et al. (HEGRA collaboration), A&A **370**, 112 (2001)
5. F.A. Aharonian et al. (HEGRA collaboration), A&A **373**, 292 (2001)
6. M.A. Malkov & L.O.C. Drury, RPPh **64**, 429 (2001)
7. F. Camilo et al. , ApJ **611**, L25 (2004)
8. E. van der Swaluw, T.P. Downes & R. Keegan, A&A **420**, 937 (2004)
9. A.R. Bell, MNRAS **353**, 550 (2004)
10. F.A. Aharonian et al. (H.E.S.S. collaboration), Nature **432**, 75 (2004)
11. H.J. Völk, E.G. Berezhko & L.T. Ksenofontov, A&A **433**, 229 (2005)
12. M. Pohl, H. Yan & A. Lazarian, ApJ **626**, L101 (2005)
13. H. Katagiri et al. (CANGAROO collaboration), ApJ **619**, L163 (2005)
14. V.S. Ptuskin & V.N. Zirakashvili, A&A **429**, 755 (2005)
15. F.A. Aharonian et al. (H.E.S.S. collaboration), Science **307**, 1938 (2005)
16. F.A. Aharonian et al. (H.E.S.S. collaboration), A&A **432**, L25 (2005)
17. F.A. Aharonian et al. (H.E.S.S. collaboration), A&A **435**, L17 (2005)
18. F.A. Aharonian et al. (H.E.S.S. collaboration), A&A **437**, 135 (2005)
19. F.A. Aharonian et al. (H.E.S.S. collaboration), A&A **437**, L7 (2005)
20. B.M. Gaensler & P.O. Slane, ARA&A **44**, 17 (2006)
21. D. Horns et al. , A&A **451**, L51 (2006)
22. E. Parizot et al. , A&A **453**, 387 (2006)
23. T.A. Porter, I.V. Moskalenko & A.W. Strong, ApJ **648**, L29 (2006)
24. R. Enomoto et al. (CANGAROO collaboration), ApJ **652**, 1268 (2006)
25. R. Yamazaki et al. , MNRAS **371**, 1975 (2006)
26. F.A. Aharonian et al. (H.E.S.S. collaboration), ApJ **636**, 777 (2006)
27. F.A. Aharonian et al. (H.E.S.S. collaboration), Nature **439**, 695 (2006)
28. F.A. Aharonian et al. (H.E.S.S. collaboration), A&A **448**, L43 (2006)
29. F.A. Aharonian et al. (H.E.S.S. collaboration), A&A **449**, 223 (2006)

30. F.A. Aharonian et al. (H.E.S.S. collaboration), A&A **457**, 899 (2006)
31. F.A. Aharonian et al. (H.E.S.S. collaboration), A&A **460**, 365 (2006)
32. D.C. Ellison et al. , ApJ **661**, 879 (2007)
33. Y. Uchiyama et al. , Nature **449**, 576 (2007)
34. J. Albert et al. , (MAGIC collaboration) A&A **474**, 937 (2007)
35. F.A. Aharonian et al. (H.E.S.S. collaboration), A&A **464**, 235 (2007)
36. F.A. Aharonian et al. (H.E.S.S. collaboration), ApJ **661**, 236 (2007)
37. F.A. Aharonian et al. (H.E.S.S. collaboration), A&A **467**, 1075 (2007)
38. F.A. Aharonian et al. (H.E.S.S. collaboration), A&A **472**, 489 (2007)
39. A.A. Abdo et al. (Milagro collaboration), ApJ **664**, L91 (2007)
40. P. Esposito et al. , A&A **467**, L45 (2007)
41. V.E. Zavlin, ApJ **665**, L143 (2007)
42. S. Gabici & F.A. Aharonian, ApJ **665**, L131 (2007)
43. F. Acero, J. Ballet & A. Decourchelle, A&A **475**, 883 (2007)
44. F.A. Aharonian et al. (H.E.S.S. collaboration), A&A **477**, 353 (2008)
45. F.A. Aharonian et al. (H.E.S.S. collaboration), A&A **481**, 401 (2008)
46. F.A. Aharonian et al. (H.E.S.S. collaboration), A&A **483**, 509 (2008)
47. F.A. Aharonian et al. (H.E.S.S. collaboration), A&A **484**, 435 (2008)
48. F.A. Aharonian et al. (H.E.S.S. collaboration), A&A **486**, 829 (2008)
49. F.A. Aharonian et al. (H.E.S.S. collaboration), A&A **488**, 219 (2008)
50. F.A. Aharonian et al. (H.E.S.S. collaboration), A&A **490**, 685 (2008)
51. A.A. Abdo et al. (Milagro collaboration), ApJ **688**, 1078 (2008)
52. R. Enomoto et al. (CANGAROO collaboration), ApJ **683**, 383 (2008)
53. W.W. Tian et al. , ApJ **679**, L85 (2008)
54. H.J. Völk, L.T. Ksenofontov & E.G. Berezhko, A&A **490**, 515 (2008)
55. E.G. Berezhko & H.J. Völk, A&A **492**, 695 (2008)
56. Y. Butt et al. , MNRAS **386**, L20 (2008)
57. D.C. Ellison & A. Vladimirov, ApJ **673**, L47 (2008)
58. R. Plaga, New Astronomy **13**, 73 (2008)
59. E. Amato, P. Blasi & S. Gabici, MNRAS **385**, 1946 (2008)
60. V.N. Zirakashvili & V.S. Ptuskin, ApJ **678**, 939 (2008)
61. A.M. Bykov, Y.A. Uvarov & D.C. Ellison, ApJ **689**, L133 (2008)
62. J.W.T. Hessels et al. , ApJ **682**, L41 (2008)
63. S. Casanova & B.L. Dingus, APh **29**, 63 (2008)
64. A. Djannati-Ataï et al. (H.E.S.S. collaboration), Proceedings of the 30th ICRC **2**, 823 (2008)
65. R.C.G. Chaves et al. (H.E.S.S. collaboration), AIP Proceedings of the 4th γ_{2008} **1085**, 372 (2008)
66. R.C.G. Chaves et al. (H.E.S.S. collaboration), AIP Proceedings of the 4th γ_{2008} **1085**, 219 (2008)
67. M. Renaud et al. (H.E.S.S. collaboration), AIP Proceedings of the 4th γ_{2008} **1085**, 285 (2008)
68. M. Renaud et al. (H.E.S.S. collaboration), AIP Proceedings of the 4th γ_{2008} **1085**, 281 (2008)
69. R. Terrier et al. (H.E.S.S. collaboration), AIP Proceedings of the 4th γ_{2008} **1085**, 316 (2008)
70. S.P. Reynolds, ARA&A **46**, 89 (2008)
71. Y. Gallant et al. , AIP Conference Proceedings of "40 years of pulsars" **983**, 195 (2008)
72. O.C. de Jager & A. Djannati-Ataï, AIP Proceedings of "Neutron Stars and Pulsars: 40 years after their discovery" in press –, – (2008)
73. A. Djannati-Ataï, NIMA **602**, 28 (2009)
74. F.A. Aharonian et al. (H.E.S.S. collaboration), ApJ **692**, 1500 (2009)
75. L.O.C Drury et al. , A&A **496**, 1 (2009)
76. D.J. Patnaude, D.C. Ellison & P. Slane, ApJ in press –, – (2009)
77. G. Morlino, E. Amato & P. Blasi, MNRAS **392**, 240 (2009)
78. F. Mattana et al. , ApJ **694**, 12 (2009)
79. R. Mukherjee, E.V. Gotthelf & J.P. Halpern, ApJ **691**, 1707 (2009)
80. A.A. Abdo et al. (*Fermi* collaboration), Submitted to ApJS –, – (2009)
81. F.A. Aharonian et al. (H.E.S.S. collaboration), Accepted in A&A –, – (2009)
82. M. Naumann-Godo et al. (H.E.S.S. collaboration), These proceedings –, – (2009)
83. W. Benbow et al. , These proceedings –, – (2009)
84. M. Punch et al. , These proceedings –, – (2009)

Gamma-Ray Pulsars Discovered by Blind Search with Fermi LAT

F. Giordano
For the Fermi LAT Collaboration
Department of Physics and INFN Sez. Bari

Just three months after launch, the Large Area Telescope (LAT) aboard the Fermi Gamma Ray Space Telescope is providing a new image of the gamma ray pulsar sky. The discovery of a new class of pulsating gamma ray emitters applying the blind period search technique is reported and discussed. These new pulsars are mostly coincident with previously unidentified EGRET gamma-ray sources, opening a new window in the studies of emission geometry, population studies and the connections with the surrounding environment

1 The EGRET heritage

Before the Fermi launch the telescopes on the Compton Gamma Ray Observatory [1] detected seven pulsating gamma ray emitters with very high confidence. In fig.1 the light curves of these seven gamma-ray pulsars are shown in five different energy bands from radio to optical, soft X-ray (<1 keV), hard X-ray/soft gamma ray (10 keV $\div$ 1MeV), and hard gamma ray (above 100 MeV). Directly from the light curves of each pulsar in each energy bin some crucial aspects regarding the acceleration mechanisms and emission model can be interpreted. For example all the light curves of the Egret pulsars show a double peak feature, but not all seven are seen at the highest energies, as well as not all the seven pulsars display a clear radio pulsations like Geminga. Before Fermi, Geminga was the unique "radio-quite" known pulsar.

2 The Fermi Era

The Fermi satellite, consisting of the Gamma-ray Burst Monitor (GBM) and the Large Area Telescope (LAT), was launched on 11 June 2008 into a low Earth circular orbit at an altitude of 550 km and an inclination of 28.5°. The LAT [2] is a pair-production telescope with large effective area ($\sim$8000 cm^2) and field of view (2.4 sr), sensitive to gamma rays between 30 MeV and > 300 GeV. A The LAT began normal science operations on 11 August 2008, and since then has been observing mostly in survey mode, scanning the entire gamma-ray sky every three hours. The overall sensitivity of the LAT is about 25 times that of EGRET, while the angular resolution is also signicantly improved (it ranges from 3$\div$6° at 100 MeV to 0.1$\div$0.2° at 10 GeV). The mission was designed with a five year lifetime and a goal of at least ten years of operations. The scientic goals of the mission include understanding particle acceleration in Active Galactic Nuclei (AGN), pulsars, and supernova remnants (SNRs), exploring the high energy emission of Gamma-ray Bursts (GRB), and probing the nature of dark matter.

Although its commissioning phase (30 June to 30 July 2008) was primarily intended for instrument performance verification and calibration, important scientic results have been obtained

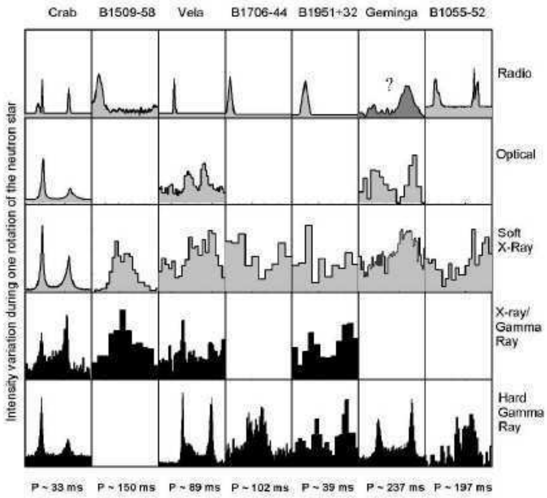

Figure 1: Light curves in different energy bands for the CGRO detected pulsars (from [1])

with these early data. The six Egret pulsars have been confirmed just during the early phase of the mission. Vela, Crab and Geminga was detected in only 15days, while the other three weaker Pulsars, the B1951+32, the B1706-44 and the B1055-52 was detected in 25 days, still during the commissioning of the mission. Moreover, after only three months of sky survey, the Fermi LAT was capable not only to confirm the 6 known Egret pulsars but also to discover 10 radio loud young galactic pulsars, 7 new ms pulsars, and 13 new $gamma - ray\ selected$ pulsars. Figure 2 shows how the Fermi pulsating gamma-ray sky looks like.

2.1 The Geminga Candidates

Radio campaigns have not always been capable to detect pulsation even from sources appearing positionally coincident with supernova remnants (SNR) or pulsar wind nebulae (PWN). Geometry consideration can explain the lack of radio pulsations from these potential pulsars, in particular in those cases where the narrow radio beams are expected to be not oriented close to the line of sight towards the Earth. According to current models of pulsar gamma-ray emission which predict a much wider gamma-ray beams than radio beams, a much larger population of potentially radio-quiet gamma-ray pulsars than the one observed is expected to be observed. A list of locations of potential pulsars which would have been investigated with the blind search was compiled almost immediately after launch. About 100 $Geminga - like$ sources was included in the list due to some peculiar features like the location in the Galactic plane, the spectral index and the emission cut-off or the lack of long-term variability as well as the presence of a very promising environment like pulsar wind nebula or SNRs. Many of these sources have been detected by EGRET, and have also been investigated in other wavelengths. Moreover, Fermi was able to detect 205 bright sources [3] in the first three months of sky survey; these sources have also been included in the $Geminga - like$ list, rejecting those clearly associated with Active Galactic Nuclei (AGN).

2.2 The Blind Period Search

Even with the advantages of the LAT in terms of field of view and timing capabilities, gamma-ray photon data are extremely sparse. For example, for the Vela pulsar, which is the brightest

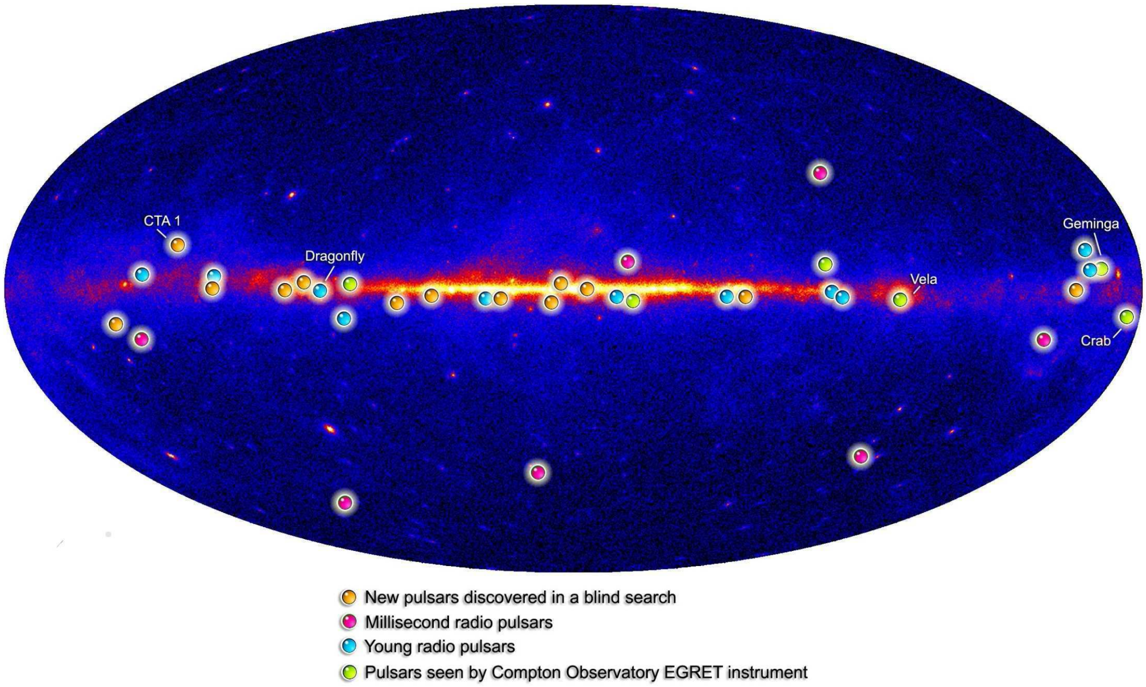

Figure 2: The Fermi pulsating gamma ray sky.

gamma-ray source in the sky, we have fewer than one photon every 4 minutes in the LAT. As a result, the detection of gamma-ray pulsations requires the accumulation of weeks or months of data. Because there is no a priori knowledge of the frequencies of any pulsars in the $Geminga - Candidates$ list, a blind frequency search over a broad range of frequencies and frequency derivatives needed to be performed. To discover a gamma ray pulsation two techniques are mostly used: the first is called epoch folding, which uses information from the ephemeris coming from other wavelengths observation. The second method uses fully coherent FFT. In a FFT the number of frequency bins increases with the length of the observational time and due to the spinning down of a pulsar which radiate away energy, in order to have a realistic scan over a frequency and frequency derivative parameter space tens of thousands FFTs need to be performed. For these reasons a fully coherent FFT is very CPU consuming and computationally intensive. An alternative method that uses truncated time differences to allow sensitive searches of sparse gamma-ray data with modest computational requirements was developed [4]. This $time - differencing$ technique was implemented and used obtaining a great simplification of the computational burden simply using a fixed coherency window of 1 week (T = 21952 s) and, despite the reduced frequency resolution due to a lower number of bins, the sensitivity is not much reduced because of a compensating reduction in the number of ferquency derivative trials

2.3 The Blind Period Pulsars

The first major Fermi discovery in blind search was the detection of the pulsation from CTA 1 [6]. This young, nearby, shell-type SNR was discovered in radio in the 1960s and X-ray observations show a well-localized central point source, RXJ0007.0+7303, embedded in a pulsar wind nebula (PWN) [7]. High energy (> 100 MeV) emission was detected by EGRET from 3EG J0010+7309, coincident with this source (see Figure 3). Moreover the period measurement and the derivative, about 315.9ms and 3.615×10^{-13} s s^{-1} respectively are very consistent with a typical young,

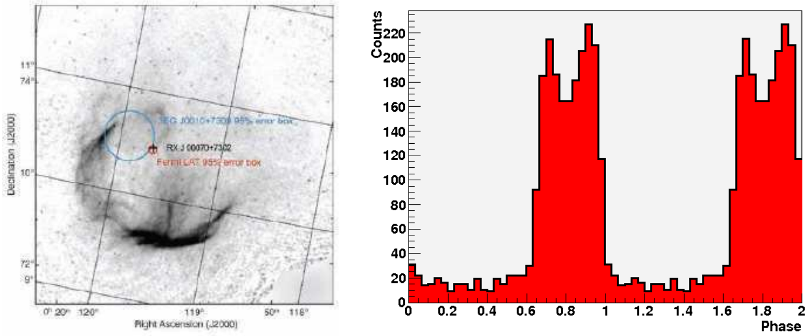

Figure 3: Left: LAT gamma-ray source location of CTA 1, superimposed on a 1420-MHz radio image of the CTA 1 SNR [6]. The red circle shows the Fermi-LAT 95% containment radius, while the cross represents the location of the X-ray point source. The large circle shows the corresponding EGRET 95% error circle . Right: Gamma-ray (> 100 MeV) folded light curve of the CTA 1 pulsar shown with two periods of rotation [6].

energetic pulsar, with a characteristic age of 14,000 years (in agreement with the estimated age of the SNR) and a spin-down power of 4.5×10^{35} erg s^{-1}.

Together with the LAT PSR J0007+7303 which was long suspected of being a pulsar because of its clear association with SNR CTA1 containing a PWN, also the LAT PSR J1418-6058, in the Kookaburra region of the Galactic plane, very close to the PSR J1420-6048, likely associated with the Rabbit PWN G313.3+0.1, [8] and the LAT PSR J1809-2332 likely powering the Taz PWN[9], have been studied with blind search and pulsation was detected (4) Another candidate pulsar investigated with the blind search was the LAT PSR J1826-1256, probably powering the Eel PWN[10] and close to the PWN HESS J1825-137, which shows emission at higher energies[12]. Fermi was capable to detect pulsation also from the LAT PSR J2021+4044, answering to the question of whether a pulsar exists in the Gamma Cygni region[13]. Also LAT PSR J0633+0632 and LAT PSR J1907+0601 had association with SNR in the complex Monoceros Loop SNR (G205.5+0.5)[14] and SNR G40.5−0.5[15] respectively, and thus they have been object of blind period search. All the light curves of all pulsar discovered are shown in Figure 4. Almost all the light curves exhibit two peaks, like the Egret ones. Eleven pulsars out of the 13 discovered in the early three months are associated with unidentified EGRET sources, while the J1907+0601, the J0357+3211 and the J2238+59 are not mentioned in the 3rd Egret Catalog, though the MGRO J1908+06 has been detected by EGRET with a energy threshold greater than 1GeV.

3 Conclusions

A time-differencing technique was used to search pulsation from gamma-ray sources whose pulsation was not detected in any other wavelengths. Thirteen new pulsars have been discovered with an age distribution from 10 kyr to 1.8 Myr and a spin-down luminosity distribution in the range 10^{33} erg/s 10^{36} erg/s. From a first preliminary comparison with the radio pulsars, this new class of gamma ray emitters show to be mostly younger, energetic and strong magnetic field gamma-ray pulsars. The detection these new gamma ray pulsars in only three months of data taking suggests that many more will be discovered in the next five years of nominal operation, which will have important implications for an entire population of previously undetected neutron stars and open a new window of new deep radio searches of these new objects, in order also to get strong constraints on the radio luminosity, geometry and emission mechanisms.

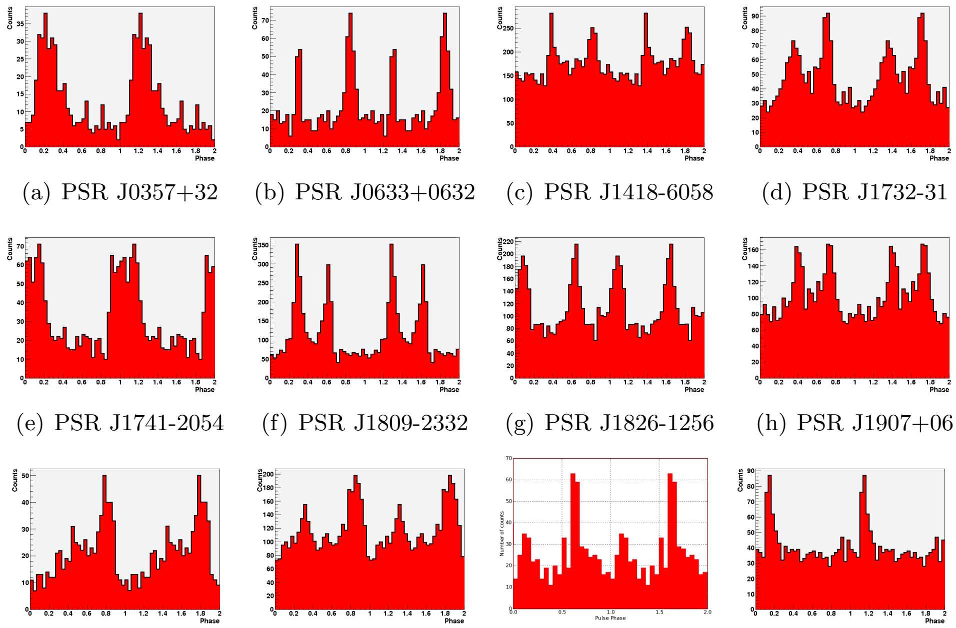

(a) PSR J0357+32 (b) PSR J0633+0632 (c) PSR J1418-6058 (d) PSR J1732-31

(e) PSR J1741-2054 (f) PSR J1809-2332 (g) PSR J1826-1256 (h) PSR J1907+06

(i) PSR J1958+2846 (j) PSR J2021+4044 (k) PSR J2032+4127 (l) PSR J2238+59

Figure 4: Light curves of the new gamma ray pulsar detected by Fermi with blind period search

References

1. D. J. Thompson, Reports on Progress in Physics 71, 116901+ (2008), 0811.0738.
2. W. B. Atwood, et al. 2009, ApJ, v.697
3. A. A. Abdo et al., Fermi Large Area Telescope Bright Gamma-ray Source List, arXiv:0902.1340
4. W. B. Atwood, M. Ziegler, R. P. Johnson, and B. M. Baughman, ApJL 652, L49L52 (2006).
5. M. Ziegler, B. M. Baughman, R. P. Johnson, and W. B. Atwood, ApJ 680, 620626 (2008).
6. A. A. Abdo et al., Science 322, 1218(2008).
7. J. P. Halpern, E. V. Gotthelf, F. Camilo, D. J. Helfand, and S. M. Ransom, ApJ 612, 398407 (2004)
8. M. S. E. Roberts, R. W. Romani, S. Johnston, A. J. Green, ApJ 515, 712 (1999).
9. M. S. E. Roberts, C. L. Brogan, ApJ 681, 320 (2008).
10. M. S. E. Roberts, R. W. Romani, N. Kawai, ApJS 133, 451 (2001).
11. M. S. E. Roberts, et al., Ap&SS 297, 93 (2005).
12. F. Aharonian, et al., A&A 460, 365 (2006).
13. K. T. S. Brazier, G. Kanbach, A. Carrami ana, J. Guichard, M. Merck, MNRAS 281, 1033 (1996).
14. D. A. Leahy, S. Naranan, K. P. Singh, MNRAS 220, 501 (1986).
15. J. Yang, J.-L. Zhang, Z.-Y. Cai, D.-R. Lu, Y.-H. Tan, Chinese Journal of Astronomy and Astrophysics 6, 210 (2006).

THE MAGIC EXTRAGALACTIC SKY

BARBARA DE LOTTO (on behalf of the MAGIC Collaboration)
University of Udine and INFN, Sezione di Trieste
Italy

The MAGIC telescope, with its 17-m diameter mirror, is currently the largest single-dish Imaging Air Cherenkov Telescope. It is located on the Canary Island of La Palma, at an altitude of 2200 m above sea level, and is operating since 2004. The accessible energy range is in the very high energy (VHE, $E > 100$ GeV) γ-ray domain, and roughly 40% of the duty cycle is devoted to observation of extragalactic sources. Due to the lowest energy threshold (25 GeV), it can observe the deepest universe, and it is thus well suited for extragalactic observations. The strategies of extragalactic observations by MAGIC are manifold: long time monitoring of known TeV blazars, detailed study of blazars during flare states, multiwavelength campaigns on most promising targets, and search for new VHE γ-ray emitters. In this talk, highlights of observations of extragalactic objects will be reviewed.

1 Introduction

One of the major goals of ground-based γ-ray astrophysics is the study of VHE γ-ray emission from active galactic nuclei (AGN). Except for the radio galaxies M87 and Centaurus A (and possibly 3C66B), and the flat-spectrum radio quasar 3C279, all the currently known VHE γ-ray emitters in the extragalactic sky are BL Lac objects. The sensitivity of the current Imaging Atmospheric Cherenkov Telescopes (IACT) has recently enabled detailed studies of these sources in the VHE γ-rays domain, providing information for advances in understanding the origin of the VHE γ-rays, as well as powerful tools for fundamental physics studies [1].

The IACT technique [2] uses the atmosphere as a calorimeter to detect the extensive air shower produced after the interaction of a VHE γ-ray. The charged particles (mainly electrons and positrons) in the air shower produce Cherenkov light that can be easily detected in the ground with photomultipliers. A Cherenkov telescope uses a large reflector area to concentrate as much as possible of these photons and focus them to a camera where an image of the atmospheric cascade is formed. By analysing this image it is possible to reconstruct the incoming direction and the energy of the γ-ray. The analysis of the images is also used to reject the much higher background of cosmic rays initiated showers.

In this paper selected results on extragalactic observations with MAGIC are presented.

2 The MAGIC telescope

MAGIC [3,4], located on the Canary Island of La Palma (2200 m a.s.l.), is currently the largest (17-m diameter) single-dish IACT. Due to its large collection area and uniquely designed camera, MAGIC has reached the lowest energy threshold (trigger threshold 50–60 GeV at small zenith angles, new trigger for pulsar observations $\sim$ 25 GeV [5]) for γ-ray emission among the existing terrestrial γ-ray telescopes.

MAGIC has a sensitivity of $\sim$ 1.6% of the Crab Nebula flux in 50 observing hours. Its energy resolution is about 30% above 100 GeV and about 25% from 200 GeV onwards. The angular resolution is 0.1 deg. The MAGIC standard analysis chain is described, e.g., in Albert et al.[6]. Observations during moderate moonshine enable a substantially extended duty cycle, which is particularly important for blazar observations. Parallel optical R-band observations are performed by the Tuorla Blazar Monitoring Program with its KVA 35-cm telescope.

A second MAGIC telescope is being commissioned [7], which is improving the sensitivity to $\sim$ 0.8% of Crab in 50 hours.

3 The propagation and absorption of γ-rays

While travelling long distances without deviations in the fields, VHE γ-rays suffer the absorption losses due to the interaction with the low energy photons from the extragalactic background light (EBL), limiting the distance to the source that could be detected. The standard process is $\gamma_{VHE}\gamma_{EBL} \rightarrow e^+e^-$ pair production. The corresponding cross section [8] reaches its maximum, $\sigma_{\gamma\gamma}^{\max} \simeq 1.70 \cdot 10^{-25}\,\mathrm{cm}^2$, assuming head-on collisions, when the background photon energy is $\epsilon(E) \simeq (0.5\,\mathrm{TeV}/E)$ eV, E being the energy of the hard (incident) photon. This shows that in the energy interval explored by the IACTs, $50\,\mathrm{GeV} < E < 100\,\mathrm{TeV}$, the resulting opacity is dominated by the interaction with infrared/optical/ultraviolet diffuse background photons (EBL), with $0.005\,\mathrm{eV} < \epsilon < 10\,\mathrm{eV}$, corresponding to the wavelength range $0.125\,\mu\mathrm{m} < \lambda < 250\,\mu\mathrm{m}$.

Based on synthetic models of the evolving stellar populations in galaxies as well as on deep galaxy counts (see, for a review, [9]), several estimates of the spectral energy distribution (SED) of the EBL have been proposed, leading to different values for the transparency of the universe to $50\,\mathrm{GeV} < E < 100\,\mathrm{TeV}$ photons [10]; the resulting uncertainties are large.

Because of the absorption produced by the EBL, the observed photon spectrum $\Phi_{\mathrm{obs}}(E_0, z)$ is related to the emitted one $\Phi_{\mathrm{em}}(E(z))$ by

$$\Phi_{\mathrm{obs}}(E_0, z) = e^{-\tau_\gamma(E_0,z)}\ \Phi_{\mathrm{em}}\left(E_0(1+z)\right)\ , \tag{1}$$

where E_0 is the observed energy, z the source redshift and $\tau_\gamma(E_0, z)$ is the optical depth [11].

The energy dependence of τ leads to appreciable modifications of the observed source spectrum (with respect to the spectrum at emission) even for small differences in τ, due to the exponential dependence described in Eq. (1). Since the optical depth (and consequently the absorption coefficient) increases with energy, the observed flux results steeper than the emitted one. The *horizon* (e.g. Ref. [12,13]) for a photon of energy E is defined as the distance corresponding to the redshift z for which $\tau(E, z) = 1$, which gives an attenuation by a factor $1/e$ (see Fig. 1). MAGIC has the lowest energy threshold, and thus is currently the best suited telescope to look farther away.

4 Multi-Wavelength Campaigns

Coordinated simultaneous multi-wavelength observations, yielding spectral energy distributions (SED) spanning over 15 decades in energy, have been recently conducted, and turn out to be essential for a deeper understanding of blazars. MAGIC participated in a number of multiwavelength-campaigns on known northern-hemisphere blazars, which involved the X-ray instruments *Suzaku* and *Swift*, the γ-ray telescopes H.E.S.S., MAGIC and VERITAS, and other optical and radio telescopes.

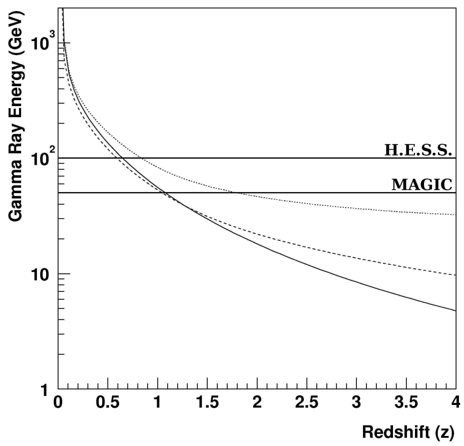

Figure 1: Gamma-ray horizon compared with the lower energy limit of the MAGIC and H.E.S.S. Cherenkov telescopes; the curves of the photon energy versus horizon are computed for different background evolution models by Blanch & Martinez in Ref. [12].

- Mkn 421 was detected in two campaigns during outbursts in 2006 and 2008; the coordinated effort allowed for truly simultaneous data from optical to TeV energies, and studies of correlations between the different energy bands [14,15].

- The VHE emission of PG 1553+113 showed no variability during the first multi-wavelength campaign on this blazar in July 2006 [16,17]; it was observed simultaneously for the first time together with AGILE during 2008 [18].

- 1ES 1959+650 showed VHE data among the lowest flux state observed from this object, while at the same time a relatively high optical and X-ray flux (both Swift/Suzaku) was found [19]. The SED could be modeled assuming a one zone SSC model, using parameters similar to the ones needed for the SED measured in 2002.

- Also campaigns on 1ES 1218+304 and 1H 1426+428 have been carried out, during both of which significant X-ray variability has been observed. The VHE data are being analyzed.

Further campaigns have been and will be organized in the future.

5 Strong Flaring of Messier 87 in February 2008

M 87 is the first non-blazar radio galaxy known to emit VHE γ-rays, and one of the best-studied extragalactic black-hole systems. To enable long-term studies and assess the variability timescales and the location of the VHE emission in M 87, the H.E.S.S., MAGIC and VERITAS collaborations established a regular, shared monitoring of M 87 and agreed on mutual alerts in case of a significant detection. During the MAGIC observations, a strong signal of $8\,\sigma$ significance was found on 2008 February 1^{st}, triggering the other IACTs as well as *Swift* observations. The analysis revealed a variable (significance: $5.6\,\sigma$) night-to-night γ-ray flux above 350 GeV, while no variability was found in the 150–350 GeV range [21]. The $E > 730$ GeV short-time variability of M 87 reported by [20] has been confirmed. This fastest variability Δt observed so far in TeV γ-rays in M 87 is on the order of or even below one day, suggesting the core of M 87 as the origin of the TeV γ-rays. M 87 is the first radio galaxy that shows evidence for a connection between simultaneously and well sampled radio and VHE flux variations, opening a new avenue for the study of AGN accretion and jet formation [22].

6 Blazars Detected during Optical Outbursts

MAGIC has been performing target of opportunity observations upon high optical states of known or potential VHE γ-ray emitting extragalactic sources. Up to now, this strategy has been proven very successful, with the detection of Mkn 180 [23], 1ES 1011+496 [24], and recently S5 0716+71 [25] (paper in preparation).

In April 2008, KVA observed a high optical state of the blazar S5 0716+71, triggering MAGIC observation, which resulted in a detection of a strong $6.8\,\sigma$ signal, corresponding to a flux of $F_{>400\mathrm{GeV}} \approx 10^{-11}\mathrm{cm}^{-2}\mathrm{s}^{-1}$. The MAGIC observation time was 2.6 h. The source was also in a high X-ray state [26].

The determination of the before-unknown redshifts of 1ES 1011+496 ($z = 0.21$) [24] and S5 0716+71 ($z = 0.31$) [27] makes these objects the third-most and second-most distant TeV blazars after 3C 279, respectively.

7 The region of 3C66A/B

The MAGIC telescope observed the region around the distant blazar 3C 66A for 54.2 h in August–December 2007. The observations resulted in the discovery of a γ-ray source centered at celestial coordinates R.A. = $2^{\mathrm{h}}23^{\mathrm{m}}12^{\mathrm{s}}$ and decl.= $43°0.'7$ (MAGIC J0223+430), coinciding with the nearby radio galaxy 3C 66B [28]. The energy spectrum of MAGIC J0223+430 follows a power law with a normalization of $(1.7 \pm 0.3_{\mathrm{stat}} \pm 0.6_{\mathrm{syst}}) \times 10^{-11}$ TeV^{-1} cm^{-2} s^{-1} at 300 GeV and a photon index $\Gamma = -3.10 \pm 0.31_{\mathrm{stat}} \pm 0.2_{\mathrm{syst}}$. A possible association of the excess with the blazar 3C 66A and nearby radiogalaxy 3C 66B is discussed in these proceedings [29].

8 Detection of the flat-spectrum radio quasar 3C 279

Observations of 3C 279, the brightest EGRET AGN [30], during the WEBT multi-wavelength campaign [31] revealed a $5.77\,\sigma$ post-trial detection on 2006 February 23rd supported by a marginal signal on the preceding night [32]. The overall probability for a zero-flux lightcurve can be rejected on the $5.04\,\sigma$ level. Simultaneous optical R-band observations by the Tuorla Observatory Blazar Monitoring Program revealed that during the MAGIC observations the γ-ray source was in a generally high optical state, a factor of 2 above the long-term baseline flux, but with no indication of short time-scale variability at visible wavelengths. The observed VHE spectrum can be described by a power law with a differential photon spectral index of $\alpha = 4.1 \pm 0.7_{\mathrm{stat}} \pm 0.2_{\mathrm{syst}}$ between 75 and 500 GeV (Fig. 2). The measured integrated flux above 100 GeV on February 23rd is $(5.15 \pm 0.82_{\mathrm{stat}} \pm 1.5_{\mathrm{syst}}) \times 10^{-10}$ photons cm^{-2} s^{-1}.

This detection extends the test on the transparency of the universe up to $z = 0.536$; the γ-ray horizon together with the IACT measurements is shown in Fig. 3 from [32].

VHE observations of such distant sources were until recently impossible due to the expected strong attenuation of γ rays by the EBL, which influences the observed spectrum and flux, resulting in an exponential decrease with energy and a cutoff in the γ-ray spectrum. The reconstructed intrinsic spectrum is difficult to reconcile with models predicting high EBL densities, while low-level models, e.g. [10], are still viable. Assuming a maximum intrinsic photon index of $\alpha^* = 1.5$, an upper EBL limit is inferred, leaving a small allowed region for the EBL.

In Fig. 4 the observed values of the spectral indexes of the blazars detected so far in VHE band are shown, together with the prediction (light grey area) of the standard scenario. The recent findings suggest a higher transparency of the universe to VHE photons than expected from current models of the EBL, and could be interpreted in terms of more exotic scenarios [34].

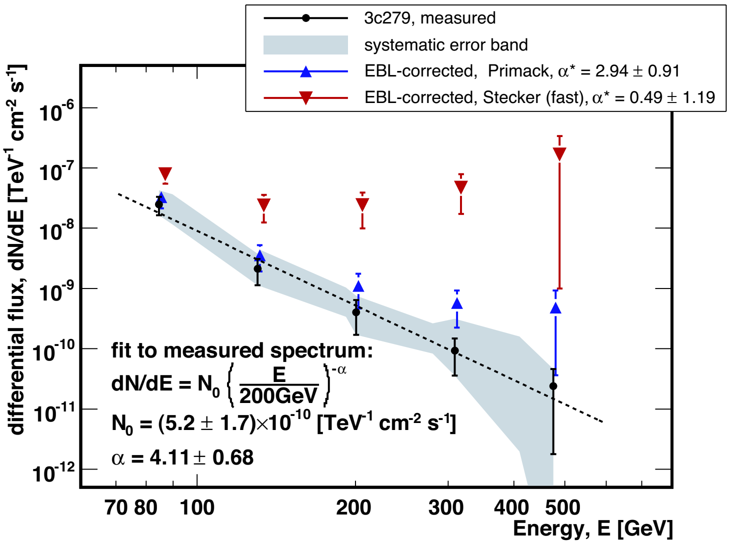

Figure 2: Spectrum of 3C 279 measured by MAGIC. The grey area includes the combined statistical (1σ) and systematic errors, and underlines the marginal significance of detections at high energy. The dotted line shows compatibility of the measured spectrum with a power law of photon index $\alpha = 4.1$. The blue and red triangles are measurements corrected on the basis of the two models for the EBL density.

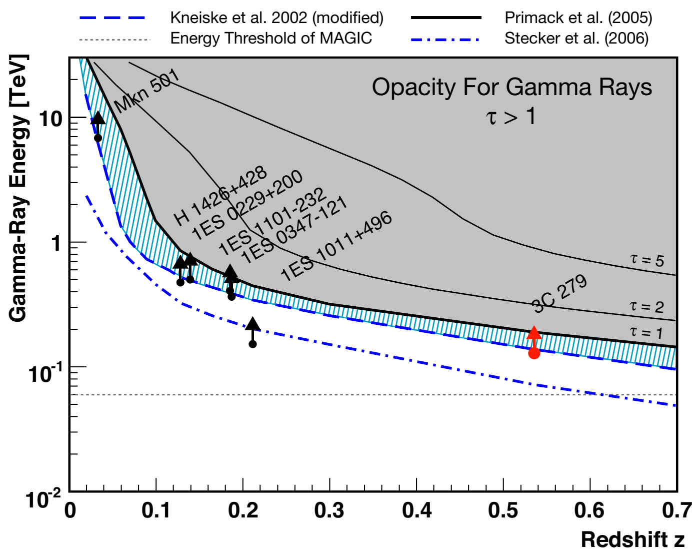

Figure 3: The γ-ray horizon. The redshift region over which it can be constrained by observations has been extended by MAGIC up to z=0.536.

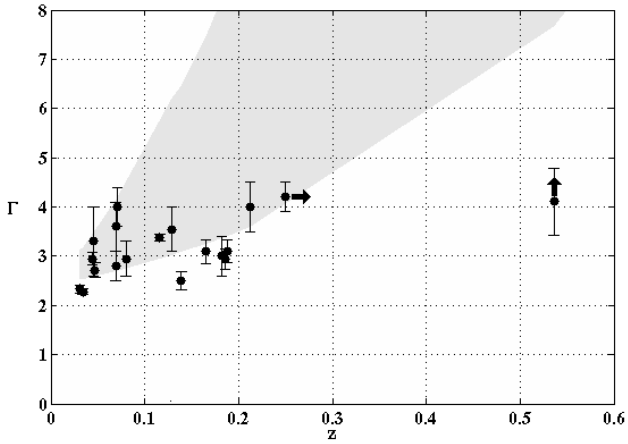

Figure 4: Observed values of the spectral indexes of all the blazars detected so far in VHE band as a function of the redshift; the grey band represents the prediction for different EBL models.

9 The July-2005 Flares of Mkn 501

Mkn 501 ($z = 0.034$) is known to be a strong and variable VHE γ-ray emitter. MAGIC observed Mkn 501 for 24 nights during six weeks in summer 2005. In two of these (one with moon present), the recorded flux exceeded four times the Crab-nebula flux, and revealed rapid flux changes with doubling times as short as 3 minutes or less. For the first time, short ($\approx$ 20 min) VHE γ-ray flares with a resolved time structure could be used for detailed studies of particle acceleration and cooling timescales. In addition, a time delay between different energy bins could be investigated, and gave some hints of a delay of the higher energy photons [35].

An energy-dependent speed of photons in vacuum is expected as a generic signature in some approaches to Quantum Gravity (QG) theories, where Lorentz invariance violation is a manifestation of the foamy structure of space-time at short distances. It could be reflected in modifications of the propagation of energetic particles, i.e. dispersive effects due to a non-trivial refractive index induced by the fluctuations in the space-time foam [38]. The dependence of the speed of light on the energy E of the photon can be parameterized as

$$c' = c\left[1 \pm \left(\frac{E}{E_{\rm S1}}\right) \pm \left(\frac{E}{E_{\rm S2}}\right)^2 \pm ...\right] . \tag{2}$$

The energy scales $E_{\rm S1}$, $E_{\rm S2}$ are usually expressed in units of the Planck mass, $M_P \equiv 1.22 \times 10^{19}$ GeV/c^2. If the linear term dominates, Eq. (2) reduces to

$$c' = c\left[1 \pm \left(\frac{E}{E_{\rm S1}}\right)\right] . \tag{3}$$

A favored way to search for such a dispersion relation is to compare the arrival times of photons of different energies arriving on Earth from pulses of distant astrophysical sources (see [39] for a review).

The reanalysis of the Mkn 501 data in [36] resulted in a much-improved estimate of the time-energy relation. At a zero-delay probability of $P = 0.026$, a marginal time delay of $\tau_l = (0.030 \pm 0.012)\,{\rm s\,GeV^{-1}}$ towards higher energies was found using two independent analyses, both exploiting the full statistical power of the dataset (see [37] for details).

Since it is not possible to exclude that this delay is due to some energy-dependent effect at the source, because the emission mechanisms are not currently understood, a lower limit of $E_{S1} > 0.21 \times 10^{18}$ GeV (95% c.l.) can be established. However, if the emission mechanism

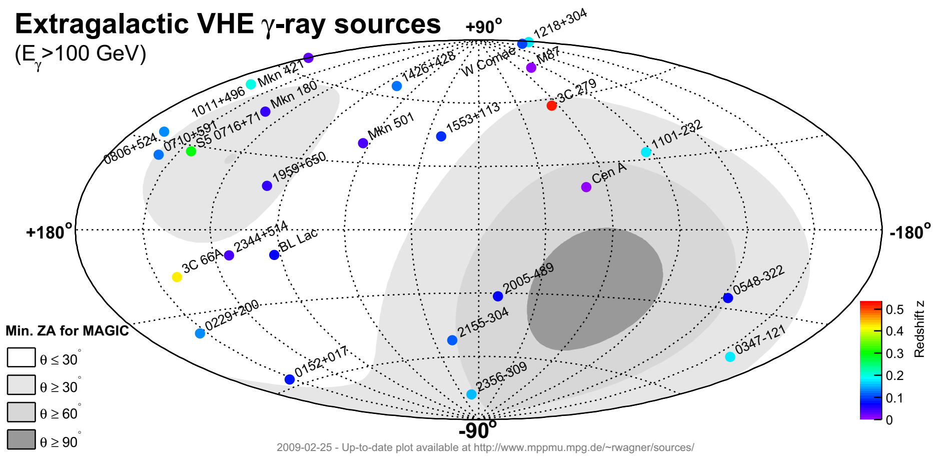

Figure 5: Skymap of extragalactic VHE γ-ray sources together with the MAGIC field of view.

at the source were understood and the observed delays were mainly due to propagation, this number could turn into a real measurement of E_{S1}.

This pioneering study demonstrates clearly the potential scientific value of an analysis of multiple flares from different sources.

10 Conclusions

After almost 4 observation cycles, MAGIC observations of the extragalactic TeV γ-ray sources contributed to many physics insights, confirming the rich potential of VHE γ-ray astrophysics. Among the currently detected 27 VHE γ-ray emitters, MAGIC has discovered 8 new sources, and detected and studied 5 known ones.

In Fig. 5 the skymap of the detected sources, together with the MAGIC field of view [40], is shown (see this reference also for an up-to-date list).

Important contributions to the understanding of active galactic nuclei have been given, allowing both to infer the intrinsic properties of the sources and to probe the nature of photon propagation through cosmic distances.

Acknowledgments

We thank the Instituto de Astrofisica de Canarias for the excellent working conditions at the Observatorio del Roque de los Muchachos in La Palma. The support of the German BMBF and MPG, the Italian INFN, the Spanish MCINN, the ETH Research Grant TH 34/043, the Polish MNiSzW Grant N N203 390834, and the YIP of the Helmholtz Gemeinschaft is gratefully acknowledged.

References

1. A. De Angelis, O. Mansutti, M. Persic, *Nuovo Cimento* **31**, 187 (2008).
2. T.C. Weekes, Proc. Int. Workshop on "Energy Budget in the High Energy Universe", Kashiwa, Japan, Feb. 22-24, (2006).
3. C. Baixeras et al., *Nucl. Instrum. Methods* A **518**, 188 (2004).
4. J. Cortina et al., Proc. 29th ICRC, 4 (2005).
5. E. Aliu et al., *Science* **322**, 1221 (2008).
6. J. Albert et al., *Astrophys. J.* **674**, 1037 (2008).

7. M. Teshima, these Proceedings.
8. W. Heitler, *The Quantum Theory of Radiation* (Oxford: Oxford University Press) (1960).
9. M.G. Hauser and E. Dwek, ARA&A, 39, 249 (2001).
10. F.W. Stecker and S.T. Scully, *Astrophys. J.* **652**, L9 (2006).
T.M. Kneiske, K. Mannheim, D.H. Hartmann, *Astron. Astrophys.* **386**, 1 (2002).
T.M.Kneiske, T. Bretz, K. Mannheim, D.H. Hartmann, *Astron. Astrophys.* **413**, 807 (2004).
J.R. Primack, J.S. Bullock, R.S. Somerville, *High Energy Gamma-Ray Astronomy*, AIP Conference Conference Series, 745, 23 (2005).
F.A. Aharonian et al., *Astron. Astrophys.* **448**, L19 (2006).
T. Stanev, D. De Marco, M.A. Malkan, F.W. Stecker, *Phys. Rev.* D **73**, 04302-2 (2006).
D. Mazin and F. Goebel, *Astrophys. J.* **655**, L13 (2007).
A. Franceschini, G. Rodighiero, M. Vaccari, *Astron. Astrophys.* **487**, 837 (2008).
M. Raue and D. Mazin, *Int. Journ. of Mod. Phys.* D **9**, 17 (2008).
11. G.G. Fazio and F.W. Stecker, *Nature* **226**, 135 (1970).
12. O. Blanch and M. Martinez, *Astrophys. J.* **23**, 598 (2005).
13. K. Mannheim, *Rev. Mod. Astron.* **12**, 167 (1999).
14. I. Donnarumma et al., *Astrophys. J.* **691**, L13 (2009).
15. V.A. Acciari et al., paper in preparation.
16. A. Reimer et al., *Astrophys. J.* **682**, 775 (2008).
17. J. Albert et al., *Astron. Astrophys.* **RN493**, (2009).
18. paper in preparation.
19. G. Tagliaferri et al., *Astrophys. J.* **679**, 1029 (2008).
20. F. Aharonian et al., *Science* **314**, 1424 (2006).
21. J. Albert et al., *Astrophys. J.* **685**, L23 (2008).
22. V.A. Acciari et al., paper in preparation.
23. J. Albert et al., *Astrophys. J.* **648**, L105 (2006).
24. J. Albert et al., *Astrophys. J.* **667**, L21 (2007).
25. M. Teshima, *Astronomer's Telegram* 1500 (2008).
26. P. Giommi et al., *Astronomer's Telegram* 1495 (2008).
27. K. Nilsson et al., *Astron. Astrophys.* **487**, L29 (2008).
28. E. Aliu et al., *Astrophys. J.* **692**, L29 (2009).
29. D. Mazin, these Proceedings.
30. A. E. Wehrle et al., *Astrophys. J.* **497**, 178 (1998).
31. M. Böttcher et al., *Astrophys. J.* **670**, 968 (2008).
32. J. Albert et al., *Science* **320**, 1752 (2008).
33. F. Aharonian et al., *Nature* **440**, 1018 (2006).
34. A. De Angelis, O. Mansutti, M. Persic, M. Roncadelli, Mon. Not. R. Astron. (2009).
35. J. Albert et al., *Astrophys. J.* **669**, 862 (2007).
36. J. Albert et al., *Phys. Lett.* B **668**, 253 (2008).
37. M. Martinez, M. Errando, preprint: arXiv:0803.2120 [astro-ph], submitted.
38. G. Amelino-Camelia, J. Ellis, N.E. Mavromatos, D.V. Nanopulos and S. Sakar, *Nature* **393**, 763 (1998).
39. D. Mattingly, *Living Rev. Rel.* **8**, 5 (2005).
40. R. M. Wagner, http://www.mpp.mpg.de/∼rwagner/sources/.

A First Look at the GeV Excess with Fermi LAT

G. Johannesson for the Fermi LAT collaboration
Stanford University

The Large Area Telescope (LAT), one of two instruments on the Fermi Gamma-ray Space Telescope (formerly GLAST, launched June 11, 2008) is a pair conversion detector designed to study the γ-ray sky in the energy range 20 MeV to $>$ 300 GeV. Fermi LAT has observed the diffuse γ-ray emission from the Galaxy with unprecedented statistics, angular and energy resolution. This provides essential information on the origin and propagation of cosmic rays, Galactic structure and the interstellar medium. We will show that the spectra of the diffuse Galactic emission at intermediate latitudes can be explained by cosmic-ray propagation models based on local observation of cosmic-ray electron and nuclei spectra. Thus the all-sky GeV excess observed by EGRET is not confirmed.

1 Introduction

The diffuse Galactic γ-ray emission (DGE) is due to interactions of cosmic-rays (CRs) with the interstellar radiation field and gas in the Galaxy. The γ-rays are produced through three main processes: inverse Compton (IC) scattering of interstellar photons, bremsstrahlung radiation and π^0-decay after production of π^0 in proton-nuclei interactions. The DGE is currently our only probe of CR fluxes in distant locations, is a complementary probe of gas density in the Galaxy, and can contain clues about physics beyond the Standard Model. It is also a very bright background for point sources and can influence determination of their positions and fluxes. The DGE is also a foreground to the fainter extragalactic γ-ray background (EGB).

Even though the DGE is produced by well-known processes, modeling it accurately is a non-trivial task. Knowledge of CR sources in the Galaxy is required, both their injection spectra and their spatial distribution [1]. Those CRs then have to be followed as they diffuse through the Galaxy, with the relevant energy losses and gains taken into account. To calculate the DGE, the CR distribution is folded with the interstellar gas and radiation field. The gas distribution is currently obtained from observation of the 21-cm spectral line of HI [2] and the 2.6-mm line of CO [3]. The interstellar radiation field is modeled using knowledge of stellar and dust distributions in the Galaxy [4]. All of this requires analysis of data from a broad range of astronomical and astroparticle instruments.

The CR intensity and spectra do not vary significantly within $\sim$ 1 kpc of the Sun so the nearby CR spectra should be similar to those observed locally. And since the scale height of the atomic gas in the Galaxy is $\sim$ 200 pc [5], most of the observed gas structures at intermediate and high Galactic latitudes are local. The DGE in the same latitude range can then be predicted from directly observed quantities of cosmic-ray fluxes and gas column densities. The contribution from IC scattering is not local in this regime, owing to the large ($\sim$ 1 kpc) scale height of CR electrons, but it is a minor component around 1 GeV.

Observations made with the Energetic Gamma-Ray Experiment Telescope (EGRET) instrument on the *Compton Gamma-Ray Observatory (CGRO)* satellite showed a clear excess in the observed emission around 1 GeV compared to DGE models based on local observations of CRs[6,7]. This effect was seen in all directions of the sky, including intermediate and high latitudes where the DGE is most straightforward to model. Explanations for this excess included everything from instrumental effects[8,9] to strong local variations in the cosmic-ray density[10,11,12] to emission from dark matter annihilation[13].

In this paper we will show that observations with the LAT[14] of the DGE in the latitude range $10^\circ < |b| < 20^\circ$ do not show this excess around 1 GeV. This region was chosen for study to maximize the signal of local DGE compared to both the isotropic component (composed of both true EGB and residual charged particle background) and DGE from further away in the Galaxy. We show that the LAT observations are consistent with models based on observations of local cosmic-rays and the full-sky nature of the EGRET GeV excess is not confirmed. A more detailed analysis of this region is presented elsewhere[15].

2 LAT Data Preparation

The LAT[14] is an electron/positron pair-production telescope featuring solid state silicon trackers and a segmented calorimeter for accurate energy measurements; it is sensitive to photons from ~ 20 MeV to > 300 GeV. It has a large $\sim$2.4 sr field of view with an on-axis effective area ~ 7000 cm^2 above ~ 1 GeV for the event selection used in this paper, for an acceptance approximately 30 times greater than EGRET. The point spread function (PSF) has a 68% containment radius of 3.5° at 100 MeV, improving to better than 1° at 1 GeV and $\sim 0.2^\circ$ at 10 GeV. Energy resolution is $\sim 15\%$ or better over the energy range considered in this paper (100 MeV to 10 GeV). The LAT normally operates in a scanning mode that surveys the whole sky every two orbits (i.e., $\sim$3 h). The improved sensitivity of the LAT, uniform and deep sky coverage, good energy resolution, and lack of consumables, provide for an exceptionally stable instrument allowing long-period studies of the γ-ray flux over large regions of the sky.

We are using 5 months worth of survey data from the LAT gathered from the beginning of August to end of December 2008. We use the most conservative classification cuts available in the standard Fermi LAT analysis, the diffuse class. This eliminates most particle background in the dataset. To reduce the effect of the earth albedo, only events coming from zenith angles $< 105^\circ$ are considered. To further reduce earth albedo, we exclude all events when the Earth was appreciably within the field of view (specifically, when the satellite is pointing more than 47° from the zenith). The exposure is calculated using the standard science tools for Fermi LAT analysis, using first post launch refinement of the instrument response, referred to as pass 6 v3. The systematic uncertainties on the effective area, evaluated by comparing the efficiencies of analysis cuts for data and simulation of observations of Vela, are energy dependent: 10% below 100 MeV, decreasing to 5% at 560 MeV, and increasing to 20% at 10 GeV and above. These are incorporated in the intensities and fluxes discussed below.

3 Analysis

Figure 1 shows the LAT data for all Galactic longitudes in the latitude range $10^\circ \le |b| \le 20^\circ$, along with EGRET data and a model from the same region. The LAT photon data is binned in energy with 5 bins per decade from 100 MeV to 10 GeV, evenly distributed logarithmically. The intensity was obtained by dividing the in-bin counts with a spectrally weighted exposure for that bin. Because the bins are relatively narrow, it was sufficient to use a power-law with an index of -2, even in the cases where the LAT effective area is strongly dependent on energy($\lesssim 500$ MeV). We are dominated by systematic error in this analysis; the statistical uncertainty is smaller

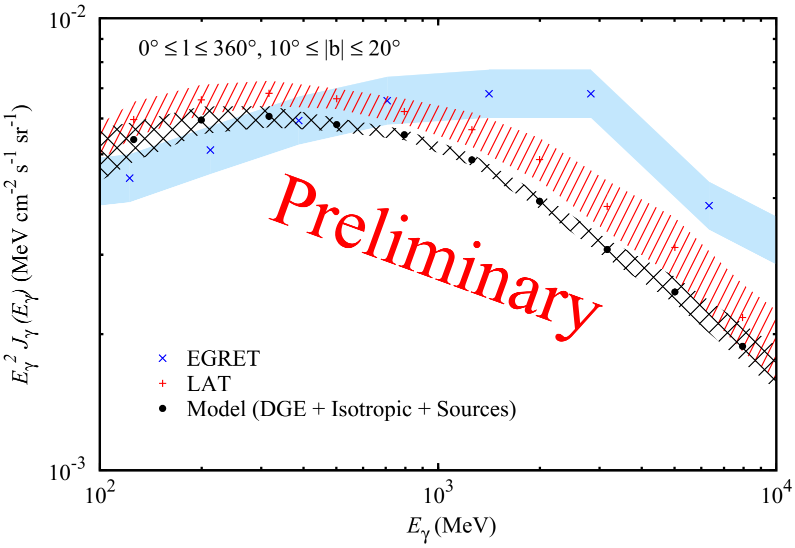

Figure 1: LAT spectrum averaged over all Galactic longitudes and latitude range $10° \le |b| \le 20°$ (plus-signs and striped region for systematic uncertainty), Also shown are the EGRET data for the same region of the sky (x-signs and solid region for systematic uncertainty). Overlaid on the data is a model composed of an a priori DGE model based on local observations of CRs, as well as a source component and an isotropic component that are determined from the LAT data (solid-rectangles and hatched region for systematic uncertainty). The model is therefore not directly compatible with the EGRET data; see text for more details. Statistical errors are less than the point size in all cases.

than the point size in figure 1. The EGRET data are derived from count maps and exposures available via the *CGRO* Science Support Center [a], processed following the procedure described in [12]. We have included the standard EGRET systematic error (13%[16]).

The model includes 3 components: DGE, an isotropic component, and point-source contribution. The DGE is fixed to an a priori CR propagation model that is an updated version of the "conventional" model from GALPROP [12,4]. Major improvements include use of a new formalism for pion production [17], a complete re-calculation of the interstellar radiation field [4], updated gas maps, and an improved line-of-sight integration routine. The source positions are taken from the 3 month Fermi LAT source list[18], although we use the LAT-internal source list going down to 5-σ. The point-source spectra were fit in a global scheme with a varying isotropic component and the fixed a priori DGE model to determine their contribution. The isotropic component contains both the true extragalactic diffuse emission, as well as residual particle background. It is determined from a fit to the LAT data using a high latitude region $|b| \ge 30°$ and all longitudes. This minimizes contamination by the significantly brighter Galactic ridge region. The a priori DGE model as well as the source contribution were included in the fit, but fixed to their initial values. The systematic uncertainty of the model shown in the figure only takes into account the contribution from the uncertainty of the effective area when determining the isotropic and point-source components.

4 Conclusion

Using the first 5 months of LAT science data we have shown that the GeV excess seen by EGRET in the latitude range $10° \le |b| \le 20°$ is not confirmed. The spectral shape of the data is adequately explained with a CR propagation model consistent with locally observed CR

[a] http://heasarc.gsfc.nasa.gov/docs/cgro/egret/

spectra. However, the model systematically underestimates the observed flux leaving room for improvement in the DGE model, both in the CR propagation part, as well as the gas distribution and the interstellar radiation field. Improved understanding of the instrument response and further development of our modeling will provide new insight into the DGE emission and origin and propagation of CRs in the Galaxy.

Acknowledgments

The *Fermi* LAT Collaboration acknowledges generous ongoing support from a number of agencies and institutes that have supported both the development and the operation of the LAT as well as scientific data analysis. These include the National Aeronautics and Space Administration and the Department of Energy in the United States, the Commissariat à l'Energie Atomique and the Centre National de la Recherche Scientifique / Institut National de Physique Nucléaire et de Physique des Particules in France, the Agenzia Spaziale Italiana and the Istituto Nazionale di Fisica Nucleare in Italy, the Ministry of Education, Culture, Sports, Science and Technology (MEXT), High Energy Accelerator Research Organization (KEK) and Japan Aerospace Exploration Agency (JAXA) in Japan, and the K. A. Wallenberg Foundation, the Swedish Research Council and the Swedish National Space Board in Sweden.

Additional support for science analysis during the operations phase from the following agencies is also gratefully acknowledged: the Istituto Nazionale di Astrofisica in Italy.

References

1. A. W. Strong, I. V. Moskalenko, and V. S. Ptuskin. Cosmic-Ray Propagation and Interactions in the Galaxy. *Annual Review of Nuclear and Particle Science*, 57:285–327, November 2007.
2. P. M. W. Kalberla, W. B. Burton, D. Hartmann, E. M. Arnal, E. Bajaja, R. Morras, and W. G. L. Pöppel. The Leiden/Argentine/Bonn (LAB) Survey of Galactic HI. Final data release of the combined LDS and IAR surveys with improved stray-radiation corrections. *Astron. & Astrophys.*, 440:775–782, September 2005.
3. T. M. Dame, D. Hartmann, and P. Thaddeus. The Milky Way in Molecular Clouds: A New Complete CO Survey. *Astrophys. J.*, 547:792–813, February 2001.
4. T. A. Porter, I. V. Moskalenko, A. W. Strong, E. Orlando, and L. Bouchet. Inverse Compton Origin of the Hard X-Ray and Soft Gamma-Ray Emission from the Galactic Ridge. *Astrophys. J.*, 682:400–407, July 2008.
5. P. M. W. Kalberla, L. Dedes, J. Kerp, and U. Haud. Dark matter in the Milky Way. II. The HI gas distribution as a tracer of the gravitational potential. *Astron. & Astrophys.*, 469:511–527, July 2007.
6. S. D. Hunter, et al. EGRET Observations of the Diffuse Gamma-Ray Emission from the Galactic Plane. *Astrophys. J.*, 481:205–+, May 1997.
7. A. W. Strong, I. V. Moskalenko, and O. Reimer. Diffuse Continuum Gamma Rays from the Galaxy. *Astrophys. J.*, 537:763–784, July 2000.
8. B. M. Baughman, W. B. Atwood, R. P. Johnson, T. A. Porter, and M. Ziegler. A Fresh Look at Diffuse Gamma-ray Emission from the Inner Galaxy. *ArXiv e-prints*, June 2007.
9. F. W. Stecker, S. D. Hunter, and D. A. Kniffen. The likely cause of the EGRET GeV anomaly and its implications. *Astroparticle Physics*, 29:25–29, February 2008.
10. T. A. Porter and R. J. Protheroe. Cosmic-ray electrons and the diffuse gamma-ray spectrum. *Journal of Physics G Nuclear Physics*, 23:1765–1784, November 1997.
11. M. Pohl and J. A. Esposito. Electron Acceleration in Supernova Remnants and Diffuse Gamma Rays above 1 GeV. *Astrophys. J.*, 507:327–338, November 1998.

12. A. W. Strong, I. V. Moskalenko, and O. Reimer. Diffuse Galactic Continuum Gamma Rays: A Model Compatible with EGRET Data and Cosmic-Ray Measurements. *Astrophys. J.*, 613:962–976, October 2004.
13. W. de Boer, C. Sander, V. Zhukov, A. V. Gladyshev, and D. I. Kazakov. EGRET excess of diffuse galactic gamma rays as tracer of dark matter. *Astron. & Astrophys.*, 444:51–67, December 2005.
14. W. B. Atwood, et al. The Large Area Telescope on the Fermi Gamma-ray Space Telescope Mission. *ArXiv e-prints*, February 2009.
15. A. A. Abdo, et al. Fermi LAT measurements of the diffuse gamma-ray emission at Galactic latitudes $10^\circ \leq |b| \leq 20^\circ$. *ArXiv e-prints*, May 2009.
16. J. A. Esposito, et al. In-Flight Calibration of EGRET on the Compton Gamma-Ray Observatory. *Astrophys. J. Supp.*, 123:203–217, July 1999.
17. T. Kamae, N. Karlsson, T. Mizuno, T. Abe, and T. Koi. Parameterization of γ, $e^{+/-}$, and Neutrino Spectra Produced by p-p Interaction in Astronomical Environments. *Astrophys. J.*, 647:692–708, August 2006.
18. A. A. Abdo, et al. Fermi Large Area Telescope Bright Gamma-ray Source List. *ArXiv e-prints*, February 2009.

The VERITAS Extragalactic Observation Program

Wystan Benbow for the VERITAS Collaboration[a]
Harvard-Smithsonian Center for Astrophysics
60 Garden St, Cambridge, MA 02138, USA

Over the past seven years remarkable progress has been made in Very High Energy (VHE; E>100 GeV) γ-ray astrophysics. The VHE source catalog has increased from only $\sim$10 sources to more than 80 sources belonging to a wide variety of source classes, and includes $\sim$25 extragalactic objects. The Very Energetic Radiation Imaging Telescope Array System (VERITAS) is currently the world's most sensitive detector of astrophysical VHE γ-rays. It has observed more than 60 extragalactic objects, primarily blazars. Highlights from the VERITAS extragalactic observation program, including several VHE source discoveries, are presented.

VERITAS, a stereoscopic array of four 12-m atmospheric-Cherenkov telescopes located in Arizona, is used to study VHE γ-rays from a variety of astrophysical sources [1]. VERITAS began scientific observations with a partial array in September 2006 and has routinely observed with the full array since September 2007. The performance metrics of VERITAS include an energy resolution of $\sim$15%, an angular resolution of $\sim$0.1°, and a sensitivity yielding a 5σ detection of a 1% Crab Nebula flux object in <50 hours. VERITAS is currently the most sensitive VHE observatory in the world, and it has an active maintenance program (e.g. frequent mirror recoating) to ensure its continued high performance over time. A VERITAS telescope will be relocated during the 2009 summer monsoons, increasing the array's sensitivity by a factor $\sim$1.2.

VERITAS is operating routinely and observes for $\sim$750 h and $\sim$250 h each year during periods of astronomical darkness and partial moonlight, respectively. A large fraction of the VERITAS observation budget is devoted to extragalactic targets. While the focus of the extragalactic program is active galactic nuclei (AGN), specifically blazars, significant observation time is also given to other extragalactic classes. These include starburst and ultra-luminous galaxies, galaxy clusters, gamma-ray bursts, and dark-matter dominated objects.

1 The Blazar Key Science Project

There are currently $\sim$25 AGN known to emit VHE γ-rays. All of these are radio-loud AGN, which are those that possess collimated, relativistic jets emanating from a central super-massive ($\sim 10^9$ solar mass) black hole. VHE γ-rays are believed to be created by these jets in a compact region very near the event horizon of the black hole. All but two VHE AGN are blazars, a class of AGN where a jet is pointed along the line of sight to Earth, causing the jet emission to be relativistically beamed. Almost 80% of the known VHE blazars are high-frequency-peaked BL Lac objects (HBL), and these are the primary targets of the blazar program. Several intermediate- (IBL) and low-peaked (LBL) objects detected at MeV-GeV energies, and several FSRQs are also included in the program. In total $\sim$50 candidates have been observed ($\sim$7 h average exposure).

[a] http://veritas.sao.arizona.edu/conferences/authors?moriond2009

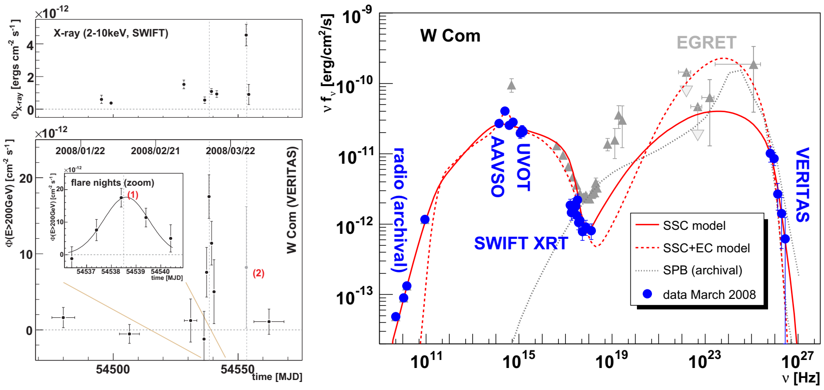

Figure 1: **Left** X-ray and VHE light curve from W Comae in early 2008. **Right** SED of W Comae.

The HBL 1ES 0806+524 ($z = 0.138$) received a 65 h exposure with VERITAS between 2006 and 2008, largely during the instrument's commissioning. Analysis of these data resulted in the discovery of VHE emission [2]. The observed excess (245 events, 6.3 standard deviations) from 1ES 0806+524 is point-like and corresponds to a flux of 1.8% of the Crab Nebula flux above 300 GeV. The measured photon spectrum is well-described by a soft power-law function with photon index $\Gamma = 3.6 \pm 1.0_{\rm stat} \pm 0.3_{\rm syst}$. The SED of 1ES 0806+524 generated from two Swift (XRT & UVOT) observations during the VERITAS exposure can be reasonably described using a synchrotron-self-Compton (SSC) model.

The VERITAS collaboration discovered VHE γ-ray emission from the HBL RGB J0710+591 ($z = 0.125$) during the conference (ATel #1941). This new VHE source was observed for ~20 h, and a preliminary analysis of these data yields a detection of ~140 γ-rays (>6σ excess). The observed VHE flux is constant at a level of ~2% of the Crab Nebula flux. A publication is in preparation that includes contemporaneous data from the Swift and Fermi satellites.

VHE γ-ray emission from the IBL W Comae ($z = 0.102$) was discovered by VERITAS in 2008 [3]. Although the source was observed (~40 h exposure) between January and April 2008, 70% (~275 γ-rays, 8.4σ) of the observed γ-rays were measured during a strong four-day outburst in the middle of March (see Figure 1). During the two brightest nights of the flare the observed flux is ~9% of the Crab Nebula flux above 200 GeV, and the measured photon spectrum is characterized by a soft power-law ($\Gamma = 3.81 \pm 0.35_{\rm stat} \pm 0.34_{\rm syst}$). Quasi-simultaneous Swift observations (XRT & UVOT) during the flare are used to generate the SED shown in Figure 1. These multi-wavelength (MWL) data can be described by SSC or external-Compton (EC) models. However, the latter yields a more natural set of fit parameters. W Comae is the first IBL known to emit VHE γ-rays, and it will be interesting to see if other VHE IBL (e.g. 3C 66A) also indicate a significant EC component.

A second VHE flare was observed from W Comae in June 2008 (ATel #1582). The flux during this two-day flare is ~3 times brighter than the first flare. During this episode contemporaneous MWL observations were made with Swift, AGILE and XMM-Newton. The VERITAS results and interpretation of the resulting SED will be the subject of a future publication.

VERITAS detected an excess of 1791 events (21.2σ) from another IBL 3C 66A during observations in 2007 and 2008 (5 h and 28 h live time, respectively) [4]. The average VHE flux is 6% of the Crab Nebula's flux above 200 GeV, and like W Comae, the VHE flux (see Figure 2) shows evidence for variability on the time-scale of days. The photon spectrum measured by VERITAS is well-fit by a soft power law ($\Gamma = 4.1 \pm 0.4_{stat} \pm 0.6_{sys}$), and does not agree with the MAGIC observation ($\Gamma = 3.1 \pm 0.3$). The catalog redshift of 3C 66A is $z = 0.444$, however this value is considered questionable [5]. If the catalog redshift is accurate, 3C 66A would represent the second most distant VHE blazar detected, and much of spectral softness (intrinsic $\Gamma_{\rm int} \sim 1.1$) would be due to the attenuation of VHE photons on the Extragalactic Background Light (EBL).

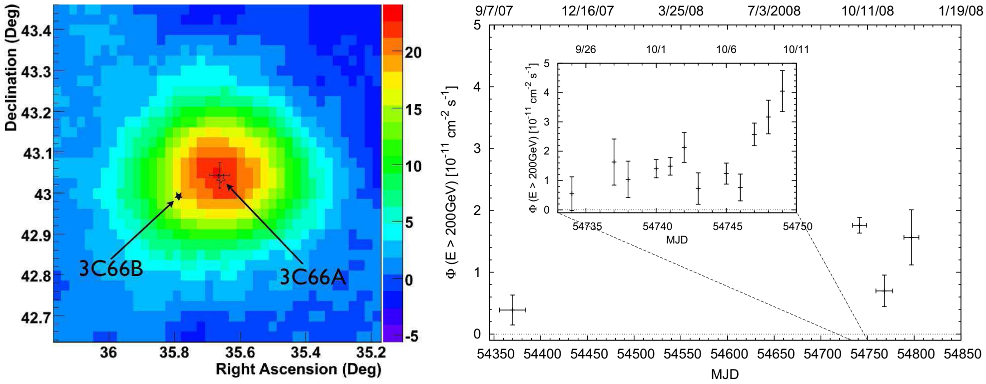

Figure 2: **Left** VERITAS sky map of the 3C 66A/B region. **Right** VHE light curve from 3C 66A.

Interestingly 3C 66A is very close (∼0.1° separation) to the radio galaxy 3C 66B (see Figure 2). As a result, there are potential issues with the identification of the VHE source. The MAGIC collaboration report VHE emission from the 3C 66A/B region in 2007 and claim marginal evidence (85% probability) for a positional association with 3C 66B [6]. In contrast, the fit position of the VERITAS excess excludes (at the 4.3σ level) the radio galaxy 3C 66B as a possible source of the VHE emission. However, it is possible that both 3C 66A and 3C 66B are variable VHE sources and the VERITAS / MAGIC detections result from different phenomena.

During the VHE flare (see Figure 2) the LAT instrument onboard the Fermi satellite also observed bright MeV-GeV γ-ray emission from 3C 66A (ATel #1759). In addition, several observations (5 satellite pointings) of the blazar were made with Swift (XRT & UVOT), and a single ∼40 ksec exposure was taken with the Chandra X-ray satellite. Analysis and modeling of these MWL observations will be the subject of a future publication.

The VERITAS blazar program also contains pre-planned and target-of-opportunity (ToO) MWL observation campaigns on known VHE blazars. For the ToO component, proposals triggered by either a VERITAS discovery or a Whipple 10-m flaring alert are submitted each year to major X-ray, optical and radio observatories. Several examples of discovery-initiated campaigns are described above. In 2008, the Whipple 10-m telescope detected an extended flaring episode (>2 Crab) from the HBL Mkn 421 ($z = 0.030$), and an alert (ATel #1506) was issued to the community. Deep ToO observations with VERITAS (∼40 h) were performed, during which more than 30000 γ-rays ($>280\sigma$) were detected. The flux observed by VERITAS ranged from 0.3 to 10 Crab. Deep contemporaneous MWL observations (with, e.g., Swift and RXTE) show a highly significant correlation between the X-ray and VHE flux, as well as spectral hardening with increased flux in both bands [7]. The VERITAS MWL campaign on the HBL 1ES 2344+514 (z=0.044) in 2007-08 is an excellent example of the pre-planned component [8]. Here, VERITAS observations (∼20 h) were scheduled over a 4-month period, along with contemporaneous Swift (XRT & UVOT) and RXTE coverage. During this campaign, the source was routinely detected (∼20σ total) in a low-flux, but weakly variable, state (8% Crab). However, VHE flaring was observed in December 2008 with one night reaching a peak flux of ∼50% Crab, the brightest VHE output observed since the source's discovery. Similar to Mkn 421, a strong VHE/X-ray flux correlation is observed as well as spectral hardening with increased flux in both bands. The MWL observations enable an SED measurement in both high- and low-flux states; both are well-described by an SSC model. VERITAS also has an active program to measure the EBL via deep observations of distant VHE blazars (see, e.g., 1ES 1218+304 [9]; $z = 0.182$).

2 Other Source Classes

Radio galaxies are AGN with jets that are not pointed towards the observer. Two, M 87 and Cen A, are currently known to emit VHE γ-rays. VERITAS has routinely monitored the VHE flux of M 87 and has performed discovery observations on several other radio galaxies (e.g. 3C 111). The VERITAS monitoring of M 87 revealed a low, constant-flux state in 2007 [10] and bright day-scale flaring state in 2008[11], similar to that observed by HESS in 2005. In 2008, the VERITAS observations were made as part of a coordinated campaign with the MAGIC and HESS instruments [11]. The highlight of this campaign is the apparent correlation of X-ray brightening in the core of M 87 with the VHE flaring, while sub-structures (knots) further out in the jet remained at a constant X-ray flux. This observation indicated that the VHE γ-ray production occurs very close to the central supermassive black hole.

Nearby starburst galaxies and ultra-luminous infrared galaxies (ULIRG) have high rates of supernova (SN) explosions, and also contain large, exceptionally dense gas clouds. This combination creates nearly ideal conditions for the generation of intense, diffuse VHE radiation, assuming that efficient hadronic cosmic-ray production takes place in the sites of the SN. VERITAS has a strong starburst galaxy (& ULIRG) observation program. The first phase of this program, a large ($\sim$100 h) exposure on M 82, is nearing completion. In future years, other starburst and ULIRG galaxies will be observed with more moderate ($\sim$25 h) exposures.

Galaxy clusters are the largest gravitationally bound objects in the Universe and the possibility of observing diffuse GeV and TeV radiation from them is widely discussed in the literature. This radiation could be produced either via standard non-thermal acceleration mechanisms or the self-annihilation of dark matter particles. VERITAS has observed the Coma ($\sim$20 h; $\sim$1% Crab limit; [13]) and Perseus ($\sim$10 h) clusters, and will observe other clusters in future seasons.

Many afterglow emission models predict a blazar-like SED for gamma-ray bursts (GRBs), implying that GRBs may produce detectable levels of VHE emission. VERITAS receives a GCN notice within seconds of a satellite's GRB detection. Whenever possible, VERITAS follow-up observations are carried out on all GRBs which are less than 3 h old and above 20° elevation. The VERITAS response time (i.e. start of on-source data taking) to a GRB alert is limited by the slewing speed of the telescopes, and is typically a few minutes, with the fastest being $\sim$90 seconds. VERITAS has observed $\sim$20 GRB afterglows, all resulting in VHE upper limits.

The indirect detection of cold dark matter (CDM), via the detection of VHE emission from the large-scale self-annihilation of CDM particles, is one of the VERITAS Key Science Projects. As there is considerable uncertainty associated with both the particle-physics and astrophysical aspects of dark matter, the VERITAS indirect CDM detection program ($\sim$50 h / year) includes VHE studies of several classes of astrophysical objects that are believed to be dark-matter dominated and may harbor dense dark-matter cores. These classes include dwarf galaxies (the primary focus), Local Group galaxies, globular clusters, and galaxy clusters. Objects from all these classes have been observed by VERITAS, resulting in VHE flux limits [11].

Acknowledgments

This research was supported by grants from the U.S. Department of Energy, the U.S. National Science Foundation and the Smithsonian Institution, by NSERC in Canada, by Science Foundation Ireland and by STFC in the UK.

References

1. J. Holder, et al., AIPC **1085**, 657 (2008).
2. V. Acciari, et al., ApJ **690**, L26 (2009).
3. V. Acciari, et al., ApJ **684**, L73 (2008).
4. V. Acciari, et al., ApJ **693**, L104 (2009).
5. J.D. Finke, et al., A&A **477**, 513 (2008).
6. E. Aliu, et al., ApJ **692**, L29 (2009).
7. L.C. Reyes, AIPC **1085**, 581 (2008).
8. J. Grube, AIPC **1085**, 585 (2008).
9. V. Acciari., et al., ApJ **695**, 1370 (2009).
10. V. Acciari, et al., ApJ **679**, 397 (2007).
11. C.M. Hui, AIPC **1085**, 407 (2008).
12. F. Aharonian, et al., Science **314**, 1424 (2006).
13. J.S. Perkins, AIPC **1085**, 569 (2008).

New Insight into Gamma-ray Blazars from the Fermi-LAT

B. Lott on behalf of the Fermi-LAT collaboration
CNRS/IN2P3, Université de Bordeaux, Centre d'Etudes Nucléaires Bordeaux Gradignan, UMR 5797, Gradignan, 33175, France

The first three months of sky-survey operation with the Large Area Telescope (LAT) on board the *Fermi* satellite reveal 132 bright sources at $|b| > 10°$ with test statistic greater than 100 (corresponding to about 10σ). Two methods, based on the CGRaBS, CRATES and BZCat catalogs, indicate high-confidence associations of 106 of these sources with known AGNs. This sample is referred to as the LAT Bright AGN Sample (LBAS). It contains two radio galaxies, namely Centaurus A and NGC 1275, and 104 blazars consisting of 58 flat spectrum radio quasars (FSRQs), 42 BL Lac objects, and 4 blazars with unknown classification. Remarkably, the LBAS includes 10 high-energy-peaked BL Lacs (HBLs). Only 33 of the sources, plus two at $|b| < 10°$, were previously detected with *EGRET*, probably due to variability. The analysis of the γ-ray properties of the LBAS sources reveals that the average GeV spectra of BL Lac objects are significantly harder than the spectra of FSRQs. Blazar $\log N - \log S$ distributions and luminosity functions enable us to investigate the evolution of the different blazar classes, with positive evolution indicated for FSRQs but none for BL Lacs.

1 Introduction

One of the legacies of EGRET was to demonstrate that, although blazars represent only a minority of active galaxies, they dominate the extragalactic high-energy sky. Blazars are characterized by powerful non-thermal emission ranging from radio to the gamma-ray bands and exhibit strong variability, over a variety of time scales from minutes to months. These properties are interpreted as resulting from the emission of high-energy particles accelerated within a relativistic jet aligned with the direction of sight and launched in the vicinity of the supermassive black hole harbored by the active galaxy. Blazars exhibit a characteristic bimodal spectral energy distribution (SED). Different classes of blazars: flat spectrum radio quasars, (FSRQs), low-frequency peaked BLLacs (LBLs), high-frequency peaked BLLacs (HBLs), can be defined depending on the presence and strength of emission lines and the position of the SED peaks. The Third *EGRET* Catalog of high-energy γ-ray sources [1] contains 66 high-confidence blazars, with $\sim$77% identified as FSRQs and the remaining $\sim$23% identified as BL Lac objects.

The recent launch of the Fermi satellite opens the exciting possibility of greatly improving our knowledge and understanding of these spectacular objects. We report here on the first results regarding AGNs obtained with 3 months worth of data. More details can be found in ref. [2].

2 The LAT Bright AGN Sample (LBAS)

Fermi's main instrument, the Large Area Telescope (LAT), offers a large field of view (2.4 sr) and an unprecedented sensitivity. It surveys the whole sky every three hours. After 6 months

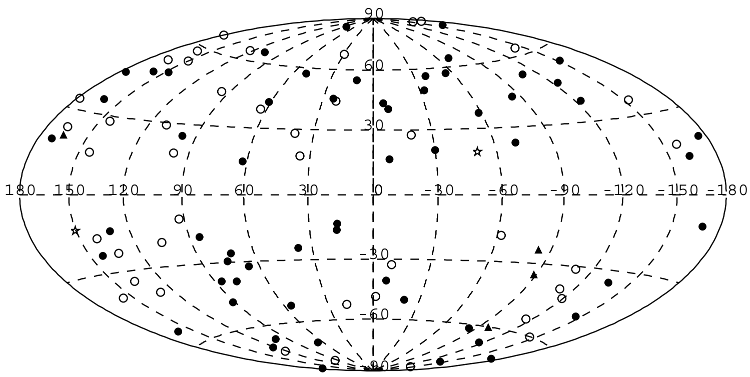

Figure 1: Locations of the LBAS sources. Filled circles: FSRQs; open circles: BL Lacs; triangles: blazars of unknown type; stars: radio galaxies.

in operation, a list of 205 bright (significance greater than 10 σ) sources has been released[3]. Of these, 132 are located at $|b| > 10°$, with 7 being pulsars with detected pulsations. Two methods, based on the CGRaBS-CRATES[4] and BZCat[5] catalogs, indicate high-confidence (Prob.> 90%) associations of 106 of these sources with known AGNs, as well as 11 additional lower-confidence associations. Only 8 bright sources remain unidentified at at $|b| > 10°$. The 106 sources with high-confidence associations with known AGNs constitute the LAT Bright AGN sample (LBAS). The LBAS comprises 58 FSRQs, 42 BL Lac objects, 2 radio galaxies, and 4 AGNs of unknown type. The location of these sources is shown in Fig. 1. BL Lac objects make up about 40% of the LBAS, a fraction much higher than observed for *EGRET* (23%). This feature most probably arises from the different instrumental responses of the two instruments. The LAT flux limit depends fairly strongly on the photon index (Fig. 2), so hard sources as BLLacs can be detected at lower fluxes than softer ones (FSRQs). A clear spectral separation is found between BL Lacs and FSRQs in the GeV γ-ray band, with FSRQs having significantly softer spectra. than BLLac objects (Fig. 3). This confirms earlier indications of the existence of spectrally distinct populations in the *EGRET* blazar sample. The average photon index is 1.99 ± 0.22 (rms) for BL Lacs, with a tendency for the HBLs to display even harder spectra, and 2.40 ± 0.17 (rms) for FSRQs. A KS test gives a probability of 2×10^{-12} that the two index samples are drawn from the same parent distribution. Spectra of some bright sources show clear sign of break/curvature.

The number of HBLs in the LBAS detected at GeV energies has risen to at least 10 (out of 42 BL Lacs) as compared to one (out of 14 BL Lacs) detected by *EGRET*, a remarkable improvement. Twelve LBAS sources are know TeV sources, representing more than 50% of the TeV blazars detected so far (21). Many of the others have been detected with a significance lower than TS = 100. The two radio-galaxies are Cen A, already detected by *EGRET* and whose detection by H.E.S.S. was announced at this conference, and NGC 1275, a peculiar radio-galaxy exhibiting many BLLac-like properties. The observed NGC1275 flux is about 8 times greater than the *EGRET* upper limit, indicating a variability time scale of a few years or less.

Only ~30% of the LBAS AGNs were also detected by *EGRET* at a comparable flux. This may be a consequence of the duty cycle and variability of GeV blazars. With ~70% of sources not previously detected in the GeV domain, the LBAS is almost a totally fresh sample.

The mean flux distribution of the *Fermi* AGNs remains similar to the corresponding one based on the *EGRET* sample while the peak flux distributions differ appreciably. This feature probably arises from the shorter sampling period for the LAT as compared to *EGRET*. In the 3-

month period considered here, a given source had much less opportunity to explore very different states than in the 4.5 years over which the *EGRET* observations were conducted.

Fermi FSRQs in the bright source list are on average more luminous and more distant than the BL Lac objects in the list; i.e., FSRQs exhibit a broad redshift distribution, starting with $z = 0.158$ (3C 273), peaking at $z \approx 1$, and extending up to $z \approx 3$ while BL Lacs are mostly found in the $z \sim 0.1$ redshift bin with a tail extending up to $z \approx 1$. No significant relation between the γ-ray photon index and redshift is found within either source class, in agreement with corresponding studies based on the *EGRET* AGN samples.

3 $\log N - \log S$ and luminosity function

Using mean fluxes, the $\log N - \log S$ distribution of all the bright sources (except the pulsars) appears compatible with a Euclidean distribution without any breaks. This is also true within 1σ for the source counts distributions of the individual FSRQ and BL Lac samples. The combined emission in the flux range $F_{100,\,\mathrm{mean}} \approx (7-10) \times 10^{-8}$ photons cm^{-2} s^{-1} observed from individually resolved AGN during this 3-month period already corresponds to $\sim$7% of the *EGRET*-detected extragalactic diffuse γ-ray background.

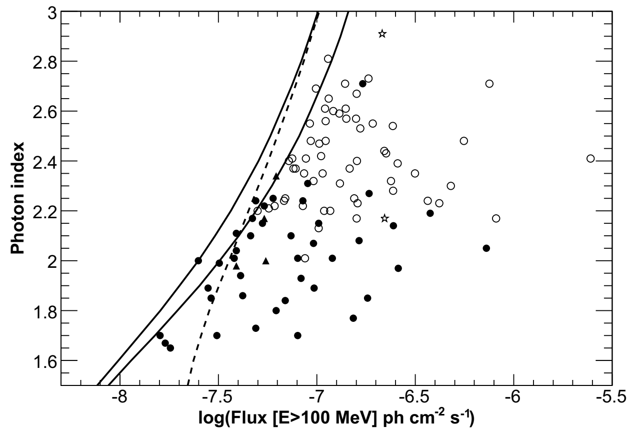

Figure 2: Flux ($E > 100$ MeV) vs. photon index for the LBAS sources. Filled circles: FSRQs; open circles: BL Lacs; triangles: blazars of unknown type; stars: radio galaxies. The solid curves represent the TS = 100 limit estimated for two Galactic latitudes $b = 20°$ and $b = 80°$ (right and left respectively) and Galactic longitude $l = 40°$. The dashed curve represents the TS = 100 limit for $b = 80°$ and 0.2 GeV $< E <$ 3 GeV.

A V/V_{max} analysis shows positive evolution at the 3σ level for the bright *Fermi*-detected FSRQs, with the most luminous FSRQs having an almost constant spatial density with redshift. For the *Fermi*-detected BL Lacs, no evolution within 1σ is apparent.

The γ-ray luminosity function of bright FSRQs can be described by a single power law with index $\Gamma \approx 2.5$ and $\Gamma \approx 1.5$ for the high ($z \geq 0.9$) and low ($z \leq 0.9$) redshift ranges, respectively, while the BL Lac γ-ray luminosity function follows a power law with index $\Gamma \approx 2.1$. The spatial density of γ-ray–emitting BL Lacs above their limiting luminosity, $\sim 3 \times 10^{44}$ erg s^{-1}, is $\sim$190 Gpc^{-3}, a factor of $\sim$200 larger than for the *Fermi*-detected FSRQs above their limiting luminosity, $\sim 7 \times 10^{45}$ erg s^{-1}. Thus, within the *Fermi* bright AGN list, BL Lacs are intrinsically more numerous than FSRQs. Bright *Fermi*-detected BL Lacs and FSRQs display comparable cumulative number counts above $\sim 10^{47}$erg s^{-1}, with BL Lacs being $\sim$3 times more numerous than FSRQs.

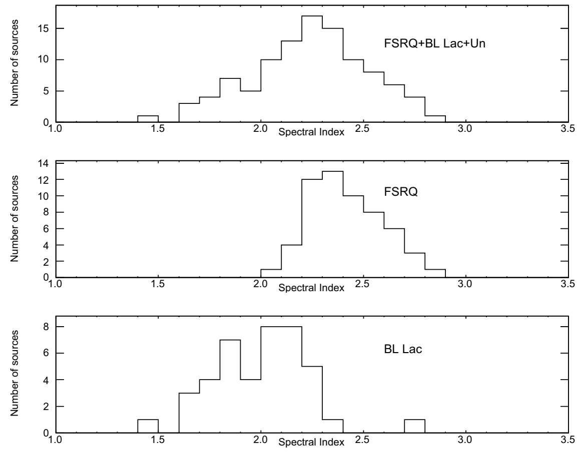

Figure 3: Photon index distributions for the LBAS blazars. Top: All sources. Middle: FSRQs. Bottom: BL Lacs.

4 Prospects

The LBAS just represents the tip of the iceberg, many more sources have already been detected. Already it is clear that the Fermi-LAT mission is living up to expectations. The excellent capabilities offered by the LAT in terms of uniform sky coverage, constant survey and improved localization open up very interesting prospects. The list includes a better understanding of the emission processes at play, the assessment of the variability patterns and corresponding duty cycles for different populations, the determination of precise luminosity functions, the assessment of the contribution of unresolved blazars to the extragalactic diffuse gamma-ray background, the investigation of the connection between gamma-ray and radio emissions, the test of the existence of a blazar sequence and its relation with a possible evolutionary link between FSRQs and BLLacs.

Acknowledgments

The *Fermi* LAT Collaboration acknowledges the generous support of the National Aeronautics and Space Administration and the Department of Energy in the United States, the Commissariat à l'Energie Atomique and the Centre National de la Recherche Scientifique / Institut National de Physique Nucléaire et de Physique des Particules in France, the Agenzia Spaziale Italiana and the Istituto Nazionale di Fisica Nucleare in Italy, the Ministry of Education, Culture, Sports, Science and Technology (MEXT), High Energy Accelerator Research Organization (KEK) and Japan Aerospace Exploration Agency (JAXA) in Japan, and the K. A. Wallenberg Foundation, the Swedish Research Council and the Swedish National Space Board in Sweden.

References

1. Hartman, R. C. et al. **1999**, ApJ, 123, 79
2. Abdo A.A. et al., arXiv:0902.1559
3. Abdo A.A. et al., arXiv:0902.1340
4. Healey S. E. et al. **2008**, ApJS, 175, 97
5. Massaro E. et al. **2009** A&A 495 691

The first multi-waveband observations with *Fermi* and H.E.S.S

D. Sanchez
Laboratoire Leprince-Ringuet Ecole polytechnique, CNRS/IN2P3

The recent (26 Aug–5 Sep 2008) multi-waveband campaign (radio to TeV) of the highly variable, high frequency peaked blazar PKS 2155−304, involving ATOM, *RXTE*, *Swift*, and for the first time *Fermi* and H.E.S.S., has provided a wealth of new and intriguing measurements. The X-ray and TeV data show significant variability on the 1–2 day time scale, even though the source remained in a relatively low TeV state during the campaign. The broadband spectral energy distribution (SED) shows the standard double humped feature, which is well described by a one-zone synchrotron self-Compton (SSC) model, but the variability patterns and the correlations seen between wavebands challenge this simple picture. In contrast to the high state in 2006, no correlation between the X-ray and TeV emission is found, which is interpreted here as being due to Klein-Nishina (KN) effects suppressing the inverse Compton scattering of the highest energy electrons. A significant correlation between optical and TeV radiation was found for the first time in this kind of object. Surprisingly, the X-ray flux correlates well with the *Fermi* daily photon index, indicating a common origin.

1 Introduction

Broadband multiwavelength (MWL) observations are a powerful tool to probe the underlying acceleration mechanism involved in blazar jets by matching spectral and temporal predictions of emission models with data. The blazar PKS 2155−304 (z=0.117) is a perfect target for such observations. Over the last 20 years this source was observed in all wavebands from radio to TeV energies. Since PKS 2155−304 is variable at all wavelengths, simultaneous data are needed to fully constrain the spectrum and determine the correlation patterns. Whereas the synchrotron part of the spectrum has been well studied during several MWL campaigns (see e.g. [4], and references therein), the rising and falling parts of the inverse-Compton emission have been poorly constrained. This is mainly due to the lower sensitivity of the previous generation of observatories in the GeV and TeV energy ranges.

In November 1997, PKS 2155−304 underwent a X-ray flare, triggering EGRET and TeV observations, and providing indications of correlations because the X-ray and GeV flares preceded the highest TeV flux observed by the Durham Mark 6 telescopes [3]. A few MWL campaigns with H.E.S.S and X-ray telescopes confirmed that there is a correlation between X-ray and TeV emission during flares. Since the demise of EGRET, and until now, no GeV observatories have been available to complement the breakthrough in sensitivity of the latest generation of atmospheric Čerenkov telescopes (ACT). In a MWL campaign in 2003, involving H.E.S.S, *RXTE* and ROSTE [1] (hereafter AH05), a wide range of fluxes was predicted in the 100 MeV-100 GeV range by either leptonic or hadronic models.

PKS 2155−304 was relatively faint for EGRET (0.1–3 GeV) since the 3EG catalogue [6] reported only a 5.9σ detection, but the H.E.S.S experiment detects it at Very High Energy (VHE, E> 200 GeV) within $\sim$ 1 h when the source is in a low state. With the successful launch of *Fermi* and its vastly improved sensitivity, PKS 2155−304 can be sampled in the GeV range on comparable time scales to H.E.S.S. providing a new spectral and timing probe in this emission regime. PKS 2155−304 was observed for the first MWL campaign involving *Fermi* and the ground-based ACT H.E.S.S. (which also included ATOM and *RXTE* and *Swift*) during 11 days.

2 Observations and analysis

Observations of PKS 2155-304 were scheduled for August 26–September 5 2008, in order to optimize the source visibility for H.E.S.S. (which is the most time-constrained instrument), as well as to ensure the best possible *RXTE* viewing efficiency (thoroughly discussed with its Science Operations Center). Such a strategy is independent of the activity of the target, as opposite to Target of Opportunity observations, but it guarantees that the needed resources are available, and in particular that *Fermi* would remain in observation mode for the duration of the campaign. Also, it was predicted that no matter the source activity, any observational outcome would have great scientific impact given the sensitivities of the instruments involved. For all the technical issues the reader is redirected to [2] (hereafter AH09), so it is only recalled here that the final data set consists of 106 ATOM observations in the BVR bands, 75 ks of *RXTE* and 5 ks of *Swift* X-ray exposures, 7.7×10^8cm^2 s *Fermi*-LAT exposure in the 0.2–300 GeV band and 32.9 hours of live time with H.E.S.S. (after standard data-quality selection are applied) above 200 GeV.

The H.E.S.S. spectrum and light curve were compatible with the source being in a low (or quiescent) state, similar to that observed by AH05. The differential flux at $E_0 = 350$ GeV (the fitted decorrelation energy) was $I_0 = 10.4 \pm 0.24_{\rm stat} \pm 2.08_{\rm sys} \times 10^{-11}\,{\rm cm^{-2}\,s^{-1}\,TeV^{-1}}$ and the spectral index $\Gamma = 3.34 \pm 0.05_{\rm stat} \pm 0.1_{\rm sys}$. The light curve showed variability, but was surprisingly uncorrelated with the X-ray flux (Fig. 1), though it appeared to correlate with the optical measurements which had so far never been the case when the source was observed in a flaring state.

The *Fermi* observations taken over the exact duration of the campaign showed a spectrum compatible with a simple power law with a flux at $E_0 = 943\,{\rm MeV}$ equal to $I_0 = (2.42 \pm 0.33_{\rm stat} \pm 0.16_{\rm sys}) \times 10^{-11}{\rm cm^{-2}\,s^{-1}\,MeV^{-1}}$, $\Gamma = 1.81 \pm 0.11_{\rm stat} \pm 0.09_{\rm sys}$. In order to increase the statistic, the data set was extended from August 4 to October 4. A broken power law was preferred with a probability of 97% for this data set with a low-energy photon index of $\Gamma_L = 1.61 \pm 0.16_{\rm stat} \pm 0.17_{\rm sys}$, a break energy of $E_{br} = 1.0 \pm 0.3\,{\rm GeV}$ a the high-energy index of $\Gamma_H = 1.96 \pm 0.08_{\rm stat} \pm 0.08_{\rm sys}$. The total flux above 200 MeV was $(1.13 \pm 0.05_{\rm stat} \pm 0.11_{\rm sys}\,{\rm cm^{-2}\,s^{-1}\,MeV^{-1}})$. The *Fermi* light curve was compatible with a constant.

The X-ray light curve clearly showed variability with a significant "harder when brighter" behavior, a doubling time scale of the order of few days. The *Fermi* photon index and the X-ray light curve were found to be correlated.

3 Discussion

The broadband time-averaged spectrum has been reasonably well fitted with a simple one-zone synchrotron self-Compton (SSC) model, Fig. 2 (see AH09 for details). Briefly a function consisting by a triple power law was used to describe the electron density with two breaks at $\gamma_1 = 1.4 \times 10^4$ and $\gamma_2 = 2.3 \times 10^5$ and a maximal energy of $\gamma_{max} = 10^{6.5}$. The magnetic field is 0.018 G, lower than the one found in AH05. Katarzyński et al. [7] used similar values for B to describe the steady emission level of PKS 2155−304 during the giant TeV flare in 2006.

There is no evidence for correlation between X-ray and VHE emission (Fig. 1), contrary to what has been reported (Ref. [5]). No clear correlation between those two energy bands was

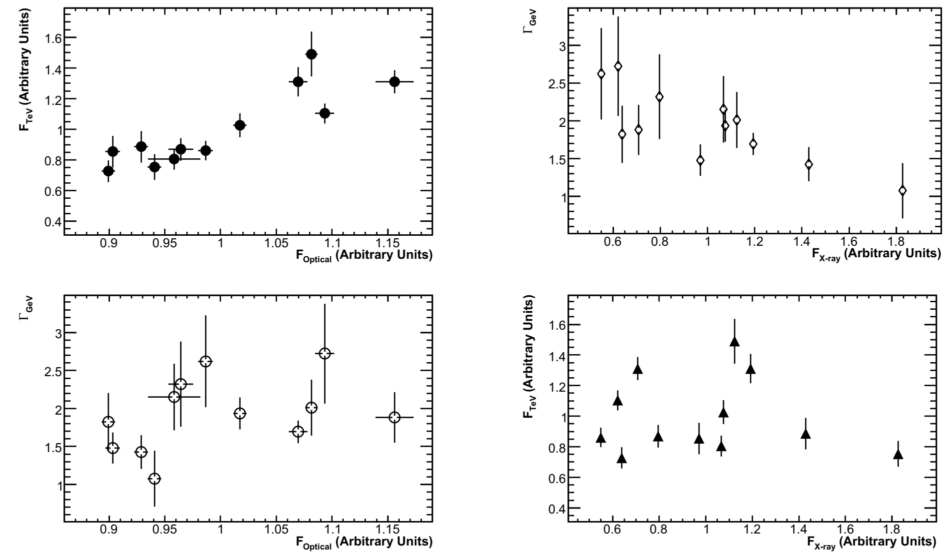

Figure 1: Top-left : TeV vs optical fluxes, top-right : GeV photon index vs X-ray flux, bottom-left : GeV photon index vs optical flux and bottom-right : TeV flux vs X-ray fluxes.

reported in AH05, when the source was also in a low TeV state. In order to check whether electrons radiating X-rays ($\gamma > \gamma_2$) are also strong contributors to the VHE γ-rays, we omitted them in our SSC calculation (black dot-dashed line in Fig. 2). This only changed marginally the VHE flux, illustrating the fact that those electrons are deep in the Klein-Nishina (KN) regime where the cross section dramatically decreases with the energy. If however B is significantly increased, electrons with $\gamma < \gamma_2$ would radiate X-rays also, and a correlation with TeV photons would appear. Interestingly, Katarzyński et al used a higher B field (by a factor 5) to describe the flaring state in their SSC description.

An increase in optical emission has been used as a tool to find new VHE sources. Here, a clear correlation between optical and VHE emission was found for the first time. This can only be explained by the fact that the same electrons producing the optical radiation and TeV emission, or by the fact that optical emission drives the VHE variability through the IC process. In our SSC model, the electrons having $\gamma < \gamma_1$ produce almost no γ-ray photons (see the red dashed line in Fig. 2), making this correlation hard to reproduce.

It appears that the X-ray flux and the *Fermi* photon index were also well correlated ($\rho_{X\Gamma} = -0.80\pm0.15$). Even if high X-ray fluxes were observed during EGRET flares[8], a clear correlation, despite the source being in a low state, is established here.

HE and VHE photons are believed to originate from the same population of electrons and the compatible *Fermi* and H.E.S.S spectra (Fig. 2) support this idea. Moreover the electrons, having an energy between γ_1 and γ_2 produce most of the γ-ray radiation from MeV to a few TeV. The lack of GeV-TeV correlation in our data is hard to understand and challenges this simple picture.

4 Conclusions

In a low flux state, PKS 2155−304 was detected by the *Fermi*-LAT to be a hard source. The study of the correlation pattern is somehow puzzling. No X-ray-TeV fluxes correlation, but significant correlations between X-ray flux and GeV photon index and optical-TeV were detected. Even though a single zone homogeneous SSC model can reasonably fit the SED, and provide an explanation for the lack of VHE-X-ray fluxes correlation in a low state, it fails to explain

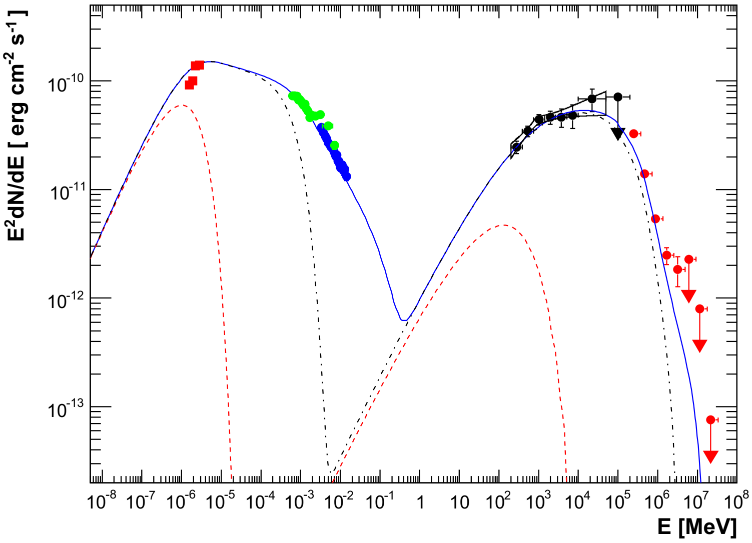

Figure 2: The SED of PKS 2155−304. The black points are *Fermi* estimate of the flux obtained by fitting a simple power law in 8 energy bins, consistent with 1σ butterfly in black. The solid blue line is the result the SSC model, absorbed by the P0.45 EBL model. The dash-dot line and the dash line are the results of the SSC model without electrons above γ_2 and γ_1, respectively.

the X-ray flux-HE photon index correlation as well as why the optical-VHE emission correlation seems to be state-dependant.

References

1. Aharonian, F., et al (H.E.S.S. Collaboration) 2005b, A&A, 442, 895
2. Aharonian, Abdo, et al. (H.E.S.S. and *Fermi* Collaborations) 2009, in Press, arXiv:0903.2924
3. Chadwick, P. M. et al, 1999, Astropart. Phys., 11, 145
4. Courvoisier, T. J.-L. et al, 1995, Apj, 438, 108
5. Giebels, B. and (H.E.S.S. Collaboration) 2005, SF2A-2005: Semaine de l'Astrophysique Francaise, 527
6. Hartman, R. C., Bertsch, D. L., Bloom, S. D., et al., 1999, ApJs, 123, 79
7. Katarzyński, K., Lenain, J.-P., Zech, A., Boisson, C., & Sol, H., 2008, MNRAS, 390, 371
8. Vestrand, W. T., & Sreekumar, P., 1999, Astropart. Phys., 11, 145

DISCOVERY OF A VERY HIGH ENERGY GAMMA-RAY SIGNAL FROM THE 3C 66A/B REGION

D. MAZIN[1],
M. Errando[1], E. Lindfors[2], E. Prandini[3], F. Tavecchio[4] for the MAGIC collaboration[5]
[1] *IFAE, Edifici Cn., Campus UAB, E-08193 Bellaterra, Spain,* [2] *Tuorla Observatory, Turku University, FI-21500 Piikkiö, Finland,* [3] *Università di Padova and INFN, I-35131 Padova, Italy,* [4] *INAF National Institute for Astrophysics, I-00136 Rome, Italy,* [5]*www.magic.mppmu.mpg.de/*

The MAGIC telescope observed the region around the distant blazar 3C 66A for 54.2 hr in 2007 August–December. The observations resulted in the discovery of a γ-ray source centered at celestial coordinates R.A. $= 2^{\mathrm{h}}23^{\mathrm{m}}12^{\mathrm{s}}$ and decl.$= 43°0.'7$ (MAGIC J0223+430), coinciding with the nearby radio galaxy 3C 66B. A possible association of the excess with the blazar 3C 66A is discussed. The energy spectrum of MAGIC J0223+430 extends up to ~ 2 TeV and follows a power law with a photon index $\Gamma = -3.10 \pm 0.31_{\mathrm{stat}} \pm 0.2_{\mathrm{syst}}$.

1 Introduction

As of today, there are 26 known extragalactic very high energy (VHE, defined here as $E > 100$ GeV) γ-ray sources. All of them are active galactic nuclei (AGNs) with relativistic jets. With the exception of the radio galaxy M 87 and Cen A all detected sources are blazars, whose jets (characterized by a bulk Lorentz factor $\Gamma \sim 20$) point, within a small angle ($\theta \sim 1/\Gamma$), to the observer. The spectral energy distribution (SED, logarithm of the observed energy density versus logarithm of the photon energy) of AGNs shows typically a two-bump structure. For the origin of the high-frequency bump, various models have been proposed, the most popular invoking inverse Compton scattering of ambient photons. There have been several suggestions for the origin of the low-frequency seed photons that are up-scattered to γ-ray energies: they may be produced within the jet by synchrotron radiation (synchrotron self-Compton or SSC mechanism[1]) or come from outside the jet (external Compton or EC mechanism[2]). Relativistic effects boost the observed emission as the Doppler factor depends on the angle to the line of sight. In case the jet angle to the line of sight is large, models that depend less critically on beaming effects are needed[3]. The VHE γ-ray emission of AGNs might also be of hadronic origin through the emission from secondary electrons[4].

3C 66A and 3C 66B are two AGNs separated by just 6′ in the sky. 3C 66B is a large Fanaroff–Riley-I-type (FRI) radio galaxy, similar to M 87, with a redshift of 0.0215, whereas 3C 66A is a blazar with uncertain redshift. The often referred redshift of 0.444[5] for 3C 66A is based on a single measurement of one emission line only, while in later observations no lines in the spectra of 3C 66A were reported[6]. Based on the marginally resolved host galaxy, a photometric redshift of ~ 0.321 was inferred. In this paper we report the discovery of VHE γ-ray emission located 6.′1 away from the blazar 3C 66A and coinciding with the radio galaxy 3C 66B in 2007. Detailed results and discussion can be found in[7].

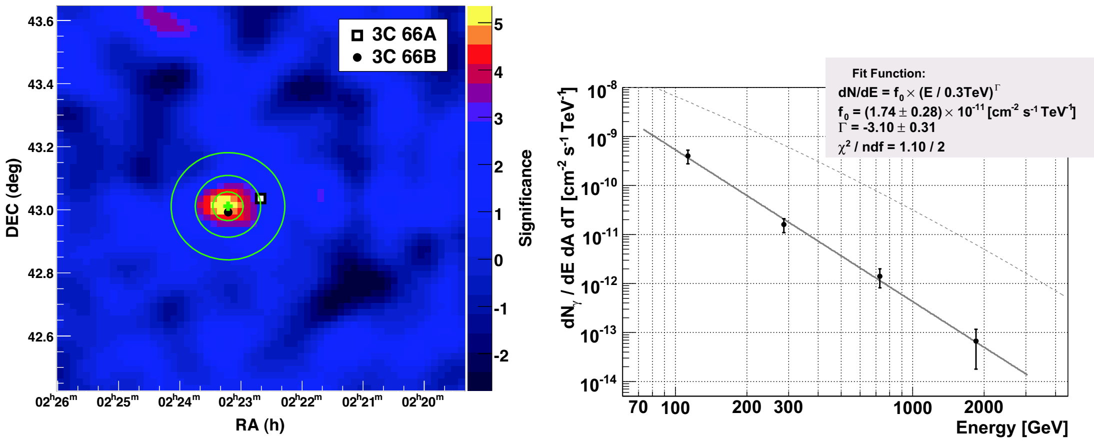

Figure 1: Left plot: Significance map for γ-like events above 150 GeV in the observed sky region. Right plot: Differential energy spectrum of MAGIC J0223+430.

2 Observations and Data Analysis

3C 66A underwent an optical outburst in 2007 August, as monitored by the Tuorla blazar monitoring program. The outburst triggered VHE γ-ray observations of the source with the MAGIC telescope following the Target of Opportunity program, which resulted in discoveries of new VHE γ-ray sources in the past.

MAGIC has a standard trigger threshold of 60 GeV, an angular resolution of $\sim 0.^\circ 1$ and an energy resolution above 150 GeV of $\sim 25\%$ (see [8] for details). The MAGIC data analysis is described in detail in [7,8].

Data were taken in the false-source tracking (wobble) mode pointing alternatively to two different sky directions, each at $24'$ distance from the 3C 66A catalog position. The zenith distance distribution of the data extends from 13° to 35°. Observations were made in 2007 August, September, and December and lasted 54.2 hr, out of which 45.3 hr passed the quality cuts based on the event rate after image cleaning. An additional cut removed the events with total charge less than 150 photoelectrons (phe) in order to assure a better background rejection.

Just before the start of the observation campaign $\sim 5\%$ of the mirrors on the telescope were replaced, worsening the optical point-spread function (PSF). As a consequence, a new calibration of the mirror alignment system became necessary, which took place within the observation campaign and improved the PSF again. The sigma of the Gaussian PSF (40% light containment) was measured to be $3.'0$ in 2007 August 12-14, $2.'6$ in 2007 August 15-26 and $2.'1$ in 2007 September and December. To take this into account, data were analyzed separately for each period and the results were combined at the end of the analysis chain. However, the realignment resulted in a mispointing, which was taken care of by a new pointing model applied offline using starguider information[9]. Considering the additional uncertainty caused by the offline corrections, we estimate the systematic uncertainty of the pointing accuracy to be $2'$ on average.

3 Results

Figure 1 (left plot) shows a significance map produced from the signal and background maps, both smoothed with a Gaussian of $\sigma = 6'$ (corresponding to the γ-PSF), for photon energies between 150 GeV and 1 TeV. For the background rejection a loose cut in the Hadronness parameter is applied to keep a large number of gamma-like events. The center of gravity of the γ-ray emission is derived from Figure 1. The fit yields reconstructed coordinates of the excess center of R.A. $= 2^{\mathrm{h}}23^{\mathrm{m}}12^{\mathrm{s}}$ and decl.$= 43^\circ 0.'7$. The detected excess, which we name

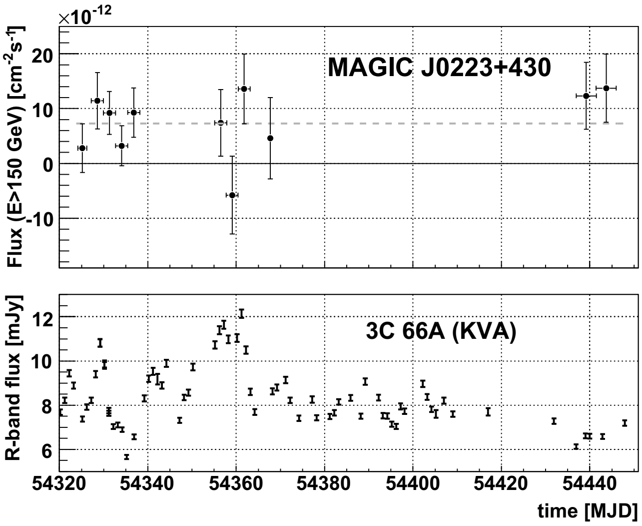

Figure 2: Light curve of MAGIC J0223+430. Upper panel: MAGIC integral flux above 150 GeV in bins of 3 days. The gray dashed line indicates the average γ-ray flux. Lower panel: optical light curve of 3C 66A as measured by the KVA telescope. While 3C 66A was very bright at optical wavelengths, the optical flux of 3C 66B remained constant, which is a typical behavior for large radio galaxies.

MAGIC J0223+430, is $6.'1$ away from the catalog position of 3C 66A, while the distance to 3C 66B is $1.'1$. We made a study to estimate statistical uncertainty of the reconstructed position. The probabilities are shown in Figure 1 by the green contours corresponding to 68.2%, 95.4%, and 99.7% for the inner, middle, and outer contour, respectively. Using this study we find that the measured excess coincides with the catalog position of 3C 66B. The origin of the emission from 3C 66A can be excluded with a probability of 95.6% (85.4%) statistically (and adding systematics), respectively.

To calculate the significance of the detection, an |ALPHA| distribution was produced, where ALPHA is the angle between the major axis of the shower image ellipse and the source position in the camera. A signal of $6.0\,\sigma$ significance (pre-trial, at the position of 3C 66B) and $5.4\,\sigma$ (post-trial, using 30 independent trials) has been calculated.

For the energy spectrum of MAGIC J0223+430, loose cuts are made to keep the γ-ray acceptance high. The differential energy spectrum was unfolded and is shown in Fig. 1 (right plot). The spectrum can be well fitted by a power law which gives a differential flux (TeV^{-1} cm^{-2} s^{-1}) of:

$$\frac{\mathrm{d}N}{\mathrm{d}E\,\mathrm{d}A\,\mathrm{d}t} = (1.7 \pm 0.3) \times 10^{-11} (E/300\,\mathrm{GeV})^{-3.1\pm0.3} \tag{1}$$

The quoted errors are statistical only. The systematic uncertainty is estimated to be 35% in the flux level and 0.2 in the power law photon index [8]. As we cannot exclude that 3C 66A contributes to the measured signal, the spectrum shown in Figure 1 (right plot) represents a combined γ-ray spectrum from the observed region.

Figure 2 shows the light curve of MAGIC J0223+430 together with the flux of 3C 66A in optical wavelengths. As we integrate over γ-ray events from a wide sky region ($\sim 0.07\,\mathrm{deg}^2$), we cannot exclude that 3C 66A contributes to the measured signal. The integral flux above 150 GeV corresponds to $(7.3 \pm 1.5) \times 10^{-12}\,\mathrm{cm}^{-2}\,\mathrm{s}^{-1}$ (2.2% of the Crab Nebula flux) and is the lowest ever detected by MAGIC. The γ-ray light curve is consistent with a constant flux within statistical errors. These errors, however, are large, and some variability of the signal cannot be excluded.

4 Discussion and conclusions

A new VHE γ-ray source MAGIC J0223+430 was detected in 2007 August to December. Given the position of the excess measured by MAGIC above 150 GeV, the source of the γ-rays is likely 3C 66B. The VHE γ-ray flux was found to be on the level of 2.2% Crab Nebula flux and was constant during the observations. The differential spectrum of MAGIC J0223+430 has a photon spectral index of $\Gamma = 3.10 \pm 0.31$ and extends up to ~ 2 TeV. In view of the recent detection of 3C 66A at VHE γ-rays [10], we note that if 3C 66A was emitting γ-rays in 2007 August to December then its flux was at a significantly lower level than in 2008.

In the unlikely case, excluded with probability 85.4%, that the total signal and observed spectrum presented in this paper originates from 3C 66A, the redshift of the source is likely to be significantly lower than previously assumed due to energy-dependent absorption of VHE γ-rays with low-energy photons of the extragalactic light[7,11]. If $z > 0.24$ for 3C 66A, an alternative explanation for a hard intrinsic spectrum at energies above 100 GeV can be given if γ-rays are passing through a narrow band of optical-infrared photons in the vicinity of the blazar [12].

3C 66B is a FRI radio galaxy similar to M 87, which has been detected to emit VHE γ-rays [13]. Since the distance of 3C 66B is 85.5 Mpc, its intrinsic VHE luminosity would be two to eight times higher than the one of M 87 (22.5 Mpc) given the reported variability of M 87 [13,14]. As in the case of M 87, there would be several possibilities for the region responsible of the TeV radiation in 3C 66B: the vicinity of the supermassive black hole, the unresolved base of the jet and the resolved jet. A possible emission scenario associated with a structured jet responsible for the observed VHE γ-ray emisson from 3C 66B is presented in [15]. Given the likely association of MAGIC J0223+430 with 3C 66B, our detection would establish radio galaxies as a new class of VHE γ-ray emitting sources (see also [16]). Further observations of radio galaxies with the Fermi Gamma-ray Space Telescope as well as by ground-based telescopes are needed to further study the γ-ray emission properties of radio galaxies.

Acknowledgments

We thank the Instituto de Astrofisica de Canarias for the excellent working conditions at the Observatorio del Roque de los Muchachos in La Palma.

References

1. Maraschi, L., Ghisellini, G., Celotti, A. 1992, *ApJ*, 397, 5
2. Dermer, C. & Schlickeiser, R. 1993, *ApJ*, 416, 458
3. Tavecchio, F. & Ghisellini, G. 2008a, *MNRAS*, 385, L98
4. Mannheim, K. 1993, *A&A*, 269, 67
5. Miller, J. S. et al., 1978, in Pittsburgh Conf. on BL Lac Objects, ed. A. M. Wolfe, 176
6. Finke, J. D., Shileds, J. C., Böttcher, M. & Basu, S. 2008, *A&A*, 477, 513
7. Aliu, E. et al. (MAGIC Collaboration) 2009, *ApJ*, 692, L29-L33
8. Albert, J. et al. 2008a, *ApJ*, 674, 1037
9. Riegel, B. et al., 2005, proc. of the 29th ICRC, Pune, India, 5, 219
10. Acciari, V.A. et al. (VERITAS Collaboration) 2009, *ApJ*, 693, L104-L108
11. Mazin, D. & Raue, M. 2007 *A&A*, 471, 439
12. Aharonian, F.A., Khangulyan, D., & Costamante, L. 2008, *MNRAS*, 387, 1206
13. Aharonian, F. et al. 2006b, *Science*, 314, 1424
14. Albert, J. et al. 2008b, *ApJ*, 685, L23
15. Tavecchio, F., Ghisellini, G., 2009, *MNRAS*, 394, L131-L135
16. Raue, M. et al. for the HESS Collaboration, 2009, these proceedings

BLAZARS: THE GAMMA-RAY VIEW OF AGILE

F. D'Ammando[1,2], S. Vercellone[3], I. Donnarumma[1], A. Bulgarelli[4], A. W. Chen[5,6], A. Giuliani[5], F. Longo[7], L. Pacciani[1] , G. Pucella[1], M. Tavani[1,2] and V. Vittorini[1,6] (on behalf of the AGILE Team)
[1]*INAF-IASF Roma, Via Fosso del Cavaliere 100, 00133 Roma, Italy*
[2]*Dip. di Fisica, Univ. "Tor Vergata", Via della Ricerca Scientifica 1, 00133 Roma, Italy*
[3]*INAF-IASF Palermo, Via Ugo La Malfa 153, 90146 Palermo, Italy*
[4]*INAF-IASF Bologna, Via Gobetti 101, 40129 Bologna, Italy*
[5]*INAF-IASF Milano, Via E. Bassini 15, 20133 Milano, Italy*
[6]*CIFS-Torino, Viale Settimio Severo 3, 10133 Torino, Italy*
[7]*Dip. di Fisica and INFN, Via Valerio 2, 34127 Trieste, Italy*

Since its launch in April 2007, the AGILE satellite detected with its Gamma-Ray Imaging Detector (GRID) several blazars at high significance: 3C 279, 3C 454.3, PKS 1510–089, S5 0716+714, 3C 273, W Comae, Mrk 421 and PKS 0537–441. Moreover, AGILE was able both to rapidly respond to sudden changes in blazar activity state at other wavelengths and to alert other telescopes quickly in response to changes in the gamma-ray fluxes. Thus, we were able to obtain multiwavelength data from other observatories such as *Spitzer*, *Swift*, RXTE, *Suzaku*, INTEGRAL, MAGIC, VERITAS, as well as radio-to-optical coverage by means of the GASP Project of the WEBT and REM. This large multifrequency coverage gave us the opportunity to study the Spectral Energy Distribution of these sources from radio to gamma-rays energy bands and to investigate the different mechanisms responsible for their emission. We present an overview of the AGILE results on these gamma-ray blazars and the relative multifrequency data.

1 Introduction

Blazars are a subclass of Active Galactic Nuclei (AGN) characterized by the emission of strong non-thermal radiation across the electromagnetic spectrum, from radio to TeV energy bands. The typical observational properties include irregular, rapid and often very large variability, apparent super-luminal motion, flat radio spectrum, high and variable polarization at radio and optical frequencies. These features are interpreted as the result of the emission of electromagnetic radiation from a relativistic jet that is viewed closely aligned to the line of sight (Blandford & Rees [1], Urry & Padovani [2]). The EGRET instrument onboard Compton Gamma-Ray Observatory (CGRO) detected for the first time strong and variable high energy γ-ray emission from blazars in the MeV–GeV region and together with coordinated multwavelength observations provided evidence that the Spectral Energy Distributions (SEDs) of the blazars are typically double humped with the first peak occurring in the IR/optical band in the Flat Spectrum Radio Quasars (FSRQs) and in UV/X-rays in the BL Lacertae objects, depending by the total jet power of the source. This first peak is interpreted as synchrotron radiation from high-energy electrons in a relativistic jet. The SED second component, peaking at MeV-GeV energies in the FSRQs and at GeV-TeV energies in the BL Lacs, is commonly interpreted as inverse Compton scattering of seed photons, internal or external to the jet, by highly relativistic electrons (Ulrich et al. [3]), although other models involving hadronic processes have been proposed (see e.g. Böttcher [4] for a recent review).

With the advent of the AGILE and Fermi-GST γ-ray satellites, together with the ground based Imaging Atmospheric Cherenkov Telescopes H.E.S.S., MAGIC and VERITAS, a new exiting era for the gamma-ray extragalactic astronomy and in particular for the study of blazars is now open and in conjunction with a complete multiwavelength coverage will allow us to shed light on the structure of the inner jet and the emission mechanisms of this class of objects.

Table 1: List of the AGILE flaring blazars. References: 1. Chen et al., 2008, A&A, 489, L37; 2. Giommi et al., 2008, A&A, 487, L49; 3. Donnarumma et al., 2009, ApJL, 691, 13; 4. Maier et al., 2009, in preparation; 5. Pucella et al., 2008, A&A, 491, L21; 6. D'Ammando et al., 2009, in preparation; 7. Pucella et al., 2009, in preparation; 8. Pacciani et al., 2009, A&A, 494, 49; 9. Giuliani et al., 2009, A&A, 494, 509; 10. Vercellone et al., 2008, ApJL, 676, 13; 11. Wehrle et al., 2009, in preparation; 12. Vercellone et al., 2009a, ApJ, 690, 1018; 13. Donnarumma et al., 2009, in preparation; 14. Vercellone et al., 2009b, in preparation; 15. TBD.

Name	**Period** *start : stop*	**Sigma**	**ATel #**	**Ref.**
S5 0716+714	2007-09-04 : 2007-09-23	9.6	1221	1
	2007-10-24 : 2007-11-01	6.0	-	2
Mrk 421	2008-06-09 : 2008-06-15	4.5	1574, 1583	3
W Comae	2008-06-09 : 2008-06-15	4.0	1582	4
PKS 1510−089	2007-08-23 : 2007-09-01	5.6	1199	5
	2008-03-18 : 2008-03-20	7.0	1436	6
	2009-03-01 : 2009-03-31	19.9	1957, 1968, 1976	7
3C 273	2007-12-16 : 2008-01-08	4.6	-	8
3C 279	2007-07-09 : 2007-07-13	11.1	-	9
3C 454.3	2007-07-24 : 2007-07-30	13.8	1160, 1167	10, 11
	2007-11-10 : 2007-12-01	19.0	1278, 1300	12
	2007-12-01 : 2007-12-16	21.3	-	13
	2008-05-10 : 2008-06-30	15.0	1545, 1581, 1592	14
	2008-07-25 : 2008-08-15	12.1	1634	15

2 Blazars and AGILE

AGILE (*Astrorivelatore Gamma ad Immagini LEggero*) is an Italian Space Agency (ASI) mission successfully launched on 23 April 2007 and capable of observing cosmic sources simultaneously in X-ray and γ-ray energy bands. The Gamma-Ray Imaging Detector (GRID) constists of a Silicon Tracker, a non-imaging CsI Mini-Calorimeter and a segmented anticoincidence system; the GRID is optimized for γ-ray imaging in the 30 MeV–30 GeV energy band. A co-aligned coded-mask hard X-ray imager (SuperAGILE) ensures coverage in the 18–60 keV energy band.

Gamma-ray observations of blazars are a key scientific project of the AGILE satellite (Tavani et al.[5]). In the last two years, the AGILE satellite detected several blazars during high γ-ray activity and extensive multiwavelength campaigns were organized for many of them. Table 1 shows the list of AGILE flaring blazars observed up now. The γ-ray activity timescales goes from a few days (e.g. S5 0716+714) to several weeks (e.g. 3C 454.3 and PKS 1510–089) and the flux variability observed has been negligible (e.g. 3C 279), very rapid (e.g. PKS 1510–089) or extremely high (e.g. 3C 454.3 and PKS 1510–089). Only few objects were detected more than once in flaring state by AGILE and only already known γ-ray emitting source showed flaring activity. This evidence together with the early results from the first three months of Fermi-LAT γ-ray all-sky survey (Abdo et al.[6]) suggest possible constraint on the properties of the most intense γ-ray emitters. In the following section we will present the most interesting results on multiwavelength observations of the individual sources detected by AGILE.

3 Individual Sources

3.1 3C 454.3

3C 454.3 is the blazar which exhibited the most variable activity in the γ-ray sky in the last two years. In the period July 2007–January 2009 the AGILE satellite monitored intensively 3C

454.3 together with *Spitzer*, WEBT, REM, MITSuME, *Swift*, RXTE, *Suzaku* and INTEGRAL observatories, yielding the longest multiwavelength coverage of this γ-ray quasar so far. The source underwent an unprecedented long period of very high γ-ray activity, showing flux levels variable on short timescales of 24–48 hours and reaching on daily timescale a γ-ray flux higher than 400×10^{-8} photons cm^{-2} s^{-1}. Also the optical flux appears extremely variable with a brightening of several tenths of magnitude in a few hours. The comparison of the light curves shows that the emission in the optical and γ-ray bands appears to be well correlated, with a time lag less than one day, as confirmed also by the analysis of the early Fermi-LAT data in Bonning et al.[7]. The dominant emission mechanism over 100 MeV seems to be the inverse Compton scattering of relativistic electrons in the jet on the external photons from the Broad Line Region (BLR), even if the γ-ray spectrum observed by AGILE in December 2007 seems to require also the contribution of external Compton of seed photons from a hot corona.

3.2 PKS 1510–089

PKS 1510–089 showed in the last two years high variability over all the electromagnetic spectrum, in particular an high γ-ray activity was detected by AGILE with two intense flaring episodes in August 2007 and March 2008 and an extraordinary actitivity during the entire March 2009 with several flaring episode and a flux reaching 500×10^{-8} ph cm^{-2} s^{-1}. The multiwavelength data carried out by GASP-WEBT and *Swift* in 2008–2009 seems to indicate the presence in the spectrum of thermal features quasar-like such as the little blue bump and the big blue bump. Instead the X-ray spectrum exhibits a soft X-ray excess, of which the nature is unclear but that could be a feature of the bulk Comptonization mechanism. Moreover, the *Swift*/XRT observations seems to show a redder-when-brighter behaviour in X-rays (i.e. the spectrum is harder when the source is brighter) already observed by Kataoka et al.[8] in this source.

3.3 3C 279

3C 279 is the first extragalactic source detected by AGILE in the γ-ray band. The average γ-ray flux over 4 days of observation is $F_{E>100MeV} = (210 \pm 38)\times10^{-8}$ ph cm^{-2} s^{-1}, similar of the high state observed by EGRET. A strong minimum in the optical band was detected by REM two months before the GRID observations. The spectrum of this source during the flaring episode observed by AGILE is soft ($\Gamma = 2.22 \pm 0.23$) and this could be an indication of a low accretion state of the disk occurred some months before the γ-ray observations, suggesting a dominant contribution of the external Compton scattering of direct disk (ECD) radiation compared to the external compton scattering of the Broad Line Region clouds (ECC). In fact the reduction of the activity of the disk should cause the decrease of the photon seed population produced by the disk and then a deficit of the ECC component with respect to the ECD, an effect delayed of the light travel time required from the inner disk to the BLR.

3.4 3C 273

3C 273 was the first extragalactic source detected simultaneously by the GRID and SuperAGILE detectors during a multiwavelength campaign over three weeks between December 2007 and January 2008 involving also simultaneous REM, *Swift*, RXTE and INTEGRAL coverage. The average flux in the 20–60 energy band is (23.9 $\pm$ 1.2) mCrab, whereas the source was detected by the GRID only in the second week, with an average flux of $F_{E>100MeV} = (33 \pm 11)\times10^{-8}$ ph cm^{-2} s^{-1}. The comparison of the light curves seems to indicate a possible anti-correlation between the γ-ray emission and the soft and hard X-rays. The SED is consistent with a leptonic model where the soft X-ray emission is produced by the combination of SSC and EC models, while the hard X-ray and γ-ray emission is due to external Compton scattering by thermal photons of the disk. The spectral variability between the first and the second week is consistent with the acceleration episode of the electron population responsible for the synchrotron emission.

3.5 S5 0716+714

The intermediate BL Lac object S5 0716+714 was observed by AGILE during two different periods: 4–23 September and 23 October – 1 November 2007. In mid September the source showed an high γ-ray activity with an average flux of $F_{E>100MeV}$ = $(97 \pm 15)\times10^{-8}$ ph cm^{-2} s^{-1} and a peak flux of $F_{E>100MeV}$ = $(193 \pm 42)\times10^{-8}$ ph cm^{-2} s^{-1}. This is one of the most high flux observed by a BL Lac object. An almost simultaneous GASP-WEBT optical campaign started after the AGILE detection and the resulting SED is consistent with a two-components SSC model. Recently Nilsson et al.[9] has estimated the redshift of the source (z = 0.31 $\pm$ 0.08) and this allowed us to calculate the total power transported in the jet, which results extremely high and at limit of the maximum power generated by a spinning black hole of 10^9 $M_\odot$.

During October 2007, AGILE detected the source at a flux about a factor 2 lower than September one with no significant variability. Instead, *Swift* observed strong variability in soft X-ray, moderate variability at optical/UV and approximately constant hard X-ray flux. Also this behaviour is compatible with the presence of two different SSC components in the SED.

3.6 Mrk 421

During a ToO towards W Comae on June 2008, AGILE surprisingly detected also this HBL object. SuperAGILE detected a fast increase of flux from Mrk 421 up to 40 mCrab in the 15–50 energy band, about a factor 10 higher than its typical flux in quiescence. The γ-ray flux detected by GRID, $F_{E>100MeV} = (42 \pm 13)\times10^{-8}$ ph cm^{-2} s^{-1}, is about a factor 3 higher than the average EGRET value, even if consistent with its maximum. An extensive multiwavelength campaign from optical to TeV energy bands was organized with the participation of WEBT, *Swift*, RXTE, AGILE, MAGIC and VERITAS. The light curves show a possible correlated variability between optical, X-rays and the high part of the spectrum. The SED can be interpreted within the framework of the SSC model in terms of a rapid acceleration of leptons in the jet. A more complex scenario is that optical and X-ray emission come from different regions of the jet, with the inner jet region that produces X-rays and is partially transparent to the optical radiation.

Acknowledgments

F. D. warmly thanks the Marie Curie Actions of the European Union for the financial support for the participation to the Conference. The AGILE Mission is funded by the Italian Space Agency (ASI) with scientific and progammatic partecipation by the Italian Institute of Astrophysics (INAF) and the Italian Institute of Nuclear Physics (INFN).

References

1. R. D. Blandford & M. Rees, *in BL Lac Objects*, ed. A. M. Wolfe, Pittsburgh Press, (1978)
2. C. M. Urry & P. Padovani, *Publications of the Astron. Soc. of the Pacific* **107**, 803 (1995)
3. M. Ulrich, L. Maraschi, C. M. Megan, *ARA&A* **35**, 445 (1997)
4. M. Böttcher, *Astrophysics and Space Science* **309**, 95 (2007)
5. M. Tavani, et al., *Astronomy and Astrophysics*, in press, (2009)
6. A. A. Abdo, et al., *submitted to ApJ*, arXiv:0902.1559, (2009)
7. E. W. Bonning, C. Baylin, C. M. Urry, et al., *submitted to ApJL*, arXiv:0812.4582, (2008)
8. J. Kataoka, G. Madejski, M. Sikora, et al., *ApJ* **672**, 787 (2008)
9. K. Nilsson, T. Pursimo, A. Sillanpää, et al., *Astronomy and Astrophysics* **487**, L29 (2008)

DISCOVERY OF VHE γ-RAYS FROM CENTAURUS A

M. RAUE[1], J.-P. LENAIN[3], F. A. AHARONIAN[7,1], Y. BECHERINI[2], C. BOISSON[3], A.-C. CLAPSON[1], L. COSTAMANTE[6], L. GÉRARD[2], C. MEDINA[3], M. DE NAUROIS[4], M. PUNCH[2], F. RIEGER[1], H. SOL[3], L. STAWARZ[5], A. ZECH[3], for the H.E.S.S. COLLABORATION

[1]*Max-Planck-Institut fuer Kernphysik, Heidelberg, Germany,* [2]*Astroparticule et Cosmologie (APC), CNRS, Université Paris 7 Denis Diderot, France,* [3]*LUTH, Observatoire de Paris, CNRS, Université Paris Diderot, Meudon, France,* [4]*LPNHE, Université Pierre et Marie Curie Paris 6, Université Denis Diderot Paris 7, CNRS/IN2P3, France,* [5]*Astronomical Observatory, Jagiellonian University, Cracow, Poland,* [6]*HEPL/KIPAC, Stanford University, US,* [7]*Institute for Advanced Studies, Dublin, Ireland*

We report the discovery of faint very high energy (VHE, $E > 100\,\mathrm{GeV}$) γ-ray emission from the radio galaxy Centaurus A in deep observations performed with the H.E.S.S. experiment. A signal with a statistical significance of $5.0\,\sigma$ is detected from the region including the radio core and the inner kpc jets. The integral flux above an energy threshold of $\sim$250 GeV is measured to be 0.8 % of the flux of the Crab Nebula and the spectrum can be described by a power law with a photon index of $2.7 \pm 0.5_{\mathrm{stat}} \pm 0.2_{\mathrm{sys}}$. No significant flux variability is detected in the data set. The discovery of VHE γ-ray emission from Centaurus A reveals particle acceleration in the source to $>$ TeV energies and, together with M 87, establishes radio galaxies as a class of VHE emitters.

1 Introduction

Centaurus A (Cen A) is the nearest active radio galaxy (3.8 Mpc [1]; for a review see [2]). At radio wavelengths rich jet structures are visible, extending from the core and the inner pc and kpc jet to giant outer lobes with an angular extension of $8^\circ \times 4^\circ$. The inner kpc jet has also been detected in X-rays, revealing a complex structure of bright knots and diffuse emission [3]. The angle of the jet axis to the line of sight is estimated to be 15-80° [see e.g. 4, and references therein]. The elliptical host NGC 5128 features a dark lane, a thin edge-on disk of dust and young stars, believed to be the remnant of a merger. Recent estimates for the mass of the central supermassive black hole give $(5.5 \pm 3.0) \times 10^7\, M_\odot$ [5]. The kpc-scale jet and the active nucleus are confirmed sources of strong non-thermal emission. In addition, more than 200 X-ray point sources with an integrated luminosity of $\mathrm{L_X} > 10^{38}\,\mathrm{erg\,s^{-1}}$ are established to be associated with the host galaxy [6].

Cen A was detected at MeV to GeV energies by all instruments on board the Compton Gamma-Ray Observatory (CGRO) in the period 1991 − 1995, revealing a peak in the spectral energy distribution (SED) in νF_ν representation at $\sim 0.1\,\mathrm{MeV}$ with a maximum flux of about $\sim 10^{-9}\,\mathrm{erg\,cm^{-2}\,s^{-1}}$ [7]. Recently, a detection of Cen A at GeV energies has been reported by the *Fermi* LAT team [8]. A tentative detection of Cen A (4.5σ) at VHE during a giant X-ray outburst in the 1970's was reported by [9]. Subsequent VHE observations made with different instruments resulted in upper limits. Cen A has been proposed as a possible source of ultra-high energy cosmic rays ([10], but see also [11]).

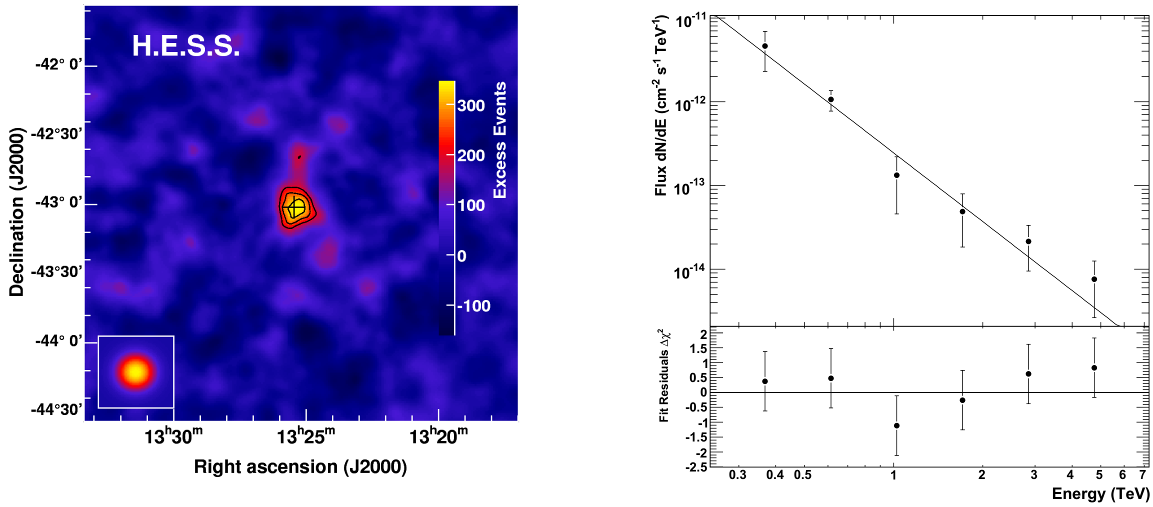

Figure 1: *Left:* Smoothed excess sky map of VHE γ-rays centered on the Cen A radio core (cross) (contours: 3, 4, and 5σ). *Right:* Differential energy spectrum of Cen A as measured by H.E.S.S.

2 H.E.S.S. observations and results

The H.E.S.S. observations of Cen A were performed between April 2004 and July 2008 (total live time: 115.0 h; zenith angles: 20° to 60°; mean zenith: $\sim 24°$). The data were analyzed with a standard Hillas-type analysis [12] with an analysis energy threshold of ~ 250 GeV for a zenith angle of 20°.

Figure 1 shows the smoothed excess sky map of VHE γ-rays as measured with H.E.S.S. centered on the Cen A radio core position. A clear excess at the position of Cen A is visible. A point source analysis, using standard cuts as described in [12], was performed on the radio core position of Cen A, resulting in the detection of an excess with a statistical significance of $5.0\,\sigma$. A fit of the instrumental point spread function to the uncorrelated sky map results in a good fit (chance probability ~ 0.7) with a best fit position of $\alpha_{J2000} = 13^{\mathrm{h}}25^{\mathrm{m}}26.4^{\mathrm{s}} \pm 4.6^{\mathrm{s}}_{\mathrm{stat}} \pm 2.0^{\mathrm{s}}_{\mathrm{syst}}$, $\delta_{J2000} = -43°0.7' \pm 1.1'_{\mathrm{stat}} \pm 30''_{\mathrm{syst}}$, well compatible with the radio core and the inner kpc jet region. Assuming a Gaussian surface-brightness profile, we derive an upper limit of 0.2° on the extension (95% confidence level).

The measured differential photon spectrum (Fig. 1) is well described by a power-law function $dN/dE = \Phi_0 \cdot (E/1\,\mathrm{TeV})^{-\Gamma}$ with normalization $\Phi_0 = (2.45 \pm 0.52_{\mathrm{stat}} \pm 0.49_{\mathrm{sys}}) \times 10^{-13}\,\mathrm{cm}^{-2}\,\mathrm{s}^{-1}\,\mathrm{TeV}^{-1}$ and photon index $\Gamma = 2.73 \pm 0.45_{\mathrm{stat}} \pm 0.2_{\mathrm{sys}}$. The integral flux above 250 GeV, taken from the spectral fit, is $\Phi(E > 250\,\mathrm{GeV}) = (1.56 \pm 0.67_{\mathrm{stat}}) \times 10^{-12}\,\mathrm{cm}^{-2}\,\mathrm{s}^{-1}$, which corresponds to $\sim 0.8\%$ Crab, or an apparent isotropic luminosity of L(>250 GeV)$= 2.6 \times 10^{39}\,\mathrm{erg\,s}^{-1}$ (adopting a distance of 3.8 Mpc). No significant variability has been found on time-scales of 28 min, nights and months (moon periods). The results have been cross-checked with independent analysis and calibration chains and good agreement was found. More details can be found in [13].

3 Discussion

Figure 2 shows the spectral energy distribution of Cen A ranging from X-rays to the VHE regime. The flux measured by H.E.S.S. is clearly below all previous upper limits in the VHE regime. Recently, the *Fermi* LAT team reported a detection of Cen A at GeV energies [8] (Fig. 2 orange bow-tie). While a simple extrapolation of the reported power law function would result in a too low flux at $\sim$TeV energies, one will have to wait until the actual spectral points are released to conclude about the compatibility of the H.E.S.S. and the *Fermi* data. In addition, the data are

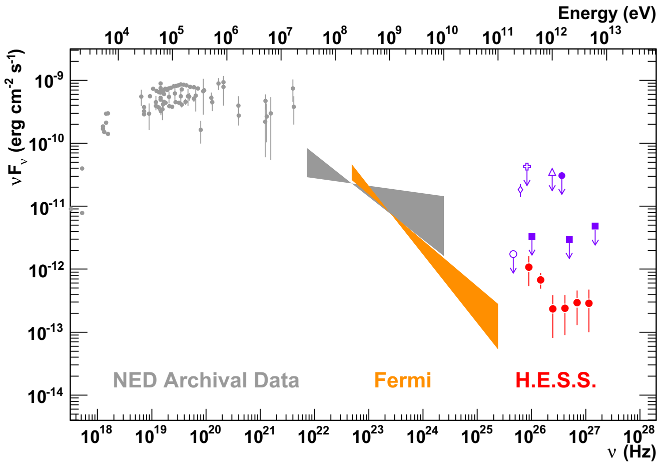

Figure 2: High energy part of the spectral energy distribution of Cen A.

not contemporaneous and variability cannot strongly be excluded from the H.E.S.S. data-set.

Several authors have predicted VHE emission from Cen A, and more generally discussed VHE emission from radio galaxies. A first class of models proposed the immediate vicinity of the supermassive black hole as the region of VHE emission, e.g. in pulsar-type scenarios [14, 15]. A second class of models propose a mechanism similar to the mechanism at work in other VHE blazars [16, 17]. [18] discussed a two-flow type model [19, 20], with a fast spine and a slower, mildly relativistic sheath propagating within the jet, which has been successfully applied to M 87 [21]. [22] modeled the VHE emission of Cen A with a multi-blob SSC model. Extended VHE emission may also be expected from Cen A. In this context, [23] proposed that γ-rays emitted in the immediate vicinity of the active nucleus are partly absorbed by the starlight radiation in the host galaxy. The created $e^{\pm}$ pairs are quickly isotropized and radiate VHE γ-rays by inverse Compton scattering the starlight radiation. The small size of the resulting isotropic pair halo ($\sim$ 4 arcmin in diameter) is fully consistent with a point-like source for H.E.S.S., but could be resolved by the future CTA (Cherenkov Telescope Array)[a] observatory. Furthermore, hadronic models have been invoked to predict VHE emission from radio galaxies [24]. The H.E.S.S. result do not yet strongly constrain these models.

Recently, [25] reported the detection of non-thermal X-ray synchrotron emission from the shock of the southwest inner radio lobe. They investigated inverse Compton scattering the starlight radiation and the CMB from high energy particles in this lobe and predicted a VHE emission well compatible with the H.E.S.S. measurement. This study would suggest Cen A is analogous to a gigantic supernova remnant (SNR). While the position is $\sim 3\sigma$ away from the best fit position of the VHE excess, it is well within the upper limit of the extension.

Cen A represents a rich potential for future VHE experiments. The current data are at the edge of differentiating the possible emitting regions. With higher sensitivity (factor 10), better astrometric accuracy and angular resolution (e.g. $\sim 5''$ and $\sim 1'$, respectively) [26], CTA would allow the localization of the site of the VHE emission, and, possibly, reveal multiple VHE emitting sources within Cen A. More generally, the detection of VHE emission from Cen A together with the detection of M 87 and the galactic center poses the question of whether VHE emission (γ-ray brightness) might be a general feature of AGN. While the sensitivity of current generation experiments is probably too low to answer this question, one can hope that the CTA experiment will be able to detect a large enough sample of sources to shed some light on this issue.

[a] http://www.cta-observatory.org/

Acknowledgments

The support of the Namibian authorities and of the University of Namibia in facilitating the construction and operation of H.E.S.S. is gratefully acknowledged, as is the support by the German Ministry for Education and Research (BMBF), the Max Planck Society, the French Ministry for Research, the CNRS-IN2P3 and the Astroparticle Interdisciplinary Programme of the CNRS, the U.K. Science and Technology Facilities Council (STFC), the IPNP of the Charles University, the Polish Ministry of Science and Higher Education, the South African Department of Science and Technology and National Research Foundation, and by the University of Namibia. We appreciate the excellent work of the technical support staff in Berlin, Durham, Hamburg, Heidelberg, Palaiseau, Paris, Saclay, and in Namibia in the construction and operation of the equipment. This research has made use of the NASA/IPAC Extragalactic Database (NED) which is operated by the Jet Propulsion Laboratory, California Institute of Technology, under contract with the National Aeronautics and Space Administration, and NASA's Astrophysics Data System.

References

[1] M. Rejkuba, *A&A* **413**, 903 (2004).

[2] F. P. Israel, *A&A Rev.* **8**, 237 (1998).

[3] R. P. Kraft, W. R. Forman, C. Jones, *et al.*, *ApJ* **569**, 54 (2002).

[4] S. Horiuchi, D. L. Meier, R. A. Preston and S. J. Tingay, *PASJ* **58**, 211 (2006).

[5] M. Cappellari, N. Neumayer, J. Reunanen, *et al.*, *MNRAS* (2008), Accepted for publication in MNRAS.

[6] R. P. Kraft, J. M. Kregenow, W. R. Forman, *et al.*, *ApJ* **560**, 675 (2001).

[7] H. Steinle, K. Bennett, H. Bloemen, *et al.*, *A&A* **330**, 97 (1998).

[8] A. A. Abdo *et al.*, *ArXiv e-prints: 0902.1559* (2009).

[9] J. E. Grindlay, H. F. Helmken, R. H. Brown, *et al.*, *ApJ* **197**, L9 (1975).

[10] G. E. Romero, J. A. Combi, S. E. Perez Bergliaffa and L. A. Anchordoqui, *Astroparticle Physics* **5**, 279 (1996).

[11] M. Lemoine, On the results of the Pierre Auger Observatory, in *SF2A-2008*, eds. C. Charbonnel, F. Combes and R. SamadiNovember 2008.

[12] F. Aharonian, A. G. Akhperjanian, A. R. Bazer-Bachi *et al.*, *A&A* **457**, 899 (2006).

[13] F. Aharonian, A. G. Akhperjanian, G. Anton *et al.*, *ApJ* **695**, L40 (2009).

[14] A. Neronov and F. A. Aharonian, *ApJ* **671**, 85 (2007).

[15] F. M. Rieger and F. A. Aharonian, *A&A* **479**, L5 (2008).

[16] J. M. Bai and M. G. Lee, *ApJ* **549**, L173 (2001).

[17] M. Chiaberge, A. Capetti and A. Celotti, *MNRAS* **324**, L33 (2001).

[18] G. Ghisellini, F. Tavecchio and M. Chiaberge, *A&A* **432**, 401 (2005).

[19] H. Sol, G. Pelletier and E. Asseo, *MNRAS* **237**, 411 (1989).

[20] A. Marcowith, G. Henri and N. Renaud, *A&A* **331**, L57 (1998).

[21] F. Tavecchio and G. Ghisellini, *MNRAS* **385**, L98 (2008).

[22] J.-P. Lenain, C. Boisson, H. Sol and K. Katarzyński, *A&A* **478**, 111 (2008).

[23] Ł. Stawarz, F. Aharonian, S. Wagner and M. Ostrowski, *MNRAS* **371**, 1705 (2006).

[24] A. Reimer, R. J. Protheroe and A.-C. Donea, *A&A* **419**, 89 (2004).

[25] J. H. Croston, R. P. Kraft, M. J. Hardcastle, M. Birkinshaw, D. M. Worrall *et al.*, *ArXiv e-prints* (2009).

[26] G. Hermann, W. Hofmann, T. Schweizer, M. Teshima for the CTA Consortium, *ArXiv e-prints* (2007).

Gamma-ray observations of galaxy clusters with H.E.S.S.

D. Nedbal[1], W. Domainko[2], J. A. Hinton[3], O. Martineau-Huynh[4]
for the H.E.S.S. Collaboration
[1]*Institute of Particle and Nuclear Physics, Charles University, V Holesovickach 2, 180 00 Prague 8, Czech Republic*
[2]*Max-Planck-Institute for Nuclear Physics, Saupfercheckweg 1, 69117 Heidelberg, Germany*
[3]*School of Physics & Astronomy, University of Leeds, Leeds LS2 9JT, UK*
[4]*LPNHE, Université Pierre et Marie Curie Paris 6, Université Denis Diderot Paris 7, CNRS/IN2P3, 4 Place Jussieu, F-75252, Paris Cedex 5, France*

Clusters of galaxies are believed to contain significant populations of cosmic rays as has been shown by radio data and indicated by hard X-ray and extreme UV observations. Due to their considerable B-field and large spatial extension, they are closed systems and accumulate hadronic cosmic rays over their entire lifetime. The cosmic rays can produce high-energy gamma rays in interactions with the intracluster medium or with radiation fields in the clusters. These gamma rays can be observed by imaging atmospheric cherenkov telescopes, such as the H.E.S.S. array. Results of recent H.E.S.S. observations of a massive cluster Abell 85 and a relaxed cluster Abell 496 are presented here and the implications of the results for the nonthermal energy content in the clusters are discussed.

1 Introduction

Galaxy clusters, the most massive gravitationally bound systems in the Universe, are the spatially most extended emitters of non-thermal radiation in the Universe. Radio observations show most significantly the presence of accelerated electrons in these systems [1], [2]. Additionally, it is also expected that clusters contain a significant population of hadronic cosmic rays since they act as storehouse for hadronic cosmic rays. Due to their spatial extension and due to the presence of magnetic fields in the μG range, clusters confine and accumulate cosmic ray protons with energies of up to $\sim 10^{15}$ eV which were accelerated in the cluster volume [3], [4].

Cosmic rays can be accelerated at several sites in galaxy clusters. These sites can be divided into external and internal sources of cosmic rays. In external mechanisms large-scale shock waves connected to cosmological structure formation are accelerators of non-thermal particles [6], [7], [8]. Particles can also be accelerated by turbulence in the intra-cluster medium(ICM) generated by major sub-cluster merger events (e.g. Brunetti et al. [9]). In internal mechanisms processes launched by the cluster galaxies lead to production of cosmic rays. Supernova remnant shocks and galactic winds have the ability to produce high-energy particles [3]. Additionally, active galactic nuclei (AGNs) can distribute non-thermal particles in the cluster volume [10], [11], [12].

A component of high energy particles should result in gamma-ray emission in galaxy clusters (see e.g. [13] for a recent review). Both cosmic ray protons and nuclei and cosmic ray electrons have the ability to generate gamma rays. Hadronic cosmic rays can produce gamma rays through inelastic collisions with thermal protons and nuclei as targets and subsequent π^0 decay [14], [3]. Alternatively, leptonic cosmic rays with sufficiently high energies can up-scatter cosmic microwave background (CMB) photons to the gamma-ray range in inverse Compton processes [15], [16], [17].

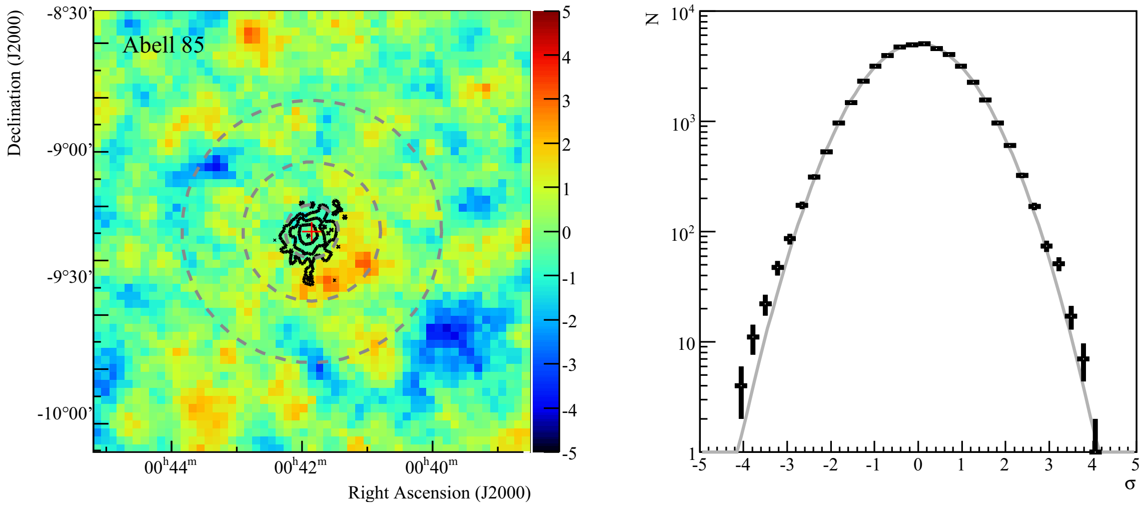

Figure 1: Left: Significance map of Abell 85 obtained with H.E.S.S. The black contours are from ROSAT PSPC X-ray observations. The dashed circles show radii of 0.4 Mpc, 1 Mpc and 1.9 Mpc. For details see main text. Right: Distribution of significances in the map of the left panel.

Despite the arguments for potential gamma-ray emission given above, no galaxy cluster has firmly been established as a gamma-ray source. Upper limits have been inferred from EGRET observations for a number of prominent galaxy clusters [18]. In the very-high energy gamma-ray range (VHE, E > 100 GeV) upper limits have been reported for several clusters by the *Whipple* [19] and *H.E.S.S.* collaboration [20], [21].

2 The H.E.S.S. experiment

The observations were performed with the H.E.S.S. telescope array, consisting of four imaging atmospheric Cherenkov telescopes located at the Khomas highlands in Namibia. See [22] for a description of the system. It has a field of view of $\sim 5°$ and observes in the VHE gamma-ray regime. The whole system is well suited to study galaxy clusters since due to its large field of view, H.E.S.S. can detect extended sources and it is expected that clusters feature extended VHE gamma-ray emission.

3 Target selection

The target clusters were selected in terms of optimal detectability, position and distance for an observation with H.E.S.S. Promising targets of this kind should be located on the southern hemisphere and at a redshift not larger than z $\sim$ 0.06, since more distant objects suffer substantial absorption from extragalactic background light. Furthermore, there should be no blazar at the location of the cluster which could superpose potential VHE emission of the galaxy cluster. In this paper the results of observations of the galaxy cluster Abell 85 with the H.E.S.S. experiment are presented. Abell 85 is a nearby (z = 0.055) massive and hot (T $\approx$ 7 keV) galaxy cluster with a complex morphology[23], [24]. It hosts a colling core at its center. In cooling core clusters, the central gas density is large enough that the radiative cooling time due to thermal X-ray emission of the intra-cluster gas is shorter than the age of the galaxy cluster. Additionally, it shows two sub-clusters merging with the main cluster which is quite uncommon for a cooling core cluster. Presumably the merging sub-clusters have not reached the central region of the main cluster and have therefore not disrupted the existing cooling core [23].

The relaxed compact cluster Abell 496 was selected in terms of a criterium of high F_X/R_X value, applied to the galaxy clusters of the REFLEX survey [5]. It has to be noted that this selection procedure prefers galaxy clusters that host a cooling core at their center.

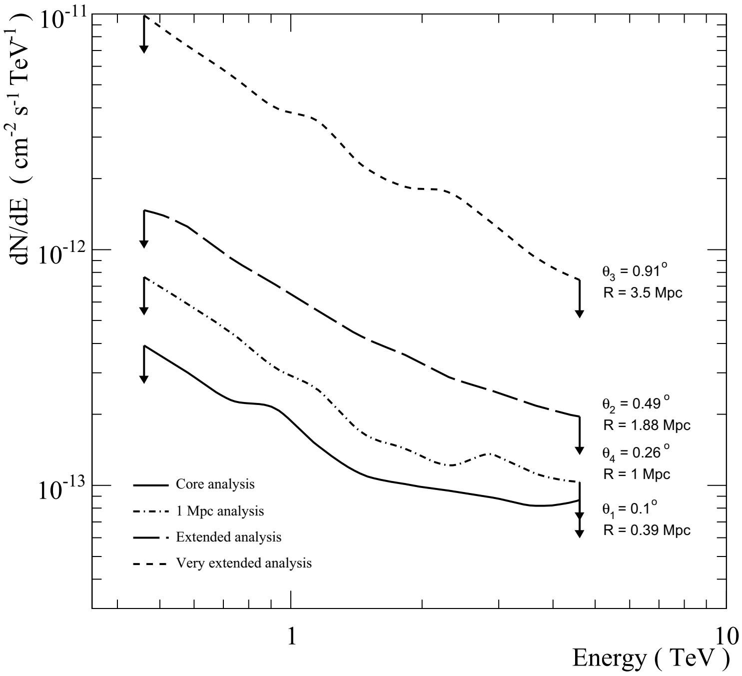

Figure 2: Upper limits on gamma-ray emission from Abell 85 for various integration regions as a function of energy. For a description of the different geometrical size cuts see main text.

4 Results

Abell 85 has been observed with H.E.S.S. for 32.5 hours live time of good quality in October and November 2006 and in August 2007. The mean zenith angle of the observations was 18° which resulted in an energy threshold of 460 GeV. H.E.S.S. standard data analysis was performed using different geometrical size cuts to account for the extended nature of the target [21]. The integration radii are chosen according to characteristic length scales of the density profile of the ICM, which acts as the target material for hadronic gamma-ray production. None of the probed regions showed a significant gamma-ray excess and hence upper limits have been derived (see Fig. 1). For obtaining the upper limits the approach of Feldman & Cousins [25] assuming a spectral index of the emission of Γ=2.1 was used. The first region for which an upper limit has been calculated is the high gas density core region. For a radius of 0.1° (0.4 Mpc at the object) around the cluster center a flux upper limit of F (>460 GeV) $<$ 3.9 $\times$ 10^{-13} ph. cm^{-2} s^{-1} has been found. As a next area, a radius of the size of the detected thermal X-ray emission of the cluster of 0.49° (1.9 Mpc) has been investigated. Here, the upper limit in VHE gamma-ray flux is F (>460 GeV) $<$ 1.5 $\times$ 10^{-12} ph. cm^{-2} s^{-1}. Finally potential emission connected to the accretion shock at the outskirts of the cluster has been searched. Therefore a very extended region with a radius of 0.91° (3.5 Mpc) has been explored. For this case the data set is reduced to 8.6 live hours due to the lack of suitable off-source data for the background estimation and there the flux upper limit was determined to F (>460 GeV) $<$ 9.9 $\times$ 10^{-12} ph. cm^{-2} s^{-1}. The upper limits on gamma-ray emission from Abell 85 for various integration regions as a function of energy can be see in Fig 2.

In case of Abell 496, 14.6 hours live time of data from 2005 and 2006 were used for analysis. Also in this case, no significant signal was found from neither of the probed regions. An upper limit on the gamma-ray flux $F(> 570\ \text{GeV}) < 4.8 \times 10^{-13}$ ph. s^{-1} cm^{-2} is found from the core region (corresponding to 0.1°) assuming a spectral index of $\Gamma = 2.1$.

5 Discussion

Based on the upper limits of the gamma-ray luminosity of the cluster Abell 85, it is possible to estimate upper limits on the total energy in hadronic cosmic rays in this cluster. For this purpose a spectral index of the cosmic rays of 2.1 is adopted and these limits are calculated for three different assumptions on the spatial distribution of cosmic rays. A hard spectral index seem to be realistic since no losses of hadronic cosmic rays at relevant energies occur in clusters and therefore the source spectrum of cosmic rays should be seen [3,4]. Firstly for the spatial distribution of the energy density in cosmic rays a scenario is adopted where it is constant throughout the cluster volume. Secondly it is assumed that the distribution of cosmic rays follows the large scale distribution of the gas density excluding the central cooling core. And thirdly it is presumed that the cosmic rays are very centrally concentrated in clusters and their distribution follow gas density profile including the central cooling core. Within a radius of 1 Mpc for the three different models of cosmic ray concentration it is found that the total energy in cosmic rays is less than 15% (constant distribution,) 8% (cosmic rays follow gas density without cooling core) and 6% (cosmic rays follow gas density including cooling core) of the thermal energy of the intra-cluster medium [21]. It has to be noted that magneto-hydrodynamic instabilities disfavor very centrally peaked distributions of cosmic rays [26,27] and an upper limit on the energy of cosmic rays of 8% seems to be realistic. This value is at the lower bounds of model predictions. Similar results have very recently also been inferred from deep radio observations for the galaxy cluster Abell 521 [28]. Therefore it seems quite likely that the next generation of gamma-ray observatories like CTA will be necessary to detect galaxy clusters in the VHE gamma-ray regime.

References

1. Giovannini, G. and Feretti, L. 2000, NewA, 5, 335
2. Gitti, M., Ferrari, C., Domainko, W., Feretti, L. and Schindler, S. 2007, A&A, 470, L25.
3. Völk, H. J., Aharonian, F. A. and Breitschwerdt, D. 1996, SSRv, 75, 279
4. Berezinsky, V. S., Blasi, P. and Ptuskin, V. S. 1997, ApJ, 487, 529
5. Böhringer, H., Schücker, P., Guzzo, L., et al. 2004, A&A, 425, 367
6. Colafrancesco, S. and Blasi, P. 2000, APh, 9, 227
7. Loeb, A. and Waxman, E. 2000, Nature, 405, 156
8. Ryu, D., Kang, H., Hallman, E. and Jones, T. W. 2003, ApJ, 593, 599
9. Brunetti, G., Blasi, P., Cassano, R. & Gabici, S. 2004, MNRAS, 350, 1174
10. Enßlin, T. A., Biermann, P. L., Kronberg, P. P. and Wu, X.-P. 1997, ApJ, 477, 560
11. Aharonian, F. A. 2002, MNRAS, 332, 215
12. Hinton, J. A., Domainko, W. and Pope, E. C. D. 2007, MNRAS, 382, 466
13. Blasi, P., Gabici, S. and Brunetti, G. 2007, Int.J.Mod.Phys. A, A22, 681
14. Dennison, B. 1980, ApJ, 239, L93
15. Atoyan, A. M. and Völk, H. J. 2000, ApJ, 535, 45
16. Gabici, S. and Blasi, P. 2003, APh, 19, 679
17. Gabici, S. and Blasi, P. 2004, APh, 20, 579
18. Reimer, O., Pohl, M., Sreekumar, P. and Mattox, J. R. 2003, ApJ, 588, 155
19. Perkins, J. S. et al. (Whipple Collaboration) 2006, ApJ, 644, 148
20. Domainko, W., et al. for the H.E.S.S. collaboration 2007, ICRC proceedings, arXiv:0708.1384
21. Aharonian, F. et al. (H.E.S.S. Collaboration) 2009, A&A, 495, 27
22. Hinton, J. A. 2004, New Astron. Rev., 48, 331
23. Kempner, J. C., Sarazin, C. L. and Ricker, P. M. 2002, ApJ, 579, 236
24. Durret, F., Lima Neto, G. B., Forman, W. 2005, A&A, 432, 809
25. Feldman, G. J. and Cousins, R. D. 1998, Phys. Rev. D, 57, 3873
26. Parker, E. N. 1966, ApJ, 145, 811
27. Chandran, B. D. and Dennis, T. J. 2006, ApJ, 642, 140
28. Brunetti, G., Giacintucci, S., Cassano, R. et al. 2008, Nature, 455, 944

GALACTIC SOURCES WITH THE *FERMI* LARGE AREA TELESCOPE

David A. Smith, *on behalf of the Fermi LAT collaboration*
Centre d'Etudes Nucléaires de Bordeaux-Gradignan
CNRS / IN2P3 and Université de Bordeaux I
Rue du Solarium, Le Haut Vigneau, B.P. 120, 33175 Gradignan cedex
smith@cenbg.in2p3.fr

The Large Area Telescope began orbiting the Earth on NASA's *Fermi* satellite on June 11, 2008, scanning the entire sky eight times per day since August. A major objective for the LAT is to characterize the large variety of GeV gamma-ray sources in the Milky Way. The emission is the by-product of charged particle acceleration to energies of GeV, TeV, and beyond. Acceleration occurs in the shocks where winds and jets collide with their surroundings, as well as across the voltage drops in pulsar magnetospheres. Many of the different Galactic GeV source classes involve either massive stars, or the remnants thereof. I will review the Galactic sources seen using the *Fermi* LAT after the first months of the sky survey.

1 Introduction

Milky Way particle accelerators have something for everybody. Astrophysicists fascinated by the mechanisms at work in a variety of types of shocks, jets, accretion flows, and rotating magnetospheres are the first concerned. But those keen on the larger scale dynamics of our Galaxy, from which to extrapolate to galaxies in general, cannot ignore these emitters as they reflect on how energy in the Galaxy is shared between the particle and photon fluxes. And finally, particle physicists bent on solving the Dark Matter puzzle need first to master the pesky foreground created by the great wealth of galactic gamma-ray sources.

The Large Area Telescope (LAT) on the *Fermi* satellite is a fabulous tool and is sparking a giant leap forward in our understanding of all of the above. The LAT is described by L. Latronico (these proceedings). Two aspects of the LAT performance are worth repeating. First, the good single-photon angular resolution combined with the large effective area and excellent charged particle rejection combine to give source localisation good enough to separate many confused sources, and is even close enough to the size of a radio-telescope lobe, or an X-ray telescope field-of-view, to simplify follow-up searches for counterparts. Second, the huge field-of-view (a fifth of the sky at a given moment), again combined with the high sensitivity, makes the sky-survey strategy possible. Imaging the whole sky 8 times per day means not only that LAT users don't need to compete for time to view their favorite objects, but also that undervalued pieces of the sky also get written to disk, and especially, that source *variability* will be seen. The LAT is truly a discovery-oriented telescope.

Table 1 lists some classes of Galactic GeV gamma-ray sources. It is striking that massive stars are present, directly or indirectly, in most of the categories. When they are still "alive", they produce intense charged-particle winds that create shocks in the dense regions where they tend to be found, such as OB associations or open clusters, long predicted to be particle accelerators, and baptised SNOBs, for "supernovae near OBs" [1,2]. The heavy elements are created in these stars. For

Table 1: Some different kinds of Galactic gamma-ray sources

Category	Sub-category	Accelerator type
Supernova remnants (SNR)		Expansion shocks
Pulsar Wind Nebulae (PWN)		Wind shocks
Massive stars	OB associations	Wind shocks
	WR stars	Wind shocks
X-ray binaries	micro-Quasars	Jets & shocks
	binary pulsars	Beams & winds
Pulsars	Young, radio-loud	Huge voltages
	Young, unknown in radio	Huge voltages
	Old (millisecond)	Huge voltages
Clusters	Globular clusters	Multi-pulsars?
	Open clusters	Wind shocks?

>9 solar masses, when the hydrogen fuel gets used up, core-collapse leads to a type II supernova explosion. The bread-and-butter of Galactic high-energy astrophysics consists of the three main leftovers from these disasters, namely, supernova remnants (SNRs), pulsar wind nebulae (PWNs), and pulsars.

Pulsars dominate the list of identified galactic sources and will be discussed below. In these proceedings, please see the contributions by D. Parent, M. Kerr, and A. Caliandro about young, radio-loud gamma-ray pulsars ; by F. Giordano for the gamma-ray pulsars discovered through the blind period search ; and by L. Guillemot for the discovery of a population of millisecond pulsars, with honorable mention for globular clusters.

2 Swan Song

To focus this sampling of early LAT results for Galactic sources I will mostly limit myself to the Cygnus region, illustrated in Figure 1. Furthermore, since most of the quantitative results are presented by other LAT team members elsewhere in these proceedings, I'll indulge the reader in a little astro-tourism suitable for summer evenings in mid-northern latitudes.

Vega is a very bright star near the zenith, to the right in the figure. Nearby is the "northern cross", the name of the asterism at the heart of the Cygnus constellation. The long-necked swan is flying along the Milky Way – visible here in gamma-rays – towards the Galactic center, in Sagittarius, near where Scorpio grazes the southern horizon. The Swan's head is the star Albireo, its tail is Deneb. The Figure includes a few Messier catalog objects, as well as the first pulsar discovered by Hewish & Bell in 1967, PSR B1919+21.

The small circles in the Figure are gamma-ray sources from the Bright Sources List [3] described by J. Ballet (these proceedings). The radius corresponds to the 95% Confidence Level for the source localization. Not shown in the figure are the several EGRET 3^{rd} catalog sources (hereafter "3EG"), most of which were unidentified [4]. The largest category of identified LAT sources is the gamma-ray pulsars: as many are visible within 20° of Cygnus as EGRET saw for the whole sky.

Most prominent in Figure 1 is the diffuse emission along the plane itself, the result of high-energy charged cosmic rays interacting with interstellar gas and dust, a separate topic covered by G. Johannesson in these proceedings. This said, one of the goals of the study of discrete gamma-ray sources is to unveil the origin of these cosmic rays.

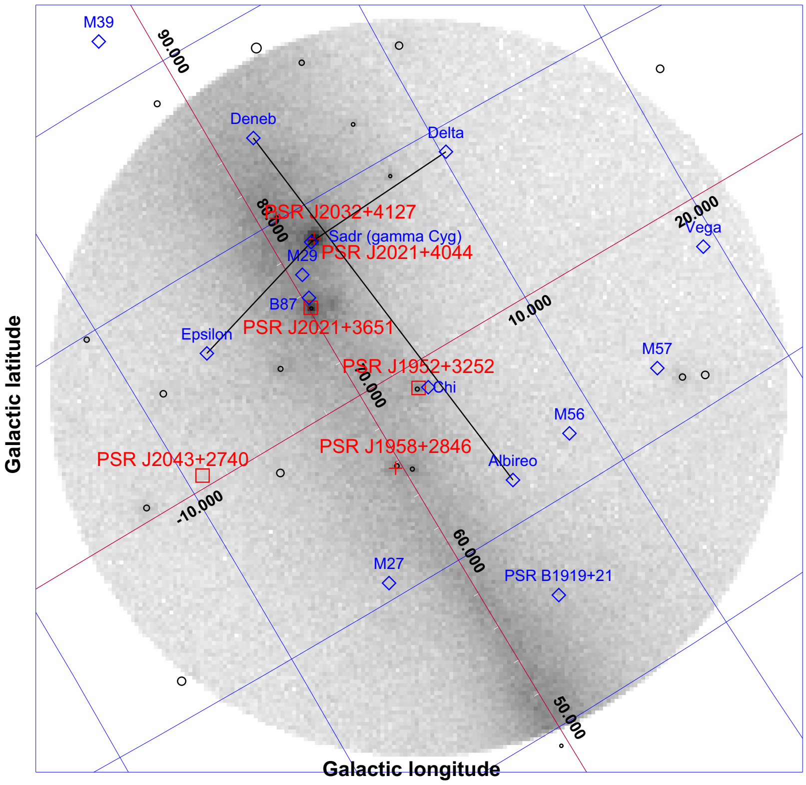

Figure 1: The Cygnus region. The grey-scale counts map shows six months of LAT > 0.1 GeV gamma-rays. The circles are the 95% C.L. radii of Bright Sources List objects. Crosses show gamma-ray pulsars found using radio ephemerides, while squares show gamma-ray pulsars found in the blind period search. Diamonds show some bright stars, Messier objects, the open cluster Berkeley 87 ("B87", see text), as well as the first pulsar discovered 42 years ago, PSR B1919+21. The coordinate scales are in degrees, galactic longitude decreases from the Swan's tail to its head.

Clusters and Associations, with and without shocks

2.1 OB associations

The gamma-ray-selected pulsar PSR J2032+4127 lies in the middle of Cygnus OB2. The name "OB" refers to the hot, blue spectral types of the many young, massive stars found grouped together [a]. The (previously) unidentified source 3EG J2033+4118 overlaps Cyg OB2 nicely. Cyg OB2 is also spatially associated with a famous TeV source, first reported by the Hegra collaboration at Moriond in 2001 (G. Rowell), and discussed extensively for years thereafter [5]. (The rapporteur was Yours Truly [6].) The TeV discovery was important because it was the first ever serendipitous discovery of a TeV gamma-ray source by an atmospheric Cherenkov detector. Furthermore, it was an apparent break in the monopoly then held by SNRs as the principal candidate source class to explain the origin of cosmic rays. The basic idea is that particle acceleration occurs in the shocks between the stellar winds. The "energy budget" argument supporting SNRs as the origin of the cosmic radiation applies nearly as well to these sorts of objects: supernovas are more powerful, but shorter-lived. Integrated over their lifetimes, OB associations fall only about an order-of-magnitude shy of the putative SN contribution to the cosmic ray energy budget. The uncertainties in the population numbers could conceivably even the footing further.

The LAT discovery of a gamma-ray pulsar that might be physically associated with Cygnus OB2 gives pause: could it be that the GeV/TeV gamma-ray source is *not* the shock of stellar winds after all? Ongoing radio and X-ray searches using the accurate LAT ephemeris could conceivably reveal a PWN [7], in which case instead of being a prototype of a new class, Cyg OB2 would turn out to be "just another" case of a pulsar giving GeV emission, and the surrounding PWN providing the TeV signal, as in the Crab (see M-H Grondin, these proceedings).

2.2 Open Clusters

Open clusters are another type of stellar grouping where massive stars are close enough together, and the interstellar medium is dense enough, that particle acceleration in shocks can occur. (Famous open clusters are the Pleiades and the Hyades, both visible by eye near the Crab, straddling Taurus and Orion.) In particular, the open cluster Berkeley 87 is shown in Figure 1. Bednarek [5] and earlier authors had predicted that shocks from the winds of massive Wolf-Rayet [b] stars could be the source of the GeV gamma-ray source reported by EGRET.

The discovery of gamma-ray pulsations from PSR J2021+3651 by the LAT [8] (M. Kerr, these proceedings), as well as by AGILE [9], means that this scenario is not dominant for this previously unidentified 3EG source. The LAT upper limit on off-pulse emission was primarily intended to search for GeV gamma-rays from the Dragonfly PWN, but it is interesting to note that the upper limit is at approximately the same level as Bednarek's prediction for the emission by the shocked winds. With increased statistics, the LAT will continue to search for off-pulse emission. It will then be a challenge to distinguish between the PWN and the open cluster as the source. The LAT localization will likely be up to this challenge in this case.

Berkeley 87 illustrates an element for understanding another problem: that of the pulsar distances d, so critical to understand their luminosity $L_\gamma = 4\pi f_\Omega d^2 h$ and thus the efficiency $\eta = L_\gamma/\dot{E}$ with which the rotational kinetic energy of neutron stars is converted to radiation in the magnetosphere. (The *"beam correction factor"* f_Ω and the spin-down energy $\dot{E}$ are discussed in Section 3, and h is the integral energy flux.) For pulsars within several hundred parsecs, parallax measurements can give accurate distances. But most known pulsars are farther, and more model-sensitive distance estimators must be used. The primary tool-of-choice is the Cordes and Lazio NE 2001 model for the free electron density throughout the Milky Way [10], which converts the measured radio

[a] The modern mnemonic for the stellar spectral types OBAFGKM is "Only Boys Accepting Feminism Get Kissed Meaningfully", from hottest to coolest.

[b] Professor Rayet founded the Bordeaux Observatory in 1893.

Dispersion Measure (DM) into a distance for a given pulsar direction ("line-of-sight"). The model uses average electron densities averaged over fairly broad swaths of the sky. For most directions, the typical distance uncertainty is ±40%. *However*, in many cases the distance can be wrong by a factor of a few! (Han, in these proceedings, addresses current knowledge of Galactic B-field and electron distributions.)

The gamma-ray pulsar PSR J2021+3651 suffers from this distance problem [8]. For its DM of 370 electrons per pc/cm^3 the nominal distance given by NE2001 is 12.1 kpc, yielding $\eta > 100\%$ for reasonable beaming models! The line-of-sight coincides with the edge of Berkeley 87. A back-of-the-envelope calculation [c] suggests that 35 electrons per pc/cm^3 could be due to the open cluster. The NE2001 distance decreases to 10.7 kpc after subtracting the "extra" electrons. This is still several times farther than argued for this pulsar and illustrates the type of work that needs to be done to obtain reliable pulsar distances.

2.3 Globular Clusters

Globular clusters (GCs) are quite different than either open clusters or OB associations. They are systems nearly as old as the Galaxy itself, judged in part by the high metal content of the stars residing therein. GCs contain many recycled pulsars (millisecond pulsars, MSPs). An important LAT result is the discovery that MSPs efficiently convert their rotation energy into GeV gamma-rays [11,12] (see also L. Guillemot, these proceedings). He also describes the LAT discovery of the globular cluster 47 Tuc as a steady gamma-ray source, and lists the MSPs known in many other GCs. There is a good chance that the LAT will be able to see pulsations from the individual MSPs in GCs.

Supernova Remnants and Pulsar Wind Nebulae

Three SNR/PWN systems are apparent in the Cygnus region (Figure 1). The γ Cygni SNR shares its name with the bright star Sadr. About half-way from Sadr to Albireo lies the variable star χ Cygni, near the SNR called CTB 80, at the heart of which lies the EGRET pulsar PSR B1951+32. Finally, the "Dragonfly" PWN surrounds PSR J2021+3651, mentioned above.

Pulsations have been discovered in the blind period search for γ Cygni [13]: a traditional SNR thus reveals that it probably has a PWN as well, coincident with 3EG J2020+4017. More generally, the many TeV PWNs discovered these last years, mainly by H.E.S.S., also host GeV pulsars, as shown by the LAT. See M-H Grondin (these proceedings) for ongoing work on the Kookaburra and Vela X PWN's.

X-ray binaries

The LAT clearly sees GeV gamma-ray emission from the high-mass X-ray binary LSI +61 303, modulated at the 26.5 day orbital period [14] (A. Hill, these proceedings). This object is a TeV source, and is one of the classic "micro-quasars". The basic idea of a μquasar is that accretion from the companion star is analogous to the accretion from the torus onto the supermassive black hole that occurs in a "real" quasar, that is, in an active galactic nucleus. Both would then produce jets wherein high-energy emission would occur. Afficionados of μquasars argue that these smaller, closer systems allow exploration of the key ideas applied to AGNs. LS 5039 is another μquasar for which evidence of a GeV gamma-ray signal is mounting.

However, in a classic paper called "Micro-quasars: Pulsars in Disguise?", G. Dubus [15] deconstructs the observational evidence that lead to the μquasar paradigm and explores the idea that a pulsar in orbit around a suitable companion could equally well explain the data in some cases. Pulsars, and massive stars, are both thus once again at the heart of the explorations of high-energy

[c] performed by S. Bontemps

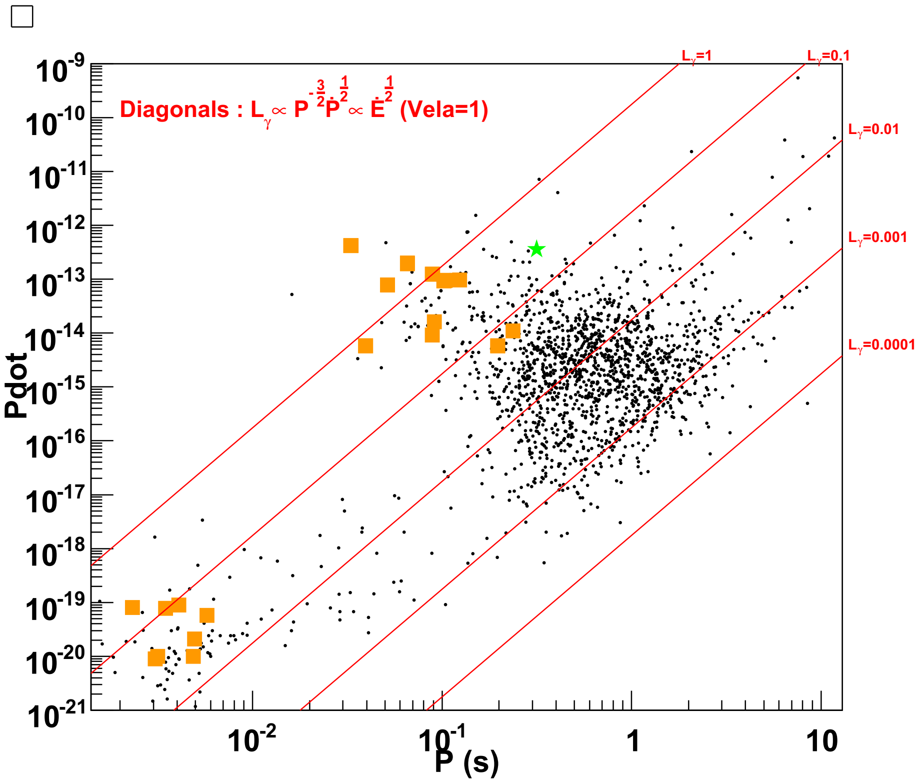

Figure 2: Period derivative versus period (seconds) of most known pulsars. Gamma-ray pulsars found by the *Fermi* LAT using rotation parameters from radiotelescopes are shown as squares, while those discovered by the blind period search are stars (only CTA 1's parameters are published so far). A total of about 50 gamma-ray pulsars have been detected, publications are in progress. Black dots show the remainder of the pulsars from the ATNF database. Diagonal lines show constant $\sqrt{\dot{E}}$, normalized to the Vela pulsar ($\dot{E} = 7 \times 10^{36}$ erg/s).

Galactic sources. As LAT data accumulates we will be able to address these issues more and more directly.

3 Gamma-ray pulsars

Pre-launch predictions for the number of gamma-ray pulsars that the LAT would detect ranged from about 100 to several hundred, and a substantial radio timing campaign was organized [18]. The differences stem from the emission model (how efficiently is the neutron star's kinetic energy of rotation transformed into high energy radiation by the electromagnetic braking process? How wide are the beams that sometimes sweep the Earth?) as well as the population model (how many neutron stars are there within a given distance of the Earth, that is, what is the supernova rate in our part of the Galaxy?). As of this writing (April, 2009), the LAT has chalked up fifty 5σ detections. These are the 6 EGRET pulsars, the 3 marginal EGRET pulsars, the new pulsars found in the blind period search [13] , and 8 millisecond pulsars [11,12]. The remaining are young radio pulsars [8,16,17], half of which are still unpublished.

Figure 2 is the standard $\dot{P}-P$ diagram, for the 1794 pulsars from the ATNF database [d], nearly all of which are radio pulsars. P is the rotation period, in seconds, and $\dot{P}=\frac{dP}{dt}$ is the rate at which the rotation slows due to electromagnetic braking. The rate at which the kinetic energy of rotation is lost by the neutron star is $\dot{E}=4\pi^2 I\dot{P}/P^3$, where the standard value for the moment of inertia used is $I=10^{45}$ gm-cm^2. Diagonal lines of constant $\sqrt{\dot{E}}$ are shown, to illustrate predictions that $L_\gamma \propto \sqrt{\dot{E}}$, normalized to Vela [19]. The position of CTA 1 is shown, and soon there will be 15 more stars [13].

The figure shows that $\dot{E}$ alone does not predict which pulsars give detectable gamma-ray pulsations. Normalizing for the distance-squared reduces the scatter, but the mix of gamma-ray bright and dim pulsars for a given $\dot{E}$ remains. The distance ambiguities discussed above are only part of the story. The geometry of the radio and gamma-ray beams is another.

Figure 3 shows the 3-dimensional gamma-ray emission predicted by a pulsar emission model (left), as well as a projection across a given line-of-sight from the Earth (right). The beams are very narrow in longitude but extended in latitude, called *"fan-like"*. To infer the total energy output in gamma-rays of the pulsar from the energy flux measured by the LAT, we use a *"beam correction factor"* f_Ω which is, for a given model and set of pulsar parameters, simply the ratio of the integrals of the two figures, normalized to 4π. Most past work has assumed a 1 sr beam (a $\sim 30°$ half-angle for a cone), which yields $f_\Omega = 1/4\pi \simeq 0.1$, corresponding to polar cap emission. Observations increasingly favor gamma-ray emission from near the pulsar light cylinder, as for example in the outer gaps or slot gaps, where the beam is broad like in the figure, and $f_\Omega \simeq 1$. This framework was developed in [20] and briefly repeated in some of the LAT pulsar papers already cited [8].

The models also predict the shapes and relative phase of the radio pulse profiles, and predict spectral parameters such as the cut-off energies. We are well-armed to compare the increasing number of LAT pulsar measurements with model predictions and expect a signficant step forward in the fundamental understanding of neutron star emission as a consequence.

4 Conclusions

Half-way through the *Fermi* LAT one-year all-sky survey, a large number of EGRET unidentifed sources have already been unambiguously associated with objects known at other wavelengths. Often, they are pulsars. Other Galactic objects which are clearly identified at GeV energies with the LAT are globular clusters and high-mass X-ray binaries. Solid identifications as pulsars means that other hypotheses have to be put aside, at least of the level of intensity that was within the reach of EGRET, and thus, just for the time being.

[d] http://www.atnf.csiro.au/research/pulsar/psrcat/

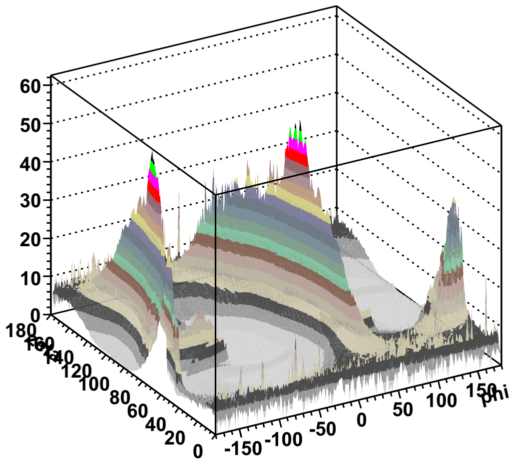

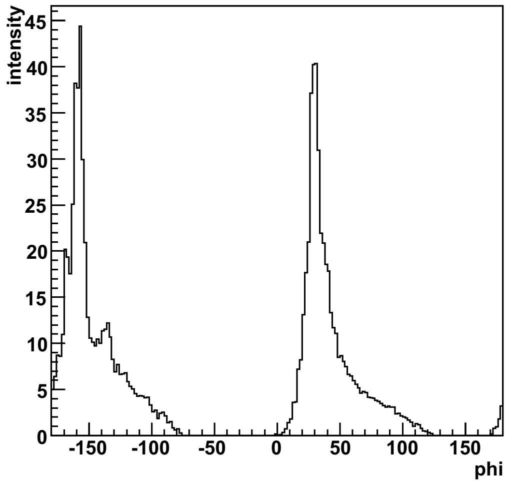

Figure 3: Simulated gamma-ray "fan-like" beam in a "slot gap" model, courtesy of A. Harding. Left: ζ versus ϕ, in degrees, where ϕ is the neutron star longitude (more commonly known as the rotation phase), and ζ is the latitude relative to the neutron star rotation axis – the line-of-sight from the neutron star to a terrestial viewer selects a value of ζ. Right: Projection along $\zeta = 80°$. The *"beam correction factor"* f_Ω is the ratio of the integrals of the two plots, normalized to 4π.

Since pulsars can be easily identifiable sources they are also easy to subtract, to open the way to analysis of more subtle objects. The nebulae sustained by pulsar winds are a second wave of objects to be scrutinized, also relatively easy to identify. As each of the many components of the Galactic gamma-ray emission is mastered and subtracted, fainter and fainter ones will come to light. Emission by the shocks in stellar winds will likely be detected, at some level. And beyond that? All guesses are fair, and we have another 9.5 years to follow through.

References

1. T. Montmerle, ApJ 231, 95 (1979)
2. M. Cassé & J. Paul, ApJ 237, 236 (1980)
3. A. Abdo et al, ApJ submitted, arXiv:0902.1340 ("Bright Sources List")
4. Hartman, R. C., Bertsch, D. L., Bloom, S. D., et al. 1999,ApJ Suppl 123, 79
5. Bednarek, W., MNRAS, 382, 367 (2007) [arXiv:0704.3517]
6. D.A. Smith, in V.H.E. Phenomena in the Universe, J. Trân Thanh Vân, editor (2003)
7. F. Camilo, P.S. Ray, et al ApJ in preparation
8. A. Abdo et al, ApJ submitted (PSR J2021+3651)
9. J.P. Halpern et al., Ap J Lett. 688, 33 (2008)
10. J. M. Cordes & T. J. W. Lazio 2002 [arXiv:astro-ph/0207156]
11. A. Abdo et al, ApJ accepted, arXiv:0904.4377 (PSR J0030+0451)
12. A. Abdo et al, Science submitted (Millisecond pulsars)
13. A. Abdo et al, Science submitted (Blind frequency search for gamma-ray pulsars)
14. A. Abdo et al, ApJ submitted (LS I +61 303)
15. G. Dubus, A&A,456,801 (2006) [arXiv:astro-ph/0605287]
16. A. Abdo et al, ApJ Lett, 695, 72, arXiv:0903.1602 (PSR J1028-5819)
17. A. Abdo et al, ApJ accepted, (PSR J0205+6449)
18. D.A. Smith, L. Guillemot, et al. A&A 492, 923 (2008)
19. A. Abdo et al, ApJ 696, 1084 (2009) (Vela)
20. K. P. Watters et al., ApJ 695, 1289 (2009) [arXiv:astro-ph/0812.3931]

LOOKING AT OUR GALAXY WITH THE MAGIC EYE

D. HADASCH FOR THE MAGIC COLLABORATION
Grup de Física de les Radiacions, Universitat Autònoma de Barcelona,
E-08193 Bellaterra

The MAGIC telescope located on the Canary Island of La Palma is a single-dish imaging atmospheric Cherenkov telescope. With a sensitivity in the 25 GeV - 30 TeV energy band it is best suited for studying very high energy γ-ray sources in the Northern hemisphere. Here we give an overview of the most recent experimental results on Galactic sources obtained with MAGIC. These include pulsars, binary systems, supernova remnants and unidentified sources.

1 What is the MAGIC eye and what does it see?

The study of very high energy (VHE, $E \geq 70$ GeV) γ-ray emission from objects in our galaxy is one of the major goals of ground-based γ-ray astronomy and one of the main issues of the Major Atmospheric Gamma Imaging Cherenkov (MAGIC) telescope located on the Canary Island of La Palma on the Roque de los Muchachos Observatory at 2250 m above see level. Its energy range spans from 50 GeV-60 GeV (trigger threshold at small zenith angles) and with a special low-energy trigger even from 25 GeV up to tens of TeV thanks to a number of technological improvements in its design. The energy resolution is better than 20% above an energy of 200 GeV. The telescope has a sensitivity of $\sim 1.6\%$ of the Crab Nebula flux in 50 observing hours. From summer 2009 on a second MAGIC telescope will allow stereoscopic observations. So the sensitivity will be improved substantially and make a deeper view in our galaxy possible.

MAGIC contributes to several fields of fundamental physics and astrophysics. It observes galactic and extragalactic objects and is active in search of Dark Matter. In this paper we highlight our latest contributions to Galactic astrophysics. Up to now MAGIC discovered four new VHE γ-ray sources in our galaxy and studied in detail eight of the previously known. The results from extragalactic observations as well as the results of the Crab Nebula and the Crab pulsar are presented elsewhere in these proceedings [1,2].

Cassiopeia A The shell type supernova remnant (SNR) Cassiopeia A located at a distance of $\sim$3.4 kpc was discovered by HEGRA at TeV energies after 232 hrs of observation time. Eight years later MAGIC observed the source between July 2006 and January 2007 for a total of 47 good-quality hours [3]. The observation resulted in the confirmation of the the HEGRA detection with a significance of $5.2\,\sigma$ and a photon flux above 1 TeV of $(7.3 \pm 0.7_{stat} \pm 2.2_{sys}) \times 10^{-13}\mathrm{cm}^{-2}\mathrm{s}^{-1}$. The spectrum is consistent with that measured by HEGRA for the energies above 1 TeV, i.e., where they overlap (see figure 1). The photon spectrum is compatible with a power law $\frac{\mathrm{d}N}{\mathrm{d}E\mathrm{d}A\mathrm{d}t} \propto E^{-\Gamma}$ with a photon index $\Gamma = 2.3 \pm 0.2_{stat} \pm 0.2_{sys}$. Furthermore, MAGIC significantly extends the energy spectrum down to about 250 GeV. The source is point-like within the angular resolution of the telescope. According to the theoretical modeling of Cassiopeia A's multi-frequency emission leptonic models of TeV emission can be disfavored because they require too low magnetic field values for the low frequency part of the spectrum. A hadronic scenario for the γ-ray production seems likely. However, it predicts for the 100 GeV - 10 TeV region a harder spectrum than the measured one (see fig. 1).

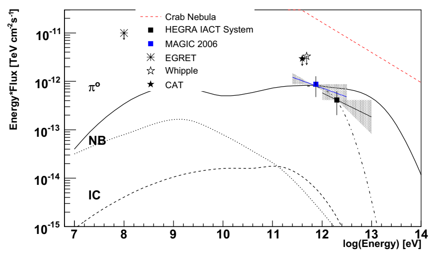

Figure 1: Spectrum of Cas A as measured by MAGIC. The upper limits given by Whipple, EGRET and CAT are also indicated, as well as the HEGRA detection. The MAGIC and HEGRA spectra are shown in the context of the model by [4].

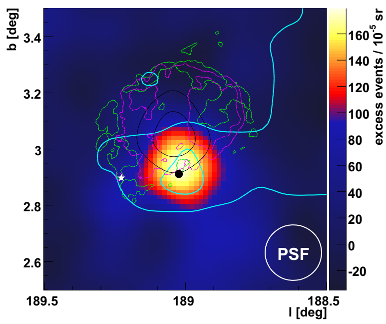

Figure 2: Sky map in direction of MAGIC J0616+225. Overlayed: ^{12}CO emission contours (cyan), contours of 20 cm VLA radio data (green), X-ray contours (purple), γ-ray contours (black) from EGRET. White star: position of pulsar CXOU J061705.3+222127. Black dot: position of 1720 MHz OH mase.

MAGIC J0616+225/ IC 443 In 2007 MAGIC discovered a new source [5] of VHE γ-ray emission, MAGIC J0616+225, located close to the Galactic Plane after an effective observation time of 29 hrs with a significance of $5.7\,\sigma$. The measured energy spectrum is well fitted by the following power law: $\frac{\mathrm{d}N}{\mathrm{d}E\mathrm{d}A\mathrm{d}t} = (1.0 \pm 0.2) \times 10^{-11}(\mathrm{E}/0.4\mathrm{TeV})^{-3.1\pm0.3}\mathrm{TeV}^{-1}\mathrm{cm}^{-2}\mathrm{s}^{-1}$. The source is point-like for MAGIC, spatially coincident with the SNR IC 443, a molecular cloud and the location of maser emission (see fig. 2), what suggest that a hadronic origin of the VHE γ-rays is likely.

Wolf-Rayet Binary Systems Wolf-Rayet stars represent an evolved stage of hot ($\mathrm{T_{eff}} > 20000$K), massive stars and are characterized by their strong winds with a velocity up to 5000 km/s and by the highest known mass loss rate $\dot{M} \sim 10^{-4}...10^{-5} M_{\odot}/yr$. Colliding winds are theoretically predicted to produce VHE γ-rays through leptonic or hadronic processes, although the evidence of this relationship has proven to be elusive so far. After the observation of the two isolated binary systems WR 146 and WR 147 containing a Wolf-Rayet star and a O8-star or a B0.5V-star, MAGIC presented the first experimental limits [6] on these objects after 30.3 hrs and 44.5 hrs, respectively (see figure 3). These limits are shown in figure 4 for the case of WR 147, compared with a theoretical model [7].

Energy [GeV]	WR 146 UL [Crab flux]	WR 147 UL [Crab flux]
> 80	5.0 %	1.5 %
> 200	3.5 %	1.4 %
> 600	1.2 %	1.7 %

Figure 3: Calculated upper limits above a certain energy for two Wolf-Rayet binary systems.

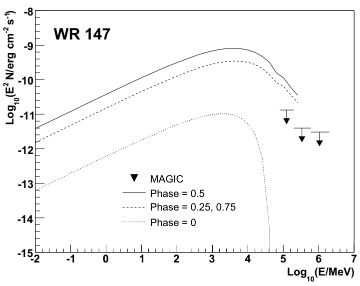

Figure 4: Inverse Compton (IC) spectra of WR 147 for orbital phases 0, 0.25, 0.5 and 0.75 together with MAGIC experimental upper limits.

Cygnus X-1 Cygnus X-1 consists of a black hole turning around an O-type star and is one of the brightest X-ray sources in the sky. During one night (24th Sept 2006) MAGIC observed a hint of a signal from Cygnus X-1 on the level of $4.1\,\sigma$ (after trials) [8], which seems to be unrelated with the nearby radio structure (see fig. 5). The observed hint of the VHE emission is in coincidence with a historically high flux in X-rays. In total the source was observed for 40 hrs in 26 nights between June and November 2006 and no steady γ-ray signal was detected. MAGIC observations have imposed the first limits to the steady γ-ray emission from this object at the level of 1 % of the Crab Nebula flux above $\sim$500 GeV.

LS I +61°303 LS I +61°303 is a γ-ray binary discovered by MAGIC [9,10,11] at TeV energies at a distance of $\sim$2 kpc. It consists of an unknown compact object (a neutron star or a black hole) orbiting a Be star and displays periodic emission throughout the spectrum from radio to X-ray wavelengths. To test for possible periodic structures in the VHE γ-ray light curve, we apply the formalism developed by Lomb and Scargle to the data taken in 2005 and 2006. We found a period of (26.8 ± 0.2) days (with a post-trial chance probability of 10^{-7}) (see fig. 6). This result is compatible with the orbital periodicity measured at other wavelengths. The peak of the emission is found always at orbital phases around 0.6-0.7. During December 2006 we detected a secondary peak at phase 0.8-0.9.

TeV J2032+4130 The first known VHE γ-ray emitting unidentified source, TeV J2032+4130, was discovered by HEGRA six years ago. MAGIC observed the source [12] for 94 hrs between 2005 and 2007 and confirmed the HEGRA

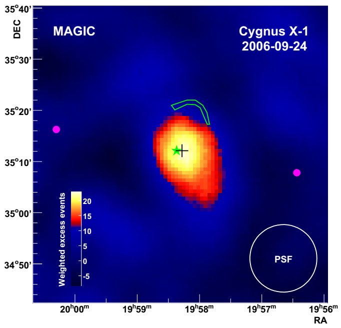

Figure 5: Sky map of Cygnus X-1 corresponding to the flare detected on 2006-09-24. The cross shows the best-fit position of the γ-ray source. The position of the X-ray source and radio emitting ring-like are marked by the star and contour, respectively.

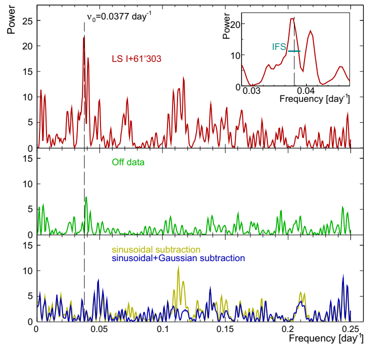

Figure 6: Lomb-Scargle periodogram for LS I $+61^{\circ}303$ data (upper panel) and simultaneous background data (middle panel). Lower panel: periodograms after subtraction of a sinusoidal signal at the orbital period (yellow line) and a sinusoidal plus a Gaussian wave form (blue line). Vertical dashed: orbital frequency. Inset: zoom around the highest peak.

detection with $5.6\,\sigma$. Also the flux, position and angular extension are compatible. The intrinsic size of the source assuming a Gaussian profile is $\sigma_{src} = 5.0 \pm 1.7_{stat} \pm 0.6_{sys}$ arcmin. The energy spectrum can be described by the power law: $\frac{\mathrm{d}N}{\mathrm{d}E\mathrm{d}A\mathrm{d}t} = (4.5 \pm 0.3) \times 10^{-13} (\mathrm{E}/1\mathrm{TeV})^{-2.0 \pm 0.3} \mathrm{TeV}^{-1}\mathrm{cm}^{-2}\mathrm{s}^{-1}$ and could be extended by MAGIC down to 400 GeV with respect to the HEGRA spectrum. Furthermore, any spectral break can be found, nor any flux variability over the three years of MAGIC observations.

Acknowledgments We thank the Instituto de Astrofísica de Canarias for the excellent working conditions at the Observatorio del Roque de los Muchachos in La Palma.

References

1. B. Delotto for the MAGIC Collaboration, these proceedings.
2. M. Lopez for the MAGIC Collaboration, these proceedings.
3. J. Albert et al. (MAGIC Coll.), *A&A* **474**, 937 (2007)
4. E.G. Berezhko et al., *A&A* **400**, 971 (2003)
5. J. Albert et al. (MAGIC Coll.), *ApJ* **664**, L87 (2007)
6. J. Aliu et al. (MAGIC Coll.), *ApJ Lett.* **685**, L71 (2008)
7. A. Reimer, M. Pohl, O. Reimer, *ApJ* **644**, 1118 (2006)
8. J. Albert et al. (MAGIC Coll.), *ApJ* **665**, L51 (2007)
9. J. Albert et al. (MAGIC Coll.), *Science* **312**, 1771 (2006)
10. J. Albert et al. (MAGIC Coll.), *ApJ* **684**, 1351 (2008)
11. J. Albert et al., (MAGIC Coll.) *ApJ* **693**, 303 (2009)
12. J. Albert et al. (MAGIC Coll.), *ApJ* **675**, L25 (2008)

Results of VERITAS Galactic Observations

A. Weinstein, for the VERITAS Collaboration[a]
Department of Physics and Astronomy, University of California Los Angeles, 430 Portola Plaza, Box 951547, Los Angeles, CA 90095-1547, USA

The Very Energetic Radiation Imaging Telescope Array System (VERITAS) is currently the world's most sensitive detector of VHE ($E > 100$ GeV) gamma rays from astrophysical sources. An overview is given of the VERITAS collaboration's galactic observation program and highlight results from that program, including several VHE gamma-ray source detections, are presented.

1 Introduction

VERITAS, a stereoscopic array of four imaging atmospheric telescopes (IACTs) in southern Arizona, is one of a new generation of observatories that have revolutionized the study of the very high energy (VHE; $E > 100$ GeV) gamma-ray sky. VERITAS, which, began routine observations with the full array in September 2007[1], has a comprehensive program of galactic source observations, including targeted observations of supernova remnants (SNRs) and pulsar wind nebulae (PWNe), galactic compact objects, and unidentified VHE gamma-ray emitters, as well as an unbiased survey of a 75 square degree portion of Cygnus region of the Galactic plane.

2 Supernova Remnants and Pulsar Wind Nebulae

Supernova remnants are thought to be responsible for the acceleration of cosmic rays up to energies of about 10^{15} eV. Particle acceleration is believed to take place at either the shock front between the expanding remnant and the interstellar medium (shell-type remnants) or at the termination shock created by the collision of the pulsar wind with the surrounding medium (plerionic remnants or pulsar wind nebulae). It remains in question whether the gamma-ray emission is produced by inverse Compton scattering of accelerated electrons or is the result of pion decay subsequent to hadronic interactions.

As not only the most established, but the strongest, non-variable source of VHE gamma-ray emission, the Crab pulsar wind nebula (PWN) is an invaluable calibration source for any new VHE gamma-ray observatory, particularly one situated in the northern hemisphere. VERITAS has observed the Crab Nebula with the two-, three-, and four-telescope array configurations; these observations have been used to validate a number of performance benchmarks, which agree well with those predicted by Monte-Carlo simulations. These performance metrics include an energy resolution of $\sim 15\%$, a single-photon angular resolution of $\sim 0.1°$, and a sensitivity that yields a 5σ detection of a gamma-ray source with a flux 1% that of the Crab Nebula in

[a] See `http://veritas.sao.arizona.edu/conferences/authors?moriond2009`

less than 50 hours. The measured Crab flux and energy spectrum are consistent with those measured by other observatories. VERITAS observations of a selection of pulsar wind nebulae associated with large energy loss ($\dot{E}/d^2$) pulsars have also yielded a set of upper limits on PWN integral flux above 300 GeV (ranging from 0.2% to 2.3% of the Crab Nebula flux) that have been reported elsewhere [3].

VERITAS has also observed a number of shell-type supernova remnants, two of which have yielded detections. The first, the young SNR Cas A, which was first detected in TeV gamma rays by HEGRA[4] is seen by VERITAS at $\sim 9.8\sigma$ in 20 hours of observation, with a flux of about 3% of the Crab Nebula flux above 1 TeV[6]. The second, supernova remnant IC 443 (G189.1 + 3.0), which not only contains a pulsar wind nebula (CXOU J061705.3+222127) but also one of the clearest examples of an SNR interacting with molecular clouds, is of especial interest. IC443 was initially co-detected in VHE gamma rays by both VERITAS and MAGIC[5]. Deep VERITAS observations taken in 2007 have now provided the first clear evidence that the VHE gamma-ray emission coincident with IC443 is extended. In 37.9 hours of observations, VERITAS detected gamma-ray emission above 300 GeV with a significance of 8.3 sigma (7.5 post-trials) in a point-source search[11]. The emission was found to be centered at $6^h16^m51^s, 22°30'11''(J2000) \pm 0.03°_{stat} \pm 0.08°_{sys}$; this location is in agreement with the MAGIC detection and coincides with a region of OH maser emission that indicates that the SNR is interacting with an encircling molecular cloud along the line of sight. Fitting the excess to a two-dimensional Gaussian profile yields an intrinsic source extension of $0.16° \pm 0.03°_{stat} \pm 0.04°_{sys}$. The spectrum agrees well with a power-law fit with a photon index of $2.99 \pm 0.38_{stat} \pm 0.3_{sys}$ and an integral flux above 300 GeV of $(4.63 \pm 0.90_{stat} \pm 0.93_{sys}) \times 10^{-12}\mathrm{cm}^{-2}\mathrm{s}^{-1}$.

The coincidence of the gamma-ray source with the densest region of the molecular cloud, only 2' from the brightest source of maser emission, suggests hadronic cosmic-ray acceleration, with the cloud acting as a target medium to amplify both pion production and the associated gamma-ray emission. However, TeV PWNe have been known to be offset from their X-ray counterparts at a level comparable to the 10'-20' displacement seen between the TeV emission from IC443 and the nearby X-ray PWN. Thus a scenario in which the gamma-ray emission originates from inverse Compton scattering off of a relic electron population from the PWN cannot be ruled out at this time. However, future studies of the energy-dependent morphology of both the TeV gamma-ray source and the nearby (possibly associated) gamma-ray source seen by the Fermi satellite may allow us to distinguish between competing scenarios.

3 High-Mass X-Ray Binaries

At this time, three high-mass X-ray binaries have been detected as gamma-ray sources at TeV energies. LSI + 61°303, first detected by MAGIC[12] is the only such source in the northern hemisphere. LSI + 61°303 consists of a Be-type star with a dense circumstellar disk, orbited once every 26.5 days by either a neutron star or a black hole. The system was thought by some to be a *microquasar*, in which accretion of material from the star onto the compact object powers relativistic jets that are the sites of gamma-ray production[13]. However, the favored hypothesis is that the gamma-rays are produced by shocks formed by collision of the relativistic pulsar wind with that of the star[14].

LSI+61°303 was initially observed by VERITAS over several orbital periods and detected at 8.4σ. The gamma-ray emission was observed to be strongly modulated by the 26.5 day orbital period, with the maximum flux for each orbital cycle appearing at apastron and corresponding to $\simeq 10\%$ of the flux of the Crab Nebula above 300 GeV[15]. Later observations in 2007 and 2008 confirmed the detection (albeit with a higher energy threshold of 500 GeV), with clear evidence for emission at apastron and marginal evidence for emission at periastron. The differential energy

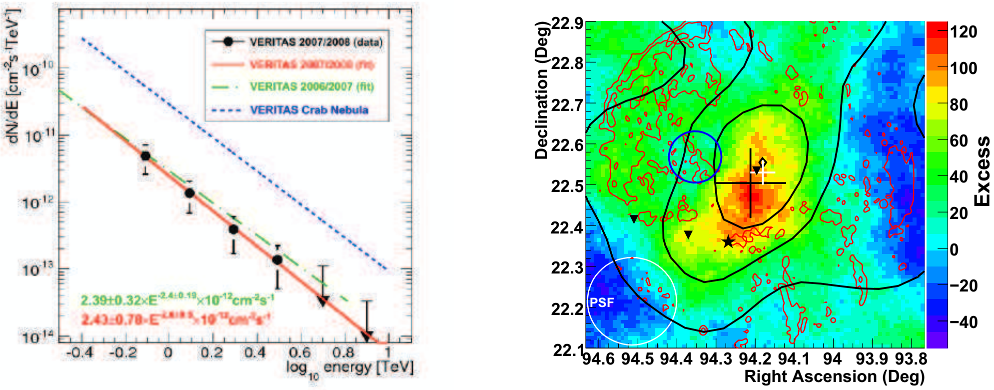

(a) (b)

Figure 1: (a) The differential energy spectra of LSI$+61°303$ from orbital phases 0.5-0.8 as measured by VERITAS during the 2006-2007 and 2007-2008 observing seasons[16]. (b) Inner 0.8° of the acceptance-corrected excess map for the IC443 field. Black circle, and cross-hair: fitted extent, position, and positional uncertainty of the VERITAS detection. White cross-hair: position and uncertainty of the MAGIC detection.[5] Red contours: optical intensity.[10] White circle: PSF of the VERITAS array. Black star: Location of PWN CXOU J061705+222127[9]. Open blue circle: 95% confidence radius of OFGL J0617.4+2234[17]. Filled black triangles: locations of OH maser emission[7]. Thick black contours: CO survey[8].

spectrum near apastron is shown in Figure 1(a). Correlation studies with contemporaneous X-ray data show no significant correlation between X-ray and TeV gamma-ray variability, but it was also shown that the TeV sampling was not dense enough for a correlation to be detected even if one were present[16]. Further observations ($\sim$ 28 hours) conducted in 2008 are contemporaneous with gamma-ray data from the Fermi satellite, which sees maximal emission from this source at periastron[17] In these observations, VERITAS detected no significant signal (2.6σ) from LSI+61 303; a 99% confidence level upper limit of $1.26 \times 10^-12\,\mathrm{cm}^{-2}\mathrm{s}^{-1}$ is placed on the gamma-ray flux above 500 GeV. However, only orbital phases 0 through 0.65 are covered with good sensitivity,; data at phases between 0.65 and 0.70 was not only limited, but taken at low elevation and under bright moonlight. Thus this non-detection is likely completely consistent with previous VHE gamma-ray observations of $\mathrm{LSI} + 61°303$ and does not imply to orbit-to-orbit variability.

4 Cygnus Region Sky Survey and Unidentified Galactic Sources

One of the key elements of VERITAS galactic observations program over the first two years was a survey of the Cygnus region of the galactic plane, covering the region between $67 < l < 82$ in galactic latitude and $-1 < b < 4$ in galactic longitude. Survey observations began in April 2007 and were completed by December 2008; analysis of survey data is on-going and will be released pending follow-up observations in Spring 2009. We report here, however, on VERITAS observations of two unidentified sources: one an unidentified TeV gamma-ray emitter being used as a calibration source for the VERITAS Sky Survey, the other a GeV gamma-ray transient occuring within the VERITAS Sky Survey region.

In 2007, the Milagro collaboration reported detections of several gamma-ray sources, including the unidentified source MGRO J1908+06 [18]. Milagro reported a 2.6° upper limit on the source extension at a median energy of 20 TeV. The H.E.S.S. experiment's extended Galactic plane survey[19] detected a source coincident with MGRO J1908+06 that had a best-fit position for the emission region of $l = 40.45 \pm 0.06^{\circ}_{stat} \pm 0.06^{\circ}_{sys}$ and $b = 0.8 \pm 0.05^{\circ}_{stat} \pm 0.06^{\circ}_{sys}$, a flux that was 14% of that of the Crab Nebula above 1 TeV, and an intrinsic extension of $\sigma_{src} = 0.21^{\circ} \pm 0.07^{\circ}_{stat} \pm 0.05^{\circ}_{sys}$. MGRO J1908+06, with its significant extension and relative strength, was an attractive calibration target for the VERITAS Cygnus region sky survey. While MGRO J1908+06 is not itself within the bounds of the survey region, the survey region is known to contain two Milagro sources, both likely to be extended, and it was clear that effective analysis of survey data would require an a good understanding of VERITAS' sensitivity to extended sources. Under the survey's aegis, VERITAS observed this source for 22 hours and detected a source at the 4.9σ level with an extension and position compatible with those of HESS 1908+063[20].

In April 2008, the AGILE satellite reported transient gamma-ray emission above 100 MeV, at a position consistent with that of the EGRET source 3EG J2020+4017[21]. The source re-brightened twice in May and June 2008, indicating a variable source[22]. VERITAS observed the region around the AGILE source for a total of 7 hours during the period from April 29th to May 6th. No significant gamma-ray emission above 300 GeV was detected anywhere in that region. A 99% confidence level upper limit on gamma-ray emission above 300 GeV has been derived, and corresponds to about 2% of the Crab Nebula flux.

5 Conclusions

VERITAS has a healthy program of galactic source observations that has already yielded a number of interesting scientific results and promises to yield more in the future. Since either the variability or morphology of a source, as a function of energy, can provide clues as to its nature, the interpretation of many of VERITAS' current and future galactic source observations will also benefit from gamma-ray data in the MeV-GeV regime provided by the Fermi satellite.

Acknowledgments

This research is supported by grants from the U.S. Department of Energy, the U.S. National Science Foundation, by NSERC in Canada, by Science Foundation Ireland, and by STFC in the UK.

References

1. J. Holder *et al.*, AIP Conf. Proc. **1085**, 657 (2009)
2. O. Celik [VERITAS Collaboration], arXiv:0709.3868 [astro-ph].
3. E. Aliu [VERITAS Collaboration], AIP Conf. Proc. **1085**, 324 (2009)
4. F. Aharonian [HEGRA Collaboration], Astron. Astrophys. **370**, 112 (2001)
5. J. Albert *et al.*, ApJ **664**, L87 (2007)
6. T. B. Humensky [VERITAS Collaboration], AIP Conf. Proc. **1085**, 357 (2009)
7. Claussen, M.J. *et al.* ApJ **489** L143 (1997)
8. Huang, Y.L. and Thaddeus, P. ApJ **309** L804 (1986)
9. Olbert, C.M. *et. al.* ApJ **554** L205 (2001)
10. McLean, B.J. *et. al.* Asp. Ser. 216, ADASS IX L145 (2000)
11. Acciari, V. A. *et al.*, ApJL accepted (2009)
12. J. Albert et al. *Science*, 312:1771–1773, 2006.
13. G. E. Romero, D. F. Torres, *et al.*, Astron. Astrophys. **410**, L1 (2003)
14. L. Maraschi and A. Treves. *MNRAS*, 194:1P–5P, January 1981.
15. V. A. Acciari *et al.*, ApJ **679**, L1427 (2008)
16. V. A. Acciari *et al.*, ApJ submitted (2009)
17. A. A. Abdo *et al.* [Fermi LAT Collaboration], arXiv:0902.1340 [astro-ph.HE].
18. A. A. Abdo *et al.*, ApJ **664**, L91 (2007) [arXiv:0705.0707 [astro-ph]].
19. A. Djannati-Atai, *et. al.* [H.E.S.S. Collaboration], arXiv:0710.2418 [astro-ph].
20. J. E. Ward [VERITAS collaboration], AIP Conf. Proc. **1085**, 301 (2009)
21. F. Longo *et. al* Astronomer's Telegram #1492 (2008)
22. A. Giuliani *et. al* Astronomer's Telegram #1585 (2008)

TeV GAMMAs AND COSMIC RAY PRODUCTION IN TYCHO'S SNR AND GEMINGA

V.G. SINITSYNA and V.Y. SINITSYNA
P.N. Lebedev Physical Institute,
119991, Leninsky pr. 53, Moscow, Russia

An information about high-energy CR population in SNRs can be obtained from gamma-ray observation. High-energy gamma-rays are produced by electronic and hadronic CR components in the inverse Compton (IC) scattering and in the hadronic collisions leading to pion production and subsequent decay respectively. SNe of type Ib and II are more numerous in our Galaxy. According to the theoretical prediction about 20 SNRs should be visible in the TeV gamma-rays whereas only two were detected up to now by SHALON, namely Tycho's SNR and Geminga. Average fluxes from two gamma-sources are found to be $I_{Tycho} = (5.2 \pm 0.9)$ and $I_{Geminga} = (4.8 \pm 1.7)$ (both unit of $10^{-13} cm^{-2} s^{-1}$). Energy spectra $F(E > 0.8TeV) \sim E^k$ of both Tycho's SNR (0.8 - 40TeV) and Geminga (0.8 - 10 TeV) are hard: for Tycho's SNR: $k_\gamma = -1.00 \pm 0.06$; for Geminga: $k_\gamma = -0.58 \pm 0.11$. Tycho's SNR has been observed by SHALON imaging Cherenkov telescope at Tien-Shan. This object, Ia SNR, has long been considered as a candidate to CR hadron source in the Northern Hemisphere. The expected pion decay gamma-flux $F_\gamma \sim E_\gamma^{-1}$ extends up to > 30 TeV, whereas the IC gamma-ray flux has a cutoff above a few TeV. So, a detection of gamma-rays at energies of 10 - 40 TeV by SHALON is an evidence for hadron origin of the rays.

Introduction

TeV energies gamma-rays, measurable by the imaging Cherenkov technique, are the most interesting for searching hadronic CRs in SNRs because they provide the information about CRs of highest possible energies $10^{13} - 10^{14}$ eV. Direct information about high-energy CR population in SNRs can be obtained from gamma-ray observation. The gamma-quantum spectra produced by the electronic and hadronic components of cosmic rays have similar shapes at the energies from 1GeV to 1 TeV due to the synchrotron losses of the electrons. So, the only observa-

Table 1: The SHALON catalogue of Galactic gamma-quantum sources with energy > 0.8 TeV

Sources	Observable flux ($\times 10^{-12} cm^{-2} s^{-1}$)	Distance (kpc)
Crab Nebula (SNR)	(1.70 ± 0.13)	2
Cygnus X-3 (binary)	(0.68 ± 0.07)	10
Geminga (radioweak pulsar)	(0.48 ± 0.17)	0.25
Tycho' SNR	(0.52 ± 0.09)	2.3
2129+47XR (binary)	(0.19 ± 0.09)	6

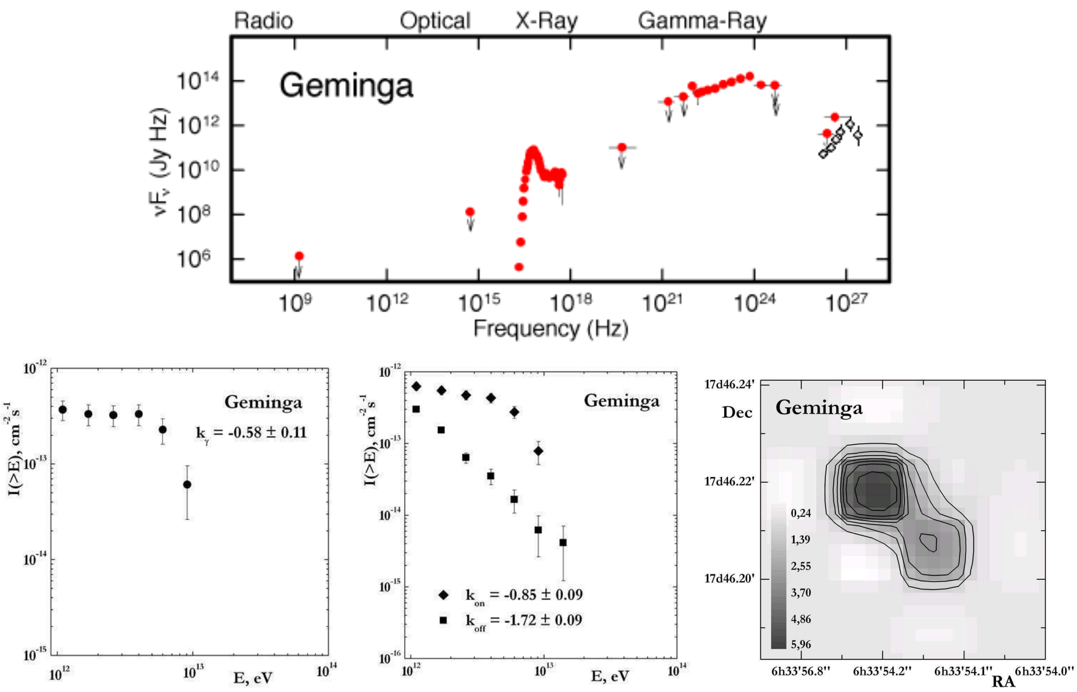

Figure 1: **top:** The broadband energy spectrum of Geminga. Upper limits correspond to that of pulsed flux whereas the data points represent the total flux. Open circles are SHALON data. **bottom:** The Geminga gamma-quantum integral spectrum with power index of $k_\gamma = -0.58 \pm 0.11$; The event spectrum from Geminga with background with index of $k_{ON} = -0.85 \pm 0.09$ and spectrum of background events observed simultaneously with Geminga with index $k_{OFF} = -1.72 \pm 0.09$; The image of gamma-ray emission from Geminga by SHALON

tional possibility to discriminate between leptonic and hadronic contributions is to measure the gamma-quantum spectrum at energies higher than 1 TeV, where these two spectra are expected to be essentially different.

The observations on Tien-Shan high-mountain station with SHALON had been carried out since 1992 year [1,2,3,4]. During this period 12 metagalactic and galactic sources have been observed. Among them are galactic sources Crab Nebula (supernova remnant), Cygnus X-3 (binary), Tycho's SNR (supernova remnant), Geminga (radioweak pulsar) and 2129+47 (binary) [1,2,3,4] and table 1. The results of observation data analysis for the each source are integral spectra, the source images and spectral energy distributions. At Figs. 1, 2, the observation results of Galaxy gamma-sources are showed.

Geminga

A neutron star in the constellation Gemini is the second brightest source of high-energy gamma-rays in the sky, discovered in 1972, by the SAS-2 satellite. For nearly 20 years, the nature of Geminga was unknown, since it didn't seem to show up at any other wavelengths. In 1991, an regular periodicity of 0.237 second was detected by the ROSAT satellite in soft X-ray emission, indicating that Geminga is almost certainly a pulsar. Geminga is the closest known pulsar to Earth. Figure 1 presents broadband energy spectrum of Geminga. Upper limits correspond to that of pulsed flux whereas the data points represent the total flux [5]. The open circles are SHALON data for steady flux.

Geminga is one of the brightest source of MeV - GeV gamma-ray, but the only known pulsar that is radio-quiet. Geminga has been the object for study at TeV energies with upper limits being reported by three experiments Whipple'93 [6], Tata'93 [7] and Durham'93 [8]. Figures 1 show the SHALON results for this gamma-source. An image of gamma-ray emission from Geminga

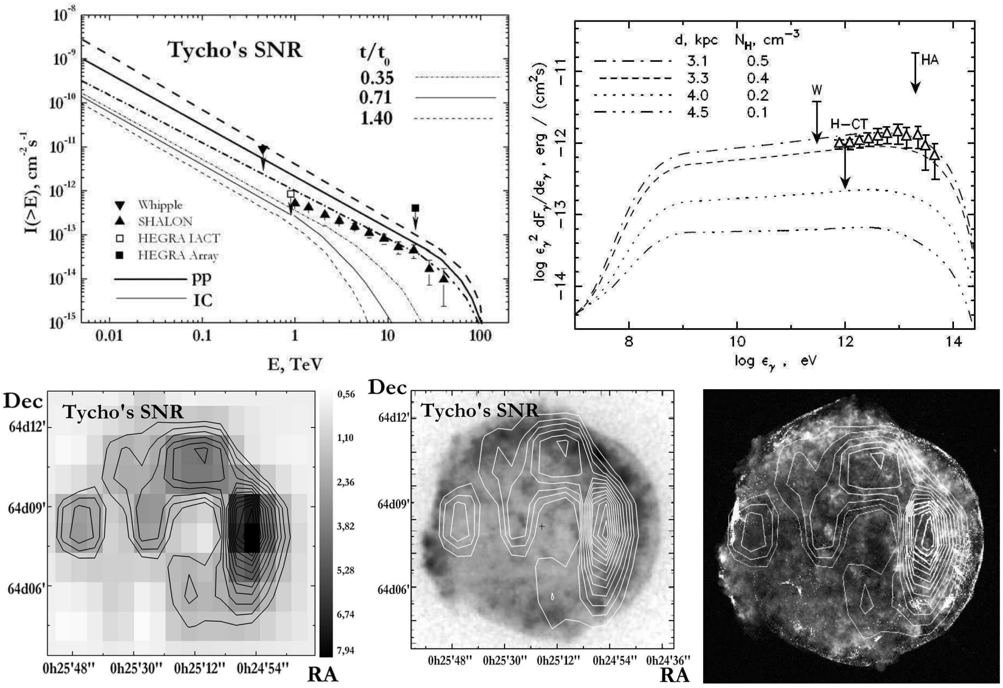

Figure 2: **top:** The Tycho's SNR gamma-quantum integral spectrum by SHALON in comparison with other experiments: the observed upper limits Whipple, HEGRA IACT system, HEGRA AIROBICC and calculations: IC emission (thin lines), π° - decay (thick lines); The spectral energy distribution of the gamma-ray emission from Tycho's SNR [L. T. Ksenofontov, H.J. Vöek, E.G. Berezhko in The Multi-Messenger Approach to High Energy Gamma-ray Sources, Barcelona, July 4-7, 2006]. **bottom:** The image of Tycho's SNR in TeV gamma-ray by SHALON (left) and image of Tycho's SNR in X-rays by ROSAT HRI (middle) and Chandra (right); white contours are SHALON data

by SHALON telescope is shown in Fig. 1, bottom. As is seen from fig.1 the value Geminga flux obtained by SHALON is lower than the upper limits published before. Its integral gamma-ray flux is found to be $(0.48 \pm 0.17) \times 10^{-12}\ cm^{-2} s^{-1}$ at energies of > 0.8 TeV. The spectrum of events coming from source and passing through distinguishing criteria with background, with index of $k_{ON} = -0.85 \pm 0.09$ and spectrum of background events observed simultaneously with source, with index of $k_{OFF} = 1.72 \pm 0.09$ are shown in comparison. The gamma-quantum spectrum of Geminga was obtained. Within the range 0.8 - 5 TeV, the integral energy spectrum is well described by the single power law $I(> E_{\gamma}) \propto E^{k_{\gamma}}$ with $k_{\gamma} = -0.58 \pm 0.11$ (Fig. 1). The energy spectrum of Geminga is harder than Crab spectrum, which has power index $k_{\gamma} = 1.44 \pm 0.07$.

Tycho's SNR

Tycho Brage supernova remnant has been observed by SHALON atmospheric Cherenkov telescope of Tien-Shan high-mountain observatory. This object has long been considered as a candidate to cosmic ray hadrons source in Northern Hemisphere, although it seemed that the sensitivity of the present generation of Imaging Atmospheric Cherenkov System's too small for Tycho's detection. Tycho's SNR has been detected by SHALON at TeV energies. The integral gamma-ray flux above 0.8 TeV was estimated as $(0.52 \pm 0.09) \times 10^{-12}\ cm^{-2} s^{-1}$ (Fig. 2).

Figures 2, show the observational results for the Tycho's SNR. An image of gamma-ray emission from Tycho's SNR by SHALON telescope is shown in Fig. 2. The correlation of TeV and X-ray (ROSAT HRI [9] and Chandra [10]) emission regions is shown at Fig. 2. The energy spectrum of Tycho's SNR at $0.8 - 20$ TeV can be approximated by the power law $F(> E_O) \propto E^{k_{\gamma}}$, with $k_{\gamma} = -1.00 \pm 0.06$. The energy spectrum of supernova remnant Tycho's SNR $F(E_O > 0.8 TeV) \propto E^{k}$ is also harder than Crab spectrum.

A nonlinear kinetic model of cosmic ray acceleration in supernova remnants is used in [11] (Fig. 2), to describe the properties of Tycho's SNR. The kinetic nonlinear model for cosmic ray acceleration in SNR has been applied to Tycho's SNR in order to compare model results with recently found very low observational upper limits on TeV energy range. In fact, HEGRA didn't detect Tycho's SNR, but established a very low upper limit at energies > 1 TeV. This value is consistent with that previously published by Whipple collaboration, being a factor of 4 lower (the spectral index of -1.1 for this comparison [11]). The π°-decay gamma-quantum flux turns out to be some greater than inverse Compton flux at 1 TeV becomes strongly dominating at 10 TeV. The predicted gamma-quanta flux is in consistent with upper limits published by Whipple [12,13] and HEGRA [14].

The spectral energy distribution of the gamma-ray emission from Tychos SNR, as a function of gamma-ray energy ϵ_{γ} , for a mechanical SN explosion energy of $E_{SN} = 1.2 \times 10^{51}$ erg and four different distances d and corresponding values of the interstellar medium number densities N_H is presented at fig. 2. All cases have dominant hadronic gamma-ray flux [L. T. Ksenofontov, H.J. Vöek, E.G. Berezhko in The Multi-Messenger Approach to High Energy Gamma-ray Sources, Barcelona, July 4-7, 2006]. The additional information about parameters of Tycho's SNR can be predicted in frame of nonlinear kinetic model [11,15] if the TeV gamma- quantum spectrum of SHALON telescope is taken into account: a source distance 3.1 - 3.3 kpc and an ambient density N_H $0.5 - 0.4$ cm^3 and the expected π°-decay gamma-ray energy spectrum extends up to about 100 TeV.

Conclusion

Since the expected flux of gamma-quanta from π°-decay, $F_{\gamma} \propto E_{\gamma}^{-1}$, extends up to ~ 30 TeV, while the flux of gamma-rays originated from the Inverse Compton scattering has a sharp cutoff above the few TeV we may conclude that the detection of gamma-rays with energies of ~ 10 to 40 TeV by SHALON is an indication of their hadronic origin [11,15].

1. V. G. Sinitsyna, AIP Conf. Proc., 515, (1999) pp. 205 and 293.
2. V. G. Sinitsyna, S. I. Nikolsky, et al.,Izv. Ross. Akad. Nauk Ser. Fiz., 66(11),(2002) pp. 1667 and 1660.
3. V. G. Sinitsyna, et al.,in Proc. 27th Int. Cosmic Ray Conf., Hamburg, 3, (2001) p. 2665; in Proc. 29th Int. Cosmic Ray Conf., Puna, 4, (2005) p. 231.
4. V. G. Sinitsyna et al.,Nucl. Phys. B (Proc.Suppl.), 151, (2006), p. 112; V. G. Sinitsyna et al., *ibid.* 122,(2003) 247; S. I. Nikolsky and V. G. Sinitsyna, *ibid.*, 122, (2003) 409; V. G. Sinitsyna et al., *ibid.*, 97,(2001) pp. 215 and 219.
5. M. S. Jackson, J. P. Halpern, and E. V. Gotthelf, ApJ, 578 (2002) p. 935.
6. C. W. Akerlof et.al in Proc. 23rd Int. Cosmic Ray Conf., Calgary, 1, (1993) p. 305.
7. P. R. Vishwanath et.al Astron.&Astrophys., 267, (1993) L5.
8. C. C. G. Bowden et.al J. Phys. G: Nucl. Part. Phys. 19, (1993) L29-L31
9. J. P. Hughes, ApJ, 545, (2000) pp. L53 - L56.
10. J. S. Warren, J. P. Hughes, C. Badenes, et al., ApJ, 634, (2005) pp. 376 - 389.
11. H. J. Völk, E. G. Berezhko, et al., in Proc. 27th Int. Cosmic Ray Conf., Hamburg, 2, (2001) p. 2469.
12. J. H. Buckley, C. W. Akerlof, D. A. Carter-Lwis, et al., Astron. Astrophys., 329, (1998) p. 639.
13. M. Catanese and T. C. Weekes, Preprint Series, no. 4811, (1999).
14. J. Prahl and C. Prosch (for the HEGRA Collaboration), in Proc. 25th Int. Cosmic Ray Conf., Durban, 3, (1997) p. 217.
15. H. J. Völk, E. G. Berezhko and L. T. Ksenofontov, in Proc. 29th Int. Cosmic Ray Conf., Pune, 3, (2005) p. 235.

Probing cosmic ray acceleration through molecular clouds in the vicinity of supernova remnants

A. Fiasson, R.C.G. Chaves, V. Marandon, M. de Naurois, K. Kosack & G. Rowell for the H.E.S.S. Collaboration

Laboratoire d'Annecy-le-Vieux de Physique des Particules, Université de Savoie, CNRS/IN2P3, 9 Chemin de Bellevue - BP 110 F-74941 Annecy-le-Vieux Cedex, France
Max-Planck-Institut für Kernphysik, P.O. Box 103980, D 69029 Heidelberg, Germany
Astroparticule et Cosmologie (APC), CNRS, Universite Paris 7 Denis Diderot, 10, rue Alice Domon et Leonie Duquet, F-75205 Paris Cedex 13, France
LPNHE, Université Pierre et Marie Curie Paris 6, Université Denis Diderot Paris 7, CNRS/IN2P3, 4 Place Jussieu, F-75252, Paris Cedex 5, France
IRFU/DSM/CEA, CE Saclay, F-91191 Gif-sur-Yvette, Cedex, France
School of Chemistry & Physics, University of Adelaide, Adelaide 5005, Australia

Very high energy γ-ray emission has been recently detected by H.E.S.S. from the direction of associations between supernova remnants and molecular clouds. In such associations dense molecular clouds may reveal accelerated cosmic rays in the vicinity of supernova remnant forward shocks. Hadronic interactions could explain part or all of the observed γ-ray fluxes. The discovery of a new VHE γ-ray source, HESS J1923+141, coincident with the supernova remnant W51C, is reported. Amongst possible associations for this source is a shocked molecular cloud.

1 Introduction

Up to hundreds of PeV, the very high energy (VHE) cosmic-ray (CR) spectrum is likely to be of Galactic origin. Since the H.E.S.S. telescope has started its observations in 2003, various shell-type SNRs have been detected. The VHE gamma-ray spectra of several of them extend to energies beyond 50 TeV, confirming that these objects indeed accelerate particles up to more than 100 TeV. The H.E.S.S. effective threshold, a few hundred GeV, is too high to probe whether these gamma rays originate from inverse Compton scattering of VHE electrons off CMB and infrared photons or from the decay of π^0 produced in hadronic showers initiated by VHE protons interacting with interstellar matter. Such interactions require a significant amount of target matter to produce a detectable γ-ray flux. Dense molecular clouds in the vicinity of SNRs could thus be such a target [1]. The presence of 1720 MHz OH masers ensures physical associations as these masers occur in shocked molecular clouds [2]. The H.E.S.S. experiment has recently detected a γ-ray emission towards several associations: W28, G359.1-0.5, CTB 37A and very recently W51C, whose detection is reported in this paper. The interpretation of these γ rays as the product of CR interactions within these molecular clouds is discussed.

2 The W28 SNR, G359.1-0.5 and CTB 37A: three association candidates

The SNRs W28, G359.1-0.5 and CTB 37A are three candidate of SNRs associated with molecular clouds. Several OH masers at 1720 MHz have been detected towards these remnants and

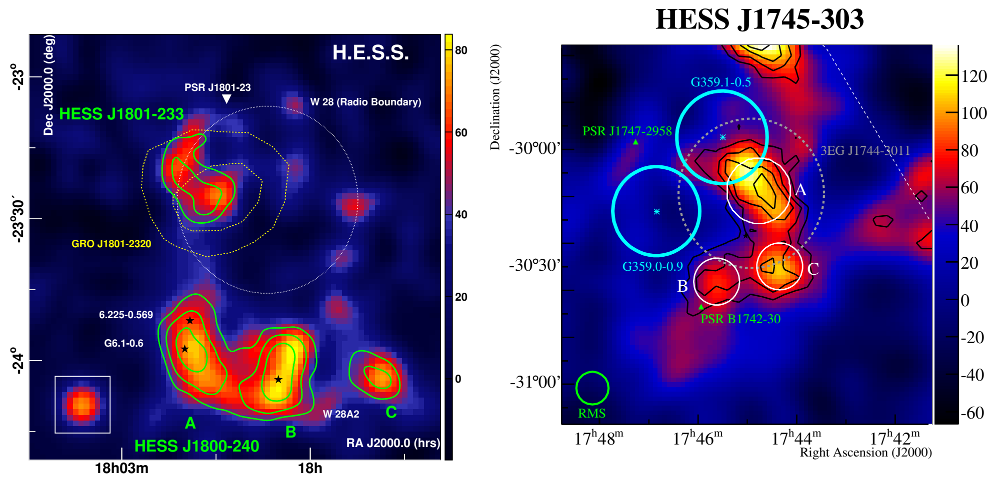

Figure 1: *Left:* H.E.S.S. γ-ray excess map Gaussian smoothed (σ=4.2′), with 4σ to 6σ significance contours overlaid. Several objects are indicated: SNR W 28 radio boundaries (thin-dashed circle), HII regions (black stars), PSR J1801-23 (white triangle), GRO J1801-2320 (dashed yellow lines - 68% and 95% position confidence levels). The inset shows the H.E.S.S. point spread function.*Right:* H.E.S.S. excess map Gaussian smoothed (σ=0.07°) of HESS J1745-303 with 4σ to 7σ statistical significance contours overlaid in black. The dashed circle is the 95% error circle for the location of 3EG J1744-3011. The Galactic plane is marked with a dotted line.

confirmed the physical associations of the SNR blast waves with dense molecular clouds. They have been observed by H.E.S.S. between 2004 and 2007.

Figure 1 *left* is the resulting VHE γ-ray excess map of the W28 field. Two sources have been detected [3] each with a statistical significance larger than 8σ: at the northeastern boundary of the remnant, HESS J1801-233, and to the South, HESS J1801-240 (possibly divided into three components, A, B and C). The W 28 SNR is interacting along its northern and northeastern boundaries with molecular clouds visible within NANTEN observations in the ^{12}CO(J=1$\rightarrow$0) line. A hadronic origin of the γ-ray emission implies a CR density enhancement of a factor 10 to 30 with respect to the local CR density; an enhancement indeed expected in the neighborhood of a CR accelerator such as W28.

Figure 1 *right* shows the VHE γ-ray source HESS J1745-303 [4]. The northern part of the H.E.S.S. source, A region, is coincident with the edge of the SNR G359.1-0.5. Observations performed in the ^{12}CO(J=1$\rightarrow$0) line [5] reveal that a fraction of a shocked ring of matter is coincident with the A region. A hadronic origin of the A region γ-ray flux infers a conversion efficiency of the mechanical explosion energy into CRs around 30%, assuming the extrapolation of the spectrum down to GeV energies. In the view of the uncertainties on this estimate, mainly the extrapolation of the spectrum down to GeV energies and the cloud mass estimation, it is in good agreement with theoretical expectations.

Finally, the discovery of the VHE γ-ray source HESS J1714-385 [6], coincident with the SNR CTB 37A, has been reported by H.E.S.S. in 2008. Figure 2 *left* shows the matter distribution superimposed with the γ-ray excess map. These molecular clouds are mostly contained within the H.E.S.S. source extension. In a hadronic scenario, the conversion efficiency of the mechanical energy of the explosion into CRs ranges between 4% and 30%, also in good agreement with theoretical expectations. However, recent X-rays observations by XMM-Newton and Chandra show a non-thermal emission coincident with the remnant. Its spectrum suggests a pulsar wind nebula (PWN) nature and it could be an alternative counterpart candidate for the γ-ray emission.

For all these VHE gamma-ray sources, a hadronic origin is also supported by the coincidence with EGRET sources. A spectral continuity to lower energy is expected in the case of a

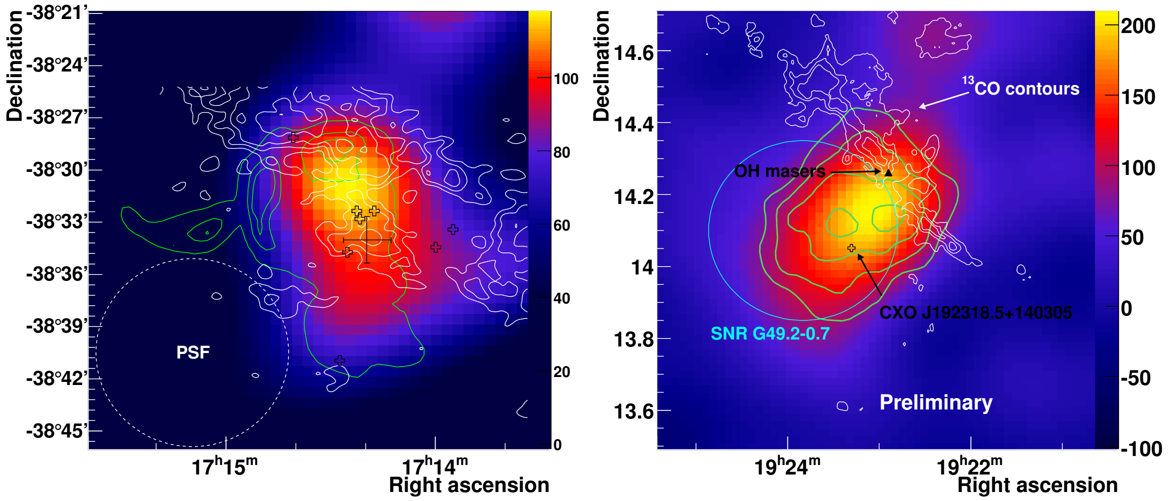

Figure 2: *Left:* HESS J1714-385 excess map, Gaussian smoothed (σ=2.9′). The 0.1, 0.9 & 1.4 Jy/beam radio contours at 843 MHz are overlaid in green and CO emission (-68 to -60 km s^{-1}) at 17, 25, 33, 41 and 49 K km s^{-1}in white. OH masers are marked with black open crosses and the best fit position for HESS J1714-385 with a large black cross. *Right:* HESS J1923+141 VHE γ-ray excess map, Gaussian smoothed (σ=7.6′). The green contours indicate the 3 σ to 6 σ significance level of the excess. The white contours show the measurement of the CO line at 30, 65 and 100 K km s^{-1}, integrated around the maser velocity between 60 km s^{-1} and 80 km s^{-1}.

hadronic origin. The H.E.S.S. spectra are compatible with extrapolations of the EGRET spectra. Although such compatibility is expected by chance [7], these H.E.S.S. sources are interesting counterpart candidates for the EGRET sources.

3 A new VHE γ-ray source: HESS J1923+141

3.1 H.E.S.S. observations

The W51 radio complex has been covered in 2007. A VHE γ-ray hotspot was visible in these observations and triggered dedicated observations performed in June 2008. After quality selection and dead-time correction, a total of ∼17 hours of observations are available within 2 degrees offset from the centre of the W51 field. These data have been analyzed using a combined Model-Hillas analysis [10]. The energy threshold for this analysis is 420 GeV. Figure 2 *right* shows the resulting excess map. An excess of VHE γ-ray is detected in the W51 region with a statistical significance of 6.7σ using an oversampling radius of 0.22°. Accounting for a number of trials updated from the HESS Galactic plane survey [11] to the current survey, this new source, HESS J1923+141, has a statistical significance post-trials of 4.4σ. The source is clearly extended compared to the H.E.S.S. PSF, and the exact morphology is still under study. The integrated flux over 1 TeV is equivalent to ∼3% of the flux from the Crab Nebula above the same energy.

3.2 The multiwavelength view

W51 is an extended radio complex composed of two HII regions W51A and W51B, embedded in a giant molecular cloud [12] hosting several star forming regions. The SNR W51C (also called G49.2-0.7) appears as a partial shell in radio continuum. It is interacting with the giant molecular cloud as evidenced by two 1720 MHz OH masers [13] and shocked material [14–15]. Fig. 2 *right* show the matter distribution revealed by the ^{13}CO line of this region. This region has been also observed with several detectors in X rays which revealed a complex region in the keV energy range. A candidate PWN, CXO J192318.5+140505, is detected coincident with the SNR W 51C [16].

3.3 Discussion on HESS J1923+141 origin

Amongst the possible counterparts, the presence of a shocked molecular cloud allows a hadronic origin. Assuming that 10% of the cloud is involved in the γ-ray production, a CR density 30 times higher than the local average value is required to produce the VHE γ-ray emission above 1 TeV. The presence of a PWN candidate provides a competitive leptonic scenario. The pulsar spin-down luminosity is estimated to be around $L_{\rm SD} = 4.5 \times 10^{36}$ erg s^{-1}, assuming a distance to the PWN of 6 kpc, identical to that of the SNR [14–17]. Using this distance, the γ-ray luminosity between 1 and 10 TeV is lower than 0.1% of the pulsar spin-down luminosity and could be explained by IC emission from relativistic electrons accelerated within the PWN. A third scenario is provided by the presence of star forming region. VHE gamma-rays have been already detected toward star forming regions by H.E.S.S. [18]. Stellar clusters could thus participate to the γ-ray emission. However, the γ-ray map does not reflect the star forming region distribution within the cloud. A VHE γ-ray emission through these scenarios cannot be excluded. More detailed spectral and morphological studies are under progress to understand the origin of this new VHE γ-ray source.

4 Summary

The γ-ray emission detected toward the SNRs of W28, G359.1-0.5 and CTB 37A, can be interpreted as originating from π^0 decay after interactions of CRs from the remnant with molecular clouds. The CR energy required is compatible with theoretical expectations. Recent observations with HESS of the W51 region led to the discovery of a new VHE γ-ray source, which could be also associated with a shocked molecular cloud. All these observations suggest that shell-type SNRs are effective hadron CR accelerators. Further studies of associations with H.E.S.S. and then FERMI and H.E.S.S. II will certainly help understanding the mechanism at the origin of the Galactic CRs.

Acknowledgments

The support of the Namibian authorities and of the University of Namibia in facilitating the construction and operation of H.E.S.S. is gratefully acknowledged, as is the support by the German Ministry for Education and Research (BMBF), the Max Planck Society, the French Ministry for Research, the CNRS-IN2P3 and the Astroparticle Interdisciplinary Programme of the CNRS, the U.K. Science and Technology Facilities Council (STFC), the IPNP of the Charles University, the Polish Ministry of Science and Higher Education, the South African Department of Science and Technology and National Research Foundation, and by the University of Namibia. We appreciate the excellent work of the technical support staff in Berlin, Durham, Hamburg, Heidelberg, Palaiseau, Paris, Saclay, and in Namibia in the construction and operation of the equipment.

References

1. F.A. Aharonian, L.O. Drury & H.J. Voelk, *A&A* **285**, 645 (1994).
2. M. Elitzur, *ApJ* **203**, 124 (1976).
3. F. Aharonian et al., *A&A* **481**, 401 (2008).
4. F. Aharonian et al., *A&A* **483**, 509 (2008).
5. M. Bitran et al., *AAS* **125**, 99 (1997).
6. F. Aharonian et al., *A&A* **490**, 685 (2008).
7. S. Funk et al., *ApJ* **679**, 1299 (2008).
8. J. M. Jackson et al., *ApJS* **163**, 145 (2006).
9. D.A. Green, *A catalogue of Galactic Supernova Remnant* (2006).
10. M. de Naurois, astro-ph/0607247 (2006).
11. F. Aharonian et al., *ApJ* **636**, 777 (2006).
12. J.M. Carpenter & D.B. Sanders, *AJ* **116**, 1856 (1998).
13. A. J. Green et al., *AJ* **114**, 2058 (1997).
14. B.-C. Koo and D.-S. Moon, *ApJ* **485**, 263 (1997).
15. B.-C. Koo and D.-S. Moon, *ApJ* **475**, 194 (1997).
16. B.-C. Koo et al., *ApJ* **633**, 946 (2005).
17. X.-H. Li, F.-J. Lu & Z. Li *ApJ* **682**, 1166 (2008).
18. F. Aharonian et al., *A&A* **467**, 1075 (2007).

Non-thermal radiation from molecular clouds illuminated by cosmic rays from nearby supernova remnants

Stefano Gabici[1], Felix A. Aharonian[1,2], and Sabrina Casanova[2]
[1] *Dublin Institute for Advanced Studies, 31 Fitzwilliam Place, Dublin 2, Ireland*
[2] *Max–Planck–Institute für Kernphysik, Saupfercheckweg 1, 69117 Heidelberg, Germany*

Molecular clouds are expected to emit non-thermal radiation due to cosmic ray interactions in the dense magnetized gas. Such emission is amplified if a cloud is located close to an accelerator of cosmic rays and if cosmic rays can leave the accelerator and diffusively reach the cloud. We consider the situation in which a molecular cloud is located in the proximity of a supernova remnant which is accelerating cosmic rays and gradually releasing them into the interstellar medium. We calculate the multiwavelength spectrum from radio to γ-rays which emerges from the cloud as the result of cosmic ray interactions. The total energy output is dominated by the γ-ray emission, which can exceed the emission from other bands by an order of magnitude or more. This suggests that some of the unidentified TeV sources detected so far, with no obvious or very weak counterpart in other wavelengths, might be associated with clouds illuminated by cosmic rays coming from a nearby source.

Galactic Cosmic Rays (CRs) are believed to be accelerated via first order Fermi mechanism at the expanding shocks of supernova remnants (SNRs). In this context, a detection of SNRs in TeV γ-rays was predicted by [1], due to the decay of neutral pions produced in interactions between the accelerated CRs and the interstellar gas swept up by the SNR shock.

The detection of several SNRs in γ-rays [2], though encouraging, cannot provide by itself the final proof that CRs are indeed accelerated at SNR shocks. This is because competing leptonic processes, namely inverse Compton scattering from accelerated electrons, can also explain the observed TeV emission, provided that the magnetic field does not significantly exceed $\sim 10\ \mu$G. Evidence for strong $\approx 100\mu$G magnetic fields, and thus indirect support to the hadronic scenario for the γ-ray emission, comes from the observation of thin X-ray synchrotron filaments surrounding some SNRs [3,4,5] and of the rapid variability time scale of the synchrotron X-rays [6]. A conclusive proof of the hadronic nature of the γ-ray emission will possibly come from the detection of neutrinos, which are produced during the same hadronic interactions responsible for the production of γ-rays [1].

The presence of a massive molecular cloud (MC) close to a SNR can provide a dense target for CR hadronic interactions and thus enhance the expected γ-ray emission. If the MC is overtaken by the SNR shock, the γ-ray emission is expected to be cospatial with the SNR shell, or a portion of it. If the MC is located at a given distance d_{cl} from the SNR, it can still be illuminated by CRs that escape from the SNR and emit γ-rays [7,8]. For this scenario, it has been shown that, for typical SNR parameters and for a distance $D = 1$ kpc, a MC of mass $10^4 M_\odot$ emits TeV γ-rays at a detectable level if it is located within few hundreds pc from the SNR [8]. In this case the angular displacement between the SNR and the γ-ray emission is $\approx 6^\circ (D/1\mathrm{kpc})^{-1} (d_{cl}/100\mathrm{pc})$. This translates in the fact that sometimes the association between SNRs and MCs can be not so

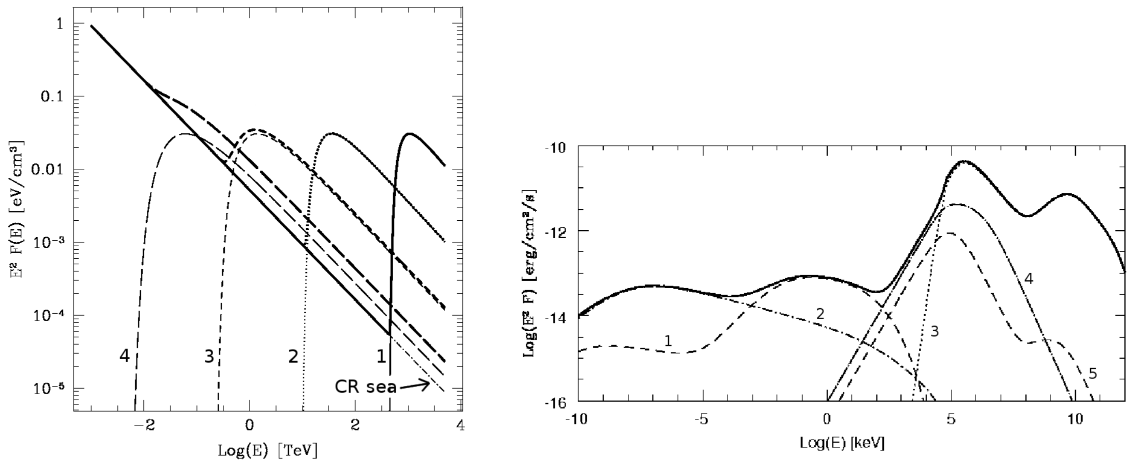

Figure 1: **LEFT:** CR spectrum in a MC located at 100 pc from a SNR. See text for details. **RIGHT:** Broad band spectrum for a MC of mass $10^5 M_\odot$, radius 20 pc, density ~ 120 cm^{-3}, magnetic field 20μG. The MC is at 100 pc from a SNR that exploded 2000 yr ago. Distance is 1 kpc. See text for further details.

obvious, given that the separation between the two objects can be bigger than the instrument field of view. Following this rationale, it was proposed [8] that some of the unidentified TeV sources [9,10] might be MCs illuminated by nearby SNRs.

In this paper, we calculate the expected non-thermal emission, from radio to multi-TeV photons, from a MC illuminated by CRs coming from a nearby SNR. We generalize the model presented in [8], which was limited to the hadronic TeV photons only, to include the generation of secondary electrons in the cloud and the related synchrotron and Bremsstrahlung emission components. Electrons accelerated at the SNR shock remain confined in the shell due to severe synchrotron losses. Similar calculations have been recently published, though they are focused on the γ-ray [11] and radio [12] emission only. We found that the total radiation energy output from a MC is dominated by the γ-ray emission, which can exceed the emission from other bands by an order of magnitude or more. This reinforces the belief that some of the unidentified TeV sources detected so far, with no obvious or very weak counterparts in other wavelengths (the so called "dark sources"), might be in fact associated with massive MCs illuminated by CRs. Moreover, under certain conditions, the γ-ray spectrum from the cloud exhibit a concave shape, being steep at low ($\sim$ GeV) energies and hard at high ($\sim$ TeV) energies. This fact might have important implications for the studies of the spectral compatibility of GeV and TeV γ-ray sources.

Cosmic ray spectrum at the cloud location

We consider a MC located at a given distance from a SNR and we calculate the CR spectrum at the cloud location. The spectrum is the sum of two components: *i)* the CRs coming from the SNR, and *ii)* the galactic CR background. While the latter contribution is constant in time, the former changes, since the flux of CRs escaping from the SNR evolves in time (full details are given in [8,13]). Fig. 1 (left) shows the CR spectrum at the location of the MC. The Galactic CR background is plotted as a thin dot–dashed line (labeled as CR sea), while the spectrum of the CRs coming from the SNR is plotted as thin lines for different times after the supernova explosion: 500 (solid, 1), 2000 (dotted, 2), 8000 (short–dashed, 3) and 32000 yr (long–dashed, 4). Thick lines represent the sum of the two contributions. The distance between the SNR and the MC is 100 pc. The total supernova explosion energy is 10^{51} ergs and the CR acceleration efficiency is 30%. The diffusion coefficient is $D(E) = 10^{28}(E/10\ GeV)^{0.5}\ cm^2/s$, compatible with CR propagation models [14].

The evolution with time of the CR spectrum at the position of the MC can be understood by recalling that CRs with different energies leave the SNR at different times [16]. The highest energy ($\sim$ PeV) CRs leave the SNR first, while CRs with lower and lower energy are released at later times. Moreover, higher energy CRs diffuse faster, thus the spectrum of CRs at the MC exhibit a sharp low energy cutoff at an energy E_{low}, which moves to lower and lower energies as time passes. The position of the cutoff represents the energy of the least energetic particles that had enough time to reach the MC. Here we assume that CR can freely penetrate the cloud. For a detailed discussion of this issue see [15].

Non-thermal radiation from the cloud

We consider a MC of mass $10^5 M_{\odot}$, radius 20 pc and uniform density ~ 120 cm^{-3}. The magnetic field is 20μG. In order to show all the different contributions to the total non-thermal emission, in Fig. 1 (right) we plot the broad band spectrum from the MC for 2000 yr after the supernova explosion. The SNR is 100 pc away from the MC. The distance to the observer is 1 kpc. The dotted line (curve 3) represents the emission from neutral pion decay (from both background CRs and CRs from the SNR), the dot–dashed lines represent the synchrotron (curve 2) and Bremsstrahlung (curve 4) emission from background CR electrons that penetrate the MC and the dashed lines represent the synchrotron (curve 1) and Bremsstrahlung (curve 5) emission from secondary electrons produced during inelastic CR interactions in the dense gas [13].

The decay of neutral pions dominates the total emission for energies above ≈ 100 MeV. The two peaks in the emission reflects the shape of the underlying CR spectrum, which, as illustrated in Fig. 1 (left), is the sum of the steep background CR spectrum, which produces the π^0–bump at a photon energy of $m_{\pi^0}/2 \sim 70$ MeV (in the photon flux F), and an hard CR component coming from the SNR that produces the bump at higher energies. The flux level at 1 TeV is approximatively 5×10^{-12}erg/cm^2/s, well detectable by currently operating Imaging Atmospheric Cherenkov Telescopes, even taking into account the quite extended ($\approx 2^{\circ}$) nature of the source. It is remarkable that such a MC would be detectable even if it were located at the distance of the Galactic centre, as can be easily estimated by taking into account that the sensitivity of a Cherenkov telescope like H.E.S.S. after 50 hours of exposure, is $\approx 10^{-13}(\theta_s/0.1^{\circ})$TeV/cm^2/s, where θ_s is the source extension. This means that very massive clouds can be used to reveal the presence of enhancements of the CR density in different locations throughout the whole Galaxy. Similar conclusions can be drawn for the expected GeV emission, which is currently probed by the AGILE and GLAST satellites. In particular, GLAST, with a point source integral sensitivity of $\approx 10^{-9}$GeV/cm^2/s at energies above 1 GeV (www-glast.slac.stanford.edu), is expected to detect such MCs as extended sources if they are within $1 \div 2$ kpc from the Earth, or as point sources if they are at larger distances.

The spectral shape in the γ-ray energy range deserves further discussion. For the situation considered in Fig. 1 (right), the $\approx 1 \div 100$ GeV γ-rays are the result of the decay of neutral pions produced by background CRs that penetrate the MC. Thus, the γ-ray spectrum at those energies mimic the underlying CR spectrum, which is a steep power law of the form $\approx E^{-2.75}$. On the other hand, the neutral pion decay spectrum at energies above ≈ 100 GeV is, in this case, dominated by the contribution from CRs coming from the nearby SNR. After 2000 yr from the supernova explosion, only CRs with energies above several tens of TeV had enough time to leave the SNR and reach the MC and thus the CR spectrum at the cloud exhibits an abrupt low energy cutoff at that energy, that we call here E_{CR}^{cut} (see Fig. 1, left). As a consequence, the γ-ray spectrum is expected to be peaked at an energy $\sim E_{CR}^{cut}/10$ of several TeV. The slope of the γ-ray spectrum below the peak is very hard and is determined by the physics of the interaction only, and not by the shape of the underlying CR spectrum. Thus, a loose association between a SNR and a MC is expected to be characterized, at least at some stage of the SNR evolution, by

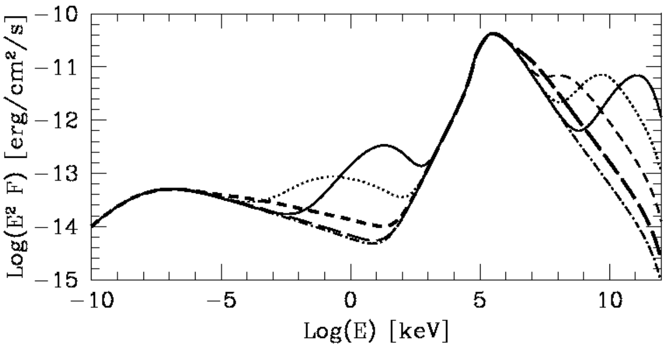

Figure 2: Radiation from the MC considered in Fig. 1. Solid, dotted, short-dashed, long-dashed, and dot-dashed lines shows the spectrum at 500, 2000, 8000, 32000 and ∞ yr after the explosion.

a very peculiar spectrum which is steep at low (GeV) energies and hard at high (TeV) energies.

The evolution with time of the emission from the MC is shown in Fig. 2, where the solid, dotted, short–dashed and long–dashed lines show the spectrum for 500, 2000, 8000 and 32000 yr after the supernova explosion respectively. For comparison, the emission from a MC with no SNR located in its proximity is plotted as a dot–dashed line. In this case only background CRs that penetrate the MC contribute to the emission.

Fig. 2 shows that the radio ($\lambda > 0.1$mm) and the soft γ-ray ($\approx 0.1 \div 1$ GeV) emissions are constant in time. This is because such emissions are produced by background CRs that penetrate the MC. The emission in the other energy bands is variable in time, being produced by the CRs coming from the SNR whose flux changes with time (see Fig. 1, left). The most prominent features in the variable emission are two peaks, in X- and γ-rays respectively. The X-ray synchrotron emission is weaker than the TeV emission for any time and for times > 2000yr the ratio between TeV and keV emission can reach extreme values of a few tens or more. These values are observed from some of the unidentified TeV sources detected by H.E.S.S. . In the scenario presented in this paper, spectra showing a high TeV/kev flux ratio can be produced very naturally if a MC is illuminated by CRs coming from a nearby SNR.

References

1. L. O'C. Drury, F. A. Aharonian, H. J. Völk, *A&A* **287**, 959 (1994)
2. J. Hinton, 2008, arXiv:0803.1609
3. A. Bamba, et al., *ApJ* **589**, 827 (2003)
4. J. Vink, J. M. Laming, *ApJ* **584**, 758 (2003)
5. H. J. Völk, E. G. Berezhko, L. T. Ksenofontov, *A&A* **433**, 229 (2005)
6. Y. Uchiyama, et al., *Nature* **449**, 576 (2007)
7. F. A. Aharonian, A. Atoyan, *A&A* **309**, 917 (1996)
8. S. Gabici, F. A. Aharonian, *ApJ* **665**, L131 (2007)
9. F. A. Aharonian, et al. (HESS coll.), *ApJ* **636**, 777 (2006)
10. B. Abdo, et al. (MILAGRO coll.), *ApJ* **664**, L91 (2007)
11. A. Y. Rodriguez Marrero, et al., 2008, arXiv:0808.1834
12. R. J. Protheroe et al., 2008, arXiv:0807.0127
13. S. Gabici, S. Casanova, F. A. Aharonian, MNRAS, in press
14. V. S. Berezinskii, et al., *Astrophysics of Cosmic Rays*, North Holland, Amsterdam, 1990
15. S. Gabici, F. A. Aharonian, P. Blasi, *Ap&SS* **309**, 365 (2007)
16. V. S. Ptuskin, V. N. Zirakashvili, *A&A* **429**, 755 (2005)
17. S. R. Kelner, F. A. Aharonian, V. V. Bugayov, *Phys. Rev. D* **74**, 034018 (2006)

CONSTRAINS ON EXTRAGALACTIC BACKGROUND LIGHT FROM CHERENKOV TELESCOPES

Daniel MAZIN[1] and Martin RAUE[2]
[1] *IFAE, Edifici Cn., Campus UAB, E-08193 Bellaterra, Spain,* [2] *Max-Planck-Institut für Kernphysik, Heidelberg, Germany*

Very high energy (VHE, E > 30 GeV) γ-rays are absorbed via interaction with low-energy photons from the extragalactic background light (EBL) if the involved photon energies are above the threshold for electron-positron pair creation. The VHE γ-ray absorption, which is energy dependent and increases strongly with redshift, distorts the VHE energy spectra observed from distant objects. The observed energy spectra of the AGNs carry therefore an imprint of the EBL. Recent detections of hard spectra of distant blazars (z = 0.11 – 0.54) by H.E.S.S. and MAGIC put strong constraints on the EBL density in the optical to near infrared waveband. Since the EBL limits depend on model assumptions, it is not yet possible to distinguish between an intrinsic softening of blazar spectra and a softening caused by the interaction with low energy EBL photons. In this paper, we give an overview of the EBL constraints, their limitations and perspectives for the joint efforts of the Fermi Gamma-Ray Space telescope and imaging atmospheric Cherenkov telescopes.

1 Introduction

During the star and galaxy formation history a diffuse extragalactic radiation field has been accumulated in the ultraviolet to far infrared wavelength regimes. This radiation field, commonly referred to as the extragalactic background light (EBL), is the second largest, in terms of the contained energy, background after the Cosmic Microwave Background of 2.7 K (CMB). While the CMB conserves the structure of the universe at the moment of the decoupling of matter and radiation following the Big Bang (at redshift z $\approx$ 1000), the EBL is a calorimetric measure of the entire radiant energy released by processes of structure formation that have occurred since the decoupling (see Hauser&Dwek[1] and Kashlinsky[2] for recent reviews).

The UV – infrared backgrounds is shown in Figure 1, left plot. From right to left, the spectral energy distributions of the three major components are shown: the cosmic microwave background (CMB), and the two components belonging to the EBL: one peaking at around 1 μm is believed to originate directly from stars. The second one, having its peak at $\sim$100 μm, results mostly from starlight that has been absorbed by dust inside galaxies and reemitted at larger wavelengths. Other contributions, like emission from AGN and quasars are expected to produce no more than 5 to 20% of the total EBL density in the mid IR (see e.g. Matute[3] and references therein). The EBL is difficult to measure directly due to strong foregrounds from our solar system and the Galaxy. The observation of distant sources of VHE γ-rays using Imaging Air Cherenkov Telescopes (IACT, such CANGAROO, H.E.S.S., MAGIC or VERITAS) provides a unique indirect measurement of the EBL due to energy dependent γ-ray absorption with the low energy photons of the EBL. The precision of the EBL constraints set by the IACT improved remarkably in the last few years. Contemporaneously with the IACT constraints, there has been rapid progress in resolving a significant fraction of this background with the deep galaxy counts at infrared wavelengths from the Infrared Space Observatory (*ISO*) and from the *Spitzer* satellite as well as at sub-millimeter wavelengths from the Submillimeter Common User Bolometer Array (SCUBA) instrument. The current status of direct and indirect EBL measurements (excluding limits from the IACTs) is shown in Fig. 1, right plot.

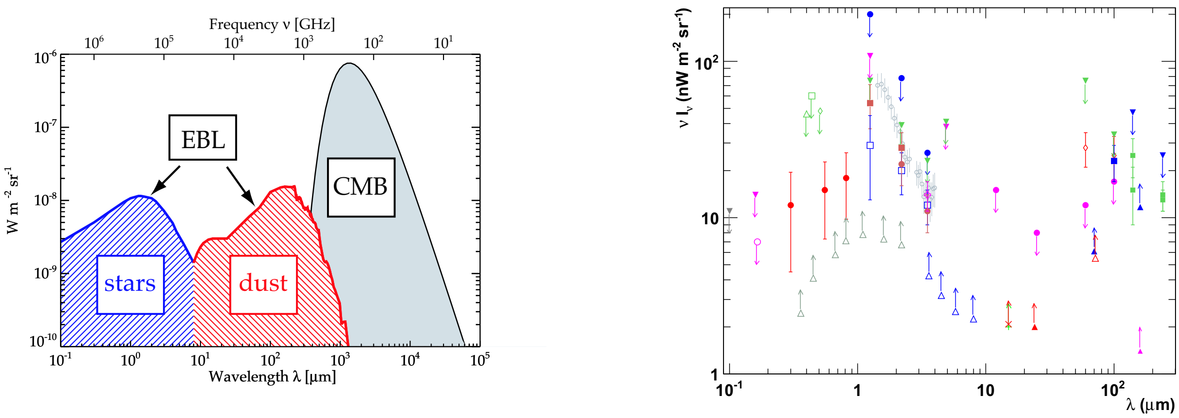

Figure 1: *Left:* Schematic Spectral Energy Distributions (SED) of the most important (by intensity) backgrounds in the universe. CMB and EBL are shown. Plot adopted from Dole et al.[4]. *Right:* EBL measurements and limits (status end 2006). Symbols see in Mazin&Raue[5].

There is fundamental entangled problem for the EBL and intrinsic blazar spectra: to study intrinsic blazar physics one needs to understand the EBL and vice versa. Therefore, one may concern that from a single observed energy spectrum of a distant VHE γ-ray source, it is rather difficult if not impossible to uniquely distinguish between the imprint of the EBL and intrinsic features of the source. Observed features can be source inherent due to an internal absorption inside the source or due to a source, which does not provide necessary conditions for acceleration of charged particles to high enough energy. However, there are many ideas how to overcome this duality: e.g., population studies of many extragalactic sources (whereas the intrinsic features might be different, the imprint of the EBL at a given redshift is the same) or/and variability of the spectra (variability is intrinsic, whereas the EBL imprint is always the same). With the current population of VHE γ-ray sources, it is only possible to set limits on the EBL, arguing that the observed spectra contain at least the imprint of the EBL.

2 Status of the EBL limits set by Cherenkov telescopes

Assuming a certain EBL density and the measured blazar spectrum, the intrinsic spectrum at the source can be calculated. By comparing the intrinsic spectra with blazar model predictions, limits on the EBL density can be derived.

The H.E.S.S. collaboration reported the detection of two intermediate redshift blazars 1ES 1101-232 (z = 0.186) and H 2356-309 (z = 0.165) [6]. Both observed spectra (measured in the range 150 GeV – 3 TeV) show a relatively hard spectral index of 2.9 and 3.1, respectively. Using the criterion that the intrinsic blazar spectrum cannot be harder than $\Gamma_{\rm int} = 1.5$, the authors derived a stringent upper limit on the EBL density in the region between 0.8 and 4 μm (see Fig. 2, left plot). The derived upper limits imply a low level EBL density in agreement with the expectations from standard galaxy evolution models. Later, the limits were confirmed using the blazar 1ES 0347-121 (Aharonian et al.[7]). The limits, in turn, rule out a cosmological origin of the near infrared excess (e.g. Matsumoto et al.[8]).

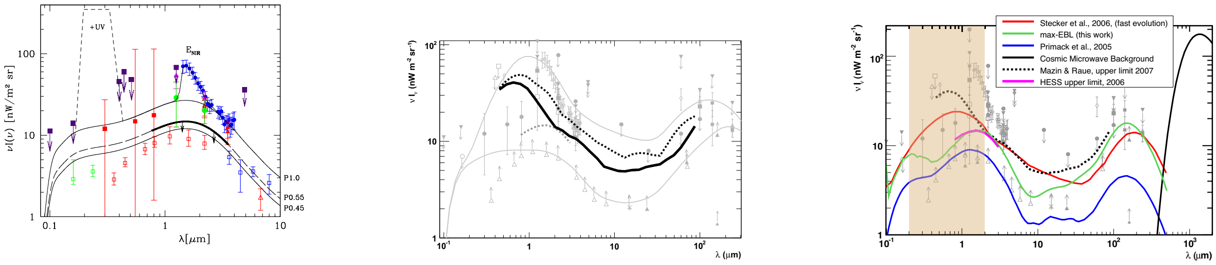

Figure 2: *Left:* Limits set by H.E.S.S. The thick black line between 0.8 and 4 μm shows the H.E.S.S. limit. *Middle:* Combined results from Mazin&Raue: the *extreme* scan (dashed black line) in comparison to the result from the *realistic* scan (solid black line). *Right:* Limits set by MAGIC using the 3C 279 spectrum. The green line inside the shadowed region corresponds to the EBL upper limit.

A common criticism of the EBL limits derived as shown above is that they use only few blazars (therefore not providing consistency with other sources) and that the limits are obtained by assuming a certain EBL model and e.g. scaling it, or by exploring just a few details, i.e. the derived limits become very model-dependent. In order to avoid this dependency Mazin&Raue[5] performed a scan over many hypothetical EBL realizations (over 8 million different ones). The authors also tested all available blazar spectra (until 2006) to generalize the EBL limits. The derived upper limits on the EBL density are shown in the middle plot of Fig. 2. Two limits are shown: the solid line represents the upper limit assuming that the intrinsic blazar spectrum cannot be harder than $\Gamma_{\rm int} = 1.5$, whereas the dashed line shows the limit for $\Gamma_{\rm int} = 2/3$. The latter one can be understood as the most conservative one as it is derived for monoenergetic electrons, which are responsible for the inverse Compton scattering of ambient photons. One can see that the derived limits favor a low EBL level and are in good agreement with galaxy counts from the optical to the mid infrared regimes. Again, the cosmological origin of the near infrared excess (e.g. Matsumoto et al.[8]) can be ruled out even for the extreme case of $\Gamma_{\rm int} = 2/3$. Using these EBL limits, constraints on the physical parameters of the early stars (z>5) were explored by Raue et al.[9].

In 2007, the MAGIC collaboration reported a detection of a very distant (z = 0.536) radio quasar 3C 279 at energies above 80 GeV [10]. The measured energy spectrum of 3C 279 extends up to ≈500 GeV, which implies a very low EBL level. In order to derive an EBL limit, the MAGIC collaboration used the EBL model of [13]. The authors [10] fine-tuned physical parameters of the EBL model in order to comply with the requirement that the intrinsic spectrum of 3C 279 cannot be harder than $\Gamma_{\rm int} = 1.5$. The resulting maximum allowed EBL model is shown by the green line in Fig. 2, right plot. The EBL limit derived by MAGIC [10] is on a similar level as limits derived earlier (H.E.S.S.[6] and Mazin&Raue[5]) and for the first time the EBL was probed at higher redshifts $0.2 < z < 0.5$. Moreover, the MAGIC limit extends into the ultraviolet regime (0.2μm to 0.8μm).[a] Tavecchio&Mazin[11] tested the effect of internal absorption on the intrinsic spectrum for several realistic scenarios and confirmed limits derived by MAGIC.

Summarizing the status of the EBL constraints obtained by the IACTs, the following can be stated:

- robust EBL upper limits are derived by different groups extending from ultraviolet through mid infrared regimes;
- the limits are close (at most factor of 2 higher) to the EBL low level inferred from the resolved galaxies by *HST*, *ISOCAM* and *Spitzer*;

[a]See Stecker&Sculy[12] for an alternative interpretation.

- this implies that instruments like *HST*, *ISOCAM* and *Spitzer* resolved most of the EBL sources;
- the resulting γ-ray horizon can be determined to lie within a narrow band between the upper limits from the IACTs and the low limits from the galaxy counts;
- the limits disfavor several EBL models which imply a late peak in the star formation history;
- the limits rule out a cosmological origin of the near infrared excess.

Even for an EBL model tuned to the level of the resolved galaxies [14], the intrinsic spectra of several TeV blazars show the maximum realistic hardness of 1.5 or close to it (e.g. Krennrich et al.[15]). This can be related to the selection effect: only blazars with extremely hard spectra can be detected because the flux of blazars with softer spectra falls below the current sensitivity limit of the IACTs. Harder than expected intrinsic spectra of VHE γ-ray sources would imply either an unnatural fine-tuning of low energy radiation fields inside the sources (e.g., Aharonian et al.[16]), different acceleration mechanisms of charged particles responsible for VHE γ-ray emission or even new physics (e.g. violation of Lorentz invariance [17] or new particles [18]). Future observations with the *Fermi* Gamma-ray observatory and new generation of IACTs such as H.E.S.S. II and MAGIC II will clarify the issue of hard intrinsic spectra due to a higher sensitivity of the instruments.

Acknowledgments

Research of D.M. is supported by a Marie Curie Intra European Fellowship within the 7th European Community Framework Programme.

References

1. M. G. Hauser and E. Dwek. *Annual Review of A&A*, 39:249, 2001.
2. A. Kashlinsky. *Phys. Rep.*, 409:361–438, April 2005.
3. I. Matute, F. La Franca, F. Pozzi, et al. *A&A*, 451:443–456, May 2006.
4. H. Dole, G. Lagache, Puget, et al. *A&A*, 451:417–429, May 2006.
5. D. Mazin and M. Raue. *A&A*, 471:439–452, August 2007.
6. F. Aharonian, A. G. Akhperjanian, A. R. Bazer-Bachi, et al. *Nature*, 440:1018–1021, April 2006.
7. F. Aharonian, A. G. Akhperjanian, A. R. Bazer-Bachi, et al. *A&A*, 473:L25–L28, 2007.
8. T. Matsumoto, S. Matsuura, H. Murakami, M. Tanaka, M. Freund, M. Lim, M. Cohen, M. Kawada, and M. Noda. *ApJ*, 626:31–43, June 2005.
9. M. Raue, T. Kneiske, and D. Mazin, A&A in press, 2009, *ArXiv e-prints: arXiv:0806.2574*,
10. J. Albert, E. Aliu, H. Anderhub, et al., *Science* **320**, 1752– (2008).
11. F. Tavecchio, and D. Mazin, *MNRAS* 392:L40-L44, January 2009
12. Stecker, F. W. and Scully, S. T. ApJ Letters 691:L91-L94, February 2009
13. T. M. Kneiske, K. Mannheim, and D. H. Hartmann. *A&A*, 386:1, 2002.
14. A. Franceschini, G. Rodighiero, and M. Vaccari, *A&A* **487**, 837–852 (2008).
15. F. Krennrich, E. Dwek, and A. Imran, *ApJ*, 689:L93 (2008).
16. F. A. Aharonian, D. Khangulyan, and L. Costamante, *MNRAS* **387**, 1206–1214 (2008).
17. R. J. Protheroe and H. Meyer. *Physics Letters B*, 493:1, 2000.
18. A. de Angelis, M. Roncadelli, and O. Mansutti, *Phys. Rev. D* **76**, 121301 (2007).

Fermi-LAT observations of Galactic X-ray binaries

A. B. HILL on behalf of the *Fermi*-LAT collaboration
Laboratoire d'Astrophysique de Grenoble, UMR 5571 CNRS, Université Joseph Fourier, BP 53, 38041 Grenoble, France

The *Fermi* Gamma-ray Space Telescope has been observing the sky in gamma-rays above 20 MeV since August 2008. The LAT (Large Area Telescope) wide field of view (>2 sr) and large effective area combine to allow the entire sky to be scanned every 3 hours with unprecedented sensitivity and source localisation in this energy range. This makes the LAT particularly suited to regular monitoring of the Galactic X-ray binary population. Observations of the bright source LS I +61°303, a well observed binary system at X-ray and TeV energies, will be presented. Discussion includes observations of variations in the flux with the orbital phase of the system and comparisons with very high-energy observations; these are the first results of orbital variations at GeV energies.

1 Introduction

The *Fermi Gamma-ray Space Telescope*, formerly GLAST, was successfully launched from Cape Canaveral, Florida on 2008 June 11. Onboard *Fermi* is the Large Area Telescope (LAT), an electron-positron pair production telescope operating in the ∼20 MeV to ∼300 GeV energy range [2]. Relative to previous high-energy gamma-ray telescopes the LAT has a large ∼2.4 sr field of view, a large effective area (∼8000 cm^2 on axis for >1 GeV) and improved angular resolution or point spread function (PSF, ∼0.8° for 68% containment at 1 GeV). The *Fermi* survey mode operations commenced on 2008 August 11. In this mode the observatory observes every part of the sky for ∼30 minutes every 3 hours making *Fermi* ideally suited for long term all-sky observations.

1.1 Gamma-ray binaries: What do we know?

Gamma-ray binaries are a subclass of X-ray binaries that show resolved radio sources and that have been detected at vergy high-energy (VHE>1 TeV). To date there are only three confirmed examples of these systems, all of which are high mass X-ray binaries: PSR B1259−63, LS 5039, and LS I +61°303 [11].

PSR B1259−63 is a system comprised of a 47.7 ms radio pulsar in a 3.4 year orbit around a B2Ve star [11]. The system has also been detected at VHE by HESS during a period of periastron passage when it exhibited flux variations on daily timescale[6].

LS 5039 comprises of an O6.5 star and an unidentifed compact object in a 3.9 day orbit. The source has been tentatively associated with the EGRET source 3EG J1824−1514 however the EGRET source has a 0.5° uncertainty in its location and shows no indications of variability [14]. The HESS detection of VHE emission within an arcmin of LS 5039 combined with VHE modulation on the known orbital period confirms the source as a gamma-ray binary [5].

LS I +61°303 is a high mass X-ray binary comprised of a Be star and an unidentified compact object in a 26.496 day orbit. As in the case of LS 5039 there was a tentative association with a high-energy source, 2CG 135+01, detected by *COS B* and then EGRET [16, 14]. However,

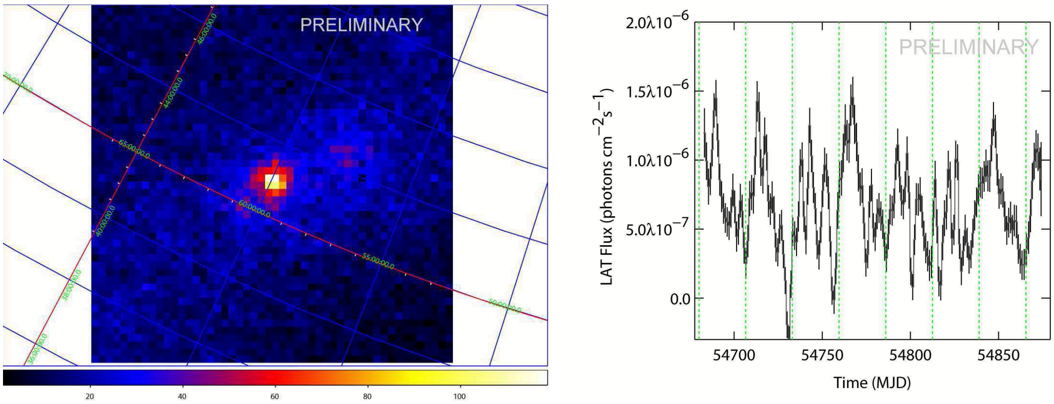

Figure 1: The 10° counts map in (RA,Dec) around the LS I +61°303 location. The source is bright and isolated with a significance of >50σ. The scale units are counts/pixel. Right: The 100 MeV to 20 GeV light curve of LS I +61°303 covering the period 2008 August 4 through 2009 February 12. The vertical lines indicate the zero phase from Gregory [12].

again the positional uncertainty was not small and variability of the EGRET light curve could neither be firmly established nor related to that seen at other wavelengths [19]. The MAGIC and VERITAS telescopes have independently reported VHE emission coincident with LS I +61°303 [9, 4]. Furthermore, the MAGIC collaboration, report the detection of a the 26.5 day orbital period in the VHE emission [7].

2 The *Fermi* detection of LS I +61°303

The *Fermi* dataset used in this analysis starts from 2008 Aug 4 through to 2009 Feb 12; this corresponds to approximately eight orbits of LS I +61°303. The data was reduced and analysed using the standard *Fermi* Science Tools package and the standard onboard filtering, event reconstruction and classification were applied to the data [2]. Only the highest quality event class ("diffuse" class) has been used. The counts map of a 10° region around LS I +61°303 is shown in Fig. 1 (left); LS I +61°303 can be seen to be the brightest source in the field lying on a background of galactic and extragalactic diffuse emission. A fit to the source yields a detection in excess of 50σ and a position of R.A. = 40.076, Dec. = +61.223 (J2000) with a 95% error of 0.069°, in good agreement with the accepted position.

2.1 Timing Analysis

Aperture photometry was used to extract a light curve of LS I +61°303 from the LAT event data, within an aperture of ∼2°, with half day binning. A version of this light curve is shown in Fig 1 (right); the light curve has been smoothed and rebinned to make the variability clearer. The light curve is clearly very variable. To explore the possibility of periodic variability in the light curve the Lomb-Scargle periodogram method was applied to the lightcurve [17, 18]. The left panel of Fig 2 shows the resultant Lomb-Scargle periodogram; the light curve points were weighted according to their exposure in the periodogram.

A solitary, high significance peak is evident in the periodogram at a period of 26.6 days; the known orbital period of 26.4960 days is marked by the vertical dashed line in Fig 2 (left). To investigate the associated error we performed a serious of Monte-Carlo simulations. Simulated light curves were constructed from the observed light curve of LS I +61°303 and randomly shuffling the flux points within their errors assuming Gaussian statistics. The Lomb-Scargle periodogram was then constructed for each simulated light curve and the period and power of the most significant peak recorded. From 200,000 simulations the distribution of detected periods gives an estimate of the period error; we find a periodicity in the LS I +61°303 light curve of P = 26.6±0.5 days.

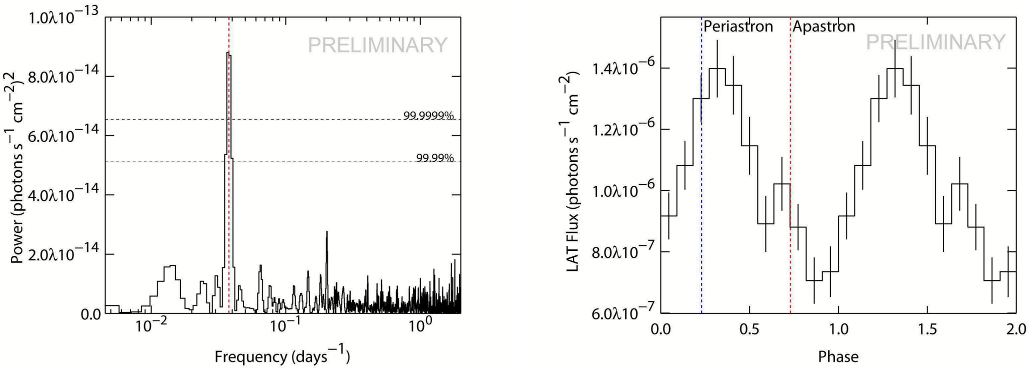

Figure 2: Left: Power spectrum of the light curve. The vertical line indicates the known orbital period from Gregory [12], coinciding with a strong peak in the spectrum, while the horizontal lines indicate the marked significance levels. Right: The light curve of Fig. 1 phase folded on the known orbital of 26.4960 days and with zero phase at MJD 43,366.2749 [13, 12].

This measurement is completely consistent with the known orbital period of 26.4960±0.0028 days Gregory [12].

Folding on the known period of LS I +61°303 yields the average phase-folded light curve shown in Fig 2 (right) with zero phase at MJD 43,366.2749 [13, 12]. The folded light curve shows a large modulation amplitude with maximum flux occuring slightly after periastron passage. This is in contrast to the variability reported at VHE by both MAGIC and VERITAS [9, 4]. The MAGIC observations of 2005-2006 report a significant flux increase from phases 0.45–0.65 and the VERITAS observations of 2006–2007 showed a strongly variable flux at 300 GeV to 5 TeV with a peak in emission at apastron during most orbital cycles.

A full and complete discussion of the LS I +61°303 *Fermi* data analysis and results is presented in [3].

3 Other X-ray binaries

LS I +61°303 is the 15^{th} brightest source in the *Fermi* 3-month Bright Source List of Abdo et al. [1] and so was an obvious candidate as the first X-ray binary to be investigated. However there are other known VHE binaries and new binaries may yet be found in the *Fermi* data set. A total of sixty eight known binary sources are monitored on a daily basis. The 3-month Bright Source List reports a gamma-ray source consistent with the position of LS 5039 [1] and investigation of the *Fermi* data are already underway. The MAGIC collaboration reported the VHE detection of Cyg X-1 in 2006 during a known X-ray flare of the source [8]. Any observations of galactic X-ray binaries are obviously made more challenging by the presence of the bright, diffuse emission across the galactic plane.

3.1 Unknown sources

There is also the possibility that previously unknown gamma-ray binary sources are detected in amongst the population of sources visible to *Fermi*. Whilst this may include those persistent sources without known counterparts it is also possible that some transient sources may also be binary systems. As of 2008 February, *Fermi* has reported the detection of two galactic plane transients, Fermi J0910−5041 [0FGL J0910.2−5044 in the 3-month Bright Source List, 1] and 3EG J0903−3531 [15, 10]. These transients may only be active for a few days and so are very challenging and interesting sources to investigate.

4 Conclusion

The early performance and results from *Fermi* are very exciting and promise many exciting discoveries for the future. A preliminary analysis of the *Fermi* data set demonstrates unambiguously that LS I $+61^{\circ}303$ is a source of GeV emission. This has been achieved through the vastly improved source location at high-energy as well as the first detection of flux variability modulated on the known orbital period at GeV energies. Based upon the *Fermi* data we estimate a period of 26.6 ± 0.5 days which is completely consistent with measurements made at other wavelengths. The source is bright, persistent and exhibits a large amount of orbit-to-orbit variability.

Future investigation of other X-ray binary systems look bright with the report of a high-energy source coincident with the position of LS 5039 in the 3-month Bright Source List [1] and the report from MAGIC that a VHE flare was seen from Cyg X-1 in 2006 [8]. The rich population of *Fermi* sources also leaves open the possibility that new binary sources are yet to be found both persistent and flaring.

Acknowledgments

The Fermi LAT Collaboration acknowledges generous ongoing support from a number of agencies and institutes that have supported both the development and the operation of the LAT as well as scientific data analysis. These include the National Aeronautics and Space Administration and the Department of Energy in the United States, the Commissariat l'Energie Atomique and the Centre National de la Recherche Scientifique / Institut National de Physique Nuclaire et de Physique des Particules in France, the Agenzia Spaziale Italiana and the Istituto Nazionale di Fisica Nucleare in Italy, the Ministry of Education, Culture, Sports, Science and Technology (MEXT), High Energy Accelerator Research Organization (KEK) and Japan Aerospace Exploration Agency (JAXA) in Japan, and the K. A. Wallenberg Foundation, the Swedish Research Council and the Swedish National Space Board in Sweden.

Additional support for science analysis during the operations phase from the following agencies is also gratefully acknowledged:the Istituto Nazionale di Astrofisica in Italy

A. B. Hill acknowledges support from the European Community via contract ERC-StG-200911

References

[1] Abdo A. A., et al., 2009a, ApJ, *submitted*, arXiv:0902.1559
[2] Abdo A. A., et al., 2009b, APh, *submitted*, arXiv:0904.2226
[3] Abdo A. A., et al., 2009c, ApJ, *in preparation*
[4] Acciari V. A., et al., 2008, ApJ, 679, 1427
[5] Aharonian F., et al., 2005a, Sci, 309, 746
[6] Aharonian F., et al., 2005b, A&A, 442, 1
[7] Albert J., et al., 2009, ApJ, 693, 303
[8] Albert J., et al., 2007, ApJ, 665, L51
[9] Albert J., et al., 2006, Sci, 312, 1771
[10] Cheung C. C., Reyes L., Longo F., Iafrate G., 2008, ATel, 1788, 1
[11] Dubus G., 2006, A&A, 456, 801
[12] Gregory P. C., 2002, ApJ, 575, 427
[13] Gregory P. C., et al., 1979, AJ, 84, 1030
[14] Hartman R. C., et al., 1999, ApJS, 123, 79
[15] Hays E., Cheung C. C., Reyes L., 2008, ATel, 1771, 1
[16] Hermsen W., et al., 1977, Nature, 269, 494
[17] Lomb N. R., 1976, Ap&SS, 39, 447
[18] Scargle J. D., 1982, ApJ, 263, 835
[19] Tavani M., Kniffen D., Mattox J. R., Paredes J. M., Foster R., 1998, ApJ, 497, L89

THE X-RAY NOVA H1743-322: THE LATE 2008 OUTBURST, AND COMPARISONS WITH PREVIOUS ONES

L. PRAT, J. RODRIGUEZ
CEA Saclay, DSM/IRFU/Service d'Astrophysique,
91191 Gif-sur-Yvette, France

We study the X-ray properties of the Black-Hole Candidate H1743−322. This source has undergone 5 outbursts of various amplitudes during the past 5 years. We analyse the 3-200 keV spectra from simultaneous INTEGRAL and RXTE observations, and follow its spectral evolution during its late 2008 outburst. We also used the timing capabilities of *RXTE* to look for QPOs in the lightcurves of this source. Using these data, we focus on the possible links in the evolution of the accretion disc and the corona of H1743−322. First, we detect an important evolution of the QPO frequency over the outburst. Under the common hypothesis that the frequency of QPOs are determined by the accretion disc, this indicates an evolution in the radius of the inner accretion disc. Then, we see a strong correlation between the QPO frequency and the photon index. Since the photon index depends directly on the characteristics of the corona, this indicates a strong link between the behaviours of the accretion disc and of the corona.

1 Introduction

Low-Mass X-ray Binaries (LMXB) are binary systems consisting of a compact object orbiting a non-degenerate low-mass star. These systems spend most of their time in a faint quiescent state, when they are barely detectable. They may undergo sudden and bright few-month-long X-ray outbursts with typical recurrence periods of many years [1]. The picture commonly accepted to explain the emission of such objects involves the emission of an optically thick and geometrically thin accretion disc, mostly emitting at typical energies of $\sim$1 keV. A second medium is detected as a power law spectrum in the $\sim$10 keV-1 MeV range. This medium of unknown geometry is called a "corona", and is probably composed of hot electrons where soft X-ray photons originating in the disc undergo inverse Comptonization. In addition, a relativistic jet, usually detectable in the radio range, might be present.

Depending on the relative strengths of these media, we can distinguish several spectral states [2,3]. The two main ones are the High Soft State (HSS), dominated by emission from the accretion disc, and the Low/Hard State (LHS), dominated by non-thermal emission. Further states have been identified as "Intermediate", depending on the details of the spectral and temporal characteristics. These features are coupled to radio changes, a compact jet being usually observed in the LHS while it is quenched in the HSS [4].

The X-ray transient H1743−322 was discovered during a bright outburst that occurred in 1977 with the *Ariel V* and *HEAO I* satellites [5]. In 2003, another bright outburst was detected with *INTEGRAL*, and has been deeply studied at all wavelengths[6,7,8]. It was shown in particular that H1743−322 had a behaviour consistent with most black-hole X-ray transients, and was, thus, classified as a Black-Hole Candidate. This 2003 outburst was followed by weaker episodes in 2004, 2005, in early 2008 [9] and in late 2008 [10].

Herein, we first present the results of the X–ray coverage of the source in late 2008, focusing on the evolution of the accretion disc. Then, we compare the variability of the source to the well-studied 2003 outburst, and try to link the evolution of the accretion disk to that of the coronal medium.

2 Available data and quick reduction description

Between 2008 September 23 [11,12] and 2008 November 19, INTEGRAL and RXTE observations of H1743−322 occurred almost every second day, while at softer X-rays, Swift (XRT) and XMM/Newton respectively provided 3 and 1 observations. All these data were reduced in a standard way. The *INTEGRAL* data were reduced using the `Off-line Scientific Analysis (OSA)` v7.0 software package, *RXTE* and *Swift*/XRT observations were reduced with the `HEASOFT` v6.5 software package, while *XMM/Newton* ones were reduced with the Science Analysis Software, `xmmsas`, v7.1 [10]. We use these data to follow the source in late 2008 from ∼1 keV to ∼200keV.

We also used the timing capabilities of *RXTE* in our analysis, and analysed light curves covering the five outbursts since 2003. We extracted high time resolution light curves from the PCA EVENT data with ∼500 μs resolution. We then produced power-density spectra (PDS) in the frequency range 0.0156–1024 Hz.

3 The late 2008 outburst

During the last outburst of H1743−322 to date, the source underwent two short spectral transitions. It began its outburst in a pure Low Hard State, then transited into a Hard Intermediate State (HIMS), and eventually went back into LHS [10]. This means that for a few days, the coronal flux decreased significantly, but the source did not reached Soft States dominated by emission from the accretion disc. In other words, and following the standard scheme, the accretion rate stayed well below the Eddington limit during the entire outburst. This makes the late 2008 outburst the fourth Hard outburst since 2003.

Using *RXTE*, we looked for Low Frequency Quasi Periodic Oscillations (LFQPOs) in the lightcurves of H1743−322. LFQPOs are present in many microquasars, mainly during states dominated by coronal or jet emission [13]. Although the precise origin of these oscillations is still unknown, QPOs are thought to be generated in the inner parts of the accretion disc. This idea stems from the fact that their frequencies are similar to the keplerian frequencies of the disc, and their evolution is correlated to the disc behaviour [14,15]. The theoretical attempts to model QPOs rely mainly on hot spots, or instabilities propagating inside the disc.

Fig. 1, left, shows the evolution of the QPO parameters over the late 2008 outburst. In the first part of the outburst, in all observations before MJD 54760, a strong QPO with its first harmonic is present. Then, during the HIMS, the QPO frequency increases dramatically, before slowly decreasing during the second LHS. This evolution in the QPO frequency is of particular interest. Indeed, if we suppose that the QPO frequency is somehow related to the Keplerian rotation frequency, then the increase in frequency can be interpreted as a movement of the inner part of the disc. Indeed, if the inner part of the disc moves in, the rotation frequency increases, and thus so does the QPO frequency. After the transition to the HIMS, when the QPO frequency increases dramatically, this would indicate that the disk had moved further inwards. Unfortunately, H1743−322 was not bright enough to enable the inner radius of the accretion disc to be determined precisely using spectral models.

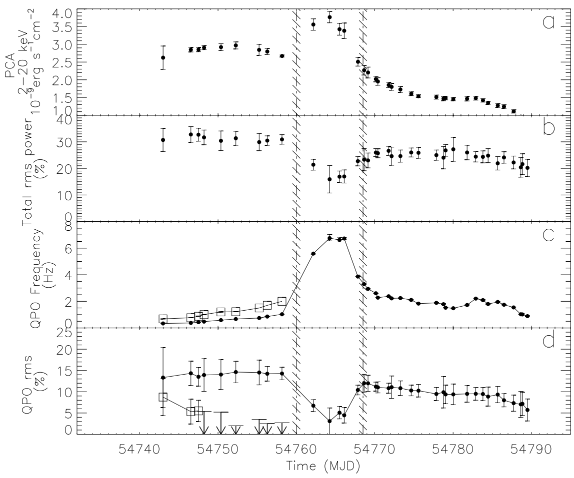

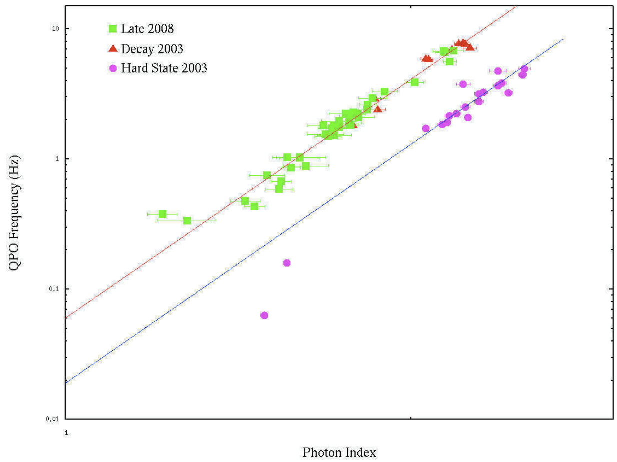

Figure 1: **Left:** Spectral and timing characteristics of H1743−322 over its late 2008 outburst. From top to bottom, **a)** lightcurve in the 2–20 keV bend, **b)** total rms power, **c)** frequencies of the two detected QPOs and **d)** rms power of these QPOs. The filled zone marks the spectral transition from the Hard State (HS) to the Hard Intermediate State (HIMS). Error bars are at the 90% confidence level. **Right:** QPO frequency as a function of the X-ray photon index, during Hard States of H1743−322. The two parallel lines are fits to the rising phase of the 2003 outburst, and to the combined decay phase of 2003 and late 2008 outburst. Between the two tracks, the QPO frequency is multiplied by 3.

4 QPO frequency / Photon index correlation

In recent years, a correlation between the QPO frequency and the photon index has also been detected in several Black-Hole Candidates [16]. The photon index is, in microquasars, characteristic of the Comptonized component that forms the corona. If now the QPO frequency is set by some disc property, then this correlation provides a strong link between the inner parts of the disc and the corona.

In the case of H1743−322, we plotted the frequency of QPOs during Hard States, versus the photon index of the Comptonized component (Fig. 1, right). QPOs were detected during the 2003 and late 2008 outbursts only. During the first Hard State of the 2003 outburst, that corresponds to the rising phase, these two parameters are linked by a power-law correlation (purple points on Fig. 1, right). Then, during the decay phase of this outburst, and during the late 2008 Hard outburst, the source follows a second track, with the same slope. Both tracks are parallel, and the intercept is multiplied by 3 between them.

The correlation between QPO frequency and photon index reveals the parallel evolution of the disc and coronal medium in H1743−322, and confirms similar results on other microquasars. However, contrary to previous observations, we detect two distinct tracks. Note that these tracks arise from observations separated by several months, but correspond to very similar spectral characteristics. This is an unexpected result, and we can only make assumptions to explain it.

An explanation for the presence of these two distinct tracks may reside in the physics of QPOs. Indeed, QPOs are known to sometimes appear together with harmonic frequencies. H1743−322 itself showed pairs of low frequency QPOs in 2003 [13] and late 2008 [10], composed of a fundamental oscillation and its first harmonic. In this respect, the two distinct tracks may come from the same oscillation that amplifies two different harmonics, depending on the initial conditions.

Theoretical models, such as the Accretion-Ejection Instability [17] (AEI), do explain QPOs. In this model, a spiral shock could result from the non-linear evolution of the AEI, just as the gas forms shocks in the arms of spiral galaxies. In some cases, several arms can develop, which explain the presence of several harmonics. The name of this instability relates to the fact that, if the disk is covered by a low-density corona, a sizable fraction of the accretion energy extracted from the disk can end up in Alfvén waves emitted by the instability in the corona, where they might energize a jet [18]. However, this model do not predict that the fundamental mode of a QPO could be quenched, while its second harmonic becomes dominant. Thus, this observation, if confirmed in the case of other microquasars, can prove to be a strong constraint on disc models.

References

1. Tanaka, Y. & Shibazaki, N. 1996, ARA&A, 34, 607
2. McClintock, J. E. & Remillard, R. A. 2006, Black hole binaries, Compact stellar X-ray sources. Edited by Walter Lewin & Michiel van der Klis: Cambridge University Press, 157
3. Homan, J. & Belloni, T. 2005, Ap&SS, 300, 107
4. Fender, R., Corbel, S., Tzioumis, T., et al. 1999, ApJ, 519, L165
5. Kaluzienski, L. J. & Holt, S. S. 1977, IAU Circ., 3099, 3
6. Parmar, A. N., Kuulkers, E., Oosterbroek, T., et al. 2003, A&A, 411, L421
7. Lutovinov, A., Revnivtsev, M., Molkov, S., & Sunyaev, R. 2005, A&A, 430, 997
8. Kalemci, E., Tomsick, J. A., Rothschild, R. E., et al. 2006, ApJ, 639, 340
9. Kalemci, E., Tomsick, J. A., Yamaoka, K., & Ueda, Y. 2008, ATel, 1348
10. Prat, L., Rodriguez, J., Cadolle Bel, M., et al. 2009, A&A, 494, L21
11. Kuulkers, E., Brandt, S., Budtz-Jorgensen, C., et al. 2008, ATel, 1739
12. Prat, L., Rodriguez, J., & Cadolle Bel, M. 2008, ATel, 1745
13. McClintock, J. E., Remillard, R. A., Rupen, M. P., et al. 2007, astro-ph, [0705.1034]
14. Rodriguez, J., Varnière, P., Tagger, M., & Durouchoux, P. 2002, A&A, 387, 487
15. Rodriguez, J., Corbel, S., Kalemci, E., Tomsick, J. A., & Tagger, M. 2004, ApJ, 612, 1018
16. Vignarca, F., Migliari, S., Belloni, T., Psaltis, D., & van der Klis, M. 2003, A&A, 397, 729
17. Tagger, M. & Pellat, R. 1999, A&A, 349, 1003
18. Varnière, P., Rodriguez, J., & Tagger, M. 2002, A&A, 387, 497

Fermi–LAT observations of Pulsar Wind Nebulae

M.-H. GRONDIN on behalf of the *Fermi*–LAT collaboration
CNRS/IN2P3, Université de Bordeaux,
Centre d'Études Nucléaires de Bordeaux Gradignan,
UMR 5797, Gradignan, 33175, France

Results on Pulsar Wind Nebulae (PWNe) obtained with the Large Area Telescope (LAT) aboard *Fermi* are reported. At GeV energies, their gamma-ray spectra can be explained by inverse Compton scattering of high energy electrons off the ambient photons (CMB, far infrared radiation from dust, synchrotron photons...). The case of the Crab nebula, the standard candle of astrophysics, is discussed in detail. The spectral energy distribution in the 200 MeV – 300 GeV energy band links up naturally with ground-based instrument results, making this source one of the best candidates to perform a cross-calibration with the Cherenkov experiments, especially with MAGIC (La Palma, Canary Islands) and VERITAS (Arizona, United States), both located in the northern hemisphere. Results on the Crab pulsar spectral analysis and its light curves at different energies are presented. Preliminary analysis of the Kookaburra and Vela X regions is also discussed.

1 Introduction

Several years after EGRET, the Large Area Telescope (LAT), aboard *Fermi*, offers the opportunity to study gamma-ray sources such as pulsars and pulsar wind nebulae (PWNe). The LAT is an electron-positron pair conversion telescope, sensitive to γ-rays with energies between 30 MeV and 300 GeV, with improved performance (a large effective area, a broad field of view, and a very good angular resolution) [1] compared to its predecessor.
Results on the Crab pulsar and nebula, both firmly detected and identified by the LAT, are presented in section 2. Sections 3 and 4 discuss preliminary results on two other gamma-ray PWNe candidates : the Kookaburra complex and Vela X.

2 The Crab nebula

The Crab nebula is known as the standard candle of astronomy, since it is detected in almost all wavelength bands of the electromagnetic spectrum. Powered by the Crab pulsar, one of the most energetic pulsars ($\dot{E} = 4.6 \times 10^{38}$ erg.s^{-1}), it is the remnant of the 1054 A.D. supernova explosion reported by Chinese astronomers and is located at a distance of 2 kpc.

2.1 Earlier gamma-ray observations

The gamma-ray detection of the Crab pulsar and nebula was reported by the EGRET collaboration in 1993 [2]. Concerning the nebula, in the 70 MeV – 30 GeV energy band, both the synchrotron radiation and inverse Compton scattering have been identified as the processes responsible for the detected emission below and above $\sim$ 200 MeV respectively [3]. The spectral

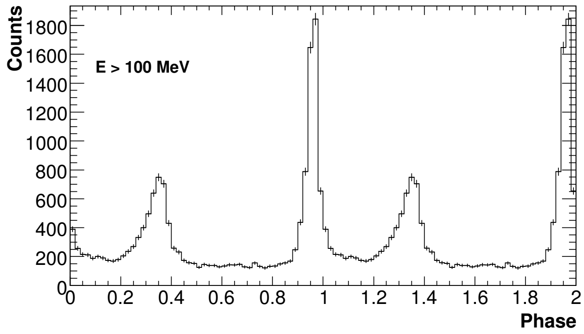

Figure 1: Phase histogram of the Crab pulsar above 100 MeV (50 bins/cycle, 2 cycles are shown)

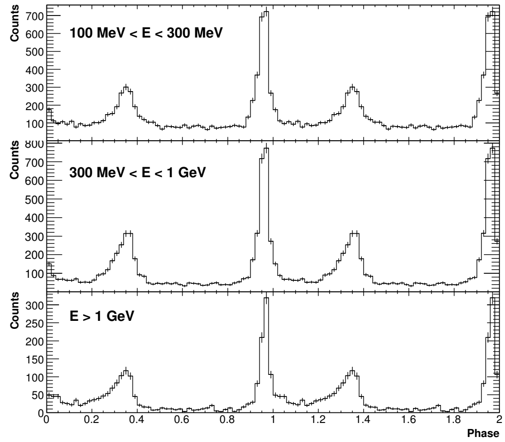

Figure 2: Phase histograms of the Crab pulsar in different energy bands (50 bins/cycle, 2 cycles are shown)

parameters of both components presented large uncertainties [4]. A spectral index of ~ 1.85 was estimated for the inverse Compton component in a 200 MeV – 30 GeV energy range but no significant cut-off or break energy could be seen with EGRET.

At very high energy, the spectral results of Cherenkov experiments nicely agree and present a steeper spectrum (spectral index of ~ 2.4) above a few hundreds of GeV. In particular, taking into account EGRET spectral results, the MAGIC collaboration estimated the energy break of the inverse Compton component at 77 ± 35 GeV [5].

2.2 Fermi results

The following results on the Crab nebula and pulsar high energy emission were obtained using five months of *Fermi*-LAT data in survey mode. To accomodate uncertainties in the instrument performance still under investigation at low energy, only events in a 200 MeV – 300 GeV energy band were selected for the spectral analysis.

Light curves

Prior to the spectral analysis of the Crab nebula, a temporal analysis of the Crab pulsar was necessary. Using an ephemeris from the Nançay radiotelescope (France), the arrival times of each event were first converted to the Solar System barycentric time and a corresponding phase ϕ was calculated with TEMPO2 [6], using the derivatives of the rotation frequency f_0.

The resulting light curve above 100 MeV is presented in figure 1. The signal-to-noise ratio has been optimized using an energy-dependent region of interest : only photons with an angle $\theta < \mathrm{Max}(6.68 - 1.76\mathrm{Log}_{10}(\mathrm{E}_{\mathrm{MeV}}), 1.3)^\circ$ from the pulsar position are selected. The light curve shows two main peaks at phase $\phi_1 \sim 0.96$ (the radio main peak being at phase 0.98), and $\phi_2 \sim 0.35$. Figure 2 presents the light curves in different energy bands. The peak positions are stable with energy while their widths and the ratio P1/P2 decrease with increasing energy.

We define the off-pulse window as the $0.45 - 0.85$ phase range. This interval will be considered for the spectral analysis of the Crab nebula, due to the bright emission of the pulsar in the rest of the phase.

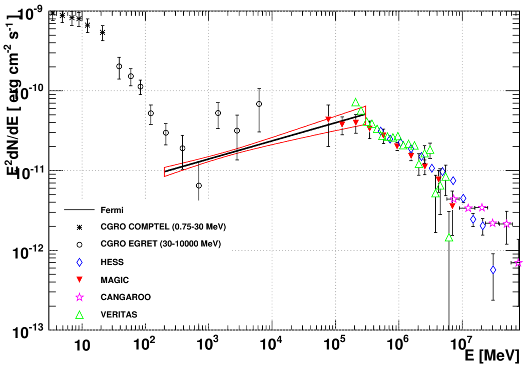

Figure 3: Spectral energy distribution of the Crab nebula (in E^2 times the differential flux) from soft to very high energy γ-rays. The fit result of the LAT data (black line) and a 1-σ contour (red lines) are represented. References : CGRO (Comptel and EGRET) [4]; MAGIC [5]; HESS [8]; CANGAROO [9], VERITAS [10]

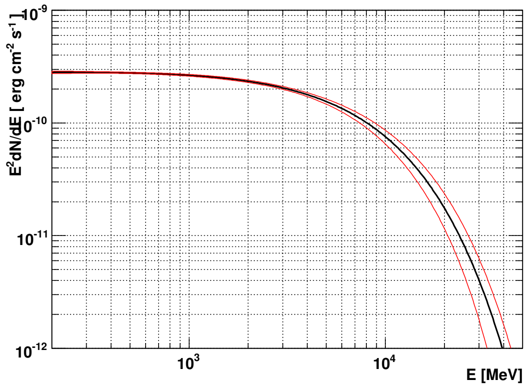

Figure 4: Spectral energy distribution of the Crab pulsar (in E^2 times the differential flux) in the *Fermi* energy band. The fit result of the LAT data (black line) and a 1-σ contour (red lines) are represented.

Crab nebula spectrum – Cross-calibration between Fermi and Cherenkov telescopes

The spectral analysis of the Crab nebula was performed using a maximum-likelihood method [7], in the off-pulse window. The best fit in the 200 MeV – 300 GeV is obtained with a simple power-law with a spectral index of ~ 1.8, a flux above 200 MeV of $(9.9 \pm 0.9) \times 10^{-8}$ cm^{-2}s^{-1} (the quoted error is statistical) for the total phase and a test statistic value of 905. These results are consistent with EGRET.

Figure 3 shows the LAT results for the source detected in the off-pulse window, represented by a 1-σ contour. Results on the Crab nebula of EGRET and other Cherenkov experiments are also shown. *Fermi* and high energy spectral points link up naturally, resulting in a firm identification of the Crab nebula.

Although no significant cut-off is observed in the LAT data with the current statistics, the determination of its value with an increased *Fermi*-LAT data sample would allow the calibration of Cherenkov telescopes [11].

Spectral analysis of the Crab pulsar

The spectral analysis of the Crab pulsar was performed on the total phase interval. The best fit in the 200 MeV – 300 GeV energy range is obtained with a power-law with an exponential cut-off of the form : $\frac{dN}{dE} \propto (\frac{E}{10^3\mathrm{MeV}})^{-\Gamma} e^{-E/E_c}\,\mathrm{cm}^{-2}\,\mathrm{s}^{-1}\mathrm{MeV}^{-1}$, where $\Gamma \sim 1.9$ is the spectral index and $E_c \sim 5 - 10$ GeV the cut-off energy. The integral flux above 200 MeV is of $(8.2 \pm 0.4) \times 10^{-7}$ cm^{-2}s^{-1} (the quoted error is statistical).

Figure 4 shows the LAT results for the pulsar, represented by a 1-σ contour. The larger energy band covered by the LAT and its better sensitivity provide a precise determination of the cut-off energy of the spectral distribution, which was not possible with EGRET.

3 The Kookaburra complex

The Kookaburra region contains several non-thermal sources, among which are two pulsar wind nebulae : Kookaburra/K3 (PWN G313.6+0.3), powered by the energetic ($\dot{E} = 10^{37}$ erg.s^{-1})

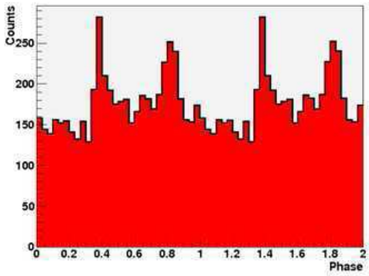

Figure 5: Phase histogram of the LAT pulsar PSR J1418.8-6058 (two cycles are shown).

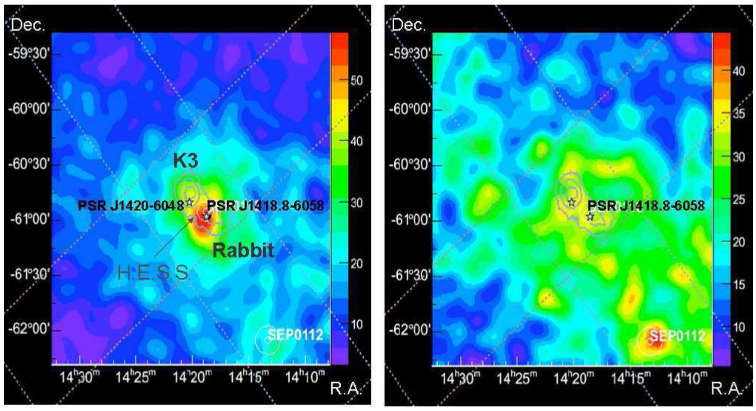

Figure 6: On- (*left*) and off-pulse (*right*) counts maps of the Kookaburra complex. H.E.S.S. contours of PWNe emission are overlaid [14]. The positions of the pulsars PSR J1420-6048 and PSR J1418.8-6058 are marked with stars.

pulsar PSR J1420-6048 and the Rabbit (PWN G313.1+0.1), possibly associated to a pulsar candidate [12].

3.1 Earlier gamma-ray observations

A gamma-ray source 3EG J1420-6038 was detected in the Kookaburra region by EGRET, but due to the poor instrumental angular resolution, the source could not be clearly identified. Re-analysis of this region demonstrated that the emission could be mainly due to K3 and its pulsar, PSR J1420-6048 [13]. Moreover, a contribution from one (or more) nebula(e) was proved by variability studies of the gamma-ray emission.
More recently, very high energy photons have been detected by H.E.S.S., coming from both K3 and the Rabbit [14]. Their spectra can only partially explain the EGRET 3EG J1420-6038 flux, allowing us to expect a pulsed contribution in this region.

3.2 Fermi preliminary results

Algorithms of periodicity search [15] are performed on each LAT bright source. In particular, significant pulsations were detected from a source LAT PSR J1418.8-6058 in the Rabbit nebula [16], with a period of P $\sim$ 110 ms (Figure 5) and a spin-down power of $\dot{E} = 4.95 \times 10^{36}$ erg s^{-1}.
This pulsar being relatively bright in gamma-rays, searches of steady emission have to be performed in the off-pulse window. Figure 6 presents the on- and off-pulse counts maps in the Kookaburra region, with H.E.S.S. contours overlaid for comparison. A precise analysis of the gamma-rays detected in the off-pulse is currently on-going and requires detailed knowledge of the galactic diffuse emission.

4 Vela X

Vela X is a PWN powered by the Vela pulsar, located at a parallax distance of 287 $\pm$ 19 pc [19]. Searches of steady emission were performed in the off-pulse window of this source. Although no significant emission from Vela X was reported by the *Fermi* collaboration, an upper limit on the flux above 100 MeV of 1.8×10^{7} cm^{-2} s^{-1} was derived in 40% of the total phase interval, using 75 days of data [20].
The Vela X spectral energy distribution can be described by leptonic scenarii : the radio to hard X-ray emission is due to synchrotron radiation, while very high energy photons are produced via

inverse Compton scattering. Models considering one single electron population can well explain the observed emission, but only assuming a second break in the leptonic spectrum [21]. Another approach consists in the injection of two electron populations, the first one responsible for the radio and potential gamma-ray emission, and the second for X-rays and very high energy gamma-rays [22]. The upper limit obtained with *Fermi* should help distinguish between the models and constrain physical parameters such as the synchrotron cut-off frequency, the electron spectrum and the magnetic field in the nebula.

5 Conclusions

The Crab nebula was firmly detected by the LAT. Its inverse Compton spectrum is well described by a simple power-law. No significant break can be seen with the current statistics. A larger data sample would allow us to estimate the cut-off energy and perform a cross-calibration study with Cherenkov telescopes.
Other very high energy PWNe are studied with the LAT, such as the Kookaburra complex and Vela X. Even if no significant detection is reported for these two regions, upper limits on the gamma-ray emission can be computed and used for multi-wavelength studies to constrain physical parameters of the models.

References

1. Atwood, W.B. et al., 2009, ApJ, submitted
2. Nolan, P.L. et al., 1993, ApJ, 409, 697
3. de Jager, 0.C.. et al., 1996, ApJ, 457, 253
4. Kuiper, L. et al., 2001, A&A, 378, 918
5. Albert, J. et al., 2008, ApJ, 674, 1037
6. Hobbs, G.B. et al., 2006, MNRAS, 369,655
7. Mattox, J.R. et al., 1996, ApJ, 461, 396
8. Aharonian, F.A. et al., 2006a, A&A, 457, 899
9. Tanimori, T. et al., 1997, arXiv/9710272
10. Celik, O., 2007, arXiv/0709.3868v1
11. Bastieri, D. et al., 2005, APh, 23, 572
12. Ng, C.-Y. and Romani, R.W., 2005, ApJ, 627, 904
13. Reimer, O. and Funk, S., 2006, arXiV/0611653
14. Aharonian, F.A. et al., 2006b, A and A 456, 245
15. Atwood, W. B. and Ziegler, M. and Johnson, R. P. and Baughman, B. M. , 2006, ApJ, 652, L49
16. Abdo, A.A. et al., 2009a, to be submitted to Science
17. Bock, D. C.-J. and Turtle, A. J. and Green, A. J., 1998, Astronom. J., 116, 1886
18. Aharonian, F.A. et al., 2006c, A and A 448, L43
19. Dodson, R. et al., 2003, ApJ, 596, 1137
20. Abdo, A.A. et al., 2009b, ApJ, in press (arXiv/0812.2960)
21. LaMassa, S.M. and Slane, P.O. and de Jager, O.C., 2008, ApJ, 689, L121
22. de Jager, O.C. and Slane, P.O. and LaMassa, S., 2008, ApJ, 689, L125

Detection of SN 1006 in Very High Energy Gamma-Rays by H.E.S.S.

M. NAUMANN-GODO, M. LEMOINE-GOUMARD and M. DE NAUROIS for the H.E.S.S. Collaboration
Laboratoire Leprince-Ringuet, Ecole Polytechnique, CNRS/IN2P3, F-91128 Palaiseau Cedex, France

The historic shell-type supernova remnant SN 1006 is a prime target for observations with Cherenkov telescopes ever since non-thermal synchrotron X-ray emission was discovered in the rims of its 30'-diameter shell. Since theoretical predictions on its TeV-luminosity were only a factor of 2 or 3 below the H.E.S.S. upper limit published in 2005, more in-depth observations of this source were carried out. In 130 h of data accumulated over the years 2003 to 2008, H.E.S.S. finally detected a gamma-ray excess from the remnant of SN 1006, with a flux level well below any previous upper limit. Latest results on the morphology of the TeV gamma-ray and non-thermal X-ray emission will be presented and the implications on the origin of the signal will be discussed.

1 Introduction

SN 1006 (G327.6+14.6) is the remnant of a galactic type Ia supernova explosion which has been historically recorded by Chinese and Arab astronomers. Presumably, SN 1006 is already in the Sedov phase and expands into the ambient insterstellar medium. The gas density of the ISM is a key parameter for the hydrodynamic evolution of the remnant. Due to its origin as type Ia supernova and also its isolated position of about 500 pc above the galactic plane, the surrounding medium is expected to be unaltered by the progenitor. The most reliable estimate of its distance is 2.2 kpc [1].

Radio and X-ray observations of the remnant show a spherical symmetry with enhanced emission towards the NE and SW limbs. Thermal X-ray (line) emission was detected in the interior of the SNR [2], whereas synchrotron emission by accelerated electrons dominates in the two bright NE and SW limbs [3]. Moreover, arc-second resolution images by Chandra reveal the small-scale structure of nonthermal X-ray filaments in the NE shell of SN 1006 [4]. These bright X-ray arcs trace the presence of strong shock fronts, where particle acceleration is most likely to occur.

Gamma-ray observations of SN 1006 were carried out by ground-based gamma-ray telescopes. A TeV γ-signal at the level of the Crab flux was claimed by the CANGAROO-I [5] and CANGAROO-II [6] telescopes but subsequent stereoscopic observations of the source with the H.E.S.S telescopes in 2003 and 2004 found no evidence of TeV γ-ray emission, thus deriving an upper limit [7] of $\Phi(> 0.26~\mathrm{TeV}) < 2.39\times10^{-12}~\mathrm{ph~cm^{-2}~s^{-1}}$. Further observations resumed by the CANGAROO-III 4-telescope array could not confirm the previous signal, thereby establishing an upper limit [8] of $\Phi(> 0.5~\mathrm{TeV}) < 3 \times 10^{-12}~\mathrm{ph~cm^{-2}~s^{-1}}$, which is consistent with the limit given by H.E.S.S.

In the following, we present preliminary analysis results from deeper very high energy (VHE) γ-ray observations of SN 1006 by H.E.S.S.

2 H.E.S.S. observations and results

2.1 Data-set and analysis methods

H.E.S.S. is an array of imaging atmospheric Cherenkov telescopes situated in the Khomas Highland of Namibia at 1800 m a.s.l. [9]. First observations on SN 1006 started as early as 2003 with an array of two telescopes only and were continued in 2004 with the complete set of four telescopes. Deeper observations followed in the years 2006 – 2008. All observations have been performed in runs of 28 min duration in the moonless part of the nights in the so-called *wobble* mode. In this mode, the telescopes are pointed to an alternating offset position of $\pm 0.5°$ in right ascension or declination with respect to the nominal source position, thereby allowing for a simultaneous background monitoring.

The data-set, selected according to standard quality criteria, has a dead-time corrected exposure (live-time) of 130 h and a mean zenith angle of 20°. The data-set was analysed using two different reconstruction algorithms: the Model analysis [10] and the 3D Model analysis [11]. The first analysis method uses raw shower images which are adjusted to a precalculated model through a log-likelihood minimisation. Through a careful treatment of the night sky background pixel per pixel and image cleaning the Model Analysis achieves a better background suppression than more conventional techniques, thus leading to an improved sensitivity. Therefore, all the results presented in the following were obtained using the Model analysis. In order to avoid trials, the analysis was performed on two pre-defined regions selected from XMM-Newton observations[3] in the non-thermal energy band, yielding a detection significance of 9.3 sigma for the NE region and 8.7 sigma respectively for the SW region.

2.2 Morphology

Fig.1 shows the H.E.S.S. excess map with a charge threshold of 200 photoelectrons (pe) overlayed with the XMM-Newton flux map in the 2 – 4.5 keV energy band which has been smoothed according to the H.E.S.S. point spread function. The striking correlation between γ and X-ray emission regions is confirmed when looking at the radial and azimuthal profiles derived from uncorrelated excess maps. Fig. 2 left shows the radial profiles of H.E.S.S. and adapted XMM-Newton excess events featuring a shell radius of $0.24° \pm 0.014°$ and the width of the radial distribution is $0.076° \pm 0.014°$, which is consistent with the H.E.S.S. point spread function, thereby showing that the emission region is compatible with a thin rim.

2.3 Spectral analysis

The spectra for the N.E. and S.W. regions (see Fig.3), obtained with a charge threshold of 60 pe, are compatible with pure power laws yielding similar indices and fluxes (Tab.1). These fluxes correspond to less than 1% of that from the Crab Nebula, well below the previously published H.E.S.S. upper limits [7], thus making SN 1006 one of the faintest known TeV sources so far.

Region	Γ	$\Phi(> 1\text{TeV})$ $(10^{-12}\text{cm}^{-2}\text{s}^{-1})$
NE	$2.36 \pm 0.1_{stat} \pm 0.2_{syst}$	0.155 ± 0.017
SW	$2.43 \pm 0.17_{stat} \pm 0.2_{syst}$	0.133 ± 0.022

Table 1: *H.E.S.S. spectra for the two regions defined from X-ray observations.*

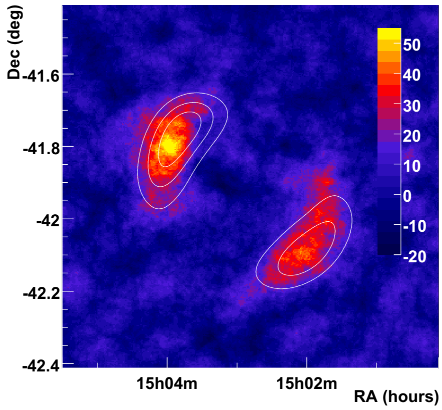

Figure 1: *H.E.S.S. gamma-ray image of SN 1006. The linear colour scale is in units of excess counts per* $\pi \times (0.1°)^2$. *The white contours correspond to the XMM-Newton flux map in the 2 – 4.5 keV energy range, which has been adapted to the H.E.S.S. point spread function.*

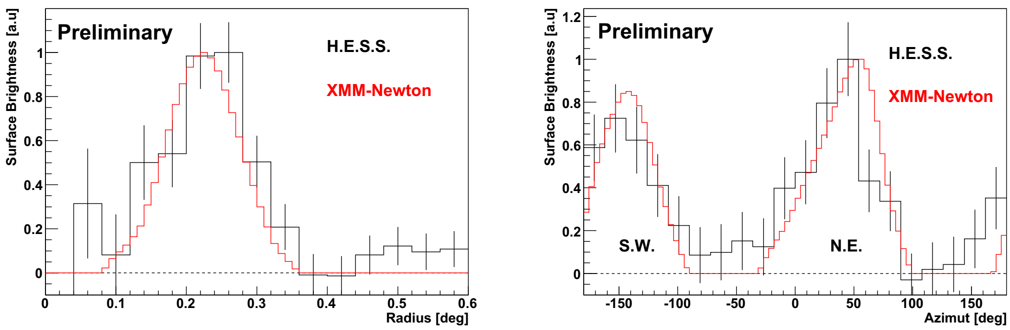

Figure 2: *Radial profile around the centre of the SNR (15h3m4.56s, -41d55'46.2") obtained from H.E.S.S. data and smoothed XMM-Newton data in the 2 - 4.5 keV energy band.*

3 Discussion

If the gamma-ray emission is solely due to inverse Compton scattering, constraints can be obtained on the magnetic field B in the acceleration region by comparing the X-ray and gamma-ray fluxes. In this case, the same population of electrons is the cause of both, the synchrotron emission of typical energy ϵ_{keV} in the X-ray band and the high-energy gamma-rays of typical energy E_{TeV}. The X-ray flux between 0.1 keV and 2 keV as measured by Allen et al. [12] is $\Phi_X([0.1 \text{ keV}, 2 \text{ keV}]) = 1.42 \times 10^{-10} \text{erg cm}^{-2}\text{s}^{-1}$. The preliminary gamma-ray energy flux as measured by H.E.S.S. between 0.4 TeV and 20 TeV is $\Phi_\gamma([0.4 \text{ TeV}, 20 \text{ TeV}]) = 2.3 \times 10^{-12} \text{erg cm}^{-2}\text{s}^{-1}$, which in the inverse Compton scenario leads to a magnetic field of B of about 30 μG.

In the case of the π^0 origin hypothesis, the gamma-ray flux is assumed to be the result of the total energy injected into cosmic rays, essentially protons. Assuming that the proton spectrum below 0.4 TeV can be described by a power law with a spectral index of 2.1, the amount of energy stored in protons can then be estimated on the basis of the total γ-ray luminosity, the characteristic cooling time due to pion production and the density of the ambient medium. Considering the recently measured gas density by Acero et al. [13] of 0.05 particles per cm^3, it is found that the energy injected into protons is approximately 2.2×10^{50} erg.

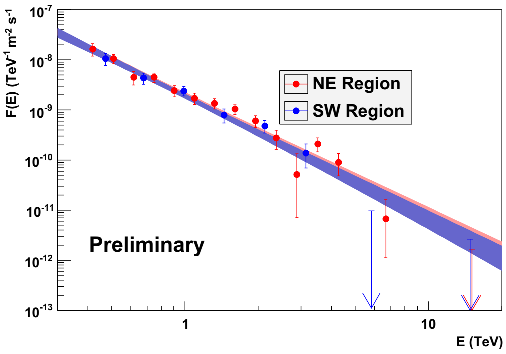

Figure 3: *Differential energy spectra of SN 1006 extracted from the two regions NE and SW.*

4 Conclusion

The detection of VHE gamma-rays from SN 1006 by H.E.S.S. has been confirmed by two independent analysis methods. The measured flux is of order 1% that detected from the Crab Nebula and therefore compatible with the previously published upper limit[7]. The bimodal morphology apparent in gamma-rays is compatible with the non-thermal emission regions visible also in X-rays. As the thickness of the TeV-shell is compatible with a thin rim emission, particle acceleration in the very narrow X-ray filaments, which have been identified as shock waves, is likely to be at the origin of the gamma-ray signal too. Given the measured flux level, the origin of the gamma-ray signal can be accommodated with both inverse Compton and π^0 production, as it leads to a reasonable magnetic field in the leptonic assumption and an acceptable energy budget for cosmic ray acceleration in the hadronic scenario.

Acknowledgments

The support of the Namibian authorities and of the University of Namibia in facilitating the construction and operation of H.E.S.S. is gratefully acknowledged, as is the support by the German Ministry for Education and Research (BMBF), the Max Planck Society, the French Ministry for Research, the CNRS-IN2P3 and the Astroparticle Interdisciplinary Programme of the CNRS, the U.K. Science and Technology Facilities Council (STFC), the IPNP of the Charles University, the Polish Ministry of Science and Higher Education, the South African Department of Science and Technology and National Research Foundation, and by the University of Namibia. We appreciate the excellent work of the technical support staff in Berlin, Durham, Hamburg, Heidelberg, Palaiseau, Paris, Saclay, and in Namibia in the construction and operation of the equipment.

References

1. P. F. Winkler, G. Gupta and K. S. Long, *ApJ* **585**, 324 (2003).
2. K. Koyama, R. Petre and E. V. Gotthelf, *Nature* **378**, 378 (1995).
3. R. Rothenflug et al., *A&A* **425**, 121 (2004).
4. A. Bamba et al., *ApJ* **589**, 827 (2003).
5. T. Tanimori et al., *ApJ* **L25**, 135 (1998).
6. T. Tanimori et al., *CRR Rep* **478**, 33 (2001).
7. F. Aharonian et al., *A&A* **437**, 135 (2005).
8. T. Tanimori et al., *29th International Cosmic Ray Conference*, ICRC 2005 Conference Proceedings, Pune, 2005, pp. 101.
9. W. Hofmann, "H.E.S.S. Status" *Towards a Network of Atmospheric Cherenkov Detectors VII*, edited by B. Degrange and G. Fontaine, Cherenkov 2005 Conference Proceedings, Ecole Polytechnique, Palaiseau, 2005, pp. 43.
10. M. de Naurois and L. Rolland, *in prep.* (2009).
11. M. Lemoine-Goumard, B. Degrange and M. Tluczykont, *Astropart. Phys.* **25**, 195 (2006).
12. G. E. Allen, R. Petre and E. V. Gotthelf, *ApJ* **558**, 739 (2001).
13. F. Acero, J. Ballet and A. Decourchelle, *A&A* **475**, 883 (2007).

INTEGRAL OBSERVATION OF GAMMA-RAY QUASAR PKS B1510-089

Anna Barnacka and Rafał Moderski
Nicolaus Copernicus Astronomical Center,
Bartycka 18, 00-716 Warsaw, POLAND

Abstract

The question of the relativistic jets composition in active galactic nuclei remains one of the unsolved mysteries of the modern astrophysics. Past multi-wavelength observations of the quasar PKS B1510-089 suggested the presence of features produced by the, so called, bulk Compton mechanism. Such features strongly support the pair plasma presence in the jet, and allow to calculate the pair to proton ratio. Here we present the results of the recent, long *INTEGRAL* observation of PKS B1510-089 in the low state.

1 Introduction

PKS B1510-089 ($\alpha_{\rm J2000} = 15^{\rm h}12^{\rm m}50.5^{\rm s}$, $\delta_{\rm J2000} = -09^{\rm d}06^{\rm m}00^{\rm s}$) at redshift $z = 0.361$ is a γ-ray blazar, first detected in MeV-GeV band by EGRET[1]. It is characterised by a highly relativistic jet that make a 3^o angle to the line of sight[2].

Last multi-wavelength campaign of the PKS B1510-089 took place in August 2006[3]. The campaign resulted in a broadband spectrum ranging from 10^9 to 10^{19} Hz and consisted of observations from *Suzaku*[4] with an approximate exposure time 3 days and energy range $0.3 - 12$ keV, *Swift*[5] XRT and UVOT monitoring over 120 ks, optical and IR observations with *REM*[6], *AIT*[7], and observations with radio telescopes *RATAN-600*[8] and *ATCA*[9].

Suzaku observations indicated that spectrum between 0.3 and 50 keV is very well represented by a very hard power law (with a photon index of $\Gamma \simeq 1.2$) augmented by a blackbody-type component (with a temperature of $kT \simeq 0.2$ keV) that accounts for the excess emission below 1 keV. Such an excess can be produced by a bulk Comptonization of external diffuse radiation by cold inhomogeneities or density enhancements within the jet.

To reproduce the overall SED of PKS B1510-089, Katoka at al.[3] adopted an internal shock scenario and assumed that shells with relativistic plasma represent regions enclosed between the reverse and forward shock fronts. Such a structure is formed by colliding inhomogeneities propagating down the jet with different Lorentz factors. In such a model, if the excess emission below 1 keV is interpreted as bulk-Compton radiation, it was possible to obtain the electron+positron to proton ratio, which in the case of PKS B1510-089 was estimated to be of the order of 10. This implies that although the number of e^+e^- pairs is larger then the number of protons, the power of the jet is dominated by the latter.

Alternatively, the observed soft X-ray excess can also be explained with the synchrotron self-Compton (SSC) model. Collected data for PKS B1510-089 are consistent with another set of model parameters for which the soft X-ray excess is due to a combination of: the tail of the synchrotron component, external Compton process and the SSC components.

Yet another alternative involves contribution from the the soft X-ray excess often observed in the non-blazar active galactic nuclei.

Suzaku observations also revealed possibility of a spectral break above 30 keV, which may indicate the peak of the external-Compton component.

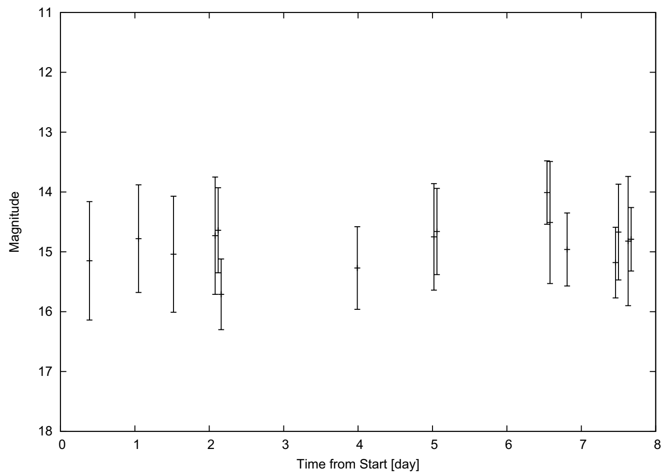

Figure 1: Optical, V band light curve of PKS B1510-089 from Optical Monitoring Camera. The "zero" point on the x-axis is Jan 18, 2008 16:08 UT.

2 INTEGRAL observation

INTEGRAL observations were performed in order to distinguish between above possibilities and to answer the questions about soft excess below 1 keV and break at high energies. These observations were carried out in January 2008 with the 600 ks exposure time. Data from all instrument were analysed using INTEGRAL Data Software package OSA 7.0. During the observation SPI spectrometer was in a service mode and thus data were not taken with this instrument.

2.1 Optical Monitoring Camera

Optical Monitoring Camera (OMC) is a CCD detector of 1024×1024 pixels located in the focal plane of a 50 mm lens with a V filter. Data from OMC were corrected for Galactic extinction using correction factor 1.32[3] and the resulting light curve is presented in Figure 1. The average luminosity of the object during the observation was 14.85 mag, which seems a little bit higher then in Aug 2006, but large uncertainties prevent us from drawing any strong conclusions. There is also no signature of large optical variability.

2.2 The Joint European X-Ray Monitor

The Joint European X-Ray Monitor (JEM-X) is a coded aperture X-ray detector which provides images with arcminute angular resolution in the $3 - 60$ keV energy range. Unfortunately the flux from PKS B1510-089 during Jan 2008 observation was not high enough to be detected by JEM-X. Consequently only the upper limits could be estimated using detector sensitivity curves. These upper limits are:

$$F_{3-10\mathrm{keV}} < 10^{-11}\mathrm{erg\,s^{-1}\,cm^{-2}}\,, \quad \text{and} \quad F_{10-25\mathrm{keV}} < 10^{-11}\mathrm{erg\,s^{-1}\,cm^{-2}}.$$

2.3 Imager on Board INTEGRAL Satellite

The imager IBIS is the main gamma-ray instrument of the *INTEGRAL* satellite. It consists of two detectors: ISGRI[10] - sensitive in the energy range 15 keV - 1 MeV, and PICsIT[11] - sensitive in the energy range 200 keV - 8 MeV. IBIS ISGRI was the only instrument which clearly detected PKS B1510-089. The significance of detection was $\sigma = 24$. The overall high energy light curve of the object is presented in Figure 2. Within observational errors the object shows no significant variability during the observation.

We fit the ISGRI data with a simple power-law model with fixed absorbing column density $N_H = 7.88 \times 10^{20}\,\mathrm{cm^{-2}}$ taken from Lockman and Savage[12]. The result of the fit is a photon

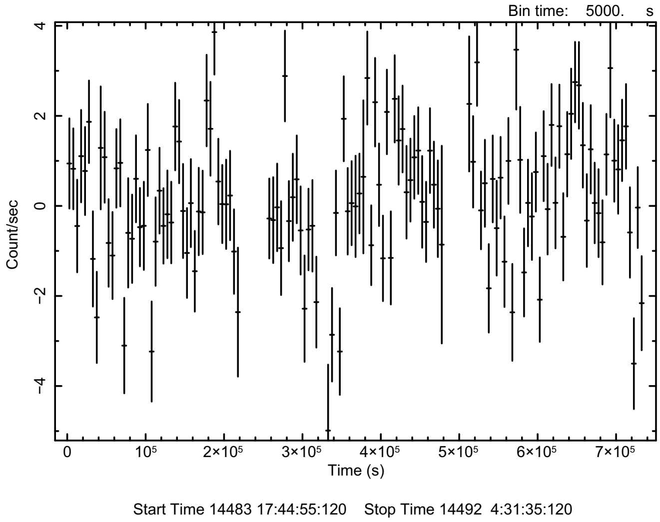

Figure 2: Light curve of PKS B1510-089 in the $20-600\,\mathrm{keV}$ energy range from Imager on Board the INTEGRAL Satellite (IBIS) ISGRI detector.

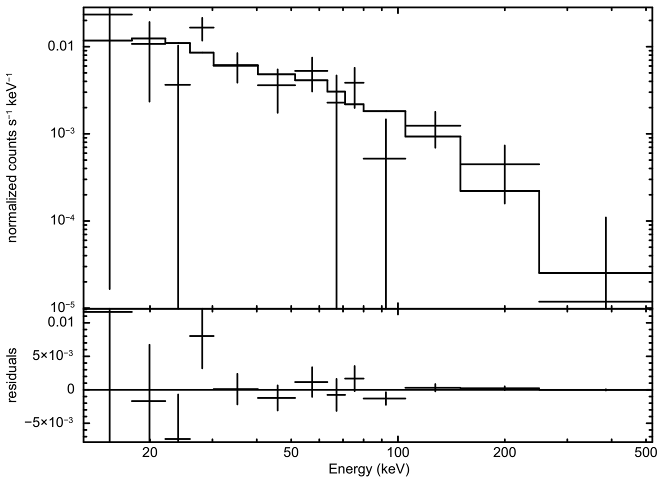

Figure 3: Result of the spectral fit to the $20-500\,\mathrm{keV}$ ISGRI spectrum with a simple power law model.

index $\Gamma = 1.2 \pm 0.3$ with $\chi^2/\mathrm{d.o.f} = 8.69/11$. The fit is presented in Figure 3. Based on the model the estimated high energy flux from PKS B1510-089 is

$$F_{13\,\mathrm{keV}-1.2\,\mathrm{MeV}} = (2.4 \pm 2.2) \times 10^{-10}\,\mathrm{ergs^{-1}cm^{-2}}\,.$$

IBIS PICsIT did not detect the object during the observation.

3 Conclusions

To compare our results with the previous *Suzaku* observation we plot both sets of data in Figure 4. *INTEGRAL* observations are consistent with the previous data from *SUZAKU* - observed spectral indexes are almost identical, 1.24 ± 0.01 for the best fit model for *Suzaku* data[3] vs. 1.2 ± 0.3 for our data. To compare fluxes we extrapolate ISGRI results to lower energies and obtain $F_{10-50\,\mathrm{keV}} = 15.5 \times 10^{-12}\,\mathrm{erg\,s^{-1}\,cm^{-2}}$. This compares to *Suzaku* flux of $F_{10-50\,\mathrm{keV}} = 38.3 \times 10^{-12}\,\mathrm{erg\,s^{-1}\,cm^{-2}}$, so the source was almost three times dimmer during Jan 2008 observation then in Aug 2006. Unfortunately the quality of *INTEGRAL* data cannot help to resolve the question of soft X-ray excess nor spectral break beyond $30\,\mathrm{keV}$.

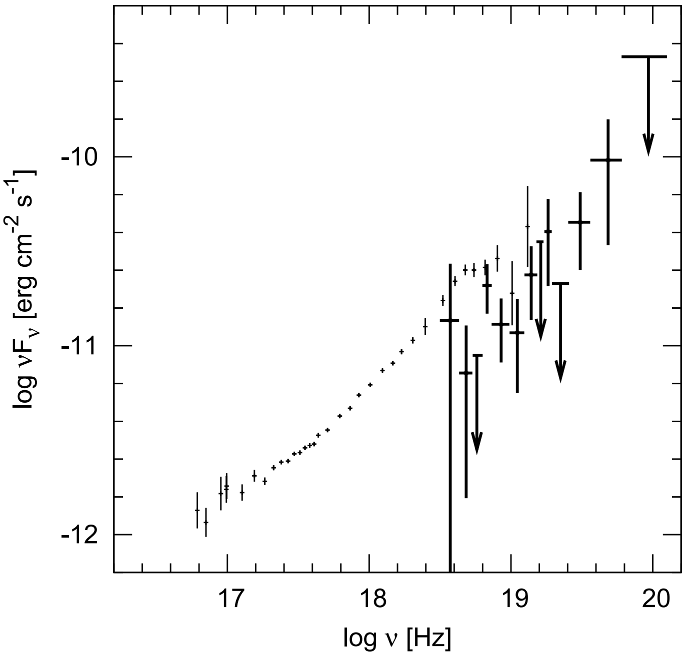

Figure 4: Comparison of the hard X-ray spectra of PKS B1510-089 from *Suzaku* (thin symbols) and *INTEGRAL* (thick symbols) observations.

Acknowledgements

The present work was partially supported by the Polish Astroparticle Network 621/E-78/BWSN-0068/2008. R.M. acknowledges support from the Polish MNiSW grant no. N N203 301635.

References

1. Hartman R.C. *et al*, ApJS **123**, 79-202 (1999).
2. Wardle J.F.C. *et al*, in *Future Directions in High Resolution Astronomy*, eds J. Romney and M. Reid, vol. 340 of *Astronomical Society of the Pacyfic Conference Series*, 67 (2005).
3. Kataoka J. *et al*, ApJ **672**, 787-799 (2008).
4. Mitsuda K. *et al*, PASJ **59**, 1-7 (2007).
5. Gehrels N. *et al*, ApJ **611**, 1005-1020 (2004)
6. Zerbi F.M. *et al*, in *SPIE Conference Series*, vol. 5492, 1590 (2004).
7. Tosti G. *et al*, in *SPIE Conference Series*, vol. 5489, 742 (2004).
8. Korolkov D.V. and Pariiskii I.N., S&T **57**, 324-329 (1979).
9. Frater R.H., Brooks J.W., and Whiteoak J.B., J. of Electronical Electron. Eng. Australia **12**, 103-112 (1992).
10. Lebrun F. *et al*, A&A **411**, L141-L148 (2003).
11. Di Cocco G. *et al*, A&A **411**, L189-L195 (2003).
12. Lockman F.J. and Savage B.D. ApJS **97**, 1-47 (1995).

SOLAR SYSTEM GAMMA-RAY ASTRONOMY WITH FERMI OBSERVATORY

M. BRIGIDA [a]
on behalf of the Fermi LAT Collaboration
Dipartimento Interateneo di Fisica "M. Merlin" dell'Univrsità degli Studi di Bari, Via Amendola 167, 70126 BARI, Italy

The Large Area Telescope (LAT), one of two instruments on the Fermi Gamma-ray Space Telescope (formerly GLAST, launched on June 11, 2008) is a pair conversion detector designed to study the gamma-ray sky in the energy range from 20 MeV to 300 GeV. Fermi has detected high-energy gamma rays from the quiet Sun and the Moon, during the first few months of the mission, thus opening a new window for detailed gamma-ray science in the Solar System. This emission is produced by interactions of cosmic rays; by nucleons with the solar and lunar surface, and electrons with solar photons in the heliosphere. The heliospheric emission is produced by inverse-Compton scattering and is predicted to be very extended. While both Sun and Moon were detected by EGRET on CGRO with low statistics, Fermi provides high-quality detections on a daily basis allow variability to be addressed. Such observations will provide a probe of the extreme conditions near the solar surface, and monitor the modulation of cosmic-rays over the inner heliosphere, impossible by any other means. Since at minimum of of the solar activty Galactic cosmic rays have their maximum flux, we expect the gamma-ray emission to be brightest at this time. Fermi is the only gamma-ray mission capable of detecting the quiet Sun and monitoring it over the full 24^{th} solar cycle. We present preliminary analyses and flux estimation for the Moon and the Sun quiet emission.

1 Introduction

The possibility of a solar quiet gamma-ray emission has been first proposed by Hudson et al., pointing out the detection capabilities of the EGRET mission [1]. The gamma emission is produced by interactions of high-energy cosmic rays (CR) with the Sun. The quiet Sun emission is expected to have two different components: the first one is the γ-ray albedo generated by the CR nuclei interactions on the solar surface. The second one is due to the Inverse-Compton (IC) scattering of CR electrons with solar photons in the heliosphere. This last component is predicted to be extended in a large region around the Sun [2 3]. The Moon emission is expected by the interaction of CR nucleons with the lunar surface (albedo).

EGRET observed high-energy gamma radiation from the Moon with an energy spectrum consistent with an albedo model [4]. Althought a similar interaction of CR occurs on the Sun, EGRET has not observed the quiet solar emission and reported a 95% confidence upper limit on the Sun gamma flux of about 2.0×10^{-7} photons $cm^{-2}\ s^{-1}$ at $E > 100\ MeV$ [5]. More recent studies [6] of EGRET solar data using both disk and halo contributions yielded a total flux of $(4.44 \pm 2.03) \times 10^{-7}$ photons $cm^{-2}\ s^{-1}$ for $E > 100\ MeV$ from the Sun, with the disk component exstimated about 1/4 of the total flux.

[a] e-mail: monica.brigida@ba.infn.it

	Sun	Moon
Expected Flux ($\times\ 10^{-7}\ ph\ cm^{-2} sec^{-1}$)	4.3 [2 3]	5.0 [4]
Egret Flux ($\times\ 10^{-7}\ ph\ cm^{-2} sec^{-1}$)	4.44±2.03 [6]	5.55±0.65 [6]
	not observed by Egret [5]	4.7±0.7 [5]

Table 1: The expected and computed EGRET fluxes ($E > 100 MeV$) for the Sun and the Moon.

2 Data selection and reduction

In this paper we analyze Fermi data collected during the first 6-month of the mission, from August 2008 to January 2009, selecting photon energies above 100 MeV. During the months covered by this analysis, the Sun is at the beginning of the 24^{th} solar cycle and hence in a period of minimum activity. As the Sun and the Moon are moving sources, we developed a code in order to perform the analysis of the data in a source-centred system: the events were mapped onto a celestial coordinate system centred on Sun and Moon instantaneous position. Coordinates were computed using JPL libraries [7] taking into account parallax corrections. In our analysis, the main sources of background are the galactic and extragalactic emission in the source centered frame. In order to have a better sensitivity to the Sun and Moon emission, other sources of background has been reduced with the following selections:

- Zenith angle $< 105°$ in order to exclude the Earth albedo;
- the Sun or the Moon should be at least 30 under or above the galactic plane in order to reduce the diffuse components and avoid the brightest sources on the galactic plane;
- the angular separation between Moon and Sun should be more than 10°, in order to remove the Moon emission component from the Sun and viceversa;

3 Sun and Moon detection

Figures 1 show the gamma-ray emission from the Sun and the Moon obtained in a 6-month accumulation of photons from August 2008 to January 2009 at energies above 100 MeV.

In order to evaluate the background, we use the "fake" source method, consisting in a "fake" source moving along the same path of the real source, but 30° displaced. In this way, the source net flux results as the difference between the total flux from the source and the flux from the "fake" source, using the same angular selection. Other methods can be used to compute the flux from a source, mainly based on a the maximum likelihood analysis [8 9]. Their application to our studies will be discussed in more detailed analysis.

Following this simple method, we have obtained a flux of (6.0±1.0) $\times\ 10^{-7}$ photons $cm^{-2}\ s^{-1}$ for $E > 100\ MeV$ from the Moon; a preliminary value of the total flux for the Sun (albedo and IC component) gives (4.0±1.0) $\times\ 10^{-7}$ photons $cm^{-2}\ s^{-1}$ for $E > 100\ MeV$.

In the table 1 the expected and the EGRET fluxes above 100 MeV are reported for the Sun and the Moon. The results obtained show a good agreement with the theoretical expectations and prevoius results reported by EGRET.

4 Conclusions

In this paper we demonstrate the observing capabilities of Fermi-LAT by presenting images of the Moon and quiet Sun accumulated over the first six months of the Mission. We also report the first exstimation of flux from the Sun and the Moon, showing the good agreement with

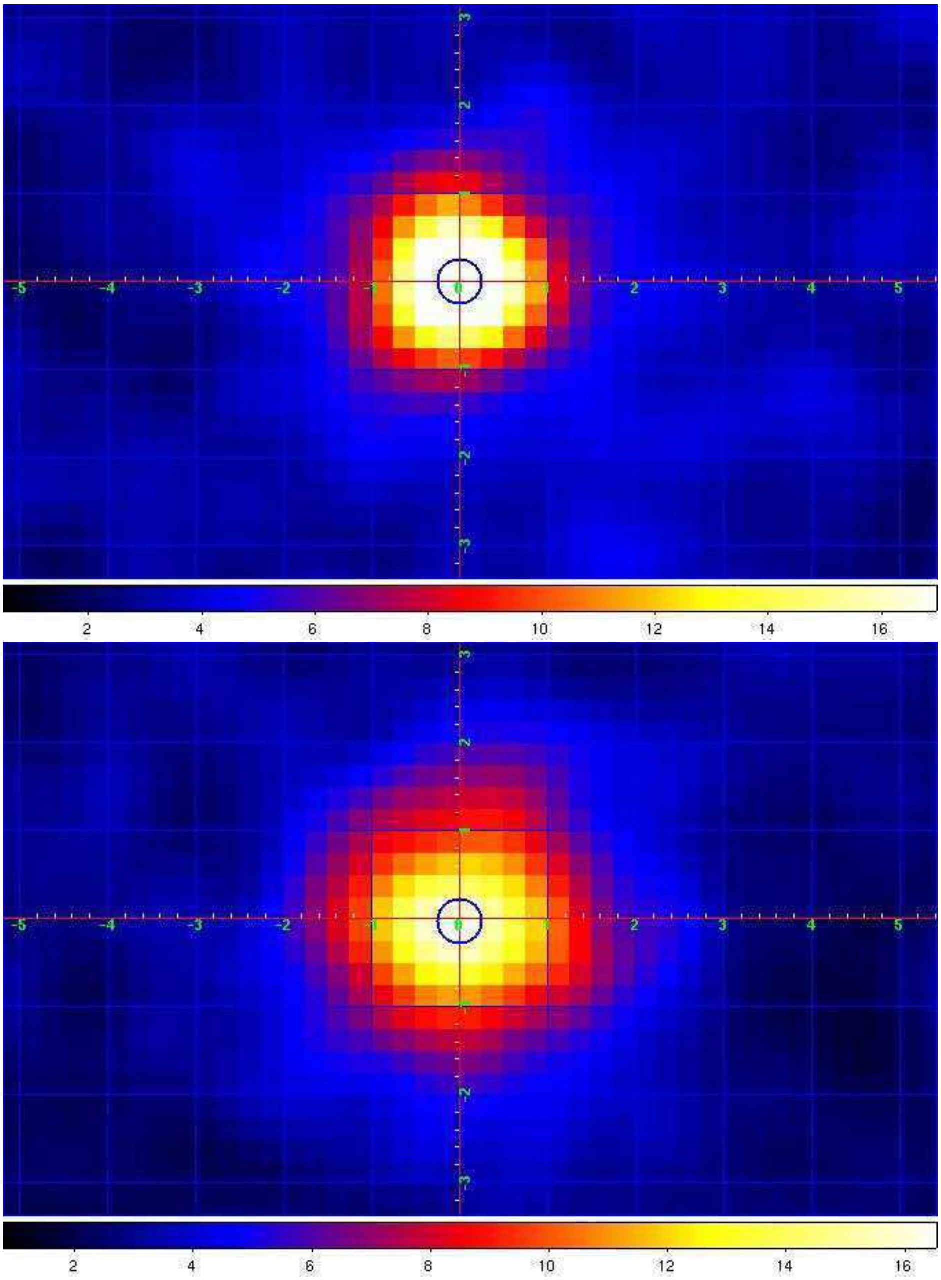

Figure 1: Sun (upper plot) and Moon (lower plot) gamma ray emission observed between August 2008 and end of January 2009. The images show the count map for $E > 100 MeV$ photons in a coordinate frame centred on the source position, the bin width used is $0.25°$. The image is then slightly smoothed; the colour bar scale used is proportional to the counts. A circle corresponding with the average Sun and Moon radius has been superimposed.

the previous observations and the theoretical evaluation. Dedicated methods will be used to compute fluxes from our Solar System sources in more detailed analysis. These results indicate that Fermi data analysis will provide fundamental information about the Sun and Moon emission and the modulation of cosmic ray fluxes during the solar cycle.

Acknowledgments

The Fermi LAT Collaboration acknowledges generous ongoing support from a number of agencies and institutes that have supported both the development and the operation of the LAT as well as scientific data analysis. These include the National Aeronautics and Space Administration and the Department of Energy in the United States, the Commissariat l'Energie Atomique and the Centre National de la Recherche Scientifique / Institut National de Physique Nuclaire et de Physique des Particules in France, the Agenzia Spaziale Italiana and the Istituto Nazionale di Fisica Nucleare in Italy, the Ministry of Education, Culture, Sports, Science and Technology (MEXT), High Energy Accelerator Research Organization (KEK) and Japan Aerospace Exploration Agency (JAXA) in Japan, and the K. A. Wallenberg Foundation, the Swedish Research Council and the Swedish National Space Board in Sweden.

Additional support for science analysis during the operations phase from the following agencies is also gratefully acknowledged:the Istituto Nazionale di Astrofisica in Italy and the K. A. Wallenberg Foundation in Sweden for providing a grant in support of a Royal Swedish Academy of Sciences Research fellowship for JC.

References

1. H. S. Hudson, Proc. Gamma-Ray Obs. Workshop (1989)
2. I. V. Moskalenko et al, ApJ 652: L65-L68 (2006)
3. E. Orlando and A. W. Strong Ap&SS, 309-359 (2007)
4. I. V. Moskalenko et al, ApJ 664: L143 (2007)
5. D. J. Thompson at al. Journal of Geoph. Res., Vol. 102, No. A7, 14,735-14,740 (1997)
6. E. Orlando and A. W. Strong, A&A 480, 847-857 (2008)
7. see http://iau-comm4.jpl.nasa.gov/access2ephs.html
8. Mattox J. R. et al. , ApJ 461:396 (1996)
9. se http://heasarc.gsfc.nasa.gov/docs/xanadu/xspec/
10. D. Seackel et al., ApJ 382:652-666 (1991)

VERY HIGH ENERGY γ-RAY OBSERVATIONS OF THE GALACTIC CENTER WITH H.E.S.S.

M. VIVIER for the H.E.S.S. collaboration
IRFU/DSM CE Saclay F-91191 Gif-sur-Yvette, cedex, France
http://www.mpi-hd.mpg.de/hfm/HESS

The inner few central parsecs of our galaxy harbour various astrophysical objects. Among these resides a supermassive black hole (SMBH) Sgr A* of mass 3×10^6 $M_\odot$ which is located at the dynamical center of our galaxy. The multi-wavelength emission of Sgr A* has been firmly established for many years with a highly variable emission in radio, infrared (IR) and X-rays. In 2004, the H.E.S.S. Imaging Atmospheric Cherenkov Telescopes (IACTs) have detected a TeV γ-ray source, HESS J1745-290, spatially coincident with the position of Sgr A*. Further data have then been taken in 2005 and 2006 to monitor the source activity and to extend the TeV spectrum at higher energies. In this paper are presented the lastest results on the HESS J1745-290 very high energy (VHE) γ-ray source position, energy spectrum and time variability.

1 Introduction

H.E.S.S. [1] is an array of four Imaging Atmospheric Cherenkov Telescopes located in Namibia. The instrument images particle showers induced by VHE γ-rays. Each telescope collects the Cherenkov light radiated by particle cascades in the air showers using a large mirror area of 107 m^2 and a camera of 960 photomultiplier tubes [2]. Each camera covers a total field of view of 5° in diameter. The four telescopes are placed in a square formation with a side length of 120 m. This configuration allows for a more precise reconstruction of the arrival direction and energy of the γ-rays using the stereoscopic technique. The energy threshold of the H.E.S.S. instrument is approximately 100 GeV when pointing to the zenith and the angular resolution is better than 0.1° per γ-rays. The point source sensitivity is $2{\times}10^{-13}\mathrm{cm}^{-2}\mathrm{s}^{-1}$ above 1 TeV for a detection at the 5σ level in a 25 hours observation time [3].
H.E.S.S. observations toward the Galactic Center (GC) region revealed in 2004 a bright TeV emission, HESS J1745-290, compatible with a point-like source and in coincidence with the supermassive black hole Sgr A*, the supernovae remnant (SNR) Sgr A East and the recently discovered pulsar wind nebulae (PWN) G359.95-0.04 [4]. A diffuse emission along the Galactic plane was also detected [5]. This diffuse emission is spatially correlated with the mass density distribution of giant molecular clouds in the central 200 pc of our Galaxy and is likely to be produced by the collisions of cosmic ray protons or nuclei with the molecular clouds [5]. The HESS J1745-290 measured energy spectrum was well-described in the energy range $160\mathrm{GeV} - 30\mathrm{TeV}$ by a power-law spectrum $dN/dE_\gamma \propto E_\gamma^{-\Gamma}$ with a spectral index $\Gamma = 2.25 \pm 0.04(\mathrm{stat.}) \pm 0.1(\mathrm{syst.})$ [6]. No deviation from a pure power-law was observed and the source was found to be stable on timescales ranging from a few minutes to a year. In 2005 and 2006, further data were collected to monitor the source activity and to extend the energy spectrum to higher energies. This paper

reports on new results concerning the source position, the source energy spectrum and the source time variability.

2 HESS J1745-290 position

The new data taken with H.E.S.S. in 2005 and 2006 have allowed a signififcant improvement in the reconstruction of the HESS J1745-290 source position [7]. A model of the telescope structure deformation has been used to compensate for systematic errors on the telescope orientation. The systematic pointing errors have then been reduced to 6" per axis, allowing for a more precise determination of the source position, compared to the one derived with the 2004 dataset [6]. Fig.1 shows the new H.E.S.S. position measurement on top of a 90 cm VLA radio image of the inner 10 pc region of the GC. The shell-like structure of the SNR Sgr A East is clearly visible. The position of HESS J1745-290 is coincident within 7.3" $\pm$ 8.7"(stat.) $\pm$ 8.5"(syst.) with the radio position of Sgr A* [8], and is also consistent with the reported position from the 2004 dataset [6]. While the latter was marginally consistent with the radio emission from Sgr A East, the new result obtained with the 2005/2006 dataset does rule out the radio emission of Sgr A East as the counterpart of HESS J1745-290 with a 7σ confidence level. The position of HESS J1745-290 agrees well with the location of the two other counterparts candidates, Sgr A* and G359.95-0.04 which are separated by only 8.7".

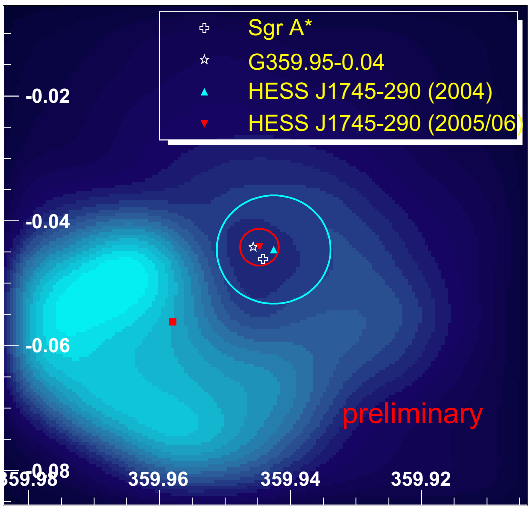

Figure 1: 90 cm VLA radio image of the SNR Sgr A East in Galactic coordinates. The position of Sgr A* and G359.95-0.04 are marked with a cross and a star, respectively. The blue triangle and circle shows the best fit position and total error (68 % C.L.) from the 2004 dataset. The best fit position and associated errors obtained with the 2005/2006 dataset is shown by the red triangle and red circle, respectively. The red square is the expected position of the centroid of the VHE γ-ray emission if it followed the observed radio flux of Sgr A East.

3 HESS J1745-290 spectrum and variability

The further data taking in 2005 and 2006 have been strongly motivated by the possibility of extending the TeV spectrum to higher energies ($\geq$ 10 TeV) and by the observed variable emission of the SMBH Sgr A*. Indeed, daily flares in the IR and X-rays domains with periodic modulations have been detected in the VLT data [9] and in the Chandra [10] and XMM-Newton [11] data, respectively. These Quasi Periodic Oscillations (QPOs) suggest that the radio to X-rays emission would be caused by the oscillation modes of an accretion disk around the SMBH [12]. Recently however, the validity of the detection of these periodic modulations has been disputed by IR observations reported by the Keck-II telescopes [13].

The new measured spectrum for the whole three-year dataset ranges from 160 GeV to 70 TeV (Fig.2). For the first time, with additional statistics, a deviation from a pure power-law starts to be visible [14]. The spectrum is well described by either a power-law of spectral index $\Gamma = 2.1 \pm 0.04(\text{stat.}) \pm 0.1(\text{syst.})$ with a high energy exponential cut-off $E_{\text{cut}} = (15.7 \pm 3.4(\text{stat.}) \pm 2.5(\text{syst.}))$ TeV (equivalent χ^2 of 23/26 d.o.f.) or by a broken power-law with spectral indices $\Gamma_1 = 2.02 \pm 0.08(\text{stat.}) \pm 0.1(\text{syst.})$, $\Gamma_2 = 2.63 \pm 0.14(\text{stat.}) \pm 0.1(\text{syst.})$ with a break energy of $E_{\text{break}} = (2.57 \pm 0.19(\text{stat.}) \pm 0.44(\text{syst.}))$ TeV (equivalent χ^2 of 20/19 d.o.f.).

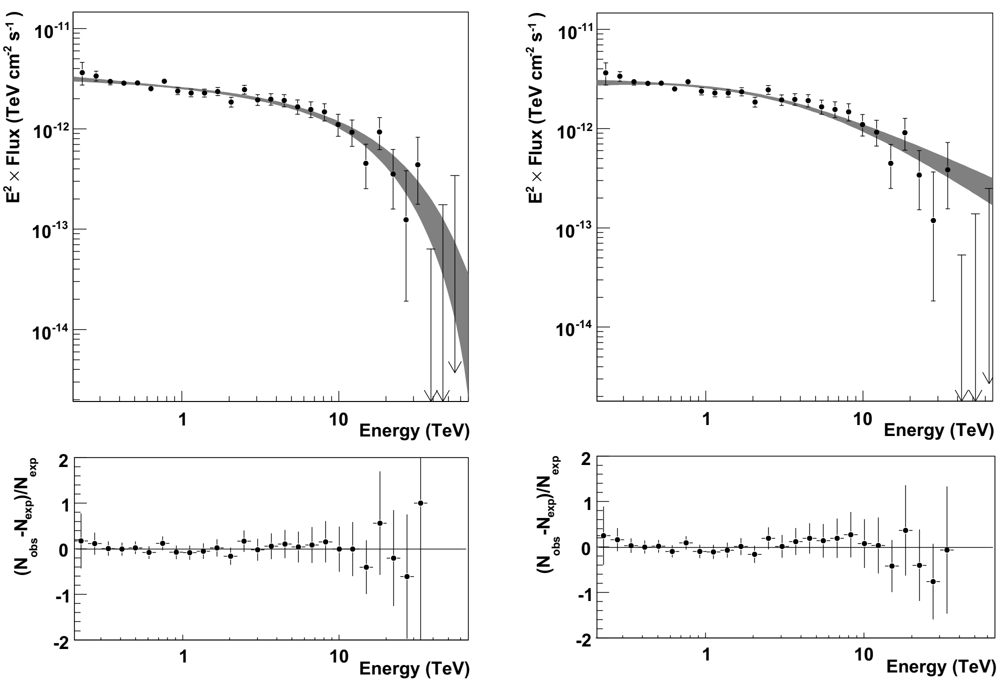

Figure 2: HESS J1745−290 spectra derived for the whole HESS GC dataset covering the three years 2004, 2005 and 2006. The shaded areas are the 1σ confidence intervals for the power law with an exponential cut-off fit (left) and the broken power law fit (right). The last points represent 95% C.L upper limits on the flux. The fit residuals corresponding to the respective fits are shown on the lower panels.

Fig. 3 shows the 2004 to 2006 light curve of the GC TeV source HESS J1745-290. The light curve points are integrated fluxes above 1 TeV calculated for 28 min time intervals. The integrated flux above 1 TeV is consistent with a flat behavior (χ^2 of 233/216 d.o.f.), leading to the non detection of any significant flaring activity of the HESS J1745-290 TeV source. Periodic modulations in the TeV flux, like those found in IR and X-rays, have also been searched for. No significant peak at the detected IR and X-rays frequencies have been observed in the Fourier power spectrum of the HESS J1745-290 signal [14].

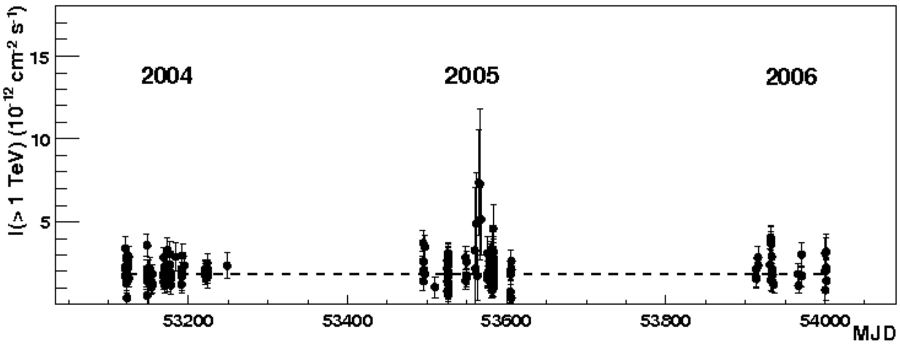

Figure 3: Run by run light curve of HESS J1745−290. The 28 min interval integrated fluxes of HESS J1745-290 are plotted for the 2004, 2005 and 2006 datasets. The dashed line shows the best fit to a constant.

4 Conclusions

The new data taken in 2005 and 2006 toward the GG region with H.E.S.S. have allowed significant improvements in characterizing the HESS J1745-290 TeV source emission. The reduction of the telescope pointing errors made possible to exclude with high significance the shell of the SNR Sgr A East as the source of the VHE γ-rays. The measured spectrum with the 2004, 2005 and 2006 data exhibits a deviation from a pure power-law at high energies ($\geq$ 10 TeV), and no significant time variability was found in the TeV emission, in contrast to the observed variable emission of Sgr A* from radio to X-rays. The point-like TeV source detected by H.E.S.S. in the GC region is not correlated with the SMBH Sgr A* activity. Thus, the emission mechanisms responsible for the TeV emission seems not to be the same as those accounting for the radio to X-rays emission.

References

1. Hofmann W., et al. (2003), Proc. of the 28th ICRC (Tsubuka), Vol.1, p.2811
2. Vincent P., et al. (2003), Proc. of the 28th ICRC (Tsubuka), Vol.5, p.2907
3. Aharonian F., et al. (2006), A&A, 457, 899
4. Aharonian F., et al. (2004), A&A, 425, 13
5. Aharonian F., et al. (2006), Nature, 439, 675
6. Aharonian F., et al. (2006), Phys. Rev. Lett., 97, 221102
7. van Eldik C., et al. (2007), Proc. of the 30th ICRC (Merida)
8. Reid M.J., et al. (1999), ApJ, 524, 816
9. Genzel, R., Schödel, R., Ott, T., et al. 2003, Nature, 425, 934
10. Baganoff, F., Bautz, M., Brandt, W., et al. 2002, Nature, 413, 45
11. Porquet, D., Predehl, P., Aschenbach, B., et al. 2003, A&A, 407, L17
12. Aschenbach, B., et al. 2004, A&A, 417, 71
13. Meyer, L., Do, T., Ghez, A., et al. 2008, ApJ, 688, L17
14. Aharonian, F., et al. 2009, accepted in A&A

Observations of the TeV γ-Ray Binaries PSR B1259−63/SS2883 and LS 5039 with H.E.S.S.[a]

M. KERSCHHAGGL
Institut für Physik, Humboldt-Universität zu Berlin

M. DE NAUROIS
LPNHE, Paris

for the H.E.S.S. Collaboration

PSR B1259−63 / SS 2883, which became known as the first galactic variable TeV γ-ray emitter since its discovery in the very high energy (VHE) regime by H.E.S.S. in 2004, as well as LS 5039 are two out of four up to now known TeV γ-ray binaries. While PSR B1259−63 is the only known binary plerion seen in this energy band, where the generation of TeV photons can be unambiguously traced back to pulsar wind (PW) interactions, LS 5039 is likely to be a microquasar and therefore accretion driven. However, the exact origins for VHE radiation in LS 5039 are still under debate. As binary plerion PSR B1259−63 is a unique laboratory for the study of PW shock dynamics with respect to interactions with ambient radiation and matter fields around a companion star. The PW interactions in PSR B1259−63 are thought to become most efficient around the system's periastron passage, occurring only every ∼3.4 years on the eccentric pulsar orbit around SS2883. A 60h H.E.S.S. observation campaign on PSR B1259−63 from April to August 2007 also covered orbital phases prior to periastron (July 27th) which were up to now unexplored in VHE γ-rays. The outline and motivation of this campaign will be discussed. Moreover, LS 5039 data will be reviewed. The flux modulation found in this VHE source provides the first indications for attenuation effects of γ-rays in the intense stellar photon field in this system. The observed spectral features, however, contradict a pure absorption by pair production scenario for LS 5039.

1 Introduction

PSR B1259−63 and LS 5039 are two TeV γ-ray binaries that have been observed by the H.E.S.S. experiment. Both systems are similar in the sense that they consist of a compact object that orbits a massive companion star, but yet very much different, especially when focusing on the nature of the compact object and related mechanisms for the genesis of VHE radiation. While the compact object in PSR B1259−63 unambiguously could be identified as a rotating neutron star, and therefore can be classified as "binary plerion" [1], the exact nature of the compact object in LS 5039 is still under debate, allowing for both, a pulsar wind interaction scenario as postulated for PSR B1259−63 as well as for an accretion driven TeV source as generally suggested for microquasars [2].

---

[a]This article has already been published in the Proceedings of the "4$^{\rm th}$ International Meeting on High Energy Gamma-Ray Astronomy" (AIP Conference Proceedings 1085)

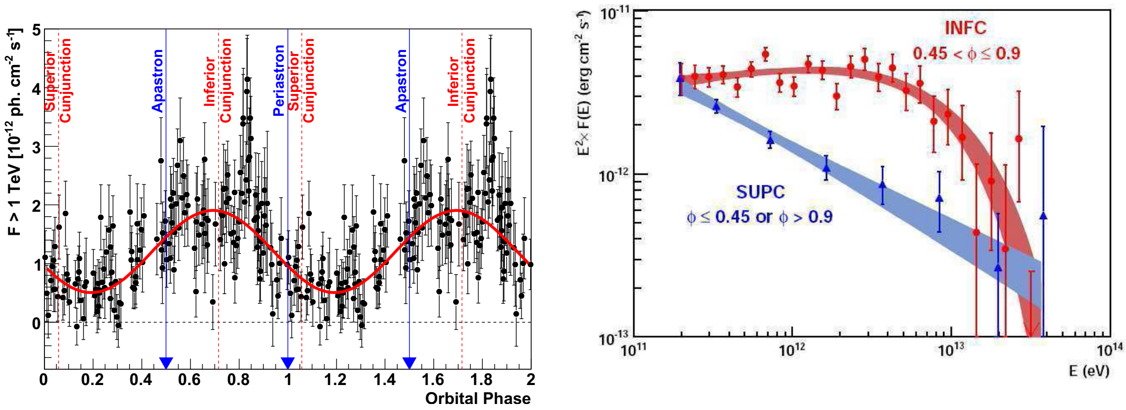

Figure 1: (left) Run-wise integrated photon flux above 1 TeV from LS 5039 as a function of orbital phase, measured by H.E.S.S. between 2004 and 2005. Each run has a duration of $\sim$ 28 min. The vertical blue lines denote the maximum and minimum in the binary separation distance at periastron and apastron respectively. (right) Differential energy spectrum of VHE photons stemming from LS 5039. The dataset has been divided into two phase bands corresponding to the high flux state around inferior conjunction (INFC) as well as low flux state centered at superior conjunction (SUPC). The shaded regions depict the 1σ confidence intervals of the according fits to the data. The spectrum clearly hardens around inferior conjunction between 200 GeV and a few TeV.

1.1 LS 5039

LS 5039 comprises a compact object that orbits a O6.5V star on a mildly eccentric ($e = 0.35$) orbit with a period of 3.9 days. Identified as massive binary X-ray system in 1997 [3], that also shows a faint radio signature [4] with resolved mildly relativistic bipolar radio jets originating from a central core [5], it has been classified as a microquasar. However, the bipolar jet structure could also be mimicked by "cometary" tails as proposed in [6] and recently observed in the similar northern object LS I+61 303 [7]. The system has been serendipitously discovered in the TeV regime by H.E.S.S. during the 2004 galactic plane scan [8]. A follow up campaign in 2005 yielded an overall dataset of 69.2 h of observations, establishing the variable nature of the flux and spectral evolution of this interesting γ-ray source [9]. A total of 1969 γ photons with a significance of 40 standard deviations were obtained from the data performing a semi-analytical model analysis method described in [10]. The corresponding excess of VHE photons was found to be coincident with the VLBA radio position of LS 5039.
Decomposition of the run-wise (28 min bins) VHE flux data above 1TeV obtained from the H.E.S.S. observations into its frequency components by means of a Lomb-Scargle [11] periodogram yields a significant peak at a period of 3.9078 ± 0.0015 days. This is fully consistent with the optical period found in [12].
The run-wise lightcurve as a function of orbital phase ϕ is shown in Fig. 1. The VHE flux of γ-rays ≥ 1 TeV follows an almost sinusoidal behavior with the emission maximum being at $\phi \approx 0.7$ which roughly coincides with the inferior conjunction of the system, i.e., when the compact object aligns with the lign of sight between the star and the observer.

The data also revealed a modulation in the differential energy spectrum of VHE photons (see Fig. 1). This is expected when considering the variable environment of the system, i.e. changing magnetic field strengths, target photon densities and relative position of the two system constituents with respect to the line of sight. Dividing the data into two broad phase intervals one centered at inferior conjunction (INFC, $0.45 < \phi \leq 0.9$) and one at superior conjunction (SUPC, $0.9 < \phi \leq 0.45$), i.e. with the compact object in front/behind the star respectively with respect to the observer, gives two distinct spectral shapes corresponding to the high and low flux states in the system. The INFC spectrum (high state) is well described by a power law with photon index $\Gamma = 1.85 \pm 0.06_{\rm stat} \pm 0.1_{\rm syst}$ and an exponential cutoff at $E_{\rm exp} = 8.7 \pm 2.0$ TeV. The

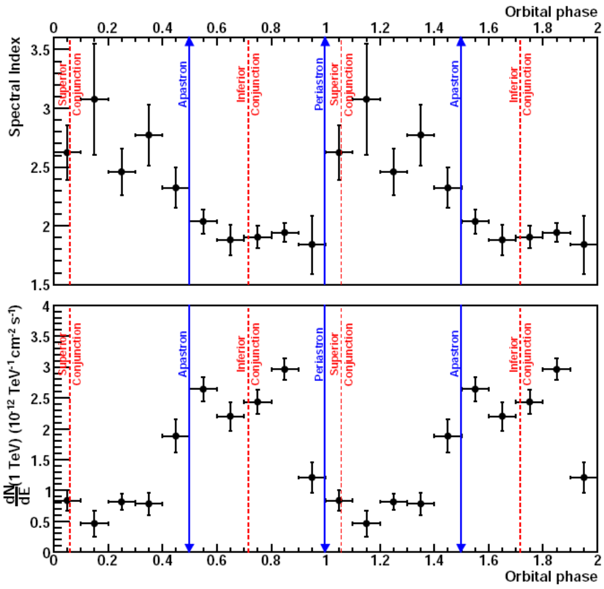

Figure 2: (Top panel) Spectral indices of a pure power law fit to VHE photons from LS 5039 below 5 TeV for phase intervals $\Delta\phi = 0.1$. (Bottom panel) Flux normalisation at 1 TeV for the same fits and phase binning.

INFC spectral behavior (low state), however, follows a pure power law with a rather steep index of $\Gamma = 2.53 \pm 0.06_{\rm stat} \pm 0.1_{\rm syst}$ ranging from 200 GeV up to $\sim$ 20 TeV. At the corresponding edges of this energy range the γ-ray spectrum seems to be almost invariable, while the maximum in modulation occurs around $\sim$ 5 TeV. Moreover, a comparison of all power law fits to the data divided into 0.1 phase bins shows a strong anti-correlation between the photon index Γ and the flux state. This has been done for photons below 5 TeV to omit effects stemming from the spectral cutoff during high state. According to this, the spectrum becomes harder in the high flux state and vice versa (see Fig. 2).

The modulation in the VHE γ-ray flux indicates that the emission zone lies relatively close, i.e. within a radius of $\sim$ 1 AU to the stellar companion. At such distances, variable absorption of γ-rays in the dense stellar photon field is expected due to the production of e^+e^--pairs [6]. In the light of a pure absorption scenario, a maximum in spectral modulation is expected around 300 GeV with a hardening of the spectrum towards the low flux state. This, however, is in contrast to the observations discussed above. This suggests more complicated scenarios for the generation of VHE radiation in this system, accounting e.g. for modulations in acceleration and cooling time scales, variations in the stellar photon field density and magnetic field strength along the compact object's orbit [13]. Time dependent accretion rates in case of a microquasar scenario should also be taken into account [14].

1.2 PSR B1259−63/SS2883

The binary system PSR B1259−63/SS2883 consists of a 48 ms pulsar orbiting a massive Be2 star at high eccentricity ($e = 0.87$) with a period of 3.4 years. It was first observed in TeV γ-rays during its periastron passage between February and June 2004 [15], establishing it as the first variable galactic TeV γ-ray source (see Fig. 3). The corresponding data showed a clear pointlike signal with a statistical significance of 13 standard deviations at the position of PSR B1259−63. A time averaged spectrum as well as a lightcurve for the integrated flux above 380 GeV from this object could be extracted (see Fig. 3 & 4). This was the first time in the history of TeV γ-ray astronomy where two sources have been discovered within the same field of view as this campaign lead to the serendipitous discovery of HESS J1303-631 [16] (see Fig. 3).

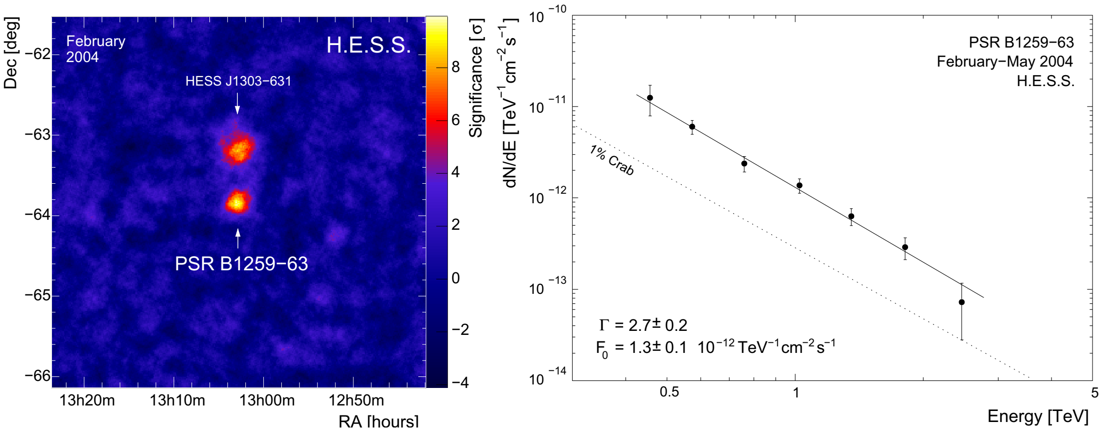

Figure 3: (left) Significance skymap of the PSR B1259−63 field of view as seen in February 2004. The unidentified γ-ray source HESS J1303−631 is located 0.6° to the north of the source. (right) Energy spectrum dN/dE of γ-rays from PSR B1259−63 determined from the H.E.S.S. 2004 data. The solid line indicates the power-law fit $F(E) = F_0 E^{-\Gamma}$.

The peculiar shape of the PSR B1259−63 lightcurve has been object of various model descriptions trying to explain the underlying physical processes causing the VHE emission. Mechanisms such as Inverse Compton (IC) scattering of ultrarelativistic electrons on the stellar photons or hadronic scenarios (e.g. $pp \to \pi^0 \to \gamma\gamma$) have been suggested as possible origins of TeV photons in the interactions of the pulsar wind with the stellar outflow and radiation field of the companion Be star (e.g. [17]). Some of these models take into account the influence of the dense stellar disc that might play a crucial role in the generation mechanism of VHE γ-rays (see[18]). In order to constrain the various parameters used in the model predictions, as well as to be able to discriminate between the models in question, data for the up to now unobserved pre-periastron period of PSR B1259−63 are needed.
As the last periastron took place on July 27, 2007, a campaign of 60 h of scheduled exposure during the pre-periastron phase from April to August 2007 has been carried out.

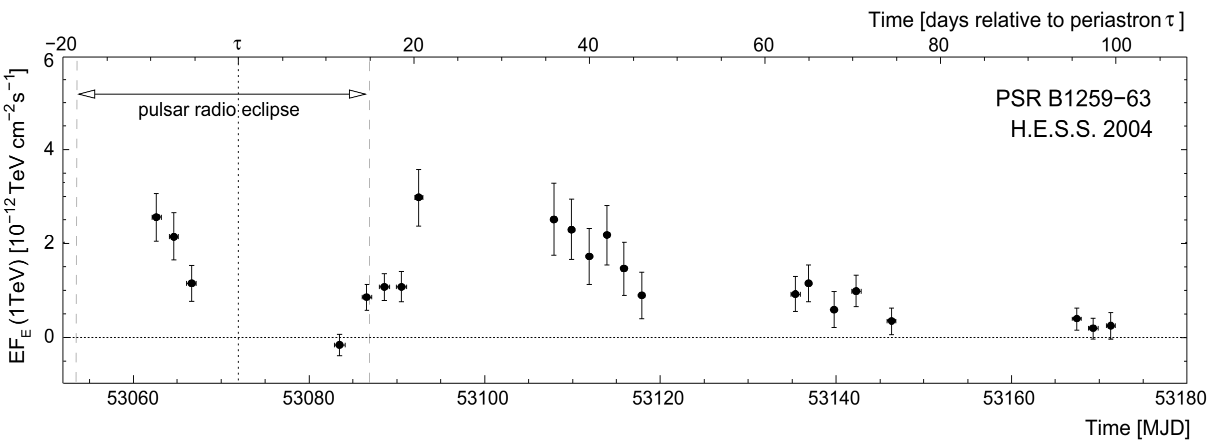

Figure 4: The PSR B1259−63 lightcurve around periastron in 2004. The vertical dashed black line indicates the position of the periastron. The data clearly indicate a variable flux.

2 The H.E.S.S. PSR B1259−63 2007 Campaign

Figure 5 shows the H.E.S.S. observation windows of PSR B1259−63 in 2007 together with data from 2004 with respect to periastron. The numbers underneath each observation slot indicate

the amount of livetime data taken for this month. The observations covered the pre-periastron orbital phase until 14 days prior to the periastron passage. The green boxes refer to the observation windows of the campaign discussed here. The overall exposure time of roughly 60 h was chosen to match the dataset from 2004, in terms of good quality data, in order to have a comparable amount of data for the pre-periastron part of the lightcurve.
The data taken have an overall livetime of 52 h.The livetime for the overall 2004 dataset was ~ 45 h. A preliminary standard point source analysis of these data (for details on the H.E.S.S. analysis chain see[15]) revealed a significance for a γ-ray excess from the source from April to August 2007 of 9 standard deviations, showing a clear signal after 3.4 years of presumed quiescence from this variable source.

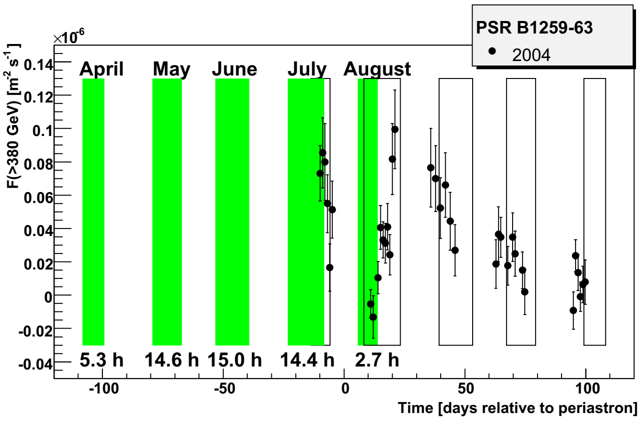

Figure 5: The PSR B1259−63 observation windows in 2007 with respect to the system's time relative to periastron (green boxes). The empty boxes are the 2007 observation windows mirrored with respect to periastron, overlaid with the 2004 data for comparison.

3 Multi Wavelength Coverage

For the sake of Multi Wavelength (MWL) coverage coincident with the TeV data provided by H.E.S.S. a cooperation with the *SUZAKU*[19] satellite project has been established. Corresponding observation schedules have been optimized for a maximum MWL coverage. *SUZAKU* planned to observe PSR B1259−63 from July to September 2007 in eight pointings of 20 ks duration each. Four pointings were scheduled in July coincident with the H.E.S.S observations covering the assumed first entrance of the pulsar into the dense circumstellar disc.

3.1 Summary & Outlook

Both TeV γ-ray binaries PSR B1259−63 and LS 5039 remain very interesting targets for VHE experiments. The corresponding source class still leaves open a number of crucial questions concerning the origin and evolution of VHE radiation in such systems. Therefore, more observational data with increasingly accurate resolution of spectral variability as well as flux behavior are desirable. PSR B1259−63 has been re-observed by the H.E.S.S. experiment in a 60 h exposure campaign lasting from April to August 2007. A preliminary point source analysis yields a significant excess from the system of 9σ.
The campaign coincided with 4 planned pointings on the target done by the X-ray satellite *SUZAKU* covering the crucial first disc crossing of the pulsar. A full scale analysis of the observational data gathered during this campaign will be presented in a future paper.
H.E.S.S. observations between 2004 and 2005 established spectral variability and periodical flux

behavior of the TeV source in LS 5039, therefore contributing to a better understanding of the VHE mechanisms present in this system.

Acknowledgments

The support of the Namibian authorities and of the University of Namibia in facilitating the construction and operation of H.E.S.S. is gratefully acknowledged, as is the support by the German Ministry for Education and Research (BMBF), the Max Planck Society, the French Ministry for Research, the CNRS-IN2P3 and the Astroparticle Interdisciplinary Programme of the CNRS, the U.K. Science and Technology Facilities Council (STFC), the IPNP of the Charles University, the Polish Ministry of Science and Higher Education, the South African Department of Science and Technology and National Research Foundation, and by the University of Namibia. We appreciate the excellent work of the technical support staff in Berlin, Durham, Hamburg, Heidelberg, Palaiseau, Paris, Saclay, and in Namibia in the construction and operation of the equipment.

1. M. Tavani, and J. Arons in *Astrophysical Journal* **477**, 439–+ (1997), `arXiv:astro-ph/9609086`.
2. G. Dubus in *ArXiv Astrophysics e-prints* (2006a), `astro-ph/0608262`.
3. C. Motch, F. Haberl, K. Dennerl, M. Pakull, and E. Janot-Pacheco in *A&A* **323**, 853–875 (1997), `arXiv:astro-ph/9611122`.
4. J. Marti, J. M. Paredes, and M. Ribo in *A&A* **338**, L71–L74 (1998).
5. J. M. Paredes, J. Martí, M. Ribó, and M. Massi in *Science* **288**, 2340–2342 (2000), `arXiv:astro-ph/0102235`.
6. G. Dubus in *A&A* **456**, 801–817 (2006b), `arXiv:astro-ph/0605287`.
7. V. Dhawan, A. Mioduszewski, and M. Rupen, "LS I +61 303 is a Be-Pulsar binary, not a Microquasar," in *VI Microquasar Workshop: Microquasars and Beyond*, 2006.
8. F. A. et al. (H.E.S.S. Collaboration) in *Science* **309**, 746–749 (2005a), `arXiv:astro-ph/0508298`.
9. F. A. et al. (H.E.S.S. Collaboration) in *A&A* **460**, 743–749 (2006), `arXiv:astro-ph/0607192`.
10. M. de Naurois in *ArXiv Astrophysics e-prints* (2006), `astro-ph/0607247`.
11. J. D. Scargle in *Astrophysical Journal* **263**, 835–853 (1982).
12. J. Casares, M. Ribó, I. Ribas, J. M. Paredes, J. Martí, and A. Herrero in *MNRAS* **364**, 899–908 (2005), `arXiv:astro-ph/0507549`.
13. D. Khangulyan, F. Aharonian, and V. Bosch-Ramon in *MNRAS* **383**, 467–478 (2008), `0707.1689`.
14. G. E. Romero, A. T. Okazaki, M. Orellana, and S. P. Owocki in *A&A* **474**, 15–22 (2007), `0706.1320`.
15. F. A. et al. (H.E.S.S. Collaboration) in *Discovery of the Binary Pulsar PSR B1259−63 in Very-High-Energy Gamma Rays around Perisatron with H.E.S.S.*, A&A 442 1 (2005) 1-10, 2005b.
16. F. A. et al. (H.E.S.S. Collaboration) in *Serendipitous discovery of the unidentified extended TeV γ-ray source HESS J1303-631 with the H.E.S.S. Cherenkov telescopes*, A&A 439 3 (2005) 1013-1021, 2005c.
17. D. Khangulyan, S. Hnatic, F. Aharonian, and S. Bogovalov in *TeV lightcurve of PSR B1259−63 / SS 2883*, astro-ph/0601241, 2006.
18. A. Neronov, and M. Chernyakova in *Radio-to-TeV γ-ray emission from PSR B1259−63*, astro-ph/0610139, 2006.
19. M. K. et al. in *The X-Ray Observatory Suzaku*, PASJ 58, 2006.

The extragalactic sky seen by H.E.S.S.

L. Gérard for the H.E.S.S. collaboration
Astroparticle et Cosmologie (APC), CNRS, Universié Paris 7 Denis Diderot, France

In the extragalactic sky, H.E.S.S. has observed Very High Energy $\gamma-$ray emission from 12 AGN, 9 being discoveries. AGN are transient objects, and short time scale variability detection opened the road to fine VHE temporal studies. Spectral hardening with increasing flux has been measured, but some new data from PKS 2155−304 indicate a more complex picture depending on the underlying flux level of the source. This source's emission provided a surprisingly strong indication for correlation between optical and VHE revealed during August 2008 multiwavelength campaign. Other studies also benefit from the observation of the extragalactic sky at VHE, indeed a very constraining upper limit on the Extragalactic Background Light density was derived from the measurement of hard spectra from distant sources.

1 Introduction

Active Galactic Nuclei (AGN) are highly transient objects emiting over the entire electromagnetic spectrum. For this reasons multiwavelength – preferably simultaneous – observations are necessary in order to get a complete vision of the processes taking place around these objects. From Namibia, the four atmospheric Čerenkov telescopes of H.E.S.S. cover the Very High Energy (VHE, > 100GeV) emission of AGN. At these energies, the falling part of what is known as the Inverse Compton (IC) peak in the leptonic model – or the hadronic models' peak – is measured. The spectral shape is a characteristic of the source and, when possible, is studied as a function of time. In case of hard spectra emitted by a distant source, the spectral index becomes a tool to put an upper-limit on the Extragalactic Background Light (EBL). Indeed the universe is not transparent to VHE $\gamma-$rays and targets need to be found over the widest possible range of distances in order to disentangle the intrinsic features of the sources from those due to absorption. The evolution of the flux in itself is a precious source of information about the emission region and the nature of the processes taking place there. And of course, the correlation of flux variability between different wavelengths is crucial to understand the links between the populations of particles responsible for the emission. These measurements constrain the emission models and therefore improve our understanding of these objects. After nearly 5 years of successful operation, what are the most relevant discoveries made by H.E.S.S. about AGN? Up to now, 12 AGN have been seen by H.E.S.S., of which 9 are discoveries. A panoramic vision of these sources is to follow, summarizing their main characteristics and the physical interpretations made thanks to their observations. Then, a closer look at PKS 2155−304, the brightest AGN seen by H.E.S.S., is taken in order to highlight the latest and some of the finest informations on AGN behaviour collected at VHE.

AGN	Redshift	Type	1st Detection		
			Year	Instrument	
Centaurus A	0.0018	FRI	2003	H.E.S.S.	1
M 87	0.004	FRI	2003	*HEGRA	2
Mkn 421	0.030	HBL	1992	*Whipple	3
PKS 0548−322	0.069	HBL	2007	H.E.S.S.	4
PKS 2005−489	0.071	HBL	2005	H.E.S.S.	5
RGB J0152+017	0.080	HBL	2007	H.E.S.S.	6
PKS 2155−304	0.116	HBL	1999	*Mark VI	7
1ES 0229+200	0.139	HBL	2006	H.E.S.S.	8
H 2356−309	0.165	HBL	2006	H.E.S.S.	9
1ES 1101−232	0.186	HBL	2006	H.E.S.S.	10
1ES 0347−121	0.188	HBL	2007	H.E.S.S.	11
PG 1553+113	>0.250	HBL	2006	H.E.S.S.	12

Table 1: *AGN detected by H.E.S.S., by order of redshift. The types comprise High-energy-peaked BL Lacs (HBL),a subcategory of Blazars, and Fanaroff-Riley type 1 (FRI) radio galaxies. The * indicates previous-generation instruments.*

2 Panoramic vision of the AGN seen by H.E.S.S.

In the extragalactic sky, H.E.S.S. monitors 12 AGN whose redshift, natures and discovery are summarized in Table 1. These objects are almost exclusively Blazars: AGN whose jet is orientated towards Earth. Centaurus A and M 87 are the only non-Blazar detected objects, their closeness compensating the lack of boosting of their emission.

2.1 Flux Variability

When looking at their flux variability, the H.E.S.S.-detected AGN can be classed in three categories. There are the AGN for which the variability cannot be detected considering the flux level of the source and the current sensitivity of the instrument. Then, those for which only long term variability is detected. And finally the rapid variability objects, generally the AGN with the highest flux hence providing the finest analysis. Centaurus A (see the related article by M. Raue et al. in these proceedings), PKS 0548−322 and 1ES 0229+200 are the AGN whose variability is not detected at VHE. A long term variability is measured for most of the detected Blazars. PKS 2005−489 [13], RGB J0152+017 [14], and H 2356−309, [13] are variable on monthly time-scales. 1ES 1101−232 [10,15], 1ES 0347−121 (2006-2007 data) and PG 1553+113 [16,17] have flux variability from one year to another. Short-term variability is measured for M 87, Mkn 421 – 15 minutes variability detected by H.E.S.S. during 2004 flare[18] and also previously by Whipple[19] – and PKS 2155−304 (see section 3.1). M 87's day-scale variability was first detected by H.E.S.S. in 2005 during a flare[20] and then confirmed by MAGIC and VERITAS in 2008[21]. Within the causality hypothesis and considering the small Lorentz factor associated to the jet of this radio-galaxy, the intra-night variability gives strong constraints on the size of the emission region, found to be of the order of the black hole's Schwarzschild radius.

2.2 Spectral characteristics

At VHE the spectral shape of all AGN is well fitted by a power law. Only the high flux states of the brightest sources meet the statistical level needed to see the expected curvature of the spectrum – due to the absortion, the IC or hadronic peak, or other intrinsic features of the source. Such a curvature has been measured by H.E.S.S. during a flare from Mkn 421 in 2004[18] and during PKS 2155−304 flaring activity[22] in 2006. Hardening spectra with increasing flux have been measured for Mkn 421 and PKS 2155−304 (see section 3.1).

2.3 Constraining the EBL

For distant sources, the absorption of the $\gamma-$ray emission by the EBL is not negligible. Measuring the VHE spectrum of such sources is a good tool to evaluate the EBL density. A very constraining upper-limit – close to the lower-limit derived from galaxy counting – was obtained from the hard spectra detection of the distant AGN 1ES 0229+200[8], H 2356−309[23], 1ES 1101−232[10,23] and 1ES 0347−121[11] – assuming the intrinsic source spectrum is not harder than $\Gamma = 1.5$. This is a very important result since the direct measurement of the EBL density is very difficult because of pollution from zodiacal light and, for a satellite measurement, that of the instrument's own emission (see D. Mazin's et al. article in these proceedings).

3 PKS 2155−304

3.1 Flux and spectral variability

PKS 2155−304 is one of the brightest AGN detected at VHE. Through regular observations, the quiescent state of the source has been determined [24]. This object also undergoes periods of high activity including flaring episodes. In Summer 2006, while in a high flux state (compared to the quiescent state), the source flared to an average of 7 times the flux of the Crab[25] (with peaks up to ~ 15 Crab). During this night, July 28$^{\mathrm{th}}$, time variability of ~ 3 min has been measured, allowing for the first VHE fine timing analysis. Under the hypothesis of causality, such a short time scale variability is of course a strong constraint on the emission region. From another view point, it has been shown that the Power Density Spectrum of the source as measured by H.E.S.S. is compatible with red noise. A study using Structure Functions has also been carried out, revealing the emission's lognormal nature during this night[26]. Also, Lorentz invariance violation effects were tested for and excluded within this data set[27] (see J. Bolmont's related article in these proceedings).

Observations from 2005 to 2007 has been combined to study the spectral evolution with flux level[24]. Though the source spectra are seen to harden with increasing flux while in a high flux state, the pattern in more complex when the flux level is lower.

3.2 Multiwavelength flux correlation

Flux correlation with other wavelengths was tested in Summer 2006[28] and Summer 2008 (first Fermi-LAT and H.E.S.S. joint campaign[29], see D. Sanchez article in these proceedings). In August 2008 – unlike during the 2006 campaign – the source was in quiescent state. When comparing the flux correlation results of these two campaigns, a two-fold behaviour depending on the flux level of the source at VHE appears. During the 2008 campaign, no correlation between VHE and X-ray was measured, whereas such a correlation was present in 2006 data set and is quite common among AGN. This correlation has previously been seen to be roughly quadratic as expected for a one-zone homogenous SSC models, but cubic correlation detected during a night flare ruled out this models. In 2008, fairly strong evidence for correlation between VHE and optical nightly averaged flux was detected. Such a correlation with optical flux is actually a first for this source and for AGN generally. This correlation pattern is a precious insight into the particle populations responsible for the multiwavelength emission.

4 Conclusion

H.E.S.S.'s contribution in observing the extragalactic sky currently consist of 12 AGN detections, from z = 0.0018 (3.8 Mpc) up to z > 0.25. Future observations should extend the AGN discovery source list beyond the current 9. The observation, with PKS 2155−304, of the shortest time scale variability for AGN – including other wavelengths– opened the road to fine temporal analysis in the VHE domain. Mkn 421 and PKS 2155−304 spectral evolution was found to harden when the flux increases, but, when looking at lower flux, the behaviour of PKS 2155−304 proved to be more complex. In August 2008, for the first time with AGN, correlation between Optical and VHE was measured during PKS 2155−304 low flux state. This source seems to exhibit a two-fold behaviour depending on its flux level, a behaviour observed on the spectral evolution (see section 3.1) and while considering the flux correlation pattern (see section 3.2). If this is confirmed, the nature of the differences between the quiescent state and the flaring episodes needs to be addressed. To further investigate this point, the knowledge of the VHE quiescent state of PKS 2155−304 need to be improved, but also that of other sources. H.E.S.S.-II (see Y. Becherini article in these proceedings) will have a large part to play in future VHE AGN studies. Indeed, with its lower energy threshold and higher sensitivity, the analysis now only possible on PKS 2155−304 should be accessible with a larger number of sources.

References

1. F. Aharonian *et al.* (H.E.S.S. collaboration), *ApJ* **695**, L40 (2009).
2. F. Aharonian *et al.* (H.E.S.S. collaboration), *A&A* **403**, L1 (2003).
3. M. Punch *et al.* (Whipple collaboration), *Nature* **358**, 477 (1992).
4. G. Superina *et al.*, *ICRC*, (2007)
5. F. Aharonian *et al.* (H.E.S.S. collaboration), *A&A* **436**, L17 (2005).
6. F. Aharonian *et al.* (H.E.S.S. collaboration), *A&A* **481**, L103 (2008).
7. P. Chadwick *et al.* (Mk V Durham collaboration), *APh* **11**, 145 (1999).
8. F. Aharonian *et al.* (H.E.S.S. collaboration), *A&A* **475**, L9 (2007).
9. F. Aharonian *et al.* (H.E.S.S. collaboration), *A&A* **455**, 461 (2006).
10. F. Aharonian *et al.* (H.E.S.S. collaboration), *A&A* **470**, 475 (2007).
11. F. Aharonian *et al.* (H.E.S.S. collaboration), *A&A* **473**, L25 (2007).
12. F. Aharonian *et al.* (H.E.S.S. collaboration), *A&A* **448**, L19 (2006).
13. L. Costamente *et al.* (H.E.S.S. collaboration), *ICRC*, (2007)
14. F. Aharonian *et al.* (H.E.S.S. collaboration), *to be submitted.*
15. F. Aharonian *et al.* (H.E.S.S. collaboration), *A&A* **477**, 481 (2008).
16. R. Wagner *et al.* (MAGIC collaboration), *ICRC*, (2007)
17. W. Benbow *et al.* (H.E.S.S. collaboration), *ICRC*, (2007)
18. F. Aharonian *et al.* (H.E.S.S. collaboration), *A&A* **437**, 95 (2005).
19. J. A. Gaidos *et al.* (Whipple collaboration), *Nature* **383**, 319G (1996)
20. F. Aharonian *et al.* (H.E.S.S. collaboration), *Science* **314**, 1424 (2006).
21. VERITAS, MAGIC and H.E.S.S. collaborations and the VLBA Team, *submitted.*
22. J.-P. Lenain *et al.* (H.E.S.S. collaboration), *AIPC*, **1085**, 415 (2008)
23. F. Aharonian *et al.* (H.E.S.S. collaboration), *Nature* **440**, 1018 (2006).
24. F. Aharonian *et al.* (H.E.S.S. collaboration), *to be submitted.*
25. F. Aharonian *et al.* (H.E.S.S. collaboration), *ApJ* **664**, L71 (2007).
26. G. Superina, B. Degrange (H.E.S.S. collaboration), *AIPC*, **1085**, 494 (2008)
27. F. Aharonian *et al.* (H.E.S.S. collaboration), *Phys. Rev. Lett.*, 101:170402 (2008).
28. F. Aharonian *et al.* (H.E.S.S. collaboration), *to be submitted.*
29. F. Aharonian, A. A. Abdo *et al.* (H.E.S.S. and *Fermi* collaborations), *ApJ*, *in press.*

SEARCH FOR LORENTZ INVARIANCE VIOLATION EFFECTS WITH PKS 2155-304 FLARING PERIOD IN 2006 BY H.E.S.S.

J. BOLMONT[1], R. BÜHLER[2], A. JACHOLKOWSKA[1], S. J. WAGNER[3],
for the H.E.S.S. COLLABORATION
[1] *LPNHE, Universite Pierre et Marie Curie Paris 6, Universite Denis Diderot Paris 7, CNRS/IN2P3, France,* [2] *Max-Planck-Institüt für Kernphysik, Heidelberg, Germany,* [3] *Landessternwarte, Universität Heidelberg, Germany*

Highly energetic, variable and distant sources such as Active Galactic Nuclei provide a good opportunity to evaluate effects due to the emission and the propagation of high energy photons. In this note, a study of possible energy-dependent time-lags with PKS 2155-304 light curve as measured by H.E.S.S. in July 2006 is presented. These time-lags could either come from the emission processes or also sign a Lorentz Symmetry breaking as predicted in some Quantum Gravity models. A Cross-Correlation function and a Wavelet Transform were used to measure the time-lags. The 95% Confidence Limit on the Quantum Gravity energy scale based on the statistical and systematic error evaluation was found to be 7×10^{17} GeV considering a linear correction in the standard photon dispersion relations and assuming that emission-induced time-lags are negligible. For now, this limit is the best ever obtained with a blazar.

1 Introduction

Quantum Gravity phenomenology [1] has known a growing interest in the past decade, especially since the time it was argued that the quantum nature of space-time could have measurable effects on photon propagation over large distances. Namely, the quantum nature of the space-time at the Planck scale could induce a dependance of the light group velocity with the energy of the photons [2,3].

It is generally assumed that the light velocity is modified following to

$$c' = c \left(1 + \xi \frac{E}{\mathrm{E_P}} + \zeta \frac{E^2}{\mathrm{E_P^2}}\right) \tag{1}$$

at the second order, where $\mathrm{E_P} = 1.22 \times 10^{19}$ GeV is the Planck energy and where ξ and ζ are free parameters which need to be determined. In the following, only the linear correction will be considered and a limit on $E_{\mathrm{QG}} = |\xi|^{-1}\mathrm{E_P}$ will be set.

As $\mathrm{E_P}$ is very large, the modification of the velocity of the photons is expected to be tiny. However, as it is related to the nature of the space-time, it was proposed [2] that these tiny effects could add up over long distances and lead to detectable time-lags between photons of different energies, assuming these photons were emitted *at the same time*. Taking into account the expansion of the Universe [4], the time-lag Δt is obtained from the dispersion relations (1):

$$\frac{\Delta t}{\Delta E} \approx \frac{\xi}{\mathrm{E_P H_0}} \int_0^z dz' \frac{(1+z')}{\sqrt{\Omega_m (1+z')^3 + \Omega_\Lambda}}, \tag{2}$$

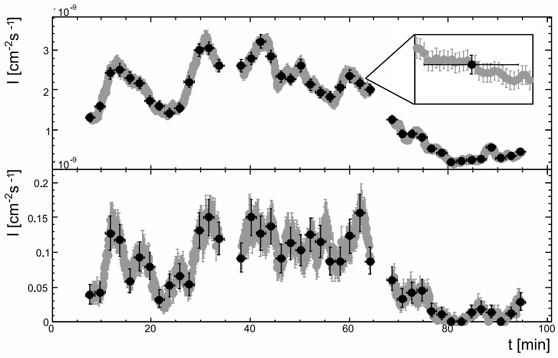

Figure 1: Light curve of the PKS2155-304 flare during the night of July 28 in 2006. Top: 200-800 GeV. Bottom: $>$ 800 GeV. The original data points (in black) are binned in two-minute time intervals. The zero time point is set to MJD 53944.02. Gray points show the oversampled light curve, for which the two-minute bins are shifted in units of five seconds.

in the case of the linear correction and where Ω_m, Ω_Λ and H_0 are parameters of the Cosmological Standard Model ($\Omega_m = 0.3$, $\Omega_\Lambda = 0.7$ and $H_0 = 70$ km s^{-1} Mpc^{-1}). ΔE is the energy difference of the photons. The time-lag may decrease or increase with ΔE depending on the model in consideration. The integral term increases with the redshift and takes into account the fact that two photons travelling with two different speeds do not take the same time to cross the Universe and then do not see the same expansion.

The goal of the 'time of flight' studies is to measure the time-lags, which should be energy dependant. For this, two kind of variable extragalactic sources may be considered: the Gamma-Ray Bursts (GRBs) and the Active Galactic Nuclei (AGNs). However, both these sources could introduce intrinsic time lags in the measurements. Therefore, it would be necessary to study the possible effects as a function of the redshift of the source. When this is not possible, the intrinsic (or source) effects are often assumed to be negligible. In the present study, this hypothesis was adopted.

2 Data and methods

In this note (more details are available elsewhere [5]), the search for propagation effects with the blazar PKS 2155-304 is described. During the night of the 28th of July 2006, the H.E.S.S. experiment detected [6] an exceptional flare of this source, located at z = 0.116, with a high flux (10 000 photons recorded in 1.5 hours) and a high variability (rise and fall times of $\sim$200 s). The over-sampled light curve of the flare is shown in Fig. 1 in two different energy bands.

To measure the time lags between photons in two different light curves, two independant analyses were carried out, using two different methods:

- The position of the maximum of the Modified Cross Correlation Function [7] (MCCF) gives directly the value of the time lag. This method was applied to the oversampled light curves of Fig. 1 in the energy bands 200-800 GeV and $>$ 800 GeV (Fig. 2, left) which corresponds to $< \Delta E > \sim$1 TeV;

- Following Ellis *et al.* [8], the Continuous Wavelet Transform [9] (CWT) was used to locate the extrema of the light curves with great precision. An extremum of the low energy band was associated with an extremum in the high energy band to form a pair. Selection criteria were applied to reject fake extrema. The energy bands 210-250 GeV and $>$ 600 GeV were used, with a bin width of one minute and no oversampling of the light curves. These energy bands give a mean ΔE of $\sim$0.92 TeV.

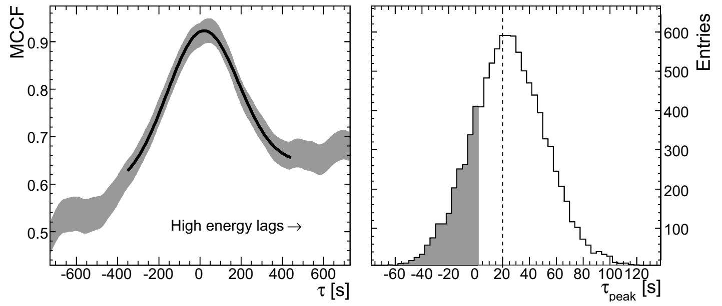

Figure 2: Left: the MCCF obtained with the two light curves of Fig. 1. Right: the MCCF peak distribution (CCPD) obtained with 10000 realizations of the light curves.

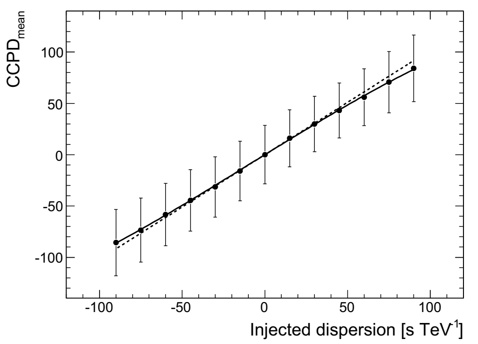

Figure 3: Mean of the MCCF peak distribution (CCPD) as a function of the injected dispersion. Each CCPD is obtained from ten thousand simulated light curves. The points have been shifted by the mean value of the CCPD of the original data (Fig. 2). The dashed line shows the linear response function.

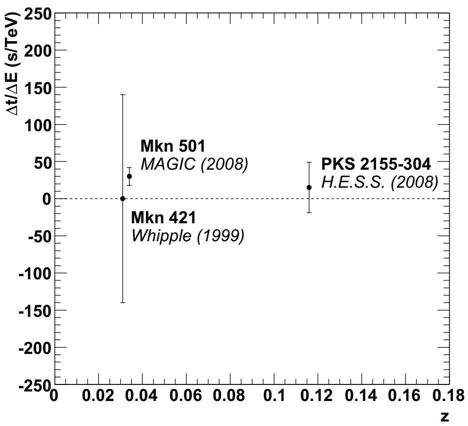

Figure 4: The dispersion measured as a function of the redshift. The results of the Whipple and the MAGIC experiments are compared with the present H.E.S.S. result.

As shown in Fig. 2 (left), the MCCF was fitted with the sum of a gaussian and a first degree polynomial to determine the position of the maximum. It gave $\tau_{\text{peak}} = 20$ s. In order to evaluate the uncertainties on this result, 10000 light curves were simulated in each energy band varying the flux within the error bars. For each pair of light curves, the MCCF was computed and its maximum was filled into the distribution shown in Fig. 2 (right). This distribution is slightly asymmetric, with a mean of 25 s and an RMS of 28 s. Another test, performed by injecting a dispersion in the data (Fig. 3), showed no significant deviation of the measured lag. Then, as the time-lag obtained was compatible with zero, a 95% confidence upper limit on the linear dispersion of 73 s/TeV was found.

With the CWT method, two pairs of extrema were obtained giving a mean time delay of 27 seconds. A method similar to the one used for the CCF was applied to determine the errors, which were found to be in a range between 30 and 36 seconds. A 95% confidence limit of 100 s/TeV was obtained for the linear correction.

3 Results and discussion

The results obtained with the two methods are summarized in Table 1 (see next page). The MCCF leads to a limit of $E_{\text{QG}} > 7.2\times10^{17}$ GeV. The CWT gives a lower limit of $E_{\text{QG}} > 5.2\times10^{17}$ GeV, mainly due to a larger measured time-lag and a lower value of $< \Delta E >$.

Table 1: The results obtained with the two methods in the case of a linear dispersion in energy.

Method	Energy bands	$< \Delta E >$	$(\Delta t/\Delta E)_{95\%\ \mathrm{CL}}$	$E_{\mathrm{QG}\ 95\%\ \mathrm{CL}}$
MCCF	200 GeV $<$ E $<$ 800 GeV and E $>$ 800 GeV	1.02 TeV	$<$ 73 s/TeV	$> 7.2 \times 10^{17}$ GeV
CWT	210 GeV $<$ E $<$ 250 GeV and E $>$ 600 GeV	0.92 TeV	$<$ 100 s/TeV	$> 5.2 \times 10^{17}$ GeV

Fig. 4 (previous page) shows all the results obtained so far with AGNs. The Whipple collaboration set a limit of 4×10^{16} GeV using a flare of Mkn 421 (z = 0.031) in 1996 [10]. More recently, the MAGIC collaboration obtained a limit of 2.6×10^{17} GeV with a flare of Mkn 501 (z = 0.034) [11]. The results obtained with H.E.S.S. are more constraining due to the fact that (*i*) PKS 2155-304 is almost four times more distant than Mkn 421 and Mkn 501, (*ii*) the statistics are higher by a factor of ten.

As mentionned above, GRBs are other good candidates for time of flight studies. Population studies have already been carried out [12] and lead to limits of the order of 10^{16} GeV. The best limit so far is $E_{\mathrm{QG}} > 2 \times 10^{18}$ GeV. It has been obtained by the Fermi experiment [13] with GRB 080916C (z = 4.35) using both GBM and LAT data. However, the time lag was obtained comparing the arrival time of the highest energy photon (13.2 GeV) with the trigger time, leading to $\Delta t = 16.5$ s. A more detailed analysis including error calibration would be necessary.

As far as the search for the Quantum Gravity propagation effect is concerned, the GRBs and the AGNs are complementary. AGN flares can be detected with high statistics with ground-based gamma-ray telescopes, which give large values of $\Delta E \sim 1$ TeV. However, the absorption of the high energy photons by the extra-galactic background light limits the distance of the observed objects. On the other hand, GRBs are easilly detected by satellite experiments at very high redshifts (up to $\sim$6) and up to a few hundreds of GeV ($\Delta E \sim 10$ GeV). Till now, no significant result has been obtained with either AGNs or GRBs for the linear and quadratic terms in the photon dispersion relations. Further observations of both a high number of AGN flares and GRBs will be necessary to give robust conclusions on possible propagation effects. Present and future experiments such as Fermi, CTA or AGIS [14] will greatly improve our capabilities in this area.

References

1. G. Amelino-Camelia, arXiv:0806.0339.
2. G. Amelino-Camelia *et al.*, Nature **395**, 525 (1998).
3. J. Ellis *et al.*, Phys. Lett. B **665**, 412 (2008), D. Mattingly, Living Rev. Rel. **8**, 5 (2005).
4. U. Jacob & T. Piran, Nature Phys. **3**, 87 (2007).
5. F. Aharonian *et al.* (HESS Collaboration), PRL **101**, 170402 (2008).
6. F. Aharonian *et al.* (HESS Collaboration), ApJL **664**, L71 (2007).
7. T.-P. Li *et al.*, Chinese J. of Astronomy and Astrophys. **4**, 583 (2004).
8. J. Ellis *et al.*, A&A **402**, 409 (2003).
9. S. Mallat, *A Wavelet Tour of Signal Processing*, ed. Academic Press (1999).
10. S. D. Biller *et al.* (Whipple Collaboration), Phys. Rev. Lett. **83**, 2108 (1999).
11. J. Albert *et al.* (MAGIC Collaboration) and J. Ellis *et al.*, Phys. Lett. B **668**, 253 (2008).
12. See e.g. J. Ellis *et al.*, Astropart. Phys. **25**, 402 (2006), J. Ellis *et al.*, Astropart. Phys. **29**, 158 (2008), J. Bolmont *et al.*, ApJ **676**, 532 (2008).
13. A. A. Abdo *et al.*, Science Express, 02/19/2009.
14. `http://www.cta-observatory.org/`, `http://www.agis-observatory.org/`.

PSR J0205+6449 and PSR J2229+6114, two young & noisy γ-ray pulsars

D. PARENT
CNRS/IN2P3, Université de Bordeaux, Centre d'Études Nucléaires de Bordeaux-Gradignan, UMR 5797, Gradignan, 33175, FRANCE

We report the discovery of gamma-ray pulsations (≥ 0.1 GeV) from two young, noisy pulsars by the Large Area Telescope aboard *Fermi*, PSR J0205+6449 and PSR J2229+6114. These pulsars, associated with pulsar wind nebulae, were discovered at radio wavelengths after the CGRO mission and are some of the most energetic in the Milky Way. The Vela-like pulsar J2229+6114, detected in the error box of the EGRET source 3EG J2227+6122, consists of one single, asymmetric peak plus an excess around 0.9 in phase, while PSR J0205+6449 located in the Galactic supernova remnant 3C 58, has a pulse profile very similar to the Vela pulsar. The γ-ray spectra above 0.1 GeV of both pulsars are fit with power laws having exponential cutoffs, leading to integral photon fluxes of $(1.37 \pm 0.14 \pm 0.30) \times 10^{-7}\,\mathrm{cm}^{-2}\,\mathrm{s}^{-1}$ for PSR J0205+6449 and $(5.86 \pm 0.22 \pm 1.17) \times 10^{-7}\,\mathrm{cm}^{-2}\,\mathrm{s}^{-1}$ for PSR J2229+6114. The first uncertainty is statistical and the second is systematic. These detections add to the growing number of young γ-ray pulsars that dominate the population of GeV γ-ray sources in the Galactic plane.

1 Introduction

Rotation-powered pulsars are rapidly rotating, strongly magnetized neutron stars, and are believed to dominate the Galactic γ-ray source population[23]. Their visibility is linked to their beam patterns. For the known γ-ray pulsars, the bulk of the electromagnetic power output is in high energies. The γ-ray emission is thus crucial for understanding the emission mechanism which converts the rotational energy of the neutron star into electromagnetic radiation, whether above the polar caps, or far from the neutron star (outer magnetospheric models). With the improvements in effective area, field of view, and angular resolution, the *Fermi* Large Area Telescope is discovering dozens of new γ-ray pulsars, measuring luminosities, light curves, and phase-resolved spectra, which will allow γ-ray tests of the theoretical models. In this proceeding we report the *Fermi* detection of the two young and noisy [a] γ-ray pulsars PSR J0205+6449 [4] and PSR J2229+6114 [5].

1.1 PSR J0205+6449

Becker et al.[7] identified an X-ray point source in the heart of the supernova remnant (SNR) 3C 58 (G130.7+3.1) as a likely pulsar, and subsequent studies yielded a distance of 3.2 kpc [19]. The pulsar J0205+6449 was finally discovered in *Chandra X-ray Observatory* data, with a period of 65.7 ms. This was followed by the detection of weak radio pulsations with a sharp

[a] The pulsar exhibits rotational instabilities.

pulse of width 2 ms [8]. The pulsar has a very high spin-down luminosity of $2.7 \times 10^{37}\,\mathrm{ergs\,s^{-1}}$ (the third most energetic of the known Galactic pulsars), a surface magnetic field strength of 3.6×10^{12} G, and a characteristic age of 5400 years. It also exhibits a high level of timing noise [18], and at least two glitches have occurred since its discovery [15]. Recently, a study by Livingstone et al.[16] presented the first measurement of the phase offset between the radio and X-ray pulse, showing that the first X-ray peak lags the radio pulse by $\phi = 0.10 \pm 0.01$.

1.2 PSR J2229+6114

PSR J2229+6114 is located at (l=106.6°, b=2.9°) within the error box of the EGRET source 3EG J2227+6122. Detected as a compact X-ray source during *ROSAT* and *ASCA* observations of the EGRET error box, it was later discovered to be a radio and X-ray pulsar [11] with a period of $P = 51.6$ ms [10]. The radio pulse profile shows a single sharp peak, while the X-ray light curve at 0.8 – 10 keV consists of two peaks, approximately separated by $\Delta\phi = 0.5$. It is almost as young as the Vela pulsar (characteristic age $\tau_c = 10\,\mathrm{kyr}$), as energetic ($\dot{E} = 2.2 \times 10^{37}\,\mathrm{ergs\,s^{-1}}$), and is evidently the energy source of the "Boomerang" arc-shaped PWN G106.65+2.96, suggested to be part of the supernova remnant (SNR) G106.3+2.7 discovered by Joncas & Higgs [13]. Studies of the radial velocities of both neutral hydrogen and the molecular material locate the system at $\sim$ 800 pc [14], while Halpern et al.[10] suggest a distance of 3 kpc estimated from its X-ray absorption. As for the distance derived from the dispersion measure (DM), it is estimated to be 7.5 kpc according to the NE 2001 model, making a large discrepancy with the association distance. Finally, AGILE has recently reported the discovery of the >100 MeV γ-ray pulsations [17].

2 Observations

The Large Area Telescope (LAT) on *Fermi*, launched on 2008 June 11, is a pair-conversion telescope [6], which consists of both a converter-tracker (direction measurement of the incident γ-rays) and a CsI(Tl) crystal calorimeter (energy measurement). The array is surrounded by segmented plastic scintillator (charged-particle background identification) and connected to a programmable trigger and data acquisition system. The instrument is sensitive to photons from 0.02 to 300 GeV over a $\sim$ 2.4 sr field of view. The LAT hardware design, event reconstruction algorithms, background selections and event quality selections determine the instrument performance [b]: a large effective area on axis (~ 0.8 m^2); superior angular resolution ($\theta_{68} \sim 0.5°$ at 1 GeV for events in the front section of the tracker); and an energy resolution better than 10% between 0.1 and 10 GeV on axis. The software timing chain deriving from a GPS clock on the satellite and the phase-folding software has been shown to be accurate to better than a few μs [21].

The data for the spectral analysis were collected during *Fermi*'s first-year all-sky survey, beginning 2008 August 4. We specially added for the timing analysis data from the detector commissioning phase from 2008 June 30 to 2008 August 3, including pointed observations of the Vela pulsar and other targets. The data for PSR J0205+6449 end 2009 March 9, while those for PSR J2229+6114 end 2009 March 23. Only γ-rays in the "Diffuse" class events (the tightest background rejection) were selected.

3 Pulsed Profiles

For the profile study of these two pulsars, we selected γ-rays over 0.1 GeV within a radius around the radio pulsar position, and then we refined them according to an energy-dependent

[b] http://www−glast.slac.stanford.edu/software/IS/glast_lat_performance.htm

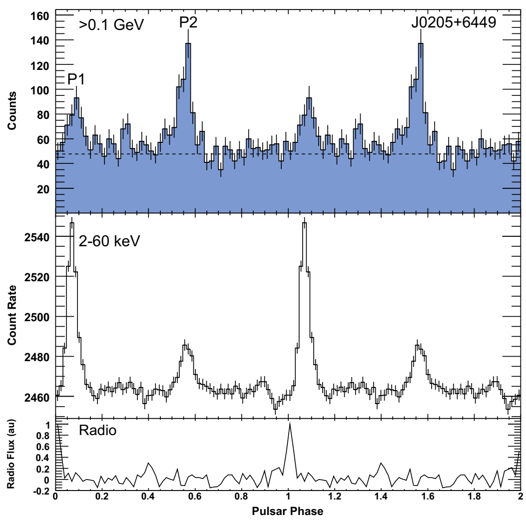

Figure 1: **Top panel:** Phase-aligned histogram of PSR J0205+6449 above 0.1 GeV. Two rotations are plotted with 50 bins per period. The dashed line shows the background level, as estimated from a ring surrounding the pulsar during the off-pulse phase. **Middle panel:** Count rate in the energy band 2−60 keV from *RXTE* data. **Bottom panel:** Radio pulse profile from GBT at a center frequency of 2 GHz with 64 phase bins.

angular radius which approximates the LAT point spread function. This selection maximizes the signal-to-noise ratio over a broad energy range. We corrected their arrival times to the Solar System Barycenter using the JPL DE405 Solar System ephemeris [22]. The events have been folded with the radio period using the ephemeris from the Green Bank Telescope (GBT) and the Lovell telescope at Jodrell Bank.

3.1 PSR J0205+6449

The pulsar is located in the Galactic plane where the diffuse gamma radiation is intense, and 5.3° from the bright LAT source 0FGL J0240.3+6113 coincident with the X-ray binary LSI+61°303 [1]. Figure 1 (top panel) shows the 50 bin γ-ray phase histograms above 0.1 GeV. The radio profile is shown at the bottom panel as a phase reference. The first γ-ray peak (P1) is offset from the radio pulse by $0.08 \pm 0.01 \pm 0.01$. The offset uncertainties arise from the γ-ray fit and from the uncertainty in the DM, respectively. The second peak (P2) is asymmetric, and centered at $0.57 \pm 0.01 \pm 0.01$. The dashed line (47 counts/bin) represents the background counts measured from a $2 - 3°$ ring surrounding the pulsar during the pulse minimum between 0.65 and 1.0 in phase. Figure 1 (middle panel) also shows the $2 - 60$ keV X-ray phase histogram measured by *RXTE* [16]. The good alignment between the X-ray and γ-ray profiles suggests a common origin for the two components. This feature is also observed in the LAT data for the Vela pulsar where the more intense X-ray pulse is aligned with the first γ-ray pulse [2].

The γ-ray profile, covering a wide range in phase, is reminiscent of the Vela light curve[2]. The γ-ray delay of 0.08 cycles and the peak separation of ~ 0.5 is becoming a consistent pattern, as the first γ-ray peaks for Vela, B1951+32, and J2021+3651 [12,3] lag the radio pulses by 0.13, 0.16, and 0.17 respectively, and the separation of the γ-ray peaks is $0.4 - 0.5$. This fits the predictions of the outer magnetospheric models quite well, whether they be the traditional outer gap model (OG) [20] or the two pole caustic gap model (TPC) [9].

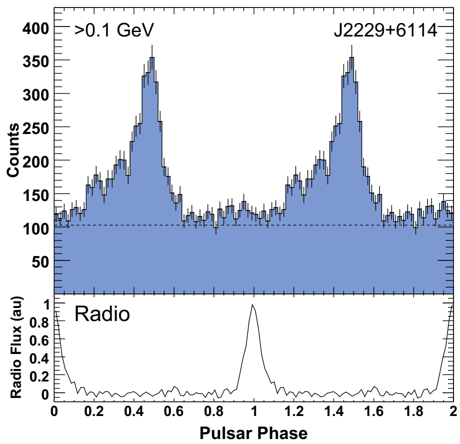

Figure 2: **Top panel:** Phase-aligned histogram of PSR J2229+6114 above 0.1 GeV. Two rotations are plotted with 50 bins per period. The dashed line shows the background level, as estimated from a ring surrounding the pulsar during the pulse minimum. **Bottom panel:** Radio pulse profile from GBT at a center frequency of 2 GHz with 64 phase bins.

Table 1: Spectral results for PSR J0205+6449 and PSR J2229+6449.

Pulsar name	F^a (>100 MeV) ($10^{-7}\,\mathrm{cm}^{-2}\,\mathrm{s}^{-1}$)	h^b (>100 MeV) ($10^{-10}\,\mathrm{ergs\,cm}^{-2}\,\mathrm{s}^{-1}$)	Γ	E_c^c GeV
J0205+6449	$1.37 \pm 0.14 \pm 0.30$	$0.67 \pm 0.05 \pm 0.10$	$2.1 \pm 0.1 \pm 0.2$	$3.0^{+1.1}_{-0.7} \pm 0.4$
J2229+6114	$5.86 \pm 0.22 \pm 1.17$	$3.15 \pm 0.08 \pm 0.63$	$2.1 \pm 0.1 \pm 0.2$	$4.2^{+0.9}_{-0.6} \pm 0.6$

3.2 PSR J2229+6114

Figure 2 (top panel) shows the 50 bin histogram of folded counts above 0.1 GeV compared with the phase-aligned radio pulse profile (bottom panel). The profile shows a single, asymmetric peak ($\phi = 0.15 - 0.65$), that has been fit by a two half-Lorentzian function. The fit places the peak at $0.49 \pm 0.01 \pm 0.01$. We estimated the background level from a $2 - 3^\circ$ ring around the pulsar during the $0 - 0.15$ pulse minimum. This is represented by the dashed line (103 counts/bin). From this, we observe an excess between 0.65 and 1.15 in phase, with a significance (signal/$\sqrt{\text{background}}$) of $7\,\sigma$.

4 Spectra and phase-averaged flux

The phase-averaged specta for PSR J0205+6449 and PSR J2229+6114 were obtained performing a maximum likelihood spectral analysis[c], using the LAT tool 'gtlike' on counts between 0.1 and 200 GeV. We fit the spectra with a power law with an exponential cutoff, that can be described by the equation:

$$\frac{dF}{dE} = N_0(E)^{-\Gamma} e^{-E/E_c}\ \mathrm{cm}^{-2}\mathrm{s}^{-1}\mathrm{GeV}^{-1} \qquad (1)$$

with E in GeV. The term N_0 is a normalization factor, Γ is the spectral index, and E_c is the energy cut-off. We summarize the results in Table 1.

[c] http://fermi.gsfc.nasa.gov/ssc/data/analysis/documentation/

5 Conclusion

Using a rotational ephemeris derived from radio observations with the GBT and at Jodrell Bank, and γ-ray data from the *Fermi* LAT, we have detected two young and noisy pulsars, PSR J0205+6449 and PSR J2229+6114. These detections increase the number of sources identified as pulsars in the Galactic plane, and confirm a bit more the assumption that the pulsars dominate the γ-ray Milky Way. Furthermore, this growing number of detected γ-ray pulsars will allow better constraints on high-energy emission models and consequently a better understanding of the pulsar magnetospheric structure and acceleration process.

References

1. Abdo, A. A., et al. 2009a, "*Fermi* LAT Bright γ-ray Source List", submitted (arXiv:0902.1340)
2. Abdo, A. A., et al. 2009b, "Fermi LAT Observations of the Vela Pulsar", ApJ, in press (arXiv:0812.2960)
3. Abdo, A. A., et al. 2009c, "Pulsed Gamma-rays from PSR J2021+3651 with the *Fermi Gamma-ray Space Telescope*", ApJ, submitted
4. Abdo, A. A., et al. 2009d, "Discovery of pulsations from the pulsar J0205+6449 in SNR 3C 58 with the *Fermi Gamma-ray Space Telescope*", ApJL, submitted
5. Abdo, A. A., et al. 2009e, "Fermi LAT Detection of Pulsed Gamma-rays from the Vela-like Pulsars PSR J1048−5832 and PSR J2229+6449", in prep.
6. Atwood, W. B., et al. 2009, ApJ, submitted (arXiv:0902.1089)
7. Becker, R. H., Helfand, D. J., & Szymkowiak, A. E. 1982, ApJ, 255, 557
8. Camilo, F., Stairs, I. H., Lorimer, D. R., Backer, D. C., Ransom, S. M., Klein, B., Wielebinski, R., Kramer, M., McLaughlin, M. A., Arzoumanian, Z., & Muller, P. 2002, ApJ, 571, L41
9. Dyks, J., & Rudak, B. 2003, ApJ, 598, 1201
10. Halpern, J. P., Gotthelf, E. V., Leighly, K. M., & Helfand, D. J. 2001a, ApJ, 547, 323
11. Halpern, J. P., Camilo, F., Gotthelf, E. V., Helfand, D. J., Kramer, M., Lyne, A. G., Leighly, K. M., & Eracleous, M. 2001b, ApjJL, 552, L125
12. Halpern, J. P., Camilo, F., Giuliani, A., Gotthelf, E. V., McLaughlin, M. A., Mukherjee, R., Pellizzoni, A., Ransom, S. M., Roberts, M. S. E., & Tavani, M. 2008, ApJ, 688, L33
13. Joncas, G., & Higgs, L. A. 1990, A&AS, 82, 113
14. Kothes, R., Uyaniker, B., & Pineault, S. 2001, ApJ, 560, 236
15. Livingstone, M. A., Ransom S. M., Camilo, F., Kaspi, V. M., Lyne, A. G., Kramer, M., & Stairs, I. H. 2008, AIP Conf. Proc., 983, 160
16. Livingstone, M. A., Ransom S. M., Camilo, F., Kaspi, V. M., Lyne, A. G., Kramer, M., & Stairs, I. H. 2009, arXiv:0901.2119
17. Pellizzoni, A. et al., 2009, ApJ, 695, L115
18. Ransom, S., Camilo, F., Kaspi, V., Slane, P., Gaensler, B., Gotthelf, E., & Murray, S. 2004, AIPC, 714, 350
19. Roberts, D. A., Goss, W. M., Kalberla, P. M. W., Herbstmeier, U., & Schwarz, U. J. 1993, A&A, 274, 427
20. Romani, R. W., & Yadigaroglu, I. A. 1995, ApJ, 438, 314
21. Smith, D. A., et al. 2008, A&A, 492, 923
22. Standish, E. M., JPL Planetary and Lunar Ephemerides, DE405/LE405, Memo IOM 312.F-98-048 (1998)
23. Yadigaroglu, I.-A., & Romani, R. W. 1995, ApJ, 449, 211

DISCOVERY OF A POPULATION OF GAMMA-RAY MILLISECOND PULSARS BY FERMI

L. GUILLEMOT
CNRS/IN2P3, Université de Bordeaux, Centre d'Études Nucléaires de Bordeaux Gradignan, UMR 5797, Gradignan, 33175, FRANCE

We report the discovery of pulsed gamma-ray emission from the 4.86 ms pulsar PSR J0030+0451 with the *Fermi*-LAT telescope. This detection makes PSR J0030+0451 the first to be firmly detected in gamma-rays, after the weak detection of PSR J0218+4232 by EGRET. This very old pulsar (characteristic age of 7.6 10^9 yrs) lowers the empirical spin-down energy lower bound of previously known gamma-ray pulsars by an order of magnitude, with an $\dot{E}$ of 3.5 10^{33} erg/s. The emission profile is reminiscent of younger gamma-ray pulsars, with two sharp peaks, separated by 0.4, and the first peak lagging the radio one by 0.1. The latest weeks of *Fermi*-LAT data though showed that not only do we firmly detect PSR J0030+0451 and confirm PSR J0218+4232, but we also detect pulsations from several other millisecond pulsars. We will review their gamma-ray characteristics and discuss which millisecond pulsars we are seeing. Finally we will discuss the emission of gamma-rays from globular clusters, where millisecond pulsars are known to be abundant.

1 Introduction

1.1 Millisecond pulsars ?

Millisecond pulsars (MSPs) are neutron stars in extremely fast rotation ($P \leq 30$ ms) and with small period derivatives ($\dot{P} \leq 10^{17}$ s/s). Roughly 10% of the pulsars listed in the ATNF catalogue [a] are MSPs [1], located at the lower-left corner of the classical $P - \dot{P}$ diagram [2]. Their high rotational rate is thought to have been acquired by accretion of matter and hence angular momentum from a binary companion [3]. Most MSPs are indeed in binary systems, while less than 1% of normal pulsars are. From the simple description of pulsars as magnetic dipoles in rotation, we know that MSPs are old stars, having characteristic spin-down ages $\tau = P/(2\dot{P})$ of the order of (0.1 - 10) $\times\ 10^9$ yrs. Their characteristic surface dipole magnetic fields $B_{\rm surf} \simeq 3.2$

[a] Available at http://www.atnf.csiro.au/research/pulsar/psrcat/expert.html

$\times\ 10^{19}\ \sqrt{P\dot{P}} < 10^{10}$ G are lower than for the normal population of pulsars, yet the magnetic field strength at the light cylinder $B_{LC} = B_{surf} \times \left(\frac{2\pi R}{cP}\right)^3$ is comparable. Furthermore, the so-called spin-down luminosity $\dot{E} \propto \dot{P}/P^3$ which represents the power output of the pulsar through electromagnetic braking, and hence the available power to be emitted from radio wavelength to gamma-rays, is comparable for MSPs and the normal population of pulsars.

1.2 MSPs at high energy

Of the nearly 170 known MSPs with $P < 30$ ms, 41 are detected as point X-ray sources, including 10 pulsed detections [4]. Although normal pulsars are much more numerous than MSPs, the number of detections reported by the different X-ray telescopes among the two populations is actually equivalent. Before the *Fermi* Gamma-Ray Telescope (FGST) was launched in June 2008, only young pulsars had been detected in gamma-rays [5], though marginal pulsations from PSR J0218+4232 in the EGRET had been reported [6]; and the various theoretical models of gamma-ray emission from pulsars predicted that some MSPs should be detectable by the *Fermi* Large Area Telescope (LAT) [7,8]. A lot of questions thus had to be answered by the LAT: *do MSPs emit gamma-rays? If they do, are the mechanisms of emission the same as for normal pulsars? Are they bright sources of gamma-rays?*

2 A search for gamma-ray MSPs with *Fermi*

2.1 The Large Area Telescope (LAT) and pulsars

The LAT on the *Fermi* spacecraft (formerly GLAST) began operating in June 2008 [9]. In brief, gamma-rays entering the LAT are converted to e^+/e^- pairs in a tracker, yielding direction information. Below the tracker is the calorimeter, giving access to the energy of the incident photon. The LAT is surrounded by an anticoincidence detector, which helps reject the charged cosmic-ray background. The LAT is sensitive to photons with energies below 20 MeV to over 300 GeV. The effective area of 8000 cm^2 at 1 GeV, the angular resolution (0.5° of 68% PSF containment at 1 GeV), the scanning observing mode and the small trigger deadtime of 26.5 μs make the LAT much more sensitive than EGRET. In addition, the timing chain from the GPS-based satellite clocks to the pulsar phase-folding software have been shown to be accurate to a few μs, which is crucial for long-term studies of MSPs [10,11].

Gamma-ray photon data are sparse: the Vela pulsar, which is the brigthest steady source of gamma-rays, triggers the LAT once every 4 minutes on average in survey operation mode. Detecting pulsars in gamma-rays therefore requires weeks to months of continuous observation; representing billions of rotations for MSPs. Accurate knowledge of rotational phase as a function of time is thus essential. We hence began a comprehensive campaign of pulsar timing observations with different radio telescopes around the world, as well as X-ray telescopes [10]. This campaign provided accurate timing for hundreds of pulsars, including MSPs, thought to be promising sources of gamma-ray emission. MSPs are stable pulsars compared to their "normal" cousins, which are usually affected by rotational instabilities (glitches, timing noise). For MSPs, the pulsar timing campaign enabled μs precision of the knowledge of the rotational phase during LAT observations.

2.2 PSR J0030+0451: first firm detection

The 4.86 ms nearby isolated millisecond pulsar J0030+0451 turned out to be the first firm detection ever of an MSP in gamma-rays [12]. The gamma-ray data was acquired during the first months of the *Fermi*'s first-year all-sky survey, from August 3 to November 2. The pulsar is

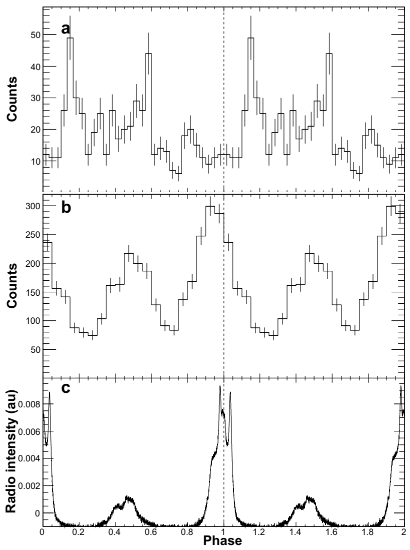

Figure 1: Multi-wavelength phase histograms of PSR J0030+0451. Two rotations are shown for clarity. a: Gamma-ray phase histogram over 100 MeV within an energy dependant ROI. Each bin is 160 μs. b: 20 bin 0.3 - 2.5 keV XMM-*Newton* light curve. c: 1.4 GHz radio profile recorded at Nançay.

outside the Galactic plane ($b = -57.6°$) and is hence in a zone of low background. We phase-folded the 563 events recorded in an energy-dependent region of interest (ROI) using high-quality radio ephemerides (rms of 4 μs) derived from seven hundred Nançay radiotelescope observations between July 1999 and November 2008. The resulting gamma-ray phase histogram is shown in Figure 1. Also shown is the XMM lightcurve that we obtained using the same ephemeris, yielding the first absolute phase alignment of radio, X-ray and gamma-rays for this pulsar. The X-ray and radio components are phase aligned, indicating that these emissions have a common origin in the magnetosphere. Conversely to what we see in X-rays, the gamma-ray profile is shifted by $\delta = 0.15$ relative to the radio; and shows two narrow peaks, separated by $\Delta = 0.44$, similarly to what is seen for normal gamma-ray pulsars, such as Vela, or B1951+32 [5]. The misalignment supports the idea that gamma-rays are produced in a different zone of the magnetosphere, as is assumed by *e.g.* Outer-Gap models [8].

A fit of the emission spectrum with an exponentially cutoff power-law of the form $\frac{dN_\gamma}{dE} = N_0 \left(\frac{E}{10^3 \text{ MeV}}\right)^{-\Gamma} e^{-E/E_c}$ where N_0 is a normalization factor, Γ is the spectral index and E_c is the energy cutoff yields $\Gamma \simeq 1.4$, $E_c \simeq 1.7$ GeV. Integrating over 100 MeV, this leads to photon and energy fluxes of 6.8 $\times 10^{-8}$ ph cm^{-2} s^{-1} and 4.9 $\times 10^{-11}$ ergs cm^{-2} s^{-1} respectively. The spectral properties of PSR J0030+0451 in gamma-rays do not differ fundamentally from what was previously seen for normal pulsars. However, with a spin-down luminosity $\dot{E}$ of 3.5 $\times$ 10^{33} erg/s, this pulsar lowers the empirical $\dot{E}$ threshold for gamma-ray emission by an order of magnitude, compared to PSR B1055$-$52 seen by EGRET [13]. In addition, PSR J0030+0451 seems to break from the trend noted for EGRET pulsars, for which the gamma-ray luminosity is in good approximation inversely proportional to $\sqrt{\dot{E}}$. However this trend is expected to saturate for low $\dot{E}$ pulsars, as they can not convert more than 100% of their spin-down luminosity into gamma-ray emission.

2.3 A whole population of gamma-ray MSPs

Two months worth of data later, PSR J0030+0451 was no longer the only gamma-ray MSP: a comprehensive search for pulsations in the LAT data from 72 galactic field millisecond pulsars

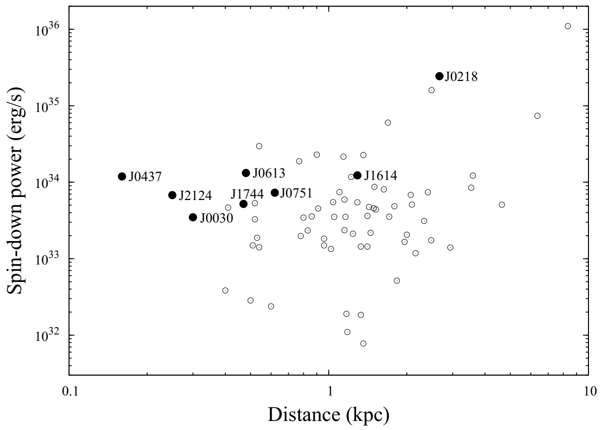

Figure 2: Spin-down luminosity $\dot{E}$ as a function of the distance for the known galactic field millisecond pulsars. Filled dots indicate pulsed gamma-ray detections. When available, parallax distances are used instead of Galactic electron density based distances.

Table 1: Galactic coordinates (l,b), rotational period P, distance D and spin-down luminosity $\dot{E}$ for the detected millisecond pulsars, as of January 2009.

JName	l (°)	b (°)	P (ms)	D (kpc)	$\dot{E}$ (10^{33} erg/s)
J0030+0451	113.1	-57.6	4.865	0.3	3.5
J0218+4232	139.5	-17.5	2.323	2.7	244
J0437−4715	253.4	-42.0	5.757	0.16	11.9
J0613−0200	210.4	-9.3	3.062	0.48	13.2
J0751+1807	202.7	-21.1	3.479	0.62	7.3
J1614−2230	352.54	20.30	3.151	1.29	12.3
J1744−1134	14.8	9.2	4.075	0.47	5.2
J2124−3358	10.9	-45.4	4.931	0.25	6.8

(that is, outside of globular clusters), again based on accurate pulsar ephemerides, led to the discovery of a whole population of pulsed gamma-ray emitters [14]. We confirmed the low-confidence EGRET detection of PSR J0218+4232 [6], a 2.32 ms pulsar in a binary orbit, relatively distant (2.7 kpc) but with a high $\dot{E}$ of 2.4 × 10^{35} erg/s, among the highest of MSPs. We also detected PSR J0437−4715, a nearby MSP in a binary orbit, searched in gamma-rays during the EGRET era, with negative results [15]. In total, we have discovered 8 MSPs in the first 6 months of LAT observations. Figure 2 shows the spin-down luminosity $\dot{E}$ as a function of the distance for the detected MSPs. Table 1 lists some of their properties.

The 8 pulsed detections, shown by filled dots in Figure 2, tend to group towards large values of the so-called spin-down flux $\dot{E}/D^2$, as expected: pulsars with high $\dot{E}$ are likely to convert more energy loss rate into gamma-ray emission. However, it is clear that some of the high $\dot{E}/D^2$ pulsars shown in this plot are missed, which can be interpreted in different ways. First, parallax distances are available for a small number of MSPs, so that distances are often calculated using the NE2001 model of Galactic electron distribution [16], which has proved to be inaccurate in some cases: for example, parallax measurements for J0613−0200 lead to $D = 480^{+190}_{-110}$ pc [17], whereas the NE2001 model gives $D = 1.7$ kpc. Second, the effective detectability of the pulsar in gamma-rays is highly dependent on the viewing geometry: depending on the inclination of the magnetic axis relative to the rotation axis (angle α) and on the inclination of the observer's line-of-sight relative to the rotation axis (angle ζ), the pulsar may radiate little gamma-ray flux towards the observer, if at all [18].

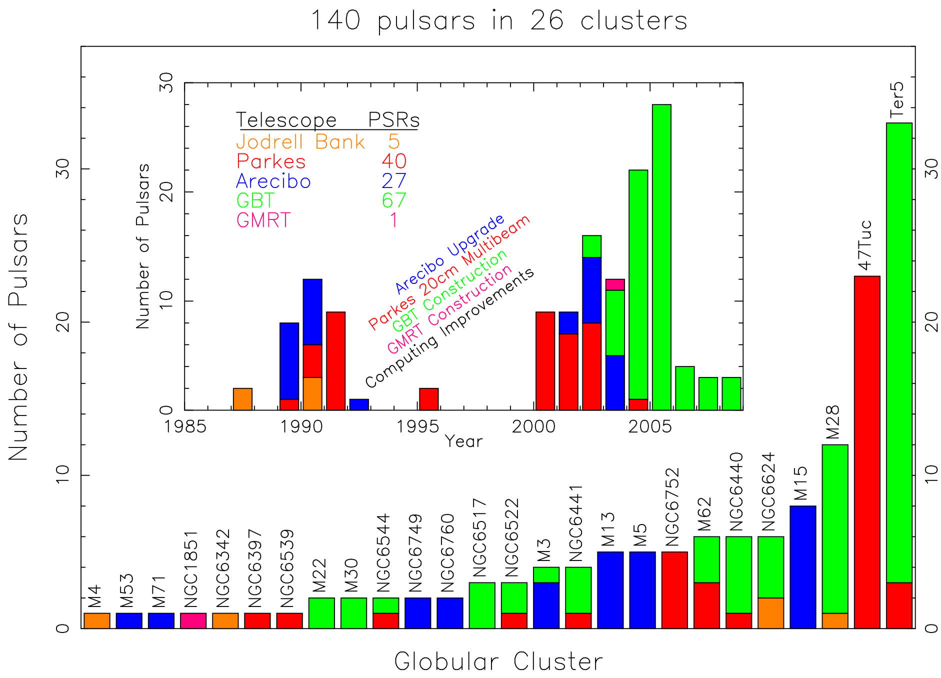

Figure 3: Number of known pulsars in globular clusters, and number of discoveries per year. Courtesy: Scott Ransom (see http://www.naic.edu/ pfreire/GCpsr.html)

3 Prospects

As the LAT continues to accumulate gamma-ray photons in the months to come, the sample of detected gamma-ray MSPs should increase, revealing high $\dot{E}/D^2$ pulsars with unfavourable geometrical configurations or conversely farther and less energetic pulsars with gamma-ray beams pointed towards the Earth. A larger sample of detections should help constrain how MSPs accelerate charged particles to high energies in their magnetosphere, and how MSPs differ from the normal population. Current analyses show that MSP spectral shapes resemble those of young pulsars [14]. In support of gamma-ray observations, precise distance measurements may enhance the interpretation of observed gamma-ray fluxes as well as the non-detections. Polarization observations, which give access to the configuration angles α and ζ, might also help understand which geometrical configurations are preferred for detection, and which ones are not.

In addition to the known galactic field millisecond pulsars, more than 100 MSPs are known in 26 globular clusters [19]. Figure 3 shows the number of known pulsars in globular clusters. The LAT has already detected steady emission from the globular cluster 47 Tuc [20], which is known to contain at least 23 MSPs. There are hence prospects that the LAT may see pulsations from individual MSPs in globular clusters. Finally, the discovery of a whole population of gamma-ray emitting millisecond pulsars strongly suggests that there must be unknown pulsars among the unidentified gamma-ray sources, such as in the *Fermi* Bright Source List [21], that could be searched for pulsations in radio wavelengths.

References

1. R.N. Manchester, G.B. Hobbs, A. Teoh and M. Hobbs, *Astronomical Journal* **129**, 1993 (2005)
2. D.R. Lorimer and M. Kramer, “Handbook of pulsar astronomy”, Cambridge University Press (2004)

3. M.A. Alpar, A.F. Cheng and M.A. Ruderman, *Nature* **300**, 728 (1982)
4. W. Becker, in "Neutron Stars and Pulsars", Astrophysics and Space Science Library **357**, 91 (2009)
5. D.J. Thompson, Reports on Progress in Physics **71**, 116901 (2008)
6. L. Kuiper, W. Hermsen, F. Verbunt, et al., *Astronomy and Astrophysics* **359**, 615 (2000)
7. A.K. Harding, V.V. Usov and A.G. Muslimov, *Astrophysical Journal* **622**, 531 (2005)
8. L. Zhang and K.S. Cheng, *Astronomy and Astrophysics* **398**, 639 (2003)
9. W.B. Atwood, A.A. Abdo, M. Ackermann, et al., *Astrophysical Journal* , submitted (2009)
10. D.A. Smith, L. Guillemot, F. Camilo, et al., *Astronomy and Astrophysics* **492**, 923 (2008)
11. A.A. Abdo, et al. (*Fermi*-LAT Collaboration), *Nuclear Instruments and Methods* , submitted (2009)
12. A.A. Abdo, et al. (*Fermi*-LAT Collaboration), *Astrophysical Journal* , accepted (2009)
13. D.J. Thompson, M. Bailes, D.L. Bertsch, et al., *Astrophysical Journal* **516**, 297 (1999)
14. A.A. Abdo, et al. (*Fermi*-LAT Collaboration), *Science* , in prep. (2009)
15. J.M. Fierro, Z. Arzoumanian, M. Bailes, et al., *Astrophysical Journal* **447**, 807 (1995)
16. J.M. Cordes and T.J.W. Lazio, arXiv:astro-ph/0207156v3 (2002)
17. A.W. Hotan, M. Bailes and S.M. Ord, *Monthly Notices of the Royal Astronomical Society* **369**, 1502 (2006)
18. K.P. Watters, R.W. Romani, P. Weltevrede and S. Johnston, *Astrophysical Journal* , in press (2009)
19. F. Camilo and F.A. Rasio, *ASP Conf. Ser.* **328**, 147 (2005)
20. A.A. Abdo, et al. (*Fermi*-LAT Collaboration), *Science* , in prep. (2009)
21. A.A. Abdo, et al. (*Fermi*-LAT Collaboration), *Astrophysical Journal* , submitted (2009)

DETECTION OF THE CRAB PULSAR WITH THE MAGIC TELESCOPE

M. LÓPEZ MOYA[1],
N. Otte[2,3], M. Rissi[4], M. Shayduk[2], T. Schweizer[2] for the MAGIC Collaboration
[1]*Istituto Nazionale di Fisica Nucleare, Sezione di Padova, I-35131 Padova, Italy,*
[2]*Max-Planck-Institut für Physik, D-80805 München, Germany,*
[3]*Santa Cruz Institue for Particle Physics, University California, Santa Cruz, CA 95064, USA,*
[4]*Swiss Federal Institute of Technology, CH-8093 Zürich, Switzerland*

For the first time, pulsed γ-rays above 25 GeV from the Crab pulsar have been detected with the MAGIC telescope [1]. The MAGIC measurements reveal that the drop-off in the emitted radiation occurs at relatively high energies, which indicates that the emission must occur far out in the Crab pulsar's magnetosphere. All models in which the emitting region is located close to the Crab pulsar's surface are ruled out by the MAGIC results.

1 Introduction

The mechanism of the pulsed electromagnetic emission in the Crab pulsar is still an open fundamental question. Observations with the EGRET instrument on-board *Compton Gamma-Ray Observatory* [2] led to the detection of the Crab pulsar up to energies of $\sim$ 10 GeV, in addition to other six γ-ray pulsars and a few more likely candidates [3] (recently confirmed by the Fermi Gamma-ray Space Telescope, see [4]). In their turn, all the groups operating Cherenkov telescopes have been trying during the last 30 years to detect the Crab pulsar without success, being only the steady emission coming from its nebula visible at TeV energies. This suggested that the Crab pulsed spectrum should terminate at energies of tens of GeV. Although the existence of a sharp cutoff in the spectrum of pulsars is a common prediction of the different theoretical models, the energy at which this cutoff happens and its spectral features change from model to model. In the polar cap model, electrons are accelerated above the polar cap radiating γ-rays via synchro-curvature radiation. Since these γ-rays are created in superstrong magnetic fields, magnetic pair production is unavoidable, and hence, only those secondary photons which survive pair creation (a few GeV for typical pulsars) escape to infinity as an observed pulsed emission. A natural consequence of the polar cap process is a superexponential cutoff of the spectrum above a characteristic energy E_0. In the outer gap model γ-ray production is expected to occur near the light cylinder of the pulsar, far away from the stellar surface. In this case the cutoff is determined by photon-photon pair production, which has a weaker energy dependence compared to magnetic pair production, and therefore a higher energy cutoff may be observable.

Thanks to its low energy threshold, MAGIC is the first ground-based γ-ray telescope able to overcome the sharp cutoffs expected near 10 GeV and detect pulsed γ-rays. This allows to measure the spectral shape of the pulsed emission in the relevant energy range, and therefore to discriminate between different emission models.

2 The MAGIC Telescope

The 17 m diameter MAGIC telescope, located on the Roque de los Muchachos Observatory (La Palma island, Spain), is currently the largest single-dish Cherenkov telescope in operation. MAGIC detects the faint flashes of Cherenkov light produced when γ-rays (or cosmic-rays) plunge into the earth atmosphere and initiate showers of secondary particles. The Cherenkov light emitted by the charged secondary particles is reflected by the telescope mirror and an image of the shower is obtained in the telescope camera. An offline analysis of the shower images allows the rejection of the hadronic cosmic ray background, the measurement of the incoming direction of the γ-rays, and the estimation of their energy. MAGIC can reach a sensitivity of 1.6% Crab in 50 hours of observation. The relative energy resolution above 100 GeV is better than 30% and the angular resolution is $\sim 0.1°$. The construction of a second telescope is now in its final stage and MAGIC will start stereoscopic observations in the coming months.

The MAGIC telescope was built with the aim of achieving the lowest possible energy threshold, and since 2004 it operates with the lowest threshold worldwide, namely ~ 50 GeV. However, this threshold turned out to be still too high to get a clear signal from the Crab pulsar [7]. This lead the MAGIC collaboration to build an innovative trigger concept with allowed us to reduced the threshold by a factor of 2. This new trigger is based on the analogue summation of the signals coming from clusters of 18 pixels, instead of discriminating single PMT signals (as it is done in the MAGIC standard trigger) [8].

3 Observations and data analysis

The observations of the Crab pulsar with the new trigger system were performed between October 2007 and February 2008. Together with each event image we recorded the absolute arrival time of the corresponding cosmic-ray with a precision of better than 1 μs from a GPS receiver, and we recorded simultaneously also the optical signal of the Crab pulsar with a special PMT located at the camera center [9]. After rejection of data taken under unfavorable weather conditions, 22.3 hours of observation remained for the analysis. We processed the data with three independent analysis chains, which all gave consistent results. In the analysis, each shower image is cleaned to remove the influence of the night sky background, and parameterized to describe its main features. One image parameter is the brightness of the image (SIZE) in photoelectrons, which is a good estimator of the energy of the primary particle. Other parameters are the orientation of the image with respect to the source position in the camera (angle ALPHA), and several additional parameters, which describe the shape of the image. We apply soft hadron rejection cuts, consisting basically in a cut in SIZE to select only low energy showers, and a SIZE dependent cut in ALPHA optimized on simulated Monte Carlo γ-ray events. For the search of pulsed emission, the arrival time of each event was transformed to the barycenter of the solar system, and the corresponding rotational phase of the Crab pulsar where calculated using contemporaneous ephemeris provided by the Jodrell Bank Radio Telescope [10].

4 Results and discussion

In figure 1 we compare our pulse phase profiles in γ-rays above 25 GeV and in the optical waveband with the measurements from the EGRET instrument above 100 MeV. In all profiles a pronounced signal is visible at the position of the main pulse (at phase 0) and at the position of the inter pulse. The significance of the pulsed signal in the γ-ray data was evaluated by three different methods. The first method is a single hypothesis test and assumes that γ-ray emission is expected in two phase intervals around the main pulse and inter pulse, respectively. For the selection of the two signal intervals we adopt the definition of the main pulse (phase -0.06 to

0.04) and inter pulse (phase 0.32 to 0.43) given by [11]. The background is estimated from the remaining events outside of the intervals. In this way we obtain a significance of 6.4 σ. The other tho methods are uniformity tests: the H-Test [12] (a periodicity test that is commonly used for periodicity searches) and the well known Pearson's χ^2 that tests the null hypothesis that the pulse profile follows a uniform distribution, both given a similar significance.

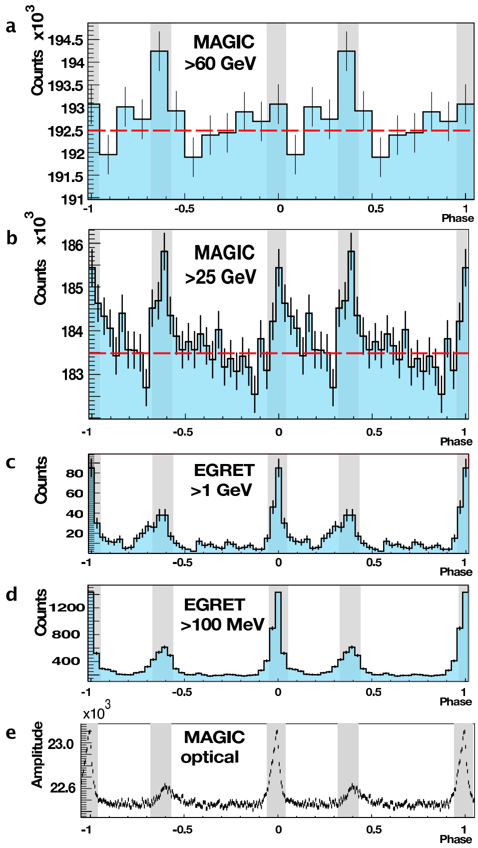

Figure 1: Crab pulsed emission in different energy bands. The shaded areas show the signal regions for P1 and P2, as defined in [11]. The optical emission measured by MAGIC with its central pixel was recorded simultaneously with the γ-rays. P1 and P2 are in phase for all shown energies and the ratio of P2/P1 increases with energy from (D) to (A).

To evaluate the cutoff energy we extrapolate the energy spectrum measured by EGRET (between 100 MeV and 1 GeV) [11] to higher energies, assuming two different cutoff shapes. If we assume an exponential cutoff (Flux$\times \exp(-E/E_0)$), the measured signal is compatible with a cutoff energy E_0 of $17.7 \pm 2.8_{\text{stat}} \pm 5.0_{\text{sys}}$ GeV. In case the cutoff is superexponential (Flux$\times \exp(-E/E_0)^2$) we determine a cutoff energy of $23.2 \pm 2.9_{\text{stat}} \pm 6.6_{\text{sys}}$ GeV. Figure 2 shows the Crab pulsar spectrum with the cutoffs obtained in this work, compared to different theoretical predictions. The values obtained for the cutoff energy are higher than expected, which allow us to draw important conclusions about the mechanism of γ-ray emission in the Crab pulsar. Using equation 1 of [13] that relates the location of the emission region, r, with the cutoff energy, one obtains for the polar cap scenario $r/R_0 > 6.2 \pm 0.2_{\text{stat}} \pm 0.4_{\text{sys}}$ (where R_0 is the neutron star radius). This contradicts the basic picture of polar cap scenarios in which γ-rays are emitted very close to the pulsar surface.

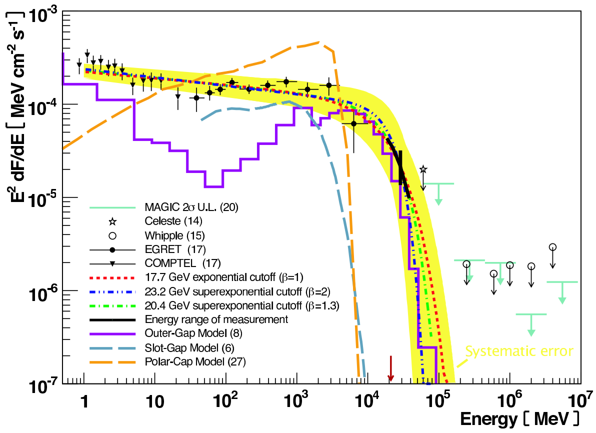

Figure 2: Crab pulsar spectrum. The solid circles and triangles on the left represent flux measurements from EGRET, while the arrows on the right denote upper limits from various previous experiments. We performed a joint fit of a generalized function F(E) $=AE^{-a}exp[-(E/E0)b]$ to the MAGIC and EGRET data. The figure shows all three fitted functions for b = 1 (red line), b = 2 (blue line), and the best-fit, b = 1.2 (green line). The black line indicates the energy range, the flux, and the statistical error of our measurement. The yellow band illustrates the joint systematic error of all three solutions.

5 Conclusions

We succeeded in the detection of pulsed γ-rays from the Crab pulsar with the MAGIC Cherenkov telescope above 25 GeV. This brought to success a 30 year-long effort of ground based γ-ray instruments to detect a pulsar at VHE γ-rays. The detection was possible after upgrading the trigger system, which substantially reduced the trigger threshold from about 50 GeV to about 25 GeV. The significance of the pulsed signal is 6.4 σ. We determine the cutoff in the energy spectrum at $17.7 \pm 2.8_{\mathrm{stat}} \pm 5.0_{\mathrm{sys}}$ GeV assuming that the cutoff is exponential in shape. The cutoff energy shifts to $23.2 \pm 2.9_{\mathrm{stat}} \pm 6.6_{\mathrm{sys}}$ GeV if the cutoff is superexponential. The high value of the cutoff, and a marginally better fit with a simple exponential hint at an acceleration region located at high altitude in the magnetosphere. We also find that the main pulse and inter pulse in the pulse profile have about equal peak amplitudes in our energy range.

1. E. Aliu et al., *Science* **322** 1221 (2008)
2. D. J. Thompson, *ApJS* **86** 629 (1993)
3. D. J. Thompson, 2001, in proceedings of *International Symposium*, Heidelberg June 2000, F.A Aharonian, H.J. Völk American Institute of Physics 558, 103.
4. L. Guillemot, these Proceedings.
5. J. K. Daugherty & A.K. Harding, *ApJ* **458** 278 (1996)
6. K. Hirotani, *ApJ* **549** 495 (2001)
7. J. Albert et al., *ApJ* **674** 1037 (2008)
8. M. Rissi et al., in proceedings of *2008 Nuclear Science Symposium*, Dresden, Germany, October 2008
9. F. Lucarelli et al., *Nucl. Instrum. Methods* **589** *415 (2008)*
10. http://www.jb.mac.ac.uk/pulsar/∼crab.html
11. *J.M. Fierro et al, ApJ* **494** *734 (1998)*
12. *O.C. de Jager, J.W.H. Swanepoel, B. Raubenheimer,* A&A **170** *187 (1989)*
13. *M.G. Baring,* Adv. Space Res. **33** *442 (2004)*

Early *Fermi*-LAT observations of the Vela pulsar

M. RAZZANO, on behalf of the *Fermi* LAT Collaboration
Istituto Nazionale di Fisica Nucleare, Sezione di Pisa, I-56127 Pisa, Italy

The Vela pulsar is one of the first targets of the Large Area Telescope, the main instrument aboard the *Fermi* Gamma-ray Space Telescope, successfully launched in June 2008. I will report on the main results coming out from the early observations of this pulsar during the first months following the launch of *Fermi*. During this period the LAT collected $\sim$ 32400 pulsed photons above 0.03 GeV and the light curve shows structures as sharp as 0.3 ms, as a result of the high timing resolution of the LAT combined with the high-quality radio ephemerides provided during the radio monitoring campaign. The study of the light curve at different energies shows that the pulse profile evolves with time, revealing a third peak at high energy. The study of the off pulse component has been useful for putting limits on the steady plerionic emission. Moreover, the analysis of the spectrum provides a much more improved measurement of the high-energy cutoff, one of the most powerful tools for constraining scenarios of gamma-ray emission in pulsars.

1 Introduction

The Vela pulsar is the brightest persistent point source in the gamma-ray sky. Because of its brightness, this source is the best studied gamma-ray pulsar, together with Crab and Geminga. Gamma-ray pulsars are believed to contribute substantially to the galactic population of EGRET unidentified sources [13], but so far only few of them have been firmly identified [6]. Gamma-ray pulsars are one of the most important targets for the recently launched *Fermi* Gamma-ray Space Telescope (previously known as GLAST). *Fermi* is an international space mission devoted to the study of the high-energy cosmic gamma-rays and carries two main instruments, the Large Area Telescope (LAT) [1] and the Gamma-ray Burst Monitor (GBM). The Large Area Telescope (LAT) is a pair-conversion telescope designed for the detection of gamma rays from <30 MeV to > 300 GeV [1]. The Vela pulsar (PSR B0833-45, PSR J0835-4510) has been one of the primary targets for *Fermi* after its successful launch of 11 June 2008. Because of its brightness, Vela is a classical target for first observations of gamma-ray space telescopes and for calibration and tuning of the instruments. This pulsar was discovered as a radio source with period of P=89 ms in the Vela supernova remnant [9]. It is bright ($S_{1.4GHz} \sim 1.5$ Jy), is surrounded by an X-ray nebula and is immersed in a radio synchrotron nebula From spin parameters it is possible to estimate the basic characteristics of the pulsar, that turns out to be quite young, with a characteristic age $\tau_c = \frac{P}{2\dot{P}} \sim 11$ kyr, and energetic, with a spin-down luminosity $\dot{E}_{SD} = 6.9 \times 10^{36} I_{45}$ erg/s[a]. The Vela pulsar is located at a distance of D = 287 pc, as based on recent VLBI parallax measurements [3]. Vela was detected as a gamma-ray emitter during the SAS-2 mission [12] and shows two peaks separated by 0.42 in phase, and past missions showed evidence of a cutoff in the range 2-4 GeV. Moreover, the Vela pulsar is one of the best targets for measuring high-energy cutoff, the most sensitive tool to test pulsar gamma-ray emission models [4].

2 LAT observations of the Vela pulsar

The initial observations of the Vela pulsar were based on 35 days of on-orbit verification tests and the initial ~ 40 days of the on-going first year sky survey. We report here the results based on this initial observations, and more details can be found at [2]. During the initial period of the *Launch and Early Orbits Operations*, the instrument configuration was being tuned for optimum performance and the results of these studies were used to verify the LAT photon selection, effective area, timing, photon energy measurement and the variation of the Point Spread Function (PSF) with energy. Since the Vela pulsar is young, it exhibits substantial timing irregularities, then it is necessary to have contemporary radio ephemeris. The radio ephemeris is obtained using observations made with the 64-m Parkes radio telescope as part of the overall program of pulsar timing in support of the *Fermi* mission [11]. Fitting the Time Of Arrivals (TOAs) obtained at Parkes lead to a timing solution with an phase with an rms residual of 90 μs throughout the LAT observations. Photon arrival times were referred to the Solar-System barycenter and pulse phases were assigned using the standard pulsar timing software TEMPO2 [7].

3 Vela pulse profile

In order to optimize the extraction of photons from the Vela pulsar, we adopt an energy-dependent Region Of Interest (ROI), defined by an angle $\theta <$ Max[1.6 − 3Log10(EGeV), 1.3] degrees from the pulsar position. This includes a larger fraction of the PSF at high energies, where the background is relatively faint. We use the $Diffuse$ class events, those reconstructed events having the highest probability of being photons. Using such a cut we collect 32,400±242 pulsed photons and 2780±53 background photons with measured energy > 0.03 GeV. Fig. 1 shows the 0.1-10GeV pulse profile from this energy-dependent cut using variable-width bins of 200 counts in order to highlight fine structures. From this light curve it is possible to see two main asymmetric peaks P1 and P2, respectively at phases $\phi = 0.130 \pm 0.001$ and $\phi = 0.562 \pm 0.002$. The outer edges of the two peaks had consistent Lorentzian half-widths of $\phi = 0.012 \pm 0.001$, while the falling edge of P1 has a Lorentzian half width of $\phi = 0.017 \pm 0.0015$, while the rising edge of P2 has a width $\phi = 0.027 \pm 0.005$. Thanks to the large energy range of the LAT, we can build energy-dependent light curves in order to see the evolution of the pulse shape with energy, as shown in 1. The main feature that can be distinguished is a decrease of P1 relative to P2 with increasing energy; P1 is not detectable above $\sim$ 10GeV. This confirms a trend seen in the EGRET data for the Crab, Vela and Geminga pulsars. The second pulse dominates at the highest energies, while interestingly at the lower energies, below $\sim$ 120MeV, the trend is reversed with P1 weakening again with respect to P2, with no statistically significant evidence for shifts in the phases of the P1 and P2 pulse components with energy. The next important feature is a distinct third peak at E > 1 GeV (P3) at ϕ 0.27 in the 3-10GeV band, which is

[a] Assuming a neutron star moment of inertia $I_{45} = 10^{45}$ g cm^2

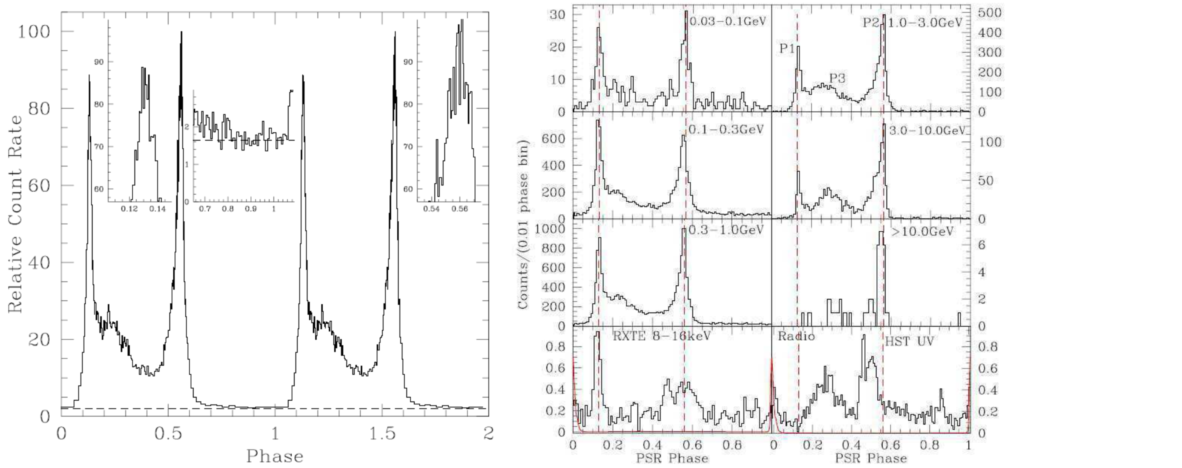

Figure 1: Right: Vela pulsar light curve for E 100 MeV. The dashed line shows the background level, as estimated from a surrounding annulus during the off-pulse phase. Insets show the pulse shape near the peaks and in the off-pulse region. Left: Energy-dependent light curve of the Vela pulsar, compared with X-rays and UV light curve. Each LAT pulsar profile is binned to 0.01 of pulsar phase, and dashed lines show the phases of the P1 and P2 peaks determined from the broad band light curve.

shifting in phase by $\delta\phi \sim 0.14$ between 0.2 and 15GeV and is present in the shoulder of P1 at $E < 1$ GeV. Comparing with lower energies, we show also in Fig. 2 the 8-16 keV non-thermal X-ray pulse measured by RXTE [5] and the 4.1-6.5 eV NUV HST STIS/MAMA pulse profile [10]. Comparing those with the gamma-ray profile, we note that P1 is dominant in the non-thermal X-rays, while it is absent in the optical/UV, but pulse profiles at these energies have a strong peak in the bridge region at $\phi \sim 0.25$, well matched in phase to the P3 structure in the GeV pulse profiles.

4 The spectrum of the Vela pulsar

We studied the phase-averaged spectrum of Vela using a standard maximum-likelihood spectral estimator, provided with the Fermi SSC science tools. This fits a source model to the data, along with models for the isotropic (instrumental and extragalactic) and structured Galactic backgrounds, comparable with pre-launch simulation [1]. The basic model is a simple power law with exponential cutoff. With the large number of events collected for Vela, the statistical errors are very small, while systematic errors are still under investigation and we adopt conservative estimates of the systematic uncertainty in the LAT effective area, derived from the on-orbit estimation of the photon selection efficiency as function of energy and offaxis angle. This varies from < 10% near 1 GeV to as much as 20% for energies below 0.1 GeV and 30% for energies greater than 10 GeV. The fit results is:

$$\frac{dN}{dE} = (2.08 \pm 0.04 \pm 0.13) \times 10^{-6} E^{-1.51 \pm 0.01 \pm 0.07} \exp[-(E/(2.857 \pm 0.089 \pm 0.17 GeV))^{b}] ph/cm^{2}/s/GeV \quad (1)$$

The first errors are the statistical values for the fit parameters, while the second errors are our propagated systematic uncertainties. The results have been compared using 3 different methods: a standard XSPEC analysis with our best model response matrices, a binned maximum likelihood estimator which computes the on-pulse photon counts in a point source weighted aperture in excess of off-pulse background counts (ptlike) and a method which propagates the model spectrum through simulated instrument response to compare with observed pulsed source counts. The resulting spectrum is shown in Fig. 2 as E^2 dN/dE along with this best fit model. In Fig. 2 we show also the EGRET points [8]: some studies have indicated that the EGRET response

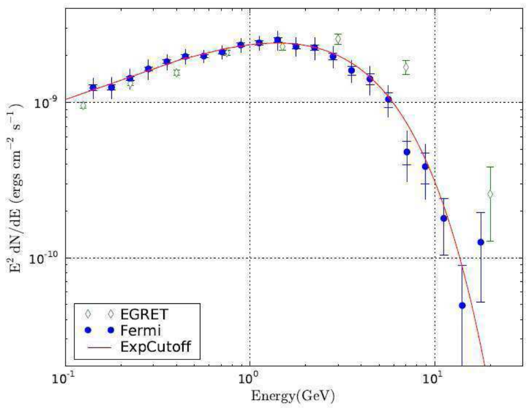

Figure 2: The phase-averaged Vela spectral energy distribution, with statistical (capped) and systematic (uncapped) errors depicted. EGRET data points are shown for comparison. The curve is the best-fit power law with a simple exponential cut-off.

was incorrectly estimated and this could explain the discrepancy with our data [2]. Trying to fix with a free exponential index b gives us an exponential index $b = 0.88 \pm 0.04^{+0.24}_{-0.52}$ so that models with a hyper-exponential behavior are well excluded and the spectrum is fully consistent with the simple exponential $b = 1$ cut-off.

5 Conclusions

We present here some highlight of the main results coming from the early observation of the Vela pulsar by the LAT [2]. The observation performed during the calibration and instrument tuning and during the first months provided a large amount of photons much higher than previous missions. The analysis of the pulse profile with energy confirmed the trend of the ratio P1/P2 and provided the evidence of a third peak at high energies, which shifts in phase with energy. The study of the phase averaged spectrum show for the first time a full coverage of the energy cutoff, that has been modeled as an exponential cutoff, providing a strong constraint favoring the outer magnetosphere emission models. In order to better use Vela pulsar as a tool for constraining theoretical models, is thus necessary to collect more data and study the detailed evolution of the spectrum with the phase.

References

1. Atwood, W. B., et al. 2009, ApJ, accepted.
2. Abdo, A. A., et al. 2009, ApJ, accepted, arXiv:0812.2960
3. Dodson, R. et al. 2003, ApJ, 596, 1137
4. Harding, A. K. 2001, American Institute of Physics Conference Series, 558, 115
5. Harding, A. K., Strickman, M. S., Gwinn, C., Dodson, R., Moffet, D., & McCulloch, P. 2002, ApJ, 576, 376
6. Hartman, R. C., et al. 1999, ApJS, 123, 79
7. Hobbs, G. B., Edwards, R. T., & Manchester, R. N. 2006, MNRAS, 369, 655
8. Kanbach, G., et al. 1994, A&A, 289, 855
9. Large, M.I., Vaughan, A.E. & Mills, B.Y. 1968, Nature, 220, 340
10. Romani, R. W., Kargaltsev, O., & Pavlov, G. G. 2005, ApJ, 627, 383
11. Smith, D. A., et al. 2008, A&A, 492, 923
12. Thompson, D. J., Fichtel, C. E., Kniffen, D. A., & Ogelman, H. B. 1975, ApJL, 200, L79
13. Yadigaroglu, I.-A., & Romani, R. W. 1995, ApJ, 449, 211

FERMI OBSERVATIONS OF PSR J2021+3651: NEW INSIGHT ON THE DISTANCE QUESTION

M. T. KERR
Department of Physics, University of Washington
Seattle, WA, United States

We report on observations of the young gamma-ray pulsar PSR J2021+3651 with the Large Area Telescope (LAT) of the Fermi Gamma-ray Space Telescope (*Fermi*). The measured high energy gamma-ray (HE) spectrum is consistent with the form $\frac{dN}{dE} = kE^{-\Gamma}\exp(-\frac{E}{E_c})$, with $\Gamma = 1.5 \pm 0.1 \pm 0.1$, $E_c = 2.4 \pm 0.3 \pm 0.5$ GeV, and an energy flux above 100 MeV of $h = 4.3 \pm 0.1 \pm 0.9 \times 10^{-11}$ erg cm^{-2} s^{-1}. The light curve morphology and spectral characteristics imply outer magnetospheric (OM) emission. Data from radio, X-ray, and HE observations consistently imply the pulsar is a nearly-orthogonal rotator. For this geometry, OM emission models predict a beaming factor $f_\Omega \equiv L_\gamma/4\pi h D^2 \approx 1.1$. The measured HE efficiency is $\eta = L_\gamma/\dot{E} = 0.25 f_\Omega (D/4\text{kpc})^2$. Comparison with the efficiency of other young pulsars suggests a distance consistent with that inferred from X-ray observations, 1-4 kpc. The large observed dispersion measure ~ 371 pc cm^{-3} remains unexplained by such small distances without an additional source of electrons along the line of sight.

1 Discovery

Although much is now known about the pulsar J2021+3651, the tale of its discovery and characterization is a rich demonstration of multiwavelength astronomy. The first sign of emission consistent with the known location of PSR J2021+3651 was detected as 2CG 075+00 by COS-B[3], and the third EGRET catalog[4] provided a much improved localization for the spatially coincident source 3EG J2021+3716. At the end of the EGRET era, pulsars remained the only firmly identified Galactic GeV class, and many low latitude unidentified EGRET sources were targeted for radio pulsation searches. To reconcile the mismatch between the large EGRET error boxes and the small radio telescope beams, Roberts et al. followed up instead on fields from a catalog of unidentified ASCA X-ray sources[1] within EGRET error circles. They discovered PSR J2021+3651 in one of the five ASCA fields[2] coincident with the EGRET source.

2 Radio Observations

Initial observations[2] with the Wideband Arecibo Pulsar Processor revealed a young $\tau_c \sim 17$ kyr and energetic $\dot{E} \sim 3.4 \times 10^{36}$ erg s^{-1} rotation-powered pulsar. The large dispersion measure DM ~ 371 pc cm^{-3} suggested a distance of 12 kpc using the NE2001 model of the Galactic free electron distribution[5]. It was noted that the observed gamma-ray flux from 3EG J2021+3716, if associated with the pulsar, implied an efficiency of 15% at 10 kpc using a 1sr emission beam, making it much more efficient than other observed young pulsars.

Recent observations associated with the timing campaign described below[9] furnish additional

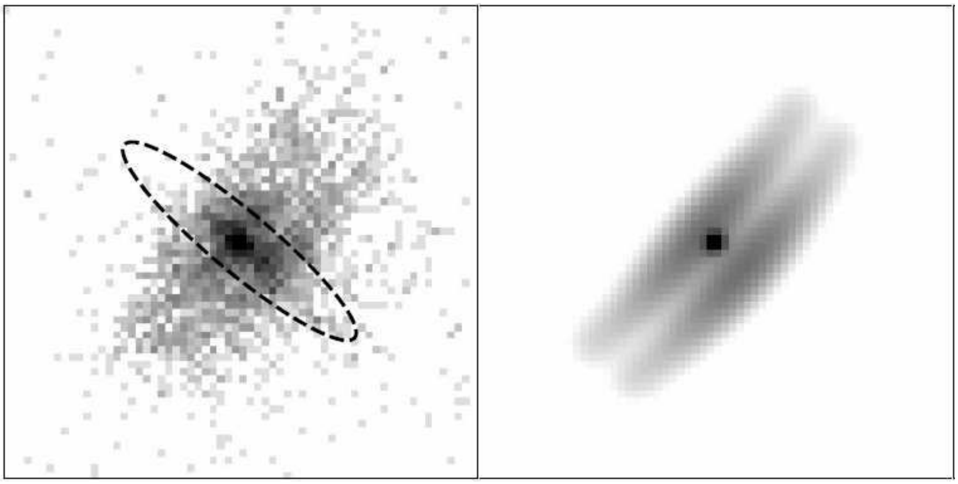

Figure 1: The Dragonfly Nebula and the (double) torus best fitting the *Chandra* counts data[8].

details[13]. In particular, a faint interpulse is detected, supportive of a picture of the pulsar as a nearly-orthogonal rotator, i.e. $\zeta \approx 90°$ and $\alpha \approx 70°$ with ζ the inclination of the pulsar spin axis to the line of sight and α the inclination of the magnetic axis from the spin axis. Polarization measurements, although from a duty cycle too short to constrain the geometry via the rotating vector model, are consistent with this geometry. The rotation measure (RM) obtained is 524 ± 4 rad m^{-2}.

3 X-ray Characteristics

The relativistic particle wind of young pulsars often powers a synchrotron pulsar wind nebula (PWN), and the discovery of a new young pulsar associated with HE emission made PSR J2021+3651 a natural target for *Chandra* observation. In addition to providing valuable probes of the relativistic wind, the high degree of symmetry of some PWN provides a measure of ζ and perhaps of α[6]. Hessels et al. obtained a 19.0 ks ACIS-S exposure[7]. They found an X-ray point source embedded in a symmetric double-torus PWN (G75.2+0.1) reminiscent of that of the Vela pulsar (see Figure 1). From the torus morphology, they inferred a spin axis inclination of $83° \pm 1°$. Their spectral measurements of the neutron star and the nebula implied a hydrogen column density of $(7.8^{+1.7}_{-1.4}) \times 10^{21}$ cm^{-2}, indicating a distance somewhat less than that implied by the DM. They further pointed out that scaling the PWN size to that of Vela, plausible given the similarity the two pulsars, would yield a distance of only 1.5 kpc.

Later observations by van Etten et al.[8] with a much longer 93.2 ks *Chandra* exposure revealed the rich morphology of the PWN; it was christened the "Dragonfly". They robustly measured the spin axis inclination $\zeta = 86° \pm 1°$. With improved spectra for the neutron star and the PWN, they made scaling, efficiency, and thermal spectrum arguments for a distance of 1-4 kpc.

4 Fermi Observations

PSR J2021+3651 is one of the 224 high-$\dot{E}$ pulsars monitored as part of the joint campaign[9] between the radio and X-ray timing communities and the LAT[14] Collaboration. Using an ephemeris furnished by the NRAO Green Bank Telescope to fold the LAT photon arrival times, pulsations were detected within the first month of data taking.

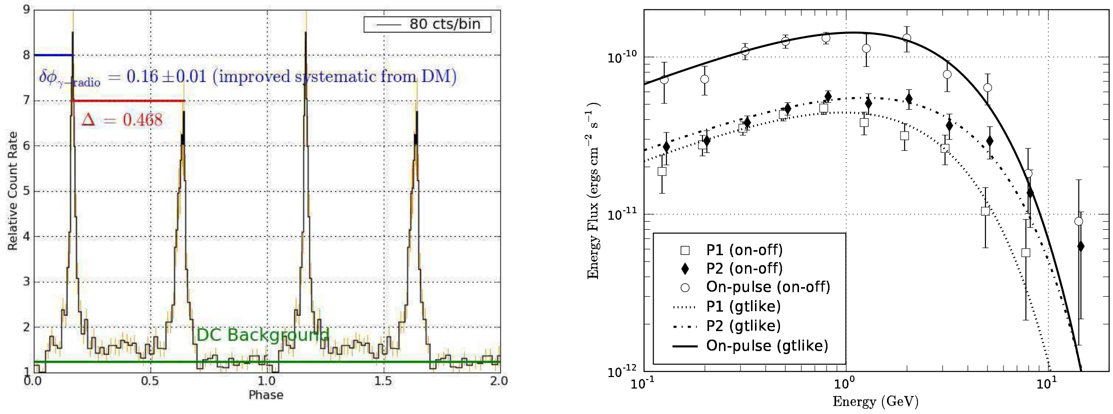

Figure 2: *Left*—Two cycles of pulsed photons in a constant photon count histogram. The lag between the radio peak and first gamma-ray peak is indicated as $\delta_r = 0.16 \pm 0.01$, while the peak separation is measured as $\Delta = 0.468$. Bridge emission is visible above the background. *Right*—The spectrum for P1 (0.13 - 0.20 cycles), P2 (0.58 - 0.68 cycles), and total pulsed (0.05 to 0.73 cycles) emission. The curves have been fit with the unbinned likelihood tool *gtlike*, while the data points are estimated with *on-off*.

4.1 Pulsations

The light curve (Figure 2) is reminiscent of that of Vela[12], showing two sharp peaks (of probable caustic origin) separated by < 0.5 cycles and lagging the radio peak by ≈ 0.1 cycles. The light curve is an important diagnostic of the pulsar beam. Watters et al. have assembled an "atlas"[10] that maps, under a given HE emission model, parameters such as the numbers of peaks and peak separation onto the most likely spin axis and magnetic axis inclinations. For this light curve, the inferred geometry is consistent with a nearly-orthogonal rotator.

4.2 Spectra

The Cygnus region is host to many gamma-ray point sources as well as a bright, structured diffuse emission stemming from trapped Galactic cosmic rays. To verify our spectral results, we used *gtlike* (an unbinned likelihood analysis employing a physics-based model of the diffuse emission), *on-off* (a joint likelihood technique that estimates the background from offpulse), and *unfolding* (an analysis using an aperture estimation of the background). All results are consistent. The spectral energy density for the pulsed emission, as well as for the two peaks, is shown in Figure 2.

We find a spectrum well-described by a power law with an exponential cutoff, $\frac{dN}{dE} = kE^{-\Gamma}\exp(-\frac{E}{E_c})$. For the pulsed emission, we find a photon index of $\Gamma = 1.5 \pm 0.1 \pm 0.1$, a cutoff energy $E_c = 2.4 \pm 0.3 \pm 0.5$ GeV, and an energy flux above 100 MeV of $h = 4.3 \pm 0.1 \pm 0.9 \times 10^{-11}$ erg cm^{-2} s^{-1}, where the former (latter) errors are statistical (systematic). Since Polar Cap models predict strong magnetic attenuation of the HE signal above a few GeV[11], the observation of a gentle cutoff and emission above 10 GeV indicate OM emission is dominant for this pulsar. While this result is interesting in its own right, it is the preference for OM emission and its characteristic fan beams that is of interest for our discussion on distance as we shall see below.

4.3 Beaming

Constraints from the X-ray torus, the radio polarization, and the gamma-ray light curve allow a robust estimation of the beam geometry for the pulsar[10]. The geometry is reflected by the model-dependent factor relating the observed flux to the total luminosity,

$$L_\gamma = 4\pi f_\Omega(\alpha,\zeta) h_\gamma D^2. \tag{1}$$

For the inferred geometry ($\alpha = 70°,\ \zeta = 85°$), both the Outer Gap and the Slot Gap models predict fan-like beams, i.e., they illuminate (nonuniformly) a large fraction of the sky, and $f_\Omega \approx 1.1$. The Polar Cap model, on the other hand, predicts $f_\Omega \leq 0.1$, more in line with the traditional assumption of a 1 sr narrow beam. The value of the geometrical information is clear: we revise our luminosity prediction upward by an order of magnitude! Scaling the observed flux to a $D_4 \equiv D/4\text{kpc}$, the efficiency for the conversion of spindown energy into HE emission is

$$\eta = L_\gamma/\dot{E} = 0.25 f_\Omega D_4^2. \tag{2}$$

5 Discussion

The gamma-ray observations add a vital piece of information to the question of the pulsar distance. As we see from Eq. 2 with an OM emission model ($f_\Omega \approx 1$), the efficiency reaches 100% at ~ 8 kpc, providing an upper limit on the distance. Further, if emission from this pulsar is similar to that from Vela, as its radio timing and HE light curve suggest, then its efficiency should be on the order of a few percent [12]. This suggests a distance consistent with the lower range of those preferred by the X-ray observations, 1-2 kpc.

However, as noted by Roberts et al.[2], Hessels et al.[7], and Van Etten et al.[8], no obvious source of excess electrons (relative to the NE2001 model) along the line of sight presents itself. The open cluster Berkeley 87, centered only 0.5° from the line of sight, has been suggested as a source for some of the observed DM[13].

The resolution of this discrepancy between X-ray and gamma-ray efficiency and radio propagation in the ISM is important for many aspects of pulsar study. The majority of pulsar distances are estimated with the NE2001 model and a significant revision impacts the distribution of pulsars both in spatial coordinates and in luminosity. Measurements of gamma-ray pulsars such as PSR J2021+3651, especially with the new paradigm of fan beam emission, will continue to place important constraints on the pulsar distances.

References

1. Roberts, M. S. E., Romani, R. W., & Kawai, N. 2001, *ApJS*, 133, 451
2. Roberts, M. S. E., Hessels, J. W. T., Ransom, S. M., Kaspi, V. M., Freire, P. C. C., Crawford, F., & Lorimer, D. R. 2002, *ApJL*, 577, L19
3. Swanenburg, B. N., et al. 1981, *ApJL*, 243, L69
4. Hartman, R. C., & EGRET Team 1998, Bulletin of the American Astronomical Society, 30, 1311
5. Cordes, J. M., & Lazio, T. J. W. 2002, arXiv:astro-ph/0207156
6. Ng, C.-Y., & Romani, R. W. 2004, *ApJ*, 601, 479
7. Hessels, J. W. T., Roberts, M. S. E., Ransom, S. M., Kaspi, V. M., Romani, R. W., Ng, C.-Y., Freire, P. C. C., & Gaensler, B. M. 2004, *ApJ*, 612, 389
8. Van Etten, A., Romani, R. W., & Ng, C.-Y. 2008, *ApJ*, 680, 1417
9. Smith, D. A., et al. 2008, *A&A*, 492, 923
10. Watters, K. P., Romani, R. W., Weltevrede, P., & Johnston, S. 2009, *ApJ*, 695, 1289
11. Daugherty, J. K., & Harding, A. K. 1996, *ApJ*, 458, 278
12. Abdo, A. A. 2009, *ApJ*, accepted, arXiv:0812.2960
13. Abdo, A. A. 2009, *ApJ*, submitted
14. Fermi/LAT Collaboration: W. B. Atwood 2009, submitted, arXiv:0902.1089

Fermi-LAT detection of pulsed Gamma-rays from the young pulsar PSR J1833-1034 in the Supernova Remnant G21.5-0.9

G.A. Caliandro on behalf of the *Fermi LAT* collaboration
Dipartimento di Fisica 'M.Merlin' dell'Universita' di Bari e del Politecnico di Bari, I-70126 Bari, Italy
Istituto Nazionale di Fisica Nucleare, Sezione di Bari, I-70126 Bari, Italy

We report the discovery of gamma-ray pulsations from the young pulsar PSR J1833-1034 with the Large Area Telescope (LAT) on board the Fermi Gamma-ray Space Telescope. This pulsar has been recently discovered in the radio energy band and is the central object of the galactic plerionic supernova remnant G21.5-0.9. The spin parameters imply a spin-down luminosity of $\dot{E}$=3.3×10^{37}ergs s^{-1} and a characteristic age of about 5kyr. On the other hand measurements of the expansion rate of the supernova remnant lead to a pulsar age lower than 1000yr, which would make the PSR J1833-1034 one of the youngest, if not the youngest, known pulsar in the Galaxy. The Gamma-ray light curve shows two peaks separated by ∼ 0.4 in phase and relative amplitude varying with energy with a behavior that much resembles the Vela light curve in shape. We discuss the implications of the presence of the supernova remnant and the connection between X-ray, GeV, and TeV energy bands.

1 Introduction

The discovery of radio pulsations of PSR J1833-1034 was announced in 2005 by two teams independently [1 2]. Its period of 61.8ms and the $\dot{P} = 2.02 \times 10^{-13}$ lead to a characteristic age of 4800yr and a spin-down luminosity of $\dot{E} = 3.3 \times 10^{37}$ erg s^{-1}, that makes PSR J1833-1034 one of the most powerful pulsars, second only to Crab in our Galaxy. It is the central object of the supernova remnant G21.5-0.9. Despite the characteristic age of the pulsar, measurements of the expansion rate of the supernova remnant give an estimated age of less than 1000yr under the assumption of undecelerated expansion [3]. If the assumption were true, this estimation would make PSR J1833-1034 the youngest known pulsar in our Galaxy. Furthermore there is good historical evidence from ancient Chinese records to believe that this pulsar is associated with a guest star supernova explosion that took place in BC 48, making the system just over 2050 years old [4].

The most recent distance estimate of G21.5-0.9 is 4.7 ± 0.4kpc [2 18]. This is a kinematic distance obtained by H_I and ^{13}CO spectra measurements, and it is in agreement with the previous estimates [20 21]. The Dispersion Measure (DM) for PSR J1833-1034 is $\sim 170 cm^{-3}pc$ [2], while the X-ray spectra of the various components of G21.5-0.9 imply a foreground absorbing column $N_H \sim 2 \times 10^{22} cm^{-2}$ [22 6]. The ratio $N_H/DM \approx 40$ is substantially higher then seen toward all but approximately three other pulsars, indicating that the source could be behind a substantial amount of molecular material [23].

G21.5-0.9 has been classified as a plerionic SNR since it has a flat radio spectrum, centrally peaked radio and X-ray emission, and highly polarized radio flux [5]. This source was chosen as a calibration target for the *Chandra X-ray observatory* and as a result very beautiful and detailed

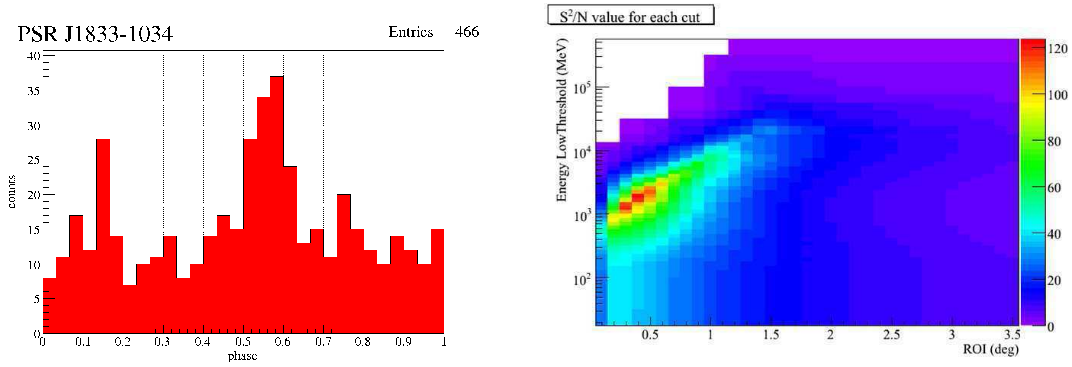

Figure 1: Left: PSR J1833-1034 light curve with optimized photon selection ($E > 1.0GeV$ $ROI = 0.5°$). Right: the color scale represents the value of the signal squared over noise (S^2/N) for each energy selection (Y axis) and ROI selection (X axis).

X-ray images of it are available [6 7 2]. The X-ray morphology of the SNR shows a central bright PWN (40″-radius) which is more compact than the radio nebula, and a faint non thermal halo, extended for $\sim$ 150″-radius, with no radio counterpart [8]. The spectrum of the central plerion steepens radially from the center [7], which is the site of a very bright compact source ($\sim$ 2″-radius) [8 6] that includes the pulsar and may delineate its wind termination shock [2]. The halo has a spatially flat spectrum with photon index of $\sim$ 2.4. It exhibits a non-thermal limb-brightened structure in the eastern section and also thermal northern knots [6 7 9].

Very recently the HESS telescope has detected Very High Energy (VHE) emission in the TeV energy range from PSR J1833-1034 and its associated PWN [10]. The photon index of the TeV spectrum is 2.1 ± 0.2 with a flux corresponding to $\sim 2\%$ of the Crab. A multiwavelength spectral analysis has been performed for the first time by De Rosa et al. 2008 [12], using *Chandra*, *INTEGRAL* and *HESS* data.

Several searches for X-ray pulsed emission have been performed either before [8 6 11] and after [2 12] the radio pulsation discovery. None of these searches has given positive results. The upper limits on the pulsed emission indicate a pulsed fraction of 50 per cent of the total pulsar flux in the 2-10keV energy range [12].

We claim in this proceeding the detection of pulsations from PSR J1833-1034 in the gamma-ray energy band by the *Large Area Telescope* (LAT) on board the *Fermi Gamma-ray Space Telescope* (hereafter *Fermi*). The gamma-ray light curve as well as the spectral features are investigated and a multiwavelength spectral study is performed from soft X-rays to TeV energies.

2 Observations and Analysis

Fermi was successfully launched on 11 June 2008 and after a phase of instrument monitoring and calibration, it began nominal sky-survey observations. The LAT is the main instrument on board. It is a pair-production telescope [13] composed of a silicon strip detector and tungsten foil tracker/converter, an hodoscopic cesium iodide calorimeter, and a plastic scintillator anti-coincidence detector. The LAT is sensitive to γ-rays in the energy range 20MeV-300GeV, its on–axis effective area is $\sim$8000cm^2 for $E >$ 1GeV and it has a large field of view of 2.4sr. In survey mode it covers all the sky in two orbits every 3hr.

In this proceeding LAT data collected through 15 January 2009 are analysed. As primary selection, we consider events with $E >$ 100MeV and belonging to "*diffuse class*" (LAT event class having the tightest cosmic-ray background rejection [13]). To avoid the γ-albedo contamination, we have selected Good Time Intervals (GTI) in a way so that we keep data only when the source and the entire Region Of Interest (ROI) selected around it are above the Earth albedo horizon,

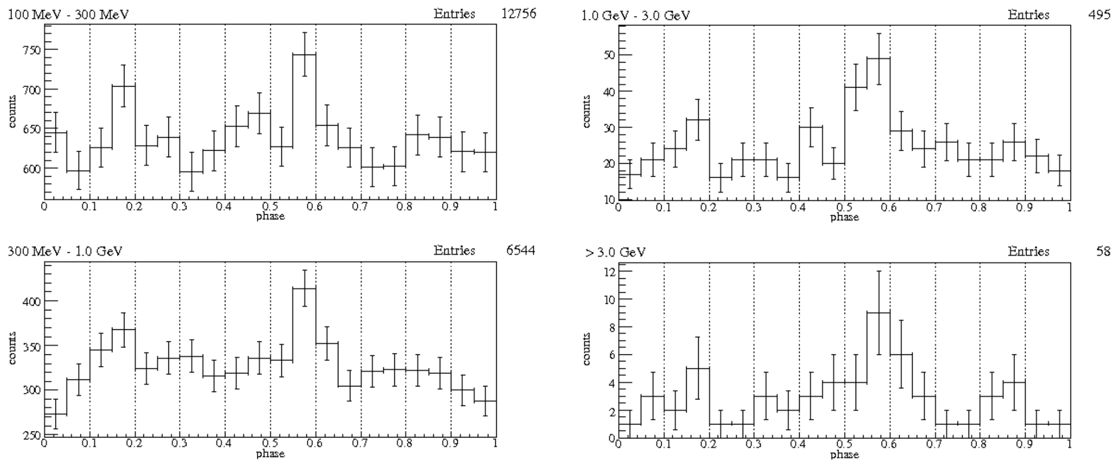

Figure 2: Light curves of PSR J1833-1034 in four energy ranges (0.1–0.3GeV, 0.3–1.0GeV, 1.0–3.0GeV, >3.0GeV).

defined to be at 105° from the Zenith.

2.1 Radio timing observations

PSR J1833-1034 is being observed by the timing consortium supporting *Fermi* observations with the NRAO Green Bank Telescope (GBT) [24]. The phase-connected ephemeris used to fold the *Fermi* data presented here was derived from nine observations obtained between 2008 June 21 and 2009 January 15 [a]. The pulsar was observed at a center frequency of 820 MHz with the Berkeley-Caltech Pulsar Machine [19], yielding total power samples every 72 μs in each of 96 frequency channels over a bandwidth of 48 MHz. Each observation lasted for about 50 minutes, from which we derived a time of arrival with typical uncertainty of 0.3 ms. We used the TEMPO timing software [b] and describe the pulsar rotation well by fitting for its frequency and first two derivatives. The dispersion measure of $169.5 \pm 0.1\,\mathrm{pc\,cm^{-3}}$ [2] was used to correct the times of arrival of the radio pulse to infinite frequency for absolute phase comparison with the gamma-ray profile, with uncertainty of ± 0.01 in phase.

2.2 Gamma-rays timing analysis

The timing analysis for PSR J1833–1034 in the γ-ray energy band is performed using an optimized photon selection criteria in terms of energy cut and radius of circular ROI. We have performed a preliminary spectral analysis, fitting the source with a simple power-law and used the result in order to evaluate the signal squared over noise ratio (S^2/N) for a dense grid of photon selection cuts (Energy Low Threshold, ROI radius). As shown in the right panel of figure 1, for PSR J1833-1034 the resulting optimal cuts are $E > 1.0$GeV and an ROI of 0.5°.

The photon arrival times have been corrected to the Solar-System barycenter using the JPL DE405 Solar System ephemeris and folded with the radio period using the Green Bank ephemeris. The H-test and Z-test with 2 harmonics give a chance probability of 4×10^{-8} and 5×10^{-10}, respectively.

The left panel of figure 1 shows the phase histogram of the 466 photons selected with the optimal cuts.

---

[a] This and other ephemerides used in *Fermi* results will be available from the Fermi Science Support Center (FSSC) data servers at http://fermi.gsfc.nasa.gov/ssc/data.

[b] http://www.atnf.csiro.au/research/pulsar/tempo/

3 Results

3.1 Pulsar Light Curve

The PSR J1833-1034 light curve shows two strong peaks separated by $\sim$ 0.41 in phase. To explore in detail the light curve, the four panels of figure 2 show the phase histograms in four energy ranges (0.1–0.3GeV, 0.3–1.0GeV, 1.0–3.0GeV, >3.0GeV) obtained selecting all the events within an energy-dependent 68% point-spread function (PSF) containment radius from the pulsar position. The main feature we can note from these phasograms is that the first peak (ϕ_1=0.15) decreases with increasing energies with respect to the second one (ϕ_2=0.56). These features strongly resemble those of Vela, as observed by EGRET [16] and now with Fermi [17].

3.2 Spectral analysis

The official tool of *Fermi-LAT* for spectral analysis is *gtlike* to perform the likelihood method. PSR J1833-1034 is in the heart of the galactic plane ($b = -0.885°$) and despite the strong pulsed signal, it does not have a high flux. It means that the signal to noise for this source is very low and so we have preferred to not use the likelihood method in a standard way. On the other hand *gtlike* was used to evaluate the differential flux in each single energy bin. The likelihood is applied in the narrow energy range of each bin assuming for our source a power-law with free prefactor and spectral index fixed to 2.0. This way has the advantage of yielding a model independent spectrum and does not need deep knowledge of the diffuse emission in the pulsar region.

The multiwavelength spectrum energy density in figure 3 shows the *LAT* points with the spectral models obtained by *Chandra* data analysis [6], *INTEGRAL* points [12], and the *HESS* spectral fit [10]. The pulsed flux calculated for PSR J1833-1034 for $E > 100 MeV$ is 1.82e-07 $\pm$ 0.24e-07 ph cm^{-2} s^{-1}.

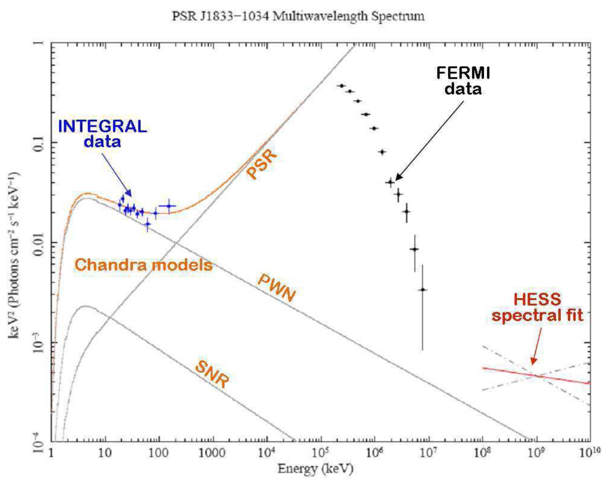

Figure 3: Spectral Energy Distribution from soft X-ray to TeV energy range. The *Fermi* data are the black crosses. Each spectral component identified through *Chandra* observations has been plotted separately. *INTEGRAL* data are plotted on the top of the model. At TeV energies the *HESS* fit is shown.

4 Conclusions

In the early months after the launch of the *Fermi* satellite, for the first time the gamma-ray pulsations of PSR J1833-1034 were detected by the *LAT* telescope with a confidence level better than 6σ. PSR 1833-1034 is a faint radio pulsar (flux density $\sim 70\mu Jy$ @ $1.4GHz$) and the central object of a very bright plerionic SNR (G21.5-0.9) in its early expansion phases, well observed in X-ray by *Chandra* and other satellites. This pulsar turn out to be one of the youngest and powerful in the Galaxy. Together with the Crab pulsar [30] and PSR J0205+6449, [29] *Fermi* is detecting a small population of extremely young γ–ray pulsars with age lower than 10000yr.

The light curve of PSR J1833-1034 shows two peaks separated by ~ 0.41 in phase and the first peak decreases with increasing energies with respect to the second one. These features are common to many γ–ray pulsars. As for Vela[17] and PSR J1028-5819[28], their easiest interpretation is in outer magnetosphere models such as the outer gap [25 26] or slot gap [27].

The spectral energy density of PSR J1833-1034 strongly suggests that the X-ray flux is mainly due to the PWN component, as well as for the TeV energy range, while in γ–ray we have a strong signature of the pulsed emission. The energy conversion efficiency for the γ–ray pulsed emission is estimated $\eta_\gamma \sim 1.0$ per cent. It is at least one order of magnitude greater than the X-ray conversion efficiency, calculated using the upper limit of the pulsed emission by *INTEGRAL* data in 20–100 keV energy range [12]. This confirms the hypothesis that the main pulsed power emission is in γ–ray energy band, as observed for the *EGRET* pulsars.

The discovery of γ–ray pulsations of PSR J1833-1034 strongly disfavor the hypothesis that the lack of a significant X-ray pulsation is due to a different pointing of the radio and X-ray beams.

Acknowledgments

The Fermi LAT Collaboration acknowledges the generous support of a number of agencies and institutes that have supported the Fermi LAT Collaboration. These include the National Aeronautics and Space Administration and the Department of Energy in the United States, the Commissariat ‘a l’Energie Atomique and the Centre National de la Recherche Scientifique / Institut National de Physique Nucleaire et de Physique des Particules in France, the Agenzia Spaziale Italiana and the Istituto Nazionale di Fisica Nucleare in Italy, the Ministry of Education, Culture, Sports, Science and Technology (MEXT), High Energy Accelerator Research Organization (KEK) and Japan Aerospace Exploration Agency (JAXA) in Japan, and the K. A. Wallenberg Foundation and the Swedish National Space Board in Sweden.

References

1. Gupta, Y., Mitra, D., Green, D. A., & Acharyya, A. 2005, Current Science, 89, 853
2. Camilo, F. et al. 2006, ApJ, 637:456-465
3. Bietenholtz, M. F., Bartel, N. 2008, MNRAS 386, 1411-1416
4. Wang, Z., Li, M., Zhao, Y. 2006 ChJAA, 6, 625
5. Green D.A.A. Catalogue of Galactic Supernova Remnants. Mullard Radio Astronomy Observatory. Cavendish Laboratory, Cambridge, 2004
6. Safi-Harb, S., Harrus, I. M., Petre R., et al. 2001, ApJ, 561, 308
7. Matheson, H. & Safi-Harb, S. 2005, AdSpR, 35, 1099
8. Slane, P., Chen, Y., Schulz, N.S., Seward, F.D., Hughes, J.P., & Gaensler, B.M. 2000, ApJ, 533, 171
9. Bocchino, F. van der Swaluw, E., Chavelier, R., & Bandiera, R. 2005, A&A, 442, 539

10. Djannati-Atai A. for HESS collaboration, 2007, Proceedings of the 30th ICRC (Merida, Mexico), arXiv:0710.2418
11. La Palombara, N., & Mereghetti, S., 2002, A&A, 383, 916
12. DeRosa, A., et al. 2008, MNRAS, arXiv0810.5230D
13. Atwood, W. B., et al. 2009, ApJ, submitted (arXiv:0902.1089)
14. DeJager, O.C., Raubenheimer, B.C., Swanepoel, J.W.H. 1989, A&A, 221, 180
15. Buccheri, R. et al. 1983, A&A, 128, 245
16. Kanbach, G. et al. 1994, A&A, 289, 855
17. Abdo, A. A., et al. 2009, ApJ, in press (arXiv:0812.2960)
18. Tian, W. W. & Leahy, 2008 D. A. MNRAS 391L..54T
19. Backer, D. C., Dexter, M. R., Zepka, A., Ng, D., Wertheimer, D. J., Ray, P. S., & Foster, R. S. 1997, PASP, 109, 61
20. Caswell, J. L.; Murray, J. D.; Roger, R. S.; Cole, D. J.; Cooke, D. J. 1975, A&A, 45, 239C
21. Davelaar, J.; Smith, A.; Becker, R. H. 1986, ApJ, 300L, 59D
22. Warwick, R. S. et al. 2001, A&A, 365L, 248W
23. Gaensler, B. M.; van der Swaluw, E.; Camilo, F.; Kaspi, V. M.; Baganoff, F. K.; Yusef-Zadeh, F.; Manchester, R. N. 2004, ApJ, 616, 383G
24. Smith, Guillemot, Camilo, et al. 2008, A&A, 492, 923
25. Cheng, K. S., Ho, C., & Ruderman, M. A. 1986, ApJ, 300, 500
26. Romani, R. W. & Yadigaroglu, I.-A. 1995, ApJ, 438, 314
27. Muslimov, A. G. & Harding, A. K. 2004, ApJ, 606, 1143.
28. Abdo, A. A., et al. 2009b, ApJ, 695L, 72A
29. Parent, D. 2009, these proceedings
30. Grondin, M.-H. 2009, these proceedings

The *Fermi* Large Area Telescope: preliminary results from on-orbit high level performance verifications and monitoring

S. Germani
for the *Fermi* LAT collaboration
Università di Perugia and INFN, via A. Pascoli, 06100, Perugia

The *Fermi* Gamma-ray Space Telescope (formerly GLAST) is an international satellite mission with a physics program spanning from gamma-ray astronomy to particle astrophysics and cosmology. The main mission instrument, the Large Area Telescope (LAT), due to the advanced particle detectors that constitute its 3 detector subsystems, studies high energy gamma rays in the range between 20 MeV and 300 GeV with much higher resolution and sensitivity compared to its predecessor EGRET. The knowledge of the instrument response functions and high level performance has direct impact on the precision of the astrophysical measurements; after the observatory launch in June 2008 from Kennedy Space Centre (NASA), a series of performance measurements and monitoring has been made using the radiation from astrophysical sources. The Vela pulsar, in particular, with its high flux pulsed emission, is a very powerful tool to study and monitor the instrument performance. Highlights of the LAT high level instrument performance and of its initial on-orbit verification and monitoring will be given.

1 Introduction

The Large Area Telescope (LAT) of the *Fermi* Gamma-ray Space Telescope mission [1] (figure 1) is a pair-conversion gamma-ray detector similar in concept to the previous NASA high-energy gamma-ray mission EGRET on the Compton Gamma-Ray Observatory [2]. High energy (20 MeV–300 GeV) gamma-rays convert into electron-positron pairs in one of 16 layers of tungsten foils. The charged particles pass through up to 36 layers of position-sensitive detectors interleaved with the tungsten, the "tracker"[3], leaving behind tracks pointing back toward the origin of the gamma ray. To optimize the angular resolution, each of the first 12 tungsten layers (Front) is only 2.7% X_0 thick, while to increase the overall conversion efficiency the last 4 layers (Back) correspond to 18% X_0 each. After passing through the last tracking layer, particles enter a calorimeter [4] composed of bars of cesium-iodide crystals read out by PIN diodes. The crystals are horizontally arranged in layers, each layer is aligned 90° with respect to its neighbors forming an hodoscopic array. This way the calorimeter can image the shower development profile providing the energy measurement of the incident gamma ray and a powerful background discriminator. A third detector system, the anti-coincidence detector [5] (ACD), surrounds the top and sides of the tracking instrument. It consists of panels of plastic scintillator read out by wavelength-shifting fibers and photo-multiplier tubes and it is used to veto charged cosmic-ray events such as electrons, protons or heavier nuclei. The ACD is highly segmented in order to minimize backsplash effects on the Effective Area and allows to extend the LAT sensitivity to much higer energies than EGRET.

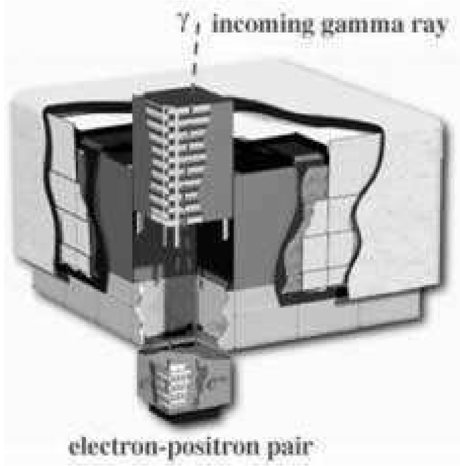

Figure 1: Schematic diagram of the LAT pair conversion telescope.

In the LAT, the tracker and the calorimeter are segmented into 16 “towers” which are covered by the ACD and a thermal blanket and meteoroid shield. An aluminum grid supports the detector modules and the data acquisition system, which is located below the calorimeter modules. The LAT is designed to improve upon EGRET’s sensitivity to astrophysical gamma-ray sources by well over a factor of 10. That is accomplished partly by sheer size, but also by use of advanced, even if well proven, particle detection technologies.

The *Fermi* observatory was successfully launched on June 11, 2008, and after a Launch and Early Operation phase (L&EO) with calibration runs and pointed observations, the LAT started its nominal scientific operation mode, consisting of a continuous all-sky survey which, due to the large field of view (~ 2.4 sr), covers the entire sky every two orbits (~ 3 hours).

2 LAT Performance

The LAT design has been optimized by means of a detailed Monte Carlo simulation of the response to $\gamma-$rays and background particles (cosmic rays) with the Geant4 toolkit [6]. Detector models, including all the subsystems, and the corresponding simulation models have been tested through an engineering model flown on a high altitude balloon [7] and subjected to an accelerator beam at SLAC [8]. Particle beam tests have been also performed at CERN [9] with spare flight tracker and calorimeter modules and a few ACD scintillator tiles.

The detector and background models have been used to develop a parameterisation of the Instrument Response Functions (IRFs) which describes the LAT performance after signal reconstruction and background rejection [a]. Since the IRFs, namely the Effective Area, the Point Spread Function (PSF), the probability distribution for the reconstructed $\gamma-$rays to form a point source, and the Energy Dispersion, may be used in scientific analyses to perform model fitting of the measured data, the validation of the pre-launch expectations with the on-orbit data and the stability monitoring are particularly important. The instrument performance have been defined for three different analysis classes corresponding to three different event selections with decreasing level of background contamination: *transient*, *source* and *diffuse*. During the early phase of the mission after launch the default class used for the analysis is the *diffuse* class which has the smallest level of background contamination.

The PSF at low energy is primarily determined by the multiple Coulomb scattering of the

[a] See http://www-glast.slac.stanford.edu/software/IS/glast_lat_performance.htm for up-to-date performance parameters.

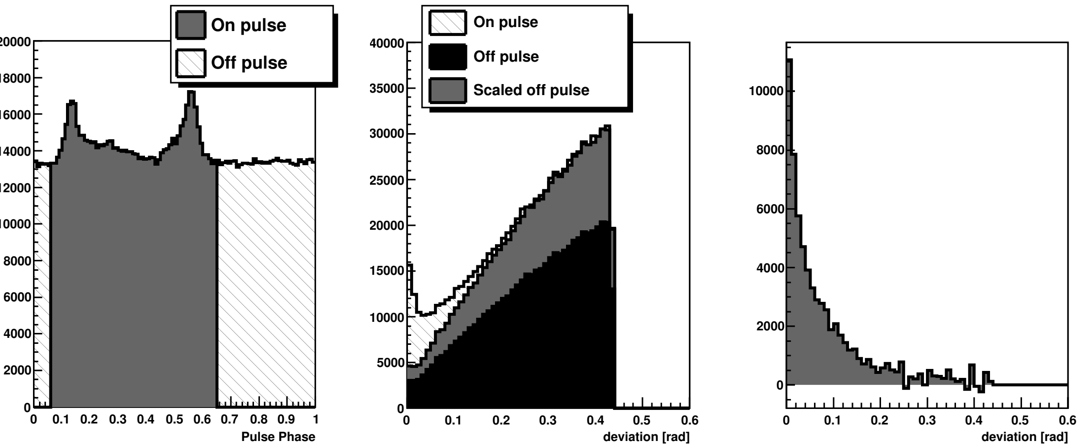

Figure 2: PSF measurement of Vela. Left panel: Vela pulsar phasogram with on-pulse and off-pulse regions highlighted. Middle panel: angular direction error for the Vela pulsar; the on-pulse, off-pulse, and scaled off-pulse histograms are shown togheter. The off-pulse scaling has been performed according to the on-pulse/off-pulse phase width ratio. Right Panel: On-Pulse angular direction error for the Vela pulsar for photons within a 20 deg radius after background subtraction.

e^+ and e^- in the converter layers, thus it improves with the photon energy. At high energy the PSF is mainly limited by the spatial resolution of the silicon detector. The amount of traversed material depends also on the incoming angle with respect to the detector axis (θ), this affects the PSF which anyway is not much deteriorated up to 60 degrees, ensuring good performance across the complete LAT field of view.

A demonstration of the observatory capabilities has been the discovery of a radio-quiet $\gamma-$ray pulsar in the CTA 1 Supernova Remnant [10] during the very early phase of the mission. Due to the much improved Effective Area and PSF, the LAT needed only a few days of data to discover a source which is positionally consistent with an unidentified EGRET source and with the much more precise position of an X-ray source. The pulsation was discovered by using $\gamma-$ray data only.

3 On-orbit PSF measurement of Vela

One of the critical analysis methods in use by the collaboration for on-orbit PSF measurement and validation takes advantage of the bright and pulsed emission from the Vela pulsar, which is the most powerful steady source in the $\gamma-$ray sky and whose emission is 100% pulsed [12]. Figure 2 summarizes the method for the PSF measurements; the left panel shows the phasogram for Vela with the on-pulse and off-pulse regions highlighted. For our analysis we select only on-pulse photons and we use the off-pulse photons to evaluate the level of the background which in this case is mainly due to the diffuse galactic emission in the selected region of interest around the source. The angular direction error with respect to the Vela position for on-pulse and off-pulse photons are shown in the central panel, where the off-pulse angular deviation scaled by the phase width ratio between the on-pulse and off-pulse region ($width_{on-pulse}/(1 - width_{on-pulse})$) is also shown. The scaled off-pulse angular deviation is used to estimate the background level for the on-pulse distribution; therefore the subtraction between the on-pulse and the scaled off-pulse angular deviation shown in the right panel of figure 2 corresponds to the direction measurement error for the Vela photons. From the distribution of the subtracted angular deviation we compute the 68% containment radius which is the figure of merit for PSF studies.

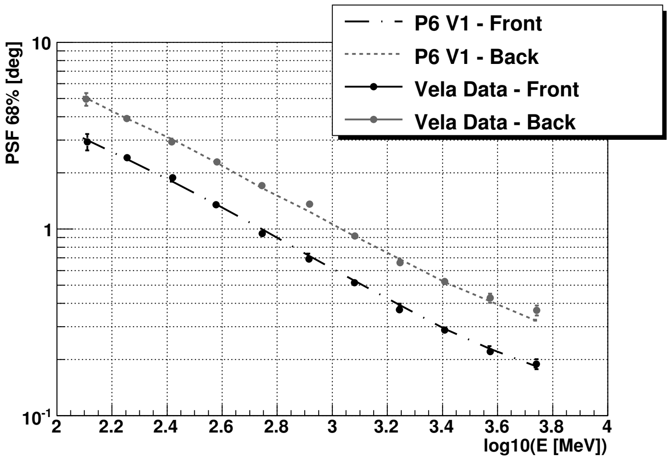

Figure 3: Front and Back 68% containment radius versus energy E for the *diffuse* class. Dots are measurements and dashed lins are the expected values.

3.1 PSF validation

Figure 3 shows the comparison between the on-orbit measurement of Vela and the pre-launch expectations for the 68% containment radius as a function of the energy. Both the Front (thin converters) and Back (thick converters) sectors are well in agreement with the expectations. This method has an intrisic limit at the energy of a few GeV since, as already hinted by EGRET [11] and confirmed by *Fermi* [12], the Vela pulsar spectrum shows an exponential cut-off at the energy of about 3 GeV. High energy PSF measurements need to be performed using other lower flux sources and more complex analysis methods.

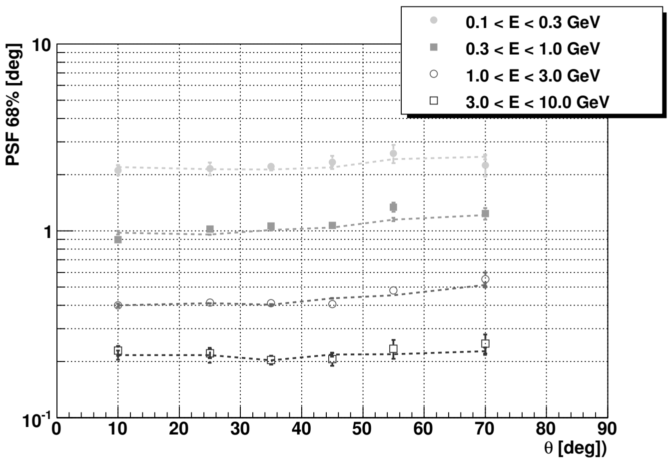

Figure 4: PSF 68% containment radius vs. θ. Dots are measurements and dashed lins are the expected values.

The on-orbit 68% containment radius dependence on the inclination angle for several energy ranges is compared to the expectations in figure 4. The agreement with the pre-launch parameterisations confirm that the LAT has good direction measurements performance even for high θ angles; this is particularly important to take full advantage of its large field of view with the all-sky scanning mode and with fast transient sources like Gamma Ray Burts (GRB) and AGN flares.

The PSF stability has been verified also for the azimuth angle of the incoming photons and

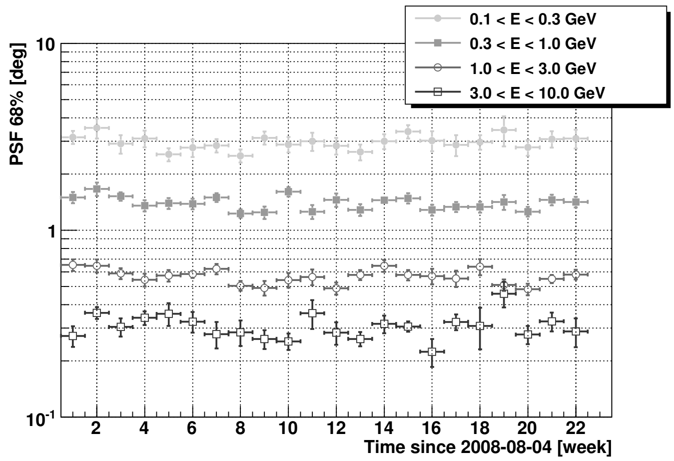

Figure 5: PSF trending with one measurement per week for different energy intervals. The trending starts on August the 4^{th}, 2008 which is the starting date for the nominal *Fermi* science operation after the conclusion of the L&EO phase.

for different geomagnetic latitudes where background rates change significantly.

3.2 PSF monitoring

Since the Instrument Response Functions are used in scientific analyses the stability of the LAT response with time is a key issue especially in the long term. Due to the high flux of the Vela pulsar we can perform a good PSF measurement per week in order to check any deviation from the nominal value. The PSF trending, see figure 5, for several energy ranges shows good stability within the errors; this plot has changed since the talk has been given and here the corrected version is shown.

The *Fermi* absolute pointing is obtained from two star trackers mounted on the spacecraft and the LAT absolute pointing can be cross-checked using an ensemble of known $\gamma-$ray sources. The alignment between the LAT and the star trackers has been calibrated on orbit and it is stable with time.

4 Conclusions

The IRF validation and monitoring is very important for the reliability of science results. The Point Spread Function has been measured up to a few GeV and shows good agreement with expectations and good stability. The global alignment is also stable with time.

Acknowledgments

The *Fermi* LAT Collaboration acknowledges generous ongoing support from a number of agencies and institutes that have supported both the development and the operation of the LAT as well as scientific data analysis. These include the National Aeronautics and Space Administration and the Department of Energy in the United States, the Commissariat à l'Energie Atomique and the Centre National de la Recherche Scientifique / Institut National de Physique Nucléaire et de Physique des Particules in France, the Agenzia Spaziale Italiana and the Istituto Nazionale di Fisica Nucleare in Italy, the Ministry of Education, Culture, Sports, Science and Technology (MEXT), High Energy Accelerator Research Organization (KEK) and Japan

Aerospace Exploration Agency (JAXA) in Japan, and the K. A. Wallenberg Foundation, the Swedish Research Council and the Swedish National Space Board in Sweden.

Additional support for science analysis during the operations phase from the following agencies is also gratefully acknowledged: the Istituto Nazionale di Astrofisica in Italy and the K. A. Wallenberg Foundation in Sweden for providing a grant in support of a Royal Swedish Academy of Sciences Research fellowship for JC.

References

1. W. B. Atwood *et al.* 2009, ApJS, in press (arXiv:0902.1089)
2. D.J. Thompson, et al. ApJ Suppl. **86**, (1993) 629.
3. W. B. Atwood *et al.*, Astropart. Phys. **28** (2007) 422.
4. E. Grove *et al.* 2009, in preparation.
5. A. A. Moiseev *et al.*, Astropart. Phys. **27** (2007) 339.
6. S. Agostinelli *et al.* Nucl. Instrum. Meth. A **506** (2003) 250.
7. D. J. Thompson *et al.* IEEE Trans. Nucl. Sci. **49** (2002) 1898.
8. E. do Couto e Silva *et al.* Nucl. Instrum. Meth. A **474** (2001) 19.
9. L. Baldini *et al.* AIP Conf. Proc. **921** (2007) 190.
10. A. A. Abdo *et al.* Science **322** (2008) 1218.
11. Kanbach, G. *et al.* *A&A.* **289** (1994) 855.
12. A. A. Abdo *et al.* Astrophys. J. **696** (2009) 1084.

TACTIC and MACE gamma-ray telescopes

K.K. Yadav (for the HIGRO collaboration)
Astrophysical Sciences Division, Bhabha Atomic Research Centre,
Trombay, Mumbai, India - 400 085

The TACTIC gamma-ray telescope, equipped with a tracking light collector of $\sim$9.5m^2 area and a 349-pixel imaging camera has been in operation at Mount Abu in Western India since 2001. Having a sensitivity of detecting the Crab Nebula above 1.2 TeV at 5.0σ signi
level in 25h of observations, this telescope has detected gamma-ray emissions from Mrk501 and Mrk421 and is presently being deployed for monitoring of AGNs. As a new Indian initiative in γ-ray astronomy we are setting up the 21-m diameter MACE γ-ray telescope at the high altitude (4200m asl) astronomical site at Hanle in North India. This telescope will deploy a 1408-pixels integrated camera at its focal plane. Designed to operate at a trigger threshold of $\sim$30 GeV, this telescope is expected to be operational in 2011. Some of the salient features of the TACTIC telescope along with the results of its recent observations and the design details of the MACE telescope are presented in this paper.

1 TACTIC telescope

The TACTIC (TeV Atmospheric Cherenkov Telescope with Imaging Camera) γ-ray telescope located at Mt. Abu (24.6° N, 72.7° E, 1300m asl), is being used to study potential TeV γ-ray sources. The telescope deploys a F/1 type tracking light collector of $\sim$9.5 m^2 area, made up of 34$\times$0.6 m diameter, front-coated spherical glass facets which have been prealigned to produce an on-axis spot of $\sim$ 0.3° diameter at the focal plane. The telescope uses a 349-pixel photomultiplier tube (ETL 9083UVB) -based imaging camera with a uniform pixel resolution of $\sim$0.3° and a field-of-view of $\sim$6°$\times$6° to record images of atmospheric Cherenkov events. The innermost 121 pixels (11$\times$11 matrix) are used for generating the event trigger, based on the NNP (Nearest Neighbour Pairs)/3NCT (Nearest Neighbour Non-Collinear Triplets) topological logic [1], by demanding a signal $\geq$ 25/8 pe for the 2/3 pixels which participate in the trigger generation. Whenever the single channel rate of any two or more pixels in the trigger region goes outside the preset operational band, it is automatically restored to within the prescribed range by appropriately adjusting the high voltage of the pixels [2]. The resulting change in the photomultiplier (PMT) gain is monitored by repeatedly flashing a blue LED, placed at a distance of $\sim$1.5m from the camera. The advantages of using such a scheme are that in addition to providing control over chance coincidence triggers, it also ensures safe operation of PMTs with typical anode currents of $\leq$ 3 μA. The back-end signal processing hardware of the telescope is based on medium channel density NIM and CAMAC modules developed inhouse. The data acquisition and control system of the telescope [3] has been designed around a network of PCs running the QNX (version 4.25) real-time operating system. The triggered events are digitized by CAMAC based 12-bit Charge to Digital Converters (CDC) which have a full scale range of 600 pC. The telescope has a pointing and tracking accuracy of better than $\pm$3 arc-minutes. The

Table 1: Observations on gamma-ray sources with TACTIC telescope

Sr.	Source	Observation period	Observation(h)	Significance/UL
1	Crab Nebula	Dec 2003 - Feb 2004	104.28	10.30σ
		Nov 2005 - Feb 2006	101.04	9.40σ
		Nov 2007 - Mar 2008	105.15	11.05σ
2	Mrk421	Dec 2005 - Apr 2006	201.72	11.5σ
		Jan 2007 - Mar 2007	83.5	$\leq 0.92 \times 10^{-12}\ ph\ cm^{-2}s^{-1}$
		Jan 2008 - May 2008	149.70	9.60σ
3	Mrk501	Mar 2005 - May 2005	46.00	$\leq 4.62 \times 10^{-12}\ ph\ cm^{-2}s^{-1}$
		Feb 2006 - May 2006	66.80	7.5σ
4	1ES2344+514	Oct 2004 - Dec 2005	60.15	$\leq 3.84 \times 10^{-12}\ ph\ cm^{-2}s^{-1}$
5	H1426+428	Mar 2004 - Jun 2007	165.70	$\leq 1.18 \times 10^{-12}\ ph\ cm^{-2}s^{-1}$

tracking accuracy is checked on a regular basis with so called "point runs", where a bright star whose declination is close to that of the candidate γ-ray source is tracked continuously for about 5 hours. The point run calibration data (corrected zenith and azimuth angle of the telescope when the star image is centered) are then incorporated in the telescope drive system software so that appropriate corrections can be applied directly in real time while tracking a candidate γ-ray source [4].

1.1 Recent TACTIC results

In order to evaluate the performance of the TACTIC telescope the Crab Nebula "standard candle" has been observed repeatedly since 2001. Operating at a γ-ray threshold energy of $\sim$1.2 TeV, the telescope records a cosmic ray event rate of $\sim$2.0 Hz at a typical zenith angle of 15°. The telescope has a 5σ sensitivity of detecting Crab Nebula in 25 hours of observation time. The consistent detection of a steady signal from the Crab Nebula along with excellent matching of its energy spectrum with that obtained by other groups, reassures that the performance of the TACTIC telescope is quite stable and reliable. The telescope has detected strong γ-ray signals from two active galactic nuclei (AGN) Mrk501 (2006 observations) [5] and Mrk421 (2005-06 observations) [6] while other two AGNs 1ES2344+514 [7] and H1426+428 observed during 2004-05 and 2004-07 respectevely have been found to be in the quiescent state. Some of the recent results obtained on various candidate γ-ray sources are listed in Table 1. We believe that there is a considerable scope for the TACTIC telescope to monitor TeV γ-ray emission from other AGNs on a long-term basis.

2 MACE telescope

Exploring the γ-ray sky in the energy range $\geq 10GeV$ with low energy threshold ground based atmospheric Cherenkov telescopes is expected to lead to a potentially rich harvest of astrophysical discoveries, as has been already demonstrated by the HESS and MAGIC telescopes at γ-ray energies $\geq 100GeV$. The low threshold energy can be attained by increasing the light collector area of the telescopes and installing them at higher altitudes where the photon density of the atmospheric Cherenkov events is higher [8]. As a new Indian initiative in gamma-ray astronomy, the Himalayan Gamma Ray Observatory (HIGRO) is being set up at Hanle (32.8° N, 78.9° E, 4200m asl) in the Ladakh region of North India. The site offers an average of about 260 uniformly distributed spectroscopic nights per year which is a major advantage in terms of sky coverage for source observations. Located closer to the shower maximum the Cherenkov photon

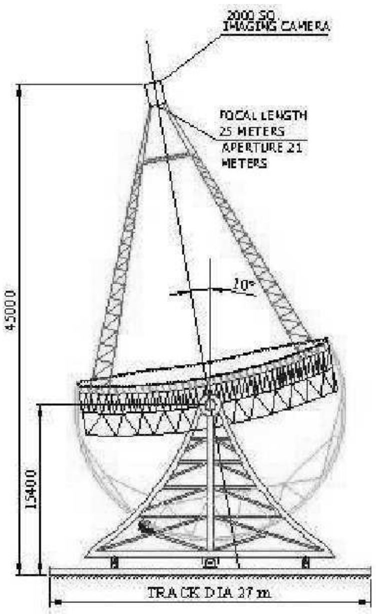

Figure 1: 21-m diameter MACE telescope

density at Hanle is substantially high as compared to the sea level[9]. The higher photon density along with the low background light level at this site helps in lowering the energy threshold of the Cherenkov telescope being setup there.

The MACE (Major Atmospheric Cherenkov Experiment) telescope with high resolution imaging camera is designed to operate in the sub-TeV energy range as part of the HIGRO collaboration. As depicted in Figure 1 the altitude-azimuth mounted telescope will deploy a 21-m diameter parabolic light collector made of 356 panels of 984 mm $\times$ 984 mm size with each panel consisting of 4 spherical mirror facets of 488 mm $\times$ 488 mm size. Each facet is diamond turned to a mirror finish yielding a reflectivity of $\geq$ 85% in the visible band. The telescope will use the graded focal length (increases towards the periphery) mirrors in order to reduce the D_{80} spot size (defined as the diameter of the circle within which 80% of the reflected rays lie) of the light collector to $\sim$15 mm for on-axis incidence. Each mirror panel will be equipped with motorized orientation controllers for aligning them to form a single parabolic light collector.

The focal plane instrumentation will have a photomultiplier tube based imaging camera covering a field of view of $4^\circ \times 4^\circ$. The imaging camera will comprise of 1408 pixels arranged in a square matrix with uniform pixel resolution of 0.1°. The inner 576 pixels with field of view of $2.4^\circ \times 2.4^\circ$ will be used for generating the event trigger. The PMTs will be provided with acrylic front-aluminized light cones for enhancing the light collection efficiency of the camera. The signal processing instrumentation will also be housed within the camera and the acquired data will be sent to the control room over the computer network for processing and archiving. Detailed Monte Carlo simulation studies have been carried out using CORSIKA[10]code and the results suggest that using a pixel threshold of $\geq$4pe and a 4 nearest neighbour pixel trigger, gamma-ray energy threshold of $\sim$30 GeV is achievable by the MACE telescope. Figure 2 shows the differential trigger rates of γ-rays for the two different types of spectra. The energy thresholds are determined to be $44 GeV$ for the Crab spectrum and $31 GeV$ for the pure power law spectrum with a diffential index of 2.59 for the above mentioned configuration.

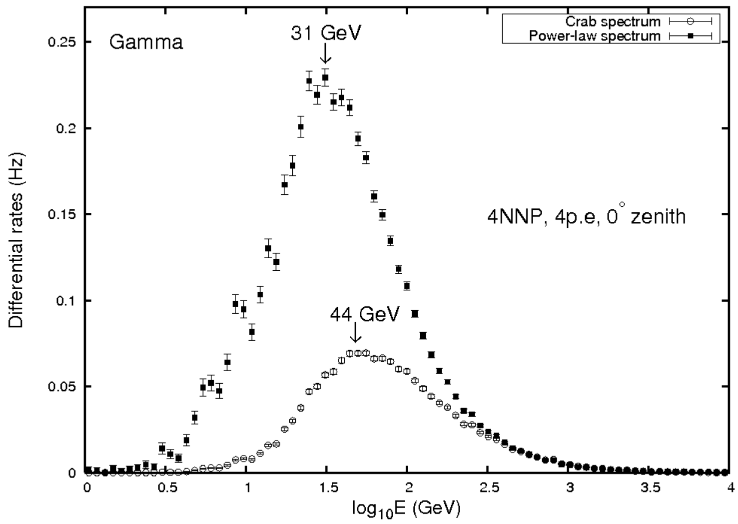

Figure 2: Gamma-ray differential rates for the two types of primary spectra calculated for the 4 nearest neighbour pixel, 4pe trigger con $\sim (44 \pm 2)GeV$ and for the power law the threshold energy is $\sim (31 \pm 2)GeV$.

2.1 Status of MACE telescope

The detailed engineering and structural design of the MACE telescope has been completed. Fabrication of the mechanical structure has started and the telescope is likely to be installed at Hanle by 2011.

Acknowledgments

We would like to thank the organizers of the "44th Rencontres de Moriond" for providing financial support to attend the conference. We would also like to thank colleagues of the Astrophysical Sciences Division for their contribution towards the operation of the TACTIC telescope and the design of the MACE telescope.

References

1. S.R. Kaul *et al*, *Nucl. Instrum. Methods* A **496**, 400 (2003).
2. N. Bhatt *et al*, *Meas. Sci. Technol* **12**, 167 (2001).
3. K.K. Yadav *et al*, *Nucl. Instrum. Methods* A **527**, 411 (2004).
4. R. Koul *et al*, *Nucl. Instrum. Methods* A **578**, 548 (2007).
5. S. V. Godambe *et al*, *J. Phys. G: Nucl. Part. Phys.* **34**, 1683 (2007).
6. K. K. Yadav *et al*, *Astropart. Phys.* **27**, 447 (2007).
7. S. V. Godambe *et al*, *J. Phys. G: Nucl. Part. Phys.* **35**, 065202 (2008).
8. F. Aharonian *et al*, *Astropart. Phys.* **15**, 335 (2001).
9. R. Cowsik *et al*, *27th ICRC, Hamburg*, OG2.05, 2769 (2001).
10. D. Heck *et al*, *FZKA 6019* Forschungszentrum Karlsruhe,(1998).

Gamma Astronomy with the ARGO-YBJ experiment

G. Marsella on behalf of ARGO-YBJ coll.
Dipartimento di Ingegneria dell'Innovazione Università del Salento and INFN, via Arnesano, 73100 Lecce, Italy

The ARGO-YBJ detector, installed at the Yangbajing Cosmic Ray Laboratory (Tibet, China), at 4300 m a.s.l., is a layer of Resistive Plate Counters (RPCs) about 6.700 m^2 wide. The high space-time granularity, the full-coverage technique and the high altitude location make this detector a unique device for a detailed study of the atmospheric shower characteristics with an energy threshold of a few hundreds GeV. These properties in addition to the large field of view and the high duty cycle make the ARGO-YBJ experiment able to monitor a large fraction of the Northern sky (ranging from -10^o to +70^o) in a continuous way. First results concerning Very High Energy Gamma Astronomy will be presented.

1 The detector features

The ARGO-YBJ (Astrophysical Radiation with Ground-based Observatory at Yangbajing) experiment is located at the Yangbajing High Altitude Cosmic Ray Laboratory (4300 m a.s.l.), 90 km North of Lhasa (Tibet, P.R.China), as an Italian-Chinese collaboration project. It has been fully operated since June 2006 with the aim of studying gamma rays and cosmic rays at an energy threshold of a few hundreds GeV, by detecting small size air showers at high altitude with wide aperture and high duty cycle.

The detector is made of a single layer of Resistive Plate Counters (RPCs)[1] fully covering an area 74 $\times$ 78 m^2, surrounded by a partially instrumented guard ring of RPCs up to 100 $\times$ 110 m^2 which allows a better core location resolution using the central carpet and therefore a better preformance in the shower direction reconstruction.The RPCs, each of dimensions 280 $\times$ 125 cm^2, are operated in streamer mode and grouped in modules made by 12 units called 'Clusters'. Each Cluster is the basic detection and Data Acquisition unit in a logical subdivision of the apparatus. The central area of the detector is made by 130 Clusters and cover about the 92% of the total area. Each RPC is divided in 10 pads 56 $\times$ 62 cm^2 that are subdivided in 8 pickup strips. The pad and the strips are respectively the time and space unitary digital elements allowing a time resolution of the order of $\sim$ 1 ns and a spatial resolution 62 $\times$ 7 cm^2. A calibration procedure is defined to correctly take into account the detector systematics to optimize the angular resolution[2]. In order to extend the energy range of the detector, each RPC is also implemented by two 'big pads' for the analogical readout of the collected charge. The high space-time granularity of the ARGO-YBJ detector (Figure 1) gives the opportunity to detect several kinds of events, characterized by different topologies and time structures and a fine sampling of the shower front close to the core [3].

The detector has two different operation modes: 'Shower Mode' and 'Scaler Mode'. In Shower Mode, for each event the location and timing of every triggered pad is recorded, allowing the lateral distribution and arrival direction reconstruction. The trigger is set to a multiplicity

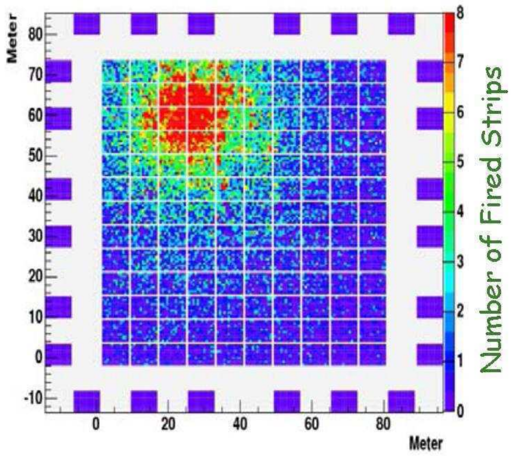

Figure 1: Shower event on the carpet

(N_{hit}) higher than 20 in 420 ns, collecting events with a rate of $\sim$ 3.7 kHz. In Scaler Mode the total counts are measured every 0.5 s, without information on both the space distribution and arrival direction of the detected particles. For each cluster, the signal coming from the 120 pads is added up and put in coincidence in a narrow time window[4] (150 ns). A detailed status report of the experiment can be found in the bibliography[5].

2 Moon and Sun shadows

Cosmic rays are hampered by the Moon and the Sun, therefore a deficit of flux in their direction is expected (the so-called "Moon and Sun shadows"). Due to the high rate of lower energy cosmic rays, the moon and the sun shadow provide the most significant signals (even if negative) in the argo-ybj sky map to which is sensitive. The measurement of the size of the deficit allows to define the detector angular resolution, while the position define the pointing accuracy. The observation of the west displacement of the Moon shadow, taking into account that charged particles traveling from the Moon to the Hearth are deflected towards East due to the geomagnetic field by an angle $\Delta\theta \sim 1.6^o/E(\mathrm{TeV})$, allows the detector calibration, as it provides a direct check of the relation between shower size and primary energy. This technique also allows to study the antiproton/proton ratio in the TeV energy range. The ARGO-YBJ experiment is observing the Moon shadow with a sensitivity of about 10 standard deviations per month at a multiplicity $N_{hit} \geq 40$, and zenith angle $\theta \leq 50^o$ (corresponding to a proton median energy $E_{50} \sim 1.8$ TeV). In the period December 2007 - August 2008 the Moon shadow has been observed (802 hours on-source) at significance of 26 standard deviations.

The shadow of the Sun has been measured in the period December 2007 - August 2008 (954 hours on-source with $\theta \leq 50^o$) for events with $N_{hit} \geq 40$ at a significance of the maximum event deficit of about 25 standard deviations.

3 Gamma Astronomy

The detector location at high altitude make it particularly suitable for Gamma Ray Astronomy. At 4300 m a.s.l. the trigger efficiency at TeV energies is about 2 times better for gamma ray showers than for hadron ones. The good angular resolution of the detector also contributes to a good sensitivity to gamma sources without any particular γ/hadron separation algorithm. Among the steady TeV gamma ray sources, the Crab Nebula is the most luminous and it is used

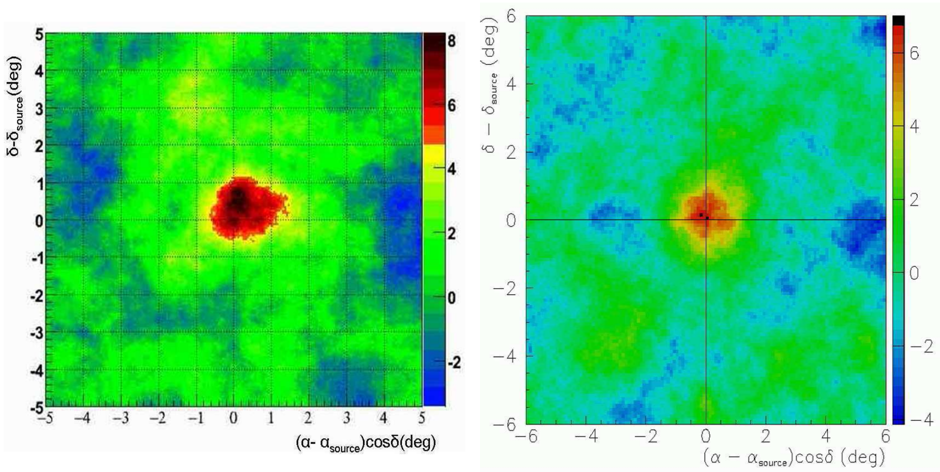

Figure 2: The Crab significance Map(left). The Mrk421 significance Map(right)

as a standard candle to check the detectors sensitivity. A map of the Crab Nebula region has been obtained by ARGO-YBJ using the events with different N_{hit} selections and zenith angle $\leq 45^o$ recorded in 2187 hours of observation, equivalent to 342 transits of the source (one transit lasts 6.4 hours). The Crab is visible with a significance of more than 7 standard deviations. Applying simple quality cuts on the conical fit reconstruction the sensitivity is increased to more than 8 σ (Figure 2). The AGN Markarian 421 has been observed since day 347 of 2007 to day 357 of 2008 (about 308 transits). In that period the source underwent an active period, with a rather strong increase of the X-ray flux. As observed in many occasions during the past years and in agreement with the Synchrotron Self-Compton (SSC) model, the X-ray flux increases are generally associated to increases in the TeV band that can reach a flux several times larger than the Crab Nebula one.

Mrk421 was flaring during the first months of 2008 and the ARGO-YBJ experiment reported evidence for a TeV emission in correlation with the X-ray flares. The significance map of the Mrk421 region is shown in Figure 2: a clear signal at about 7 standard deviations level is visible during 2008. The observation refers to a multiplicity $N_{hit} \geq 60$. A correlation of TeV photons detected by the ARGO-YBJ experiment with the X-ray events detected by the Rossi RXTE Satellite[6] is evident (Figure 3). We note that an all-sky VHE gamma-ray telescope as the ARGO-YBJ experiment is able to monitor the Mrk421 in a continuous way.

ARGO-YBJ allows to study Gamma Ray Bursts (GRBs) in the GeV energy range, where gamma rays are less affected by the absorption due to pair production in the extragalactic space.

A search for γ emission has been done in coincidence with 39 GRBs detected by satellites (mainly by Swift) in ARGO-YBJ field of view with zenith angle $\theta \leq 45^o$. Using the 'Scalar Mode' technique, four multiplicity channel ($\geq 1, \geq 2, \geq 3, \geq 4$) have been analyzed either in coincidence with the low energy emission, either in an interval of 2 hours around it. No excess has been found allowing a corresponding fluence upper limits[7], of the order of $10^{-5} erg/cm^2$ in the energy range 1-100 GeV during the satellite time detection, obtained assuming a power law spectrum with a differential index $\alpha = 2.5$.

4 Conclusions

The ARGO-YBJ detector has been completely installed and is taking data since June 2006, in particular with a high duty cycle ($\geq 95\%$) since November 2007. The first Analysis on the Moon and Sun shadows allowed to detect these signals at more than 25 standard deviations. The Crab

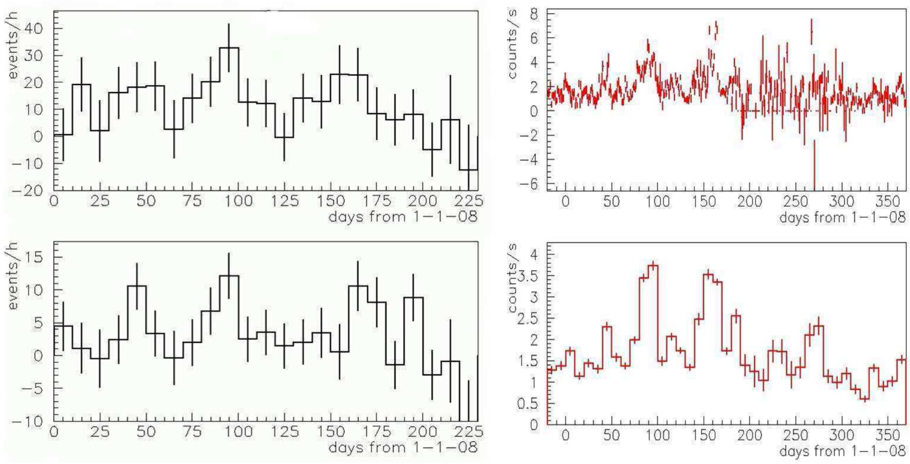

Figure 3: The Mkr421 fluxes as seen by ARGO(left). At top with a $N_{hit} \geq 40$ and at bottom with a $N_{hit} \geq 100$ selection respectilvely. On the right a comparison with Mrk 421 X-ray fluxes as seen by RXTE with two different integration windows

Nebula has been observed at more than 7 standard deviation, and enhanced to about 8 standard deviation using simple quality cuts on the conical fit used in shower direction reconstruction without any γ/hadron separation algorithm. Mrk421 flares have been observed in 2008. An all sky survey is going on and upper limits to GRBs flux at GeV energies have been calculated.

For the future the collaboration is optimizing the shower reconstruction and studying algorithms for gamma-hadron discrimination to enhance its sensitivity to gamma sources, but the results presented in this work confirm that ARGO-YBJ is a unique device for a continuous monitoring of the sky at TeV energies in the declination band -10^o to +70^o.

1. Aielli G. at al. NIM A562 (2006), 92-96.
2. Aielli G. et al. Astroparticle Physics 30 (2009) 287-292
3. Calabrese Melcarne K. et al. in Proc. 30th ICRC 2007
4. Aielli G. et al. Astroparticle Physics 30 (2008) 85-95
5. Di Sciascio G. et al. arXvi:0811.0997
6. http://heasarc.gsfc.nasa.gov/doc/xte/asm_products.html
7. Di Girolamo T. et al. in Proc.30th ICRC 2007

The phase II of H.E.S.S.

Y. Becherini, A. Djannati-Atai, M. Punch for the H.E.S.S. Collaboration
Astroparticule et Cosmologie (APC), CNRS/Univ. Paris 7 Denis Diderot,
Paris, France

In 2010 the H.E.S.S. experiment will enter its phase II where the present 4-telescope configuration will be enriched with a new very-large telescope at the centre of the array. The $600\,\mathrm{m}^2$ mirror area and high-resolution camera will permit the lowering of the threshold to about 30 GeV in the single-telescope mode, opening a new observational window to a large number of new high-energy phenomena. Adding a new very-large telescope also helps to enhance the detection sensitivity in the multi-telescope mode. The status of the project and the preliminary estimates of the angular resolution and effective area in the low energy domain will be presented and discussed.

1 Scientific objectives

Very high-energy (VHE) γ-ray astronomy has been living through a very exciting era with the advent of the H.E.S.S. experiment: in 2003 there were only twelve VHE sources detected in total but at present the extra-galactic VHE sky is composed of 27 Active Galactic Nuclei (*AGN*), while the Galactic sky is composed of about 60 sources. Concerning H.E.S.S. about 52 galactic and extra-galactic sources have been published between 2004 and 2009 and the majority of these were discoveries. With the sensitivities given by the present atmospheric Cherenkov experiments, it is becoming more and more difficult to augment the VHE catalogue as the brightest sources have been detected. A 5σ detection of a flux level below 1% percent of the Crab Nebula (a *faint source*) currently requires a typical observation time of the order of 100 hours, due to the fact that the H.E.S.S. mirror reflectivity has been degrading over years, causing a significant loss in sensitivity. Faint fluxes are expected from new classes of high-energy phenomena as the *starburst* galaxies or *Ultra Luminous Infra Red Galaxies* (ULIRG), as well as from galaxy clusters and from radio-galaxies. For the moment only two sources having a flux level of the order of 1% of the Crab have been discovered by H.E.S.S. [1,2] after a significant amount of observation time integrated over several years. Efforts to improve the sensitivity by optimising shower reconstruction algorithms and γ/hadron discrimination procedures are ongoing [3]. But in parallel, in order to further enhance the experiment detection capability, the project is entering in its new phase planned since 2005, called HESS-II. The first objective of this phase is the lowering of the energy threshold to about 30 GeV in the single-telescope (or *mono*) mode and the second objective is a sensitivity improvement better than a factor of two in the multi-telescope mode. A considerable amount of new physics subjects will be accessible with a 30 GeV energy threshold. Since a negligible γ-ray absorption is expected in the [30–100] GeV energy range, more distant objects will become visible with their intrinsic features, enriching the extra-galactic source catalogue and permitting to put stronger constraints on the

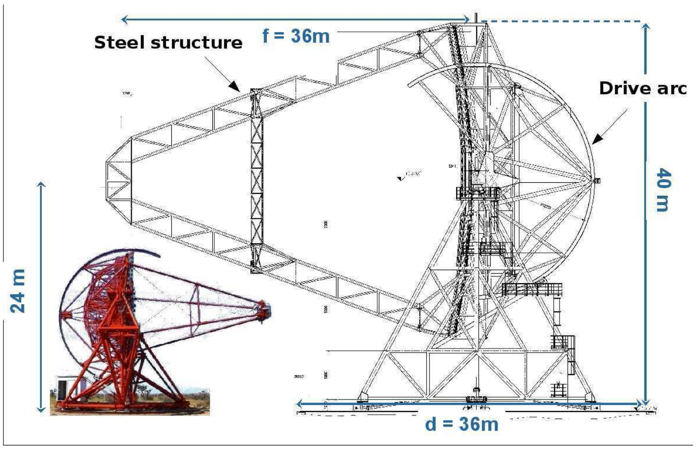

Figure 1: Sketch of the new very-large HESS-II telescope next to the former H.E.S.S. one shown on the left side of the figure.

EBL[a] absorption and on quantum gravity. Having access to the lower energy spectra will also permit the study of pulsar emission and to distinguish between different scenarios in several hadronic candidate sources thanks to the large effective area (see Par. 4) which allows results to be obtained in a reasonable observation time. It is worth noting that the H.E.S.S. studies of the [30–100] GeV energy spectra will be overlapping the Fermi analysis in the same energy range thus giving the chance to cross-check the different observations. Since the energy threshold is inversely proportional to square root of the reflecting mirror area, such a threshold level is being reached with the addition of a new very-large Cherenkov telescope (VLCT) at the centre of the present 4-telescope array.

2 The new 600 m^2 telescope

The HESS-II telescope design is optimised for the detection of low energy γ-ray induced showers and has a field-of-view of 3.5°. The installation phase is planned for the end of 2009 and the system is expected to be ready for the first data taking runs in the upgraded configuration for mid-2010. The telescope is a sturdy steel structure of remarkable size (see Fig. 1): the system is 40-m high when pointing at the horizon and 50-m high when pointing at the Zenith. The reflector of HESS-II is composed of 850 hexagonal mirror facets of 90 cm width (flat-to-flat) installed on a 30 m diameter parabolic surface, in order to minimize the time dispersion of the photons forming the image on the focal plane. The Cherenkov photons reflected by the mirror surface are detected on the focal plane which is connected to the reflective surface by four steel arms. A minimal focal length over diameter ratio of 1.2 is required to achieve very good imaging over the field of view, therefore the focal length has been chosen to be 36 m. The focal plane is equipped with a high-resolution camera composed of 2048 photo-multipliers each having a 0.07° diameter. The depth of field of the VLCT is such that for optimum shower imaging the telescope should be focused on the average shower maximum. Since the distance to the average shower maximum varies with elevation, the telescope needs to be refocused by moving the camera closer towards the dish along the optical axis for observations at large zenith angles. The maximum shift of the camera is about 10 cm. The focal plane is instrumented with new electronics using the *SAM* (Swift Analogue Memory) which will allow an accurate digitisation of the arrival time (about 1 ns resolution) and charge of the detected pulses. A level-2 trigger is foreseen for the VLCT which should allow some extra discrimination based on the pixel topology above two

[a]Extra-Galactic Background Light

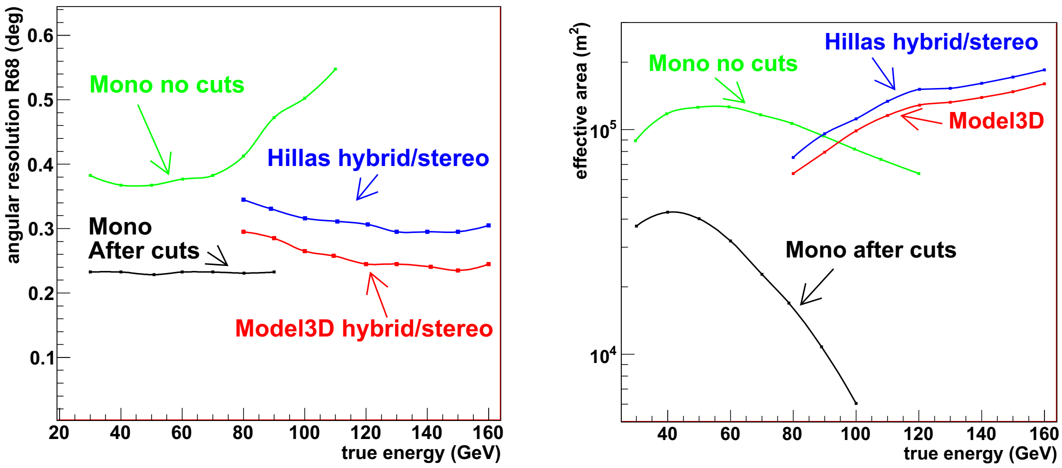

Figure 2: Left: Angular resolution for the different HESS-II detection regimes. The upper line *Mono no cuts* shows the curve for the pure *mono* events hitting the very-large telescope only, after image cleaning and reconstruction only, with no analysis cuts yet applied. For energies greater than 80 GeV the performance starts to worsen because the *mono* events in this range have a large impact parameter thus an image approaching the edge of the camera. The lower line *Mono after cuts* shows the angular resolution after background rejection cut and nominal distance cut (see text). The remaining curves show where the hybrid and stereo range take over and are obtained at trigger and image cleaning level i.e. no analysis cuts were applied (the upper line is for the Hillas case while the lower line is for the Model3D case). The final hybrid/stereo angular resolution is expected to be much better: 0.06° for H.E.S.S. after cuts. Right: Effective area given in m^2 for the different HESS-II detection regimes. The upper line *Mono no cuts* is again the curve obtained for the pure *mono* events after trigger and image cleaning, the curve after cuts is also indicated (*Mono after cuts*). The effective areas at higher energy after trigger and image cleaning (so no analysis cuts were applied) for the hybrid and stereo events for two different reconstruction algorithms are also shown by the upper line (*Hillas* case) and the lower line (*Model3D* case).

threshold levels.

3 Three-energy domain analysis

The inter-telescope trigger system of the HESS-II configuration will allow to trigger on three classes of events in parallel: at very low energies on purely mono-telescope events of the VLCT (*Mono* domain), at mid energies on combined events with an image from the VLCT and one from the smaller H.E.S.S. telescopes often with rudimentary information in the latter (*hybrid*[b] domain), and at even higher energies on current H.E.S.S. - Phase I type events with additional rich information in the central telescope (*full-stereo* domain). For the evaluation of the low energy performance of the upgraded system we simulated gamma and proton showers between 20 and 150 GeV at a zenith angle of 18° assuming an optimal optical efficiency in the five telescopes: all the results presented here have then to be considered valid only in the case of full-recoating of the four mirror dishes of H.E.S.S. phase I. The γ-ray source is simulated on the optical axis, so the source is projected at the centre of the cameras, and the simulations are carried out over a sufficiently large radius (500 m) from the centre of the array. The local trigger configuration used in this analysis can be summarised as follows: for the smaller telescopes we required a pixel threshold of 4 p.e. and a minimum number of pixels of 2.5, while for the VLCT we raised these values to 5 and 3.5 to allow a better online rejection of low energy hadrons. The event is then kept only if it has at least one telescope satisfying the local trigger condition. The

[b]The term hybrid is used in this paper to denote a particular event topology and should not be confused with the HESS-II “hybrid trigger mode” used in other contexts

algorithms for the level-2 trigger are still under development, so these are not included in the current study.

4 Performance in the [30–100] GeV range

A preliminary analysis aiming to evaluate the performance of the system in terms of angular resolution and effective area has been performed for the [30–100] GeV energy range. Images detected by the VLCT are used to reconstruct the parameters characterising the shower with the *Hillas* algorithm [4]. The resulting shower properties plus other robust parameters characterising the event has been used for the definition of a hadron rejection cut in a multi-variate approach. A cut on the nominal distance is required in order to reject the events giving images at the border of the camera, and to reject the events hitting the telescope too close to the source direction, which give non-elliptical images. Only the events giving images at a nominal distance greater than $> 0.45°$ and smaller than $< 1°$ are kept for further analysis.

The angular resolution, defined as 68% containment radius for all the pure *mono* events after image cleaning and reconstruction, is shown in Fig. 2 (left) with the upper line *Mono no cuts*, while the resulting curve after the background rejection and nominal distance cuts is shown with the lower line *Mono after cuts*. The angular resolution of the hybrid and stereo events, i.e. at higher energy, after reconstruction has been estimated with the Hillas and the Model3D [5] algorithms without any cuts, for comparison. The angular resolution for the pure *mono* events after cuts is of the order of $0.25°$.

For the calculation of the effective area for a point-like source analysis, an additional cut on the squared angular deviation between the source position and the reconstructed direction θ^2 is applied: we select all the events having a $\theta^2 < 0.13$ deg^2. The effective area resulting after the three analysis cuts is shown in Fig. 2 on the right. The area in the *mono* range after cuts is also shown with the lower curve *Mono after cuts*: it has a maximum around 40 GeV then it drops quickly at about 80 GeV where the hybrid and stereo detection regimes take over.

It should be noted however that the three cuts applied to study the performance presented in this work are only roughly estimated and will be optimised with more enhanced analyses.

5 Conclusions

Monte-Carlo studies of the performance of the full H.E.S.S. system after the addition of the phase-II VLCT at the centre of the current array shows that the goals of lowered threshold will be achievable (down to 30 GeV in *mono* mode). Studies will continue to characterise the improvement in the sensitivity which will be attained in the hybrid/stereo ranges, together with the development of adapted analysis methods. HESS-II has great new physics potential, with results expected on AGNs, pulsars, and the differentiation of leptonic/hadronic models in SNRs in the lower energy range, and detection of weaker source classes thanks to the improved sensitivity. The first results are expected soon after first light, in 2010.

References

1. M. Naumann-Godo et al, *Proc. for the 4th Heidelberg International Symposium on Gamma-Ray Astronomy, Heidelberg, Germany* **1085**, 304-307 (2008).
2. F. Aharonian et al, *Astrophys. Journal Lett.* **695**, 40-44 (2009).
3. Stefan Ohm et al., *Gamma-Hadron Separation in Very-High-Energy gamma-ray astronomy using a multivariate analysis method*, accepted for publication in *Astropart. Phys.*
4. W. Hoffman, I. Jung, A. Konopelko et al, *Astropart. Phys.* **12**, 135 (1999).
5. M. Lemoine-Goumard, B. Degrange, M. Tluczykont, *Astropart. Phys.* **25**, 195-211 (2006).

GAW - A very large field-of-view Imaging Atmospheric Cherenkov Telescope

Luísa Arruda, on behalf of the GAW collaboration
LIP
Av. Elias Garcia, 14, 1º andar
1000-149 Lisboa, Portugal
e-mail: luisa@lip.pt

GAW (Gamma Air Watch) is a pathfinder experiment in the TeV range to test the feasibility of a new generation of Imaging Atmospheric Cherenkov Telescopes (IACT). It combines high flux sensitivity with large field-of-view (FoV = $24^{\mathrm{O}} \times 24^{\mathrm{O}}$) using Fresnel lenses, stereoscopic observational approach and single-photon counting mode. This particular counting mode, in comparison with the usual charge integration one, allows the triggering of events with a smaller number of collected Cherenkov photons keeping a good signal/background separation. GAW is conceived as an array of three identical imaging telescopes with 2.13 m diameter placed at the vertices of an equilateral triangle of 80 m side. The telescope will be built at the Calar Alto Observatory site (Sierra de Los Filabres - Almeria Spain, 2168 m a.s.l.) and is a joint effort of research institutes in Italy, Portugal and Spain. The main characteristics of the experiment will be reported.

1 Introduction

High energy gamma-rays are a powerful probe for several astrophysical quests. During the recent years a new window has been opened in the observation of gamma-rays from about few tens of MeV up to EeV thanks to the availability of new photon detectors built using technologies imported from experimental particle physics. Satellites cover the lowest energy range of detection (few MeV up to few tens GeV) while ground-based detectors like Imaging Atmospheric Cherenkov Telescopes (IACTs) and Extensive Air Shower (EAS) arrays cover higher energy regions (the former from 50 GeV up to more than 10 TeV and the latters with a threshold at 0.5-1 TeV). The aim of this article is to introduce a Research and Development experiment for the construction of a new IACT to detect very high energy (VHE) gamma-rays [a]. Although this is a young research field, VHE gamma-ray astronomy is a well established discipline with several identified sources, steady and variable, galactic and extragalactic.

The existing and planned ground-based IACT observatories aim to lower the energy threshold to few tenths of GeV to overlap with satellite detection region. The second goal is to improve the flux sensitivity in the region above 100 GeV through a stereoscopic observational approach. Another important purpose is to do a full sky coverage since astronomical events can occur at unkown locations and/or randomly in time. A current IACT telescope consists of an optical system with few degrees field-of-view (FoV $\leq 5^{\mathrm{o}}$) and of a pixelized camera placed at its focus. They can not achieve larger FoV due to mirror optical aberrations that rapidly increase with off-axis angles. Moreover, the increasing of the detector area required to cover large FoV would

[a] As a rule of thumb, VHE γ-rays are classified as γ-rays with energies from $\sim$30 GeV up to $\sim$30 TeV [1]

unavoidably produce a strong reduction of the light collecting area due to the shadow of the detection matrix onto the reflector. Such limitation has to be overcomed to significantly improve the capability of surveying large sky areas since detection of transient phenomena is a goal. An alternative solution might be the usage of refractive optics like Fresnel lenses as light collectors instead of the classical mirror. Fresnel lenses enable large FoV, they have good transmittance and avoid the shadow problem. Since they are easy to replicate Fresnel lenses appear as an affordable solution however chromaticity should be controlled. The study of the feasibility of such solution is the aim of the GAW experiment as explained below.

1.1 The GAW experiment

The design of the GAW telescope includes a Fresnel lens and a focal surface detector formed by a grid of **M**ulti**A**node pixelized (8x8) **P**hoto**M**ultiplier **T**ubes (MAPMT) coupled to light guides. A schematic view of the GAW telescope is depicted in Figure 1. A detailed description of the GAW detector is given in reference [2]. The design of the GAW experiment was made to prove the feasibility of the usage of a Fresnel lense as an efficient light collector allowing an enlargement of the field of view. Another innovative idea is that instead of the usual charge integration method, GAW front-end electronics design will be based on single photoelectron counting mode [3]. In such working mode, the effects of the electronic noise and the photomultiplier gain differences are kept negligible. This method strongly reduces the minimum number of photoelectrons (p.e.) required to trigger the system and, consequently a low telescope energy threshold ($\sim$ 700 GeV) is achieved despite the relatively small dimension of the Cherenkov light-collector (2.13 m diameter). The pixel size is small enough (3.3425 mm) to reduce the photoelectrons pile up within intervals shorter than sampling time (10 ns). Current camera design is confortable with a threshold of 14 p.e per event per trigger-cell (2×2 multianode photomultipliers) since the expected night sky background (NSB) contribution is 2-3 p.e. per sample per trigger-cell.

The light collector is a non-commercial Fresnel lens with focal length of 2.56 m and 3.2 mm thick. The lens is made of UltraViolet transmitting polymetacrilate with a nominal transmitance of $\sim 95\%$ from 330 nm to 600 nm. The lens design is optimized for the maximum wavelength of photon detection ($\lambda \sim 360$ nm). The lens is composed of a central core ($\varnothing$ 50.8 cm) surrounded by a corona of 12 petals extending for 40.6 cm and by a second level of 20 petals for the outer corona extending for more 40.6 cm. A mechanical spider support will keep all pieces together.

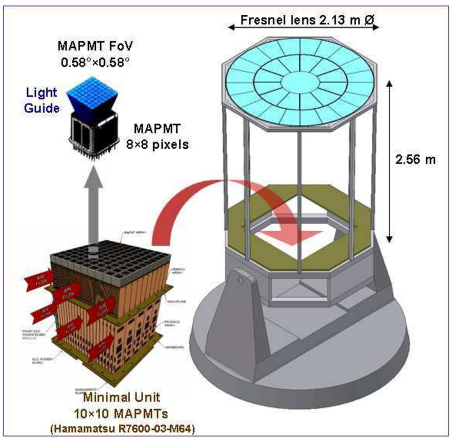

Figure 1: Schematic view of the GAW telescope.

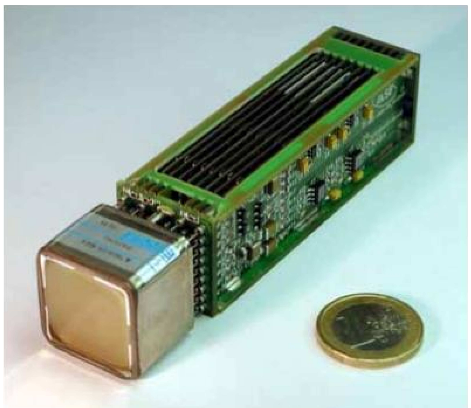

Figure 2: FEBrick with a MultiAnode PMT

The MAPMT used for GAW focal surface detector is the Hamamatsu R7600-03-M64 (Figure 2) with 64 anodes arranged in an 8×8 matrix. The physical dimension of the tube section is

$25.7 \times 25.7\,\mathrm{mm}^2$ while the effective area is $18.1 \times 18.1\,\mathrm{mm}^2$. The tube is equipped with a bialkali photocathode and a 0.8 mm thick UV-transmitting window (from 200 up to 680 nm). This ensures good quantum efficiency for wavelengths longer than 300 nm with a peak of 20% at 420 nm. The Metal Channel Dynode structure with 12 stages provides a gain of the order of 3×10^5 for an applied voltage of 800 V. This PMT provides a fast response (of the order of 10 ns) in order to disentangle the Cherenkov light, which is produced coherently in space and time, from the incoherent but significantly fluctuating NSB.

In order to reduce dead areas between adjacent photomultipliers and consequently to increase the photon collection efficiency, an array of light guides was added, coupled to each photomultiplier. Due to the dead areas between adjacent PMTs around 55% of the photons would be lost without any guiding device. A light guide unit is a pyramidal polyhedron composed of 8×8 independent, plastic tubes glued on a plastic plate. The tubes are made of a polymetacrilate (PMMA) from Fresnel Technologies with a refractive index of 1.489 close to the one of the PMT window ($n = 1.5$). These characteristics were chosen to obtain a transmittance as high as possible over the wavelength range of the PMT detection. The 64 pieces that constitute the light guide, with ten different shapes, are held together by a thin layer (1 mm) on the top made of an anti-reflective PMMA. Inside the light guide, photons are conducted by internal reflections. The light guide unit is optically coupled to the active area of phototube cathode through a 1 mm flexible optical pad. With a total height of 35 mm, and a collecting surface of $26.74{\times}26.74\,\mathrm{mm}^2$, it presents a readout pixel size of 3.3425 mm which renders in a spatial granularity of $\sim 0.1^{\mathrm{o}}$ suitable for Cherenkov imaging. The optimum dimensions have been determined to maximize the photon collection efficiency (~71%), to minimize the cross talk between adjacent pyramidal frustuns (~6.5%) and to achieve the higher spatial uniformity in the photon collection efficiency (uniform at the level of 0.01). All these parameters were evaluated with simulated samples for the photon incident angles on the top of the light guide within the GAW FoV.

1.2 The GAW project timeline

The chosen site for the telescope placement is the Calar Alto Observatory (Sierra de Los Filabres, Almeria, Spain), at 2168 m above sea level. The civil engineeering work at the Calar Alto site is close to be finished and, in particular, the construction of the building to house the telescope is finished as can be seen in Figure 3(b). The telescope mechanical structure, which is depicted in Figure 3(a), and the spider support for the lens petals were manufactured by a specialized company (ASTELCO Systems) and shipped to the site, after validation tests carried at the company headquaters. The telescope and lens comissioning will be undertaken in 2009/2010. The main goal for this stage is to prove the feasibility of the GAW concept, in particular the optics and the data acquisition systems. A reduced Fresnel lens with a single central petal will be installed in the centre of the supporting spider and the lens design will be validated by measuring the spot size with Vega spectrum. The first tests of GAW electronics will also be carried out. Afterwards the project will start with a first phase where only one telescope will be assembled, with a reduced focal surface detector (10×10 MAPMT), covering a FoV of $6^{\mathrm{o}}{\times}6^{\mathrm{o}}$. This phase, starting in 2010, will be suited to test this detector principle in "on-axis" mode and in "off-axis" observation mode. The focal surface will be mounted on a rack frame (Figure 3(c)) and moved to enable sensitivity measurement by observing the Crab Nebula, on-axis and off-axis, up to 12^{o}, the edge of the GAW FoV. Obtained the R&D results and in case of a sucessful confirmation of the GAW concept a second phase is foreseen, with a fully equipped focal plane with $24^{\mathrm{o}}{\times}24^{\mathrm{o}}$ FoV. For this phase three identical telescopes will be constructed, placed at the vertexes of a equilateral triangle (80 cm side) and will work in the stereoscopic mode, improving the angular resolution, the cability of identifying gamma-ray induced showers and the determination of the primary photon energy.

(a)

(b)

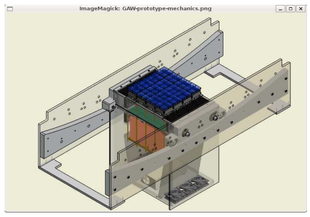

(c)

Figure 3: (a) GAW telescope mechanical structure. (b) Telescope housing in Calar Alto. (c) Artistic view of the detector focal surface mounted on a rack frame.

2 Summary

IACTs with large FoV will offer two important advantages: they will survey the sky for serendipitous TeV detections and, at the same time, will increase the IACT collection area, triggering events whose core is far away from the telescope axis and therefore improving the statistics of the high energy tail of the source spectra. Presently, GAW is a R&D experiment to build a Cerenkov telescope that will test the feasibility of a new generation IACT that joins large FoV and high flux sensitivity. Large FoV will be achieved by using refractive optics made of Fresnel lens of moderate size. The focal camera will use the single photon counting mode instead of the charge integration mode widely used in the present IACT experiments. This working mode will allow the detector to be operated with a low photoelectron threshold and a consequent lowering of the energy threshold. The stereoscopic observational approach will improve the angular resolution. GAW is a collaboration effort of several Research Institutes in Italy, Portugal and Spain. It will be erected in the Calar Alto Observatory (Sierra de Los Filabres - Andalucia, Spain). The first telescope is forseen for 2010.

3 Acknowledgments

I would like to express my acknowledgments to the GAW collaboration for giving me the opportunity to attend the 44^{th} Rencontres de Moriond on *Very High Energy Phenomena in the Universe*. I also express my gratitude to the organizers for the financial support to participate in the meeting.

References

[1] de Angelis, A. *et al.*, *Riv.Nuovo Cim.*, **31**, 4 (2008) 187-246.

[2] GAW Collaboration, GAW, Gamma Air Watch - Concept Design and Science Case, http://gaw.iasf-palermo.inaf.it/2005.

[3] Catalano, O. *et al.*, *Astroparticle Physics*, **29**, 2 (2008) 104-116.

CTA – the Cherenkov Telescope Array

M. Punch for the CTA collaboration
Astroparticule et Cosmologie (APC), CNRS, Universite Paris 7 Denis Diderot, 10, rue Alice Domon et Leonie Duquet, F-75205 Paris Cedex 13, France UMR 7164 (CNRS, Université Paris VII, CEA, Observatoire de Paris)

High energy gamma-ray astronomy is a newly emerging and very successful branch of astrophysics. Exciting results have been obtained by the current generation Cherenkov telescope systems. The design study of the very large Cherenkov Telescope Array system (CTA) with a sensitivity about an order of magnitude better than current instruments and a wider energy coverage from a few tens of GeV to over 100 TeV is ongoing, with a baseline solution based on proven technology, the main challenges being on the cost and reliability fronts. This new facility — CTA — will be operated as an observatory for the science community, based on two sites: Southern, with a wide energy range covering especially the Galactic sources; and Northern, with a focus on low energies for Extragalactic objects. This observatory will reveal an order of magnitude more sources than in the current VHE catalogues, allowing for example population studies of classes such as Pulsar Wind Nebulae (PWNe) and Active Galactic Nuclei (AGN). Due to its higher sensitivity and better angular resolution it will be able to detect new classes of objects and phenomena that have not been visible until now. The scientific potential and status of the design study of CTA are reported.

1 Introduction

The domain of Very High Energy (VHE) Gamma-Ray astronomy has reached maturity with the advent of the latest generation of gamma-ray telescope systems, which have developed the Atmospheric Cherenkov Technique (ACT) to sensitivities which are an order of magnitude over the previous generation. In Europe, H.E.S.S. and MAGIC are the leaders in this domain, having advanced the techniques of stereoscopy for the former and large mirror area for the latter, with both using fast, fine-imaging cameras. With the second phase of these experiments soon in operation, HESS-II will explore the gain from very large image mirror area, while MAGIC-II will introduce stereoscopy. So, there is a clear convergence in operation for the latest generation of ACT telescopes. The idea of launching a large project in Cherenkov astronomy, gathering all the current European expertise in the domain, rapidly took form thanks to the success of this current generation of experiments.

2 Goals of CTA

The goal of CTA is to create the future ground-based gamma-ray observatory, with a jump of a factor of 10 in sensitivity over the currently-operating experiments (down to a milliCrab level), providing a deeper vision of the gamma-ray sky, and allowing much finer temporal resolution for variable sources (e.g. AGNs). In parallel, the energy range to be explored should extend from a few 10's of GeV to above 100 TeV, allowing new source classes to be discovered, and the emission mechanisms in the known source classes to be better investigated (e.g., comparison of leptonic vs. hadronic models in SNRs, binaries), and a wide parameter space for possible Dark Matter annihilation sources to be explored. Additionally, an improvement in angular resolution will not only provide increased background rejection for the point-like sources (AGNs, binaries), but will allow also fine mapping of the extended Galactic sources (PWNe and SNRs) and possibly the nearest extragalactic sources (M87, Cen A). Given that the gamma-ray sky is already known to contain a rich catalogue of sources, full-sky coverage is most desirable, with Northern and Southern installations of the observatory, adapted to the sky coverage, i.e. better low-energy coverage for the Northern installation where the extragalactic sky would be the preferred target, and with a wider energy range for the Southern one for which the region around the Galactic centre will be fully accessible. These goals could be achieved by means of two extended, mixed arrays of Cherenkov telescopes (detailed below) with the additional advantage that such large, extended arrays would have an inherent flexibility of operation, allowing both deep field investigations and surveys, in parallel with monitoring of the brightest variable sources and reactivity to alerts from other instruments.

3 Conceptual Design of CTA

On the basis of the experience with and convergence of the current generation of ACT Telescopes, it is clear that the technology to achieve the goals of the CTA is available, with the current generation being considered as “Prototypes”. The goals can be achieved with extended, mixed arrays of Cherenkov telescopes, with a gradation in telescope performance:

- Detection at the highest energies, from 10–100 TeV, encounter the major difficulty of the sparseness of the signal even from strong sources. This leads to the requirement of an extended array comprising a couple of tens of telescopes over $\sim 10\,\mathrm{km}^2$, of small size ($\sim$ 5–7m diameter) but with very wide Field-of-View (FoV, 7–10°) in order for air-showers to be seen in stereo by widely-separated detectors, and relatively coarse pixelization ($\sim 0.25°$ or larger). Such an array is mainly required on the Southern site, where Galactic sources — unaffected by absorption of the extragalactic background light — are the preferred target.

- In the core energy range from 100–10 TeV, where the current generation of ACT telescopes operates most efficiently, an extended array is also required for increased collection area, providing a higher proportion of “golden events” where the shower impact parameter is contained within the array (giving better angular resolution and increased sensitivity), and which will also provide flexibility of use of sub-arrays. An array of a few tens of telescopes covering $\sim 1\,\mathrm{km}^2$, of mid-size (10–13m diameter), with wide FoV (5–8°, for mapping of extended objects) and moderate pixelization ($\sim 0.2°$ or smaller) is under consideration.

- At the lowest energies, a central section of a few large telescopes (0–25m diameter), with improved photo-detector performance and a FoV of 4–6° with finer pixelization ($\sim 0.1°$), will provide access to the lowest energies, and therefore to the most distant AGNs and to Galactic sources with spectral cut-offs (e.g. pulsars), as well as linking up to the spectral information provided by satellite detectors (FermiGST, AGILE) at lower energies. As detailed above, the Northern site will concentrate more on this low-energy regime.

The parameters concerning the mix of telescopes, layout, mirror area, camera pixelization, and the electronics' trigger and sampling rapidity are part of the Design Study which is underway within the collaboration, and are optimized in a multi-dimensional parameter space with consideration given to performance for the physics goals, and to cost and reliability/durability.

4 The CTA Design Study

The Design Study on CTA is proceeding, based on a large consortium of institutes, including most European groups in this and related fields, and interested parties from the US and Japan.

The cost and reliability/durability challenges are primordial in these studies, the latter being of particular importance for such a large project of long duration, since the installations will operate as an observatory with a life-time of the order of 30 years. The cost envelope within which the optimization is being performed supposes that 100k€ will be needed for the Southern site, and 50k€ for the Northern (capital costs). To achieve this goal will already require advances in the cost model for some components, and implies that a gain of a factor of 10 in sensitivity can be achieved with a factor of 10 cost ratio over the current generation.

It should be noted that the project aims to have of the order of 100 telescopes operating in remote locations (on two sites), with of the order of 100,000 electronics channels, and 10,000 m^2 of mirror area. So, as an indication, an savings/increase of 10k€ per telescope, or 10€ per channel, or 100€/m^2 per mirror is equivalent to a saving/increase in overall cost of 1 M€.

The Design Study has been divided into a number of Work Packages (WPs) in the management structure, including Physics, Monte Carlo & Data Analysis, Site evaluation & infrastructure, Mirror (optics, control), Telescope (structure, drives, control systems), Focal Plane Instrumentation (photo-detectors, light-guides, mechanics), Electronics (read-out and trigger), Atmosphere Studies and Calibration, Observatory Operation & Access, Data (handling, processing, management, access), and Quality Assurance & risk assessment. The aims of some of these WPs are briefly described below (space does not permit all to be described).

The physics goals are taken into account in the optimization based on certain "benchmark" sources (being defined by the Physics WP given the key physics topics for CTA). The Monte Carlo WP provides the instrument response for a number of base configurations, initially defined using "Toy Model" methods based on full simulations, but a number of these base configurations will be fully simulated using the codes extended from the previous generations (air-shower and instrument simulations). The cost of each element of the base configurations (e.g., mirror area, photo-detectors, electronics, telescope mounts) allows the overall cost to be found, and together with the instrument response should allow the "physics bang-for-the-buck" to be estimated, and the base configurations to be winnowed and adjusted — in a complex feedback loop between the Physics, Monte Carlo, and technical WPs which it is hoped will converge rather rapidly.

The Site WP concerns the evaluation of sites based on a number of defined meteorological, technical, and infrastructural criteria based on existing data (meteo stations, satellite measurements), to achieve a candidate shortlist for which more precise measurements, infrastructure and political evaluations can be made for comparison in the definitive choice.

The Telescope WP goals, as described in the conceptual design above, requires the definition and evaluation of three sizes of telescope, using standard optics (parabolic or Davies-Cotton dishes, with no secondary mirror) as a base-line. The dish type will be adapted to the telescope size, while in general the focal distance relative to the diameter will be kept as large as affordable (1.4–2), for better isochronicity and lower aberrations. For the larger telescopes, active mirror control may be used if the inherent telescope stiffness would not allow a Point Spread Function (PSF) less than 1 mrad. Commercial components will be used as much as possible, for reliability and cost concerns. Note that the 30-year lifetime aimed for requires a failure rate an order of magnitude below the current generation.

In the Mirror WP, the goal is to achieve a 1–2.5 m^2 hexagonal mirror panel, with a reflectance above 80% in the wavelength range which is useful for the ACT (300–600 nm), weighing less than 30 kgs, with a PSF below 0.6 mrad. Proven solutions exist for this, based either on aluminized monolithic glass or on machined aluminium plate on a aluminium honeycomb, but these suffer from fast aging and high weight, or from high cost, respectively. New solutions based on carbon-epoxy composites or aluminized glass sheets on a polymer foam substrate are being investigated, with the long-term performance over many weather cycles and response to frosting problems being key issues under evaluation.

Concerning the cameras, the Focal Plane Instrumentation (FPI) and Electronics WPs are major cost drivers. A clear decision has been reached to have a fully-integrated camera, in which the signals from the photo-detectors are processed all the way to digitization and the resulting data are sent over optical fibres to the central data acquisition systems. This approach simplifies the communication and cabling, and allows full advantage to be taken of the rapidity of the Cherenkov signals by telescope-triggering within the cameras. It will also allow a modularity at the camera level to be achieved (in which a "spare" camera can be installed in case of breakdown, pending repair in a central workshop). However, it does engender a heavier camera, requiring careful consideration of the problems of temperature stabilization and weather protection.

The FPI WP is leading studies with industrial partners on the photo-detectors, where the base-line solution of Photo-Multiplier Tubes (PMTs) is being extended with the examination and comparison of new products (super/ultra-bialkali photo-cathodes, hemispherical windows, ...) on the basis of photo-detection efficiency in the relevant wave-length range, accessibility of the single-photo-electron signal for calibration purposes, and low after-pulsing rate for the reduction of random coincidence triggers. The FPI WP also is investigating the camera mechanics and optics, with Winston-cone light guides and protective windows for the cameras, with optimally light-weight, robust, and easy-access camera mechanics.

Within the Electronics WP, major efforts are underway to integrate as many elements of the electronics chain as possible within a single custom Integrated Circuit. These elements include the pre-amplification, pixel-level trigger comparators, analogue signal storage, analogue-to-digital conversion (ADCs), digital signal buffering in FIFOs, and data transfer (LVDS, Ethernet...). Such integration will allow unit costs to be brought down (lower component cost, simpler integration on circuit boards), and will increase the reliability and robustness of the electronics. Partial solutions of this type exist already in current instruments (the "Swift Analogue Memory", SAM, used in HESS-II and the "Domino Ring Sampler" DRS-2 used in MAGIC-II), but increased integration is sought with the NeCTAr project and the "Dragon" card based around the DRS-4 chip, on which developments are proceeding. The Electronics WP is also concerned with the camera and array triggering for which several solutions exist in current instruments.

Note also that parallel developments proceed on more speculative research efforts (e.g. advanced photo-detectors such as silicon PMs), for which the planned design should not preclude their integration if such technologies mature early, or their integration in later upgrade cycles.

5 Conclusions

The CTA project for the future major of Atmospheric Cherenkov Observatory is proceeding in the Design Study phase, organized in a number of Work Packages whose work is advancing. Prototypes of components are being constructed, which will allow the design decisions to be made and construction to begin in 2012/13, with aim of completion of the full arrays in 2018. CTA will then be the major observatory in VHE gamma-ray astronomy, combining guaranteed astrophysics and physics returns with significant discovery potential.

References

1. Please see the many contributions to these proceedings concerning the current physics from the ACT detectors, and also the contributions for HESS-II and MAGIC-II in near-future upgrades, and that on AGIS for the similar future concept from the mainly North American consortium.

AGIS: The Advanced Gamma Ray Imaging System

Wystan Benbow for the AGIS Collaboration
Harvard-Smithsonian Center for Astrophysics
60 Garden St, Cambridge, MA 02138, USA

With the construction and subsequent operation of several third-generation observatories (VERITAS, HESS & MAGIC), very high energy (VHE; E > 100 GeV) γ-ray astronomy has undergone a revolution in the past 10 years. The VHE source catalog has grown from ~10 objects in 2002, to more than 80 in 2009, and should continue to increase. In addition, the number of VHE source classes has grown considerably, revealing a diverse range of astrophysical phenomena. It is clear that if the sensitivity of VHE observatories is improved, more sources and more source classes will be discovered. The Advanced Gamma ray Imaging System (AGIS) is a concept for a ten times more sensitive, fourth-generation VHE observatory that will hopefully begin construction in 2012, and commence partial and full scienti
in ~2015 and ~2019, respectively. The AGIS concept is described in this proceeding.

1 Introduction

The rapid growth of VHE γ-ray astronomy was achieved primarily through the development of stereoscopic arrays of large-diameter imaging atmospheric-Cherenkov telescopes (IACTs). Using current technology and effectively scaling the technique, the sensitivity of an IACT observatory can be improved by an order of magnitude. It is also relatively straight-forward to increase the field-of-view (FoV), lower the energy threshold, and improve the angular resolution of a future VHE detector. Indeed it would seem that the major technology development will be to affordably achieve these improvements, and ensure reliable operation of the instruments.

The AGIS concept consists of an array of 50 wide-FoV IACTs that use a challenging optical design to reduce the plate scale of the instrument, enabling a cost-effective modular camera. Although the construction of an independent experiment is possible, the AGIS collaboration anticipates merging with European groups formulating the Cherenkov Telescope Array (CTA) to create a major international VHE observatory. In this scheme, the AGIS collaboration would contribute a 36-IACT system to a larger array of IACTs. The AGIS component of this array would primarily focus on the 100 GeV to 10 TeV range, while enhancing the overall capabilities of the observatory in the 20 GeV to 100 TeV range.

2 Key Science Goals

It is likely that sensitivity of AGIS will enable an increase of the VHE source catalog to ~1000 sources, going out to redshifts of $z \approx 1$. For an example of the potential impact on VHE observations of the inner Galaxy, see Figure 1. The increase in the number of sources should provide an impact on VHE astronomy similar to that of the Fermi Gamma-ray Space Telescope's effect on MeV-GeV astronomy, and will have considerable implications for many important topics in astrophysics, astroparticle physics, and cosmology. It will enable deep probes of the physics at

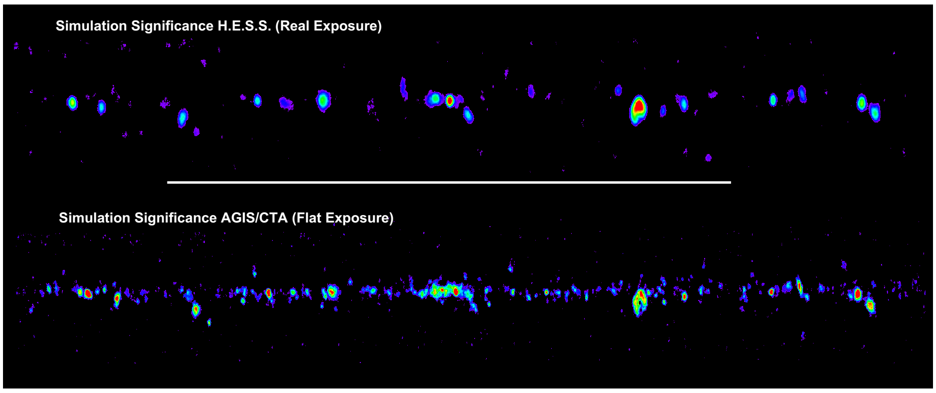

Figure 1: A simulated sky map of the inner Galaxy that would be observed by AGIS (Funk et al. 2008).

the sites of high-energy acceleration and particle interaction, as well as allow an interpretation of the numerous classes of VHE emitters based on VHE population studies, rather than a few remarkable objects. AGIS will also expand on the science from the Fermi satellite by extending the broad-band spectrum of numerous γ-ray sources from 100 GeV up to to 100 TeV, covering a total energy range of six decades, and improving on the γ-ray source localizations. Detailed discussion[a] of the galactic, extragalactic, and astroparticle physics topics addressed by AGIS can be found in the White Paper[b] on the *Status and Future of Gamma-ray Astronomy* commissioned by the American Physical Society. The following list contains the key scientific questions to be addressed by AGIS:

- How and where does nature produce very energetic particles in general, and hadronic cosmic rays in particular? In detail, what are the roles of Poynting fluxes, electromagnetic turbulence, and shocks?
- How do black holes form relativistic jets in AGNs and GRBs, and how do these jets interact with their environment?
- How do energetic particles influence or generate the magnetic field that permeates interstellar space?
- What is the nature of dark matter, and how is it distributed in galactic halos?
- Does spacetime show evidence for structure on TeV^{-1} to Planck scales? Is Lorentz invariance a good symmetry at these energies?

3 Technical Details

The primary objective of AGIS is to construct an instrument that is 10 times more sensitive (1 mCrab or $\sim 10^{-13}$ erg cm^{-2} s^{-1} at 1 TeV) than current instruments (e.g. VERITAS) in the 100 GeV to 10 TeV band. This can be accomplished by increasing the collection area of the array to ~ 1 km^2 and by improving both the angular resolution and the background rejection from the current capabilities. To achieve this objective, the conceptual design[2,3,4] of AGIS consists of 36 wide-FoV (8°) telescopes each with an effective mirror area of ~ 100 m^2. The specifications of the AGIS conceptual design are listed in Table 1. Many design parameters (e.g. pixel size, telescope spacing, optical PSF) are not finalized, and are the subject of further simulation studies.

Figure 2 shows the expected angular resolution and effective area for AGIS. In comparison to VERITAS, a $2-3$ times better angular resolution, along with a ~ 10 times higher collection area, is achieved. It is possible to further improve (by $\sim 40\%$) the angular resolution by decreasing

[a] www.agis-observatory.org/RFI
[b] http://cherenkov.physics.iastate.edu/wp/

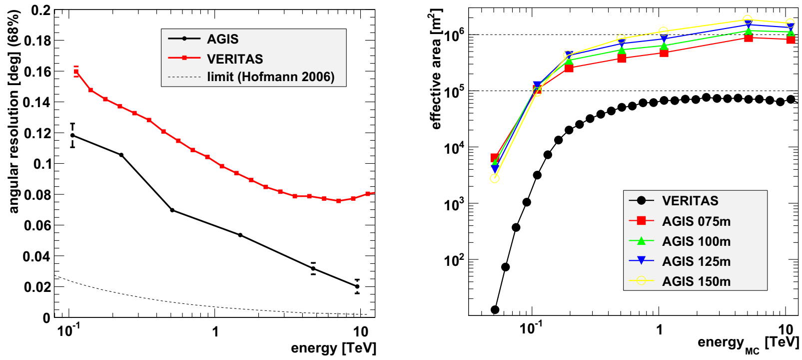

Figure 2: Left: Angular resolution (0.1° camera pixels) vs energy for AGIS (36 telescopes with baseline spacing of 125 m) compared with VERITAS (Holder et al. 2008) and the theoretical limit (Hofmann 2005). Right: Effective area vs energy for the AGIS (36-telescope) array with different telescope distances.

Table 1: Speci

Telescope Spacing	120 - 150 m
Effective Mirror Area per Telescope	100 m^2
Field of View (FoV)	8°
Pixel Size	0.05 - 0.10°
Effective Collection Area	1 km^2
Energy Threshold	100 GeV
Angular Resolution	0.02 - 0.05°

the pixel size from 0.1° to 0.05°. Although AGIS has considerable sensitivity both below 100 GeV and in the range 10 TeV to 100 TeV, expansions of the 36-IACT array are envisioned to improve the coverage at the lowest and highest energies. Indeed this expansion may be part of a joint international collaboration, and the final detector may consist of a hybrid array with several different telescope designs and baseline spacings. For example this hybrid array might also consist of a dense core of larger IACTS and an array of small IACTs spread over a large area.

The angular resolution of the traditional IACT design (Davies-Cotton, DC) used by HESS and VERITAS is limited by aberrations (e.g. coma) which are particularly apparent off the main optical axis. These limiting effects can be reduced by placing the camera at a large focal distance. However, this requires a large, expensive camera, and thus an IACT with an 8° FoV camera has not yet been built. To create a cost-effective, compact camera, a new IACT telescope design with a considerably shorter focal length is proposed for AGIS. This design consists of a two-mirror Schwarzchild-Couder (SC) optical system [5] that uses complex aspheric mirror surfaces (see Figure 3). The preliminary design consists of an 11.5 m diameter primary mirror with a 5.63 m central hole, and a 6.6 m diameter secondary mirror. The SC design will reduce the plate scale of the telescope such that integrated photo-sensors (e.g. multi-anode photomultiplier tubes (MAPMTS)) can be used in a modular camera (see Figure 3). In addition the degradation of the off-axis optical PSF in the SC design is much less than in the DC design, and a low-cost fast mount can be used.

Although the SC design is almost 100 years old, an SC telescope has never been built due to the lack of technology for producing the complex mirror surfaces at reasonable cost. In addition, the design requires precision alignment (less than 0.1 mm deviation across a length of 1 m) of the optics that must be maintained during observing, despite dependence on the tracking position and temperature in the optical surfaces and support structure. The results of recent research and development efforts have made it possible to overcome these issues [2].

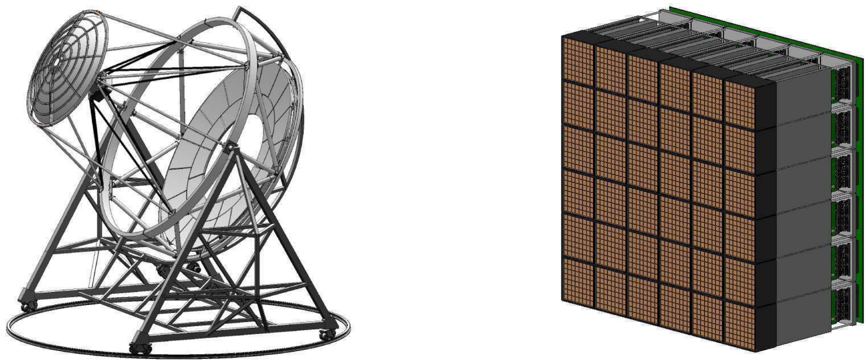

Figure 3: Left: Conceptual drawing of the SC telescope (OSS, positioning system and 8° camera. Right: Conceptual drawing of one sub $\times$6 2” MAPMT modules plugged into a backplane.

The AGIS camera will employ a modular design based on MAPMTS and highly-integrated waveform sampling ASICS. The camera will be divided into subfields, each covering a FoV of about $2-3°$. Each subfield will interface with a front-end pattern trigger, and will be composed of a number of camera modules, consisting of several MAPMT modules and front-end ASIC cards. Although an array trigger using a simple telescope coincidence substantially reduces the number of background events recorded, a topological array trigger will be constructed to further suppress background events and ultimately reduce the array's energy threshold [8].

The AGIS collaboration has not yet selected a site, but locations are being considered in the United States (Utah, Arizona & New Mexico), Mexico (e.g., Sierra Negra & San Pedro Matir), India (e.g., Hanle), and South America (e.g. Argentina & Chile). A Southern Hemisphere location is most likely given the large number of known and potential VHE sources near the Galactic Center (see Figure 1), unless a different, independent instrument (e.g. CTA) is constructed there first. However, should the AGIS collaboration merge with the CTA groups, it is possible that similar instruments in both Northern and Southern Hemispheres will eventually be built.

4 Conclusion

The rapid evolution of VHE astronomy has clearly demonstrated the need for a next-generation VHE observatory with 10 times higher sensitivity and 3 times better angular resolution. AGIS, is a concept for this observatory that uses an array of 36 wide-FoV IACTs with a novel two-mirror SC design. This complex design should decrease the cost and improve the reliability of a large IACT array. Although the SC design proposed for AGIS is challenging, the technology is available to quickly turn this concept into a reality. The cost of constructing the AGIS 36-telescope component is expected to be ∼130 million US dollars, along with another ∼20 million US dollars for infrastructure and a project office. Research and development efforts for AGIS, including the development of a prototype telescope, are expected to continue in the near term. Construction of the AGIS array is anticipated to begin in 2012, pending approval from the funding agencies, and scientific observations are expected to commence in 2015 and 2019 with a partial and full array, respectively.

References

1. S. Funk, et al., AIPC **1085**, 886 (2008).
2. V. Bugaev, et al., AIPC **1085**, 834 (2008).
3. A.N. Otte, et al., AIPC **1085**, 866 (2008).
4. G. Maier, et al., AIPC **1085**, 862 (2008).
5. V. Vassiliev, et al., Astroparticle Physics **28**, 10 (2007).
6. J. Holder, et al., AIPC **1085**, 657 (2008).
7. W. Hofmann, Proc. of Cherenkov 2005 **Palaiseau**, 393 (2005).
8. F. Krennrich, et al., AIPC **1085**, 894 (2008).

2.
High Energy Cosmic Rays

On (shock) acceleration of very high energy cosmic rays

Martin Lemoine
Institut d'Astrophysique de Paris,
CNRS, UPMC,
98 bis boulevard Arago, F-75014 Paris, France

This talk discusses the acceleration of very high energy cosmic rays in astrophysical sources, with a strong emphasis given to the recent developments in our understanding of relativistic shock acceleration.

1 Introduction

The number one question for ultra-high energy cosmic ray astrophysics is how to produce particles with an energy as high as $\sim 10^{20}\,$eV. The famous Hillas criterion [1] allows to set a strict upper bound on the maximal energy $E_{\rm max}$ produced in an object of size R, magnetic field B containing scattering centers moving at velocity βc: $E_{\rm max} \leq Ze\beta BR \simeq 10^{20}\,{\rm eV}\,Z\,B_{\mu{\rm G}}R_{100{\rm kpc}}$ ($B_{\mu{\rm G}} \equiv B/1\,\mu{\rm G}$, $R_{100{\rm kpc}} \equiv R/100\,{\rm kpc}$), neglecting relativistic boost effects. It is a strict upper bound in the sense that it does not consider the possible limitations associated with energy losses inside this source or the details of particle escape (nevertheless discussed in some detail in Ref. [1]). In order to make progress, one must consider these objects on a case by case basis and better quantify the maximal acceleration energy by comparing the acceleration timescale with the age of the source, the escape timescale and the energy loss timescale [2]. Of course, the conclusions then depend on the assumptions made regarding the acceleration mechanism, the chemical composition, the environment and the magnetic fields inside the source. Nevertheless, magnetars [3], gamma-ray bursts [4,5] and giant radio-galaxies [6] emerge as the most promising candidates.

Given the breadth of this subject, it is very difficult to do justice and discuss in detail all the acceleration models that have been suggested. The present discussion rather focuses on relativistic shock acceleration, which is generically considered as the standard acceleration mechanism in these objects[a]. Furthermore, the interest of relativistic Fermi acceleration goes beyond the problematic of the origin of $10^{20}\,$eV cosmic rays. In particular, it is viewed as the generic mechanism through which the primary particles that give rise to secondary high energy radiation (synchrotron or inverse Compton photons, neutrinos) are accelerated, in a variety of objects (e.g. blazars or gamma-ray bursts). Finally, our understanding of relativistic shock acceleration has evolved significantly in the past decade, revealing in more than one place substantial differences with non-relativistic Fermi acceleration, and in some other cases interesting parallels, as discussed below.

[a] for exceptions, see for instance [3] in the context of magnetar winds, [7] for acceleration in the core of active galactic nuclei (AGN), see also Refs. [1,8,9,10] for general discussions.

This discussion is organized as follows. Section 2 discusses relativistic shock acceleration and Section 3 applies the results to the above topic, namely the acceleration of ultra-high energy cosmic rays. In order to remain as general as possible, a generic lower bound on the magnetic luminosity of the source of 10^{20} eV particles will also be discussed in the frame of recent data.

2 Acceleration at relativistic shock waves

2.1 General considerations

The mechanism of Fermi acceleration at non-relativistic shock waves is well understood in the test particle limit in which one neglects the backreaction of the accelerated particles on the magnetized environment of the shock wave [11,12]. Considering a shock wave of velocity $\beta_{\rm sh}c$ (respectively to the unshocked upstream medium at rest), propagating in a fixed magnetized turbulence, one can show that a test particle bouncing back and forth across the shock wave acquires a net energy gain at each up $\rightarrow$ down $\rightarrow$ up cycle through its interactions with the ambient electromagnetic fields:

$$g \equiv \frac{\Delta E}{E} = \Gamma_{\rm rel}^2\left(1+\beta_{\rm rel}\cos\theta_{\rm d\rightarrow u}\right)\left(1-\beta_{\rm rel}\cos\theta_{\rm u\rightarrow d}\right) - 1 \ . \qquad (1)$$

Here, $\beta_{\rm rel}$ ($\Gamma_{\rm rel} \equiv (1-\beta_{\rm rel}^2)^{1/2}$) denotes the relative velocity between upstream and downstream, $\theta_{\rm u\rightarrow d}$ is the angle (with respect to the shock normal) with which the particle crosses the shock from upstream to downstream, as measured relatively to the upstream plasma rest frame, and $\theta_{\rm d\rightarrow u}$ is the same angle for the return from downstream to upstream, albeit in the downstream plasma rest frame. This formula is general and it remains valid in the relativistic limit. It is obtained thanks to two consecutive Lorentz transformations, from the upstream to the downstream plasma rest frame and back, implicitly assuming that the particle gets deflected but its energy is conserved in the rest frame of the plasma in which it propagates. This of course neglects any Fermi type 2 process.

In the upstream rest frame, the shock wave moves forward (towards upstream) and so does the downstream shocked plasma, albeit at a smaller velocity $\beta_{\rm rel} < \beta_{\rm sh}$. As viewed in the rest frame of the shock wave, the upstream plasma moves toward the shock front at speed $-\beta_{\rm sh}$, while downstream moves away from the shock front at velocity $-\beta_{\rm sh|d}$, with $\beta_{\rm sh|d} = \beta_{\rm sh}/4$ if $\beta_{\rm sh} \ll 1$ and $\beta_{\rm sh|d} \simeq 1/3$ when $\beta_{\rm sh} \rightarrow 1$ (for strong shocks). Accordingly, the particle has a net probability $P_{\rm esc}$ of escaping the shock wave by being advected away in the downstream region, at each Fermi cycle. Then, if one injects particles from upstream and follows the evolution of this population, one finds that at cycle N, the population has decreased in size by a factor $(1-P_{\rm esc})^N$ but its average energy has increased by $(1+g)^N$, with $g \equiv \Delta E/E$ the energy gain per cycle.

The addition of the spectra of the particles that have gone through 1, 2,..., N cycles and then escaped far downstream produces a remarkable powerlaw with index s. The above accounting gives $s = 1 - \log(1-P_{\rm esc})/\log(1+g)$; the generalization of this formula for relativistic shocks has been formulated by Vietri [13], see also [14]. For $\beta_{\rm sh} \ll 1$ and $\beta_{\rm rel} \simeq 3\beta_{\rm sh}/4$, one finds $g \simeq \beta_{\rm sh}$ after appropriate statistical averages on the ingoing and outgoing angle cosines in Eq. (1); furthermore $P_{\rm esc} \simeq \beta_{\rm sh}$ in the diffusive approximation, thus giving $s \simeq 2.0$ for strong non-relativistic shocks. The acceleration timescale is given by the time taken to execute a full cycle, divided by the fractional energy gain, i.e. $t_{\rm acc} \sim t_{\rm scatt}/\beta_{\rm sh}^2$ for $\beta_{\rm sh} \ll 1$, where $t_{\rm scatt}$ denotes the typical scattering (or turn-around) time in the plasma turbulence. Fermi acceleration is thus fully characterized in this non-relativistic strong shock, test particle limit. Most of the recent action in this field has been to understand the impact of the accelerated population on the magnetized environment and the shock structure, e.g. [15]. Detailed observations of supernovae remnant shock waves have indeed revealed amplification of the magnetic field by one to two orders of magnitude, e.g.[16]. The accelerated particles are considered as the possible agents of this amplification through the streaming instability that they seed in the upstream plasma, e.g. [17]. Such amplification is actually a necessary condition for supernovae remnant shock waves to be able to accelerate particles up to the knee[18]. For comparable shock speeds and magnetic fields, one needs giant shock waves of size $\gtrsim 1\,\mathrm{Mpc}$ in order to reach energies of order $10^{19}\,\mathrm{eV}$[2], possibly $10^{20}\,\mathrm{eV}$ if the composition is predominantly heavy nuclei[19]. Trans-relativistic supernovae, with $\beta_{\rm sh} \lesssim 1$, might however accelerate particles up to $\sim 10^{19}\,\mathrm{eV}$[20,21].

2.2 Relativistic regime

As $\beta_{\rm sh} \to 1$, the above discussion has to be revised, because the shock wave then never trails far behind the accelerated particle. This induces a strong anisotropy in the distribution of outgoing angles which significantly affects the energy gain [22,23]. A blunt averaging of the angle cosines in Eq. (1) would give $g \sim \Gamma_{\rm rel}^2 \sim \Gamma_{\rm sh}^2 \gg 1$. This actually holds for the first cycle, in which the upstream plasma particles are injected with arbitrary pitch angles. However, in subsequent Fermi cycles, the particle is overtaken by the shock wave nearly as soon as it has been deflected by an angle $\sim 1/\Gamma_{\rm sh}$ in the upstream frame, because its velocity along the shock normal then becomes smaller than $\beta_{\rm sh}c$. Taking $\cos\theta_{\rm up\to down} \sim 1$ in Eq. (1) now leads to $g \sim 2$. The escape probability is significantly larger than in the non-relativistic limit, $P_{\rm esc} \sim 0.4$, nevertheless this combination of energy gain and escape seemingly allows for a powerlaw to develop with index $s = 2.3$, as observed in Monte Carlo simulations [24,23,14,25], semi-analytical calculations [26] or analytical estimates[27].

However, the above conclusions have been revised rather dramatically in the past few years, with the realization that the generic superluminal nature of relativistic shock waves generally inhibits Fermi acceleration. It was known that for a uniform magnetic field making an angle $\Theta_{B|\rm u} > 1/\Gamma_{\rm sh}$ with respect to the shock normal, particles cannot execute more than a few Fermi cycles[28]. This result has been generalized to more realistic situations involving large scale turbulence, where large scale means a coherence length $l_{\rm coh} \gg r_{\rm L}$ with $r_{\rm L}$ the typical Larmor radius of accelerated particles[29], a result that conforts the numerical findings of Ref.[30]. In short, Fermi acceleration in the ultra-relativistic regime is inhibited because the particle is captured by and advected away with a downstream magnetic field line, which is mostly perpendicular with respect to the shock front in the downstream plasma, due to shock compression ($\Theta_{B|\rm d} \simeq \pi/2$ to within $1/\Gamma_{\rm sh}$ if $\Theta_{B|\rm u} > 1/\Gamma_{\rm sh}$).

The development of powerlaws around relativistic shock waves, which are seemingly indirectly observed through the synchrotron radiation of accelerated electrons, thus requires some instability to remodel the magnetic field on small spatial scales ($\ll r_{\rm L}$). Monte Carlo simulations[31] indeed indicate that, provided the level of small scale turbulence is large enough, Fermi cycles develop. The level of turbulence required has been calculated analytically in Ref.[32], where it is shown that, if short scale turbulence exists downstream, powerlaws should form over the range of Larmor radii:

$$\ell_{\delta B} < r_{\rm L} < \ell_{\delta B}\frac{\delta B}{B}\ , \tag{2}$$

with $\ell_{\delta B}$ the typical scale of short scale fluctuations of amplitude δB ($\delta B > B$ is assumed). The Larmor radius is here calculated with respect to the total magnetic field. It is interesting to note that the above inequality defines a maximal energy beyond which acceleration shuts off. One can understand this limitation by noting that the particle is subject to two competing effects: the helical motion around the average transverse field line, which tends to advects the particle away from the shock front, and the scattering in the small scale turbulence which may allow it to catch back the shock front. While the timescale associated with the former scales

$\propto (\delta B/B) r_{\rm L}/c$, the timescale associated to the latter $\propto r_{\rm L}^2/(\ell_{\delta B} c)$, hence at sufficiently large Larmor radii, the former effect is dominant, i.e. escape losses become catastrophic. As discussed in Ref. [32], this cut-off has probably been observed in the Monte Carlo simulations of Ref. [31].

Quite interestingly, amplification of the magnetic field has been observationally inferred from the synchrotron interpretation of gamma-ray burst early afterglows, both downstream (e.g. [33] for a detailed review) and upstream [34]. This latter result suggests that the accelerated particle population plays an important role in the development of the instabilities. With respect to the magnetization of the downstream plasma, the relativistic two stream Weibel instability operating in the shock transition layer has been raised a lot of attention [35,36,37,38].

2.3 Electromagnetic instabilities

At this stage, it is probably important to recall that one is dealing here with non-collisional shock waves, for which electromagnetic micro-instabilities are to play a key role in the formation of the shock. The development of such micro-instabilities and the formation of the shock wave have been simulated ab initio through powerful particle-in-cell (PIC) simulations, see [39,40,41,42,43,44,45] for the latest simulations of the formation of a ultra-relativistic shock front. On scales much larger than the shock width (of order of a few tens of ion skin depths in the PIC simulations), the shock does appear as a discontinuity and the shock crossing conditions derived in the fluid limit apply [46]. The PIC simulations have recovered these shock crossing conditions in their ab initio simulations in several cases.

Recent simulations indicate that the level of magnetization around the shock keeps evolving in time, beyond the timescale of shock formation, and that the influence of accelerated particles controls the evolution of the magnetisation. [42]. More recent simulations have observed the development of Fermi cycles around the shock wave [47]; they have also shown, however, that for a sufficiently large upstream magnetisation, the growth of instability is suppressed and Fermi cycles do not emerge [44]. The latter point is easily understood when one recalls from the above discussion that the generation of short scale instabilities is a necessary condition for Fermi acceleration to develop in the ultra-relativistic limit [29].

Once the shock has formed and the downstream populations are thermalized, one expects that magnetic amplification can only be triggered by the accelerated population which penetrates into the upstream plasma, thereby seeding beam plasma type instabilities. The relativistic generalization of the Bell instability that is likely at play at supernovae remnant shock waves is a natural candidate [48,49], but it appears limited to the parallel configuration $\Theta_B < 1/\Gamma_{\rm sh}$ which is non-generic [32]. Various instabilities have been discussed [50,51]. The latter work also discusses the limitations due to the advection of the upstream plasma, i.e. the time that is available for mode growth is the crossing time of the shock precursor $\sim r_{\rm L}/\Gamma_{\rm sh}^3 c$ [48], where $r_{\rm L}$ is the typical Larmor radius of the accelerated population in the background magnetic field. Obviously, as the upstream background magnetisation level increases, the precursor length diminishes, hence the instabilities are progressively quenched. In this way, one can understand the results of the PIC simulations [51]. The outcome of Fermi acceleration has been discussed in some detail in this latter work and several useful criteria have been obtained on the level of upstream magnetisation. In practice, it is found that Fermi acceleration should be inhibited in pulsar winds, for the magnetisation is so high that instabilities do not have time to grow on the very short precursor timescale. Regarding the initial ultra-relativistic phase of gamma-ray burst external shock waves with $\Gamma_{\rm sh} \sim 300$, the results indicate that Fermi acceleration should develop if the upstream magnetic field is as "low" as in the interstellar medium ($\sim 1\,\mu$G) but could be inhibited if the magnetic field is as large as 1 mG as expected for some Wolf-Rayet winds.

3 Acceleration to 10^{20} eV

The above requirements generically imply that acceleration to ultra-high energy cannot take place at ultrarelativistic shock waves, because one needs to accomodate two conflicting requirements: that the magnetisation be sufficiently large to satisfy the (necessary but not sufficient) condition $t_{\rm acc}(10^{20}\,{\rm eV}) \ll R/c$, with R the radius of the shock wave; and secondly, that the magnetisation be sufficiently low for waves to grow on the precursor timescale and for Fermi cycles to develop [51]. In particular, if scattering takes place in short scale turbulence upstream, the acceleration timescale $t_{\rm acc} \sim r_{\rm L}^2/(\Gamma_{\rm sh}^2 c\ell_{\delta B})$ increases quadratically with E, therefore the maximal energy $E_{\rm max} \lesssim ZeB\Gamma_{\rm sh}\sqrt{R\ell_{\delta{\rm B}}}$, which is smaller than that derived from the Hillas criterion by a factor $\Gamma_{\rm sh}\sqrt{\ell_{\delta B}/R} \ll 1$, with $\ell_{\delta B} \approx c\omega_{\rm pe}^{-1}$. In the particular situation in which the magnetisation is such that scattering is governed by the background field in the upstream plasma but by short scale fluctuations downstream, with a downstream residence time smaller than the upstream residence time, corresponding to upstream Alfvén speed [51] $\Gamma_{\rm sh}^{-1}\xi_{\rm e.m.}(m_e/m_p)^{1/2} \ll \beta_{\rm A} \ll \xi_{\rm e.m.}$, acceleration becomes more efficient but the bounds on $\beta_{\rm A}$ impose strong lower limits on the size R ($\xi_{\rm e.m.} \sim 0.01-0.1$ is the fraction of shock energy density dumped into short scale electromagnetic modes). The efficiency of Fermi acceleration could also improve if the accelerated particles interact with ambient photon fields through photo-hadronic interactions, thereby benefiting from the so-called converter effect [52].

One of the main conclusions of this discussion is that mildly relavistic shocks with $\Gamma_{\rm sh}\beta_{\rm sh} \sim 1$ are the most efficient (Fermi) accelerators. Indeed, anisotropy effects are not as pronounced as in the ultra-relativistic case, the precursor length is larger hence electromagnetic waves have more time to grow and subluminal configurations are easier to achieve. One may expect an acceleration timescale of the form $t_{\rm acc} \sim t_{\rm scatt}$, with $t_{\rm scatt}$ the scattering timescale in the upstream turbulence. If the scattering is of the Bohm type, which is the most favorable case with respect to particle acceleration, then $t_{\rm scatt} \sim r_{\rm L}/c$; whether this applies or not depends however on the shape of the upstream turbulence spectrum, including the backreaction of the accelerated particles, which remains an open question.

From this point on, this discussion follows two different paths, specializing first on the particular case of gamma-ray bursts fireballs, then discussing a generalized Hillas criterion for sources of ultra-high energy cosmic rays. Focusing on one type of sources allows one to make more quantitative predictions with respect to the possibility of acceleration, the maximal energy and the flux produced. Even then, this example shows that there remain nagging uncertainties related to the physical conditions inside the source which prevent from making definite predictions.

3.1 Acceleration in gamma-ray burst fireballs

According to the standard fireball scenario of gamma-ray bursts, particle acceleration is expected at the internal and external (forward and reverse) shock waves, in order to produce the prompt emission through synchrotron emission in the former, and the afterglow emission in the latter. Internal shock waves are mildly relativistic in the wind frame with $\Gamma_{\rm sh}\beta_{\rm sh} \sim 1-$a few, while the external shock wave is initially ultrarelativistic, $\Gamma_{\rm sh} \sim 300$, then decelerates to non-relativistic velocities; the reverse shock is expected to be mildly relativistic.

Gamma-ray bursts can account for the observed flux of cosmic rays at the highest energies if they output a similar amount (possibly up to an order of magnitude more) of energy in such cosmic rays as in photons [4,5]. There are quite a few proposals for accelerating particles up to 10^{20} eV in gamma-ray bursts. For instance, Fermi acceleration to 10^{20} eV may occur in the internal shock phase at small radii $\sim 10^{13}$ cm [5,53]. In order to escape further expansion losses, it is mandatory that the protons convert into neutrons through photo-hadronic interactions. For generic gamma-ray bursts parameters, the optical depth for photo-hadronic interactions turns out of order unity at the highest energies, hence cosmic rays should escape along with a significant neutrino signal at PeV energies. This scenario however assumes that the magnetic field energy density is continuously replenished to a constant fraction of shock energy density, corresponding to a scaling $B \propto r^{-1}$. This non-trivial assumption might be satisfied if the backreaction of the accelerated particles on the shock turbulence is efficient. If B decreases faster, then expansion losses prevent acceleration to ultra-high energies, unless the acceleration process takes place at the reverse shock [53]. Cosmic rays could also be accelerated to ultra-high energies by interacting with multiple internal shocks [54]. In this case, the acceleration process is more akin to type 2 Fermi acceleration with scattering on relativistic fronts of Lorentz factor $\gamma_{\rm int} \sim$ a few. With an energy gain of order $\gamma_{\rm int}^2$, this process is highly efficient. Decoupling from the flow now occurs because the background magnetic field is assumed to decay faster than r^{-1} (so that $r_{\rm L}/r$ increases as a powerlaw with r). It has also been suggested to accelerate cosmic rays at the ultra-relativistic external shock wave, either through type 1 Fermi acceleration [22,55,56] or type 2 [57] in the downstream turbulence. However, the above discussion argues against type 1 acceleration at the ultra-relativistic shock, unless it occurs in a one shot regime on pre-existing 10^{16} eV particles [22]. Type 2 acceleration is also unlikely, because it requires large scale relativistic turbulence in order to achieve an acceleration timescale comparable to the Larmor radius in the downstream frame, whereas the electromagnetic instabilities at ultra-relativistic shock waves discussed before generally lead to short scale ($\ell_{\delta B} \sim c/\omega_{\rm pe}$) turbulence with $\beta_{\rm A} \ll 1$, implying a rather large scattering timescale. Finally, ultra-high cosmic rays might also be accelerated through shear acceleration, which is a variant of the Fermi mechanism taking place not at a shock wave but in the velocity gradient in the direction perpendicular to that of the flow [58]. Interestingly, these various acceleration mechanisms lead to different predictions for secondary products such as neutrinos and high energy photons, as discussed in particular in Refs. [53,55,57,59,60,61].

3.2 A general luminosity bound on the source of ultra-high energy cosmic rays

The Hillas criterion, discussed in Section 1 can be recast as a useful lower limit on the magnetic luminosity of the source [2], which for spherical symmetry and non-relativistic motion with speed βc reads: $L_{\rm B} \simeq B^2R^2\beta c/2 \geq 1.2\times 10^{45}\,\beta Z^{-2}E_{20}^2\,{\rm erg/s}$ ($E_{20} \equiv E/10^{20}\,{\rm eV}$). Obviously, this limit is quite stringent. A more stringent bound on L_B can be obtained at the expense of considering the acceleration process in more detail [62,63,64]. To this effect, one writes the acceleration timescale as $t_{\rm acc} = \mathcal{A}t_{\rm L}$ and one assumes an outflow with bulk Lorentz factor γ and half-opening angle Θ. In the comoving frame, the maximal energy is limited by the condition $t_{\rm acc} < t_{\rm dyn} = R/(\gamma\beta c)$, with R the distance to the origin the outflow, the quantity $t_{\rm dyn}$ defining the dynamical timescale. This can be rewritten as a lower bound on $L_B = R^2\Theta^2\gamma^2\beta c B^2/4 \gtrsim 0.65\times 10^{45}\,\Theta^2\gamma^2\mathcal{A}^2\beta^3 Z^{-2}E_{20}^2\,{\rm erg/s}$, L_B being defined in the source rest frame, and $E_{20} = E/10^{20}$ eV. This bound is more severe than that derived from the Hillas criterion for several reasons. First of all, one must expect $\mathcal{A} > 1$ and possibly $\mathcal{A} \gg 1$. For instance, non-relativistic Fermi acceleration leads to $\mathcal{A} \sim \alpha/\beta_{\rm sh}^2$ for Fermi acceleration at a shock of velocity $\beta_{\rm sh} \ll 1$ or $\alpha/\beta_{\rm A}^2$ for Fermi 2, and $\alpha \equiv t_{\rm scatt}/t_{\rm L} > 1$ [65]. If acceleration takes place in a (non-relativistic) shear flow with velocity gradient $\Delta u/\Delta x$, the timescale $t_{\rm acc} \sim \Delta x^2/(\Delta u^2 t_{\rm scatt})$ [10]; the deconfinement limit corresponds to $t_{\rm scatt} \sim \Delta x$, in which case the limiting acceleration timescale becomes comparable to $t_{\rm scatt}/\Delta u^2$, as above. Finally, ultra-relativistic shock acceleration is inefficient at ultrahigh energies, as discussed above; mildly relativistic shocks lead to $\mathcal{A} \sim \alpha$. All in all, $\mathcal{A} \sim 1$ can be seen as a limiting regime of maximally efficient acceleration, for moderately relativistic shocks and assuming a Bohm diffusion regime $\alpha = 1$.

In these respects, the above bound is very restrictive because very few sources are capable of emitting such magnetic power. One can check that the bound remains robust in the limit $\beta \to 0$, since $\mathcal{A}^2 \propto \beta_{\rm sh}^{-4}$ then more than compensates for this term. The Hillas criterion, which scales as

β, is less stringent in this respect. Similarly, as $\Theta \to 0$, lateral escape losses become prominent when $\Theta < \Gamma^{-1}$ and the above limit remains essentially unchanged. From a theoretical point of view, it is natural to expect $Z \sim 1$ in regards of the tiny cosmic abundance of iron and other heavy nuclei, but the bound is certainly less stringent with respect to the acceleration of heavy nuclei as it scales as Z^{-2}. Experimental determinations of the composition at ultra-high energies disagree with each other: the Pierre Auger Collaboration has measured a composition that seemingly becomes heavier at higher energies $> 10^{19}$ eV [66], although the recently reported correlation with nearby active galaxies suggests that the primaries are light [67]. The most recent results of the HiRes collaboration rather point toward a pure proton composition at the highest energies $> 10^{19}$ eV [68]. One may nevertheless conclude that the Seyfert galaxies, which have been seen in the arrival directions of most of the high energy events of the Pierre Auger Observatory [67] cannot be the sources of these cosmic rays because they do not satisfy the above luminosity bound. Note that the possibility of having sources such as AGN showing episodic outbursts to luminosities in excess of 10^{46} erg/s is also strongly constrained by existing X-ray surveys [69]. Even Centaurus A, our nearest radio-galaxy, cannot accelerate protons to ultra-high energies, since its jet kinetic power $L_{\rm j} \sim 2 \times 10^{43}$ ergs/s. For $L_B \lesssim 10^{43}$ ergs/s and mildly relativistic motion $\beta \sim 0.3$, one infers a maximal energy $E_{\rm max} \lesssim Z \times 10^{18}$ eV for this object.

Acknowledgments. It is a pleasure to acknowledge the Weizmann Institute of Science for hospitality, where part of this paper was written, as well as Guy Pelletier and Alexandre Marcowith for collaboration on some the issues discussed here.

References

1. Hillas, A. M., *Ann. Rev. Astron. Astrophys.* **22** (1984) 425
2. Norman, C. A., Melrose, D. B., & Achterberg, A., *Astrophys. J.* **454** (1995) 60
3. Arons, J., *Astrophys. J.* **589** (2003) 871
4. Vietri, M., *Astrophys. J.* **453** (1995) 883
5. Waxman, E., *Phys. Rev. Lett.* **75** (1995) 386.
6. Rachen, J. P., & Biermann, P. L., *Astron. Astrophys.* **272** (1993) 161
7. Neronov, A., Semikoz, D., Tkachev, I., 2007, arXiv:0712.1737
8. Berezinskii, V. S., Bulanov, S. V., Dogiel, V. A., & Ptuskin, V. S., *Astrophysics of cosmic rays* (Amsterdam: North-Holland, 1990), ed. Ginzburg, V.L.
9. Pelletier, G., *Lect. Not. Phys.* **576** (2001) 58
10. Rieger, F. M., Bosch-ramon, V., Duffy, P., *Astrophys. Sp. Sc.* **309** (2007) 119
11. Bell, A., *Month. Not. Roy. Astron. Soc.* **182** (1978) 147
12. Blandford, R., Eichler, D., *Phys. Rep.* **154** (1987) 1
13. Vietri, M., *Astrophys. J.* **591** (2003) 954
14. Lemoine, M., Pelletier, G., *Astrophys. J.* **589** (2003) L73
15. Ellison, D., 2008, in *37th COSPAR*, (July 2008, Montr??l, Canada), p.805
16. Vink, J., Laming, J. M., *Astrophys. J.* **584** (2003) 758
17. Bell, A., *Month. Not. Roy. Astron. Soc.* **353** (2004) 550
18. Lagage, P.-O., Césarsky, C., *Astron. Astrophys.* **125** (1983) 249
19. Inoue, S., Sigl, G., Miniati, F., Armengaud, E., 2007, arXiv:0701167
20. Wang, X.-Y., Razzaque, S., Mészáros, P., Dai, Z.-G., *Phys. Rev.* **D76** (2007) 083009
21. Budnik, R., Katz, B., MacFadyen, A., Waxman, E., *Astrophys. J.* **673** (2008) 928
22. Gallant, Y., Achterberg, A., *Month. Not. Roy. Astron. Soc.* **305** (1999) L6
23. Achterberg, A., Gallant, Y., Kirk, J. G., Guthmann, A. W., *Month. Not. Roy. Astron. Soc.* **328** (2001) 393
24. Bednarz, J., Ostrowski, M., *Phys. Rev. Lett.* **80** (1998) 3911

25. Ellison, D. C., Double, G. P., *Astropart. Phys.* **22** (2004) 323
26. Kirk, J. G., Guthmann, A. W., Gallant, Y. A., Achterberg, A., *Astrophys. J.* **542** (2000) 235
27. Keshet, U., Waxman, E., *Phys. Rev. Lett.* **94** (2005) 111102
28. Begelman, M. C., Kirk, J. G., *Astrophys. J.* **353** (1990) 66
29. Lemoine, M., Pelletier, G., Revenu, B., *Astrophys. J.* **645** (2006) L129
30. Niemiec, J., Ostrowski, M., *Astrophys. J.* **641** (2006) 984
31. Niemiec, J., Ostrowski, M., Pohl, M., *Astrophys. J.* **650** (2006) 1020
32. Pelletier, G., Lemoine, M., Marcowith, A., *Month. Not. Roy. Astron. Soc.* **393** (2009) 587
33. Piran, T., *Rev. Mod. Phys.* **76** (2005) 1143
34. Li, Z., Waxman, E., *Astrophys. J.* **651** (2006) L328
35. Gruzinov, A., Waxman, E., *Astrophys. J.* **511** (1999) 852
36. Medvedev, M. V., Loeb, A., *Astrophys. J.* **526** (1999) 697
37. Wiersma, J., Achterberg, A., *Astron. Astrophys.* **428** (2004) 365
38. Lyubarsky, Y., Eichler, D., *Astrophys. J.* **647** (2006) L1250
39. Kato, T. N., *Astrophys. J.* **668** (2007) 974
40. Chang, P., Spitkovsky, A., Arons, J., *Astrophys. J.* **674** (2008) 378
41. Dieckmann, M. E., Shukla, P. K., Drury, L. O., *Astrophys. J.* **675** (2008) 586
42. Keshet, U., Katz, B., Spitkovsky, A., Waxman E., *Astrophys. J.* **693** (2009) L127
43. Spitkovsky, A., *Astrophys. J.* **673** (2008) L39
44. Sironi, L., Spitkovski, A., 2009, arXiv:0901.2578
45. Nishikawa, K.-I., et al., 2009, arXiv:0904.0096
46. Blandford, R., McKee, C., *Phys. Fluids* **19** (1976) 1130
47. Spitkovsky, A., *Astrophys. J.* **682** (2008) L5
48. Milosavljević, M., Nakar, E., *Astrophys. J.* **651** (2006) 979
49. Reville, B., Kirk, J. G., Duffy, P., *Plasma Phys. Contr. Fus.* **48** (2006) 1741
50. Bret, A., 2009, arXiv:0903.2658
51. Lemoine, M., Pelletier, G., 2009, arXiv:0904.2657
52. Derishev, E. V., Aharonian, F. A., Kocharovsky, V. V., Kocharovsky Vl. V., *Phys. Rev.* **D68** (2003) 043003
53. Waxman, E., *Lect. Notes Phys.* **576** (2001) 122.
54. Gialis, D., Pelletier, G., *Astron. Astrophys.* **425** (2004) 395
55. Dermer, C. D., *Astrophys. J.* **574** (2002) 65
56. Vietri, M., de Marco, D., Guetta, D., *Astrophys. J.* **592** (2003) 378
57. Dermer, C. D., Humi M., *Astrophys. J.* **556** (2001) 479
58. Rieger, F. M., Duffy, P., *Astrophys. J.* **632** (2005) L21
59. Gialis, D., Pelletier, G., *Astrophys. J.* **627** (2005) 868
60. Murase, K., Nagataki, S., *Phys. Rev. Lett.* **97** (2006) 051101
61. Murase, K., Nagataki, S., *Phys. Rev.* **D73** (2006) 063002
62. Lyutikov, M., & Ouyed, R., arXiv:astro-ph/0507620 (2005)
63. Waxman, E., *Physica Scripta* **T121** (2005) 147.
64. Lemoine, M., Waxman, E., in prep., 2009
65. Casse, F., Lemoine, M., Pelletier, G., *Phys. Rev.* **D65** (2002) 023002
66. Unger, M., et al. (Pierre Auger Collaboration), *Astron. Nach.* **328** (2007) 614
67. Abraham, J. et al. (The Pierre Auger Collaboration), *Science* **318** (2007) 938
68. Belz, J. (HiRes Collaboration), *proc. CRIS-2008* (Malfa, Italy, Sept. 2008)
69. Waxman, E., Loeb, A., 2008, arXiv:0809.3788

RECENT RESULTS FROM THE HIGH-RESOLUTION FLY'S EYE

J. Belz
Department of Physics and Astronomy
Salt Lake City, Utah 84112, U.S.A.

We present an overview of the most recent results from the High-Resolution Fly's Eye (HiRes) observatory. These include both monocular and stereo energy spectra, the results of a search for correlations between event arrival directions and active galactic nuclei, and new results on composition studies using airshower maximum.

1 THE HIGH RESOLUTION FLY'S EYE

The High Resolution Fly's Eye (HiRes) observartory was operated from May 1997 to April 2006 on the Dugway Proving Grounds in Utah, U.S.A. HiRes consisted of two nitrogen fluorescence detectors: HiRes-I at (40.2° N, 112.8° W, 1597 meters M.S.L.) and HiRes-II at (40.1° N, 113.0° W, 1553 meters M.S.L.), separated by approximately 13 km.

HiRes-I consisted of a single ring of fluorescence cameras viewing elevation angles from 3° to 17°. HiRes-II, which became operational in December 1999, consisted of two rings of cameras viewing elevation angles from 3° to 31°. Each camera consisted of a 16×16 array of photomultiplier tubes (PMTs) at the focus of a 4 m^2 spherical mirror. HiRes-II also made use of a 100 ns clock flash ADC aystem [1], which allowed grouping of PMT pulse-height information from different tubes with the same hit times. This feature played an important role in the analyses described in this paper.

2 ENERGY SPECTRA

Reconstruction of airshower events proceeds by using the fluorescence light signal to infer the number of charged particles as a function of depth in the atmosphere (Figure 1). By comparing the profiles of observed events to CORSIKA [2] simulated airshower events, primary particle energy and airshower characteristics (including X_{max}) are estimated.

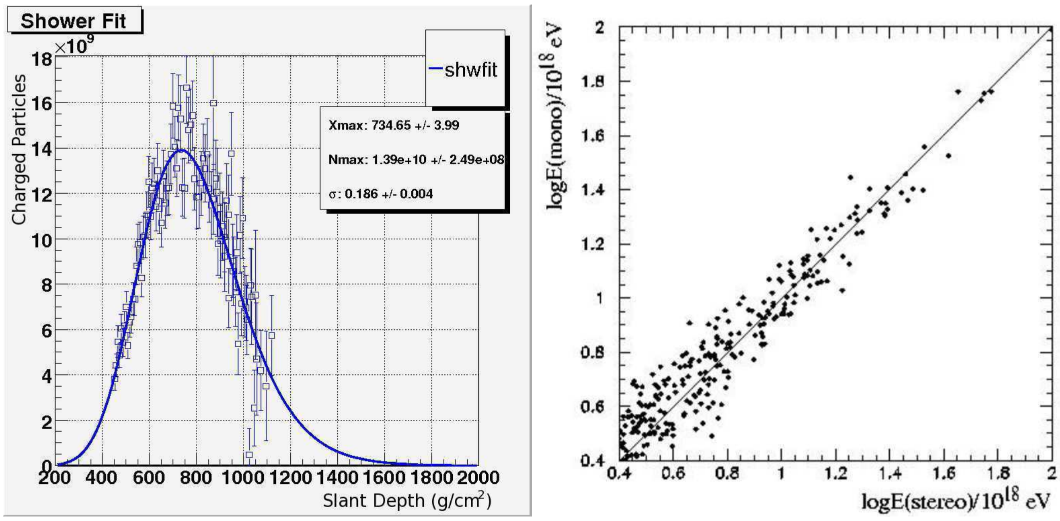

Figure 1: *Left:* Shower profile of HiRes stereoscopic event. Phototube pulses are sorted into time bins, the y-axis is converted from fluorescence light output (proportional to energy deposition) to the number of charged particles assuming an average energy deposition per particle of 2.4 MeV/g cm^2. *Right:* HiRes-I monocular energy versus stereo energy, for the subset of events reconstructed in both modes.

HiRes recently reported the first observation at the 5σ level of the GZK [3] suppression feature in monocular measurements of the ultra-high energy cosmic ray spectrum [4]. This result, confirming a 40 year old prediction, establishes the extragalactic nature of the highest energy cosmic rays.

HiRes however was designed as a stereo fluorescence experiment, and obtains its best event reconstruction in stereoscopic mode. The stereo event sample, while consisting of fewer events, can thus serve as an important confirmation of the monocular results as well as a check of monocular systematic uncertainties. Figure 1 illustrates the consistency of HiRes-I monocular and stereo energy measurements for individual events.

Major systematic uncertainties in the stereo energy measurements are given in Table 1. The photometric calibration of the HiRes telescopes has been described previously [5], and is based on a xenon flash lamp that is placed at the center of each mirror which illuminates the phototube camera.

Table 1: Systematic uncertainties in HiRes stereo energy spectrum

Item	Uncertainty
Photonic scale	10%
Fluorescence yield	6%
Deposited energy calculation	10%
Aerosol concentration	6%
TOTAL	17%

The intensity of fluorescence light emitted from a cosmic ray shower is proportional to the total ionization energy deposited by the charged particles in the shower [6]. We have used an average of the fluorescence yield measurements from the first three papers of reference [7]; Our fluorescence uncertainty is derived from the averaging procedure.

We estimate a systematic uncertainty of 10% from the energy deposition model used in determining the charged particle counts from the fluorescence signal. Our last major systematic uncertainty comes from variability of the aerosol concentrations, an effect minimized by monitoring of aerosols at the HiRes site on an hourly basis.

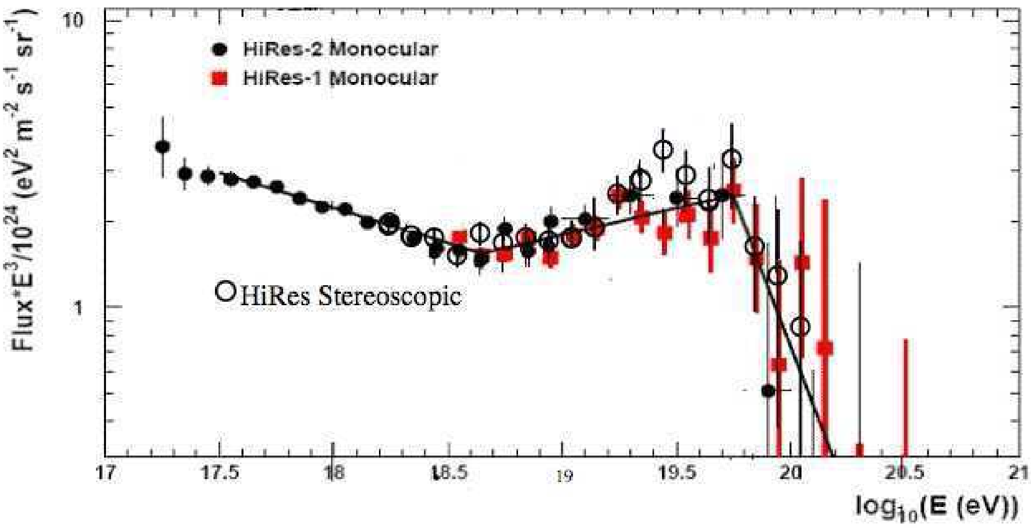

Figure 2: HiRes monocular (black circles and red squares) and stereoscopic (open circles) spectra.

The HiRes monocular and stereo spectra are illustrated in Figure 2. The stereo spectrum is consistent in both magnitude and shape to the monocular spectra, confirming the finding of both an "ankle" at $\log E(eV) = 18.6$ and a high-energy cutoff at $\log E(eV) = 19.7$.

3 Anisotropy: AGN CORRELATIONS

Motivated by the finding of the Pierre Auger Observatory (PAO) [8] of correlations between UHECR arrival directions and Southern Hemisphere Active Galactic Nuclei (AGN) from the 12th Véron catalog [9] , we report the results for of a similar search in the Northern Hemisphere.

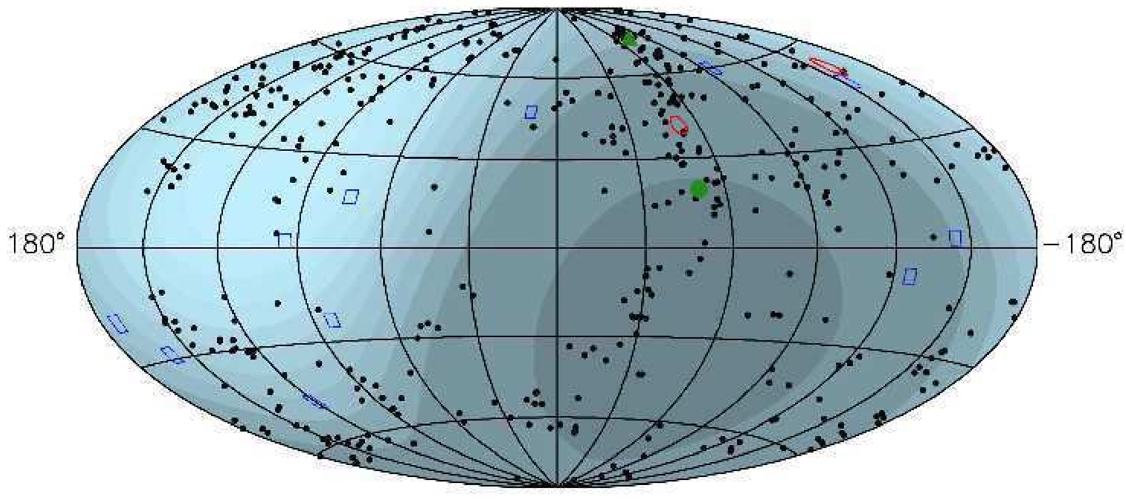

Figure 3: Sky map in galactic coordinates. Black circles: AGN with $Z < 0.018$. Blue squares: uncorrelated HiRes stereo events above 56 EeV. Red circles: HiRes stereo events within a space angle $\theta < 3.1^\circ$ of a candidate AGN. The green circle represents Cen A, and the green triangle represents M87. The blue shaded regions delineate regions of constant exposure, the darkest indicating no exposure.

The PAO AGN signal was established in an exploratory scan of data collected between

January 2004 and May 2006. In this scan, it was established that requiring that the opening angle $\theta < 3.1^\circ$, the energy $E > 56$ EeV, and AGN redshift $Z < 0.018$ maximized the correlation of UHECR arrival directions with AGN. A subsequent sequential analysis of independent events collected between June 2006 and August 2007 found correlations between AGN and 8 of 13 events above 56 EeV. Accounting for the statistical effects of the sequential analysis, the chance probability of such an effect was estimated to be approximately 1%.

The HiRes AGN analysis consisted of two parts, a direct test of the PAO criteria as well as an independent scan of the HiRes stereo dataset. For the direct test, HiRes event energies were shifted downwards by 10% to correct for an apparent energy scale mismatch between the two experiments [4,10]. The results of this search are shown in Figure 3. Using the scan criteria established by the PAO, HiRes finds 2 of 13 events above 56 EeV correlate with AGNs, where 3.2 are expected randomly. With a chance probability of 83%, the HiRes data is consistent with no correlation effect.

In a second test of the AGN-as-source hypothesis, we conducted an independent scan of the HiRes stereo data using the method suggested by Finley and Westerhoff [11]. We find the most significant effect occurs at the opening angle $\theta < 2.0^\circ$, the energy $E > 16$ EeV, and AGN redshift $Z < 0.016$. Using this criteria, 36/198 events have their arrival directions correlate with AGN. The chance probability of this correlation is 24%, hence we conclude that the HiRes data is consistent with no significant deviation from isotropy.

Taken together, these findings weaken the general AGN hypothesis, while making no statement about Southern Hemisphere AGN. This result was recently published by HiRes [12].

4 COMPOSITION WITH X_{max}

A simple extension [13] of Heitler's model for electromagnetic cascades [14] shows that we can expect the average value of *airshower maximum* $\langle X_{max} \rangle$ to follow the relation

$$\langle X_{max} \rangle = \lambda_r \left(\ln \frac{E}{\xi_c^e} - \ln A \right) + C \tag{1}$$

where λ_r is the radiation length of the medium (air), ξ_c^e the critical energy (at which radiative energy loss equals collisional energy loss), and E and and A are respectively the energy and atomic mass of the primary cosmic ray. C is model-dependent, and approximately independent of energy.

Differentiating this relation we obtain the *elongation rate* Λ_A

$$\Lambda_A = \frac{d \langle X_{max} \rangle}{d \log E} \approx \lambda_r \left(2.3 - \frac{d \ln A}{d \log E} \right) \tag{2}$$

which is a common choice as a composition discriminant because of its simple dependence on A.

We derive X_{max} from a shower (Figure 1) by recasting the charged particle profile in terms of the age parameter:

$$s = \frac{3X}{X + 2X_{max}} \tag{3}$$

and fitting the result to a Gaussian distribution with X_{max} as its peak. We find the Gaussian-In-Age (GIA) functional form to have smaller residuals over the fit range than the more commonly used Gaisser-Hillas (GH) parametrization [15], and that the GIA parametrization results in more stable fits.

For comparison with airshower model predictions, we make use of a QGSJET01 shower library, consisting of both proton and iron-initiated airshowers. Before being propagated through the HiRes detector Monte Carlo, we determine the model predictions for $\langle X_{max} \rangle$ by fitting the

Table 2: QGSJET-I predictions for $<X_{max}>$.

Primary	Elongation Rate	$<X_{max}>$ at $\log E = 19.0$
proton	47.9 g/cm^2/decade	763.2 g/cm^2
iron	58.9 g/cm^2/decade	683.0 g/cm^2

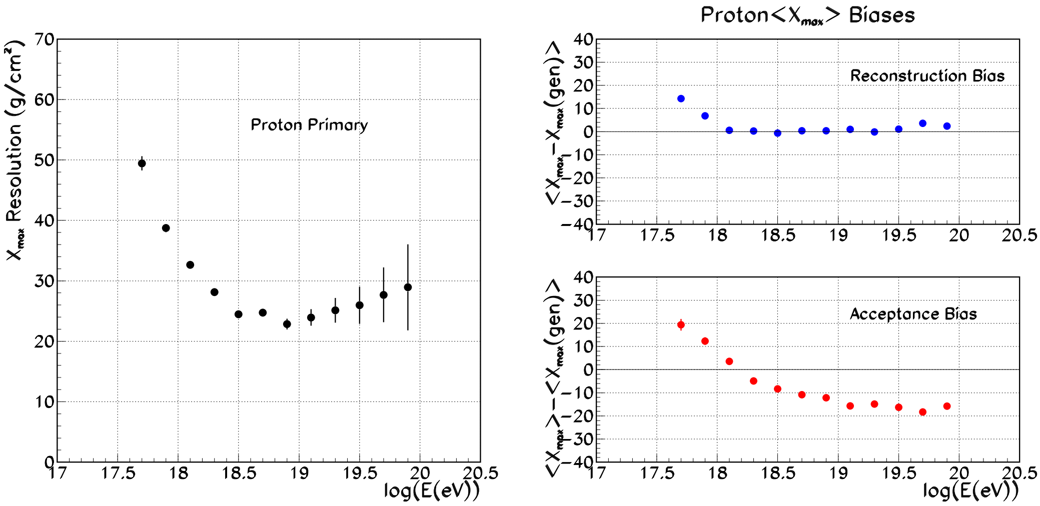

Figure 4: *Left:* X_{max} resolution for airshowers initiated by proton primary cosmic rays, as determined using a QGSJET01 shower library and the HiRes detector Monte Carlo. *Right:* $<X_{max}>$ reconstruction (top) and acceptance (bottom) biases for QGSJET01 proton Monte Carlo, after application of all cuts applied in the text.

thrown proton and iron shower profiles to the same GIA function used in event reconstruction. The results of these fits are given in Table 2.

The critical issue in comparing experimental $<X_{max}>$ distributions to the model predictions lies in understanding the various biases that the detector acceptance and reconstruction programs can impart on the data. It is useful to categorize these biases into two types:

1. *Reconstruction bias*: Due to events which are successfully reconstructed and pass data quality cuts which have the wrong X_{max}.

2. *Acceptance bias*: Due to events which fail reconstruction altogether, at preferentially shallow or deep levels in the atmosphere.

The current analysis takes the approach of choosing the simplest cuts consistent with obtaining minimal reconstruction bias, and then applying acceptance corrections to the data in order to arrive at an elongation rate which can be compared to predictions.

Event geometry for this study is determined using both the HiRes-I and HiRes-II detector sites. Only the HiRes-II information is used in forming the shower profile. All events are required to undergo a successful profile fit, in addition to:

- having a zenith angle $< 70°$
- having X_{max} be “bracketed” by the observed bins
- having the shower impact parameter with respect to HiRes-II be greater than 5 km
- having the angle of the airshower in the HiRes-II shower-detector plane ψ satisfy the condition $40° < \psi < 130°$

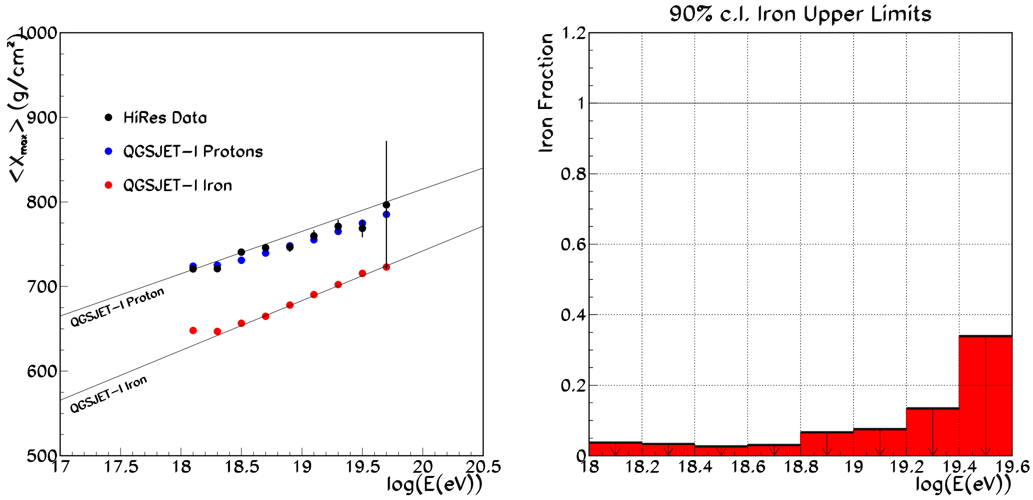

Figure 5: *Left:* $<X_{max}>$ for the HiRes stereo data, along with QGSJET01 proton and iron showers passing through a detector Monte Carlo and the full analysis chain. Also shown are the "rails" (Table 2) from the shower library predictions. Acceptance corrections have not yet been applied. *Right:* 90% c.l. upper limits on the iron fraction in the data, within the QGSJET01 two-component ansatz. A likelihood fit is performed in which the X_{max} distribution in the data (in each energy range) is compared to a sum of QGSJET01 proton and iron distributions.

The X_{max} resolution for HiRes stereo events satisfying the above criteria is illustrated in Figure 4 (left).

Figure 4 (right) illustrates the reconstruction and acceptance biases, as determined from QGSJET01 proton Monte Carlo, after application of the above criteria. There is essentally no reconstruction bias above 1 EeV. Below this, we see the effects of shallow showers being reconstructed systematically deeper than they actually are, as at their true depth they would fail the bracketing requirement. As Figure 4 (right) also shows, there remains an acceptance bias of approximately 15 g/cm^2 at the highest energies, for which we will later correct.

$<X_{max}>$ for the HiRes stereo data, along with QGSJET01 proton and iron showers passing through a detector Monte Carlo and the full analysis chain, are shown in Figure 5. The data is clearly most like the QGSJET01 proton prediction. Figure 5 shows the result of fitting the X_{max} distributions in a given energy bin to a sum of QGSJET01 proton and iron distributions. Under this ansatz, we place 90% c.l. upper limits on the iron fraction of less than 0.1 over most of the HiRes energy range.

Finally, to do a direct comparison with the shower library predictions as well as to determine experimental values for $<X_{max}>$ and the elongation rate we perform an acceptance correction to the data using the QGSJET01 proton prediction. Results are shown in Figure 6 [16]. Results agree well with previous HiRes published data, within uncertainties. Figure 6 overlays the present result with that of the hybrid HiRes prototype/MIA array [17]. The apparent change in elongation rate in the 0.1–1.0 EeV decade is a strong motivation for future experiments such as the TALE project, which seek to understand the composition of primary UHECR over the full range of energies contained in this plot.

Acknowledgements

This work is supported by US NSF grants PHY-9321949, PHY-9322298, PHY-9904048, PHY-9974537, PHY-0098826, PHY-0140688, PHY-0245428, PHY-0305516, PHY-0307098, and by the DOE grant FG0392ER40732. We gratefully acknowledge the contributions from the technical

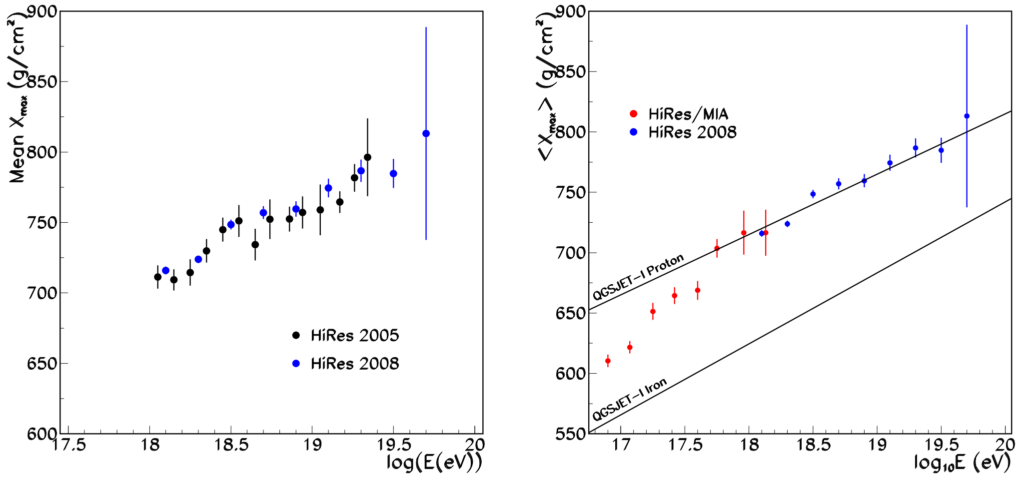

Figure 6: *Left:* Current HiRes <X_{max}> result (blue points), after acceptance correction is applied, superimposed on previously published HiRes results (black points). *Right:* Current HiRes <X_{max}> result (blue points), after acceptance correction is applied, superimposed on previously published HiRes prototype/MIA results (red points). Also shown are QGSJET01 predictions for protons and iron.

staffs of our home institutions. The cooperation of Colonels E. Fisher, G. Harter and G. Olsen, the US Army, and the Dugway Proving Ground staff is greatly appreciated.

References

1. J. H. Boyer *et al.*, *Nucl. Instrum. Methods* **A482** 457 (2002).
2. D. Heck *et al.*, CORSIKA: A Monte Carlo code to simulate extensive air showers, Forschungszentrum Karlsruhe technical note FZKA 6019 (1998).
3. K. Greisen, *Phys. Rev. Lett.* **16** 748 (1966).
   G. Zatsepin and V. Kuz'min, *J. Exp. Theor. Phys. Lett* **4** 78 (1966).
   G. Zatsepin and V. Kuz'min, *J. Exp. Theor. Phys. Lett* **4** 114 (1966).
4. R. Abbasi *et al.*, *Phys. Rev. Lett.* **100** 101101 (2008).
5. R. Abbasi *et al.*, *Astropart. Phys.* **23**, 157 (2005).
6. J.W. Belz *et al.*, *Astropart. Phys.* **25**, 57 (2006).
7. F. Kakimoto *et al.*, *Nucl. Instrum. Meth.* **A** (1996)
   M. Nagano *et al.*, *Astropart. Phys.* **20**, 293 (2003).
   J.W. Belz *et al.*, *Astropart. Phys.* **25**, 129 (2006).
   A.N. Bunner, Ph.D. thesis, Cornell University, 1967.
8. J. Abraham *et al.*, *Science*, **318** 938 (2007).
   J. Abraham *et al.*, *Astropart. Phys.*, **29** 188 (2008).
9. M.P. Véron-Cetty and P. Véron, *Astron. Astrophys.* **455** 773 (2006).
10. J. Abraham *et al.*, *Phys. Rev. Lett.*, **101** 061101 (2008).
11. C. Finley and S. Westerhoff, *Astropart. Phys.* **21**, 359 (2004).
12. R. Abbasi *et al.*, *Astropart. Phys.* **30** 175 (2008).
13. J. Matthews, *Astropart. Phys.* **22** 387 (2005).
14. W. Heitler, *The Quantum Theory of Radiation*, Oxford University Press (1954).
15. T. Gaisser and A. Hillas, *Proc. 15th ICRC, Plovdiv, Bulgaria* **12** 89 (1977).
16. R. Abbasi *et al.*, *Ap. J.* **622** 910 (2005).
17. T. Abu-Zayyad *et al.*, *Phys. Rev. Lett.* **84** 4276 (2000).

The energy spectrum of cosmic rays measured with the Pierre Auger Observatory

F. Schüssler for the Pierre Auger Collaboration
Karlsruhe Institute of Technology (KIT), Postfach 3640, 76021 Karlsruhe, Germany

Surface detector data of the Pierre Auger Observatory has been used to measure the energy spectrum of ultra-high energy cosmic rays with unprecedented statistics and a flux suppression at highest energies has been established. Simultaneous air shower observations with fluorescence and surface detectors are used to extend the nominal range of the observatory to lower energy, i.e. fully covering the region of the ankle. Both measurements and the observed spectral features are discussed in relation with different astrophysical scenarios.

1 Introduction

The energy spectrum of high energy cosmic rays shows an almost perfect power-law behavior over many order of magnitude in energy and flux. Over the last decades only two distinct features could be resolved at ultra-high energies. At very high energies ($> 5 \times 10^{19}$ eV) the presence of a flux suppression compatible with the predicted energy loss due to interactions of cosmic rays with the microwave background radiation [1,2] has been established recently [3,4]. It should be noted that this suppression, rather that originating from the *GZK-effect*, could also be related to the upper end of the, yet unknown, acceleration mechanisms.

Between 10^{18} and 10^{19} eV a hardening of the spectrum has been observed [5,6,7,8]. This break in the power-law behavior, called the *ankle*, has been traditionally attributed to the transition from cosmic rays of galactic origin to a flux dominated by extra-galactic sources [9,10]. Assuming that this transition to extra-galactic cosmic rays happens at lower energies ($< 10^{18}$ eV), the ankle feature could also be explained by energy losses of protons due to $e^{\pm}$ pair production with photons of the cosmic microwave background [11,12]. Over the last years, it has become clear that a discrimination between these different astrophysical scenarios is only possible with new, high resolution and high statistics measurements of the cosmic ray flux and the primary mass composition.

The Pierre Auger Observatory is the world's largest cosmic ray observatory. Data taking started in early 2004 during the construction phase. In June 2008 the southern site located

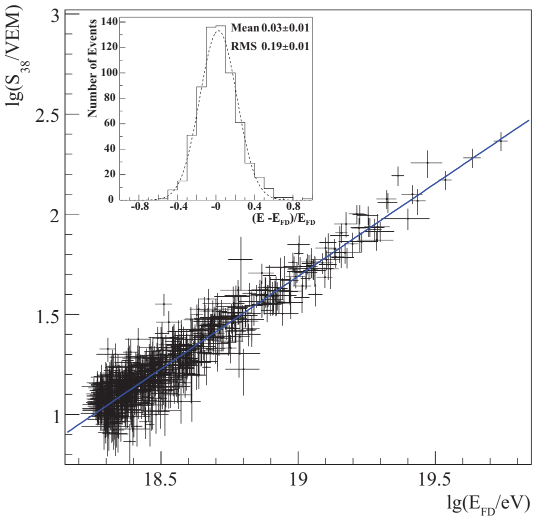

Figure 1: Energy calibration of the surface detector via the correlation between $\lg S_{38^\circ}$ and $\lg E_{\mathrm{FD}}$. The fractional differences between the FD and SD energies are inset (from [4]).

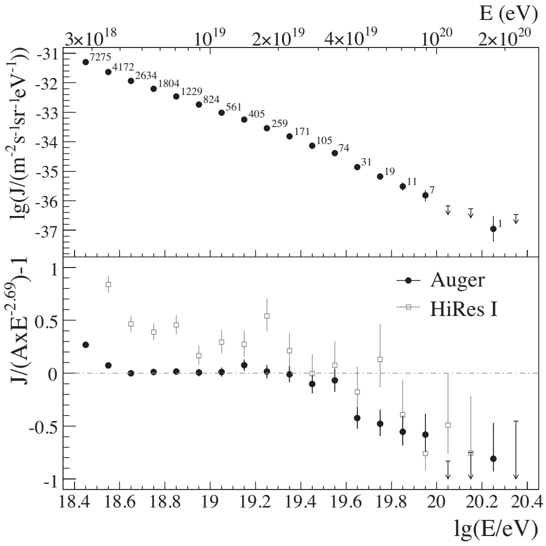

Figure 2: Energy spectrum derived from surface detector data of the Pierre Auger Observatory in comparison with HiRes data (from [4]).

in the province of Mendoza, Argentina, was completed. The Pierre Auger Observatory now comprises more than 1600 water Cherenkov detectors placed on a triangular grid with 1.5 km spacing. This surface detector array (SD) covers about 3000 km^2 and samples the secondary particles of the extensive air showers initiated by the primary cosmic rays in the atmosphere at ground level. The SD is overlooked by 24 optical telescopes grouped in units of 6 at four locations on its periphery. This fluorescence detector (FD) records images of the ultra-violet fluorescence light emitted by the nitrogen molecules excited by the extensive air showers. It is able to observe the longitudinal shower development and provides a calorimetric measurement of the primary energy with little dependence on hadronic interaction models.

2 Energy spectrum from surface detector data

The surface detector is able to operate with an almost 100% duty cycle and collected the largest data set of ultra-high energy cosmic rays (UHECR) already during the construction phase. During the time between 01/2004 and 08/2007 an exposure of $7{\cdot}10^3$ km^2 sr yr could be accumulated. The definition of quality selection criteria which remove events having their shower core outside the boundary of the active array enables the determination of the exposure on a purely geometrical basis by counting the number of active elementary cells as function of time [13]. The status of each detector station is stored every second and the exposure is know with an uncertainty of about 3%.

The design of the Pierre Auger Observatory allows us to observe air showers simultaneously with both the SD and the FD. Although the duty cycle of about 13% of these *hybrid* measurements limits the available statistics, a reliable energy calibration of the high statistics surface detector data can be performed. The recorded SD signal has to be corrected for attenuation effects. The applied constant-intensity procedure is relying on measured data only and allows to relate the signal measured at any zenith angle with the signal measured at a reference angle of 38°. The derived parameter S_{38° is then compared to the energy measured with the fluorescence telescopes on an event-by-event basis. The obtained calibration curve is shown in Fig. 1. It should be stressed that the dependence of this energy calibration on hadronic interaction mod-

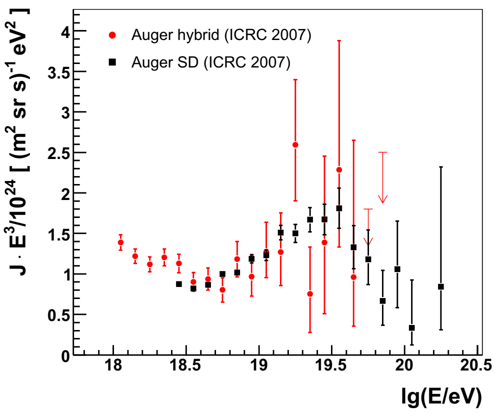

Figure 3: Energy spectrum derived from hybrid and surface detector data of the Pierre Auger Observatory [16,18].

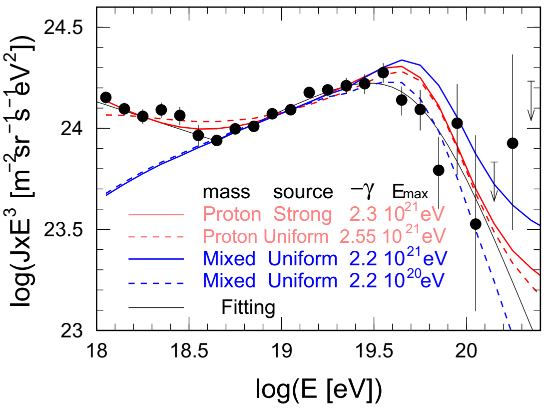

Figure 4: The combined energy spectrum of the Pierre Auger Observatory in comparison with astrophysical models (from [19]).

els is limited to the determination of the energy fraction transfered into particles which are not contributing to the electromagnetic energy deposit. The connected systematic uncertainty is 4% [14].

The derived UHECR energy spectrum is shown in Fig. 2. A flux suppression at the highest energies is clearly visible in the lower panel, where the measured flux is shown relative to a power-law following $E^{-2.69}$. The differences relative to the measurement of the HiRes experiment [3] are under study, but it should be noted that they are within the systematic uncertainty of the energy assignment (22% for the Pierre Auger Observatory [15] and 17% quoted by HiRes [3]).

3 Energy spectrum from fluorescence detector data

To perform conclusive comparisons with astrophysical models of ultra-high energy cosmic rays the cosmic ray flux has to be measured also well below the region of the ankle. This requires an extension of the nominal energy range of the Pierre Auger Observatory which is given by the surface array becoming 100% efficient above 3×10^{18} eV. Lower energies can be reached in a model independent way with the fluorescence detector. Fortunately, all air showers above 10^{18} eV that are recorded by the fluorescence detector have a coincident signal in at least one surface detector station [16]. This additional information can be used to improve the event reconstruction of the fluorescence signal significantly [17] and allow for a very precise determination of the primary energy.

On the other hand, the accumulated exposure of hybrid air shower observations is depending on a large number of parameters. Extensive Monte Carlo simulations reproducing the very time dependent data taking conditions are used to determine the detector efficiency and integrated exposure. These simulations rely on a large variety of monitoring information and atmospheric measurements. The time dependent response of all detector components down to the level of single PMTs is simulated. Event selection criteria are applied to simulated and real events to assure a high energy resolution ($\sigma(E)/E < 10\%$). The definition of an energy dependent fiducial volume around the fluorescence detectors allows us to reduce the intrinsically different trigger and selection efficiencies for air showers initiated by light and heavy primaries significantly.

The first energy spectrum derived from hybrid data of the Pierre Auger Observatory is shown in Fig. 3 together with the corresponding surface detector data. The two measurements are in good agreement. They are combined to yield a cosmic ray flux measurement covering a large energy range with high statistics and accuracy. In Fig. 4, first comparisons of this combined spectrum with the pure proton *Dip*-model and the mixed composition *Transition*-model are shown [20]. It is possible to reproduce the derived flux with the proton model if a strong cosmological source evolution with redshift z is assumed ($(z + 1)^5$). The mixed composition model is able to described the data down to the ankle, below which an additional component is required. It should be noted that a pure proton composition at highest energies seems to be disfavored by the comparison between the Auger measurements of the longitudinal shower development with prediction from hadronic interaction models [21].

References

1. K. Greisen. *Phys. Rev. Lett.*, 16:748–750, 1966.
2. G. T. Zatsepin and V. A. Kuzmin. *Pis'ma Zh. Eksp. Teor. Fiz.*, 4:114, 1966.
3. R. Abbasi et al. (HiRes Collaboration) *Phys. Rev. Lett.*, 100:101101, 2008.
4. J. Abraham et al. (Pierre Auger Collaboration) *Phys. Rev. Lett.*, 101:061101, 2008.
5. J. Linsley. *Proc of 8th Int. Cosmic Ray Conf., Jaipur*, 4:77–99, 1963.
6. M. A. Lawrence, R. J. O. Reid, and A. A. Watson. *J. Phys.*, G17:733–757, 1991.
7. M. Nagano et al. (Akeno Collaboration). *J. Phys.*, G18:423–442, 1992.
8. D. J. Bird et al. (Fly's Eye Collaboration). *Phys. Rev. Lett.*, 71:3401–3404, 1993.
9. A. M. Hillas. *J. Phys.*, G31:R95–R131, 2005.
10. T. Wibig and A. W. Wolfendale. *J. Phys.*, G31:255–264, 2005.
11. V. Berezinsky, A. Z. Gazizov, and S. I. Grigorieva. *Phys. Lett.*, B612:147–153, 2005.
12. R. Aloisio, V. Berezinsky, P. Blasi, and S. Ostapchenko. *Phys. Rev.*, D77:025007, 2008.
13. D. Allard et al. for the Pierre Auger Collaboration. *Proc. of 29th Int. Cosmic Ray Conf., Pune*, page 71, 2005.
14. T. Pierog et al. *Proc. 30th Int. Cosmic Ray Conf. (Merida, Mexico)*, 2007.
15. B. R. Dawson et al. for the Pierre Auger Collaboration. *Proc. of 30th Int. Cosmic Ray Conf., Merida*, 4:425, 2007.
16. L. Perrone for the Pierre Auger Collaboration. *Proc of 30th Int. Cosmic Ray Conf., Merida*, 4:331, 2007.
17. P. Sommers. *Astropart. Phys.*, 3:349–360, 1995.
18. M. Roth for the Pierre Auger Collaboration. *Proc. of 30th Int. Cosmic Ray Conf., Merida*, 4:327, 2007.
19. T. Yamamoto for the Pierre Auger Collaboration. *Proc. of 30th Int. Cosmic Ray Conf., Merida*, 4:335, 2007.
20. D. Allard, E. Parizot, and A. V. Olinto. *Astropart. Phys.*, 27:61–75, 2007.
21. M. Unger for the Pierre Auger Collaboration. *Proc of 30th Int. Cosmic Ray Conf., Merida*, 4:373, 2007.

Propagation of extragalactic ultra-high energy cosmic-ray nuclei : implications for the observed spectrum and composition

Denis Allard
Laboratoire Astroparticule et Cosmologie (APC), CNRS/Paris VII
10 rue Alice Domon et Léonie Duquet, 75205 Paris Cedex 13, France.

In this paper, we study the propagation of cosmic-ray nuclei and protons. We emphasize the influence of the source composition on the expected spectrum and composition on earth as well as on the phenomenology of the transition from Galactic to extragalactic cosmic-rays and the interpretation of the ankle. We point out that the different source composition models cannot be distinguished on the sole basis of the cosmic-ray spectrum but that the the energy evolution of $\langle X_{\max} \rangle$ should remove this degeneracy. Finally, we compare the prediction of the different source composition models with the available data and discuss the implications of our results.

1 Introduction

The cosmic-ray (CR) spectrum has been measured for half a century over 12 order of magnitude in energy and 32 in Flux. This spectrum shows an extraordinary regularity as it can almost be fitted by a single power law between $\sim 10^{10}$ and 10^{20} eV. One can however notice that this regularity is broken at least in two places : the so-called "knee" (a steepening around 3-5$\times 10^{15}$ eV[1]) and the "ankle" (a hardening around 3-5$\times 10^{18}$ eV). These features are of considerable interest for astrophysics. At the highest energies a suppression of the flux seems to be observed independently by two experiments (HiRes[2] and Auger[3]) above $4-5 \times 10^{19}$ eV probably corresponding to the expected GZK cut-off[4,5]. However, at high energy, composition analyses are difficult to perform due to the large hadronic model dependance of air showers properties. As a result, a clear understanding of the highest energy cosmic-ray spectrum and its composition cannot yet be obtained. In particular, the question of the transition from Galactic (GCR) to extragalactic cosmic-rays (EGCR) is under intense debates. Moreover, a clear identification of the UHECR sources, crucial to constrain the acceleration mechanisms at play is not possible yet. In this context, propagation studies of extragalactic ultra-high energy cosmic-ray (UHECR) nuclei can be very useful to identify spectral and composition signatures of different source composition models that can be compared to the available data.

In this proceeding, we study the propagation of cosmic-ray protons and nuclei. After presenting the relevant photon backgrounds and interaction processes relevant at the highest energies, we calculate propagated spectra and the expected energy evolution of $\langle X_{\max} \rangle$ under different assumptions for the source composition and cosmological evolution of the source luminosities. We finally compare the model predictions with recent cosmic-ray data and discuss our results.

2 Interactions of protons and nuclei with photon backgrounds

In the following sections we consider the interaction of protons and nuclei with the CMB and the infra-red, optical and ultraviolet backgrounds (hereafter we group these three backgrounds under IR/Opt/UV for short). To model the IR/Opt/UV backgrounds and their cosmological evolution, we use the latest estimate of[6] which is based on the earlier work of the authors updated with recent data on history of the star formation rate and the evolution of galaxy luminosity functions. We use IR/Opt/UV calculated at 26 different redshifts ($\Delta z = 0.2$) between 0 and 5.

Protons and nuclei propagating in the extragalactic medium interact with CMB and IR/Opt/UV background photons. These interactions produce features in the propagated UHECR spectrum such as the GZK cutoff[4,5] and their decay products generate the cosmogenic neutrino flux[7]. In the case of protons the energy losses are dominated at low energy by adiabatic losses. Interactions with CMB photons become relevant at $\sim 10^{18}$ eV (at z=0) through the pair production process, dominant up to $\sim 7 \times 10^{19}$ eV where the pion production, responsible for the GZK suppression, takes over. Interaction of protons with IR/Opt/UV photons are subdominant on the whole energy range.

The interactions experienced by nuclei with photon backgrounds are different from the proton case. Pair production (for which we use the mass and charge scaling given in[8]) and adiabatic losses result in a decrease of the Lorentz factor of the UHE nucleus, whereas photodisintegration (also called photoerosion) processes lead to the ejection of one or several nucleons from the nucleus. Different photoerosion processes become dominant in the total interaction cross section at different energies[9]. The lowest energy disintegration process is the Giant Dipole Resonance (GDR) which results in the emission of one or two nucleons and α particles. The GDR process is the most relevant as it has the highest cross section with thresholds between 10 and 20 MeV for all nuclei. For nuclei with mass $A \geq 9$, we use the theoretically calculated GDR cross sections presented in[10], which take into account all the individual reaction channels and are in better agreement with data than previous treatments. For nuclei with $A < 9$, we use the phenomenological fits to the data provided by[8]. Around 30 MeV in the nucleus rest frame and up to the photopion production threshold, the quasi-deuteron (QD) process becomes comparable to the GDR and dominates the total cross section at higher energies. The photopion production (or baryonic resonances (BR)) of nuclei becomes relevant above 150 MeV in the nuclei rest frame (e.g., $\sim 5 \times 10^{21}$ eV in the lab frame for iron nuclei interacting with the CMB), and we use the parametrization given in[8] where the cross section in this energy range is proportional to the mass of the nucleus (nuclear shadowing effects are expected to break this scaling above 1 GeV). The reference for this scaling is the deuteron photoabsorption cross section which is known in great detail.

The contribution of the different photoerosion processes and the different backgrounds to the total mean free path for iron nuclei are displayed in Fig. 1a. The photoerosion is dominated by the GDR process through most of the Lorentz factor range. The baryonic resonances begin to dominate only above $10^{21.5}$ eV where the effect of the GDR starts to decrease. Fig. 1b shows the contribution of pair production and photoerosion processes to the total attenuation length of iron nuclei. Photoerosion processes dominate through most of the energy range and the effect of pair production is small at low redshifts. Although the competition between pair production off the CMB and photoerosion processes with IR/Opt/UV photons depends on the redshift (e.g., at high redshifts pair production increases due to the stronger evolution of the CMB), the propagation of nuclei is mainly dominated by photoerosion processes. A comparison between the attenuation lengths of different species is displayed in Fig. 1c. The figure shows what is known since[9], that the attenuation length of low mass nuclei are smaller than that of protons and heavy nuclei above 10^{19} eV and, as a consequence, light nuclei should not contribute as significantly at the high energy end of the spectrum. Furthermore, iron nuclei have larger or similar attenuation lengths to protons up to $\sim 3\times10^{20}$ eV. However, the energy loss processes are different for protons and nuclei and the sole comparison of attenuation lengths can be misleading and is not straightforward to interpret : most of the energy losses of nuclei result in nucleon ejection, thus, unlike protons, a given nucleus does not remain on “the same attenuation length curve” during its propagation.

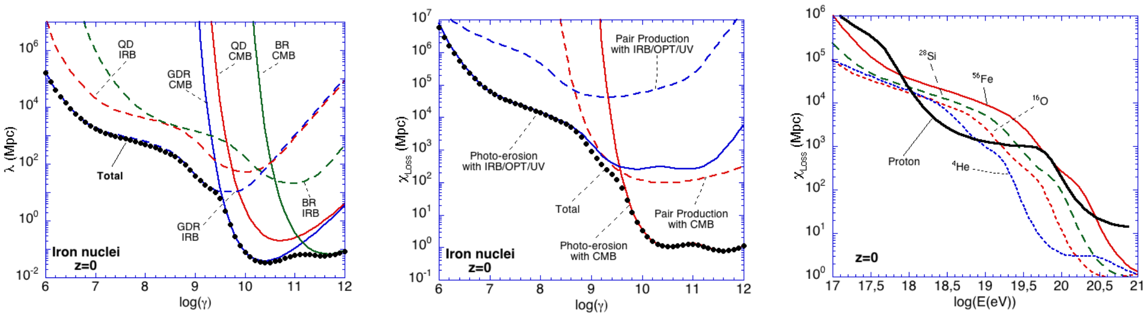

Figure 1: Left: Evolution of the iron nucleus mean free path as a function of the Lorentz factor for the different photoerosion processes and interactions with the CMB and IR/Opt/UV photons at $z = 0$.Center: Evolution of the attenuation length at $z = 0$. The contribution of pair production and photoerosion processes off the CMB and IR/Opt/UV photons are separated. Right: Comparison of the energy evolution of the attenuation length of different nuclei at $z = 0$.

3 Propagated spectra

For the following calculation we use a Monte-Carlo code to propagate nuclei from the source to Earth as described in detail in [11,12]. We consider the classical pure proton scenarios and the extragalactic mixed composition models. For our generic mixed nuclei case (see [11] for more details), we assume that the EGCR source composition matches that of the GCRs observed at lower energies, and that the maximum energy achieved by nuclei of species i in EGCR sources scales with their charge Z_i, i.e. $E_{\mathrm{max},i} = Z_i E_{\mathrm{max}}(^1H)$, as expected if the acceleration mechanism is controlled by magnetic confinement and limited by particle escape. In the following, we assume a power-law source spectrum with spectral index β and set the maximum proton energy to $10^{20.5}$ eV, unless otherwise specified, referring to [14] for a discussion on the influence of E_{max}.

We find that the observed UHECR spectra are best fitted with spectral indices between 2.1 and 2.3, which corresponds to a proton dominated composition with significant fractions of He and CNO, and a lower fraction of heavier nuclei [12]. However, another important ingredient of EGCR models is the time evolution of the power and/or number density of sources. Indeed, the link between the spectrum of the sources and the observed one (and thus the determination of the “best fit spectral indices”) depends strongly on the assumed redshift evolution of the sources. Here, we consider three different source evolution models. The first one corresponds to no evolution at all – hereafter referred to as the uniform source distribution model. In the so-called “SFR model”, we assume that the EGCR injection power is proportional to the star formation rate, which correspond a to redshift evolution in $(1+z)^3$ for $z < 1.3$ and a constant injection rate for $1.3 < z < 6$ (with a sharp cutoff at $z = 6$). Finally, we consider a stronger source evolution favoured by the recent infra-red survey of the Spitzer telescope. In this so-called “strong evolution model”, we assume a injection rate proportional to $(1+z)^4$ for $z < 1$ and a constant rate for $1 < z < 6$, followed by a sharp cut-off (see [12] for more details and references on the sources evolution models).

In the case of pure proton EGCR sources, the best fit $\beta = 2.6$ if one assumes a uniform distribution of sources (no evolution), while it goes down to 2.5 in the case of an SFR-like evolution, and 2.4 in the strong evolution case (see Fig. 2a and[15,17,18]). As shown in previous works[16,18], the

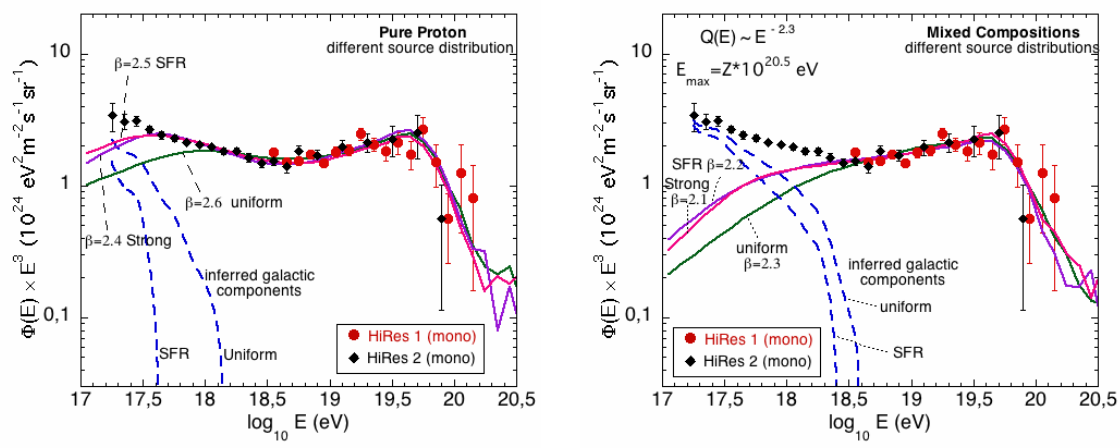

Figure 2: Propagated spectra, $E^3\Phi(E)$, for pure proton models (left) and mixed composition models (right) compared with HiRes monocular data[13]. Different source evolution models are indicated by the labels. The corresponding galactic components are inferred from the overall spectrum by subtracting the EGCR component, in the case of the uniform and SFR source evolution models.

propagated proton spectrum and the concave shape known as the "pair production dip" (with a minimum around $10^{18.7}$ eV on Fig. 2a, for the uniform source model) are only mildly dependent on the source evolution hypothesis. However, the energy where this e^+–e^- dip begins depends on the relative weight of energy losses related to pair production, which dominate at high energy, and energy losses associated with the universal expansion, which dominate at low energy (see [15] for more details). Therefore, the beginning of the dip depends on the redshift evolution of the source density (or power): the transition between the two energy loss processes occurs at a lower energy in the SFR and strong evolution cases (see Fig. 2a). In these cases the extragalactic component can account for the whole CR flux down to much lower energies ($\sim 4\,10^{17}$ eV), which correlatively allows/requires the GCR component to cut at relatively low energies, notably lower than the confinement limit of charged nuclei in the Galaxy. Thus, in the pure proton case, the energy $E_{\rm end}$ at which the GCR/EGCR transition ends (i.e, above which cosmic-rays are purely extragalactic) depends on the source evolution scenario. The highest value of $E_{\rm end}$ is obtained in the case of a uniform source distribution, around 1–1.5 10^{18} eV. This energy range is significantly lower than in the case of mixed composition scenarios (see below) – a distinctive feature that can be used to discriminate between the models, using composition analyses.

The propagated EGCR spectra obtained with a mixed source composition are shown in Fig. 2b. The best fit of the high-energy data is obtained in these cases for significantly smaller spectral indices, i.e., harder source spectra: $\beta \simeq 2.3$ in the uniform case, going down to 2.2 for SFR-like source evolution and 2.1 for the strong evolution model. In all these mixed composition cases, the end of the GCR/EGCR transition roughly coincides with the ankle[11,14]. Above $10^{18.5}$ eV, the predicted spectrum is quite insensitive to the source distribution, as can be seen in Fig. 2b. It is also important to note that the mixed composition models do not imply/require any definite value of the highest energy of cosmic rays in the Galactic component, as long as GCRs represent a sufficiently small fraction of the total spectrum around E_{ankle} not to influence the overall spectrum and composition. Therefore, the Galactic component does not necessarily vanish above $E_{\rm ankle}$, nor is it required that cosmic rays be accelerated above $E_{\rm ankle}$ at all. At energies below the ankle, the inferred fraction of GCRs depends on the source evolution model, just as in the pure proton case (see [20] for more details). We stress that the energy at which the Galactic and extragalactic components have an equal contribution to the CR flux lies between $\sim 5\,10^{17}$ eV and $\sim 10^{18}$ eV . Note also that in our mixed composition models the cosmic rays can be dominated by light nuclei at energies below 10^{18} eV, which is a major difference

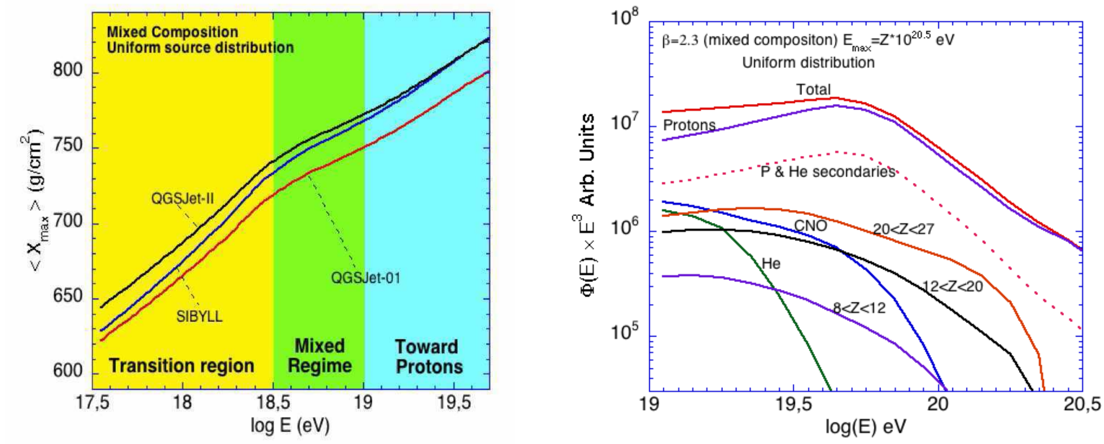

Figure 3: Left: $\langle X_{\max}\rangle$ evolution for an extragalactic mixed composition and uniform source evolution model for three different hadronic models (see labels). Right: Predicted spectrum for a mixed extragalactic composition above 10^{19} eV decomposed in its elemental components.

with the GCR/EGCR transition scenario studied in [19].

4 The shape of $\langle X_{\max}\rangle(\mathbf{E})$

Having identified the value of β that provides the best fit of the data in each scenario, and obtained the corresponding fractions of GCRs and EGCRs at all energies, we can now deduce the evolution of the cosmic-ray composition as a function of energy and predict the values of the associated observables. The *propagated* EGCR composition in each case is a direct output of our computations, and we assume that the Galactic component is essentially made of Fe nuclei above $10^{17.5}$ eV (relaxing this assumption would slightly flatten the $\langle X_{\max}\rangle$ evolution in the transition region). From the relative abundance of all elements at a given energy, we derive the average value of the atmospheric depth (in g/cm^2) at which the maximum shower development is reached, $\langle X_{\max}\rangle$, using Monte-Carlo shower development simulations [14,20].

In the pure proton case, the interpretation of the evolution of $\langle X_{\max}\rangle$ with energy is straightforward (figures are shown in [14,20]). The transition from Galactic iron nuclei to extragalactic protons being quite narrow (i.e., it occurs over a small energy range, in a decade or even half a decade), the evolution of $\langle X_{\max}\rangle$ with energy is very steep and then gets flatter when the transition is over and the composition does not change anymore, all EGCRs being merely protons. The point where the $\langle X_{\max}\rangle$ evolution can be observed to break simply indicates the energy E_{end}, corresponding to the end of the transition. Characteristically, an early break in the elongation rate at $\sim 4\,10^{17}$ eV is expected in the strong and SFR source evolution models, whereas the break is found around 1–1.5 10^{18} eV for a uniform source distribution. No break is expected at the ankle. Indeed, the ankle is consistently interpreted in pure proton models as the signature of the interactions between EGCR protons and CMB photons producing e^+e^- pairs. Obviously, the resulting "pair production dip" would not be visible if the EGCR component did not consist almost exclusively of protons. Quantitatively, nuclei heavier than H cannot contaminate the EGCR component at a higher level than ~ 15 %[19,16,11].

The case of mixed composition models is illustrated in Fig. 3a. The evolution of $\langle X_{\max}\rangle$ is relatively steep in the transition region, below E_{ankle}, because the composition evolves rapidly from the dominantly heavy Galactic component to the light extragalactic mixed composition. However, the evolution is significantly slower than in the case of pure proton models, because the transition is wider and the cosmic-ray composition does not turn directly into protons only. As can be seen on Fig. 3a, an intermediate stage appears, which may be called the mixed-

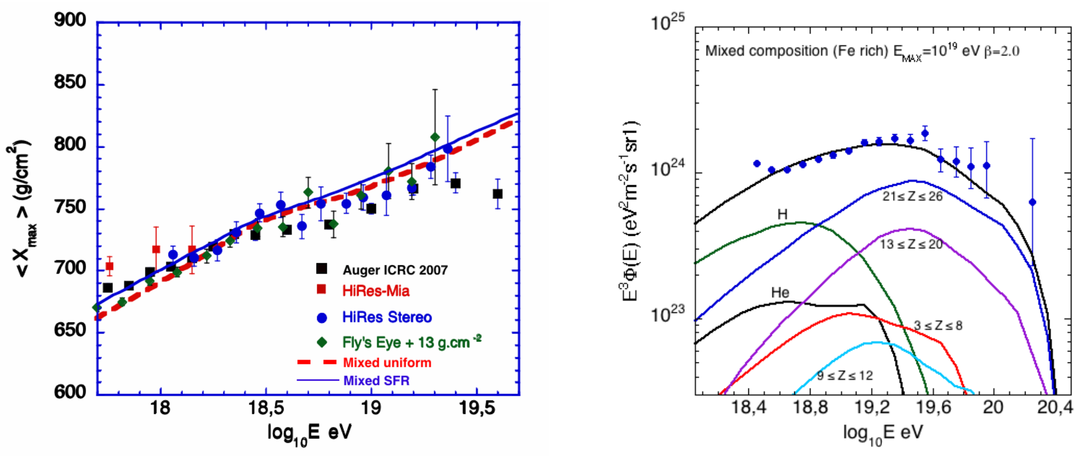

Figure 4: Left: $\langle X_{\rm max}\rangle$ evolution for an extragalactic mixed composition above 10^{19} eV, for the SFR and uniform source evolution compared to cosmic-ray data (see legend). Right: Predicted spectrum for a mixed extragalactic composition ($E_{max} = Z \times 10^{19}$ eV) decomposed in its elemental components and compared to Auger data [3].

composition regime, where a break in the evolution of $\langle X_{\rm max}\rangle$ around E_{ankle} is followed by a flattening up to $\sim 10^{19}$ eV, reflecting the fact that the (propagated) EGCR composition does not change much in this energy range. This is because among the different EGCR nuclei, only He nuclei interact strongly with infrared photons at these energies. Between E_{ankle} and $\sim 10^{19}$ eV, the evolution of $\langle X_{\rm max}\rangle$ is actually compatible with what is expected from a constant composition. Then around 10^{19} eV, the relative abundance of nuclei heavier than protons starts to decrease significantly as a result of photo-disintegration processes: the CNO component starts interacting with the infrared background and the CMB photons eventually cause the He component to drop off completely (see Fig. 3b). The evolution of $\langle X_{\rm max}\rangle$ therefore steepens again, accompanying the progressive evolution towards an almost pure proton composition as each type of nuclei reaches its effective (mass dependent) photo-disintegration threshold. Even though slight differences may be expected from one model to the other, the above evolution of $\langle X_{\rm max}\rangle(E)$ in a three steps process is a characteristic prediction of mixed-composition models, or generically of any type of EGCR sources allowing for the acceleration of a significant fraction of nuclei heavier than He.

5 Comparison with data and discussion

The high-energy cosmic ray spectrum can be satisfactorily accounted for within either the pure proton or the mixed composition models (and many other source composition models, see [21]). However, we have shown that the corresponding phenomenology of the GCR/EGCR transition is very different in each case, which results in distinct shape of $\langle X_{\rm max}\rangle$ as a function of energy. The currently available data do not allow one to draw definitive conclusions yet. However, we argued in [14] that the predictions of the mixed-composition models appear to be in better agreement with the current data from fluorescence detectors. In particular, a good agreement is found with Fly's Eye results above $10^{17.5}$ eV [22]. Concerning the slope of the $\langle X_{\rm max}\rangle$ evolution in the transition region (i.e., below the ankle), mixed-composition models typically predict values for the slope of the $\langle X_{\rm max}\rangle$ evolution compatible with what is observed. Furthermore, both the predicted break at the ankle and the steepening above 10^{19} eV are compatible with the HiRes Stereo data [23]. Fig. 4a shows the comparison between the $\langle X_{\rm max}\rangle$ evolution for a mixed composition in the SFR evolution case and the data of HiRes Stereo, HiRes-Mia, Fly's Eye (rescaled by 13 $g\,cm^{-2}$, as suggested in [25]) and Auger [26]. As can be seen, Fly's Eye and Stereo HiRes data are consistent with the predicted break in the $\langle X_{\rm max}\rangle$ evolution between 3 and 4 EeV, which also corresponds to the energy of the ankle reported by both experiments. Note that HiRes-Mia results at lower energy are also compatible with pure proton models, as well as with mixed-composition models except at one point around $5\,10^{17}$ eV. The data best agree with the absolute scale of $\langle X_{\rm max}\rangle$ computed with the QGSJet-II model. However, it is important to note that the results obtained with QGSJet01 show exactly the same features shifted downwards by $\sim$20 $g\,cm^{-2}$, and are still well within the systematic uncertainties of the different experiments. This illustrates once more that the choice of the hadronic model is not critical in the present discussion [20].

When comparing the mixed composition model predictions with the recent data of the Pierre Auger observatory, the agreement appears less good. Auger data are compatible with a break in the $\langle X_{\rm max}\rangle$ evolution in an energy range close to the ankle (which is, as mentioned before, difficult to handle for a pure proton model) and the overall shape of the evolution below 10^{19} eV, although flatter, is compatible with the mixed model predictions. Above $\sim 10^{19}$ eV, however, the composition seems to be getting heavier where the mixed model would predict a lightening. This trend, if confirmed by a larger statistics, would then represent a major incompatibility with our "generic" mixed composition model. Though the reality of this trend is still quite speculative due to the low statistics accumulated at the highest energies, it is interesting to investigate what could cause the composition to get heavier at the highest energies.

In the case of our generic mixed composition, one actually expects that the composition could get heavier above 5×10^{19} eV if heavy nuclei are accelerated at the highest energies. Indeed, above energy, the proton flux decreases sharply due to photopion interactions with CMB photons. Between 5×10^{19} eV and $\sim 2.5\times10^{20}$ eV, heavy nuclei (Fe) only interact with the less dense far-IR photons and the decrease of their flux is then slower (see Fig. 3b) than for protons, implying an increase of their relative abundance. This trend ends when the heavy component disappears due to interaction with CMB photons (see [20] for more details). However, the energy range where this feature is expected does not seem to be compatible with Auger data. Invoking a heavy dominated or possibly pure iron composition at the sources would presumably not solve the problem either. The composition analyses at lower energy seem to favor a transition from heavy galactic to light extragalactic cosmic-rays which does not look compatible with the expectations of an extragalactic heavy source composition (see discussion of the pure iron sources in [14]). Let us note that the latter point is somehow alleviated but remains true if one assumes a strong evolution of source luminosity with redshift for which spectral indices of 2.0-2.1 would be required to fit the observed spectra.

In this context, a possible explanation for this trend would be to infer that most of the sources are not able to accelerate protons up to the highest energies and that only heavy nuclei are accelerated above 10^{20} eV (in the case of a maximum energy scaling with the charge of the nucleus, this kind of scenario is proposed for instance in [27]). As we discussed in [14], low E_{max} proton solutions do not work very well with our usual mixed composition hypothesis. Some tuning of the composition is then necessary for this type of scenario to be compatible with the data. However, good fits of the data can be obtained with a moderate increase of the overall abundance of heavy elements at the source, by a factor of three or so with respect to low-energy Galactic cosmic rays. This is illustrated in Fig. 4b where expected spectra are displayed and compared with data assuming a mixed composition, $\beta = 2.0$, $E_{max} = Z\times10^{19}$ eV and $\sim 30\%$ of Fe nuclei at the sources. One can see that the agreement with data is reasonable and that the composition, proton dominated at low energy, becomes gradually heavier and very dominated by iron above $5\,10^{19}$ eV. Such a scenario would have implications on the cosmogenic neutrino flux that should be extremely low above 10^{17} eV. Neutrinos and photons fluxes from interactions during the acceleration at the sources would as well be presumably very low (see discussion in [28]). To conclude, let us note that, at the current level of statistics, it seems difficult to argue that the recent anisotropy claim by the Pierre Auger collaboration [29] disfavors heavy compositions at the highest energie (see for instance [30]). However, a significant small scale clustering, if observed in the future, would challenge this type of scenario.

Although the available cosmic-ray data already allow to put encouraging constrains on the different models we presented, a clear picture of the GCR to EGCR transition, the composition and the origin of the UHECR is still difficult to draw. Future data of the Pierre Auger Observatory, its low energy extension as well as the future very large aperture projects such as Auger North[31] and JEM-EUSO[32] should allow a clearer view on these questions in the next few years.

References

1. Antoni, T., et al., (KASCADE), 2005, Astropart. Phys., 24, 1, astro-ph/0505413.
2. Thomson, G.B., 2006, astroph/0609403.
3. Abraham J., et al., 2008, PRL V 101 I 6.
4. Greisen K 1966 PRL 16 748.
5. Zatsepin G T and Kuzmin V A 1966 Sov. Phys. JETP Lett. 4 78.
6. Stecker, F. W., Malkan, M. A. and Scully, S. T., 2005, astro-ph/0510449, ApJ in press.
7. Berezinsky, V.S. & Zatsepin, G.T., 1969, Phys. Lett. 28B, 423
8. Rachen, J. P., 1996, Interaction processes and statistical properties of the propagation of cosmic-rays in photon backgrounds, PhD thesis of the Bohn University.
9. Puget, J. L., Stecker, F.W. and Bredekamp, J.H., 1976, ApJ. 205, 638.
10. Khan, E. , et al., 2005, Astropart. Phys., 20, 53.
11. Allard, D., Parizot, E., Khan, E., Goriely, S., and Olinto, A. V., 2005, A&A Letters, 443, 29, astro-ph/0505566.
12. Allard, D., et al., 2006, JCAP09(2006)005, astro-ph/0605357.
13. Bergman, D., (HiRes), 2005, Proceeding of the 29^{th} ICRC conference, Pune (India).
14. Allard, D., Parizot, E. and Olinto, A. V., 2007, Astropart. Phys., V27 issue 1, 61-75. astro-ph/0512345.
15. Berezinsky, V. S., Gazizov, A. Z., & Grigorieva, S. I., 2006, Phys. Rev. D74:043005, hep-ph/0204357.
16. Berezinsky, V. S., Gazizov, A. Z., & Grigorieva, S. I., 2005, Phys. Lett. B, 612, 147.
17. De Marco, D, Blasi P and Olinto A V 2003 *Astropart. Phys.* **20** 53.
18. De Marco, D., Stanev, T., 2005, Phys. Rev. D, 72, 081301.
19. Wibig, T. and Wolfendale, A. W., 2004, astro-ph/0410624.
20. Allard, D., Parizot, E. and Olinto, A. V., 2007, A&A, V473, Issue 1, pp.59-66, astro-ph/0703633.
21. Allard, D., Busca, N. G., Decerprit, G., Olinto, A. V., & Parizot, E. 2008, Journal of Cosmology and Astro-Particle Physics, 10, 33
22. Bird, D., et.al, 1993, Phys. Rev. Let. 71, 3401.
23. Abbasi, R.U., et al., (HiRes), 2005, Ap.J. 622, 910.
24. Abu-Zayyad, T., et. al., (HiRes-Mia), 2000, Phys. Rev. Lett. 84, 4276.
25. Sokolsky, P. (HiRes Collaboration), 2005, Proceeding of the 29^{th} ICRC, Pune (India).
26. Unger, M., et al., [Auger Collaboration], 2007, proceedings of the 30^{th} International Cosmic-Ray Conference, Merida (Mexico), astro-ph/0706.1569.
27. Inoue, S., Sigl, G., Miniati, F. and Armengaud, E., 2007, proceedings of the 30^{th} International Cosmic-Ray Conference, Merida (Mexico), astro-ph/0711.1027.
28. Allard, D. and Protheroe, R. J., 2009, astro-ph/0902.4538, submitted to A&A.
29. The Pierre Auger Collaboration, 2007, Science 318, 938-943.
30. Wibig, T. and Wolfendale, A. W., 2007,astro-ph/0712.3403v1.
31. Nitz, D. et al., [Auger Collaboration], 2007, proceedings of the 30^{th} International Cosmic-Ray Conference, Merida (Mexico), astro-ph/0706.3940.
32. Takizawa, Y., et al., 2007, Nuclear Physics B - Proceedings Supplements, V166, 72-76.

Magnetic fields in our Galaxy and nearby universe

JinLin Han
National Astronomical Observatories, Chinese Academy of Sciences,
Jia-20, DaTun Road, Chaoyang District, Beijing 100012, China
E-mail: hjl @ bao.ac.cn

The magnetic fields in our Galaxy and nearby universe are crucial knowledge to understand the origin and propagation of cosmic rays. Magnetic fields in our Galaxy have been most effectively revealed by Faraday rotation measures (RMs) of pulsars and background radio sources. In the Galactic disk, the large-scale magnetic field structure and field strength can be derived from pulsar RMs and Dispersion measures (DMs). From the sky distribution of RMs of extragalactic radio sources, the toroidal fields in the Galactic halo can be identifield from the antisymmetric distribution. To explore the magnetic fields of cosmological scale, the RMs in the Galactic pole regions can be used, because the foreground RM contribution from our Galaxy is minimized and can be eliminated easily. RMs have a larger deviations towards higher redshift, which is evidence for intergalactic magnetic fields. However, it is hard to disentangle it from the combination with unknown electron distribution in the intergalactic space.

1 Introduction

The first idea about the Galactic magnetic fields was proposed by Fermi [7] when he suggested the origin of cosmic rays from interstellar space and the acceleration by interstellar magnetic fields. Though Alfvén [2] insisted for the solar origin of cosmic rays, he first estimated the strength of Galactic fields amplified by motion of interstellar medium, $B \sim$ a few μG, which is correct, using the equipartition of magnetic field energy with motion of gas in the form of $B^2/8\pi \sim \rho v^2/2$ and adopting interstellar gas density $\rho \sim 10^{-24}$g cm^{-3} and typical gas velocity of 10 km s^{-1}. These are only very basic concepts on the extent and strength of Galactic magnetic fields.

At present, the new detection of ultrahigh energy (50 Eev) cosmic rays [1], which probably origin from AGNs in the nearby universe (<∼80 Mpc), leads to think about the magnetic fields in the intergalactic space. There is not yet helpful measurement on the the immediately intergalactic magnetic fields ourside our Galaxy, though “extragalactic magnetic fields” [4] have been detected in the nearby spiral galaxies and the intergalactic medium inside a few clusters of galaxies.

Our own Galaxy is so bright in sky not only in optical and radio bands, but also in the polarized radio sky [24,26] and the Faraday's sky or the Rotation Measure (RM) Sky which are closely related to the magnetic fields of our Galaxy. The RM sky is strikingly antisymmetric in the inner Galaxy [13]. Faraday rotation of polarized emission from a radio source ($*$) to us ($\oplus$) is defined by

$$\psi = 810 \int_{\oplus}^{*} \lambda^2(l) n_e(l) \mathbf{B}(l) \cdot d\mathbf{l}, \tag{1}$$

here, ψ is total rotation angle (in rad), λ is wavelength (in m), $n_e(l)$ is intervening electron density (in cm^{-3}), $\mathbf{B}$ is vector magnetic field (in μG), and $d\mathbf{l}$ is the unit vector of the line of sight (in kpc) pointing towards us. Electron density and magnetic field vary along the line of sight. *To reveal the intervening magnetic fields, it is necessary to know the distribution of electron density along the line of sight.* For a cosmological radio source at a given location in the universe, e.g. at redshift z, the wavelength $\lambda(z)$ is also specifically related to observed wavelength by $\lambda_{\rm obs} = (1+z)\lambda(z)$. So, the rotation measure (RM, in rad m^{-2}) of a radio source at a redshift, z_s, should be defined as

$$RM_{\rm obs} = \frac{\psi_1 - \psi_2}{\lambda^2_{\rm obs1} - \lambda^2_{\rm obs2}} = 810 \int_0^{z_s} (1+z)^{-2} n_e(z)\, \mathbf{B}(z) \cdot d\mathbf{l}. \quad (2)$$

In different cosmological models, the dl and dz are related by

$$\frac{dl}{dz} = \frac{c}{H_0}(1+z)^{-1}[\Omega_{\rm m}(1+z)^3 + (1-\Omega_{\rm m}-\Omega_\Lambda)(1+z)^2 + \Omega_\Lambda]^{-1/2}. \quad (3)$$

Here, $H_0 = 100h$ km s^{-1}Mpc^{-1} is the Hubble constant, h is the dimensionless factor, c is the speed of light, $\Omega_{\rm m}$ is the dimensionless ordinary matter density, and Ω_Λ is the vacuum energy density. Most recent measurements [8,27] show that $h = 0.72 \pm 0.05$, $\Omega_{\rm m} \sim 0.3$ and $\Omega_\Lambda \sim 0.7$. Observed Faraday rotation consists of three contributions,

$$RM_{\rm obs} = RM_{\rm in} + RM_{\rm ig} + RM_{\rm fg}, \quad (4)$$

namely, the intrinsic rotation measure local to a source, $RM_{\rm in}$, the rotation measure from the intergalactic medium, $RM_{\rm ig}$, and the foreground RM from our Galaxy, $RM_{\rm fg}$. The foreground RM from our Galaxy are common contribution to RMs of radio sources located in a small sky region. To reveal the properties of intergalactic magnetic fields, the effect of intrinsic and foreground rotation measures should be eliminated from the observed values of $RM_{\rm obs}$.

2 Magnetic fields in our Galaxy

Pulsars in our own Galaxy emit polarized radio emission, and their RMs can be used to measure the interstellar magnetic fields [20]. Observed Faraday rotation of pulsars does not have any intergalactic contribution or intrinsic contribution, nor do we have to consider the cosmological effect on the wavelength. Therefore, the RM (in radians m^{-2}) of a pulsar at distance D (in kpc) can be simply given by RM $= 810 \int_0^D n_e \mathbf{B} \cdot d\mathbf{l}$. Positive RMs correspond to the average fields directed toward us. In addition, the electron density between a pulsar and us can be measured by the pulse delay between the high and low radio frequencies. This is the dispersion measure (DM) of a pulsar, DM $= \int_0^D n_e dl$. From the two observables, DM and RM, we obtain a direct estimate of the field strength weighted by the local free electron density,

$$\langle B_{||} \rangle = \frac{\int_0^D n_e \mathbf{B} \cdot d\mathbf{l}}{\int_0^D n_e dl} = 1.232\, \frac{\rm RM}{\rm DM}. \quad (5)$$

where RM and DM are in their conventional units of rad m^{-2} and cm^{-3} pc and $B_{||}$ is in μG.

Previous analysis of pulsar RM data often used the model-fitting method [17,19], i.e., to model magnetic field structures in the all paths from pulsars to us (observer) and fit them together with the electron density model to observed RM data. *Significant improvement* can be obtained now when RM and DM data are available for many pulsars in a given region with similar lines of sight. Measuring the gradient of RM with distance or DM is the most powerful method of determining both the direction and magnitude of the large-scale field in that particular region

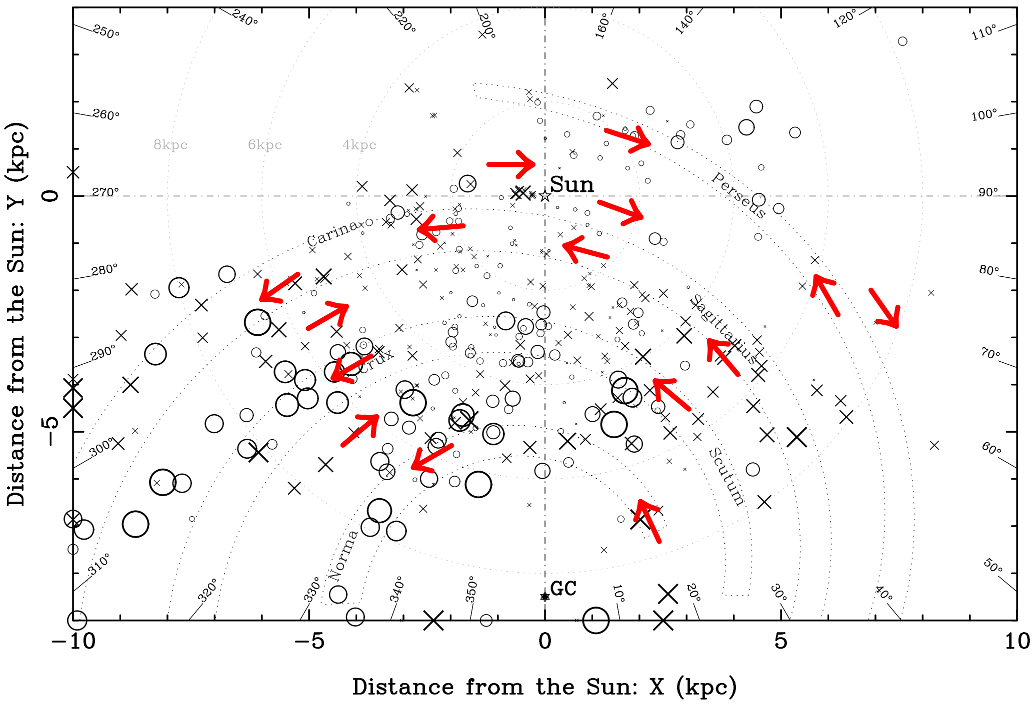

Figure 1: The RM distribution of 374 pulsars with $|b| < 8°$, projected onto the Galactic Plane. The linear sizes of the symbols are proportional to the square root of the RM values. The crosses represent positive RMs, and the open circles represent negative RMs. The approximate locations of four spiral arms are indicated. The large-scale structure of magnetic fields derived from pulsar RMs are indicated by thick arrows [15].

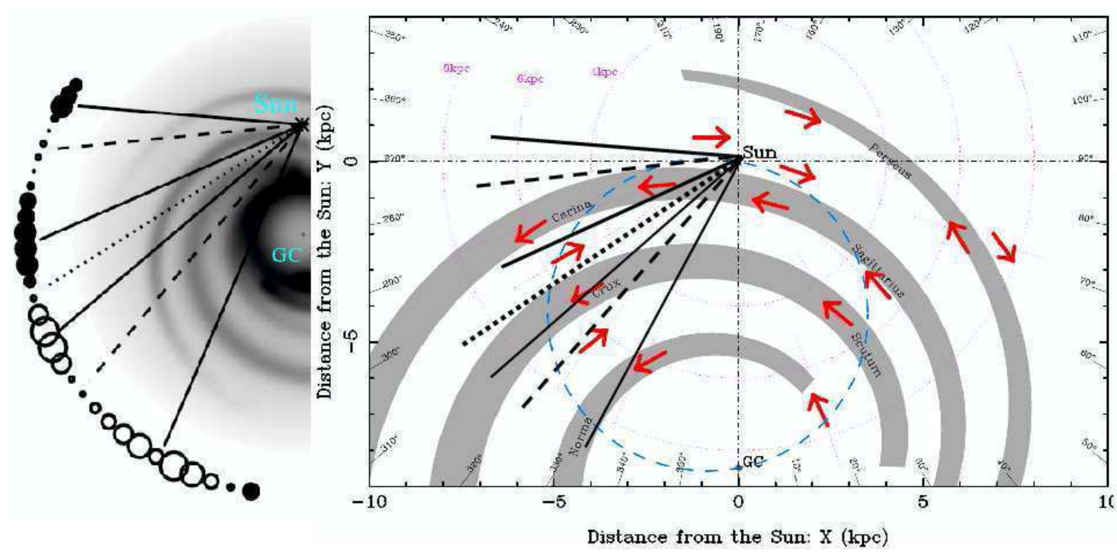

Figure 2: The general tendency of RM variations of extragalactic radio sources along the Galactic longitude, peaks and valleys [6], is very consistent with the large-scale structure of magnetic fields in the tangential regions derived from pulsar RMs [15].

of the Galaxy [21,15]. Field strengths in the region can be *directly measured* (instead of *modeled*) from the slope of trends in plots of RM versus DM. Based on Equation 5, we get

$$\langle B_{||}\rangle_{d1-d0} = 1.232\frac{\Delta\mathrm{RM}}{\Delta\mathrm{DM}} \tag{6}$$

where $\langle B_{||}\rangle_{d1-d0}$ is the mean line-of-sight field component in μG for the region between distances $d0$ and $d1$, $\Delta\mathrm{RM} = \mathrm{RM}_{d1} - \mathrm{RM}_{d0}$ and $\Delta\mathrm{DM} = \mathrm{DM}_{d1} - \mathrm{DM}_{d0}$.

Up to now, RMs of 550 pulsars have been observed [9,16,30,15]. Most of the new measurements lie in the fourth and first Galactic quadrants and are relatively distant, which enable us to investigate the structure of the Galactic magnetic field over a much larger region than was previously possible. We detected counterclockwise magnetic fields in the most inner arm, the Norma arm [14]. A more complete analysis for the fields near the tangential regions of the most probable spiral of our Galaxy [15] gives such a picture for the coherent large-scale fields aligned with the spiral-arm structure in the Galactic disk, as shown in Fig.1: magnetic fields in all inner spiral arms are counterclockwise when viewed from the North Galactic pole. On the other hand, at least in the local region and in the inner Galaxy in the fourth quadrant, there is good evidence that the fields in interarm regions are similarly coherent, but clockwise in orientation. There are at least two or three reversals in the inner Galaxy, probably occurring near the boundary of the spiral arms. The magnetic field in the Perseus arm can not be determined well. The negative RMs for distant pulsars and extragalactic radio sources [5] (see Fig. 1) in fact suggest the interarm fields both between the Sagittarius and Perseus arms and beyond the Perseus arm are predominantly clockwise. The average RM variation along the Galactic longitude of extragalactic radio sources [6], especially these of the fourth Galactic quadrant, are very consistent with the magnetic field directions derived from the tangential regions of the arms (see Fig. 2). This implies that the dominant contribution to RMs of extragalactic radio sources behind the Galactic disk comes from the interstellar medium mainly in tangential regions.

Stronger regular magnetic fields in the Galactic disk towards the Galactic Center have been suggested previously [18,28]. Measurements of the regular field strength in the Solar vicinity give values of 1.5 ± 0.4 μG [25,17,19], but near the Norma arm it is 4.4 ± 0.9 μG [14]. With significant more pulsar RM data now available, Han et al. were able to measure the regular field strength near the tangential points in the 1st and 4th Galactic quadrants [15], and then plot the dependence of regular field strength on the Galactoradii (see Fig. 3). Although uncertainties are large, there are clear tendencies for fields to be stronger at smaller Galactocentric radii and weaker in interarm regions. To parameterize the radial variation, an exponential function was used as following,

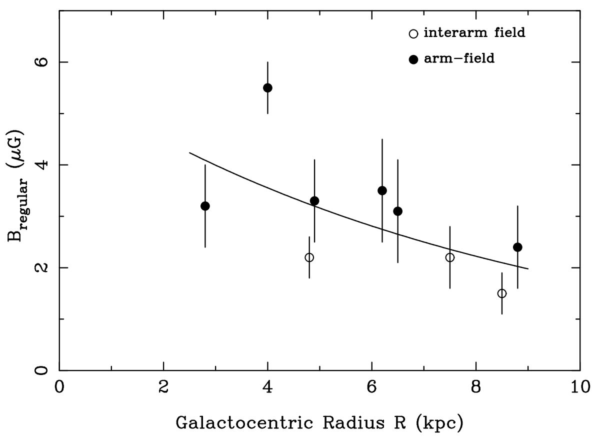

Figure 3: Variation of the large-scale regular field strength with the Galactocentric radius derived from pulsar RM and DM data near the tangential regions [15]. Note that the "error-bars" are not caused by the uncertainty of the pulsar RM or DM data, but reflect the random magnetic fields in the regions.

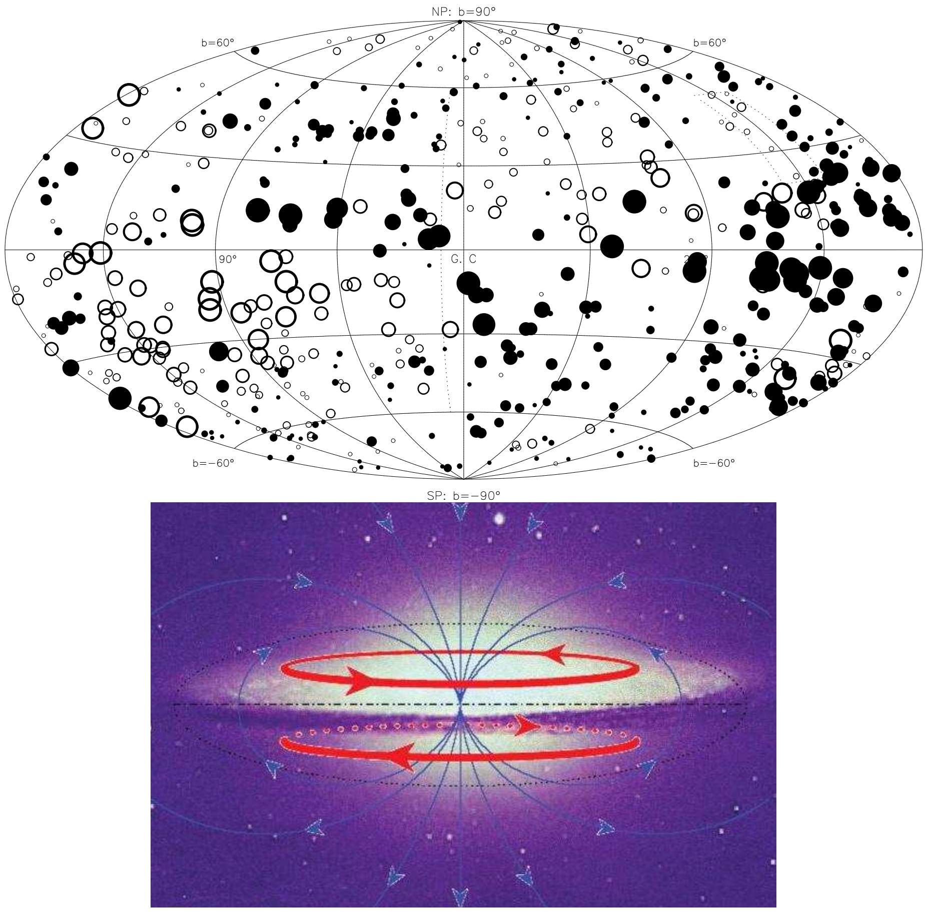

Figure 4: The antisymmetric rotation measure sky, derived from RMs of extragalactic radio sources after filtering out the outliers of anomalous RM values, should correspond to such a magnetic field structure in the Galactic halo as illustrated [13,16].

which not only gives the smallest χ^2 value but also avoids the singularity at $R = 0$ (for $1/R$) and unphysical values at large R (for the linear gradient). That is,

$$B_{\rm reg}(R) = B_0 \ \exp\left[\frac{-(R - R_\odot)}{R_{\rm B}}\right], \tag{7}$$

with the strength of the large-scale or regular field at the Sun, $B_0 = 2.1 \pm 0.3$ μG and the scale radius $R_{\rm B} = 8.5 \pm 4.7$ kpc.

The magnetic field structure in halos of other galaxies is difficult to observe. Our Galaxy is a unique case for detailed studies, since polarized radio sources all over the sky can be used as probes for the magnetic fields in the Galactic halo. As we mentioned before, the foreground RM from our Galaxy are common contribution to RMs of radio sources. That is to say, an "averaging process", which eliminates the random intrinsic RMs and discards the anonymous RMs, should be used to reveal the Galactic RM contribution. We removed any source if its RM value deviates from the average of their neighbours by 3 sigma, i.e. filtering out the outliers of RM values that is probably significantly from intrinsic RM, then from such a "cleaned" RM distribution in the sky, Han et al. identified the striking antisymmetry in the inner Galaxy respect to the Galactic coordinates [13,16]. This RM sky can result from the azimuth magnetic fields in the Galactic halo with reversed field directions below and above the Galactic plane (see Fig.4). Such a field can be naturally produced by an A0 mode of dynamo [31], and it is necessary to include this into any reasonable model for interstellar medium [29]. The observed filaments

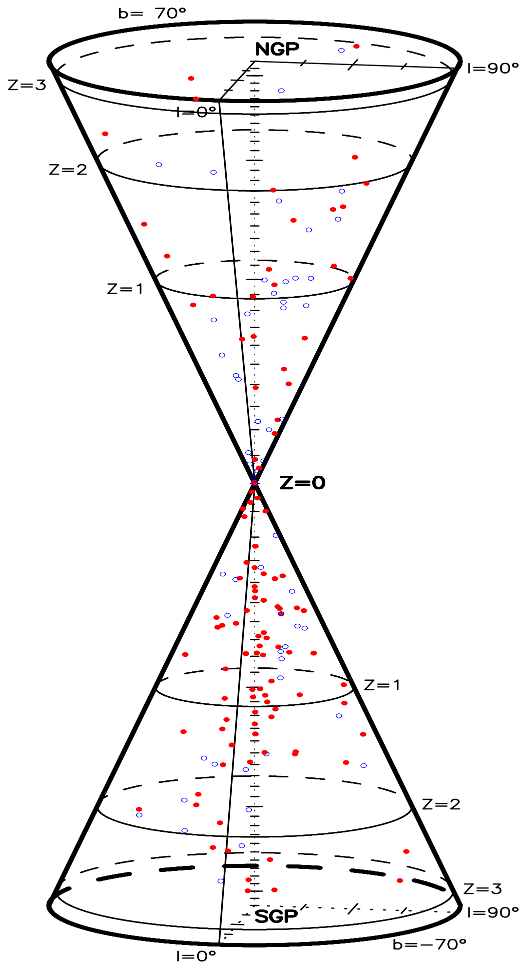

Figure 5: The space distribution of radio sources in the Galactic pole regions which we have their rotation measures observed. The red points stand for the positive RMs and blue ones for the negatives. It is clear that the rotation measures tend to be more positive (red) in the south Galactic pole and negative in the north pole, indicating the local vertical Galactic magnetic fields [12].

near the Galactic center should result from the dipole field in this scenario. The local vertical field component of ∼0.2 μG [17,16] may be related to the dipole field in the solar vicinity.

3 RM tomography for magnetic fields in the nearby universe

To probe the magnetic fields on cosmological scales, we have to look at the variation of RMs of radio sources with the redshift of the sources after the foreground Galactic RM contribution is eliminated. Three conditions have to be satisfied: 1). We have to measure the foreground RM sky to a certain level of accuracy. Looking at the RM sky in Fig.5, one can immediately see that the RMs near the two Galactic poles are on average very small. Whilst in other regions, the Galactic RMs are more difficult to assess accurately. A more extensive RM sky survey is required for this purpose. 2). To reveal the intergalactic RMs of a few rad m^{-2}, the measurements of each RM should be at least accurate to this level. With current technicques this is now acheivable using the wide-band spectral-polarimeters available at many radio telescopes. 3). The redshift of measured objects must also be known. This is now becoming possible for large numbers of sources by virtue of new large-scale optical spectrum survey, such as SDSS.

We have observed 110 objects with known redshift in the pole regions [12]. Together with previously published data, we found from RM data of two poles, see Fig. 6, that: 1). RM data clearly tend to have opposite signs which indicate a small but significant local vertical Galactic magnetic fields of 0.2 μG; 2) the deviations get larger at higher redshifts, which implies clearly that there is some kind of random RM contribution from intergalactic medium.

To understand the intergalactic magnetic fields, we still have three barriers to overcome. In each redshift range, we require a large number of objects with measured RMs, so that effect of their intrinsic RMs does not dominant. Second, we do not have enough information about the electron density distribution, such as whether it is clouded in the intergalactic space and how it couples with magnetic fields[32]. To delineate the intergalactic magnetic fields, there is still a long way to go.

Acknowledgments: I am very grateful to colleagues who have collaborated with me: Dr. R.N. Manchester from Australia Telescope National Facility, CSIRO (Australia), Prof. G.J. Qiao from Peking University (China), Prof. Andrew Lyne from Jodrell Bank Observatory (UK), and Dr. Katia Ferriére from Observatory of Midi-Pyrénées (France), Dr. Willem van Straten from Swinborne University (AU). The author is supported by the National Natural Science Foundation (NNSF) of China (10821061 and 10773016) and the National Key Basic Research Science Foundation of China (2007CB815403).

References

1. Abraham, J., et al. 2007, Science, 318, 938
2. Alfév, H. 1949, *Phys. Rev.* **75**, 1732
3. Armstrong, J. W., Rickett, B. J., & Spangler, S. R. 1995, ApJ, 443, 209
4. Beck, R. 2008, AIPC 1085, 83
5. Brown, J. C., Taylor, A. R., Wielebinski, R., & Mueller, P. 2003, ApJ, 592, L29
6. Brown, J. C., Haverkorn, M., Gaensler, B. M., & et al. 2007, ApJ, 663, 258
7. Fermi, E. 1949, *Phys. Rev.* **75**, 1169
8. Freedman, W. L., Madore, B. F., Gibson, B. K., et al. 2001, ApJ, 553, 47
9. Hamilton, P. A. & Lyne, A. G. 1987, MNRAS, 224, 1073
10. Han, J. L. 2004, In: The Magnetized Interstellar Medium, Copernicus GmbH, p.3
11. Han, J. L., Ferriere, K., & Manchester, R. N. 2004, ApJ, 610, 820
12. Han, J. L., Man, H., Zhao J. 2008, in preparing
13. Han, J. L., Manchester, R. N., Berkhuijsen, E. M., & Beck, R. 1997, A&A, 322, 98
14. Han, J. L., Manchester, R. N., Lyne, A. G., & Qiao, G. J. 2002, ApJ, 570, L17
15. Han, J. L., Manchester, R. N., Lyne, A. G., Qiao, G. J., & van Straten, W. 2006, ApJ, 642, 868.
16. Han, J. L., Manchester, R. N., & Qiao, G. J. 1999, MNRAS, 306, 371
17. Han, J. L. & Qiao, G. J. 1994, A&A 288, 759
18. Heiles, C. 1996b, in ASP Conf. Ser. 97: in: Polarimetry of the Interstellar Medium, 457
19. Indrani, C. & Deshpande, A. A. 1999, New Astronomy 4, 33
20. Lyne, A. G. & Smith, F. G. 1989, Nature, 218, 124
21. Lyne, A. G. & Smith, F. G. 1989, MNRAS, 237, 533
22. Minter, A. H. & Spangler, S. R. 1996, ApJ, 458, 194
23. Ohno, H. & Shibata, S. 1993, MNRAS, 262, 953
24. Page, L. and Hinshaw, G. and Komatsu, E. et al. 2007, ApJS, 170, 335
25. Rand, R. J. & Kulkarni, S. R. 1989, ApJ, 343, 760
26. Reich, W. 2007, "Galactic polarization surveys", in: Cosmic Polarization,ed. Roberto Fabbri, Publisher: Research Signpost
27. Riess, A. G., Filippenko, A. V., Challis, P., et al. 1998, AJ, 116, 1009

28. Strong, A. W., Moskalenko, I. V., & Reimer, O. 2000, ApJ, 537, 763
29. Sun, X. H., Reich, W., Waelkens, A., Enßlin, T. 2007, A&A, in press
30. Weisberg, J. M., Cordes, J. M., Kuan, et al. 2004, ApJS, 150, 317
31. Wielebinski, R., Krause, F., 1993, A&AR, 4, 449
32. You, X.P., Han, J.L., Chen, Y. 2003, Acta Astronomica Sinica, Vol.44, Suppl. p.155

Conference organizors on nice Banquit.

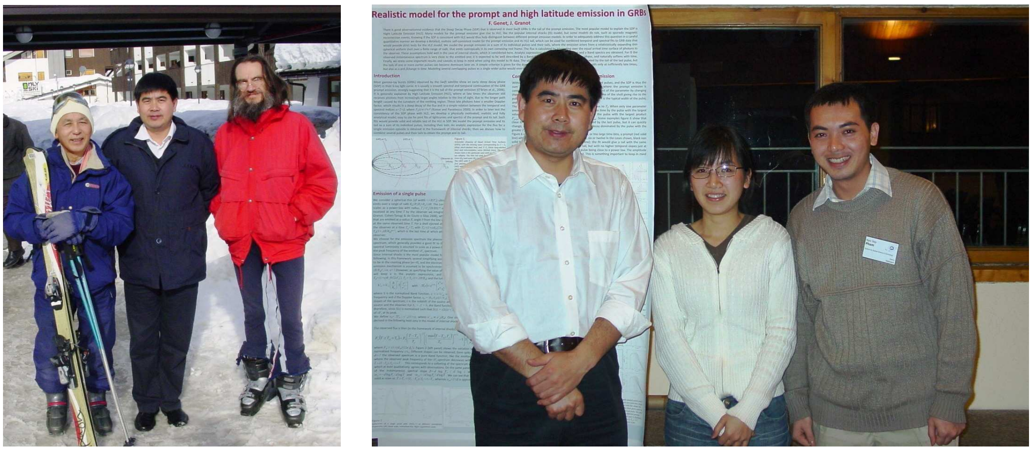

J.L.Han with the conference organizers: Dr. J. Dumarchez and Dr. J. Trân Thanh Vân and with the two vietnam participants: Ms. Tuyet Nhung Pham and Mr. Ngoc Diep Pham.

OBSERVABLES SENSITIVE TO PRIMARY MASS COMPOSITION AT THE PIERRE AUGER OBSERVATORY

A.G. MARIAZZI FOR THE PIERRE AUGER COLLABORATION
IFLP (CONICET - La Plata/Universidad Nacional de La Plata),CC67 - 1900,
La Plata, Argentina

The knowledge of the mass composition of the ultra high energy cosmic rays (UHECR) is a crucial point towards the determination of their origin, acceleration and propagation mechanism. A unique feature of the Pierre Auger Observatory is its hybrid nature, where showers are observed simultaneously by fluorescence telescopes and water Cherenkov tanks. The combined use of these two detection techniques provides cross-calibration and a better event reconstruction accuracy. Ideally all mass-sensitive observables should be combined to maximise the discrimination, but the 10% duty cycle of the fluorescence detector limits the use of direct measurements of shower maximum at the highest energies. Mass-sensitive observables accessible with the surface detectors alone are investigated. These are the signal risetime in the Cherenkov stations, the muon content, and the azimuthal signal risetime asymmetry. The mass sensitivity of these variables is demonstrated and their application for composition studies is discussed.

1 Introduction

The aim of the Pierre Auger Observatory is to measure the flux, arrival direction distribution and mass composition of ultra-high energy cosmic rays with unprecedented statistical precision over the whole sky. The Surface Detector (SD) of the southern site of the Pierre Auger Observatory [1] consists of 1600 water Cherenkov detectors equally spaced on a triangular grid (1.5 km) over an area of approximately 3000 km^2. The Fluorescence Detector (FD) consists of 4 eyes with 6 telescopes, each located at the border of the SD array overlooking it. The SD records the shower front, by sampling the particle density at ground level, with a duty cycle of 100%. The FD measures the fluorescence light emitted as the shower develops through the atmosphere. As it can only operate on clear, moon-less nights, its duty cycle is about 10%. This unique combination of both techniques in a hybrid detector offers huge advantages. For example, the SD can measure the energy parameter S(1000), the signal at 1000 m from the core, with high, easily calculated aperture, while the FD calorimetric shower energy determination provides the conversion between S(1000) and primary energy. This allows one

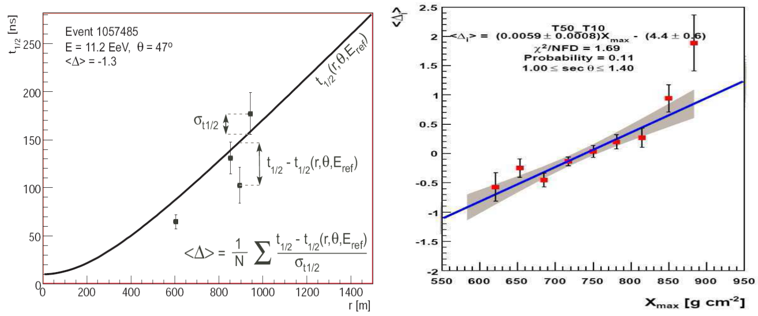

Figure 1: (left)Risetime vs. distance to the core: the curve is the benchmark risetime and the data points represent the measurements of risetime of each detector with error bars for this particular event. (right) Correlation of risetime and X_{max} for the selected hybrid events

to determine the energy of a cosmic ray without having to rely on models. Another feature of this hybrid design is a much improved resolution in direction and energy determination as compare to the results obtained by any detector system on its own. The systematic errors of both methods are of different origin, thus, allowing a valuable cross check of the results.

The hybrid events provide a direct measurement of X_{max}, which is the main parameter to infer mass composition [2], but the bulk of events collected by the Observatory have information only from the surface array. Therefore, observables from the array are very useful for composition analysis at the highest energies. Ideally all mass-sensitive observables should be combined to maximise the discrimination. Because of this, and the obviously independent systematic uncertainties, it is worthwhile to study ground level observables that are sensitive to the primary composition as well. A variety of experimental variables are currently investigated like the signal rise time, its asymmetry and the muon content from the signal shape analysis.

2 The risetime of the signal

For each event, the water Cherenkov detectors record the signal as a function of time (FADC traces). Muons travel in straight lines through the atmosphere with hardly any interaction, whereas the electromagnetic particles undergo multiple scattering on their way to ground. The first portion of the signal of the stations is dominated by the muon component which tends to arrive earlier and over a period of time shorter than the electromagnetic particles, which are spread out on time. Air showers with more muon content (like those produced by heavy primary cosmic rays) have a narrower distribution in arrival times than showers with large fractions of electromagnetic particles (like those produced by light primaries).

The risetime is the time it takes to reach from 10% to 50% of the total integrated signal in each station. It was shown to be sensitive to primary mass composition, and is highly correlated with the shower development and the depth of its maximum [3].

The risetime as a function of core distance for a particular event it is shown in Figure 1 (left). It is desirable to assimilate these individual measurements of risetime into a single parameter which can be used on an event-by-event basis as a surrogate for X_{max} over a wide range of energies. The parameter introduced here is the average deviation of the risetimes of signals in an event, $< \Delta_i >$, from those evaluated from a fit to the average $t_{1/2}$ as a function of core distance (r) and zenith angle(θ) for showers at a fixed reference energy ($10^{19} eV$). This function is called the benchmark function. Then, for each selected detector in a given event, the deviation of the measured risetime from the benchmark function is calculated in units of measurement uncertainty, $\sigma^i(t_{1/2})$, and averaged for all detectors in the event as shown in equation 1, enabling a new observable, $< \Delta >$ to be introduced.

$$< \Delta >= \frac{1}{N} \sum_{i=1}^{N} \frac{t^i_{1/2} - t_{1/2}(\theta, r, E_{ref})}{\sigma^i(t_{1/2})} \tag{1}$$

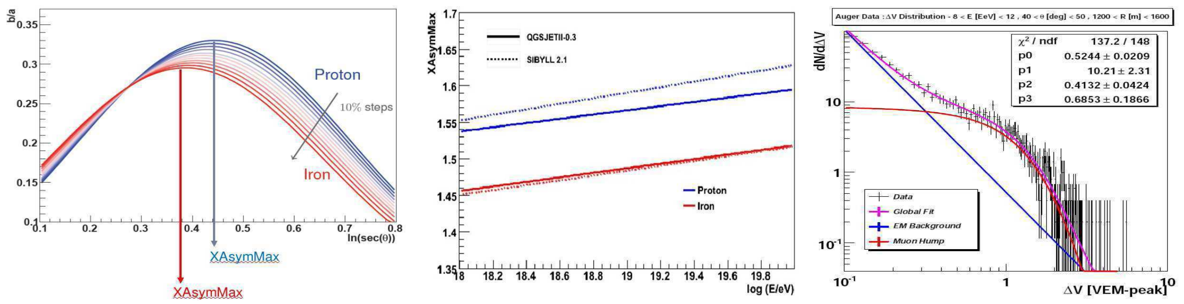

Figure 2: (left)Asymmetry development for the different samples with mixed composition, going from pure proton to pure iron in steps of 10%.(center)Position of maximum asymmetry vs. primary energy for different models and primaries.(right)Distribution of jumps for events at a given energy, zenith angle and distance to the core range. Lines correspond to the different fitted distributions of muons and electromagnetic signal.

This new observable does not involve any fit function that may fail in a shower by shower basis and it can be determined in events with only one detector satisfying the selection criteria.

The correlation of the chosen parameter with X_{max} is measured using a sample of hybrid events. This is shown in Figure 1(right), where a linear dependence is found allowing an estimation of X_{max} from events observed by the SD alone. Mass composition studies could be done afterwards by means of the obtained elongation rate. To improve accuracy in the correlation, signals for each individual detector are deconvolved to minimize detector response effects.

3 The longitudinal development of the asymmetry in risetime

The azimuthal asymmetry of time distributions from signals of inclined showers have been measured in the Pierre Auger Observatory [4]. The SD stations measure one stage of the shower development for near vertical events. But in the case of inclined showers, considerably different shower ages are observed, depending on whether the station is up- or downstream of the incoming shower direction. The upstream trace is rather broad, which is compatible with a large fraction of electromagnetic particles. The downstream trace is narrower indicating that most of the electromagnetic component has been attenuated and the signal is dominated by muons.

The risetime asymmetry can be measured by selecting events in bins of reconstructed energy and $\sec\theta$. Then, for these events the average risetime of those detectors passing quality cuts is determined. For each $(E, \sec\theta)$ bin, a fit of $< t_{1/2}/r >$ to a linear cosine function of ξ (azimuthal angle in the shower plane) provides the asymmetry factor b/a : $< t_{1/2}/r >= a + b\, cos\xi$. The amplitude of the asymmetry changes with the zenith angle, θ, i.e. atmospheric depth traversed. The main idea behind the method is to reconstruct a longitudinal development of the observed asymmetry which is reminiscent of the longitudinal development of the extensive air shower. The asymmetry has a maximum, which is in a different position for different primaries, as it is shown in Figure 2(right). In Figure 2(center) the values of the position ($\sec\theta$) at which the asymmetry longitudinal development reaches its maximum (XAsymMax) are plotted vs. primary energy for data collected by the Pierre Auger Observatory. Predictions for SIBYLL2.1 and QGSJETII03 hadronic models are included. The corresponding linear fits of both primary types are clearly separated, thus allowing discrimination of heavy and light primaries [5].

4 Muon content from signal shape

The muon content of the extensive air showers is a quantity highly sensitive to mass composition. The FADCs of the SD detectors show a characteristic time structure from which the muon content can be measured. Since muons muon deposits much more energy (typically 240 MeV) than electrons or photons (about 10 MeV), spikes are produced over the smoother electromagnetic background in the

FADC time traces. Usual methods exploiting the detailed time structure are referred as muon counting methods. They consist in identifying and counting muon peaks over the background. The following a method is based on the derivative of the FADC traces, where high values indicate the occurrence of a muon. FADC jump is the delta $V = V(ti + 1) - V(ti)$, between consecutive bins (25 ns) where $V(ti)$ is the FADC signal. In Figure 2(right) the distribution of jumps for real events is shown. The asymmetry of the jump distribution is induced by the muon component. It was found that the jump distribution can be described by a sum of pure muonic and electromagnetic distributions, represented with almost universal analytical functions. This behavior has been established on data and checked by Monte Carlo simulations. By measuring in the data the relative weight of each component one could in principle obtain the number of muons.

The main idea behind using the jump feature relies on the fact that the number of muons in a station is related to the area below the curve, above a given jump threshold. In practice, the so called jump estimator from the FADC waveform is calculated, which is simply related to the number of muons in the surface detector by a proportionality factor. The number of muons in an Auger surface detector could be estimated by this simple formula within an appropriate range of energy, zenith angle and radial distances. The value of the proportionality factor is directly determined from the analysis of fits on the Auger data and, consequently, is independent of Monte Carlo simulations. By fitting a muonic lateral distribution function for each event the muon density at 1000 m for each event is estimated.

In that way, the muonic signal can be determined on a statistical basis with a resolution of about 25% and the number of muons as a function of energy can be compared to predictions from air shower simulations to estimate the primary composition.

5 Conclusions

A variety of surface detector observables are sensitive to the mass composition. The mass sensitivity of risetime, azimuthal asymmetry in risetime and muon content from the signal, as examples of SD observables, have been studied.

The assimilation of individual risetime measurements into an event-wide parameter has been achieved through the introduction of the average fluctuation in $t_{1/2}$, $< \Delta >$. This parameter has been proven to correlate with X_{max}, having established that $< \Delta >$ is an X_{max}-sensitive variable.

The longitudinal development of the observed asymmetry in time distributions from SD detector signals of inclined showers is an indicator of the shower development and it is different for different primaries. The zenith angle at which it reaches its maximum can be used as an estimator for the primary composition. The method was validated using hypothetical data samples corresponding to pure proton, pure iron and a mixed composition.

A method to estimate the number of muons in each station for individual events was presented. This method is based on the distribution of a quantity called the "jump" calculated from the surface detector waveform recorded in FADC traces.

In summary, the capability of the SD array for determining mass composition has been shown.

References

1. J. Abraham et al., *Nucl. Instrum. Meth.* A **523**, 50 (2004).
2. M. Unger et al., Proc. 30th ICRC, Merida, Mexico (2007).
3. R. Walker & A.A. Watson, *J. Phys.* G **7**, 1279 (1981).
   A.A. Watson. & J.G.Wilson, *J. Phys.* A **7**, 1199 (1974)
4. M. D. Healy et al., Proc. 30th ICRC, Merida, Mexico (2007).
5. M. T. Dova et al., *Astropart. Phys.* in press (2009).
   (http://dx.doi.org/10.1016/j.astropartphys.2009.03.001)

SURVIVAL OF ULTRAHIGH ENERGY NUCLEI PROPAGATING IN CLUSTERS OF GALAXIES

K. Kotera
Institut d'Astrophysique de Paris, 98 bis boulevard Arago, 75014 Paris, France

We study the survival of ultrahigh energy nuclei injected in magnetised clusters of galaxies, using a complete numerical propagation method and a realistic modelling of the baryonic and photonic density backgrounds. It is found that the survival of heavy nuclei highly depends on the injection position and on the profile of the magnetic field. Taking into account the limited lifetime of the central source can also lead in some cases to the detection of a heavier chemical composition at the highest energies.

1 Introduction

The chemical composition of ultrahigh energy cosmic rays is still an open question. Measurements prior to the Pierre Auger Observatory (PAO) indicate a light composition above energy $E \sim 10^{18.5}$ eV[1,2]. The results of the PAO on the contrary tend to suggest a mixed composition above the knee, that might even get heavier at the highest energy end.[3] Ultrahigh energy nuclei (mass number $A > 1$ and atomic number Z) have triggered the interest of many authors for two main properties: for a given set of physical parameters, they can be accelerated to an energy typically Z times larger than protons, and the heaviest particles can propagate on distances of hundreds of megaparsecs before losing their energy. The paramount issue in this subject is then the survival of these heavy nuclei in the dense medium in the source, or nearby the source. In particular, this question can be addressed in the context of propagation inside clusters of galaxies, considering that they produce particles or host powerful accelerators.

Clusters of galaxies are indeed dense regions of the Universe that harbour many candidate sources for ultrahigh energy cosmic rays, such as Active Galactic Nuclei (AGN), compact stellar remnants and cosmological shocks. The propagation of produced particles in these object is not straightforward though, as they have particularly enhanced photonic and baryonic backgrounds that will lead to interaction processes and secondary particle production. Most of all, clusters of galaxies host strong magnetic fields that can easily confine cosmic rays of energy $E < Z \times 10^{17.5}$ eV, for several hundreds of millions of years, leading galaxy clusters to act like storage rooms for these particles. Because the diffusion time in a magnetic field increases with the charge Ze of the particle, heavy nuclei should remain confined longer times in the structure, leading to an enhanced number of interactions and thus possibly to complete depletion of the original particle. Distinct signatures of these propagation effects should be observed in the produced spectrum as well as in the neutrino and gamma-ray fluxes.

We explore in this work the consequences of the injection of a mixed chemical composition in galaxy clusters, by calculating numerically the propagated primary particle fluxes. Effects due to the limited lifetime of the central source will also be briefly discussed.

2 Modelling clusters of galaxies for ultrahigh energy cosmic ray propagation

Clusters of galaxies can be roughly split into two categories in terms of temperature and emission: cool core clusters and non cool core clusters. This bimodality has also some significant consequences when it comes to modelling magnetic fields: cool core clusters are reported to have a much stronger magnetic field in the core, as well as a higher turbulence rate, as compared to non cool core clusters[4]. We model our cluster magnetic field using the three dimensional outputs of the MHD simulations run by Dubois & Teyssier[5]. We re-normalise arbitrarily the overall field by setting the maximum value to 10 and 30 μG for the cool core cluster (following values derived by Enßlin & Vogt 2006[6]) and we take a value of 1 μG at the center of non cool core clusters, that corresponds to the same scaling as for the cool core case at 30 μG. The magnetic field coherence lengths are calculated consistently from the simulation outputs in increasing spherical shells.

If ultrahigh energy cosmic rays are not injected in the central region of clusters of galaxies, we do not expect any striking signatures on the propagated spectra, as the background densities leading to interactions decrease very rapidly with the radial distance. Transient sources like gamma ray bursts and high Mach number accretion and merger shocks being mainly located in the peripheral regions, we will rather concentrate on central AGN as sources of ultrahigh energy particles in this work. Radio observations indeed indicate a strong presence of radio-loud Faranoff Riley type I (FRI) galaxies in the centre of galaxy clusters[7,8].

We consider in this study the interaction of high energy protons and nuclei with the Cosmic Microwave Background (CMB) and with the infrared (IR) background. We calculate the latter by adding the contribution of the diffuse extracluster IR photon density and the intracluster density created by galaxies inside the cluster. We model the diffuse IR background according to the studies of Stecker et al. (2006)[9] and the intracluster IR background by assuming that local ($z < 0.2$) clusters of galaxies are mostly populated by elliptical galaxies that moderately enrich the cluster with infrared photons.

Our ultrahigh energy nuclei propagation code combines a fast and accurate semi-analytical trajectory integration method in the magnetic field, and complete Monte Carlo calculations of photonic and baryonic energy losses for primary and secondary nuclei. Details of this method can be found in Kotera & Lemoine (2008)[10], Allard et al. (2005)[11] and Kotera et al. (2009)[12].

3 Results and discussion

Figure 1 shows our resulting cosmic ray spectra after propagation in the the indicated type of cluster and magnetic field normalisation. We present total and secondary nuclei fluxes as well as the contribution of different chemical species (see legend in the upper right panel). We assume in these plots that the source emits particles continuously and that the stationary regime has been reached. The effects of propagation in the extragalactic medium is not included in these results but they should not affect importantly the composition obtained in these spectra.

One observes that the production of secondary nuclei mainly differs in the four panels around energies $E \sim 10^{17.5-19}$ eV. The depletion of heavy nuclei in this range of energies is due to the combined effects of magnetic confinement and interactions on the infrared background. The gap is especially pronounced for iron which has a very low mean free path to photo-disintegration at these energies. Lighter nuclei are confined at lower energies and thus suffer less interactions. These figures demonstrate that with a high (but realistic) magnetic field of $B_{\rm c} \sim 30$ μG at the centre of a cool core cluster (bottom left), the heaviest nuclei hardly survive, and escape the structures only for energies around $E \sim 10^{20}$ eV. For lower magnetic fields though, a reasonable amount of iron can still survive the propagation inside clusters. One can also note that no heavy nuclei survive at the highest energies ($E > 10^{20.5}$ eV) due to photo-disintegration on the CMB photons, meaning that the composition becomes pure proton in this region.

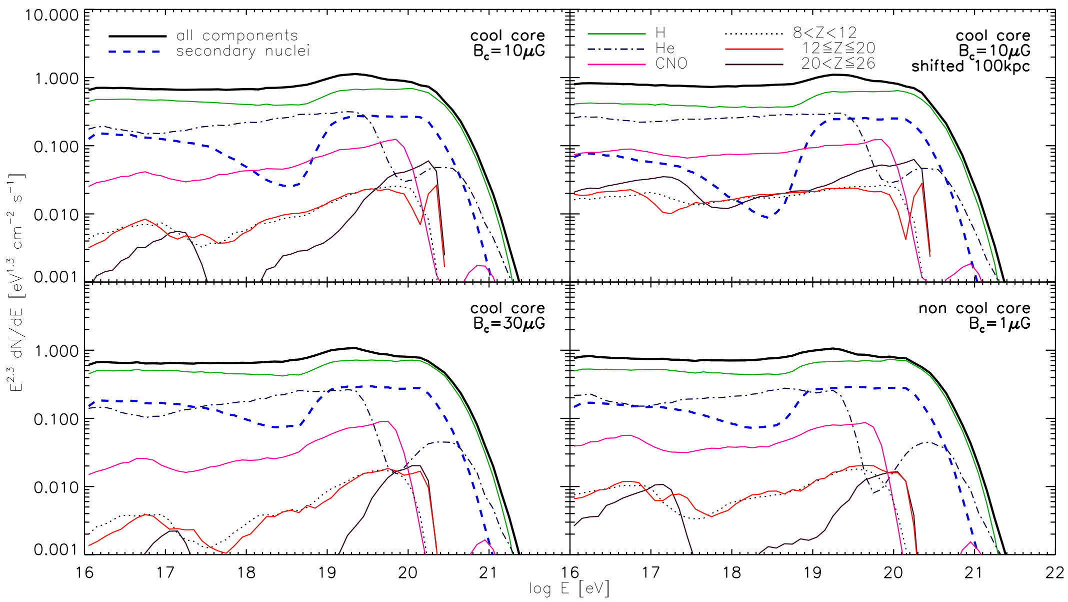

Figure 1: Cosmic ray energy spectra for (*left*) central injection and cool core cluster with magnetic field at the centre $B_\mathrm{c} = 10\mu$G (*top*) and 30μG (*bottom*) and (*upper right*) cool core cluster with $B_\mathrm{c} = 10$ μG and source shifted of 100 kpc from the centre, and (*bottom right*) central source and non cool core cluster with $B_\mathrm{c} = 1$ μG. These spectra are normalised to unity at $E = 10^{19}$ eV.

The bottom right panel presents the cases of a non cool core cluster with central magnetic field $B_\mathrm{c} = 1$ μG with the source located at the centre. This panel should be compared to the bottom left panel, as the scaling coefficient is the same in both cases, meaning that the magnetic field profiles differ here only in the core of the cluster. The higher magnetic field and the enhanced baryonic density in the cool core case definitely play a role at lowest energies ($E < 10^{17.5}$ eV): the confinement in the core is more efficient and heavy nuclei are more depleted by hadronic interactions than in the non cool core case.

It is very plausible that the acceleration sites of ultrahigh energy cosmic rays are not at the very centre of the cluster of galaxies, but shifted of some hundreds of kiloparsecs (for lobes or hot spots of radio galaxies for example). The upper right panel presents the resulting spectrum obtained if the injection of ultrahigh energy cosmic rays happens at 100 kpc of the centre of the cluster. In a cool core cluster, the baryonic density falls quite steeply with the distance from the centre: at 100 kpc, the average density is already two magnitudes lower than at the centre. This explains why nuclei survive much better in this case, especially at low energy. The position of the source will thus have a deep impact on the resulting composition of ultrahigh energy particles.

It is of common knowledge that AGN remain active only during a limited time, typically of order $\sim 10^7$ yrs for luminosities of 10^{43-44} erg/s[13]. Figure 2 presents the evolution of the cosmic ray spectra in time, assuming a limited AGN lifetime of $t_\mathrm{AGN} = 10$ Myr. The cosmic ray afterglow observed after the extinction of the source is due to the confinement times of different species at different energies and to their variance around their mean value. While time goes, we observe the progressive apparition of low energy particles and of heavier nuclei. The variance σ_conf around the confinement time t_conf is globally proportional to the latter, meaning that high energy light nuclei have a small variance. For this reason, high energy protons and helium quickly disappear as the source dies, while heavy nuclei with larger confinement time and variance remain present a much longer time. This leads interestingly to a heavy composition at the highest energies for times greater than $\sim t_\mathrm{AGN} + t_\mathrm{esc}$, where t_esc is the escaping time of

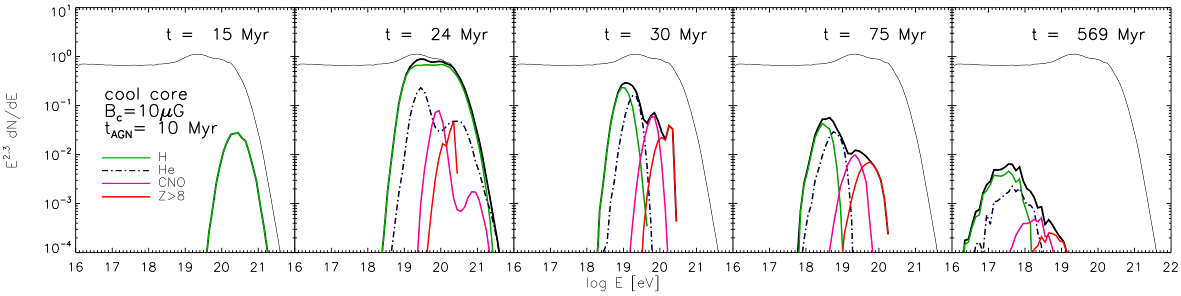

Figure 2: Evolution of the cosmic ray spectrum in time, assuming a lifetime of $t_{\rm AGN} = 10$ Myr for the central AGN, for the case of a cool core cluster of central magnetic field $B_{\rm c} = 10\ \mu$G. Each panel presents the spectrum at the time indicated at the top-right hand corner. The injection from the source is assumed to begin at $t = 0$. The thick black line is the total spectrum and the thin black line indicates the total flux obtained for a stationary regime, as in figure 1. These spectra are normalised to unity at $E = 10^{19}$ eV.

protons propagating rectilinearly from the cluster. After $\sim 10\,t_{\rm AGN}$, the flux is considerably diminished at all energies.

Such effects could be detectable if a few nearby clusters of galaxies with an extinguished AGN contribute to the observed diffuse flux of ultrahigh energy cosmic rays. Indeed, in this configuration, the composition at the highest energies should become heavy, and even be mainly iron enriched. The duration of the duty cycle of AGN will set the average cosmic ray emission state at which one expects to observe a cluster of galaxies hosting an AGN. According to it, one might expect the absence of powerful sources in the arrival directions of the observed highest energy events: magnetised clusters of galaxies hosting an extinguished AGN can be emitting cosmic ray afterglows, and contribute to the overall observed spectrum, provided that their density and source luminosity are high enough. We may also notice that in the presence of more than one AGN at the centre of the cluster, there might be a spread in the effective injection duration, which can mimic a time-independent permanent regime. In such a case, the obtained fluxes are those calculated in figure 1.

Further features on ultrahigh energy nuclei survival and secondary neutrinos and gamma ray emissions are discussed in Kotera et al. (2009)[12].

References

1. Shinozaki, K., *et al.* in International Cosmic Ray Conference, Vol. 7,151–+ (2005)
2. Abbasi, R. U., *et al.* Astrophysical Journal **622**, 910 (2005)
3. Unger, M., Engel, *et al.* Astronomische Nachrichten **328**, 614 (2007)
4. Carilli, C. L., & Taylor, G. B. ARA&A **40**, 319 (2002)
5. Dubois, Y., & Teyssier, R. A&A **482**, L13 (2008)
6. Enßlin, T. A., & Vogt, C. A&A **453**, 447 (2006)
7. Best, P. N. MNRAS **35**, 70 (2004)
8. Gilmour, R., Best, P., & Almaini, O. MNRAS **392**, 1509 (2009)
9. Stecker, F. W., Malkan, M. A., & Scully, S. T. Astrophysical Journal **648**, 774 (2006)
10. Kotera, K., & Lemoine, M. *Phys. Rev.* D **77**, 023005 (2008)
11. Allard, D., Parizot, E., Olinto, A. V., Khan, E., & Goriely, S. A&A **443**, L29 (2005)
12. Kotera, K., Allard D., Murase, K., Aoi J., Dubois, Y., Pierog, T. & Nagataki, S., in prep.
13. Schmidt, M. Astrophysical Journal **146**, 7 (1966)

PERFORMANCES OF THE KASCADE-Grande EXPERIMENT

A. Chiavassa[c,1], W.D. Apel[a], J.C. Arteaga[b,2], F. Badea[a], K. Bekk[a], M. Bertaina[c], J. Blümer[a,b], H. Bozdog[a], I.M. Brancus[d], M. Brüggemann[e], P. Buchholz[e], E. Cantoni[c,f], F. Cossavella[b], K. Daumiller[a], V. de Souza[b,3], F. Di Pierro[c], P. Doll[a], R. Engel[a], J. Engler[a], M. Finger[a], D. Fuhrmann[g], P.L. Ghia[f], H.J. Gils[a], R. Glasstetter[g], C. Grupen[e], A. Haungs[a], D. Heck[a], J.R. Hörandel[b,4], T. Huege[a], P.G. Isar[a], K.-H. Kampert[g], D. Kang[b], D. Kickelbick[e], H.O. Klages[a], Y. Kolotaev[e], P. Łuczak[h], H.J. Mathes[a], H.J. Mayer[a], J. Milke[a], B. Mitrica[d], C. Morello[f], G. Navarra[c], S. Nehls[a], J. Oehlschläger[a], S. Ostapchenko[a,5], S. Over[e], M. Petcu[d], T. Pierog[a], H. Rebel[a], M. Roth[a], H. Schieler[a], F. Schröder[a], O. Sima[i], M. Stümpert[b], G. Toma[d], G.C. Trinchero[f], H. Ulrich[a], J. van Buren[a], W. Walkowiak[e], A. Weindl[a], J. Wochele[a], M. Wommer[a], J. Zabierowski[h]

[a] *Institut für Kernphysik, Forschungszentrum Karlsruhe, 76021 Karlsruhe, Germany*
[b] *Institut für Experimentelle Kernphysik, Universität Karlsruhe, 76021 Karlsruhe, Germany*
[c] *Dipartimento di Fisica Generale dell'Università, 10125 Torino, Italy*
[d] *National Institute of Physics and Nuclear Engineering, 7690 Bucharest, Romania*
[e] *Fachbereich Physik, Universität Siegen, 57068 Siegen, Germany*
[f] *Istituto di Fisica dello Spazio Interplanetario, INAF, 10133 Torino, Italy*
[g] *Fachbereich Physik, Universität Wuppertal, 42097 Wuppertal, Germany*
[h] *Soltan Institute for Nuclear Studies, 90950 Lodz, Poland*
[i] *Department of Physics, University of Bucharest, 76900 Bucharest, Romania*

[1] *email address: andrea.chiavassa@to.infn.it*
[2] *now at: Universidad Michoacana, Morelia, Mexico*
[3] *now at: Universidade de São Paulo, Instituto de Fisica de São Carlos, Brazil*
[4] *now at: Dept. of Astrophysics, Radboud University Nijmegen, The Netherlands*
[5] *now at: University of Trondheim, Norway*

The KASCADE-Grande experiment, located at Forschungszentrum Karlsruhe, Germany, is a multicomponent extensive air shower detector to study cosmic rays in the energy range from 10^{16} to 10^{18} eV. Due to its multicomponent characteristics, namely the former KASCADE experiment enriched by a large acceptance (0.5 km^2) scintillator detector (Grande) KASCADE-Grande is a suitable array to provide refined measurement in the 10^{16} to 10^{18} eV primary cosmic rays energy region. In this paper we will briefly discuss the relevance of performing high precision measurements in this energy range and the consequences expected both at higher (transition from galactic to extragalactic radiation) and lower (details about the knee) energies. The resolutions obtained with the KASCADE-Grande experiment are presented.

1 Introduction

The cosmic rays spectrum at energies above 10^{14} eV must be studied by ground based experiments detecting the secondary particles produced in Extensive Air Showers (EAS) generated in the atmosphere by the interaction of a primary cosmic ray.

A recent review of experimental results [1] is shown in Figure 1 (for the single experiments see referecences therein). It can be seen that the energies from 10^{16} to 10^{18} eV are the less

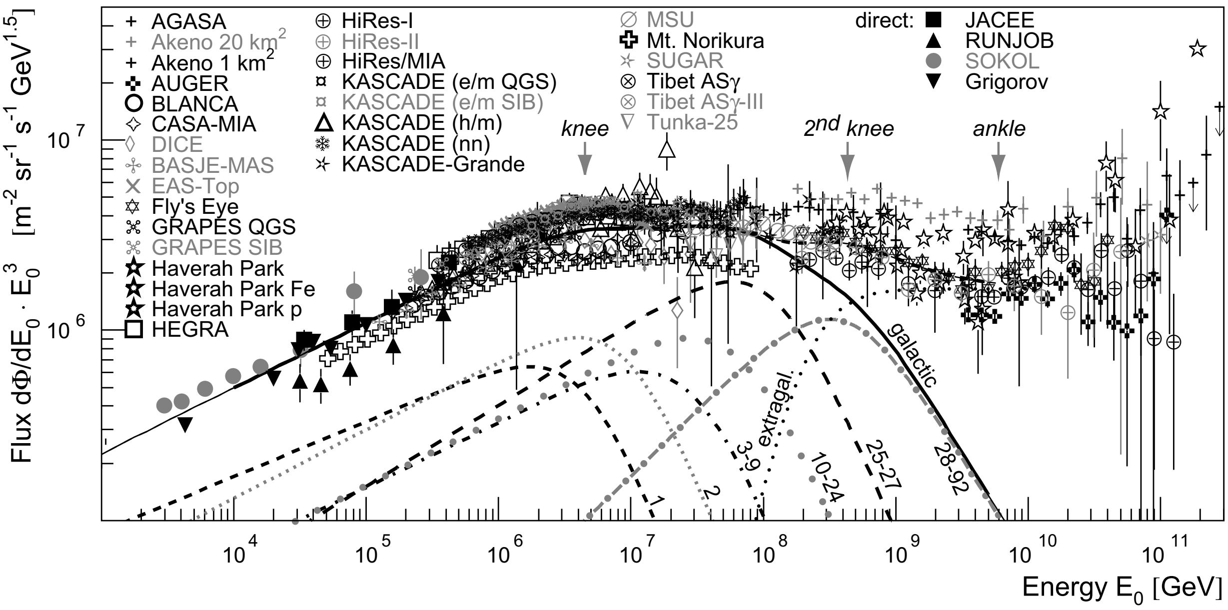

Figure 1: Review of measurements of the primary cosmic rays spectrum.

widely covered, the few available results are those of the Akeno [2] and MSU [3] experiments. In the last decade no arrays have explored this energy range, hence there is high interest in new measurements performed with high resolution detectors.

Concerning the energies just below 10^{16} eV we are dealing with the well known structure in the primary cosmic ray spectrum known as the knee, this feature has been widely investigated in the last decade and relevant experimental results have been obtained.

The change of slope has been observed in the spectra of all EAS components (electromagnetic [4 5 6], muonic [7 8] and hadronic [9]) and at different stages of the shower development, thus demonstrating that the knee is a feature of the primary cosmic ray spectrum and it is not due to a change in the interaction mechanism.

Moreover the charactheristics of the observed change of slopes, namely the integral fluxes above the knee and the number of electrons and muons at the knee, agree with the expectations of shower development in the atmosphere [7].

The EAS-TOP [7] and CASA-MIA [10] experiments have measured, through the correlation of the mean values of electrons and muons detected in the shower, that the primary chemical composition becomes heavier for increasing energies.

A more refined analysis performed mainly by the KASCADE experiment show that: the knee is due to the light component of cosmic rays [8] and that the spectra of single components (grouped in five groups) show knees at energies increasing with the primary atomic number [11] (a similar result has been obtained by the EAS-TOP collaboration [7]). The resolutions reached (by both experiments) do not allow to discriminate between a Z or A dependence.

All these analyses concerning the primary chemical composition heavily depend (at least for the quantitative aspects) on a complete EAS simulation, and thus suffer from the lack of knowledge of primary interactions at the energies under investigation. Moreover, at colliders the forward region of the interactions (the one relevant for the EAS development) is not studied.

We can conclude that the favoured scenario to explain the knee deals with astrophysical mechanisms: either the acceleration or the propagation of galactic cosmic rays. In both scenarios a change of the slope of the spectra of single elements is expected at an energy scaling with Z, thus we expect the iron knee at an energy equal to $ZE_{knee} \sim 10^{17}$ eV. This energy is above the range covered by recent experiments and it is thus important to study it with detectors allowing a separation between different elements or at least between the light and heavy components.

Concerning energies above 10^{18} eV the interest is connected with the transition from galactic to extragalactic cosmic rays.

In the so called "dip model" (Berezinsky et al. [12]) the fluxes of galactic and extragalactic cosmic rays become equal at $E \sim 5 \cdot 10^{17}$ eV, i.e. the energy of the faint spectral feature known as the second knee. The spectral shape observed (i.e. the ankle) is reproduced in the model by pair production of protons interacting with photons of cosmic microwave background. At energies above $\sim 10^{18}$ eV the authors predict a chemical composition dominated by protons (the fraction of heavier elements expected is lower than 15%).

In the model of Allard et al.[13] the ankle is due to the transition from galactic to extragalactic primaries and the chemical composition is assumed to be similar to the one observed at lower energies, thus a mixed composition is predicted. The transition to extragalactic radiation is supposed to happen at energies $\sim 3 \cdot 10^{18}$ eV.

It is thus of main importance to perform accurate measurements of the primary chemical composition in the whole energy range from 10^{16} to 10^{18} eV.

Chemical composition measurements in this energy range can be mainly performed using the N_e, N_μ ratio. The precision required was not yet reached by past experiments and we can expect relevant information in the next years.

Apart from the KASCADE-Grande experiment, that will be fully described in the following section, the $10^{16} - 10^{18}$ eV energy range will be covered, in the near future, by the ICE-TOP [14], TUNKA-133 [15] experiments and by the low energy extensions of the Pierre Auger Observatory [16] and of the Telescope Array [17].

2 The KASCADE-Grande experiment

The KASCADE-Grande experiment [18] is a multi-detector setup consisting of the KASCADE [19] experiment, the trigger array Piccolo and the scintillator detector array Grande (the experimental layout is shown in Figure 2). Additionally, KASCADE-Grande includes an array of digitally read out dipole antennas (LOPES) to study the radio emission in air showers at $E > 10^{16}$ eV [20]. Most important for the analysis presented here are the two scintillator arrays: KASCADE and Grande. The KASCADE experiment is itself a multiple detector setup and its major parts are an array of 252 scintillator detector stations, a streamer tube Muon Tracking Detector ($E_\mu > 800$ MeV) [21], and a multiwire proportional chamber muon detector ($E_\mu > 2.4$ GeV).

The KASCADE array is structured in 16 clusters. Each detector station houses two separate detectors for the electromagnetic (unshielded liquid scintillators) and muonic components (shielded plastic scintillators, $E_\mu > 230$ MeV). Muon detectors are housed only in 12 clusters (or 192 stations). This enables to reconstruct the lateral distributions of muons and electrons separately on an event-by-event basis.

The Grande array is formed by 37 stations of plastic scintillator detectors, 10 m^2 each (divided into 16 individual scintillators) spread on a 0.5 km^2 surface, with an average grid size of 137 m. All 16 scintillators are viewed by a high gain photomultiplier (for timing and low particle density measurements), the four central ones are additionally viewed by a low gain one (for high particle densities). The signals are amplified and shaped inside the Grande stations, and, after transmission to a central DAQ station, they are digitized by peak sensing ADCs. The dynamic range of the detectors is $0.3 - 8000$ particles $/10m^2$. Grande is arranged in 18 hexagonal clusters formed by six external detectors and a central one. The minimum triggering requirement is the coincidence of the central and three neighboring stations in one hexagon (4/7, rate 5 Hz). A stricter implemented mode, that is required for triggering the KASCADE array, is the 7/7 trigger mode, requiring all stations in a hexagon being fired (0.5 Hz).

Figure 3 show the detection and reconstruction efficiency, inside an internal fiducial area of

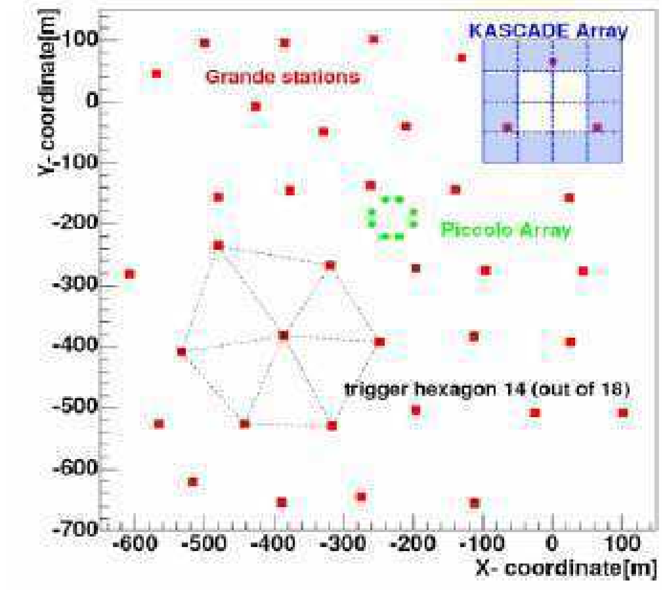

Figure 2: Layout of the KASCADE-Grande experiment.

$\sim 0.3\ km^2$, as a function of the shower size. Full efficiency is reached at $\sim 10^6$ shower size, i.e. a primary energy of $\sim 10^{16}$ eV.

2.1 Reconstruction Accuracy

The main shower parameters that are measured for each event are: the arrival direction, the total number of muons (N_μ) and the total number of charged particles (N_{ch}) in the shower.

The arrival direction of the events is determined fitting the arrival time of the particles in the Grande detectors to a curved shower front [22]. The core position, the shower age and the shower size (N_{ch}) are obtained fitting the particles densities measured by the Grande stations with a NKG like function [22].

The total number of muons is calculated using the core position determined by the Grande array and the muon densities measured by the KASCADE muon detectors [23].

The precisions obtained in the reconstruction of the shower parameters are evaluated exploiting the unique feature of the KASCADE-Grande experiment of having two independent samplings of the same event by the KASCADE and the Grande arrays. Selecting showers with core located in a region that is internal for both arrays (i.e. a ring around one of the Grande station located inside the KASCADE array) we have a set of events that are independently reconstructed by both arrays. We can thus compare the Grande results to those obtained by the KASCADE array that, having a better and known resolution, is used as reference (the distance between two KASCADE detectors is just 13 m). Dividing events in bins of shower size (N_{ch}^{KA} determined by KASCADE) we construct the distributions of the difference of the arrival directions $\Delta\Phi$ and of the core positions Δr. Fitting these distributions with a Rayleigh function we determine the Grande resolution as a function of the shower size. Figure 4 shows that the angular resolution is better than $1°$ (the increase of the errors for shower size greater than 10^7 is due to a lack of statistics). Figure 5 shows that the error on the determination of the core position is clearly lower than 10 m. The same procedure is followed for the shower size, the distributions of $\Delta N_{ch} = (N_{ch}^{KA} - N_{ch}^{Gr})/N_{ch}^{KA}$ are fitted with a gaussian distribution. The mean value (full squares in Figure 6) represent the systematic difference in the shower size obtained by KASCADE (N_{ch}^{KA}) and by Grande (N_{ch}^{Gr}); while the RMS gives the precision of the Grande

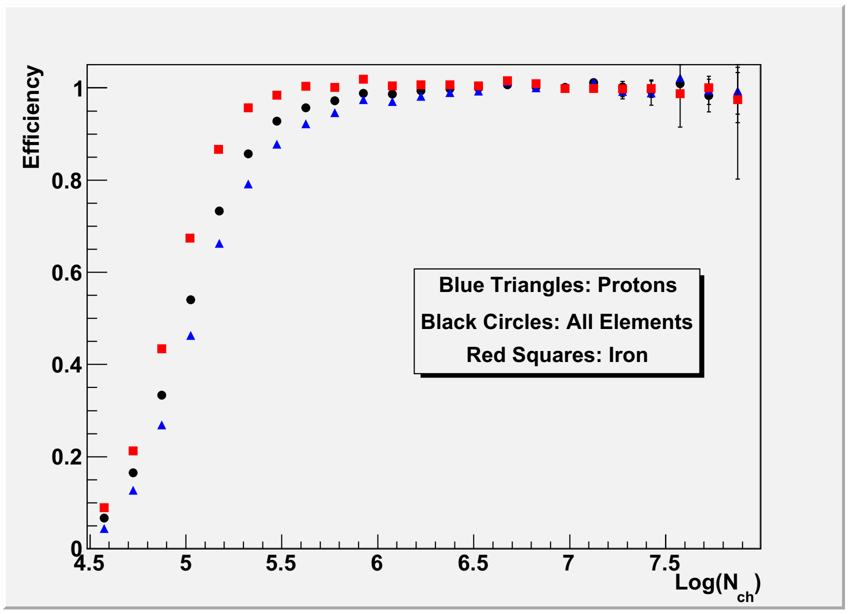

Figure 3: Detection and reconstruction efficiency as a function of the total number of charged particles of the KASCADE-Grande experiment.

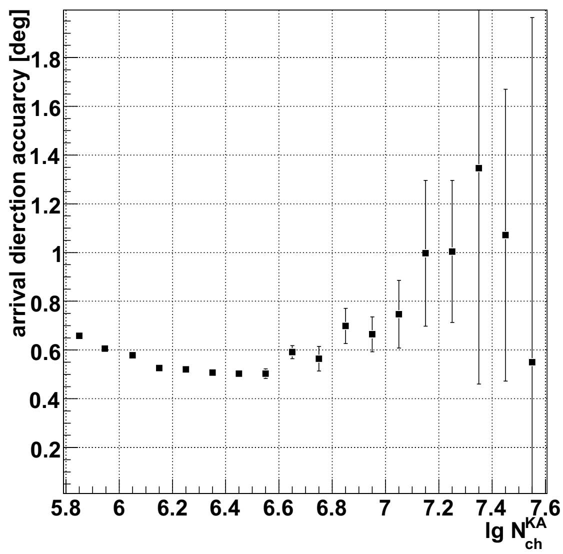

Figure 4: Grande array angular resolution measured comparing the arrival direction with the one obtained by the KASCADE array.

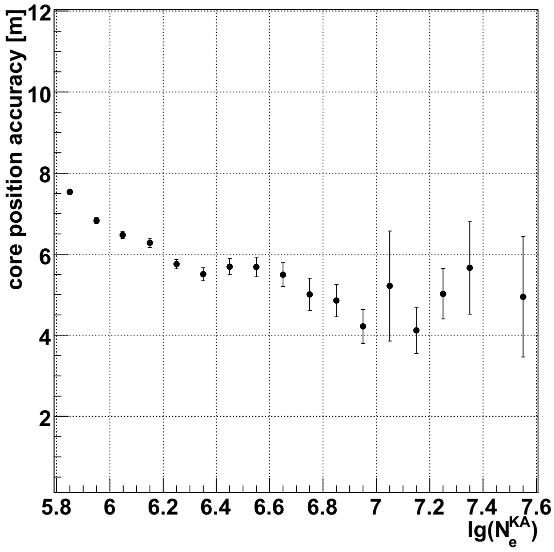

Figure 5: Grande array core position resolution obtained by the comparison with the KASCADE array.

array (open squares in Figure 6). We can see that the systematic difference between Grande and KASCADE is lower than 5% and that the error in the determination of the shower size is lower than 20%.

The errors on the shower parameters that have been obtained are those foreseen in the proposal of the KASCADE-Grande experiment. The KASCADE-Grande experiment is in continuous data taking since January 2004, a conclusive evaluation of systematic effects and the whole data processing are currently in progress.

As an example of the KASCADE-Grande potentialities we mention the measurements of the all particle spectrum that are currently undergoing following different approaches. One technique is based on the well known constant intensity cut method applied both to the muon and to the charged particle size spectra. Preliminary studies show that the resolution that can be reached is about 22% at $E \sim 10^{17}$ eV. In a different approach we try to measure the primary energy for single events using the shower size weighted with the N_μ/N_{ch} ratio. The systematic errors and the accuracy of this procedure are currently under investigation.

3 Conclusions

We have presented the resolutions obtained by the KASCADE-Grande experiment in the measurement of the EAS parameters. These performances have been evaluated in a purely experimental way using the KASCADE array as reference. The results are those expected in the proposal of the experiment: $< 1°$ on the arrival direction, < 10 m on the core location and $< 20\%$ on the shower size. Thus allowing investigations of cosmic rays in the energy range from 10^{16} to 10^{18} eV with a previously unreached precision.

Acknowledgments

The authors would like to thank the members of the engineering and techcnical staff of the KASCADE-Grande collaboration, who contributed to the success of the experiment. The KASCADE-Grande experiment is supported by the BMBF of Germany, the MIUR and INAF

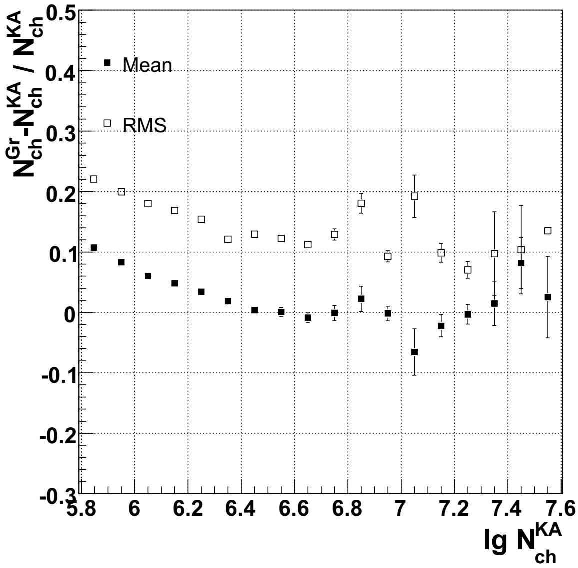

Figure 6: Grande array precision in the determination of the shower size. Full squares show the systematic difference between the Grande and the KASCADE determination of N_{ch}; open squares show the Grande precision in the single event measurement of the shower size N_{ch}^{GR}

of Italy, the Polish Ministry of Science and Higher Education and DAAD (PPP grant for 2009-2010), and the Romanian Ministry of Education and Research (grant CEEX05-D11_79/2005).

References

1. J. Hörandel, Advances in Space Research, 41 (2008) 442.
2. M. Nagano et al., J. Phys. G: Nucl. Part. Phys., 10 (1984) 1295.
3. Y.A. Fomin et al., Proc. of the 25^{th} ICRC, 1 (1999), 337.
4. M. Aglietta et al., Astroparticle Physics, 10 (1999), 1.
5. T. Antoni et al., Astroparticle Physics, 19 (2003), 703.
6. M.A.K. Glasmacher et al., Astroparticle Physics, 10 (1999), 291.
7. M. Aglietta et al., Astroparticle Physics, 21 (2004), 583.
8. T. Antoni et al., Astroparticle Physics, 16 (2002), 373.
9. J. Hörandel eet al., Proc. of the 26^{th} ICRC, 1 (1999), 337.
10. M.A.K. Glasmacher et al., Astroparticle Physics, 12 (1999), 1.
11. T. Antoni et al., Astroparticle Physics, 24 (2005), 1.
12. R. Aloisio et al., Astroparticle Physics, 27 (2007), 76.
13. D. Allard et al., Astroparticle Physics, 27 (2007), 61.
14. T. Gaisser et al., arXiv:0711.0353v1.
15. N.M. Budnev et al, arXiv:080:3037
16. H.O. Klages et al, Proc of the 30^{th} ICRC, 5 (2007), 849.
17. http://www.telescopearray.org
18. G. Navarra et al., Nucl. Instr. and Meth., A 518 (2004), 207.
19. T. Antoni et al. Nucl. Instr. and Meth., A 513 (2003), 429.
20. H. Falcke et al., Nature, 435 (2005), 313.
21. P. Doll et al., Nucl. Instr. and Meth., A 488 (2002), 517.
22. R. Glasstetter et al., Proc. of the 29^{th}, 6 (2005), 293.
23. J. Van Buren et al., Proc. of the 29^{th}, 6 (2005), 301.

Cosmic-ray knee and flux of secondaries from interactions of cosmic rays with dark matter

Manuel Masip[1], Iacopo Mastromatteo[2]

[1]*CAFPE and Departamento de Física Teórica y del Cosmos Universidad de Granada, E-18071 Granada, Spain*

[2]*International School for Advanced Studies (SISSA) Via Beirut 2-4, I-34014 Trieste, Italy*

We discuss possible implications of a large interaction cross section between cosmic rays and dark matter particles due to new physics at the TeV scale. In particular, in models with extra dimensions and a low fundamental scale of gravity the cross section grows very fast at *transplanckian* energies. We argue that the knee observed in the cosmic ray flux could be caused by such interactions. We show that this hypothesis implies a well defined flux of secondary gamma rays that seems consistent with MILAGRO observations.

1 New physics at the TeV scale

We know from collider experiments that there are three basic interactions between elementary particles. These interactions are understood in terms of a $SU(3)_C \times SU(2)_L \times U(1)_Y$ gauge symmetry, and have been confirmed by all data during the past decades: the standard model is basically *correct* up to energies around 200 GeV. On the other hand, we also observe gravitational interactions. Their strength is set by Newton's constant, which in natural units defines the Planck mass, $M_P = G_N^{-1/2}$. Gravity is much weaker than gauge interactions and not detectable at colliders. It has been tested only at macroscopic distances, in processes involving the exchange of *quanta* of up to 10^{-13} GeV.

What do we expect at higher energies? If we extrapolate what we *know* in a straightforward way, we find that the three gauge couplings have log corrections that point towards a grand unification scale at $M_X \approx 10^{16}$ GeV. Gravity is different, it grows quadratically with the energy and becomes of order one at the Planck scale, $M_P \approx 10^{19}$ GeV. Below M_P one needs a consistent framework for the four interactions, and string theory is the only available candidate. The LHC is going to explore energies of up to 1 TeV. It could find, for example, supersymmetry, a discovery for the next decades that would provide consistency to the whole picture. But such discovery would leave us still very far from the fundamental scale. String theory and quantum gravity are in this framework *non-reachable*, almost non-physical.

However, this is not the only possibility. In a different framework that has been discussed a lot recently the fundamental scale of gravity (M_D) is pushed down to the TeV. This can be done, for example, with flat extra dimensions that accelerate the running of G_N, or with a warped metric, the popular Randall-Sumdrum models[1]. In any case, within this framework the LHC could see exciting physics, maybe even a hint of the string scale itself. The *transplanckian* regime ($s \gg M_D^2$) would probably be not accessible there, but it would be clearly at the reach of very energetic cosmic rays. Collisions in this regime are really different from what we have seen so far in colliders. In particular, the spin 2 of the graviton implies that gravity becomes strong and dominates over gauge interactions at distances that increase with $\sqrt{s}$.

The range of energies that cosmic rays provide is very wide, exceeding the 14 TeV to be reached at the LHC. In the collision of a cosmic proton with a dark matter particle χ in our galactic halo we have

$$\sqrt{s} = \sqrt{2m_\chi E} \lesssim 10^7 \text{ GeV} . \tag{1}$$

One would obtain even higher energies, up to 10^{11} GeV, in the head on collision of two cosmic rays[3]: these are the most energetic elementary processes that we know are occurring in nature, and would be clearly transplanckian within the TeV gravity picture. Here we will focus on the first type of processes.

2 Transplanckian collisions

Can one calculate a cross section at $\sqrt{s} \gg M_D$ without knowing the details about the fundamental theory? The answer is *yes* as far as the fundamental theory does not change the long distance properties of gravity at these transplanckian energies. It is the case, for example, in string theory, where the Regge behaviour implies that at $s \gg M_s^2$ only the low t (forward) contributions of the massless string modes survive. And due to the spin 2 of the graviton, in this regime gauge contributions are negligible, only gravity matters.

In a collision at transplanckian energies we expect two basic processes[2]. At small impact parameters we expect *capture*, the collapse of the two particles into a mini black hole of mass $M \approx \sqrt{s}$ and radius

$$R \approx \left(\frac{M}{M_D}\right)^{\frac{1}{n+1}} \frac{1}{M_D} . \tag{2}$$

At larger impact parameters we expect processes where the incident particle transfers a small fraction y of its energy and keeps going. These elastic processes can be calculated in the eikonal approximation, that provides a resummation of ladder and cross-ladder contributions.

An important observation is that these are long-distance processes, the typical distance is larger than $1/M_D$ and grows with the energy. To *see* quantum gravity, string theory or even a Z boson the incident particle needs to go to short distances (of order $1/M_{Z,S,D}$) *inside* the black hole horizon, so all these details become irrelevant. The higher the energy in the collision, the more reliable is the estimate based on classical gravity (strongly coupled but tree level).

Another important point is that, although the typical distance is longer than $1/M_D$, it is still shorter than the proton radius and the exchanged gravitons *see* the partons inside the proton. A parton carrying a fraction x of the proton momentum hits χ and, as a result, the proton breaks into a scattering parton or a black hole plus the proton remnant. From the analysis of these jets using HERWIG we obtain

(i) The scattering parton and the proton remnant define jets giving a very similar spectrum of stable particles. This spectrum is only mildly sensitive to the fact that the parton may be a quark or a gluon.

(ii) In the center of mass frame of the two jets the final spectrum of stable particles is dominated by energies around 1 GeV, almost independently of the energy of the parton starting the shower.

(iii) The stable species (particle plus antiparticles) are produced with a frequency f_i that is mostly independent of the energy or the nature of the two jets. We obtain an approximate 55% of neutrinos, a 20% of photons, a 20% of electrons, and a 5% of protons.

(iv) The spectrum of stable particles resulting from a mini BH in its rest frame is very similar to the one obtained from the quark and gluon jets.

A parametrization of the final spectra of stable particles from quark and gluon jets and from black hole evaporation can be found in[4].

3 Secondaries from collisions of cosmic rays with dark matter

Let us now discuss if there is any observable effects from these processes. When a ultrahigh energy cosmic ray reaches the Earth coming from outside the galaxy, it has crossed a certain dark matter column density x. The probability of interaction is just

$$p(x) \approx \frac{\sigma\, x}{m_\chi}\,. \tag{3}$$

Since the depth x from the border of the galaxy can vary in a factor of ten, more cosmic rays will interact from deeper directions, which could imply an anisotropy in the flux of extragalactic cosmic ray that has not been observed. We find, however, that for cross sections up to the mbarn and for the expected dark matter densities the probability of interaction is too small to produce an observable effect.

The effect on lower energy cosmic rays, however, could be more relevant. The crucial difference is that cosmic rays of energy below 10^8 GeV are trapped inside the galaxy by random magnetic fields of order μG. Their trajectory from the source to the Earth is not a straight line, it is more similar to a random walk. The depth that they face grows with time, and a fraction of them could interact with a dark matter particle before reaching the Earth. Now, in these models the cross section grows very fast at center of mass energies above M_D, so there could be a critical energy giving a cross section large enough for cosmic rays to interact. At larger energies the interaction would break them and produce an effect that could explain the *knee* (the change in the spectral index from -2.7 to -3) observed in the cosmic ray spectrum.

If gravitational interactions were responsible for this change, then there would be a flux of secondary particles that could be readily estimated. Let us assume that, on absence of gravitational interactions, the flux $\propto E^{-2.7}$ would have extended up to 10^8 GeV. This means that the flux

$$\Phi_N \approx \int_{10^6\ \mathrm{GeV}}^{10^8\ \mathrm{GeV}} \mathrm{d}E\ 1.8\ (E^{-2.7} - 10^{1.8} E^{-3})\ \frac{\mathrm{nucleons}}{\mathrm{cm}^2\ \mathrm{s\ sr}} \tag{4}$$

had been *processed* by these interacions into secondary particles of less energy. In Fig. 1 we plot the fluxes of secondary protons and gamma rays together with the flux of dark matter particles boosted by eikonal scatterings. The flux of $e = e^+ + e^-$ is similar to the photon flux, although the propagation effects (synchroton emission, etc.) that may distort the spectrum have not been included. Recent data from PAMELA[5] signals an excess in the positron flux above 10 GeV, although the contribution that we find seems well below these data. We add in the plot the diffuse gamma-ray flux measured by MILAGRO[6] at energies around 15 TeV, which seems to indicate an excess versus the expected values from some regions in the galactic plane. The contribution that we find could explain anomalies in the gamma-ray flux above 10 GeV or in the positron and antiproton fluxes above 1 TeV. The diffuse photon flux that we obtain is always around MILAGRO data and proportional to E^{-2} at energies between 100 and 10^6 GeV for any values of the dark matter mass and the number of extra dimensions.

4 Summary

Strong gravity at the TeV scale would affect the propagation of the most energetic cosmic rays. In particular, cosmic protons could interact with the WIMP χ that constitutes the dark matter of our universe. These interactions could break the incident proton and produce a deflection in the flux (the cosmic ray knee), together with a flux of secondary antiparticles and gamma rays.

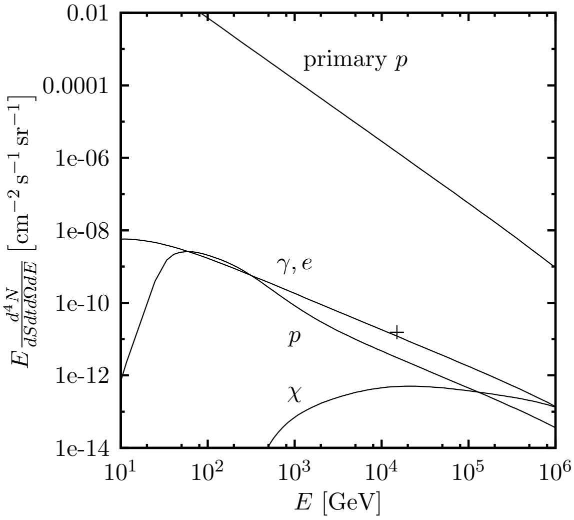

Figure 1: Secondary fluxes from p–χ gravitational collisions for $n = 6$, $M_D = 5$ TeV and $m_\chi = 200$ GeV. The point at 15 TeV indicates the gamma-ray flux measured by MILAGRO.

The analysis of the cross sections and dark matter densities required for this hypothesis to work will be presented elsewhere[7]. In any case, it is puzzling that the change in the spectral index in the flux appears at center of mass energies $\sqrt{2m_\chi E_{knee}} \approx 10$ TeV, where the new physics is expected.

Acknowledgments

This work has been supported by MEC of Spain (FPA2006-05294) and by Junta de Andalucía (FQM-101 and FQM-437). IM acknowledges a fellowship from SISSA (2007JHLPEZ).

References

1. N. Arkani-Hamed, S. Dimopoulos and G. R. Dvali, Phys. Lett. B **429** (1998) 263; L. Randall and R. Sundrum, Phys. Rev. Lett. **83** (1999) 3370.
2. G. F. Giudice, R. Rattazzi and J. D. Wells, Nucl. Phys. B **630** (2002) 293; J. I. Illana, M. Masip and D. Meloni, Phys. Rev. D **72** (2005) 024003;
3. P. Draggiotis, M. Masip and I. Mastromatteo, JCAP **0807** (2008) 014.
4. M. Masip and I. Mastromatteo, JCAP **0812** (2008) 003.
5. O. Adriani *et al.*, "Observation of an anomalous positron abundance in the cosmic radiation," arXiv:0810.4995 [astro-ph].
6. A. A. Abdo *et al.*, Astrophys. J. **688** (2008) 1078.
7. R. Barcelo, M. Masip and I. Mastromatteo, "Cosmic ray knee and new physics at the TeV scale," arXiv:0903.5247 [hep-ph].

RADIODETECTION AND CHARACTERIZATION OF THE COSMIC RAYS AIR SHOWER RADIO EMISSION WITH THE CODALEMA EXPERIMENT

T. SAUGRIN for the CODALEMA collaboration
SUBATECH, Université de Nantes, IN2P3/CNRS, Ecole des Mines de Nantes, 4 rue Alfred Kastler, 44000 Nantes

The radiodetection experiment CODALEMA allows to study cosmic ray air showers on an event-by-event basis through the detection of the radiated electric field. Since its creation in 2001, the set-up has received a major evolution of its experimental configuration and is un particular able to characterize the electric signal induced by an EAS, according to the physical parameters of the shower.
Evidences for a geomagnetic origin of EAS radioelectric field are presented. A first study of electric field lateral distribution functions, and the correlation between primary particles energies and EAS electric field is also discussed.

1 Introduction

The idea of extensive air showers (EAS) radio-detection first appeared in the 60's (Askaryan 1962) : among all the particles created by the interaction between primary cosmic particles and Earths atmosphere, the charged particles, especially electron-positron pairs, lead to the creation of a coherent induced radioelectric field which could be measured.

Historically, the charge excess mechanism, was the first to be assumed at the origin of induced radioelectric field (Allan 1971). Positrons created in the particle shower interact with atmospheric electrons: a negative charge excess appears, moves across the atmosphere and creates a subsequent electromagnetic field. Several geomagnetic mechanisms can also be inferred like a dipolar field creation mechanism (Scholten, 2008), or the geosynchrotron radiation contribution (Huege 2005).

After early and promising results (Jelley 1961, Allan 1971), the radiodetection method has been abandonned in favour of more usual techniques, like ground detection. Today, with the availability of fast electronics, EAS radio detection becomes again an operational technique. Indeed, several experiments, like LOPES in Germany or CODALEMA located at the radio observatory of Nanay, France, have already obtained evidence for a radio emission counterpart in atmospheric showers.

The CODALEMA experiment is a ground detector triggered experiment in order to correlate the measured electric transients with particles detected by a scintillator based detector-array. Currently 17 ground detectors are in operation, and the experiment is triggered by coincidences between the 5 central scintillators.

To measure the induced radio electric field, CODALEMA uses 24 dedicated antennas (Ardouin 2007, Charrier 2007), mainly deployed over 2 lines of 473 and 612 meters in the North-South axis and the East-West axis. The recorded radio signals are identified by an off-line analysis (Ardouin 2009).

2 Energy threshold

The present results have been acquired using data measured between November 2006 and March 2008. During this period of 355 effective days of data acquisition, 619 true EAS radio events have been detected by CODALEMA. The number of radio events triggered with the internal criterion (relevant estimate of the shower energy) is 157. By using EAS radio events correlated with internal trigger events, we obtain a first energy distribution of radio detected events. The energy threshold of the radio detector is clearly visible below 10^{17} eV, even though the energy threshold of the scintillator array is around 10^{15} eV (Fig. 1 (a)). A comparison with the energy distribution of internal events shows that the two distributions converge when energy increases.

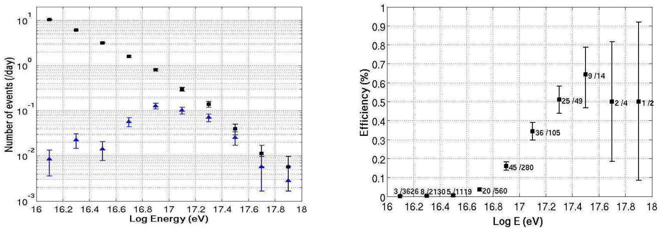

(a) (b)

Figure 1: (a) Energy distributions of internal events measured by the scintillators (squares) and seen in coincidence with the antennas (triangles) (b) Efficiency of the radio detector versus EAS energy

The radio detection efficiency, defined as the ratio of the number of radiodetected internal events over the total number of internal events, rises with energy and reaches about 50% at 2.10^{17} eV (Fig. 1 (b)). This efficiency is highly related to the geomagnetic origin of the produced electric field.

3 Geomagnetic effect

The arrival direction distribution of our 619 EAS radio events shows a deficit of events in the South direction (Fig. 2 (a)). However, the arrival distribution of trigger events is uniform, so the North-South asymmetry only appears with correlated radio events. A possible explanation of this phenomenon could be related to geomagnetic mechanisms: the closer the arrival direction is with respect to the geomagnetic field, the less geomagnetic effects should occur.

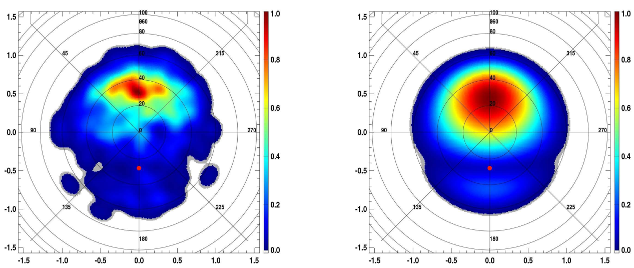

(a) (b)

Figure 2: (a) 10^o gaussian smoothed sky map of radiodetected events. The zenith is at the center, the azimuth is: North (top, 0^o), West (left, 90^o), South (bottom, 180^o) and East (right, 270^o); the direction of the geomagnetic field at Nanay is indicated by the red dot. (b) Geomagnetic toy model predicted sky map. The color scale is normalized to 1 in the maximum direction

To characterize the possible relationship between the observed North-South asymmetry and a potential geomagnetic origin of the electric field, we use a geomagnetic toy model. This model is based on the hypothesis that the radioelectric field characteristics are highly related to the Lorentz force induced by the geomagnetic field on EAS charged particles. We will then made several assumptions. First, the signal amplitude given by the CODALEMA East-West polarized antenna is proportional to $|\vec{q}\Lambda\vec{B}|_{EW}$ which is the EW component of the Lorentz force. We also assume that the electric field polarization is linear and oriented along the Lorentz force. Finally, because the CODALEMA experiment detects EAS near the radio detector energy threshold, we can assume that the signal magnitude is proportional to the radio detection efficiency.

By correcting this efficiency by the zenithal distribution of the ground detectors events and by the antenna gain pattern, we can finally compute a predicted event sky map, which appears to be similar to the observed sky map (Fig. 2 (b)). Simulated zenithal and azimutal distributions are compared to the observed ones in Fig. 3. , and both show good agreement. This result confirms the importance of geomagnetic mechanisms in the radioelectric field creation process, and explain the observed maximum radio efficiency of 50% induced by events with a low value of the Lorentz force EW component For higher energy events, radioelectric field will be high enough to be detectable for any EAS arrival direction, and the radio detection efficiency will then become independent of the value of the Lorentz force.

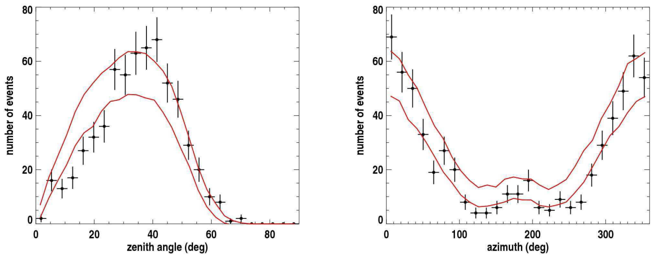

(a) (b)

Figure 3: Zenithal (a) and azimuthal (b) angular distributions (black crosses) observed for the radio events.The red lines define the +/- 1σ band around the prediction.

Nevertheless, we cannot conclude on the contribution of others creation mechanisms, which could be detectable only at higher energy; and on the exact geomagnetic mechanism in action, which need multiple polarization measurement to be study.

4 Electric field lateral distribution and energy calibration

The experimental set-up of the CODALEMA experiment allows a measurement of the radioelectric field for each antenna, individually. The electric field lateral distribution, which is simply the signal amplitude as a function of the distance to the shower axis, may then be easily built event by event. An example of lateral distribution obtain for a CODALEMA radiodetected event is show on Fig. 4 (a)). .

Allan empirically parameterized the radioelectric field lateral profile (Allan, 1970) with :

$$E(d) = E_0 \cdot e^{\frac{d}{d_0}} \qquad with \qquad E_0 = E_p \cdot \sin\alpha \cdot \cos\Theta$$

where Ep is the primary particle energy, α the angle between the shower arrival direction and the geomagnetic axis, Θ the zenithal angle, d the distance to the shower axis and (E_0,d_0) the parameters of an exponential. By fitting the observed lateral distribution with a decreasing exponential, the electric field on the shower axis may be estimated. According to the Allan formula, this E_0 parameter is directly proportional to the shower energy. The energy radio estimator E_{radio} is then defined by:

$$E_{radio} = \frac{E_0}{|\vec{q}\Lambda\vec{B}|_{EW} \cdot \cos\Theta}$$

where the Lorentz force EW component is substitute to the Allan original geomagnetic effect correction, according to the geomagnetic toy model.

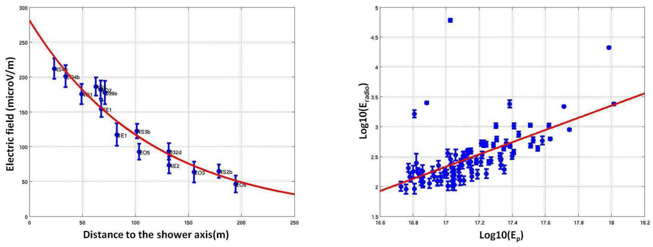

(a) (b)

Figure 4: (a) Example of CODALEMA radiodetected event electric field lateral distribution. The errorbars define the radio noise on each antenna at measurement time. The red line define the exponential fit. (b) Preliminary correlation between the radio and scintallator energy estimator in logarithmic scale.

A preliminary correlation between E_{radio} and the shower energy (estimated by the scintillator array) is show on (Fig. 4 (b)). with a restricted selection of events (high SNR, high quality of exponential fit). The relation between the radio and scintillators estimators is linear as expected, and seems to confirm the validity of Eradio as a relevant radio estimator. Further details on radio energy calibration are in progress.

5 Outlooks

The CODALEMA experiment shows very promising results and, in particular, the geomagnetic mechanism in the electric field production as well as a preliminary energy. Nevertheless, because of CODALEMA experimental limitations notably related to the energy threshold of both detector arrays, a new technical evolution is required.

The radio detection autonomous station presently in developpement in the CODALEMA collaboration will allow us to detect EAS at higher energies and at higher impact parameters. To reach this objective, the autonomous stations will be deployed at the same time on the CODALEMA site in order to build a 1 km^2 antenna array, and on the Pierre Auger Observatory for the Radio@Auger project.

References

1. G. A. Askar'yan, Soviet Physics, J.E.T.P., 14, (2) 441 (1962)
2. H. R. Allan, Elem. part. ansd Cos. Ray Phys., 1971, Vol. 10, 171-302
3. O. Scholten, K. Werner et F. Rusydi, Astroparticle Physics, 2008 Vol. 19, 477-494
4. T. Huege et H. Falcke, Astroparticle Physics, 2005, Vol. 24, 116-136
5. J. V. Jelley et al., Nature, 1965, Vol.205, 327
6. D. Ardouin et al., Astroparticle Physics vol 26 (2007) p.341-350
7. D. Charrier, Proceeding ISAP, 2007
8. D. Ardouin et al.,Astroparticle Physics vol 31 (2009) p.192-200

Influence of the hadronic interaction models on the size of the missing energy of cosmic ray showers

Michal Nyklíček, Petr Trávníček
Institute of Physics of the AS CR, v. v. i., Na Slovance 2,
CZ-182 21 Praha 8, Czech Republic

The missing energy is a part of primary particle energy which cannot be detected by the fluorescence detectors. It can be calculated only from Monte Carlo simulations and it is thus affected by a choice of the high energy interaction model and also by the mass of the primary particle. The influence of high energy interaction model and of the mass of the primary particle to the size of the missing energy is described. A new idea, how to make the correction for the missing energy more independently on the assumed primary particle type and the choice of the high energy interaction model is introduced.

1 Introduction

The longitudinal development of the shower of secondary particles can be detected by fluorescence telescopes and the energy of primary particle can be then reconstructed. Some part of the primary energy can not be detected, because a fraction of the energy is carried away by neutrinos and due to the small energy deposit of muons. This part of primary energy is invisible to detectors and it is called the missing energy. The size of the missing energy is therefore important parameter to be taken into account in the energy reconstruction of the shower by fluorescence technique. In the case of real air showers the primary particle type and the most relevant model of hadronic interactions are unknown. The correction to the missing energy is usually taken from Monte Carlo simulations as an average between primary particle types for a given interaction model.

2 Method

One of the possible ways, how to determine the size of the missing energy is to simulate longitudinal profiles of the atmospheric showers. For purposes of this work, the CONEX [1,2] simulation code was used together with following high energy hadronic interaction models: SIBYLL[3], QGSJET01[4], QGSJET02 and neXus[5]. In all cases GHEISHA[6] was taken as a low energy hadronic interaction model. The showers were simulated for protons and iron nuclei as a primary particles with the zenith angle $\Theta = 0°$. For each high energy interaction model and each primary particle 500 showers were simulated.

The longitudinal profile can be described by Gaisser-Hillas equation[7]:

$$f_{GH}(X) = \frac{dE}{dX_{max}} \left(\frac{X - X_0}{X_{max} - X_0} \right)^{\frac{X_{max}-X_0}{\lambda}} e^{\frac{x_{max}-X}{\lambda}}, \tag{1}$$

where $\frac{dE}{dX_{max}}$ is the energy deposit at the shower maximum, X is the slant depth, X_0 is the point of the first interaction, X_{max} is the point of the shower maximum and λ is a constant (identified as the interaction length).

The calorimetric energy (E_{cal}), which can be measured by the detectors is then given by the integral of the energy deposit profile:

$$E_{cal} = \int_0^\infty f_{GH}\,(X)\,dX,$$

where f_{GH} is the GH function (see eq. 1).

It can be shown, that $f_{GH}(X)$ can be parametrized[8] by E_{cal} and using gamma function Γ:

$$f_{GH} = \frac{E_{cal}}{\lambda} e^{\frac{X_0 - X}{\lambda}} \left(\frac{X - X_0}{\lambda}\right)^{\frac{X_{max} - X_0}{\lambda}} \Gamma\left(\frac{X_{max} - X_0}{\lambda} + 1\right). \tag{2}$$

Then the missing energy (E_{miss}) can be easily computed as:

$$E_{miss} = E_{prim} - E_{cal}, \tag{3}$$

where E_{prim} represents the primary particle energy.

3 Results

Using the method, described above, the missing energy is calculated separately for each interaction model and for both assumed types of primary particles. Figure 1 shows examples of the distribution of the missing energy for 500 showers with the same primary energy and the same interaction model (neXus). Distribution of the size of the missing energy is generally much wider in the case of protons as primary particles than in the case of iron nuclei. This is due to the shower to shower fluctuations, which are larger for protons.

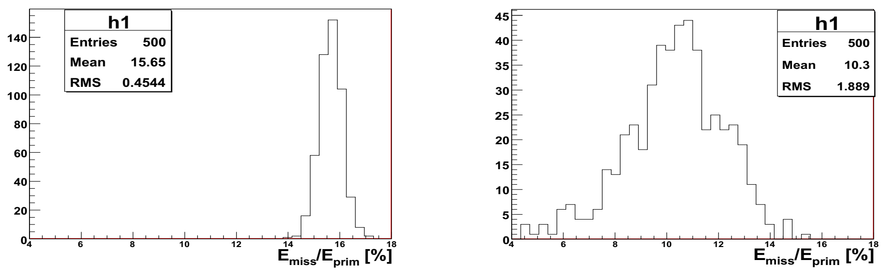

(a) neXus, iron nuclei, $E = 10^{17.5}$ eV.

(b) neXus, protons, $E = 10^{17.5}$ eV.

Figure 1: The distribution of relative missing energy, neXus high energy interaction model.

For each interaction model and type of primary particle the value of the missing energy is obtained as the average from 500 simulated showers. The results of the size of the missing energy as a function of primary energy are shown in figure 2(a). The average mean missing energy obtained as the average from different high energy interaction models is depicted. The bottom line (red) is for protons as primary particles, the upper one (blue) is for iron nuclei and the middle one (green) represents the optimal choice of the missing energy correction if the primary particle type is unknown. The middle line is computed for mixture composition (50% protons and 50% iron nuclei). The results for protons and iron nuclei are shown with error bars. They represent the range of the values of the missing energy, which can be obtained for the set of high energy interaction models (QGSJET01, QGSJET02, SIBYLL, neXus).

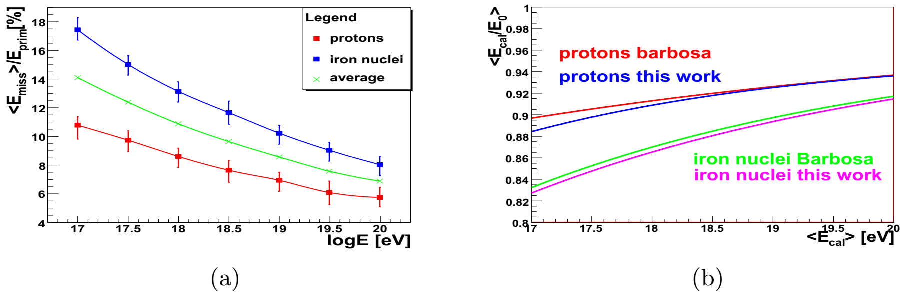

Figure 2: (a) The average relative mean missing energy for protons and iron nuclei and the total average mean missing energy as the function of the primary energy and the influence of the high energy interaction models (error bars). (b) The relative calorimetric energy as the function of 'measured' calorimetric energy and the comparison of results from this work using CONEX with the results from the paper[9] using CORSIKA. The plot is for QGSJET01 and vertical showers.

Generally it can be concluded that the relative fraction of the missing energy is decreasing with increasing primary energy. The relative fraction of missing energy is higher in the case of iron nucleus as the primary particle. The influence of high energy interaction models is approximatelly about 1%, while the most important contribution to uncertainity to the exact determination of the missing energy is our absence of knowledge about the exact chemical composition of the cosmic rays with such energies. The total uncertainity is approximately 4% at the primary energy 10^{17}eV and with increasing energy it decreases to 2% at 10^{20}eV. The results are similar to work[9] where CONEX was used to determine the mising energy for the first time.

4 Comparison with previous calculations using CORSIKA

The results were compared with the previous work done by Barbosa[10] (using detailed simulation in CORSIKA). This comparison is shown in figure 2(b) for QGSJET01 and vertical showers. For this comparison, following parametrization[10] was used:

$$\frac{E_{cal}}{E_0} = a - b\left(\frac{E_{cal}}{1EeV}\right)^c, \tag{4}$$

where a, b and c are constants.

The results generally agree within 0.5% in the relative calorimetric energy. The larger discrepancies for protons at lower energies are under investigations.

5 New Approach

The big part of the missing energy is caused by the fact that the energy deposit of muons is small. From this it follows that there is a natural correlation between the number of muons on the ground and the size of the missing energy. Experiments under construction HEAT[11] and AMIGA[12] will combine measurements of fluorescence profile and muon component on the ground.

Figures 3(a),(b) show, how the dependency of the number of muons on the ground (muons with energy > 1 GeV) on the relative size of the missing energy looks like. Data are for interaction models: QGSJET01, SIBYLL and neXus; for both primary particles - protons and iron nuclei, and for zenith angles between $0° - 60°$ (with the step of $10°$). Data for different models and primary particles follows the same line. Hence the size of the missing energy can be parametrized as a function of the number of muons on the ground universally for all interaction models and primary particle types.

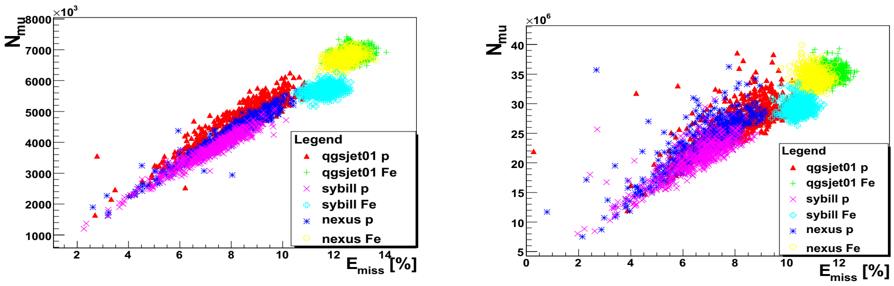

(a) 10^{18}eV, $\Theta = 0°$ (b) 10^{19}eV, $\Theta = 60°$

Figure 3: Number of muons (E>1 GeV) on the ground and the relative size of the missing energy selected for two energies and zenith angles Θ.

6 Conclusions

The method using CONEX to determine the size of the missing energy is very fast and easy to use. The results from this method are comparable to study[10] (detailed simulation in CORSIKA) and paper[9] (simulation in CONEX). Results of missing energy calculations were presented for different high energy hadronic interaction models and primary particles types.

New idea, how to make correction for the size of the missing energy, using information about the amount of muons on the ground is introduced. It seems that the influence of high energy interaction models and the type of primary particle to the energy reconstruction can be reduced in the experiments measuring fluorescence profile and muon component on the ground.

Acknowledgments

The contribution is prepared with the support of Grant Agency of the Academy of Sciences and Ministry of Education, Youth and Sports of the Czech Republic within the projects KJB100100904 and LA08016.

References

1. T. Bergmann *et al*, Astropart. Phys., vol. 26, pages 420-432,astro-ph/0606564 (2007).
2. T. Pierog *et al*, Nucl. Phys. Proc. Suppl., vol. 151, pages 159-162, astro-ph/0411260 (2006).
3. Fletcher, R.S.; Gaisser, T.K.; Lipari, P.; Stanev, T. (1994): SIBYLL: An Event generator for simulation of high-energy cosmic ray cascades. *Phys. Rev. D50 5710.*
4. Kalmykov, N.N.; Ostapchenko, S.S.; Pavlov, A.I.; (1997): Quark-Gluon String Model And EAS Simulation Problems at Ultra-High Energies. *Nucl. Phys. Proc. Suppl. 52B, 17.*
5. Bossard, G. et al. (2001): Cosmic Ray Air Shower Characteristics in the Framework of the Parton-based Gribov-Regge Model NEXUS. *Phys. Rev.,* D63:054030, 2001.
6. Fesefeldt, H. (1985): The simulation of hadronic showers. *PITHA 85/02, Aachen.*
7. Gaisser, T.K.; Hillas, A.M. (1977): Proc. 15th ICRC.
8. Unger, M. *et al* (2008): Nucl.Instrum.Meth.A588:433-441,2008.
9. Pierog, T. *et al*, Proceedings of the 30th ICRC (2007), contributionID 899.
10. Barbosa, H.M.J. *et al* (2004): Astropart. Phys. 22, 159.
11. Klages, H.O. (2007): Proceedings of the 30th ICRC (2007), contribution ID 65.
12. Etchegoyen, A. (2007): Proceedings of the 30th ICRC (2007), contribution ID 1307.

The FLUKA high energy cosmic ray generator: predictions for the charge ratio of muons detected underground

G. Battistoni, S. Muraro
INFN, Sezione di Milano, Via Celoria 16, I-20133, Milano, Italy

A. Margiotta, M. Sioli
Universitá di Bologna and INFN, Sezione di Bologna, Dipartimento di Fisica, V.le Berti Pichat 6/2, I-40127, Bologna, Italy

for the FLUKA Collaboration

A new generator for high energy cosmic ray physics based on FLUKA Monte Carlo code is under development. This will be primarily dedicated to the physics of high energy muons detected underground, exploiting the full integration in the calculation of both air shower development and muons transport in the rock. This generator will be used for experiments at Gran Sasso laboratory (ICARUS and OPERA). As a first application we analyze the predictions for the charge ratio of underground muons, with the aim of investigating some features of the high energy particle production model. This measurement is particularly sensitive to the π/K ratio of secondary mesons produced in the proton-Air and Nucleus-Air collisions. We compare preliminary results with data from ongoing experiments.

1 Introduction

In the framework of the application of the FLUKA Monte Carlo code to cosmic rays physics, a new generator for high energy cosmic rays is under development, with the aim of extend the existing FLUKA cosmic rays library to include the TeV region.
The FLUKA code [1] is a general purpose Monte Carlo code for the interaction and transport of particles. It is built and maintained with the aim of including the best possible physical models in terms of completeness and precision.
The application of FLUKA in cosmic ray physics arises from the interest in applied physics topics, such as radioprotection in space or in atmosphere [2,3], and in basic research (e.g. the calculation of atmospheric neutrino fluxes [4,5]).
In both cases it is important to check the reliability of calculations produced with a model which is benchmarked using only data coming from well controlled accelerator experiments. In this context, an important issue in the evaluation of a Monte Carlo calculation concerns the quality of the hadronic interaction models, i.e. their capability of reproducing the existing data.
The FLUKA hadronic models are based as far as possible on a theoretical microscopic approach, having care to preserve correlations and fulfilling the necessary conservation laws in every single interaction. Free parameters are set by comparing predictions to data from thin target experiments at accelerators and are in general kept fixed for all projectile-target combinations and energies. This approach ensures predictivity also in regions where experimental data are not available [6].

2 Generation of high energy muons

The generator is primarily dedicated to the physics of high energy muons detected underground, exploiting the full integration in the calculation of both air shower development and muons transport in the rock.
The aim is to predict multiple muon rates for different primary masses and energy within the framework of a unique simulation model. This work is under way, for instance within both the ICARUS [9] and OPERA [10] collaborations at Gran Sasso. Starting from an atmospheric shower generation, particles are transported in Gran Sasso rock. A threshold is applied to select only muons with energy larger than 1 TeV.
The main reasons which led to conceive a FLUKA-based generator for TeV muons are the following:

- to provide a tool which has been validated and benchmarked along the years with the latest experimental results, outside the cosmic ray community and independently from the existing generators;
- to provide a self-consistent generator all in one, namely a generator able to handle all the simulation steps in a unique framework, from the primary interaction in atmosphere, to the shower development, particle transport in the overburden, sampling at the detector level and, in principle, the detector itself.

One of the feature of this package is that it is fully optimized for TeV cosmic ray muons, i.e. we adopted many biasing solutions in different phases of the simulation in order to speed up the production chain.
Moreover, we stress that the package is flexible enough to include different underground and/or underwater sites, provided that a detailed map of the overburden is fed to the generator (in the underground case). In the present version the LNGS underground site has been implemented, while the ANTARES underwater site [11] is in preparation.

Main features of the underground muons generator:

- the geometry description in a given reference frame, namely the physical volumes which fill the empty space together with their chemical composition and physical properties;
- a given source beam (sampled from a primary mass composition model at present derived from [13], i.e. a description of the relative abundances of cosmic rays and their energy spectra), defined by the type of primary particles to be propagated throughout the geometry setup, their kinetic energy, injection point and direction and
- a given hadronic interaction model.

Once this set of information are supplied, a FLUKA run can start producing a user-defined number of stories which can be translated a-posteriori in the corresponding lifetime.

3 The muon charge ratio R_{μ^+/μ^-}

In order to improve the models of the interactions of cosmic rays in the atmosphere, we present a comparison with MINOS N_{μ^+}/N_{μ^-} ratio experimental data [17].
The muon charge ratio reflects the excess of π^+ over π^- and K^+ over K^- in the forward fragmentation region of proton initiated interaction together with the fact that there are more protons than neutrons in the primary spectrum.
Because of their strangeness (S = +1), K^+ and K^0 can be yielded in association with a leading

barion Λ o Σ. On the other hand, the production of K^-,$\bar{K^0}$ requires the creation of a sea-quark pair $s - \bar{s}$ together with the leading nucleon and this is a superior order process [14]. For this region K^+ yield is greater than K^- yield, differently from π^+ and π^- yields because of their isospin symmetry. So the K^+/K^- ratio is larger than the π^+/π^- ratio.

The muons result from pions and kaons decaying before their interaction in the atmosphere, so muons charge ratio reflect kaons and pions charge ratio.
As energy increases, the fraction of muons seen from kaon decays also increases because the longer-lived pions ($\pi^\pm$: $c\tau_0$ = 780 cm, ϵ = 115 GeV) begin more likely to interact before decaying than the shorter-lived kaons ($K^\pm$: $c\tau_0 = 371$ cm, $\epsilon = 850$ GeV)[a]. Consequently, kaon decays begin to make an increasingly more important contribution to the muon charge ratio at these energies. Since strong interaction production channels lead to a muon charge ratio from kaon decays that is greater than that from pion decays, the measured charge ratio is expected to increase.
Several competing processes, however, could counterbalance this increase at even higher energies. Decay of charmed hadrons is one of such processes.
There is also the possibility that heavier elements become a more important component of cosmic ray primaries as the energy increases. This increasingly heavy composition would decrease the ratio of primary protons to neutrons, thereby decreasing the muon charge ratio.

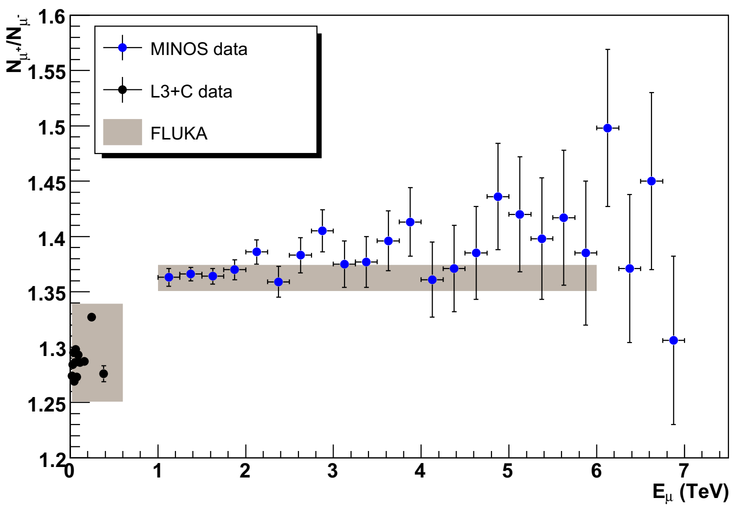

Figure 1: FLUKA comparison with L3+C and MINOS $N_{\mu+}/N_{\mu^-}$ experimental data.

4 Results and conclusions

The FLUKA models have been benchmarked with experimental data from accelerator experiments and from atmospheric muons experiments. The L3+C charge ratio experimental data [15] in the energy region $E_\mu < 1$ TeV has been bechmarked with FLUKA. The agreement is within 0.8 % [16].

$$R^{FLUKA}_{\mu^+/\mu^-} = 1.29 \pm 0.05 \qquad R^{L3+C}_{\mu^+/\mu^-} = 1.285 \pm 0.003(stat.) \pm 0.019(sys.) \tag{1}$$

[a] *critical energy* ϵ = energy where interaction and decay processes have the same magnitude. Beyond this energy interaction process dominates on decay.

The MINOS [17] experiment has recently published the muon charge ratio at the surface in the energy region 1 TeV $< E_\mu <$ 7 TeV:

$$R^{MINOS}_{\mu^+/\mu^-} = 1.374 \pm 0.004(stat.) + 0.012 - 0.010(sys.). \tag{2}$$

In this work, the muon charge ratio in the TeV energy region, as results from the underground muons simulation with the FLUKA Monte Carlo code is:

$$R^{FLUKA}_{\mu^+/\mu^-} = 1.362 \pm 0.012 \tag{3}$$

$$R^{FLUKA}_{\mu^+/\mu^-(from\ \pi\ decay)} = 1.26 \pm 0.01 \qquad R^{FLUKA}_{\mu^+/\mu^-(from\ K\ decay)} = 1.98 \pm 0.04 \tag{4}$$

The agreement with MINOS data is within 0.6 %. Fig. 1 shows the comparison between FLUKA and experimental data.

The agreement between data and simulation suggests the possible predictivity of the code even in the High Energy Cosmic Rays energy range, namely in a region where experimental data from accelerator experiments are not available.

Acknowledgments

This work has been carried out in the framework of the FLUKA Collaboration.

References

1. A. Fass‘o, A. Ferrari, J. Ranft and P.R. Sala, CERN Yellow Report 2005 - 10 (2005), INFN/TC 05/11; A. Fass‘o et al., Proc. of CHEP2003, eConf C0303241, arXiv:hep-ph/0306267.
2. G. Battistoni, A. Ferrari, M. Pelliccioni and R. Villari, Rad. Prot. Dosim. 112 (2004) 331.
3. F. Ballarini et al. Journal of Physics: Conference Series 41 (2006) 135.
4. G. Battistoni et al., Astropart. Phys. 123152000.
5. G. Battistoni et al., Astropart. Phys. 192692003 [Erratum-ibid. 19 291 (2003)].
6. A. Ferrari and P.R. Sala, Proceedings of Workshop on Nuclear Reaction Data and Nuclear Reactors Physics, Design and Safety, A. Gandini, G. Reffo eds., Trieste, Italy, April 1996, n. 2 (1998) 424.
7. S. Roesler, R. Engel, J. Ranft, Proc. MonteCarlo 2000 Conference, Lisboa, 23 - 26 October 2000, Springer Verlag eds. (2001) 1033.
8. J. Ranft, Phys. Rev. D 51 (1995) 64.
9. S. Amerio et al., Nuclear Instruments & Methods A 526 (2004) 329.
10. M. Guler at al., OPERA Experimental Proposal, CERN/SPSC 2000-028, SPSC/P318, INFN-LNGS P25/2000.
11. ANTARES Collaboration, Proposal, astro-ph/9907432 (1999).
12. M. Ambrosio et al., Phys. Rev. D5614181997.
13. J.R. Hörandel, Astroparticle Physics 19 (2003) 193-220
14. “Cosmic Rays and Particle Physics”. Gaisser, T.K., Cambridge University Press 1990.
15. P. Achard *et al.* Phys. Lett. B **598**, 15 (2004)
16. S. Muraro, ”The calculation of atmospheric muon flux using the FLUKA Monte Carlo code”, Ph.D. Thesis, Milano University, 2006.
17. P. Adamson *et al.* Phys. Rev. D **76**, 052003 (2007)

TIERRAS:AN AIRES PACKAGE TO SIMULATE HIGH ENERGY COSMIC RAY SHOWERS UNDERGROUND AND UNDERWATER

M.J. TUEROS
IFLP (CONICET - La Plata/Universidad Nacional de La Plata),CC67 - 1900, La Plata, Argentina

TIERRAS is a Montecarlo simulation program based on the well known AIRES air shower simulations system designed to propagate high energy particle cascades underground, providing a tool to study particles arriving underground from a primary cosmic ray on the atmosphere or to initiate cascades directly underground and propagate them, exiting into the atmosphere if necessary. In this presentation we show a cross-check of its results against experimental data and the first results of full underground shower simulations, as an example of the package capabilities.

1 Introduction

Muons are usually called the "penetrating component" of cosmic ray induced Extended Air Showers (EAS). Due to their small cross section, high energy muons are able to reach deep underground without interacting in the atmosphere, carrying information about the primary particle mass, the inelastic cross section and other physical properties of the processes that originated them. To tackle these problems many shallow underground detectors studying the total muon content, muon multiplicity, and muon lateral distribution function have been successfully used(AGASA, CASA-MIA, MINOS) and more are going to be built (AMIGA).

To aid in the interpretation and design of this type of experiments we present TIERRAS, an extension of the well known AIRES [1] simulation code that has been originally designed to continue the EAS simulation underground and study the design and performance of the AMIGA detectors but quickly showed its potential for other underground experiments. TIERRAS can also be useful to study the phenomenology of underground showers, and explore the signatures that exotic decays or interactions could present in underground detectors.

Throughout this document we refer in a generic way to "underground" environments, referring to rock, soil, water, ice or even moon regolith. The material composition is irrelevant for the discussion given in this article, and all these media can be simulated in TIERRAS.

2 Underground Simulations

The algorithms needed to simulate the propagation of high energy particles through matter are virtually independent of the state of aggregation of the medium through which particles propagate, as are the physical routines needed for the calculation of energy losses or for the evaluation of collision products. In the energy range of interest in cosmic ray showers the main dependences of physical processes are the mass and the charge of the projectile and the target

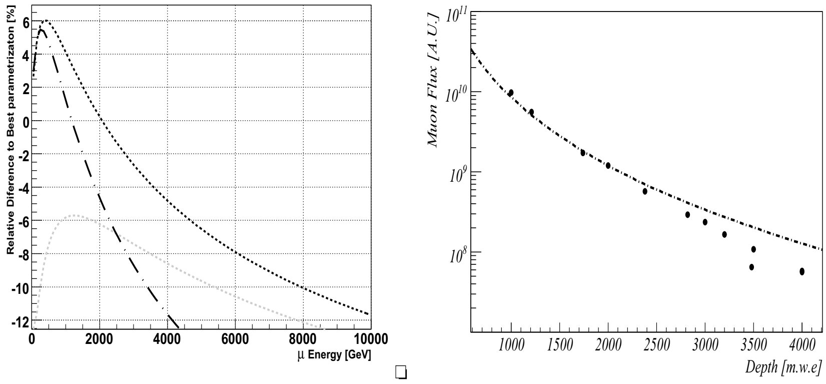

Figure 1: (Left) Relative difference to the most accurate parametrization of the muon energy loss found in literature [3] vs Energy. The black slash-dot-slash line parametrizes TIERRAS simulations. The light dotted line and the black dotted line are usual parametrizations given in [4].(Right) Total muon vertical flux vs. depth. Black slash-dot line is the TIERRAS simulation, black dots are experimental points from Baksan[5] and MACRO[6]experiments.

material and the medium density. This makes it possible to take a simulation software used to propagate particles on air and adapt it to simulate other media.

Although most algorithms are independent of the media, some major differences in the phenomenology of particle showers are introduced by the change from air to ground. For example, Pions in air have a high chance of decaying instead of interacting with other hadrons, producing high energy muons and neutrinos. In the higher density of underground environments, pions are more likely to interact than to decay giving rise to a higher amount of hadronic particles, specially neutrons, that can travel relatively long distances. Another effect of the higher density is to lowers the threshold energy at which the the Landau-Migdal-Pomeranchuk (LPM) and Dielectric Suppression (DS) effects start affecting the gamma cross section, making gamma rays above some PeV much more penetrating than on air.

Ionization dominates the energy loss at low energies both in air and rock, and it can be considered fairly constant at energies below 10 GeV. Bremsstrahlung and Pair Production for muons is negligible in air at all but very high energies, while it is increasingly important underground for energies above 50 GeV. Ionization, Bremsstrahlung and Pair production are simulated including the effects of the effective Z , Z/A and medium density, making results accurate for all media.

Photo-production however requires special attention. The original AIRES code does not take into account muon induced spallation [2], and in the current version neither does the TIERRAS package. This will make TIERRAS to underestimate muon energy loss at very high muon energies (above 2 TeV).

Several parametrizations of the muon energy loss are available on the literature [3 4]. To show the effect that the omission of photo-production processes has on muons, the mean energy loss per $g.cm^{-2}$ was calculated and compared with the reference parametrizations in Figure 1.

It can be seen that TIERRAS has good agreement with these parametrizations up to around 2 TeV, where the effect of muon induced spallation starts to be important. To study how this affects muon propagation underground, we studied the total vertical muon flux at different depths using a parametrization of the muon flux at the earth surface [4]. Comparison with measurements from Basin [5] and the MACRO experiment [6] are shown in Figure 1.

We see that for very deep sites (below 2.5 kilometers of water equivalent, 2 TeV mean muon energy), our results depart from the experimental data, showing the limit to which this simulation code can be used. This is not a limitation for cosmic ray studies in shallow underground sites. The energy spectrum of the muons produced in an EAS peaks between 1 and 500 GeV and

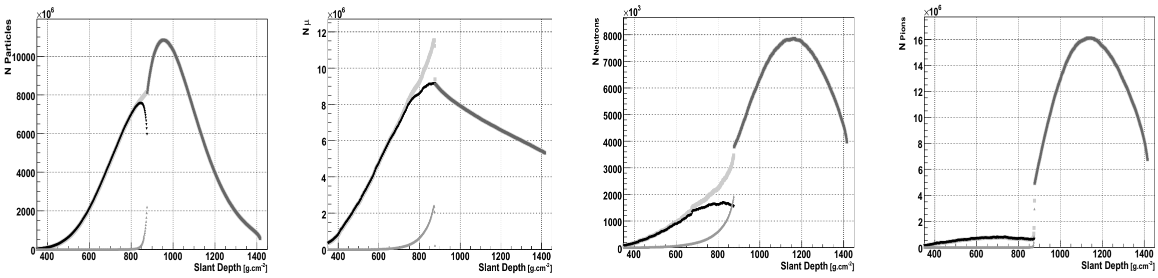

Figure 2: *Longitudinal development of All Particles, Muons, Neutrons and Pions (from left to right). Black correspond to AIRES simulation, dark gray to the TIERRAS underground simulation and light gray to the Albedo component. In very light gray AIRES+Albedo components are added.*

particles of more than 1 TeV have almost no influence on the total muon signal. On experiments interested only in muons far from the shower core like AMIGA, this is even less of a problem as no particle exceeds 500 GeV in a 10^{19} eV shower at more than 200m from the core.

3 Sample Results for the AMIGA case

We show here the results of a TIERRAS simulation for a 1 EeV proton air shower penetrating 3 m in "Standard Soil" (proposed AMIGA design [7,8]), to illustrate the power of this new tool and some qualitative aspects of underground showers.

Primary cosmic rays have their first interaction at high altitudes, and traverse many interaction lengths before reaching ground. As a result at ground level the air shower is well developed, the energy spectra of the different shower particle types are in dynamic equilibrium and passage through more air would not substantially change it. When the shower reaches ground it encounters an abrupt change in medium density, atomic number and atomic weight that provokes a sudden rearrangement of the particles energy spectra. High energy particles encounter a higher cross section, and a lot of low energy particles are generated until the particles reach a new equilibrium spectrum some interaction lengths later. Note that this is just a redistribution of energy as the energy loss per $g.cm^{-2}$ increases only 30% due to the medium change. The back-scattering cross section is also increased producing a noticeable "albedo" effect, mainly in the shower core where most of the high energy particles reside. These albedo particles are very numerous but have very low energy and are stopped in a few hundred meters in air.

Figure 2 shows an example of how all this phenomena affects the longitudinal development of the different particle types. It is important to note that there are up-going particles at any stage of shower development. As a regular AIRES simulation ends when the particles reach ground, the lower part of the simulation lacks the up-going portion of the shower that should have been generated lower in the ground. This can be seen in Figure 2 as the sudden decrease in particle number in the last 25 $g.cm^{-2}$ before reaching ground level at 875 $g.cm^{-2}$. The profile regains its continuity when albedo particles are added to the AIRES simulation.

Gamma emission from bremsstrahlung of charged particles scales as Z^2 , so the emission is doubled passing from Z=7.26 in air to Z=11 underground, as most cross sections do. The number of gammas is nearly doubled when changing the medium, but the mean energy reduces indicating again that a lot of low energy emission is occurring. The development of the longitudinal profile of electrons is tightly related to the gammas profile, and shows the same albedo effect on the air/ground interface. As this two are the more numerous particles, the profile of the total number of particles exhibits the main characteristics of this two particle types, and can be seen in the left side of Figure 2.

Figure 2 also shows the longitudinal development of muons. It can be seen that there is a great contribution of "albedo" muons, and that the transition is not continuous. The excess muons are secondary muons produced by the decay of other albedo particles, specially pions. This is evident from the fact that the albedo component rises abruptly about 1.5 $g.cm^{-2}$ above ground level, showing that the up-going pions start to decay after exiting ground, reaching the maximum about 40 m above ground. Muons can travel far in air, and the effect on the total number of muons is more than 10% up to 800 $g.cm^{-2}$ or 700 m height. All this up-going muons have relatively little energy (mean muon energy is 0.2 GeV against the 5 GeV of the down-going component), and there is little transfer of energy to the muonic energy content.

The passage trough soil stops most of the electrons and low energy muons, making the mean muon energy to rise nearly 50%. The electron component of the shower is reduced nearly two decades, inverting the relation of the muonic and electronic component energies. At ground level, the electrons carry about 5 times more energy than muons.At AMIGA level muons carry more than 10 times more energy than electrons.

Pions endure one of the more important redistributions of energy due to the change in cross section. The increased density underground make pions more likely to suffer an hadronic interaction with a nucleus than to decay as it is normally the case in air, generating a 10 fold increase in their number. Nearly half of the pions generated near the surface exit upwards as albedo, as seen in Figure 2. Pions on air decay to muons (plus neutrino), explaining the increase in the number of muons seen in the muon albedo.

There is an important amount of low energy neutrons being generated below ground due to the increase in nuclear interactions, and almost half of the neutrons are produced upwards. Up-going neutrons carry however only 5% of the total neutron energy at ground level, their mean energy being 0.27 GeV, against the 3.3 GeV of the down-going component. This up going neutrons can be very important in simulations of neutron monitors.

4 Conclusions

The simulation of cosmic ray showers underground using TIERRAS provides an important tool for designing, calibrating and validating underground experiments. The good agreement with experimental results for muon energy loss assures the applicability for muon content and muon lateral distribution up to 1 km depth (2.5 km water equivalent). For deeper sites, an effort should be made to include muon induced spallation. Including the propagation of neutrinos is also feasible, and both modifications together would render the simulation code useful for very deep neutrino detectors.

First results indicate that albedo effects can be important close to the shower core and deserve more attention. This package can be used to make further studies on this subject, and its possible impact on detectors signal. The rearrangement of the particle spectrum in the first meters of shower development underground also call for detailed simulations on shallow detectors that sample particles from the "out of equilibrium" stage of the cascade.

References

1. S. Sciutto, AIRES 2.6 user Manual, www.fisica.unlp.edu.ar/aires
2. A.N. Cillis et al., Phys. Rev. D 64,013010 (2001)
3. Formaggio, Martoff,Annu. Rev. Nucl. Part. Sci. 54, 361-412 (2004)
4. T.K. Gaisser,Cosmic Rays and Particle Physics, UK:Cambridge Univ. Press (1990)
5. Andreev Yu M, et al., Proc. 16th ICRC (Moscow) 6,200 (1987)
6. MACRO Collaboration, Phys. Rev. D 52:3793 (1995)
7. M.C. Medina et al., Nucl. Inst. and Methods in Phys. Res. A 2006.2:302-311
8. M.C. Medina et al., American Inst. of Phys. Conf. Proceedings 2007.884:405-410

THE COSMIC-RAY POSITRON AND ELECTRON EXCESS: AN EXPERIMENTALIST'S POINT OF VIEW

M. SCHUBNELL
Department of Physics, University of Michigan, 450 Church Street, Ann Arbor, MI, USA

The recent report by the PAMELA team of the observed rise in the cosmic-ray positron fraction above a few GeV and the report of an excess of cosmic-ray electrons around a few hundred GeV by the ATIC collaboration has resulted in a flurry of publications interpreting these observations either as a possible signature from the decay of dark matter or as a contribution from isolated astrophysical sources. While those interpretations are scientifically exciting, the possibility that measurements are contaminated by misidentified cosmic ray protons can not be ignored.

1 Introduction

Positrons and electrons constitute only a small fraction of the cosmic-ray intensity measured near earth but the observation of these particles has long been recognized as a powerful tool for the investigation of cosmic-ray production and acceleration as well as transport and interaction in the interstellar medium. Direct observation of the all-electron (electrons *and* positrons, $e^{\pm}$) component is feasible up to energies of about a few TeV by balloon or satellite experiments while at higher energies the low particle fluxes require indirect techniques with effective detection areas much larger than the instrument itself.

From the measurement of the relative abundances of positrons and electrons it is evident that the all-electron component consists of mainly electrons. These are generally thought to originate from the same sources as the hadronic component of the cosmic radiation but unlike the much more massive hadrons, electrons experience severe energy loss during propagation, dominantly through synchrotron losses and inverse Compton scattering on interstellar photons. Above GeV energies $\leq 10\%$ of the electrons in the cosmic radiation and an nearly equal amount of positrons are produced through the decay of secondary particles, mostly pions, generated in hadronic interactions of energetic protons with the interstellar medium. The relative fraction of positrons, $N_{e^+}/(N_{e^-} + N_{e^+})$, is expected to fall slowly with energy because of the declining path length of the primary nuclei at high rigidities. The pure secondary nature of the positron component makes it a good

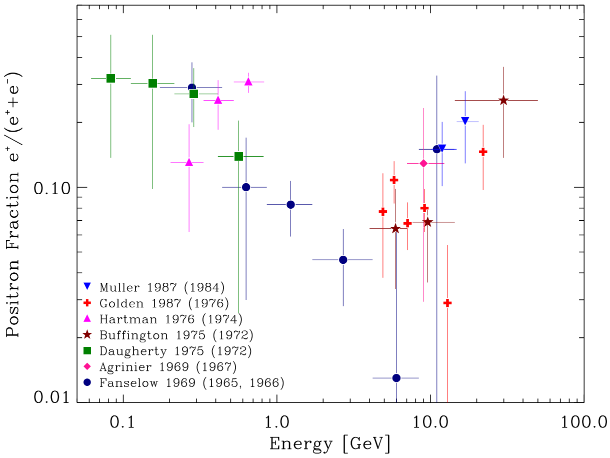

Figure 1: Measurements of the positron fraction prior to the 1990s. The year(s) the data was taken is indicated in parenthesis. For references see Barwick *et al*[4].

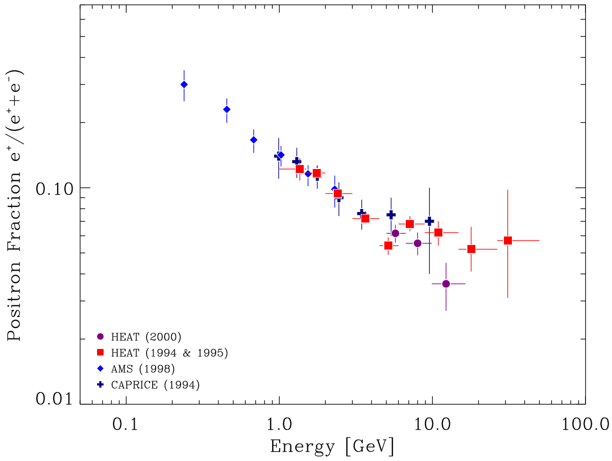

Figure 2: Recent measurements of the positron fraction do not confirm the rise seen in earlier data[4,5,6,3]. The HEAT group reports a possible structure at ≈7 GeV[4].

probe of cosmic-ray propagation and the precise understanding of this constituent of the all-electron intensity allows to isolate the characteristics of the primary electron component.

The absolute intensities of cosmic ray protons and electrons has been measured extensively and can, in the energy region between about 1 GeV and 100 GeV, be represented by a power-law of the form $I(E) = b \times E^{-\alpha}$, with the spectral index $\alpha_p \approx 2.7$ for protons and $\alpha_e \approx 3.4$ for electrons.

2 Cosmic-Ray Positron and Electron Measurements

The majority of early cosmic-ray positron measurements (prior to the 1990s), mostly utilizing small permanent magnet spectrometers and detector systems with limited particle identification capability, observed an unexpected rise in the positron fraction above ≈5 GeV (Fig. 1). Subsequent measurements by instruments with more powerful particle identification showed the almost exclusively secondary nature of positrons with no evidence for a steeply rising positron fraction (Fig. 2). At the same time a possible structure near 7 GeV was reported by the HEAT-$e^{\pm}$ collaboration [4]. These results were confirmed by the CAPRICE instrument [6] and the AMS-1 instrument [3], albeit with lower resolution and energy reach. The unexpected feature in the positron fraction was discussed by many authors as a possible signature of dark matter. Very recently, the PAMELA satellite experiment extended the cosmic-ray positron and electron observations to higher energies [1], confirming the measurements by HEAT but also claiming a dramatic rise in the positron fraction starting at 10 GeV and extending up to 100 GeV, reminiscent of the rise observed at lower energies by early observations (Fig. 3). At yet higher energies, around a few 100 GeV, the ATIC instrument reports a significant excess in the all-electron intensity [7]. The PAMELA and ATIC measurements have motivated a great number of interpretations, from possible signatures of dark matter to astrophysical sources[a]. While such explanations are very attactive and exciting one has to use caution when interpreting cosmic-ray positron and electron measurements.

The intensity of cosmic-ray protons at 10 GeV exceeds that of positrons by a factor of about 5×10^4. Therefore a proton rejection of about 10^6 is required if one wants to obtain a positron sample with less than ≈5% proton contamination. Thus, from an experimental point of view, the single biggest challenge in measuring cosmic-ray positrons is the discrimination against the vast proton background. Furthermore, because the proton spectrum is much harder than the electron and positron spectrum the proton rejection has to improve with energy. In addition, any small

[a] An up-to-date selection can be found at the astrophysics archive: http://arxiv.org/archive/astro-ph.

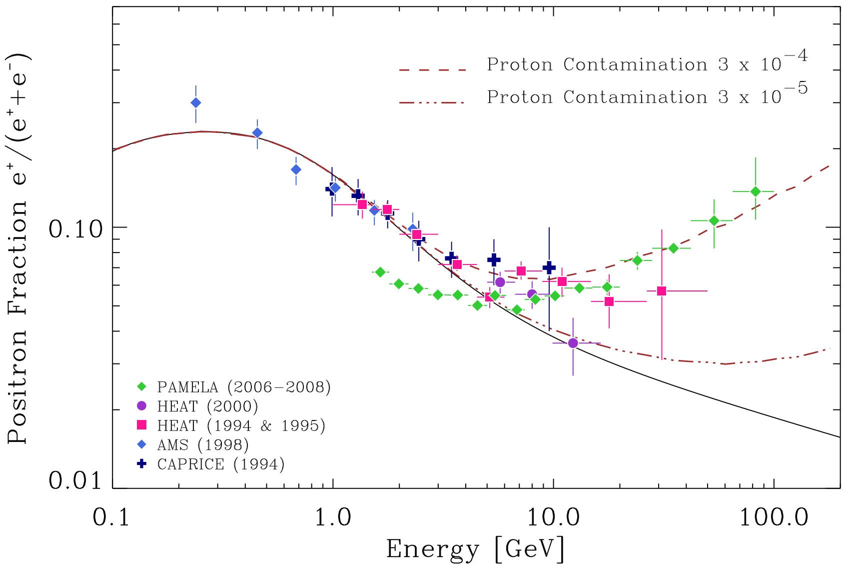

Figure 3: Recent measurements of the positron fraction overlaid with a pure secondary production prediction for cosmic-ray positrons [10] and the same prediction including residual proton contamination. Below ≈5 GeV solar modulation affects the particle intensities observed near Earth and may explain the discrepancy between the PAMELA data and older measurements, obtained at distinctively different solar epochs [8]. In the region between 5 and 50 GeV measurements by PAMELA are consistent with previous data from the HEAT experiment, while the dramatic rise at high energies is reminiscent of an earlier era when particle identification was insufficient.

amount of spillover from tails in lower energy bins can become problematic.

Keeping this in mind it is easy to see why proper particle identification is crucial for the measurements and becomes more important at higher energies. Excellent particle identification requires multiple detector systems and techniques, ideally redundant and complementary, allowing for in-situ determination of hadronic rejection efficiency. Such an instrument will typically employ a powerful magnet spectrometer which measures the particle's charge sign and rigidity. The higher the magnetic field strength and the finer the granularity of the hodoscope's tracking layers the higher the rigidities that can be reached. The particle's charge and direction is typically measured by 'time of flight' scintillator layers. Hadron/electron separation is achieved with transition radiation detectors (TRDs) which measure the ratio of a particle's mass and energy and therefore are ideal for this purpose. Finally, an electromagnetic calorimeter below the magnet spectrometer results in particle identification and energy determination through shower shape and electromagnetic energy deposition. Because of weight restrictions, for balloon borne and satellite instruments the calorimeter depth is typically limited to 10-15 radiation lengths.

The PAMELA instrument suffers from the lack of a second, powerful hadron/electron discrimination detector element (such as a TRD) and therefore relies on the electromagnetic calorimeter for hadron rejection. This impacts positron measurements because with increasing energy not only does the proton background increase but also the discrimination of electromagnetic showers inside the calorimeter becomes more difficult. The probability that hadronic particles mimic electromagnetic showers through early π^0 production is problematic. Very small amounts of spill-over from lower energy bins adds to the list of potential problems. The neutron detector on PAMELA can come to the rescue at high energies but is inefficient below about 100 GeV. However, in the case of early π^0 production with no further hadronic interaction, the neutron detector will be inefficient.

The published all-electron measurements by the ATIC group are difficult to reconcile with previous measurements. The claimed excess has given rise to numerous speculative publications interpreting the data as evidence for primary electrons from dark matter decay. However, from an experimentalist's perspective, the reported data are suspicious as the authors do not properly take into account the uncertainties associated with potential hadronic background particle interactions inside the graphite target on top of the detector. Indeed, this experiment was designed and optimized to detect hadronic particles and while the low Z target is good for detecting nuclei it increases the probability of hadronic contamination. Additionally, uncalibrated leakage of the electromagnetic shower out the back of the calorimeter can lead to pile-up at lower energies.

3 Conclusions and Outlook

Cosmic-ray electron and positron measurements are uniquely capable of illuminating the century old question of the origin of cosmic rays. Electromagnetic process are well understood (at least at the energies in question) and experiments, while challenging, can precisely measure the two components to energies up to at least 100 GeV. The HEAT-$e^{\pm}$ instrument has shown that the combination of powerful detector systems can successfully suppress the hadronic background to the required level. The data reported by PAMELA are, if correct, exciting and confirm the HEAT results of an excess in the positron fraction above a few GeV. While cosmic-ray experiments are and will continue to be important in searching for possible dark matter signatures in cosmic rays, it has to be emphasized that the observation of such an excess is not necessarily linked to dark matter and may well reflect the contribution of primary astrophysical sources to the positron flux. Any potential dark matter 'signature' observed in cosmic rays will ultimately rely on confirmation through accelerator data.

Caution should be exercised when interpreting cosmic-ray positron and electron data above a few GeV because of possible proton contamination of the measurements. The ATIC results in particular are suspicious and will be scrutinized by the forthcoming results from FERMI. Balloon borne instruments have been pathfinding in measuring cosmic-ray particles and have produced the majority of currently available data. While space borne instruments have the advantage of much longer exposure, they have to overcome the technical, financial, and often political hurdles to bring such an instrument into space. The AMS team for instance has been struggling for a decade to get a shuttle flight for deployment on the International Space Station. At costs in excess of $1.5 billion one must ask if a similar size balloon borne instrument flown on several long duration balloon flights would not have been scientifically and financially more prudent. Typical long duration flights from McMurdo, Antarctica achieve now in excess of 40 days at float altitude. A single such flight would give an experiment like HEAT$e^{\pm}$ roughly 3 years worth of PAMELA data during a single flight. At energies above a few TeV, the particle rates become so small that the direct detection of cosmic-ray electrons and positrons becomes difficult at best. Indirect observations with ground based instruments such as HESS [2] will extend the energy reach to ≈5-10 TeV but with large systematic errors. Above 10 TeV the CREST instrument has the potential to measure the electron spectrum and to detect isolated sources of cosmic rays [11].

References

1. O. Adriani *et al*, Nature **458**, 607 (2009).
2. F. Aharonian *et al*, *Phys. Rev. Lett.* **101**, 261104 (2008).
3. J. Alcaraz *et al*, *Phys. Lett.* B **484**, 10 (2000).
4. S.W. Barwick *et al*, *Astrophys. J* **482L**, 191 (1997).
5. J.J. Beatty *et al*, *Phys. Rev. Lett.* **93**, 241102 (2004).
6. G. Barbielliniet *al*, *A&A* **309**, L15 (1996).
7. J. Chang *et al*, Nature **456**, 362 (2008).
8. J. Clem *et al*, *Astrophys. J* **464**, 507 (1996).
9. M.A. DuVernois *et al*, *Astrophys. J* **559**, 296 (2001).
10. I. Moskalenko & A. Strong, *Astrophys. J* **493**, 694 (1998).
11. M. Schubnell *et al*, *Proc. 30th ICRC, Merida, Mexico* **2**, 305 (2007).

Continuous Injection of High Energy Positrons from an Astrophysical Object: Can a Pulsar Account for the Cosmic Ray Electron/Positron Data?

Norita Kawanaka, Kunihito Ioka and Mihoko M. Nojiri
Institute of Particle and Nuclear Studies, KEK (High Energy Accelerator Research Organization), 1-1 Oho, Tsukuba 305-0801, Japan

We investigate the observed spectrum of cosmic-ray electrons and positrons from astrophysical sources, especially pulsars, considering continuous cosmic-ray injections. We find that a continuous injection produces a broad peak and a high energy tail above the peak, which can constrain the source duration ($< 10^5$yr with the current data). We also show that the H.E.S.S. data in the TeV range suggest that young sources with age less than $< 3 \times 10^4$yr are an order-of-magnitude less energetic than the average. These spectral diagnostics can be refined in the near future by the Fermi and CALET experiments.

1 Introduction

Recently, the cosmic-ray electron and positron excess has been measured by PAMELA satellite [1], ATIC balloon experiment[2], and PPB-BETS[3]. These observations strongly indicate nearby sources of $e^{\pm}$ pairs within $d \sim$ 1kpc since high energy electrons/positrons lose their energy during propagation. Furthermore, the H.E.S.S. experiment has extended the electron observations up to 5TeV[4]. Possible candidates of electron/positron sources include a pulsar [5], a gamma-ray burst [6](GRB), a supernova remnant [7] and dark matter annihilations/decays [8].

It is remarkable that an astrophysical source can make a peak with a sharp cutoff that is similar to the dark matter predictions, if the source is a transient object like a GRB[6]. However, other astrophysical sources like pulsars or microquasars are not transient and expected to have a finite spread in the cutoff, as suggested by Ioka (2008)[6].

We investigate the effects of continuous pair injections on the observed electron/positron spectrum. Especially, we discuss the range of physical parameters of the sources (total electron/positron energy, the source duration, etc.) that are consistent with the current observational data. For the detail of this study, see Kawanaka et al. (2009)[9].

2 Injection Models and Calculations

We assume that a point-like source starts injecting $e^{\pm}$ pairs a time $t_{\rm age}$ ago with total energy $E_{e^+} \sim E_{e^-}$ at a distance d ($\sim$ 1kpc) from the Earth. The diffusion equation which describes the propagation of electrons/positrons in the interstellar medium should be

$$\frac{\partial}{\partial t} f = K(\varepsilon_e)\nabla^2 f + \frac{\partial}{\partial \varepsilon_e}[B(\varepsilon_e)f] + Q(t, \boldsymbol{r}, \varepsilon_e), \tag{1}$$

where $f(t, \boldsymbol{r}, \varepsilon_e)$ is the distribution function of particles at time t and position $\boldsymbol{r}$ with energy ε_e. Here $K(\varepsilon_e) = K_0(1 + \varepsilon_e/3\text{GeV})^{\delta}$ is the diffusion coefficient, $B(\varepsilon_e)$ is the energy loss rate, and Q is the injection rate of electrons/positrons. We adopt $K_0 = 2.0 \times 10^{28}\text{cm}^2\ \text{s}^{-1}$, $\delta = 0.6$, that are compatible with the B/C ratio analysis, and $B(\varepsilon_e) = -b\varepsilon_e^2$ with $b = 10^{-16}\text{GeV}^{-1}\ \text{s}^{-1}$ which includes synchrotron and inverse Compton scattering energy losses[10].

Assuming that the injection has been done instantaneously with a power-law spectrum from a point-like source (i.e. $Q(t, \boldsymbol{r}, \varepsilon_e) \propto \varepsilon_{e,0}^{-\alpha}\delta(t - t_0)\delta(\boldsymbol{r} - \boldsymbol{r_0})$, the resulting $e^{\pm}$ spectrum would be

$$G(t, \boldsymbol{r}, \varepsilon_e; t_0, \boldsymbol{r}_0) = \frac{Q_0(t_0)\varepsilon_{e,0}^{-\alpha} B(\varepsilon_{e,0})}{\pi^{3/2} B(\varepsilon_e) d_{\text{diff}}^3} \times \exp\left(-\frac{|\boldsymbol{r} - \boldsymbol{r}_0|^2}{d_{\text{diff}}^2}\right), \tag{2}$$

where $\varepsilon_{e,0} = \varepsilon_e/[1 - b(t - t_0)\varepsilon_e]$ is the energy of electrons/positrons at the time t_0 which are cooled down to ε_e at the time t[11].

We can approximate the diffusion length as

$$d_{\text{diff}} \simeq 2\sqrt{K(\varepsilon_e)(t - t_0)\frac{1 - (1 - \varepsilon/\varepsilon_{\text{cut}})^{1-\delta}}{(1 - \delta)\varepsilon_e/\varepsilon_{\text{cut}}}}, \tag{3}$$

where $\varepsilon_{\text{cut}} = [b(t - t_0)]^{-1}$.

We can obtain the observed spectrum for a continuous injection by integrating over time $G(t, \boldsymbol{r}, \varepsilon_e; t_0, \boldsymbol{r}_0)$ multiplied with the injection luminosity which varies with time. We consider two types of continuous injection. One is the pulsar-type decay:

$$Q_0(\tau) \propto \frac{1}{(1 + \tau/\tau_0)^2}. \tag{4}$$

This is the similar function of time as the spin-down luminosity of a pulsar with a surface magnetic field

$$B = 8.6 \times 10^{11} P_{10\text{msec}} \left(\tau_{0,4}\right)^{-1/2}, \tag{5}$$

where $P_{10\text{msec}}$ is the pulsar period normalized by 10msec and $\tau_{0,4} = \tau_0/10^4$year. The other is the exponential decay:

$$Q_0(\tau) \propto \exp\left(-\frac{\tau \ln 4}{\tau_0}\right). \tag{6}$$

which may be realized by a pulsar that initially confines $e^{\pm}$ in its nebula and releases them afterward, or by a microquasar ceasing its activity.

In Fig. 1 we show the electron plus positron flux resulting from above two injection models in addition to the transient model ($\tau_0 = 0$) and the background (dotted line). The remarkable point is that an astrophysical source can make a spectral peak that is similar to the ATIC/PPB-BETS excess and also to the dark matter case. The peak energy is determined by

$$\varepsilon_{e,\text{peak}} = \left[bt_{\text{age}} + \frac{1}{\varepsilon_{e,\text{max}}}\right]^{-1}, \tag{7}$$

because the electrons/positrons with initially higher energy cool down via synchrotron and inverse Compton emission within time t_{age}. We can inversely estimate the source age as $t_{\text{age}} \sim 5 \times 10^5$years from the peak energy for $\varepsilon_{e,\text{max}} > 1$TeV.

As is clear from Fig. 1, the spectral cutoff becomes shallower for the continuous injection models than the transient one ($\tau_0 = 0$; short dot-dashed line). This is because the significant fraction of $e^{\pm}$ pairs are produced recently (i.e. injected long after the birth of the source) and they have shorter time for the energy loss via synchrotron and inverse Compton emission. Then their energy is still higher than the peak energy when they reach the Earth, and they produce a broader peak.

The thick solid line represents the total (the primary plus background electron and positron) flux assuming that the source starts emitting $e^{\pm}$ pairs with total energy $\sim 10^{50}$erg, a power-law index $\alpha \sim 1.5$ and a maximum energy ~ 5TeV at a distance ~ 1kpc from the Earth a time $t_{\text{age}} \sim 5 \times 10^5$yr ago, and decays exponentially with the duration of $\tau_0 \sim 10^5$year. This model looks better for the ATIC/PPB-BETS peak, though we cannot conclude that the duration is finite with the current data. The positron fraction predicted from this parameter set is also consistent with the PAMELA results, in almost the same way as Fig. 1 of Ioka (2008)[6].

In the case of pulsar-type injection, there is another interesting spectral feature resulting from a long duration. In Fig. 1, the high energy tail above the peak energy is more enhanced for the long duration case ($\tau_0 = 10^5$years, double dashed line) than the short duration case ($\tau_0 = 10^4$years, long dashed line). This is because the longer the duration of injection is, the larger fraction of $e^{\pm}$ pairs are freshly produced and they do not lose their energy during the propagation so much (see also Atoyan et al. 1995[11]). Especially, the flux of the long duration model may exceed the H.E.S.S. observations around $\sim$ 4TeV if we add the background (dotted line) while that of the short duration model does not. As the errorbars are still large, however, we should await future observations.

The H.E.S.S. data also put constraints on the total $e^{\pm}$ pair energy from young sources. We plot in Fig. 1 the spectrum from the source with the age of $\sim 3 \times 10^4$years. We find the total electron energy of the source should be small (10^{48}erg) if their birth rate is of the order of 10^4 years so that they do not exceed the HESS data points. If the birth rate of the energy source should account for the ATIC peak, the birth rate should be at least $< 10^{-5}$years^{-1}.

3 Discussion and Conclusion

We investigate the astrophysical origin for the PAMELA and ATIC/PPB-BETS excesses and in particular the effects of the finite duration and the multiple sources on the electron and positron spectra, as expected for pulsars and microquasars. We find the followings:

(1) A non-transient source can make a spectral peak that is similar to the ATIC/PPB-BETS excess (see Fig. 1) around the peak energy in Eq. (7). The peak is generally broad with a width

$$\left|\frac{\Delta\varepsilon_{e,\mathrm{peak}}}{\varepsilon_{e,\mathrm{peak}}}\right| \approx \frac{\tau_0}{t_{\mathrm{age}}} \sim 10\% \ \tau_{0,4}\left(\frac{t_{\mathrm{age}}}{10^5\mathrm{years}}\right)^{-1}, \tag{8}$$

which could provide a method to measure the source duration τ_0 by the Fermi satellite or the future CALET experiments. We also note that the peak becomes smoother if the injection rises gradually in the initial stage.

(2) The spectrum from a long duration source has a high energy tail above the peak energy (see Fig. 1). Especially the flux of this tail plus the background may exceed the H.E.S.S. data points when assuming a pulsar-type decay with a duration $\tau_0 > 10^5$years. This implies that the source is not likely a single pulsar with magnetic fields weaker than a few times 10^{11}G. However, we cannot rule out the long-duration pulsar model if the maximum energy of injected $e^{\pm}$ pairs is smaller than $<$ TeV, or the injection is not the pulsar-type in Eq. (4) but the exponential-type in Eq. (6). The latter is possible if high energy pairs generated in the pulsar magnetosphere are not injected into the space instantaneously but initially confined in a pulsar wind nebula and they diffuse out after the nebula gets broken.

(3) The H.E.S.S. data suggest that young sources with age less than 3×10^4yr are two orders-of-magnitude less energetic than the source making the ATIC/PPB-BETS peak. Note that the lifetime of the pulsar nebula is around $\sim 10^5$yr and younger pulsars could not contribute by the cosmic-ray confinement in the nebula.

1. Adriani, O. et al. *Nature* **458**, 607 (2008)
2. Chang, J. et al. *Nature* **456**, 362 (2008)
3. Torii, S. et al. arXiv:0809.0760
4. Aharonian, F. et al. *Phys. Rev. Lett.* **101**, 261104 (2008)
5. Chi, X., Cheng, K. S. & Young, E. C. M. *ApJL* **459**, 83 (1996); Zhang, L. & Cheng K. S. *A&A* **368**, 1063 (2001); Grimani, C. *A&A* **474**, 339 (2007); Kobayashi, T., Komori, Y., Yoshida, K. & Nishimura, J. ApJ **601**, 340 (2004); Büesching, I., de Jager, O. C., Potgieter, M. S. & Venter,

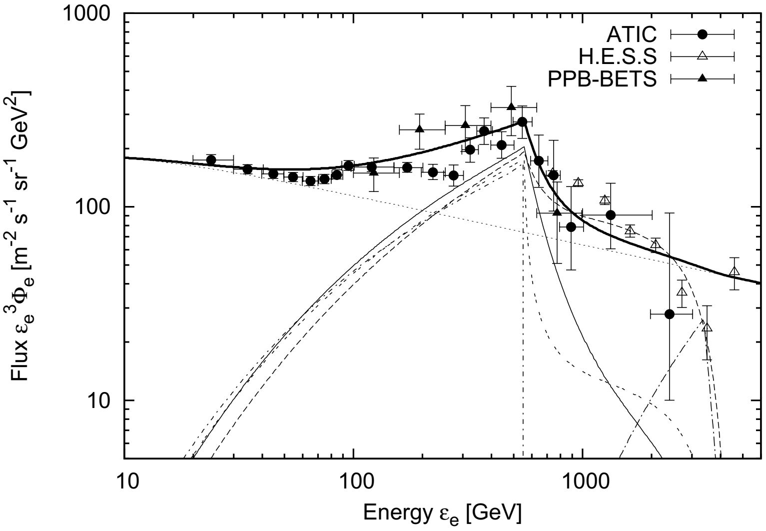

Figure 1: The electron plus positron flux predicted from a source that continuously injects pairs for a finite duration $\tau_0 = 10^5$years with the exponential decay (thin solid line), and its sum (thick solid line) with the background (dotted line), compared with the ATIC/PPB-BETS/H.E.S.S. data. We also show the pulsar-type injection with $\tau_0 = 10^5$years (long dashed line) and $\tau_0 = 10^4$years (double dashed line), in addition to the transient injection ($\tau_0 = 0$; short dot-dashed line). We assume that a source at $d = 1$kpc from the Earth a time $t_{\rm age} = 5.0 \times 10^5$years ago produces $e^\pm$ pairs with total energy $E_{e^+} = E_{e^-} = 0.8 \times 10^{50}$erg and spectral index $\alpha = 1.7$ up to $\varepsilon_{\rm e,max} = 5$TeV. The flux from a young ($\sim 3 \times 10^4$years) and much less energetic ($\sim 2 \times 10^{48}$erg) source with the pulsar-type decay (long dot-dashed line) is also shown.

C. ApJL **678**, 39 (2008); Hooper, D., Blasi, P & Serpico, P. D. *JCAP* **01**, 025 (2009); Yuksel, H., Kistler, M. D. & Stanev, T. arXiv:0810.2784; Profumo, S. arXiv:0812.4457; Malyshev, D., Cholis, I. & Gelfand, J. arXiv:0903.1310

6. Ioka, K. arXiv:0812.4851
7. Shaviv, N. J., Naker, E. & Piran, T. arXiv:0902.0376; Fujita, Y., Kohri, K., Yamazaki, R. & Ioka, K. arXiv:0903.5298
8. Asano, M., Matsumoto, S., Okada, N. & Okada, Y. *Phys. Rev.* D **75**, 063506 (2007); Arkani-Hamed, N., Finkbeiner, D. P., Slatyer, T. & Weiner, N. *Phys. Rev.* D **79**, 015014 (2009); Bergstrom, L., Bringmann, T. & Edsjö, J. *Phys. Rev.* D **78**, 103520 (2008); Hamaguchi, K., Shirai, S. & Yanagida, T. T. arXiv:0812.2374; Cirelli, M. & Strumia, A. arXiv:0808.3867; Cholis, I., Finkbeiner, D. P., Goodenough, L. & Weiner, N. arXiv:0810.5344; Cholis, I., Dobler, G., Finkbeiner, D. P., Goodenough, L. & Weiner, N. arXiv:0811.3641; Chen, C. R., Hamaguchi, K., Nojiri, M. M., Takahashi, F. & Torii, S. arXiv:0812.4200; Chen, C. R., Nojiri, M. M., Takahashi, F. & Yanagida, T. T. arXiv:0811.3357; Chen, C. R. & Takahashi, F. *JCAP* **02**, 004 (2009); Chen, C. R., Takahashi, F. & Yanagida, T. T. *Phys. Lett.* B **671**, 71 (2009); Hisano, J., Matsumoto, S., Nojiri, M. M., Saito, O. *Phys. Rev.* D **71**, 063528 (2005); Hisano, J., Kawasaki, M., Kohri, K. & Nakayama, K. arXiv:0810.1892; Hisano, J., Kawasaki, M., Kohri, K. & Nakayama, K. arXiv:0812.0219; Hisano, J., Kawasaki, M., Kohri, K., Moroi, T. & Nakayama, K. arXiv:0901.3582; Ishiwata, K., Matsumoto, S. & Moroi, T. *Phys. Rev.* D **78**, 063505 (2008); Ishiwata, K., Matsumoto, S. & Moroi, T. arXiv:0811.0250; Ishiwata, K., Matsumoto, S. & Moroi, T. arXiv:0811.4492; Zhang, J. et al. arXiv:0812.0522; March-Russell, J. D. & West, S. M. arXiv:0812.0559; Hooper, D., Stebbins, A. & Zurek, K. M. arXiv:0812.3202; Pohl, M. *Phys. Rev.* D **79**, 041301 (2009)
9. Kawanaka, N., Ioka, K. & Nojiri, M. M. arXiv: 0903.3782
10. Baltz, E. A. & Edsjö, J. *Phys. Rev.* D **59**, 023511 (1999); Moskalenko, I. V. & Strong, A. W. ApJ **493**, 694 (1998)
11. Atoyan, A. M., Aharonian, F. A. & Völk, H. J., *Phys. Rev.* D **52**, 3265 (1995)

Inhomogeneity in the Supernova Remnants as a Natural Explanation of the PAMELA/ATIC Observations.

Tsvi Piran[1], Nir J. Shaviv[1] and Ehud Nakar[2]
1. Racah Institute for Physics, The Hebrew University, Jerusalem 91904, Israel
2. The Raymond and Beverly Sackler School of Physics & Astronomy, Tel-Aviv University, Tel-Aviv 69978, Israel

Recent measurements of the positron/electron ratio in the cosmic ray (CR) flux exhibits an apparent anomaly[1], whereby this ratio increases between 10 and 100 GeV. In contrast, this ratio should decrease according to the standard scenario, in which CR positrons are secondaries formed by hadronic interactions between the primary CR protons and the interstellar medium (ISM)[2]. The positron excess is therefore interpreted as evidence for either an annihilation/decay of weakly interacting massive particles, or for a direct astrophysical source of pairs. The common feature of all proposed models is that they invoke new physics or new astrophysical sources. However, this line of argumentation relies implicitly on the assumption of a relatively homogeneous CR source distribution. Inhomogeneity of CR sources on a scale of order a kpc, can naturally explain this anomaly. If the nearest major CR source is about a kpc away, then low energy electrons ($\sim$ 1 GeV) can easily reach us. At higher energies ($\gtrsim$10 GeV), the source electrons cool via synchrotron and inverse-Compton before reaching the solar vicinity. Pairs formed in the local vicinity through the proton/ISM interactions can reach the solar system also at high energies, thus increasing the positron/electron ratio. A natural origin of source inhomogeneity is the strong concentration of supernovae to the galactic spiral arms. Assuming supernova remnants (SNRs) as the sole primary source of CRs, and taking into account their concentration near the galactic spiral arms, we consistently predict the observed positron fraction between 1 and 100 GeV, while abiding to different constraints such as the observed electron spectrum and the CRs cosmogenic age. ATIC's[3] electron spectrum excess at $\sim$ 600 GeV can be explained, in this picture, as the contribution of a few known nearby SNRs.

PAMELA[1] discovered that the CR positron/electron ratio increases with energy above $\sim$ 7 GeV. The apparent discrepancy between the theoretical standard prediction of a decreasing ratio and these measurements is now commonly known as the "PAMELA anomaly"[4]. It is commonly interpreted as evidence for a new source of primary CR positrons, most likely WIMPs. Measurements of the electron spectrum at $0.1-1$ TeV by ATIC[3] show an excess of CR electrons at energies of $300-800$ GeV, and at even higher energies ($1-4$ TeV) HESS measures[5] a sharp decay in the electron spectrum. ATIC's results are usually considered as support of a dark matter origin for the PAMELA anomaly, where the observed spectral bump corresponds to the WIMP mass.

In the standard picture[2], the majority of CRs are thought to originate in SNR shocks. SNRs, however, are not expected to be a major source of CR positrons. Instead, as CR protons diffuse through the Galaxy, they collide with interstellar medium (ISM) nuclei, producing "secondary" positrons and electrons. CRs diffuse within the disk, and escape the Galaxy once they reach the halo height, $l_H \sim 1$ kpc above the disk. The diffusion coefficient can be approximated as $D = D_0(E/E_0)^\beta$. Most CR diffusion models assume that CRs are produced with a power-law spectrum, $N_E \equiv dN/dE \propto E^{-\alpha}$. The observed spectrum is then a convolution of the source spectrum and propagation losses, giving for the primary electrons $N^{(e)}_{E,obs} \propto E^{-(\alpha_e+\beta)}$. Positrons are secondary CRs formed from CR protons, and suffer additional propagation loses, implying $N^{(s)}_{E,obs} \propto N^{(p)}_{E,obs}E^{-\beta} \propto E^{-(\alpha_p+2\beta)}$. The predicted flux ratio is $\phi^+/(\phi^- + \phi^+) \approx \phi^+/\phi^- \propto E^{\alpha_e-\alpha_p-\beta}$, where α_e and α_p are the source power-law indices of electrons and protons respectively. Both electrons and protons are expected to have similar spectral slopes, i.e., $\alpha_e \approx \alpha_p$, which is somewhat larger than 2. Consequently, $\alpha_p - \alpha_e < \beta \approx 0.3 - 0.6$ and the standard model predicts, in contrast to PAMELA observations, a CR positron/electron ratio which decreases with energy.

This standard model assumes a homogenous, source distribution[2,6]. However, as star formation in spiral galaxies is concentrated in spiral arms[7,8] one should consider the effect of inhomogeneities in the CR source distribution on the CR spectrum. This inhomogeneity of sources influences the electrons/positrons spectra via cooling which sets a typical distance scale that an electron/positron with a given energy can diffuse away from its source. For a homogenous distribution cooling affects the spectra of (primary) electrons and (secondary) positrons in the same way and their ratio is unaffected. On the other hand, primary electrons will be strongly affected by an inhomogeneous source distribution at energies for which the diffusion time is longer than the cooling time. Protons are not affected by cooling and are therefore distributed rather smoothly in the galaxy even if their sources are inhomogeneous. The secondary positrons (that are produced by the smoothly distributed protons) are only weakly affected by the inhomogeneity of the sources. This effect would induce an observed signature on ϕ^+/ϕ^-, with similar properties to the one observed by PAMELA.

We [9] considered a simple analytic model for diffusion from a source at a distance d from Earth. We model the galaxy as a two dimensional slab. The Galactic plane is infinite and the disk height is finite, l_H. The source is at a distance d from Earth. A CR diffuses within this slab with a constant diffusion coefficient $D(E)$, and it escapes once $|y| > l_H$. We find that for a a turnover in ϕ^+/ϕ^- is observed at E_b which satisfies $\tau_c(E_b) \approx \min\{\tau_x(E_b), (\tau_e(E_b)\tau_x(E_b))^{1/2}\}$. ϕ^+/ϕ^- for $E < E_b$ decreases, while it increases for $E > E_b$. This is the observed behavior seen by PAMELA, provided that $E_b \approx 10$ GeV, which the case using typical parameters for cooling and diffusion from a source at $d \approx 1$ kpc [9]. The nearest spiral arm to the solar system is the Sagittarius-Carina arm at a distance of ≈ 1 kpc.

At the same time the typical age of CR protons with energy E_b is $a \sim \max\{\tau_e, (\tau_e\tau_d)^{1/2}\}$. Therefore a natural prediction of the model is $a(E_b) \gtrsim \tau_c(E_b)$ and a comparison of the two observables can be used as a consistency test for the model. Moreover, over a wide range of the parameter space for which $d \gtrsim l_H$, the model predicts $a(E_b) \approx \tau_c(E_b)$ regardless of the value of the diffusion coefficient D.

To demonstrate quantitatively the potential of this model to recover the observed behavior of ϕ^+/ϕ^-, we [9] (see also ref. 8 simulated numerically the CR diffusion for a realistic spiral-arm concentrated source distribution. Before presenting these results we stress that all other models explaining PAMELA invoke a new ad hoc source of high energy CR positrons which has a negligible effect on low energy CR components. However, in our model, the PAMELA explanation is intimately related to low and intermediate energy CR propagation in the Galaxy. Namely, by revising the source distribution of CRs, we affect numerous properties of $\sim$ GeV CRs. Given that the interpretation of observations (in particular, isotopic ratios) used to infer model parameters (such as D_0, β or l_H) depend on the complete model, one should proceed while baring in mind that these parameters may differ in our model from present canonical values. In this sense, the objective is not to carry a

comprehensive parameter study, fitting the whole CR data set to an inhomogeneous source distribution model. Instead, our goal is to demonstrate the potential of the model to explain naturally the PAMELA anomaly. To this end we use the simplest possible model, fixing all parameters with the exception of the halo size, l_H, and the normalization of the diffusion coefficient, D_0, that we vary to fit the data.

Small scale inhomogeneities are important at energies larger than a few hundreds GeV, for which the lifetime, and therefore propagation distance, of electrons is so short that the electron spectrum is dominated by a single, or at most a few nearby sources[10,11,12]. To take this effect into account we truncate the "homogeneous" disk component at $r < 0.5$ kpc and age less than $t < 0.5$ Myr, and we add all SNRs within this 4-volume: Geminga, Monogem, Vela, Loop I and the Cygnus Loop, as discrete instantaneous sources. These sources were described using the analytical solution[10] for the diffusion and cooling from an instantaneous point source.

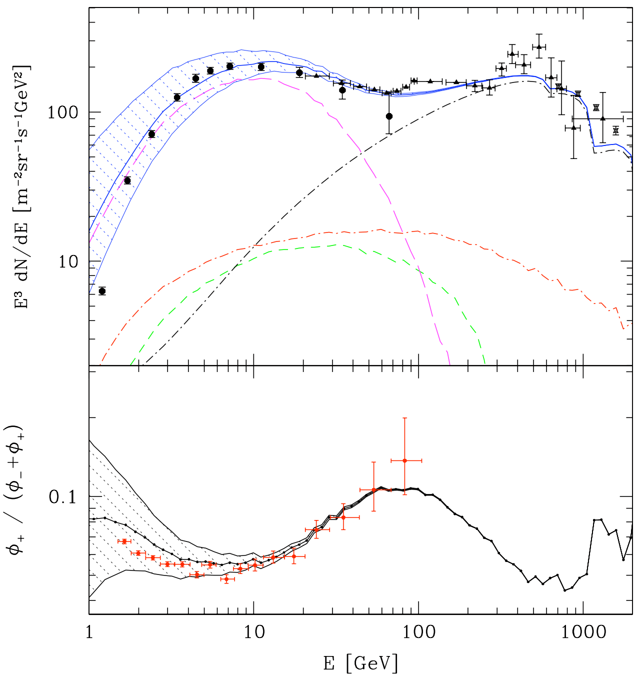

Figure 1: *Bottom Panel*: Model results and the measured PAMELA points for the positron fraction. The shaded region is the variability expected from solar modulation effects[13]. *Top Panel*: The expected electron and positron spectra – Primary arm electrons (long dashed purple), primary disk electrons with nearby sources excluded (short dashed green), nearby SNRs (dot-dashed black), secondary positrons (dot-dashed red), and their sum (blue). The hatched region describes the solar modulation range (from 200 MV to 1200 MV). The three data sets plotted are of HEAT[14] (circles), ATIC[3] (triangles) and HESS[5] (open squares).

The lower panel of fig. 1 depicts $\phi^+/(\phi^+ + \phi^-)$. As expected from the simple analytical model, the fraction decreases up to ~ 10 GeV and then it starts increasing. At about 100 GeV, the ratio flattens and it decreases above this energy because of the injection of "fresh" CRs from recent nearby SNRs whose high energy primary electrons don't have time to cool. These sources also contribute to higher energy electrons detected by ATIC. The cosmogenic age we obtain in this model for 1 GeV per nucleon particles is 14 Myr.

The upper panel of fig. 1 depicts the electronic spectrum and its constituents—primary spiral arm electrons, primary disk electrons (without nearby sources), the spectrum of the nearby sources and the secondary pairs. Evidently, there are two bumps in the $E^3 N_E$ plot. The lower energy bump arises from spiral arm electrons, the higher energy of which cannot reach us due to cooling. The higher energy bump, which corresponds to the ATIC peak, is due to a few nearby SNRs. The three "steps" are due to the cooling cutoffs from Geminga, Loop I and the Monogem SNRs. Note that the average CR flux from these sources is about 3 to 6 times higher than can be expected from the average disk population were it not truncated. This is not surprising given that our local inter-arm region is perturbed by the Orion Spur.

While the predictions for the positron/electron ratio for the spiral arms CR model are very different than for a homogenous sources distribution, the effect on the electron spectrum is much more subtle. Both models predict a break of the electron spectrum at 10 GeV. The break predicted by spiral arm model is from a power law to an exponential, while in the homogenous model it is a broken power-law. Given that above ~ 100 GeV the electron spectrum is strongly affected by the sources that produce the ATIC bump (e.g., local SNRs), the energy range between 10 to 100 GeV is too short to distinguish, based on the electron spectrum alone, between the two models. Thus, while both models can adequately reproduce the observed electron spectrum (at least up to 100 GeV), only the inhomogeneous source model can explain the positron/electron ratio.

One of the interesting predictions of this model where both the PAMLEA and the ATIC anomalies are explained as consequences of propagation effects from SNRs, is that the positron fraction should start dropping with energy at ~ 100 GeV, just above the present PAMELA measurement. It should reach a minimum around the ATIC peak, where it should start rising again. Whether or not it can go up to about 50% at a few TeV depends on whether the CRs from very recent SNe, the Cygnus Loop and Vela, could have reached us or not. This critically depends on the exact diffusion coefficient. Here it is also worth pointing out that above a few TeV the secondaries must be produced within the local bubble, implying that their normalization should be ten times lower than for the lower energy secondaries. These predictions are in contrast to the case where the ATIC peak is due to a primary source of pairs, in which case the positron fraction is expected to keep rising also at a few hundreds GeV. With these predictions, it will be straightforward in the future to distinguish between propagation induced "anomalies", and real anomalies arising from primary pairs (in particular, when PAMELA's observations will extend to higher energies). Of course, it is possible that the ATIC peak is due to a source of primary pairs, while the PAMELA anomaly is a result of SNRs in the spiral arms, but then it would force us to abandon the simplicity of the model, that the anomalies are all due to propagation effects from a source distribution borne from the known structure of the Milky Way.

Acknowledgments

TWe thank Marc Kamionkowski, Re'em Sari and Vasiliki Pavlidou for helpful discussions. The work was partially supported by the ISF center for High Energy Astrophysics, an ISF grant (NJS), an IRG grant (EN) an ERC excellence grant and the Schwartzman Chair (TP).

References

1. O. Adriani, et al., Nature, **458**, 607 (2009).
2. Moskalenko, I. V. & Strong, A. W. *ApJ.* **493**, 694 (1998).
3. Chang, J. *et al.* *Nature* **456**, 362 (2008).
4. See talk by F. Cafagna, A. Morselli, M. Raidal, N. Kawanaka at this conference.
5. H. E. S. S. Collaboration. *ArXiv e-prints* (2008). 0811.3894.
6. Strong, A. W. & Moskalenko, I. V. *ApJ.* **509**, 212 (1998).
7. Lacey, C. K. & Duric, N. *ApJ.* **560**, 719 (2001).
8. Shaviv, N. J. *New Astron.* **8**, 39 (2003).
9. Shaviv, N. J., Nakar, E., & Piran, T., *ArXiv e-prints* (2009). 0902.0376.
10. Atoyan, A. M., Aharonian, F. A. & Völk, H. J. *Phys. Rev. D* **52**, 3265–3275 (1995).
11. Kobayashi, T., Komori, Y., Yoshida, K. & Nishimura, J. *ApJ.* **601**, 340 (2004).
12. Profumo, S. *ArXiv e-prints* (2008). 0812.4457.
13. Clem, J. M. *et al.* *ApJ.* **464**, 507 (1996).
14. DuVernois, M. A. *et al.* *ApJ.* **559**, 296 (2001).

VERY HIGH ENERGY EMISSION FROM THE VICINITY OF SUPERMASSIVE BLACK HOLES

G. PEDALETTI* & S. J. WAGNER
Landessternwarte, Universität Heidelberg,
Königstuhl, D 69117 Heidelberg, Germany
* *IMPRS Fellow*

Galactic nuclei are among the hypothesized sources of Ultra High Energy Cosmic Rays (UHECR; $E > 10^{19}$ eV). If this hypothesis holds, very high energy (VHE; >100 GeV) γ-rays are expected to be emitted from the vicinity of super-massive black holes (SMBH), irrespective of their activity state. VHE emission from the accelerated particles is feasible via leptonic or hadronic processes. The main parameters to be determined are the mass of the central object and the value of the magnetic field. The giant elliptical galaxy NGC1399 is the best candidate for this kind of study in the southern hemisphere. Conclusions on the physical parameters of the system are drawn from VHE observations of this system.

1 Introduction

Super-massive black holes with masses in the range $M_{\rm BH} = 10^6 - 10^9 M_\odot$ are ubiquitously found in the central region of spheroidal systems (such as elliptical galaxies, lenticular galaxies, and early-type spiral galaxies with massive bulges).

Blazar-type Active Galactic Nuclei (AGN) are established emitter of VHE γ-rays[17]. In addition, VHE emission in the vicinity of SMBH in non-blazar galactic nuclei is also expected.

The Pierre Auger Collaboration claimed a correlation between the arrival direction of UHECR and a class of object whose spatial distribution follows that of local AGN[1]. A direct connection between AGN and UHECR is controversial up to date and it has to be kept in mind that nothing is known about UHECR sources, but the fact that they have to satisfy the so-called "Hillas criterion": the particles have to be confined in the acceleration region[9]. Galactic nuclei are considered among the possibilities because of the expected high magnetic field in their compact nuclear region; several authors explored already this possibility (see e.g.[6]). If these systems are indeed the sources of UHECR, there will be VHE γ-ray emission associated, the detection of which would uniquely pinpoint the source.

Furthermore, SMBH could be associated with VHE emission also in the case of radiogalaxies. Radiogalaxies are established VHE emitters since M87[4] and CenA[15] were detected using Cherenkov telescopes. Interestingly, the radiogalaxy M87 also shows fast variability in the VHE domain of the order of few days[4], constraining the size of a non-relativistically moving emitting region down to few Schwarzschild radii ($R_{\rm S}$).

Local SMBH in non-blazar AGN can therefore be regarded as a prime candidate for VHE emission. While the detection of VHE gamma-rays in blazar-type systems is facilitated by the superluminal motion (the apparent luminosity is boosted and the optical depth related to photon-photon absorption is reduced, see[17]), this is not the case for non-blazar systems. Hence, proximity and low luminosity in the IR/optical domain increase the possibility of a detection in the VHE band. In most of the models a high mass of the central black hole is also a parameter that increases the expected flux.

The parameters relative to the SMBH in the center of the giant elliptical galaxy NGC 1399 will be used in the following in order to test the different scenarios. This system can be regarded as the perfect test for such kind of studies because of its proximity (D=20.3 Mpc), high mass of the central black hole ($M_{\rm BH} = 10^9 M_\odot$) and low luminosity in low-energy bands[12].

2 Expected Emission

The power that can be extracted from a spinning SMBH is represented by

$$W_{\rm max} \sim 10^{45} a^2 \left(M_9\right)^2 \left(B_4\right)^2 \ \text{erg s}^{-1}, \tag{1}$$

where $M_9 = M_{\rm BH}/(10^9 M_\odot)$, $B_4 = (B/10^4 \text{ G})$ and $a = J/J_{\rm max} = 1$ ($J_{\rm max} = GM/c$ is the maximum angular momentum per unit mass)[19].

Assuming that there is an emission process that can effectively tap into this power and that $M_{\rm BH}$ and the magnetic field are high enough, this kind of luminosity output from a nearby system could be easily detected by current generation of Cherenkov telescopes.

2.1 Emission Processes

VHE emission from the accelerated particles is feasible via leptonic or hadronic processes irrespective of the acceleration mechanism.

Accelerated protons can collide with other protons present in the accretion disk producing pions, some of which decay into VHE γ-rays. With $t_{\rm pp} \simeq (\sigma_{\rm pp} n_{\rm max} c)^{-1} \simeq 15$ yr, where t_{pp} and $\sigma_{pp} \sim 4 \cdot 10^{-26}$ cm^2 are the timescale and the cross-section of proton-proton collision, variability is not expected on timescales shorter than a few years. $n_{\rm max} \sim 10^7$ cm^{-3} is the plasma density at R_S extrapolated from the value at the accretion radius $n(\mathrm{r_{acc}}) = 0.23$ cm^{-3} ([14]), in the test case of NGC 1399, assuming a free-fall profile.

In some models[10,11,16] VHE γ-rays originate from leptonic processes, i.e. curvature emission or inverse Compton (IC) scattering. However, the energy of curvature photons does not depend on the mass of the particle and is identical for photons emitted by electrons or protons. Equating the maximum energy gain from acceleration ($E_{\rm gain} = \eta q B c$, with $\eta = 1$ the efficiency of the acceleration mechanism[2]) and the energy loss for curvature, the maximum energy attained by the accelerated proton is:

$$E_{\rm p,curv} \simeq 1.5 \times 10^{19} \left(\frac{R_{\rm curv}}{R_{\rm S}}\right)^2 \left(M_9\right)^{1/2} \left(B_4\right)^{1/4} \text{eV}, \tag{2}$$

where $R_{\rm curv}$ is the curvature radius of the magnetic field lines. The emitted photon will have an energy of $E_{\gamma,\rm curv} \simeq 5 \left(\frac{R_{\rm curv}}{R_{\rm S}}\right)^{1/2} \left(M_9\right)^{1/2} \left(B_4\right)^{3/4}$ TeV. It is easily seen from Eq. 2 that a proton can be accelerated to UHE provided that the mass of the central black hole and the associated magnetic field are high enough.

Another energy loss mechanism that might not be negligible for the accelerated particles is due to Inverse Compton (IC) collision with a low-energy photon field. Being $L_{\rm IR}, R_{\rm IR}, \epsilon_{\rm IR}$ respectively the luminosity, radius of the region and energy of the infrared soft photon field, it is possible to calculate the maximum energy attainable by the electrons in the case of maximum efficiency of the acceleration process:

$$E_{\rm e,max} \simeq 280 \ B_4^{1/2} M_9 \left(\frac{R_{\rm IR}}{R_S}\right) \left(\frac{10^{41} \text{erg s}^{-1}}{L_{\rm IR}}\right)^{1/2} \text{TeV}. \tag{3}$$

It is then possible to calculate: the average energy of a Compton upscattered photon (Thomson regime) $E_{\gamma,\mathrm{IC}} =\sim 5\left[\frac{\epsilon}{10^{-2}\mathrm{eV}}\right]\left[\frac{E_e}{10\mathrm{TeV}}\right]^2$ TeV; the average energy of a Compton upscattered photon (KN regime) $E_{\gamma,\mathrm{IC}} = E_{\mathrm{e}}$.

3 VHE Data and their Interpretation

NGC 1399 was observed with the H.E.S.S. array of imaging atmospheric-Cherenkov telescopes in 2005 and 2007 for a total of 38 h exposure (88 runs of ∼28 min each). After applying the standard H.E.S.S. data-quality selection criteria[3] a total of 18 hours live time remain. The mean zenith angle is $Z_{\mathrm{mean}} = 19.6°$ and the mean offset is $\Psi_{\mathrm{mean}} = 0.85°$. The data were reduced using standard analysis tools and selection cuts (standard cuts[3]) and the Reflected-Region method[5] for the estimation of the background. A point source analysis was performed with an angular cut of $\theta^2 = 0.0125$ and a size cut of 80 photo-electrons (details in[3]). This leads to a post-analysis threshold of 260 GeV at Z_{mean}. No significant excess (-26 events, -1.1 standard deviations) is detected from NGC 1399 (see Fig. 1).

Assuming a photon index of Γ=2.6, the upper limit (99.9% confidence level[8]) on the integral flux above 260 GeV is:

$$I\,(>260\mathrm{GeV}) < 1.1\times10^{-12}\ \mathrm{cm}^{-2}\mathrm{s}^{-1}, \tag{4}$$

or 0.7% of the Crab Nebula flux (CF). Changing the assumed value of Γ does not change the upper limit by much; it can vary from 0.53% CF (hard spectrum, $\Gamma = 2.0$) to 0.94% CF (soft spectrum, $\Gamma = 4.0$).

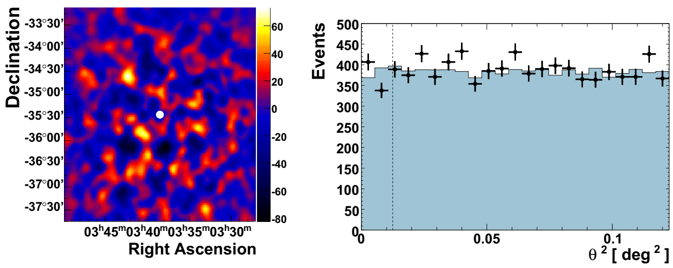

Figure 1: **Left:** The smoothed (smoothing radius r=0.09°) VHE excess in the region centered on NGC 1399. The central white dot indicates the position of the optical center of NGC 1399. There is no significant excess at any point in the sky map. **Right:** Distribution of events as a function of squared angular distance from NGC 1399 for gamma-ray-like events in the ON region (points) and in the OFF region (filled area, normalized). The dotted line represents the cut for point-like sources.

3.1 *Absorption*

The optical depth resulting from photon-photon pair absorption, in a source of luminosity L and radius R, is given by: $\tau\,(E, R) = (L\,(\epsilon)\,\sigma_{\gamma\gamma})\,/\,(4\pi R\epsilon c)$. In the NGC 1399 system, the visibility of a 200 GeV photon ($L_\gamma < 6.16\times10^{40}$ erg s^{-1}) requires $L\,(\epsilon = 5eV) < 2.83\times10^{42}$ erg s^{-1}, if the region containing the soft photon field is of the order of 100 times the Schwarzschild radius of the black hole. This condition seems to be satisfied looking at the very low luminosity detected by HST[12]. If instead more energetic hard photons are considered, $E > 1$TeV, the fairly high emission detected in the near infrared[18] requires the size of the emitting region to be $R \sim 10^3 R_{\mathrm{S}}$.

Moreover, a magnetized system can sustain pair production on its own and degrade the energy of a VHE photon. However, this mechanism will not lead to efficient absorption as long as the magnetic field is $B < 10^6 G$, see[7].

Therefore, it can be assumed that, if VHE radiation is produced in the NGC 1399 system, such emission should not have been absorbed.

3.2 *Magnetic Field and Maximum Particle Energy*

Independently from which emission process is dominating, a high value of the magnetic field will lead to a higher flux (see Eq. 1). The black hole alone cannot sustain magnetic fields, but the accreting plasma will form a magnetosphere (of unknown configuration). Indeed, as shown in[13], the magnetic field depends ultimately on the mass accretion rate.

If it is assumed that all the power coming from Eq. 1 is radiated in the VHE domain (maximum efficiency), the upper limit derived by the VHE observation of NGC 1399 allows to set a limit for a homogeneous magnetic field based on Eq. 1:

$$B < 74.0\ a^{-1}\ \mathrm{G}. \tag{5}$$

This translate on an upper limit on the mass accretion rate $\dot{m} = \dot{M}/\dot{M}_{\mathrm{Eddington}} < 10^{-6}$ ([13]).

Substituting the upper limit on the magnetic field derived from the H.E.S.S. observation of NGC 1399, it's easy to see that such kind of systems are not able to accelerate UHECR. The maximum energy attainable by a proton, when curvature losses are dominating, it is *"only"* $E_{\mathrm{p,curv}} < 4 \times 10^{18}$eV (see Eq. 2). If the hypothesized emission would be related to IC losses, then the maximum energy of an accelerated electron would be $E_{\mathrm{e,max}} \sim 2 \times 10^{13}$eV (see Eq. 3).

4 Conclusions

The low value of the magnetic field $B < 74.0\ a^{-1}$ G ($\dot{m} < 10^{-6}$) derived from the VHE observations of NGC 1399, would not rule out VHE emission via IC scattering or proton proton interactions, but would translate into the need of probing lower fluxes. However, such kind of systems as the one described here cannot accelerate particles to ultra high energies.

Acknowledgments

This work has been supported by the International Max Planck Research School (IMPRS) for Astronomy & Cosmic Physics at the University of Heidelberg.
Special thanks to G. Bicknell, J. Kirk and F. Rieger for useful discussions.

References

1. Abraham, J. et al. (Pierre Auger Collaboration) 2007, Science 318, 938
2. Aharonian, F. et al. 2002, Phys Rev D, 66b, 3005
3. Aharonian, F. et al. (H.E.S.S. Collaboration) 2006, A&A, 457, 899
4. Aharonian, F. et al. (H.E.S.S. Collaboration) 2006,Science, 314, 1424A
5. Berge, D. et al. 2007, A&A, 466, 1219
6. Boldt, E. & Gosh, P. 1999, MNRAS, 307, 491
7. Erber, T. 1966, RvMP, 38, 626E
8. Feldman, G. J. & Cousins, R. D. 1998, Phys. Rev. D, 57, 3873
9. Hillas 1984,ARA&A, 22, 425H
10. Levinson, A. 2000, Phys. Rev. Let., 85, 912
11. Neronov, A. & Aharonian, F. 2007, ApJ, 671, 85
12. O' Connell, R. W. et al. 2005, ApJ, 635, 305
13. Pedaletti, G., Wagner, S. J., Bicknell, G. V. 2008, AIPC, 1085, 530P
14. Pellegrini, S. 2005, ApJ, 624, 155
15. Raue et al. for the H.E.S.S. Collaboration, this conference
16. Rieger, F. M. & Aharonian, F. A. 2008, A&A, 479, L5
17. Schlickeiser, R. 1996, A&AS, 120C, 481S
18. Skrutskie, M. F. et al 2006, AJ, 131, 1163S
19. Thorne, Price & Macdonald 1986, Black Holes: The Membrane Paradigm (Yale University Press)

RESULTS ON ULTRA HIGH ENERGY COSMIC RAYS PRIMARY COMPOSITION AND SEARCH FOR PHOTONS WITH THE PIERRE AUGER OBSERVATORY

V. SCHERINI FOR THE PIERRE AUGER COLLABORATION
Bergische Universität Wuppertal, Department of Physics, 20 Gaußstr., 42119 Wuppertal, Germany

The Pierre Auger Observatory is the world's largest instrument conceived to study the origin and nature of the highest energy cosmic rays, i.e. $E > 10^{18}$ eV. The "hybrid" design combines the ground array and the fluorescence detection techniques in order to characterize the extensive particle showers induced by the cosmic primaries in the Earth atmosphere. Data taking at the southern site has been running stable since 2004. Results on the UHECR primary composition studies are presented, focusing in particular on the search for photon primaries at these extreme energies.

1 Introduction

Composition studies are a key to understand the nature of the Ultra High Energy Cosmic Rays (UHECR). Measurements at the transition region from galactic to extra-galactic cosmic rays are especially crucial to clarify their origin and characterize their sources. Data collected at the Pierre Auger Observatory [1] suggest a mixed composition over the whole energy range [2]. Results from the different experiments are compatible within the quoted systematics and the characterization of the astrophysical sources is still an open issue. Interpretation of the observations in terms of mass composition depends strongly on the assumed hadronic interaction models and related uncertainties [3]. Further improvement of the detection techniques and better knowledge of the experimental systematics, together with the increase of statistic are necessary. An overlap of the range of study between different experiments making use of complementary techniques will also be decisive.

In addition to nuclear primaries, a UHE photon component at the level of $\sim 0.1\%$ is also expected from the decay of neutral pions produced in the interaction of nucleons with the CMB [4]. Larger photon fractions (up to $\sim$50% at the highest energies) are predicted by the non-acceleration models [5]. Discrimination between the different scenarios for the origin of the UHECR is possible, based on observables sensitive to the distinctive characteristics of extensive atmospheric showers initiated by photons. So far no observation of UHE photons has been claimed, but stringent limits on their fraction in the integral CR flux have been placed. These limits also help to reduce uncertainties related to photon contamination in other measurements (i.e. derivation of energy spectrum [6], proton-air cross section [7]). The detection of primary photons at these extreme energies will in turn open a new window to the Universe, with large impact also on fundamental physics [8].

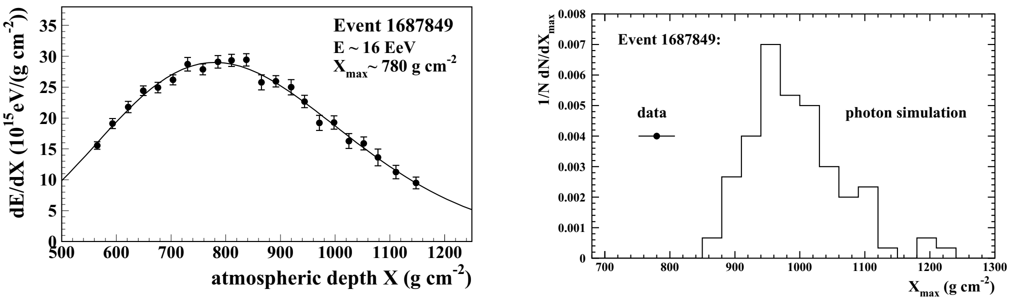

Figure 1: Left: longitudinal shower profile of a typical event recorded by the Auger fluorescence detector. Right: data point with statistical uncertainty along with X_{max} distribution from photon simulations. Figures from Ref. [9].

2 Photon searches with the Pierre Auger Observatory

Deviation of the recorded data from expectations for showers induced by nuclear primaries can offer a clear signature, which is detectable by fluorescence telescopes as well as by arrays of surface detectors, by using the most sensitive observables connected to the cascade development. By combining both the detection techniques, the Pierre Auger Observatory hybrid instrument has an unique potential for these kind of searches.

Based on the direct observation of the longitudinal shower profile by the Auger fluorescence detector a limit of 16% (95% c.l.) was obtained on the photon fraction in the integral cosmic ray flux above 10 EeV (see Ref. [9]). For a sample of high quality reconstructed events, the measured discriminant observable, the depth of shower maximum X_{max}, was compared to the theoretical expectations for showers of the same geometry and energy, but assuming a primary photon origin. In Fig. 1 (left) the reconstructed longitudinal profile is plotted for a typical event. In the right panel the data point is plotted along with the corresponding photon simulations. The difference between data and average photon X_{max} value is $\sim 200\ \mathrm{g\,cm}^{-2}$, which corresponds to a deviation of 2.9 in units of standard deviations, i.e. a photon origin is unlikely for this event.

The results from the search for UHE photons with the Auger ground array have been published in Ref. [10]. The sensitive observable was in this case a combination of the risetime of the signal at 1000 m from shower core and the estimated shower front curvature. A detailed Monte Carlo study was performed to characterize the behavior of photon induced showers. A limit to the photon flux was derived by comparing photon-like events to the well known experimental exposure. The limit on the photon fraction was placed at the level of 2% (95%c.l.), see Fig. 4. In Fig. 2 shower front curvature and signal risetime are shown for data and photon simulations.

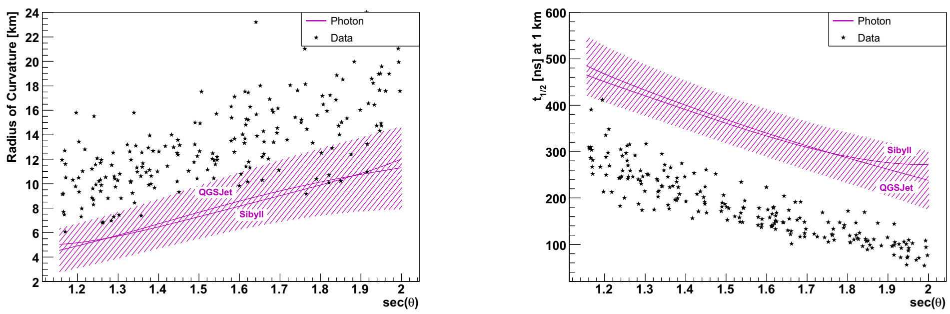

Figure 2: Shower front curvature (left) and signal risetime (right) for events recorded with the Auger surface detector (black) along with parameterizations from simulations of photon induced showers. Figures from Ref. [10].

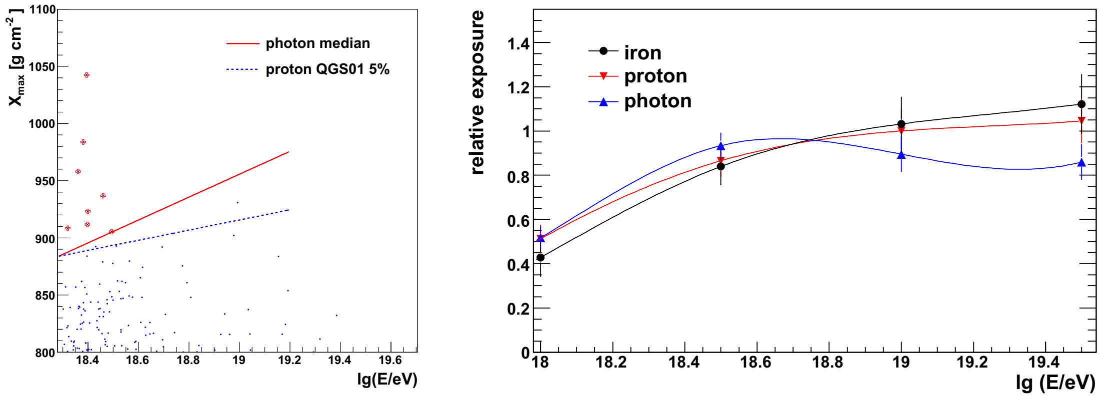

Figure 3: Left: closeup of the scatter plot of $X_{\max}$ vs energy for all events (blue dots) with $X_{\max}$ above 800 g cm^{-2} and energy above 2 EeV, all cuts applied. Red crosses show the 8 photon candidate events (see text). The solid red line indicates the typical median depth of shower maximum for primary photons. The dashed blue line results from simulations of primary protons. A fraction of 5% of the simulated proton showers had $X_{\max}$ values larger than indicated by the line. Right: relative exposure to primary photons, protons and iron nuclei normalized to protons at 10 EeV. Polynomial fits are superimposed to the obtained points. Figures from [11].

3 First limits on the photon fraction at EeV energies

Observations in hybrid mode (i.e. observed by both the fluorescence and surface detectors) are also possible at energies below 10 EeV. Decreasing the energy threshold increases the event statistics, which to some extent balances the factor ∼10 smaller duty cycle compared to observations with the ground array alone.

A high quality hybrid data sample has been selected applying a set of reconstruction quality, fiducial volume and cloud cuts (for details see Ref. [11]). The closeup of the $X_{\max}$ vs energy plot for all the selected events with $X_{\max}$ above 800 g cm^{-2} and energy above 2 EeV is shown in Fig. 3 (left). Events with large $X_{\max}$ values are of interest, in particular events having $X_{\max}$ above the photon median value have been deemed as "photon candidates". The observed $X_{\max}$ of all the photon-like events has been compared with expectations from photon induced showers of the same geometry and energy. 8, 1, 0, 0 photon candidate events have been found with energies greater than 2, 3, 5 and 10 EeV, respectively (red crosses in Fig. 3 left panel). Their number, compatible with expectations from nuclear background, has been used to obtain an upper limit to the photon fraction in data by accounting for the corresponding cut efficiency. The limit is conservative and model independent as no nuclear background is subtracted.

A detailed study of the detector efficiency as a function of energy for different primary particles has been performed. The acceptance for photons is close to the acceptance for nuclear primaries, and the relative abundances are preserved to a good approximation at all energies, see Fig. 3 (right). A correction factor, conservative and independent of assumptions about the actual primary fluxes, has been derived and applied to the selected data [11].

Upper limits of 3.8%, 2.4%, 3.5% and 11.7% on the fraction of cosmic-ray photons above 2, 3, 5 and 10 EeV have been obtained at 95% c.l.. Uncertainties connected to the variation of the selection cuts within the experimental resolution don't affect the derived limits. The total uncertainty in $X_{\max}$ is ∼16 g cm^{-2} . Increasing (reducing) *all* reconstructed $X_{\max}$ values by this amount changes the limits to 4.8% (3.8%) above 2 EeV and 3.1% (1.5%) above 3 EeV, while the limits above 5 and 10 EeV are unchanged. The new hybrid limits [11] (Auger HYB) and surface array limits [10] (Auger SD) are shown in Fig. 4 along with other experimental results, model predictions and GZK bounds.

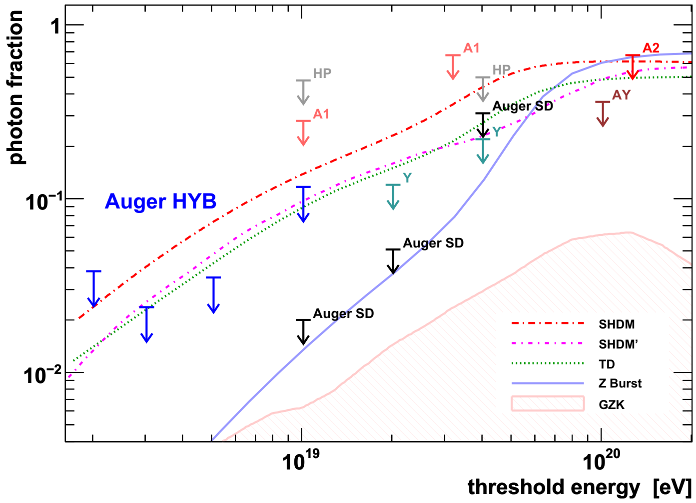

Figure 4: Upper limits on the photon fraction in the integral cosmic-ray flux for different experiments: AGASA (A1, A2), AGASA-Yakutsk (AY), Yakutsk (Y), Haverah Park (HP). In black limits from the Auger surface detector (Auger SD) [10], in blue new hybrid limits above 2, 3, 5, and 10 EeV (Auger HYB) [11]. Lines indicate predictions from top-down models. The shaded region shows expected GZK bounds [4]. Figure taken from Ref. [11].

4 Conclusions

The Pierre Auger Observatory already demonstrated its unique potential both for UHECR composition studies and UHE photon searches. The derived photon bounds provide a test of model predictions in different energy ranges and using different experimental techniques thus giving an independent confirmation of the model constraints. When completed by the northern site its collection area will increase by a factor 8 and gain unprecedented statistics at the highest energies. Photon fractions well below 0.1% (as expected from the GZK process) will be in reach.

Acknowledgments

This work was supported by BMBF (Bundesministerium für Bildung und Forschung). Special thanks to the organizers and the staff of the XLIV Rencontres de Moriond. Thanks to all the colleagues for the stimulating discussions and for the very good time in the snow.

References

1. Pierre Auger Collaboration [J. Abraham et al.], *Nucl. Instr. Meth. A* **523** (2004), 50–95.
2. M. Unger [Pierre Auger Collaboration], *30th ICRC, Mérida, Mexico,* **4** (2007), 373.
3. D. Allard, E. Parizot, and A. V. Olinto, *Astropart. Phys.* **27** (2007), 61–75.
4. G. Gelmini, O. Kalashev, and D. V. Semikoz, (arXiv:0706.2181 [astro-ph]).
5. P. Bhattacharjee and G. Sigl, *Phys. Rep.* **327** (2000), 109.
6. Pierre Auger Collaboration [J. Abraham et al.], *Phys. Rev. Lett.* **101** (2008), 061101.
7. R. Ulrich *et al.*, *Nucl. Phys. B Proc. Suppl.* **175** (2008), 121–124.
8. M. Risse and P. Homola, *Mod. Phys. Lett. A* **22** (2007), 749.
9. Pierre Auger Collaboration [J. Abraham et al.], *Astropart. Phys.* **27** (2007), 155.
10. Pierre Auger Collaboration [J. Abraham et al.], *Astropart. Phys.* **29** (2008), 243.
11. Pierre Auger Collaboration [J. Abraham et al.], (arXiv:0903.1127 [astro-ph]).

MULTI-FREQUENCY SEARCH FOR ASTROPHYSICAL SOURCES OF THE AUGER UHECR EVENTS

S. COLAFRANCESCO
ASI-ASDC, c/o ESA/ESRIN, Via G. Galilei,
I-00040 Frascati, Italy

We present the results of a multi-frequency search for the possible astrophysical counterparts of Pierre Auger Observatory UHECR events. We further discuss the methodology, the main results and the implications of our search.

1 Introduction

The recent observation of a directional correlation of the most energetic $E > 57$ EeV) Pierre Auger Observatory (PAO) events with the position of nearby AGNs [1], [2], complemented with the observation of he GZK effect [4], provides hints for an extragalactic origin of the most energetic cosmic rays reaching the Earth. The correlation has maximum significance for CRs with energies greater than $5.7 \cdot 10^{19}$ eV and AGNs at a distance less than $\lesssim 71$ Mpc. At this energy threshold, 20 of the 27 events correlate within 3.2 degrees with positions of a nearby AGNs from the Veron-Cetty catalog [3,1]. In addition, the spatial distribution of the Auger events seems to cluster in the direction of the nearby radio galaxy Centaurus A. This source, together with the other radio galaxy M87 in Virgo, has already been singled out as a potential cosmic ray accelerator on the basis of gamma-ray data [5]. Such kind of anisotropy – if confirmed by the increasing event statistics that will be accumulated by the PAO – can be considered as a strong hint for an extragalactic origin of the most energetic CRs [6].

Various studies have already searched for a statistical association of various populations of active and/or normal galaxies with the Auger events: X-ray selected AGNs (mostly Sy1, Sy2 galaxies, LINERS [7]), spiral HI galaxies (in search for possible magnetars association [8]), IRAS galaxies (in search for a cross-Correlation between UHECR arrival distribution and Large-Scale Structures [9]), AGNs from the the incomplete VCV2001 catalog plus a NED search extension [10,11]. However, all studies based on such population analysis are biased by the fact that there is no complete nearby AGN catalogue.

The interest for nearby AGNs as viable counterparts of the Auger UHECRs is motivated by the fact that they can eject highly relativistic particles in their jets. It has been speculated in the past that supermassive black holes at the centers of active galaxies power particle flows that create the opportunity for particle acceleration to super-EeV energy [12]. However, it has been shown that conventional long-lived AGN jets cannot be the primary site of UHECR acceleration since they fall short of satisfying that power threshold $L_{bol} \gtrsim 10^{45} E_{20}^2$ erg/s necessary to recover the flux of UHECRs from nearby sources (see e.g. [13]). In addition, acceleration (Fermi-I and/or Fermi-II types) at relativistic or ultra-relativistic shocks does not seem to be very efficient in accelerating particles to UHECRs (see Lemoine at this Meeting, see also Ostrowki 2009).

However, one possibility to overcome the previous power threshold is to invoke bursts of cosmic rays of extreme energy [13,14] (and neutrinos [15]) produced in objects dominated by SMBHs like AGNs. In such flares of CRs their acceleration mechanism has to be anyway sufficiently efficient as to produce the flux and energy spectra of UHECRs observed.

2 A multifrequency approach

In this study we summarize the results of an extensive study of the possible astrophysical counterparts of the 27 PAO events with $E > 57$ EeV taking into account all the following selection criteria:

Spatial constraints. We search for high energy cosmic sources (galactic: PSRs, SNRs, Molecular Clouds; and extragalactic: AGNs, Radio Galaxies, Galaxies, galaxy Clusters) spatially associated with PAO events within a circle of 3 deg radius on the sky from the arrival direction of each PAO event (the circle radius of 3 deg has been choosen as a reference value for the association).

Spectral constraints. We search for high energy cosmic sources associated with non-thermal synchrotron emission at high frequency in the WMAP all sky survey (covering the frequency range from 23 to 94 GHz). The synchrotron emission features of the cosmic sources would indicate the presence of high-E particles ($\nu_{synch} \approx 3.7MHz \cdot B_{\mu G}(E_e/GeV)^2$, where E_e is the particle energy in units of GeV and $B_{\mu G}$ is the strength of the magnetic field). We select the possible candidates according to their multi-frequency emission features and especially according to their possible X-ray emission and gamma-ray emission from Gev to TeV range.
Sources that are observed in the radio, X-ray and gamma-ray ranges simultaneously show, in general, quite flat particle spectra that makes more likely their extension up to very high energy. Finally we select as the most likely candidates those sources that are variable in these frequency ranges.

Horizon constraints. We select as possible candidates only those sources that have redshift $z < 0.02$ corresponding to a distance of $\sim 100h_{70}^{-1}$ Mpc in a flat, vacuum-dominated CDM cosmology with H_0=70 km s^{-1} Mpc^{-1}, Ω_M=0.3, Ω_Λ=0.7.

We report in Table 1 the list of the likely candidates (sources that satisfy all the previous constraints and that have a known redshift) as well as of the other possible associations (sources that do not have a definite counterpart) to the observed PAO events. Fig.1 shows the distribution of the PAO events superposed to the WMAP Q-band all sky map and with the most likely associated astrophysical candidates. Blazars and radio galaxies are considered in our approach as likely candidates (apart from some non secure identification in NED astronomical database), while Sayfert galaxies, Liners, SNe, SNR and unidentified radio sources are only considered as possible associations because of either lack of strong variability or lack of source identification. We also perform the same analysis on two different kind of random realizations, i.e. a completely random distribution of UHECR events (labelled in Tab1 as Random) and a distribution of UHECR events that maintain the same spatial pattern on the sky of the Observed one but with a random rotation angle (labelled in Tab1 as Random rotated). The results of the association study is also reported Tab1 and it shows a systematic decrease in both the number of UHECR events that are associated to astrophysical sources (13 in the Random and Random rotated vs. 25 in the Observed realization out of 27 observed by the PAO) and in the number of candidate and possible associations.

Table 1: PAO events: statistics.

Events with candidates	BLLac	Radio galaxies	Seyfert galaxies	Liner	SN SNR	Other sources	Radio Sources
Observed							
25							
candidates	2	7					
possible	4		27	8	4	10	21
Random							
13							
candidates	1	4					
possible			3	3			6
Rotated random							
13							
candidates	1						
possible			4				9

3 Discussion

The multi-frequency study of the possible astrophysical association to the PAO events that we present here is strictly valid under the small angle approximation hypothesis, i.e. that all of the UHECRs are protons. PAO events that are close to each other (forming doublets and/or triplets) require, in our analysis only one candidate source being their spatial separation consistent with the average angle deflection for protons.
If the UHECRs are instead heavy nuclei (see Allard at this Meeting) the spatial association study is not meaningful because of the large angle deflection expected for nuclei while diffusing in the Galactic and extra-galactic magnetic fields. Even though the average angular deflection of such nuclei is not fully understood, a lower number of astrophysical sources are sufficient in principle to reproduce the whole PAO event distribution of the sky. In fact, we found that, e.g, only 8 sources (3 radio galaxies, 1 BL Lac and 4 Sy2 galaxies with radio jet emission) are sufficient to reproduce the arrival directions of 22 out of the 27 PAO events with $E > 57$ EeV assuming a 30 deg radius uncertainty circle (note also that three of these events, events no. 23, 24 and 25, form a triplet).

All of the most likely association sources (radio galaxies, Blazars and Sy2 galaxies) are likely variable sources thus making them good candidates from the point of view of both the energetics and acceleration mechanism. In our model, the acceleration of UHECRs occurs as magnetically confined blobs (as those seen in the jets of many Blazars and radio galaxies) ejected from the inner regions of the SMBH-accretion disk system with a Lorentz bulk motion factor γ, travel through the surrounding galaxy medium and encounter particles (protons, nuclei, seen from the blob's rest frame as relativistic particles with a Lorentz factor γ), isotropize them magnetically within the blob and up scatter them with an effective Lorentz factor γ^2 seen in the observer's rest frame (see [14] for details).
Such a scenario produces both CR acceleration and high-E emission of radiation by accelerating leptons by the same mechanisms. Therefore, the scenario here proposed predicts that all of the very high-E emission from Blazars and radio galaxies is variable and due to the interaction a set of relativistic, magnetically-confined plasmoids with the ambient medium / radiation fields; in these respects such a model can be tested through multi-frequency and multi-time scale observations of AGN-like (Blazar, radio galaxies, Sy-like galaxies) objects that are becoming available with the advent of the new generation GeV (Fermi, AGILE) and TeV (HESS, MAGIC,

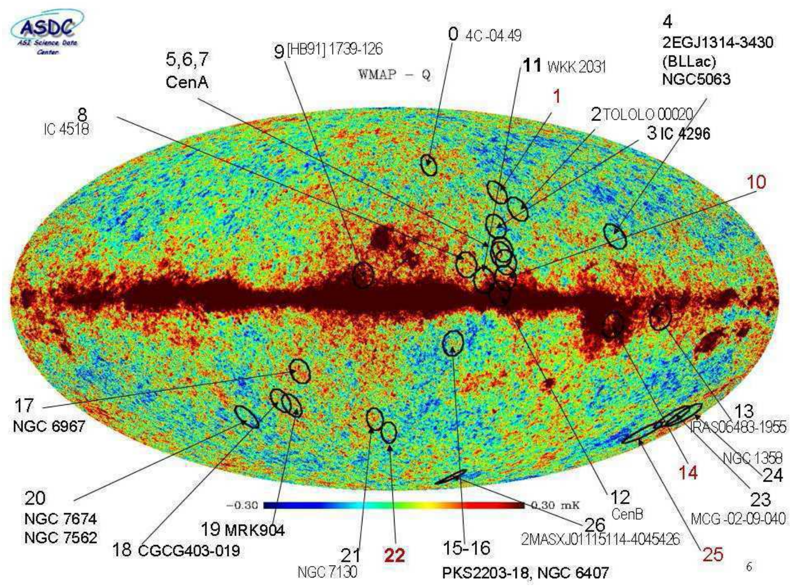

Figure 1: The WMAP Q-band (23 GHz) all sky map and the PAO events superposed (circles) with the most likely associated astrophysical candidates as labelled.

CTA) experiments.

The possibility to perform a true astrophysical study of the cosmic sources of UHECR events is strictly related to the possibility that the UHECRs are protons (i.e. we have small angle deflection of such particles by intervening magnetic fields) and that the CR sources produce a relative accelerated leptonic counterpart that could emit radiation visible through a multi-frequency strategy.

References

1. Abraham, J. et al. [Pierre Auger Collaboration] 2007, Science, 318, 938
2. Abraham, J. et al. [Pierre Auger Collaboration] 2007, arXiv:0712.2843v1
3. M-P Veron-Cetty and P Veron, 2006, A&A, 455, 773 accessed via http://vizier.u.strasbg.fr/viz-bin/VizieR
4. K. Greisen, 1966, Phys. Rev. Lett. 16 748; G.T. Zatsepin and V.A. Kuz'min 1966, Sov. Phys. JETP. Lett. 4 78
5. Anchordoqui, L.A. et al. 2004, Phys.Lett.B, 600, 202
6. Kampert, K.H. 2008, arXiv:0801.1986
7. M R George et al. 2008, arXiv:0805.2053v1
8. G Ghisellini et al. 2008, arXiv:0806.2393v1
9.) Takami, H. et al. 2008, arXiv:0812.0424
10. I V Moskalenko et al. 2008, arXiv:0805.1260v1
11. Gureev, S. & Troitsky, S. 2008, arXiv:0808.0481
12. Gaisser, T.K. 1996, AAS, 189, 5902
13. Farrar, G. & Gruzinov, A. 2008, arXiv:0802.1074
14. Colafrancesco, S. 2009, preprint
15. Halzen, F. 2008, arXiv:0809.1874v1

3. Gamma Ray Bursts

Gamma Ray Burst results from the Swift mission

P.A. Evans

X-ray and Observational Astronomy Group, Department of Physics and Astronomy, University of Leicester, LE1 7RH, UK

In this review I introduce the Gamma Ray Burst phenomenon, and overview the contribution of the *Swift* satellite to this field in the 4 years since its launch. I focus on some of the questions which *Swift* has helped to answer, as well as the new mysteries it has uncovered. I also introduce the automated analysis of the *Swift* X-ray data for GRBs, which makes *Swift* the first mission to provide public, reduced, analysed data products, ready for scientific use within hours of the data being collected.

1 Introduction

Gamma Ray Bursts are the most powerful phenomena currently known, with isotropic luminosities of order 10^{53} erg s^{-1}. They were originally discovered by the Vela satellites (Klebesadel, Strong & Olson[1]) looking for violations of the Nuclear Test Ban Treaty. Later the Burst and Transient Source Experiment (BATSE) on board the Compton Gamma Ray Observatory discovered thousands of bursts, which were isotropically distributed on the sky (Fig. 1, e.g. Meegan et al.[2]), suggesting a cosmological origin.

BATSE also found evidence for two classes of GRBs. The histogram of GRB durations (Fig. 1) shows a strong bimodality, indicative of 2 populations of bursts. Further, the shorter population tended to have harder spectra than the long ones (Kouveliotou et al.[3]).

A watershed event in the history of GRBs occurred in 1997, when BeppoSAX discovered the first afterglow – a fading, uncatalogued X-ray source at the location of GRB 970228 (Costa et al.[4]; van Paradijs et al.[5]; Frail et al.[6]). Subsequent (optical and X-ray) afterglow discoveries and redshift measurements confirmed the cosmological nature of GRBs. Long GRBs were found to be associated with star forming galaxies, supporting the idea that they represent the death of massive stars (Paczynski[7]).

Afterglows fade rapidly, and typically follow-up observations began several hours post-trigger. Because of this, no afterglow of a short GRB (which are intrinsically fainter than their long counterparts) was detected prior to the launch of *Swift*. The most widely accepted progenitor model for a short burst was the merging of two neutron stars or a black hole-neutron star binary (e.g. Narayan, Paczynski & Piran[8]).

The generally accepted model for emission from a GRB is the fireball model (e.g. Rees & Mészáros[9], Sari, Piran & Narayan[10]). In this model the GRB launches a jet of highly relativistic material towards the observer. This jet contains 'shells' moving with different bulk Lorenz factors. Collisions between these shells ('internal shocks') dissipate the energy which we see as the GRB itself – the 'prompt emission'. The interaction of the jet with the ambient medium forms an external shock, which emits via synchrotron radiation and produces the afterglow. For

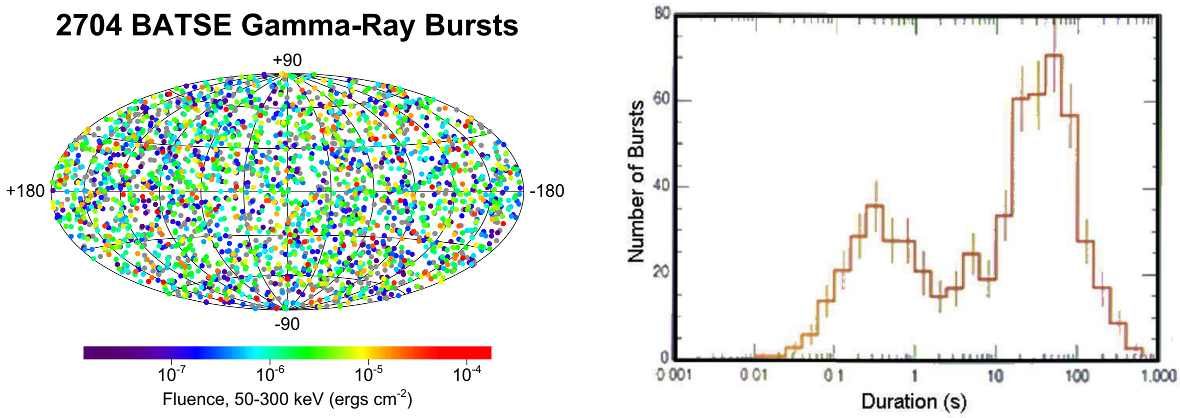

Figure 1: The distribution of GRB positions and durations as seen by BATSE[2], 3.

detailed reviews of GRBs, see e.g. Piran[11]).

2 Swift

The *Swift* satellite (Gehrels et al.[12]), launched in November 2004, is a NASA/UK/Italy mission whose primary goal is to study the GRB phenomenon. To this end it contains 3 instruments and has a unique, rapid and accurate slewing capability. The Burst Alert Telescope (BAT; Barthelmy et al.[13]) has a ∼2-sr field of view, in the 15–350 keV energy range, and detects GRBs at a rate of ∼100 per year. The 0.3–10 keV X-ray Telescope (XRT; Burrows et al.[14]) and the UV/Optical Telescope (UVOT; Roming et al.[15]) have smaller fields of view, and are capable of performing detailed follow-up analysis. As soon as BAT trigger on a new GRB, the satellite determines immediately if it is safe to observe the burst with the XRT & UVOT, and if so it automatically slews to the burst, typically arriving on-target within ∼100 s. While UVOT has detected only ∼40% of these GRBs, the XRT has detected >90%, the majority of them within minutes of the event. Thanks to recent improvements in the XRT position determination (Goad et al.[16]; Evans et al.[17]) *Swift* currently rapidly provides positions accurate to ∼2 arcsec for most GRBs. In this talk I was invited to review the contribution of the *Swift* satellite to GRB research.

Prior to launch there were many outstanding questions about GRBs, and it was hoped that *Swift* would answer many of them. Zhang & Mészáros[18] detailed many of these. As Zhang[19]) points out, while *Swift* has helped solve many of those puzzles, it has also asked many new questions.

In Section 3 I consider some of the answers that *Swift* has provided, and in Section 4 I present some of the new questions. In Section 5 I introduce a catalogue of XRT results for GRBs which can be (and is being) used to explore some of these questions. I also present tools which allow users to easily analyse XRT observations of any source.

3 Questions and answers

3.1 Short GRBs and GRB progenitors

One of the big hopes for *Swift* was that, given its rapid slewing ability, it would find the elusive afterglows of short GRBs. This goal was realised on May 9th 2005, when Swift-BAT triggered on GRB 050509B; an X-ray afterglow was reported two and a half hours later (Kennea et al.

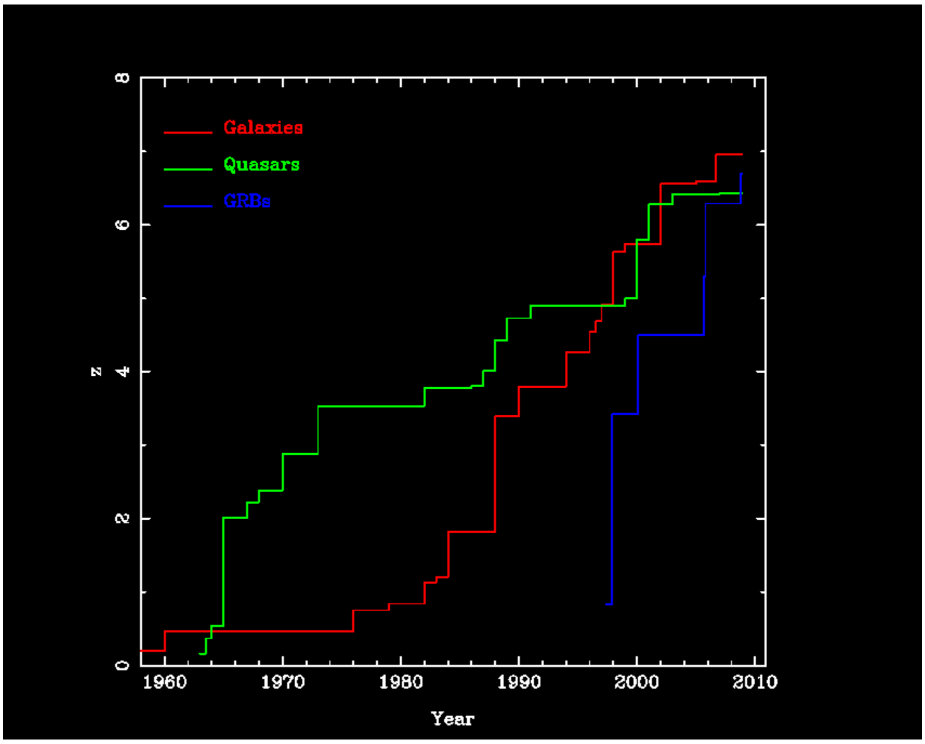

Figure 2: The evolution of redshift record holder with time, for GRBs, Galaxies and QSOs (courtesy of Nial Tanvir).

[20]), once the dataset had been received on the ground (note that, due to operational changes, were the same burst observed today the position would have been available within ∼10 minutes of the trigger and would have been a factor of four more precise). The afterglow was on the outskirts of an elliptical galaxy, confirming that the short GRB progenitors are distinct from long GRB progenitors. The first optical afterglow for a short GRB was not for a *Swift* burst, but one discovered by HETE: GRB 050709 (Butler et al.[21]; Fox et al.[22]), however subsequently *Swift* has found and localised many short GRBs, and they have been found in all types of galaxy. This supports the idea that short bursts arise from the merger of two compact objects.

Swift has also provided accurate localisations for hundreds of long GRBs, many of which also have ground-detected afterglows and over a hundred of which have spectroscopic redshifts (more than 70% of GRBs with redshifts were detected by *Swift*). Unlike short GRBs, long GRBs are only ever found in star-forming galaxies, and where the positions are accurate enough, they occur in the star forming regions of such galaxies. This provides strong support for the massive star progenitor model for long bursts.

3.2 New subclasses

One of the questions mentioned by Zhang & Mészáros (2004) was whether there were more subclasses of GRBs than the long & short types known prior to *Swift*. *Swift* has shown that the situation is more complex than was previously thought. GRB 050724 (Barthelmy et al.[23]) was a GRB with a short, hard pulse, followed by a longer period of softer emission. *Swift* classified this burst as long, whereas BATSE would have labelled it a short burst. This alone suggests that the 'long/soft' classification is GRB is far from ideal, since it is detector-dependent. Around half of the short GRBs seen by *Swift* to date have this extended soft emission, and a significant fraction of the BATSE short bursts also show it.

Further, GRBs 060614 and 060505 were nearby, long GRBs with no observed supernovae, down to very deep limits (e.g. Gehrels et al.[24]). Long GRBs are thought to signal the deaths of massive stars, and for nearby bursts an associated supernova is usually seen (e.g. Kulkarni et al.[25]; Galama et al.[26]; Stanek et al.[27]; Hjorth et al.[28]).

Whether these short bursts with extended emission and long bursts with no supernovae represent new classes of GRB is not currently clear; however *Swift* has shown that the old classification scheme is a oversimplified.

3.3 High redshift bursts

Due to their brightness GRBs are potentially extremely useful cosmological probes, and it was hoped pre-launch that *Swift* would detect high redshift bursts and allow us to probe the early universe. This hope has definitely been realised. As Fig. 2 shows, the redshift of the most distance observed GRB is rising rapidly, and it is likely that the most distant object known will soon be a GRB. To date, *Swift* has observed sixteen GRBs at $z > 3.5$, nine at $z > 4$ and four at $z > 5$. The most distant GRB with a spectroscopic redshift is GRB 080913 (Greiner et al. [30]) at $z = 6.7$. With an increasing number of telescopes capable of rapid infrared observations of GRBs, and instruments such as GROND and X-Shooter online, the likelihood of identifying high redshift bursts is ever-increasing.

4 New mysteries

4.1 X-ray flares

Although rebrightening features had been seen by BeppoSAX (e.g. Amati et al.[31]), it was not until the launch of *Swift* that the rate and brightness of X-ray flares was revealed. Flaring behaviour is seen in the majority of X-ray afterglows, and studies of *Swift* data (Falcone et al. [32]; Chincarini et al.[33]) have shown them to have similar properties to the prompt emission. They also appear superimposed on the afterglow, rather than being part of it. It is currently believed that flares arise from late internal shocks, however flares can be seen more than a day after the trigger, suggesting that the GRB must be active for much longer than originally thought. This presents a challenge to central engine models.

4.2 Jet breaks

If the outflow from a GRB is collimated in a jet, as widely believed, one should observe a 'jet break' as the material decelerates. Two factors contribute to this: the relativistic beaming angle becomes wider than the physical opening angle of the jet, and the sideways expansion velocity of the jet becoming non-negligible compared to the forward velocity. Observationally, this jet break should appear as an achromatic steepening of the light curve. In fact, this phenomenon has been seen very infrequently in *Swift* data, the reason for which is currently unclear. Curran et al.[36] suggested that the signal-to-noise ratio of the XRT data is not sufficient to reliably detect jet breaks. Racusin et al.[37] considered a wide range of theoretical models for the break, and found that many of the bursts could potentially harbour jet breaks. Alternatively, de Pasquale et al.[38] suggested that the jet is much more complex than previously thought, with the optical and X-ray emission arising from different physical regions; an achromatic break thus ceases to be the observational signature of the jet break. The authors suggest that the end of the plateau phase in the X-ray (see below) could be a jet break. Support for a complex jet structure can be found, for example, in the very bright and well studied GRB 080913B (Racusin et al.[39]), at $z = 0.9$.

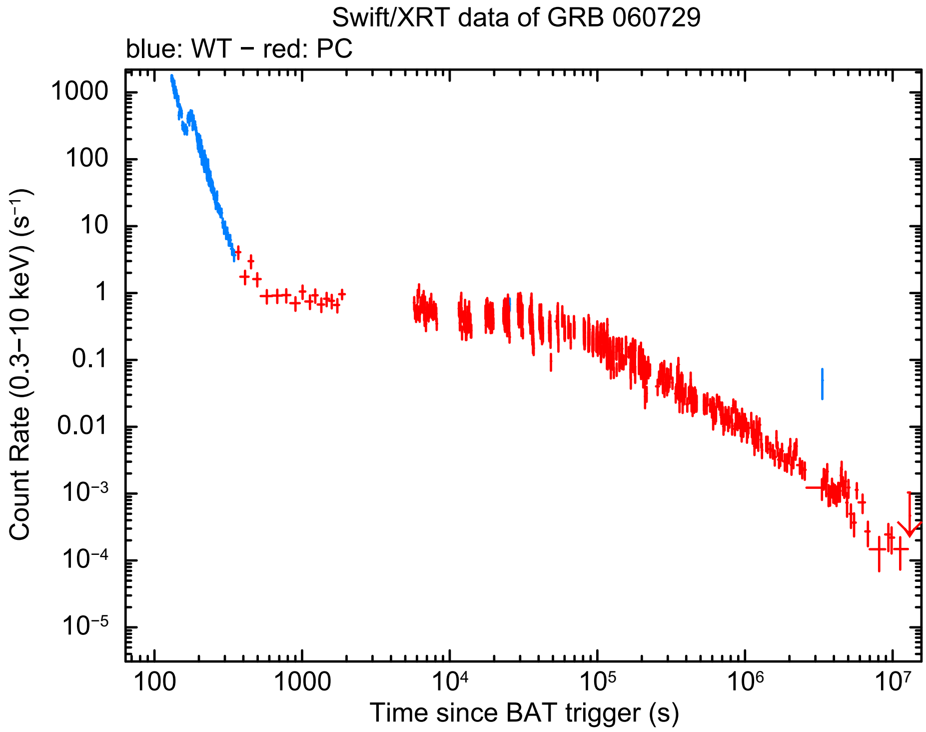

Figure 3: GRB 060729 (Grupe et al. [34]); an example of the 'canonical' light curve (light curve from Evans et al. [17,35]

At present there is no definitive, widely accepted answer to the question of how many jet breaks *Swift* has seen, and whether this matches expectations, and if not, why not.

4.3 Complex X-ray afterglows

Prior to *Swift* almost all X-ray afterglow observations were sparse, showing simple power-law decays believed to arise from synchrotron radiation from the external shock. It was anticipated that the rapid *Swift* observations would show the same at early times.

In fact, *Swift* X-ray afterglows were seen to be much more complex than this. The most common morphology is the so-called 'canonical light curve' (Fig. 3) which shows a steep decay, a shallow 'plateau' and then a moderate decay. The former is interpreted as 'high latitude' emission, that is the prompt emission seen from off-axis and hence arriving at the observer after the main, on-axis emission has ceased. This was predicted prior to the launch of *Swift* (Kumar & Panaitescu[29]) but was expected to be hidden beneath the afterglow emission. The final, moderate decay is believed to be the normal synchrotron emission from a forward shock, as seen prior to *Swift*, although Evans et al. [17] have shown that in many cases the data are not consistent with this interpretation within the standard fireball model.

The plateau phase is less well understood, and has been much discussed in the literature (e.g. Nousek et al. [40]; Liang et al. [41]; Dado et al. [42]). It is generally believed to indicate energy injection into the afterglow, for example from ongoing activity of the central engine, although no consensus has yet been reached on the details of this emission, or even if this is the cause of the plateau.

This 'canonical' light curve shape, while common, accounts for less than half of the GRBs. Evans et al. [17] recently produced the first XRT catalogue of GRBS, and they identified four different common types of light curve, shown schematically in Fig. 4, as well as a class of 'oddballs' – unique light curve morphologies which do not fit the classes in Fig. 4. For the four

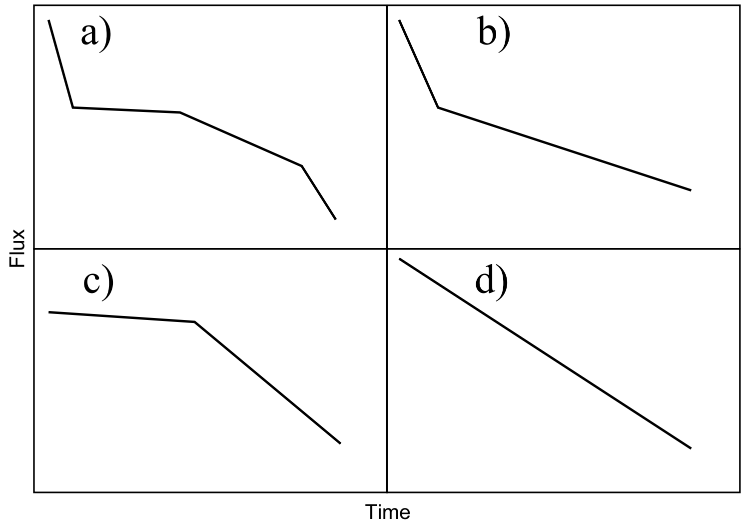

Figure 4: Schematic diagrams of the different light curve morphologies seen, from Evans et al. [17]. Panel a) shows the so-called 'canonical' light curves. Panels b)–c) are those with one break, either flattening (b) or steepening (c). Panel d) are those with no breaks. There are also 'oddballs' - uniquely shaped light curves which do not fit any of these classes.

types of curve in Fig. 4 Evans et al. produced a spectrum for each phase of the light curve, and compared the resulting temporal index (α) and spectral index (β) pair with those predicted by theory. As seen in Fig. 5, the majority of the data points do not lie in the region permitted by the standard fireball model.

If energy injection takes place, the grey bands mark the lower limit of the (α, β) space permitted by the fireball model, however this reduces the diagnostic power of the model unless some physical limit on the rate of energy injection is derived. Of particular note are the points in panel d). These correspond to canonical bursts which show a break after the 'final' decay phase; a break usually interpreted as a jet break. However Fig. 5 shows that these points are inconsistent with post-jet break theory: either the break reflects the end of energy injection but not a jet break – in which case energy injection must continue for $\sim$days, or the break is a jet break, but energy injection is still ongoing, lasting $\sim$weeks. Either scenario is difficult to explain in the context of central engine models.

5 Online *Swift*-XRT data

Evans et al. [17] presented a catalogue of XRT observations of GRBs complete to GRB 080723B. The creation of the light curves, spectra and high-precision localisations used in this paper was fully automated and extensively verified. The tools which achieve this are automatically applied to any new GRB observed by *Swift* and the light curves, spectra and positions are available to view (and download) as soon as the observation data are available, via http://www.swift.ac.uk/xrt_products. Full details of how these are produced are given in Evans et al. [17].

As well as observing GRBs, *Swift* provides Target of Opportunity and Guest Investigator programs and spends much of its time observing targets approved through these schemes. The XRT data can be analysed online using the web tools at http://www.swift.ac.uk/user_objects/. These produce publication-quality light curves, spectra and positions automatically, for any given point-source observed by the XRT.

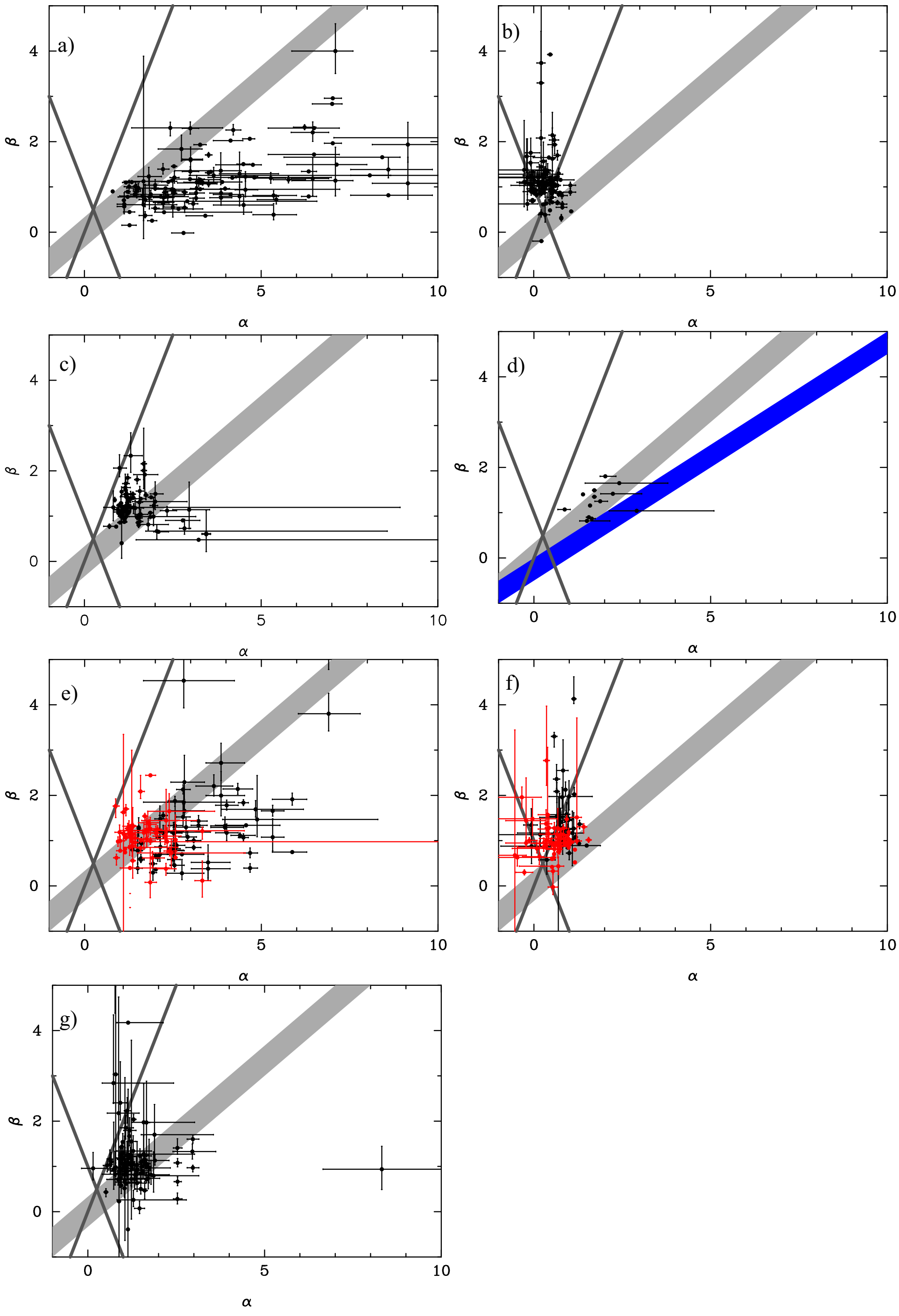

Figure 5: Spectral indices (β) vs temporal indices (α) for different light curve phases; see Fig. 4. Panels a)–d) are for the 'canonical' light curves and show the values from the steep decay, plateau, 'normal' and 'post-jet-break' phases. Panels e)–f) show the values from those light curves showing a single break; the steeper of the segments are plotted in e) and the shallower in f). The black and red points indicate type b and c light curves respectively (see Fig. 4). Panel g) show the values for those light curves which do not contain a break. The grey bands mark the areas permitted by standard afterglow closure relationships; the narrow grey lines are for the fast-cooling regime. The blue band in panel d) marks the range permitted by post-jet-break closure relationships.

References

1. R.W. Klebesadel, I.B. Strong, R.A. Olson, Ap.J **182**, L85 (1973)
2. C. Meegan et al. Nature **355**, 143 (1992)
3. C. Kouveliotou et al., Ap.J **413**, L101 (1993)
4. E. Costa et al. Nature **387**, 783 (1997)
5. J. van Paradijs et al. Nature **386**, 686 (1997)
6. D. Frail et al. Nature **389**, 261 (1997)
7. B. Paczynski Ap.J **494**, 45 (1998)
8. R. Narayan, B. Paczynski, T. Piran Ap.J **395**, L83 (1992)
9. M.J. Rees & P. Mészáros ApJ **430**, L93 (1994)
10. R. Sari, T. Piran, R. Narayan ApJ **497**, 17 (1998)
11. T. Piran RvMP **76**, 1143 (2005)
12. N. Gehrels et al., ApJ **611**, 1005 (2004)
13. S.D. Barthelmy et al., SP.Sci. Rev **120**, 143 (2005)
14. D.N. Burrows et al., SP.Sci. Rev **120**, 165 (2005)
15. P.W.A. Roming et al., SP.Sci. Rev **120**, 95 (2005)
16. M.R. Goad et al., AA **476**, 1401 (2007)
17. P.A. Evans et al., MNRAS, in press, (arXiv 0812.3662)
18. B. Zhang & P. Mészáros JMPA **19**, 2385 (2004)
19. B. Zhang ChJAA **7**, 1 (2007)
20. J.A. Kennea et al., GCN Circ , 3383 (2005)
21. N.R. Butler GCN. Circ , 3570 (2005)
22. D.B. Fox Nature **437**, 845 (2005)
23. S.D. Barthelmy et al. ApJ **635**, L133 (2005)
24. N. Gehrels et al. Nature **444**, 1044 (2006)
25. S.R. Kulkarni et al., Nature **393**, 35 (1998)
26. T.J. Galama et al., Nature **395**, 670 (1998)
27. K.Z. Stanek et al., Ap.J **591**, L17 (2003)
28. J. Hjorth et al., Nature **423**, 847 (2003)
29. P. Kumar & A. Panaitescu, ApJ **541**, 51 (2000)
30. J. Greiner et al., ApJ **693**, 1610 (2009)
31. L. Amati et al., NuPhS **69**, 656 (1999)
32. A.D. Falcone et al., ApJ **671**, 1912 (2007)
33. G. Chincarini et al., ApJ **671**, 1903 (2007)
34. D. Grupe et al., ApJ **662**, 443 (2007)
35. P.A. Evans et al., A&A **469**, 379 (2007)
36. P.A. Curran, A.J. van der Horst, R.A.M.J. Wijers MNRAS **386**, 859 (2008)
37. J.L. Racusin et al., ApJ., in press (arXiv 0812.4780)
38. M. de Pasquale et al., MNRAS **392**, 153 (2009)
39. J.L. Racusin et al., Nature **455**, 183 (2008)
40. J.A. Nousek et al., ApJ **642**, 389 (2006)
41. E. Liang, B.-B. Zhang, B. Zhang, ApJ **670**, 565 (2007)
42. S. Dado, A. Dar, A. De Rujula ApJ **646**, L21 (2006)

WHY THE SWIFT GRB REDSHIFT DISTRIBUTION IS CHANGING IN TIME

D. M. COWARD AND I. IMERITO
School of Physics, University of Western Australia
M013, Crawley WA 6009, Australia

We show how the observed gamma ray burst (GRB) redshift distribution is changing in time from time-dependent selection effects. For a subset of *Swift* triggered long duration bursts, we show that the mean time taken to acquire spectroscopic redshifts for a GRB afterglow has evolved to shorter times. We identify a correlation between the mean time taken to acquire a spectroscopic redshift and the measured redshift. This correlation reveals that shorter telescope response times, on average, capture more numerous smaller redshift bursts. This is evidence for a selection effect that biases longer response times with relatively brighter high redshift bursts. Conversely, for shorter response times, optically fainter bursts that are relatively closer are bright enough for spectroscopic redshifts to be acquired. This Malmquist type selection effect explains why the average redshift, z = 2.8 measured in 2005, has evolved to z = 2 by mid 2008.

1 Introduction

GRBs[a] are extremely bright transient events observed out to very high-z. Because of their high luminosity in γ-rays, they are an important probe to their host galaxies. Some GRBs have been associated with the collapse of massive stars via supernova signatures identified with the fading GRB optical afterglow[1,2]. The GRB-supernova connection implies that GRBs should follow the star formation rate of massive stars, and could be used as a complementary probe of the star formation rate in the high-z regime where optical data is deficient.

The XRT on board *Swift* provided the means to rapidly find GRBs with small error boxes, enabling fast follow up of the optical afterglow by dedicated ground-based telescopes. Prior to *Swift*, only about 50% of localized GRBs were identified with an optical afterglow. The high

[a] Hereafter GRB refers to bursts classified as long.

sensitivity of *Swift* coupled with the growing number of rapid response ground-based telescopes capable of spectroscopy were expected to fill the gaps. Despite this optimism, optical/NIR afterglows have been found for nearly 80% of GRBs, but only 40–50% of these have measured redshifts [3]. It is now very likely that some GRBs may not have an afterglow at all, and are defined as 'dark' bursts. Jakobsson et al. [4] define a dark burst from the spectral slope between the optical and X-ray.

The probability of obtaining a reliable GRB redshift is determined by the signal-to-noise ratio of the absorption or emission lines. Usually, multiple 'strong' lines are required, but this is hampered because many GRB OAs fade rapidly. Also, many GRB host galaxies are too faint for redshifts to be obtained, so the time taken to image the OA with medium to large telescopes capable of spectroscopy becomes critical. In addition to the afterglow extinction induced biases above, the so-called 'redshift desert' in $z \approx 1 - 2$ is a region where it is difficult to measure redshifts because of the lack of strong emission lines [8]. However, we note that for absorption lines, the Mg II doublet is prominent in $0.4 < z < 2.2$, so that the redshift desert may not play such a prominent role in redshift determination.

These problems were further highlighted by Coward et al. [5] and Coward [6]. They argued that in $z = 0 - 1$, the GRB redshift distribution should increase rapidly because of increasing differential volume sizes and evolution in the rate of star formation. This characteristic in the *Swift* redshift distribution was not apparent up to mid 2007. To account for this discrepancy, it is clear that other biases, independent of the *Swift* sensitivity, must be invoked.

A shift of the mean of the GRB redshift distribution was observed in the early part of the *Swift* mission [7] and by Burrows (private communication). This was attributed, partly to the improved sensitivity and more accurate localisation by *Swift*, resulting in a bias for fainter and higher redshift bursts. Jakobsson et al. [9] showed that within the first year of *Swift* the mean redshift for a subset of 28 bursts had drifted to about 2.8, about double that of the pre-*Swift* average redshift. This could explain the difference between the *Swift* redshift distribution compared to the other satellites prior to *Swift*, but it does not explain the trends occurring over a period of several years over the life-time of the *Swift* mission. In this study, we first identify the significance of the trends, and also show that they are a selection effect related to the efficiency of ground based telescopes performing spectroscopy of the GRB OAs.

2 Data analysis and results

We select 110 GRBs detected by *Swift* from 2005 March to 2008 September with high-energy emission duration greater than 4 s and with absorption and emission spectra of the OA that allowed a redshift measurement. From this population, we select a subset of 82 from GCN circulars that have response times, T_z, from when the burst was triggered by *Swift's* BAT to the acquisition of a spectroscopic redshift. We exclude those redshifts measured from the host galaxy at very late times as obtaining these spectra did not depend critically on the response time of the telescope.

We employ the time of the burst with the redshift data and analyse this data as a time series to probe how the statistical moments–i.e. the mean, variance and the discovery rate–evolve over the mission time of *Swift*. To determine if the data is non-stationary in time, a moving average filter spanning 4 nearest neighbours on each side of an event is employed.

Fig. 1, left panel, plots the raw redshifts and output from the moving average filter (using 4 nearest neighbours) as a time-series. Although there are fluctuations over periods of months, there is a clear downward trend in the redshift averages over a 3 year period. We test if the observed non-stationarity of the redshift time-series is related to how the redshifts are measured, in particular the time taken to obtain spectroscopic redshifts. The right panel plots both the response times to acquire these 82 redshifts and a moving average of this data, $< T_z >$, against

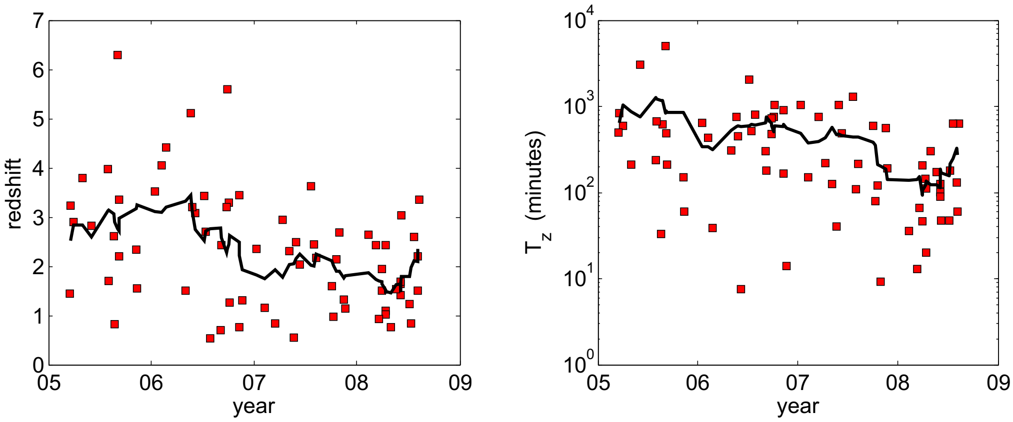

Figure 1: **Left panel**–Plot showing the time-series of 82 measured redshifts from 2005 March to 2008 September. A moving average filter using 4 nearest neighbours, solid line, reveals a trend towards smaller redshift. The non-stationarity of the time-series is evidence for a selection effect. **Right panel**–Time-series of the response time to acquire a spectroscopic redshift for the same GRBs as above. Over the same period, the average response time has reduced from about 1000 min to several 100s of minutes.

the time when the burst occurred. The plots shows a definite long term trend in the response times.

To investigate how T_z is affecting the selection of GRBs in a certain distance range, Fig. 2 plots T_z with z. Using a Spearman's correlation test, we find a correlation of 0.2 with a probability of a random correlation of 6%. This is compelling evidence that a selection effect is at work. Because the correlation coefficient is not large (but still significant), it is likely that there is a subset of redshifts that are responsible for this effect. In a preliminary study by Coward (in preparation), we find evidence that a subset of redshifts associated with faint OAs are the main contributors to the correlation. The dependance on OA brightness is a strong indicator of a Malmquist type bias at work.

3 Discussion

The correlation between $T - z$ and z has its root in the Malmquist bias. This type of brightness–distance relation plagues many survey galaxy catalogues. In our analysis, we assume that T_z has an affect on the observed sample of GRB OA brightness, which in turn affects the probability of obtaining a redshift. The Malmquist bias is more subtle in this case, but nonetheless has a significant impact on the GRB redshift distribution. The very fact that there is a measurable correlation at all implies the existence of a selection effect. What effect does this have on the potential for using the GRB redshift distribution to map out the evolution of the GRB progenitors over cosmic time? We point out that a simple mapping from the redshift distribution to GRB progenitor rate evolution will not be accurate unless the $T_z - z$ correlation is corrected for.

Another fascinating aspect of this study is the identification of the importance of the GRB OA luminosity function in determining the strength of the $T_z - z$ correlation. Recent simulations by Imerito et al. (in preparation) have shown that the Malmquist bias causing the correlation is sensitive to the relative numbers of bright OAs at low-z and high-z. This implies that the $T_z - z$ correlation may actually be used to probe the OA luminosity function. Instead of hindering work using the GRB redshift distribution, the $T_z - z$ relation may actually be a useful tool that will potentially provide new insight into GRB progenitor rate evolution.

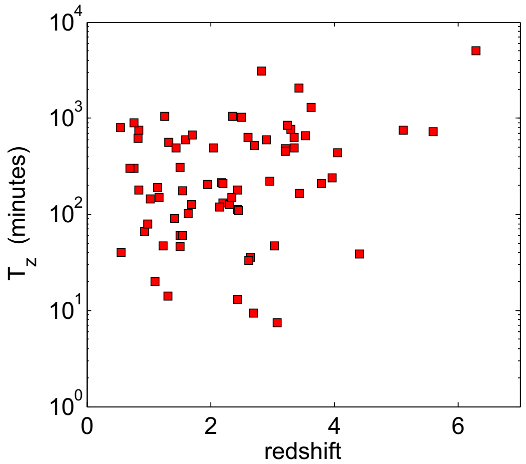

Figure 2: Scatter plot of the response time to acquire a redshift, T_z with the measured redshift, z. A Spearman's correlation test yields a positive correlation of 0.2, with a probability of a random correlation of 6%. The explanation for the correlation is a selection effect driven by the optical facilities engaged in spectroscopy. The evolving T_z causes a Malmquist type bias for redshift selection, via the optical brightness required to obtain a redshift measurement.

Acknowledgments

D. M. Coward thanks the organisers of the 2009 Rencontres de Moriond (Very High Energy Phenomena in the Universe) for providing a superb environment that fostered many exciting collaborative discussions. In particular, D.M. Coward thanks P. Evans of the *Swift* XRT team for taking an active interest in this study and taking the time to discuss the results with other *Swift* scientists. D. M Coward is supported by ARC grants DP0877550, LP0667494 and the University of Western Australia.

References

1. J. Hjorth *et al*, *Nature* **423**, 847 (2003)
2. K.Z Stanek, *et al*, *ApJ* **591**, L17 (2003)
3. N.R. Tanvir and P. Jakobsson, *Phil. Trans. Royal Society A* **366**, 1377 (2007)
4. P. Jakobsson *et al*, *ApJ* **617**, L21 (2004)
5. D. Coward, *New Astron. Rev.* **51**, 539 (2007)
6. D.M. Coward, D. Guetta D, R.R. Burman, A. Imerito, *MNRAS* **386**, 111 (2008)
7. E. Berger *et al*, ApJ **634**, 501 (2005)
8. F. Fiore., D. Guetta, S. Piranomonte, V. D'Elia, L.A. Antonelli, *Astronomy and Astrophysics* **470**, 515 (2007)
9. P. Jakobsson *et al*, *Astronomy and Astrophysics* **447**, 897 (2006)

GRB OBSERVATIONS WITH THE FERMI GBM

R.D. PREECE (for the Fermi GBM Team)
Department of Physics, University of Alabama in Huntsville,
Huntsville, AL, USA

The Fermi GBM is performing on orbit as expected. We have triggered on over 100 gamma-ray bursts, with four or so in common with the LAT. GBM covers the energies 8 keV to 40 MeV using two sets of overlapping detectors, with moderate energy resolution. I discuss the on-orbit performance of GBM, as well as the GRB global properties we are collecting, with an emphasis on burst spectroscopy.

1 Introduction

The *Fermi* Gamma-ray Burst Monitor (GBM) was designed for gamma-ray burst (GRB) spectroscopy, localization, and other analyses especially to support the Large Area Telescope (LAT). As such, it is not as sensitive as other, currently operating instruments, such as the Swift Burst Alert Telescope, nor is it required to pinpoint burst localizations for large ground-based telescopes. What it is designed for, to work in tandem with the LAT to identify interesting events and to provide continuum spectroscopy in the energies below the LAT threshold, it has done quite well.

The GBM consists of two type of detectors, 12 sodium iodide (NaI) detectors, placed around the *Fermi* spacecraft to preferentially cover the sky above the Earth's limb (assuming zenith pointing, on the average), plus two bismuth germanate (BGO) detectors, one each on opposite sides of the spacecraft. The NaI detectors cover the low-energy regime, 8 – 1000 keV, while the BGO detectors cover the energies in the middle regime between the NaI range up to the LAT threshold, 200 keV – 40 MeV. The placement and energy coverage of the NaI detectors make them suitable for coarse-grained GRB localization, with an estimated systematic error of roughly 3 degrees to be combined in quadrature with the statistical error. In Table 1, we present the average location errors for the different stages of the location process, as of February 2009: done on-board by the GBM Flight Software (FSW), done automatically on the ground using FSW generated background and source data selections, and performed by a human using their best judgement for data selection. This last method also includes a much better determination of the scattering of gamma-rays from the Earth's atmosphere than is possible on-board, as well as a one-degree grid of fluxes for each detector mapped onto the sky. The on-board grid has five degree resolution. The FSW localizations provide the basis for the LAT decision to repoint the spacecraft autonomously; with a fairly large field of view, the LAT needs only to know whether the trigger is on or out of the field of view. The requirement for GBM is $15°$ for this case.

Table 1: GBM Localizations.

Type of localization	Average Error (deg.)
FSW (on-board)	8.6
Ground (auto)	8.3
Human in-the-loop	4.4

2 Calibration

Extensive validation of our energy calibration has been done both before launch and also during flight. The flight electronics have been verified to be highly linear, so it becomes important to map out the non-linear light output of the NaI detectors, especially at the low energy end. We used several radioactive sources at various stages in the assembly and integration of the instrument, as well as accelerators in Germany (BESSY) and Stanford University [1]. In orbit, there are a number of lines at known energies in the background spectra that may be used both to validate the calibration as well as to serve as features to lock in the automatic gain control (AGC) function of the GBM FSW. For the NaI detectors, we use the 511 keV annihilation line for AGC, which is nearly always visible, as in Figure 1. As another valuable reference point, each spectrum exhibits a shoulder below the 32 keV Iodine K-shell electron escape feature. The BGO background spectrum is rich and varying, with spectral features due to activation from the hard radiation that the observatory passes through in the South Atlantic Anomaly, as well as persistent atmospheric features. The GBM team has settled on a line at 2.2 MeV for the AGC, which is also present nearly all the time (see Figure 1).

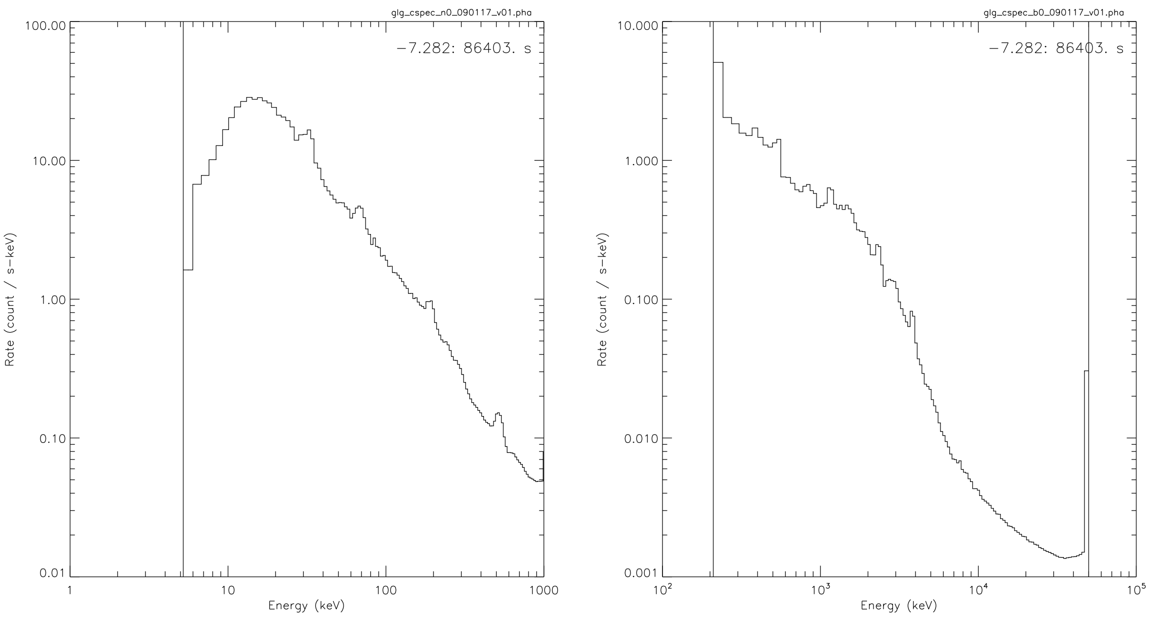

Figure 1: Typical GBM background spectra. *left*: NaI *right*: BGO

3 Data Products

As a service to the GRB community, the GBM team will provide a series of successively more refined data products, all in FITS (Flexible Image Transport System) format. The first, of course, will be the data themselves, which consist of three types: CPSEC, fully energy resolved (128 channel) spectroscopy data, one file for each detector, at medium time resolution (0.256 s during a trigger), spanning T $\pm$ 4000 s. CTIME data consists of 8 energy channels at 0.064 s time resolution, spanning T $\pm$ 1000 s. Both of these data products are delivered as a time series of spectra, FITS PHA Type-II. Finally, Time-Tagged Event files consist of FITS EVENT data, 128 energy channels, spanning T $-20+300$ s. Detector response matrices are provided for each data type (the TTE data share responses with CSPEC).

At a higher level of abstraction, the GBM team will be performing several global catalog tasks for each trigger and publishing the catalog results. First of all, the human-in-the-loop ground localization of each trigger will provide consistency checks on the on-board performance, as well as serving as the input for the response matrix generation, when localizations derived externally to GBM can not be obtained. Next, the burst duration calculation determines the T90 and T50 values, the peak flux value and integration interval and the total fluence, both in photon and energy units. The duration calculation uses a spectral deconvolution in each time interval in order to take out the effects of bandpass and spacecraft slew. Essentially, a spectral model is fit to each of a series of background subtracted spectra, over a time span that includes many of the background spectra themselves. In calculating the cumulative fluence, the background subtracted background fitted spectra should more or less sum to zero, and only those portions of the time history where count from the trigger itself are present should contribute to the sum. The cumulative fluence plot over time can be seen in Figure 2, with a plateau before any emission begins, a rising portion as the trigger progresses, followed by another flat plateau after the end of the emission. As it is difficult to determine exactly where the emission begins or ends in any given trigger, the T90 statistic marks where the 5th and 95th percentile of the emission fall on the time axis.

3.1 Spectral Catalog

At the highest level, the GBM team will produce a Spectral Catalog, similar to the series produced while BATSE was operating [2]. As much as possible, a time-integrated plus a peak flux spectrum for every GRB trigger will be fitted with a standard set of spectral models, with increasing numbers of spectral shape parameters: power-law, exponentially attenuated power law, Band 'GRB' function [3], and smoothly broken power law. For brighter events, these models will be used in time series of spectral fits to determine the characteristics of the spectral evolution through the burst. Most importantly for corellation studies, several of these models produce parameters that are either identical to, or comparable to, E_{peak}.

The catalog will consist of a series of model fit result FITS files for each trigger, where the fit parameters are stored in a data extension, which may be read by any FITS reader, including FV. In most cases, where it makes sense, the data from the brightest detectors, both NaI and BGO, will be jointly fitted. The temporal history will be constructed to obtain equal significance in each time bin (using the signal to noise ratio) and each spectrum will be entirely independent. Typically, CSPEC or binned TTE data will be used.

3.2 GRB Trigger Properties

As of the time of the Moriond Meeting in February 2009, GBM had triggered on 109 GRBs. Based upon preliminary spectral analyses of the time-integrated spectra, these break down as follows:

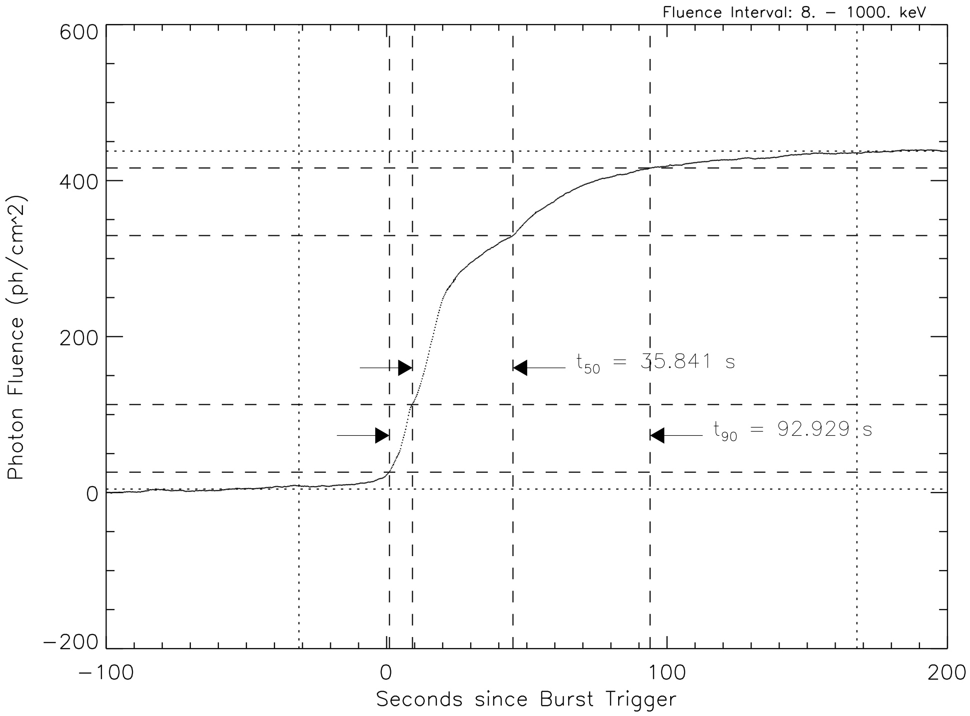

Figure 2: GRB080817: Burst Duration.

- 20 consistent with single Power Law (all of these had low fluence $< 1 \times 10^{-6}$ erg/cm^2),
- 43 consistent with Exponentially attenuated Power Law,
- 47 consistent with Band GRB model,
- 9 more are too weak to make much of a guess for the spectrum.

In addition, joint fits with spectral data obtained from the LAT for the burst in common so far give us confidence in our energy calibration.

References

1. E. Bissaldi, et al. *Experimental Astronomy* **24**, 47 (2009).
2. Y. Kaneko, et al. *ApJS* **166**, 298 (2006).
3. D. L. Band, et al. *ApJ* **413**, 281 (1993).

OBSERVATIONS OF GRB HIGH-ENERGY PROPERTIES WITH *Fermi*

V. PELASSA
on behalf of the Fermi LAT and GBM collaborations
LPTA (CNRS/IN2P3 - Montpellier 2 University)
Montpellier, France

The Large Area Telescope (LAT) on the *Fermi* Gamma-ray Space Telescope observatory is a pair conversion telescope sensitive to gamma rays over more than four energy decades, between 20 MeV and more than 300 GeV. Acting in synergy with the Gamma-ray Burst Monitor (GBM) - the other instrument onboard the mission - the LAT features unprecedented sensitivity for Gamma-Ray Bursts (GRB) in terms of spectral coverage and instrumental dead time. During the first six months of mission *Fermi* detected more than one hundred GRB. Four of them had a significant high-energy emission and could be studied with the Large Area Telescope. After reviewing *Fermi* performance for GRB studies, we present here these four GRB and their temporal and spectral characteristics.

1 Introduction

Before *Fermi*, two experiments have performed GRB observation above 20 MeV : the Energetic Gamma-Ray Experiment Telescope (EGRET) onboard the Compton Gamma-Ray Observatory (CGRO) from 1991 to 2000 and the Italian experiment Astro-rivelatore Gamma a Immagini LEggero (AGILE) operating since 2007.

Three types of emission have been observed :

- a prompt high-energy emission coincident with the keV-MeV emission ;
- a temporally extended high-energy emission in the case of GRB 940217, with a 18 GeV photon recorded ~75 minutes after the prompt emission. The origin of this extended emission may require more than one emission mechanism [1] ;
- a high-energy extra spectral component has been observed for GRB 941017. Its temporal evolution is decorrelated from the low-energy emission, and the wide band spectrum is inconsistent with a pure synchrotron model [2].

Little is known so far about GRB emission above 100 MeV, and *Fermi* LAT observations should help to shed light on the underlying acceleration mechanisms. In section 2 we describe *Fermi* performance and operations for GRB studies. Section 3 presents the four *Fermi* LAT detections after six months of operations. Their temporal and spectral characteristics are detailed, in particular the very bright GRB 080916C.

2 GRB observations with *Fermi*

2.1 GRB detection and localization

The *Fermi* observatory consists of two instruments. The LAT is a pair conversion telescope which allows independent on-board and ground burst trigger and spectral analysis up to more

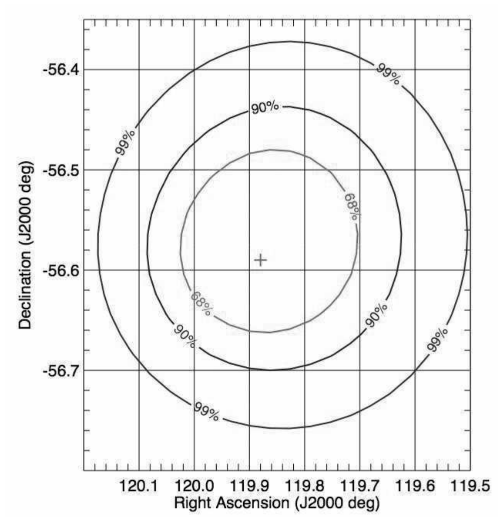

Figure 1: GRB 080916C LAT localization with 68%, 90% and 99% C.L. error contours.

than 300 GeV. The GBM is a set of 14 photomultipliers (12 NaI and two BGO) allowing burst trigger, localization over the entire unocculted sky and spectral analysis from 8 keV to 40 MeV.

The combined use of these two instruments allows a spectral coverage of seven energy decades that matches the typical spectrum of a GRB prompt emission. Besides, the GBM observations give the low-energy context without which the LAT data would be difficult to understand.

The wide field of view of both instruments (the LAT field of view is $\sim$2.4 sr) and their low deadtimes (2.6μs for the GBM, a minimum of 26.5μs for the LAT) confer them good detection capabilities for intense transient sources such as GRB. A study based on BATSE (Burst And Transient Sources Experiment, onboard CGRO) bursts characteristics yields a detection rate of $\sim$200 GRB per year for the GBM and $\sim$13 GRB per year for the LAT, which is consistent with the actual detections so far (the actual GBM detection rate is slightly higher, see section 3). LAT on-ground detection search is generally more sensitive than the onboard search, as it uses fully reconstructed events. As an example GRB 080916C could have triggered the onboard algorithm, whereas GRB 080825C was just above on-ground detectability threshold.

GRB localization is performed onboard and on-ground. For GBM triggers, NaI data are used and a location is derived onboard within 2 s to better than 15°. An automatic refinement to better than 5° is done on-ground within a few minutes. Finally, a human-in-the loop localization is performed.

A LAT location is derived for LAT triggers using the GBM onboard location as seed. LAT localization studies based on simulations have shown that the position accuracy depends on the burst's characteristics (fluence, hardness, duration) and its position in the LAT field of view. The detection of events above 1 GeV strongly improves the localization. For example, GRB 080825C with no photon above 1 GeV was localized with an error radius of $\sim$1°, whereas GRB 080916C localization yielded an error radius of $\sim$0.1° (see figure 1).

2.2 Alerts and notices

For every detection, a GCN notice is sent to the ground within 10 s through the TDRSS network. Several update messages are issued within a few minutes. These automated messages contain the following information : localization, significance of the detection, and for GBM triggers also the most probable nature of the source (e.g. GRB, Soft Gamma Repeater, Anomalous X-ray Pulsar, Terrestrial Gamma-ray Flash, solar flare, accidental event) according to a Bayesian classification scheme. GBM notices are publicly available since October 17th, 2008, and LAT notices since February 28th, 2009. A ground notice containing an improved localization is also sent for GBM triggers, that involves a more sophisticated software algorithm than for the onboard notices.

Circulars are sent by GBM and LAT team members. In the case of a common GBM/LAT detection, a first GBM circular is sent rapidly , it contains a refined manual localization and a preliminary lightcurve based on the so-called trigger data, sent to the ground along with the alert messages. A second circular is sent after the full science data have been sent to the ground, processed, and the studies have been performed.

LAT processed data are available to the Burst Advocate in average eight hours after their acquisition. The Automated Science Processing that is a part of the LAT data processing pipeline searches for a prompt emission or an afterglow in LAT data, for every *Fermi* or *Swift* detection. Counts maps and lightcurves are produced, a localization and a first spectral analysis are performed. After a detailed manual study a circular is issued, containing a localization, along with spectral and temporal analyses, and possible results of the search for a high-energy afterglow.

2.3 LAT follow-up observations

In case of a bright GBM trigger or a LAT detection, an Autonomous Repoint Recommendation (ARR) can be sent to the spacecraft 2 to 600 s after the trigger time. The spacecraft will slew so as to keep the burst location as close as possible to the LAT Z-axis, as long as it remains above the Earth horizon by at least 20° (i.e. the nominal Earth avoidance angle). During occultations of the target by the Earth the spacecraft will slew at a constant angle from the Earth limb until the target rises on the other side. If no interrupt occurs, this maneuver lasts five hours, then the LAT resumes normal data taking in survey mode.

Since this maneuver impacts other observation activities, the threshold on the brightness of the burst has been set so that roughly one ARR per week can be accepted for a burst occuring within the LAT field of view. Bursts occuring outside the LAT field of view require a larger slew and the threshold is higher : roughly one such ARR per month should be accepted.

Spacecraft response to ARR was enabled on October 8th, 2008. Since then five ARR were accepted, the latter two for real bursts occuring in late March, 2009. These two ARR allowed a follow-up of GRB extended emission by the LAT.

3 GRB observations with the LAT

As shown in figure 2 about 120 GRB have been detected by the *Fermi* Gamma-ray Burst Monitor between July 14th 2008 and February 1st 2009, along with two SGR, two AXP, a few TGF and a solar flare. Four GRB have been detected by the *Fermi* Large Area Telescope as well :

- GRB 080825C [3,4] was the first significant detection (6.15 σ in the LAT) of a GRB in the LAT with 10 events seen above 100 MeV;
- GRB 080916C [5,6] was the brightest LAT detection with 10 events above 1 GeV and more than 140 events used for the spectral analysis above 100 MeV. A follow-up observation by the ground optical telescope GROND allowed its redshift measurement : $z = 4.35 \pm 0.15$ [12]. We will discuss the consequences of this measure;
- GRB 081024B [7,8] was the first short burst with emission above 1 GeV. It was a LAT detection with a significance of 8.4 σ;
- GRB 081215A [9,10] was not in the field of view of the LAT, but it was bright enough to produce a significant increase of the raw count rate in the tracker (more than 8 σ).

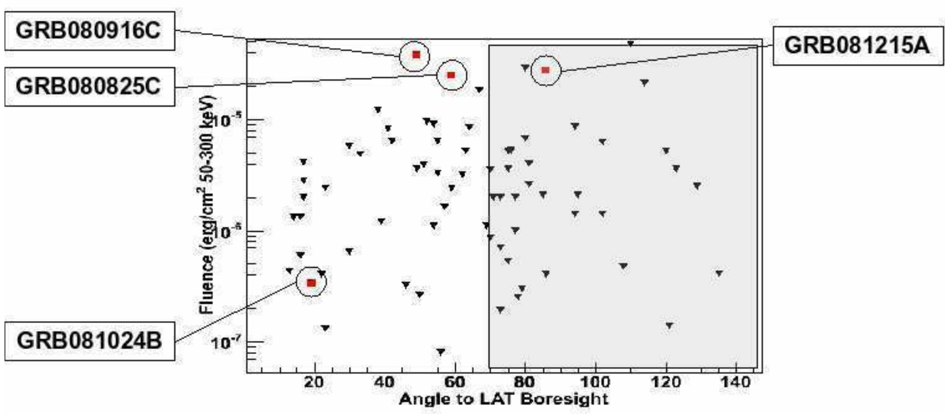

Figure 2: GRB detected by *Fermi*-GBM from July 14th, 2008, to February 1st, 2009. Fluence in range [50 – 300] keV is shown vs angle to LAT boresight. Four out of these ∼120 GRBs were detected in the LAT as well.

3.1 Temporal Characteristics

The multiwaveband lightcurve of GRB 080916C is shown in figure 3. The emission in the GBM energy range shows two peaks, the first of these is not observed in the LAT. This 4.5 s delay between high-energy and low-energy emissions is a hint of spectral evolution.

The emission in the LAT energy range was also temporally extended with respect to the emission in the GBM.While the GBM emission drops off 55 s after trigger time, the LAT emission remains significant for 1400 s. The analysis of this extended emission has been performed using tight cuts adapted to weak sources studies. A likelihood ratio test performed at the location given by GROND observation yielded a significance of 5.6 σ in the last time interval from T_0+200 s to T_0+1400 s. The flux above 100 MeV decays continuously from the main peak to these late times, and also the spectrum is consistent with the trend from the prompt emission : a power-law shape of similar slope.

GRB 080825C emission in the GBM energy range shows multiple peaks, with two main peaks in the first 5 s, and lasts 35 s. The emission above 100 MeV shows one main peak, coincident with the second main GBM peak, although the significance of this delay is poor because of the low statistics. Some events are detected when the signal in the GBM is already very weak, with a reasonable evidence (more than 3 σ) for an extended emission [3 4] .

GRB 081024B is a short burst. The emission in the GBM lasts only 0.8 s and shows two main peaks. The LAT lightcurve above 100 MeV shows one main peak in this interval, and a few events arrive after the end of the emission in the GBM energy range [7 8] .

The common feature to these three bursts is an extended emission in the LAT above 100 MeV with respect to the emission in the GBM. The delay observed in GRB 080916C does not significantly appear in the latter two bursts, but this effect might be a common property of GRB high-energy emission that future observations will confirm.

GRB 081215A is almost transverse and thus the LAT emission is studied from the raw tracker trigger rate. It shows one single pulse, simultaneous to the single pulse observed in the GBM. Although we have no accurate energy information on the corresponding LAT events, they are likely below 150 MeV according to a LAT simulation of this burst based on the extrapolation of the GBM spectral measurement [9 10] .

3.2 GRB080916C spectral characteristics

On-going analyses of all LAT detected GRB show that their spectra are well fit with a Band function[13]. In the case of the bright GRB 080916C, a detailed time-resolved spectroscopy could

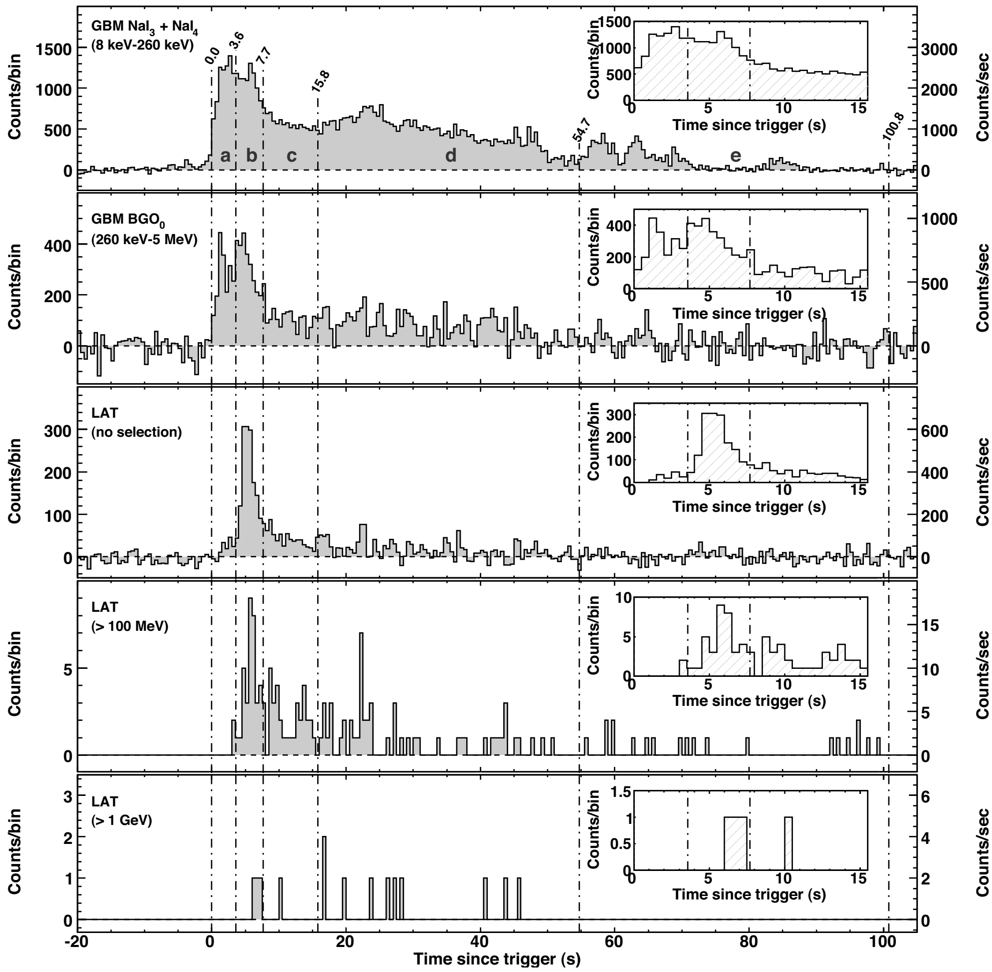

Figure 3: GRB 080916C multiwaveband lightcurve. From top to bottom : NaI (low-energy detectors of the GBM), BGO (intermediate energies), LAT raw counts (no quality cuts or spatial selection have been applied), LAT events used for spectroscopy above 100 MeV, and LAT events above 1 GeV. The first three lightcurves are background subtracted. More than 3000 LAT raw counts were observed, most of them are likely to be below 100 MeV. More than 140 events could be used for spectroscopy above 100 MeV, 14 of them above 1 GeV. The most energetic event has an energy of 13.2 GeV and was detected 16.5 s after the trigger time.

be performed.

The combined GBM-LAT spectrum for the interval containing the main LAT peak is shown in figure 4. Its best fit has a reduced chi-square of 0.96 and good residuals, and the Band parameters are given in table 1. This spectrum shows no evidence for any additional component as could be seen for GRB 941017. Neither does it show any roll-off.

The lightcurve of GRB 080916C was divided in five time bins, and a GBM/LAT combined spectral analysis was performed in each one. The second time bin contains the main LAT peak discussed above. In every bin the spectrum is best fit with a Band function. The evolution is shown in figure 5 : soft-to-hard with the late arrival of the LAT emission, then hard-to-soft which is consistent with the emission from a cooling particle outflow. None of these spectra shows evidence for an extra component or a cutoff.

The measurement of GRB 080916C redshift, $z = 4.35 \pm 0.15$, has important consequences. As far as the enrgetics is concerned, thehuge isotropic energy release $E_{iso} \simeq 8.8 \times 10^{54} erg$ strongly favours the hypothesis of a narrow collimated jet as the source of the emission. The highest energy photon has an observed energy of 13.2 GeV and an energy of 70.6 GeV in the

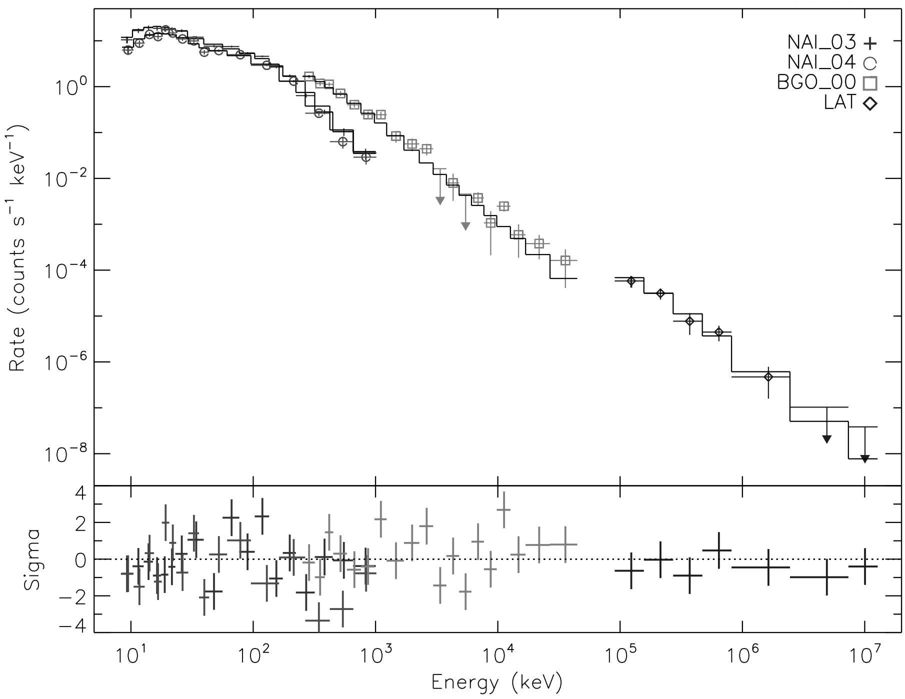

Figure 4: GRB 080916C main LAT peak counts spectrum — photon spectrum convolved with the instruments responses. Crosses and circles are fluxes in the GBM NaI, squares are fluxes in the GBM BGO, and diamonds show LAT signal above 100 MeV. This multi-detector spectrum is best fit with a Band function (two smoothly joined powerlaws) see table 1. 68% C.L. error bars are given, or 95% C.L. upper limits.

Table 1: GRB 080916C : spectral parameters for main LAT peak. Band function fit.

Parameter	Value	Error (68% C.L.)	
Alpha	-1.02	0.02	low-energy slope
Beta	-2.21	0.03	high-energy slope
E_{peak} (keV)	1170	142	νF_ν spectrum maximum
Amplitude ($s^{-1}.cm^{-2}.keV^{-1}$)	0.035	0.001	

source frame. Its delayed arrival, 16.5 s after the trigger time, allows to put strong and robust constraints on Lorentz invariance violation, and more particularly on the Quantum Gravity mass scale : $M_{\rm QG} > 1.50 \times 10^{18} GeV/c^2 \sim 0.1 M_{\rm Planck}$ [14].

GRB 080916C spectrum shows no evidence of a spectral cutoff in any time bin, in particular at early times. This probably excludes pair-production opacity effects as the main cause of the delay observed in the high-energy emission. This actually allows to put a high lower limit on the bulk Lorentz factor in the jet : $\Gamma_{min} = 600$ from bin d, $\Gamma_{min} = 890$ from bin b [14], which is the highest obtained so far.

Finally, no extra spectral component is observed in any time bin. This suggests that the emission from keV to GeV range comes from a unique mechanism, but its origin remains unclear. In a leptonic model framework, this observation suggests that the inverse Compton emission would peak well above 10 GeV. In a hadronic model, Ultra High Energy Cosmic Rays production would produce an extra component in the photon spectrum, which is not observed.

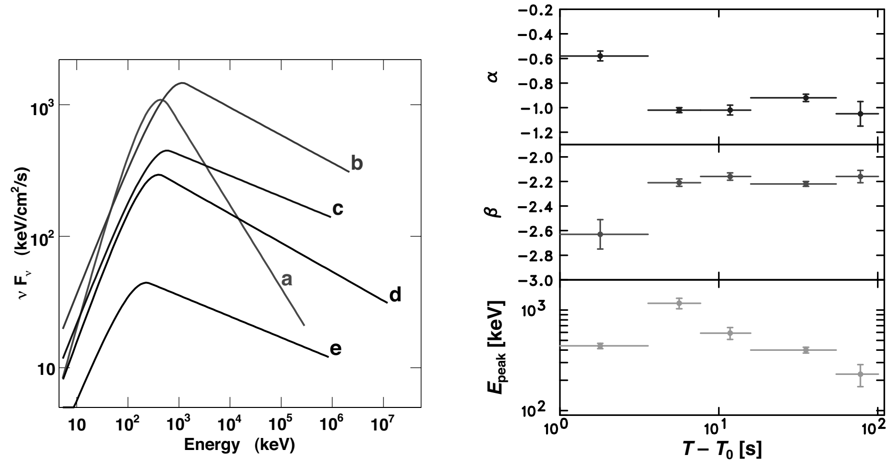

Figure 5: GRB 080916C spectrum temporal evolution. Left : νF_ν photon models for all 5 time bins. Right : fitted parameter values in each time bin (Band function) The high-energy slope beta hardens and the flux increases in the second time bin when the LAT emission arrives. Then the total flux decreases and the high-energy slope remains constant.

Conclusion

In six months of operations, *Fermi* GBM detected $\sim$120 bursts, including 4 LAT detections. Detailed temporal and spectral analyses have been performed for these four bursts, combining data from both instruments.

GRB 080916C is a very bright event allowing a rich analysis. It shows evidence for a delayed and temporally extended high-energy emission, lasting up to 23 minutes after the low-energy trigger. It was the most energetic burst ever observed, among bursts of known redshift. All time-resolved spectra are consistent with a Band function.

GRB 080916C analysis strongly suggests the existence of a narrow collimated jet, and that the emission in the whole keV–GeV range is due to a unique mechanism. It is not clear yet whether this emission is of leptonic or hadronic origin. Finally, we were able to put the best constraints ever on the jet bulk Lorentz factor $\Gamma > 600$ to 900 and on the Quantum Gravity mass scale $M_{\rm QG} > 1.50 \times 10^{18} GeV/c^2 \sim 0.1 M_{\rm Planck}$.

References

1. K. Hurley, Dingus B. L., Mukherjee R., et al., *Nature* **372**, 652 (1994)
2. M. M. González, B. L. Dingus, Y. Kaneko et al., *Nature* **424**, 749 (2003)
3. A. J. van der Horst, V. Connaughton, GCN Circular 8141
4. A. Bouvier et al., GCN Circular 8183
5. A. Goldstein, A. J. van der Horst, GCN Circular 8245
6. H. Tajima, J. Bregeon, J. Chiang, G. Thayer, GCN Circular 8246
7. V. Connaughton, M. S. Briggs, GCN Circular 8408
8. N. Omodei, GCN Circular 8407
9. R. Preece, GCN Circular 8678
10. J. McEnery, GCN Circular 8684
11. A. Abdo et al., *Science* **323**, 1688 (2009)
12. J. Greiner et al., *A & A* submitted, *arXiv:0902.0761*
13. D. Band et al., *Astrophys. Journ.* **413**, 281 (1993)
14. J. Granot, *these proceedings*

GRB Theory in the Fermi Era

J. Granot
on behalf of the Fermi LAT and GBM collaborations
Centre for Astrophysics Research, University of Hertfordshire, College Lane, Hatfield AL10 9AB, UK

Before the launch of the Fermi Gamma-ray Space Telescope there were only a handful of gamma-ray bursts (GRBs) detected at high energies (above 100 MeV), while several different suggestions have been made for possible high-energy emission sites and mechanisms. Here I briefly review some of the theoretical expectations for high-energy emission from GRBs, outline some of the hopes for improving our understanding of GRB physics through Fermi observations of the prompt GRB emission or the early afterglow (first few hours after the GRB), and summarize what we have learned so far from the existing Fermi GRB observations (over its first half-year of operation). Highlights include the first detection of > GeV emission from a short GRB, as well as detailed temporal and spectral information for the first GRB with > GeV emission and a measured redshift, that has the highest measured apparent (isotropic equivalent) radiated energy output (for any GRB), the largest lower limit on the bulk Lorentz factor of the emitting region, and constrains possible Lorentz invariance violation by placing a robust lower limit on the quantum gravity mass.

1 Introduction: pre-Fermi high-energy GRB observations

High-energy emission from GRBs was first detected by the Energetic Gamma-Ray Experiment Telescope (EGRET) on-board the Compton Gamma-Ray Observatory (CGRO; 1991−2000). While EGRET detected only five GRBs with its Spark Chambers (20 MeV – 30 GeV) and a few GRBs with its Total Absorption Shower Counter (TASC; 1 − 200 MeV), these events already showed diversity. Most noteworthy are GRB 940217, with high-energy emission lasting up to ~ 1.5 hr after the GRB including an 18 GeV photon after ~ 1.3 hr, [1] and GRB 941017 which had a distinct high-energy spectral component [2] detected up to ~ 200 MeV with $\nu F_\nu \propto \nu$. This high-energy spectral component had ~ 3 times more energy and lasted longer (~ 200 s) than the low-energy (hard X-ray to soft gamma-ray) spectral component (which lasted several tens of seconds), and may be naturally explained as inverse-Compton emission from the forward-reverse shock system that is formed as the ultra-relativistic GRB outflow is decelerated by the external medium. [3,4] Nevertheless, better data are needed in order to determine the origin of such high-energy spectral components more conclusively. The Italian experiment Astro-rivelatore Gamma a Immagini LEggero (AGILE; 2007−) has detected GRB 080514B at energies up to ~ 300 MeV, and the high-energy emission lasted longer (> 13 s) than the low-energy emission (~ 7 s). [5]

Fermi has raised great expectations for probing the high-energy emission from GRBs as its Large Area Telescope (LAT; from 20 MeV to > 300 GeV) significantly improves upon previous missions, mainly in terms of its large effective area, small dead-time and large field of view. Together with its Gamma-ray Burst Monitor (GBM; 8 keV – 40 MeV) Fermi has an unprecedented energy range of ~ 7.5 decades, which is extremely useful for studying the GRB emission.

2 Expectations from Fermi

Prompt emission: most people hoped for, or even expected, the detection of a distinct high-energy spectral component. Such a detection can shed light on the prompt GRB emission mechanism at low energies (for which the νF_ν spectrum which typically peaks at $E_{\rm peak}$ of around a few hundred keV), which is still unclear, as well as the emission mechanism at high energies. A high-energy spectral component may arise either from leptonic processes, namely inverse-Compton scattering by the same population of relativistic electrons responsible for the observed low-energy prompt emission, [6,7] or from hadronic processes [8] such as proton synchrotron, photo-pair production, and pion production via photo-meson interaction or p-p collisions, that may lead to pair cascades. Moreover, if the energy output in such a high-energy spectral component is comparable to or even larger than that in the low-energy spectral component (as seen by EGRET for GRB 941017) then this will increase the already very tight requirements on the source in terms of the total radiated energy and the efficiency of the gamma-ray emission. [9]

Many hopes were raised to detect a high-energy spectral cutoff or steepening due to opacity to pair production ($\gamma\gamma \to e^+e^-$) at the source.[10,11] Such a detection would determine $\Gamma^{-2\beta}R$, where Γ and R are the bulk Lorentz factor and distance from the source of the emitting region, and β is the (directly measurable) high-energy photon index. Thus, it would determine both Γ and R for models (such as the popular internal shocks model) in which $R \sim \Gamma^2 c\Delta t$, where Δt is the observed variability time of the prompt GRB emission, or test whether this relation holds if Γ can be estimated independently (e.g. from the afterglow onset time).

Longer lived high-energy emission: several possible mechanisms have been suggested for long lived high-energy emission from GRBs, which may be detectable well after the end of the prompt GRB emission. Synchrotron self-Compton (SSC – the inverse-Compton scattering of seed synchrotron photons emitted by the same population of relativistic electrons) emission at GeV energies is expected from the afterglow (i.e. the long lived forward shock going into the external medium). Early on, when there is also a reverse shock going into the ejecta, it can also produce inverse-Compton emission at high energies, either via SSC, or by "external-Compton" (EC; inverse-Compton scattering in which the seed photons are produced in a different region), where reverse shock electrons scatter the forward shock synchrotron photons, or vice versa.[12] In some models[13,14] the reverse shock can be long-lived, lasting for hours or even days, in which case such high-energy emission involving the reverse shock would be similarly long-lived. Other inverse-Compton processes involving two different emission regions have also been suggested. In particular, the *Swift* satellite detects flares in the early X-ray afterglow in about half of the GRBs it observes, typically from hundreds to thousands of seconds after the GRB. These X-ray flares are often attributed to sporadic late-time activity of the central source, and are believed to be emitted at a smaller radius than that of the contemporaneous afterglow shock. In this scenario, EC may operate where afterglow electrons scatter flare photons[15] or vice versa.[16]

Another mechanism that may produce long lived high-energy emission is a pair echo. In this scenario $\gtrsim$ TeV photons that escape the source pair produce with the cosmic infrared background (or the cosmic microwave background – CMB), producing e^+e^- pairs with $\sim$ TeV energies, that in turn inverse-Compton scatter CMB photons to $\sim$ GeV energies. This emission can potentially be detected up to thousands of seconds after the GRB, if the inter-galactic magnetic fields are sufficiently low ($\lesssim 10^{-20}$ G for a correlation length of ~ 1 Mpc). [17,7] Finally, hadronic processes involving high-energy cosmic-rays accelerated in the prompt GRB emission region, or in the afterglow shock, could potentially produce long-lived high-energy emission.

High-energy GRB observations by Fermi on a time scale of up to hours after the GRB can either detect some of these emission components or alternatively place interesting limits on them. In both cases, the hope is that Fermi would thus be able to constrain the physical conditions at the source and help determine the dominant high-energy emission mechanisms.

3 First results from Fermi

GBM: the GBM has a very wide field of view (full sky, half of which is occulted by the Earth at any time) and is only slightly less sensitive than the Burst and Transient Source Experiment (BATSE, that was on-board the CGRO), thus resulting in a comparable (only slightly lower) GRB detection rate of $\sim 250\ \mathrm{yr}^{-1}$, where $\sim 18\%$ of them are of the short duration spectrally hard class of GRBs. A good fraction of GBM GRBs are within the LAT field of view.

LAT GRB detection rate: during the first ~ 9 months of operation Fermi LAT has clearly detected high-energy emission from 7 GRBs, corresponding to a detection rate of $\sim 9\ \mathrm{yr}^{-1}$. A detailed comparison to the expected detection rate requires specifying the number of detected photons above a certain energy. The preliminary results (which suffer from a large statistical uncertainty due to the small number of detected GRBs) are $\sim 7-8\ \ \mathrm{yr}^{-1}$ ($\sim 1-2\ \ \mathrm{yr}^{-1}$) with at least 10 photons above 100 MeV (1 GeV). This is compatible (perhaps slightly lower but well within the errors) with the expected rate[18] based on a sample of bright BATSE GRBs for which the fit to a Band spectrum over the BATSE energy range (30 keV – 2 MeV) is extrapolated into the LAT energy range, and excluding cases with a rising νF_ν spectrum at high energies (i.e. a high-energy photon index $\beta > -2$).[a] This suggests that, on average, there is no significant excess (perhaps even a slight deficit) of high-energy emission in the LAT energy range relative to such an extrapolation from lower energies. Note that this expected detection rate (that is close to the observed rate) is smaller than that for a larger sample of BATSE bursts that includes events that are dimmer in the BATSE range, some of which have $\beta \gtrsim -2$ and would be detectable by the LAT upon extrapolation, thus increasing the expected LAT detection rate. It should be noted, however, that for such GRBs that are relatively dim in the BATSE range it is hard to determine the value of β very accurately, and it might suffer from some systematic error.

GRB 081024B: this GRB was detected by the LAT with more than 10 photons above 100 MeV, and is the first clearly short GRB that is detected at high energies (up to a few GeV). Its spectrum is consistent with a single Band function, similar to the LAT long GRBs. Its high-energy emission (> 100 MeV) lasts about 3 s, while its low-energy emission goes back to background levels after 0.8 s. Even though it was not possible to determine its redshift (due to the lack of an afterglow detection), the lack of a high-energy cutoff in its spectrum up to the highest detected photon energies implies a fairly high lower limit on its bulk Lorentz factor for any reasonable redshift: $\Gamma_{\rm min}(z = 0.1) \approx 150$ while $\Gamma_{\rm min}(z = 3) \approx 900$. These values are significantly higher than the pre-Fermi conservative estimates for short GRBs[19], that were based on the prompt emission spectrum of many short BATSE GRBs being well-fit by a power-law with a high-energy exponential cutoff, where such an exponential cutoff at high energies results in a much lower $\Gamma_{\rm min}$ compared to a (reasonably hard) power-law at high energies.

4 A minimal Lorentz factor of the emitting region from compactness arguments

The large isotropic equivalent luminosities ($L \sim 10^{50} - 10^{53}\ \mathrm{erg\ s^{-1}}$) and short observed variability time ($\Delta t \sim 1\ \mathrm{ms} - 1\ \mathrm{s}$) of GRBs would imply a huge opacity to pair production ($\gamma\gamma \to e^+e^-$) within the source ($\tau_{\gamma\gamma} \gg 1$) if the source (i.e. the emitting region) is at rest or moving at a sub-relativistic velocity relative to us. Neglecting cosmological factors of $(1+z)$ for simplicity, an order of magnitude estimate of the optical depth at a dimensionless photon energy $\varepsilon \equiv E_{\rm ph}/m_e c^2$ gives $\tau_{\gamma\gamma} \sim \sigma_T n_{\rm ph}(1/\varepsilon) R \sim \sigma_T L_{1/\varepsilon}/(4\pi m_e c^3 R) \gtrsim 10^{14}(L_{1/\varepsilon}/10^{51}\ \ \mathrm{erg\ s^{-1}})(\Delta t/1\ \mathrm{ms})^{-1}$, where $R \lesssim c\Delta t$ is the source size and $n_{\rm ph}(1/\varepsilon)$ is the number density of the target photons (near the threshold for pair production) that provide most of the opacity. Such a huge optical depth would

[a] Such a hard high-energy photon index may be an artifact of the limited energy range of the fit to BATSE data, and even if such a hard spectrum is present in the BATSE range it is not very likely that νF_ν continues to smoothly rise well into the LAT energy range.

result in a (quasi-) thermal spectrum, in stark contrast with the significant high-energy power-law tail observed in most GRBs. This is known as the compactness problem.[20] Its solution is that the source moves toward us at a very high Lorentz factor, $\Gamma \gg 1$. This reduces $\tau_{\gamma\gamma}$ due to three effects. First, the threshold for pair production is $\varepsilon_1\varepsilon_2 > 2/(1-\cos\theta_{12})$ where ε_1 and ε_2 are the two photon energies and θ_{12} is the angle between their directions. For a source at rest, $\theta_{12} \sim 1$ and $\varepsilon_1\varepsilon_2 \gtrsim 1$, while for a relativistic source $\theta_{12} \sim 1/\Gamma$ (due to relativistic beaming) and $\varepsilon_1\varepsilon_2 \gtrsim \Gamma^2$ (in the source rest frame $\theta'_{12} \sim 1$ and $\varepsilon'_1\varepsilon'_2 \gtrsim 1$ where $\varepsilon' \sim \varepsilon/\Gamma$). Thus $L_{1/\varepsilon}$ is replaced by $L_{\Gamma^2/\varepsilon} = L_{1/\varepsilon}\Gamma^{2(1+\beta)}$, adding a factor of $\sim \Gamma^{2(1+\beta)}$ to the expression for $\tau_{\gamma\gamma}$, where β is the high-energy photon index ($L_\varepsilon = L_0\varepsilon^{1+\beta}$ in the relevant energy range). Second, R should now represent the distance in the lab frame over which $n_{\rm ph}$ is large enough to significantly contribute to $\tau_{\gamma\gamma}$, i.e. roughly the distance of the emitting region from the source, and $R \lesssim \Gamma^2 c\Delta t$ is possible since $\Delta t \sim R/(c\Gamma^2)$ is the time delay in the arrival of photons from an angle of $\sim 1/\Gamma$ from the line of sight relative to the line of sight itself for an emitting region with a radius of curvature $\sim R$ (in the lab frame), as well as the difference in arrival time of two photons emitted along the line of sight over a radial interval $\Delta R \sim R$. This adds a factor of $\sim \Gamma^{-2}$ to the expression for $\tau_{\gamma\gamma}$. Finally, there is a factor of $1-\cos\theta_{12} \sim \Gamma^{-2}$ in the differential expression for $\tau_{\gamma\gamma}$, due the the rate at which the photons pass each other and have a chance of interacting (exactly parallel photons will never interact). This results in an additional factor of $\sim \Gamma^{-2}$ in the expression for $\tau_{\gamma\gamma}$. Altogether, $\tau_{\gamma\gamma}$ includes a factor of $\sim \Gamma^{2(1-\beta)}$, and since typically $-\beta \sim 2-3$, this typically requires $\Gamma > \Gamma_{\rm min} \sim 100$ in order to achieve $\tau_{\gamma\gamma} < 1$. In particular, when there is no high-energy cutoff or steepening in the spectrum up to an observed photon energy of $\varepsilon_{\rm max}$, then the requirement that $\tau_{\gamma\gamma}(\varepsilon_{\rm max}) < 1$ leads to $\Gamma_{\rm min} \propto (L_0/\Delta t)^{1/2(1-\beta)}(\varepsilon_{\rm max})^{(-1-\beta)/2(1-\beta)}$.

5 GRB 080916C

GRB 080916C was the second GRB detected by the LAT and the brightest so far. It had > 3000 raw LAT counts (after background subtraction) in the first 100 s, with 145 events above 100 MeV that could be used for spectral analysis, and 14 photons above 1 GeV.[21] The accurate localization by the LAT (to within $\sim 0.1^\circ$) enabled the detection of its X-ray afterglow after 17 hr in a follow-up observation by the *Swift* X-ray telescope,[22] which in turn provided a much better localization (to within 1.9") that enabled follow-up observations by ground based telescopes and the detection of the optical/NIR afterglow by the Gamma-Ray Burst Optical/Near-Infrared Detector (GROND), which was able to measure a photometric redshift of $z = 4.35 \pm 0.15$.[23]

Energetics and beaming: GRB 080916C was a very bright long GRB. It had a very high fluence of $f = 2.4 \times 10^{-4}$ erg cm^{-2}, corresponding to an isotropic equivalent energy output of $E_{\gamma,\rm iso} \approx 8.8 \times 10^{54}$ erg $\approx 4.9 M_\odot c^2$, which is the highest measured so far for any GRB, and strongly suggests that the outflow was collimated into a narrow jet, in order to alleviate the otherwise very extreme energy requirements from the source.

Spectral evolution: the time resolved spectrum of the prompt emission in GRB 080916C was analyzed in five different time bins (chronologically labeled **a**-**e**; see *left* and *middle panels* of Fig. 1) and found to be well-fit by a single Band spectrum (featuring a smooth transition between two power-law segments) in a combined fit of the LAT and GBM data. The peak of the νF_ν spectrum, $E_{\rm peak}$, first increases between the first and second time bins, and then gradually decreases with time (see *middle panel* of Fig. 1). The photon indices at low energies, α, and at high energies, β, both change between the first and second time bins, α becoming softer and β becoming harder, and are then consistent with remaining constant in time.

Implications of a single dominant spectral component: the fact that the spectrum in time bins **a-e** is consistent with a single Band function suggests that a single spectral component, arising from a single emission mechanism, dominates throughout the observed energy range, which cover 6 decades in energy (roughly 10 keV – 10 GeV). This provides interesting constraints

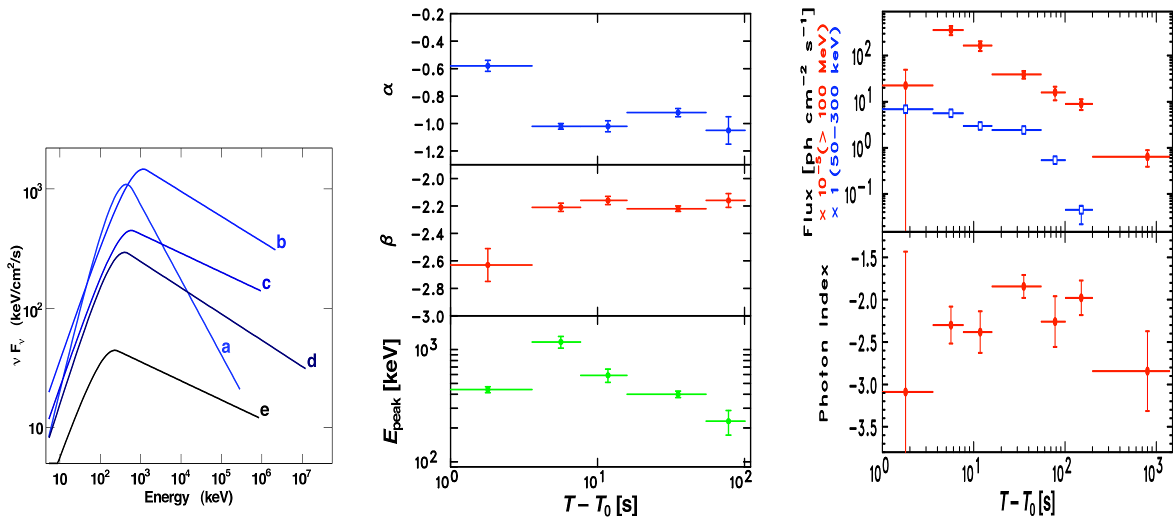

Figure 1: Spectral evolution of GRB 080916C. [21] **Left panel**: The best-fit model νF_ν spectra for all five time intervals. The changing shapes show the evolution of the spectrum over time. The curves end at the energy of the highest-energy photon observed in each time interval. **Middle panel**: Fit parameters for the Band function – the photon index at low (α) and high (β) energies, and the photon energy ($E_{\rm peak}$) where the νF_ν spectrum peaks – as a function of time. Error bars indicate 1 σ uncertainty. **Right panel**: Fluxes (*top*) for the energy ranges $50 - 300$ keV (blue open squares) and > 100 MeV (red solid squares) and power-law index as a function of the time from the GRB trigger time T_0 to $T_0 + 1400$ s [(*bottom*) LAT data only].

on any emission mechanism. For example, if the observed emission is synchrotron radiation, then an SSC component may peak in the LAT energy range, and the fact that it is not detected suggests that either (i) it has a lower luminosity, its peak νF_ν being at least ~ 10 times lower than that of the synchrotron component, if the SSC component peak around several GeV, implying at least ~ 10 times more energy in relativistic electrons than in the magnetic field in the emission region, or (ii) the SSC component may have a comparable or even higher luminosity than that of the synchrotron component if it peaks well above 10 GeV, in which case it will be hard to detect it due to the smaller number of photons at higher energies and attenuation due to pair production with the extra-Galactic background light (EBL).

EBL: in time bin **d** there is weak evidence for a possible high-energy excess relative to a Band spectrum. [21] The chance probability of such an excess is 1%, and taking into account the 5 trials (for bins **a-e**) it increases to 5% (or 2 σ). For some EBL models the optical depth for pair production with the EBL of the highest energy detected photon, $13.22^{+0.70}_{-1.54}$ GeV, is $\tau_{\gamma\gamma} \sim 3-4$, in which case the significance of an additional high-energy spectral component would be increased to $\sim 3-4\ \sigma$. Such a spectral component may increase the already extreme apparent radiated energy in GRB 080916C. However, for many other EBL models $\tau_{\gamma\gamma}(13\ {\rm GeV}) \ll 1$, resulting in a mere 2 σ hint of a possible excess, which is not very significant.

Delayed high-energy onset: the high-energy emission in GRB 080916C starts $\sim 4-5$ s after the low-energy emission. After the onset of the LAT emission it quickly rises to a bright sharp peak – the main peak in the LAT lightcurve, which coincides with the second peak in the GBM lightcurve (in time bin **b**). If indeed the observed spectrum in the GBM and LAT energy range is dominated by a single spectral component, as suggested by the fact that it is well-fit by a single Band spectrum, then the delayed HE onset may be attributed mainly to a change in the high-energy photon index β between the first and second pulses in the GBM lightcurve (as was measured; see Fig. 1). This, in turn, may naturally occur if these two pulses originated in two distinct physical regions (e.g. two sets of colliding shells in the internal shocks model) with different physical conditions, resulting in a different power-law index of the energy distribution of the accelerated relativistic electron population that is responsible for the observed emission.

Opacity effects do not work well as an alternative explanation since there is no sign of a high-energy cutoff or steepening in the spectrum (that must be present in the observed energy range in order for opacity effects to be the major cause for the observed delayed onset).

Contribution from an additional spectral component at high energies may be possible if together with the spectral component that dominates at low energies the combined spectrum is still well-fit by a single Band function (which is not always that easy to achieve). In this case, however, it is not obvious why the effective value of β (or the luminosity ratio of the two components) should remain constant for the remainder of the GRB (time bins **b-e**). If the main LAT peak is attributed to emission from the same physical region as the first GBM peak (e.g. due to the gradual acceleration of high-energy protons or heavier ions that produce pair cascades) then it is not clear why it should coincide with the second GBM peak or why the main LAT peak is as sharp as it is (as a much smoother peak would be expected in this case). Altogether, the exact cause for the delayed high-energy onset is still not clear, and more detailed modeling could help address this question.

Long lived high-energy emission: while the low-energy emission lasted several tens of seconds, with some low level emission detected up to 200 s after the GRB trigger time, high-energy emission was detected by the LAT for more than 1000 s. In particular, the LAT detected emission above 100 MeV in two additional time bins (just after time bins **a-e**), $100-200$ s and $200-1400$ s (see *right panel* of Fig. 1). The >100 MeV LAT flux decayed as $t^{-1.2\pm0.2}$ from several seconds and up to 1400 s, while during the last time bin ($200-1400$ s) the photon index was $\beta=-2.8\pm0.5$. The GBM flux decayed more slowly ($\sim t^{-0.6}$) up to ~ 55 s, and faster ($\sim t^{-3.3}$) at later times (until fading below detection threshold around 200 s).

Different possible mechanisms may account for such a long lived high-energy emission. A natural possibility is afterglow SSC emission, but spectral hardening is expected when this component becomes dominant, and this is not seen in the data. Some time delay may be caused by scattering of photons emitted at a smaller radius [15] (e.g. an inner set of colliding shells in the internal shock model) or due pair cascades induced by ultra-relativistic ions accelerated in the prompt emission region. [24] In both cases, however, it might be hard to produce the relatively slow decay rate, due to adiabatic losses on a much shorter timescale (that of the observed prompt emission pulses). Other options are scattering of photons from early X-ray flares (undetected in this case, but detected by *Swift* in many other GRBs) by afterglow electrons, or a pair echo. It is hard to conclusively determine the exact mechanism at work here, but further study may help distinguish between the different possibilities.

Comparison to other GRBs: while there is a hint of a delayed onset of the high-energy emission in other LAT GRBs, in those cases it is not nearly as significant as in GRB 080916C. However, a longer duration of the high-energy emission compared to the low-energy emission appears in most LAT GRBs so far, and seems to be a common feature in GRBs. Moreover, it also appeared in EGRET GRBs (especially in GRB 940217) and in the AGILE GRB 080514B. It is hard to tell whether the longer lived high-energy emission is from a similar mechanism in all these cases or from different mechanisms in different GRBs, due to the rather low photon statistics of this long-lived emission and the lack of good broad-band monitoring of the contemporaneous afterglow emission at lower frequencies (mainly X-ray and optical). Nevertheless, such broad-band coverage may improve in the near future and help in distinguishing between the different possible physical origins of the long lasting high-energy emission.

Minimum Lorentz factor: the very high isotropic equivalent luminosity together with the fact that the spectrum did not show any significant deviation from a Band spectrum up to the highest observed photon energies (of $E_{\rm max}\gtrsim$ a few GeV) require a very large bulk Lorentz factor of the emitting region, $\Gamma>\Gamma_{\rm min}$, in order for the optical depth to pair production in the source to satisfy $\tau_{\gamma\gamma}(E_{\rm max})<1$ (see § 4). For time bin **d** this implies $\Gamma_{\rm min}=608\pm15$. For time bin **b**

$\Gamma_{\rm min} = 887{\pm}21$ for an observed variability time of $\Delta t = 2$ s (the time for a factor of ~ 2 GBM flux variation). A more careful inspection of the low-energy lightcurve in time bin **b** shows significant variability at least down to timescales of 0.5 s, and adopting $\Delta t = 0.5$ s results in $\Gamma_{\rm min} \approx 1100$. Even the more conservative value of $\Gamma_{\rm min} \approx 900$ is more than twice the previous largest $\Gamma_{\rm min}$ for any other GRB from opacity considerations.[10] Moreover, our limit is more robust than previous ones, since in our case the target photons that provide the opacity for the highest energy observed photon are within the observed energy range ($E_{\rm ph} \ll E_{\rm max}$), while for previous limits they were well above the observed energy range ($E_{\rm ph} \gg E_{\rm max}$), and therefore it was not clear whether they were indeed present at the source. Note that for the conservative assumption that the photon spectrum reaches only up to $E_{\rm max}$, $\Gamma_{\rm min} \lesssim (1+z)E_{\rm max}/m_e c^2 \approx 200(1+z)(E_{\rm max}/100\ {\rm MeV})$, and therefore a large $\Gamma_{\rm min}$ requires the detection of high-energy photons. Our lower limit on Γ for time bin **b** implies a fairly large emission radius, $R \sim \Gamma^2 c\Delta t/(1+z) \gtrsim 10^{16}$ cm.

Limits on Lorentz invariance violation: some quantum gravity models predict energy dispersion in the propagation speed of photons, where high-energy photons travel slower[b] than low-energy photons.[25] The Lorentz invariance violating terms in the dependence of the photon momentum $p_{\rm ph}$ on the photon energy $E_{\rm ph}$ can be expressed as a power series,

$$\frac{p_{\rm ph}^2 c^2}{E_{\rm ph}^2} - 1 = \sum_{k=1}^{\infty} \left(\frac{E_{\rm ph}}{\xi_k M_{\rm Planck} c^2}\right)^k = \sum_{k=1}^{\infty} \left(\frac{E_{\rm ph}}{M_{{\rm QG},k} c^2}\right)^k \ , \tag{1}$$

in the ratio of $E_{\rm ph}$ and a typical energy scale $M_{\rm QG,k}c^2 = \xi_k M_{\rm Planck} c^2$ for the $k^{\rm th}$ order, which is expected to be of the order of the Planck scale, $M_{\rm planck} = (\hbar c/G)^{1/2} \approx 1.22\times 10^{19}\ {\rm GeV/c^2}$. That is, $\xi_k \sim 1$ may naively be expected for the coefficients that are not infinite (some terms may not appear in this sum). Since we observe photons of energy well below the Planck scale, the dominant Lorentz invariance violating term is associated with the lowest order non-zero term in the sum, of order n, which is usually assumed to be either first order ($n = 1$) or second order ($n = 2$). The photon propagation speed is given by the corresponding group velocity,

$$v_{\rm ph} = \frac{\partial E_{\rm ph}}{\partial p_{\rm ph}} \approx c\left[1 - \frac{n+1}{2}\left(\frac{E_{\rm ph}}{M_{{\rm QG},n} c^2}\right)^n\right] \ . \tag{2}$$

Taking into account cosmological effects, this induces a time delay in the arrival of a high-energy photon of energy $E_{\rm h}$, compared to a low-energy photon of energy $E_{\rm l}$, of[26]

$$\Delta t \approx \frac{(1+n)}{2H_0}\frac{(E_{\rm h}^n - E_{\rm l}^n)}{(M_{{\rm QG},n}c^2)^n}\int_0^z \frac{(1+z')^n}{\sqrt{\Omega_M(1+z')^3 + \Omega_\Lambda}}\,dz' \ . \tag{3}$$

We apply this formula to the highest energy photon detected in GRB 080916C, with an energy of $E_{\rm h} = 13.22^{+0.70}_{-1.54}$ GeV, which arrived at $t = 16.54$ s after the GRB trigger (i.e. after the onset of the hard X-ray to soft gamma-ray, sub-MeV emission: $E_l \sim 0.1$ MeV). Since we have $E_{\rm h}/E_{\rm l} \sim 10^5 \gg 1$, the term $E_{\rm h}^n$ in eq. (3) can be neglected, and $\Delta t \propto (E_{\rm h}/M_{\rm QG,n})^n$. Since it is hard to associate the highest energy photon with a particular spike in the low-energy lightcurve, we make the conservative assumption that it was emitted sometime between the GRB trigger and the time that it was observed, i.e. $\Delta t \leq t$. This results in the following limits[21] for $n = 1$,

$$M_{\rm QG,1} > (1.55 \pm 0.04)\times 10^{18}\left(\frac{E_{\rm h}}{13.22\ {\rm GeV}}\right)\left(\frac{\Delta t}{16.54\ {\rm s}}\right)^{-1}\ {\rm GeV/c^2} \ , \tag{4}$$

and for $n = 2$, $M_{\rm QG,2} > (9.66 \pm 0.22)\times 10^8 (E_{\rm h}/13.22\ {\rm GeV})(\Delta t/16.54\ {\rm s})^{-1/2}\ {\rm GeV/c^2}$. Our limit for $n = 1$ is the strictest of its kind, and only a factor of 10 below the Planck mass.

[b] In principle they could also travel faster (or even faster in some photon energies and slower in others). For GRB 080916C, however, there is no high-energy photon detected before the onset of the low-energy emission (i.e. the GRB trigger), and in fact the first of the 14 photons with energies above 1 GeV arrives several seconds after the GRB trigger. Therefore, a comparable or perhaps an even somewhat stricter limit may be put on such a "negative delay" in the arrival time of high-energy photons relative to low-energy photons.

6 Conclusions

Fermi has raised great expectations that, similar to previous major new relevant space missions, it would also significantly contribute to the progress in the GRB field. The main expectations are to improve our understanding of the prompt GRB emission mechanism and the physical properties of the emission region, possibly by observing a distinct high-energy spectral component or signatures of opacity to pair production in the source, as well as improving our understanding of the early afterglow. While most of these hopes will have to wait a bit longer, Fermi has already provided some very interesting initial results during its first half-year of operation. The spectrum of most GRBs detected so far by both the GBM and the LAT is consistent with a single Band function, suggestive of a single dominant emission mechanism in the observed energy range, as is also suggested by the LAT GRB detection rate. Longer lived high-energy emission compared to the low-energy emission (in some cases lasting $> 10^3$ s) appears to be common in LAT GRBs. Particularly interesting LAT GRBs are GRB 081024B, the first clearly short GRB detected above 1 GeV, and the exceptionally bright and energetic GRB 080916C that provided a wealth of information leading to tight lower limits on the bulk Lorentz factor of the emitting region and the quantum gravity mass. Finally, there is still a lot to look forward to from Fermi.

Acknowledgments

The author gratefully acknowledges a Royal Society Wolfson Research Merit Award.

References

1. K. Hurley *et al.*, *Nature* **372**, 652 (1994).
2. M. M. Gonźalez *et al.*, *Nature* **424**, 749 (2003).
3. J. Granot and D. Guetta, *Astrophys. J.* **598**, L11 (2003).
4. A. A. Pe'er, E. Waxman, *Astrophys. J.* **613**, 448 (2004).
5. A. Giuliani *et al.*, *Aston. & Astrophys.* **491**, L25 (2008).
6. H. Papathanassiou and P. Mészáros, *Astrophys. J.* **471**, L91 (1996).
7. D. Guetta and J. Granot, *Astrophys. J.* **585**, 885 (2003).
8. M. Bottcher and C. Dermer, *Astrophys. J.* **499**, L131 (1998).
9. J. Granot, A. Königl and T. Piran, *Mon. Not. R. Astron. Soc.* **370**, 1946 (2006).
10. Y. Lithwick and R. Sari, *Astrophys. J.* **555**, 540 (2001).
11. J. Granot, J. Cohen-Tanugi and E. do Couto e Silva, *Astrophys. J.* **677**, 92 (2008).
12. X.Y. Wang, Z.G. Dai and T. Lu, *Astrophys. J.* **556**, 1010 (2001).
13. R. Sari and P. Mészáros, *Astrophys. J.* **535**, L33 (2000).
14. F. Genet, F. Daigne and R. Mochkovitch, *Mon. Not. R. Astron. Soc.* **381**, 732 (2007).
15. X.Y. Wang, Z. Li and P. Mészáros, *Astrophys. J.* **641**, L89 (2006).
16. A. Panaitescu, *Mon. Not. R. Astron. Soc.* **383**, 1143 (2008).
17. R. Plaga, *Nature* **374**, 430 (1995).
18. D. L. Band *et al.*, *Astrophys. J.* accepted (2009)
19. E. Nakar, *Phys. Rep.* **442**, 166 (2007).
20. M. Ruderman, *Ann. NY Acad. Sci.* **262**, 164 (1975).
21. A. B. Abdo *et al.*, *Science* **323**, 1688 (2009).
22. M. Perri *et al.*, GCN Circ. 8261 (2008)
23. J. Greiner *et al.*, *preprint*, http://arxiv.org/abs/0902.0761 (2009).
24. C. D. Dermer and A. Atoyan, *New J. Phys.* **8**, 122 (2006).
25. G. Amelino-Camelia *et al.*, *Nature* **393**, 763 (1998).
26. U. Jacob and T. Piran, JCAP **01**, 031 (2008).

On the Prompt Emission Mechanism in Gamma-Ray Bursts

Tsvi Piran[1a], Re'em Sari[1] and Yuan-Chuan Zou[1,2]
1. Racah Institute for Physics, The Hebrew University, Jerusalem, 91904 Israel
2. School of Physics, Huazhong University of Science and Technology, 430074 Wuhan, China

We examine the prompt emission mechanisms that take place in Gamma-Ray Bursts (GRBs). The nature of this process is still one of the interesting puzzles in GRBs. Recent simultaneous observations of both optical and gamma-rays from 080319c, the naked eye bursts, suggested, at first, that the observed gamma-rays are Inverse Compton (IC) scattering of the optical emission. However, optical upper limits rule out this possibility for most burst and even for 080319c, whose optical emission was extremely powerful.

1 Introduction

The mechanism that produces the prompt gamma-ray emission in Gamma Ray Burst (GRBs) is still uncertain. The non-thermal character together with the short time scale variability led to the compactness problem[1]. The resolution of the compactness problem have led to the commonly accepted paradigm that the emitting regions must be moving relativistically (at 0.99c or faster) towards us and to the fireball model. While this was an important step in understanding GRBs we still have to understand what is the origin of the non-thermal emission.

Among non-thermal emission processes two: Inverse Compton (IC) and synchrotron, stand out as the natural candidates. Other processes like curvature emission, or cascade due to proton proton collisions are incapable of producing the huge observed luminosities with reasonable physical parameters. Among IC and synchrotron the latter become, somehow, the "standard" process but the former remained always a serious alternative [2−9] The observations of numerous bursts with low energy spectral slopes that are inconsistent with synchrotron [10,11,12,7] provided additional motivation to consider IC. Recently, Kumar & McMahon [13] have argued that the overall synchrotron model is inconsistent and suggested that Synchrotron Self-Compton (SSC) can resolve some of the problems.

The observations [14,15,16] of a naked eye optical flash that coincided with the prompt $\gamma-$ray emission from GRB080319b provided further motivation to consider IC as the source of the prompt γ-rays. Among the different models that appeared so far [17−21], several favor scenarios in which the prompt γ-ray emission is IC of the optical flash and there have been suggestions that this is generic.

Motivated by these ideas we [22] have explored the possibility that SSC is the source of the prompt γ-ray emission in GRBs. The analysis is very general. It depends only on the observed fluxes (in the optical and in soft γ-rays, as well in the GeV-TeV regime) and on the conditions in the emitting regions, where the main parameters of interest are the Lorentz factor of the emitting electrons, γ_e, and the bulk Lorentz factor, Γ. It is independent of the nature of the relativistic

[a]Talk given by T. Piran

ejecta (baryonic or Poynting flux), of the relativistic electrons (internal or external shocks, or something else) and of the acceleration process. We don't even use the usual constraints on the size of the emitting region and the Lorentz factor that arise from variability considerations[23]. We show that current observations rule out the possibility that the soft γ-ray emission is produced via SSC or more generally of IC of low energy photons that are produced in the moving jet. We then [19] turn to GRB080319b, that has motivated this research, and show that even though its optical emission was much brighter even in this case the soft γ-ray emission was not an SSC of the optical signal and that the optical photons and γ-rays must have arisen from different sources.

2 Inverse Compton

IC requires a soft seed component at the IR-UV range. The flux of these seed photons is constrained by observations (or upper limits) of the prompt optical emission. GRB 990123 [24] and GRB 080319B [14] are rare exceptions with very strong optical emission, ~ 9 and ~ 5.3 mag respectively. However most bursts are much dimer optically with observations or upper limits around 14 mag [25] (In the following we use very conservatively optical upper limits of 11 mag corresponding to $F_{opt} \approx$100 mJy). . This should be compared with fluxes of mJy in soft gamma rays for a modest burst. The flux ratio F_γ/F_{opt} which is typically larger than 0.01 (corresponding to an energy ratio, $\nu_\gamma F_\gamma/\nu_{opt} F_{opt} > 1500$) during the peak soft γ-rays emission [25] .

If the low energy seed emission is in the optical and the observed soft γ-rays are the first IC component, then the Y parameter ($\equiv \nu_\gamma F_g/\nu_{opt} F_{opt}$) is very large, typically greater than thousands. In this case the second IC component would be in the GeV-TeV range and it would carry an even larger amount of energy than the soft γ-rays. This will pose an "energy crisis" and even more important would violating upper limits from EGRET [26,27] and Fermi (even the powerful high energy emission of GRB080916C[28] did not carry that much energy)[b]. This problem is generic and it does not depend on the specific details of the overall model.

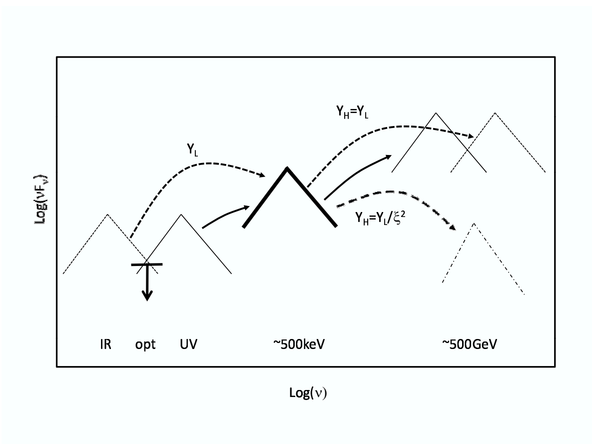

Figure 1: A schematic description of the IC process. Low energy photons at the IR (marked in dotted lines), optical or UV (marked in solid thin lines) are IC scattered to produce the observed soft gamma ray emission (marked in bold lines). A second IC scattering brings the soft gamma photons to the TeV region. If the initial seed photons are softer the higher energy component is harder. If the initial seed is in the IR then the second IC process might be in the KN regime, in which case this component is suppressed (dashed-dotted line). The seed low energy emission is constraint by upper limits on the optical prompt observations (bold solid arrow).

Two factors may alleviate the energy catastrophe. First, the frequency of the seed photons may differ from those where upper limits exist, allowing larger seed flux and reducing the lower limits on Y. Second, the Klein-Nishina (KN) suppression, which does not affect the first scattering, may affect the second, resulting in a lower Y parameter for the second scattering

[b] If the second IC component is in the TeV it will be absorbed by the IGM and won't be observed. Still the "energy crisis" problem will persist.

than the first one. However [22], even when these factors are taken into account the IC solution is problematic.

Consider IC scattering of seed photons with a peak frequency ν_s and a peak flux F_s (both measured at the observer's frame). We assume that the seed photons are roughly isotropic in the fluid's frame. This would be the case if the seed photons are produced by a mechanism local to the moving fluid, synchrotron radiation is an example. For simplicity we assume that all the photons have the same energy and all the electrons have the same Lorentz factor. The energy and flux of the scattered photons are:

$$\nu_{IC} = \nu_s \gamma_e^2 \min(1, \xi^{-1}); \quad \nu_{IC} F_{IC} = Y \nu_s F_s \min(1, \xi^{-2}) \tag{1}$$

where $Y \equiv \tau\gamma_e^2$ and τ are the Compton parameter and the optical depth in the Thomson scattering regime. The factor, $\xi \equiv (\gamma_e/\Gamma)h\nu_s/m_e c^2$ describes the correction that arises if the scattering is in the KN regime ($\xi > 1$).

Extrapolating from ν_{opt} we can set a limit on the low energy peak flux F_L:

$$F_L \leq (\nu_L/\nu_{opt})^\alpha F_{opt}, \tag{2}$$

where ν_L is the frequency of the peak and α is the spectral index in the range (ν_L, ν_{opt}) or (ν_{opt}, ν_L). F_{opt} is taken as an upper limit. An *UV solution* is characterized by $\nu_L > \nu_{opt}$ and an *IR solution* is characterized by $\nu_L < \nu_{opt}$. Since by definition, the seed photon energy peaks at ν_L, we must have $\alpha > -1$ in the *UV solution* and $\alpha < -1$ in the *IR solution* . Moreover, since the spectrum around ν_L is up-scattered to create the familiar Band spectrum [29] around ν_γ, we can expect $\alpha \approx -1.25$ for the IR solution and $\alpha \approx 0$ for the *UV solution* .

Using Eqs. (1,2) we set a limit on the Compton parameter Y_L, in the first scattering:

$$Y_L \geq \left(\frac{\nu_\gamma F_\gamma}{\nu_{opt} F_{opt}}\right) \left(\frac{\nu_L}{\nu_{opt}}\right)^{-(1+\alpha)}. \tag{3}$$

The second IC scattering produces photons in the GeV-TeV range. Y_H is the ratio of energy emitted via the second IC scattering in the high energy (GeV- TeV) band and in the lower energy gamma-rays:

$$h\nu_H = 0.08\mathrm{TeV} \left(\frac{h\nu_\gamma}{500\mathrm{keV}}\right) \left(\frac{\gamma_e}{400}\right)^2 \min\left[1, \frac{\Gamma m_e c^2}{\gamma_e h\nu_\gamma}\right] \tag{4}$$

and

$$Y_H \geq 1500 \left(\frac{F_\gamma}{10^{-26}} \frac{10^{-24}}{F_{opt}}\right) \left(\frac{h\nu_\gamma}{500\,\mathrm{keV}} \frac{8\cdot 10^{14}\,\mathrm{Hz}}{\nu_{opt}}\right) \left(\frac{\nu_L}{\nu_{opt}}\right)^{-(1+\alpha)} \min\left[1, \left(\frac{\Gamma m_e c^2}{\gamma_e h\nu_\gamma}\right)^2\right]. \tag{5}$$

We have used here typical values $\nu_{opt} = 8\cdot 10^{14}$Hz and $h\nu_\gamma = 500$keV (both are before cosmological redshift hence they are larger by a factor of $(1+z) \approx 2$ than the observed frequencies, R band and 250keV). For the canonical values of the observer fluxes we use very conservative values: R magnitude of 11.2, ($F_{opt} \leq 10^{-24}\mathrm{ergs\,cm^{-2}\,s^{-1}\,Hz^{-1}}$), as an upper limit on the optical flux, while many limits are much stronger. Similarly, for the γ-ray flux we take, $F_\gamma = 10^{-26}\mathrm{erg\,cm^{-2}\,s^{-1}\,Hz^{-1}}$, which is quite modest.

The very large value of Y_H is the essence of the IC problem. It arises from the fact that the energy released in prompt gamma-rays is at least a factor of 1500 larger than the energy released in prompt optical emission (see Eq. 3). The large values of Y_H implies that the energy emitted in the GeV-TeV range would exceeds the observed soft γ-rays by a few orders of magnitude.

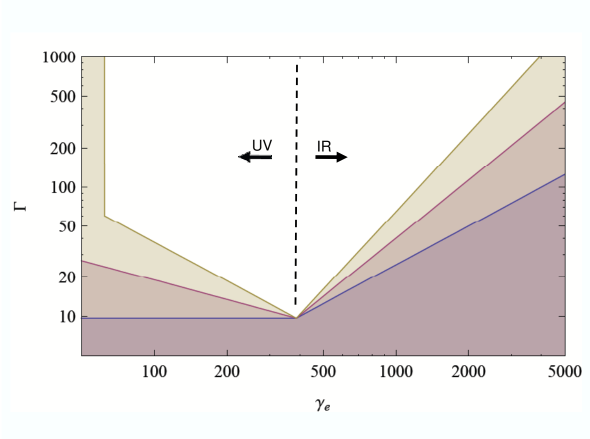

Figure 2: The allowed (colored) phase space in which $Y_H \leq 1$. For three spectral indexes $\alpha = 0, 0.5, 1$ (from bottom to top) for $\nu_L > \nu_{opt}$ and $\alpha = -1, -1.5, -2$ for $\nu_L < \nu_{opt}$(from bottom to top). Parameters used are: $F_\gamma/F_{opt} = 0.01$, $\nu_{opt} = 8 \cdot 10^{14}$Hz and $h\nu_\gamma = 500$keV. The γ_e axis corresponds to values of ν_L ranging from $15\nu_{opt} = 4.8 \cdot 10^{16}$Hz=0.2keV for $\gamma_e = 50$ to $0.006\nu_{opt} = 4.8 \cdot 10^{12}$Hz for $\gamma_e = 5000$.

To demonstrate the severity of the constraint we plot (Fig. 2) the "allowed region" in the (γ_e, Γ) phase space for which $Y_H < 1$. The expected parameter region for internal shocks $\gamma_e \approx 500$, $\Gamma \approx 300$ is deep inside the ruled out region. We find two possible regions which don't over produce GeV-TeV emission: An *IR solution* with a very large γ_e and a *UV solution* with a very low γ_e. In both cases ν_L is far from the optical regime and hence the observational limits on F_L are weak, allowing a modest Y solution. We consider these two possibilities now.

2.1 The UV solution

For low values of γ_e the whole Γ range is seemingly allowed. This happens at rather low values $\gamma_e < 62, 34, 10$ for $\alpha = 1., 0.5, 0$ respectively, corresponding to seed photon energies in the hard UV. The second Compton scattering is not in the KN regime and therefore $Y_L \approx Y_H$. The total energy, given by $(1/Y_L + 1 + Y_H)E_\gamma$, is at least $3E_\gamma$. UV solutions with $Y_L = Y_H < 1$ are therefore also somewhat wasteful as they require a large (E_γ/Y_L) low energy component. A second problem arises, for this solution, with the spectral shape. The observed low energy spectral index (in the X-ray band) is typically close to zero, while this solution requires a steeply rising flux from ν_{opt} to ν_L.

The analysis above is based on the optical limits but for the modest values of γ_e needed for the *UV solution* , ν_L, the peak flux frequency of the seed photons becomes large (Eq. 1) and F_L is now limited also by prompt soft X-ray observations. We use α_1 and α_2 as the low energy and high energy spectral indices in the γ-ray band, respectively. As stated before, the canonical values are $\alpha_1 = 0$ and $\alpha_2 = -1.25$ [29c]. One can estimate the X-ray flux at $\nu_x = 20$ keV directly from the observations at this energy or using the flux at $\nu_\gamma \approx 500$ keV and the low energy spectral slope α_1. Recalling that the IC does not change the spectral slope, we use the same indices both around ν_γ and around ν_L. Therefore:

$$F_L < (\nu_L/\nu_x)^{\alpha_2}(\nu_x/\nu_\gamma)^{\alpha_1}F_\gamma. \tag{6}$$

Using Eq. 1 we obtain:

$$Y > \frac{\nu_\gamma^{\alpha_1+1}\nu_x^{\alpha_2-\alpha_1}}{\nu_L^{\alpha_2+1}} = (\nu_\gamma/\nu_x)^{\alpha_1-\alpha_2}\gamma_e^{2(\alpha_2+1)}. \tag{7}$$

If we impose the condition $Y \cong 1$ (where the total energy required is minimized to $3E_\gamma$), we find that $\gamma_e > 3000$ or $\nu_L < \nu_{opt}$ - thus the whole UV regime is ruled out. This condition depends

[c] Since we consider flux rather than photon counts the indices are shifted by 1 relative to Band's.

strongly on the spectral indices: α_1 and α_2. Clearly if α_2 is smaller (a steeper drop on the high energy side) ν_L can be larger and Y is smaller. Thus, the available X-ray data rules out the *UV solution* for most of the phase space.

2.2 The IR Solution and Self Absorption

The *IR solution* holds for $\nu_L < 0.1\nu_{opt} = 8 \cdot 10^{13}$Hz and $\alpha \leq -1.5$. It requires a large electron's Lorentz factor $\gamma_e \geq 1000$ and a relatively low bulk Lorentz factor $\Gamma < 300$. The solution is deep in the KN regime and the KN suppression is very significant. It allows for a large amplification between the IR and the soft γ-rays and no amplification between the low energy γ and the TeV emission. A solution is possible in a small region of the parameter space if the high energy spectrum is steep ($\alpha \leq -1.5$) - this increases the allowed flux at ν_L. Such a spectrum above the peak frequency, though steeper than the canonical $\alpha = -1.25$, is not rare in the observations of prompt γ-ray bursts. However, the large seed flux that is needed at such low frequencies is usually limited by self absorption.

Self absorption limits the flux at ν_L to be below the black body flux, F_{sa}, for a local temperature $kT \approx \Gamma\gamma_e m_e c^2$:

$$\begin{aligned} F_{sa}(\nu_L) &= \frac{2\pi_L^2}{c^2}\gamma_e m_e c^2 \frac{R^2}{\Gamma d_L^2} \\ &\approx 1.3 \cdot 10^{-20} \mathrm{erg\,cm^{-2}\,s^{-1}\,Hz^{-1}} \frac{(R/10^{17}\mathrm{cm})^2}{d_L^2(z=1)} \frac{(\nu_\gamma/500)^2}{(\gamma_e/400)^3(\Gamma/300)}, \end{aligned} \tag{8}$$

where R is the radius of the source and $d_L(z=1)$ is the luminosity distance for z=1. In the following examples we use conservatively $R = 10^{17}$cm as the emission radius of the prompt emission.

The combined limits on the (Γ, γ_e) parameter space from self absorption with $Y_H = 1$ are shown in fig. 2.2. Only an extremely small region around $\gamma_e \approx 1800$ (corresponding to $\nu_L = 3.7 \cdot 10^{13}$Hz) and $\Gamma \approx 120$ is allowed. This used a conservative over estimate for the emission radius $R = 10^{17}$ cm. If we use the variability time scale $\delta t < 1$sec, with $R \sim \Gamma^2 c\delta t$ and the low values of Γ obtained, R will be much smaller, invalidating even this solution. The self absorption limit rules out also the region in the parameter space that corresponds to external shocks ($\Gamma \approx 100$, $\gamma_e \approx 5 \times 10^4$). This solutions requires a very low seed frequency that would have implied a very small self-absorption limit.

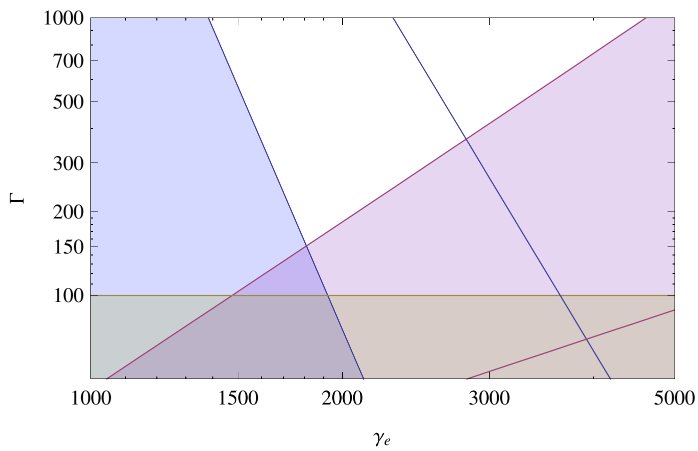

Figure 3: Allowed region for the *IR solution* in the (Γ, γ_e) parameter space. The limit on the left (decreasing curve) corresponds to the condition $F_{sa} \geq F_L$. The limit on the right (increasing curve) corresponds to $Y_H = 1$. Also marked is $\Gamma = 100$, which is considered as a minimal value for the bulk Lorentz factor to resolve the compactness problem. The limits are shown for $\alpha = -2$. (On the right side around $\gamma_e = 4000$ shown are the corresponding curves for $\alpha = -1$.). The γ_e range from 1000 to 5000 corresponds to $\nu_L = 1.2 \cdot 10^{14}$Hz to $\nu_L = 4.8 \cdot 10^{12}$Hz. Parameters used in this figure are: $F_\gamma/F_{opt} = 0.01$, $\nu_{opt} = 8 \cdot 10^{14}$Hz and $h\nu_\gamma = 500$keV. For $\alpha = -2$ an extremely small region around $\gamma_e \approx 1800$ (corresponding to $\nu_L = 3.7 \cdot 10^{13}$Hz) and $\Gamma \approx 120$ is allowed.

3 GRB080319B

GRB080319B [14] was most notable due to its huge total energy and its extremely strong prompt optical emission that could have been seen with naked eyes. This burst was located at redshift $z = 0.937$. Its duration T_{90} was ~ 57s. The peak flux is $F_p \sim 2.26 \pm 0.21 \times 10^{-5} \mathrm{erg\,cm^{-2}s^{-1}}$ at peak energy of the νF_ν spectrum $E_p \simeq 675{\pm}22$keV(i.e., $\nu_p \sim 1.6 \times 10^{20}$Hz, and consequently $f_{\nu,p} \sim 2.7 \times 10^{-25} \mathrm{erg\,cm^{-2}Hz^{-1}s^{-1}}$), and the photon indexes lower and higher than the E_p are $-0.855^{+0.014}_{-0.013}$ and $-3.59^{+0.32}_{-0.62}$ respectively [14]. Choosing standard cosmological parameters $H_0 = 70 \mathrm{km\,s^{-1}\,Mpc^{-1}}, \Omega_m = 0.3, \Omega_\lambda = 0.7$, we have a peak luminosity $L_p \sim 9.7 \times 10^{52} \mathrm{erg}\,s^{-1}$ and an isotropic energy $E_{\gamma,\mathrm{iso}} \simeq 1.3 \times 10^{54}$ erg.

GRB 080319B was different from most other bursts (but similar in many ways to GRB990123, whose optical emission was slightly weaker) because of its enormous optical luminosity. The extremely bright optical flash that accompanied GRB 080319B suggested, at first glance, that the prompt γ-rays in this burst were produced by SSC. In fact the arguments presented above (that depend on F_γ/F_{opt}) cannot be used to constrain directly the IC process. However, a detailed analysis [19] reveals that the very strong optical emission poses, due to self absorption, very strong constraints and puts the origin of the optical emission at a very large radius, almost inconsistent with internal shock. Alternatively it requires a very large random Lorentz factor for the electrons. Both are inconsistent with the conditions needed for the γ-rays being IC of this optical emission. In fact the optical emission and the γ rays could not even have been produced by synchrotron emission from two populations of electron within the same emitting region. Thus we must conclude that the optical and the γ-rays were produced in different physical regions. A possible interpretation of the observations is that the γ-rays arose from internal shocks but the optical flash resulted from external reverse shock emission. This would have been consistent with the few seconds delay observed between the optical and γ-rays signals. Naturally the analysis of this burst is more specific and not as generic as the earlier discussion.

The very strong optical flash that accompanied GRB 080319B poses the strongest constraints on the emission mechanism. A lot can be learnt from studying this flash on its own. The observed optical signal, $F_{\nu,\mathrm{opt}}$, must be less or equal than the corresponding black body emission:

$$F_{\nu,\mathrm{opt}} \le F_{BB} = 2\pi(1+z)^3 \nu_{\mathrm{opt}}^2 \Gamma \gamma_e m_e \left(\frac{R}{\Gamma d_L}\right)^2 = 1.1 \times 10^{-24} \left(\frac{\gamma_e}{100}\right) \left(\frac{R}{10^{15}\mathrm{cm}}\right)^2 \left(\frac{\Gamma}{1000}\right)^{-1}, \quad (9)$$

where R is the emission radius and d_L is the luminosity distance. This value should be compared with the observed optical flux $F_{\nu,\mathrm{opt}} \sim 2.9 \times 10^{-22} \mathrm{erg\,cm^{-2}\,Hz^{-1}\,s^{-1}}$ which is more than two orders of magnitude larger than the one found for F_{BB} with "typical" values. This is the essence of the problem of finding a reasonable solution for the emission mechanism in GRB080319B. By itself this constraint imposes a rather large γ_e for reasonable values of R and Γ, or alternatively a very large value of R.

The black body limit Eq. (9) can be compared now with two expression that link R and Γ: The angular time scale $\delta t > R/2\Gamma^2 c$, and the deceleration radius: $R < R_\gamma = (3E/4\pi n \Gamma^2 m_p c^2)^{1/3}$, (for uniform ISM), where E is the energy of the outflow and n is the ISM density. This comparison shows that while the Black Body limit pushes the emitting radius to large values, the two others limit R to small values. The allowed region is rather small and the radii are typically large and they won't be consistent with those needed for emitting the γ-rays. Note that the allowed region shrinks to zero if we take $\delta t \le 0.1$sec as implied from the γ-ray observations.

To examine the SSC model we use the four observables, $F_{\nu,\gamma}$, $F_{\nu,\mathrm{opt}}$,ν_γ, ν_{opt} to determine the conditions N_e, B, Γ, γ_e and R in the emitting region [19]. The overall spectral distribution is shown in Fig. 3. As there are five variables and four equations we need to have one free parameter, which we conveniently choose to by the Compton parameter Y. Once we solve for these parameters we plug the results into the black body equation Eq. (9 and find[19]:

$$F_{\nu,opt} = 500 F_{BB} Y^{-1.75} \frac{\Gamma}{1000}. \tag{10}$$

For reasonable values of Γ and for Y less than unity, the observed optical flux is larger than the black body limit. This is the essence of the optical self-absorption problem that forbids any low Y SSC solution for GRB 080319B. A large Y will lead to an energy crisis where most of the energy of this (already very powerful) burst would have been emitted in the GeV regime leading to a huge overall energy requirement.

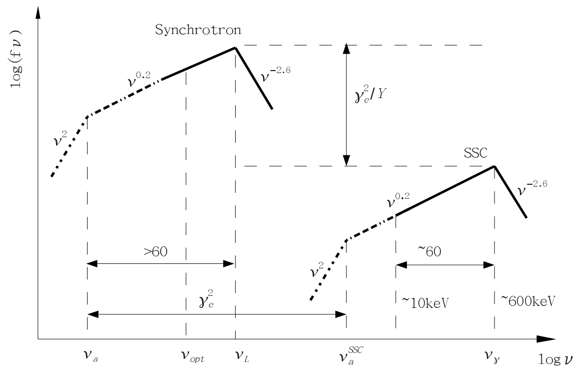

Figure 4: A schematic description of the spectrum in an SSC model. Note that if $10\mathrm{keV}/\gamma_e^2 > \nu_{opt}$, that is if γ_e is small enough, ν_{opt} might be below ν_a.

4 Conclusions

For a typical GRB, IC has to amplify the total energy of a low energy seed photon flux by a factor of $\approx$ 1000 to produce the observed prompt gamma-ray flux. The same relativistic electrons will, however, continue and upscatter the gamma-ray flux to very high energies in the TeV range. In many cases this second generation IC will be in the Klein-Nishiha regime (that is the photon's energy will be larger than the electrons rest mass, in the electron's rest frame). This will suppress somewhat the efficiency of conversion of γ-rays to very high energy gamma-rays, however it won't stop it altogether. Our analysis focused on the case that the low energy seed photons are produced within the moving region that includes the IC scattering relativistic electrons. Such will be the case, for example, in SSC. The analysis is also limited to the important implicit assumption that the emitting region is homogenous. It is possible that very strong inhomogeneities could change this picture.

Under quite general conservative assumptions, if IC produces the prompt sub-MeV photons, then a second scattering will over produce a very high (GeV-TeV) prompt component that will carry significantly more energy than the prompt gamma-rays themselves. On the theoretical front such a component will cause an "energy crisis" for most current progenitor models. From an observational point of view, this component is possibly already ruled out by EGRET upper limits[26,27]. Fermi should have seen such strong emission had it existed. For example, a burst with a "modest" isotropic energy $E_{\gamma,iso} = 10^{53}$erg, locating at $z = 1$, should produce $\sim 10 Y_H (E_H/10\mathrm{GeV})$ photons detected by Fermi.

It turns out that even for GRB080319B, the naked eye burst, that motivated this study, the observed fluxes are inconsistent with a simple SSC model. In fact one can even show that it is unlikely that the prompt γ-rays and the optical have been emitted from the same emitting region. Such a conclusion was reached, based on much less detailed data for GRB990123 as well.

Acknowledgments

We thank R. Mochkovitch, E. Nakar, J. Poutanen, P. Kumar and X. F. Wu for helpful discussions. The research was partially supported by the ISF center for excellence in High Energy Astrophysics , by an Israel-France collaboration grant, by an IRG grant , by an ATP grant , by an Advanced ERC grant and by the Schwartzman chair.

References

1. Piran, T. 2005, Reviews of Modern Physics, 76, 1143
2. Shemi A., 1994, MNRAS, 269, 1112
3. Shaviv Nir J.; Dar A., 1995, MNRAS, 277, 287
4. Sari R., Narayan R., Piran T., 1996, ApJ, 473, 204
5. Sari R., Piran T., 1997, MNRAS, 287, 110
6. Waxman E., 1997, ApJ, 485, L5
7. Ghisellini, G., Lazzati, D., Celotti, A., & Rees, M. J. 2000, MNRAS, 316, L45
8. Stern B. E., Poutanen J., 2004, MNRAS, 352, L35
9. Kobayashi S., Zhang B., Mészáros P., Burrows D., 2007, ApJ, 655, 391
10. Cohen E., Katz J. I., Piran T., Sari R., Preece R. D., Band D. L., 1997, ApJ, 488, 330
11. Preece R. D., et al., 1998, ApJ, 506, L23
12. Preece R. D., et al, 2002, ApJ, 581, 1248
13. Kumar P., McMahon E., 2008, MNRAS, 384, 33
14. Racusin, J. L., et al. 2008, Nature, 455, 183
15. Bloom, J. S., et al. 2009, ApJ, 691, 723
16. D'Elia V., et al., 2008, ApJL submitted (arXiv:0804.2141)
17. Kumar, P., & Panaitescu, A. 2008, MNRAS, 391, L19
18. Fan Y. Z., Piran T., 2008, Front. Phys. China. in press (arXiv:0805.2221)
19. Zou, Y.-C., Piran, T., & Sari, R. 2009, ApJL, 692, L92
20. Yu Y. W., Wang X. Y., Dai Z. G., 2008, arXiv:0806.2010
21. Mochkovitch R., et al., 2008, in preparation
22. Piran, T., Sari, R., & Zou, Y.-C. 2009, MNRAS, 393, 1107
23. Sari, R., & Piran, T. 1997, ApJ, 485, 270
24. Akerlof C., et al., 1999, Nature, 398, 400
25. Yost S. A., et al., 2007, ApJ, 669, 1107
26. Gonzalez Sanchez, M. M. 2005, Ph.D. Thesis
27. Ando S., Nakar E., Sari R., 2008, arXiv:0807.0012
28. Abdo, A. A., et al. 2009, Science, 323, 168
29. Band, D., et al., 1993, Astrophys. J. 413, 281

The Early Time properties of GRBs: Canonical Afterglows and the Importance of Prolonged Central Engine Activity

A. Melandri
Astrophysics Research Institute, Liverpool John Moores University,
Twelve Quays House, Egerton Wharf, CH41 1LD, UK

We classified the observed afterglows of a sample of 63 Gamma Ray Bursts (GRBs) into four main classes and discuss the underlying physics that can explain them. The unprecendented temporal coverage of this sample allow us to use the presence or absence of temporal breaks in X-ray and optical bands to test the standard model. Although the standard model works well in general, a growing number of GRBs are shown to deviate from the forward shock model even with inclusion of energy injection or ambient density gradients. We show that additional emission in the early-time X-ray afterglow due to late-time central engine activity is key and may explain GRBs whose afterglows do not fit the standard model.

1 The Sample

Optical light curves at early times should show different shapes depending on the relative contribution of the forward and reverse shock emission (see Kobayashi & Zhang 2003 for more details on the theoretical predictions); possible light curve shapes are illustrated in Figure 1. Case 1: the light curve will show a transition from steep to shallow power law decay index if the peak of the forward shock emission (solid line) is masked by the reverse shock emission (dashed line). If the peak of the forward shock is detected together with the ongoing emission from the reverse shock, the light curve should look as in case 2. Finally, if there is energy injection to the forward shock emission then the light curve should appear as in case 3; this behaviour can be explained by long-lived central engine activity. Similar shapes has been observed by Oates et al. (2009).

We present the analysis of a sample of 63 GRBs observed with the network of three 2-m telescopes, formed by the Liverpool Telescope (LT, La Palma, Canary Islands), the Faulkes Telescope North (FTN, Haleakala, Hawaii) and the Faulkes Telescope South (FTS, Siding Spring, Australia). In this paper we discuss only the light curve properties for the detected afterglows and compare optical and X-ray data. For a complete analysis of the properties of the sample within the theoretical framework of the fireball model and the intrinsic rest frame properties of those bursts with known spectroscopic redshift refer to Melandri et al. (2008).

1.1 Optical/X-ray light curves comparison

For the majority of the bursts the behaviour in the X-ray and optical bands is different, especially at early times where in the X-ray band the temporal decay is steep, showing the hints of large flare activity. Those features are likely to be due to central engine activity or possibly reverse shock emission.

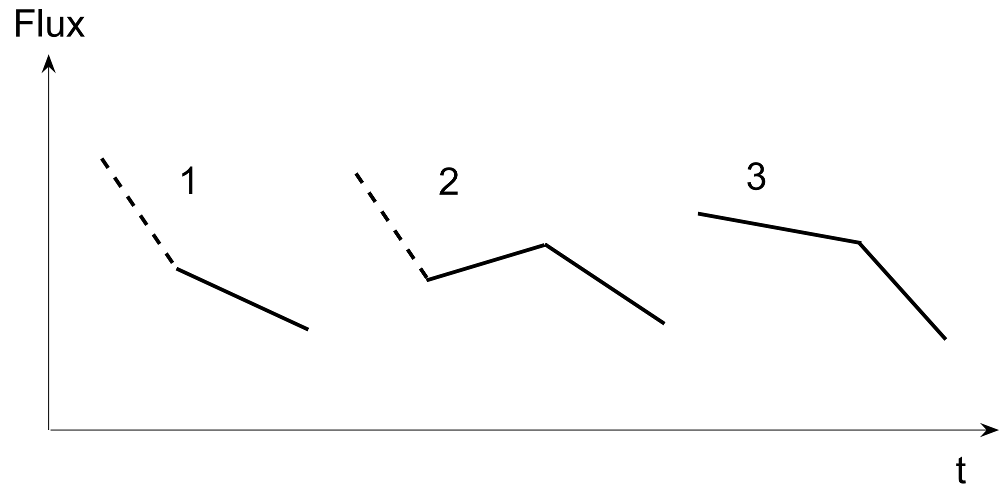

Figure 1: Possible shapes of the optical light curves at early times as a result of the contribution of reverse (dashed line) and forward (solid line) shock emissions (case 1 and 2) or due to energy injection (case 3).

The bursts in our sample (Melandri et al. 2008) can be divided into four classes (Figure 2 based on detected breaks in the optical and the X-ray afterglow light curves during the decay phase:

- Class A : no break in the optical or in the X-ray band;
- Class B : no break in the optical band, break in the X-ray band;
- Class C : break in the optical band, no break in the X-ray band;
- Class D : break in the optical and in the X-ray band.

The observed breaks in the light curves can be the result of different mechanisms: 1) the cooling break (chromatic break), 2) the cessation of the energy injection (achromatic), 3) the jet break (achromatic), 4) a change in the ambient distribution (chromatic or achromatic) or 5) by an additional emission component (chromatic). As the emission process at the time of our observations is in the slow cooling regime, one of the most natural explanations for a break in a light curve is the cooling break. However the other mechanisms can be relevant, at early and late-time, and we took them all into account in our analysis.

2 Results

Using the temporal and spectral properties of the X-ray and optical afterglows we investigated the blastwave physics around the break times within the framework of the standard fireball model (Melandri et al. 2008). The majority of the bursts in our sample (14 out of 24) are consistent with the standard model. However, for a significant fraction of our sample (10 bursts) the data cannot be explained by the standard model, even if modifications to the simple model are made (i.e. energy injection or variation in the ambient matter). A possible explanation beyond the standard model is that the early X-ray afterglow is not due to forward shock emission but is instead produced by late-time central engine activity. Enhanced X-ray emission from late-time central engine activity plays a big role and may explain non-standard light curves (e.g. Melandri et al. 2009) and the high fraction of optically dark GRBs (Melandri et al. 2008).

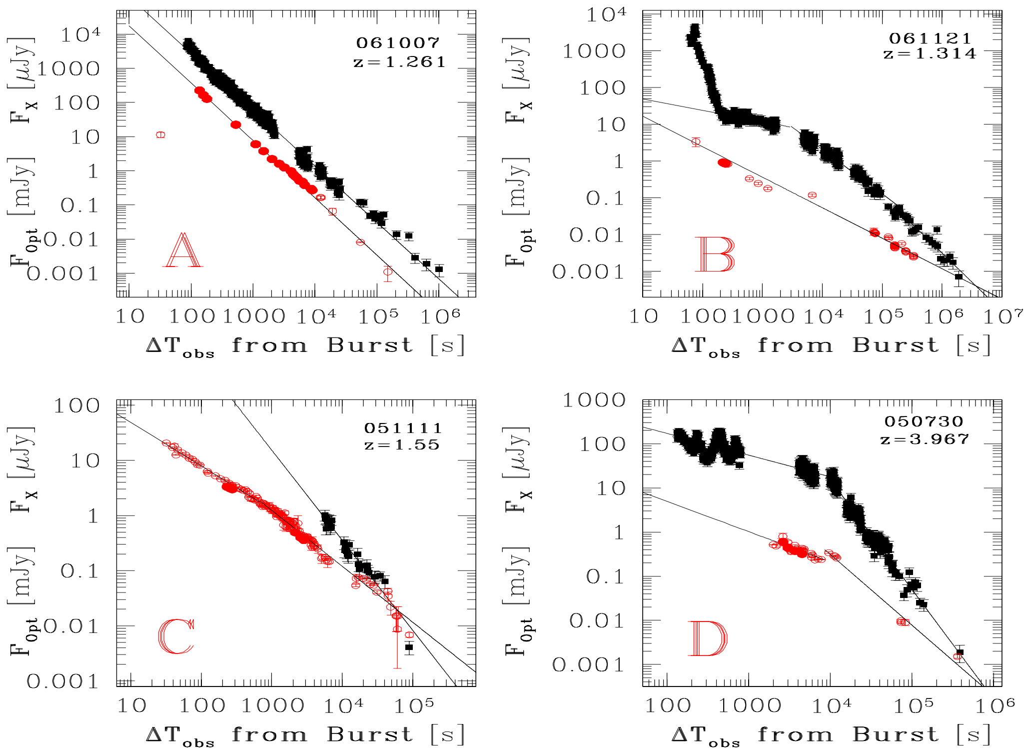

Figure 2: Examples of optical/X-ray light curves for bursts belonging to each different class. See text for details.

Acknowledgments

AM acknowledges funding from the Particle Physics and Astronomy Research Council (PPARC). The Liverpool Telescope is operated by Liverpool John Moores University at the Observatorio del Roque de los Muchachos of the Instituto de Astrofisica de Canarias. The Faulkes Telescopes, now owned by Las Cumbres Observatory, are operated with support from the Dill Faulkes Educational Trust.

References

1. S. Kobayashi and B. Zhang, ApJ **582**, L75 (2003)
2. A. Melandri *et al*, ApJ **686**, 1209 (2008)
3. A. Melandri *et al*, arXiv:0903.1414 , (2009)
4. S. Oates *et al*, MNRAS **295**, 490 (2009)

Testing an unifying view of Gamma Ray Burst afterglows

M. Nardini[1], G. Ghisellini[2], G. Ghirlanda[2], A. Celotti[1]
[1] *SISSA/ISAS, Via Beirut 2-4, 34014 Trieste, Italy*
[2] *Osservatorio Astronomico di Brera, via E. Bianchi 46, I23807 Merate, Italy*

Four years after the launch the *Swift* satellite the nature of the Gamma Ray Bursts (GRBs) broadband afterglow behaviour is still an open issue ad the standard external shock fireball models cannot easily explain the puzzling combined temporal and spectral optical to X–ray behaviour of a large number of afterglows. We analysed the rest frame de–absorbed and K–corrected optical and X–ray multi–wavelength light–curves of a sample of 33 GRBs with known redshift and optical extinction at the host frame. We modelled their broadband behaviour as the sum of the standard forward shock emission due to the interaction of a fireball with the circum–burst medium and an additional component. We are able to obtain a good agreement with the observed light–curves despite their complexity and diversity and can also account for the lack of achromatic late times jet breaks in several GRBs and explain the presence of chromatic breaks. Even if the second component is treated in a phenomenological way, we can identify it as a "late prompt" emission due to a prolonged activity of the central engine produced by a mechanism similar to the one responsible for the early prompt emission. Our attempt can be considered as a first step towards the construction of a more physical scenario. A first important hint is that the "late prompt" temporal decay is intriguingly consistent with what expected with the the accretion rate of fallback material. In order to test our model also from the spectral point of view, we analysed the X–ray time resolved spectra and when possible the evolution of the optical to X–ray spectral energy distribution. All the events are found to be fully consistent with what predicted by our model. Furthermore our analysis can give an alternative view to the connection between the host galaxy dust reddening and the estimate of the $N_{\rm H}$ column derived from the X–ray spectra.

1 Introduction

The launch of the *Swift* satellite represented a great improvement for the early time observations of Gamma Ray Bursts (GRBs) afterglows. The precise GRB localisation and the fast X–ray follow–up opened a new window on the understanding of the GRB afterglow emission. The behaviour of the X–ray light curves of a large fraction of events in the first thousands of seconds appeared much more complex than what had been observed and predicted in the pre–*Swift* era when it was possible to observe the X–ray afterglow only after some hours after the trigger. Most of the observed GRBs show a steep decay phase after the end of the prompt γ–ray emission that lasts for several dozens of seconds and is usually interpreted as the high latitude emission of the fireball (Nousek et al. [1], Zhang et al. [2]). This sudden flux decay is followed by a phase in which the flux remains almost constant for a time that lasts from hundreds to hundred of thousand seconds depending on the specific GRB. This "flat" phase triggered the interest of many groups and a large number of possible explanations have been proposed in literature. In Ghisellini et al. [3] a brief summary of some of the proposed models is given. After the end of the shallow phase (at a time called $T_{\rm A}$) the X–ray light curve changes behaviour and starts to decline as a power law $F \propto t^{-\alpha}$ with an index $\alpha \approx 1.3$ that represents the typical afterglow behaviour observed in the pre–*Swift* era. The optical light–curves instead seem not to trace the behaviour observed in the X–rays in a large number of events.

In this work we focus in particular on the model proposed by Ghisellini et al. [4]. In this model, after the standard prompt emission, a prolonged activity of the central engine keeps producing shells with decreasing power and decreasing bulk Lorentz factor Γ. In this scenario during the shallow phase the decreasing Lorentz factor allows to see an increased portion of the emitting area. This effects ends at a characteristic time $T_{\rm A}$ when $1/\Gamma$ becomes equal to the jet opening angle $\theta_{\rm j}$. The observed radiation (both in the X–ray and in the optical bands) during the shallow phase is thus explained as the superposition of a "standard" forward shock afterglow emission and this second "late prompt" component.

2 Light–curve modelling

2.1 The sample

We analysed a sample of long GRBs with known redshift, optical and XRT follow up, and a published estimate of the host galaxy dust absorption $A_{\rm V}^{\rm host}$. As at the end of March 2008 we found 33 GRBs fulfilling all our selection criteria. When possible, if multiple $A_{\rm V}^{\rm host}$ estimates for an individual burst are present in literature, we choose the one obtained analysing the optical data only, without assuming any connection with the X–rays data. We collected all the multi–band photometric data reported in literature for the GRBs in our sample and converted the observed magnitudes to monochromatic luminosities (de–reddened an K–corrected; see the relevant data and references in Ghisellini et al. [3]). The observed XRT 0.3–10 keV fluxes have been corrected for the Galactic and host frame $N_{\rm H}$ absorption and converted into rest frame K–corrected 0.3–10 keV luminosities.

2.2 Phenomenological model

We modelled the rest frame luminosity light–curves as the sum of two separate components. The first one is modelled as a "standard" forward shock afterglow component following the analytical description given in Panaitescu and Kumar [5]. This parametrisation needs 6 free parameters. Since we do not have a complete physical description of the second component we treated it in a completely phenomenological way with the aim of minimising the number of free parameters and to make a first step towards a more physical modelling. The second component spectral energy distribution is modelled as a smoothly joining double power–law whose shape, for simplicity, is assumed not to evolve in time.

$$\begin{aligned} L_{2^{nd}}(\nu,t) &= L_0(t)\,\nu^{-\beta_{\rm x}}; && \nu > \nu_b \\ L_{2^{nd}}(\nu,t) &= L_0(t)\,\nu_{\rm b}^{\beta_{\rm o}-\beta_{\rm x}}\nu^{-\beta_{\rm o}}; && \nu \le \nu_{\rm b}, \end{aligned} \tag{1}$$

where L_0 is a normalisation constant. The temporal behaviour of the second component is also described by a double power–law, with a break at $T_{\rm A}$ and with decay indices $\alpha_{\rm flat}$ and $\alpha_{\rm steep}$ (before and after $T_{\rm A}$). This modelling has 7 free parameters. Some of them can be well constrained directly by the observations (such as $T_{\rm A}$ and the spectral indices when the second component dominates the observed flux).

There is instead some degeneracy between the values of $\beta_{\rm o}$ and $\nu_{\rm b}$. In our modelling we did not take into account X–ray flares and possible optical re–brightenings and bumps.

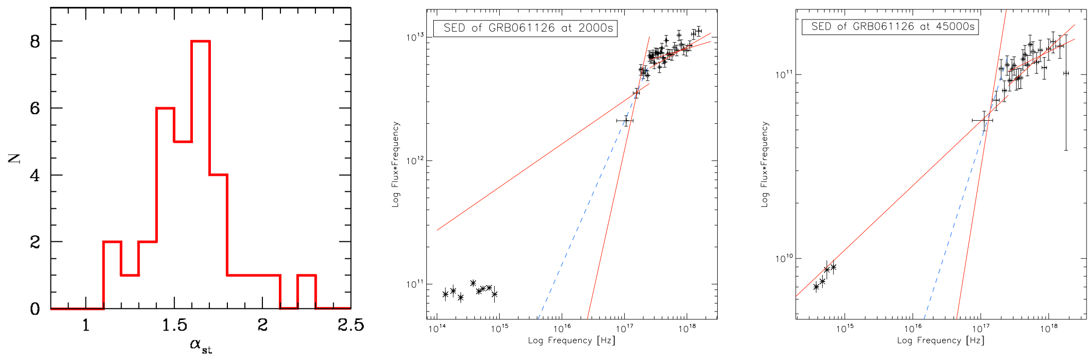

Figure 1: *Left panel*: The distribution of the decay index $\alpha_{\rm steep}$ of the second component. This is the decay index after $T_{\rm A}$. *Central panel*: Early time SED of GRB 061126. *Right panel*: Late time SED of GRB 061126.

2.3 Results

All the optical and X–ray light–curves of the GRBs in our sample can be simultaneously reproduced rather well by our modelling. In 2 cases both the optical and X–ray light–curves are dominated by the second component while in 4 cases they are both dominated by the standard afterglow. The second component is dominant especially in the X–ray band (15 GRBs) while in the optical it dominates only in 3 GRBs. The afterglow dominates mainly in the optical (19 GRBs) while it is less important in the X–rays (6 GRBs). The remaining light–curves can be well described by a combination of the two components having almost the same importance or that dominate the light–curves in different time intervals. The distributions of the afterglow component parameters are similar to the ones obtained by Panaitescu and Kumar [6]. The distributions of the second component parameters show some interesting features. In particular the values of the post break second component decay index $\alpha_{\rm steep}$ cluster around 1.6: this is remarkably close to 5/3 (see fig. 1) that is the predicted decay of the accretion rate of fallback material onto the black hole (Chevalier [7]). It is also the average decay of the X–ray flare luminosity (Lazzati et al. [8]). We also found an interesting correlation between the total energy emitted in γ–rays during the prompt event $E_{\gamma,\rm iso}$ and the energetics of the second component, estimated as $T_{\rm A} L_{\rm T_A}$. This correlation is stronger than the one between $E_{\gamma,\rm iso}$ and the kinetic fireball energy E_0, implying that it is not simply due to the common redshift dependency.

The small number of simultaneous breaks in optical and X–rays light curves in the *Swift* era opened a hot discussion about the nature of the jet breaks. In our scenario a jet break is expected only when the standard afterglow dominates the observed emission. When instead the flux is mainly produced by the second component, no jet break should be visible. This can explain the lack of breaks at late times, the presence of chromatic breaks (when X–rays and optical bands are due to different components), and a post–break light curve decaying in a shallower way than predicted (due to the contribution of the second component).

3 Spectral check

If the optical and the X–ray bands are produced by different processes there must be a spectral break in the spectral energy distribution between these two bands. For the light–curves modelling we assumed – for simplicity – that such a break always falls right in–between the optical and the X–ray bands, but sometimes this break could occur in the observed XRT spectra. We then re–analysed all the XRT spectra of the GRBs in our sample selecting time intervals not affected by prompt or high latitude emission or flaring activity. We first fitted the data with an absorbed single power–law model with frozen Galactic absorption plus a host frame absorption that was left free to vary. Our results are consistent with the ones found in literature and with the ones obtained using the automatic spectral analysis tool developed by Evans et al. [9]. We confirm the absence of spectral evolution around $T_{\rm A}$, as predicted by the late prompt model that explains $T_{\rm A}$ as a purely geometrical effect. With the single power–law fitting we also confirm the inconsistency between the small $A_{\rm V}^{\rm host}$ derived in the optical and the usually large $N_{\rm H}^{\rm host}$ derived by the X–ray analysis, if one assumes a standard $A_{\rm V}/N_{\rm H}$ relation (see e.g. Stratta et al. [10]; Schady et al. [11]). We selected a sample of events with higher statistics spectra and we tried to fit them using a broken power–law model with the same two absorption components used in the case of the single power law fitting. In this GRB sub–sample we found 7 cases in which the presence of a break in the XRT observed spectra gives a better fit ($\Delta\chi^2 > 5.5$) than the single power–law. In 8 GRBs instead the broken power–law model is excluded (break energy outside the considered energy range).

For the 7 GRBs requiring a break in the X–ray band we can test if this break is consistent with what observed in the optical band. We can also check if this is consistent with what predicted by our double component model. We then constructed and analysed the optical to X–rays SEDs at different times. The results are encouraging, since for all bursts where the optical and X–ray fluxes were predicted to be produced by the same component, the optical lies on the extrapolation of the low energy index of the X–ray spectra. Instead, when the optical and X–rays were predicted to be produced by different components, the extrapolation of the low energy spectral index to the optical band underestimates the observed flux. Furthermore, in GRB 061126 we can clearly see the transition between two phases. The entire X–rays light–curve is dominated by the second component, while the optical flux is dominated by the standard afterglow emission at early times. Reassuringly, at these early times the optical SED is inconsistent with the extrapolation of the XRT spectrum. After about 2500 s, instead, the optical to X–ray SED can be described by a single component, and at these times the optical light–curve was indeed predicted to be dominated by our second component (see fig. 1). In the 7 GRBs fitted with a broken power–law model the derived $N_{\rm H}^{\rm host}$ is smaller than the one obtained with a single power–law model, and closer to the values expected from $A_{\rm V}^{\rm host}$. On the other hand we derive very large $N_{\rm H}^{\rm host}$ columns also in some of the GRBs in which a broken power–law fitting is excluded. This means that the large $N_{\rm H}/A_{\rm V}$ ratios observed in several GRBs can be sometimes due to an intrinsic spectral feature, but this can not be considered as a general solution of the large $N_{\rm H}/A_{\rm V}$ issue.

References

1. J.A. Nousek *et al*, ApJ **642**, 389 (2006).
2. B. Zhang *et al*, ApJ **642**, 354 (2006).
3. G. Ghisellini *et al*, ApJ **658**, L75 (2007)
4. G. Ghisellini *et al*, MNRAS **393**, 253 (2009)
5. A. Panaitescu & P. Kumar, ApJ **543**, 66 (2000)
6. A. Panaitescu & P. Kumar, ApJ **571**, 779 (2002)
7. R.A. Chevalier, ApJ **346**, 847 (1989)
8. D. Lazzati, MNRAS **388**, L15 (2008)
9. P.A. Evans, MNRAS submitted arXiv:0812.3662v1
10. G. Stratta, ApJ **608**, 846 (2004)
11. P. Schady, MNRAS **377**, 284 (2007)

SEARCH FOR NEUTRINOS FROM GAMMA-RAY BURSTS WITH THE ANTARES TELESCOPE

D. Dornic
on behalf of the ANTARES Collaboration
CPPM, CNRS/IN2P3 - Université de Méditerranée, 163 avenue de Luminy, 13288 Marseille Cedex 09, France

Gamma-ray bursts (GRBs) are powerful cosmic particle accelerators producing a highly variable flux of high energy gamma-rays. Under the assumption of hadronic acceleration in jets, a copious flux of neutrinos can be expected. Among the possible astrophysical sources, GRBs offer one of the most promising perspectives for the detection of cosmic neutrinos thanks to an almost background free search. The ANTARES neutrino telescope is running in a complete mode since May 2008. The collaboration has implemented two different methods to search for GRBs: the first one is based on the search for neutrino candidates relying on the time and position information provided by an external trigger and the second one is based on the optical follow-up of special neutrino events. The use of these two complementary techniques provides enhanced sensitivity to these transient sources.

1 Introduction

The ANTARES neutrino telescope[1] is located 40 km off shore Toulon, in the South French coast, at about 2500 m below sea level. The complete detector is composed of 12 lines, each including 75 photomultipliers spread on 25 storeys, which are the sensitive elements. Data taking started in 2006 with the operation of the first line of the detector. The construction of the 12 line detector was completed in May 2008. The main goal of the experiment is to detect high energy muon induced by neutrino interaction in the vicinity of the detector. The detection of these neutrinos would be the only direct proof of hadronic accelerations and so, the discovery of the ultra high energy cosmic ray sources without ambiguity.

Among all the possible astrophysical sources, transients offer one of the most promising perspectives for the detection of cosmic neutrinos thank to the almost background free search. The fireball model, which is the most commonly assumed, tells us how the GRBs operate but there are still remaining important questions such as which processes generate the energetic ultra-relativistic flows or how is the shock acceleration realized. The observation of neutrinos in coincidence in time and position with a GRB alert could help to constrain the models.

In this paper, we discuss the different strategies implemented in ANTARES for the transient sources detection. To detect transient sources, two different methods can be used [2]. The first one is based on the search for neutrino candidates in conjunction with an accurate timing and positional information provided by an external source: the triggered search method. The second one is based on the search for high energy or multiplet of neutrino events coming from the same position within a given time window: the rolling search method.

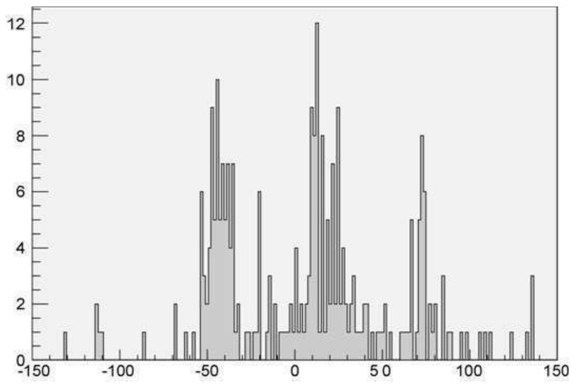

Figure 1: Detector response time (in seconds) to the GRB satellite alerts (Oct 2006 to Dec 2008).

2 The triggered search method

Classically, GRBs or flare of AGNs are detected by gamma-ray satellites which deliver in real time an alert to the Gamma-ray bursts Coordinates Network (GCN [4]). The characteristics (mainly the direction and the time of the detection) of this alert are then distributed to the other observatories. The small difference in arrival time and position expected between photons and neutrinos allows a very efficient detection by reducing the associated background. This method has been implemented in ANTARES mainly for the GRB detection since the end of 2006. Today, the alerts are primarily provided by the Swift [5] and the Fermi [6] satellites. Data triggered by more than 500 alerts (including the fake one) have been stored up to now.

The "all data to shore" concept used in ANTARES allows to store all the data unfiltered during short periods. Based on the time of the external alert, in complement to the standard acquisition strategy, an on-line running program stores the data coming from the whole detector during 2 minutes without any filtering. This allows to lower the energy threshold of the event selection during the off-line analysis with respect to the standard filtered data. Due to a continuous buffering of data (covering 60s) and thanks to the very fast response time of the GCN network (figure 1), ANTARES is able to recorded data before the detection of the GRB by the satellite [7].

Due to the very low background rate, even the detection of a small number of neutrinos correlated with GRBs could set a discovery. But, due to the relatively small field of view of the gamma-ray satellites (for example, Swift has a 1.4 sr field of view), only a small fraction of the existing bursts are triggered. Moreover, the choked GRBs without photons counterpart can not be detected by this method.

3 The rolling search method

This second method, originally proposed by Kowalski and Mohr [8], consists on the detection of a burst of neutrinos in temporal and directional coincidence. Applied to ANTARES [3], the detection of a doublet of neutrinos is almost statistically significant. Indeed, the number of doublets due to atmospheric neutrino background events is of the order of 0.05 per year when a temporal window of 900 s and a directional one of 3° x 3° are defined. It is also possible to search for single cosmic neutrino events by requiring that the reconstructed muon energy is higher than a given energy threshold (typically above a few tens of TeV). This high threshold reduces significantly the atmospheric neutrino background [9].

In contrary to the current gamma-ray observatories, a neutrino telescope covers instantaneously at least an hemisphere if only up-going events are analyzed and even 4π sr if down-going

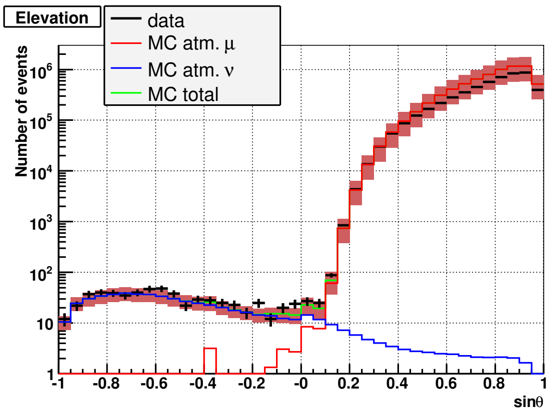

Figure 2: Elevation distribution of the well reconstructed muon tracks (black dots with error bar) recorded in 2008. The blue and red lines represent the Monte-Carlo distribution for atmospheric neutrinos and atmospheric muons (the shaded band contains the systematic error).

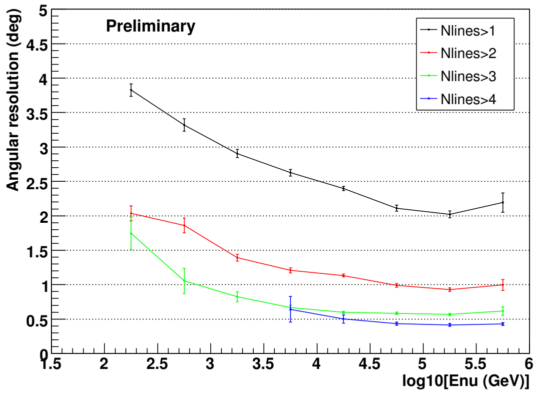

Figure 3: Angular resolution evolution with energy for the event reconstructed with at least 2, 3, 4 and 5 lines.

events are considered. When the neutrino telescope is running, this method is almost 100% efficient. Moreover, this method applies whenever the neutrinos are emitted with respect to the gamma flash. More importantly no assumption is made on the nature of the source and the mechanisms occurring inside. The main drawback of the rolling search is that a detection is not automatically associated to an astronomical source. To overcome this problem, it is fundamental to organize a complementary follow-up program. The observation of any transient sources will require a quasi real-time analysis and an angular precision lower than a degree.

3.1 The ANTARES neutrino triggers

Since the beginning of 2008, ANTARES has implemented an on-line event reconstruction. This analysis strategy contains a very efficient trigger based on local clusters of photomultiplier hits and a simple event reconstruction. The two main advantages are a very fast analysis (between 5 and 10 ms per event) and an acceptable angular resolution. The minimal condition for an event to be reconstructed is to contain a minimum of six storeys triggered on at least two lines. To select a high purity sample of up-going neutrino candidates, one quality cut is applied to the result of the χ^2 minimisation of the muon track reconstruction based on the measured time and amplitude of the hits. In order to obtain a fast answer, the on-line reconstruction does not use the dynamic reconstructed geometry of the detector lines. This has the consequence that the angular resolution is degraded with respect to the one obtained with the standard off-line ANTARES reconstruction (of about 0.2 - 0.3 °) which includes the detector positioning.

In order to set the cuts used for our "golden" neutrino event selection, we have analysed the data taken in 2008 corresponding to 173 active days. During this period, around 582 up-going neutrino candidates were recorded. The figure 2 shows the elevation distribution of the well reconstructed muon events. This plot shows as the same time the distribution of the down-going atmospheric muons and the up-going neutrino candidates compare to the distribution predicted by the Monte-Carlo simulations. In order to obtain an angular resolution lower than the field of view of the telescope used for the follow-up (around 1.9 °), we select reconstructed events which trigger several hits on at least 3 lines. The dependence of this resolution with the number of lines used in the fit is shown in the figure 3. For the highest energy events, this resolution can be as good as 0.5 degree. An estimation of the energy in the on-line reconstruction is indirectly determined by using the number of hits of the event and the total amplitude of these hits. In order to select events with an energy above a few tens of TeV, a minimum of about 20 hits and about 180 photoelectrons per track are required. These two different trigger logics applied on the 2008 data period select around ten events.

3.2 Optical follow-up network

ANTARES is organizing a follow-up program in collaboration with TAROT (*Télescope à Action Rapide pour les Objets Transitoires*, Rapid Action Telescope for Transient Objects, [10]). This network is composed of two 25 cm optical robotic telescopes located at Calern (South of France) and La Silla (Chile). The main advantages of the TAROT instruments are the large field of view of 1.86 ° x 1.86 ° and their very fast positioning time (less than 10 s). These telescopes are perfectly tailored for such a program. Since 2004, they observe automatically the alerts provided by different GRB satellites [11].

As it was said before, the rolling search method is sensitive to all transient sources producing high energy neutrinos. For example, a GRB afterglow requires a very fast observation strategy in contrary to a core collapse supernovae for which the optical signal will appear several days after the neutrino signal. To be sensitive to all these astrophysical sources, the observational strategy is composed of a real time observation followed by few observations during the following month. Such a program does not require a large observation time. Depending on the neutrino trigger settings, an alert sent to TAROT by this rolling search program would be issued at a rate of about one or two times per month.

4 Summary

The detection of neutrinos from transient sources is favoured by the fact that external triggers are provided by satellite currently in operation. The analysis of the data relying on those alerts is on-going in the ANTARES Collaboration.

The follow-up of golden events would improve significantly the perspective for neutrino detection from transient sources. The most important point of the rolling search method is that it is sensitive to any transient source. A confirmation by an optical telescope of a neutrino alert will not only give the nature of the source but also allow to increase the precision of the source direction determination in order to trigger other observatories (for example very large telescopes for the redshift measurement). The program for the follow-up of ANTARES golden neutrino events is operational with the TAROT telescopes since February 2009. It would be also interesting to extend this technique to other wavelength observation such as X-ray or radio.

References

1. N. Cottini, these proceedings.
2. S. Basa, D. Dornic et al, arXiv:astro-ph/0810.1394
3. D. Dornic et al, arXiv:astro-ph/0810.1416
4. GCN network, http://gcn.gsfc.nasa.gov
5. S.D. Barthelemy , L.M. Barbier, J.R. Cummings et al, 2005, space Science Reviews, 120, 143
6. R. Preece, these proceedings.
7. M. Bouwhuis, 2005 PhD Thesis, University of Amsterdam
8. M. Kowalski and A. Mohr, Astroparticle Physics, 27 (2007) 533-538
9. D. Dornic et al, arXiv:astro-ph/0810.1412
10. M. Bringer, M. Boer et al, 1999, A&AS, 138 581
11. A. Klotz, M. Boer, J.L. Atteia, B. Gendre, AJ 2008 submited

GAMMA-RAY BURST HOST GALAXIES: A LEGACY APPROACH

DANIELE MALESANI, JENS HJORTH, JOHAN P. U. FYNBO, BO MILVANG-JENSEN
Dark Cosmology Centre, Niels Bohr Institute, Juliane Maries Vej 30, 2100 Copenhagen Ø, Denmark.

PÁLL JAKOBSSON
Centre for Astrophysics and Cosmology, University of Iceland, Dunhagi 5, 107 Reykjavík, Iceland.

ANDREAS O. JAUNSEN
Institute of Theoretical Astrophysics, University of Oslo, PO Box 1029 Blindern, N-0315 Oslo, Norway.

Long-duration gamma-ray bursts are related to the deaths of young, massive stars. GRBs thus provide a precious cosmological tool, since they pinpoint locations in the Universe where active star formation is ongoing. We here describe the preparation and collection of a large, unbiased sample of GRB host galaxies. The goals of our program are the detection of the hosts, the search for reddened systems, the determination of redshifts, and the study of Lyα emission. Preliminary results include a large detection rate in the optical, a low fraction of red systems, an increase of the redshift completeness (including several systems in the "redshift desert"), and a lower-than-expected recovery of Lyα emission.

1 Introduction

Long-duration gamma-ray bursts (GRBs) are associated with the deaths of massive stars[12,23,26]. This fact allows their use as powerful tools to study star formation in the Universe. GRBs offer many advantages: they are very bright and detectable up to any redshift (the current record[10] being $z = 6.7$); the gamma- and X-ray emission is not affected by dust, hence they can be detected also inside highly obscured environments; their explosion relies on the existence of a single stellar progenitor, hence they select galaxies independent of their brightness; last, the study of the (bright) afterglows often provides valuable information about the hosts, including redshift, metallicity, dust content, presence of molecules, and so on.

This brief summary outlines that GRB host galaxies constitute a new sample of high-redshift star-forming systems, with selection criteria different from existing samples. Up to now, many studies of GRB hosts have been carried out (e.g.[6,25,21,3,8]), however hampered by the non-homogeneity of the adopted samples. In particular, before the launch of *Swift*[9], an optical afterglow was needed to locate a host galaxy, thus introducing selection effects against dusty systems. Nowadays, the X-Ray Telescope (XRT) onboard *Swift* routinely provides arcsecond-sized error positions for almost all GRBs, which allows carrying out effective, unbiased host searches.

1.1 Our sample

We aim at selecting a representative, unbiased sample of GRB host galaxies. To optimize the survey, we focus on those systems with the best available information, by selecting bursts with the following properties: (1) triggered on board by *Swift*; (2) be in the long class, with

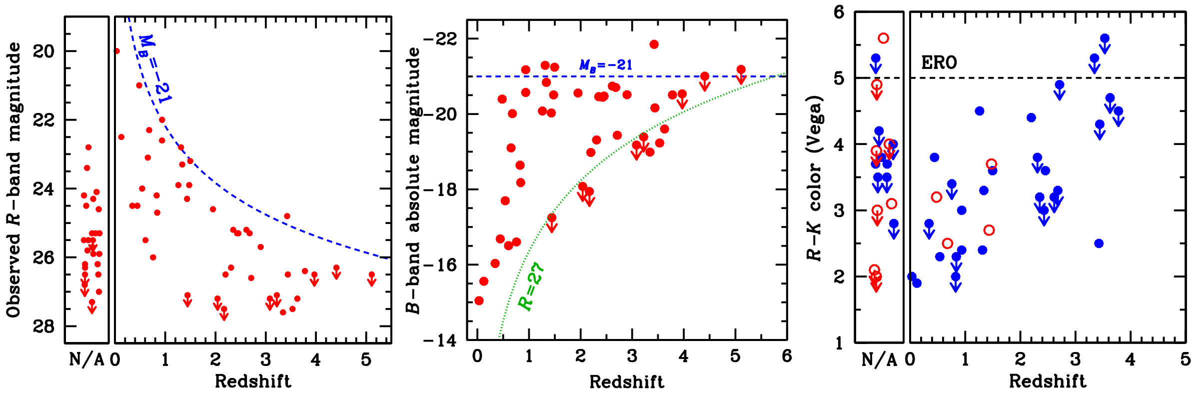

Figure 1: Left: observed R-band magnitudes of the hosts in our sample as a function of redshift. The left box shows objects with unknown redshift (the abscissa value is arbitrary). The dashed line shows the magnitude of an L^* galaxy ($M_B = -21$) as a function of redshift. Middle: absolute luminosity of hosts as a function of redshift. The dashed line shows the level of L^*, while the dotted curve indicates the effective survey limit ($R \approx 27$). Right: $R-K$ color of the hosts in our sample as a function of z. Only the galaxies with optical detection are shown. The box on the left shows systems with no known redshift (arbitrary absissa value). The horizontal line marks the boundary of extremely red objects (EROs; $R-K > 5$).

a duration $T_{90} > 2$ s; (3) detected between March 2005 and August 2007; (4) low Galactic extinction ($A_V \leq 0.5$ mag); (5) prompt XRT localization (< 12 hr); (6) good observability from the VLT ($-70° < \delta < +27°$); (7) small positional uncertainty (error radius $\leq 2''$).

Note that criteria 3–6 do not introduce selection effects in the sample, since they do not rely on physical properties of the bursts. Only criterium 7 may in principle bias against faint events (which have on the average worse localizations), however in practice it only excludes a few events (10% of the total). In the end, a burst satisfying the above criteria has a greater chance to be well studied and characterized, since its afterglow was more easily observable.

Following the above criteria, we are left with a sample of 71 GRBs. Among these, 55 (77%) have an optical/NIR afterglow and 40 (56%) have a measured redshift ($0.033 < z < 6.295$). These numbers fare significanly better than considering the full *Swift* sample (393 GRBs up to 2009 January), where only 53% and 33% have an optical counterpart and a redshift, respectively. For more details about our program, we refer to reference[13].

2 Results

Luminosities. As a first task, we searched for and localized the hosts. The survey was quite successful, with a detection rate of 80%. The success drops significantly at large redshifts, with a recovery fraction of 45% at $z > 3$. Figure 1 shows the distribution of the observed (left) and absolute (middle) magnitudes. As can be seen, GRB hosts are mostly subluminous, at a level $(0.01\text{–}1) \times L^*$. This is in line with previous findings based on smaller and less complete samples[17,6], and confirms that GRBs can pinpoint faint galaxies at high redshifts. The search of missing hosts will be carried out through dedicated HST observations.

Colors. The detection rate at NIR wavelengths is significantly lower than in the optical. This is due to a combination of instrument sensitivity and blue host colors. We found hosts in about 35% of the searched systems. Overall, colors are in the range $2 < R-K < 4.5$, with a single possible example of an extremely red object (ERO). The candidate ERO-GRB had no reported optical afterglow; while the lack of optical emission is consistent with the presence of dust, we cannot exclude a chance association given the relatively large error circle. Figure 1 (right) shows the distribution of observed colors for bursts with and without an optical afterglow. Note that the two groups have a comparable distribution of colors. Overall, even considering

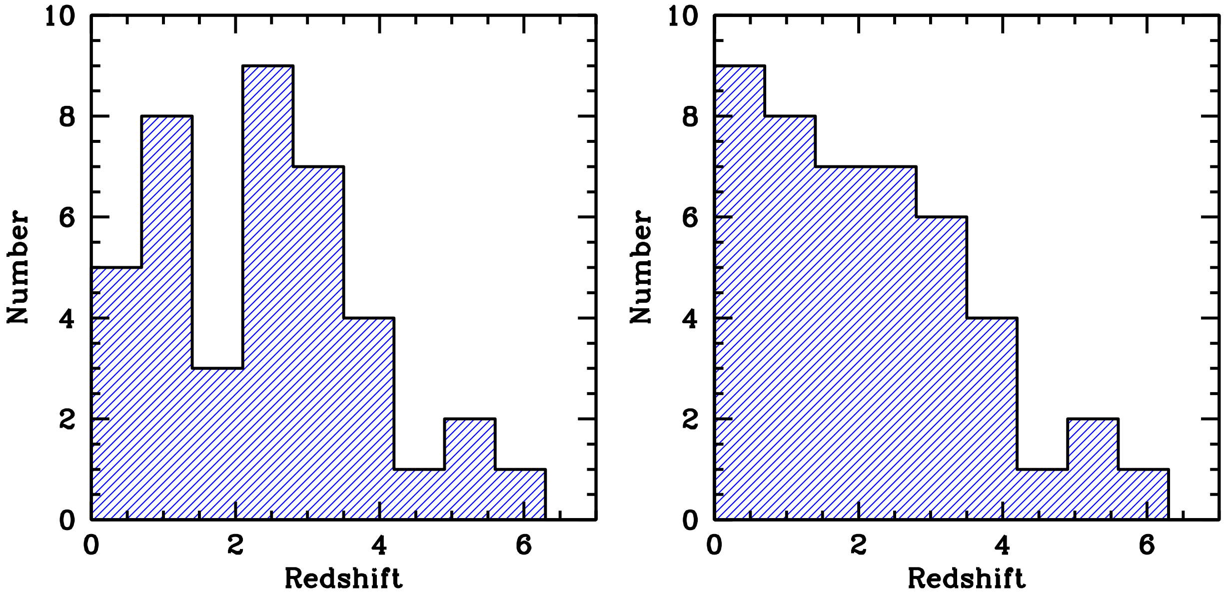

Figure 2: Redshift distribution of GRBs in our sample. Left panel: redshifts taken from the literature. Right panel: including the results from our program.

bursts with no afterglow, we can confirm earlier findings[17] that GRB hosts have mostly blue colors (though a few cases of red systems have been found[18,2]). Since reddened afterglows exist, this does not exclude that dust is present in some GRB hosts (e.g.[16,24,19]).

Redshifts. We followed up hosts without redshift with a variety of spectroscopic setups. In several cases, despite not being able to measure a secure redshift, we could set valuable limits due to the lack of expected features. Many GRBs are bound to be in the so-called redshift desert ($1 \lesssim z \lesssim 2$), where the most prominent nebular lines are shifted into wavelength regions difficult to observe. In some cases, we could confirm this hypothesis thanks to the use of red grisms sensitive up to 10,000 Å. We plan to follow up fainter or unclear cases with the upcoming optical/NIR X-shooter spectrograph[4] at the VLT, which we can access through guaranteed time.

Overall, we could measure nine new redshifts, and, surprisingly, we found a few of the redshifts reported in the literature to be likely wrong. For eight more systems we could constrain $1 \lesssim z \lesssim 2$. None of the targeted systems have a redshift larger than 2. While this is partly due to the selection of the brightest systems for spectroscopy, it also shows that many dark or faint GRBs probably lie at moderate redshift. Figure 2 shows the redshift distribution of our sample, outlining the contribution from our program. We caution that the analysis of the spectroscopic data[15] is not yet complete. The most noticeable effect is the elimination of the "gap" at $z \sim 1.7$, likely due to selection effects[5] (the prominent Lyα feature is not visible for $z \lesssim 2$). Our program was hence successful in filling the "redshift desert". Many authors have argued that the GRB redshift distribution is skewed towards higher redshifts compared to the evolution of the overall cosmic star formation (e.g.[14,11,27,22]). We here caution that a more complete sample is needed before drawing robust conclusions.

Lyα emisson. We have looked for Lyα emission in all hosts with a known redshift in the range $2 < z < 4.5$ (where the Lyα feature is redshifted in a favorable wavelength range). We did not require the presence of a detected host galaxy. These spectra also provided a way to doublecheck some of the redshifts reported in the literature (leading to the mentioned discovery of a few likely wrong redshifts). The analysis of these data is still ongoing, but the recovery fraction for these *Swift* GRB hosts appears lower than in earlier cases. Lyα is detected in about 20% of the cases. For comparison, pre-*Swift* studies provided five detections out of five studied cases[7]. The peak of the Lyα line is observed redshifted by a few hundreds km s^{-1} with respect to the absorption-line redshift inferred from afterglow spectra. This has already been observed in Lyman break galaxies[1]. We refer to reference[20] for a full description of our Lyα studies.

3 Legacy value

The results mentioned above are only the first steps to exploit the rich dataset collected in our program. The selection of the sample itself is valuable as an attempt to define a "good" set of GRBs upon which any kind of studies can be carried out, from the prompt emission properties, to the study of afterglows, to the characterization of the hosts and environments. The epoch when a single burst could bring significantly new and surprising elements is nearing an end, and it is now important to focus on well-characterized samples and population studies, where systematic effects are controlled and possibly minimized. Our group in Copenhagen has consistently concentrated the efforts on bursts selected according to the criteria outlined above, and will continue to follow this track in the future, also thanks to the new available instrumentation, such as X-shooter at the VLT.

Acknowledgements

The Dark Cosmology Centre is funded by the Danish National Research Foundation. The research of DM has been partly supported by the Instrument Centre for Danish Astrophysics. DM thanks Lorenzo Amati, David Coward, Arnon Dar, Phil Evans, Diego Götz, Andrea Melandri, Marco Nardini, and Danka Paraficz for stimulating discussion.

1. K. L. Adelberger et al.. 2003, ApJ, 584, 45
2. E. Berger et al. 2007, ApJ, 660, 504
3. H.-W. Chen et al. 2009, ApJ, 691, 152
4. S. D'Odorico et al. 2004, procs. SPIE, 5492, 220
5. F. Fiore, et al. 2007, A&A, 470, 515
6. A. S. Fruchter et al. 2006, Nature, 441, 463
7. J. P. U. Fynbo et al. 2003, A&A, 406, L63
8. J. P. U. Fynbo et al. 2008, ApJ, 683, 321
9. N. Gehrels et al. 2004, ApJ, 611, 1005
10. J. Greiner et al. 2009, ApJ, 693, 1610
11. D. Guetta and T. Piran 2007, JCAP, 7, 003
12. J. Hjorth et al. 2003, Nature, 423, 847
13. J. Hjorth et al. 2009, in preparation
14. P. Jakobsson et al. 2006, A&A, 447, 897
15. P. Jakobsson et al. 2009, in preparation
16. A. O. Jaunsen et al. 2008, ApJ, 681, 453
17. E. Le Floc'h et al. 2003, A&A, 400, 499
18. A. J. Levan et al. 2006, ApJ, 647, 471
19. M. J. Michałowski et al. 2008, ApJ, 672, 817
20. B. Milvang-Jensen 2009, in preparation
21. J. X. Prochaska et al. 2007, ApJ, 666, 267
22. R. Salvaterra et al. 2009, MNRAS, in press (arXiv:0805.4104)
23. K. Z. Stanek et al. 2003, ApJ, 591, L17
24. N. R. Tanvir et al. 2008, MNRAS, 388, 1743
25. C. Wolf and P. Podsiadlowski 2007, MNRAS, 375, 1049
26. S. E Woosley and J. S. Bloom 2006, ARA&A, 44, 507
27. H. Yüksel et al. 2008, ApJ, 683, L5

COSMOLOGY WITH GAMMA–RAY BURSTS

L. AMATI
INAF - IASF Bologna, via P. Gobetti 101,
I-40129 Bologna, Italy

Gamma–Ray Bursts (GRBs) are the brightest sources in the universe, emit mostly in the hard X–ray energy band and have been detected at redshifts up to ∼8.1. Thus, they are in principle very powerful probes for cosmology. I shortly review the researches aimed to use GRBs for the measurement of cosmological parameters, which are mainly based on the correlation between spectral peak photon energy and total radiated energy or luminosity. In particular, based on an enriched sample of 95 GRBs, I will provide an update of the analysis by Amati et al. (2008) aimed at extracting information on Ω_M and, to a less extent, on Ω_Λ, from the $E_{p,i}$ – E_{iso} correlation. I also briefly discuss the perspectives of using GRBs as cosmological beacons for high resolution absorption spectroscopy of the IGM (e.g., WHIM), and as tracers of the SFR, up to the "dark ages" ($z > 6$) of the universe.

1 Introduction

After ∼40 years since its discovery, the GRB phenomenon is still one of the most intriguing and hot topics in modern astrophysics. Indeed, despite the huge observational advances occurred since the late 90s, with the discovery of the afterglow emission, optical counterparts, host galaxies, the determination of the cosmological distance scale and huge luminosity and the evidences of association with peculiar SNe, our understanding of GRBs origin and physics is still affected by several open issues [1]. Among these, one of the most intriguing and debated is the possible use of GRBs as comological probes, which has been proposed in the last few years by several authors, following the mounting evidence that they are the brightest and farthest sources in the universe. In particular, many efforts have been done in order to extract information on cosmological parameters in an independent, or complementary, way to type Ia SNe and other cosmological probes (e.g., BAO, galaxy clusters, the CMB) by "standardizing" GRBs with the so called spectrum–energy correlations. Also, the high X–ray flux and the association of long GRBs with the death of young massive stars prompted the investigation of GRBs as background sources for high resolution spectroscopy of the IGM with next generation experiments and as tracers of the star formatin rate (SFR) up tp the re–ionization epoch.

In this article, after summarizing the properties that make GRBs potentially powerful cosmological probes (Section 2), I will discuss and update the analysis aimed at estimating cosmological parameters by using the $E_{p,i}$ – E_{iso} correlation, the simplest and first discovered among spectrum–energy correlations (Sections 3 and 4). Then, I will review (Section 5) the results on cosmological parameters obtained by using other spectrum–energy correlations found by adding to $E_{p,i}$ and E_{iso} a third observable. Historically, these correlations were the first to be used to this purpouse since 2004. Methods based on the joint use of spectrum–energy correlations with Type Ia SNe or other GRB correlations are outlined in Section 6. Finally, in Section 7 I briefly

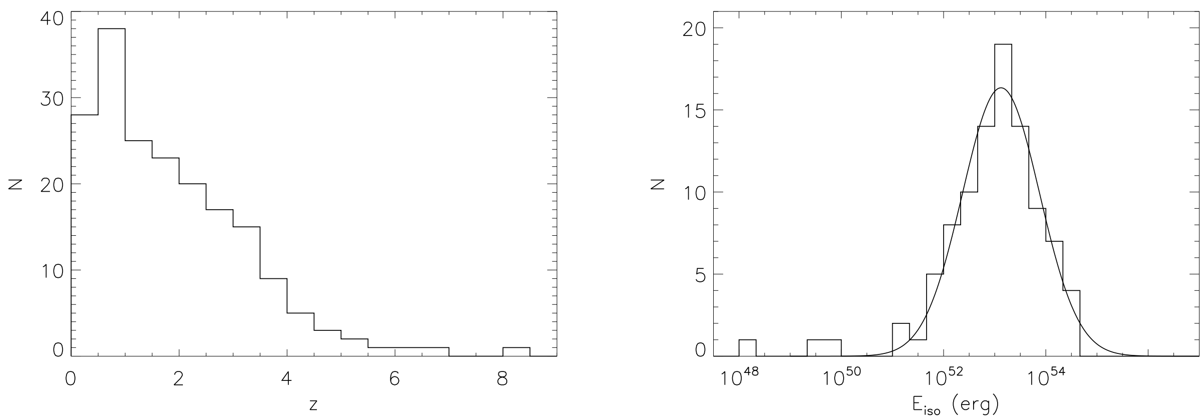

Figure 1: Left: redshift distribution for the 189 GRBs with known redshift as of April 2009. Right: $E_{\rm iso}$ distribution for the 95 GRBs with known redshift and spectral parameters as of April 2009.

discuss the possible use of GRBs as cosmological beacons and tracers of the star formation history of the universe.

For reasons of space, the citations in the text cannot be exgaustive, and the given references are reviews or examples. The analysis reported in Sections 2, 3 and 4 are based on data available as of April 2009 and have been performed specifically for this work.

2 Gamma–Ray Bursts as cosmological probes

In the last years, the use of Type Ia SNe as standard candles, combined with CMB measurements, has revolutioned our view of the history of the cosmic expansion of the universe. Indeed, within the standard CDM cosmological model the evidence, based on CMB observations and the implications of inflation, that the universe is flat (Ω=1) and the location of high–z SNe Ia in the Hubble diagram imply that the universe is presently accelerating and that $\sim$73% of Ω is determined by an unknown and mostly unpredicted component or field (e.g., dark energy, quintessence, cosmological constant) [2,3,4]. However, SN Ia as standard candles are affected by possible systematics, like, e.g., different explosion mechanisms and progenitor systems, evolution with z, possible dependence on z of the light curve shape correction for luminosity normalization, signatures of evolution in the colours, correction for dust extinction, anomalous luminosity–color relation, contaminations of the Hubble Diagram by no–standard SNe-Ia and/or bright SNe-Ibc (e.g. HNe) [5]. In addition, this sources are found only up to moderate redshift ($\sim$1.4–1.7).

Thus, the quest for alternative astrophysical sources capable to provide estimates of the cosmological parameters in an independent way and at higher z with respect to SNe Ia is a central topic in modern astrophysics. The sources under investigation for this purpouse include, e.g., galaxy clusters and BAO, but a lot of interest has been raised in the last years by the redshift and luminosity properties of GRBs.

In Figure 1, I show the updated distributions of z (189 events with measured redshift) and $E_{\rm iso}$ (95 events with measured redshift and spectral parameters) of GRBs as of April 2009. The redshift values were taken from the GRB table by J. Greiner [a] and references therein, whereas the values of $E_{\rm iso}$ were computed based on the spectral parameters and fluences reported in Amati et al. (2008) [6], 70 events, and Amati et al. (2009) [7], 25 more events, and by assuming a standard ΛCDM cosmology with $H_0 = 70$ km s^{-1} Mpc^{-1}, $\Omega_M = 0.27$ and $\Omega_\Lambda = 0.73$. As can be seen, GRBs are the brightest sources in the universe, with values of the isotropic–equivalent

[a] http://www.mpe.mpg.de/jcg/grbgen.html

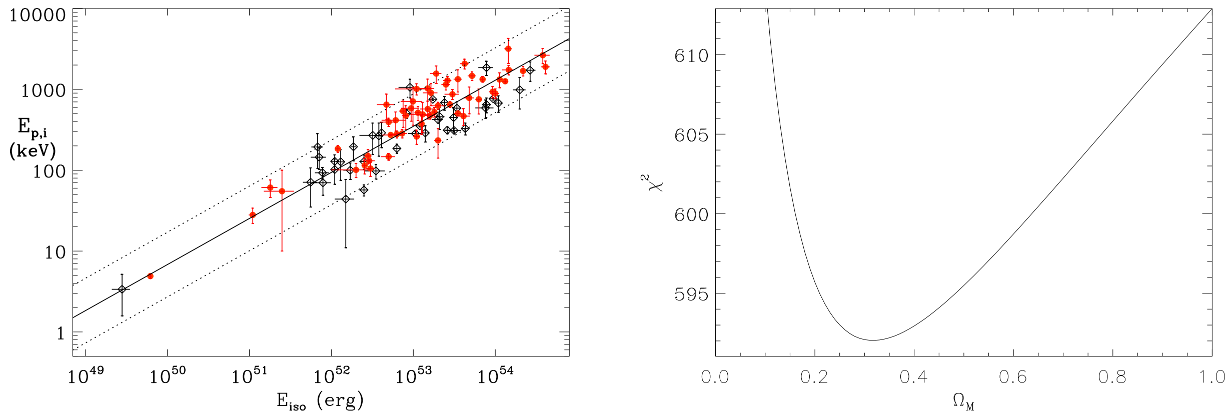

Figure 2: Left: $E_{\rm p,i}$ – $E_{\rm iso}$ correlation withe the prsent sample of 95 GRBs with known redshift and $E_{\rm p,i}$. Red dots are those GRBs localized by *Swift*. Right: χ^2 value of the fit of the updated $E_{\rm p,i}$ – $E_{\rm iso}$ correlation (95 GRBs) with a simple power–law as a function of the value of $\Omega_{\rm M}$ assumed to compute the $E_{\rm iso}$ values. A flat univese is assumed.

radiated energies, $E_{\rm iso}$, that can exceed 10^{54} erg, emit most of their radiated energy in the hard X–rays, and thus are not affected by dust extinction problems which affect, e.g., type Ia SNe, and show a redshift distribution extending at least up to ∼8.1, much above that of any other class of astrophysical sources.

Thus, in principle GRBs are the most suitable cosmological probes. However, as can be seen in Figure 1, they are not standard candles, showing radiated energies, and luminosities, spanning several orders of magnitude. In the past it was proposed that the collimation–corrected radiated energy, E_γ (see Section 5) could be clustered at around $\sim 10^{51}$ erg [8,9], but this evidence was not confirmed by subsequent observations. The investigation of GRBs as a new and alternative tool for the measurement of cosmological parameters was then prompted by the discovery of a strong correlation between the spectral peak photon energy, a quantity independent on the cosmological model, and the event intensity (radiated energy, average luminosity, peak luminosity), which depends on the assumed cosmological parameters. This correlation and the methods proposed to derive from it information on cosmological parameters are the subject of the next three Sections.

3 The $E_{\rm p,i} - E_{\rm iso}$ correlation

GRB spectra are non thermal and are well described by a smoothed broken power–law ("Band" function) with low and high energy photon indices in the ranges ∼0.5–1.5 and ∼2.1–3, respectively [10,11]. Thus, when expressed in terms of νF_ν, GRB spectra show a peak. The photon energy at which this peak occurs is hence called "peak energy" and indicated as $E_{\rm p}$ when referring to the observed spectrum or $E_{\rm p,i}$ for the cosmological rest–frame (i.e., "intrinsic") spectrum. $E_{\rm p,i}$ values range from a few keV up to several thousands of keV and its distribution has the shape of a Gaussian centered at around 200–300 keV with a low energy tail [12]. This spectral parameter is a relevant observable for models of the physics of GRB prompt emission [13], whose understanding is one of the main still open issues in this field of research.

Evidence for a strong correlation between $E_{\rm p,i}$, and $E_{\rm iso}$ was first reported by Amati et al. (2002)[14], based on a limited sample of *Beppo*SAX GRBs with known redshift. This correlation was later confirmed and extended to softer/weaker events (X–Ray Flashes, XRFs) by measurements by other satellites, mainly HETE–2, *Konus*/WIND and, more recently also *Swift* and *Fermi*/GBM [12,6,15] The recent estimates of z for some short GRBs provided the evidence that

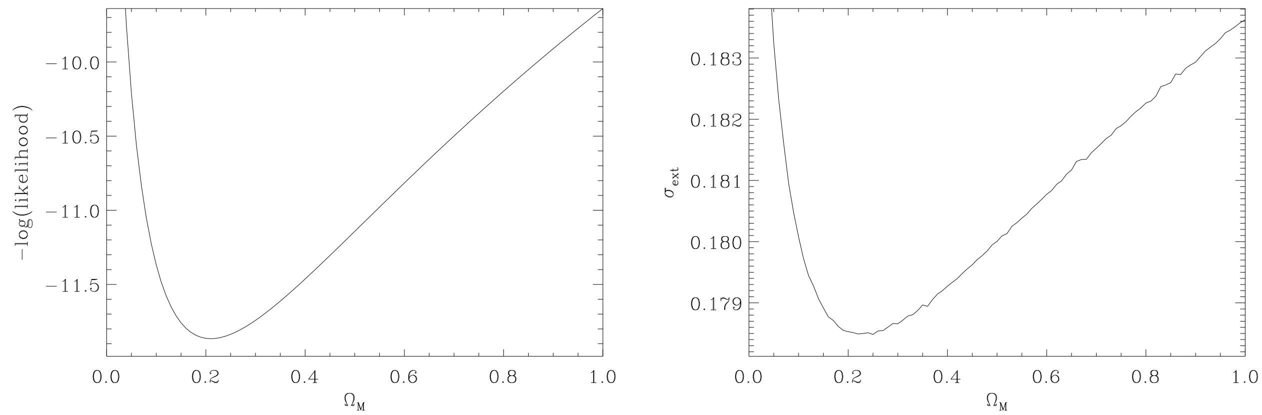

Figure 3: Values of log(likelihood)(left) and $\sigma_{\rm ext}$ (right) of the fit of the updated $E_{\rm p,i} - E_{\rm iso}$ correlation (95 GRBs) with a maximum likelihood method accounting for extrinsic variance (see text) as a function of the value of $\Omega_{\rm M}$ assumed to compute the $E_{\rm iso}$ values. A flat univese is assumed.

the $E_{\rm p,i} - E_{\rm iso}$ correlation holds only for long GRBs [16,17], with the exception of the peculiar sub–energetic GRB 980425. It was also found that the correlation holds as well if $E_{\rm iso}$ is substituted with the average or peak luminosity ($L_{\rm iso}$ and $L_{\rm p,iso}$, respectively [18,19]), which is not surprising given that these "intensity indicators" are strongly correlated. In Figure 2, I show the $E_{\rm p,i} - E_{\rm iso}$ correlation for the most updated (April 2009) sample of GRBs with known z and $E_{\rm p,i}$. The main features of the $E_{\rm p,i} - E_{\rm iso}$ correlation are that it extends over several orders of magnitude both in $E_{\rm p,i}$ and $E_{\rm iso}$, it can be modeled by a power–law with slope $\sim$0.5 and it is characterized by an extra–scatter, with respect to Poissonian fluctuations, of $\sim$0.2 dex [15,12,6].

As already discussed by several authors [13,20,12], this observational evidence has relevant implications for the geometry and physics of GRB prompt emission and can be used to identify and understand sub–classes of GRBs (e.g., short, sub–energetic, XRFs). In the recent years some authors argued that the correlation may be an artifact of, or at least significantly biased by, a combination of selection effects due to detectors sensitivity and energy thresholds [21,22,23]. However, the fact that GRBs detected, localized and spectroscopically characterized by different instruments all follow the same $E_{\rm p,i} - E_{\rm iso}$ correlation, as can be see in Figure 2 by comparing the location of *Swift* GRBs with respect to those detected by other instruments, supports the hypothesis of a low impact of selection and detectors threshold effects. Moreover, time resolved analysis of large samples of GRBs provide evidence that the correlation holds also within single bursts [24,25], thus pointing to a physical origin of it.

4 Estimating cosmological parameters with the $E_{\rm p,i} - E_{\rm iso}$ correlation

As discussed in the previous Section, the $E_{\rm p,i} - E_{\rm iso}$ correlation is highly significant, holds for all long GRBs with known redshift and $E_{\rm p,i}$ and is likely not strongly affected by selection and detectors threshold effects. Thus, given that it links a cosmology independent quantity, $E_{\rm p,i}$, to the burst radiated energy or luminosity, in principle it could be used to "standardize" GRBs, in a way similar to what is done with SNe Ia with the "Phillips" relation. However, the dispersion of the points around the best fit power–law is significanlty in excess to the Poissonian one, indicating the presence of an extrinsic variance of unknown origin. In addition, given the lack of a sufficient number of GRBs at very low or at the same redshift (Figure 1), the correlation cannot be calibrated, as can be done, instead, for Type Ia SNe. Because of this problems, in the last years the "cosmological use" of this correlation, and/or the $E_{\rm p,i}$–$L_{\rm p,iso}$ correlation, consisted in the estimate of pseudo–redshifts for those GRBs without measured redshift. This can be

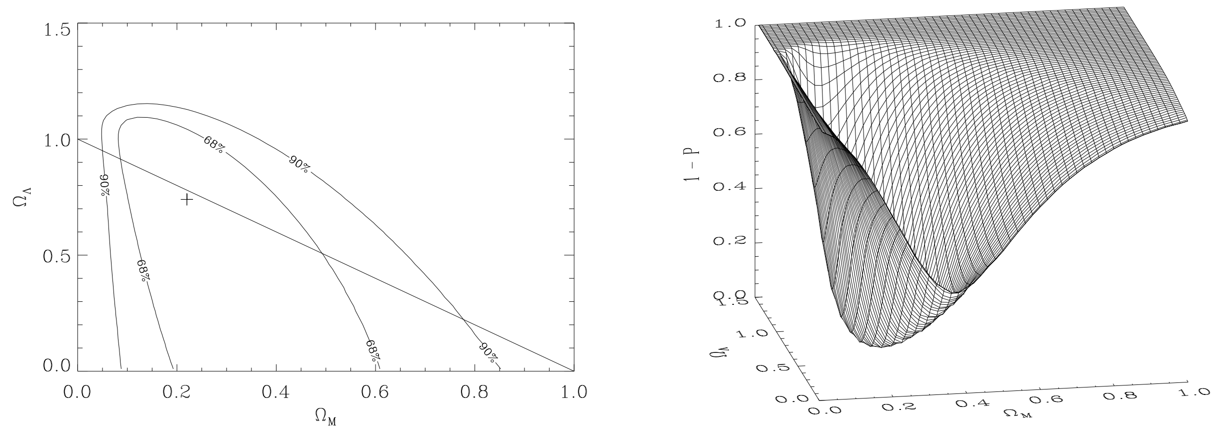

Figure 4: Contour (left) and surface (right) plots showing the probability associated to $\Omega_{\rm M}$ and Ω_Λ found by fitting the updated $E_{\rm p,i} - E_{\rm iso}$ correlation (95 GRBs) with a maximum likelihood method accounting for extrinsic variance (see text) and releasing the hypothesis of a flat universe. The cross in the left panel indicates the best fit values.

done by simply studying the track of a GRB in the $E_{\rm p,i} - E_{\rm iso}$ plane as a function of redshift, or by using quantities involved in the correlation to build a pseudo–redshift estimator [26]. Some authors applied these methods on large sample of GRBs in order to reconstruct the luminosity function or, assuming the association of GRB with very massive stars, the star formation rate (SFR) evolution (Section 7).

However, recently Amati et al. (2008) [6] have shown that the $E_{\rm p,i} - E_{\rm iso}$ correlation can also be used to obtain information on cosmological parameters. Their work was prompted by the evidence that, in the assumption of a flat universe, the trend of the χ^2 of the fit with a simple powerlaw as a function of the value of $\Omega_{\rm M}$ adopted to compute the luminosity distance and hence the values of $E_{\rm iso}$ shows a nice parabolic shape minimizing at $\Omega_{\rm M}{\sim}0.3$, as can be seen in Figure 2. This is a qualitative but simple, and independent on other cosmological probes, indication that if the universe is flat, as predicted by inflation and implied by CMB measurements, the universe expansion is presently accelerating and an unknown component or field (e.g., dark energy, quintessence, cosmological constant) is dominating over matter and/or gravity. In order to quantify the estimate of $\Omega_{\rm M}$, Amati et al. (2008) adopted a likelihood method which accounts for uncertainties on both X and Y quantities and parametrizes the extrinsic variance (i.e. the variance in excess to the Poissonian one) of the data, $\sigma_{\rm ext}$. In this way, they found $\Omega_{\rm M} = 0.15^{+0.25}_{-0.11}$ at 68% c.l. and $\Omega_{\rm M} < 1$ at a significance level higher than 99%. This result is fully consistent with that obtained with type Ia SNe. By means of simulations, they also showed that with the substantial increase of the number of GRBs with known z and $E_{\rm p,i}$ expected in the next years, these constraints will be significantly reduced.

In Figures 3 I show the results obtained by repeating the same analysis on the updated sample of 95 GRBs. As can be seen, both the −log–likelihood and $\sigma_{\rm ext}$ minimize for $\Omega_{\rm M}{\sim}0.2$. In particular, I find $\Omega_{\rm M} = 0.21^{+0.27}_{-0.13}$ at 68% c.l. and $\Omega_{\rm M} = 0.21^{+0.53}_{-0.16}$ at 90% c.l. These constraints are slightly tighter than those obtained by Amati et al. (2008), confirming the expected effect of the sample enlargement. Moreover, as can be seen in Figure 4, by releasing the assumption of a flat universe, the best–fit values of $\Omega_{\rm M}$ and Ω_Λ are 0.22 and 0.74, respectively, i.e. very close to the standard cosmology values and to the flat universe hypothesis. Also in this case, even if at 68% c.l. they still provide only an upper limit to Ω_Λ, the contour confidence levels are tighter than what found by Amati et al. (2008).

5 Cosmology with three-parameters spectrum–energy correlations

Soon after the first detections of GRB optical counterparts, it was found that in some cases the optical afterglow light curve shows a steepening of its power–law decay [27,28]. Within the standard fireball – external shock scenario for the afterglow emission, this "break" can be interpreted as due to collimated emission [29] (even though other explanations are possible). In this view, the jet opening angle can be derived from the break time $t_{\rm b}$ by making some assumptions on the circum–burst medium average density and profile and on the efficiency of conversion of the fireball kinetic energy into radiated energy. The jet opening angle, in turn, can be used to derive the collimation–corrected, or "true", radiated energy, E_γ, from $E_{\rm iso}$. As mentioned in Section 2, E_γ is sitll not standard and is tipically in the range from $\sim 5\times10^{49}$–10^{52} erg.

In 2004 it was found that when substituing $E_{\rm iso}$ with E_γ, the $E_{\rm p,i} - E_{\rm iso}$ correlation becomes tighter, i.e. its extrinsic scatter reduces by a factor of ~ 2 [28]. Even if based on a rather low number of events, this evidence prompted the first systematic investigations of GRBs as cosmological rulers [30,28,31]. Despite the advantage of a reduced scatter with respect to the $E_{\rm p,i} - E_{\rm iso}$ correlation, the problem of the lack of calibration with low z events cannot be solved anyway, and different methods were proposed in order to avoid "circularity". The most common are the so called "scatter methods", consisting in fitting the correlation for each set of cosmological parameters under study, deriving a χ^2 distribution and use it to obtain best fit values and confidence intervals. This can be done either directly in the $E_{\rm p,i} - E_\gamma$ plane or in the Hubble diagram obtained by deriving E_γ from $E_{\rm p,i}$ and hence the luminosity distance from E_γ and the measured fluence. More sophisticated methods based on Bayesian statistics were also proposed [31].

The constraints on $\Omega_{\rm M}$ and the limits to Ω_Λ obtained with the $E_{\rm p,i} - E_\gamma$ correlation were similar to those derived a few years later from the $E_{\rm p,i} - E_{\rm iso}$ correlation and described in the previous Section. The main drawbacks that prevented, up to now, the expected improvements in the accuracy and reliability of the cosmological parameters estimates with this method include: i) the very slow increase of GRBs with evidence of a break in the optical afterglow light curve, mainly due to the lack of systematic monitoring (the number of GRBs that can be used for the $E_{\rm p,i} - E_\gamma$ correlation are $\sim 25\%$ with respect to the $E_{\rm p,i} - E_{\rm iso}$ correlation); ii) the evidence from *Swift*/XRT measurements of the X–ray afterglow that, contrary to what expected in the basic jet scenario,in several cases there are not X–ray breaks or the breaks are achromatic; iii) the debate on the real dispersion and possible existence of outliers of the $E_{\rm p,i} - E_\gamma$ correlation [32,33]; iv) the fact that the $E_{\rm p,i} - E_\gamma$ correlation is model dependent, i.e. requires assumptions on the circum–burst density profile and, more in general, a jet model. Concerning points ii) and iv), it was noted that the correlation between $E_{\rm p,i}$, $E_{\rm iso}$ and $t_{\rm b}$ holds even without the need of a jet interpretation, i.e. at a purely empirical level [34]. Thus, also the $E_{\rm p,i} - E_{\rm iso} - t_b$ correlation was investigated for the estimate of cosmological parameters. However, under this respect it is still affected by the low number of events that can be used, the existence of possible outliers and the uncertainty on its true dispersion.

In 2006, it was also found that the dispersion of the $E_{\rm p,i}$–$L_{\rm p,iso}$ correlation decreases substantially when including the "high signal time scale" $\rm T_{0.45}$, a parameter often used in GRB variability studies. Thus, also this correlation was proposed as a tool to standardize GRBs, similarly to the $E_{\rm p,i} - E_\gamma$ and $E_{\rm p,i} - E_{\rm iso} - t_b$ correlations, but with the advantage of a higher number of events, being based on prompt emission properties only. However, subsequent analysis on larger samples showed that the extrinsic scatter of this correlation may not be significantly lower than that of the simple $E_{\rm p,i} - E_{\rm iso}$ or $E_{\rm p,i}$–$L_{\rm p,iso}$ correlations [35,36].

6 Calibrating GRBs with SNe Ia and multi–correlation studies

As mentioned in the previous Sections, one of the most liming features of spectrum–energy correlations as tools to standardize GRBs is the lack of low redshift GRBs, or of a sufficient number of GRBs at the same redshift, allowing to calibrate them. On the other hand, if one believes that SN Ia are reliable distance indicators, then can use them to calibrate GRB spectrum–energy correlations and take advantage of the GRB redshift distribution in order to extend the Hubble diagram from z $\sim$ 1.7 up to $\sim$8. This approach has been followed by several authors [37,38], allowing them not only to tighten the constraints on $\Omega_{\rm M}$ and Ω_Λ but also to obtain information on the the dark energy equation of state and its evolution, or to test cosmological models alternative to the standard ΛCDM.

The obvious drawback of this use of GRBs for cosmology is that it introduces a "circularity" with type Ia SNe, i.e., GRBs are no more independent probes and all the systematics and uncertainties associated with SNe propagates into the results obtained with this method.

The spectrum–energy correlations discussed in previous Sections are the tightest but not the only ones linking GRB observables to their luminosity. For instance, significant correlations were found between prompt emission variability and peak luminosity or between prompt emission time–lag and luminosity. Some authors developed methods for putting together several correlations in order to derive estimates of cosmological parameters [39]. However, adding to spectrum–energy correlations more dispersed correlations adds, thus preventing a significant improvemnt with respect to using spectrum–energy correlations alone.

7 Gamma–Ray Bursts as cosmological beacons and SFR tracers

Besides the estimate of cosmological parameters, GRBs are also very promising tools for cosmology under other respects. The association of long GRBs with peculiar type Ib/c SNe or hypernovae, and thus the death of very massive stars, is supported both by theories and observations [40]. Thus, given their huge luminosity and redshift distribution extending up to at least $z \sim 8$, GRBs may be considered powerful and unique tracers of the SFR evolution up to the re-ionization epoch. For instance, the recent detection of GRB 090423 at $z \sim 8.1$ is a simple and direct evidence that stars were already there at about 600 millions of year from the big–bang and with explosion mechanism not markedly different from that of stars born several billions of years later [41]. Several authors addressed this issues, either by comparing directly the GRB redshift distribution with the SFR up to $z \sim 4$ reconstructed from other observations, or by reconstructing the GRB luminosity function and its evolution by computing the pseudo–redshift of large numbers of GRB based on spectrum–energy correlations [19]. The results of these analysis indicate that GRBs are a biased tracer of the SFR evolution, which may be due to the fact, supported both by theory and observations, that GRBs are produced by low metallicity stars in low metallicity galaxies. Under this respect, GRBs provide information on the metallicity evolution [42].

Another interesting and promising cosmological use of GRBs is to use their X–ray afterglow emission as background source for X–ray high resolution spectroscopy of the inter–galactic medium (IGM) and of the host galaxies inter–stellar medium (ISM). This kind of investigations is the subject of future missions under study, like, e.g., the EDGE mission proposed to the ESA Cosmic Vision [43] or the XENIA mission submitted to the NASA Decadal Survey. As discussed, e.g., by Branchini et al. (2009) [44], with state of the art X–ray microcalorimeters, allowing energy resolutions of the order of $\sim$2–3 eV in the 0.2–2 keV energy range, an effective area of $\sim$1000 cm^2 energy range, spacecraft slewing capabilities of the order of 1 min and by assuming the X–ray afterglow photon fluence distribution measured by *Swift*/XRT, sensitive spectroscopy of tens of WHIM system per year could be done. In addition, by exploiting, e.g., resonant absorption lines, such instrumentation would allow the study of the galaxy ISM properties and their evolution with redshift.

References

1. P. Meszáros, Prog.Phys. **69**, 2269 (2006).
2. S. Perlmutter, G. Aldering, M. Della Valle *et al*, Nature **391**, 51 (1998).
3. A.G. Riess, A.V. Filippenko, P. Challis *et al*, AJ **116**, 1009 (1998).
4. A.G. Riess, L-G. Strolger, J. Tonry *et al*, ApJ **607**, 665 (2004).
5. M. Della Valle, L. Amati AIPC **1059**, 63 (2008).
6. L. Amati, C. Guidorzi, F. Frontera *et al*, MNRAS **391**, 577 (2008).
7. L. Amati, C. Guidorzi, F. Frontera, A&A **submitted**, (2009).
8. D.A. Frail, S.R. Kulkarni, R. Sari *et al*, ApJ **562**, L55 (2001).
9. E. Berger, S.R. Kulkarni, D.A. Frail, ApJ **590**, 379 (2003).
10. D. Band, J. Matteson, L. Ford *et al*, ApJ **413**, 281 (1993).
11. Y. Kaneko, R.D. Preece, M.S. Briggs *et al*, ApJS **166**, 298 (2006).
12. L. Amati, MNRAS **372**, 233 (2006).
13. B. Zhang, P. Mészáros, ApJ **581**, 1236 (2002).
14. L. Amati, F. Frontera, M. Tavani *et al*, A&A **390**, 81 (2002).
15. G. Ghirlanda, L. Nava, G. Ghisellini *et al*, MNRAS **387**, 319 (2008).
16. L. Amati, NCimB **121**, 1081 (2006).
17. G. Ghirlanda, L. Nava, G. Ghisellini *et al*, A&A **496**, 585 (2009).
18. D.Q. Lamb, G.R. Ricker, J-L. Atteia *et al*, NewAR **48**, 323 (2004).
19. D. Yonetoku, T. Murakami, T. Nakamura *et al*, ApJ **609**, 935 (2004).
20. D.Q. Lamb, T.Q. Donachy, C. Graziani, ApJ **620**, 355 (2005).
21. D. Band, R.D. Preece, ApJ **627**, 319 (2005).
22. E. Nakar, T. Piran, MNRAS **360**, L73 (2005).
23. N.R. Butler, D. Kocevski, J.S. Bloom, ApJ **694**, 76 (2009).
24. E. Liang, Z.G. Dai, X.F. Wu, ApJ **606**, L29 (2004).
25. C. Firmani, J.I. Cabrera, V. Avila–Reese *et al*, MNRAS **392**, 1209 (2008).
26. J–L. Atteia, A&A **407**, L1 (2003).
27. F.A. Harrison, J.S. Bloom, D.A. Frail *et al*, ApJ **523**, L12 (1999).
28. G. Ghirlanda, G. Ghisellini, D. Lazzati, ApJ **616**, 331 (2004).
29. R. Sari, T. Piran, J.P. Halpern, ApJ **519**, L17 (1999).
30. Z.G. Dai, E.W. Liang, D. Xu, ApJ **12**, L101 (2004).
31. G. Ghirlanda, G. Ghisellini and C. Firmani, NJP **8**, 123 (2006).
32. S. Campana, C. Guidorzi, G. Tagliaferri *et al*, A&A **472**, 395 (2007).
33. G. Ghirlanda, L. Nava, G. Ghisellini *et al*, A&A **466**, 127 (2007).
34. E. Liang, B. Zhang, ApJ **633**, 611 (2005).
35. F. Rossi, C. Guidorzi, L. Amati *et al*, MNRAS **388**, 1284 (2008).
36. A.C. Collazzi, B.E. Schaefer, ApJ **688**, 456 (2008).
37. Y. Kodama, D. Yonetoku, T. Murakami *et al*, MNRAS **391**, L1 (2008).
38. N. Liang, W.K. Xiao, Y Liu *et al*, ApJ **685**, 354 (2008).
39. B.E. Schaefer, ApJ **660**, 16 (2007).
40. S.E. Woosley, J.S. Bloom, ARA&A **44**, 507 (2006).
41. R. Salvaterra, M. Della Valle, S. Campana *et al*, Nature **submitted**, arXiv:0906.1578 (2009).
42. L–X. Li, MNRAS **388**, 1487 (2008).
43. L. Piro, J.W. den Herder, T. Ohashi *et al*, Exp.Astron. **23**, 67 (2009).
44. E. Branchini, E. Ursino, A. Corsi *et al*, ApJ **685**, 354 (2009).

RECENT RESULTS ON MAGNETARS

SANDRO MEREGHETTI
INAF - Istituto di Astrofisica Spaziale e Fisica Cosmica Milano,
v. E.Bassini 15, I-20133 Milano, Italy

Several observations obtained in the last few years indicate that Soft Gamma-ray Repeaters (SGRs) and Anomalous X-ray Pulsars (AXPs) are basically a single class of isolated neutron stars. Their properties are well explained by the magnetar model, based on neutron stars powered by magnetic fields as high as 10^{14}–10^{15} G. Here I report some recent results obtained for the transient Soft Gamma-ray Repeater SGR 1627–41, that started a new outburst after about 10 years from the previous one, and for the Anomalous X–ray Pulsar 1E 1547.0–5408. The latter source recently showed a remarkable bursting activity, that reinforces the similarity between AXPs and SGRs.

1 Anomalous X-ray Pulsars and Soft Gamma-Ray Repeaters

Two small classes of peculiar high-energy sources, the Anomalous X-ray Pulsars (AXPs) and the Soft Gamma-Ray Repeaters (SGRs), have attracted increasing attention in the last decade. Their classification in two distinct groups reflects the different manifestations that led to their discovery, but there is mounting evidence that they are probably a single class of objects. Namely, observations performed in the last few years showed many similarities between AXPs and SGRs [34,18].

AXPs were first detected as persistently bright pulsars in the soft X-ray range (<10 keV) and thought to belong to the population of galactic accreting binaries. When more X–ray data accumulated, and deeper optical/IR searches excluded the presence of bright companion stars, their peculiar properties started to emerge and led to classify them as a separate class of pulsars [16]. Their common properties are periods of a few seconds, secular spin-down in the range 10^{-13} – 10^{-10} s s^{-1}, relatively soft spectra below 10 keV, and, in some cases, associations with supernova remnants.

SGRs were discovered through the detection of short bursts in the hard X-ray/soft gamma-ray range and initially considered as a subclass of gamma-ray bursts[13,1]. During sporadic periods of activity, lasting from days to months, they emit short bursts (<1 s) of hard X–rays/soft γ-rays reaching L$\sim 10^{41}$ erg s^{-1}. Occasionally, SGRs emit much more energetic "giant flares" with luminosity up to 10^{47} erg s^{-1}. Only three of these rare events have been observed, each one from a different source [15,8,22,20]. When good positions for the SGRs bursts could be obtained it became possible to identify their X-ray counterparts, finding that they are pulsating sources very similar to the AXPs.

It is generally believed that both SGRs and AXPs are Magnetars: neutron stars with extremely high magnetic fields, B$\sim 10^{14}$-10^{15} G, i.e. 100-1000 times stronger than those of the typical neutron stars observed as radio pulsars powered by rotational energy or as X–ray pulsars powered by accretion from their binary companions. In this interpretation, the magnetic field

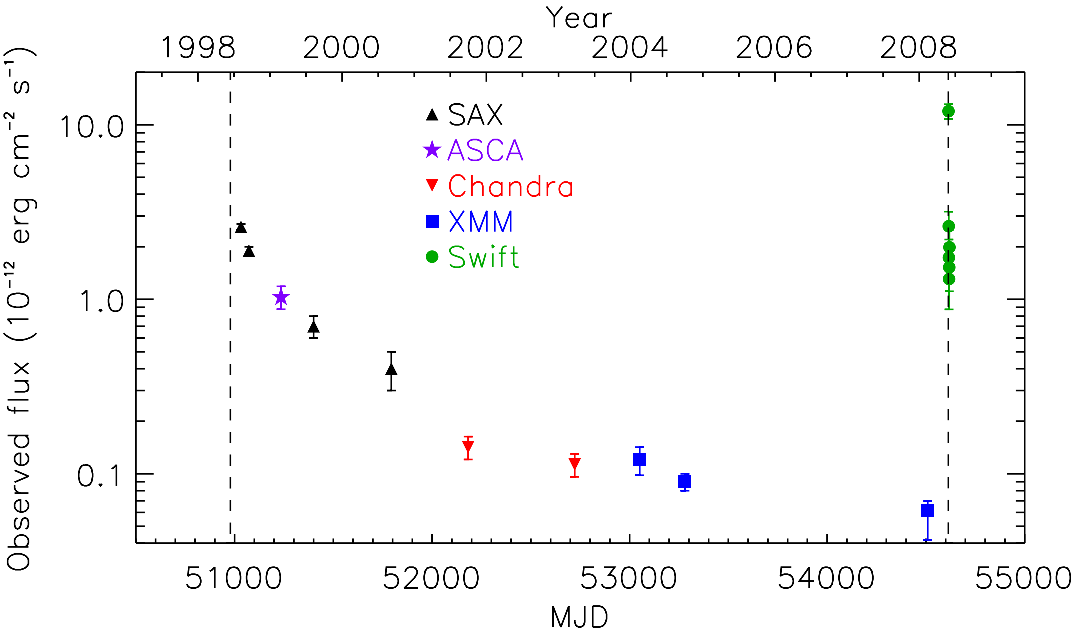

Figure 1: X–ray light curve of SGR 1627–41 spanning ten years of observations with different satellites (observed flux in the 2-10 keV energy range). The vertical lines indicate the two periods of bursting activity seen from this source (June 1998 and May 2008).

is the ultimate energy source of all the persistent and bursting emission observed in AXPs and SGRs [25,26].

Here I present some results on two sources that entered new periods of strong activity in the last months: the SGR 1627–41 and the AXP 1E 1547.0–5408. These results further support the similarity between these two classes of sources.

2 The 2008 reactivation of SGR 1627–41

SGR 1627–41 was the first SGR to show a transient behavior. It was discovered in 1998, during a bursting state that lasted about six weeks [32]. At the time of the outburst its X-ray counterpart had a luminosity of $\sim 10^{35}$ erg s^{-1}, but in the following years its X-ray luminosity gradually decreased [17], as shown in Fig. 1. This long-term decay was interpreted as the cooling of the neutron star after the heating that occurred during the outburst [11]. In principle, the modelling of the long term light curve could provide information on the mechanism for (and location of) the heating and on the neutron star structure. However, uncertainties in the relative cross calibrations of the different instruments as well as the limited spectral information make it difficult to obtain reliable results [17].

An XMM-Newton observation carried out in February 2008 revealed SGR 1627–41 at only $\sim 10^{33}$ erg s^{-1} (for d=11 kpc), the lowest luminosity observed for a SGR [4]. In May 2008 SGR 1627–41 started a new outburst, during which several short bursts were detected and a peak luminosity higher than that observed in 1998 was attained (Fig. 1). The subsequent evolution could be monitored by a series of Swift observations that showed an initial rapid decrease followed by a shallower phase [4]. The 2008 light curve is compared in Fig. 2 with that of the previous outburst and with the behavior seen in a few other AXPs/SGRs [4]. When early data are available, they show that a single power law decay cannot reproduce the source fading, owing to the presence of a steeper initial phase in the first days after the outburst. This suggest

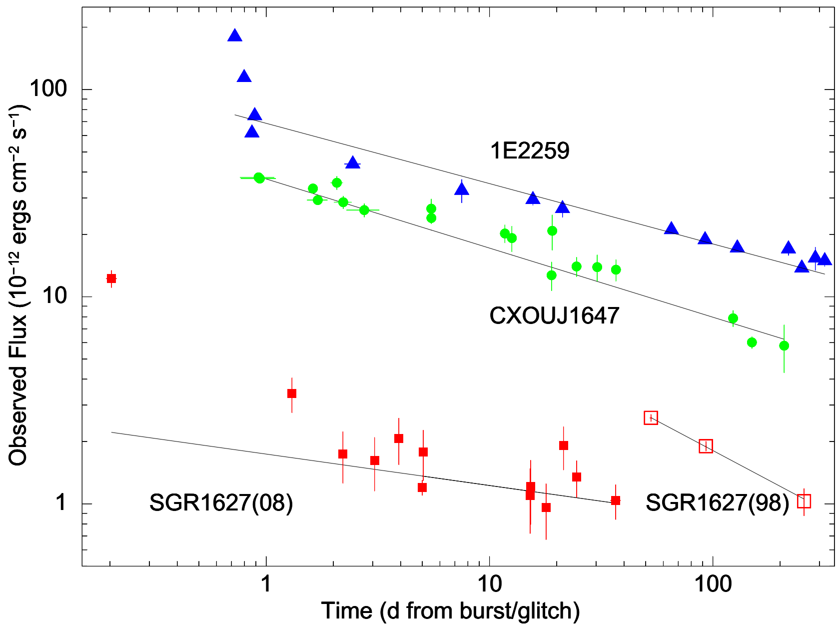

Figure 2: Comparison of the long term flux decays following outbursts of SGRs and AXPs. For SGR 1627–41 both the 1998 and 2008 events are plotted. Note the good coverage of the early phases of the 2008 outburst that could be obtained thanks to the prompt observations with Swift. The lines are power laws with time decay index ranging from –0.2 (SGR 1627–41 in 2008) to –0.6 (SGR 1627–41 in 1998).

the presence of two different mechanisms at play. One possibility is that the steep phase be due to magnetospheric currents dissipation while the later phase reflect the effect of crustal cooling. It is also possible that X-rays emitted during the initial bright burst, delayed by interstellar dust scattering, contribute to the initial steep phase (see below).

Due to visibility constraints, the brightest part of the SGR 1627–41 outburst could not be observed by XMM-Newton, but we requested a Target of Opportunity observation to be performed as soon as possible, in order to take advantage of the source brightness to measure its still unknown spin period. The observation was done on 2008 September 27-28, and despite the low source flux $\sim 3 \times 10^{-13}$ erg cm^{-2} s^{-1}, the large effective area of the EPIC instrument allowed us to collect enough counts and to discover the long-sought pulsations[5]. The spin period is 2.6 s, one of the shortest among magnetar candidates. The X–ray pulse profile, characterized by two peaks of different intensity, is shown in Fig. 3.

The deep XMM-Newton observation led also to the discovery of diffuse X–ray emission from the vicinity of SGR 1627–41, as shown in Fig. 4. Spectral and spatial analysis shows that the resolved source about 1.5 arcmin south of the SGR is most likely due to a cluster of galaxies, while the more extended and softer emission is related to the supernova remnant / HII region complex CTB 33[24].

3 The January 2009 outburst of 1E 1547.0–5408

The transient X–ray source 1E 1547.0–5408 was discovered almost 30 years ago[12] in the supernova remnant G 327.24–0.13, but it attracted little interest until it was proposed as a possible AXP on the basis of new X-ray and optical studies ruling out more standard interpretations[6]. Radio pulsations with $P = 2.1$ s and period derivative $\dot{P} = 2.3 \times 10^{-11}$ s s^{-1} were subsequently discovered[2], confirming its AXP nature. In October 2008 1E 1547.0–5408 started an outburst with the emission of several short bursts and a significant increase in its X-ray flux[10].

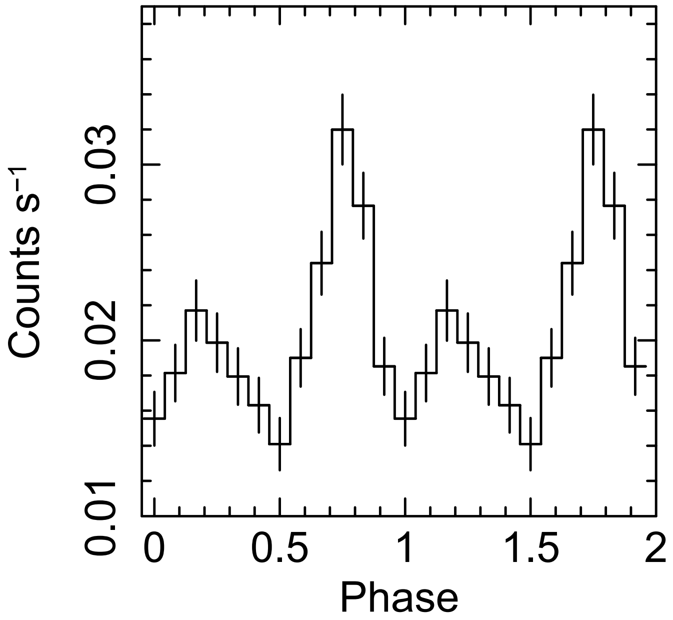

Figure 3: X-ray light curve of SGR 1627–41 folded at the spin period of 2.59 s discovered by Esposito et al. (2009). The data have been obtained with the XMM-Newton EPIC pn camera in the 2-12 keV energy range.

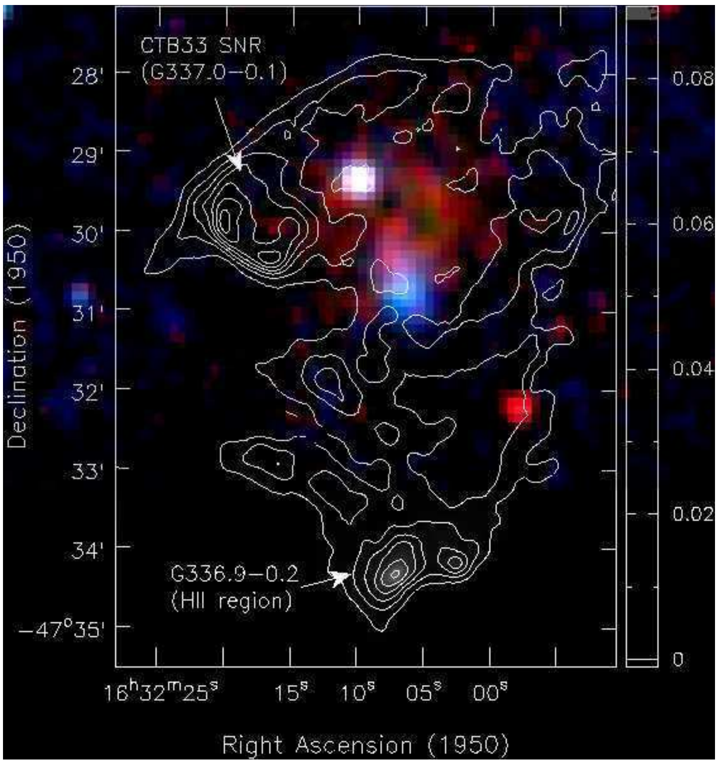

Figure 4: XMM-Newton EPIC X-ray image of the region of SGR 1627–41 with overlaid contours from the 1375 MHz radio map of Sarma et al. (1997). The colors indicate the photon energy (1.7–3.1 keV in red, 3.1–5 keV in green, and 5–8 keV in blue). The bright source in white is SGR 1627–41. The bluish diffuse source is most likely a cluster of galaxy in the background, as indicated by its high absorption and redshifted Fe line. The soft X–ray (in red) diffuse emission can be associated to the SNR G337.0–0.1.

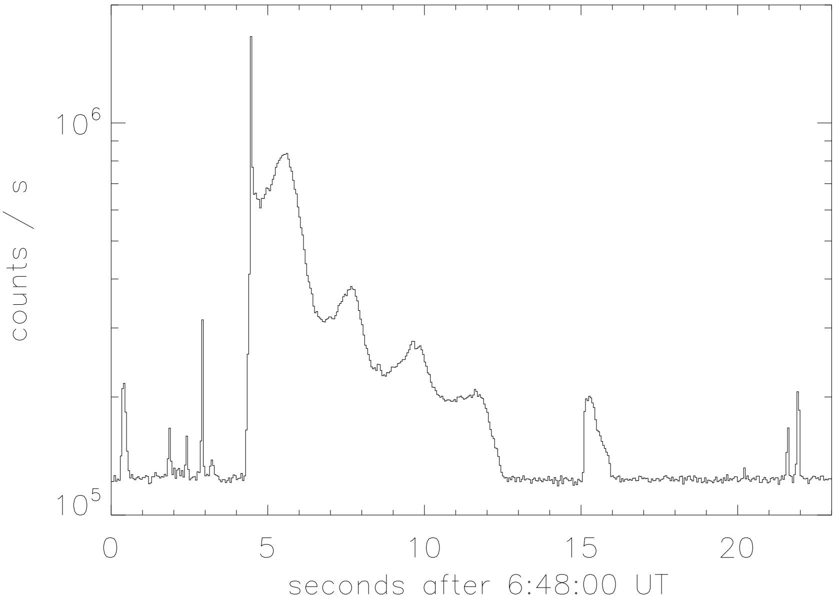

Figure 5: Bursts from 1E 1547.0–5408 observed at E>80 keV with the Anti-Coincidence System of the SPI instrument on board INTEGRAL on January 22, 2009. The initial spike of the longest burst had a duration of ~0.3 s and reached a peak flux greater than 2 10^{-4} erg cm^{-2} s^{-1} (25 keV - 2 MeV). A modulation at 2.1 s, reflecting the neutron star rotation period, is clearly visible in the burst tail.

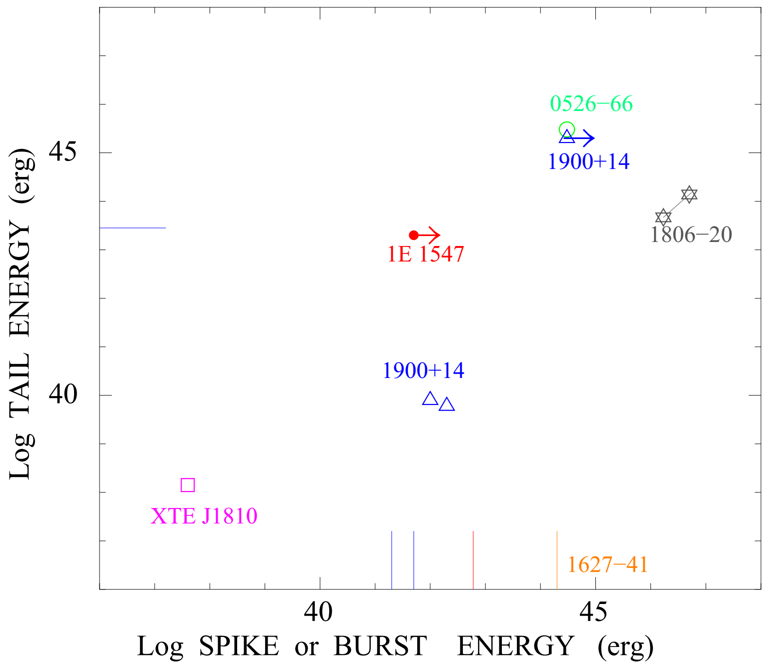

Figure 6: Energetics of flares and peculiar bursts from SGRs and AXPs. The different sources are distinguished by the symbols color. The ordinate gives the energy in the pulsating tails that often follow the brightest bursts, while the abscissa reports the energy in the initial spikes (data from Mereghetti et al. (2009) and references therein). The vertical/horizontal lines refer to events in which only one of these components has been observed. The three historical giant flares from SGRs are in the upper right corner. Note that in some cases only lower limits to the total energy could be derived due to instrument saturation. The two points for SGR 1806–20 are for the generally assumed distance of 15 kpc and for the more recent estimate d=8.7 kpc. The energetics of the burst from 1E 1547.0–5408 for an assumed distance of 10 kpc, is in the range of the so called "intermediate flares".

More recently, a new period of strong activity culminated on 2009 January 22, when more than 200 bursts were detected in a few hours. Some of these bursts were particularly bright, and two had durations sufficiently long to show a clear modulation at the neutron star spin period. Of particular interest is the burst shown in Fig. 5, that started with a very bright and short initial spike (∼0.3 s) followed by a ∼8 s long pulsating tail [19]. Although these features are typical of giant flares from SGRs [15,8,22,20], the energy released in this event was not as large as that of the three historical giant flares. This is shown in Fig. 6, where the energetics of the strongest bursts and flares from SGRs/AXPs are compared. Although the plotted data are affected by some uncertainties, especially for the brightest events that caused instrument saturation, it is clear that there is a rather continuum distributions of intensities, from the normal short bursts up to the brightest giant flares. It is also noteworthy that extended pulsating tails have been detected not only for the three giant flares, but also after less intense bursts [9,14,33]. Conversely, also a few examples of pulsating tails apparently without a bright initial hard spike have been observed [7,19]. This is possibly an indication that the spike emission is non-isotropic, a fact that adds a further uncertainty to proper estimates of the involved energy.

Immediately after the discovery of the strong bursting activity of January 22, several follow-up pointings of 1E 1547.0–5408 were carried out with Swift. During the first XRT observations, the imaging mode could not be used because the source was too bright. The first data providing full imaging (Fig. 7) were obtained on January 23 at ∼15:30 UT and showed the presence of remarkable dust scattering rings around the source position [28]. Dust scattering X-ray halos around bright galactic sources were predicted well before their observations with the first X-ray imaging instruments [21]. Their study allows to get information on the properties and spatial distribution of the interstellar dust. When the scattered radiation is a short burst/flare and the dust is concentrated in a relatively narrow cloud, an expanding ring (instead than a steady diffuse halo) appears, due to the difference in path-lengths at different scattering angles. Halos in the form of expanding rings have been observed in a few gamma-ray bursts, and their study allowed to determine accurate distances for the scattering dust clouds in our galaxy [30,27,31].

The dust scattering rings around 1E 1547.0–5408 are the brightest ever observed and the first ones for an AXP/SGR. Further observations carried out with Swift, XMM-Newton and Chandra clearly show that their angular size is increasing with time. By fitting their expansion law it is possible to determine the burst emission time, which is found to coincide with the interval of highest activity including the bright event of ∼6:48 UT shown in Fig. 5. A comprehensive spectral analysis of all the available X–ray data of the expanding rings around 1E 1547.0–5408 will allow to determine the distances of the source and of the three dust layers [29].

4 Conclusions

The two sources described here have many similarities. Their spin periods (2.1 and 2.6 s) are the shortest of all the AXPs/SGRs, both are located in supernova remnants (and are in the same region of the galactic plane), both are transient sources and emitted short bursts when in the high state. If 1E 1547.0–5408 had not been previously known as a weak X-ray source, but discovered through its bursts it would have been baptized SGR, as it recently happened for the new source SGR 0501+4516 [3,23]. This underlines once more that the distinction between AXPs and SGRs does not reflect a real difference in the two classes of sources, that can be well explained by the same physical model.

Acknowledgments

The results described in this work have been possible thanks to a large international collaboration including P.Esposito, A. De Luca, D.Götz, G.L.Israel, N.Rea, L.Stella, A.Tiengo, R.Turolla,

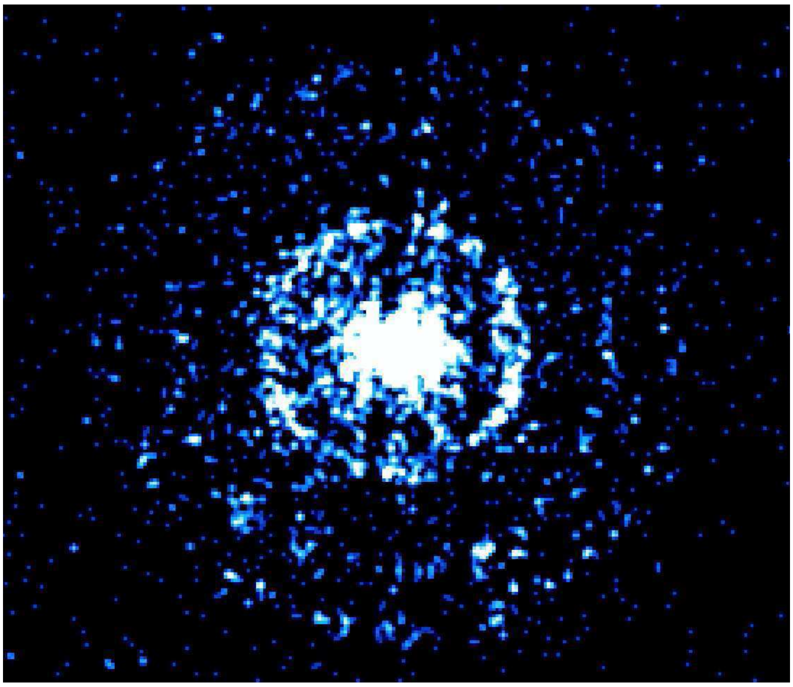

Figure 7: X-ray rings produced by dust scattering around 1E 1547.0–5408. In this image, obtained with the Swift/XRT instrument on January 23, the innermost and brightest ring has a radius of ∼1 arcmin. Two outer rings, produced by closer dust layers are also visible. The ring dimensions were seen to increase in later observations, as expected for scattering by narrow dust layers of the X–ray flux emitted during the strong bursting activity that took place around 6:48 UT of January 22.

G.Vianello, A. von Kienlin, G.Weidenspointner, S. Zane and others.

References

1. Atteia, J.L., Boer, M., Hurley, K., Niel, M., Vedrenne, G., Fenimore, E.E., Klebesadel, R.W., Laros, J.G., Kuznetsov, A.V., Sunyaev, R.A., Terekhov, O.V., Kouveliotou, C., Cline, T., Dennis, B., Desai, U., Orwig, L. 1987, *ApJ*, 320, L105
2. Camilo, F., Ransom, S. M., Halpern, J. P., & Reynolds, J. 2007, *ApJ*, 666, L93
3. Enoto, T., et al. 2009, *ApJ*, 693, L122
4. Esposito, P., et al. 2008, *MNRAS*, 390, L34
5. Esposito, P., et al. 2009, *ApJ*, 690, L105
6. Gelfand, J. D. & Gaensler, B. M. 2007, *ApJ*, 667, 1111
7. Guidorzi, C., Frontera, F., Montanari, E., et al. 2004, *A&A*, 416, 297
8. Hurley, K., Cline, T., Mazets, E., et al. 1999, *Nature*, 397, 41
9. Ibrahim, A. I., Strohmayer, T. E., Woods, P. M., et al. 2001, *ApJ*, 558, 237
10. Israel, G. L., et al. 2009, *MNRAS*, submitted
11. Kouveliotou C. et al., 2003, *ApJ*, 596, L79
12. Lamb, R. C. & Markert, T. H. 1981, *ApJ*, 244, 94
13. Laros, J.G., Fenimore, E.E., Fikani, M.M., Klebesadel, R.W., Barat, C. 1986, *Nature*, 322, 152
14. Lenters, G. T., Woods, P. M., Goupell, J. E., et al. 2003, *ApJ*, 587, 761
15. Mazets, E. P., Golentskii, S. V., Ilinskii, V. N., Aptekar, R. L., & Guryan, I. A. 1979, *Nature*, 282, 587
16. Mereghetti, S., Stella, L. 1995, *ApJ*, 442, L17

17. Mereghetti, S., Esposito, P., Tiengo, A., Turolla, R., Zane, S., Stella, L., Israel, G.L., Feroci, M., Treves, A. 2006, *A&A*, 450, 759
18. Mereghetti, S. 2008, *A&A Rev*, 15, 225
19. Mereghetti, S., Götz, D., Weidenspointner, G., von Kienlin, A., Esposito, P., Tiengo, A., Vianello, G., Israel, G.L., Stella, L., Turolla, R., Rea, N., Zane, S. 2009, *ApJ*, 696, L74
20. Mereghetti, S., Götz, D., von Kienlin, A., et al. 2005, *ApJ*, 624, L105
21. Overbeck, J.W. 1965, *ApJ*141, 864
22. Palmer, D. M., Barthelmy, S., Gehrels, N., et al. 2005, *Nature*, 434, 1107
23. Rea, N. et al. 2009, *MNRAS*in press
24. Sarma, A. P., Goss, W. M., Green, A. J., & Frail, D. A. 1997, *ApJ*, 483, 335
25. Thompson, C. & Duncan, R. C. 1995, *MNRAS*, 275, 255
26. Thompson, C. & Duncan, R. C. 1996, *ApJ*, 473, 322
27. Tiengo, A. & Mereghetti, S. 2006, *A&A*449, 203
28. Tiengo, A., Mereghetti, S., Vianello, G., et al. 2009, GCN circ. 8848
29. Tiengo, A., et al. 2009, in preparation
30. Vaughan, S., Willingale, R., O'Brien, P.T., et al. 2004, *ApJ*603, L5
31. Vianello, G., Tiengo, A., & Mereghetti, S. 2007, *A&A*473, 423
32. Woods, P.M., Kouveliotou, C., van Paradijs, J., Hurley, K., Kippen, R.M., Finger, M.H., Briggs, M.S., Dieters, S., Fishman, G.J. 1999, *ApJ*, 519, L139
33. Woods, P. M., Kouveliotou, C., Gavriil, F. P., et al. 2005, *ApJ*, 629, 985
34. Woods, P.M., Thompson, C., 2006, in Compact stellar X-ray sources, pp. 547–586

Angular Energy Distribution of Relativistic Jets from Collapsars

Akira Mizuta[1] and Miguel, A. Aloy[2]
[1] *Center for Frontier Science, Chiba University Yayoi-cho 1-33, Inage-ku, Chiba, 263-8522 Japan*
[2] *Departamento de Astronomía y Astrofisíca, Universidad de Valencia, 46100-Burjassot (Valencia), Spain*

Angular energy distribution of the highly relativistic jets from collapsars is studied, using 19 different progenitor models whose radial mass profile, total mass, radius of the progenitor of each models are different each other. The jet propagation is followed from deep inside of the progenitor to outside of the progenitor surface. The angular energy distribution strongly depends on the mass of the progenitors at pre-supernova stage. The distribution of the jets from lighter progenitors is steeper than that of the jets from heavier progenitor models.

1 Introduction

The connection between the long duration gamma-ray bursts (GRBs) and the type Ib/c supernovae (SN) has been strongly suggested by some observations, for example, SN1998bw/GRB980425 [1,2] and GRB030329/SN2003dh [3]. SN1998bw and SN2003dh are type Ic SN and categorized within a special class of supernova explosions, so-called hypernovae, whose explosion energy is about ten times higher, i.e., $\sim 10^{52}$ erg, than that of ordinary supernova. The properties of the progenitor have been investigated. Unfortunately we do not know any direct information on the most other GRB progenitors, since the burst usually occurs far away from us.

It is an interesting question weather it is possible to get any information on the nature of a GRB progenitor from the observation of the afterglow emission. Following collapsar model [4,5], we study propagation of the relativistic jets from collapsars to see the dependence of the progenitor properties for the GRB jet. The angular energy distribution, which is integrated energy per unit of solid angle, is the useful diagnostics for this, since the angular energy distribution directly affects the observation. Lazzati et al.[6] discussed theoretically such an angular distribution and concluded that the energy distribution per solid angle ($dE/d\Omega$) of the jet displays a θ^{-2} dependence with the viewing angle after its eruption through the progenitor surface. Recently, Morsony et al.[7] have used hydrodynamic simulations to test the theoretical prediction of Lazzati et al.[6], and found that their numerical models do not follow the inferred theoretical angular energy distribution. In this paper we discuss the dependence of progenitor properties on the angular energy distribution of relativistic jets from collapsars.

2 Model and Numerical Method

We use 19 progenitor models developed Woosley & Heger [8] (the models HE16A-P and 16TB, 16TC and 16OC). They traced the massive star evolution, including the effects of initial angular momentum, dynamo, metallicity, and mass loss rate. The models used in this study can be divided into three groups by the mass of the progenitors at pre-supernovae stage. Those are light ($\simeq 5M_\odot$: type L), middle ($\simeq 10M_\odot$ type M), and heavy ($\simeq 15M_\odot$ type H) progenitor models. The radial mass profiles and radii are different from each other, even if they are in the same group. We extend the mass profile up to 10^{11} cm, which is outer computational boundary of spherical coordinate, assuming a r^{-2} dependence. The inner computational boundary is at $r = 10^8$ cm. We assume that our models are axial and equatorially symmetric and, therefore, specify reflection boundary conditions at the polar axis ($\theta = 0°$) and at the equator ($\theta = 90°$).

It is assumed that a jet has been generated by the central engine, and that at a certain distance, quasi-steady injection conditions are settled through a well defined circular nozzle. Thus, we inject plasma, in the radial direction, through the innermost radial boundary at $r = 10^8$ cm in a cone of half-opening angle $\theta_{\rm j} = 5°$. The jet injection proceeds for a period $t_{\rm inj} = 4$ s. We parametrize the outflowing plasma by assuming that it is hot (we set $\epsilon_{\rm j}/c^2 = 30$) and moderately relativistic (the Lorentz factor being $\Gamma_{\rm j,0} = 5$). We adopt the convention that the parameters of the outflow at the injection point are named with a subscript 'j'. The injected flows have the potential to accelerate to bulk Lorentz factors larger than 100 [12], converting thermal energy to kinetic energy. During the first 3 s, the power of the injected outflow is $L_{\rm j,0} \equiv \rho_{\rm j}\Gamma_{\rm j,0}v_{r{\rm j}}(h_{\rm j}\Gamma_{\rm j,0} - 1)c^2\Delta S = 10^{51}$ erg s^{-1}, where ΔS is the area of the injection surface, $h(\equiv 1 + \epsilon/c^2 + p/\rho c^2)$ is the specific enthalpy, and v_r is the radial component of the 3-velocity. The density and pressure of the injected outflow are obtained by setting $\Gamma_{\rm j,0}$, $\epsilon_{\rm j}$, $L_{\rm j,0}$, $\theta_{\rm j}$, and $r_{\rm min}$. We fix $L_{\rm j,0} = 10^{51}$ erg s^{-1}, which is higher than that adopted in previous studies [9,10,7]. Thus the total injected energy is several times 10^{51} erg. Since the main purpose of this study is to see the jet propagation and expansion of the cocoon into the interstellar medium after the shock breakout, we adopt this power to obtain a rapid propagation of the jet in the progenitor. This fast propagation is necessary to be consistent with the fact that we neglect the self-gravity of the star. If the jet crosses the progenitor much faster than the typical hydrodynamic timescale in the system, the progenitor remains roughly unchanged during the complete jet propagation through it and, therefore, we do not need to care about the progenitor evolution during such short timescales.

3 Results and Discussion

The dynamical evolution of the jet from collapsars can be split in two phases. Those are before and after the shock break, at which the head of the jet reaches progenitor surface and erupts from the surface. The dynamics of our models during this two phases if roughly similar to that outlined by some previous works [11,9,10,12,7]. When the head of the jet is inside of the jet, the jet keeps good collimation, forming a strong bow shock at the head of the progenitor. A high pressure plasma driven by the bow shock and high pressure cocoon support the collimation of the jet. After the shock breaks out from the surface of the progenitor, the jet proceeds into ISM which is assumed to be dilute gas. The jet still keeps good collimation with a half opening angle of several degrees, though cocoon component spreads out.

The evolution of our models has been followed until the head of the jet reaches the outermost radial computational boundary at $r = 10^{11}$ cm. Assuming the dynamics of the jet is at quasi self-similar phase, we derive the angular energy distribution per unit solid angle ($dE/d\Omega$) that can be potentially emitted at the afterglow phase. In order to derive $dE/d\Omega$ we have to make several assumptions. First, we assume that a fix fraction (the same everywhere) of the total energy (internal plus kinetic) will be converted into electromagnetic radiation. Basically, this assumption is equivalent to state that the angular profile of the observed non-thermal radiation is simply a scaled version of the total energy angular profile. Certainly, this is a rough approximation, since the non-thermal radiation from γ-rays to radio frequencies will be produced by synchrotron (and, perhaps, inverse Compton) processes of particles accelerated at shocks (or, maybe, along the jet boundary layer; e.g., Aloy et al.[13]). Obviously, there are shocks of very different properties in the ultrarelativistic beam and in the cocoon and, thus, we may expect somewhat different conversion efficiencies of the outflow energy into radiation in the beam and in the cocoon. Finally, we assume that the angular energy distribution is *frozen-in* by the time when the head of the jet reaches the outer computational boundary. The radiation contributions coming from regions outside of the line of sight is considered when the angular energy distribution is derived (see Janka et al.[14]). In order to avoid accounting for subrelativistic regions, which will not contribute to the afterglow energetics, we exclude the contributions of numerical cells where $v_r < 0.7c$ and $h\Gamma < 4$.

The absolute value of the observed $dE/d\Omega(\theta)$ along every radial direction forming an angle θ with the polar axis depends, among other things, on two parameters whose exact value is not well constrained, neither by observations nor by the present day theory. These are (i) the efficiency of energy conversion to radiation, and (ii) the total energy injected. Therefore, we will show only the angular profiles of $dE/d\Omega(\theta)$ normalized to the maximum value $dE/d\Omega(\theta)|_{\max}$ found for each model. Figure 1 shows the normalized isotropic angular energy distributions corresponding to models HE16C, HE16L and HE16N, which are prototypes of the types L, M and H, respectively. In the same figure we overplot fits to the normalized $dE/d\Omega(\theta)$ profiles. The fitting function is a smoothly broken power law (SBP) of the form,

$$F(\theta) = 2^{-1/n} A \left[\left(\frac{\theta}{\theta_0} \right)^{\alpha_l n} + \left(\frac{\theta}{\theta_0} \right)^{\alpha_h n} \right]^{1/n}, \tag{1}$$

where A is the value of the function F at $\theta = \theta_0$, θ_0 is the angular location of the break point between the prebreak and postbreak power-laws, whose slopes are α_l and α_h, respectively, and n is a numerical factor that controls the sharpness of the break.

By inspection of Fig. 1, the angular energy distributions are remarkably well fitted by the function of Eq. (1) in the interval $0 < \theta \lesssim 3.4°$, i.e., in the angular region occupied by the beam of the jet. At smaller latitudes ($5° \lesssim \theta \lesssim 8°$) the model data separates from the fitting function and presents systematically larger values than the latter. Indeed, the data in such an interval can be well fitted by a simple power law, with a slope in the range $[-3.6, -4.5]$ The deviation from the SPB function in this angular range is due to the contribution of the expanding, mildly relativistic cocoon.

In order to show more clearly the existence of correlations between the properties of the progenitor star and the $dE/d\Omega$ distribution, we show in Fig. 2 the dependence of the postbreak slope α_h and on the stellar progenitor mass M. There exists a correlation between α_h and M, such that the slope of lighter progenitors is steeper than that of heavier ones. There is roughly a linear dependence of α_h on M, which displays a relatively large dispersion. The reason for the dispersion being that for very similar values of the total progenitor mass, the rest-mass density radial profiles are different. This is particularly true in heavy progenitor model. For the prebreak slope α_l we find no obvious correlation with the progenitor mas. We have not found any other good correlation between the fit parameters (other than α_h) and the gross properties of the progenitors (radius, average density, total angular momentum, rotation period, mass of the iron core, etc.).

The dependence of the angular energy distribution on the progenitor mass comes from the difference of the pressure at the shock break. The jet is well confined and high pressure for heavier progenitor case, since the higher density progenitor envelope prevents the jet to expand during its propagation. Such high pressure jet can expand faster after shock break. As the result, the angular energy distribution extends to larger latitude.

4 Summary

Angular energy distribution of the highly relativistic jets from collapsars is studied. The distribution is well fitted by smoothly broken power law. We show the dependence of the distribution on the progenitor mass. The distribution of the jets from lighter progenitors is steeper than that of the jets from heavier progenitor models.

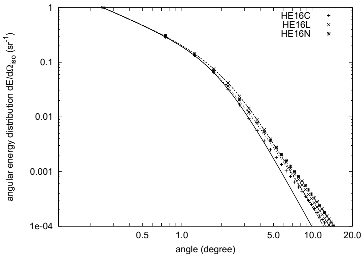

Figure 1: Equivalent isotropic angular energy distribution of models, HE16C, HE16L, and HE16N, when the head of the jet reaches the outer computational boundary. With lines we also show the fitting functions to SBPs (Eq. 1) for each model. The solid, dashed, and dotted lines are the fitting functions of Eq. 1 corresponding to models HE16C, HE16L, and HE16N, respectively.

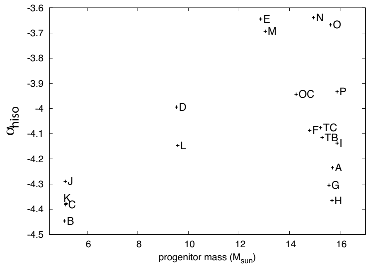

Figure 2: Dependence of the index α_h on the total mass of the progenitor. We identify the models by the last letter in the model name, e.g., the label 'A' stands for model HE16A. The labels 'TB', 'TC', and 'OC' stand for the models 16TB, 16TC, and 16OC, respectively.

Acknowledgments

We would like to thank A. Heger for his kindness to allow us to use his progenitor models for this study. This work is partly supported by the Grants-in-Aid of the Japanese Ministry of Education, Science, Culture, and Sport (19540236, 20041002, 20340040 A.M.), the grants of the Spanish Ministry of Science and Innovation CSD2007-00050 and AYA2007-67626-C03-01. M. A. A. is a Ramón y Cajal fellow of the Spanish Ministry of Education and Science. The calculations were carried out on a NEC SX8, at the Cybermedia Center, Osaka University, on a NEC SX8, at Yukawa Institute for theoretical physics, Kyoto University, on the Space Science Simulator (NEC SX6), at the Japan Aerospace Exploration Agency, and on a NEX SX9, at the Center for Computational Astrophysics, National Astronomical Observatory of Japan.

References

1. Galama, T. J., et al. 1998, Nature, 395, 670
2. Iwamoto, K., et al. 1998, Nature, 395, 672
3. Stanek, K. Z., et al. 2003, ApJ, 591, L17
4. Woosley, S. E. 1993, ApJ, 405, 273
5. MacFadyen, A. I., & Woosley, S. E. 1999, ApJ, 524, 262
6. Lazzati, D., & Begelman, M. C. 2005, ApJ, 629, 903
7. Morsony, B. J., Lazzati, D., & Begelman, M. C. 2007, ApJ, 665, 569
8. Woosley, S. E., & Heger, A., 2006, ApJ, 637, 914
9. Zhang, W., Woosley, S. E., & MacFadyen, A. I. 2003, ApJ, 586, 356
10. Zhang, W., Woosley, S. E., & Heger, A. 2004, ApJ, 608, 365
11. Aloy, M. A., et al. 2000, ApJ, 531, L119
12. Mizuta, A., Yamasaki, T., Nagataki, S., & Mineshige, S. 2006, ApJ, 651, 960
13. Aloy, M. A., & Rezzolla, L. 2006, ApJ, 640, L115
14. Janka, H.-T., Aloy, M.-A., Mazzali, P. A., & Pian, E. 2006, ApJ, 645, 1305

Introducing the *SVOM* mission for Gamma-Ray Bursts Studies

Diego Götz
CEA Saclay - DSM/Irfu/SAp - Orme des Merisiers, F-91191, Gif-sur-Yvette, France

on behalf of the *SVOM* Collaboration
CESR Toulouse; APC Paris; LAM Marseille; IAP Paris; LATT Toulouse; INAF Milano; NAOC Beijing; IOPM Xi'an; IHEP Beijing

We present the *SVOM* (Space-based multi-band astronomical Variable Object Monitor) mission, that is being developed in cooperation between the Chinese National Space Agency (CNSA), the Chinese Academy of Science (CAS) and the French Space Agency (CNES), and is expected to be launched in 2014. Its scientific objectives include the study of the GRB phenomenon (diversity and unity), GRB physics (particle acceleration, radiation mechanisms), GRB progenitors, cosmology (host galaxies, intervening medium, star formation history, re-ionization, cosmological parameters), and fundamental physics (origin of cosmic rays, Lorentz invariance, gravitational waves sources). *SVOM* is designed to detect all known types of Gamma-Ray Bursts (GRBs), to provide fast and reliable GRB positions, to measure the broadband spectral characteristics and temporal properties of the GRB prompt emission. Four space borne instruments have been selected for phase A study: a wide field (∼2 sr) coded mask telescope (ECLAIRs), operating in the 4–250 keV energy range, will provide the triggers and localizations, while a gamma-ray non-imaging spectrometer (GRM), sensitive in the 50 keV-5 MeV domain, will extend the prompt emission energy coverage. After a satellite slew, in order to place the GRB direction within field of view of the two narrow field instruments - a soft X-ray (XIAO), and a visible telescope (VT) - the GRB position will be refined and the study of the early phases of the GRB afterglow will be possible. A set of three ground based dedicated instruments, two robotic telescopes (GFTs) and a wide angle optical monitor (GWAC), will complement the space borne instruments. Thanks to the low energy trigger threshold (∼4 keV) of the ECLAIRs, *SVOM* is ideally suited for the detection of soft, hence potentially most distant, GRBs. Its observing strategy is optimized to facilitate follow-up observations from the largest ground based facilities.

1 Introduction

Despite recent observational progress, the 40 years old Gamma-Ray Bursts (GRBs) mystery is far from being completely solved (see e.g. Mészáros (2006)[1] for a review). There is general consensus on the cosmological nature of these transient sources of gamma-ray radiation, and, at least for the long burst category, the association with the explosion of massive stars (>30 $M_\odot$) is a scenario that reproduces most observed features. Whatever the exact progenitors of long GRBs are, they have been detected up to redshift 6.7 [2], making them powerful tools to investigate the early Universe (star formation history, re-ionization, etc.), and to possibly derive cosmological parameters. For short bursts, on the other hand, the situation is less clear, mainly because of the lack of a statistically compelling number of good quality observations of their afterglows. Many questions concerning GRBs are still open, such as the physical processes at work during the prompt phase, in terms of particle acceleration and radiation processes, the GRBs classification, a better characterization of GRB host galaxies and progenitors, as well as some fundamental physics issues like Lorentz invariance, the origin of cosmic rays and gravitational waves.

In order to contribute to address the above questions, the French Space Agency (CNES), the Chinese Academy of Sciences (CAS) and the Chinese Space Agency (CNSA) are developing the *SVOM* mission (Space-based multi-band astronomical Variable Object Monitor). *SVOM* has successfully reached the end of its phase A design study, and is planned to be launched in 2014 in a circular orbit with an inclination of $\sim 30°$ and altitude of $\sim$600 km. For Phase A study four instruments have been selected: ECLAIRs, a coded mask wide field telescope that will provide real time localizations of GRB to arcminute level, two GRMs units, non-imaging gamma-ray spectrometers, and two narrow-field instruments, XIAO and VT, for arcsecond localizations, and for the study of the early afterglow phases in the X-ray and optical bands. Indeed, once a GRB is detected within field of view of ECLAIRs, the satellite will autonomously perform a slew towards the GRB direction, in order to allow the observations of the afterglow by the XIAO and VT telescopes. The *SVOM* pointing strategy derives from a combination of two main constraints: the avoidance of bright X-ray galactic sources and an anti-solar pointing, to have the GRBs always detected on the night side of the Earth. Even if the latter choice induces some dead time at mission level, due to the Earth passages occulting ECLAIRs field of view once per orbit, it will enhance the possibility of successful follow-up with large ground based facilities, with a goal of 75% of *SVOM* GRBs easily observable during their early afterglow phase.

Besides the space flown instruments, the *SVOM* mission includes a set of ground based instruments, in order to broaden the wavelength coverage of the prompt and of the afterglow phase: GWACs are a set of wide field optical cameras that cover a large fraction of ECLAIRs field of view. They will be based in China and will follow ECLAIRs pointings, in order to catch the prompt optical emission associated with GRBs. Two robotic telescopes (GFTs), one based in China, and one provided by CNES, complete the ground based instrumentation. Their goal is to measure the photometric properties of the early GRB error region from the near infra-red to the optical band, and to refine the afterglow position provided by the on-board instruments. In the following sections the instruments and the mission are described in some detail.

2 ECLAIRs

ECLAIRs[3] is made of a coded mask telescope working in the 4–250 keV energy range (CXG), and a real-time data-processing electronic system, UTS[4], which is in charge of analyzing ECLAIRs data stream in real-time and of detecting and localizing the GRBs occurring within its field of view. The CXG has a wide field of view ($\sim$ 2 sr), and a fair localization accuracy ($\sim$10 arcmin error radius (90% c.l.) for the faintest sources, down to a couple of arcmin for the brightest ones). Its detector plane is made of 80$\times$80 CdTe pixels yielding a geometrical area of 1024 cm^2. The telescope is passively shielded, and a new generation electronics allows to lower the detection threshold with respect to former CdTe detectors by about 10 keV, reaching $\sim$4 keV. The CXG, in spite of its rather small geometrical surface, is thus more sensitive to GRBs with soft spectra, potentially the most distant ones, than currently flying telescopes, see Fig. 1.

The ECLAIRs/CXG telescope is expected to localize about 70 GRBs per year. This estimate takes into account the dead time induced by the passages over the Southern Atlantic Anomaly, that increase significantly the instrumental particle induced background, and by the passage of the Earth in the CXG field of view.

3 GRM

The Gamma-Ray Monitor (GRM) on board *SVOM* is composed of two identical units each made of a phoswich (NaI/CsI) detector of 280 cm^2, read by a photomultiplier. In front of each detector there is a collimator in order to reduce the background and to match the CXG and GRM fields of view. The GRM does not have imaging capabilities, however as can be seen from Fig. 1, the GRM extends the spectral coverage of the *SVOM* satellite to the MeV range. This is an important point, since the current detectors like BAT on board *Swift*[5] or IBIS/ISGRI on board *INTEGRAL*[6] have a comparable or better localization accuracy with respect to the CXG, but they lack a broad band coverage, hampering a correct spectral characterization of the prompt high-energy emission of GRBs, which is a key input of any sensible modeling of GRBs' radiative processes. The recent successful launch of *Fermi*, and the availability of the GBM detectors (non-imaging spectrometers with a 2π field of view) used in synergy with BAT and ISGRI will partially fill this need before the launch of *SVOM*, but the different orbits, pointing constrains, and sensitivities of the three instruments imply a low rate of simultaneous detections. On the other hand, for every *SVOM* GRB a good localization and good spectral information will be available at the same time.

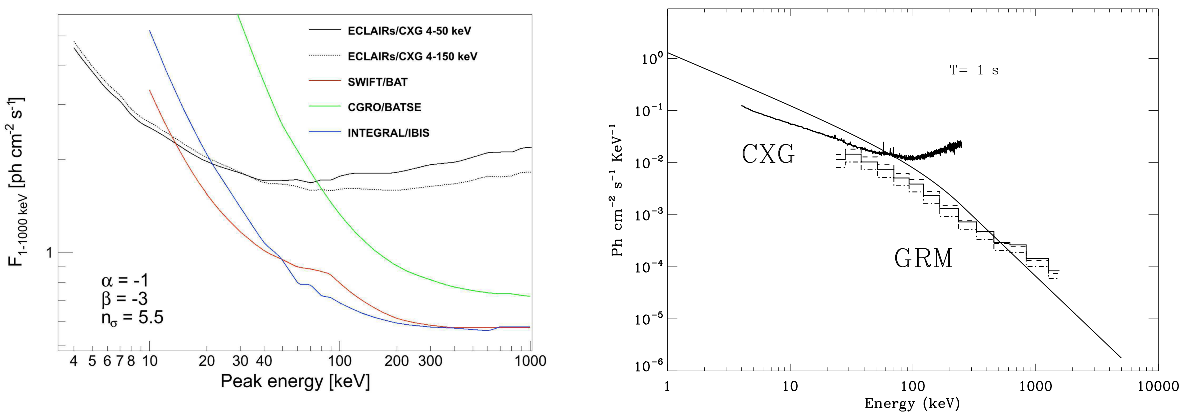

Figure 1: Left: ECLAIRs/CXG sensitivity compared to previous and current instrumentation. The curves have been computed as a function of the GRB peak energy for a 5.5 σ detection assuming a Band spectrum (Band et al. 1993) with the other spectral as parameters reported in the plot. Right: Combined GRM (two units) ECLAIRs on axis sensitivity for a 1 s integration time and a 5 σ detection. A Band spectrum with α=–1, β=–2.5, E_0=100 keV, and $F_{50-300keV}$=1 photon cm^{-2} s^{-1} is overplotted for comparison.

4 XIAO

The X-ray Imager for Afterglow Observations (XIAO[8]) has been proposed by an Italian consortium, lead by the INAF-IASF institute in Milan. It is a focusing X-ray telescope, based on the grazing incidence (Wolter-1) technique. It has a short focal length of ∼0.8 m, and a field of view (25 arcmin diameter) adequate to cover the whole error region provided by the CXG telescope, so that after the satellite slew the GRB position should always be inside the XIAO field of view. XIAO has an effective area of about 120 cm^2 and the mirrors are coupled to a very compact, low noise, fast read out CCD camera, sensitive in the 0.5–2 keV energy range.

5 VT

The space-borne Visible Telescope will be able to improve the GRB localizations obtained by the CXG and XIAO to sub-arcsecond precision through the observation of the optical afterglow. In addition it will provide a deep and uniform light-curve sample of the detected optical afterglows, and allow to do primary selection of optically dark GRBs and high-redshift GRB candidates (z>4). The field of view of the telescope will be 21×21 arcmin, sufficient to cover the error box of the CXG. The detecting area of the CCD has 2048 × 2048 pixels to ensure the sub-arcsecond localization of detected sources. The aperture of the telescope should guarantee a limiting magnitude of $M_V = 23$ (5σ) for a 300 s exposure time. Such a sensitivity is a significant improvement over the UVOT on board the *Swift* satellite and over existing ground-based robotic GRB follow-up telescopes. The VT is expected to detect nearly 70% of SVOM GRBs for which a slew is performed. The telescope will have at least two bands in order to select high-redshift GRB candidates. They are separated at 650 nm, which corresponds to a redshift of z∼4-4.5 using Lyα absorption as the redshift indicator.

6 Ground segment

The ground segment of the mission will be composed of X- and S-band antennas (for data and housekeeping telemetry download), a mission operation center, based in China, two science centers (based in China (CSC) and France (FSC) and in charge of operations and monitoring of the scientific payload), and a VHF alert network. The latter will be composed of a series of receivers distributed over the globe in order to guarantee continuous coverage for the alerts dispatched by the platform. The alerts will contain the information about the GRB positions, that will be sent to the ground as soon as more accurate information is derived on board, followed by complementary quality indicators (light curves, images, etc.) produced on board. The VHF network is directly connected to the FSC, which is in charge of formatting and dispatching the alerts to the scientific community through the Internet (GCNs, VO Events, SVOM web page, etc.). The first alerts corresponding to the initial localization by the CXG are expected to reach the recipients one minute after the position has been derived on board. Then the following alerts, containing the refined positions derived on-board, will reach the scientific community within 10 minutes from the first notice. In case of a refined (sub-arcsec) position is available from the prompt data analysis of the GFTs or GWACS, this information will immediately reach the the FSC, and dispatched to the scientific community through the channels mentioned above. For more details on the alert distribution strategy, see Claret (2008)[9]. In addition the FSC will be on charge of publishing the CXG pointing direction in order to facilitate ground based robotic telescopes to quickly react, minimizing the slew time.

Acknowledgments

D.G. acknowledges the LATT Toulouse and the French Space Agency (CNES) for financial support.

References

1. Mészáros, P. , 2006, Reports on Progress in Physics, 69, 2259
2. Fynbo, J. P. U., Greiner, J., Kruehler, T., et al. 2008, GRB Coordinates Network, 8225, 1
3. Remoué, N., Barret, D., Godet, O., et al. 2009, Proceedings of the Sixth Hunstville Symposium on Gamma-Ray Bursts, AIP, in press
4. S. Schanne, 2008, Proceedings of the Santa Fe Conference. AIP Conference Proceedings, Volume 1000, 58
5. Gehrels, N., Chincarini, G., Giommi, P., et al. 2004, ApJ, 611, 1005
6. Lebrun, F., Leray, J. P., Lavocat, P., et al. 2003, A&A, 411, L141
7. Band, D., Matteson, J., Ford, L., et al. 1993, ApJ, 413, 281
8. Mereghetti, S., De Luca, A., Fiorini, M., et al. 2008, SPIE Meeting, arXiv:0807.0893v1
9. Claret, A., 2008, Proceedings of the Santa Fe Conference. AIP Conference Proceedings, Volume 1000, 569

4.
Dark Matter

SEARCH FOR DARK MATTER IN THE SKY

ALDO MORSELLI
INFN Roma Tor Vergata,
Via della Ricerca Scientifica 1, Roma, Italy

The detection of γ-rays, antiprotons and positrons due to pair annihilation of dark matter particles in the Milky Way halo is a viable indirect technique to search for signatures of supersymmetric dark matter where the major challenge is the discrimination of the signal from the background generated by standard production mechanisms. The new PAMELA antiproton data are consistent with the standard secondary production and this allows us to constrain exotic contribution to the spectrum due to neutralino annihilations. In particular, we show that in the framework of minimal supergravity (mSUGRA), in a clumpy halo scenario (with clumpiness factor ≥ 10) and for large values of $\tan(\beta) \geq 55$, almost all the parameter space allowed by WMAP is excluded. Instead, the PAMELA positron fraction data exhibit an excess that cannot be explained by secondary production. PPB-BETS and ATIC reported a feature in electron spectrum at a few hundred GeV. The excesses seem to be consistent and imply a source, conventional or exotic, of additional leptonic component. Here we discuss the status of indirect dark matter searches and a perspective for PAMELA and Fermi γ-ray space telescope (Fermi) experiments.

1 Antiproton to proton ratio data

The PAMELA (a Payload for Antimatter Matter Exploration and Light-nuclei Astrophysics) experiment is a satellite-borne apparatus designed to study charged particles in the cosmic radiation with a particular focus on antiparticles (antiprotons and positrons) [1]. The PAMELA antiproton data [2] are shown in figure 1 together with the antiproton flux expected from standard secondary production. Cosmic ray propagation and production of secondary particles and isotopes is calculated using the GALPROP code [3]. The lines show the minimal and maximal fluxes as calculated in models with different propagation parameters tuned to match the boron-to-carbon ratio in cosmic rays ([4, 5, 6, 7]). The antiproton data collected by PAMELA [2] and BESS [8] are consistent with each other and with predictions for secondary antiproton flux thus excluding a strong antiproton signal from exotic processes. Figure 2 is made in the framework of minimal supergravity (mSUGRA) by fixing the less sensitive parameters A_0, $\tan\beta$ and $\text{sign}(\mu) = +1$ and in the case of a clumpiness factor 10 and $\tan(\beta) = 55$. Following the analysis in [6], the region below the line in figure 2 can be excluded based on antiproton data.

This result can be compared with estimates based on Fermi five-years sensitivity to WIMP annihilation photons (continuum spectrum) from the Galactic center as shown in figure 3 [10,11]. The red band is the cosmologically allowed region by WMAP [12]; the region above the blue line ($M_{WIMP} \sim 200$ GeV) is not observable by Fermi due to the higher WIMP mass as one moves to higher $M_{1/2}$. The dark matter halo used for the Fermi indirect search sensitivity estimate is a truncated Navarro, Frank and White (NFW) halo profile. For steeper halo profiles (like the Moore profile) the Fermi limits move up, covering a wider WMAP allowed region, while for

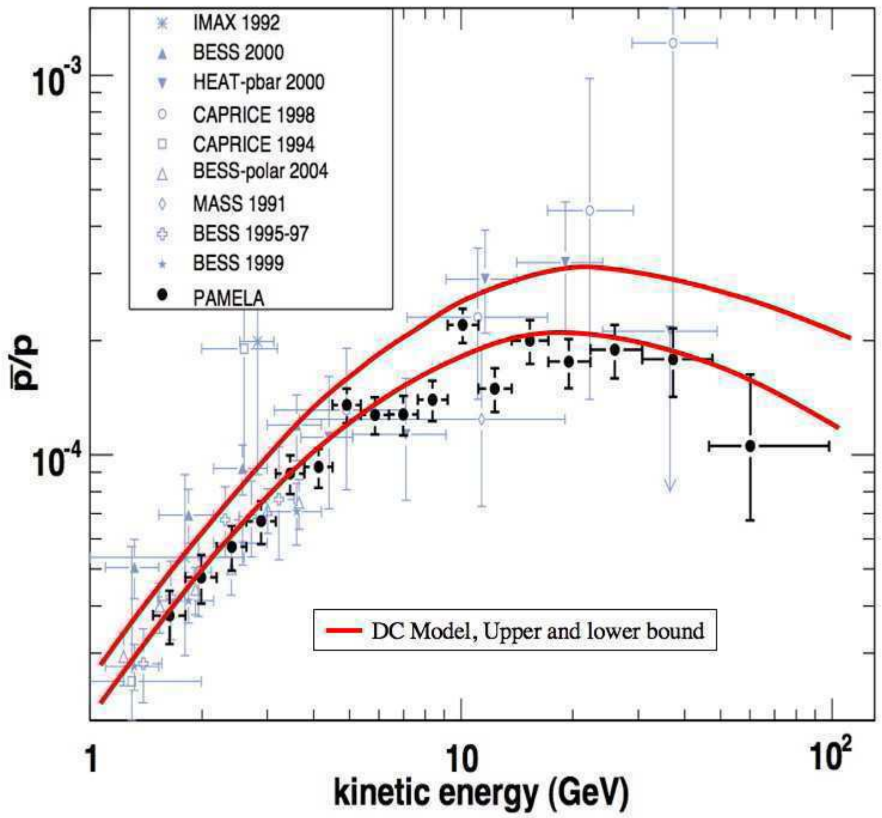

Figure 1: The antiproton-to-proton flux ratio as measured by PAMELA The lines show an approximate range expected for the standard secondary production

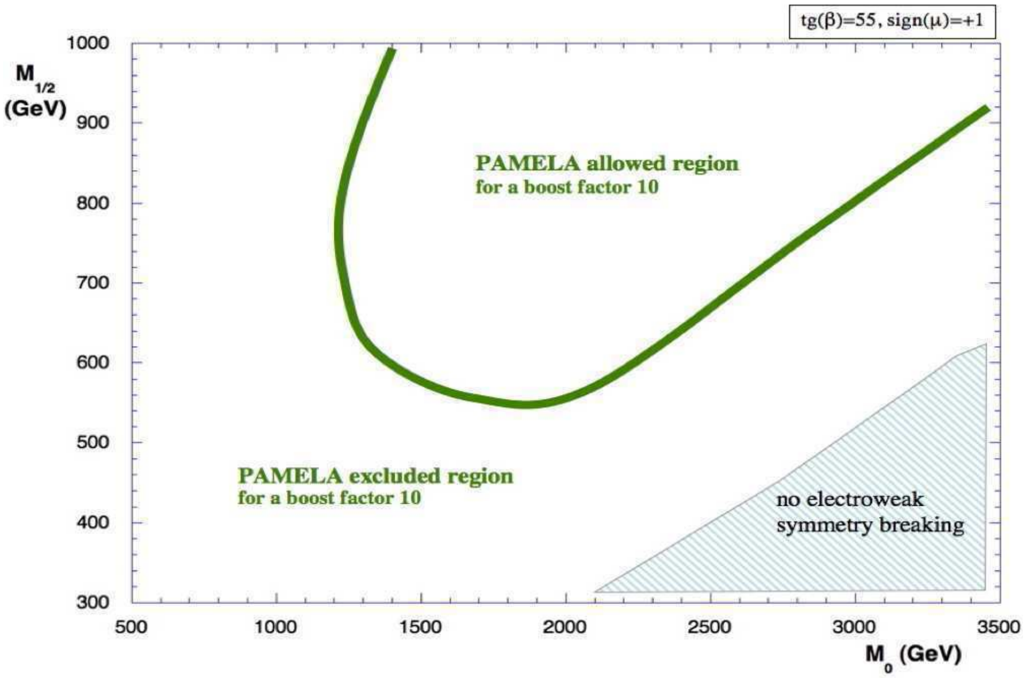

Figure 2: PAMELA excluded region in a clumpy halo scenario for a boost factor 10 in the framework of minimal supergravity (mSUGRA) in the case of $\tan(\beta) = 55$.

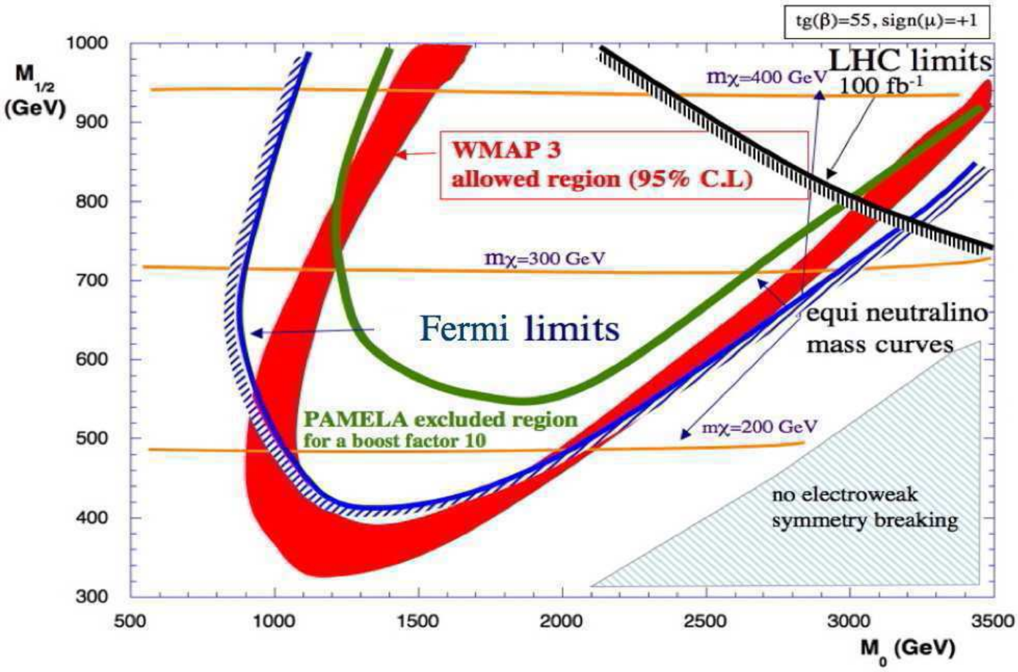

Figure 3: Sensitivity plot for observation of mSUGRA for LHC and Fermi for $\tan(\beta) = 55$

less steep profile (like the isothermal profile) the Fermi limits move down, covering less WMAP allowed region. The LHC accelerator limits are from [13].

Figure 4 is the same of figure 3 but for $\tan(\beta) = 60$. It can be seen that for a clumpiness factor 10 all the WMAP region is already excluded. For larger value of $\tan(\beta)$ the excluded parameter space is even larger, while for lower values the capability of the antiprotons flux to probe the mSUGRA scenario is very weak ([6,9]).

2 Positron fraction and electron excess

Contrary to the antiproton to proton ratio data, the PAMELA positron fraction data [14] exhibit an excess above ∼10 GeV that cannot be explained by secondary production[4,6]. We note that the change in the positron fraction data below ∼10 GeV is probably due to the solar modulation (e.g., [15]) and change in the polarity of the solar magnetic field compared to the previous cycle. The temptation to claim the discovery of dark matter is strong, but there are competing astrophysical sources, such as pulsars, that can give strong flux of primary positrons and electrons [16, 17], [18]. In figure 5 the PAMELA data are shown with a possible pulsar contribution scaled from [16].

An independent confirmation that something interesting is going on with leptons in cosmic rays came from measurements of high-energy electrons. The cosmic-ray electron flux has not been measured very well in the past and especially at very-high energies because of the very steep spectrum and thus the need for high rejection power and long exposure. Simulations of the electron propagation from local sources [26] has shown that features in the electron spectrum may be expected in the TeV range where the flux of Galactic cosmic-ray electrons gradually steepens. On the other hand, annihilation of Kaluza-Klein particles may produce spectral features in sub-TeV range [20]. The first indication of a feature (or excess) in the electron spectrum at a few hundred GeV came from PPB-BETS flight a couple of years ago [23]. A recent confirmation of the excess by ATIC [24] gives more confidence that this is not an instrumental artefact. In the coming years, the electron spectrum will be measured again and again until the last doubt in

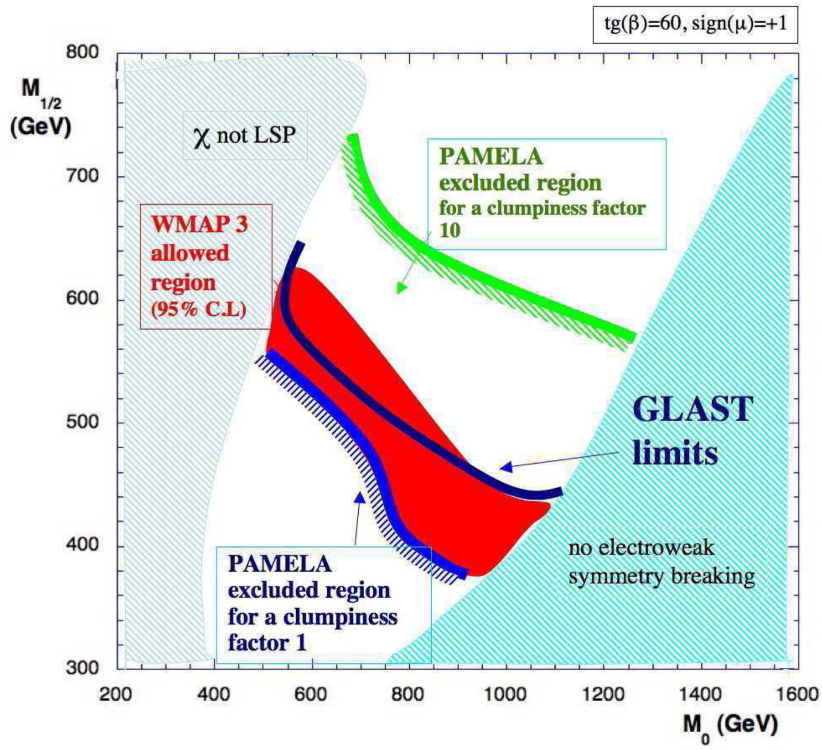

Figure 4: Sensitivity plot for observation of mSUGRA for LHC and Fermi for $\tan(\beta) = 60$

the reality of this feature has gone away or a proof of its instrumental nature is found.

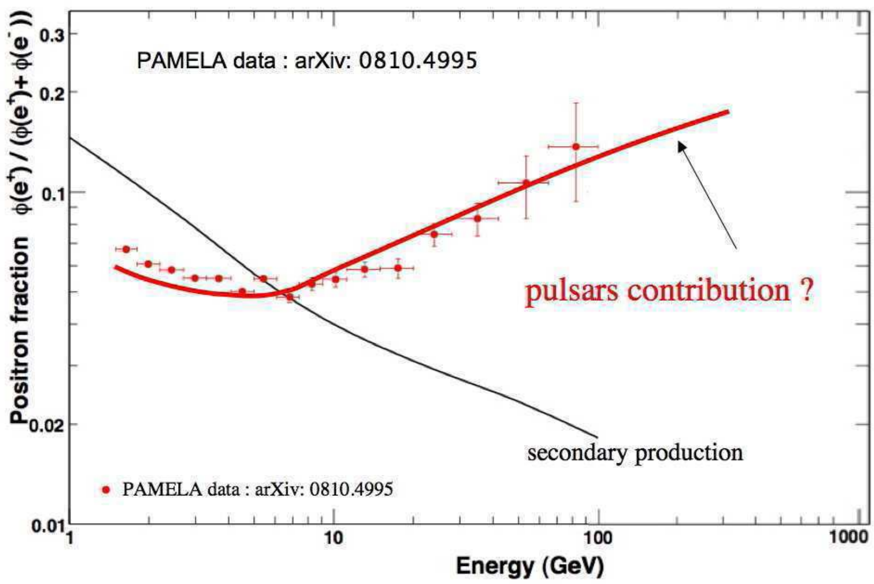

Figure 5: PAMELA data and a possible contribution from pulsars. Black solid line shows the background from secondary positrons in cosmic rays from GALPROP

How can one distinguish between the contributions of pulsars and dark matter annihilations? Most likely, a confirmation of the dark matter signal will require a consistency between different experiments and new measurements of the reported excesses with large statistics. The observed excess in the positron fraction should be consistent with corresponding signals in abso-

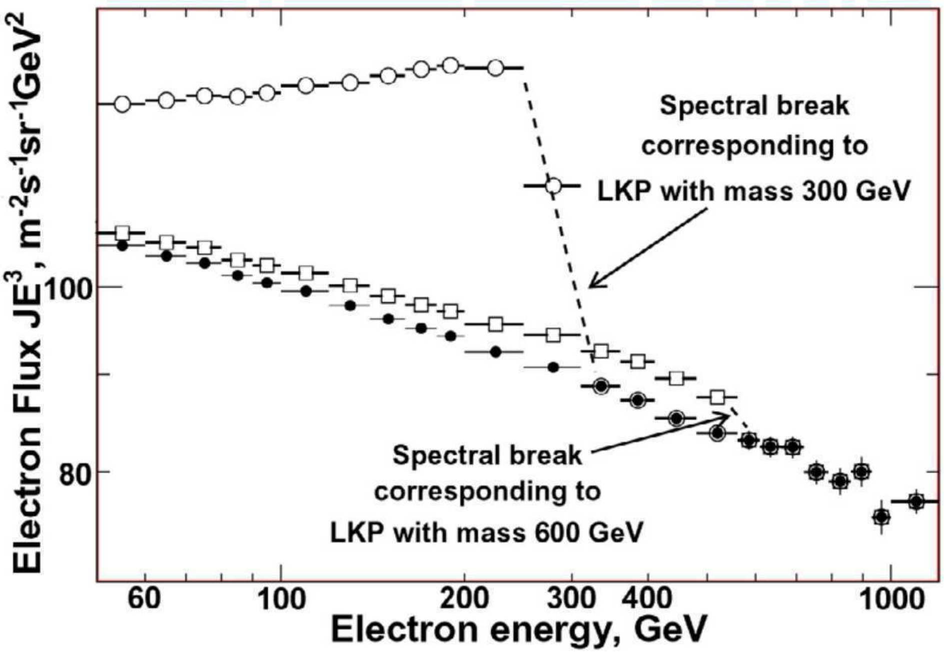

Figure 6: Simulated detection of lightest Kaluza-Klein particles (LKPs) with masses of 300 and 600 GeV in the LAT electron spectrum to be collected in five years of operation. Filled circles: "conventional" electron flux; open circles: the same but with added signal from 300 GeV LKPs; open squares: the same with added signal from 600 GeV LKPs.

lute positron and electron fluxes in the PAMELA data and all lepton data collected by Fermi [19]. Fermi has a large effective area and long projected lifetime, 5 years nominal with a goal 10 years mission, which makes it an excellent detector of cosmic-ray electrons up to $\sim$1 TeV [25]. Fermi measurements of the total lepton flux with large statistics will be able to distinguish a gradual change in slope with a sharp cutoff with high confidence [20]. The latter, as shown in figure 6 for a NFW DM distribution with boost factor of 5 and local density of 0.4 GeV cm^{-3} , can be an indication in favor of the dark matter hypothesis. A strong leptonic signal should be accompanied by a boost in the γ-ray yield providing a distinct spectral signature detectable by Fermi [21,22]. Antiproton data with higher statistics and at higher energies collected by PAMELA could also give us some clue. If in the future PAMELA will not observe a change in the slope, there is a possibility to observe it in the total electron + positron flux with Fermi. Fermi will be able to measure the total flux with high statistic up to $\sim$ 1 TeV [20] and a sharp change in the slope, as shown in figure 6, can be an indication in favor of the dark matter hypothesis, while a smoother change can be an indication of pulsars contributions. Finally, if the sources of positrons are pulsars, they should be quite close and we should probably be able to see them with Fermi in the γ-rays data or in the anisotropy of the total lepton (electron+positron) spectrum [18].

If the sources of the excess positrons are pulsars, they should be quite close to us and, therefore, may be detectable in γ-rays with Fermi. In this case, one has to expect broader features in the electron and positron spectra without sharp cutoffs. Meanwhile, the proposed test of the anisotropy in the total lepton (electron+positron) flux [18] may not work. First, the predicted anisotropy is very small, at the fraction of a per cent. Second, the so-called heliospheric modulation strongly affects the flux of cosmic-ray species below 20-50 GeV. The extended heliospheric magnetic field and the solar wind may affect the arriving directions of cosmic-ray particles at even higher energies. Therefore, even if the anisotropy is observed it may be connected with configuration of the heliospheric magnetic field rather then due to the local sources of primary leptons.

3 Conclusion

Recent accurate measurements of cosmic-ray positrons and electrons by PAMELA, PPB-BETS, and ATIC have open a new era in particle astrophysics. The observed features or excesses break a boring single-power-law behavior of the cosmic-ray spectrum. Their exotic origin has to be confirmed by complimentary findings in γ-rays by Fermi and atmospheric Cherenkov telescopes, and by LHC in the debris of high-energy proton destructions. A positive answer will be a major breakthrough and will change our understanding of the universe forever. On the other hand, if it happens to be a conventional astrophysical source of cosmic rays, it will mean a direct detection of particles accelerated at an astronomical source, again a major breakthrough. In this case we will learn a whole lot about our local Galactic environment. However, independently on the origin of these excesses, exotic or conventional, we can expect very exciting several years ahead of us.

References

1. P. Picozza et al. [PAMELA Coll.], Astropart. Phys. 27 (2007) 296 [astro-ph/0608697], P. Picozza and A. Morselli, J. Phys. G: Nucl. Part. Phys. 29 (2003) 903 [astro-ph/0211286], P. Picozza and A. Morselli, World Scientific Publishing Co. [astro-ph/0604207]
2. O. Adriani et al. [PAMELA Coll.], arxiv:0810.4994
3. A. W. Strong, I. V. Moskalenko, and V. S. Ptuskin, Annu. Rev. Nucl. Part. Sci. 57 (2007) 285
4. A. W. Strong and I. V. Moskalenko, ApJ 509 (1998) 212
   I. V. Moskalenko and A. W. Strong, ApJ 493 (1998) 694
5. I. V. Moskalenko et al., ApJ 565 (2002) 280
6. A. Lionetto, A. Morselli, and V. Zdravkovic, J. Cosmol. Astropart. Phys. JCAP09 (2005) 010 [astro-ph/0502406]
7. V. S. Ptuskin et al., ApJ 642 (2006) 902
8. K. Abe et al. [BESS Coll.], arXiv:0805.1754
9. A. Morselli, ICHEP 2006, 33rd Int. Conf. 2007 Word Scientific, pg 222-225, SBN-13 978-981-270-385-9
10. A. Morselli at al., Nucl. Phys. 113B (2002) 213
11. A. Cesarini, F.Fucito, A.Lionetto, A.Morselli, P. Ullio, Astropart. Phys. 21 (2004) 267 [astro-ph/0305075]
12. D. N. Spergel, et al. [WMAP Coll.], ApJS 170 (2007) 377 [astro-ph/0603449]
13. H. Baer, et al., JCAP 0408 (2004) 005
14. O. Adriani et al. [PAMELA Coll.], arxiv:0810.4995
15. J. M. Clem et al., ApJ 464 (1996) 507
16. F. A. Aharonian, A. M. Atoyan and H. J. Völk, Astron. Astrophys. 294 (1995) L41
17. S. Coutu et al., Astropart. Phys. 11 (1999) 429
18. D. Hooper et al., arXiv:0810.1527
19. W. B. Atwood et al., ApJ (2008) submitted
20. E. Baltz et al., JCAP07 (2008) 013 [arXiv:0806.2911]
21. L. Bergström, T. Bringmann and J. Edsjö, arXiv:0808.3725
22. N. Arkani-Hamed et al., arXiv:0810.0713
23. K. Yoshida et al., Adv. Space Res. 42 (2008) 1670
24. J. Chang, et al., Nature 456 (2008) 362
25. A. A. Moiseev, E. A. Baltz, J. F. Ormes, and L. G. Titarchuk, arXiv:0711.3033
26. T. Kobayashi, Y. Komori, K. Yoshida, and J. Nishimura, ApJ 601 (2004) 340

COSMIC RAYS FROM ANNIHILATING DARK MATTER

MARTTI RAIDAL

NICPB, Ravala 10, 10143 Tallinn, Estonia

I review the study of DM masses, annihilation channels and cross sections that can reproduce the PAMELA indications of an e^+ excess consistently with the PAMELA $\bar{p}$ data and the ATIC/PPB-BETS $e^+ + e^-$ data. From the PAMELA data alone, two solutions emerge: (i) either the DM particles that annihilate into W, Z, h must be heavier than about 10 TeV or (ii) the DM must annihilate only into leptons. The solution (ii) implies a peak in the $e^+ + e^-$ energy spectrum, which, indeed, seems to appear in the ATIC/PPB-BETS data around 700 GeV. Thus in both cases a DM particle compatible with the PAMELA excess seems to have quite unexpected properties.

1 Introduction

Cosmological observations imply that about 80% of the mass of the Universe is some unknown form of cold Dark Matter (DM) [1]. Presently the origin and nature of the DM particles, their mass, spin, couplings and other properties remain completely unknown. Among many possible cold DM candidates the most popular ones are the stable weakly interacting massive particles (WIMPs) which occur in many extensions of the Standard Model (SM), most notably in supersymmetry. If the DM WIMPs are thermal relics, their annihilation cross section must be $\sigma v \sim 3 \cdot 10^{-26}\,\mathrm{cm}^3/\mathrm{sec}$, which indeed is typical of a weakly interacting TeV-scale particle.

The recently reported results by the PAMELA experiment [3] have the opportunity, if confirmed, of establishing a breakthrough in the cosmic antimatter searches. The PAMELA data show (i) a steep increase in the energy spectrum of the positron fraction, $e^+/(e^+ + e^-)$, in cosmic rays above 10 GeV [3], compatibly with previous less certain hints from HEAT [4] and AMS-01 [5]; (ii) no excess in the $\bar{p}/p$ energy spectrum [6] compared with the predicted background; (iii) at low energy, $E_{e^+} < 10$ GeV, the positron flux is presently suppressed by the solar magnetic polarity state A^- [7]. In addition, the PPB-BETS balloon experiment reported an excess in the $e^+ + e^-$ energy spectrum between 500-800 GeV [8], confirming the similar earlier claim by the ATIC-2 balloon experiment [9].

In this talk I review the results of the work [10]. In this paper we studied whether galactic DM annihilations can account for the observed excesses in the data. We performed a model independent analysis of the PAMELA positron and antiproton data with and without the electron plus positron data obtained from the balloon experiments. Our aim was to study if and how one can get model independent information on the DM mass, spin, interactions to the SM particles and on the DM annihilation cross section from the experimental data.

2 Model independent analyses

We study the non-relativistic DM annihilation cross sections into the set of all possible SM particle final states, DM DM $\to$ SM SM, where

$$\mathrm{SM} = \{e, \mu_L, \mu_R, \tau_L, \tau_R, W_L, W_T, Z_L, Z_T, h, q, b, t\},$$

taking into account the allowed polarizations (Transverse, Longitudinal, Left, Right). Using Monte Carlo tools, partly written by us, we try to keep the polarizations/helicities of the DM annihilation products and compute the energy spectra of the final state $e^\pm, p^\pm, \gamma, \nu_{e,\mu,\tau}$ coming from their decays. For technical details of the treatment of DM profile models and cosmic ray propagation models we refer the reader directly to Ref. [10]. Here we present the most important results.

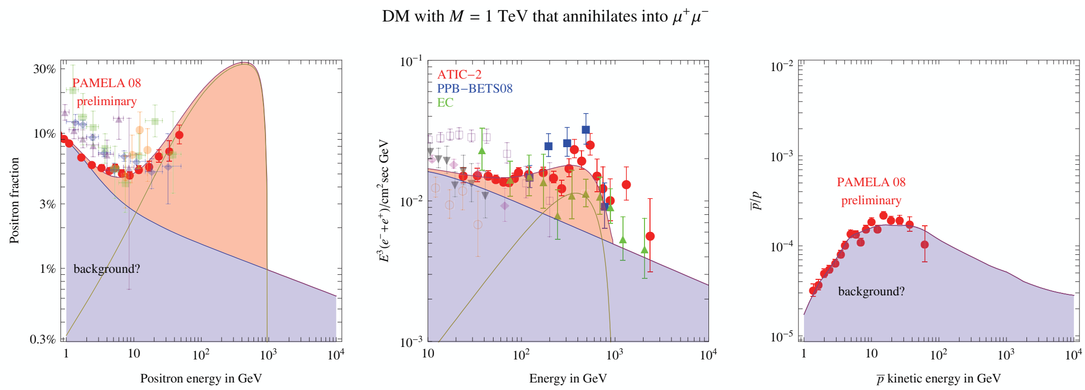

Figure 1: *An example of a preferred fit of* e^+ *(left),* $e^+ + e^-$ *(center),* $\bar{p}$ *(right) data for* $M = 1\,\mathrm{TeV}$. *Galactic DM profiles and propagation models are varied to provide the best fit.*

To illustrate our results, as well as to present the PAMELA and balloon $e^+/(e^+ + e^-)$, $(e^+ + e^-)$ and $\bar{p}/p$ data, we show in Fig. 1 one of the best example fits for the DM mass 1 TeV that annihilate into $\mu^+\mu^-$. The first panel presents the predictions for the positron fraction, the second for the total electron and positron flux and the third for the antiproton over proton flux. Because the antiproton data agrees with the background, PAMELA essentially excludes the possibility of DM annihilation into quarks and particles which decay predominantly to quarks, such as the gauge and Higgs bosons W, Z, h. This result has important implications for discriminating between different DM models as the conventional WIMP DM candidates such as supersymmetric Wino [11] or extra dimensional Kaluza-Klein states [12] are excluded by the non-observation of antiproton excess [10]. The PAMELA positron fraction data can be fitted by the annihilation of DM with large range of masses. However, inclusion of the ATIC data to the fit fixes the DM mass from the observed $(e^+ + e^-)$ excess. As seen in Fig. 1, 1 TeV DM annihilating to muons gives a good fit to data provided the annihilation cross section is enhanced by a factor of thousand compared to the annihilation cross section at DM freeze-out. This can be achieved by Sommerfeld enhancement [10] of todays annihilation cross section by the velocity dependent factor $1/v$ where today $v \sim 10^{-3}$ while $v \sim 0.2$ at freeze-out.

To present our best fit results we show in Fig. 2 the combined fit of PAMELA and balloon $(e^+ + e^-)$ data. Clearly data selects out only the leptonic annihilation modes of DM while all other modes give considerably poorer fits. At the same time, if the positron excess is induced by a nearby pulsar which creates positron flux proportional to $E^{-p}e^{-E/M}$, good fit to data is also obtained.

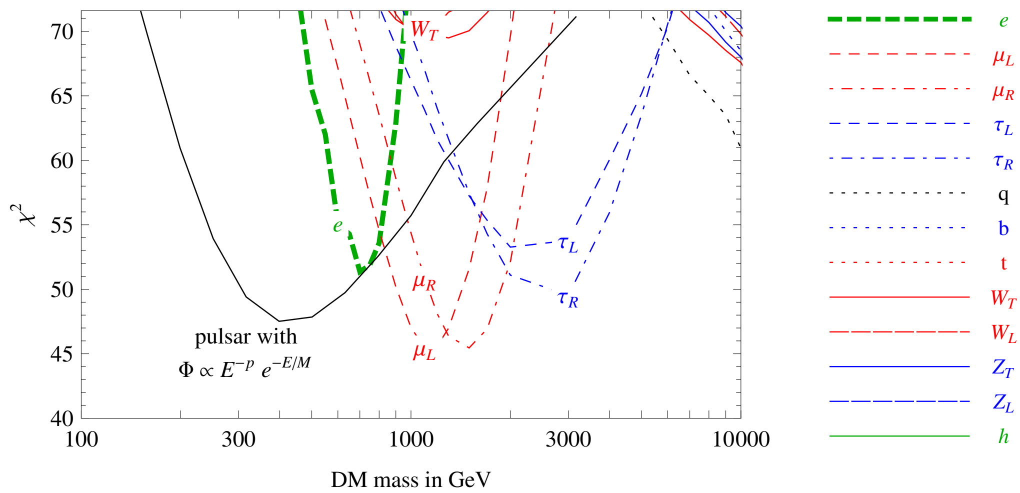

Figure 2: *Combined fit of PAMELA positron and balloon $e^+ + e^-$ data.*

3 Conclusions

In Ref. [10] we studied if DM annihilations into two-body SM states can reproduce the features that seem present in the energy spectra of e^+, e^-, $\bar{p}$ cosmic rays recently measured at energies between about 10 GeV and 3 TeV by the PAMELA [3], ATIC-2 [9] and PPB-BETS [8] experiments.

We found that:

- Considering the PAMELA positron data alone, the observed positron excess can be well fitted by DM annihilations into W, Z, e, μ, τ with any DM mass, and by DM annihilations into q, b, t, h with a multi-TeV DM mass.

- Adding the PAMELA anti-proton data suggests that the positron excess can be fitted by DM annihilations into W, Z, h (annihilations into q, b, t give poorer fits) only with a multi-TeV DM mass, unless boost factors or propagation strongly differentiate between e^+ and p^-. DM annihilations into leptons are still viable for any DM mass.

- Adding the balloon $e^+ + e^-$ data similarly suggests that DM annihilations into W, Z, h, b, q, t can fit the PAMELA excess only with a multi-TeV DM mass. Annihilations into e, μ, τ predict a feature in the $e^+ + e^-$ spectrum that, for a DM mass around one TeV, is compatible with the hint present in ATIC-2 and PPB-BETS data.

- The annihilation cross section suggested by the PAMELA data is a few orders of magnitude larger than what naturally suggested by the cosmological abundance, unless DM formed sub-halos. This enhancement could be due to a Sommerfeld non-relativistic enhancement of the annihilation cross section. Alternatively, this may indicate for non-thermal production of DM.

In the light of our results two solutions emerge for the DM.

1. The first possibility is a heavy DM, $M \gtrsim 10\,\text{TeV}$, that annihilates into W^+W^- or hh (an example of a DM candidate of this sort is provided by the model of [13]).

2. The second, more exciting, possibility is that the PAMELA excess has also been seen in $e^+ + e^-$ data, by ATIC and PPB-BETS. The forthcoming ATIC-4 and FERMI data should

soon clarify this issue. In such a case the best fit is obtained for $M \approx 1\,\text{TeV}$ with DM annihilating into $\mu^+\mu^-$, and good fits are also obtained for $M \approx 800\,\text{GeV}$ if DM annihilates into e^+e^-, or $M \approx 2\,\text{TeV}$ if DM annihilates into $\tau^+\tau^-$. The needed 'boost times cross section' is $B_e\,\sigma v \sim 3\ 10^{-23}\ \text{cm}^2/\text{sec}$.

In both cases, a DM particle compatible with the PAMELA anomaly has therefore unexpected properties.

Acknowledgments

This work was supported by the ESF Grant 8090 and by the Ministry of Education and Research of the Republic of Estonia.

References

1. E. Komatsu *et al.* [WMAP Collaboration], Astrophys. J. Suppl. **180** (2009) 330 [arXiv:0803.0547 [astro-ph]].
2. J. Silk and M. Srednicki, Phys. Rev. Lett. 53, 624 (1984); J. R. Ellis, R. A. Flores, K. Freese, S. Ritz, D. Seckel and J. Silk, Phys. Lett. B 214, 403 (1988).
3. O. Adriani *et al.* [PAMELA Collaboration], Nature **458** (2009) 607 [arXiv:0810.4995 [astro-ph]].
4. S. W. Barwick *et al.* [HEAT Collaboration], Astrophys. J. **482** (1997) L191 [arXiv:astro-ph/9703192].
5. M. Aguilar *et al.* [AMS-01 Collaboration], Phys. Lett. B **646** (2007) 145 [arXiv:astro-ph/0703154].
6. O. Adriani *et al.*, Phys. Rev. Lett. **102** (2009) 051101 [arXiv:0810.4994 [astro-ph]].
7. J.M. Clem *et al.*, The Astrophysical Journal 464, 507 (1996).
8. S. Torii *et al.* [PPB-BETS Collaboration], arXiv:0809.0760 [astro-ph].
9. ATIC collaboration, Nature 456 (2008) 362.
10. M. Cirelli, M. Kadastik, M. Raidal and A. Strumia, Nucl. Phys. B **813** (2009) 1 [arXiv:0809.2409 [hep-ph]].
11. G. Servant and T. M. P. Tait, Nucl. Phys. B 650, 391 (2003) [arXiv:hep-ph/0206071].
12. T. Moroi and L. Randall, Nucl. Phys. B 570, 455 (2000) [arXiv:hep-ph/9906527].
13. M. Cirelli, N. Fornengo and A. Strumia, Nucl. Phys. B **753** (2006) 178 [arXiv:hep-ph/0512090].

DARK MATTER ANNIHILATION IN SMALL-SCALE CLUMPS

V.S. BEREZINSKY[1,2], V.I. DOKUCHAEV[1] AND Yu.N. EROSHENKO[1]
[1] *Institute for Nuclear Research of the Russian Academy of Sciences, 60th October Anniversary Prospect 7a, 117312 Moscow, Russia*
[2] *INFN, Laboratori Nazionali del Gran Sasso, I-67010 Assergi (AQ), Italy*

The small-scale clumps of dark matter particles are efficiently disrupted at the early stages of hierarchical structure formation and later in the Galaxy by tidal interactions with stars. It is shown that a substantial fraction of clump remnants survive through the tidal destruction during the lifetime of the Galaxy if a clump core radius is rather small. The resulting mass spectrum of survived clumps is extended down to the core mass of a minimal mass clump. These survived dense remnants of tidally destructed clumps provide a suitable contribution to the amplification (boosting) of dark matter annihilation signal in the Galaxy.

Results of numerical simulations and theoretical models of Dark Matter (DM) clustering at the scales of subhalos and smaller heavily depend on the (unknown) form of initial perturbation spectrum. The form of perturbation spectrum at small scales cannot be recovered from the nowadays and future cosmic microwave background observations. In the lack of unique fundamental theory of cosmological inflation, the only possible chance to obtain information on the perturbation spectrum at small scales is the observation of annihilation boosting produced by the clumpy DM structures in the Galaxy.

The cold DM component is gravitationally unstable and is expected to form the gravitationally bounded clumpy structures from the scale of superclusters of galaxies and down to very small clumps of DM. The minimum mass of clumps (the cutoff of the mass spectrum), $M_{\rm min}$ is determined by the collisional and collisionless damping processes (see e. g. [1] and references therein). Recent calculations [2] show that the cutoff mass is related to friction between DM particles and cosmic plasma similar to the Silk damping. In the case of the Harrison-Zeldovich spectrum of primordial fluctuations with CMB normalization the first small-scale DM clumps are formed at redshift $z \sim 60$ with a mean density 7×10^{-22} g cm^{-3}, virial radius 6×10^{-3} pc and internal velocity dispersion 80 cm s^{-1} respectively. Only very small fraction of these clumps survives the early stage of tidal destruction during the hierarchial clustering[3]. Nevertheless these survived clumps may provide the major contribution to the annihilation signal in the Galaxy [3,4,5,6,7].

The unresolved problem of DM clumps is a value of the central density or core radius. Numerical simulations give a nearly power density profile of DM clumps. Both the Navarro-Frenk-White (NFW) and Moore profiles give formally a divergent density in the clump center. A theoretical modelling of the solitary clump formation by Gurevich and Zybin [8,9] predicts a power-law profile of the internal density of clumps

$$\rho_{\rm int}(r) = \frac{3-\beta}{3}\,\bar{\rho}\left(\frac{r}{R}\right)^{-\beta}, \qquad (1)$$

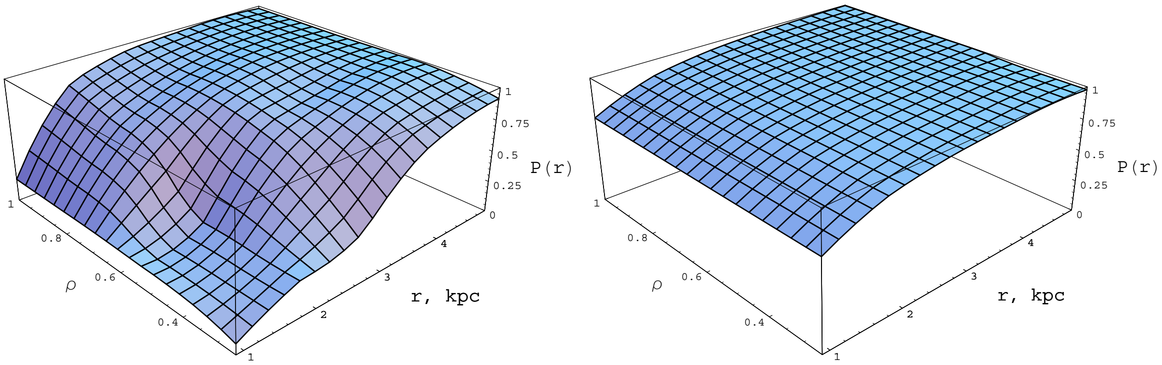

Figure 1: The survival probability $P(r,\rho)$ for clumps, which survives the tidal destruction by the stellar disk and the halo stars, plotted as as a function of distance from the galactic center r and a mean internal clump density ρ in the case $x_c = 0.1$ (left panel) and $x_c = 0.05$ (right panel). The density of clumps is normalized to the density 7.3×10^{-23} g cm^{-3} valid for clumps with mass $M = 10^{-6}$M$_{\odot}$.

where $\bar{\rho}$ and R are the mean internal density and a radius of clump, respectively, $\beta \simeq 1.8 - 2$ and $\rho_{\rm int}(r) = 0$ at $r > R$. A near isothermal power-law profile (1) with $\beta \simeq 2$ has been recently obtained in numerical simulations of small-scale clump formation [10]. Additional indication that mergers do not play a pivotal role in establishing the universal internal clump density profile comes from the recent numerical simulation [11]. We consider the relative core radius $x_c = R_c/R$ of DM clumps as a free parameter in the range $0.001-0.1$ and investigate the dependence of the probability of clump survival in the Galaxy on this parameter under the action of tidal forces from galactic disk and stars. The numerically calculated survival probability $P(r,\rho)$ for clumps, which survives the tidal destruction by the stellar disk and the halo stars is shown in the Fig. 1.

It must be noted that density profiles of small-scale DM clumps and large-scale DM halos may be quite different. The galactic halos are well approximated by the Navarro-Frenk-White profile outside the central core where dynamical resolution of numerical simulations becomes insufficient. The theoretical estimation of the relative core radius of DM clump $x_c = R_c/R$ was obtained in [8,9] from the energy criterion, $x_c \equiv R_c/R \simeq \delta_{eq}^3$, where δ_{eq} is a value of density fluctuation at the beginning of matter-dominated stage. A similar estimate for DM clumps with the minimal mass $\sim 10^{-6}$M$_{\odot}$ originated from 2σ fluctuation peaks gives $\delta_{eq} \simeq 0.013$ and $R_c/R \simeq 1.8 \times 10^{-5}$ respectively. The other possibility is that a real core radius is determined by the relaxation of small-scale perturbations inside the forming clump [12].

We describe a gradual mass loss of small-scale DM clumps assuming that only the outer layers of clumps are involved and influenced by the tidal stripping. In this approximation we calculate a continues diminishing of the clump mass and radius during the successive galactic disk crossings and encounters with the stars. An effective time of mass loss for DM clump remains nearly the same as in our previous calculations [3,13]. However the clump destruction time has now quite different physical meaning: it provides now a characteristic time-scale for diminishing of clump mass and size instead of the total clump destruction. This means that small remnants of clumps may survive in the Galaxy. See details in [14]. In the Fig. 2 is shown the final mass function of small-scale in the halo at the present epoch for two distances from the Galactic center [14]. We supposed in numerical calculations that a core radius is very small and all masses of remnants are admissible. The final mass function of clump remnants has a cut-off near the mass of the core of clump with a minimal mass $M_{\rm min}$. One can see from in the Fig. 2 that clump remnants exist below the $M_{\rm min}$. Deep in the bulge (very near to the Galactic center) the clump remnants are more numerous because of intensive destructions of clumps in the dense

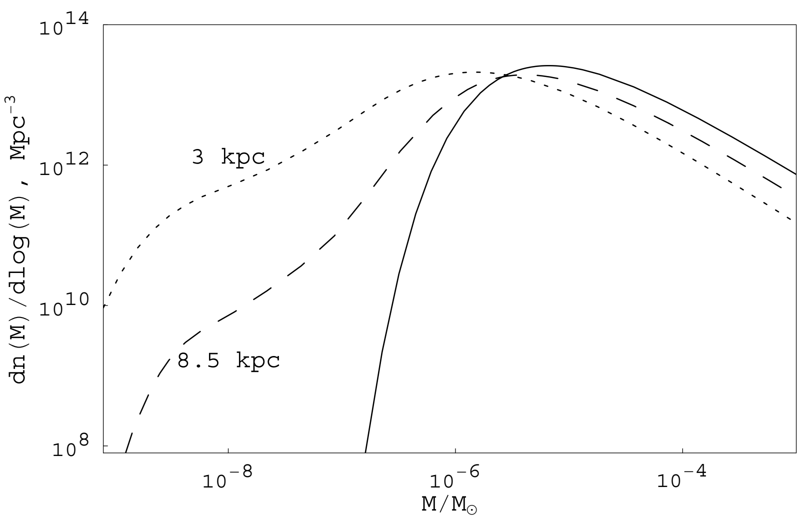

Figure 2: Numerically calculated modified mass function of clump remnants for galactocentric distances 3 and 8.5 kpc. The solid curve shows the initial mass function.

stellar environment in comparison with the rarefied one in the halo. The main contribution to the low-mass tail of the mass function of remnants comes from the clumps with the near-disk orbits where the destructions are more efficient.

As a representative model we use the standard Navarro-Frank-White profile of the DM Galactic halo

$$\rho_{\rm H}(r)=\frac{\rho_0}{(r/L)\,(1+r/L)^2}, \tag{2}$$

where $L=45$ kpc, $\rho_0=5\times10^6{\rm M}_\odot$ kpc^{-3}. The gamma-ray flux from annihilation of diffuse distribution (2) of DM in the halo is proportional to

$$I_{\rm H}=\int\limits_0^{r_{\rm max}(\zeta)}\rho_H^2(\xi)\,dx, \tag{3}$$

where the integration is over r goes along the line of sight, $\xi(\zeta,r)=(r^2+r_\odot^2-2rr_\odot\cos\zeta)^{1/2}$ is the distance to the Galactic center, $r_{\rm max}(\zeta)=(R_{\rm H}^2-r_\odot^2\sin^2\zeta)^{1/2}+r_\odot\cos\zeta$ is a distance to the external halo border, ζ is an angle between the line of observation and the direction to the Galactic center, $R_{\rm H}$ is a virial radius of the Galactic halo, $r_\odot=8.5$ kpc is the distance between the Sun and Galactic center. The corresponding signal from annihilations of DM in clumps is proportional to the quantity [3]

$$I_{\rm cl}=S\int\limits_0^{r_{\rm max}(\zeta)}dx\int\limits_{M_{\rm min}}^{M_{\rm max}}\rho\rho_H(\xi)P(\xi,\rho)f(M)\,dM, \tag{4}$$

where $\rho(M)$ is the mean density of clump. The function S depends on the clump density profile and core radius of clump [3] and we use $S\simeq14.5$ as a representative example. The observed amplification of the annihilation signal is defined as $\eta(\zeta)=(I_{\rm cl}+I_{\rm H})/I_{\rm H}$ is shown in the Fig. 3 for the case $x_c=0.1$. It tends to unity at $\zeta\to0$ because of the divergent form of the halo profile (2). The annihilation of diffuse DM prevails over signal from clumps at the the Galactic center. The $\eta(\zeta)$ very slightly depends on x_c, and corresponding graphs for $x_c<0.1$ are almost indistinguishable from the one in the Fig. 3. This is because the observed signal is obtained by integration along the line of sight and the effect of clumps destruction at the Galactic center is masked by the signal from another regions of the halo.

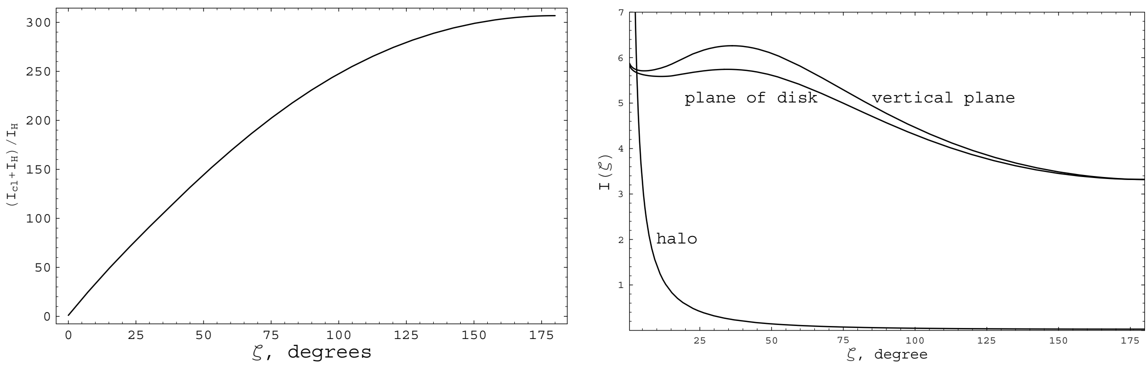

Figure 3: Left panel: the amplification (boosting) of the annihilation signal $(I_{\rm cl} + I_{\rm H})/I_{\rm H}$ as function of the angle between the line of observation and the direction to the Galactic center. Right panel: the annihilation signal in the Galactic disk plane, in the vertical plane crossing the Galaxy rotation axis and from the diffuse DM halo.

Conclusion

The dense remnants of small-scale DM clumps survive the tidal destruction and provide the enhancement of DM annihilation in the Galaxy. These remnants of DM clumps form the low-mass tail in the standard mass distribution of small-scale clumps extended much below the minimal clump mass $M_{\rm min}$ of the standard distribution. Despite the small survival probability of clumps during early stage of hierarchial clustering, they provide the major contribution to the annihilation signal (in comparison with the diffuse DM). The amplification (boost-factor) can reach 10^2 or even 10^3 depending on the initial perturbation spectrum and minimum mass of clumps.

Acknowledgments

This work was supported in part by the Russian Ministry of Science grant LSS 959.2008.2.

References

1. A.M. Green, S. Hofmann and D.J. Schwarz, JCAP **0508**, 003 (2005).
2. E. Bertschinger, *Phys. Rev.* D **74**, 063509 (2006).
3. V. Berezinsky, V. Dokuchaev and Yu. Eroshenko, *Phys. Rev.* D **68**, 103003 (2003).
4. V. Berezinsky, V. Dokuchaev and Yu. Eroshenko, *Phys. Rev.* D **73**, 063504 (2006).
5. M. Kamionkowsky and S.M. Koushiappas, *Phys. Rev.* D **77**, 103509 (2008).
6. L. Pieri, G. Bertone and E. Branchini, Mon. Not. Roy. Astron. Soc. **384**, 1627 (2008).
7. S. Ando and E. Komatsu, *Phys. Rev.* D **73**, 023521 (2006).
8. A.V. Gurevich and K.P. Zybin, Sov. Phys. – JETP **67**, 1 (1988).
9. A.V. Gurevich and K.P. Zybin, Sov. Phys. – Usp. **165**, 723 (1995).
10. J. Diemand, B. Moore and J. Stadel, Nature **433**, 389 (2005).
11. J. Wang and S.D. M. White, arXiv:0809.1322v1 [astro-ph].
12. A. G. Doroshkevich, V. N. Lukash and E. V. Mikheeva in *XLIst Rencontres de Moriond. La Thuile, Aosta Valley, Italy (March 11–18, 2006). From Dark Halos to Light*, eds. Sophie Maurogordato, Jean Trân Thanh Vân, Laurence Tresse (Thê Gióí Publishes, Vietnam, 2006); *ibid.* arXiv:0712.1688 [astro-ph].
13. V. Berezinsky, V. Dokuchaev and Yu. Eroshenko, JCAP **07**, 011 (2007).
14. V. Berezinsky, V. Dokuchaev and Yu. Eroshenko, *Phys. Rev.* D **77**, 083519 (2008).

Spiral Galaxies without CDM halo?

Ł. BRATEK[A], J. JAŁOCHA[A], M. KUTSCHERA[A,B], P. SKINDZIER[B]
[A]*Henryk Niewodniczański Institute of Nuclear Physics, Polish Academy of Sciences, Radzikowskego 152, PL-31342 Kraków, Poland*
[B]*M. Smoluchowski Institute of Physics, Jagellonian University, Reymonta 4, PL-30059 Kraków, Poland*

The global disk model is applied to find mass distribution by iterations in spiral galaxies with rotation curves breaking sphericity condition at larger radii. The iteration scheme's role is to overcome the ambiguity of determination of mass density of a flattened mass distribution from naturally cutoff rotation curves. Our findings suggest that the amount of cold dark matter in the examined galaxies may be smaller than that predicted by other mass models, or even absent.

1 Global thin disc model and flattened (disk-like) galaxies

Toomre's model of rotating axisymmetric and infinitely thin disc of dust matter (*i.e.*, pressureless perfect fluid) [5], offers a tool for determining the equilibrium mass distribution in a highly flattened system, directly from its rotation law, provided the approximation of circular motion of matter around the galactic center is applicable. In the latter case, a mass distribution is flattened rather than spherical if the sphericity condition is broken, that is, when the 'spherical' mass function $M(r) = Grv_c^2(r)$, corresponding to rotation curve v_c, is not everywhere nondecreasing. If this happens at larger radii, the CDM halo, which dominates gravitation of baryonic matter, must be either non-spherical or absent. Moreover, the gravitational potential from the internal mass distribution is almost spherically symmetric at large distances, thus, irrespectively of their geometry, the central bulge and the internal disc may be described by an equivalent column mass density. These allows us to use a substitute global disc component to describe whole galaxy which is flattened at larger radii.

SMD-RC relations for disk-like systems are nonlocal.[a] SMD is a functional of the global shape of RC [1]

$$\sigma(\rho) = \frac{1}{\pi^2 G}\mathcal{P}\left[\int_0^\rho v_c^2(\chi)\Big(\frac{K\left(\frac{\chi}{\rho}\right)}{\rho\,\chi} - \frac{\rho}{\chi}\frac{E\left(\frac{\chi}{\rho}\right)}{\rho^2-\chi^2}\Big)\mathrm{d}\chi + \int_\rho^\infty v_c^2(\chi)\frac{E\left(\frac{\rho}{\chi}\right)}{\chi^2-\rho^2}\,\mathrm{d}\chi\right]. \tag{1}$$

Here, $\mathcal{P}$ stands for the 'principle value integral'; K and E are elliptic functions. Thus, for unambiguous determination of the SMD from a RC, one needs the RC to be measured out to the Keplerian falloff ($v_c^2(\rho) \propto \rho^{-1}$), otherwise the SMD cannot be determined even within the observed region! The inverse of relation (1) shows that rotational velocity on a circular orbit is

[a] SMD = 'surface mass density', RC = 'rotation curve'

related to masses distributed both inside and outside that orbit

$$\frac{v_c^2(\rho)}{4\,G\,\rho} = \mathcal{P}\left[\int\limits_0^{\rho} \sigma(\chi)\frac{\chi E\left(\frac{\chi}{\rho}\right)}{\rho^2-\chi^2}\,\mathrm{d}\chi - \int\limits_{\rho}^{\infty} \sigma(\chi)\left(\frac{\chi^2 E\left(\frac{\rho}{\chi}\right)}{\rho\,(\chi^2-\rho^2)} - \frac{K\left(\frac{\rho}{\chi}\right)}{\rho}\right)\mathrm{d}\chi\right]. \tag{2}$$

This leads to some unexpected features of disk-like mass distributions. Eg., in the presence of a flat disk, rotation curve can be strictly Keplerian in an infinite region where mass density is nonzero, cf. figure (1). Due to the non-locality of SMD-RC relations, SMD of a flattened system

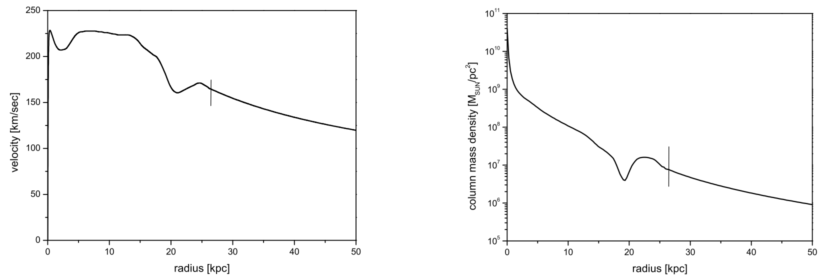

Figure 1: Rotation curve and surface mass density of an infinitely large disk-like system of which rotation curve is exactly Keplerian outside radius $\rho \approx 26kpc$ (shown by vertical bar) and the same as for NGC 891 inside that radius.

cannot be determined unambiguously since RC is measured out to some finite radius R. Eg., the value of integral (1) can be changed significantly by appropriate extrapolation of RC beyond radius R.

To obtain results close to reality one has to supplement RC measurements with additional data. For self-consistency we divide all the data between two complementary spatial domains (we take RC data in the region inside a disk of radius R, and H+He density measurements outside it) and combine them by iterations. The resulting global SMD and RC, apart from accounting for the observed part of RC and for the amount of matter seen outside radius R, should be such that the SMD-RC relations (1) and (2) were satisfied globally.

2 An iteration scheme for the global thin disc model

In the first iteration step, one approximates the disc SMD for radii $\rho < R$ with the values obtained by cutting integration in integral (1) at a cutoff radius $\rho = R$ at which rotation data end. At all other radii and at those where the value of $\sigma(\rho)$ in (1) falls below the observed SMD (bounded from below by H+He data), one can use the observed SMD as the actual density. We consider such constructed density as the first approximation to the unknown global SMD, and calculate the corresponding RC from integral (2), *cf.* figure (2). Let denote these functions by $\sigma_1(\rho)$ and $v_1(\rho)$, respectively. Rotational velocity $v_1(\rho)$ is lower than the observed one, $v_{obs}(\rho)$, thus more mass, which must be added to $\sigma_1(\rho)$, is needed to account for the galaxy's rotation. The missing mass is calculated using integral (1) cut off at $\rho = R$ in which, in place of $v^2(\chi)$, the difference $v_{obs}^2 - v_1^2$ is substituted. Next, the resulting correction is added to $\sigma_1(\rho)$ and continued with the observed SMD, $\sigma_{obs}(\rho)$, in the regions where the corrected $\sigma_1(\rho)$ falls below σ_{obs}. This we consider as the global SMD in the second approximation and denote by σ_2. This procedure is to be repeated iteratively until the global RC calculated from the found global SMD in the last iteration step gets overlapped for radii $\rho < R$ with the observed part of RC.

In fact, to obtain our results, we applied for calculation of the missing mass, a slightly modified method, as described in more detail in [2]. However, the general idea of the iterations

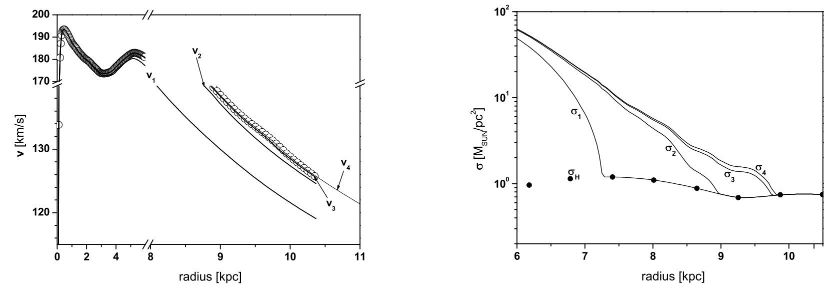

Figure 2: Iteration steps for galaxy NGC 4736. Rotational velocities v_1, v_2, v_3, and v_4 calculated for global surface densities σ_1, σ_2, σ_3 and σ_4 obtained in four consecutive iteration steps. The open circles in the first figure represent the measured rotation curve. Solid circles in the second figure represent the observed column mass density of HI.

remains the same. Finally, one should verify that $\sigma(\rho)$ and $v(\rho)$ from the last iteration step satisfy (1) and (2).

Figure (3) shows the results. Since rotation curves of NGC 4736, NGC 1365 and NGC 7793 break sphericity condition at larger radii, we expect they have no CDM halo. Indeed, the surface mass distribution found in these galaxies converges to that of gas (H+He), and in addition, mass-to-light (M/L) ratios are low even if mass of the gas is included. But it should be clear that a M/L profile should be rather calculated only for the luminous mass in a given frequency band, that is, without inclusion of the mass of hydrogen and He which are invisible in this band. Such obtained M/L profile is decreasing with radius, which provides another argument for that the CDM halo cannot be present in these galaxies. Note, that NGC 1365 was already reported to contain only a small amount of dark matter [3].

3 Summary

Among spiral galaxies one can find such whose rotation can be explained in the framework of Newtonian gravitation and without recourse to the presence of CDM halo. This is unusual from the point of view of our understanding of galactic evolution.

The general prescription is the following. Take a spiral galaxy with rotation curve breaking the sphericity condition (the halo, if present, is then expected to be flattened). Use the global disk model to find the column mass density of a presumably flattened mass distribution (geometry of the central bulge is irrelevant for the rotation of distant matter). To minimize the ambiguities inherent to disk geometry, find the global mass density by iterations using as many observational constraints as possible.

For the several galaxies we have examined so far, luminous matter accounts for their rotation, mass-to-light ratios falloff with radius and are low, and surface mass densities smoothly overlap with that of hydrogen+helium observed at large radii. The galaxies are much less abundant in CDM than other models of galaxies predict (a model with dark halo [4] predicts for galaxy NGC 4736, a spherical dark matter halo containing 70% of total mass and 1.5 times greater total galaxy mass than we find, *cf.* [2]). We stress also that first we find the global mass distribution and the rotation law and then we calculate the resulting M/L profiles, which is the opposite to what is usually done.

Since different mass models give quantitatively and qualitatively different results for the same galaxies, more realistic mass models than the naive few-component parametric models used so far, are required.

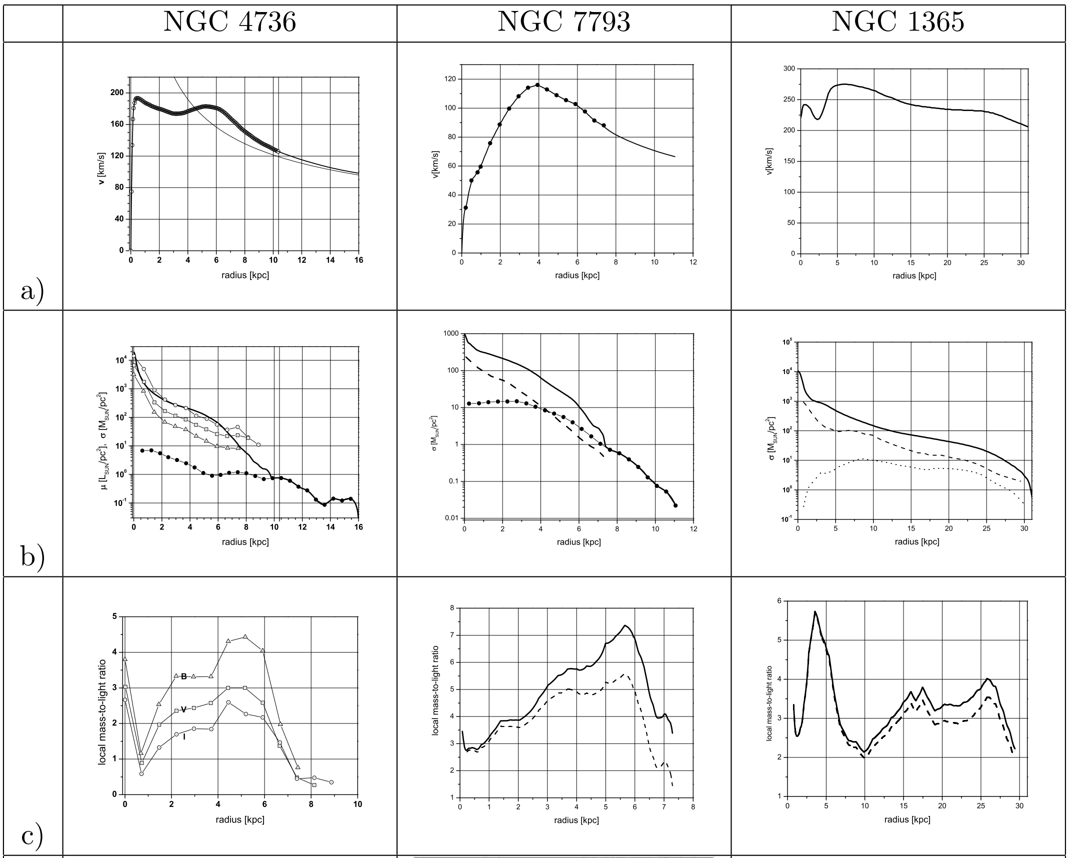

NGC 4736

M_{TOT}	$3.43 \times 10^{10} M_\odot$
M_{HI}	$6.00 \times 10^{8} M_\odot \Rightarrow 0.02 M_{TOT}$
L_I	$2.87 \times 10^{10} L_{I,\odot} \Rightarrow M/L_I = 1.2$
L_V	$2.14 \times 10^{10} L_{V,\odot} \Rightarrow M/L_V = 1.6$
L_B	$1.54 \times 10^{10} L_{B,\odot} \Rightarrow M/L_B = 2.2$

NGC 7793

M_{Gal}	$2.35 \cdot 10^{11} M_\odot$
M_{HI+He}	$1.66 \cdot 10^{10} M_\odot$
L_B	$6.9 \cdot 10^{10} L_\odot$
M_{Gal}/L_B	$3.4 M_\odot/L_\odot$
$(M_{Gal} - M_{gaz})/L_B$	$3.16 M_\odot/L_\odot$

NGC 1365

M_{Gal}	$1.00 \cdot 10^{10} M_\odot$
M_{HI+He}	$1.2 \cdot 10^{9} M_\odot$
L_B	$2.4 \cdot 10^{9} L_\odot$
M_{Gal}/L_B	$4.17 M_\odot/L_\odot$
$(M_{Gal} - M_{gaz})/L_B$	$3.67 M_\odot/L_\odot$

Figure 3: Results obtained in the framework of the global disk model. I) NGC 4736: a) rotation curve (RC): solid circles – measurements, solid thick line – model, solid thin line - Keplerian asymptote; b) solid line – surface mass density (SMD) – model, solid circles – measured SMD of hydrogen HI, empty circles, squares, triangles – the observed luminosity in I, V, B filters; c) the resulting M/L ratio profiles in filters I,V and B. II) NGC 7793: a) RC: solid circles – measurements, solid thick line – model, b) solid line – model SMD, dashed line – luminosity in filter B, solid circles – SMD of HI and He; c) solid line – M/L ratio profile, dashed line – M/L ratio profile with excluded HI and He . III), NGC 1365: a) RC model and measurements, b) solid line – model SMD, dashed line – luminosity in filter B, dotted line – SMD of HI and He; c) solid line – M/L ratio profile, dashed line – M/L ratio profile with excluded HI and He .

References

1. Bratek Ł., Jałocha J., Kutschera M. 2008, MNRAS 391, 1373-1383
2. Jałocha J., Bratek Ł., Kutschera M. 2008, ApJ 679, 373-378
3. S. Jorsater, G.A. van Moorsel, 1995, AJ 110, 2037
4. Kent, S. M. 1987, AJ 93, 816
5. Toomre A. 1963, ApJ 138, 385

A NEW LIGHT BOSON FROM CHERENKOV TELESCOPES OBSERVATIONS?

MARCO RONCADELLI
INFN, Sezione di Pavia, via A. Bassi 6, I – 27100 Pavia, Italy

ALESSANDRO DE ANGELIS
Dipartimento di Fisica, Università di Udine, Via delle Scienze 208, I – 33100 Udine, and INAF and INFN, Sezioni di Trieste, Italy

ORIANA MANSUTTI
Dipartimento di Fisica, Università di Udine, Via delle Scienze 208, I – 33100 Udine, and INFN, Sezione di Trieste, Italy

Early indications by H.E.S.S. and the subsequent detection of blazar 3C279 by MAGIC show that the Universe is more transparent to very-high-energy gamma rays than previously thought. We demonstrate that this circumstance can be reconciled with standard blazar emission models provided that photon oscillations into a very light Axion-Like Particle occur in extragalactic magnetic fields. A quantitative estimate of this effect indeed explains the observed spectrum of 3C279. Our prediction can be tested by the satellite-borne *Fermi*/LAT detector as well as by the ground-based Imaging Atmospheric Cherenkov Telescopes H.E.S.S., MAGIC, CANGAROO III, VERITAS and by the Extensive Air Shower arrays ARGO-YBJ and MILAGRO.

1 Introduction

A characteristic feature of the very-high-energy (VHE) band is that the horizon of the observable Universe rapidly shrinks above 100 GeV as the energy further increases. This is due to the fact that photons from distant sources scatter off background radiation permeating the Universe, thereby disappearing into electron-positron pairs [1]. The corresponding cross section $\sigma(\gamma\gamma \to e^+e^-)$ peaks where the VHE photon energy E and the background photon energy ϵ are related by $\epsilon \simeq (500\,\mathrm{GeV}/E)\,\mathrm{eV}$. We recall that Imaging Atmospheric Cherenkov Telescopes (IACTs) probe the energy interval $100\,\mathrm{GeV} - 100\,\mathrm{TeV}$. Consequently, observations performed by the IACTs are affected by an opacity dominated by the interaction of the beam photon with ultraviolet/optical/infrared diffuse background photons (frequency band $1.2 \cdot 10^3\,\mathrm{GHz} - 1.2 \cdot 10^6\,\mathrm{GHz}$, corresponding to the wavelength range $0.25\,\mu\mathrm{m} - 250\,\mu\mathrm{m}$), usually called Extragalactic Background Light (EBL) and produced by galaxies during the whole history of the Universe. Neglecting evolutionary effects for simplicity, photon propagation is then controlled by the photon mean free path $\lambda_\gamma(E)$ for $\gamma\gamma \to e^+e^-$, and so the observed photon spectrum $\Phi_{\mathrm{obs}}(E, D)$ is related to the emitted one $\Phi_{\mathrm{em}}(E)$ by

$$\Phi_{\mathrm{obs}}(E, D) = e^{-D/\lambda_\gamma(E)}\ \Phi_{\mathrm{em}}(E)\ . \tag{1}$$

Within the considered energy range, $\lambda_\gamma(E)$ decreases like a power law from the Hubble radius 4.3 Gpc around 100 GeV to nearly 1 Mpc around 100 TeV [2]. Thus, Eq. (1) implies that the observed flux is *exponentially* suppressed both at high energies and at large distances, so that sufficiently far-away sources become hardly visible in the VHE range and their observed spectrum should anyway be *much steeper* than the emitted one.

Yet, the behaviour predicted by Eq. (1) has *not* been detected by observations. A first indication in this direction was reported by the H.E.S.S. collaboration in connection with the discovery of the two blazars H2356-309 ($z = 0.165$) and 1ES1101-232 ($z = 0.186$) at $E \sim 1$ TeV [3]. Stronger evidence comes from the observation of blazar 3C279 ($z = 0.536$) at $E \sim 0.5$ TeV by the MAGIC collaboration [4]. In particular, the signal from 3C279 collected by MAGIC in the region $E < 220$ GeV has more or less the same statistical significance as the one in the range 220 GeV $< E <$ 600 GeV (6.1σ in the former case, 5.1σ in the latter) [a].

A possible way out of this difficulty involves the modification of the standard Synchro-Self-Compton (SSC) emission mechanism. One option invokes strong relativistic shocks [6]. Another is based on photon absorption inside the blazar [7]. While successful at substantially hardening the emission spectrum, these attempts fail to explain why *only* for the most distant blazars does such a drastic departure from the SSC emission spectrum show up.

Our proposal – usually referred to as the DARMA scenario – is quite different [8]. Implicit in all previous considerations is the hypothesis that photons propagate in the standard way throughout cosmological distances. We suppose instead that photons can oscillate into a new very light spin-zero particle – named Axion-Like Parlicle (ALP) – and vice-versa in the presence of cosmic magnetic fields, whose existence has definitely been proved by AUGER observations [9]. Once ALPs are produced close enough to the source, they travel *unimpeded* throughout the Universe and can convert back to photons before reaching the Earth. Since ALPs do not undergo EBL absorption, the *effective* photon mean free path $\lambda_{\gamma,\text{eff}}(E)$ gets *increased* so that the observed photons travel a distance in excess of $\lambda_\gamma(E)$. Correspondingly, Eq. (1) becomes

$$\Phi_{\text{obs}}(E, D) = e^{-D/\lambda_{\gamma,\text{eff}}(E)}\ \Phi_{\text{em}}(E)\ , \tag{2}$$

which shows that even a *small* increase of $\lambda_{\gamma,\text{eff}}(E)$ gives rise to a *large* enhancement of the observed flux. It turns out that the DARMA mechanism makes $\lambda_{\gamma,\text{eff}}(E)$ shallower than $\lambda_\gamma(E)$ although it remains a decreasing function of E. So, the resulting observed spectrum is *much harder* than the one predicted by Eq. (1), thereby ensuring agreement with observations even for a *standard* SSC emission spectrum. As a bonus, we get a natural explanation for the fact that only the most distant blazars would demand $\Phi_{\text{em}}(E)$ to substantially depart from the emission spectrum predicted by the SSC mechanism.

We proceed to review the main features of our proposal as well as its application to blazar 3C279.

2 DARMA scenario

Both phenomenological and conceptual arguments entail that the Standard Model (SM) of particle physics should be viewed as the low-energy manifestation of some more fundamental and richer theory of all elementary-particle interactions including gravity. Therefore, the SM lagrangian is expected to be modified by small terms describing interactions among known and new particles. Many extensions of the SM which have attracted considerable interest in the last few years indeed predict the existence of ALPs. They are spin-zero light bosons defined by the low-energy effective lagrangian

$$\mathcal{L}_{\text{ALP}} \;=\; \frac{1}{2}\,\partial^\mu a\,\partial_\mu a - \frac{1}{2}\,m^2\,a^2 - \frac{1}{4M}\,F^{\mu\nu}\,\tilde{F}_{\mu\nu}\,a\ , \tag{3}$$

[a] See ref. [5] for a different view.

where $F^{\mu\nu}$ is the electromagnetic field strength, $\tilde{F}_{\mu\nu}$ is its dual, a denotes the ALP field and m stands for the ALP mass. According to the above view, it is assumed $M \gg G_F^{-1/2} \simeq 250\,\mathrm{GeV}$. On the other hand, it is supposed that $m \ll G_F^{-1/2} \simeq 250\,\mathrm{GeV}$. The standard Axion [10] is the archetype of ALPs and is characterized by a specific relation between M and m, while in the case of *generic* ALPs M and m are to be regarded as *independent*. So, the peculiar feature of ALPs is the trilinear γ-γ-a vertex described by the last term in $\mathcal{L}_{\mathrm{ALP}}$, whereby one ALP couples to two photons.

Owing to such a vertex, ALPs can be emitted by astronomical objects of various kinds, and this fact yields strong bounds: $M > 0.86 \cdot 10^{10}\,\mathrm{GeV}$ for $m < 0.02\,\mathrm{eV}$ [11] and $M > 10^{11}\,\mathrm{GeV}$ for $m < 10^{-10}\,\mathrm{eV}$ [12]. Moreover, the same γ-γ-a vertex produces an off-diagonal element in the mass matrix for the photon-ALP system in the presence of an external magnetic field $\mathbf{B}$. Therefore, the interaction eigenstates differ from the propagation eigenstates and photon-ALP oscillations show up [13].

We imagine that a sizeable fraction of photons emitted by a blazar soon convert into ALPs. They propagate unaffected by the EBL and we suppose that before reaching the Earth a substantial fraction of ALPs is back converted into photons. We further assume that this photon-ALP oscillation process is triggered by cosmic magnetic fields (CMFs), whose existence has been demonstrated very recently by AUGER observations [9]. Owing to the notorious lack of information about their morphology, one usually supposes that CMFs have a domain-like structure [14]. That is, $\mathbf{B}$ ought to be constant over a domain of size L_{dom} equal to its coherence length, with $\mathbf{B}$ randomly changing its direction from one domain to another but keeping approximately the same strength. As explained elsewhere [15], it looks plausible to assume the coherence length in the range $1 - 10\,\mathrm{Mpc}$. Correspondingly, the inferred strength lies in the range $0.3 - 1.0\,\mathrm{nG}$.

3 Predicted energy spectrum

Our ultimate goal consists in the evaluation of the probability $P_{\gamma\to\gamma}(E, D)$ that a photon remains a photon after propagation from the source to us when allowance is made for photon-ALP oscillations as well as for photon absorption from the EBL. As a consequence, Eq. (2) gets replaced by

$$\Phi_{\mathrm{obs}}(E, D) = P_{\gamma\to\gamma}(E, D)\, \Phi_{\mathrm{em}}(E) \ . \tag{4}$$

Our procedure is as follows. We first solve exactly the beam propagation equation arising from $\mathcal{L}_{\mathrm{ALP}}$ over a single domain, assuming that the EBL is described by the "best-fit model" of Kneiske *et al.* [16]. Starting with an unpolarized photon beam, we next propagate it by iterating the single-domain solution as many times as the number of domains crossed by the beam, taking each time a *random* value for the angle between $\mathbf{B}$ and a fixed overall fiducial direction. We repeat such a procedure 10'000 times and finally we average over all these realizations of the propagation process.

We find that about 13% of the photons arrive to the Earth for $E = 500\,\mathrm{GeV}$, representing an enhancement by a factor of about 20 with respect to the expected flux without DARMA mechanism (the comparison is made with the above "best-fit model"). The same calculation gives a fraction of 76% for $E = 100\,\mathrm{GeV}$ (to be compared to 67% without DARMA mechanism) and a fraction of 3.4% for $E = 1\,\mathrm{TeV}$ (to be compared to 0.0045% without DARMA mechanism). The resulting spectrum is exhibited in Fig. 1. The solid line represents the prediction of the DARMA scenario for $B \simeq 1\,\mathrm{nG}$ and $L_{\mathrm{dom}} \simeq 1\,\mathrm{Mpc}$ and the gray band is the envelope of the results obtained by independently varying $\mathbf{B}$ and L_{dom} within a factor of 10 about such values. These conclusions hold for $m < 10^{-10}\,\mathrm{eV}$ and we have taken for definiteness $M \simeq 4 \cdot 10^{11}\,\mathrm{GeV}$ but we have cheked that practically nothing changes for $10^{11}\,\mathrm{GeV} < M < 10^{13}\,\mathrm{GeV}$.

Our predictions can be tested by the satellite-borne *Fermi*/LAT detector as well as by the ground-based IACTs H.E.S.S., MAGIC, CANGAROO III, VERITAS and by the Extensive Air Shower arrays ARGO-YBJ and MILAGRO.

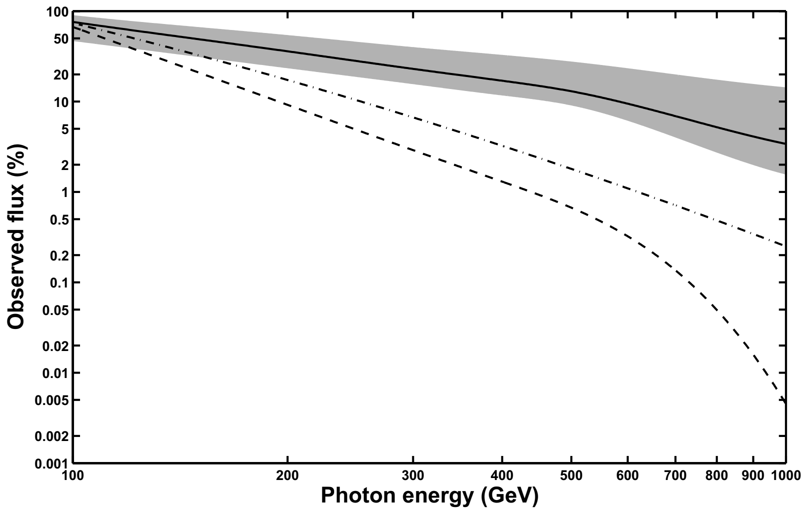

Figure 1: The two lowest lines give the fraction of photons surviving from 3C279 without the DARMA mechanism within the "best-fit model" of EBL (dashed line) and for the minimum EBL density compatible with cosmology (dashed-dotted line), which are discussed by Kneiske *et al.* (see reference in the text). The solid line represents the prediction of the DARMA mechanism.

References

1. G. G. Fazio and F. W. Stecker, Nature **226**, 135 (1970).
2. P. Coppi and F. Aharonian, Astrophys. J. **487**, L9 (1997).
3. F. Aharonian *et al.* (H.E.S.S. Collaboration), Nature **440**, 1018 (2006).
4. J. Albert *et al.* (MAGIC Collaboration), Science **320**, 1752 (2008).
5. F. W. Stecker and S. T. Scully, Astrophys. J. **691**, L91 (2009).
6. F. W. Stecker, M. G. Baring and E. J. Summerlin, Astrophys. J. **667**, L29 (2007). F. W. Stecker and S. T. Scully, Astron. Astrophys. **478**, L1 (2008).
7. F. Aharonian, D. Khangulyan and L. Costamante, Mon. Not. R. Astron. Soc. **387**, 1206 (2008).
8. A. De Angelis, M. Roncadelli and O. Mansutti, *Phys. Rev.* D **76**, 121301 (2007).
9. J. Abraham *et al.* [Pierre Auger Collaboration] Science **318**, 939 (2007).
10. J. H. Kim, Phys. Rep. **150**, 1 (1987). H. Y. Cheng, Phys. Rep. **158**, 1 (1988).
11. K. Zioutas *et al.*, *Phys. Rev. Lett.* **94**, 121301 (2005). S. Andriamoje *et al.*, JCAP **04**, 010 (2007).
12. G. G. Raffelt, *Stars as Laboratories for Fundamental Physics* (University of Chicago Press, Chicago, 1996).
13. P. Sikivie, *Phys. Rev. Lett.* **51**, 1415 (1983); *Phys. Rev. Lett.* **52**, 695 (1984). L. Maiani, R. Petronzio and E. Zavattini, *Phys. Lett.* B **175**, 359 (1986). G. G. Raffelt and L. Stodolsky, *Phys. Rev.* D **37**, 1237 (1988).
14. P. P. Kronberg, Rept. Prog. Phys. **57**, 325 (1994). D. Grasso and H. Rubinstein, Phys. Rep. **348**, 163 (2001).
15. A. De Angelis, M. Persic and M. Roncadelli, Mod. Phys. Lett. **A 23**, 315 (2008).
16. T. M. Kneiske, T. Bretz, K. Mannheim and D. H. Hartmann, Astron. Astrophys. **413**, 807 (2004).

Probing eV-scale axions with CAST.

Jaime Ruz[1]*, on behalf of the CAST Collaboration.*
[1]*Instituto de Física Nuclear y Altas Energías, Universidad de Zaragoza, Zaragoza, Spain*

CAST (CERN Axion Solar Telescope) is a helioscope looking for axions coming from the solar core to the Earth. The experiment, located at CERN, is based on the Primakoff effect and uses a magnetic field of 9 Tesla provided by a decommissioned LHC magnet. CAST is able to follow the Sun during sunrise and sunset having four X-ray detectors mounted on both ends of the magnet to look for photons from axion-to-photon conversions. During its First Phase, which concluded in 2004, CAST searched for axions with masses up to 0.02 eV. By using a buffer gas the coherence needed to scan for axions with masses up to 1.20 eV is re-established in CAST's Second Phase. This technique enables the experiment to study the theoretical regions for axions. During the years 2005 and 2006, the use of ^{4}He has already enabled the search for axions with masses up to 0.39 eV. Up to present time, CAST has upgraded its experimental setup to operate with ^{3}He in the magnetic field.

1 Helioscopes axion searches

The strong CP-problem of QCD might be solved by the introduction of a chiral symmetry [1] whose spontaneous breakdown implies the appearance of a new particle [2, 3]:

$$\mathcal{L}_\theta \equiv \mathcal{L}_{\mathrm{a}} = \Big(\frac{\mathrm{a}}{\mathrm{f_a}}\Big)\xi\Big(\frac{\mathrm{g}^2}{32\pi^2}\Big)\mathrm{G}^{\mu\nu}_{\mathrm{a}}\widetilde{\mathrm{G}}^{\mathrm{a}}_{\mu\nu}. \tag{1}$$

The axion, as the new particle was named, is a very light pseudoscalar Goldstone boson that could be produced via the so-called Primakoff effect [4] in the presence of strong electromagnetic fields. The solar core is an ideal environment to produce those particles due to the strong electric fields of the solar plasma.

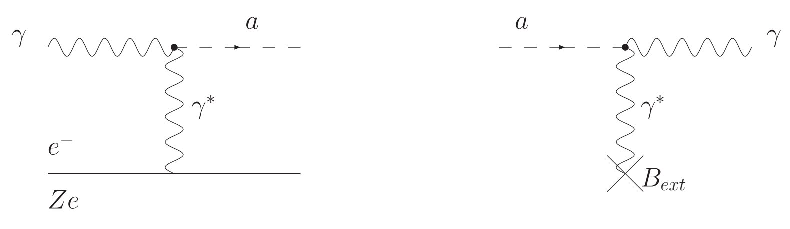

Figure 1: Feynman diagrams for the Primakoff production of axions in the solar core (left) and axion-to-photon conversion in the presence of a magnetic field (right).

In such conditions, a real photon (X-ray) and a virtual photon (electromagnetic field) might couple and result in an axion that is able to reach the Earth's surface. These axions, could be reconverted into X-ray photons in a transverse magnetic field. Therefore, they can be detected by using a magnet pointing to the solar core and an X-ray detector attached to its end [5].

2 The CERN Axion Solar Telescope (CAST)

Twice per day, CAST points towards the Sun making use of a decommissioned superconducting LHC magnet of 9.26 meter length and 9 Tesla field in order to look for a signal of axions according to the expected differential axion flux at the Earth's surface [6]:

$$\frac{d\phi_a}{dE_a} = 6.020 \times 10^{10} \cdot \left[\frac{g_{a\gamma\gamma}}{10^{-10}GeV^{-1}}\right]^2 \cdot E_a^{2.481} e^{-E_a/1.205}\,\mathrm{cm}^{-2}\mathrm{s}^{-1}\mathrm{keV}^{-1}. \tag{2}$$

Four X-ray detectors are mounted on both sides of the magnet: two sunset Micromegas that replace the previously used Time Projection Chamber [7], a sunsrise Micromegas [8] and a Charge Coupled Device [9]. This latter detector is used together with an X-ray telescope that improves its signal to background ratio. Each one of the detectors is daily aligned with the solar core during 1.5 hours in order to look for a photon arising from an axion-to-photon Primakoff conversion suitable to happen in the magnet of CAST. The probability for such an event can be written as:

$$\mathcal{P}_{a\rightarrow\gamma} = \left[\frac{g_{a\gamma\gamma}}{10^{-10}GeV^{-1}}\right]^2 \left[\frac{B_\perp}{2}\right]^2 \cdot \frac{1}{q^2+\Gamma^2/4} \cdot [1 + e^{-\Gamma L} - 2e^{-\Gamma L/2}\cos qL]. \tag{3}$$

From this we can observe that a possible axion-to-photon Primakoff conversion has the following coherence condition:

$$\left(\mathrm{m_a^2/keV^2}\right) \ll \left(\mathrm{m_\gamma^2/keV^2}\right) + 2\left(\frac{\mathrm{E_a/keV}}{\mathrm{L \cdot keV}}\right). \tag{4}$$

These coherence requirements of the conversion probability restricted CAST's First Phase search to axion masses below 0.02 eV [10, 11].

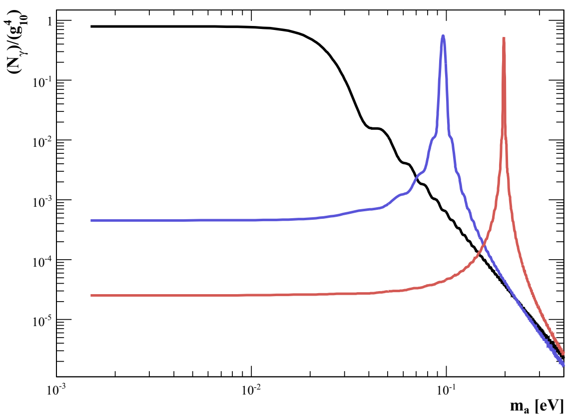

Figure 2: Expected photons arriving CAST for the First Phase (black line) and for two different settings of CAST's Second Phase (red and blue lines). It can be observed how CAST's First Phase loss of coherence is restored during the Second Phase.

However, the loss of coherence over the full magnet length as encountered in CAST's First Phase (vacuum) has been restored for the Second Phase of the experiment. This has been accomplished by filling the magnet with a buffer gas such that the photon acquires an effective mass (see figure 2). The CAST experiment has been upgraded in order to be able to have gases at various pressures in the magnet bores. A complete gas system has been designed and built to control the use of the buffer gas and monitor its density.

Cooling the superconducting CAST magnet down to 1.8 K by using superfluid Helium causes the employed gas in the magnet conversion region to saturate. ^{4}He for instance, is able to restore CAST's coherence for axions masses up to 0.39 eV. However, at the given temperature it saturates when its pressure reaches 16.4 mbar. Therefore, in order to extend the search for axion masses up to 1.20 eV, the use of a lighter gas like ^{3}He is required (see figure 3).

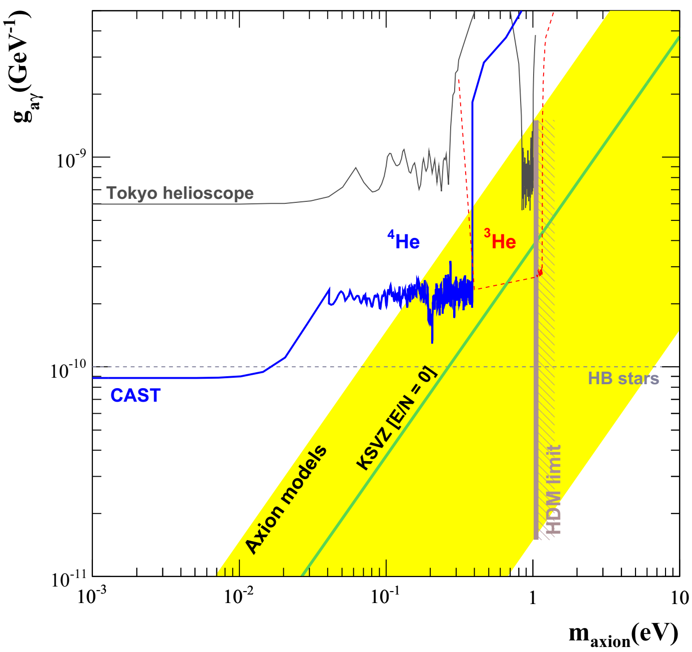

Figure 3: CAST exclusion plot for axion mass versus coupling constant to photon in the experimental panorama of the rest of stelar axion search experiments. In the figure, it can be observed the result achieved by CAST during its first and the ^{4}He run of Second Phase [11] (thick blue line). The thin red line is the expectation for the ^{3}He run of CAST's Second Phase. In light grey the results from the Tokyo helioscope [13–15]

The CAST data taking procedure during the Second Phase was choosen in a way such that it allows for scans of axion masses from 0.02 to 1.20 eV. For the ^{4}He run, during 2005 and 2006 the ^{4}He gas density was increased in the magnet bore daily by a certain number of atoms. The overall range of pressure inside the bore reached from 0 to 13.43 mbar. This mechanism has already allowed CAST to restore the coherence of axion masses up to 0.39 eV (see figure 3). The ^{3}He run of CAST's Second Phase is ongoing and the Primakoff coherence condition has already been fulfilled for axions of masses up to 0.66 eV.

3 Conclusion

During its First Phase, while having vacuum in the magnet bores, CAST looked for traces of axion-to-photon conversions via the Primakoff effect for axions coming from the solar core. However, coherence restrictions constrainted the axion search to masses below 0.02 eV [10, 11].

CAST's Second Phase has already started and the extension of sensitivity using ^{4}He gas has been accomplished during the years 2005 and 2006. The analysis of the ^{4}He run has finished [12] and the final result can be seen in the figure 3. The extension of sensitivity in CAST up to axions masses of 1.20 eV is being accomplished by using ^{3}He and axions masses have already been probed up to 0.66 eV.

4 Bibliography

1. R. D. Peccei and H. R. Quinn, Physical Review Letters **38** (1977) 1440.
2. S. Weinberg, Physical Review Letters **40** (1978) 223.
3. F. Wilczek, Physical Review Letters **40** (1978) 279.
4. H. Primakoff, Physical Review Letters **81** (1951) 899.
5. P. Sikivie, Physical Review Letters **51** (1983) 1415 [Erratum ibid. **52** (1984) 695].
6. K. van Bibber *et al*, Physical Review D. **39** (1989) 2089.
7. D. Autiero *et al.*, New Journal of Physics **9** (2007) 171.
8. P. Abbon *et al.*, New Journal of Physics **9** (2007) 170.
9. M. Kuster *et al.*, New Journal of Physics **9** (2007) 169.
10. K. Zioutas *et al.* [CAST Collaboration], Physical Review Letters **94** (2005) 121301.
11. S. Andriamonje *et al.* [CAST Collaboration], Journal of Cosmology and Astroparticle Physics **0704** (2007) 010.
12. E. Arik *et al.* [CAST Collaboration], Journal of Cosmology and Astroparticle Physics **0902** (2009) 008.
13. S. Moriyama *et al.* Physics Letterss B **434** (1998) 147-152.
14. Y. Inoue *et al.* Physics Letters B **536** (2002) 18-23.
15. Y. Inoue *et al.* Physics Letters B **668** (2008) 9397.

Dark Matter Properties and LSST: Measuring the Invisible with Gravitational Lensing

M. Bradač* and LSST Collaboration
Department of Physics,
University of California,
Santa Barbara, CA 93106, USA

The cluster of galaxies 1E0657-56 (The Bullet Cluster) has been the subject of intense research in the last few years. This system is remarkably well-suited to addressing outstanding issues in both cosmology and fundamental physics. However this is not the only object where properties of dark matter can be studied. Here I will present our measurements on the limits that can be placed on the intrinsic properties of dark matter particles from the Bullet cluster and newly discovered Bullet-like cluster MACSJ0025-1222. Further I will describe how we can tackle the questions of dark matter properties using a large sample of galaxies and galaxy clusters that act as gravitational lenses. With its excellent imaging capabilities and color coverage, LSST will play a leading role in this endeavor.

1 Introduction

The currently accepted cold dark matter model makes very precise predictions for the properties of galaxies and galaxy clusters that can be tested in great detail. There seem to be two crises; namely the amount of substructure in galaxies, and cuspy mass profiles, seen in simulations do not match the observations. These crises can be solved by invoking for example warm and/or self interacting dark matter; consequently they make forecasts about the properties of galaxy clusters (see e.g. [1] and references therein). In self-interacting dark matter scenarios, cores of dark matter halos are heated by collisions, and at least initially have lower central densities and shallower density profiles than in CDM. In warm dark matter scenarios the cluster profiles are also predicted to be less steep. The merger dynamics is also affected by the dark matter microphysics. In addition clusters provide a critical test for alternative gravity theories, that have been proposed to eliminate the need of dark matter altogether. By using gravitational lensing to measure the mass profiles of (merging) clusters, we are in a position to distinguish between different forms of dark matter (and gravity) from astrophysical observations. This will give a measurement of the interaction properties in advance of the expected direct detection of the dark matter particles. Finally, it is difficult to measure the properties of dark matter in galaxy clusters due to the presence and strong influence of baryons. However, by combining all observations we will not only learn about dark matter, but also be able to place meaningful constraints on the formation and evolution of clusters, further testing the ΛCDM paradigm.

The most striking example of such investigations to date has been the Bullet cluster 1E0657−56 [2, 3] and MACS J0025.4−1222 [4]. In these system, the positions of dark matter halos and the dominant baryonic component (i.e. hot gas) are well separated, leading us to infer the clear presence and domination of a dark matter component (see Fig. 1 and [3, 4, 2]). A union of the strong lensing data (information from highly distorted arcs) and weak lensing data (weakly distorted background galaxies) for the cluster mass reconstruction has been demonstrated to be very successful in providing a high-fidelity, high signal-to-noise mass reconstruction over a large area.

2 The Two Bullet-like Clusters 1E0657-56 and MACSJ0025-1222

The cluster of galaxies 1E0657−56 is one of the hottest, most X-ray luminous clusters known. Since its discovery [5], it has been the subject of intense and ongoing research. In particular, Chandra X-ray observations by [6] revealed the cluster to be a supersonic merger in the plane of the sky with a textbook example of a bow shock, making this cluster a unique case in which to study hydrodynamical properties of interacting systems. The optical images show that the cluster has two distinct components, and the X-ray analysis reveals that the lower mass sub-cluster's gas has recently exited the core of the main cluster with a relative velocity of $4500^{+1100}_{-800}\mathrm{kms}^{-1}$. Detailed simulations of this system by [7] revealed that the sub-cluster itself (galaxies and dark matter component) is likely moving with lower velocity of $\sim 2700\mathrm{kms}^{-1}$.

Just like its cousin, MACS J0025.4−1222 consists of two merging subclusters of similar richness at $z = 0.586$ [4]. It was discovered using deep, ground-based optical imaging and short, snapshot Chandra exposures of clusters in the all-sky, X-ray flux-limited MAssive Cluster Survey (MACS) [8, 9]. MACS J0025.4−1222 emerges as a massive, merging cluster with an apparently simple geometry, colliding in approximately the plane of the sky. We measure the distribution of X-ray emitting gas from Chandra X-ray data and find it to be clearly displaced from the distribution of galaxies. A strong (information from highly distorted arcs) and weak (using weakly distorted background galaxies) gravitational lensing analysis based on Hubble Space Telescope observations and Keck arc spectroscopy confirms that the subclusters have near-equal mass. The total mass distribution in each of the subclusters is clearly offset (at $> 4\sigma$ significance) from the peak of the hot X-ray emitting gas (the main baryonic component), but aligned with the distribution of galaxies. We measure the fractions of mass in hot gas ($0.09^{+0.07}_{-0.03}$) and stars ($0.010^{+0.007}_{-0.004}$), consistent with those of typical clusters, finding that dark matter is the dominant contributor to the gravitational field.

Due to their unique geometries and physical state, these cluster are the best known system in which to test the dark matter hypothesis [2, 4]. The observed offsets between the gravitational lensing mass peaks (presented in Fig. 1) and the X-ray gas component give the most direct evidence for the presence of dark matter yet available.

Merging clusters are, however, not the only places where dark matter can be studied. Clusters in general can be used to probe the spatial distribution of dark matter and its interplay with the baryonic mass component [RXJ1345−1145; 10], and thereby allow us to study effectively their formation and evolution, one of the more robust predictions of currently favoured ΛCDM cosmologies. The key requirement for this is to obtain high-resolution, absolutely-calibrated mass maps, from the cluster core region ($\sim$ 10kpc) to the outskirts ($\sim$ 1000kpc) of a representative sample of clusters. LSST is an ideal instrument to achieve this goal, since it combines multi-color high-resolution imaging over a large field of view. This will allow us to identify multiply imaged sources as well as perform weak lensing measurements all the way out to the virial radius. We showed that our method is able to provide mass estimates to 10% accuracy, with high spatial resolution in the center of the cluster, provided the weak lensing analysis can be supported by secure multiple image systems with redshifts in the strong lensing regime.

3 Dark Matter Properties

The clear offset between the peaks of the major baryonic component (hot gas) and the total mass distribution (obtained from gravitational lensing) gives a strong evidence for the existence of dark matter. In addition, we see (see e.g. Fig. 1) that the total mass peak is consistent with the centroids

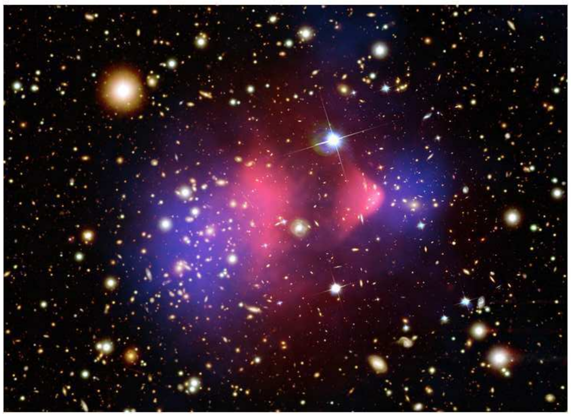 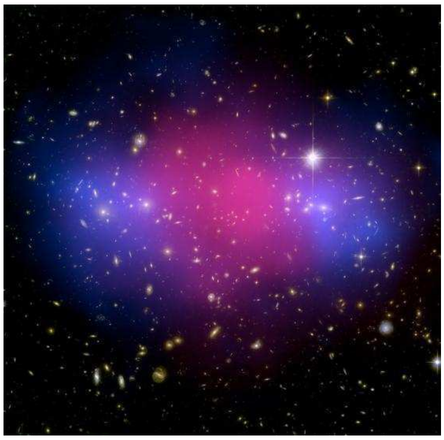

Figure 1: The color composite of the Bullet cluster 1E0657−56 (left) and MACS J0025.4−1222 (right). Overlaid in *blue* shade is the surface mass density map from the weak lensing mass reconstruction. The X-ray emitting plasma is shown in *red*. Both images subtend $\sim$ 10 arcmin on the vertical axis. Credit (left): X-ray NASA/CXC/CfA Optical: NASA/STScI; Magellan/U.Arizona; [2, 4] (right) X-ray (NASA/CXC/Stanford/S.Allen); Optical/Lensing (NASA/STScI/UCSB/M.Bradac); [4].

of the collisionless galaxies belonging to the cluster (which can be recognized by their orange-yellow color in Fig. 1).

These observation already give us a hint that dark matter is collisionless; in addition with detailed simulations (see [11]) we were able to place upper limit on self-interaction cross-section of dark matter per unit mass of dark matter particle, σ/m. We take advantage of new, higher-quality observational datasets by running N-body simulations of 1E0657-56 that include the effects of self-interacting dark matter, and comparing the results with observations of the hot gas (X-rays) and total matter distribution (strong and weak lensing). The addition of strong lensing is crucial here, as the results are sensitive to the central mass distribution in the cluster, the latter is difficult to obtain with weak lensing data only, since the signal-to-noise ratio of the weak lensing measurement is much lower (galaxy shapes are a noisy estimator of the underlying mass distribution) and consequently reconstructions need to be heavily smoothed.

This new method places an upper limit (68% confidence) of $\sigma/m < 1.25\text{cm}^2/\text{g} = 2.25\text{barn/GeV}$. If we make the assumption that the subcluster and the main cluster had equal mass-to-light ratios prior to the merger, we derive our most stringent constraint of $\sigma/m < 0.7\text{cm}^2/\text{g} = 1.3\text{barn/GeV}$, which comes from the consistency of the subcluster's observed mass-to-light ratio with the main cluster's, and with the universal cluster value, ruling out the possibility of a large fraction of dark matter particles being scattered away due to collisions. A similar experiment for MACS J0025.4−1222 (although full simulation will only be performed after the dynamical data becomes available) yielded $\sigma/m < 4\text{cm}^2/\text{g} = 7\text{barn/GeV}$ [4]. This limit will be further improved in the near future with improved dynamical analysis of this system.

Our limits rule out most of the $\sigma/m < 0.5-5\text{cm}^2/\text{g} = 1-10\text{barn/GeV}$ range invoked to explain inconsistencies between the standard collisionless cold dark matter model and observations[12].

4 Towards a kilo-cluster sample with LSST

Massive and interacting clusters, while quite rare, are remarkably well-suited to addressing outstanding issues in both galaxy evolution and fundamental physics. However, in order to study the mass distribution, methods relying on hydrostatic (X-rays) or dynamical equilibrium are ill-suited for such systems. With a large sample of clusters observed at various wavelengths with LSST we will therefore be able to obtain an absolutely calibrated mass map from the very core regions ($\sim$ 10 to 100kpc from strong lensing) to the largest scales ($\sim$ 1000kpc from weak lensing). When combined these data will have an as of yet unexplored potential to study clusters of galaxies and use them as dark matter and in larger samples as dark energy laboratories.

Our main conclusions are the following:

1. The majority of the mass is spatially coincident with the galaxies, which implies that the cluster mass must be dominated by a relatively collisionless form of dark matter. Combining these findings with detailed simulations we obtain upper limit on dark-matter self interaction cross section of $\sigma/m < 0.7\mathrm{cm}^2/\mathrm{g} = 1.3\mathrm{barn}/\mathrm{GeV}$.

2. Using the combined strong and weak lensing mass reconstruction we derive a high-resolution, absolutely calibrated mass map. We detect the main cluster peak and a distinct mass concentration at the subcluster position, both clearly offset from the location of the X-ray gas in the system in both 1E0657−56 and MACS J0025.4−1222.

3. The high resolution data allow us to significantly detect the shapes of both the main mass component and the subcluster with no prior assumptions on their positions or profiles.

The rough limits on the dark-matter self interaction cross section from the pioneering work on 1E0657−56 and MACS J0025.4−1222 can be substantially improved: by using more obviously merging systems. We are currently analysing the data from more such systems. In addition, large samples of clusters will allow us to derive constraints on the mass distribution of clusters from their very center to their outskirts, thereby providing a unique tool to study clusters and use them as dark matter laboratories.

Acknowledgments

I would like to thank the organizers for their kind invitation to this meeting. Support for this conference was provided through LSST collaboration, through Hubble Fellowship grant # HST-HF-01206.01, and through Training and Mobility of Researchers grant.

References

[1] J. P. Ostriker and P. Steinhardt. New Light on Dark Matter. *Science*, 300:1909–1914, June 2003.
[2] D. Clowe, M. Bradač, A. H. Gonzalez, M. Markevitch, S. W. Randall, C. Jones, and D. Zaritsky. A Direct Empirical Proof of the Existence of Dark Matter. *ApJ*, 648:L109–L113, September 2006.
[3] M. Bradač, D. Clowe, A. Gonzalez, P. Marshall, W. Forman, C. Jones, M. Markevitch, S. Randall, T. Schrabback, and D. Zaritsky. Strong and weak lensing united III: the cluster mass distribution of the merging cluster 1E0657−56. *ApJ*, 652:937–951, December 2006.
[4] M. Bradač, T. Schrabback, T. Erben, M. McCourt, E. Million, A. Mantz, S. Allen, R. Blandford, A. Halkola, H. Hildebrandt, M. Lombardi, P. Marshall, P. Schneider, T. Treu, and J.-P. Kneib. Dark Matter and Baryons in the X-Ray Luminous Merging Galaxy Cluster RX J1347.5-1145. *ApJ*, 681:187–196, July 2008.
[5] W. H. Tucker, H. Tananbaum, and R. A. Remillard. A search for 'failed clusters' of galaxies. *ApJ*, 444:532–547, May 1995.
[6] M. Markevitch, A. H. Gonzalez, L. David, A. Vikhlinin, S. Murray, W. Forman, C. Jones, and W. Tucker. A Textbook Example of a Bow Shock in the Merging Galaxy Cluster 1E 0657-56. *ApJ*, 567:L27–L31, March 2002.
[7] V. Springel and G. R. Farrar. The speed of the 'bullet' in the merging galaxy cluster 1E0657-56. *MNRAS*, 380:911–925, September 2007.
[8] H. Ebeling, A. C. Edge, and J. P. Henry. MACS: A Quest for the Most Massive Galaxy Clusters in the Universe. *ApJ*, 553:668–676, June 2001.
[9] H. Ebeling, E. Barrett, D. Donovan, C.-J. Ma, A. C. Edge, and L. van Speybroeck. A Complete Sample of 12 Very X-Ray Luminous Galaxy Clusters at z ¿ 0.5. *ApJ*, 661:L33–L36, May 2007.
[10] M. Bradač, S. W. Allen, T. Treu, H. Ebeling, R. Massey, R. G. Morris, A. von der Linden, and D. Applegate. Revealing the Properties of Dark Matter in the Merging Cluster MACS J0025.4-1222. *ApJ*, 687:959–967, November 2008.
[11] S. W. Randall, M. Markevitch, D. Clowe, A. H. Gonzalez, and M. Bradač. Constraints on the Self-Interaction Cross Section of Dark Matter from Numerical Simulations of the Merging Galaxy Cluster 1E 0657-56. *ApJ*, 679:1173–1180, June 2008.
[12] R. Davé, D. N. Spergel, P. J. Steinhardt, and B. D. Wandelt. Halo Properties in Cosmological Simulations of Self-interacting Cold Dark Matter. *ApJ*, 547:574–589, February 2001.

SEARCH FOR VISIBLE AND INVISIBLE LIGHT HIGGS DECAYS AT *BABAR*

The *BABAR* Collaboration, represented by J. Albert
Department of Physics & Astronomy, University of Victoria, 3800 Finnerty Rd., Victoria V8P 5C2, Canada

We search for evidence of a light scalar (*e.g.* a Higgs boson) in two radiative decay channels of the narrow $\Upsilon(3S)$ resonance: $\Upsilon(3S) \to \gamma A^0$, followed by either $A^0 \to \mu^+\mu^-$ or $A^0 \to$ invisible. Such an object appears in extensions of the Standard Model, where a light *CP*-odd Higgs boson naturally couples strongly to *b*-quarks. We find no evidence for such processes in 122×10^6 $\Upsilon(3S)$ decays collected by the *BABAR* collaboration at the PEP-II B-factory, and set 90% C.L. upper limits on the branching fraction products $\mathcal{B}(\Upsilon(3S) \to A^0) \times \mathcal{B}(A^0 \to \mu^+\mu^-)$ at $(0.25 - 5.2) \times 10^{-6}$ in the mass range $0.212 \leq m_{A^0} \leq 9.3\,\mathrm{GeV}$ and $\mathcal{B}(\Upsilon(3S) \to A^0) \times \mathcal{B}(A^0 \to$ invisible) at $(0.7 - 31) \times 10^{-6}$ in the mass range $m_{A^0} \leq 7.8$ GeV. The results are preliminary.

1 Introduction

The Higgs mechanism is a theoretically appealing way to account for the different masses of elementary particles [1]. It implies the existence of at least one new scalar particle, the Higgs boson, which is the only Standard Model (SM) [2] particle yet to be observed.

A number of theoretical models extend the Higgs sector to include additional Higgs fields, some of them naturally light [5]. Similar light scalar states appear in models motivated by astrophysical observations [6]. Direct searches typically constrain the mass of such a light particle, A^0, to be below $2m_b$ [7] or lighter [6], making it accessible to radiative decays of Υ resonances [8]. Model predictions for the branching fraction (BF) of $\Upsilon \to \gamma A^0$ decays range from 10^{-6} to as high as 10^{-4} [6,9]. Empirical motivation for a low-mass Higgs search comes from the HyperCP experiment [10], which observed three anomalous events in the $\Sigma \to p\mu^+\mu^-$ final state, that have been interpreted as production of a scalar with the mass of 214.3 MeV decaying into a pair of muons [11]. The large datasets available at *BABAR* allow us to place stringent constraints on such models.

If a light scalar A^0 exists, the pattern of its decays would depend on its mass. In certain Next-to-Minimal Supersymmetric Standard Model scenarios [5], particularly those in which the mass of the lightest supersymmetric particle (LSP) is above m_τ or if $m_{A^0} < 2m_\tau$, the dominant decay mode of A^0 may be invisible: $A^0 \to \chi^0\bar{\chi}^0$, where the neutralino χ^0 is the LSP. If there are no invisible (neutralino) decays, for low masses $m_{A^0} < 2m_\tau$ the dominant decay mode should be $A^0 \to \mu^+\mu^-$. Significantly above the tau threshold, $A^0 \to \tau^+\tau^-$ would dominate, and the hadronic decays may also be significant.

In the following, we describe a search for monochromatic single photons in decays $\Upsilon(3S) \to \gamma A^0$, either in the absence of other decay products, or with a resonance in the dimuon invariant mass distribution for the fully reconstructed final state $A^0 \to \mu^+\mu^-$. In the latter case, we assume that the decay width of the dimuon resonance is negligibly small compared to the experimental resolution, as expected[6,12] for m_{A^0} sufficiently far from the mass of the η_b[13]. In both cases, we further assume that the resonance is a scalar (or pseudo-scalar) particle. While significance of any observation would not depend on this assumption, the signal efficiencies and, therefore, the extracted BFs are computed for a spin-0 particle.

2 The *BABAR* Detector and Dataset

We search for two-body transitions $\Upsilon(3S) \to \gamma A^0$, followed by the decay $A^0 \to \mu^+\mu^-$ or an invisible decay of the A^0, in a sample of $(121.8 \pm 1.2) \times 10^6$ $\Upsilon(3S)$ decays collected with the *BABAR* detector at the PEP-II asymmetric-energy e^+e^- collider at the Stanford Linear Accelerator Center. We use a sample of $78.5\,\mathrm{fb}^{-1}$ accumulated on $\Upsilon(4S)$ resonance ($\Upsilon(4S)$ sample) for studies of the continuum backgrounds; since $\Upsilon(4S)$ is three orders of magnitude broader than $\Upsilon(3S)$, the BF $\Upsilon(4S) \to \gamma A^0$ is expected to be negligible. For characterization of the background events and selection optimization we also use a sample of $2.4\,\mathrm{fb}^{-1}$ collected 30 MeV below the $\Upsilon(3S)$ resonance (henceforth referred to as off-resonance samples).

3 Event Selection and Signal Yields for the $A^0 \to$ Invisible Decay Channel

We split the dataset into two broad energy ranges based on the energy of the highest-energy electromagnetic cluster in the center-of-mass (CM) frame. The high-energy region corresponds to $3.2 < E^*_\gamma < 5.5$ GeV. The backgrounds in this region are dominated by the process $e^+e^- \to \gamma\gamma$, especially near $E^*_\gamma = E_{cm}/2$, where the photon energy distribution for $e^+e^- \to \gamma\gamma$ events peaks. The event selection is optimized to reduce this peaking background as much as possible.

The second energy range is $2.2 < E^*_\gamma < 3.7$ GeV. Background in this region is dominated by the low-angle radiative Bhabha events $e^+e^- \to e^+e^-\gamma$, in which both electron and positron miss the sensitive detector volumes. In the region $3.0 < E^*_\gamma < 3.7$ GeV, the tail from the $e^+e^- \to \gamma\gamma$ background is significant.

A limited number of variables are available for these very low-multiplicity event samples. We use photon quality and fiducial criteria, as well as rejecting events with charged tracks and muon clusters, to select the events of interest.

We optimize the event selection to maximize $\varepsilon_S/\sqrt{\varepsilon_B}$, where ε_S is the selection efficiency for the signal, and ε_B is the background efficiency. We use Monte Carlo (MC) samples[17,15] generated over a broad range $0 < m_{A^0} \leq 8$ GeV of possible A^0 masses for the signal events. We also use approximately 10% of the available dataset as a background sample for the selection optimization. This sample is included in the final fit.

In the following, we present the analysis of the data in each energy range separately. We use the high-energy region to measure the signal yields in the mass range $0 < m_{A^0} \leq 6$ GeV. We measure the yields in the region $6 < m_{A^0} \leq 7.8$ GeV using the low-energy region. The overlap between the two regions is minimal, and the events yields are consistent in the range of m_{A^0} where the regions overlap.

3.1 $A^0 \to$ Invisible: High-Energy Region

The selection efficiency for signal is 10-11%, depending on m_{A^0}, and is below 10^{-5} for $e^+e^- \to \gamma\gamma$ events. Most of the signal efficiency loss occurs due to fiducial selection of the photon.

We extract the yield of signal events as a function of the assumed mass m_{A^0} in the interval $0 < m_{A^0} \leq 6$ GeV by performing a series of unbinned extended maximum likelihood fits to the distribution of the missing mass squared $m_X^2 \equiv m^2_{\Upsilon(3S)} - 2E^*_\gamma m_{\Upsilon(3S)}$ in fine steps of $\Delta m_{A^0} =$ 0.1 GeV. After the final selection, 955 events remain in the data sample in the interval $-5 \leq$

$m_X^2 \leq 40$ GeV^2. The dominant background in this region is from $e^+e^- \to \gamma\gamma$, radiative Bhabha, and two-photon fusion events.

Our MC simulations estimate that the backgrounds from the generic $\Upsilon(3S)$ decays or mis-reconstructed vector mesons produced through initial-state radiation (ISR) processes are negligible. The ISR processes can potentially contribute peaking backgrounds at low m_X^2. We see no evidence for these extra contributions in the off-resonance sample, but also vary the peaking $e^+e^- \to \gamma\gamma$ PDF to estimate potential systematic effects.

The signal PDF is described by a Crystal Ball [18] function centered around the expected value of $m_X^2 = m_{A^0}^2$. We determine the PDF as a function of m_{A^0} using high-statistics simulated samples of signal events, and we determine the uncertainty in the PDF parameters by comparing the distributions of the simulated and reconstructed $e^+e^- \to \gamma\gamma$ events. The resolution for signal events varies between $\sigma(m_X^2) = 1.5$ GeV^2 for $m_{A^0} \approx 0$ to $\sigma(m_X^2) = 0.7$ GeV^2 for $m_{A^0} = 8$ GeV.

3.2 $A^0 \to$ Invisible: Low-Energy Region

The selection efficiency for signal is 20%. Most of the signal efficiency loss occurs due to the fiducial requirement on the CM polar angle $|\cos\theta_\gamma^*| < 0.46$, applied to suppress the background from $e^+e^- \to e^+e^-\gamma$, which rises steeply in the forward and backward directions. We restrict the photon energy range to avoid the region $E_\gamma^* < 2.2$ GeV where the backgrounds are excessively high and the single-photon trigger selection requires further investigation.

We extract the yield of the signal events as a function of the assumed mass m_{A^0} in the range $6 < m_{A^0} \leq 7.8$ GeV by performing a set of unbinned extended maximum likelihood fits to the distribution of the missing mass squared m_X^2 in steps of $\Delta m_{A^0} = 0.025$ GeV. After the final selection, 14,947 events remain in the data sample in the interval $30 \leq m_X^2 \leq 62$ GeV^2. The dominant background in this region is from radiative Bhabha events, with contributions from $e^+e^- \to \gamma\gamma$ becoming relevant at low values of m_X^2 (high photon energy). The signal PDF is described by the same Crystal Ball [18] function as in the high-energy region.

4 Event Selection and Signal Yields for the $A^0 \to \mu^+\mu^-$ Decay Channel

For this channel, we select events with exactly two oppositely-charged tracks and a single energetic photon with a CM energy $E_\gamma^* \geq 0.2$ GeV, allowing other photons to be present in the event as long as their CM energies are below 0.2 GeV. We assign a muon mass hypothesis to the two tracks (henceforth referred to as muon candidates), and require that they form a geometric vertex with the $\chi^2_{\rm vtx} < 20$ (for 1 degree of freedom), displaced transversely by at most 2 cm from the nominal location of the e^+e^- interaction region. We perform a kinematic fit to the Υ candidate formed from the two muon candidates and the energetic photon, constraining the CM energy of the Υ candidate, within the beam energy spread, to the total beam energy $\sqrt{s}$. We place a requirement on the kinematic fit $\chi^2_{\Upsilon(3S)} < 39$ (for 6 degrees of freedom). We further require that the momentum of the dimuon candidate A^0 and the photon direction are back-to-back in the CM frame to within 0.07 radians, and select events in which the cosine of the angle between the muon direction and A^0 direction in the center of mass of A^0 is less than 0.88. We reject events in which neither muon candidate is positively identified.

After the selection, the backgrounds are dominated by two types of QED processes: "continuum" $e^+e^- \to \gamma\mu^+\mu^-$ and the initial-state radiation (ISR) production of the vector mesons J/ψ, $\psi(2S)$, and $\Upsilon(1S)$. In order to suppress contributions from ISR-produced $\rho^0 \to \pi^+\pi^-$ final state in which a pion is misidentified as a muon, we require that both muons are positively identified when we look for A^0 candidates in the range $m_{A^0} < 1.05$ GeV. Finally, when selecting candidate events in the η_b mass region with dimuon invariant mass $m_{\mu\mu} \sim 9.39$ GeV, we require that no secondary photon above a CM energy of $E_2^* = 0.08$ GeV (0.08 GeV) is present in the event. This requirement suppresses decay chains $\Upsilon(3S) \to \gamma_2\chi_b(2P) \to \gamma_1\gamma_2\Upsilon(1S)$ in which the photon γ_2 has a typical CM energy of ≈ 100 MeV.

We use MC samples generated at 20 values of m_{A^0} over a broad range $0.212 < m_{A^0} \leq 9.5\,\text{GeV}$ of possible A^0 masses to measure selection efficiency for the signal events. The efficiency varies between 24-44%, depending on the dimuon invariant mass.

We extract the yield of signal events as a function of the assumed mass m_{A^0} in the interval $0.212 \leq m_{A^0} \leq 9.3\,\text{GeV}$ by performing a series of unbinned extended maximum likelihood fits to the distribution of the "reduced mass" $m_R = \sqrt{m_{\mu\mu}^2 - 4m_\mu^2}$. Each fit is performed over a small range of m_R around the value expected for a particular m_{A^0}. We use the $\Upsilon(4S)$ sample to determine the probability density function (PDF) for the continuum background in each fit window, which agrees within statistics to MC simulations. We use a threshold (hyperbolic) function to describe the background below $m_R < 0.23$ GeV; its parameters are fixed to the values determined from the fits to the $\Upsilon(4S)$ dataset. Elsewhere the background is well described in each limited m_R range by a first-order ($m_R < 9.3\,\text{GeV}$) or second-order ($m_R > 9.3\,\text{GeV}$) polynomial.

The signal PDF is described by a sum of two Crystal Ball functions [18] with tail parameters on either side of the maximum. The signal PDFs are centered around the expected values of m_R and have the typical resolution of $2 - 10\,\text{MeV}$, which increases monotonically with m_{A^0}. We determine the PDF as a function of m_{A^0} using a set of simulated signal samples, and we interpolate PDF parameters and signal efficiency values linearly between simulated points. We determine the uncertainty in the PDF parameters by comparing the distributions of the simulated and reconstructed $e^+e^- \to \gamma_{\text{ISR}} J/\psi$, $J/\psi \to \mu^+\mu^-$ events.

Known resonances, such as J/ψ, $\psi(2S)$, and $\Upsilon(1S)$, are present in our sample in specific intervals of m_R, and constitute *peaking background*. We include these contributions in the fit where appropriate, and describe the shape of the resonances using the same functional form as for the signal, a sum of two Crystal Ball functions, with parameters determined from the dedicated MC samples. We do not search for A^0 signal in the immediate vicinity of J/ψ and $\psi(2S)$, ignoring the region of $\pm 40\,\text{MeV}$ around J/ψ and $\pm 25\,\text{MeV}$ around $\psi(2S)$.

In the $0.212 \leq m_{A^0} < 0.5\,\text{GeV}$ region, we fit over a fixed interval $0.01 < m_R < 0.55\,\text{GeV}$, near the J/ψ resonance, we fit over the $2.7 < m_R < 3.5\,\text{GeV}$ interval, and near the $\psi(2S)$ resonance we fit over the range $3.35 < m_R < 4.1\,\text{GeV}$. Elsewhere, we use sliding intervals $\mu - 0.2 < m_R < \mu + 0.1\,\text{GeV}$, where μ is the mean of the signal distribution of m_R. We search for A^0 signal in fine mass steps $\Delta m_{A^0} = 2 - 5\,\text{MeV}$.

5 Systematic Uncertainties

5.1 $A^0 \to$ Invisible

The largest systematic uncertainties in the signal yield come from the estimate of the $e^+e^- \to \gamma\gamma$ peaking background yield in the high-energy region and its shape (in both energy regions). Varying the peaking $e^+e^- \to \gamma\gamma$ background contribution by its uncertainty changes the signal yield by ± 38 events for $m_{A^0} = 0$, with the effect decreasing with increased m_{A^0}. The uncertainty due to the $e^+e^- \to \gamma\gamma$ PDF is largest in the low-energy region, where it contributes up to ± 70 events (for $m_{A^0} = 7.4$ GeV) to the uncertainty in the signal yield.

We determine the uncertainty in the signal PDF by comparing the data and simulated distributions of $e^+e^- \to \gamma\gamma$ events. We correct for the differences observed, and use half of the correction as an estimate of the systematic uncertainty. The effect on the signal yield is generally small, except for the region near $m_{A^0} = 7.4$ GeV, where the systematic variation of the signal PDF changes the yield by ± 64 events. Such large variation is caused by high correlation with the $e^+e^- \to \gamma\gamma$ yield in this region. The total additive systematic uncertainty on the yield is ranges between 1 and 100 events, depending on m_{A^0}.

We measure the trigger and filter selection efficiency using single-photon $e^+e^- \to \gamma\gamma$ and $e^+e^- \to e^+e^-\gamma$ events selected from a sample of unbiased randomly accepted triggers. We find excellent agreement with the MC estimates of the trigger efficiency, within the systematic uncertainty of 0.4%. We measure the efficiency of single photon reconstruction in a large sample of $e^+e^- \to \mu^+\mu^-\gamma$, $e^+e^- \to \tau^+\tau^-\gamma$, and $e^+e^- \to \gamma\omega$ events, and assign a systematic uncertainty on the reconstruction efficiency of 2%. We assign an additional 2% systematic uncertainty on the single photon selection. The uncertainty on the total number of recorded $\Upsilon(3S)$ decays is estimated to be 1.1%. The total multiplicative error on the branching fraction is 3.1%.

5.2 $A^0 \to \mu^+\mu^-$

We compare the overall selection efficiency between the data and the MC simulation by measuring the absolute cross section $d\sigma/dm_R$ for the radiative QED process $e^+e^- \to \gamma\mu^+\mu^-$ over the broad kinematic range $0 < m_R \leq 9.6\,\mathrm{GeV}$, using the off-resonance sample. We use the ratio of measured to expected cross sections to correct the signal selection efficiency as a function of m_{A^0}. This correction reaches up to 20% at low values of m_{A^0}. We use half of the applied correction, or its statistical uncertainty of 2%, whichever is larger, as the systematic uncertainty on the signal efficiency. This uncertainty accounts for effects of selection efficiency, reconstruction efficiency (for both charged tracks and the photon), trigger efficiency, and the uncertainty in estimating the integrated luminosity.

We determine the uncertainty in the signal and peaking background PDFs by comparing the data and simulated distributions of $e^+e^- \to \gamma_{\mathrm{ISR}} J/\psi$ events. We correct for the observed difference (5.3 MeV in MC versus 6.6 MeV in the data) in the width of the m_R distribution for these events, and use half of the correction to estimate the systematic uncertainty on the signal yield. This is the dominant systematic uncertainty on the signal yield for $m_{A^0} > 0.4$ GeV. Likewise, we find that changes in the tail parameters of the Crystal Ball PDF describing the J/ψ peak lead to variations in event yield of less than 1%. We use this estimate as a systematic error in the signal yield due to uncertainty in tail parameters. The systematic uncertainties due to the fixed continuum background PDF for $m_R < 0.23$ and the fixed contribution from $e^+e^- \to \gamma\phi$ do not exceed $\sigma(\mathcal{B}) = 0.3 \times 10^{-6}$.

We test for possible bias in the fitted value of the signal yield with a large ensemble of pseudo-experiments. The bias is consistent with zero for all values of m_{A^0}, and we assign a BF uncertainty of $\sigma(\mathcal{B}) = 0.02 \times 10^{-6}$ at all values of m_{A^0}.

6 Results and Conclusions

Since we do not observe a significant excess of events above the background in either channel in the A^0 mass ranges considered, we set upper limits on the branching fractions. The 90% C.L. Bayesian upper limits, computed with a uniform prior and assuming a Gaussian likelihood function, are shown in Fig. 1. The limits fluctuate depending on the central value of the signal yield returned by a particular fit, and range from $(0.7-31)\times 10^{-6}$ for the $A^0 \to$ invisible channel and $(0.25-8.1)\times 10^{-6}$ for the $A^0 \to \mu^+\mu^-$ channel. Our limits rule out much of the parameter space allowed by the light Higgs [9] and axion [6] models. These results are preliminary.

Acknowledgements

We are grateful for the excellent luminosity and machine conditions provided by our PEP-II colleagues, and for the substantial dedicated effort from the computing organizations that support *BABAR*. The collaborating institutions wish to thank SLAC for its support and kind

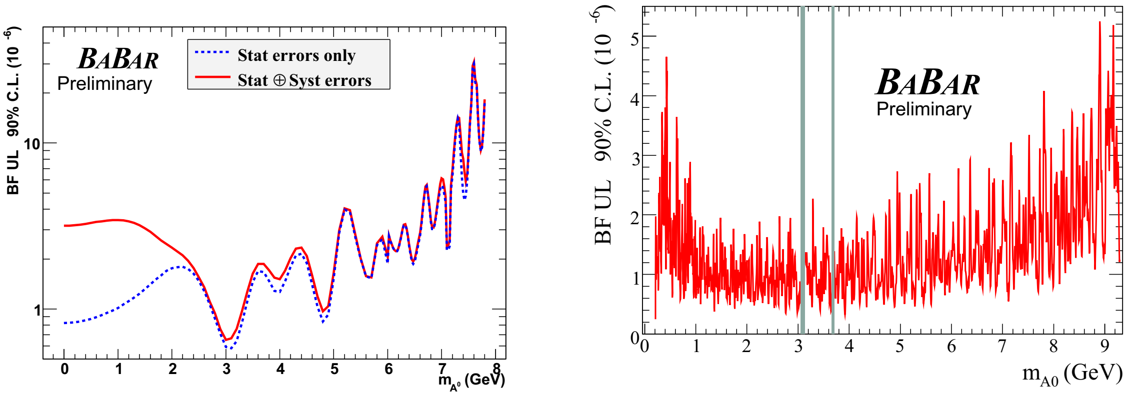

Figure 1: (Left) 90% C.L. upper limits on the branching fraction $\mathcal{B}(\Upsilon(3S) \to \gamma A^0) \times \mathcal{B}(A^0 \to \text{invisible})$. The dashed blue line shows the statistical uncertainties only, the solid red line includes the systematic uncertainties. (Right) Upper limits on the branching fraction $\mathcal{B}(\Upsilon(3S) \to \gamma A^0) \times \mathcal{B}(A^0 \to \mu^+\mu^-)$ as a function of m_{A^0} from the fits to $\Upsilon(3S)$ data. The shaded areas show the regions around the J/ψ and $\psi(2S)$ resonances excluded from the search.

hospitality. This work is supported by DOE and NSF (USA), NSERC (Canada), CEA and CNRS-IN2P3 (France), BMBF and DFG (Germany), INFN (Italy), FOM (The Netherlands), NFR (Norway), MES (Russia), MEC (Spain), and STFC (United Kingdom). Individuals have received support from the Marie Curie EIF (European Union) and the A. P. Sloan Foundation.

References

1. P.W. Higgs, Phys. Rev. Lett. **13**, 508 (1964).
2. S. Weinberg, Phys. Rev. Lett. **19**, 1264 (1967); A. Salam, p. 367 of *Elementary Particle Theory*, ed. N. Svartholm (Almquist and Wiksells, Stockholm, 1969); S.L. Glashow, J. Iliopoulos, and L. Maiani, Phys. Rev. D **2**, 1285 (1970).
3. LEP Working Group for Higgs boson searches, R. Barate *et al.*, Phys. Lett. B **565**, 61 (2003).
4. LEP-SLC Electroweak Working Group, Phys. Rept. **427**, 257 (2006).
5. R. Dermisek and J.F. Gunion, Phys. Rev. Lett. **95**, 041801 (2005).
6. Y. Nomura and J. Thaler, preprint arXiv:0810.5397 [hep-ph] (2008).
7. R. Dermisek and J.F. Gunion, Phys. Rev. D **73**, 111701 (2006).
8. F. Wilczek, Phys. Rev. Lett. **39**, 1304 (1977).
9. R. Dermisek, J.F. Gunion, and B. McElrath, Phys. Rev. D **76**, 051105 (2007).
10. H. Park *et al.*, HyperCP Collaboration Phys. Rev. Lett. **94**, 021801 (2005).
11. X. G. He, J. Tandean and G. Valencia, Phys. Rev. Lett. **98**, 081802 (2007).
12. E. Fullana and M.A. Sanchis-Lozano, Phys. Lett. B **653**, 67 (2007).
13. *BABAR* Collaboration, B. Aubert *et al.*, Phys. Rev. Lett. **101**, 071801 (2008); preprint arXiv:0903.1124, submitted to Phys. Rev. Lett.
14. *BABAR* Collaboration, B. Aubert *et al.*, Nucl. Instr. Meth. A **479**, 1 (2002).
15. The *BABAR* detector Monte Carlo simulation is based on GEANT4: S. Agostinelli *et al.*, Nucl. Instrum. Methods Phys. Res., Sect. A **506**, 250 (2003).
16. ARGUS Collaboration, A. Drescher *et al.*, Nucl. Instr. Meth. A **237**, 464 (1985).
17. D. Lange, Nucl. Instrum. Methods Phys. Res., Sect. A **462**, 152 (2001).
18. M. J. Oreglia, Ph.D Thesis, report SLAC-236 (1980), Appendix D; J. E. Gaiser, Ph.D Thesis, report SLAC-255 (1982), Appendix F; T. Skwarnicki, Ph.D Thesis, report DESY F31-86-02(1986), Appendix E.

Indirect search for Dark Matter with the ANTARES neutrino telescope

V. Bertin, on behalf of the ANTARES Collaboration
C.P.P.M., CNRS/IN2P3-Université de la Méditerranée,
163, avenue de Luminy - Case 902 - 13288 Marseille cedex 9, France

Indirect search for Dark Matter trapped inside celestial bodies is one of the main physics goal of neutrino telescopes. The expected flux coming from supersymmetric Dark Matter annihilations into the Sun and the sensitivity of the ANTARES and KM3NeT detectors to such a signal are presented. The ANTARES detector has been taking data during its building phase in 2007 with five lines operational. This allowed to set a first limit on the neutrino flux coming from Dark Matter annihilations into the Sun with this experiment.

1 Introduction

The most popular paradigm of modern cosmology considers the Dark Matter as a population of stable weakly interacting massive particles (WIMPs) relic from the Big Bang, although not yet discovered. Those particles would gravitationally accumulate in the core of massive celestial bodies such as stars or in a less extend planets, where they could self-annihilate into ordinary matter and eventually produce significant high energy neutrino fluxes. Indirect search for Dark Matter looking at such neutrino fluxes coming from the core of the Sun, the Earth or the galactic centre is thus one of the main physics goal of the current and future neutrino telescopes.

2 The ANTARES neutrino telescope

The ANTARES detector [1] is the first undersea neutrino telescope and the largest one of the Northern hemisphere. It is composed of 12 mooring lines, each holding 75 photomultipliers spread on 25 storeys, installed at a depth of about 2500 metres off shore the Provençal coast of France, in order to form a 3D-matrix of 900 photodetectors. The main goal of the experiment is to look for the Cherenkov light emitted by high energy muons during their travel in the sea water throughout the detector. The trajectory of the muon track is reconstructed from the detection timing of the Cherenkov photons as well as from the positions of the photodetectors. An indirect search for neutrinos can then be performed by selecting the upward-going muons produced by neutrinos which have passed through the entire planet and interacted in the vicinity of the detector. The direction of the incoming neutrino, being almost collinear with the secondary muon, can then be determined with an accuracy reaching $0.2°$ for high energy neutrinos above 10 TeV. Due to its size and the spacing of the photomultipliers, the ANTARES detector has a low energy threshold of ~ 20 GeV for reconstructed neutrinos and an effective area of $\sim 10^{-3}$ m^2 for neutrinos with an energy of 500 GeV. The effective area increases strongly with the neutrino energy and reaches ~ 1 m^2 for PeV energy neutrinos.

Data taking with the ANTARES detector started after the undersea connection of the first line in February 2006 followed by the second line in September 2006. A further three lines were connected in January 2007, with another five connected in December 2007. The apparatus reached its complete configuration with the last two lines being connected in May 2008.

3 Sensitivity to neutralino annihilations in the Sun in mSugra models

The supersymmetric extensions of the Standard Model provide a natural Dark Matter candidate in the form of the lightest neutralino, a supersymmetric partner of the neutral gauge and Higgs bosons. In models with conserved R-parity, the neutralino is a Majorana particle and a stable WIMP which can have a relic density in close agreement with the one derived from the WMAP measurements [2] of the Cosmic Microwave Background.

The signal of neutralino annihilations into the Sun has been studied within the context of the mSugra scenario in which the neutralino properties depend on the four parameters $m_0, m_{1/2}, A_0, \tan\beta$ and $sign(\mu)$. From those parameters defined at the GUT energy scale, the properties of the supersymmetric particle spectrum including the neutralino at the electroweak scale are calculated using renormalization group equations (RGE). The expected neutrino flux resulting from neutralino annihilations into the Sun was calculated for approximately four million parameter sets with a modified version of DarkSUSY 4.1 [3] using a random walk method to scan the regions of the parameter space allowed by theoretical and experimental constraints and to highlight models predicting a neutralino relic density in close agreement with the WMAP constraints. The RGE code ISASUGRA [4] was used for the calculation of the supersymmetric particle spectrum and the halo model of Navarro, Frenk and White [5] was assumed with a local Dark Matter density of 0.3 GeV/cm^2 per cm^3. The flux calculation takes into account the effect of absorption and oscillations of neutrinos inside the Sun as well as during their propagation through vacuum from Sun to Earth.

Knowing the effective area of the ANTARES detector as a function of the neutrino energy, an estimated detection rate can then be calculated from the neutrino flux. Taking into account the irreducible background coming from atmospheric neutrinos as well as an additional background due to misreconstructed atmospheric muon events, a sensitivity is derived considering the signal and background events integrated within a cone of 3° radius around the direction of the Sun. Assuming that only the averaged background rate will be measured, an achievable upper limit for three years of data taking with the complete ANTARES detector can be derived and compared to the detection rate predicted for each individual mSugra model. Figure 1 highlights the models which can be excluded by three years of data taking with the complete ANTARES detector, as well as with a future kilometre-scale undersea neutrino telescope KM3NeT [6]. The sensitivity of ANTARES will allow to put constraints on part of the mSugra parameter space, in particular in the so-called Focus-Point region [7] where the neutralino is mainly Higgsino type and for which higher neutrino fluxes and harder neutrino spectra are expected.

4 Limit on neutrino and muon flux from Dark Matter annihilations in the Sun with ANTARES

A search for neutrinos produced by Dark Matter annihilations into the Sun has been carried out in the data sample collected by the ANTARES detector during its five line operation phase in 2007. During this period, corresponding to 167 days of effective lifetime of data taking, more than 15 millions of muon events have been recorded. After reconstruction and selection cuts, essentially based on the quality of the track fit, a sample of about 200 upward-going events representing the neutrino candidates are selected. This total event rate as well as their zenith

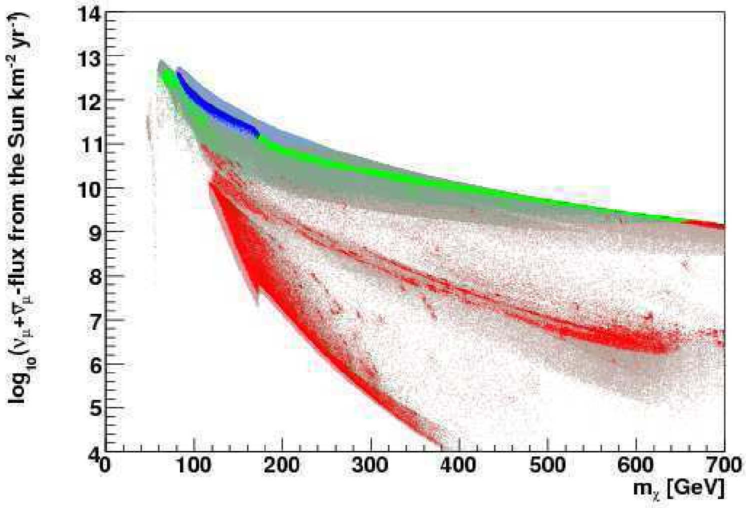

Figure 1: Sensitivity of ANTARES and KM3NeT to neutrinos produced by annihilations of neutralinos into the Sun in mSugra models. The flux of $\nu_\mu + \bar{\nu_\mu}$ integrated for neutrino energies above 10 TeV is given as a function of the neutralino mass. Blue and green points indicate models within the sensitivity of ANTARES and KM3NeT respectively, while red points show models outside the reach of both experiments. Brightly coloured points indicate models with a relic density predicted within 2σ of the WMAP region, shaded ones are those outside.

angle distribution is found to be in good agreement with expectations from the background of atmospheric neutrinos [1].

This sample of upward-going events has been used to look for a possible excess of neutrinos coming from the direction of the Sun. With the condition that the Sun has to be below the horizon, and taking into account some trigger dead-time, the effective lifetime of this search period reduces to 68.4 days. The analysis is performed by counting the number of observed events inside a search cone centered towards the direction of the Sun. The expected background, mainly due to atmospheric neutrino events, has been estimated as a function of the cone opening angle by Monte Carlo simulation. This has been found in very good agreement with an alternative estimation obtained with the data sample by randomizing the direction of the upward-going events. In the data sample recorded with the ANTARES 5-line detector, the distribution of events observed towards the direction of the Sun as a function of the cone opening angle is found to be in good agreement with background expectation. A limit on a possible excess of events as a function of the cone opening angle has then been derived following the unified approach method of Feldman and Cousins [8].

Using the two extreme cases of a hard and a soft neutrino spectrum resulting from neutralino annihilations into W^+W^-/ZZ and $b\bar{b}$ respectively, an optimal cone size has been derived for every neutralino mass before analyzing the data. This allowed to set a limit on the flux of neutrinos, integrated above an energy threshold of 10 GeV, produced by neutralino annihilations inside the Sun as a function of the neutralino mass for these two hard and soft spectra, as shown in figure 2 (left). In order to compare this result with the limits published by other indirect detection experiments, the corresponding neutrino induced muon flux integrated above an energy threshold of 1 GeV was calculated. The limits obtained on that quantity are presented in figure 2 (right). Although they are not yet competitive, the limits obtained by ANTARES based on a data sample of about six months recorded with half of its final detector design are already promising.

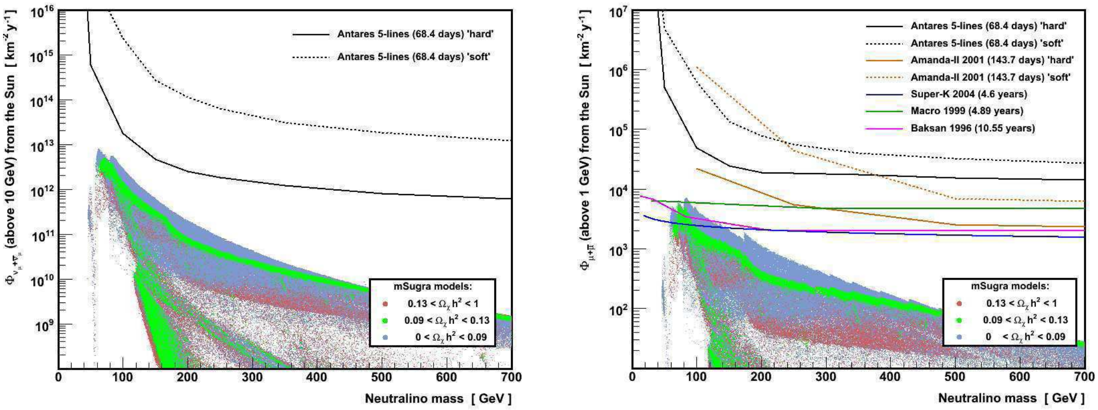

Figure 2: Limit on neutrino flux ($E_\nu > 10$ GeV) (left) and neutrino induced muon flux ($E_\mu > 1$ GeV) (right) coming from the Sun obtained by ANTARES with the data of the 5-Line period in comparison to the expected flux from neutralino annihilations in mSugra models. Existing limits from other experiments are also shown. Green points indicate models with a relic density within 2σ of the WMAP region, blue and red points show models predicting respectively a lower or larger relic density.

5 Conclusion and perspectives

The ANTARES detector, which was completed in May 2008, is the first undersea neutrino telescope and the largest one in the Northern hemisphere. A sample of about 200 neutrino events have been recorded during the building stage of the experiment in 2007, when five lines were operational. This set of events is found to be in good agreement with expectations from the atmospheric neutrino background. In particular, no excess has been found towards the direction of the Sun allowing to set a promising limit on the flux of neutrinos produced by Dark Matter annihilations inside the Sun. A similar analysis looking for signals of Dark Matter annihilations in the Earth or towards the centre of the galaxy is currently under progress.

Further studies of supersymmetric models show that the ANTARES experiment and a future km-scale undersea neutrino telescope KM3NeT will be sensitive to neutrino fluxes predicted by an interesting class of models for which the Dark Matter relic density is in agreement with current cosmological constraints.

References

1. N. Cottini on behalf of the ANTARES Collaboration, these proceedings.
2. D.N. Spergel *et al., Astrophys. J. Suppl.* **148**, 175 (2003).
3. P. Gondolo *et al., JCAP* **0407**, 008 (2004).
4. F.E. Paige, S.D. Protopescu, H. Baer and X. Tata, Isajet 7.69: A Monte Carlo generator for p p, anti-p p and e+ e- reactions, hep-ph/0312045 (2003).
5. J.F. Navarro, C.S. Frenk and S.D.M. White, *Astrophys. J.* **490**, 493 (1997).
6. C. Naumann on behalf of the KM3NeT Consortium, these proceedings.
7. J.L. Feng, K.T. Matchev and T. Moroi, *Phys. Rev.* D **61**, 075005 (2000).
8. G.L. Feldman and R.D. Cousins, *Phys. Rev.* D **57**, 3873 (1998).

LOW-SCALE GRAVITY BLACK HOLES at LHC

E. REGŐS, A. DE ROECK, H. GAMSIZKAN, Z. TRÓCSÁNYI
CERN, Geneva

We search for extra dimensions by looking for black holes at LHC. Theoretical investigations provide the basis for the collider experiments. We use black hole generators to simulate the experimental signatures (colour, charge, spectrum of emitted particles, missing transverse energy) of black holes at LHC in models with TeV scale quantum gravity, rotation, fermion splitting, brane tension and Hawking radiation. We implement the extra-dimensional simulations at the CMS data analysis and test further beyond standard models of black holes too.

1 Introduction

1.1 Quantum gravity and accelerator physics

Quantum gravity is becoming a testable theory with the Large Hadron Collider program starting soon at CERN. We can obtain bounds from collider experiments. One considers graviton interference effects at the LHC. In extra-dimensional models the Planck scale can be as low as the TeV scale which is going to be accessible for the LHC. Quantum gravity can affect the decay modes of particles with mass in the TeV range. In hadron/lepton scatterings and decays the cross sections and branching ratios receive a contribution from quantum gravity in extra-dimensional models. We can consider limits from cosmology and astrophysics as well, e.g. cosmic rays and supernovae. Of particular interest is particle astrophysics, evidence from astronomical observations for extra dimensions.

1.2 Cosmic rays and supernovae – cosmic rays are Nature's free collider

Supernova cores emit large fluxes of Kaluza – Klein gravitons producing a cosmic background which by radiative decays provides a diffuse gamma-ray background. The cooling limit from the SN 1987A neutrino burst puts a bound on the radius of extra dimensions.

Cosmic neutrinos produce black holes, and the energy loss from graviton mediated interactions cannot explain cosmic ray events above a limit. Black holes are produced in observable collisions of elementary particles if extra dimensions exist. Leading to giant air showers, the Auger Observatory will probe the Planck mass up to 4 TeV and may observe hundreds of black holes (Anchordoqui et al. 2002).

1.3 Quantum black holes

Quantum black holes provide limits on gravity as well, the transitions in their energy spectra (quasi-normal modes) depend on the parameters of space-times around the black holes, e.g. in string theories.

2 Stringy black holes at LHC

Alternatives to the hierarchy problem (Planck scale of 10^{19} GeV, electro-weak scale of 240 GeV) are supersymmetry (fundamental theory at $M_{\rm Pl}$, EW derived from radiative corrections) and extra dimensions (EW scale fundamental, $M_{\rm Pl}$ derived). In the latter, matter is confined in 4D while gravity propagates in all dimensions and is weak as the compact space dimensions are large compared to the EW scale (Arkani-Hamed, Dimopoulos, Dvali, 1998).

While there is a large variety of stringy black holes (Youm, 1999) we consider brane world models of black hole generators BlackMax (Dai et al. 2007) and Charybdis (Harris et al. 2003). While the latter has no rotation, BlackMax generates rotating black holes in split fermion models (Arkani-Hamed, Schmaltz 2000, fermions live on separate branes) and models with brane tension. We simulate the experimental signatures of black holes formed at the LHC and the particle decay. We interface BlackMax for CMS analysis.

Further models of Dvali (copies of standard model, non-integer extra dimensions) suggest black hole detection is even more likely (with somewhat different particle decay) and provide explanations for astrophysical dark matter.

2.1 BlackMax simulations, analysis

We have studied rotating and non-rotating blackholes and extra-dimensional scenarios with branes of various dimensions, fermion splitting dimensions and tension. The hoop conjecture assumes a black hole forms if the impact parameter of colliding particles is less than two times the gravitational radius corresponding to their COM energy.

We examine non-rotating models of BlackMax for comparison with Charybdis, 3 models with 5, 3 and 3 extra dimensions, Planck mass of 2, 2 and 5 TeV, and minimum black hole mass of 4, 5 and 7 TeV, respectively. The center-of-mass energy of protons at LHC is taken 14 TeV.

BlackMax controls mass loss, momentum loss, angular momentum loss, angular momentum suppression, charge suppression and colour suppression. In Charybdis-I these loss factors are treated differently (keep the colour minimum, etc).

For the Giudice – Wells (PDG, particle data group) definition of Planck mass the cross sections are 2E-10 b, 2E-11 b and 8E-14 b in BlackMax for the 3 models, respectively. (Rates are the number of events (per given interval) per total number of black holes multiplied by cross section of black holes and integrated luminosity.)

PDG gives higher multiplicities in higher dimensions than the Dimopoulos – Landsberg definition of Planck mass. For the BlackMax – Charybdis comparison we use Dimopoulos Planck mass and BlackMax-II (beta version, with baryon and lepton number conservation).

We find that the mass function of microscopic black holes is "universal", that is, the initial distribution of black hole mass per event (normalized to the total number of events) is almost the same for the three models examined. We plot $M - M_{min}$ vs. $log\ N$ (per event) and they are almost identical straight lines with slopes very close. Here we used the Dimopoulos Planck mass (and 60000 events) but models with rotation and brane tension give similar mass functions too.

We have studied the distribution of black hole colours and charges as well.

The multiplicity (average number of emitted particles per black hole) in model 2 (for PDG Planck mass) is distributed as 4.5 quarks, 1 lepton, 1 gluon, 0.5 gauge boson W,Z, less than 0.1 for Higgs bosons, for photons and gravitons.

As we expect quarks/jets dominate, and charged antileptons are more abundant due to their positive charge.

Due to equipartition the average energy of emitted particles shows an opposite tendency to their multiplicity with parameters (e.g. black hole mass). Rotating models have higher energies and lower multiplicities.

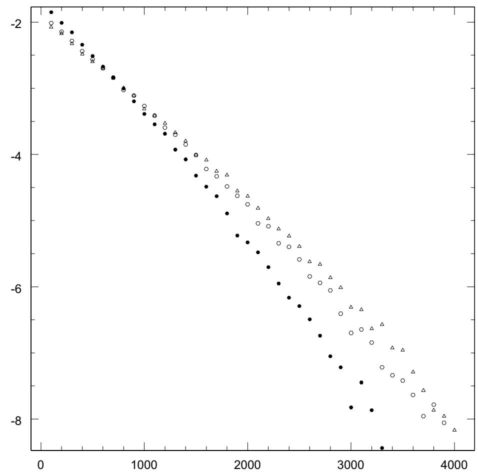

Figure 1: The distribution of black hole mass M [GeV] (per event) (vs. $M - M_{min}$) in models 1, 2, and 3 in BlackMax-II.

2.2 Pseudorapidity

We characterise the angular distribution by the pseudorapidity and compare various beyond standard models to the standard by the ratio of integrated pseudorapidity between [0.5, 1] and [0, 0.5]. Values for various extra-dimensional black holes differ from the QCD value.

The η ratios for quarks, anti-quarks, charged leptons, anti-leptons, electrons, muons, photons in all models are significantly lower than the asymptotic QCD value.

η is also used as angular cut for detector acceptance (< 2.5 for leptons, < 5 for jets, quarks, W,Z).

2.3 Electrons/positrons, muons/anti-muons, photons

We study electrons, muons and photons (anti-particles are included for the experiment).

The energy distributions of emitted particles show the expected spectrum shape.

The distribution of transverse momentum of leptons and antileptons can be used as they are easy to identify.

3 Transverse momentum

The distribution of transverse momentum is an important distribution to distinguish extra-dimensional and super-symmetric scenarios from the standard model. The standard model cuts off for low values of p_T and the mean value for single top quarks is 66 GeV. Our extra-dimensional models have values an order of magnitude larger.

The extra-dimensional models have even higher transverse momentum tails than super-symmetric/SUGRA models as in SUSY the missing particle, the neutralino does not interact strongly (no high-p_T tail). In the extra-dimensional models the higher the dimension and the number of split dimensions the higher p_T tail we get.

The distributions for electrons and muons are not significantly different.

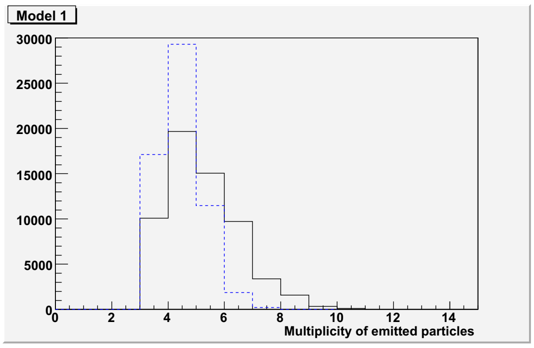

Figure 2: The relative distributions of multiplicity of emitted particles in model 1 (average number of particles per black hole) in BlackMax-II and Charybdis-I.

3.1 Standard and beyond standard models

Apart from the MET, SUSY models tend to give higher multiplicities than extra-dimensional (but not always, e.g. q$q_R \Longrightarrow q\chi_0$).

We calculate the standard model background by Pythia. We consider pp$\Longrightarrow q\bar{q}$, pp$\Longrightarrow t\bar{t}$ and plot the distribution of transverse momentum p_T of top quarks (t+$\bar{t}$) emitted in the standard model.

4 Graviton emission and MET

One can use the missing transverse energy MET (reconstructed from the energy deposits in the calorimeter and the reconstructed muon tracks) to distinguish amoung various gravity models. In addition to the neutrino emission the gravitons contribute to the missing energy.

BlackMax-I has graviton emission in the Hawking radiation phase and BlackMax-II has gravitons in the final burst too. Charybdis-I considers only neutrinos for MET as graviton emission is not included even for non-rotating black holes.

The MET from neutrinos is higher for extra-dimensional scenarios than for super-symmetry.

5 Comparison of BlackMax with Charybdis

The cross sections for BlackMax (I,II) and Charybdis-I are significantly different. In addition Yoshino – Rychkov suppression in BlackMax-II decreases the cross sections by several orders of magnitude.

For the varying cross sections we compare BlackMax-II with Charybdis-I by normalizing to the total number of black hole events (60000 for Dimopoulos Planck mass).

We find that the relative distributions of initial black hole mass are in remarkable agreement in BlackMax and Charybdis. That is because the mass loss mechanisme does not affect the initial mass distribution. We have found a universal (exponential) mass function for the three models as well.

In the following figures we show model 1 in BlackMax and Charybdis. Model 1 is also experimentally the most accessible as it has the lowest minimum black hole mass.

BlackMax gives higher multiplicities and correspondingly lower transverse momentum and energy than Charybdis. The MET is higher in BlackMax with gravitons.

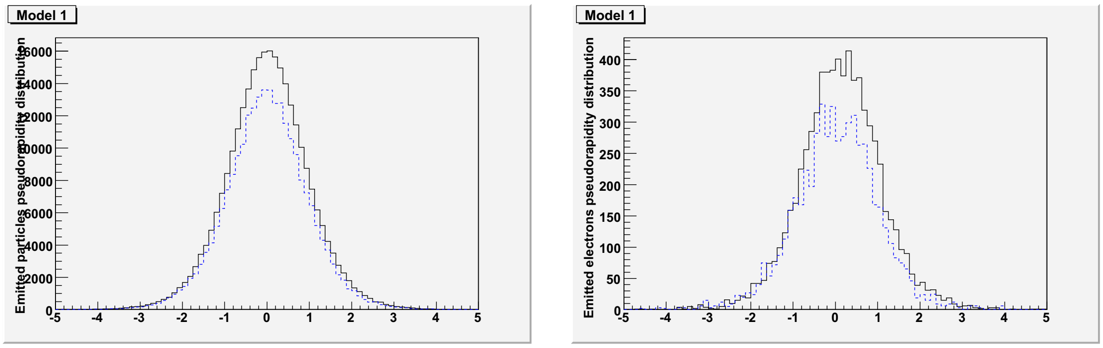

Figure 3: The relative distributions of pseudorapidity η of all particles (left) and electrons + positrons (right) emitted from black holes in model 1 in BlackMax and Charybdis (blue).

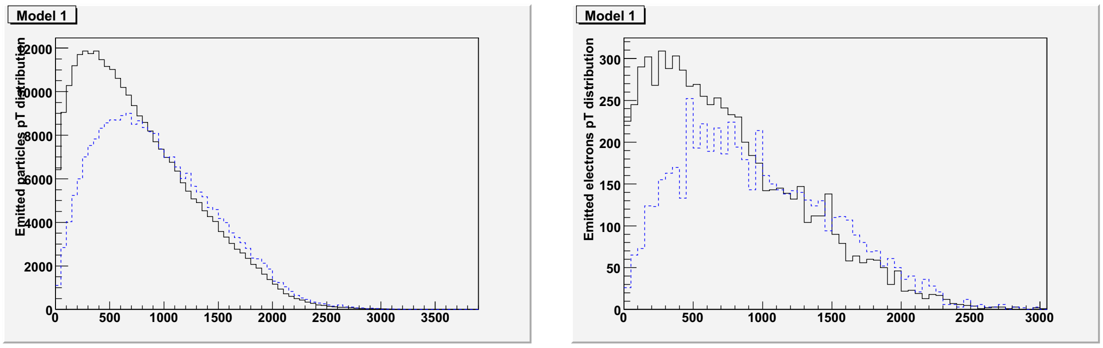

Figure 4: The relative distributions of transverse momentum p_T [GeV] of all particles (left) and electrons + positrons (right) emitted from black holes in model 1 in BlackMax and Charybdis.

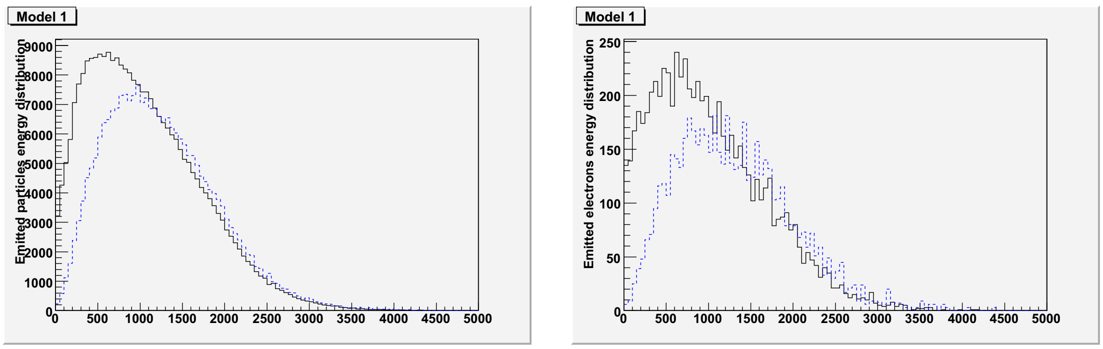

Figure 5: The relative distributions (spectrum) of energy E [GeV] of all particles (left) and electrons + positrons (right) emitted from black holes in model 1 in BlackMax and Charybdis.

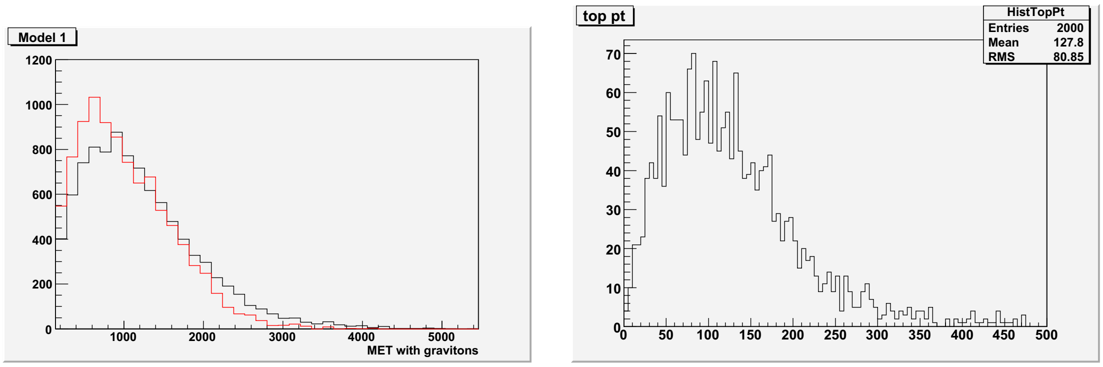

Figure 6: The relative distributions of missing transverse energy MET [GeV] including gravitons in model 1 in BlackMax and Charybdis (red)(left) and the distribution of transverse momentum p_T [GeV] of top quarks (t+$\bar{t}$) emitted in the standard model (right).

References

1. L.A. Anchordoqui, J.L. Feng, H. Goldberg, A.D. Shapere, PRD**65**,124027(2002)

2. N. Arkani-Hamed, S. Dimopoulos, G.R. Dvali, PLB**429**,263(1998)

3. N. Arkani-Hamed, M. Schmaltz, PRD**61**,033005(2000)

4. D. Youm, Phys. Rept.**316**,1(1999)

5. D. Dai, G. Starkman, D. Stojkovic, C. Issever, E. Rizvi, J. Tseng, PRD**77**,076007(2008)

6. C.M. Harris, P. Richardson, B.R. Webber, JHEP**0308**,033(2003)

WARM DARK MATTER, PHASE SPACE DENSITY AND THE LHC

A. KHMELNITSKY, D. GORBUNOV AND V. RUBAKOV
Institute for Nuclear Research of the Russian Academy of Sciences,
60th October Anniversary Prospect, 7a, 117312 Moscow, Russia

Some problems concerning small scale structure recently emerged in Cold Dark Matter scenario: missing satellites problem, cusped density profiles and lack of galactic angular momentum. All these problems seem to have solution in scenarios with Warm Dark Matter. We make use of the phase space density approach to discuss keV gravitino as a warm dark matter candidate. Barring the fine tuning between reheat temperature in the Universe and superpaticle masses, we find that warm gravitinos have both appropriate total mass density and suitable primordial phase space density at low momentum provided that their mass is in the range 1 keV $\lesssim m \lesssim$ 15 keV, reheat temperature in the Universe is low, $T_R \lesssim$ 10 TeV, and masses of some of the superpartners are sufficiently small, $M \lesssim$ 350 GeV. The latter property implies that the gravitino warm dark matter scenario will be either ruled out or supported by the LHC experiments.

1 Motivation and Recipe

The predictions of the ΛCDM model are in outstanding consistency with the bulk of cosmological observations (see Ref. [1] and references therein). Yet there are clouds above the collisionless cold dark matter scenario, which have to do with cosmic structure at subgalactic scales. Three most notable of them are missing satellites, cuspy galactic density profiles and too low angular momenta of spiral galaxies. All these suggest that CDM may be too cold, i.e. that the vanishing primordial velocity dispersion of dark matter particles may be problematic. Hence, one is naturally lead to consider warm dark matter (WDM) scenarios [2]. In this work we present the ways to quantify the notion of Warm Dark Matter and consider the particular WDM candidate — light gravitino[a].

There are several ways to describe the difference between WDM and CDM scenarios. The simplest one is to say that warm dark matter particles have larger free streaming length l_{fs}. Density fluctuations on scales smaller than l_{fs} do not grow. Thus free streaming length on the moment of matter-radiation equality (since this time density fluctuations begin to grow rapidly) defines the scale of the smallest objects formed in WDM cosmology. For non-interacting particles it is possible to estimate $l_{fs}(t_{eq})$ as

$$l_{fs}(t_{eq}) \sim v \cdot t_{eq} = \frac{p}{T}\frac{T_{eq}t_{eq}}{m},$$

with v, p, m being typical velocity and momentum and the mass of dark matter particles correspondingly. For thermal-like distribution $p/T \sim 3$, and present size of suppression scale is given

[a] The talk is largely based on papers [3], where one can find additional details and references.

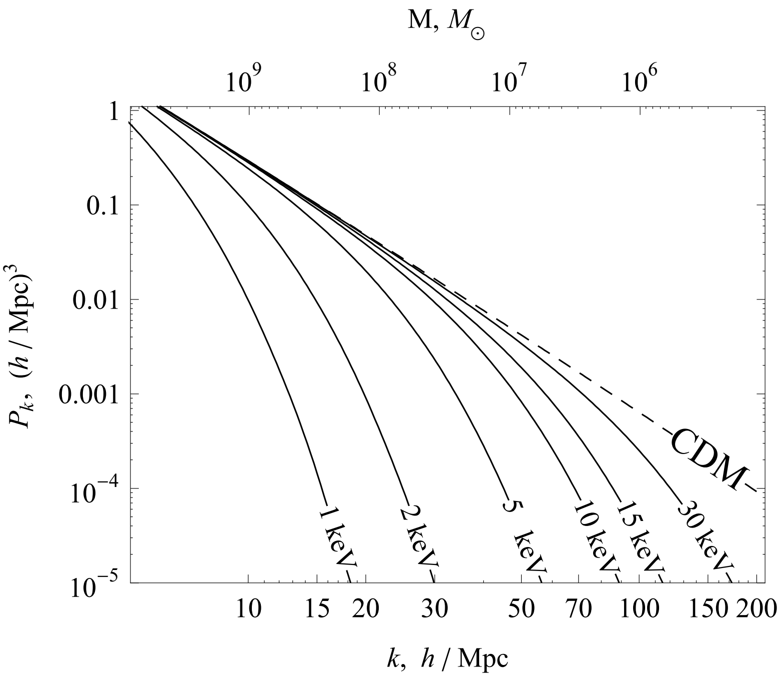

Figure 1: Linear matter power spectrum for standard ΛCDM cosmology (dashed line) and ΛWDM (solid lines) assuming the normalized Fermi–Dirac distribution of WDM particles with masses $m = 1, 5, 10, 15, 20$ and 30 keV and $g_* = g_{\mathrm{MSSM}}$.

by

$$l_0 \sim 200 \text{ kpc} \frac{1 \text{ kev}}{m}.$$

Perturbations on this scale correspond to the objects with mass

$$M \simeq \rho_{DM} \cdot \frac{4\pi}{3} l_0^3 \sim 10^9 M_\odot \left(\frac{1 \text{ keV}}{m}\right)^3.$$

The scale of missing satellites is believed to be of order $10^7 - 10^8 M_\odot$ [4], which suggest that m should be in the keV range.

To be more precise one can calculate the linear power spectrum of density perturbations by solving numerically the Boltzmann evolution equations. Warm particles filter primordial power spectrum on small scales, and thus the formation of small halos is suppressed. The filtering scale must be small enough, since the power spectrum shows no significant deviations from the CDM prediction on scales within reach of current observations. This leads to constraints on the primordial velocity dispersion of WDM particles(cf. [5] and references therein). On the other hand, in order to improve on structure formation, the filtering scale must be of the order of the scale of missing satellites.

We have calculated linear matter power spectrum in ΛWDM cosmology assuming that dark matter particles have the Fermi–Dirac primordial distribution function, normalized to correct present total density. To this end we have modified the Boltzmann evolution equations implemented in the Code for Anisotropies in the Microwave Background (CAMB) [6]. Figure 1 presents the resulting ΛWDM power spectrum for $m = 1, 2, 5, 10, 15$ and 30 keV (solid) in comparison with ΛCDM (dashed). One concludes that the power spectrum is suppressed by about an order of magnitude on the scales corresponding to $10^8 M_\odot$ and smaller provided the WDM particle mass is about $10 - 15$ keV. Of course, this is an indicative figure.

Alternative way to quantify the notion of warm dark matter is to make use of the phase space density approach [7]. Its key ingredient is the ratio between the mass density and the cube of the one-dimensional velocity dispersion in a given volume, $Q \equiv \rho/\sigma^3$. On the one hand, this quantity is measurable in galactic halos; on the other hand, it can be used as an estimator for coarse-grained distribution function of halo particles. Namely, for non-relativistic dark matter particles

$$Q \simeq m^4 \cdot \frac{n}{\langle \frac{1}{3} p^2 \rangle^{3/2}} ,$$

where m is the mass of these particles and n is their average number density in a halo. Assuming that the coarse-grained distribution of halo particles is isotropic, $f_{halo}(\mathbf{p}, \mathbf{r}) = f_{halo}(p, r)$, one estimates

$$\frac{n}{\langle p^2 \rangle^{3/2}} = \frac{\left[\int f_{halo}(\mathbf{p}, \mathbf{r}) d^3\mathbf{p}\right]^{5/2}}{\left[\int f_{halo}(\mathbf{p}, \mathbf{r}) \mathbf{p}^2 d^3\mathbf{p}\right]^{3/2}} \sim f_{halo}(p_*, r) ,$$

where p_* is a typical momentum of the dark matter particles. In this way the magnitude of the coarse-grained distribution function in galactic halos is estimated as

$$f_{halo} \simeq \frac{Q}{3^{3/2}\, m^4} . \tag{1}$$

Coarse-grained distribution function is known to decrease during violent relaxation in collisionless systems [8]. Hence, the primordial phase space density of dark matter particles cannot be lower than that observed in dark halos. This leads to the Tremaine–Gunn-like constraints on dark matter models [7]. The strongest among these constraints are obtained by making use of the highest phase space densities observed in dark halos, namely those of dwarf spheroidal galaxies (dSph) [4,7]. dSph's are the most dark matter dominated compact objects, and seem to be hosted by the smallest halos containing dark matter [4]. In recently discovered objects Coma Berenices, Leo IV and Canes Venaciti II, the value of Q ranges from $5 \cdot 10^{-3}\, \frac{M_\odot/\mathrm{pc}^3}{(\mathrm{km/s})^3}$ to $2 \cdot 10^{-2}\, \frac{M_\odot/\mathrm{pc}^3}{(\mathrm{km/s})^3}$ [9]. In what follows we use the first, more conservative value,

$$Q = 5 \cdot 10^{-3}\, \frac{M_\odot/\mathrm{pc}^3}{(\mathrm{km/s})^3} . \tag{2}$$

By requiring that the primordial distribution function exceeds the coarse-grained one, $f > f_{halo}$, one arrives at the constraint

$$3^{3/2} m^4 f > Q . \tag{3}$$

This constraint gives rise to a reasonably well defined lower bound on m in a given model.

If the primordial distribution is such that (3) is barely satisfied, the formation of high-Q objects like dSph's is suppressed. In fact, it may be suppressed even for larger f, since the coarse-grained distribution function may decrease considerably during the evolution. The parameter

$$\Delta \equiv \frac{3^{3/2} m^4 f}{Q}$$

shows how strongly the coarse-grained distribution function f must be diluted due to relaxation processes in order that the formation of dense compact dark matter halos be suppressed. It is known from simulations that the phase space density decreases during the structure formation. In particular, during the nonlinear stage it decreases by a factor of 10^2 to 10^3 [10], or possibly higher. Hence, the primordial distribution function of WDM particles should be such that $\Delta \gtrsim 10^2 - 10^3$. At least naively, obtaining the dilution factor in a given model in the ballpark $\Delta = 1 - 10^3$ would indicate that the primordial phase space density is just right to make dwarf galaxies but not even more compact objects. Interestingly, we will find that Δ is indeed in this ballpark for WDM gravitinos.

2 Results

We make use of this phase space density criterion to examine light ($m \lesssim 15$ keV) gravitino as a warm dark matter candidate, assuming that R-parity is conserved and hence gravitino is stable. We find that gravitino mass should be in the range

$$1\,\mathrm{keV} \lesssim m_{\tilde{G}} \lesssim 15\,\mathrm{keV}\ .$$

In the early Universe, light gravitinos are produced in decays of superparticles and in scattering processes [12]. For so light gravitinos, their production in decays of superparticles plays an important role [13]. This process is most efficient at temperatures of the order of decaying particles mass. At lower temperatures number density of decaying particles is suppressed by Boltzmann factor and at higher temperatures expansion rate of the Universe is higher so the gravitino production rate is lower. Most notably, gravitinos serve as warm dark matter candidates only if other superparticles are rather light. We find that superparticles whose mass M is below the reheat temperature should obey

$$M \lesssim 350\ \mathrm{GeV}\ , \tag{4}$$

otherwise gravitinos are overproduced in their decays and in scattering and/or relic gravitinos are too cold. Barring fine tuning between the reheat temperature in the Universe and superparticle masses, this means that gravitino as warm dark matter candidate will soon be either ruled out or supported by the LHC experiments.

Gravitino production in scattering processes operates most efficiently at the highest possible temperatures in the early Universe, so the requirement that gravitinos are not overproduced restricts severely the reheat temperature T_R, cf. [13,14]; we find that T_R must be at most in the TeV range.

The bound (4) is to be compared to the experimental bounds on masses of gluino and quarks of the 1st and 2nd generations, $M_{\tilde{q},\tilde{g}} \geq 250 - 325$ GeV [1]. Given the narrow interval between these bounds, we find it disfavored that squarks and gluinos participate in gravitino production processes. Hence, we elaborate also on a scenario with relatively light colorless superparticles whose masses M obey (4), heavy squarks and gluinos, and reheat temperature in between,

$$M \lesssim T_R \ll M_{\tilde{q},\tilde{g}}\ . \tag{5}$$

In this scenario, squarks and gluinos do not play any role in gravitino production, while the important production processes are decays and collisions of sleptons, charginos and neutralinos. We find that in this case, the overall picture is consistent in rather wide range of parameters, with the reheat temperature extending up to 10 TeV.

We conclude that unlike in the WIMP case, gravitino WDM does not automatically have the present mass density in the right ballpark. If the heaviest superparticles are squarks and gluinos, and they were relativistic in the cosmic plasma (the first scenario), the allowed range of parameters is rather narrow. We consider least contrived the possibility that the masses of sleptons, charginos and neutralinos are in the range $M = 150-300$ GeV, the reheat temperature is $T_R = 200\ \mathrm{GeV} - 10$ TeV and the masses of gluinos and squarks are higher, $M_{\tilde{g},\tilde{q}} \gg T_R$ (second scenario). Then for masses $m_{\tilde{G}} = 1 - 15$ keV, gravitinos can indeed serve as warm dark matter particles. In any case, gravitino as warm dark matter candidate will be either ruled out or supported by the LHC experiments.

Acknowledgments

AKh gratefully acknowledges the conference organizers for support and hospitality. We are indebted to F. Bezrukov, A. Boyarsky, S. Demidov, V. Lukash, O. Ruchayskiy, M. Shaposhnikov and I. Tkachev for the interest to this work and useful discussions. This work was supported in part by the grant of the President of the Russian Federation NS-1616.2008.2, by the RFBR grant 08-02-00473-a and by the Russian Science Support Foundation (DG).

References

1. C. Amsler *et al.* [Particle Data Group], Phys. Lett. B **667** (2008) 1.
2. P. Bode, J. P. Ostriker and N. Turok, Astrophys. J. **556** (2001) 93 [arXiv:astro-ph/0010389]; V. Avila-Reese, P. Colin, O. Valenzuela, E. D'Onghia and C. Firmani, Astrophys. J. **559** (2001) 516 [arXiv:astro-ph/0010525].
3. D. Gorbunov, A. Khmelnitsky and V. Rubakov, JCAP **0810** (2008) 041 [arXiv:0808.3910 [hep-ph]]; D. Gorbunov, A. Khmelnitsky and V. Rubakov, JHEP **0812** (2008) 055 [arXiv:0805.2836 [hep-ph]].
4. M. Mateo, Ann. Rev. Astron. Astrophys. **36** (1998) 435 [arXiv:astro-ph/9810070].
5. A. Boyarsky, J. Lesgourgues, O. Ruchayskiy and M. Viel, dark matter models," arXiv:0812.0010 [astro-ph].
6. A. Lewis, A. Challinor and A. Lasenby, Astrophys. J. **538** (2000) 473 [arXiv:astro-ph/9911177], URL `http://camb.info`.
7. C. J. Hogan and J. J. Dalcanton, Phys. Rev. D **62** (2000) 063511 [arXiv:astro-ph/0002330]; J. J. Dalcanton and C. J. Hogan, Astrophys. J. **561** (2001) 35 [arXiv:astro-ph/0004381]; D. Boyanovsky, H. J. de Vega and N. Sanchez, Phys. Rev. D **77** (2008) 043518 [arXiv:0710.5180 [astro-ph]].
8. D. Lynden-Bell, Mon. Not. Roy. Astron. Soc. **136** (1967) 101; S. Tremaine, M. Henon and D. Lynden-Bell, Mon. Not. Roy. Astron. Soc. **219** (1986) 285; P. H. Chavanis, "Statistical mechanics of violent relaxation in stellar systems," [arXiv:astro-ph/0212205].
9. J. D. Simon and M. Geha, Astrophys. J. **670** (2007) 313-331 [arXiv:0706.0516 [astro-ph]].
10. S. Peirani, F. Durier and J. A. De Freitas Pacheco, Mon. Not. Roy. Astron. Soc. **367** (2006) 1011 [arXiv:astro-ph/0512482]; S. Peirani and J. A. de Freitas Pacheco, [arXiv:astro-ph/0701292].
11. J. Madsen, Phys. Rev. D **44** (1991) 999; J. Madsen, Phys. Rev. D **64** (2001) 027301 [arXiv:astro-ph/0006074].
12. V. S. Rychkov and A. Strumia, Phys. Rev. D **75** (2007) 075011 [arXiv:hep-ph/0701104].
13. T. Moroi, H. Murayama and M. Yamaguchi, Phys. Lett. B **303** (1993) 289.
14. J. Pradler and F. D. Steffen, Phys. Lett. B **648** (2007) 224 [arXiv:hep-ph/0612291].

PHASES OF ADS BLACK STRINGS

Térence Delsate
Theoretical and Mathematical Physics Department,
Université de Mons-Hainaut, 20, Place du Parc
7000 Mons, Belgium
terence.delsate@umh.ac.be

We review the recent developements in the stability problem and phase diagram for asymptotically locally AdS black strings. First, we quickly review the case of locally flat black string before turning to the case of locally AdS spacetimes.

1 Introduction

This decade has witnessed a growing interest for solutions of general relativity in AdS spaces. This is due to the celebrated AdS/CFT correspondance conjecture[1], relating solutions of general relativity in asymptotically AdS spaces to conformal field theories defined on the conformal boundary of the AdS space. In this context, black hole solutions play an important role[2].

In more than four dimensional spacetime, the uniqueness theorem on black holes, garantying that the horizon topology of a black object is always S^2 is no longer true. Various black objects have been constructed in higher dimensions, such as black strings with horizon topology $S^{d-3}\times S^1$ in contrast with black holes with horizon topology S^{d-2}.

On the other hand, in 1993, R. Gregory and R. Laflamme have shown that black strings and branes are unstable towards long wavelength perturbations[3]. The Gregory-Laflamme instability was originally discovered in the framework of asymptotically locally flat spacetimes but it is believed to be a generic feature of black extended objects. In particular, it will be argued that this instability persists in asymptotically locally AdS spacetimes, where a black string solution has been found recently by R. Mann, E. Radu and C. Stelea[4].

This proceeding is organised as follows: we review the black string instability and phase diagram in asymptotically locally flat spacetimes in section 2 before turning to asumptotically locally AdS spacetimes in section 3.

2 Asymptotically locally flat space

Thoughout this section, we consider the d-dimensional Einstein-Hilbert action

$$S = \frac{1}{16\pi G}\int_{\mathcal{M}} \sqrt{-g}Rd^dx + \frac{1}{8\pi G}\int_{\partial\mathcal{M}} \sqrt{-h}Kd^{d-1}x, \tag{1}$$

where G is the d-dimensional Newton constant which we set to one, $\mathcal{M}$ is the spacetime manifold, g is the determinent of the metric, R is the scalar curvature and K is the extrinsic curvature of the boundary manifold $\partial\mathcal{M}$. The equation of motion resulting form the variation of the Einstein-Hilbert action is given by

$$R_{MN} = 0,\ \ M, N = 0, \ldots, d-1, \tag{2}$$

where R_{MN} is the Ricci tensor.

The black string solution to equation (2) is given by

$$ds^2 = -\left(1 - \left(\frac{r_0}{r}\right)^{d-4}\right) dt^2 + \frac{dr^2}{\left(1 - \left(\frac{r_0}{r}\right)^{d-4}\right)} + r^2 d\Omega_{d-3}^2 + dz^2,\ \ z \in [0, L], \tag{3}$$

where L is the length of the coordinate z, r_0 is the horizon radius and $d\Omega_{d-3}$ is the line element of the unit $(d-3)$-sphere.

The black string (3) is characterised by thermodynamical quantities, namely the mass M, associated to the time translation, the tension $\mathcal{T}$, associated with z-translation invariance, the temperature T_H, which can be obtained by demanding regularity at the horizon in the euclidean section, the entropy S, defined as one quarter of the horizon area and the length in the extradimension L.

These thermodynamical quantities can be used to define a thermodynamical phase diagram in temperature-entropy coordinates $(T_H, S/L)$ or in a mass-tension diagram (μ, n), with the dimensionless quantities $\mu = M/L^{d-3}, n = \mathcal{T}L/M$[5].

The uniform black string solution is subject to a dynamical instability which manifests itself already at the linearised level[3]. The equations for the perturbations admit unstable solutions with small wavenumber k in the extradirection as well as stable solutions with a large wavenumber. The wavelengths of the various modes are given by $\lambda = 2\pi/k$. There is a static solution between these two regimes for $k = k_c$, where k_c is called the critical wavenumber.

This dynamical instability is related to the thermodynamical stability of the black string: long black strings are unstable while short black strings are stable We refer the reader to the original paper[3] for more details.

Initially, it was widely believed that the unstable black string should decay to an array of localised black holes but it has been shown that this decay would take an infinite proper time at the horizon[6]. This suggested the existance of another phase, the non uniform black string. Non uniform black strings were first constructed in a perturbative way then by solving numerically the full system of non-linear partial differential equations[7]. All these three phases, the black string, non uniform black string and the localised black hole are static solution; these static solutions should be the equilibrium configurations since they don't evolve by definition.

A possible way to have an idea of the endpoint of the black string instability consists in comparing the thermodynamical properties of the three phases in a phase diagram[5].

3 Asymptotically AdS space

In this section, we present the recent results obtained in the stability problem for black strings in AdS spacetime. We consider the d-dimensional Einstein-Hilbet action with a negative cosmological constant,

$$S = \frac{1}{16\pi G}\int_{\mathcal{M}} \sqrt{-g}\left(R + \frac{(d-1)(d-2)}{\ell^2}\right) d^d x + \frac{1}{8\pi G}\int_{\partial\mathcal{M}} \sqrt{-h} K d^{d-1} x, \tag{4}$$

with the same convention as in the previous section and where ℓ is the AdS radius, related to the cosmological constant Λ by $\Lambda = -(d-1)(d-2)/2\ell^2$.

The uniform black string solution is obtained by using the spherically symmetric ansatz

$$ds^2 = -b(r)dt^2 + \frac{dr^2}{f(r)} + r^2 d\Omega^2_{d-3} + a(r)dz^2 \qquad (5)$$

and solving numerically the equations of motion resulting from the variation of (4)[4]. The asymptotic behaviour of the metric fields is given by $a, b, f \approx r^2/\ell^2$ at the leading order.

The thermodynamical quantities characterising the solution (5) are the same as in the asymptotically locally flat case, but have to be computed in a regularised version of the action which diverges because of the AdS asymptotic. The regularised action is obtained by adding appropriate boundary counterterms[8].

However, there is a new lengthscale in the theory, namely the AdS radius which affects the thermodynamical properties of the black string. In particular, it allows a new phase of thermodynamically stable black string, namely big AdS black strings, characterised by a large horizon radius r_0 - AdS length ratio. Small AdS black strings, with $r_0/\ell << 1$, are thermodynamically unstable.

We investigated the existance of a Gregory-Laflamme instability by considering non uniform black strings within the ansatz

$$ds^2 = -b(r)e^{2A(r,z)} + e^{2B(r,z)}\left(\frac{dr^2}{f(r)} + a(r)dz^2\right) + e^{2C(r,z)}d\Omega^2_{d-3}, \; z \in [0, L], \qquad (6)$$

where a, b, f is the solution of Mann, Radu and Stelea and A, B, C are smooth functions of r and z. In the perturbative approach, we develop the non uniformity in a Fourier series of the variable z and in term of a small parameter ϵ according to $X(r,z) = \epsilon X_1(r)\cos(kz) + \epsilon^2(X_0(r) + X_2(r)\cos(2kz)) + \mathcal{O}(\epsilon)^2$, X generically denoting A, B, C. Then we solve at each order in ϵ the corresponding equations of motion. Order ϵ^0 is just the uniform solution while order ϵ gives access to the linear stability problem. The modes X_1 correspond to the static perturbation in the Gregory-Laflamme picture. The equations for these modes form an eigenvalue problem, where the eigenvalue is the square of the Gregory-Laflamme critical wavenumber. If the eigenvalue is real, there exists a Gregory-Laflamme instability, if it is imaginary, the solution is always stable[9]. It turns out that small AdS thermodynamically unstable black strings are dynamically unstable while big AdS thermodynamically stable black strings are dynamically stable, confirming the Gubser-Mitra conjecture[11] in this case.

The order ϵ^2 contains two independant modes: the backreactions, X_0 and massive modes X_2. Thermodynamical corrections for the non uniform phase arise at this order where only the backreactions contribute[10]. We investigated the non uniform solutions emanating from the unstable modes at the order ϵ^2 for small AdS black strings. The new lengthscale provided by ℓ implies a new dimensionless quantity, $\mu_2 = L/\ell$ characterising the non uniform solutions. It turns out that for small value of μ_2, the picture is essentially similiar to the case of asymptotically locally flat spacetimes while for large μ_2 enough, the small AdS phase becomes thermodynamically stable. In other words, the length L plays an important role in the thermodynamical stability of non uniform black strings, just like r_0 does for uniform black strings; small ($r_0/\ell << 1$) and short ($L/\ell << 1$) AdS non uniform black string are thus thermodynamically unstable while small and long ($L/\ell \approx 1$) non uniform black strings are thermodynamically stable[10].

The first results in the nonperturbative approach (the full non linear system of partial differential equations) confirms the perturbative approach and provides numerical evidences for the existence of the non uniform black string phase.

4 Acknowledgement

I would like to thank the organisers of the Rencontres de Moriond 2009 - La Thuile for giving me the opportunity of presenting this talk and for the good time in the conference. I also would like to thank Yves Brihaye, Eugen Radu and Georges Kohnen for usefull discussions and advices.

1. J. M. Maldacena, Adv. Theor. Math. Phys. 2 (1998) 231 [Int. J. Theor. Phys. 38 (1999) 1113], hep-th/9711200; E. Witten, Adv. Theor. Math. Phys. 2 (1998) 253, hep-th/9802150.
2. S. W. Hawking and D. N. Page, Commun. Math. Phys. 87 (1983) 577.; E. Witten, Adv. Theor. Math. Phys. 2 (1998) 505, arXiv:hep-th/9803131.
3. R. Gregory and R. Laflamme, Phys. Rev. Lett. 70 (1993) 2837, hep-th/9301052.
4. R. Mann, E. Radu and C. Stelea, JHEP 09 (2006) 073, hep-th/0604205.
5. T. Harmark, N. A. Obers, Nucl. Phys. B 684 (2004) 183-208, hep-th/0309230.
6. G. T. Horowitz and K. Maeda, Phys. Rev. Lett. 87 (2001) 131301, hep-th/0105111.
7. S. Gubser, Class. Quant. Grav. 19 (2002) 4825-4844, hep-th/0110193; T. Wiseman, Class. Quant. Grav. 20 (2003) 1137, hep-th/0209051.
8. V. Balasubramanian and P. Kraus, Commun. Math. Phys. 208 (1999) 413, hep-th/9902121.
9. Y. Brihaye, T. Delsate and E. Radu, Phys. Lett. B662 (2008) 264-269, hep-th/00710.4034.
10. T. Delsate, Phys. Lett. B663 (2008) 118-124; T. Delsate, in preparation.
11. S. S. Gubser, I. Mitra, JHEP 08 (2001) 018, hep-th/0011127.

Solution to the Kadanoff-Baym equations for
Scalar Fields in a Thermal Bath

A. Anisimov

Deutsches Elektronen-Synchrotron DESY, Hamburg, Germany

We study the approach to equilibrium for a scalar field which is coupled to a large thermal bath. Our analysis of the initial value problem is based on Kadanoff-Baym equations which are shown to be equivalent to a stochastic Langevin equation. The interaction with the thermal bath generates a temperature-dependent spectral density, either through decay and inverse decay processes or via Landau damping. In equilibrium, energy density and pressure are determined by the Bose-Einstein distribution function evaluated at a complex quasi-particle pole. The time evolution of the statistical propagator is compared with solutions of the Boltzmann equations for particles as well as quasi-particles. The dependence on initial conditions and the range of validity of the Boltzmann approximation are determined.

The current standard model of cosmology explains many features of our universe as the result of out-of-equilibrium processes during its very early high-temperature phase (cf. [1,2]). This includes the matter-antimatter asymmetry, i.e. the origin of matter, the production of dark matter, the formation of light elements and the decoupling of photons leading to the cosmic microwave background.

Many nonequilibrium processes in the early universe can be treated in the canonical way by means of Boltzmann equations (cf.[1]) with sufficient accuracy. In some cases, however, quantum effects play a crucial role. This applies in particular to baryogenesis, the generation of the matter-antimatter asymmetry. Here the CP asymmetry, which leads to the baryon asymmetry, is the result of a quantum interference. It is therefore important to go beyond the classical Boltzmann equations and to treat the entire baryogenesis process quantum mechanically.

The treatment of nonequilibrium processes in quantum field theory is usually based either on Kadanoff-Baym equations and the Schwinger-Keldysh formalism [3,4,5] or on stochastic Langevin equations [6,7,8]. Boltzmann equations are first-order differential equations for number densities, which are local in time. They represent a valuable approximation for nonequilibrium processes in a dilute, weakly coupled gas. However, when the interactions between the quanta of the thermal plasma are strong, which is certainly the case in the presence of non-Abelian gauge interactions, the validity of the Boltzmann approximation is questionable. Correspondingly, the notion of number density becomes ambiguous, although several useful definitions have been suggested [8].

In this paper we study the approach to equilibrium for a scalar field which is coupled to a thermal bath with many degrees of freedom such that backreaction effects can be neglected. We shall focus on the description of this nonequilibrium process in terms of Green's functions rather than number densities.

Knowing the exact solution of the initial value problem for the Green's function of the scalar field, we can systematically study the conditions for the validity of ordinary Boltzmann equations as well as Boltzmann equations for quasi-particles. At large times the scalar field reaches equilibrium. As we shall see, this state does not correspond to a gas of quasi-particles. There is an additional thermal 'vacuum' contribution which in principle can even lead to a negative pressure of low-momentum modes. The general solution of the Green's function also allows us to study the dependence of the equilibration on the initial conditions.

The letter is organized as follows. In Section 2 we quote the known nonequilibrium solutions of the Kadanoff-Baym equations. Then thermal equilibrium and the quasi-particle picture are discussed in Section 3. A brief summary and outlook is given in Section 4.

In what follows we will qoute the solution to KB equations for the scalar Φ linearly coupled to some strongly interacting thermal bath.

The *spectral functinon* wqhich we denote as Δ^- can be found as

$$\Delta^-_{\mathbf{q}}(y) = i\int_{-\infty}^{\infty} \frac{d\omega}{2\pi} e^{-i\omega y} \rho_{\mathbf{q}}(\omega) \ , \tag{2.1}$$

where the spectral function $\rho_{\mathbf{q}}(\omega)$ is given in terms of real and imaginary part of the self-energy $\Pi^R_{\mathbf{q}}(\omega)$,

$$\rho_{\mathbf{q}}(\omega) = \frac{-2\mathrm{Im}\Pi^R_{\mathbf{q}}(\omega) + 2\omega\epsilon}{[\omega^2 - \omega^2_{\mathbf{q}} - \mathrm{Re}\Pi^R_{\mathbf{q}}(\omega)]^2 + [\mathrm{Im}\Pi^R_{\mathbf{q}}(\omega) + \omega\epsilon]^2} = i\tilde{\Delta}^-_{\mathbf{q}}(i\omega) \ . \tag{2.2}$$

The spectral function describes a quasi-particle resonance at finite temperature with energy $\Omega_{\mathbf{q}}$,

$$\Omega^2_{\mathbf{q}} - \omega^2_{\mathbf{q}} - \mathrm{Re}\Pi^R_{\mathbf{q}}(\Omega_{\mathbf{q}}) = 0, \quad \Omega^2_{\mathbf{q}}|_{T=0} = \omega^2_{\mathbf{q}} \ , \tag{2.3}$$

and decay width

$$\Gamma_{\mathbf{q}} \simeq -\frac{1}{\Omega_{\mathbf{q}}} \mathrm{Im}\Pi^R_{\mathbf{q}}(\Omega_{\mathbf{q}}) \ . \tag{2.4}$$

For simplicity, we have neglected the effect of $\mathrm{Im}\Pi^R_{\mathbf{q}}$ on the quasi-particle energy.

The solution for the *statistical propagator* the equation for which is given by

$$(\partial^2_{t_1} + \omega^2_{\mathbf{q}})\Delta^+_{\mathbf{q}}(t_1, t_2) + \int_0^{t_1} dt' \Pi^-_{\mathbf{q}}(t_1 - t')\Delta^+_{\mathbf{q}}(t', t_2) = \zeta(t_1, t_2) \ , \tag{2.5}$$

with

$$\zeta(t_1, t_2) = \int_0^{t_2} dt' \Pi^+_{\mathbf{q}}(t_1 - t')\Delta^-_{\mathbf{q}}(t' - t_2) \ . \tag{2.6}$$

can be found as

$$\begin{aligned}
\Delta^+_{\mathbf{q}}(t_1, t_2) &= \Delta^+_{\mathbf{q},}\dot{\Delta}^-_{\mathbf{q}}(t_1)\dot{\Delta}^-_{\mathbf{q}}(t_2) + \ddot{\Delta}^+_{\mathbf{q},}\Delta^-_{\mathbf{q}}(t_1)\Delta^-_{\mathbf{q}}(t_2) \\
&+ \dot{\Delta}^+_{\mathbf{q};}\left(\dot{\Delta}^-_{\mathbf{q}}(t_1)\Delta^-_{\mathbf{q}}(t_2) + \Delta^-_{\mathbf{q}}(t_1)\dot{\Delta}^-_{\mathbf{q}}(t_2)\right) \\
&+ \Delta^+_{\mathbf{q},}(t_1, t_2) \ ,
\end{aligned} \tag{2.7}$$

where

$$\Delta^+_{\mathbf{q},}(t_1, t_2) = \int_0^{t_1} dt' \int_0^{t_2} dt'' \Delta^-_{\mathbf{q}}(t_1 - t')\Pi^+_{\mathbf{q}}(t' - t'')\Delta^-_{\mathbf{q}}(t'' - t_2) \ . \tag{2.8}$$

This contribution to the statistical propagator, which is independent of the initial conditions, is often referred to as *memory integral.* It can be expressed in the form

$$\Delta^+_{\mathbf{q},}(t_1, t_2) = -\int_{-\infty}^{\infty} \frac{d\omega}{2\pi} e^{-i\omega(t_1 - t_2)} \mathcal{H}^*_{\mathbf{q}}(t_1, \omega)\mathcal{H}_{\mathbf{q}}(t_2, \omega)\Pi^+_{\mathbf{q}}(\omega) \ , \tag{2.9}$$

where [8]

$$\mathcal{H}_{\mathbf{q}}(t, \omega) = \int_0^t d\tau e^{-i\omega\tau} \Delta^-_{\mathbf{q}}(\tau) \ . \tag{2.10}$$

The expression (2.9) will be the basis of our numerical analysis in Section 7.

Let us now verify that the solution (2.7) for the statistical propagator approaches thermal equilibrium at late times. This means that the quantity

$$\Delta^+_{\mathbf{q}}(t, \omega) = \int_{-2t}^{2t} dy e^{i\omega y} \Delta^+_{\mathbf{q}}\left(t + \frac{y}{2}, t - \frac{y}{2}\right) \ , \tag{3.1}$$

which becomes a Fourier transform for $t \to \infty$, satisfies the KMS condition asymptotically,

$$\Delta^+_{\mathbf{q}}(\infty,\omega) = -\frac{i}{2}\coth\left(\frac{\beta\omega}{2}\right)\Delta^-_{\mathbf{q}}(\omega) \ . \tag{3.2}$$

For late times only the memory integral is relevant, since $\Delta^-_{\mathbf{q}}(t)$ and $\dot{\Delta}^-_{\mathbf{q}}(t)$ fall off exponentially for $t \gg 1/\Gamma$. One then obtains

$$\Delta^+_{\mathbf{q}}(\infty,\omega) = \Delta^+_{\mathbf{q},}(\infty,\omega) = -|\mathcal{H}_{\mathbf{q}}(\infty,\omega)|^2\Pi^+_{\mathbf{q}}(\omega) \ . \tag{3.3}$$

The quantity $\mathcal{H}_{\mathbf{q}}(\infty,\omega)$ is the Laplace transform of the spectral function,

$$\begin{aligned}
\mathcal{H}_{\mathbf{q}}(\infty,\omega) &= \int_0^\infty d\tau e^{-i(\omega-i\epsilon)\tau}\Delta^-_{\mathbf{q}}(\tau) \\
&= \tilde{\Delta}^-_{\mathbf{q}}(i\omega+\epsilon) \\
&= \frac{1}{s^2+\omega_q^2+\tilde{\Pi}_{\mathbf{q}}(s)}\bigg|_{s=i\omega+\epsilon} \\
&= -\frac{1}{\omega^2-\omega_q^2-\mathrm{Re}\Pi^R_{\mathbf{q}}(\omega)-i\mathrm{Im}\Pi^R_{\mathbf{q}}(\omega)} \ ,
\end{aligned} \tag{3.4}$$

which yields

$$\begin{aligned}
|\mathcal{H}_{\mathbf{q}}(\infty,\omega)|^2 &= \frac{1}{(\omega^2-\omega_{\mathbf{q}}^2-\mathrm{Re}\Pi^R_{\mathbf{q}}(\omega))^2+(\mathrm{Im}\Pi^R_{\mathbf{q}}(\omega))^2} \\
&= -\frac{\rho_{\mathbf{q}}(\omega)}{2\,\mathrm{Im}\,\Pi^R_{\mathbf{q}}(\omega)} \ .
\end{aligned} \tag{3.5}$$

Inserting this expression into (3.3), using the KMS condition

$$\Pi^-_{\mathbf{q}}(\omega) = 2i\mathrm{Im}\Pi^R_{\mathbf{q}}(\omega) \ ,$$

one obtains (cf. (2.1),(2.2)),

$$\begin{aligned}
\Delta^+_{\mathbf{q}}(\infty,\omega) &= -\coth\left(\frac{\beta\omega}{2}\right)\frac{\mathrm{Im}\Pi^R_{\mathbf{q}}(\omega)}{(\omega^2-\omega_{\mathbf{q}}^2-\mathrm{Re}\Pi^R_{\mathbf{q}}(\omega))^2+(\mathrm{Im}\Pi^R_{\mathbf{q}}(\omega))^2} \\
&= -\frac{i}{2}\coth\left(\frac{\beta\omega}{2}\right)\Delta^-_{\mathbf{q}}(\omega) \ .
\end{aligned} \tag{3.6}$$

Hence, our solution for the statistical propagator indeed fulfills the KMS condition in the limit $t \to \infty$, which proves that the system reaches thermal equilibrium. It is instructive to evaluate the statistical propagator in thermal equilibrium at equal times, i.e., $y = t_1 - t_2 = 0$,

$$\Delta^+_{\mathbf{q}}\big|_{y=0} = \frac{1}{2}\int_{-\infty}^\infty \frac{d\omega}{2\pi}\coth\left(\frac{\beta\omega}{2}\right)\rho_{\mathbf{q}}(\omega) \ . \tag{3.7}$$

For a free field one has

$$\rho_{\mathbf{q}}(\omega) = 2\pi\mathrm{sign}(\omega)\delta(\omega^2-\omega_{\mathbf{q}}^2) \ , \tag{3.8}$$

which yields the well know result

$$\Delta^+_{\mathbf{q}}|_{y=0} = \frac{1}{\omega_{\mathbf{q}}}\left(\frac{1}{2}+n(\omega_{\mathbf{q}})\right) \ , \tag{3.9}$$

with the temperature dependent Bose-Einstein distribution function

$$n(\omega_{\mathbf{q}}) = \frac{1}{e^{\beta\omega_{\mathbf{q}}}-1} \ . \tag{3.10}$$

Generically, the interaction with the thermal bath changes the energy $\omega_{\mathbf{q}}$ of a free particle to a temperature dependent complex energy $\hat{\Omega}_{\mathbf{q}}$ which appears as a pole of the spectral function $\rho_{\mathbf{q}}(\omega)$ and the integrand of (3.7). The spectral function then has t For a specific example the approach to equilibrium will be studied numerically in Section 7. two poles in the upper plane, $\hat{\Omega}_{\mathbf{q}}$ and $-\hat{\Omega}^*_{\mathbf{q}}$, which are determined by the condition

$$\hat{\Omega}_{\mathbf{q}} - \left(\omega^2_{\mathbf{q}} + \Pi^R_{\mathbf{q}}\left(\hat{\Omega}_{\mathbf{q}}\right)\right)^{1/2} = 0 \ . \tag{3.11}$$

Assuming that the integral can be closed in the upper half-plane, one obtains for the statistical propagator in equilibrium,[a]

$$\Delta^+_{\mathbf{q}}|_{y=0} = \mathrm{Re}\left(\frac{1}{\hat{\Omega}_{\mathbf{q}}}\left(\frac{1}{2} + n(\hat{\Omega}_{\mathbf{q}})\right)\right) \ . \tag{3.12}$$

Compared to (3.8), the Bose-Einstein distribution function has been replaced by the complex distribution function $n(\hat{\Omega}_{\mathbf{q}})$.

At high temperatures, where $\beta\omega_{\mathbf{q}} \ll 1$, the Bose-Einstein distribution has a well-known infrared divergence,

$$n(\omega_{\mathbf{q}}) \simeq \frac{1}{\beta\omega_{\mathbf{q}}} \gg 1 \ . \tag{3.13}$$

For quasi-particles, where $\omega_{\mathbf{q}}$ is replaced by $\hat{\Omega}_{\mathbf{q}} = \Omega_{\mathbf{q}} + i\Gamma_{\mathbf{q}}/2$, this divergence is cut off by the finite width,

$$|n(\hat{\Omega}_{\mathbf{q}})| \simeq \frac{1}{|\beta(\Omega_{\mathbf{q}} + \frac{i}{2}\Gamma_{\mathbf{q}})|} \leq \frac{2}{\beta\Gamma_{\mathbf{q}}} \ , \tag{3.14}$$

which remains finite even if the real part $\Omega_{\mathbf{q}}$ vanishes.

Comparison of equations (3.9) and (3.12) suggests that in thermal equilibrium the Φ particles may form a gas of quasi-particles. This question can be clarified by evaluating energy density and pressure of the Φ particles. Since the expectation value of Φ vanishes, one obtains from the energy momentum tensor[b]

$$T_{\mu\nu} = \partial_\mu\Phi\partial_\nu\Phi - \eta_{\mu\nu}L \tag{3.15}$$

for the contribution of a mode with momentum $\mathbf{q}$ to energy density and pressure,

$$\epsilon_{\mathbf{q}} = \langle T_{00}\rangle|_{\mathbf{q}} = \frac{1}{2}\langle\dot{\Phi}^2 + (\vec{\nabla}\Phi)^2 + m^2\Phi^2\rangle|_{\mathbf{q}} \ , \tag{3.16}$$

$$p_{\mathbf{q}} = \langle T_{ii}\rangle|_{\mathbf{q}} = \langle\frac{1}{3}(\nabla\Phi)^2 + \frac{1}{2}(\dot{\Phi}^2 - (\nabla\Phi)^2 - m^2\Phi^2)\rangle|_{\mathbf{q}} \ . \tag{3.17}$$

This yields for the energy density

$$\begin{aligned}\epsilon_{\mathbf{q}}(\infty) &= \frac{1}{2}\left(\partial_{t_1}\partial_{t_2} + \omega^2_{\mathbf{q}}\right)\Delta^+_{\mathbf{q}}(t_1,t_2)\big|_{t_1=t_2=\infty} \\ &= \frac{1}{2}\left(\Omega^2_{\mathbf{q}} + \omega^2_{\mathbf{q}}\right)\frac{1}{\Omega_{\mathbf{q}}}\left(\frac{1}{2} + n(\Omega_{\mathbf{q}})\right) \ ,\end{aligned} \tag{3.18}$$

and for the pressure

$$\begin{aligned}p_{\mathbf{q}}(\infty) &= \left(\frac{1}{3}^2 + \frac{1}{2}\left(\partial_{t_1}\partial_{t_2} - \omega^2\right)\right)\Delta^+_{\mathbf{q}}(t_1,t_2)\big|_{t_1=t_2=\infty} \\ &= \left(\frac{1}{3}^2 + \frac{1}{2}\left(\Omega^2 - \omega^2\right)\right)\frac{1}{\Omega}\left(\frac{1}{2} + n(\Omega_{\mathbf{q}})\right) \ ,\end{aligned} \tag{3.19}$$

where, for simplicity, we have neglected the quasi-particle width.

In summary, the energy momentum tensor in thermal equilibrium can be expressed as sum of a quasi-particle gas contribution and a temperature dependent 'vacuum' term,

$$\langle T_{\mu\nu}\rangle|_{\mathbf{q}} = u_\mu u_\nu\left(\epsilon_{\mathbf{q}} + p_{\mathbf{q}}\right) - \eta_{\mu\nu}p_{\mathbf{q}} + \eta_{\mu\nu}\kappa_{\mathbf{q}} \ . \tag{3.20}$$

Here $u^\mu = (1, \vec{0})$ is the 4-velocity of the thermal bath, and

$$\epsilon_{\mathbf{q}} = \Omega_{\mathbf{q}}\left(\frac{1}{2} + n(\Omega_{\mathbf{q}})\right) \ , \tag{3.21}$$

$$p_{\mathbf{q}} = \frac{1}{3}\frac{^2}{\Omega_{\mathbf{q}}}\left(\frac{1}{2} + n(\Omega_{\mathbf{q}})\right) \ , \tag{3.22}$$

---

[a]Here we restrict ourselves to the case where there are no additional poles.

[b]We use the convention diag $(\eta_{\mu\nu}) = (1, -1, -1, -1)$.

$$\kappa_{\mathbf{q}} = \frac{\omega_{\mathbf{q}}^2 - \Omega_{\mathbf{q}}^2}{2\Omega_{\mathbf{q}}} \left(\frac{1}{2} + n(\Omega_{\mathbf{q}})\right) . \tag{3.23}$$

Energy density and pressure of the quasi-particle gas agree with the corresponding expressions for a free gas, with the energy $\omega_{\mathbf{q}}$ of a free particle replaced by the quasi-particle energy $\Omega_{\mathbf{q}}$. The 'vacuum contribution' $\kappa_{\mathbf{q}}$ vanishes for $\Omega_{\mathbf{q}} = \omega_{\mathbf{q}}$. For large thermal effects, i.e. $\Omega_{\mathbf{q}} \gg \omega_{\mathbf{q}}$ or $\Omega_{\mathbf{q}} \ll \omega_{\mathbf{q}}$, the equation of state differs significantly from the one of a free gas. Note that for $\Omega_{\mathbf{q}}^2 < \omega_{\mathbf{q}}^2$, the pressure can even become negative!

We have studied the approach to equilibrium for a real scalar field coupled to a large thermal bath. We have computed the exact two-point functions, the spectral function and the statistical propagator, for arbitrary initial conditions. This is possible for a thermal bath with many degrees of freedom such that the backreaction of the scalar field can be neglected.

The self-energy representing the thermal bath is time-translation invariant. We have shown that this is also the case for the spectral function, whereas the statistical propagator depends on two time coordinates, t_1 and t_2, and also the time t_i where the initial conditions are specified.

We have obtained the two-point functions by solving the Kadanoff-Baym equations. As expected, the relaxation time is determined by the imaginary part of the self-energy, i.e., a 'quasi-particle width' Γ. For $t > 1/\Gamma$, the statistical propagator becomes independent of the initial conditions. It is then given by a memory integral which depends on the real and imaginary part of the self-energy.

It is interesting to study the contribution of the thermalized scalar field to energy density and pressure. For a free field these observables are determined by the Bose-Einstein distribution function. Interaction with the thermal bath can significantly modify energy density and pressure, and therefore the equation of state. The Bose-Einstein distribution as function of the complex quasi-particle pole is now the relevant quantity. Energy density and pressure differ from the expressions for a free gas of quasi-particles by a temperature-dependent 'vacuum term' which can become important at high temperatures.

1. E. W. Kolb and M. S. Turner, *The Early Universe*, Addison-Wesley, New York, 1990.
2. V. Mukhanov, *Physical Foundations of Cosmology*, Cambridge University Press, Cambridge, 2005.
3. L. P. Kadanoff and G. Baym, *Quantum Statistical Mechanics*, Benjamin, New York, 1962.
4. J. Schwinger, J. Math. Phys. (1961) 407;
   P. M. Bakschi and K. T. Mahanthappa, J. Math. Phys. (1963) 1;
   P. M. Bakschi and K. T. Mahanthappa, J. Math. Phys. (1963) 12;
   L. V. Keldysh, Zh. Eksp. Teor. Fiz. (1964) 1515 [Sov. Phys. JETP (1965) 1018].
5. M. Le Bellac, *Thermal Field Theory*, Cambridge University Press, Cambridge, 1996.
6. J. Zinn-Justin, *Quantum field theory and critical phenomena*, Int. Ser. Monogr. Phys. (1993) 1.
7. J. Yokoyama, Phys. Rev. D (2004) 103511 [arXiv:hep-ph/0406072].
8. D. Boyanovsky, K. Davey and C. M. Ho, Phys. Rev. D (2005) 023523 [arXiv:hep-ph/0411042].
9. J. Berges, A. Rothkopf and J. Schmidt, Phys. Rev. Lett. (2008) 041603 [arXiv:0803.0131].
10. H. A. Weldon, Phys. Rev. D (1983) 2007.

5.
High Energy Neutrino Astronomy

STATUS AND RESULTS FROM THE ICECUBE NEUTRINO OBSERVATORY

GEORGES KOHNEN for the IceCube Collaboration[a]
Service de Physique des Particules Elémentaires
Université de Mons-Hainaut
20, place du parc
B-7000 Mons, Belgium

The IceCube neutrino observatory is currently under construction in the deep ice at the geographic South Pole, reaching 75% completion whilst already taking data. When completed in 2011, it will consist of nearly 5000 digital optical modules on more than 80 strings, capable of detecting the Cherenkov radiation from high-energy neutrino-induced charged leptons. The detection of astrophysical neutrinos can help identify the sources of the high energy cosmic rays since other messengers, such as photons or protons, are absorbed or deflected during propagation. The cubic-kilometer under-ice instrument, complemented by an extensive air-shower array, allows access to neutrino energies up to the PeV range, and to sensitivities below expected neutrino fluxes from some astrophysical sources if they accelerate hadrons. I will summarize current results of IceCube and its predecessor AMANDA, as well as the physics capabilities of the full observatory.

1 Introduction

The main goal of the IceCube neutrino observatory[1] is the search for high-energy extraterrestrial neutrinos, which may reveal the origin of cosmic rays and offer insight into the most energetic phenomena in the universe. Neutrinos have very small interaction cross sections, travelling astronomical distances freely. In addition, they cannot be deflected by intergalactic magnetic fields due to the absence of electric charge, and thus they point back to their origin (see figure 1 (a)).

The most interesting neutrino sources include Active Galactic Nuclei and Gamma-Ray Bursts (GRBs). According to our understanding, these very energetic astronomical phenomena can produce mesons when the ejected particle beams interact with matter and photons near the sources. Very high energy neutrinos are then produced through decays such as $\pi^{\pm} \rightarrow \mu^{\pm}\nu_{\mu}$ and, subsequently, $\mu^{\pm} \rightarrow e^{\pm}\nu_{\mu}\nu_{e}$.

I will first present the IceCube observatory, its design and current status, as well as the detection principle. Then, I will review several recent physics results and ongoing searches, and conclude with a description of our future plans.

2 The IceCube Neutrino Observatory

IceCube was planned and designed following the success of its predecessor AMANDA (Antarctic Muon And Neutrino Detector Array[3]), which is now a part of IceCube. The baseline design

[a] See http://icecube.wisc.edu/ for a full list of authors.

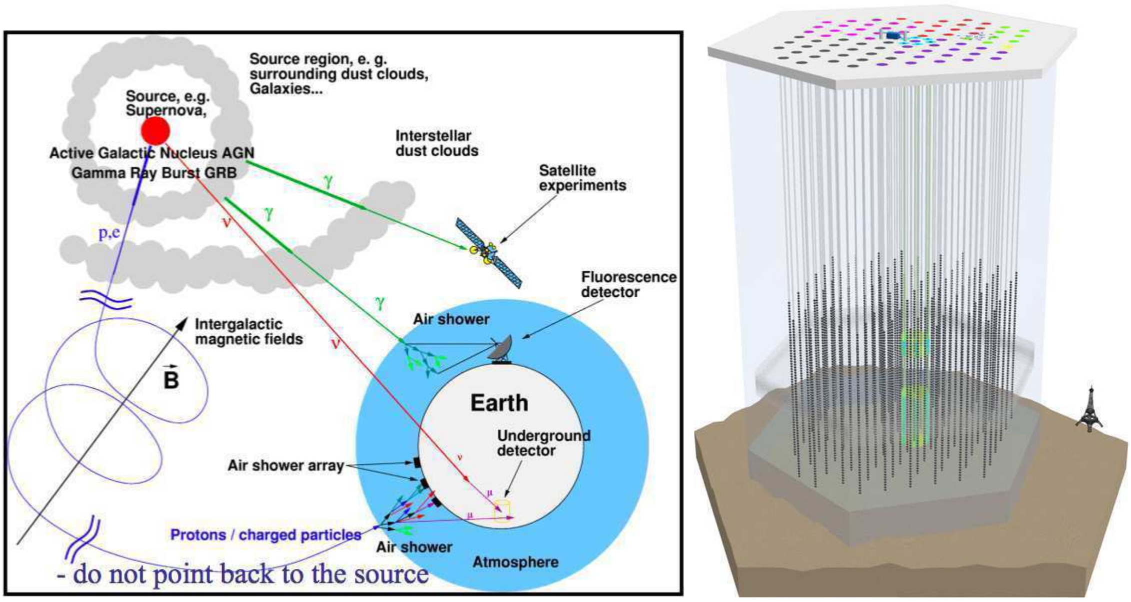

Figure 1: Left (a): Multi-Messenger astronomy. Right (b): The complete IceCube neutrino observatory, including DeepCore and the most dense dust layer at a depth of 2100 m.

of IceCube consists of 4800 digital optical modules (DOMs [2]) on 80 vertical cables (strings), arranged in a hexagonal grid and placed at depths between 1450 m and 2450 m in the clear ice beneath the surface of the South Pole (see figure 1 (b)). The strings are deployed into water-filled holes, previously bored to a depth of 2500 m with a hot-water drill. Once deployed and frozen in, the DOMs become permanently inaccessible. The ice layer above the detector efficiently shields it from low-energy atmospheric muons. The vertical distance between consecutive DOMs is 17 m, and neighbouring strings are 125 m apart on average. The housing of the DOMs consists of a 33 cm glass sphere, capable of withstanding very high pressure. With an improved detector technology and a size of one cubic kilometre, IceCube is expected to drastically improve timing and angular resolutions with respect to AMANDA.

In addition, IceCube also includes an air-shower array called IceTop, located at the surface above the in-ice telescope. It consists of 80 stations, each equipped with four DOMs in two tanks filled with optically clear ice. IceTop was designed to study cosmic ray and air shower physics up to 10^{18} eV by itself and in coincidence with the in-ice array. By tagging air showers with downgoing muons, it also provides an alternative calibration scheme for the in-ice array and a veto against downgoing muon background.

The particle detection principle relies on the blue and near-UV Cherenkov light emission from relativistic charged leptons moving faster than the speed of light in the ice. The DOMs include a 10-stage 25 cm Hamamatsu photomultiplier tube (PMT) capable of detecting this faint light. A DOM can record the signal waveform whenever one or more photons are detected and produce a "hit". In order to avoid noise i.e. isolated hits (with no nearby hits in space or time), a local coincidence condition requires neighbouring DOMs to record a hit before an event trigger is formed. Single Majority Triggering (SMT) requires the coincidence of hits in at least eight DOMs within a time window of 5 μsec (for the 40-string detector), or at least 6 DOMs for IceTop.

The signal from the PMT is digitized, time-stamped and buffered by the onboard electronics, and sent to the surface data acquisition system, where the DOM pulses are sorted into a time-ordered stream. Two different waveform digitizers are contained onboard: an Analog Transient Waveform Digitizer (ATWD) at a sample rate of up to 300 MHz during 400 ns, and a Fast

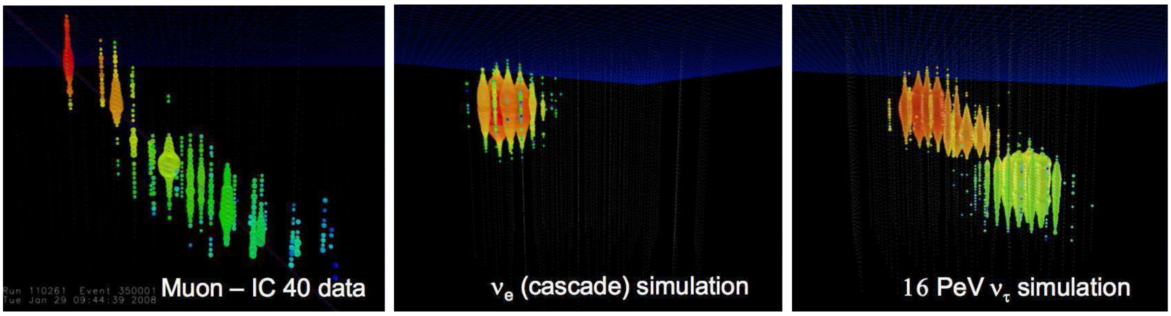

Figure 2: Neutrino signatures: a track-like muon signature, a cascade-like electron signature, and a double bang from a tau creation/decay.

Analog to Digital Converter (FADC) at 40 MHz for 6400 ns. All DOMs are synchronized to a GPS clock with an accuracy of 2 ns. Moreover, calibration runs for neighbouring DOMs can be taken using the integrated LEDs. Cables from all strings converge into the IceCube Laboratory (ICL), a two-story elevated building on the surface, in the middle of the array. It was commissioned in January 2007 and houses all the electronics needed for data-taking, archiving, filtering and data reduction. Due to the limited bandwidth for transfer over NASA's Tracking and Data Relay Satellite System (TDRSS, 55 GB/day in 2009), the data needs to be processed and filtered on-line. Only triggered events that passed the filters are sent to the northern hemisphere. Additionally, all raw data is being written to tapes.

IceCube started data-taking in 2006 with a nine-string array, continued in 2007 with 22 strings, and in 2008 with 40 strings, demonstrating an excellent stability (see table 1). Nineteen additional strings have been deployed during the 2008-2009 austral summer.

3 Event detection and reconstruction

Maximum likelihood fitting techniques are used to reconstruct the direction and energy of each event, taking into account corrections for the absorption and scattering properties of photons in the ice as a function of depth.

The three different flavours of neutrinos can be identified by their distinctive patterns (see figure 2):

- A ν_e interaction in the ice ($\nu_e + N \rightarrow e + X$) produces a small ($\sim$ 10 m) electromagnetic shower. As the typical cascade size and scattering length ($\lambda_{scattering} \sim 20$ m) are small compared to the inter-string distance, the direction of the incoming electron neutrino is difficult to reconstruct. However, as these events are mostly contained in the detector, the energy reconstruction is quite accurate ($\sigma \sim 0.18$ in $log_{10}(E/GeV)$). The Cherenkov light spreads over a spherical volume relative to the electron energy.

- A ν_μ interaction in the ice gives rise to a secondary muon that travels long distances in the ice in a straight line. The light pattern is a Cherenkov cone along a straight track (see figure 2), with additional light from stochastic processes such as bremsstrahlung, pair-production and photo-nuclear interactions (if the muon energy is high enough). Due to the large detection volume, providing long lever arms, and the digitization inside the DOMs, allowing for an excellent time resolution, the angular resolution of the track-like events is below 1° at an energy of 1 TeV in the 40-string detector, and the energy resolution ~ 0.3 - 0.4 in $log_{10}(E/GeV)$. These values may be further improved using new reconstruction techniques and a more precise ice model.

- One of the characteristic signatures of a ν_τ interaction is the so-called "double bang": two consecutive cascades, one at the production and one at the decay of the tau lepton. Additionally, the tau produces Cherenkov radiation between the cascades. Another possible signature is the "(inverted) lollipop", where the tau decay (production) cascade is outside the detector volume. At high energy, cascades from tau production/decay are easy to distinguish from electron neutrino cascades.

The main background to point source search in IceCube are muons and neutrinos from cosmic ray interactions in the atmosphere (see table 1). Point source searches expect a signal excess from the direction of known sources. At the depth of the detector, the flux of atmospheric muons (downgoing) is a factor 10^6 larger than the flux of atmospheric neutrinos. Most of the atmospheric muons can be cut away by considering only upgoing events, but the atmospheric neutrinos will have to be distinguished from their astrophysical counterparts using other characteristics such as energy deposition.

Year	IceCube Strings	Cosmic Ray muon rate	Atmospheric neutrino rate
2005	1	5 Hz	
2006	9	80 Hz	1.5/day
2007	22	550 Hz	28/day
2008	40	1000 Hz	110/day
2011	80	1650 Hz	220/day

Table 1: Atmospheric event rates for different IceCube configurations

The pointing resolution of the 40-string detector has also been studied in a moon shadow analysis. The moon can block cosmic rays from reaching the earth, and a 4.2 σ deficit of atmospheric muons from cosmic rays was observed within 0.7° around the direction of the moon, using 3 months of data taken with the 40-string detector in 2008.

4 Results

4.1 Point source search

Point source searches are one of the main goals of IceCube, and the most promising way to detect astrophysical neutrinos. Figure 3 shows the limits on the neutrino flux from various point sources, for the AMANDA [4] and IceCube [5] detectors (9 strings and 22 strings). The skymap obtained with IceCube 22 strings can be seen in figure 4. The most significant excess of events in the sky at 2.2 sigma after accounting for all trials.

4.2 Gamma ray bursts

Being amongst the most energetic astronomical phenomena, Gamma ray bursts may produce very high energy neutrinos along with photons, and have been proposed as possible sources of ultra-high energy cosmic rays [11]. The detection of neutrinos from a GRB would provide evidence for the acceleration of ultra-high energy cosmic rays in GRBs. The best limit on neutrino emission from GRBs comes from the AMANDA telescope: the upper limit on the diffuse flux normalization times E^2 for the Waxman-Bahcall model at 1 PeV is 6×10^{-9} GeV cm^{-2} s^{-1} sr^{-1} with 90% of the events expected within the energy range from ~ 10 TeV to ~ 3 PeV [12, 13]. The limit was obtained in a search for muon neutrinos from 419 GRBs detected by the BATSE satellite between 1997 and 2003.

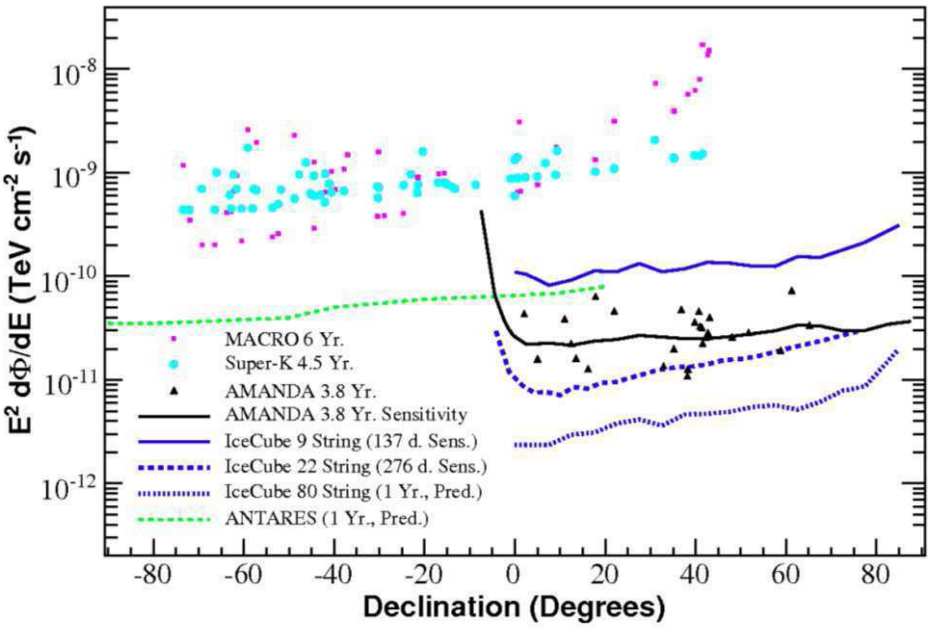

Figure 3: Limits on the neutrino flux from various point sources as a function of declination. Note that IceCube looks through the earth at the northern hemisphere. Also shown are limits from MACRO [6], Super-K [7], and predicted sensitivity for ANTARES [8].

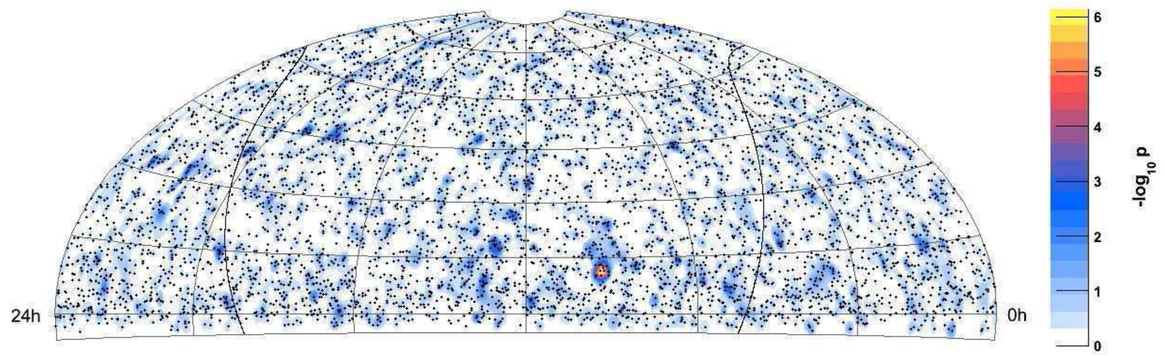

Figure 4: Equatorial sky map of events (points) and pre-trial significances (p-value) obtained with IceCube 22 strings in the unbinned point source search in 2007. The solid curve is the galactic plane.

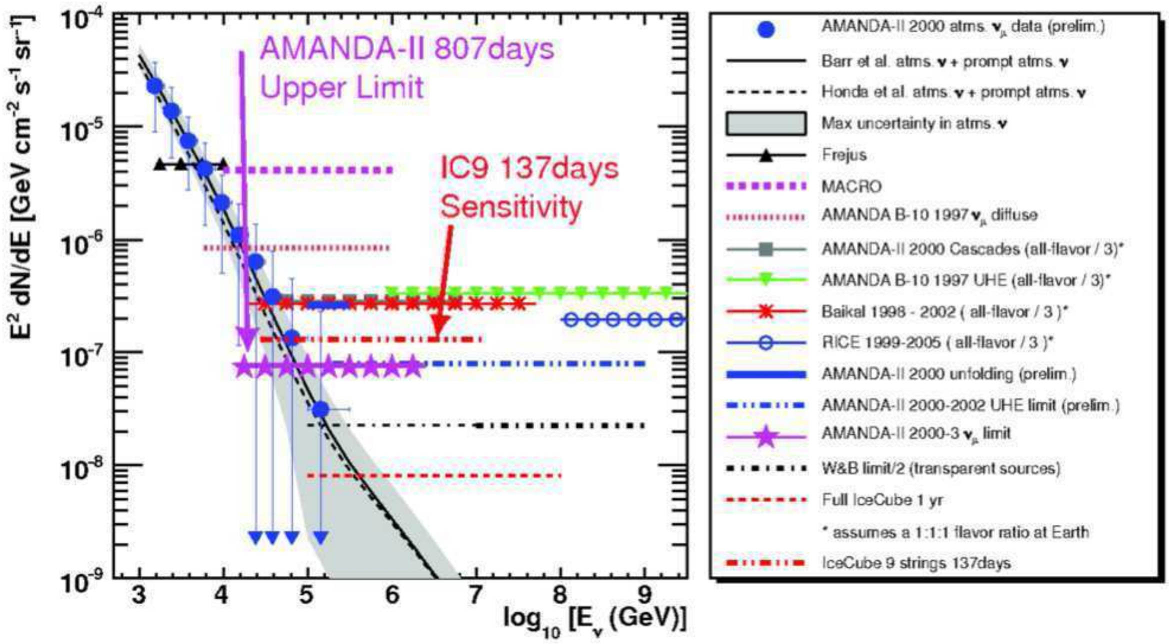

Figure 5: Upper limits on the ν_μ flux from diffuse sources with an E^{-2} energy spectrum [9].

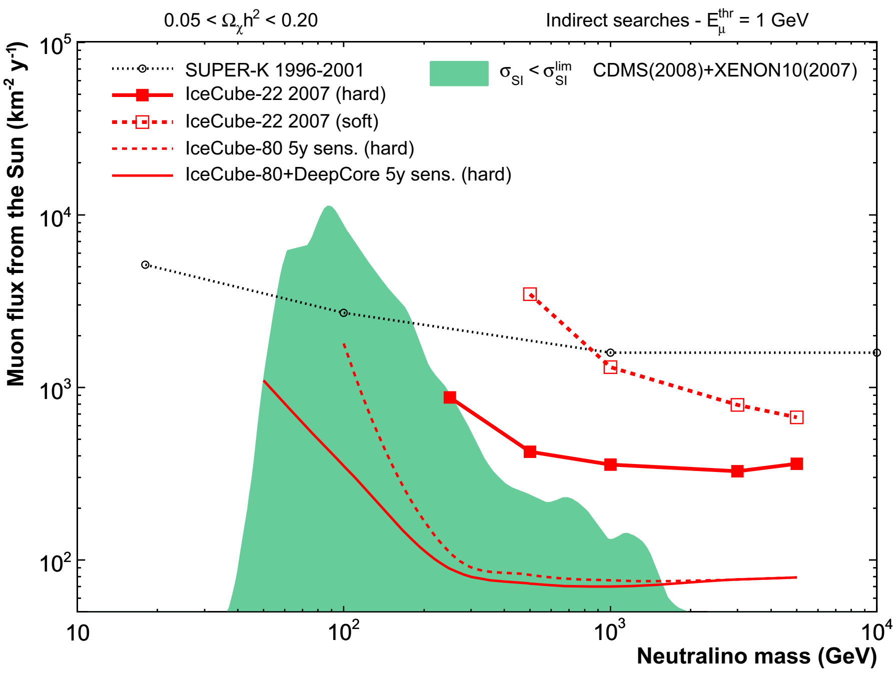

Figure 6: Upper limits at the 90% confidence level on the muon flux from neutralino annihilations in the Sun with IceCube 22-strings for the soft ($b\bar{b}$) and hard ($W^+W^-/\tau^+\tau^-$) annihilation channels [16]. The shaded area represents MSSM models not disfavoured by direct searches. Also shown is the expected sensitivity of full IceCube + DeepCore, as well as limits from Super-K [10].

A search for neutrinos from GRBs using the 22-string IceCube detector is currently nearing completion. Time and position information is now obtained from the Swift and Fermi satellite data.

The analysis of the brightest ever GRB, 080319B, yielded no excess above the background[14]. Unfortunately, IceCube was running in a nine-string configuration at the time of this GRB.

4.3 Diffuse search

Several diffuse neutrino flux analyses are looking for extraterrestrial neutrinos from unresolved sources. These can be astrophysical neutrinos from objects that produce a flux that is too faint to be detected individually, or cosmogenic neutrinos that originate in interactions of high-energy protons with the cosmic microwave background. A signal would be an excess of high-energy events over the expected atmospheric neutrino background, which has a softer energy spectrum than extraterrestrial neutrinos[15]. Searches have been performed with the AMANDA detector[15], and with the 9-string IceCube detector in 2006. Upper limits on the ν_μ flux have been derived (see figure 5).

4.4 Indirect dark matter search

IceCube is also actively looking for neutrinos as a signature of dark matter in the centre of the Sun (or the Earth) where weakly interacting massive particles (WIMPs) can accumulate and annihilate. One of the most promising candidate particles is the stable and massive neutralino, that can self-annihilate to Standard Model particles that produce neutrinos in the energy range from a few GeV to tens of TeV.

No excess over the expected background has been observed for this indirect search in the centre of the Sun with the 2007 data[16]. Upper limits have been obtained on the annihilation rate of captured neutralinos in the Sun and converted to limits on WIMP-proton cross-sections, for neutralino masses in the range 250 - 5000 GeV. Figure 6 shows upper limits at the 90% confidence level on the muon flux from neutralino annihilations in the Sun with IceCube 22-strings. These results are the most stringent limits to date on neutralino annihilation in the Sun.

4.5 Other physics objectives

Other topics and active analyses not described here include cosmic ray physics with IceTop[17], the search for exotic particles and processes (magnetic monopoles[18], Q-Balls, SUSY, TeV gravity), the search for violation of Lorentz Invariance[19], neutrino oscillation studies[20] and searches for neutrinos from Supernovae.

5 Future plans

IceCube plans to finish the baseline construction by the end of the 2010/2011 austral summer, including six extra strings with high quantum efficiency DOMs, making up a dense inner core of strings ("DeepCore")[21], hence improving the detection efficiency of low energy events. Both the horizontal interstring (72 m) and vertical DOM spacings are denser in this section. Out of the 60 DOMs on these strings, 10 will be placed above the central dust layer in the ice (with a vertical spacing of 10 m), and the remaining 50 at a vertical spacing of 7 m in the clearest ice below ($\lambda_{scattering} \sim$ 40-50 m and $\lambda_{absorption} \sim$ 220-230 m at 440 nm light wavelength, compared to ($\lambda_{scattering} \sim$ 20 m and $\lambda_{absorption} \sim$ 110 m above). This, combined with the use of the surrounding standard IceCube modules as a veto, will lower the detection threshold below 100

GeV, allowing more efficient neutrino oscillation and WIMP studies, as well as tau physics and southern sky point source searches.

The possibility of increasing the sensitivity of IceCube at higher energies is also under consideration. One idea is to surround IceCube by another ring of strings, increasing the sensitivity to weak astrophysical signals with hard spectra. New techniques for covering much larger volumes are also being tested with radio and acoustic devices deployed on IceCube strings.

6 Conclusion

Within the next few years, the cubic-kilometre neutrino telescope IceCube will collect an unprecedented number of neutrino events over a broad energy region, which will guarantee a high discovery potential. The ongoing searches for point sources, WIMP annihilations and GRBs look promising. DeepCore as well as the hybrid high-energy extensions will take IceCube's physics potential beyond what was originally planned.

Acknowledgments

The author would like to express his gratitude to the conference organizers for the opportunity to participate in the XLIVth Rencontres de Moriond, the European Union for travel grants, as well as IISN and BELSPO, Belgium.

References

1. A. Achterberg, et al. (IceCube collaboration), Astropart. Phys. 26, 155 (2006)
2. R. Abbasi, et al. (IceCube collaboration), Nucl. Inst. Meth. A601, 294 (2009)
3. J. Ahrens, et al. (AMANDA Collaboration), Phys. Rev. D66, 012005 (2002)
4. R. Abbasi, et al. (IceCube collaboration), Phys. Rev. D79, 062001 (2009)
5. P. Berghaus, for the IceCube collaboration, Preprint arXiv:0812.2883 (2008)
6. M. Ambrosio et al., ApJ 546, 1038 (2001)
7. S. Desai et al., Astropart. Phys. 29, 42 (2008)
8. J. Aguilar, for the ANTARES Collaboration, Preprint arXiv:0710.0252 (2007)
9. K. Hoshina, for the IceCube collaboration, Preprint arXiv:0711.0353 (2008)
10. S. Desai et al., Phys. Rev. D70, 083523 (2008)
11. E. Waxman, Phys. Rev. Lett. 75, 386 (1995)
12. A. Achterberg, et al. (IceCube collaboration), ApJ 674, 357 (2008)
13. A. Achterberg, et al. (IceCube collaboration), ApJ 664, 397 (2007)
14. R. Abbasi, et al. (IceCube collaboration), Preprint arXiv:0902.0131 (2009)
15. A. Achterberg, et al. (IceCube collaboration), Phys. Rev. D76, 042008 (2007)
16. R. Abbasi, et al. (IceCube collaboration), Preprint arXiv:0902.2460 (2009)
17. S. Klepser, for the IceCube collaboration, Preprint arXiv:0811.1671 (2008)
18. H. Wissing, for the IceCube collaboration, Preprint arXiv:0711.0353, 139 (2007)
19. R. Abbasi, et al. (IceCube collaboration), Preprint arXiv:0902.0675 (2009)
20. C. Rott, for the IceCube collaboration, Preprint arXiv:0810.3698 (2008)
21. O. Schulz, for the IceCube collaboration, AIP Conf. Proc. 1085, 783 (2009)

THE ANTARES NEUTRINO TELESCOPE: A STATUS REPORT

NICCOLÒ COTTINI
DSM/Irfu, CEA/Saclay
F-91191 Gif-sur-Yvette Cédex

The ANTARES detector consists of a three dimensional array of 885 photomultipliers, arranged in 12 lines anchored at a depth of about 2500 m in the Mediterranean Sea, detecting the Cherenkov light produced by neutrino-induced muons. An additional instrumented line is used for environmental monitoring and for R&D of acoustic neutrino detection. Five lines of the detector have been operated since January 2007, followed by 5 additional lines in December 2007. Since May 2008 the detector is complete. The detector performance and its long-term stability are discussed. The results obtained with the first 5 line data on the atmospheric neutrino detection and the search for a cosmic neutrino signal are presented.

1 Introduction

The detection of high energy cosmic neutrinos is a major challenge in astroparticle physics: the discovery of extraterrestrial sources of these particles may answer some fundamental questions, such as the origin of high energy cosmic rays. The ANTARES neutrino telescope is being operated at about 2500 m depth in the Mediterranean sea, 40 km off the French coast. The detector consists of a three dimensional array of 885 photomultipliers (PMTs).
The detected neutrinos have energies in the range 10 GeV - 100 PeV. The main detection channel is given by muon neutrinos ν_μ, crossing the Earth and interacting by a charge current process with a nucleon of the matter in the crust: $\nu_\mu + N \rightarrow \mu + X$. Above a few TeV, the generated muon is (almost) collinear with the incident neutrino and can travel up to 10 km in the rock. When this upward going muon gets from the crust to the sea water, it emits Cherenkov light with an angle $\theta_C \simeq 42^\circ$ with respect to its direction. The photons are detected by the PMT array: their time, position and charge represent the raw data, to be used for the muon trajectory reconstruction.
At energies higher than 500 GeV, the muons produced by the cosmic ray interactions in the atmosphere above the detector can reach the ANTARES site and constitute a source of background. Another background is due to the atmospheric neutrinos, generated at the antipodes

of the detector and having the same signature as the cosmic signal: an upward going muon. Three thousands of these atmospheric neutrino events are detected each year. Moreover, for some fraction of the total downward going muon flux, the produced Cherenkov light is misinterpreted as an upward going track signal. The flux difference between the downward going muons and the muons induced by atmospheric neutrinos at the ANTARES site is about six order of magnitudes (see figure 1). Therefore dedicated analysis are needed to first reject the upward going reconstructed atmospheric muons and then to disentangle a possible cosmic component from a pure sample of upward going tracks.

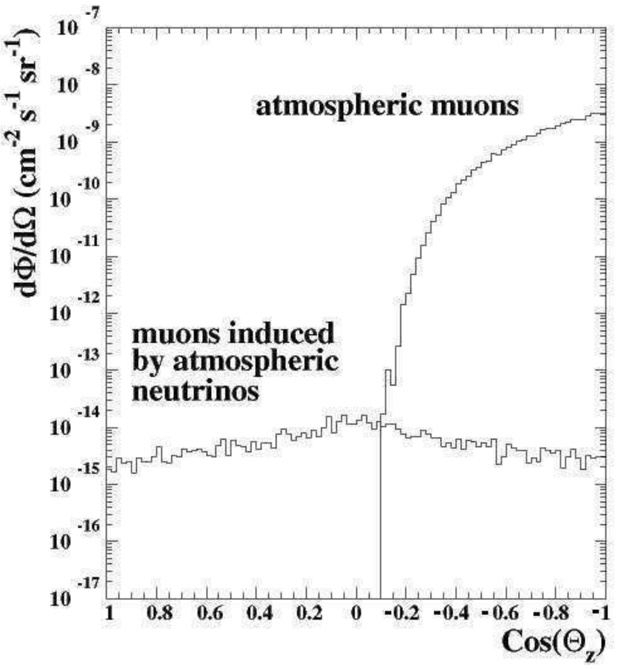

Figure 1: Muon flux at 2400 m depth in the sea. The flux is given as a function of the muon flight direction with respect to the vertical axis.

The PMTs also detect the light generated by ^{40}K decays in the sea water and by some organisms. These two light sources give a continuous background, which varies between 60 and 100 kHz and is conventionally called baseline. Peaks of biological activity can occasionally rise the counting rate up to the order of 1 MHz. In figure 2, the typical background behaviour during the data taking is shown.

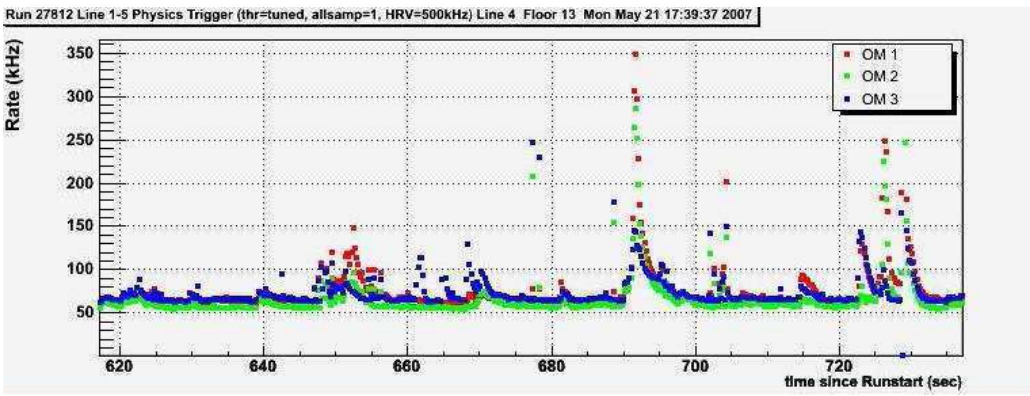

Figure 2: Optical background rate measured by 3 PMTs of a storey, in a time window of 2 minutes (May 2007).

2 The ANTARES detector

In figure 3, an artist's view of the ANTARES telescope is shown. The detector consists of 12 lines spread over a 200 × 200 m^2 area and spaced by about 65 m. The lines have a height of ∼450 m, are anchored to the sea bed and held nearly vertical by a buoy at the top. Each line is divided in 25 storeys, which represent the fundamental units of the detector. A storey is composed of 3 optical modules, which consist of 10 inch photomultipliers (PMTs) housed in glass spheres [1, 2] and 45° downward oriented to increase the sensitivity to upward going tracks. The first storey is 100 m above the sea bed, and the spacing between the storeys is 14.5 m. Each storey is also equipped with a titanium electronic container, where the analogue electrical outputs of the PMTs are digitised in a custom built microchip with an analogue ring sampler architecture (called ARS). Each readout channel includes two ARS working in a token ring mode to reduce the dead time. The signal is then treated in real time by a data acquisition card. The result is finally sent to the bottom of the line through optical fibres and then to a junction box. In the junction box the outputs from the lines are connected to a 40 kilometre electro-optical submarine cable and sent to the experiment shore station in the town of La Seyne-sur-Mer, in France.

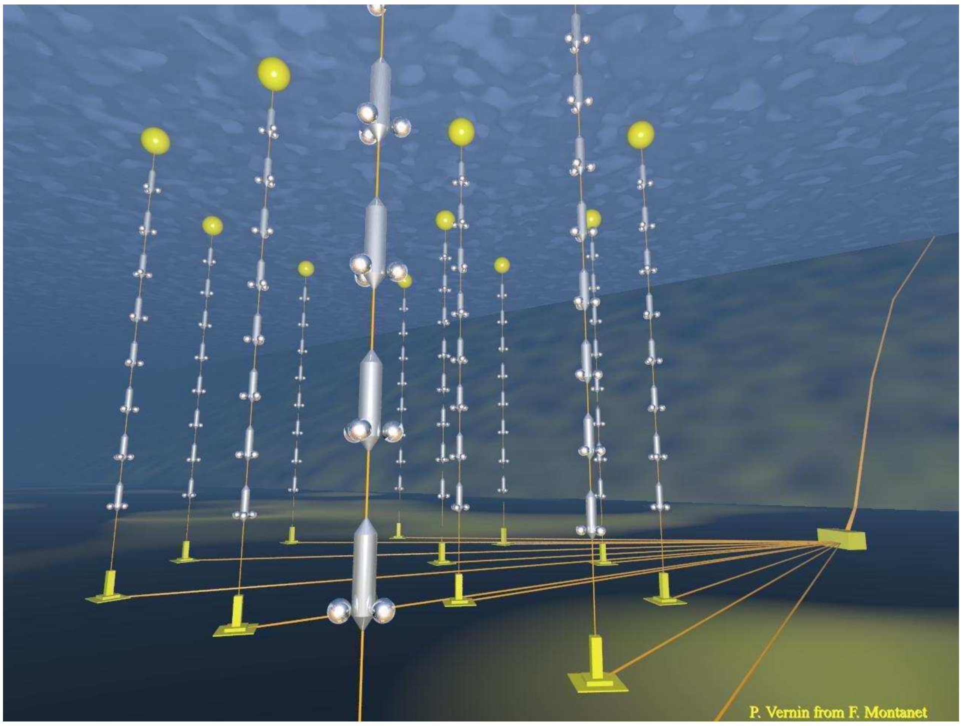

Figure 3: Artist's view of the ANTARES detector.

ANTARES is also a multidisciplinary underwater science infrastructure continuously recording various types of data for studies related to oceanography, climatology or geophysics. A R&D system for neutrino acoustic detection also records sounds from the deep sea (see reference [3] for further details).
The first ANTARES detection line was connected in March 2006. Five lines of the detector have been operated since January 2007, followed by 5 additional lines in December 2007. The detector has been completed on May 30th, 2008, with the connection of the last two lines.

3 The detector operations

The median optical background rate recorded between March 2006 and May 2008 by the PMTs of the first ANTARES detection line is shown in figure 4. In 2006, the biological activity was exceptionally high but has gradually returned to its nominal value of about 60 kHz. No firm explanation for this phenomenon has been found yet.

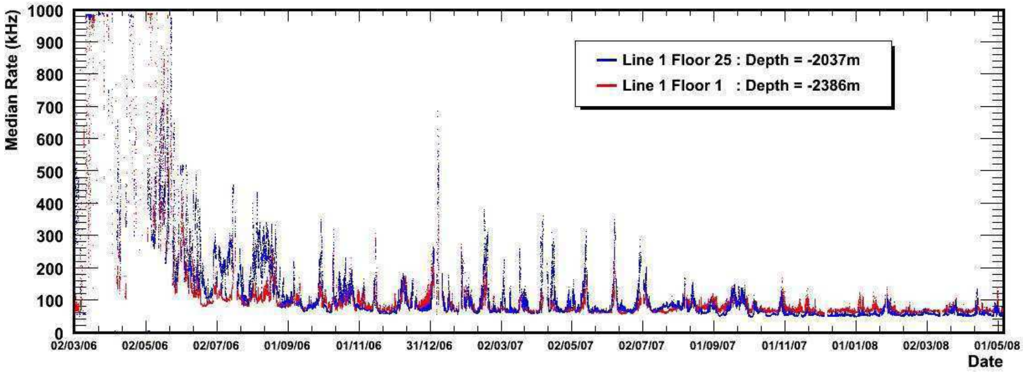

Figure 4: Median rate recorded between March 2006 and May 2008 by the PMTs of the first and the last storey of the first ANTARES detection line.

Since no filtering is made offshore, the data stream is dominated by the background light. On shore, a computer farm runs various software triggers [4] to select the photon hits on the PMTs supposed to be due to muon tracks. Indeed these hits are correlated in time and position as a consequence of the properties of the Cherenkov light, while the hits produced by ^{40}K decays and bioluminescence are mostly uncorrelated. Therefore only the data corresponding to a sufficient number of correlated hits imply the presence of a muon signal and are selected for off line analysis; all the other data are discarded. The main trigger requires at least 5 pairs of optical modules in the same storey to have signals coincident within 20 ns; these 5 pairs must be compatible with the Cherenkov light given by a muon propagating in the detector. This condition can be modified to address a particular physics target: for instance, the trigger settings for GRB analysis are described in [5].

The evolution of the number of triggered events as a function of time during the year 2007 and 2008 is shown in the figure 5 and the figure 6 respectively. The black line correspond to all data, while some quality criteria have been applied for the other lines. The data taking is organised in runs of a duration of some hours (tipically 5). The violet line correspond to runs in which 80% of the detector electronic channels were giving data. For the blue line, runs are considered for which the bioluminescence produce a PMT rate beyond 20% of the baseline for no more than 40% of the run duration. For the red line, this condition is strenghten to 20% of the run duration.

The photon hits filtered by the trigger make up a so-called event. All the events are stored on disks for further track reconstruction and analysis. The knowledge of the hit charge, position and arrival time allows the reconstruction of the muon trajectory thus giving information on the parent neutrino. The reconstruction algorithm used in this proceeding is described in [6]; its overall structure consists of four steps:

1. a linear fit through the (x,y,z,t) coordinates of the photon hits, called prefit;

2. a χ^2 minimization: the muon track parameters are fitted using the time of the photon hits, weighted by the measured charge;

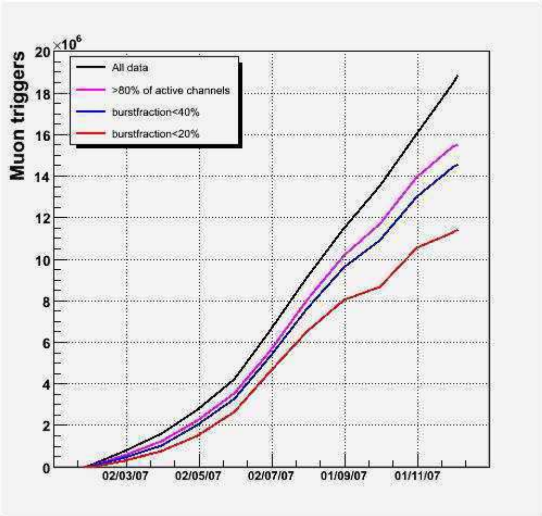

Figure 5: Evolution of the number of triggered events as a function of time (black line), during the 2007 data taking campaign. The other lines correspond to different data quality criteria, depending on the level of the optical background (see text).

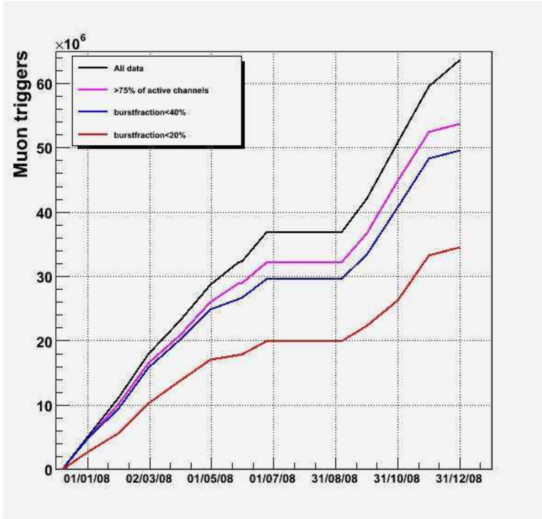

Figure 6: Evolution of the number of triggered events as a function of time (black line), during the 2008 data taking campaign. The other lines correspond to different data quality criteria, depending on the level of the optical background (see text).

3. a first maximum likelihood fit: a Monte Carlo simulation is used to draw the probability density function (pdf) of the time residuals. This pdf shows a narrow peak of a few nanoseconds around 0 ns offset (the ANTARES resolution is about 1 ns in time), followed by a tail due to light diffusion in water and Bremsstrahlung. For each possible set of track parameters, the pdf is used to compute the likelihood of the observed event; the set of parameters which gives the maximum likelihood is kept.

4. a second maximum likelihood fit, differing from the first by its pdf including the light intensity information and the presence of a continuous uncorrelated background.

In order to decrease the fraction of minimizations ending in a local minimum, the second and third steps are repeated with 8 different starting points, resulting from transformations of the prefit track. The final solution is chosen as the one giving the highest likelihood value. The atmospheric muons reconstructed as upward going tracks usually result in a small likelihood value. In particular, the following reconstruction quality variable has been considered:

$$\Lambda = -\frac{lnL}{N_{DOF}} + 0.1 \cdot (N_{comp} - 1), \tag{1}$$

where L is the value of the likelihood of the fit, divided by the number of degrees of freedom N_{DOF}, and N_{comp} is a term related to the number of local minima found in the track fit. A cut on Λ can be set, so that genuine neutrino events are selected with a certain level of atmospheric muon contamination.

The simulations have shown that this reconstruction achieves better than 0.3° angular resolution for neutrinos above 100 TeV. At lower energy, the neutrino angular resolution deteriorates because the muon is no longer collinear with the incident neutrino. This performance is made possible by the excellent properties of the water at the ANTARES site (absorption and scattering lengths are of about 60 m and 265 m in the blue wavelength [7]). An optical module positioning

with 10 cm resolution is also needed to obtain the quoted reconstruction precision.
Indeed, the ANTARES lines are flexible and move in the sea current, with movements of about one metre at the top for a typical sea current of 5 cm/s. The required spatial precision is obtained through an acoustic positioning system, with components installed at several points along the line and on the sea bed, coupled to tiltmeters and compasses on each storey.

4 The first physics analyses

The analysis of the data taken in 2006 with the first detection line has been reported in [8]. From January to December 2007, ANTARES has taken data with 5 lines (see figure 7) for 310 days. The duty cycle of the data taking in this period has been of about 80%. As a first step, it has been decided to restrict the analysis to runs with a particularly low biological activity, that is the presence of peaks of bioluminescence for less than 40% of the time of a run. This corresponds to an equivalent data taking time of about 160 days, in which 14.5 million events were triggered (see the blue line on figure 5).

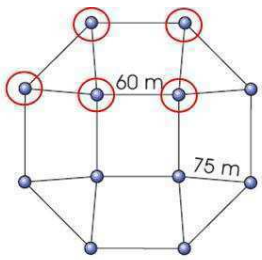

Figure 7: Array of the ANTARES lines on the sea bed. The five lines taking data in 2007 are emphasized by a circle.

The event reconstruction described in section 3 has been applied to the 5 line events. A measurement of the downward going muon flux (see reference [9]) has been performed. The result is in agreement with the Monte Carlo predictions, thus proving that the detector behaves as expected for the atmospheric muon background.
Then the atmospheric neutrino background has been analyzed. A sample of neutrino events has been selected with a cut on the Λ variable (equation 1), requiring an atmospheric muon contamination below 10%. Keeping this level of purity, an improvement of the selection efficiency has been studied through a likelihood ratio analysis, based on some variables discriminating the neutrino signal from the atmospheric muon background. Four variables have been used: the muon track elevation obtained by the reconstruction prefit; the fraction of hits with time residual smaller than 3 ns; the distance covered by the last in time photon, from the muon track to the fired PMT; the measured PMT charges per unit time. For each variable i, a probability density function $s(x_i)$ for neutrinos and $b(x_i)$ for atmospheric muons have been obtained by Monte Carlo and the following likelihood ratio has been computed:

$$y = \frac{\prod_i s(x_i)}{\prod_i s(x_i) + \prod_i b(x_i)} \qquad (2)$$

The y variable has been found to be weakly correlated with Λ. A bidimensional cut in Λ and y has shown an increase of the selection efficiency by a factor of two with respect to a simple Λ cut only. In the end, 185 neutrino events have been selected from the data, while $218 \pm 41(\mathrm{theo}) \pm 4(\mathrm{stat})\ ^{+3}_{42}(\mathrm{syst})$ were expected from a Monte Carlo simulation. The Bartol model [10] has been used to simulate the atmospheric neutrino flux. The main contribution to systematics are given by the uncertainties on the optical modul response and on the detector

calibrations. Further studies are ongoing; therefore the systematic contribution is expected to be reduced and become symmetric around the number of expected neutrinos.
The distribution of the elevation (θ) and the azimuth (φ) of the neutrino events is compared to the Monte Carlo expectation in the figure 8 and the figure 9 respectively. The non uniform detector response is due to the geometry of the 5 line detector (see figure 7), much higher than wide and asymmetric in azimuth.

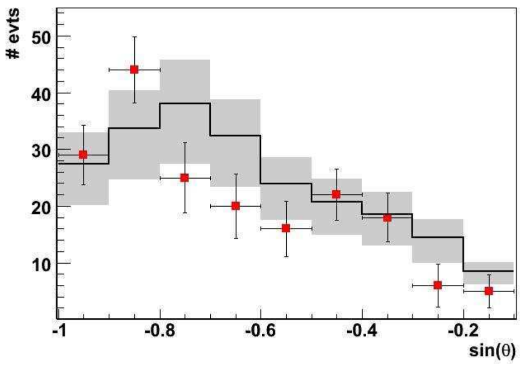

Figure 8: Distribution of the cosine of the elevation (θ) for the neutrino tracks selected from the 5 line data (squares, with statistical error bars), compared to the simulation (line). The grey band corresponds to the quadratic sum of the theoretical, statistical and systematic errors.

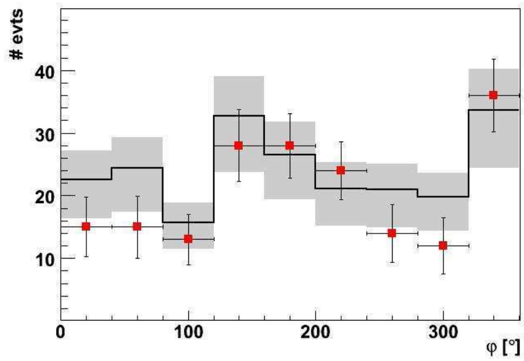

Figure 9: Distribution of the azimuth (φ) for the neutrino tracks selected from the 5 line data (squares, with statistical error bars), compared to the simulation (line). The grey band corresponds to the quadratic sum of the theoretical, statistical and systematic errors.

A good agreement between the data and the simulation is also found with another independent atmospheric neutrino analysis [11], which is based on a different reconstruction algorithm and obtains a comparable selection efficiency. These results prove the correct detector response to a known neutrino source such as the atmospheric neutrinos. Therefore the time has come for ANTARES to start the quest for cosmic neutrinos.
Using the 5 line data, a first limit to the neutrino flux from supersymmetric dark matter annihilation in the core of the Sun has been determined [12]. A search for high energy neutrinos produced with an E^{-2} energy spectrum by a mechanism of particle shock acceleration [13] has also been performed on the basis of a potential source list. The sky map of the 94 neutrino events considered in the analysis [14] is shown in figure 10. No cosmic neutrino signal has been found in the 5 line data; see reference [14] for the analysis details.

5 Conclusion

The analysis of the data taken in 2007 with the first 5 lines of the ANTARES telescope shows that the detector behaviour complies with the expectations. The measured downward going muon flux and the number of detected atmospheric neutrinos are found in fair agreement with the Monte Carlo simulations. This good performance allows the search for an extraterrestrial neutrino signal, which has not been found yet.
The detector construction has been completed on May 30$^{\text{th}}$, 2008. The analysis of the data taken in 2008 is ongoing. The search for neutrino cosmic sources continues...

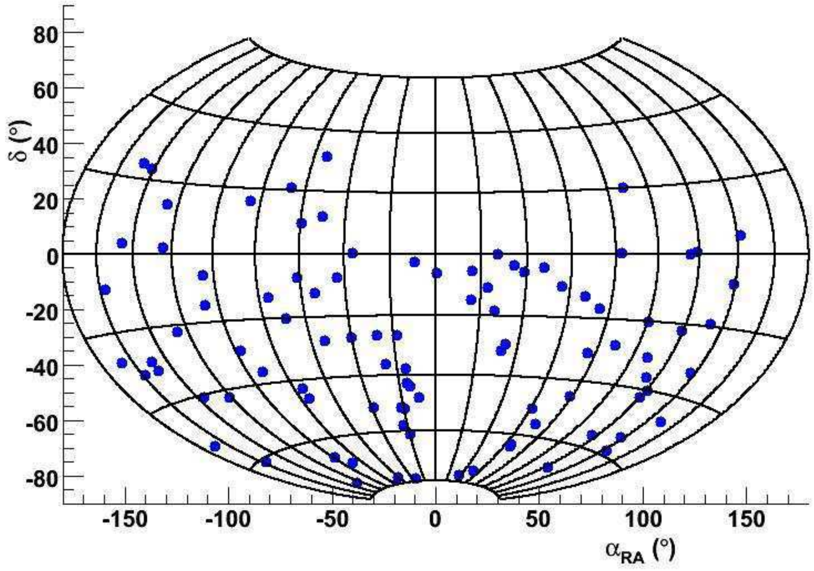

Figure 10: Sky map in equatorial coordinates of 94 neutrino events detected with 5 ANTARES lines.

References

1. The ANTARES Collaboration, Nucl. Instr. Meth. A **484**, 369 (2002).
2. The ANTARES Collaboration, Nucl. Instr. Meth. A **555**, 132 (2005).
3. K. Graf, these proceedings.
4. The ANTARES Collaboration, Nucl. Instr. Meth. A **570**, 107 (2007)
5. D. Dornic, these proceedings.
6. A. Heijboer, PhD thesis, http://antares.in2p3.fr (2005).
7. The ANTARES Collaboration, Astropart. Phys. **23**, 131 (2005).
8. The ANTARES Collaboration, arXiv:0812.2095v1 [astro-ph] (2008).
9. C. Picq, these proceedings.
10. G. Barr *et al.*, Phys. Rev. D **39**, 3532 (1989).
11. J. Brunner, private communications.
12. V. Bertin, these proceedings.
13. F. Halzen, arXiv:astro-ph/0506248v1 (2005).
14. K. Fratini, these proceedings.

PHYSICS RESULTS AND PERSPECTIVES OF THE BAIKAL NEUTRINO PROJECT

A. AVRORIN[a], V. AYNUTDINOV[a], V. BALKANOV[a], I. BELOLAPTIKOV[d], D. BOGORODSKY[b], N. BUDNEV[b], I. DANILCHENKO[a], G. DOMOGATSKY[a], A. DOROSHENKO[a], A. DYACHOK[b], Zh.-A. DZHILKIBAEV[a], S. FIALKOVSKY[f], O. GAPONENKO[a], K. GOLUBKOV[d], O. GRESS[b], T. GRESS[b], O. GRISHIN[b], A. KLABUKOV[a], A. KLIMOV[h], A. KOCHANOV[b], K. KONISCHEV[d], A. KOSHECHKIN[a], V. KULEPOV[f], D. KULESHOV[a], L. KUZMICHEV[c], E. MIDDELL[e], S. MIKHEYEV[a], M. MILENIN[f], R. MIRGAZOV[b], E. OSIPOVA[c], G. PAN'KOV[b], L. PAN'KOV[b], A. PANFILOV[a], D. PETUKHOV[a], E. PLISKOVSKY[d], P. POKHIL[a], V. POLESCHUK[a], E. POPOVA[c], V. PROSIN[c], M. ROZANOV[g], V. RUBTZOV[b], A. SHEIFLER[a], A. SHIROKOV[c], B. SHOIBONOV[d], Ch. SPIERING[e], O. SUVOROVA[a], B. TARASHANSKY[b], R. WISCHNEWSKI[e], I. YASHIN[c], V. ZHUKOV[a]

[a] *Institute for Nuclear Research, 60-th October Anniversary pr. 7a, Moscow 117312, Russia*
[b] *Irkutsk State University, Russia*
[c] *Skobeltsyn Institute of Nuclear Physics MSU, Moscow, Russia*
[d] *Joint Institute for Nuclear Research, Dubna, Russia*
[e] *DESY, Zeuthen, Germany*
[f] *Nizhni Novgorod State Technical University, Nizhni Novgorod, Russia*
[g] *St.Petersburg State Marine University, St.Petersburg, Russia*
[h] *Kurchatov Institute, Moscow, Russia*

The Neutrino Telescope NT200 is operated since 1998 and was upgraded to the 10 Mton detector NT200+ in 2005. The preparation towards a km3-scale (Gigaton volume) detector in Lake Baikal is currently a central activity. As an important milestone, a km3-prototype string, based on completely new technology, has been installed and was operating together with NT200+ since April 2008. Also selected astroparticle physics results from the long-term operation of NT200 are presented.

1 Introduction

The Baikal Neutrino Telescope NT200 is operating in Lake Baikal at a depth of 1.1 km and is taking data since 1998. Since 2005, the upgraded 10-Mton scale detector NT200+ is in operation. Detector configuration and performance have been described elsewhere [1 2]. The most recent milestone of the ongoing km3-telescope research and development work (R&D) was the installation of a "new technology" prototype string in spring 2008, as a part of NT200+. Fig.1 (left plot) gives a sketch of the current status of the telescope NT200+, including the km3-prototype string.

In this paper we review selected astroparticle physics results from long-term operation of NT200, in particular, an improved limit on a diffuse astrophysical neutrino flux, upper limits on the muon flux from annihilations of hypothetical weakly interacting massive particles (WIMPs) in the Earth and the Sun, and we also discuss the R&D activities towards a km3-scale Baikal telescope. Other results, also on related science and new acoustic technology tests, can be found in [3].

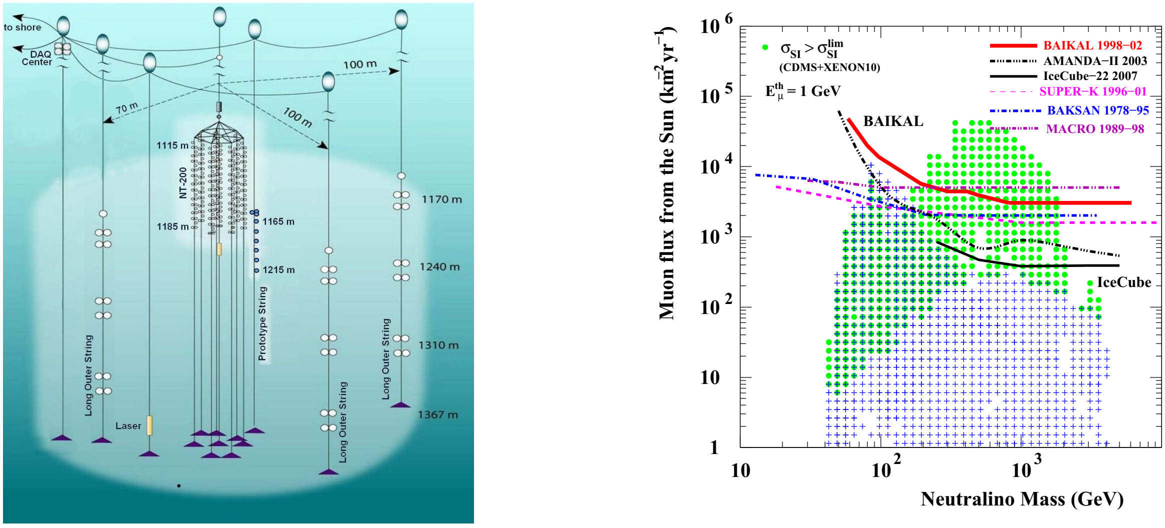

Figure 1: The Lake Baikal neutrino telescope: the compact NT200 (center), 3 long outer strings and the new technology km3-prototype string. Right panel: The NT200 upper limits at 90% c.l. on muon flux from WIMP annihilation in the Sun versus WIMP mass (see text).

2 Selected physics results from NT200

2.1 A search for neutrinos from WIMPs in the Earth and in the Sun

A possible signal from dark matter WIMP annihilations in the Earth and in the Sun would reveal as an excess of upward going muons over atmospheric neutrinos arriving either from near vertical or from the direction of the Sun, respectively. We have used the experimental data of NT200 taken between April, 1998 and March, 2003. In case of the Earth signal, event selection relies on a series of quality cuts which are tailored to the response of the telescope to nearly vertically upward going muons. The energy threshold is about $E_{thr} \sim 10$ GeV in this analysis. We have selected 48 neutrino events for 1038 live days, compared to 56.6 events expected from atmospheric neutrinos with oscillation parameters of Super-Kamiokande results [4], and 73.1 events without oscillations. With no evidence for an excess above the atmospheric neutrino expectation, the upper limit at 90% confidence level (c.l.) on the muon flux from the center of the Earth was determined as $F < 3.7 \cdot 10^{-15}$ cm^{-2}s^{-1} (for WIMP masses greater than 100 GeV, and normalized to $E_{thr} = 1$ GeV).

In case of the Sun we have applied two sorts of quality cuts according to two angular resolutions $\delta\Theta = 3.9°$ and $\delta\Theta = 5.3°$. Respectively, we have selected 510 and 2376 upward going muons in two data samples for 1007 live days. For both samples the distributions of correlation angles between these muons and the Sun were compared to the corresponding off-source background expectation. No indication for excess muons were found. The obtained upper limits at 90% c.l. on an additional muon flux from the Sun are shown in Fig.1 (right) as function of the WIMP mass. In Fig.1 (right), adapted from [5], also gives results from other neutrino telescopes: Baksan, MACRO, Super-Kamiokande, AMANDA-II, IceCube (22 strings), and also minimal supersymmetric neutralino model predictions (see ref. [5]).

2.2 A search for extraterrestrial high-energy neutrinos

The BAIKAL survey for high energy neutrinos searches for bright cascades produced at the neutrino interaction vertex in a large volume around the telescope. A full cascade reconstruction algorithm (for vertex, direction, energy) was applied to the data[6]. Cuts were then placed on this

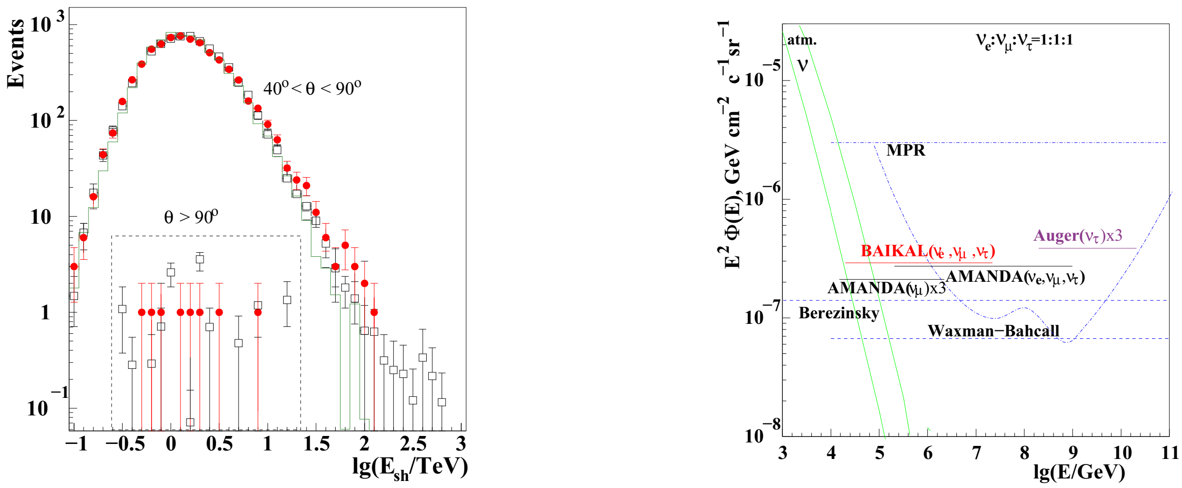

Figure 2: Left panel: Reconstructed cascade energy distribution for data (red dots) and for MC-generated atmospheric muons (boxes); true MC energy distribution given as histogram. Right panel: All-flavor neutrino flux limits and theoretical bounds (see text).

reconstructed cascade energy to select neutrino events. The reconstructed energy distribution of data is shown in Fig.2 (left panel: dots). Eight events were reconstructed as upward going cascades (zenith angle $\theta > 90°$, distribution in dashed box in Fig.2). Also the MC-generated (histogram) and reconstructed (boxes) energy distributions from simulated atmospheric muons are shown in Fig.2 (left panel); 12 upward reconstructed cascade-like events are expected. As seen from Fig.2, within systematic and statistical uncertainties there is no significant excess above the background from atmospheric muons. We introduce the following final neutrino signal cuts on the cascade energy: E_{sh} >130 TeV and E_{sh} >10 TeV for downward and upward going cascades, respectively. With zero observed events and 2.3±1.2 expected background events, a 90% confidence level upper limit on the number of signal events of $n_{90\%}$ =2.4 is obtained. For an E^{-2} behaviour of the neutrino spectrum and a flavor ratio $\nu_e : \nu_\mu : \nu_\tau = 1 : 1 : 1$, the 90% C.L. upper limit on the neutrino flux of all flavors obtained with the Baikal neutrino telescope NT200 is: $E^2\Phi < 2.9 \times 10^{-7}\mathrm{cm}^{-2}\mathrm{s}^{-1}\mathrm{sr}^{-1}\mathrm{GeV}$, for 20 TeV < E_ν < 20 PeV. Fig. 2 (right panel) shows our upper limit on the all-flavor E^{-2} diffuse flux, which is a significant improvement of the earlier obtained limit [7]. Also shown are the limits obtained by AMANDA [8,9] and Pierre Auger Observatory [10], theoretical bounds obtained by Berezinsky [11], by Waxman and Bahcall [12], by Mannheim et al.(MPR) [13], as well as the atmospheric conventional neutrino fluxes [14].

3 Towards a km3 detector in Lake Baikal: the new technology string

The Baikal collaboration pursues since several years a R&D program for a km3-scale neutrino telescope in Lake Baikal. The construction of NT200+ was a first step in this direction. The existing NT200+ is a natural laboratory to verify many new key elements and design principles of the new telescope. A Baikal km3-detector could be made of building blocks similar to NT200+, but with NT200 replaced by a single string, still allowing separation of high-energy neutrino induced cascades from background. It will contain a total of 1700–2300 optical modules (OMs), arranged at 90–100 strings with 16–24 OMs each, and an instrumented length of 350–460m. Interstring distances will be ∼100 m. The effective volume for cascades events above 100 TeV is 0.5–0.8 km^3, the threshold for muons is 10–30 TeV. The most recent km3-milestone was the construction and installation of a new technology prototype string in spring 2008. This string is operating as an integral part of NT200+. Prototype string design and first results are described in detail in [15]. First calibration and verification tests have been successful. MC-optimization for the km3-detector design is going on, as well as studies for optimal trigger technologies.

4 Conclusion

The Baikal neutrino telescope NT200 is working since April 1998. On the road towards a km3-scale neutrino telescope in Lake Baikal, significant upgrades of the detector have been done in spring 2005. Up to now the NT200+ telescope of 5 Mton enclosed volume is in operation, together with a km3-prototype string installed in spring 2008. An analysis of the NT200 data samples for the 1998-2002 seasons has been carried out. With an improved method, based on reconstructed cascade energy, a significantly lowered upper limit for a diffuse astrophysical $(\nu_e + \nu_\mu + \nu_\tau)$ E^{-2}-fluxes has been obtained. The same data samples were analyzed for neutrinos from WIMP annihilation in both the Sun and the Earth. No excess signals were found, therefore upper limits on an additional muon flux from the Sun and the Earth in dependence on the WIMP mass have been set. The results are comparable with other searches.

Acknowledgements

This work was supported in part by the Russian Ministry of Education and Science, by the German Ministry of Education and Research, by the Russian Found for Basic Research (grants 08-02-00432-a, 09-02-10012-k, 07-02-00791, 08-02-00198, 09-02-10001-k, 09-02-00623-a), by the grant of the President of Russia NSh-321.2008-2, by the program "Development of Scientific Potential in Higher Schools" (projects 2.2.1.1/1483, 2.1.1/1539, 2.2.1.1/5901), and by NATO-Grant NIG-9811707(2005).

References

1. V. Aynutdinov et al., *Nucl. Instrum. Methods* A **588**, 99 (2008).
2. V. Aynutdinov et al., *Nucl. Instrum. Methods* A **567**, 433 (2006).
3. V. Aynutdinov et al., *Nucl. Instrum. Methods* A **602**, 14 (2009).
4. Y. Fukuda et al., *Phys. Rev. Lett.* **81**, 1562 (1998).
5. C. De Clercq et al., *Proc. of IDM2008*, Stockholm, 2008; R. Abbasi et. al., arXiv:0902.2460v1; M. Ackermann et. al., *Astropart. Phys.* **24**, 459 (2006)
6. A. Avrorin et al., *Astronomy Letters*, in press.
7. V. Aynutdinov et al., *Astropart. Phys.* **25**, 140 (2006).
8. A. Achterberg et al., *Phys. Rev.* D **76**, 042008 (2007),
9. M. Ackermann et al., *Astrophys. J.* **675**, 1014 (2008).
10. J. Abraham et al., *Phys. Rev. Lett.* **100**, 211101 (2008).
11. V. Berezinsky, arXiv.org: astro-ph/0505220 (2005).
12. E. Waxman and J. Bahcall, *Phys. Rev.* D **59**, 023002 (1999).
13. K. Mannheim, R. Protheroe and J. Rachen, *Phys. Rev.* D **63**, 023003 (2001).
14. L. Volkova *Yad. Fiz.* **31**, 1510 (1980).
15. V. Aynutdinov et al., *Nucl. Instrum. Methods* A **602**, 227 (2009).

Current status of KM3NeT

C.L. NAUMANN for the KM3NeT consortium
CEA Saclay, DSM / Irfu / SPP,
91191 Gif-sur-Yvette, France

One of the most important unsolved questions in modern astrophysics concerns the origin of the high-energy cosmic rays, which were first detected nearly a century ago. A direct identification and study of their sources is only possible using the electrically neutral components of the cosmic radiation, such as photons and neutrinos, which are not deflected by interstellar magnetic fields. For this purpose, the KM3NeT consortium is currently designing a km^3-sized neutrino telescope in the Mediterranean, as a successor to the recently completed ANTARES telescope off the French coast and the design studies NEMO (near Sicily) and NESTOR (Greece). One of the principal tasks is the definition of the detector design - both its layout and the technology used - with the aim of maximising its physics potential within the constraints of financial and technological feasibility. An overview of the current status of this design study is presented, together with some implications for scientific output.

1 Introduction

1.1 Physics Goals

Neutrinos at TeV energies are thought to be produced in large numbers as a by-product in cosmic accelerators, via the decay of pions produced by interactions of highly energetic protons. The fluxes and spectra of these neutrinos depend strongly on the details of the acceleration process, in particular on the relative importance of hadronic acceleration processes (as opposed to leptonic models, which do not imply TeV neutrino production). Thus, the detection of TeV neutrinos from known astrophysical objects would provide a 'smoking gun' for hadronic acceleration, and allow a better understanding of the internal processes. Furthermore, as neutrinos are very deeply penetrating and suffer no deflection, they themselves constitute ideal probes for sources hidden from view in other observational channels. Therefore, neutrino telescopes offer a new window to astrophysics, in particular complementary to the currently highly successful gamma-ray astronomy. However, due to low interaction cross-sections, large detection volumes are needed; recent studies for known HESS sources[1] have shown that interaction volumes of the order of at least 1 km^3 will be required.

1.2 Detection Principle

The detection of TeV energy muon neutrinos in water or ice is performed by measuring the Cherenkov light emitted by muons crossing the detector in a three-dimensional array of photomultiplier tubes (PMTs) distributed in the deep sea or ice. From the distribution of hits in the array, the muon track can be reconstructed, and thus the direction of the neutrino. An important background comes from atmospheric muons; this is reduced by installing the detectors at depths of several kilometers to use the water or ice above for shielding, and by accepting only upgoing tracks, as only the neutrinos can traverse the earth. Thus, a neutrino telescope principally views the sky on the opposite side of the earth.

The choice of target material affects the detector performance: Water has high transparency for blue light and is very homogeneous. However, radioactive ^{40}K decays and bioluminescent organisms create a non-negligible optical background, and biofouling can reduce the transparency of the optical sensors. Ice, on the other hand, is essentially free from intrinsic background light but the strong light scattering on dust particles in ice limits these telescopes' angular resolution.

1.3 Existing Neutrino Telescopes

Around the world, several neutrino telescopes are already operating or under construction. The longest-running of these is the Baikal Deep Underwater Neutrino Telescope, located in Lake Baikal, Siberia, operating since 1993. The two Antarctic neutrino telescopes, AMANDA and IceCube, work in the clear ice of the South Pole. AMANDA has been running since 1996, and is now being superseeded by IceCube (under construction since 2005), which will be the first cubic kilometre sized neutrino telescope. As the location on the South Pole renders the potentially interesting galactic centre invisible to these telescopes, a location in the Mediterranean Sea seems more rewarding. There the construction of the ANTARES neutrino telescope was completed in summer 2008. The size of this detector is roughly 0.01 km^3, comparable with AMANDA. In addition, R&D projects for a cubic-kilometre size neutrino telescope in the Mediterranean have been undertaken: the NEMO project with a test infrastructure and a prototype string off the coast of Sicily and NESTOR, with a detection unit prototype off the Greek coast.

2 The KM3NeT consortium

To better coordinate the construction of such a cubic-kilometre size neutrino telescope in the Mediterranean and to bundle the return of experience from ANTARES, NEMO and NESTOR, the KM3NeT consortium has been founded, currently supported by about 40 laboratories from ten European countries (Cyprus, France, Germany, Greece, Ireland, Italy, the Netherlands, Romania, Spain and the UK). A Design Study was initiated, co-funded by the European Union through the FP6 program. It will end in 2009 with the publication of the Technical Design Report (TDR). The Preparatory Phase (PP), which began in March 2008, will prepare the construction of the detector; this phase is funded by the EU FP7 program. The KM3NeT project has been recognised by the ESFRI (European Strategy Forum on Research Infrastructures) as a *research infrastructure of pan-european interest*, and has been included on the ESFRI roadmap for future large-scale infrastructures[2].

3 Design Optimisation Studies

3.1 Design Goals

The design goals for the KM3NeT telescope have been set in the Conceptual Design Report[3]. A lifetime of at least 10 years is planned, with a construction period of at most 4 years. To be complementary to IceCube but with a better sensitivity in particular to neutrino point sources, several requirements have been formulated: The detector has to be optimised for a focus energy range between roughly 1 TeV and 1 PeV. For pointing accuracy, the angular resolution for muons is required to be better than 0.1°, corresponding to the kinematic deviation between the neutrino and the muon at 30 TeV. Accordingly, a good timing resolution in the order of nanoseconds and the possibility to make use of local triggering schemes between detection units for optical background suppression are important.

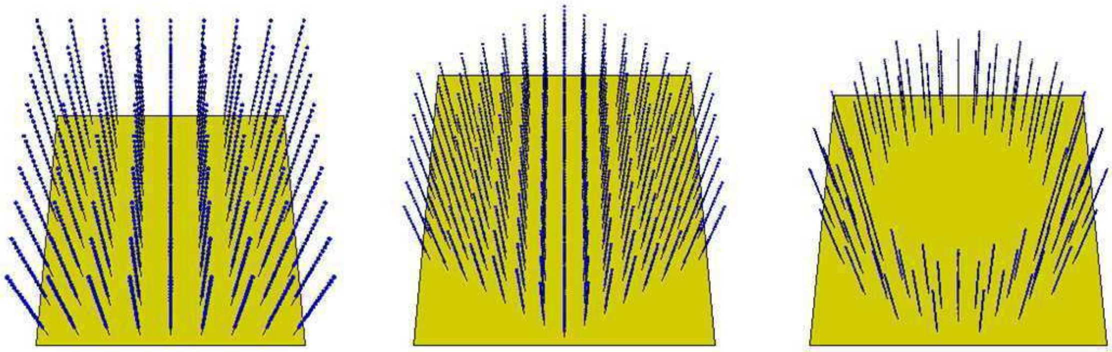

Figure 1: Some sea floor layout options studied for KM3NeT.

For this reason, a large variety of design options has been studied, both for the layout of the detector and for the properties of the detection units. In each case, the design with optimised physics performance has to be found, under the constraints given by the technical and financial feasibility and the time available for the construction of the detector. For this purpose, Monte-Carlo simulation and reconstruction studies are being undertaken, aided by the return of experience from ANTARES, NEMO and NESTOR.

3.2 Detection Units

The basic building blocks of the detection units are the photomultiplier tubes. For KM3NeT, a variety of different options for the type of photomultiplier tubes (PMTs) and their grouping in so-called storeys has been investigated. These options include one-dimensional 'strings' and three-dimensional 'tower' structures with horizontal extentent of several metres. For photodetection, optical modules containing either large PMTs (8 to 10 inches) or groups of up to 31 smaller PMTs (3 inch) are under study. Other options include novel PMTs with higher quantum efficiency or directional sensitivity, or the replacement of traditional PMTs with hybrid photodetectors. As the choice of the detection units affects the efficiency and angular acceptance of the detector, each of these options has to be included in the simulations.

3.3 Detector Layout

In the course of the optimisation study, several possible string or tower layouts have been investigated, including homogeneous designs such as cubes or hexagons and inhomogeneous options such as rings and clusters (figure 1). For each option, the number and the horizontal and vertical distances between detection units has been varied. No single design is optimum for the whole energy range of interest, with denser designs generally performing better at low energies, while at high energies only the total size is important.

3.4 The Reference Detector

While the final detector design has not yet been fixed, a preliminary design has been chosen as a basis for further studies. This so-called 'reference detector' configuration consists of 255 detector lines arranged in a cubic 15x15 grid with a horizontal inter-line distance of 95 metres and 37 storeys per line, with vertical distances of 15.5 metres. Each detector storey contains a single optical module with 21 3-inch photomultiplier tubes. This detector design was used as a basis for the optimisation studies described above. As it can be deemed representative for the KM3NeT designs under study, it allowed the calculation of preliminary values for physics sensitivities, some of which will be presented in the following section.

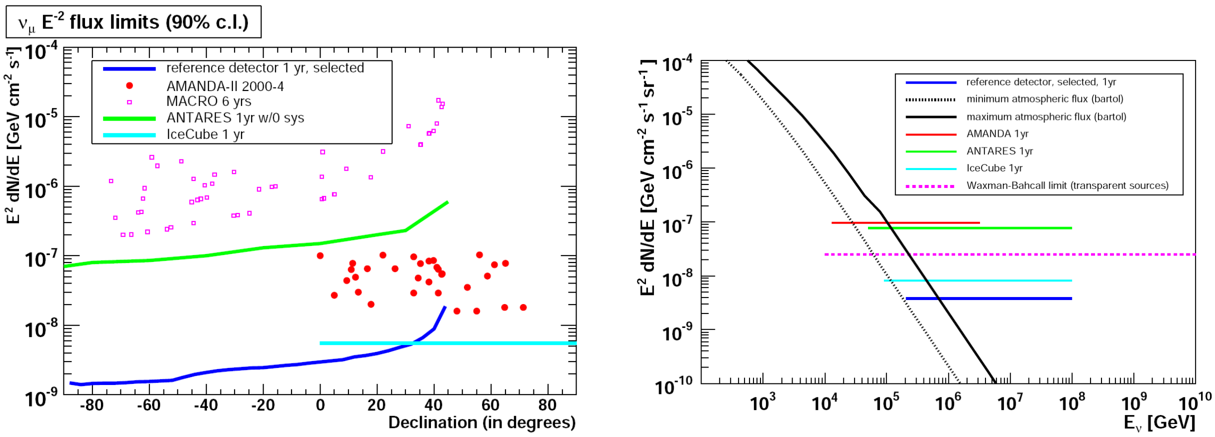

Figure 2: Sensitivity of the reference detector (blue, solid) to point sources as a function of source declination (left). Also shown are the sensitivities of IceCube and other experiments. Right: Sensitivity for diffuse fluxes after 1 year of measurement.

3.5 Preliminary Results

Figure 2 gives preliminary sensitivities of the reference detector for neutrino point sources (left) and diffuse neutrino fluxes (right). The sensitivity for point sources is about a factor 30 better than for ANTARES; due to its larger photocathode area and better angular resolution, it is also better than for IceCube. The predicted sensitivity lies within reach of model predictions for several known cosmic ray sources.

4 Conclusions

The KM3NeT consortium is on its way to the definition of the design of a cubic kilometre sized neutrino telescope in the Mediterranean Sea. The EU-funded Design Study will provide the Technical Design Report in 2009, containing the technical specifications for the KM3NeT infrastructure. Construction is planned to begin shortly afterwards and is expected to be finished after three years. First results from the Design Study containing a reference detector and its expected performance have been published in the Conceptual Design Report[3] in April 2008.

Acknowledgments

This work is supported through the EU-FP6 KM3NeT Design Study Contract No. 011937.

References

1. A. Kappes *et al.*, 'Potential Neutrino signals from Galactic γ-ray sources', *ApJ*, vol. 656, p. 870, 2007, astro-ph/0607286
2. European Strategy Forum on Research Infrastructures (ESFRI), 'Esfri Roadmap'. Available under http://cordis.europa.eu/esfri/home.html
3. The KM3NeT Consortium, *Conceptual Design Report for a Deep-Sea Research Infrastructure in the Mediterranean Sea Incorporating a Very Large Volume Neutrino Telescope*, www.km3net.org/CDR/CDR-KM3NeT.pdf, ISBN 978-90-6488-031-5, 2008.

ATMOSPHERIC MUONS IN ANTARES

C. PICQ
CEA Saclay/IRFU/SPP, 91191 Gif-Sur-Yvette, France
Laboratoire APC Paris 7, Bâtiment Condorcet
10 rue Alice Domon et Lonie Duquet, 75205 Paris Cedex 13, France

Antares in an underwater neutrino telescope entirely deployed in the Mediterranean Sea. The telescope consists of a 3D network of photomultipliers aiming to detect the Cerenkov light emitted by relativistic charged particles. From January to December 2007 the Antares detector was composed of 5 lines, from December 2007 to May 2008, it was composed of 10 lines. The full 12 line detector is completed since May 30$^{\text{th}}$ 2008. In this paper we present a measurement of the muon flux with the 5 line detector and some systematic uncertainties. The muon flux is estimated as a function of the zenith angle and leads to the usual Depth Intensity Relation.

1 Introduction

The determination of the downgoing muon flux is an important check of the ANTARES behavior. As it has been measured by other experiments, it can be used as a check of the knowledge of the detector. Moreover, understanding downgoing muons is important for their rejection, since they constitute the largest background to the upgoing muons signal.

The two main difficulties of this measurement are the detector geometry and the muons multiplicity. The detector was designed to detect upgoing muons (coming from neutrinos): optical modules are looking downward with a 45° angle and the upper part of the sphere is painted in black. Downgoing muons will be detected by a region of the optical module where the acceptance is marginal and subject to large relative uncertainties.

The second difficulty is due to the unknown number of muons arriving at the same time in the detector [1]. When a primary cosmic ray (mostly proton) collides with a nitrogen or an oxygen nucleus, it produces an atmospheric cascade of secondary particles (called "shower" or "bundle" of particles). During its development, the shower produces charged mesons which decay into muons and neutrinos.

These atmospheric muons propagate to the sea level. Only the most energetic ones (E> 500 GeV) can go through more than two kilometers of water and reach the detector. For muon energies above 1 TeV at the detector, the down-going flux is dominated by atmospheric muons, six orders of magnitude above muons from the atmospheric neutrinos. This explains the importance of measuring the muon flux.

2 Muon flux measurement

The measurement of the muon flux is computed according to the relation:

$$\frac{d\phi}{dSdtd\Omega} = \langle m \rangle_{MC}(\cos\theta) \left(\frac{dN(\cos\theta)}{d\cos\theta}\right)_{\text{data}} \frac{1}{\text{Eff}_{\text{reco}}(\cos\theta) \times \mathcal{A}_{Eff}(\cos\theta)} \times \frac{1}{2\pi\Delta T} \tag{1}$$

where the mean multiplicity $\langle m \rangle_{MC} \approx 1.19$, the effective area after filtering $\mathcal{A}_{Eff}$ (figure 1), the reconstruction efficiency $\text{Eff}_{\text{reco}} \approx 95\%$ are estimated from Monte Carlo. We use a simulation based on CORSIKA [2], with a primary composition coming from poly-gonato model [3], the hadronic model is QGSJET0.1. The variable $\left(\frac{dN(\cos\theta)}{d\cos\theta}\right)_{\text{data}}$ is the number of events in the data and $\Delta T \approx 427,2$ hours of data taking during the 5 line period (June 2007).

3 Measurement uncertainties

Statistical uncertainties are negligible. Some systematic uncertainties have been taken into account for this analysis. Each photomultiplier signal is digitized. This signal is saved through its charge and the time of threshold crossing of this signal. The data filtering reacts differently when the value of the threshold is different. This effect will not be taken into account as the trigger efficiency is calculated on Monte Carlo. An error on the charge calibration or on the value of the threshold leads to a difference between Monte Carlo and data. An error on this charge calibration can lead to an effect of ±10% on the measurement of the muon flux.

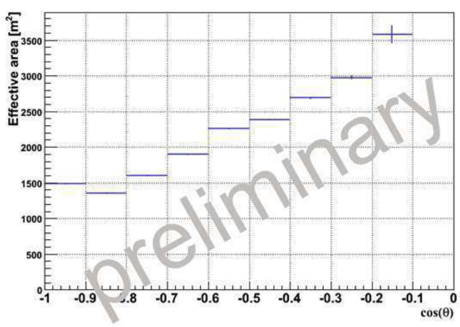

Figure 1: Effective area after filtering for muons with energy above 20 GeV.

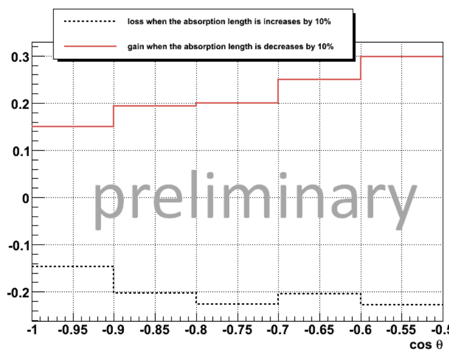

Figure 2: When the absorption length is decreased(increased) by 10%, the muon flux is higher(lower) of ≈ 20%

A second effect comes from the absorption length used in the simulation. The value is around 55 m. In situ measurements show that an uncertainty of 10% is expected. The uncertainty on the muon flux is presented figure 2. When the absorption length is decreased (increased) by 10%, the number of events in the simulation and the effective area decreased (increased): the muon flux is higher (lower) of ≈ 20%.

The last effect taken into account in this measurement is the uncertainty of the angular acceptance of the photo-multiplier. The angular acceptance is the probability of a muon to be detected by our photo-multiplier. The difference between measurements and simulations can be explained by the limited size of the setup used, leading to parasitic light reflexions on the tank wall. The measurement of this angular acceptance is difficult as we are looking at very small effects and we would like to obtain a very high precision. Any parasitic light will produce a huge error on the measurement. This error between the measured angular acceptance and the simulated one leads to a decrease of $\approx 35\%$ on the muon flux when the angular acceptance used in the Monte-Carlo is the measured one. Different measurements of the angular acceptance have been done with two different optical modules. The difference on measured angular acceptance gives an effect by $\approx 20\%$ on the muon flux.

The systematic uncertainties on the muon flux (added quadratically) are estimated individually for each angular bin, and amounts on average to $[-44\%; +33\%]$.

4 Results

The measured muon flux with 5 line data is presented on figure 3. The blue dots represent the measured muon flux and the band the systematic uncertainties on this measurement. The red line is the Okada parameterization [4] which gives the muon flux depending on the depth, the energy and the zenith angle. The threshold of the energy of the muons detected in ANTARES is 20 GeV, as we need 10 hits to reconstruct an event. To know the number of muons crossing the detector, we use a can surrounding the detector. This can has a mean depth of ≈ 1995 m which is the depth used in the Okada parameterization. The green line is a parameterization [5] taking into account the bundle of muons. The measurement is in agreement with both parameterizations within measurement uncertainties.

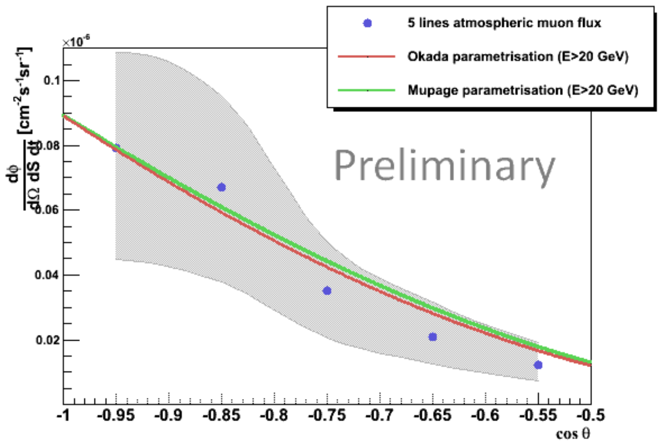

Figure 3: Muon flux versus the zenith angle at a mean depth of ≈ 1995 m for muon energy above 20 GeV.

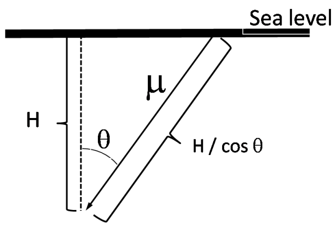

Figure 4: Method to verticalize the flux

To compare with other experiments, we computed the vertical flux at different depths. For a detection depth H (figure 4), the slant depth of the muon is $H/\cos\theta$. In addition the zenith dependence of the muon flux at sea level is proportional to $\sec\theta$. To transform the muon flux depending on zenith angle to a vertical flux depending on slant depth, we use the relation:

$$I_v\left(\frac{H}{\cos\theta}\right) \approx I\left(\Delta\theta, H\right) \times \cos\theta \tag{2}$$

This formula can be used up to $\theta = 60°$ where Earth curvature effects can be neglected.

Figure 5 presents the result obtained with the 5 line detector. It can be compared to other results from Amanda [6], Dumand [7] and Baïkal NT-36 [8]. Our results are in agreement with these

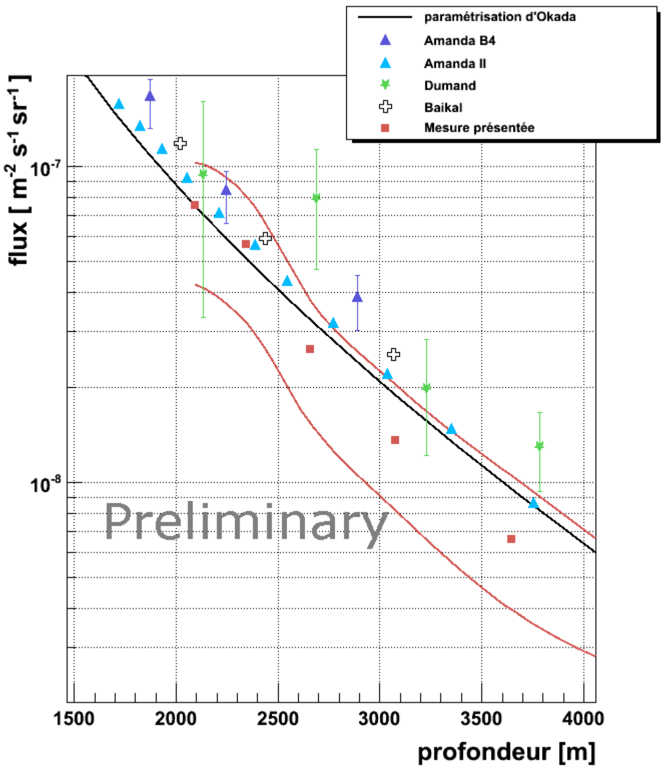

Figure 5: Vertical flux at different depths for ANTARES 5 line compared with the results of other experiments.

measurements so the global understanding of the detector is satisfactory. However, systematic uncertainties are quite large and we are currently working to decrease them: new measurements of the absorption length and of the angular acceptance of the optical module.

5 Conclusion

In deep sea neutrino telescopes, the upgoing muon sample (from neutrinos) is polluted by a fraction of muons coming from atmospheric bundles. In this study, we presented a measurement of the muon flux in agreement with worldwide data, showing a satisfactory understanding of our detector and of the muons coming from atmospheric showers.

References

1. Picq C., 43^{th} *Rencontres de Moriond: EW Interactions and Unified Theories, 2008*
2. *Heck D. et al, Forschungszentrum Karlsruhe Report FZKA 6019 (1998)*
3. *Horandel J. R.,* ICRC Report *, (2001).*
4. *Okada, Atsushi,* ICRC Report *, 319-94-1 (1994).*
5. *Becherini Y. et al,* Astropart. Phys. **25***, 1-13 (2006).*
6. *Andrés E. et al,* Astropart. Phys. **13***, 1 (2000), Desiati P.,Bland K. et al,18732003.*
7. *Babson J. et al,* Phys. Rev. *D* **42***, 3613 (1990).*
8. *Belolaptikov I.A. et al,* Astropart. Phys. **7***, 263 (1997).*

POINT-LIKE SOURCE SEARCH WITH THE 5-LINE ANTARES DATA

KATIA FRATINI
INFN-Genova,
via Dodecaneso 33, Genova, Italy

ANTARES, the world's largest operational underwater neutrino experiment, is taking data with its complete layout since the end of May 2008. During the year 2007 it has been operating with 5 active detector lines out of 12. Results of the point-like search analyses performed on the data collected in this period are presented, showing that even for this first small data sample, the limits are competitive with previous experiments looking at the Southern hemisphere.

1 Introduction

The search for high energy (10 TeV - 100 PeV) neutrino sources is one of the most interesting challenges faced in the astroparticle physics field. It is strongly linked to the problem of the origin of the cosmic rays: in fact, the discovery of the neutrino production from a source is the only clear evidence for the source to be a cosmic ray emitter [1].
The ANTARES experiment and its main physics results have already been presented in this Conference [2]. Here, the point-like source search carried out by the ANTARES collaboration is described. The general approach is to perform a blind analysis of the 5-line data, which consists in scrambling the right ascension coordinate. Two kinds of search have been developed: the fixed source search (Sec. 5), where the direction of the source is assumed to be known, and the all sky search (Sec. 6), where the whole sky is probed. Two different methods, previously optimised by calculating the sensitivity as a function of the declination, have been used in these searches for point-like sources: the cone method (Sec. 3) and the Expectation Maximisation (EM) method (Sec. 4): the first one has been used as a cross-check of the second one, which is more powerful, as expected from being an unbinned method [3]. The results obtained after unblinding the data are discussed in Sec. 5 and Sec. 6.

2 Data selection

In 2007 the duty cycle was $\sim 80\%$. After excluding high bioluminescence periods, the number of effective data taking days is 140. The data are selected by applying two cuts: a cut on the elevation, $\Theta < -10^\circ$, to reduce further the contamination from the atmospheric muons, and a cut on a reconstruction quality parameter Λ [2], $\Lambda > -4.7$. In Figure 1(a) the number of events selected as a function of the cut value on the Λ parameter shows that the applied cut selects 96 events. In figure 1(b), the distribution of the elevation, resulting after applying the cut on Λ, for real (black line), MC atmospheric muon (red line) and MC neutrino (green line) data, shows that the final selection results in a high purity sample (~ 80 %). In the region selected there is a good agreement between real and MC data. The distribution of the time residuals of the hits used in the reconstructed tracks (Fig. 1(c)) also shows a good agreement between real (black line) and MC (blue histogram) data. The angular resolution obtained at high energy depends on the reconstruction algorithm used which is based on the time residuals: the good agreement shown, supports our estimation of the angular resolution.

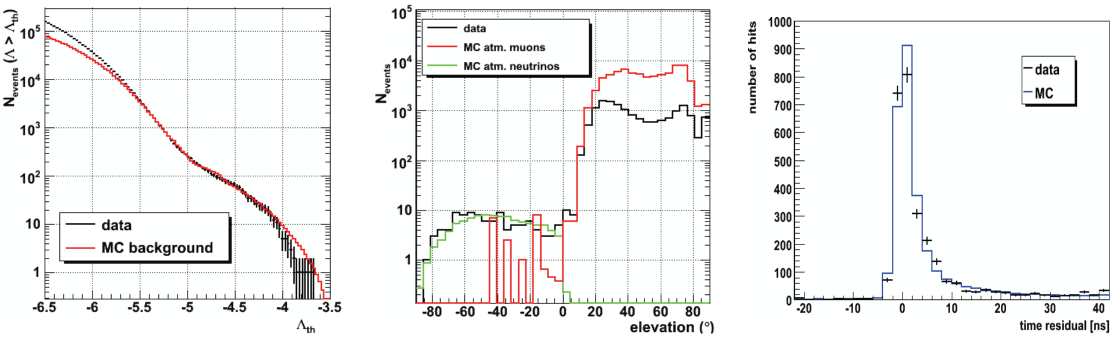

(a) (b) (c)

Figure 1: Integrated distribution of the Λ parameter, an indicator of the reconstruction quality, for real (black line) and MC (red line) data (a). Elevation distribution, for real (black line), MC atmospheric muon (red line) and MC atmospheric neutrino (green line) data when $\Lambda > -4.7$ (b). Time residual distribution of the hits used in the reconstructed tracks for real (black line) and MC (blue line) data.

3 The cone method

The cone method provides the source to be observed inside a cone having the centre in the source position and the opening angle chosen in order to minimise the sensitivity to the source flux (optimum cone aperture). In the Feldman and Cousin framework [4], the sensitivity is defined as the average upper limit at a given confidence level (90%) over all the possible experiments with number of expected background events n_b and no signal. Assuming the background follows a Poisson distribution, the average upper limit on the number of observed event is:

$$\bar{\mu}_{90}(n_b) = \sum_{n_{obs}=0}^{\infty} \mu_{90}(n_{obs}, n_b) \cdot \frac{(n_b)^{n_{obs}}}{(n_{obs})!} \exp(-n_b) \tag{1}$$

where n_{obs} is the total number of detected events and $\mu_{90}(n_{obs}, n_b)$ the set upper limit, for each experiment. The average upper limit on the flux is:

$$\bar{\Phi}_{90}(E, \Theta) = \frac{\bar{\mu}_{90}(n_b)}{n_s} \cdot \Phi(E, \Theta) \tag{2}$$

where n_s is the number of signal events expected from a source emitting the flux $\Phi(E, \Theta)$, which is supposed to be a power law with spectral index $\gamma = -2$. The ratio MRF $= \frac{\bar{\mu}_{90}(n_b)}{n_s}$ is called Model Rejection Factor. The method consists in the minimisation of this ratio as a function of the cone aperture, with the aim of finding the optimum cone which minimises the sensitivity. In order to calculate the MRF, n_b and n_s have been estimated from the angular error distribution, inferred by MC simulation of an energy spectrum like E^{-2} and real scrambled data respectively, for each declination band. The optimum cone aperture ranges from $3\,^\circ$ to $4.5\,^\circ$. Figure 2(a) (red line) shows the sensitivity as a function of the declination.

4 The Expectation-Minimisation (EM) method

The identification of signal events coming from a source above the background level from the atmospheric neutrino events can be performed by a clustering analysis, which looks for structures in the data. In the framework of the mixture model method [5], the probability density function for the ANTARES data can be described by the sum of two components:

$$p(\mathbf{x}) = \Pi_{BG} P_{BG}(\delta) + \Pi_S P_S(\mathbf{x}; \mu, \mathbf{\Sigma}) \tag{3}$$

where $\mathbf{x} = (\delta, RA)$ is the event position and Π_{BG} and Π_S are the fractions of the background and signal component respectively. The pdf of the background component P_{BG} is inferred by the real scrambled data and the pdf of the signal one is supposed to be a two-dimension Gaussian function, with μ and Σ being the mean and covariance vector respectively. In this description, the values ($\Psi_1^{(m)}$) of the parameters left floating in the fit which maximise the likelihood function related to our data sample are calculated by means of the EM algorithm [5]. The two possible hypotheses, signal + background (M_1) and the background-only (M_0), are compared using the Bayesian Information Criterion (BIC), which basically uses the maximum likelihood ratio of the models with a penalty that takes into account the number of free parameters ν_1 weighed by the number of the events n in the data sample {x}:

$$BIC = 2\log(p\{x\})|\Psi_1^{(m)}, M_1) - 2\log(p\{x\})|M_0) - \nu_1 \log(n) \tag{4}$$

Each experiment is characterised by a BIC value. In order to calculate the sensitivity, the average value of the background-only BIC distribution, calculated over a set of scrambled real data samples, has been chosen as the BIC observed value: BIC_{obs}. The signal hypothesis which produces a probability equal to 90% of obtaining a BIC value equal or higher than BIC_{obs} has been taken as the sensitivity (Fig. 2(a) blue line).

5 Fixed point-like source search

25 sources, listed in table 1, have been selected among the most promising neutrino source candidates in the ANTARES field of view for the 5-line point-like source analysis.

Table 1: List of the selected sources, their position and the calculated p-value.

Source	DECL	RA	$pvalue_{bin}$	$pvalue_{unbin}$
PSR B1259-63	-63.83	195.70	1	1
RCW 86	-62.48	220.68	1	1
ESO139-G12	-59.94	264.41	1	1
HESS J1023-575	-57.77	155.82	0.062	0.004
Cir X-1	-57.17	230.17	1	1
HESS J1614-518	-51.82	243.58	0.086	0.088
PKS 2005-489	-48.82	302.37	1	1
GX 339	-48.79	255.70	1	1
RX J0852.0-4622	-46.37	133.00	1	1
Centaurus A	-43.02	201.36	1	1
RX J1713.7-3946	-39.75	258.25	1	1
PKS 0548-322	-32.27	87.67	1	1
H 2356-309	-30.63	359.78	1	1
PKS 2155-304	-30.22	329.72	1	1
Galactic Center	-29.00	266.42	0.140	0.055
1ES 1101-232	-23.49	165.91	1	1
W28	-23.33	270.42	1	1
LS 5039	-14.82	276.56	1	1
1ES 0347-121	-11.99	57.34	1	1
HESS J1837-069	-6.95	279.41	1	1
3C 279	-5.79	194.05	0.11	0.03
RGB J0152+017	1.79	28.17	1	1
SS 433	4.98	287.96	1	1
HESS J0632+057	5.80	98.24	1	1
IceCube HotSpot	11.00	153.00	1	1

The p-value, which is the probability of the background to produce the measured (or higher) value for the observable (BIC for the EM method or n_{obs} for the cone one), has been calculated for each source. No statistically significant excess has been found. The lowest value corresponds to a pre-trial p-value of 2.8σ found with the EM method. It is expected in 10% of the experiments when looking at 25 sources (post-trial probability). In the case of the EM method, the upper limits (Fig. 2(a) blue square) come out considering the signal hypothesis which produces a probability equal to 90% to obtain a BIC value equal or higher than BIC_{obs}, calculated on the real data sample after unblinding it. In the case of the cone method the upper limits (Fig. 2(a) red square) are given by $\mu(n_{obs}, n_b)$ defined in Eq.1.

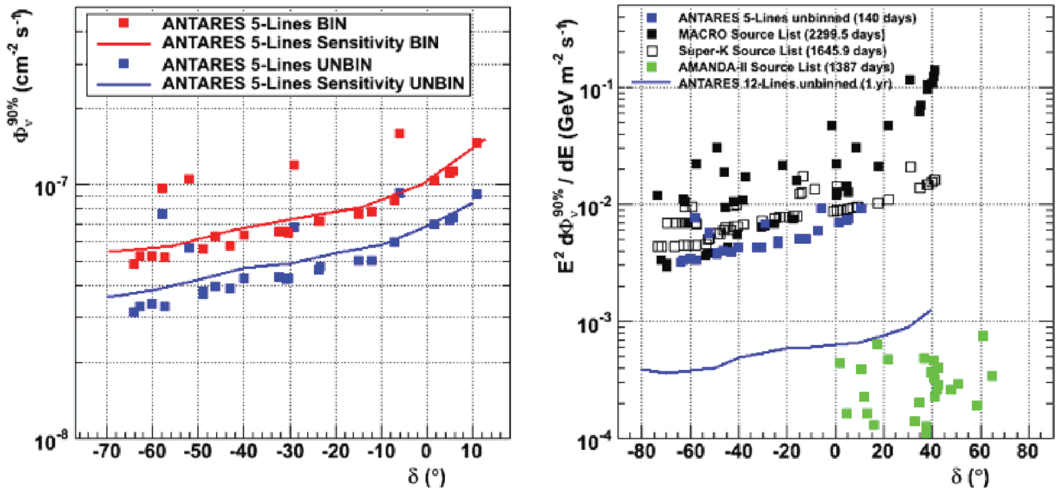

(a) (b)

Figure 2: The sensitivity (line) and the upper limits (square) calculated with the 5-line ANTARES data by means of the cone (red) and EM (blue) method respectively (a). Comparison of the ANTARES 5-line data upper limits with those from other experiments: MACRO, AMANDA, Super-K. The ANTARES sensitivity for the 12-line detector in one year of data taking is also shown (b). The sensitivity and the upper limits are calculated in terms of the integrated flux in plot (a) and of the differential flux in plot (b).

6 All sky point-like source search

In this kind of search, sources are looked for in the whole sky, and no assumption on their position is made. In the case of the EM method, a pre-clustering algorithm searches for event accumulations within a cone with aperture $5\,^\circ$. The center of gravity of each identified cluster has been used as initial value of the position of the source candidate and finally the cluster with the highest significance (evaluated respect to the only background BIC distribution) has been selected. In the ANTARES data sample the highest BIC value found is $BIC_{obs} = 1.4$, corresponding to a p-value $= 0.3$ (1σ excess) in the position $\delta = -63.7\,^\circ$ $RA = 243.9\,^\circ$.

7 Conclusion

The point-like source search on the 5-line data has been performed by means of two different methods: EM method and the cone method. The first one is more powerful: the second one has been used as a cross check. The sensitivity as a function of the declination has been calculated for both methods: the EM one, in average, is 27% more sensitive than the cone one. Unblinding the 5-line data did not show any statistically significant excess in both the fixed source search and the all sky search. The upper limits set with less than a half of the detector and in only 140 days of data taking are competitive with those calculated by other experiments which have run for a much longer time in the Northern hemisphere.

References

1. F. Halzen *et al*, *Rep. Prog. Phys.* **65**, 1025-1078 (2002).
2. N. Cottini, these proceedings.
3. J. Braun *et al*, *Astropart. Phys.* **29**, 299-305 (2008).
4. G. Feldman and R. Cousins *Phys. Rev.* D **57**, 3873 (1998).
5. J.A. Aguilar and J.J. Hernandez-Rey, *Astropart. Phys.* **29** **2**, 117-124 (2008).

Update of neutrino flux limit from the Pierre Auger Observatory

D. Góra[a] for the Pierre Auger Collaboration
Karlsruhe Institute of Technology (KIT), D-76021 Karlsruhe, Germany
Institute of Nuclear Physics PAN, ul. Radzikowskiego 152,31-342 Cracow, Poland

The surface detector array of the Pierre Auger Observatory is sensitive to ultra high energy neutrinos. The properties of such showers that can start deep in the atmosphere are very different at ground level from those of showers initiated in the upper atmosphere by protons or nuclei. The neutrino events would have a significant electromagnetic component leading to a broad time structure of detected signals in contrast to nucleonic-induced showers. In this paper we study the signature of up-going ν_τ-induced showers and we report the recent result of the Observatory: an upper limit on the diffuse flux of up-going ν_τ. Assuming an E^{-2} differential energy spectrum the limit at 90% C.L. is $E^2 dN_{\nu_\tau}/dE < 1.3 \times 10^{-7}$ GeV cm^2 s^{-1} sr $^{-1}$ using the data collected between 1 January 2004 and 31 August 2007. Although the largest contribution to the total expected event rate comes from up-going ν_τ, the contribution of down-going neutrinos can not be neglected. Down-going neutrinos of any flavour may interact through charged and neutral current. Simulations suggest that a good identication criterium requires broad signals in time in the first triggered tanks of the event.

1 Introduction

The detection of ultra high energy (UHE) cosmic neutrinos, above 1 EeV, is important as it may allow to identify the most powerful sources in the Universe. In general, a low incoming flux of neutrinos is expected. Due to their low interaction probability, neutrinos need to interact with a large amount of matter in order to be possibly detected. One of the detection techniques is based on the detection of extensive air showers (EAS) in the atmosphere. Propagating through the Earth only the so-called Earth skimming tau neutrinos may initiate detectable air showers above the ground [1]. In this case tau neutrinos may interact within the Earth and produce charged leptons which in turn decay into neutrinos with lower energies. Since the interaction length for the produced tau lepton is a few kilometers at the energy of about 1 EeV, the leptons produced close to the Earth's surface may emerge from the Earth, decay above the ground and produce EAS potentially detectable by a large ground detector [2,3].

In this paper we study the signature neutrino induced showers in the case of the surface detector (SD) of the Pierre Auger Observatory [4] and we report about one of the most recent results of the Observatory: an upper limit on diffuse flux of tau neutrinos [5].

2 Identifying and discriminating ν-induced showers

One of the experimental challenges for the Auger Observatory is to discriminate neutrino-induced showers from the background of showers initiated by cosmic rays. The underlying concept

[a] The author gratefully acknowledge the financial support by the HHNG-128 grant of the Helmholtz association and the Ministry of Science and Higher Education under Grant 2008 No. NN202 127235.

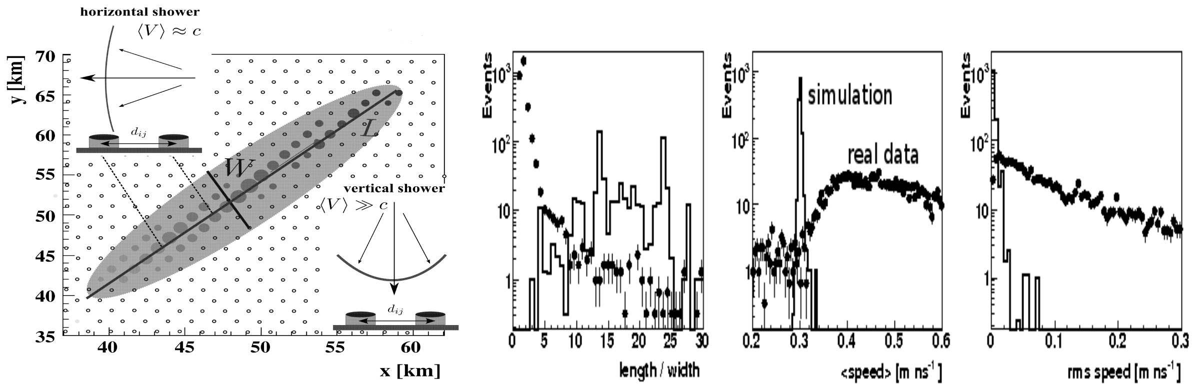

Figure 1: (Left panel) Sketch of length (L) over width (W) of a footprint and determination of the apparent velocity v_{ij} between two stations; (three right panels) distribution of discriminating variables for showers initiated by τs decaying in the atmosphere;

of neutrino identification is rather straightforward. Whereas proton or nuclei and photons interact shortly after having entered the atmosphere, neutrinos may penetrate undisturbed a large amount of matter and generate showers close to the surface array consisting of 1600 water-cherenkov detectors with 1.5 km spacing. The differences between showers developing close to the detector – so-called young showers – and showers interacting early in the atmosphere – old showers – is getting more and more pronounced as we consider larger zenith angles. In case of showers initiated by protons and nuclei, which interact soon after entering the atmosphere, only high–energy muons can survive for high energy angles. As a result, the detected showers show a thin and flat front which leads to short detected signals ($\sim$ 100 ns). In case of young neutrino-induced showers a significant electromagnetic component is present at the ground as well. The shower front is curved and thick and leads to broad signals, lasting up to a few microseconds.

The first step towards identification of showers induced by Earth-skimming ν_τ implies searching for very inclined young showers. Young showers are expected to trigger detector stations with broad signals[3]. Such signals are clearly broad signals and counting them can help in identifying young showers. Then the topology of the footprints is important ingredient[3]. Elongated footprints identify inclined showers, Figure 1 (left panel). A tensor of inertia was calculated to evaluate the length (L) over the width (W) of the patterns on ground. The positions of the stations were weighted by their signals. The elongation of a footprint is defined as L/W. The additional parameter which was taken into account is the so-called mean apparent velocity of a shower on the ground, $\langle V \rangle$[b]. The mean apparent velocity is expected to be compatible with the speed of light for quasi-horizontal showers, within its statistical error $\sigma_{\langle V \rangle}$. In Figure 1 (right panels), the distributions of these discriminating variables for small fraction of the real data (used without any preselection cuts) and simulated τ induced showers are shown. We can see that neutrino candidates are required to have elongated patterns on the ground with ratio $L/W > 5$ and the average speed is expected to be very close to the speed of light, in the range (0.29, 0.31) m ns^{-1} with r.m.s. scatter below 0.08 m ns^{-1}. Finally contiguous configurations of selected ToTs complete the expected picture of young ν-induced shower footprints[3].

3 Results: Neutrino exposure and flux limit

Data from January 2004 until August 2007, which corresponds to about 1 year from the completed surface detector, have been analysed. Over the period analyzed, no candidate events were found that fulfilled the selection criteria. Based on this, the Pierre Auger Observatory data can

[b]The mean apparent velocity is given by averaging the apparent velocity, defined as $v_{ij} = \frac{d_{ij}}{\Delta t_{ij}}$ where d_{ij} is the distance between the couples of stations, projected onto the direction defined by the length of the footprint, and Δt_{ij} the difference in their signal start times.

be used to set a limit on the diffuse flux of UHE ν_τ. For this purpose the exposure of the detector must be evaluated. The total exposure is the time integral of the instantaneous aperture which has changed as the detector has grown while it was being constructed and set into operation.

The expression for the exposure can be written as

$$\mathrm{Exp} = \int_\Omega \mathrm{d}\Omega \int_0^{E_\nu} \mathrm{d}E_\tau \int_0^\infty \mathrm{d}h_c \frac{\mathrm{d}^2 N_\tau}{\mathrm{d}E_\tau \mathrm{d}h_c} P_\tau, \tag{1}$$

where $d^2N_\tau/dE_\tau dh_c$ is the flux of emerging τs after folding with the probability of tau decaying in the atmosphere and $P_\tau(E_\tau, h_c) = \int_T \mathrm{d}t \int_S \mathrm{d}S \, \cos\theta \, \epsilon(E_\tau, h_c, x, y, t)$, where $\epsilon(E_\tau, h_c, x, y, t)$ is the probability to identify a τ lepton (identification efficiency) which depends on the energy E_τ, the altitude above ground of the central part of the shower h_c defined at 10 km after the decay point, the position (x, y) of the shower core in the surface S covered by the array, and the time t through the instantaneous configuration of the array. The θ and Ω are the zenith and solid angles.

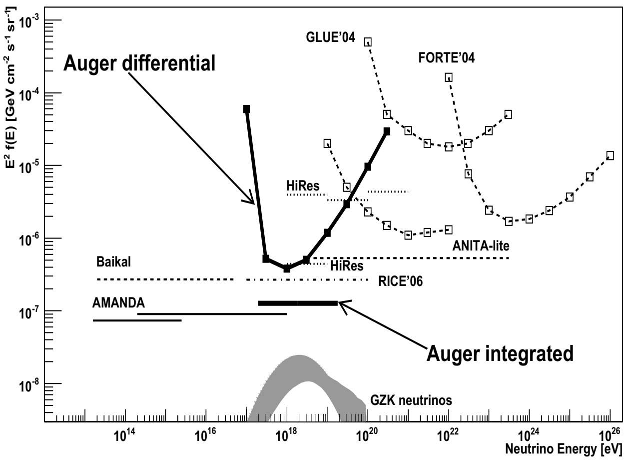

Figure 2: Limits at 90% C.L. for a diffuse flux of ν_τ from the Pierre Auger Observatory along with limits from other experiments, see References in[5].

Calculating the flux limit requires physical quantities that have not been experimentally measured in the relevant energy range, namely, the interaction cross-section, the energy loss, and the polarization. The influence of different cross sections on the calculated exposure is about 15%. The differences in existing calculations for the energy losses [7] leads to 40% uncertainty on calculated exposure and the conservative estimation of the systematic uncertainty for a tau polarization results in a 30% difference of the exposure. Other systematic uncertainties come from additional matter (Andes) around the site of the Pierre Auger Observatory (18%) and from (25%)[5] uncertainties of the EAS MC generator.

Finally, on the basis of the exposure calculations, the limit for an injected spectrum $K \times \Phi(E_\nu)$ with a known shape $\Phi(E_\nu)$ was calculated. The 90% C.L. on the value of K, according to Ref. [8] is $K_{90\%} = 2.44/N_{WB}$ for negligible background and zero neutrino events observed by the Auger Observatory in case of the $f(E_\nu) \sim E_\nu^{-2}$ differential flux of ν_τ. In such a case the upper limit for tau neutrinos is

$$E_\nu^2 \Phi(E_\nu) < 1.0 \left(^{+0.3}_{-0.5}\right) \times 10^{-7} \ \mathrm{GeV\ cm^{-2} s^{-1} sr^{-1}}. \tag{2}$$

In Figure 2 the integrated limit is shown along with the typical spectra of astrophysical neutrinos[9] (GZK neutrinos). Alternatively, a differential sensitivity (being proportional to the inverse of the acceptance, i.e. $2.3/(E_\nu \, Exp(E_\nu))$ is plotted. The best sensitivity is reached at about 1EeV.

4 Down-going neutrinos

The surface detector of the Pierre Auger Observatory is also sensitive to down-going neutrinos in the EeV range and above[6]. Down-going neutrinos of any flavour may interact through both charged (CC) and neutral current (NC) interactions producing hadronic and/or electromagnetic showers. In case of NC reaction the fragments of a target nucleus induce a pure hadronic shower with a small fraction (about 20%) of energy transfer to EAS. In CC ν_e interaction the rest of

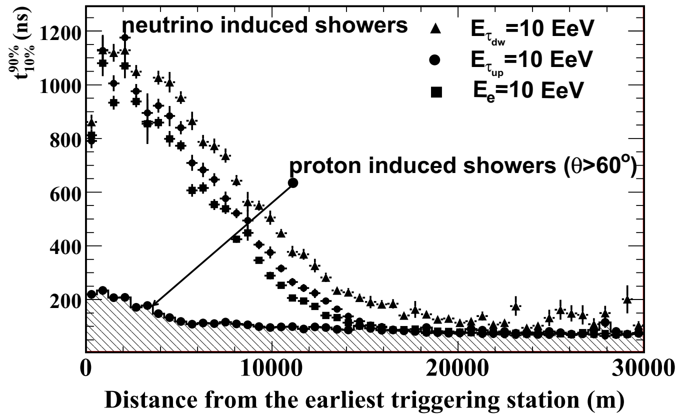

Figure 3: Average signal duration of the station versus distance from earliest triggering station. The $t^{90\%}_{10\%}$ is the time when integrated station signal takes rise from 10% to 90% of its maximum.

energy goes to an additional electromagnetic shower, making the ν_e CC induced showers the main contribution to the expected event rate. In CC ν_τ interaction, if the τ lepton decays in flight a fraction of its energy is also converted into a shower.

The criterium to identify young, inclined, down-going showers consists of looking for a broad time signals as in the case of up-going neutrinos, at least in the early region, i.e. in those tanks triggered before the shower core hits the ground [6]. This has been confirmed by simulations of ν-induced showers as is shown in Figure 3. The signal for ν-showers is broader around the position of the maximum of the shower development. Broader signals are expected to last about 1000 ns, while the duration decreases to a value of about 150 ns downstream in the latest stations which are hit by the muonic tail of the shower development. For hadronic showers with $\theta > 60^\circ$, the expected duration of the signals is almost constant along the shower development at ground with an average value of about 150 ns.

Preliminary MC simulations show that the ratio between expected rate for down- and up-going neutrino events is about 50%. This demonstrates that down-going neutrino induced showers contribute significantly to the expected event rate. The search for down-going showers and a precise calculation of the expected contributions from different interactions channels to the total rate is in progress.

5 Conclusions

To conclude, the dataset from January 2004 until August 2007, is used to present an upper limit on the diffuse incident ν_τ flux. The Pierre Auger Observatory will keep taking data for about 20 years over which the bound will improve by over an order of magnitude if no neutrino candidate is found.

References

1. A. Letessier-Selvon, AIP Conf. Proc. 566 (2001) 157–171; D. Fargion, Astrophys. J. 570 (2002) 909–925.
2. X. Bertou et al., Astropart. Physc. 17 (2002) 183.
3. P. Billoir, O. Blanch Bigas, Nucl. Phys. Proc. Suppl. 168 (2007) 225–231.
4. J. Abraham, et al., Nucl. Instrum. Meth. A523 (2004) 50–95.
5. J. Abraham, et al., Phys. Rev. Lett. 100 (2008) 211101.
6. J. Alvarez-Muniz, Proc. of the 30th Intern. Cosmic Ray Conference, Merida, Mexico.
7. E. Bugaev et al., Astropart. Phys. 21 (2004) 491; S. I. Dutta et al., Phys. Rev. D72 (2005) 013005; C. Aramo, et al., Astropart. Phys. 23 (2005) 65–77.
8. G. J. Feldman, R. D. Cousins, Phys. Rev. D57 (1998) 3873–3889.
9. R. Engel et al., Phys. Rev. D64 (2001) 093010; D. Allard et al., JCAP 0609 (2006) 005.

An Overview of the ANITA Experiment

E. W. Grashorn[1], for the ANITA Collaboration[2]
[1] *Center for Cosmology and AstroParticle Physics, Ohio State University, 191 W. Woodruff Ave., Columbus, OH 43210, USA*
[2] *http://www.physics.ohio-state.edu/ grashorn/anita/Authors.pdf*

The ANITA (ANtarctic Impulsive Transient Antenna) experiment is a balloon-borne, broadband antenna array flown over the Antarctic continent. It is designed to detect radio Cherenkov emission from UHE astrophysical neutrino (E> 10^{12} MeV) interactions in the ice below. ANITA 1 completed a 35 day flight during the Austral summer of 2006-2007. ANITA 2, with increased sensitivity over ANITA 1, was launched December 20, 2008 and flew for 30 days. Initial analysis of ANITA 1 data shows that no neutrino candidates were detected with no physics background. In the absences of a signal, an upper limit was set on the high energy neutrino flux that begins to eliminate the highest cosmogenic neutrino models.

1 Introduction

The detection of cosmogenic neutrinos has profound astrophysical implications. The sun produces a steady flux of MeV neutrinos [1], and it is expected that it is an ordinary star. Supernovae have been shown to produce a burst of 10 MeV neutrinos [2,3] that precede the optical burst; the total energy of the neutrino flux is orders of magnitude higher. Gamma ray bursts (GRBs) are expected to produce an enormous, beamed burst of $10^8 - 10^{11}$ MeV neutrinos in coincidence with the burst of gamma rays [4]. The detection of such neutrinos would confirm the hadronic nature of the GRB jets. The interaction of Ultra-High Energy Cosmic Rays with the Cosmic Microwave Background (CMB) is expected to produce neutrinos [5] with energy greater than 10^{12} MeV, the guaranteed cosmogenic neutrino flux. The detection of these neutrinos would indicate that the GZK process [6,7] is responsible for the decrease in UHECR flux above 6×10^{13} MeV, and a measurement of their flux could give an indication of the UHECR composition. A *lack* of these neutrinos could mean that Lorentz invariance is wrong, or could imply new physics [5].

Since neutrinos are neutral, they point back to a distant origin through galactic and intergalactic magnetic fields much better than charged cosmic rays and are not subject to the same short GZK horizon. Neutrinos only interact weakly, so they can travel cosmological distances before annihilating with the cosmic microwave background radiation, unlike the very high energy gamma rays. As such, neutrinos are cosmological probes.

Neutrinos rarely interact, so massive detectors are required to observe them. Cubic kilometer water (ice) detectors are being built, but the expected fluxes are so low that these detectors might have to run for many years before detecting even a single cosmogenic neutrino. The flux of neutrinos could be as small as one per km^2 per *week*. The ANITA payload flies 35 Km above the Antarctic ice, which allows it to observe nearly the entire $\sim 10^6$ km^3 of the continent, though geometry reduces the effective aperture to $\sim 10^3$ km^{3}sr. ANITA is designed to detect broadband radio pulses (200-1200 MHz) that arise from the Cherenkov radiation caused by the charge asymmetry induced by the interaction of a neutrino in the ice[8]. Positrons are annihilated, and electrons are scattered into the shower, which results in a 20% charge excess. The charge excess produces a fast, impulsive RF signal. This is known as the Askaryan effect [9]. Though it was introduced in the 1960s, little work was done with it until the 1990s. The Askaryan effect has been confirmed for sand, salt and ice in laboratory experiments with test beams at the Stanford Linear Accelerator Center [10,11,12].

2 ANITA Technology

The broadband receivers used by ANITA are dual polarization, quad ridged feedhorn antennas canted 10° downward to observe the ice below. There are 32 antennas arranged in two rows (the antennas in the top row are vertically offset by one antenna width; see Fig. 1) to observe the full 360° in azimuth for ANITA 1; ANITA 2 has an additional lower row of eight antennas (Fig. 1). Each antenna has an effective field of view of 45°, and each antenna is separated by 22.5°, so there is full overlap with adjacent antennas. Each antenna in the top row is aligned with an antenna in the bottom row, facing a patch of ice at the same phi-angle; this is referred to as a "phi sector".

Figure 1: The ANITA 2 payload, on the hook in Antarctica. ANITA 1 lacked the lowest row of eight feedhorns, but appeared similar in every other way.

The impulsive broadband signals for which ANITA is searching require fast giga-sample (GSa) digitization, which are commercially available, relatively inexpensive, but consume as much as 10 W/ch. Balloon borne devices, powered by the sun and on-board batteries, have a limited power budget. To overcome this problem, an ASIC Switched Capacitor Array was developed by members of the ANITA team [13]. It continuously samples the raw RF waveform, but is not read out until the fulfillment of a trigger condition. This method uses an order of magnitude less power of a commercial GSa digitizer and reduces the processing load and data rate considerably.

When a waveform is received by the system, it is split and part of the signal is sent to a hardware trigger unit, where it is filtered into four sub-bands (ν_c = 265, 435, 650 and 900 Hz) for each polarization. This results in a total of eight trigger channels for each antenna. There are three levels of trigger to reject non-directional thermal backgrounds (the level 1 trigger was ANITA 1 only).

- *Level 1 trigger.* The first level trigger requires that the impulse exceeds the SNR in three of eight trigger channels on a particular antenna. The level 1 trigger rate is about 150 kHz.
- *Level 2 trigger.* The second level trigger requires a coincidence between two L1 triggers in the same ring, which is the expected result of a true neutrino because the antennas have overlapping acceptance regions. The level 2 trigger rate is about 40 kHz
- *Level 3 trigger.* The highest level trigger requires coincidence between L2 triggers in the same phi-sector. The level 3 trigger rate is about 5 Hz, and provides a "heartbeat" that the instrument is alive and still communicating properly.

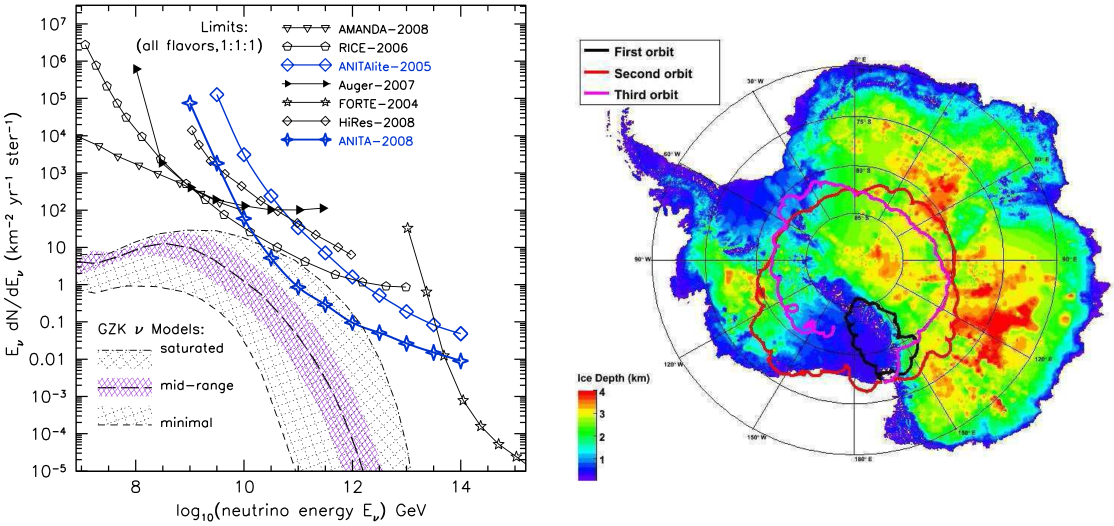

Figure 2: **(L)** The ANITA 1 ultra-high energy neutrino flux limits as a function of energy, the first flux limits to restrict theoretical GZK neutrino predictions. **(R)** The ANITA 2 flight path. More time was spent over deep ice (E. Antarctica) and less time over the South Pole than ANITA 1.

The probability of a thermal fluctuation reconstructing coherently to mimic a true signal event gives of order 0.003 events for the entire ANITA 1 flight [8].

The fast electronics required to digitize a broadband impulse give timing of about 60 ps. Pulse-phase interferometry of the coincident RF signals result in event pointing less than 0.3° in elevation and about 1° in azimuth. Backgrounds come in two flavors, "Carrier Wave" (CW, nearly sinusoidal) and impulsive. CW signals have high narrow band power that can saturate the system, but are easy to identify and remove. Impulsive backgrounds can come from electronic switching phenomena. The major source of these backgrounds are anthropogenic, and are easy to identify because encampments are sparse. The Fresnel transmission coefficient of horizontally polarized (H-pol) signals suggests that they must originate above the ice, so a true neutrino candidate must be strongly vertically polarized (V-pol). It has been suggested that cosmic ray airshowers could produce an H-pol signal in ANITA [8], but there are no known physics phenomena above ground that could produce a V-pol signal that could be seen by ANITA.

3 ANITA 1 Results

ANITA 1 spent 35 days aloft, but a lot of that time was spent over the South Pole, which caused a lot of human initiated (anthropogenic) carrier wave noise and overwhelmed the detector. This reduced the overall livetime to 17.3 days, in which 8.3 million event triggers were recorded. Cuts were optimized on a 10% data set to blind the analysis to selection bias. Cuts were applied that required upcoming plane wave, vertically polarized, broadband signals. These signals were required to be isolated from camps and isolated from other events [8]. No neutrino candidates were observed. In the absence of a neutrino signal, flux limits were established [14], shown in Fig. 2(L). These are the first flux limits to begin to restrict the theoretical GZK flux predictions.

4 ANITA 2

A new front-end on ANITA 2 significantly reduced the overall T_{sys} of the electronics by ∼40 K. The inclusion of a bottom row of eight "nadir" antennas (see Fig. 1), where each antenna is shared between adjacent phi sectors, allows a third possibility for phi-sector coincidence. The trigger conditions were changed to V-pol only and now require two of three channels plus full band. These improvements taken together could improve the energy threshold by as much as a factor of 1.7, and ANITA gains sensitivity as E_{th}^{-2}, giving a factor of 3 event rate increase.

The ANITA 2 flight path is greatly improved over the ANITA 1 path [8] because there was more time spent over the deep ice of East Antarctica and less time over the South Pole, shown in Fig. 2(R). ANITA 1 bore the misfortune of an anomalous polar vortex that set up far from the South Pole, which pushed it away from the deep ice of East Antarctica. "Dynamic Phi-Masking", an automatically activated, active suppression of readout during transit over noisy areas, greatly decreased the dead time caused by stations such as McMurdo. The combination of the dynamic phi-masking and improved flight path could improve the exposure by as much as 30% over ANITA 1, though the actual exposure has not yet been calculated.

A total of 26.8 million events were recorded by ANITA 2, more than a three-fold increase over ANITA 1, which gives preliminary confirmation that the improvements to ANITA 2 resulted in the expected sensitivity gains. The data are being analyzed and results are forthcoming.

5 Summary

The science case for neutrino astronomy is compelling, and there is great need for more sensitive detectors. The technology of RF detection of neutrino induced Cherenkov radiation has matured, resulting in orders of magnitude greater sensitivity than current water (ice) Cherenkov detectors. ANITA 1 has produced significant results and ANITA 2, with increased sensitivity, should greatly improve the probability of detecting a cosmogenic neutrino. Results are coming soon.

This work was funded directly by the Center for Cosmology and AstroParticle Physics at Ohio State University. ANITA is funded by the National Aeronautics and Space Administration, the National Science Foundation Office of Polar Programs, the US Department of Energy Office of Science High Energy Physics Division, the UK Science and Technology Facilities Council and the Taiwan National Science Council. Special thanks to the staff of the Columbia Scientific Balloon Facility.

References

1. R. J. Davis, D. S. Harmer and K. C. Hoffman, Phys. Rev. Lett. **20**, 1205 (1968).
2. R. M. Bionta *et al.*, Phys. Rev. Lett. **58**, 1494 (1987).
3. K. Hirata *et al.* [KAMIOKANDE-II Collaboration], Phys. Rev. Lett. **58**, 1490 (1987).
4. E. Waxman and J. N. Bahcall, Phys. Rev. Lett. **78**, 2292 (1997) [arXiv:astro-ph/9701231].
5. V. S. Beresinsky and G. T. Zatsepin, Phys. Lett. B **28** (1969) 423.
6. K. Greisen, Phys. Rev. Lett. **16**, 748 (1966).
7. G. T. Zatsepin and V. A. Kuzmin, JETP Lett. **4**, 78 (1966) [Pisma Zh. Eksp. Teor. Fiz. **4**, 114 (1966)].
8. P. W. Gorham *et al.* [ANITA collaboration], arXiv:0812.1920 [astro-ph].
9. G. A. Askaryan, JETP, **14**, 441 (1962); JETP, **21**, 658 (1966);
10. D. Saltzberg *et al.*, Phys. Rev. Lett. **86**, 2802 (2001) [arXiv:hep-ex/0011001].
11. P. W. Gorham, D. Saltzberg, R. C. Field, E. Guillian, R. Milincic, D. Walz and D. Williams, Phys. Rev. D **72**, 023002 (2005) [arXiv:astro-ph/0412128].
12. P. W. Gorham *et al.* [ANITA Collaboration], Phys. Rev. Lett. **99**, 171101 (2007) [arXiv:hep-ex/0611008].
13. G. S. Varner, L. L. Ruckman, P. W. Gorham, J. W. Nam, R. J. Nichol, J. Cao and M. Wilcox, Nucl. Instrum. Meth. A **583**, 447 (2007) [arXiv:physics/0509023].
14. P.W. Gorham *et al.* [ANITA collaboration], arXiv:0812.2715 [astro-ph].

Development of a Radio Detection Array for the Observation of Showers Induced by UHE τ Neutrinos

C. Cârloganu[a], on behalf of D. Ardouin[b], D. Charrier[b], H. Hongbo[c], P. Lautridou[b], O. Martineau-Huynh[c,d,e], V. Niess[a], O. Ravel[b], X.P.Wu[e], M, Zhao[e], Y. Zhiguo[c]

[a]*Laboratoire de Physique Corpusculaire de Clermont Ferrand, IN2P3/CNRS, Université Blaise Pascal, Clermont Ferrand, France*

[b] *SUBATECH, Université de Nantes, IN2P3/CNRS, Ecole des Mines Nantes, France*

[c] *Particle Astrophysics Center, Institute of High Energy Physics, Chinese Academy of Science, Beijing, 100049, China*

[d] *Laboratoire de Physique Nucléaire et des Hautes Energies, Universités Paris 6-7, IN2P3/CNRS, Paris Cedex 05, France*

[e] *National Astronomical Observatories , Chinese Academy of Science, Beijing 100012, China.*

The running radio-detector 21CMA is being currently adapted for ν_τ searches. 10287 antennas sit along two high altitude valleys, surrounded by mountain chains, in an exceptionally low electromagnetic noise environment. Firsts measurements obtained with the in situ, 6-antennas prototype, show the great potential for shower detection of the array. Preliminary simulations of the foreseen setup indicate that an one year exposure of $\sim 10^{13}\mathrm{cm}^2{\cdot}\mathrm{s}{\cdot}\mathrm{sr}$ for 10^{17} eV ν_τ's may be attainable using 80 dedicated antennas.

1 Introduction

The probing of the UHE component of the far away Universe relies heavily on the detection of the UHE neutrinos [1]. Unfortunately, they can be observed only indirectly, through their interaction with target nucleons. The very low interaction cross section, combined with the already small fluxes predicted [1], require detection volumes of the order of cubic kilometers.

The UHE neutrinos are produced either by the interaction of the UHE cosmic rays within their sources, or in their subsequent interactions with the background radiation fields. In both cases, tau neutrinos are much suppressed at production since they are not a decay product of the dominating pions. However, approximately equal fluxes for each flavour are expected after traveling cosmological distances to the Earth due to neutrino flavour oscillations [2,3].

There are several running experiments looking for ν_τ's, as the dedicated neutrino telescopes ANTARES [4] and IceCube [5]. The extensive air shower (EAS) detector AUGER [6] looks for ν_τ's which enter the Earth just below the horizon and produce τ leptons which can escape the Earth; subsequently, the τ's decay in flight in the atmosphere produces showers visible both in their surface array and fluorescence telescopes. The AUGER collaboration showed accumulated exposures of the order of $3 \cdot 10^{16}$ $\mathrm{cm}^2{\cdot}\mathrm{s}{\cdot}\mathrm{sr}$, which allowed them to place an upper limit on the ν_τ flux approaching the theoretical predictions for the GZK neutrinos [7].

Lately, two collaborations, CODALEMA [8] and LOPES [9], showed the feasibility of radio-detection of the EAS's using an external trigger provided by ground detectors. Moreover, signal patterns obtained with a standalone, self-triggered antenna have provided convincing signatures

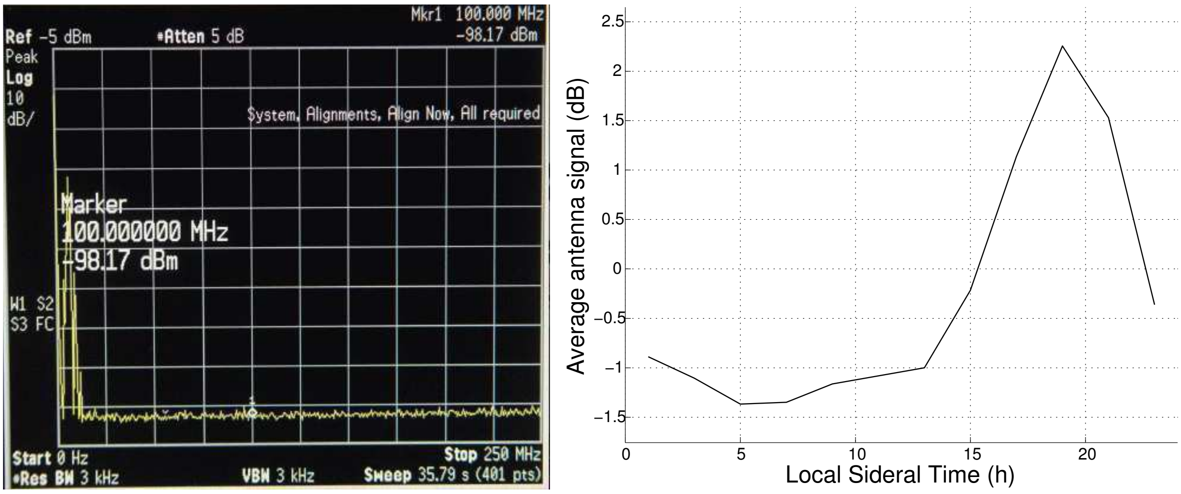

Figure 1: *Left:* average Fourier transform of the background noise for a 21CMA antenna. *Right:* antenna signal averaged over 15 hours of data taking as a function of the local sideral time, peaking to the galactic radio emission.

of EAS's [8]. An accuracy of the order of the degree was obtained by CODALEMA for the reconstruction of the arrival directions of radio transients generated by solar flares. The same reconstruction method was used for the EAS's. Under the assumption that the EAS's can be measured by standalone radio sensors with a direction accuracy of the order of the degree, we present here a proposition to look for ν_τ's using some dedicated sensors from an already existing radio array, 21CMA [10]. It is argued that the experimental site is particularly appropriate for the ν_τ detection and generally for radio detection. The status of the project is shown, as well as our expectations for the physics outreach based on preliminary simulations of the experimental setup.

2 21CMA experiment and the present setup for τ 21CMA

The 21CMA experiment is situated in the Ulastai Valley, in the Western-China province of XinJiang, at 2700 m of altitude. It is the only running experiment dedicated to re-ionisation studies. The detector consists of 10287 [50-100 MHz] log-periodic antennas, distributed over 81 groups of 127 antennas each (called in the following pods). It has two arms of 4 and 3 km length, oriented North-South and East-West respectively, which follow two almost perpendicular valleys.

On each pod, the analog signals of the 127 antennas are added and amplified by ∼60 dB before being sent over an optical fibre to the control room. Prior to their recording on disk, they are digitised using 81 8-bits ADCs (one for each pod), working synchronously at 200 MHz.

The first measurements performed on site showed a unique radio environment: the radio transmitters above 15 MHz are quasi-absent (Figure 1, left). The galactic plane thermal emission in the radio waveband is visible after only one day of data taking (Figure 1, right), showing that the antennas have the sensitivity requiered for EAS detection.

The first phase of the project is meant to prove the principle of the EAS detection with a self-triggering array. Six antennas were positioned as seen in Figure 2, left and self-triggered using an amplitude threshold set at 6 times the standard deviation of the electronics noise and read independently of the 21CMA array. A triangulation reconstruction leads to the signal origin in case of coincident signals on more than three antennas.

The time calibration of the setup was checked by reconstructing a nearby radio source of known position. The dispersion of the reconstructed position of the source (Figure 2, right), is

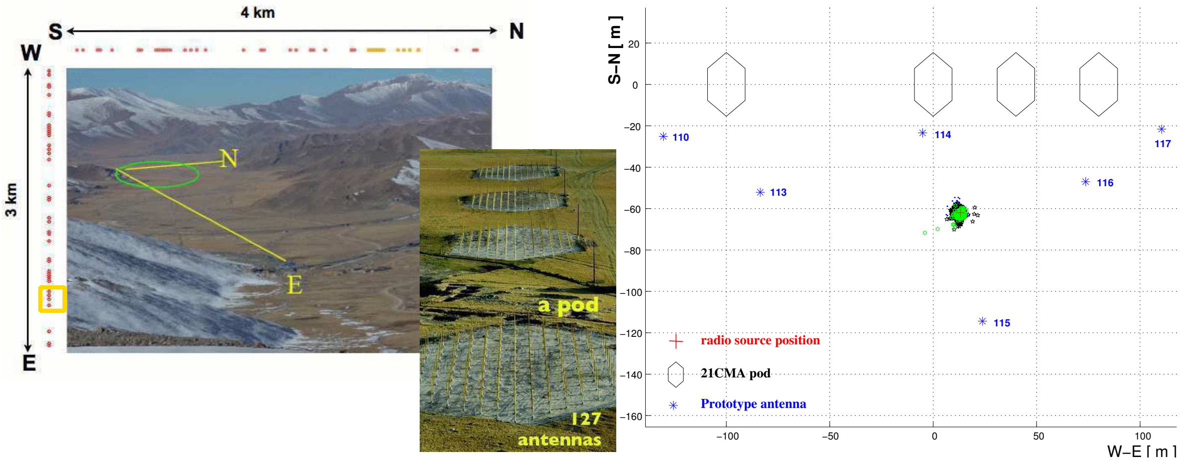

Figure 2: *Left:* the positions of the 81 pods in the two valley are shown (the red dots). The 6 pods housing our supplementary antennas are highlighted by the yellow rectangle. *Middle:* a close view of the pods. *Right:* the position of the six antennas (blue stars), the position of the car used as radio source (red cross) and the reconstructed origin of the signal (green and black points).

compatible with a time resolution of an antenna of few ns.

3 Simulation Chain

The detection principle for ν_τ's at 21 CMA is the following: a UHE, almost horizontal ν_τ, interacts with the mountains surrounding the antennas. The produced τ can escape the mountains and if it decays within the valley it produces a shower which can be seen by the antennas. The mountains act also as shielding against the EAS's due to the cosmic ray interactions in the atmosphere. An angular resolution of $\sim$degree should prevent contamination from downgoing CR EAS's.

Starting with a diffuse neutrino flux, the τ flux will depend on the depth of matter crossed, which is calculated from satellite data[11]. The ν_τ-nucleon interaction is simulated with Pythia[12]. The τ propagation assumes continuous losses [14] and its decay is simulated with the TAUOLA package [13]. The radio signal is generated following the longitudinal and radial profiles of the shower and it has an exponential fall with the distance [15]. The typical electronics noise is simulated and the trigger is defined by three or four coincident antennas with signals above the threshold. With a complete detector with 81 antennas (one per pod) the expected effective surface at the trigger level is shown in Figure 3, left, as function of the incoming ν_τ angle with the local vertical for an energy of 10^{19} eV. It reaches $3.5 \cdot 10^3 \mathrm{m}^2$ for horizontal ν_τ's in the case of four coincident antennas. On the right of the same figure, the achievable exposure in one year of data taking is shown as function of the incident neutrino energy.

4 Conclusion

The project of using the running 21CMA radio detector for $\nu_\tau$searches started in June 2008 and the first results are very encouraging. The radio environment is ideal: almost no terrestrial noise, the measurement of the radio signal from the galactic plane offers a reliable calibration of the antenna sensitivity. A lot of effort is ongoing for the time inter-calibration of the prototype using known radio sources. If clear measurements of the EAS will be available before summer 2009, the prototype will be then upgraded to the full 81 antennas. Simulation studies show that the 21CMA layout is very efficient for the detection of ν_τ's with energies between 10^{16}- 10^{19} eV,

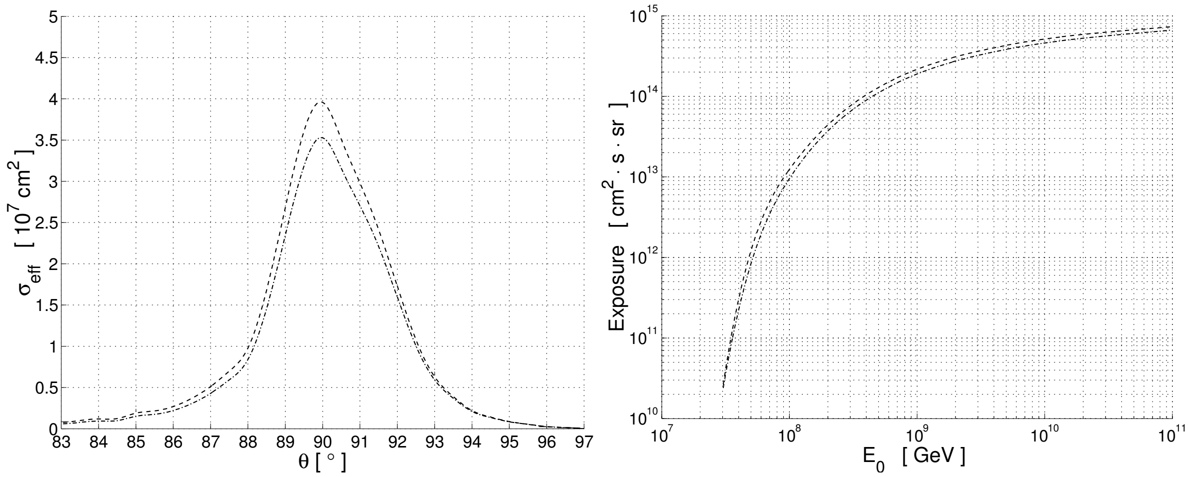

Figure 3: *Left:* effective surface at the trigger level as a function of the incoming ν_τ angle with the local vertical for 10^{19} eV ν_τ. *Right:* expected exposure in one year of data taking as function of the incident neutrino energy. The different curves correspond to triggers requiring 3 or 4 coincident antennas.

though further up-scaling is necessary for it to be competitive with existing detectors.

References

1. T.K. Gaisser, F. Halzen, T. Stanev, *Phys. Rept.* **258**, 173 (1995), E. Waxman, *New J. Phys.* **6**, 140 (2004)
2. F. Fukuda *et al*, *Phys. Rev. Lett.* **86**, 5656 (2001).
3. J.G. Learned, S. Pakvasa, *Astropart. Phys.* **3**, 267 (1995).
4. N. Cottini (ANTARES collaboration), these proceedings.
5. A. Achterberg *et al.* (IceCube Collaboration), *Astropart. Phys.* **26**, 155 (2006), G. Kohnen (IceCube Collaboration) these proceedings.
6. The Pierre Auger Collaboration, ar-Xiv:0903.3385v1, 19 March 2009.
7. F.W. Stecker, C. Done, M.H. Salamon, P. Sommers *Phys. Rev. Lett.* **66**, 2697 (1991).
8. D. Ardouin *et al.*, *Nucl. Instrum. Methods* A **555**, 148 (2005), J. Lamblin (CODALEMA Collaboration), proceedings “30th International Cosmic Ray Conference”, Mérida, México, 2007, P. Lautridou (CODALEMA Collaboration), proceedings ARENA 2008, B. Revenu (CODALEMA Collaboration), proceedings ARENA 2008.
9. A. Nigl *et al.*, Astronomy & Astrophysics, **488**, 807 (2008), A. Nigl *et al.*, Astronomy & Astrophysics, **487**, 781 (2008),
10. X.-P. Wu, National Astronomical Observatories, Chinese Academy of Science, personal communication (2007).
11. CGIAR-CSI (Consortium for Spatial Information), http://srtm.csi.cgiar.org.
12. T. Sjostrand et al, hep-ph/0603175.
13. Z. Was, proceedings “Sixth international workshop on tau lepton physics”, Victoria Canada, September 2000, Nucl.Phys.Proc.Suppl. 98 (2001) 96-102
14. model 3 in Dutta et al, *Phys. Rev.* D **72**, 013005 (2005).
15. A. Horneffer *et al*, proceedings “30th International Cosmic Ray Conference”, Mérida, México, 2007.

ANTARES: TOWARDS ACOUSTIC DETECTION OF HIGHEST ENERGY NEUTRINOS

K. GRAF for the ANTARES Collaboration
Erlangen Centre for Astroparticle Physics (ECAP), University of Erlangen,
Erwin-Rommel-Str. 1, 91058 Erlangen, Germany

Neutrinos within a wide energy range are predicted to originate from very-high-energy phenomena in the Universe. Acoustic neutrino detection is a promising option to enlarge the discovery potential for astrophysical sources in the highest-energy regime above 10^{18} eV. In order to investigate the techniques for acoustic particle detection in the deep-sea, the AMADEUS set-up has been integrated into the ANTARES neutrino telescope in the Mediterranean Sea. The research pursued with AMADEUS spans a wide range of topics, amongst them the study of the deep-sea ambient acoustic background: the characterisation of the noise level and of the location, the rate and the correlation length of transient signals.
In this article we describe the basic principles of acoustic neutrino detection and the AMADEUS array of acoustic sensors and we summarise the recent results achieved by the project.

1 Introduction

Several questions in astrophysics, cosmology and particle physics can be pursued using cosmic neutrinos of ultra-high-energies (*UHE*, $E_\nu \gtrsim 10^{18}$ eV) as messenger particles. Among these questions are the origin of UHE cosmic rays (*UHECR*), the Greisen-Zatsepin-Kuzmin (*GZK*) effect, cosmological top-down scenarios and topological defects. New results on the particle properties, e.g. the neutrino cross section, are expected at these energies which are not reachable in particle accelerators on Earth. The faint neutrino fluxes at ultra-high energies, e.g. expected from the GZK suppression of UHECR as indicated by the results of the HiRes and Auger Collaborations[1,2], are at the edge of detectability for current or future cubic-kilometre-sized Cherenkov neutrino telescopes (e.g. IceCube and KM3Net). Hence for the study of cosmic UHE neutrinos new approaches in the detection technique are required. We discuss one of those approaches in this article: an acoustic detection method.

2 Acoustic Neutrino Detection

The acoustic detection method is based on sound emission as an effect of the propagation of neutrino-induced particle cascades in liquid and solid media[a]. The sound generation process is described by the *thermo-acoustic model*[3,4]. According to this model, the energy deposition of particles transversing the medium leads to a local heating of the water which is fast with respect to the hydro-dynamical time scale. The temperature change is accompanied by an expansion or contraction of the medium according to volume expansion coefficient and the specific heat capacity. This translates into a pressure wave or acoustic pulse which propagates through the medium. The main input to the calculation of a thermo-acoustic pulse[4] is the superposed energy deposition density in the medium of all particles in a cascade. The evolution of particle cascades resulting from neutrino interactions and their energy deposition need to be simulated with Monte Carlo particle interaction codes like CORSIKA and GEANT[5].

Due to the approximately cylindric cascade geometry, the pressure pulse is emitted in a cylindric wave pattern, i.e. its isobars are located in a disk-shape perpendicular to the cascade axis defined by the neutrino direction[b]. At each point in space within the sonic disk, the thermo-

[a] Only sea water is regarded here.
[b] At the high energies regarded here, the neutrino direction aligns almost completely with the cascade direction.

acoustic signal is bipolar in time with a peak-to-peak amplitude of the order of 10 mPa per 1 EeV cascade energy at 200 m distance from the cascade; the signal is largely reduced outside the disc. The signal energy spectral density is peaking around 10 kHz and the signal length is several tens of microseconds. The propagation of the sonic wave through the medium is accompanied by attenuation, much lower than the one of optical Cherenkov light, and refraction. The attenuation length for sound propagation in sea water decreases with frequency; for 10 kHz (20 kHz) signals it is on the order of 5 km (1 km).

A three-dimensional array of acoustic sensors with an instrumented volume of $\gtrsim 10\,\mathrm{km}^3$ and with a sensor density of $\approx 100\,\mathrm{sensors/km}^3$ is required to detect acoustic signals for GZK neutrinos with a significant rate. In such a hypothetical detector, the signature of a neutrino-induced sound pulse has to be recognised among the ambient noise and has to be distinguished from background transients which can originate from either surface or under-sea sound sources (fauna or anthropogenic). In the frequency range of interest for acoustic detection, from 1 to 100 kHz, the ambient noise in the deep-sea is primarily generated by agitation of the sea surface – through precipitation, cavitation and spray[6].

3 The AMADEUS Project

The main goal of the AMADEUS (**A**ntares **M**odules for **A**coustic **DE**tection **U**nder the **S**ea) project[7] is to conclude on the feasibility of acoustic UHE neutrino detection in large, sea-based acoustic detector arrays. This study is carried out by means of a dedicated acoustic sensor array constantly operated during several years in a detector environment. The research topics span a wide range: under study are e.g. the distribution, the rate and the correlation length of background events and the level of background noise which determine the achievable acoustic detection sensitivity for UHE neutrinos. In addition, by integrating AMADEUS into the ANTARES neutrino telescope (cf. Sec. 3.1), we will have the opportunity to study hybrid opto-acoustical detection possibilities. For all studies mentioned above, adapted filtering, triggering and reconstruction algorithms are developed and tested on the acoustic data.

3.1 AMADEUS Set-Up

The AMADEUS set-up[c] is part of the ANTARES Cherenkov neutrino telescope[8] (cf. Fig. 1). ANTARES is located off-shore in the Mediterranean Sea about 40 km south of Toulon (France) at a water depth of about 2500 m. It comprises 12 vertical structures, the detection lines labelled *L1* – *L12*; the additional line *IL07* is instrumented with several apparatus for environmental monitoring. Each detection line holds 25 *storeys*, the main active part of the detector housing the optical sensors and read-out hardware. The storeys are vertically separated by 14.5 m starting at a height of about 100 m above sea floor. Each line is fixed to the sea floor by an anchor and held vertically by a buoy.

Acoustic sensing is fully integrated into the detector in form of six *Acoustic Storeys* (*AS*) which are modified versions of standard ANTARES storeys. At the AS, the three PMTs are substituted by six acoustic sensors and custom-designed electronics are used for the digitisation and preprocessing of the analogue signals. The distances between sensors in the AMADEUS set-up vary from ≈ 1 m within the storeys to a maximum of ≈ 350 m between two storeys. At the storeys, the sensor data are by default amplified to a sensitivity of ≈ 0.5 V/Pa, filtered with an $\approx 1 - 100$ kHz bandpass and digitised with 250 kSamples per second with a 16bit sampling over the input voltage range from -2 to $+2$ V. All data (up to 1.5 TByte/day) is sent to an on-shore server cluster for filtering and storing. On-line filters are implemented for all goals stated in Sec. 3: a minimum bias filter, recording 10 s samples of data every hour for each sensor, a

[c] For a detailed description cf.[7].

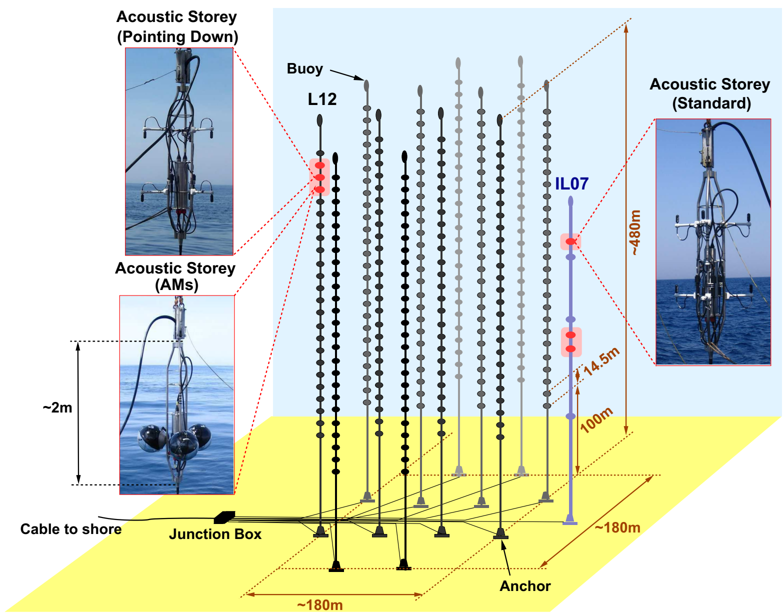

Figure 1: A sketch of the ANTARES detector[7]. The six Acoustic Storeys are highlighted and their three different set-ups, implemented to test acoustic detector designs and sensing methods, are shown.

threshold based filter, and a matched filter based on cross correlation with the expected bipolar signal; the latter two require coincidences between the sensors in a storey. These filters reduce the data volume by a factor of more than 100, constituting the data sample for off-line analysis.

The three acoustic storeys on the IL07 started operation in December 2007, the ones on L12 with the completion of ANTARES in May 2008. AMADEUS is now fully functional with 34 out of its 36 sensors active. After the first year of operation, the system has demonstrated excellent long-term stability and data-taking characteristics. During the ANTARES data-taking periods, the AMADEUS set-up has been continuously active for about 85% of the time. The excellent characteristics can be illustrated using the minimum bias data: the noise levels (root-mean-square of the signal amplitudes in each 10 s sample) recorded at the same time with any two active sensors are highly correlated with coefficients between 93% and 100%. The stability of the data-acquisition electronics is illustrated by the low standard deviation of the distribution of the mean signal amplitude of each sample which is only $\approx 1/10\,000$ of the input range.

As a major analysis example, the reconstruction of arrival direction of acoustic signals is presented in the following.

3.2 Reconstruction of Arrival Directions

Position reconstruction of acoustic point-like sources is implemented by reconstructing first their arrival direction from individual storeys, taking advantage of these local sensor groups. The combination of reconstructed directions from three or more storeys in a second step results in the source position. For the first step, the direction is identified from the differences in the arrival times of the acoustic wave in the sensors of one storey[9].

Fig. 2 shows a qualitative mapping of the arrival directions of transient acoustic signals originating in the vicinity of the ANTARES detector for the second storey from the bottom on IL07. The data sample has been collected with the minimum bias filter during the time period 29.01. to 05.06.2008. The figure shows the directions of all reconstructed signals ($\approx 200\,000$) which have an amplitude greater than eight times the standard deviation of the ambient noise. As expected, the majority of the sources are received from directions in the upper hemisphere, including all kinds of transient signals, e.g. dolphins click and shipping noise. In the lower

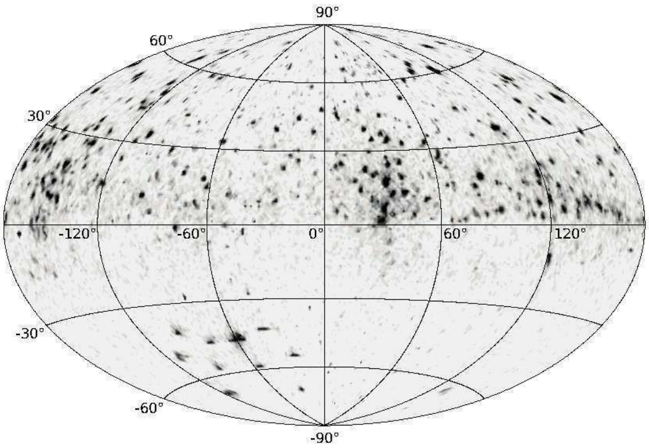

Figure 2: A qualitative mapping in Aitoff projection of the arrival directions of transient acoustic signals[9] for the second storey from the bottom on IL07, 180 m above the sea-bed. The centre direction is defined by the westward direction towards the horizon of that storey. $90°$ ($-90°$) in longitude corresponds to north (south), $90°$ ($-90°$) in latitude to vertically upwards (downwards).

hemisphere only few sources are observable with the layout pattern of the ANTARES detector evident on the lower left part of the figure. Those sources constitute the ANTARES acoustic positioning system[10], emitting signals from acoustic beacons at the bottom of each line.

4 Conclusions

The acoustic neutrino detection technique is a promising option to extend the study of cosmic neutrinos to the ultra-high-energy regime. The AMADEUS system, dedicated to the investigation of this technique, has been successfully installed together with the ANTARES neutrino telescope. Except for size, the system has all features required for concluding on the feasibility of neutrino detection with a potential future acoustic neutrino telescope. AMADEUS can also be used as a multi purpose device, e.g. for studies of hybrid opto-acoustical neutrino detection techniques, marine acoustic source distributions, and marine research.

Acknowledgements

The presented work is performed within the ANTARES collaboration and the author is supported by the German government through BMBF grants 05CN5WE1/7 and 05A08WE1. The author wishes to thank the organisers for a most interesting conference.

References

1. HiRes Coll., R.U. Abbasi *et al.*, preprint *arXiv:astro-ph/0703099v2* (2007).
2. Auger Coll., A. Watson *et al.*, *Nucl. Instrum. Methods* A **588**, 221 (2008).
3. G.A. Askariyan, B.A. Dolgoshein *et al.*, *Nucl. Instrum. Methods* **164**, 267 (1979).
4. J.G. Learned, *Phys. Rev.* **19**, 3293 (1979).
5. Acorne Coll., S. Bevan *et al.*, preprint *arXiv:astro-ph/0903.0949v1* (2009).
6. R.J. Urick, *Ambient Noise in the Sea*, Peninsula Publishing, Los Altos, USA (1986).
7. R. Lahmann, *et al.*, *Nucl. Instrum. Methods* A , doi:10.1016/j.nima.2009.03.058 (2009).
8. N. Cottini, these proceedings.
9. C. Richardt, *et al.*, *Nucl. Instrum. Methods* A , doi:10.1016/j.nima.2009.03.074 (2009).
10. M. Ardid, *Nucl. Instrum. Methods* A **602**, 174 (2009).

6. Summary

HIGH ENERGY PHENOMENA IN THE UNIVERSE - SUMMARY TALK

ARNON DAR
Technion, Israel Institute of Technology, Haifa 32000, Israel

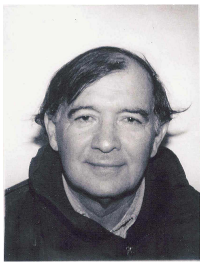

Highlights of the 44th Rencontre de Moriond on High Energy Phenomena in the Universe held in La Thuile, Italy during February 1-8, 2009

1 Introduction

More than 110 talks and 10 posters were presented at the 44th Rencontre De Moriond on high energy phenomena in the universe. They reflect the flood of new and important results in the fields of cosmic ray astrophysics, high energy gamma ray astronomy, high energy neutrino astronomy and the search for astrophysical evidence for physics beyond the standard models of particle physics, general relativity and cosmology. Unable to cover in a short summary all the talks and the new results, I will limit my summary to results which were presented and discussed in this Rencontre and which to the best of my judgment are the most important and fundamental ones.

2 Ultra-high Energy Cosmic Rays

If the ultra-high energy cosmic rays (UHECRs) are extragalactic in origin, as suggested by the isotropy of their arrival directions and the lack of correlation with the Galactic plane, than inelastic collisions with the cosmic background radiation (CBR) and cosmic expansion are expected to degrade their energies during their travel from their extragalactic sources to Earth. If the UHECRs are protons, pion production in collisions with the cosmic microwave background radiation (MBR) strongly degrades their energy above an effective threshold of $\sim 5 \times 10^{19}$ eV, the so called Greisen-Zatsepin-Kuzmin (GZK) threshold [1, 2] , while e^+e^- pair production in collisions with the CBR degrades their energy above an effective threshold of $\sim 10^{18}$ eV just below the CR ankle at $\sim 3 \times 10^{18}$ eV. If the UHECRs are nuclei, nuclear photodissociation in collisions with the CBR begins to be effective at a slightly lower energy for light nuclei and around the GZK threshold energy for iron-like nuclei [3]. Thus, the suppression of the flux of CR protons above the GZK threshold is expected to be accompanied by even a stronger suppression of the flux of heavier nuclei.

Early measurements by the Akeno Giant Air Shower Array (AGASA), which detects air showers at ground level with scintillators, reported the detection of UHECRs above the GZK threshold not showing the expected GZK suppression [4] but showing strong clustering in their arrival direction. These led to variety of interpretations including speculations on physics beyond the standard particle physics model and on violation of Lorentz invariance and special relativity. However, later results from the High Resolution Fly's Eye (HiRes) experiment [5, 6], which detect the fluorescence emitted in the air by nitrogen molecules excited by the passage of the shower, observed the GZK suppression above the expected threshold and did not find a significant anisotropy in the arrival directions of UHECRs. The AGASA and HiRes results were based on a small number of events and used different techniques. Results from measurements of UHECRs by the Pierre Auger Observatory which was conceived as a hybrid detector combining the two detection methods and covering an area 30 times bigger than that of AGASA, that were obtained during its construction confirmed the GZK suppression above the expected threshold [7, 8] and appeared to indicate that UHECRs above the GZK threshold arrive from nearby active galactic nuclei [9, 10].

The fast falling spectrum of the ultra-high energy cosmic rays (UHECRs), up to energies of about 10^{20} eV where the CR flux is of the order of 1 particle per km^2 per a couple of centuries, their arrival directions and their composition have now been measured by HiRes [6] and by the PAO [8, 11, 13] with sizable statistics (roughly twice and four times, respectively, the exposure of AGASA). The main results can be summarized as follows:

- **GZK Suppression Confirmed:** Allowing for 10% adjustment in the CR energies inferred either by HiRes or PAO from the fluorescence light emitted by air molecules excited by the CR induced atmospheric showers, because of a 10% difference in the adopted fluorescence yield in the showers, the energy spectra of UHECRs measured by both experiments are identical (Fig. 1a) and show the expected GZK suppression beyond $\sim 4\times 10^{19}$ eV, consistent with the highest energy CRs being extragalactic protons. (The power law $E^{-2.69}$ which fits the PAO spectrum below 40 EeV predicted 163±3 events above 40 EeV and 35±1 above 100 EeV, while 69 events and 1 event were observed by PAO, clearly confirming the GZK suppression).

- **Composition:** The atmospheric depth (in g/cm^2) of shower maximum, X_{max}, has been used both by HiRes[6] and PAO[11, 12] to infer the composition of UHECRs. Both experiments report a mixed composition that is becoming lighter with energy up to 3 EeV. However, HiRes results indicate a light composition all the way up to the GZK threshold around 40 EeV where it runs out of statistics, whereas PAO results indicate that the composition becomes heavier above 3 EeV and more so beyond the GZK threshold (Fig. 1b). These conclusions are valid provided that hadron physics does not change above 3 EeV.

- **Isotropy:** Below the GZK threshold both the HiRes and the PAO CR events are completely consistent with statistical fluctuations of an isotropic distribution of arrival directions.

- **UHECRs-AGN correlation:** At energies above the GZK threshold only CRs from nearby sources can reach Earth. If they are not deflected much by the intergalactic and Galactic magnetic fields, their arrival directions should point back to their sources, opening the window to UHECR astronomy. The evolution with energy of the distribution of

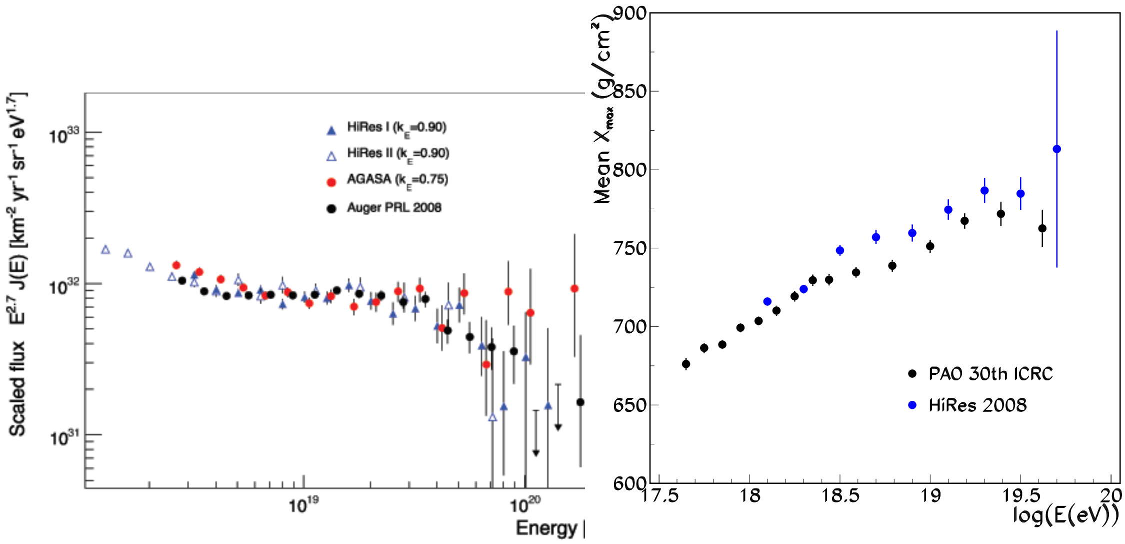

Figure 1: **Left (a):** Comparison between the spectra of UHECRs multiplied by $E^{2.69}$ measured by PAO, HiRes (with energy rescaled by a factor 0.9) and AGASA (with energy rescaled by a factor 0.7). The PAO and HiRes data are consistent and show the expected GZK suppression above 4×10^{19} eV. **Right (b):** Comparison between the mean depth of shower maximum of UHECRs as measured by HiRes and by PAO.

arrival directions of UHECRs measured by PAO shows a sharp transition from isotropy to anisotropy beyond the GZK threshold. The arrival directions of UHECRs with energy above 57 EeV show a correlation on angular scales of less than 6^o with the sky positions of AGNs within 71 Mpc, which are concentrated near the supergalactic plane. Intrinsic (catalog independent) properties of these events, such as their auto-correlation function, show a clear departure from isotropy in a large angular range[13]. The correlation/anisotropy observed by PAO was not confirmed by HiRes which reported [6] lack of arrival-direction correlation of their highest energy events with local AGNs (in the Northern Hemisphere). PAO found that out of their 27 UHECRs events with energy above 56 EeV, 20 were found to lie within 3.2^o of the line of sight to an AGN nearer than 71 Mpc while only 6 were expected to be found by chance from an isotropic distribution of arrival directions (the threshold energy, maximal angular deviation, and maximal AGN distance were chosen to maximize the UHECRs-correlation) (Fig. 2a). HiReS found that using the PAO criteria only 2 of their 13 events above 56 EeV correlated with AGN (Fig. 2b), while 3.2 were expected randomly, ruling out the correlation at a probability of 83%. The PAO collaboration has stressed that even though the correlation with nearby AGN seems to be quite robust in their sample, the angular scale of $\sim 6^o$ does not make possible to unambiguously identify the sources and sources which are distributed similar to AGNs cannot be excluded as the true sources.

- **UHEGRs:** Showers initiated by ultra-high energy gamma rays (UHEGRs) develop differently from showers induced by nuclear primaries. Particularly, the depth of shower maximum is much larger and the shower is much poorer in muons relative to those of CR nuclei. Upper limits on the presence of photons in the primary cosmic-ray flux were obtained by PAO; in particular a limit of 2% (at 95% c.l.) above 10 EeV on the flux of UHEGRs relative to UHECRs was derived by PAO [12]. This limit improves previous constraints on Lorentz violation parameters by several orders of magnitude due to the extreme energy in case of UHEGRs.

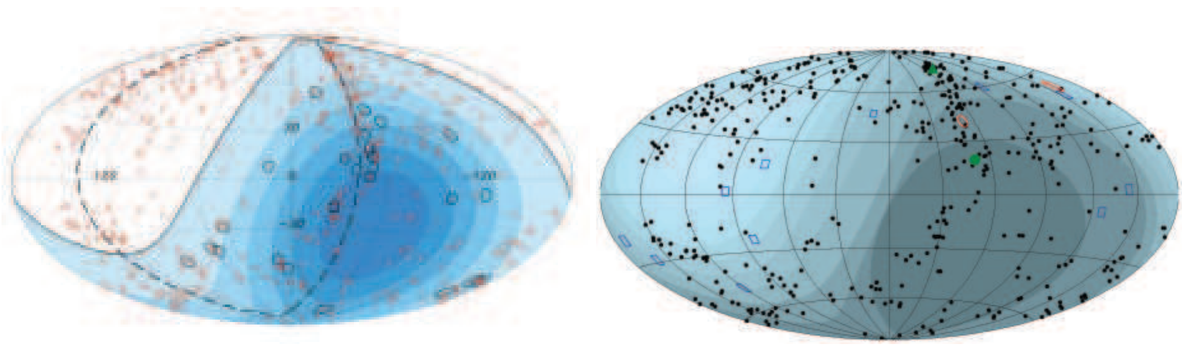

Figure 2: **Left:** The arrival directions of UHECRs with energy above 57 EeV, measured by PAO and plotted as circles with an angular radius of 3.2^o centered on their arrival direction on a sky map (Galactic coordinates) of AGNs within 71 Mpc from Earth. Colors indicate equal exposure. **Right:** The arrival directions of UHECRs with energy above 57 EeV, measured by HIRES and plotted as circles with an angular radius of 3.2^o centered on their arrival direction on a sky map (Galactic coordinates) of AGNs within 71 Mpc from Earth. Colors indicate equal exposure.

Although AGN are a natural source of extragalactic UHECRs, the directional correlation found by Auger is surprising in many respects. A 3.2^o deviation is of the order of magnitude of that inflicted on UHECRs by the magnetic field of the Galaxy, it would be surprising if extragalactic CRs did not encounter intergalactic magnetic fields with similar or larger effects. The Veron catalog of AGN is not complete and not directionally uniform in its coverage and sensitivity, unlike the Auger coverage within its field of view. The Auger correlation is purely directional, not investigated case-by-case for the possible effects of AGN distance, luminosity, jet direction and radio loudness. The effect of distance is obvious, the correlation with luminosity is very plausible. Concerning jet-direction, one has to understand how the UHECRs from AGNs could be fairly isotropically emitted, given that AGNs produce extremely collimated jets, and that they are seen in gamma-rays as very luminous blazars only when the jets are pointing in our direction. The proton- and electron-acceleration efficiencies of CR sources are presumably correlated. The radio loudness is a measure of the number of high energy synchrotron-radiating electrons. The jets of an AGN may accelerate CRs to well above the GZK limit and collimate them forward in a cone of aperture $1/\Gamma$ where Γ is their bulk motion Lorentz factor. But the PAO results suggest a more isotropic source, the end lobe of an AGN jet being the obvious choice [14]. These lobes have radii R_l of a few kpc. They are steadily energized by the incoming jet. Traveling in a medium swept up by previous jet components, a jet may deposit in its lobe an energy in excess of 10^{60} erg, emitted by the central black hole during the AGNs active life. An equipartition magnetic field B in these end lobes can exceed a milli Gauss. The Larmor limit energy for the acceleration of a proton in a lobe is then $E_{max} \approx e\, B\, R_L \approx 3 \times 10^{21}$ eV, well above the GZK threshold.

However, the PAO UHECRs-AGN correlation is puzzling in other respects. E.g., why there are no events from the direction of the Virgo cluster, that contains powerful AGN such as M87 at 14 Mpc? Why the maximal correlation for UHECRs with E$\geq$57 EeV is with AGN at distance less than 71 Mpc - Such UHECRs should come from distances up to 200 Mpc and not only from less than 71 Mpc.

All together, the results from PAO are very important in many respects and are pointing towards a potential breakthrough in UHECR and UHEGR astronomies, but much more statistics are needed in order to establish that. With a main goal of full sky coverage, the Auger Observatory is to be completed by a northern site. Current plans aim at a significantly ~ 7 times larger array to proceed with UHECR and UHEGR astronomies.

To reach even larger exposures, dedicated observatories in space which can observe UHECR induced atmospheric showers by looking down towards the Earth are planned. The Extreme Universe Space Observatory (EUSO) on the Japanese Experiment Module (JEM), which will detect fluorescence from UHECR events within 60^o field of view, is being planned for deployment on the International Space Station. JEM-EUSO may detect $\sim 1,000$ particles above 70 EeV in a three year mission. The Orbiting Wide-Angle Light Collectors (OWL) will stereoscopically image fluorescence from UHECRs. Such missions may observe a significant fraction of the ~ 10 million showers generated in the Earth atmosphere per year by UHECRs with energy above the GZK threshold.

3 Dark Matter

3.1 Evidence from cosmic colliders

Dark matter is an hypothetical matter that does not emit electromagnetic radiation, whose presence has been inferred consistently from gravitational effects on visible matter, on light trajectories, on the space-time geometry of the universe, on structure formation in the universe and on cosmic evolution.

The observed phenomena which imply that the universe contains much more dark matter than visible matter, include the rotational speeds of galaxies, orbital velocities of galaxies in clusters, gravitational lensing of background objects by galaxies and galaxy clusters and the temperature distribution of hot gas in galaxies and clusters of galaxies. Dark matter also plays a central role in structure formation and galaxy evolution, and has measurable effects on the anisotropy of the cosmic microwave background radiation. At present, the density of ordinary baryons and radiation in the universe is estimated about 4% of the total energy density in the universe. About 22% is thought to be composed of dark matter. The remaining 74% is thought to consist of dark energy, distributed diffusely in space.

The dark matter hypothesis has generally been the preferred solution to the missing mass problems in astronomy and cosmology over alternative theories of gravity based on modifications to general relativity which have been used to model dark matter observations without invoking dark matter [15, 16]. However, until recently there was no conclusive evidence that dark matter really exists. This has changed dramatically by X-ray and optical observations of collisions between galaxy clusters [17, 18, 19], such as in 1E0657-558 at z=0.296 (the 'Bullet Cluster'), MACS J0025 at z=0.586 and A520 at z=0.201 (the 'Cosmic Train Wreck'). In such collisions the clusters' galaxies and dark matter halos are affected only by gravity while the electromagnetic interactions between the clusters' X-ray emitting ionized gas produce an additional drag on the gas. Consequently, after the collision the galaxies and their associated dark matter halos lead the slower moving X-ray emitting gas clouds stripped off from the galaxy clusters, as seen in Figs. 3a,b. The galaxies in these Figures were observed from the ground with Magellan and from space with the HST, the stripped off X-ray emitting gas was mapped with Chandra and the dark matter halos of the clusters were mapped by measuring the distortion of the images of background galaxies by the deflection of light as it passes the clusters dark matter halos. Such observations require that regardless of the form of the gravitational force law at large distances and low accelerations, the majority of the mass of the system be some form of dark matter. Many more cases of cluster collisions will be studied through gravitational lensing of background galaxies with a dedicated large telescope such as the 8.4m Large Synoptic Survey Telescope (LSST) which is under design and development and scheduled to be commisioned at Cerro Pachòn (Chile) by 2017 [17].

Figure 3: Composite images of the bullet cluster (1E 0657-56) **(Left)** and the cluster MACS J0025 **(Right)**. Both clusters were formed by a collision of two galaxy clusters. The major components of the clusters are shown in different colors., The galaxies whose stars makes them visible in optical light are shown in orange and white, the ionized gas in the clusters which is visible in X-rays is shown in pink and the putative dark matter, which dominates their gravitational potential and is inferred through gravitational lensing of background galaxies, is shown in blue. After the collision, most of the matter in the clusters (in blue) is well separated from most of the normal matter (the gas in pink) and moves ahead of it. This separation provides direct evidence that most of the matter in the clusters is dark matter which cannot be represented by modified gravity of the cluster gas which contains most of the baryons in clusters. Credits 1E0657-56: X-ray NASA/CXC/CfA Optical: NASA/STScI; Magellan/U.Arizona; Clowe et al. (2006); Bradac et al. (2006) MACS J0025.4-1222: X-ray(NASA/CXC/Stanford/S.Allen); Optical/ Lensing(NASA/STScI/UCSB/M.Bradac) Bradac et al. (2008)

3.2 Direct and indirect detections ?

Determining the nature of the dark matter particles is one of the most important problems in modern cosmology and particle physics. Both direct detection in which the interaction of dark matter particles are observed in a detector and indirect detection that looks for the products of dark matter annihilation or decay products have been conducted extensively and are ongoing. Dark matter detection experiments have ruled out some WIMP (Weakly Interacting Massive Particle) and axion models. There are also several claims of direct detection of dark matter particles in lab experiments such as DAMA/NaI (Dark Matter/Sodium Iodine) in the Gran Sasso underground laboratory, and possible detections of astrophysical gamma rays, positrons and electrons from dark matter annihilation, by EGRET aboard the CGRO, by ATIC and by PAMELA, respectively, but all these are so far unconfirmed and difficult to reconcile with the negative results of other experiments. In particular:

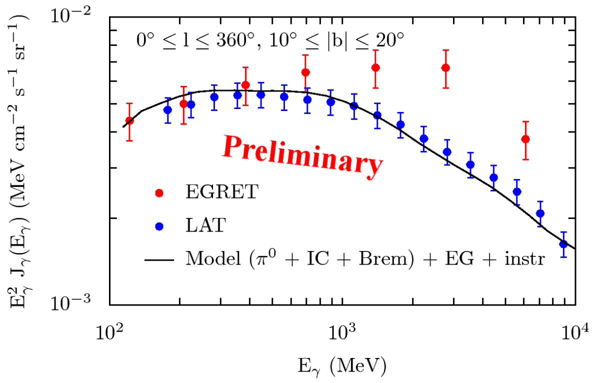

Figure 4: Comparison between the spectra of the diffuse gamma ray background radiation at intermediate latitude which were measured by EGRET and by LAT. The LAT data do not confirm the existence of the EGRET GeV excess and can be fitted by the standard model of Galactic cosmic ray electrons and nuclei with densities normalized to their respective locally observed densities.

The EGRET GeV excess:

The spectrum of the diffuse γ background radiation (GBR) that was measured by EGRET aboard the Compton Gamma Ray Observatory showed an excess above 1 GeV in comparison with the flux expected from interactions of cosmic ray (CR) nuclei and electrons in the Galactic interstellar medium (ISM) [20]. The origin of this GeV excess has been unknown. Among its suggested origins was annihilation or decay of WIMPs [21]. However, recent measurements with the Large Area Telescope (LAT) aboard the Fermi observatory have yielded preliminary results [22] which do not show a GeV excess at small Galactic latitudes and agree with the flux expected from CR interactions in the Galactic ISM (Fig. 4). Moreover, by comparing the spectra of gamma-rays around GeV from nearby Galactic pulsars, which were measured by EGRET and LAT, the Fermi collaboration confirmed [22] previous conclusions [23] that the origin of the EGRET GeV excess is instrumental and not a dark matter annihilation/decay signal.

The ATIC GeV excess:

The Advanced Thin Ionization Calorimeter (ATIC) experiment aboard balloon flights over Antarctica [24] reported an excess in the flux of CR electrons at energies between 300-800 GeV. Several papers suggested that this excess in cosmic ray electrons (and positrons) arises from annihilation of dark matter particles such as Kaluza-Klein particles with a mass of about 620 GeV/c^2 [25]). However, in this meeting caution was advocated when interpreting cosmic ray electron and positron data above a few GeV because of possible proton contamination of the measurements and it was pointed out that the ATIC reported data should be suspected as the authors did not properly take into account the uncertainties associated with a potential hadronic background due to particle interactions inside the graphite target on top of the detector [26].

Moreover, it was pointed out [27] that if the ATIC electron excess was due to dark matter annihilation, such an excess of Galactic cosmic ray electrons would have produced a detectable GeV excess in the diffuse Galactic GBR at large latitudes, while dark matter annihilation in external galaxies would have produced a detectable GeV excess in the diffuse EXTRAGALACTIC GBR at all latitudes, which was not observed by EGRET (Figs. 5a,b).

After the Rencontre de Moriond it was shown that the ATIC excess is probably instrumental due to misidentified proton induced electron-like events in the ATIC detector by cosmic ray protons [29]. Moreover, the HESS collaboration reported a measurement of the cosmic-ray electron spectrum above 340 GeV which does

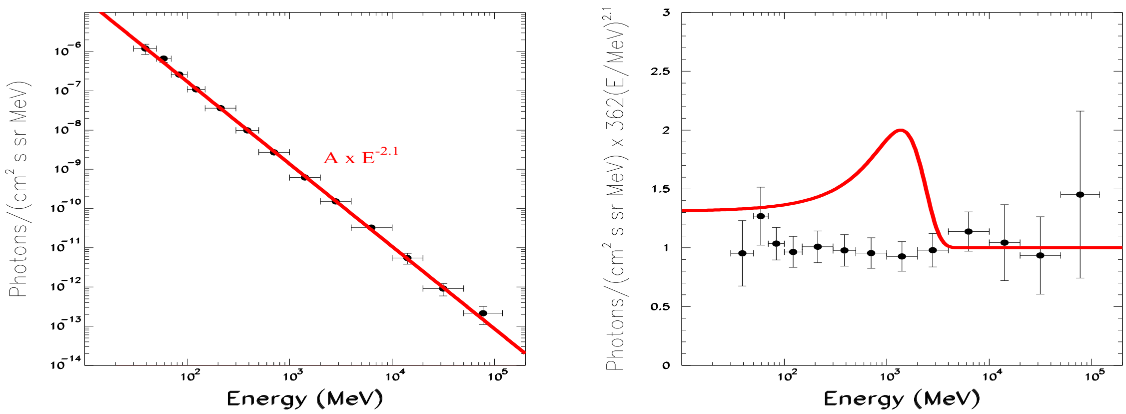

Figure 5: **Left:** The spectrum of the extragalactic gamma ray background radiation (GBR) which was measured by EGRET [28] and is well represented by a single power law $dn/dE \propto E^{-2.10\pm 0.03}$. **Right:** Comparison between the spectrum of the extragalactic GBR measured by EGRET [28] and the GBR spectrum which is produced by ICS of MBR photons in external galaxies by a universal power-law spectrum of high energy CR electrons, $dn_e/dE \propto E^{-3.2}$ plus an excess such as that measured by ATIC [24] between 300-800 GeV. Both spectra were divided by the best fitted power-law to the EGRET GBR spectrum.

not show the ATIC peak [30] and the LAT collaboration reported a high precision measurement of the steeply falling cosmic ray electron spectrum between 20 GeV and 1 TeV which also does not show the prominent ATIC peak [31].

The PAMELA positron fraction:

In the standard leaky box models, CR sources accelerate primary cosmic ray nuclei and electrons while secondary electrons and positrons are produced by the decay of charged π's and K's produced in hadronic collisions of primary cosmic ray nuclei in the interstellar medium (ISM). The primary particles are injected with roughly the same energy spectrum $dn/dE \sim E^{-p_{inj}}$ with $p_{inj} \approx 2.2$, but the escape by diffusion from the Galaxy increases the spectral index of the primary CR nuclei to $p_N \approx 2.7$ while cooling by synchrotron radiation and inverse Compton scattering of background photons increases the spectral index of the primary CR electrons by one unit to $p_e \approx 3.2$. Because of Feynman scaling the secondary electrons and positrons, which are produced by CR interactions in the ISM, have a spectral index $p_{inj} \approx 2.7$, which increases to $p_e \sim 3.7$ by cooling. Consequently, in the standard CR model the positron fraction decreases like $\sim E^{-0.5}$ at high energies (where solar modulation and geomagnetic effects are negligible). Contrary to this expectation the PAMELA satellite experiment has recently reported [32, 33, 34], a dramatic rise in the positron fraction starting at 10 GeV and extending up to 100 GeV in complete disagreement with the standard cosmic ray model calculations [35]. These observations have created much excitement and motivated many papers claiming that the observed rise is produced by the annihilation of dark matter particles. Other publications related the excess to a local enhancement of the flux of electrons and positrons due to nearby galactic sources of positrons and electrons such as pulsars [36] or to secondary production in the ISM by CRs from nearby sources such as supernova remnants in the nearest spiral arm [37].

However, the rise of the positron fraction with increasing energy beyond 10 GeV may be entirely due to hadronic production of positrons (and electrons) in the cosmic ray sources [27]: In fact, if Fermi acceleration of highly relativistic particles results in a universal power-law distribution of Lorentz factors of the accelerated particles, $dn/d\gamma \propto \gamma^{-p_{inj}}$, with an injection spectral index $p_{inj} \approx 2.2$, than the injected flux of high energy electrons is suppressed by a factor $(m_e/m_p)^{p_{inj}-1} \approx 10^{-4}$ compared to that of protons at the same energy [38], which is much

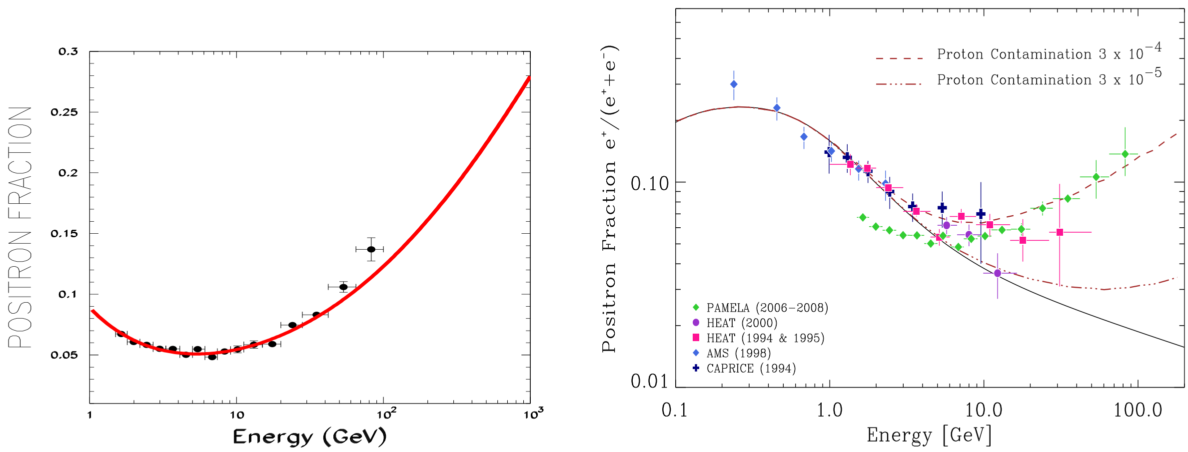

Figure 6: **Left (a):** Comparison between the positron fraction measured with PAMELA and that expected from secondary production of electrons and positrons in the CR sources and in the ISM. **Right (b):** Recent measurements of the positron fraction overlaid with a the standard leaky box model prediction [35] of secondary production of cosmic-ray positrons in the ISM and the same prediction including residual proton contamination [26]. Below 5 GeV solar modulation affects the particle intensities observed near Earth and may explain the discrepancy between the PAMELA data and older measurements, obtained at distinctively different solar epochs. In the region between 5 and 50 GeV measurements by PAMELA are consistent with previous data from the HEAT experiment.

smaller than their observed ratio in the Galaxy. Cosmic ray nuclei, however, may encounter in/near source a total column density comparable to a mean free path for hadronic interactions during their acceleration and before being injected into the ISM. In that case, due to Feynman scaling, they generate an electron+positron spectrum identical to that of the CR protons but with a normalization which is larger by roughly two orders of magnitude than that of the primary Fermi accelerated electrons. The combination of Fermi acceleration of electrons and hadronic production of electrons and positrons in/near the CR sources plus hadronic production of electrons and positrons in the ISM can naturally explain the rise of the positron fraction beyond 10 GeV [27].

Finally, despite of the above, caution must be applied also to the PAMELA results as emphasized in this Rencontre by M. Schubnell [26]: the intensity of cosmic-ray protons at 10 GeV exceeds that of positrons by a factor of about 5×10^4. Therefore a proton rejection of about 10^6 is required if one wants to obtain a positron sample with less than 5%. Furthermore, because the proton spectrum is much harder than the electron and positron spectra, the proton rejection has to improve with energy. In addition, any small amount of spillover from tails in lower energy bins can become problematic [26]. Fig. 6 demonstrates that a proton contamination of 3×10^{-4} can explain the PAMELA positron fraction.

The PAMELA antiproton to proton ratio:

The recent measurements of the antiproton to proton ratio measured by PAMELA [32, 33] agrees with that expected from secondary production in the ISM, but the measurements do not extend to high enough energy (see Fig. 7 where the energy dependence can distinguish between secondary production in the CR sources which yields a constant ratio and secondary production in the ISM that yields a ratio which decreases like $E^{-0.5}$).

4 High Energy Gamma Ray Astronomy

The tremendous progress made in high energy gamma ray astronomy during the past two decades is due to many instruments with increasing sensitivity covering now the entire MeV-PeV energy

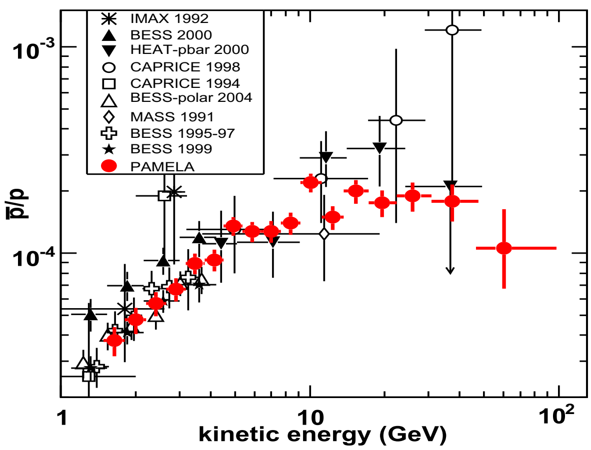

Figure 7: Comparison between the antiproton to proton ratio in Galactic cosmic rays as function of energy as measured by PAMELA and by previous experiments. The results of PAMELA cannot distinguish yet between a decreasing ratio with energy, expected from secondary production of antiprotons in the ISM, and a constant ratio expected from secondary production in the CR sources.

range, as summarized in Fig. 8 borrowed from Aldo Morselli.

This progress has culminated with the successful completion and operation of the large imaging Cherenkov telescope systems, HESS, MAGIC and VERITAS and the launch of the Fermi Gamma-ray Space Observatory on June 11, 2008 with its two main instruments, the Large Area Telescope (LAT) for all-sky survey studies of astrophysical and cosmological point and diffuse sources of high energy ($30 < E < 300$ GeV) and Gamma-ray Burst Monitor (GBM) to study gamma-ray bursts. These studies led to an explosion of newly discovered Galactic and extragalactic sources.

Most of the 125 bright non-pulsar gamma ray sources detected by LAT at high latitude ($b > 10^O$ in the first 3 months of operation are AGNs (57 FSRQ, 42 BLLac, 6 of uncertain class and 2 radio galaxies)[39]. The Galactic gamma ray sources include 13 new pulsars[40] (radio-quiet pulsars, young radio pulsars and millisecond pulsars), pulsar wind nebulae[41](PWNe), supernova remnants, molecular clouds, X-ray binaries[42], Wolf-Rayet stars, OB associations, open clusters and globular clusters[43].

4.1 High energy gamma ray astronomy and the origin of Galactic CRs

In 1934, Baade and Zwicky proposed that supernovae are the main sources of galactic CRs which were first discovered by Hess in 1912. Today diffusive shock acceleration in the blast wave driven into the ISM by a supernova shell is the most popular model for the origin of galactic cosmic rays. Despite the general consensus and exciting recent results, the origin of these particles is still debated and an unambiguous and conclusive proof of the supernova remnant hypothesis is still missing. In particular, the recent detection of a number of supernova remnants in TeV gamma rays by HESS, MAGIC and VERITAS still does not constitute a conclusive proof that galactic cosmic rays nuclei with energies below the cosmic ray knee are accelerated mainly in supernova remnants (SNRs). In particular, it was found that it is difficult to disentangle the hadronic and leptonic contributions to the observed gamma ray emission (for an excellent review see[44]).

In some shell SNRs such as RX J1713.7-3946 and Vela Junior the non-thermal synchrotron emission exhibits a striking morphological similarity with the TeV gamma ray image. Such a correlation is naturally expected in leptonic models, where both X-rays and gamma rays are emitted by the same population of electrons via synchrotron and inverse Compton scattering,

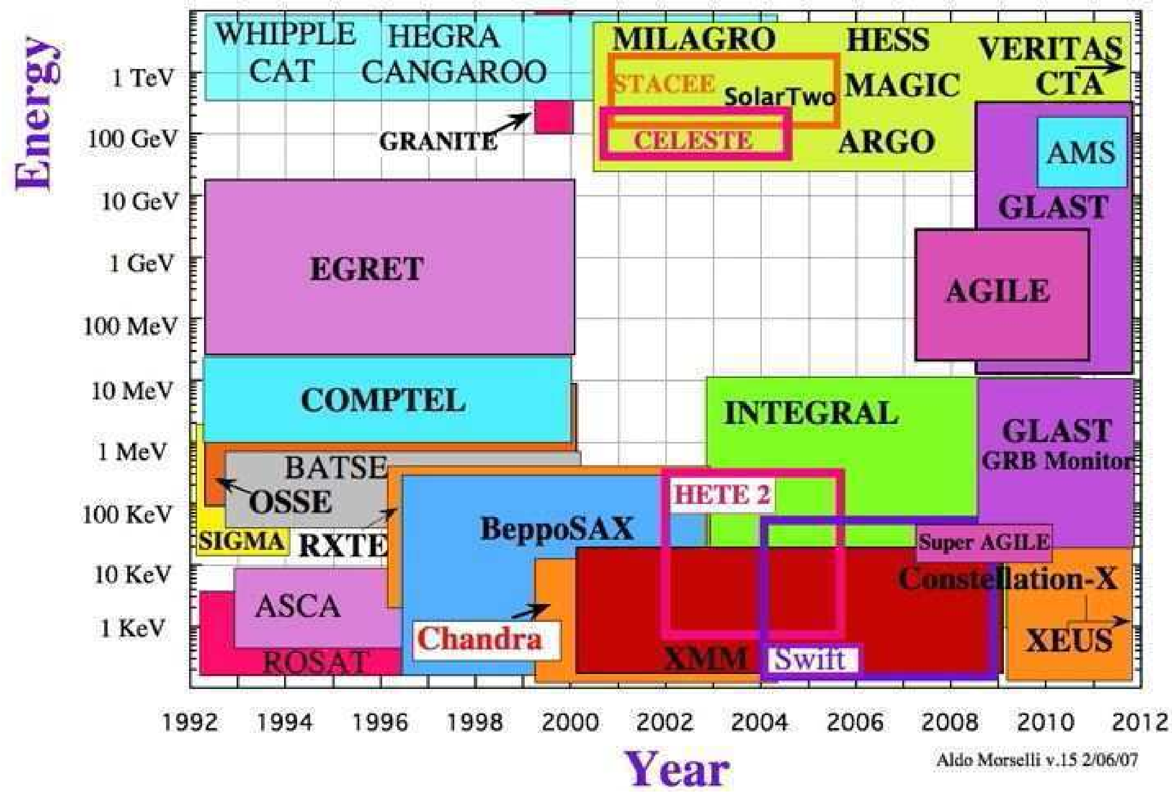

Figure 8: The recent rapid progress in gamma ray astronomy is due to the increasing energy range and sky coverage by both air-shower Cherenkov telescopes and gamma ray telescopes aboard satellites

respectively. Although the correlation can be accommodated also within hadronic models if most of the gamma ray emission is through π^0 decay and the X-ray emission is the result of synchrotron emission from secondary electrons from $\pi^\pm$ decay. In such a scenario the energy flux in TeV gamma rays must exceed that in X-rays since the electrons from $\pi^\pm \to \mu^\pm \to e^\pm$ decay carry less energy than the γ's from π^0 decay, while the opposite is observed in RX J1713.7-3946. But, the assumed synchrotron radiation from secondary electrons plus positrons may not be the correct origin of the X-ray emission from RX J1713-394 (e.g. bremsstrahlung from ISM protons which enter the SN shell rest-frame with $\sim$200 keV kinetic energy). In fact, the gamma ray spectrum that was measured from this SNR by HESS up to almost 100 TeV has a knee (or an exponential cutoff) around $E \sim 5$ Tev which suggest that protons are accelerated in RX J1713.7-3946 up to the CR knee energy around 2 PeV: at 2 PeV the mean charge multiplicity (mostly pions) in pp collisions is around 50 and that of the π^0's is about 25. Pions carry about 35% of the incident proton energy and about 1/3 of that energy is carried by π^0's. Consequently, the typical energy of photons from the decay of π^0 produced by 2 PeV protons in pp collisions is roughly 5 TeV.

However, the safest way of proving or rejecting acceleration of CR nuclei in RX J1713.7-3946 (and in SNRs in general) is to search for neutrinos produced in the decays of charged pions (by stacking all the neutrino events from the direction of known SNRs).

4.2 High energy gamma ray emission from GRBs

During nearly 20 years of observations the Burst And Transient Source Experiment (BATSE) on board the Compton Gamma Ray Observatory (CGRO), has detected and measured light curves and spectra in the keV-MeV range of several thousands Gamma Ray Bursts (GRBs). Higher-energy observations with its EGRET instrument aboard CGRO were limited to those GRBs which happened to be in its narrower field of view. Its large calorimeter measured the light-curves and spectra of several GRBs in the 1-200 MeV energy range. Seven GRBs were detected also with the EGRET spark chamber, sensitive in the energy range 30 MeV - 10 GeV. The EGRET detections indicated that the spectrum of bright GRBs extends at least out to 1 GeV, with no evidence for a spectral cut-off (see, e.g., Dingus 2001, and references therein). However, a few GRBs, such as 940217 [45] and 941017 [46] showed evidence for a high energy component in the GRB pulses which begins significantly after the beginning of the keV- MeV pulse and has a slower temporal decay than that of the keV-MeV emission, suggesting that the high-energy emission, at least in some cases, is not a simple extension of the main component, but originates from a different emission mechanism and/or region. This has been confirmed recently by observations of high energy photons from several GRBs with the Fermi LAT [49, 50, 51], and AGILE [48] However, the flux levels of TeV gamma rays from a couple of GRBs which were inferred from ground level measurements of atmospheric showers were not confirmed by HESS with its high sensitivity array which produced upper limits much smaller than the flux levels predicted by standard fireball models where TeV photons are produced by inverse Compton scattering, decay of π^0's from proton-gamma collisions and by synchrotron radiation from UHE protons.

Not only the observed flux levels but also the spectral and temporal behaviour of the high energy emission are not those predicted by the popular fireball (FB) models of GRBs. This is not completely surprising in view of the fact that the rich and accurate data, which have been accumulated in recent years from space-based observations with Swift and ground based observations with robotic telescopes, have already challenged the prevailing popular views on GRBs: Synchrotron radiation (SR) cannot explain simultaneously their prompt optical emission and their hard X-ray and gamma-ray emission which were well measured in some bright GRBs such as 990123 and 080319B. The prompt hard X-ray and gamma-ray pulses cannot be explained by synchrotron radiation from internal shocks generated by collisions between conical shells. Neither can SR explain their typical energy, spectrum, spectral evolution, pulse-shape, rapid spectral softening during their fast decay phase and the established correlations between various observables. Moreover, contrary to the predictions of the FB model, the broadband afterglows of GRBs are highly chromatic at early times, the brightest GRBs do not show jet breaks, and in canonical GRBs where breaks are present, they are usually chromatic and do not satisfy the closure relations expected from FB model jet breaks. In spite of all the above, the GRB community is not so critical and many authors believe that the GRB data require only some modifications of the standard FB model in order to accommodate the observations. Other authors simply ignore the failures of the FB model and continue the interpretation of observations with the FB model hypotheses (colliding conical shells, internal and external shocks, forward and reverse shocks, continuous energy injection, refreshed shocks) and parametrize the data with freely adopted formulae (segmented power laws, exponential-to power-law components) which were never derived explicitly from any underlying physical assumptions.

The situation of the cannonball (CB) model of GRBs is entirely different. In a series of publications, which were largely ignored by the rest of the GRB community, it was demonstrated repeatedly that the model correctly predicted the main observed properties of GRBs and reproduces successfully the diverse broad-band light-curves of both long GRBs [53] and short hard bursts (SHBs) [54]. In fact since the discovery of GRBs in 1967 and the beginning of the GRB debate, the majority view on key GRB issues was wrong almost always, while a minority view turned out to be the right one, as demonstrated in Table I where the 'correct view' is indicated by bold letters.

In the CB model, a highly relativistic jet of plasmoids (CBs) from the central engine first

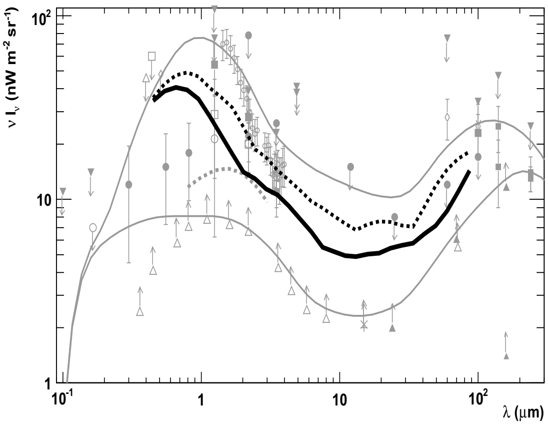

Figure 9: Limits and estimates of the spectrum of the extragalactic background light (EBL) as extracted from different measurements and theoretical models prior to the detection of the blazar 3C279 by MAGIC in TeV gamma rays [56].

crosses a quasi isotropic radiation field (glory) produced around the central engine by wind/mass ejection episodes from the progenitor star/binary system prior to the GRB. The prompt gamma-ray and X-ray emission is dominated by inverse Compton scattering (ICS) of this glory light. A simultaneous broad band synchrotron radiation (SR) and inverse Compton scattering of this radiation to much higher energy begin slightly after the CBs have swept in enough electrons and ionized nuclei of the ejecta/wind in front of them, isotropized them and Fermi accelerated them and the knocked-on (Bethe-Bloch) electrons and nuclei in the CBs to high energy by their turbulent magnetic fields. SR from these electrons dominates the optical radiation, while the ICS of these SR photons (SSC) produces high energy photons with an energy flux density that extends beyond TeV. Production of π^0's in collisions between the Fermi accelerated nuclei and the ambient matter in the CBs and the wind produces a power-law distribution of high energy photons which extends to much higher energies. The same mechanisms can produce also the observed high energy emission from short hard bursts (SHBs). As in the case of blazars, the observed flux of high energy photons from ordinary GRBs and SHBs is significantly suppressed at TeV energies by pair production in the IGM, while in the energy range covered by LAT, the absorption of photons by the extragalactic background light is much smaller.

5 High energy gamma ray astronomy, UHECRs and the extragalactic background light

Pair production in collisions of high energy photons with extragalactic background light (EBL) from the far infrared strongly modifies the flux and spectrum of high energy (0.1-100 TeV) photons from distant point and diffuse sources. Measurements of these fluxes from various bright sources such as AGNs and GRBs as function of redshift can be used to test and constrain theoretical models of star and dust formation, structure formation in the early universe, astrophysical models of HE cosmic sources and photon-photon interaction at very high energies. Photodisintegration of UHECR nuclei in their collisions with EBL photons strongly affects their composition [55]. TeV gamma rays from blazars have been used extensively to test the measurements and theoretical estimates of the EBL (see [56] and Fig. 9), the strongest constraints come from the most distant blazar 3C279 at z=0.536, which has been detected by MAGIC [58] in TeV gamma rays. Detection of a 13 GeV photon from GRB 080916C with the Fermi LAT at redshift z=4.35 has also been used already to test different EBL models [52].

5.1 HE gamma rays from extragalactic sources

Despite the detection of a dozen of extragalactic blazars in TeV by HESS [57], MAGIC [58] and VERITAS [59] and ten times more in GeV photons by Fermi LAT [60,39] and despite the multi wavelength campaigns (e.g. [61] where a few of these extragalactic sources were observed simultaneously in the radio, optical, X-ray, GeV and TeV bands, beside constraining some theoretical models, not much better understanding of how massive black holes launch their mighty jets has been achieved. This is because of the complexity of the black hole engine, the complexity of its environment, the complex time variability of the observed emission and the very many adjustable parameters and assumptions in the theoretical models. Roughly, most observations are consistent with a leptonic SSC model where synchrotron radiation from a population of Fermi accelerated electrons with a typical peak flux energy E_{SR} suffers inverse Compton scattering by the same population of electrons. The relativistic kinematics and the energy dependence of the Klein-Nishina cross section of ICS produces a second peak at $E_{SSC} \approx (m_e c^2)^2 \delta^2 / 3\, E_{SR}\, (1+z)^2$ where δ is the Doppler factor of the Blazar's jet.

Acknowledgments

The author would like to thank all the speakers at the 44th Rencontre De Moriond on High Energy Phenomena in the Universe, the scientific organizing committee for a most interesting program, and in particular Jean Tran Thanh Van and Kim who step aside after having initiated and organized the past 44 Rencontres de Moriond in order to promote scientific collaboration, scientific exchange and spread of scientific knowledge beyond borders and ideological and racial barriers. John Belz, Marusa Bradac, Francesco Cafana, Gudlaugur Johannesson, Daniel Mazin, Aldo Morselli and Michael Schubnell are gratefully acknowledged for supplying original figures for this summary.

References

1. K. Greisen, *Phys. Rev. Lett.* **16**, 748 (1966).
2. G.T. Zatsepin, V.A. Kuz'min, *JETP Lett.* **4**, 78 (1966).
3. D. Allard, *these proceedings and references therein.*
4. M. Takeda et al. *Phys. Rev. Lett.* **81**, 1163 (1998).
5. A. Abbasi et al, *Phys. Rev. Lett.* **100**, 101101 (2008).
6. J. Belz, *these proceedings and references therein.*
7. J. Abraham et al., *Phys. Rev. Lett.* **101**, 061101 (2008)
8. F. Schuessler, *these proceedings and references therein.*
9. J. Abraham et al. [The Pierre Auger Collaboration], *Science* **318**, 939 (2007).
10. J. Abraham et al. [The Pierre Auger Collaboration], *Astropart. Phys.* **29**, 188 (2008).
11. A. Mariazzi, *these proceedings and references therein.*
12. V. Scherini, *these proceedings and references therein.*
13. R. Knapik, *these proceedings and references therein.*
14. J.P. Rachen, P. L. Biermann, *Astron. & Astroph.*, **272**, 161 (1993).
15. J.D. Beckenstein, *Phys. Rev. D*, **70** 083509 (2004).
16. J.R. Brownstein & J.W. Moffat, *MNRAS*, **367**, 527 (2006).
17. M. Bradac, *these proceedings and references therein.*
18. M. Bradac et al., *Astrophys. J.* **652**, 937 (2006).
19. M. Bradac et al., *Astrophys. J.* **687**, 959 (2008).
20. S.D. Hunter et al., *Astrophys. J.* **481**, 205 (1997).
21. W. de Boer et al., *Phys. Rev. Lett.* **95**, 209001 (2005) and references therein.

22. G. Johannesson, *these proceedings and references therein.*
23. F.W. Stecker, S.D. Hunter & D. A. Kniffen, *Astropart. Phys.* **29**, 25 (2008).
24. J. Chang et al., *Nature*, **452**, 362 (2008).
25. C. Cheng, J. L. Feng & K. T. Matchev, *Phys. Rev.Lett.* **89**, 211301 (2002); D. Hooper & K. Zurek, arXiv:0902.0593 2009) and references therein.
26. M. Schubnell, *these proceedings and references therein.*
27. S. Dado & A. Dar, arXiv:0903.0165 (2009).
28. P. Sreekumar et al., *Astrophys. J.* **494**, 523 (1998).
29. A.R. Fazely, R.M. Gunasingha, S.V. Ter-Antonyan, arXiv:0904.2371v3 (2009)
30. F. Aharonian et al., arXiv:0905.0105 (2009).
31. A.A. Abdo et al., arXiv:0905.0025 (2009).
32. F. Cafagna, *these proceedings and references therein.*
33. A. Morselli, *these proceedings and references therein.*
34. O. Adriani et al., *Nature* **458**, 607, 2009
35. I.V. Moskalenko & A.W. Strong, *Astrophys. J.* **493**, 694 (1998).
36. N. Kawanaka, *these proceedings and references therein.*
37. T. Piran, N. Shaviv & E. Nakar, *these proceedings.*
38. A. Dar & A. De Rújula, *Phys. Rep.* **466**, 179, (2008).
39. B. Lott, *these proceedings and references therein.*
40. F. Giordano, *these proceedings and references therein.*
41. M.H. Grondin, *these proceedings and references therein.*
42. A. Hill, *these proceedings and references therein.*
43. D.A. Smith, *these proceedings and references therein.*
44. S. Gabici arXiv:0811.0836 (2008).
45. K. Hurley et al., *Nature* **372**, 652 (1994).
46. M.M. Gonzalez et al., *Nature* **424**, 749 (2003).
47. B.L. Dingus, *in High Energy Gamma Ray Astronomy, AIP Conf. Proc.* **558**, 383 (2001).
48. A. Giuliani et al., *Aston. & Astrophys.* **491**, L25 (2008).
49. L. Baldini, *these proceedings and references therein.*
50. V. Pelassa, *these proceedings and references therein.*
51. J. Granot, *these proceedings and references therein.*
52. A.B. Abdo et al., *Science* **323**, 1688 (2009).
53. S. Dado, A. Dar & A. De Rújula *Astrophys. J.* **696**, 994 (2009).
54. S. Dado, A. Dar & A. De Rújula, *Astrophys. J.* **693** 311 (2009).
55. J.L. Puget et al., *Astrophys. J.* **205** 638, (1976).
56. D. Mazin, *these proceedings and references therein.*
57. L. Gerard, *these proceedings and references therein.*
58. B. De Lotto, *these proceedings and references therein.*
59. W. Benbow, *these proceedings and references therin*
60. J. Ballet, *these proceedings and references therein.*
61. D. Sanchez, *these proceedings and references therein*

Table 1: Evolution of the GRB debate

Issue	Majority View	Minority View	Observational Proof (Year)
Origin	Man Made	**Nature Made**	Vela Satellites (1967-1973)
Location	Solar System	**More Distant**	Vela Satellites (1967-1973)
	Galactic Disk	**Cosmological**	CGRO (1992)
	Galactic Halo	**Distant Galaxies**	BeppoSAX+HST+GBTs (1997)
Event	n^*-n^* Merger	**SN Explosion**	BeppoSAX+HST+GBTs (1998-2003)
Source	Relativistic Fireball	**Relativistic Jet**	CGRO, BeppoSAX (1992-1999)
	Collimated Fireball		Swift+GBTs (2004-2009)
	Conical Jet		
Prompt Radiation:			
keV-MeV	Synchrotron	**Inverse Compton**	BeppoSAX, Swift (1999-2009)
"Prompt Optical"	Reverse Shock	**Synchrotron**	Robotic Telescopes (1999-2009)
Afterglow:			
Chromaticity	Achromatic	**Chromatic**	Swift+Robotics+GBTs (2004-2009)
Plateau phase	Reenergization	**Slow Deceleration**	Swif+GBTs 2004-2009
t_b when:	$1/\Gamma_{jet}\approx\theta_{jet}$	$\mathbf{\Delta M\approx M_0}$	Swift+GBTs (2004-2009)
"Missing break"	Very Late Break	**Very Early Break**	Swift+GBTs (2004-2009)
		To be decided ?	
Jet Geometry	Conical Shells	Cannonballs	Swift, Fermi, HST, GBTs ?
Jet Composition	e^+e^- plasma	Ordinary Matter	Swift, Fermi, HST, GBTs ?
Source	Hypernova	Normal SNIb/c	Integral, Swift, Fermi, HST, GBTs ?
	(Rare SNIb/c)	Most SNIb/c	Integral, Swift, Fermi, HST, GBTs ?
Radiations:			
keV-MeV	SSC ?	ICS of Glory Light	Swift, Fermi, GBTs ?
HE γ's	?	SSC + π^o	LAT,HESS,MAGIC,VERITAS,PAO
HE Neutrinos	Detectable	Non Detectable	ICE CUBE,ANTARES,PAO
Remnant	BH, Magnetar	n^*, BH	Swift , Fermi, HST, GBTs ?

7.
Posters

Realistic model for the prompt and high latitude emissions in GRBs

F. Genet & J. Granot
University of Hertfordshire, Center for Astrophysics Research, Hatfield AL10 9 AB, England

There is good observationnal evidence that the Steep Decay Phase (SDP) that is observed in most *Swift* GRBs is the tail of the prompt emission. The most popular model to explain the SDP is Hight Latitude Emission (HLE). Knowing if the SDP is consistent with HLE would help distinguish between prompt emission models giving rise to HLE and those who do not. We describe the realistic self-consistent model we developped for the prompt emission and its HLE tail, here in the case of internal shocks (IS) only. The prompt emission is modeled as the sum of independent pulses. A single pulse is modeled as emission from an ultra-relativistic thin spherical expanding shell. We obtain analytic expressions for the flux. We find that the observed spectrum is also a Band function, naturally softening with time. The decay of the SDP is initially dominated by the tail of the last pulse, but other pulses can dominate later.

1 Introduction

Most gamma-ray bursts (GRBs) observed by the *Swift* satellite show an early steep decay phase (SDP) in their X-ray light curve. It is usually a smooth spectral and temporal continuation of the GRB prompt emission, strongly suggesting that it is the tail of the prompt emission[1]. It is generally explained by High Latitude Emission[2] (HLE), where at late times the observer still receives photons from increasingly larger angles relative to the line of sight, due to the longer path lenght caused by the curvature of the emitting region. These late photons have a smaller Doppler factor, which results in a steep decay of the flux and in a simple relation between the temporal and spectral indices $\alpha = 2 + \beta$, where $F_\nu(T) \propto T^{-\alpha}\nu^{-\beta}$. We describe first our model for a single pulse, before to combine several pulses to model the prompt emission.

2 Emission of a single pulse

We consider an ultra-relativistic ($\Gamma \gg 1$) thin (of width $\ll R/\Gamma^2$) spherical expanding shell emitting over a range of radii $R_0 \leq R \leq R_f \equiv R_0 + \Delta R$. Considering only the internal shocks model, the Lorentz factor of the emitting shell is assumed to be constant equal to Γ_0, and electrons are expected to be in fast cooling regime. In order to calculate the flux received at any time T by the observer we intergrate over the Equal Arrival Time Surface[3] (EATS), which is the locus of points from which photons reach the observer at the same observed time T. For a shell ejected at an observer time T_{ej}, the first photon reaches the observer at a time $T_{ej} + T_0$ with $T_0 = (1+z)R_0/(c\Gamma_0^2)$. The last photons emitted from the line of sight reach the observer at $T_f \equiv T_0(R_f/R_0) = T_0(1+\Delta R/R_0)$. We choose for the emission spectrum the phenomenological Band[4] function spectrum. The emission mechanism is assumed to be synchrotron. The observer flux is then

$$F_\nu(T \geq T_{\rm ej} + T_0) = F_0 \left(\frac{T - T_{\rm ej}}{T_0}\right)^{-2} \left[\left(\frac{\min(T - T_{\rm ej}, T_f)}{T_0}\right)^3 - 1\right] S\left(\frac{\nu}{\nu_0}\frac{T - T_{\rm ej}}{T_0}\right) \;, \quad (1)$$

where S is the normalized Band function, ν is the observed frequency, $F_0 \equiv (1+z)L_0/(12\pi d_L^2)$ with z the redshift of the source; $\nu_0 = 2\Gamma_0\nu_0'/(1+z)$, where ν_0' is defined as the peak of the Band function spectrum at R_0. The shape a single pulse can vary from spiky to rouder. The observed spectrum is a pure Band function, just like the emitted spectrum, where the observed peak frequency ν_p of the νF_ν spectrum decreases with time as $\nu_p = \nu_0/\tilde{T}$, and $\tilde{T} = (T - T_{\rm ej})/T_0 = 1+\bar{T}$. This corresponds to a softening of the spectrum with time which agrees with observations. The calculation of the instantaneous spectral slope $\beta \equiv -d\log F_\nu/d\log\nu$ and temporal slope $\tilde{\alpha} \equiv -d\log F_\nu/d\log\tilde{T}$, where $\tilde{T} = (T - T_{\rm ej})/T_0 = 1+\bar{T}$ show that the HLE relation $\tilde{\alpha} = 2+\beta$ is valid as soon as $\bar{T} > \bar{T}_f$. One should be careful that this is true only in the framework of internal shocks model, and with this definition of the temporal slope (for exemple, $\bar{\alpha} \equiv -d\log F_\nu/d\log\bar{T}$, which is another definition of the temporal slope, approaches $2+\beta$ only at late time).

3 Combining pulses to obtain the prompt emission

Within our model, the prompt emission is the sum of independent pulses, and the SDP is thus the sum of the tails of these pulses. For a prompt emission composed of several equal pulses, at late time the contribution of each pulse is equal, and the temporal slope just after the peak of a pulse increases with its ejection time T_{ej}. When varying several parameters among the different pulses, the late time flux ratio of the pulse tails is the ratio of their $F_{peak}T_f^{2+\beta}$. Just after the peak of the last pulse, the SDP is dominated by the last pulse. This shows that several pulses can dominate the SDP at different times. Because of noisy data or coarse time bins, a prompt emission which is actually composed by several pulses can be seen and fitted by one broad pulse: the fit would give a tail with the same temporal slope at late time than the actual prompt tail, but with a different behaviour at its beginning. Moreover, this overestimates the flux of the SDP.

4 Conclusion

We have outlined a model for the prompt emission and its tail. This model contains a restricted number of free parameters (7 per pulse in the case for internal shocks), and gives rise to many different shapes for a pulse, from very spiky to rounder, which qualitatively reproduces the observed diversity. The observed spectrum is a pure Band function as the emitted one in the case of internal shocks, and our model naturally produces a softening of the spectrum, as is observed. When combining several pulses to model the prompt emission, the Steep Decay Phase is initially dominated by the last pulse, and is dominated at late times by the pulse with the largest $F_{peak}T_f^{2+\beta}$ (essentially the widest pulse), but can be dominated by other pulses in between. When fitting data, one should be careful not to consider several overlapping pulses as a single broad pulse, which would lead to an overestimate of the prompt tail flux and a misinterpretation of the steep decay phase.

References

1. O'Brien P.T., et al., *ApJ* **647**, 1213 (2006)
2. Kumar P. & Panaitescu A., *ApJL* **541**, L51 (2000)
3. Granot J., Cohen-Tanugi J. & do Couto e Silva E., *ApJ* **677**, 92 (2008)
4. Band D., et al., *ApJ* **413**, 281 (1993)

THE STATUS OF VIRGO

L. ROLLAND, on behalf of the Virgo collaboration
LAPP, Université de Savoie, CNRS/IN2P3, Annecy-le-Vieux, France

1 Introduction

The Virgo [1,2] detector is designed to detect gravitational waves (GW) emitted by astrophysical sources in the frequency range from a few Hz to 10 kHz. It is a recycled interferometer with two 3-km long Fabry-Perot cavities, located close to Pisa (Italy). The expected sources of GWs are continuous wave signals from neutron stars, burst signals ($< 100\,\mathrm{ms}$) from supernova core collapses, 'modeled signals' ($\sim 0.1\,\mathrm{s}$ to a few $10\,\mathrm{s}$) from coalescences of binary compact objects – neutron stars (NS) and black holes (BH) – and stochastic signals from cosmological sources. A detection of a GW signal would be of main interest to study the inner structure of the objects. However, as it is discussed later, useful limits can be derived from non-detections.

2 Virgo first science run and data analysis with LIGO and GEO

During its first science run (VSR1), from May 18th to October 1st 2007, the detector was in *science mode* for 81% of the time. The sensitivity of Virgo at the end of the run is shown along with the LIGO [3] and GEO [4] sensitivities in figure 1. The detector range is defined as the distance of a coalescing binary system whose signal would be seen with a signal-to-noise ratio of 8, averaged over the source sky position, inclination and polarization. During VSR1, the range reached 3.5 Mpc for binary neutrons stars – $(1.4, 1.4)\,M_\odot$ – and 15 Mpc for binary black holes – $(10, 10)\,M_\odot$.

The data from the different detectors, LIGO, GEO and Virgo are being jointly analysed since May 2007. The agreement was made in order to reconstruct the source parameters (direction, polarization), to improve the time and sky coverage and to reduce the false detection rate. Joint analysis is on-going and results will be published soon.

2.1 "All-sky" searches

All-sky searches are being done for the different types of GW signals. A non-detection would result in upper limits on the rate of the detectable events or on the GW strain amplitude.

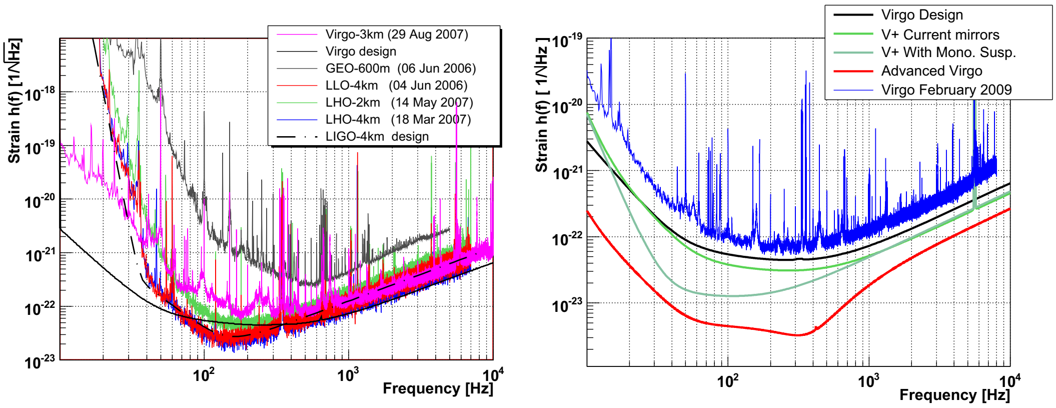

Figure 1: (a) Sensitivity of Virgo, LIGO and GEO during the run VSR1. The design sensitivity of Virgo and LIGO are also given. (b) Design sensitivity of Virgo, Virgo+ and Advanced Virgo along with the Virgo real sensitivity in February 2009.

2.2 Known pulsars

GW emission from known pulsars is being searched for. The non-detection of GW emission sets upper limits on the fraction of the spin-down energy emitted through GWs and on the pulsar ellipticity.

2.3 Astrophysical triggers

Emphasis is put on searches that focus on astrophysical triggers[5] detected through other messengers (γ-rays, X-rays, optical light, radio, neutrinos). It allows to search for GW with amplitude closer to the noise floor of the detector. Such a multi-messenger detection would improve our understanding of the stucture of the objects. However, useful limits can be derived from non-detections in the GW domain. For example, assuming that a given γ-ray burst (GRB) is emitted by the merging of a binary system, a GW signal is searched using a matched-filtering method. A non-detection of GW from the GRB would allow to place limits on the distance and mass of the system[6,7]. A non-detection of GRB events using a burst analysis would place limits on the energy emitted in GW by the event.

Using different detectors together, the reconstruction of the location of the detected GW events gives the possibility to follow-up observations with optical telescopes. This approach is currently being developed to get ready for the advanced detectors area.

3 Status of Virgo+

The aim of Virgo+ is to gain a factor two in sensitivity compared to the Virgo design (see figure 1) and start a run (VSR2) mid-2009. The expected values for some figures of merit of Virgo+ are given in table 1.

To achieve such sensitivity, different upgrades were done from June 2008. To reduce the shot noise, a new input mode-cleaner end mirror, a new laser amplifier (50 W) with compliant injection system optics and a system to compensate the thermal deformation of the mirrors have been installed. New control electronics was installed to reduce the control noise. To reduce the thermal noise and further increase sensitivity, new mirrors suspended to monolithic suspensions are expected to be installed during a suitable interruption of data taking.

The Virgo+ commissioning is ongoing. In February 2009, without increased laser power yet, a range of 7 Mpc for BNS was reached.

Table 1: Figures of merit of the different phases of the detector: range for binary systems and typical strain sensitivity level to bursts and to the Crab pulsar (integrating over 1 year, with 1% false alarm rate and 90% detection efficiency). AdvVirgo sensitivity to the Crab pulsar ellipticity will be of the order of 10^{-5}. Virgo+: (1) without and (2) with monolithic suspensions.

	BNS (Mpc)	BBH (Mpc)	Sensitivity at 1 kHz	Crab (at 60 Hz)
Virgo design	11	58	7.2×10^{-23}	1.4×10^{-25}
Virgo+ (1)	15	76	5.1×10^{-23}	$\sim 1 \times 10^{-25}$
Virgo+ (2)	54	272	5.0×10^{-23}	$\sim 3 \times 10^{-26}$
Advanced Virgo	149	753	1.8×10^{-23}	$\sim 10^{-26}$

4 Towards Advanced Virgo

The goal of Advanced Virgo is to improve the sensitivity by a factor 10 (increasing the observed volume by a factor 1000) compared to the nominal Virgo design (see table 1 and figure 1 for some figures of merit). A document describing the AdvVirgo baseline design has been released with preliminary budget and execution plans. The schedule is in parallel with the upgrades towards Advanced LIGO.

5 Conclusion

The Virgo detector made its first scientific run in coincidence with the three LIGO detectors in 2007. A first detection is unlikely, but several upper limits on GW emission will be set in the next months.

The upgraded detector, Virgo+, will start a new run in 2009, making a first detection plausible. The proposal for Advanced Virgo, designed to achieve a sensitivity a factor 10 better in all the detection band, should allow to detect several events per month, opening the GW astronomy area.

Astrophysical triggered searches are being developed and might help to give confidence in the first GW detections.

References

1. http://wwwcascina.virgo.infn.it
2. F. Acernese et al., J.Phys.:Conf.Ser. **120**, 032007 (2008)
3. http://www.ligo.caltech.edu/
4. http://geo600.aei.mpg.de/
5. B. Abbott et al., Class. Quantum Grav. **25**, 114051 (2008)
6. F. Acernese et al., Class. Quantum Grav. **25**, 225001 (2008)
7. B. Abbott et al., Astrophys.J. **681**, 1419 (2008)

The puzzling clustering and bimodality of long GRBs optical afterglow luminosities

M. Nardini[1], G. Ghisellini[2], G. Ghirlanda[2]
[1] *SISSA/ISAS, Via Beirut 2-4, 34014 Trieste, Italy*
[2] *Osservatorio Astronomico di Brera, via E. Bianchi 46, I23807 Merate, Italy*

The study of the rest frame properties of long Gamma-Ray bursts (GRBs) afterglows is a fundamental aspect for a better understanding of the nature of these powerful explosions. The launch of the Swift satellite (November 2004) marked a strong improvement of the observational capabilities of X-rays and optical afterglows. We studied the intrinsic optical afterglows of a sample of long GRBs finding an unexpected clustering and a hint of bimodality of the optical luminosity distribution (at 12h after the trigger). Through a Montecarlo simulation we proved that both the observed clustering and bimodality are not simply due to selection effects but should hide important informations in the understanding of the nature of the afterglow emission. These findings can shed also light on the nature of the large fraction of optically dark GRBs.

1 Optical luminosity distribution

The study of the long GRBs optical luminosity light–curves rest frame properties in pre-*Swift* era showed that the luminosity distribution of most GRBs clusters around a typical value. The optical luminosity distribution is much narrower than the observed flux distribution and is also narrower than the distributions of the prompt gamma ray energetics (Nardini et al. [1]; see also Liang & Zhang [2]). We also found a hint of bimodality in the optical luminosity distribution since 3 underluminous GRBs were at more than 4 σ below the brighter events mean luminosity.

The launch of the *Swift* satellite combined with the availability of a net of fast pointing ground based optical telescopes allowed a fast and rich optical follow–up starting from a few dozen of seconds after the trigger for a large number of events. In more recent works we verified whether the clustering and the bimodality obtained in the pre–*Swift* optical luminosity distribution of long GRBs is confirmed by more abundant data of the *Swift*–era. We selected a sample of all the long GRBs with known redshift, good optical photometry coverage at some hours after the trigger and with a published estimate of the host galaxy dust absorption $A_{\rm V}^{\rm host}$. As of the end of March 2008 we found a sample of 33 GRBs fulfilling our selection criteria (golden sample) and 20 without the $A_{\rm V}^{\rm host}$ estimate. In the left panel of Fig. 1 we plot the rest frame K–corrected and de–reddened monochromatic luminosity light–curves at the central frequency of the R band in the rest frame time. At very early times (accessible now with *Swift*, and poorly sampled in pre–*Swift* era) the luminosities span some orders of magnitudes, but at later times we confirm both the clustering and bimodality observed in Nardini et al. [1]. The right panel of Fig. 1 shows the luminosity distribution at the common rest frame time of 12 h after trigger. Note the presence of a gap between the underluminous and the brighter events families (for more details see Nardini et al. [3].

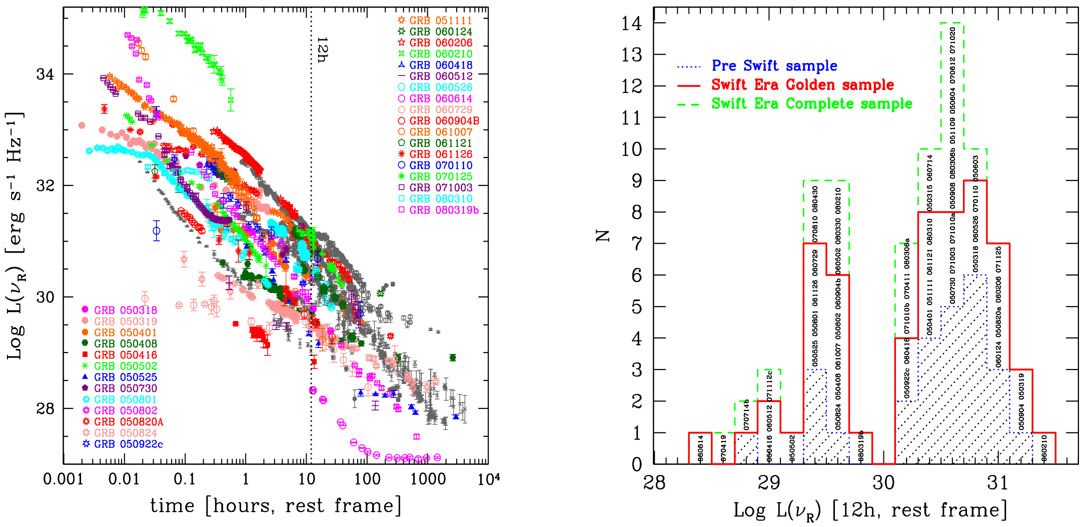

Figure 1: *Left panel*: Rest frame L_{ν_R} light–curves of the *Swift* GRBs in our sample superposed to the pre-*Swift* ones. *Right panel*: Optical luminosity distribution at 12 h after trigger (rest frame time).

2 The role of selection effects and dark bursts

In order to test whether the observed clustering and bimodality are real or just due to observational biases we applied the method developed in Nardini et al. [4]. We analysed all the telescopes limiting magnitudes of the optically dark GRBs observations and we obtained the probability distribution for a GRB to be observed in the R band at 12h after trigger with a given limiting magnitude (TSF). Through a Montecarlo simulation we generated a large number of optical afterglows assuming i) a redshift distribution following the star formation rate (Porciani & Madau [5]), ii) different luminosity functions and iii) A_V^{host} distributions. We then check if they would be observable using the limiting magnitudes described by the TSF. The luminosity distribution of the observable simulated events was then compared with the real one.

We found that no unimodal intrinsic luminosity function can reproduce the real observed distribution. This can be reproduced either assuming an intrinsically bimodal luminosity function or assuming a strong achromatic absorption (grey dust) for about half of the simulated afterglows. In our simulation most of the GRBs belonging to the bright family events are usually observable even at large redshifts, while most of the faint family bursts are below the telescope sensitivity. The ones we observe are then the tip of the iceberg of a large family of optically faint bursts. The optically dark GRBs can therefore belong to these unobservable low luminosity events.

References

1. M. Nardini *et al*, A&A **451**, 821 (2006)
2. E. Liang & B. Zhang, ApJ **638**, 67 (2006)
3. M. Nardini *et al*, MNRAS **386**, L87 (2008)
4. M. Nardini *et al*, MNRAS **383**, 1049 (2008)
5. C. Porciani & P. Madau, ApJ **548**, 522 (2001)

STATUS OF HAGAR EXPERIMENT AT HANLE

B.S. ACHARYA
(On behalf of HIGRO Collaboration)
Dept. of High Energy Physics, Tata Institute of Fundamental Research, Dr Homi Bhabha Road, Colaba, Mumbai 400 005, India

A new ground-based high altitude γ-ray observatory was recently set up at Hanle in the Ladakh region of the Himalayas. It consists of wavefront sampling array of 7 non-imaging telescopes (named HAGAR), the first of its kind to be set up at so high an altitutude. The details of setup, performence studies and observation status are presented in this paper.

1 Introduction

The ground-based atmospheric Cherenkov technique has been successful in detecting celestial sources VHE γ-rays. The recent emphasis is to reduce the energy threshold further to overlap the energy range between the satellite- and ground-based detectors. One such possibility is to install telescopes at high altitudes[1,2]. We have set up the Himalayan Gamma Ray Observatory (HIGRO)[3] at Hanle ($32^\circ.8\ N$, $78^\circ.9\ E$, 4300 m amsl) in the Ladakh region near a 2 m Himalayan Chandra Telescope (HCT). Recently, an array of 7 non-imaging Cherenkov telescopes (HAGAR) has been commissioned. This will be followed by a large 21-m dia. imaging telescope (MACE).

2 HAGAR telescope array

The HAGAR (High Altitude GAmma Ray) telescope array[4] is based on wavefront sampling technique. It consists of 7 non-imaging telescopes deployed as shown in figure 1. Each telescope has 7 para-axially mounted F/1 mirrors of 90 cm dia. viewed by an UV sensitive photomultiplier tube (Photonis XP2268B) mounted at the focus behind 3° diameter mask. Each telescope's pointing is modelled by sighting large number of bright stars.

Pulses from individual PMTs are brought to the control room through coaxial cables. Signals from the 7 PMTs of a telescope are added linearly to yield a suitable trigger pulse. A real time clock synchronized to 1 Hz pulse from GPS clock, is used for recording absolute time with a resolution of 1 μs. The interrupt driven PC based data acquisition and recording system employs CAMAC based instrumentation. The trigger for data acquisition is obtained from a coincidence of any 4 out of 7 telescope pulses. For each trigger informations regarding pulse height, relative arrival time of pulses from all PMTs etc. are recorded. The typical trigger rate is about 14 Hz.

3 Performance of HAGAR from Monte Carlo simulation studies

Monte Carlo simulation of Cherenkov showers have been carried out using CORSIKA code[5]. Showers initiated by γ-rays, e^-, p and α particles incident at the top of the atmosphere were

Figure 1: Photograph of HAGAR array (left) & Layout of telescopes (right)

Figure 2: Threshold energy vs Trigger rate (left) Sensitivity of HAGAR array (right)

simulated. The γ/hadron segregation potential of various parameters like Cherenkov photon density fluctuations, relative timing jitter, pulse decay time etc. have been investigated[6]. Taking into account various design details, the energy thresholds, trigger rates and the sensitivity are estimated for γ-rays and cosmic rays[6]. The expected rate of trigger events and the corresponding energy threshold is shown in figure 2 together with the expected 5σ sensitivity. Dotted line corresponds to the case without rejection of cosmic ray showers. Solid line is for 98% rejection of hadronic showers and retention of 35% gamma ray showers. The energy threshold of the HAGAR system is in the range of 60 to 200 GeV.

4 Present status and Conclusions

Regular observations using the 7 element HAGAR array have started in Sept 2008. We have observed pulsars (Crab and Geminga) and AGNs (Mkn421 and 1ES2344+514). The angular resolution at present is 0.2 ± 0.1 deg. The analysis of data is going on.

Acknowledgements

We are thankful to colleagues from TIFR, IIA and BARC for their contributions towards the design, fabrication and testing of HAGAR system.

References

1. F. Aharonian *et al.*, *Astropart. Phys.* **15**, 335 (2001).
2. R. Cowsik *et al.*, *in proc. of 27th ICRC, Hamburg* **OG 2.05**, 2769 (2001).
3. R. Koul *et al.*, *in [proceedings of* 29^{th} *ICRC, Pune*, **5**, 243 (2005).
4. B.S. Acharya *et al.*, *in proc. of 30th ICRC, Merida* **3**,1361 (2007).
5. D. Heck *et al.*, *Forschungszentrum Karlsruhe Report*, **ZKA 6019** (1998).
6. V.R. Chitnis *et al.*, *in proceedings of* 29^{th} *ICRC, Pune*, **5**, 235 (2005).

Introduction of the AMBER Experiment

E. W. Grashorn, for the AMBER Collaboration
Center for Cosmology and AstroParticle Physics, Ohio State University, 191 W. Woodruff Ave., Columbus, OH 43210, USA

The AMBER (Air-shower Microwave Bremsstrahlung Radiometer) uses a novel technique for microwave detection of cosmic ray airshowers. Laboratory experiments have shown that the observed microwave emission scales with energy, which will provide a high duty cycle complement to current nitrogen fluorescence methods. A prototype detector is deployed at University of Hawaii, USA, and prototypes are being developed at Ohio State University, USA and the Pierre Auger Observatory in Mendoza, Argentina.

1 Introduction

The origin and acceleration of Ultra High Energy Cosmic Rays (UHECRs) is one of the most vexing problems in astrophysics. Despite well over four decades of study, these fundamental aspects remain a mystery. The combination of power law energy spectrum and Greisen-Zatsepin-Kuzmin (GZK) suppression [1,2] above $6{\times}10^{19}$ eV makes it difficult to obtain a high statistics sample, and the fact that UHECRs are charged particles traveling through galactic and extra-galactic magnetic fields makes it hard to trace them back to their origin. Recent projects such as AGASA [3], Hi-Res [4] and Pierre Auger Observatory [5] have yet to discover an incontrovertible source. The two most widely deployed detection methods, surface detection (AGASA, Auger) and fluorescence detection (Hi-Res, Auger) present particular challenges. A surface detector array employs ground stations spaced over kilometers to collect a small fraction of the particles produced by the airshower. Due to the limited sampling of the shower, this method relies on Monte Carlo for particle interactions at energies orders of magnitude above current accelerators or average shower behavior determined empirically, resulting in an energy resolution of order $\sim$20%. A fluorescence detector directly images the fluorescence of nitrogen excited by the passage of an UHECR air shower. The amount of light collected scales with energy, which provides excellent energy resolution, and the observation of shower development provides strong constraints on primary particle type. These detectors can only operate on clear, moonless nights, however, which limit their duty cycle to around 10%. A new method of radio air shower detection via the collection of broadband molecule Bremsstrahlung radiation has been demonstrated recently by a project called the Air-shower Molecular Bremsstrahlung Radiometer (AMBER) [6].

2 Molecular Bremsstrahlung Radiation

An Ultra-High Energy Cosmic Ray air shower dissipates most of its substantial energy budget through ionization, producing a tenuous plasma. The plasma cools on a nanosecond time scale, distributing its thermal energy through collisions with neutral molecules, which leads to the nitrogen fluorescence currently observed. These electrons can produce their own emission, including continuum Bremsstrahlung radiation. The violation of equilibrium conditions in this process produces a signal enhancement, a partially coherent emission. This radiation has been shown to scale with energy in laboratory experiments at the Argonne Wakefield Accelerator (AWA) and at the Stanford Linear Accelerator Center (SLAC) [6].

3 Current Efforts

AMBER exploits the economy of scale by buying off-the-shelf satellite television components for its prototypes. University of Hawaii, Manoa, has operated a 1.8 m broadband antenna with four C-band (3.7-4.2 GHz) feedhorns arranged in a diamond pattern (similar to Fig. 1) on the roof of the Physics building periodically since 2005. Ten candidates were observed over several months [6]. A similar array is under construction at the Ohio State University ElectroScience Laboratory, using a slightly larger (2.4 m) antenna. This is pictured in Fig. 1.

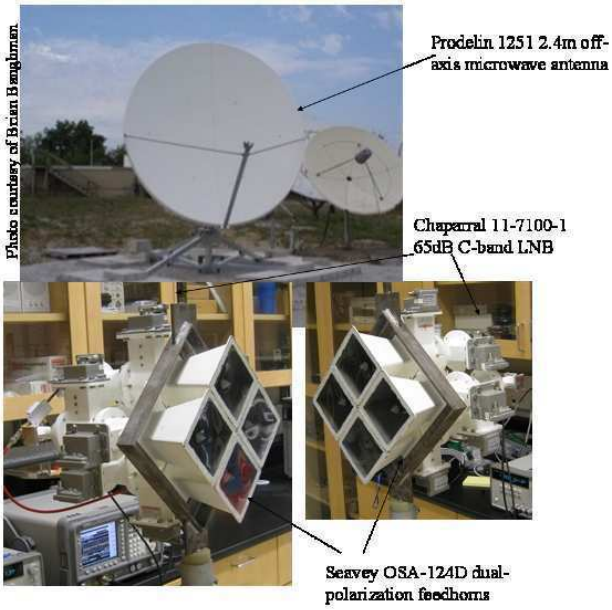

Figure 1: The prototype feedhorn array at OSU

4 Future Plans

Two four pixel arrays similar to the one shown in Fig. 1 will be installed in the Austral Autumn at the Coihueco Fluorescence Detector site of the Pierre Auger Observatory in Mendoza, Argentina. This is the site of many new R&D efforts at the Observatory including HEAT and AMIGA, projects seeking to lower the Auger energy threshold for fluorescence detection and surface detection, respectively. This site is a natural location for AMBER to verify its use as a cosmic ray detector.

Acknowledgments

This work was funded directly by the Center for Cosmology and AstroParticle Physics at Ohio State University. AMBER is funded by the US Department of Energy High Energy Physics Division.

1. K. Greisen, Phys. Rev. Lett. **16**, 748 (1966).
2. G. T. Zatsepin and V. A. Kuzmin, JETP Lett. **4**, 78 (1966) [Pisma Zh. Eksp. Teor. Fiz. **4**, 114 (1966)].
3. N. Chiba *et al.*, Nucl. Instrum. Meth. A **311**, 338 (1992).
4. T. Abu-Zayyad *et al.*, Nucl. Instrum. Meth. A **450**, 253 (2000).
5. J. Abraham *et al.* [Pierre Auger Collaboration], Nucl. Instrum. Meth. A **523**, 50 (2004).
6. P. W. Gorham *et al.*, Phys. Rev. D **78**, 032007 (2008) [arXiv:0705.2589 [astro-ph]].

Fermi-LAT search for gamma-ray pulsations in 2 young radio pulsars in the Carina region

M. RAZZANO on behalf of the *Fermi* LAT Collaboration
Istituto Nazionale di Fisica Nucleare, Sezione di Pisa, I-56127 Pisa, Italy

Thanks to its large effective area, resolution and sensitivity, the *Fermi* Gamma-ray Space Telescope is opening a new era for gamma-ray astronomy. In particular the Large Area Telescope, the main instrument aboard *Fermi*, is going to detect and identify many new gamma-ray pulsars, helping to better understand the emission mechanism of these fascinating sources. I report on the observations of two young radio pulsars within EGRET sources in the Carina region, a portion of the sky populated by many gamma-ray sources. The first one is PSR J1048-5832, located well within a 3EG source and detected with low-confidence as a gamma-ray pulsar by EGRET. The second one, PSR J1028-5819, is a young radio pulsar recently discovered in a search of 3EG error circles, and its association with the source 3EG J1027-5817 makes it an excellent candidate to be a gamma-ray pulsar.

1 Introduction

With the advent of the *Fermi* Large Area Telescope (LAT) [1] most of the EGRET unidentified gamma-ray sources are going to be identified. In particular most of the Galactic sources are expected to be identified as gamma-ray pulsars [9,15]. Right after its launch, *Fermi* has shown its potential in studying in great details the already known pulsars [2] and detecting new ones [3]. Among the several gamma-ray complexes along the Galactic plane, the Carina region is crowded with unidentified EGRET and COS B sources[9,14] and thus is among the best targets for focusing the search for pulsations from gamma-ray pulsars.

2 PSR J1028-5819

PSR J1028-5819 lies in the error circle of the EGRET source 3EG J1027-5817 and has been discovered in radio just few months prior to *Fermi* launch [12] as part of a search of three EGRET sources at high frequency. It is a young pulsar, with period P = 91.4 ms, period derivative $\dot{P}$ = 1.61×10^{-14} s s^{-1} and characteristic age $\tau_c = 9.21 \times 10^4$ yr. The derived spin-down power,

$\dot{E}_{SD} = 8.43 \times 10^{35}$ erg s^{-1} combined with its dispersion measure derived distance of 2.3 kpc makes it a plausible counterpart for the EGRET source with flux of (6.6±0.7) $\times$ 10^{-7} ph cm^{-2} s^{-1}. The data has been collected during the initial 35 days of on-orbit verification, including sky-survey tuning and pointed-mode tuning on Vela pulsar [3], from June 30 to August 3 2008, as well as the initial 15 weeks of sky survey, from August 3 to November 16 2008, and using the *Diffuse* class in order to minimize the background contamination. The full details of the results have been recently published [5].

The right panel of Fig. 1 shows the profile of PSR J1028-5819 in gamma-rays compared with the radio profile obtained at Parkes 64 m. telescope. Two peaks are clearly visible at $\phi = 0.200 \pm 0.003$ and $\phi = 0.661 \pm 0.003$, separated by ~ 0.46 in phase, with no significant evolution of the pulse profile with energy. The LAT point source 0FGL J1028.6-5817 from the Fermi LAT bright source list [4] corresponding to PSR J1028-5819 is located at (R.A., decl.)=(157.166, -58.292), and there are two other LAT point sources nearby, 0FGL J1024.0-5754 and 0FGL J1018.2-5858, 0.73° and 1.52° away respectively. The COS-B source 2CG 284-00 [14] was apparently made up of contributions from all three LAT sources, while the EGRET source 3EG J1027.5817 has now been resolved by the Fermi LAT into contributions from the two sources, 0FGL J1028.6-5817 and 0FGL J1024.0-5754. The spectrum has been fit using a standard maximum likelihood estimator (gtlike) provided in the *Fermi* Science Tools, with a power law with index $\Gamma = 1.22 \pm 0.2 \pm 0.12$ and energy cutoff $E_c = 2.5 \pm 0.6 \pm 0.5$ GeV (the first errors are statistical and the second are systematic). These values lead to a gamma luminosity of 1.1×10^{35} f erg/s (f is a beaming correction factor) and an efficiency $\eta_\gamma = 0.13$ f/I_{45} (I_{45}= I/10^{45}gcm^2). Using the gamma-ray light curve Atlas of [16] we have estimated $f \sim 1.1$ for the Outer Gap model [13] and $f \sim$ 0.9-1.0 for the Two Pole Caustic Model [6] or Slot Gap models [10].

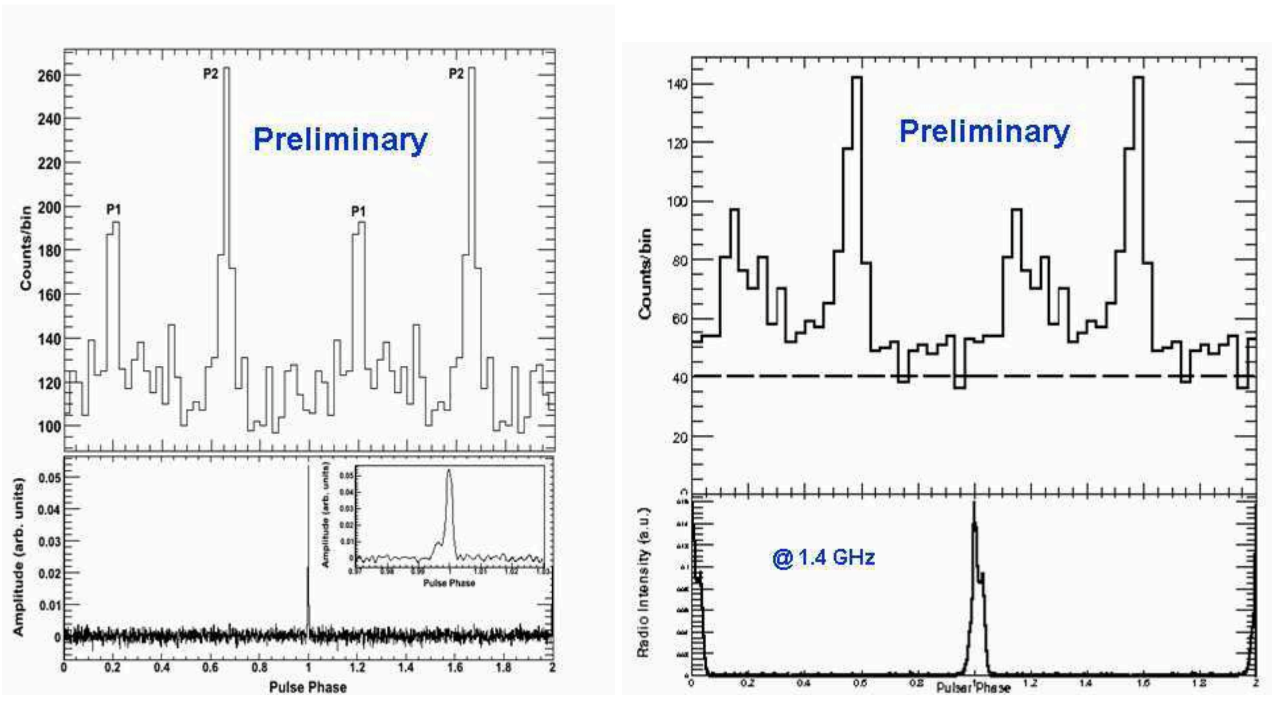

Figure 1: Left: 40 bin light curve of PSR J1028-5819 for E>100 MeV compared with the radio profile obtained at Parkes 64 m telescope. Right: 30 bin 30 bin light curve of PSR J1048-5832 for E>100 MeV compared with the radio profile obtained at Parkes 64 m telescope.

3 PSR J1048-5832

PSR J1048-5832 was discovered at radio wavelengths in a Parkes survey [7] within the error circle of the EGRET source 3EG J1048-5840 and the COS-B source 2CG 288-00 [14]. This pulsar is young, with period $P = 123.7$ ms, period derivative $\dot{P} = 9.6 \times 10^{-14}$ s s^{-1} and characteristic age τ_c 2.0×10^4 yr. The derived spin-down power, $\dot{E}_{SD} = 2.0 \times 10^{36}$ erg s^{-1} combined with its HI derived distance of 2.5-6.6 kpc [8] makes it a plausible counterpart for the EGRET source with flux of $(6.2 \pm 0.8) \times 10^{-7}$ ph cm^{-2} s^{-1}. A previous study of the EGRET data suggested the possibility of a gamma-ray pulsation [11], that the *Fermi*-LAT has now confirmed with high confidence. The first light curve is shown in Fig. 1, where data were collected in the same period as J1028-5819. The gamma-ray light curve, compared with the radio profile, shows two clear peaks at $\phi \sim 0.14$ and $\phi \sim 0.56$, and the profile clearly resembles that of the Vela pulsar.

4 Conclusions

In this contribution we have shown a short highlight of the results of observations of two new gamma-ray pulsars in the Carina region, which turn out to give clear pulsed signals modulated at the same period as the radio pulsar. These two pulsars are then clear examples of the large potential of the *Fermi*-LAT for discovery and identification of gamma-ray sources, in particular those that contribute to the highly-structured Galactic gamma-ray emission.

References

1. Atwood, W. B., et al. 2009, ApJ, accepted.
2. Abdo, A. A., et al. 2008, Science, 322, 1218
3. Abdo, A. A., et al. 2009, ApJ, accepted, arXiv:0812.2960
4. Abdo, A. A. 2009, arXiv:0902.1340
5. Abdo, A. A., et al. 2009, ApJL, 695, L72
6. Dyks, J., & Rudak, B. 2003, ApJ, 598, 1201
7. Johnston, S., Lyne, A. G., Manchester, R. N., Kniffen, D. A., D'Amico, N., Lim, J., & Ashworth, M. 1992, MNRAS, 255, 401
8. Johnston, S., Koribalski, B., Weisberg, J. M., & Wilson, W. 1996, MNRAS, 279, 661
9. Hartman, R. C., et al. 1999, ApJS, 123, 79
10. Muslimov, A. G., & Harding, A. K. 2004, ApJ, 606, 1143
11. Kaspi, V. M., Lackey, J. R., Mattox, J., Manchester, R. N., Bailes, M., & Pace, R. 2000, ApJ, 528, 445
12. Keith, M. J., Johnston, S., Kramer, M., Weltevrede, P., Watters, K. P., & Stappers, B. W. 2008, MNRAS, 389, 1881
13. Romani, R. W. 1996, ApJ, 470, 469
14. Swanenburg, B. N., et al. 1981, ApJL, 243, L69
15. Yadigaroglu, I.-A., & Romani, R. W. 1995, ApJ, 449, 211
16. Watters, K. P., Romani, R. W., Weltevrede, P., & Johnston, S. 2009, ApJ, 695, 1289

Gravitinos, the Lithium problem, and DM production: Is there a corresponding neutrino physics linkage?

A.W. Beckwith
American Institute of Beam Energy Propulsion,
P.O. Box 1907, Madison, Alabama, 35758
beckwith@aibep.org, abeckwith@uh.edu

Studies are cited indicating that gravitino production acts as a natural upper bound to Li^6 and Li^7 levels, based on what happens after hadronic decay of relic 1 TeV into 100 GeV gravitinos at 1000 s. after the Big Bang. The produced gravitinos contribute a large fraction of required dark matter density. Whether or not gravitinos can be linked to neutrino production depends on which model of dark matter (DM) is assumed or used. A model presented by the author in 2008 links DM of about 100 GeV -- based on a phenomenological Lagrangian creating different Neutrino masses without SUSY -- with a dark matter candidate of about 100 GeV. This may tie in 100 GeV gravitinos with neutrino physics.

Introduction

The author has presented (Beckwith, 2008a and 2008b) arguments relating the number of computational operations for production of entropy -- given by Seth Lloyd (2001) and modified by Beckwith (2009) -- to graviton production:

$$I = S_{total} / k_B \ln 2 = [\#operations]^{3/4} = \left[\rho \cdot c^5 \cdot t^4 / \hbar\right]^{3/4} \tag{1}$$

Where I is total entropy divided by Boltzman's constant , k_B is Boltzmann's constant, S_{total} is the entropy generated by emergent space time up to a time t, and ρ density is the "time component" of the usual stress-energy expression of general relativity $\rho \equiv T^{00}$. This formulation of entropy provides a way to obtain a numerical count (at or before 1000 s. after the Big Bang) of gravitons ($\Delta S \approx \Delta N_{gravitons} \approx 10^{20}$) as part of an emergent field representation of gravity/gravitational waves, a starting point for determining increasing net universe cosmological entropy. To tie in the use of Eqn. (1) with dark matter/neutrino physics, it should be noted that gravitinos (the SUSY "partner" of gravitons) are modeled by Karsten Jedamzik et al. (2008), as having a mass of 100 GeV at 1000 seconds after the Big Bang. The author's model of DM (2009) also estimated, via a non-SUSY Lagrangian argument, a mass range on the order of 100 to 400 GeV. If there is an early universe production of gravitinos as a super partner to gravitons, suppression of Li^6 levels is assumed to be linked to the relic production of 100 GeV gravitinos. If Li^6 levels are also linked to DM mass values, this may say something about relic neutrino data sets, especially if Beckwith's (2009) linkage of the Meissner and Nicholai Lagrangian for neutrino physics and DM -- using Ng's equivalence between entropy and numerical production values (2007) – is confirmed.

Models of suppression of Li^6 and Li^7 levels due to 100 GeV gravitino generation

Jedamzik (2008, page 7) estimates that the suppression of Li^7 is linked to gravitinos, based on the idea that supersymmetry relates a boson to a fermion. The lack of experimental evidence of, say, a selectron (bosonic particle having all the properties of an electron except that it has zero spin) suggests that supersymmetry is broken. This selectron could then acquire large mass corrections, which would have prevented us from finding it thus far. If there is, say, a change in entropy, and the number of relic, emergent gravitational field "gravitons" from the Big Bang (the number is defined as $\Delta S \approx \Delta N_{gravitons} \approx 10^{20}$ within 1000 seconds after the Big Bang) and supersymmetry creates a similar number of super partner gravitinos, each of mass of about 100 GeV, Beckwith (2009) proposes (assuming each gravitino is paired with a relic graviton) that the number of relic neutinos is roughly equivalent to the number of relic gravitinos. This is in line with $\Delta S \approx \Delta N_{gravitons} \approx 10^{20}$ in the first 1000 s. after the big bang. Does this lead to limits on Lithium 6 and Lithium 7 production?

Conclusion: A certain number of gravitons/gravitinos produced leads to Lithium 6 and 7 numerical production. Does this imply relic neutrino data sets?

If a certain number of neutrinos of mass of at least 28 to 100 GeV is produced, as implied by G. Belanger (2004), the following needs to be investigated: is there roughly a one-to-one correspondence between gravitinos, neutrinos, and relic gravitons, leading to $\Delta S \approx \Delta N_{gravitons} \approx 10^{20}$ in the first 1000 s.? And if true, are there enough gravitinos and neutrinos to account for Jedamzik's (2008) data, indicating suppression of Lithium 6 and 7? The payoff of this linkage would be linking relic neutrinos and relic gravitons – leading to possibly linking the data sets of the IceCube neutrino telescope with the NIST experiment on primordial early universe gravitational waves (2009). If this linkage is confirmed, it could indicate that there are, indirectly through supersymmetry, enough neutrino-gravitino "objects" produced in the early universe to confirm the suppression of Lithium 6 and 7. It should be noted that this investigation would be more sophisticated than what McElrath (2007) suggested for limits to dark matter searches, which would require LHC style accelerator searches. .

References

Beckwith, A.W. "Several routes to determining entropy generation in the early universe" (2008a), arXiv:0712.0029

Beckwith, A.W., "Implications for the Cosmological Landscape: Can Thermal Inputs from a Prior Universe Account for Relic Graviton Production?" AIP Conference Proceedings 969, (2008b), pp. 1091-1102

Beckwith, A.W.," Hypothetical Dark Matter/Axion rockets: What can be said about Dark Matter in terms of space physics propulsion", AIP Conf.Proc.1103:276-284, (2009), http://arxiv.org/abs/0810.1493

Belanger, G.; Boudjema, F.; Cottrant, A.; Pukhov, A.; Rosier-Lees, S, "Lower limit on the neutralino mass in the general MSSM,".(2004) JHEP0403:012,2004, http://arxiv.org/abs/hep-ph/0310037

Jedamzik, K. "Neutralinos, Gravitinos, and the Cosmic Lithium Problem," (2008), http://www.oamp.fr/lam/equipes/inter/jedamzik.pdf

Jedamzik, K.; Choi, K-Y; Roszkowski, L; Ruiz de Austri, R., "Solving the Cosmic Lithium Problems with Gravitino Dark Matter in the CMSSM," JCAP 0607 (2006) 007, http://arxiv.org/abs/hep-ph/0512044

Lloyd, S., "Computational capacity of the universe," (2001), http://arxiv.org/abs/quant-ph/0110141

McElrath, R., "Light Higgses and Dark Matter at Bottom and Charm Factories", (2008) http://arxiv.org/abs/0712.0016

Meissner, K.A.,Nicolai, H., "Neutrinos, Axions, and Conformal Symmetry,",arXiv: 0803.2814v2, 2 April 2008

NIST, "Super-Sensors to Measure 'Signature' of Inflationary Universe," (2009) http://www.nist.gov/public_affairs/releases/aps_050209.html

XLIVth Rencontres de Moriond

Very High Energy Phenomena in the Universe

List of Participants

Last Name	First Name	City	Country	email
Abdou	Yasser	Gent	**Belgium**	yasser@inwfsun1.ugent.be
Acharya	Bannanje	Mumbai	**India**	acharya@tifr.res.in
Albert	Justin	Victoria	**Canada**	jalbert@uvic.ca
Allard	Denis	Paris	**France**	allard@apc.univ-paris7.fr
Amati	Lorenzo	Bologna	**Italy**	amati@iasfbo.inaf.it
Anisimov	Alexey	Hamburg	**Germany**	alexey.anisimov@desy.de
Ansari	Reza	Orsay	**France**	ansari@lal.in2p3.fr
Armengaud	Eric	Gif sur Yvette	**France**	armengau@in2p3.fr
Arruda	Maria Luisa	Lisbon	**Portugal**	luisa@lip.pt
Baldini	Luca	Pisa	**Italy**	luca.baldini@pi.infn.it
Ballet	Jean	Gif sur Yvette	**France**	jballet@cea.fr
Barnacka	Anna	Warszawa	**Poland**	abarnack@camk.edu.pl
Becerra Gonzalez	Josefa	Tenerife	**Spain**	jbecerra@iac.es
Becherini	Yvonne	Paris	**France**	yvonne.becherini@ apc.univ-paris7.fr
Beckwith	Andrew	Moriches	**USA**	abeckwith@uh.edu
Belz	John	Salt Lake City	**USA**	belz@cosmic.utah.edu
Benabderrahmane	Mohamed L.	Zeuthen	**Germany**	mohamed.lotfi.benabderrahmane@desy.de
Benbow	Wystan	Cambridge	**USA**	wbenbow@cfa.harvard.edu
Bertin	Vincent	Marseille	**France**	bertin@cppm.in2p3.fr
Bolanos Carrera	Azucena	Mexico	**Mexico**	azucena@fis.cinvestav.mx
Bolmont	Julien	Paris	**France**	bolmont@in2p3.fr
Bonifazi	Carla	Paris	**France**	bonifazi@lpnhe.in2p3.fr
Bradac	Marusa	Santa Barbara	**USA**	marusa@physics.ucsb.edu
Bratek	Lukasz	Krakow	**Poland**	lukasz.bratek@ifj.edu.pl
Brigida	Monica	Bari	**Italy**	monica.brigida@ba.infn.it
Cadolle Bel	Marion	V.N. de Cañada	**Spain**	marion.cadolle@sciops.esa.int
Cafagna	Francesco	Bari	**Italy**	francesco.cafagna@ba.infn.it
Caliandro	Giuseppe	Bari	**Italy**	andrea.caliandro@ba.infn.it
Caraveo	Patrizia	Milano	**Italy**	pat@iasf-milano.inaf.it
Carloganu	Cristina	Aubiere	**France**	carlogan@in2p3.fr
Caruso	Rossella	Catania	**Italia**	rossella.caruso@ct.infn.it
Cesarini	Andrea	Galway	**Ireland**	andycaesar@gmail.com
Chiavassa	Andrea	Torino	**Italy**	achiavas@to.infn.it
Colafrancesco	Sergio	Frascati	**Italy**	cola@mporzio.astro.it
Cottini	Niccolo	Gif sur Yvette	**France**	niccolo.cottini@cea.fr
Coward	David Martin	Crawley	**Australia**	coward@physics.uwa.edu.au
D Ammando	Filippo	Roma	**Italy**	filippo.dammando@iasf-roma.inaf.it
Dar	Arnon	Haifa	**Israel**	arnon@physics.technion.ac.il
De Lotto	Barbara	Udine	**Italy**	delotto@fisica.uniud.it
De Ona Wilhelmi	Emma	Paris	**France**	emma@apc.univ-paris7.fr
Delsate	Terence	Mons	**Belgium**	terence.delsate@umh.ac.be
Diago Ortega	Alicia	Tenerife	**Spain**	adiago@iac.es
Dokuchaev	Viacheslav	Moscow	**Russian Fed.**	dokuchaev@ms2.inr.ac.ru
Dornic	Damien	Marseille	**France**	dornic@cppm.in2p3.fr
Dumarchez	Jacques	Paris	**France**	jacques.dumarchez@cern.ch
Evans	Philip	Leicester	**UK**	pae9@star.le.ac.uk
Fiasson	Armand	Annecy-le-Vieux	**France**	fiasson@in2p3.fr
Fratini	Katia	Genova	**Italia**	fratini@ge.infn.it
Gabici	Stefano	Dublin	**Ireland**	sgabici@cp.dias.ie
Genet	Franck	Hatfield	**UK**	f.genet@herts.ac.uk
Gerard	Lucie	Paris	**France**	lucie.gerard@apc.univ-paris7.fr
Germani	Stefano	Perugia	**Italy**	stefano.germani@pg.infn.it
Giordano	Francesco	Bari	**Italy**	francesco.giordano@ba.infn.it
Goetz	Diego	Gif sur Yvette	**France**	diego.gotz@cea.fr
Gora	Dariusz	Karlsruhe	**Germany**	dariusz.gora@ik.fzk.de
Graf	Kay	Erlangen	**Germany**	kay.graf@physik.uni-erlangen.de
Granot	Jonathan	Hatfield	**UK**	j.granot@herts.ac.uk
Grashorn	Eric	Columbus	**USA**	grashorn@mps.ohio-state.edu

Grondin	Marie-Hélène	Gradignan	**France**	grondin@cenbg.in2p3.fr
Guardincerri	Yann	Buenos Aires	**Argentina**	yguardin@df.uba.ar
Guilet	Jérôme	Gif sur Yvette	**France**	jerome.guilet@cea.fr
Guillemot	Lucas	Gradignan	**France**	guillemo@cenbg.in2p3.fr
Hadasch	Daniela	Bellaterra	**Spain**	daniela.hadasch@gmail.com
Han	Jinlin	Beijing	**China**	hjl@bao.ac.cn
Hill	Adam	Grenoble	**France**	adam.hill@obs.ujf-grenoble.fr
Insolia	Antonio	Catania	**Italy**	antonio.insolia@ct.infn.it
Jalocha-Bratek	Joanna	Krakow	**Poland**	joanna.jalocha@ifj.edu.pl
Johannesson	Gudlaugur	Stanford	**USA**	gudlaugu@stanford.edu
Kawanaka	Norita	Tsukuba	**Japan**	norita.kawanaka@kek.jp
Kerr	Matthew	Seattle	**USA**	kerrm@u.washington.edu
Kerschhaggl	Matthias	Berlin	**Germany**	mkersch@physik.hu-berlin.de
Khmelnitsky	Andrew	Moscow	**Russian Fed.**	khmeln@inr.ac.ru
Klepser	Stefan	Bellaterra	**Spain**	klepser@ifae.es
Knapik	Robert	Fort Collins	**USA**	knapik@lamar.colostate.edu
Kohnen	Georges	Mons	**Belgium**	kohnen@umh.ac.be
Kotera	Kumiko	Paris	**France**	kotera@iap.fr
Latronico	Luca	Pisa	**Italy**	luca.latronico@pi.infn.it
Lemoine	Martin	Paris	**France**	lemoine@iap.fr
Lopez Moya	Marcos	Padova	**Italy**	mlopez@pd.infn.it
Lott	Benoit	Gradignan	**France**	lott@cenbg.in2p3.fr
Magneville	Christophe	Gif sur Yvette	**France**	cmv@hep.saclay.cea.fr
Malesani	Daniele	Copenhagen	**Denmark**	malesani@astro.ku.dk
Marcisovsky	Michal	Prague	**Czech Rep.**	marcisov@fzu.cz
Mariazzzi	Analisa	La Plata	**Argentina**	mariazzi@fisica.unlp.edu.ar
Marsella	Giovanni	Lecce	**Italy**	marsella@le.infn.it
Masip	Manuel	Granada	**Spain**	masip@ugr.es
Mazin	Daniel	Barcelona	**Spain**	mazin@ifae.es
Medina	Maria Clementina	Meudon	**France**	clementina.medina@obspm.fr
Melandri	Andrea	Liverpool	**UK**	axm@astro.livjm.ac.uk
Mereghetti	Sandro	Milano	**Italy**	sandro@iasf-milano.inaf.it
Mizuta	Akira	Chiba	**Japan**	mizuta@cfs.chiba-u.ac.jp
Morselli	Aldo	Roma	**Italy**	aldo.morselli@roma2.infn.it
Muraro	Silvia	Milan	**Italy**	silvia.muraro@mi.infn.it
Murugan	Jeff	Cape Town	**South Africa**	jeff@nassp.uct.ac.za
Nardini	Marco	Trieste	**Italy**	nardini@sissa.it
Naumann	Christopher	Gif sur Yvette	**France**	christopher.naumann@cea.fr
Naumann-Godo	Melitta	Palaiseau	**France**	naumann-godo@llr.in2p3.fr
Nedbal	Dalibor	Prague	**Czech Rep.**	nedbal@ipnp.troja.mff.cuni.cz
Nyklicek	Michal	Prague	**Czech Rep.**	nyklicek@fzu.cz
O Murchadha	Aongus	Madison	**USA**	omurchadha@wisc.edu
Paraficz	Danuta	Copenhagen	**Denmark**	danutas@astro.ku.dk
Parent	Damien	Gradignan	**France**	parent@cenbg.in2p3.fr
Pedaletti	Giovanna	Heidelberg	**Germany**	g.pedaletti@lsw.uni-heidelberg.de
Pekala	Jan	Krakow	**Poland**	jan.pekala@ifj.edu.pl
Pelassa	Véronique	Montpellier	**France**	pelassa@lpta.in2p3.fr
Pham	Ngoc Diep	Hanoi	**Vietnam**	diep@mail.vaec.gov.vn
Pham	Tuyet Nhung	Hanoi	**Vietnam**	ptnhung@mail.vaec.gov.vn
Picq	Claire	Gif sur Yvette	**France**	claire.picq@cea.fr
Piran	Tsvi	Jerusalem	**Israel**	tsvi@phys.huji.ac.il
Prat	Lionel	Gif sur Yvette	**France**	lionel.prat@cea.fr
Preece	Robert	Huntsville	**USA**	rob.preece@nasa.gov
Prosperi	Giovanni	Milano	**Italy**	prosperi@mi.infn.it
Punch	Michael	Paris	**France**	punch@in2p3.fr
Raidal	Martti	Tallinn	**Estonia**	martti.raidal@cern.ch
Raue	Martin	Heidelberg	**Germany**	martin.raue@mpi-hd.mpg.de
Razzano	Massimiliano	Pisa	**Italy**	massimiliano.razzano@pi.infn.it
Regos	Eniko	Geneva	**Switzerland**	eniko@ast.cam.ac.uk

Renaud	Matthieu	Paris	**France**	mrenaud@apc.univ-paris7.fr
Rodriguez	Jerome	Gif sur Yvette	**France**	jrodriguez@cea.fr
Rodriguez-Martino	Julio	Catania	**Italy**	julio.rodriguez@ct.infn.it
Rolland	Loic	Annecy	**France**	rollandl@in2p3.fr
Roncadelli	Marco	Pavia	**Italy**	marco.roncadelli@pv.infn.it
Rouille D Orfeuil	Benjamin	Paris	**France**	rouille@apc.univ-paris7.fr
Ruz	Jaime	Zaragoza	**Spain**	jaime.ruz@cern.ch
Ruzicka	Pavel	Prague	**Czech Rep.**	ruzicka@fzu.cz
Sanchez	David	Palaiseau	**France**	dsanchez@llr.in2p3.fr
Saugrin	Thomas	Nantes	**France**	thomas.saugrin@subatech.in2p3.fr
Savvidy	George	Athens	**Greece**	savvidy@inp.demokritos.gr
Scherini	Viviana	Wuppertal	**Germany**	scherini@physik.uni-wuppertal.de
Schubnell	Michael	Ann Arbor	**USA**	schubnel@umich.edu
Schuessler	Fabian	Karlsruhe	**Germany**	fabian.schuessler@ik.fzk.de
Seery	David	Cambridge	**UK**	djs61@cam.ac.uk
Shoibonov	Bair	Dubna	**Russian Fed.**	bair@nusun.jinr.ru
Siemieniec Ozieblo	Grazyna	Krakow	**Poland**	grazyna@oa.uj.edu.pl
Sinitsyna	Vera Y.	Moscow	**Russian Fed.**	verasinsin@mail.ru
Skindzier	Piotr	Krakow	**Poland**	piotr.skindzier@uj.edu.pl
Smith	David	Gradignan	**France**	smith@cenbg.in2p3.fr
Stasielak	Jaroslaw	Krakow	**Poland**	jstasielak@gmail.com
Teshima	Masahiro	Munich	**Germany**	mteshima@mppmu.mpg.de
Tran Thanh Van	Jean	Orsay	**France**	moriond@wanadoo.fr
Trap	Guillaume	Gif sur Yvette	**France**	trap@apc.univ-paris7.fr
Tueros	Matias	La Plata	**Argentina**	secre@fisica.unlp.edu.ar
Vanlaer	Pascal	Brussels	**Belgium**	pascal.vanlaer@ulb.ac.be
Vivier	Matthieu	Gif sur Yvette	**France**	matthieu.vivier@cea.fr
Weinstein	Amanda	Los Angeles	**USA**	amandaw@astro.ucla.edu
Weltman	Amanda	Cambridge	**UK**	a.weltman@damtp.cam.ac.uk
Yadav	Kuldeep	Mumbai	**India**	kkyadav@barc.gov.in